

Springer Proceedings in Physics 175

Ivan A. Parinov
Shun-Hsyung Chang
Vitaly Yu. Topolov *Editors*

Advanced Materials

Manufacturing, Physics, Mechanics and
Applications

 Springer

Springer Proceedings in Physics

Volume 175

More information about this series at <http://www.springer.com/series/361>

Ivan A. Parinov · Shun-Hsyung Chang
Vitaly Yu. Topolov
Editors

Advanced Materials

Manufacturing, Physics, Mechanics
and Applications

 Springer

Editors

Ivan A. Parinov
Southern Federal University
Rostov-on-Don
Russia

Vitaly Yu. Topolov
Rostov-on-Don
Russia

Shun-Hsyung Chang
Department of Microelectronics Engineering
National Kaohsiung Marine University
Kaohsiung City
Taiwan

ISSN 0930-8989

Springer Proceedings in Physics

ISBN 978-3-319-26322-9

DOI 10.1007/978-3-319-26324-3

ISSN 1867-4941 (electronic)

ISBN 978-3-319-26324-3 (eBook)

Library of Congress Control Number: 2015954957

Springer Cham Heidelberg New York Dordrecht London

© Springer International Publishing Switzerland 2016

This work is subject to copyright. All rights are reserved by the Publisher, whether the whole or part of the material is concerned, specifically the rights of translation, reprinting, reuse of illustrations, recitation, broadcasting, reproduction on microfilms or in any other physical way, and transmission or information storage and retrieval, electronic adaptation, computer software, or by similar or dissimilar methodology now known or hereafter developed.

The use of general descriptive names, registered names, trademarks, service marks, etc. in this publication does not imply, even in the absence of a specific statement, that such names are exempt from the relevant protective laws and regulations and therefore free for general use.

The publisher, the authors and the editors are safe to assume that the advice and information in this book are believed to be true and accurate at the date of publication. Neither the publisher nor the authors or the editors give a warranty, express or implied, with respect to the material contained herein or for any errors or omissions that may have been made.

Printed on acid-free paper

Springer International Publishing AG Switzerland is part of Springer Science+Business Media
(www.springer.com)

Preface

The modern theoretical, experimental, and computational methods provide R&D of numerous processing techniques for different advanced materials and composites. Based on last achievements and proposed solutions of Materials Science, Condensed Matter Physics and Mechanics of Deformable Solids, novel materials and structures meet broad applications in the modern science, techniques and technologies operating in the ranges from nano- up to macroscale. Modern requirements for improvement of material properties, obtainment of preliminary given characteristics, and extension of possibilities of devices, created on their base, support tremendous and continuous interest to fast development of the theoretical, experimental, and numerical methods. These methods create new knowledge and are capable to ensure control and prediction of critical phenomena and improvement of very fine processes (for instance, nano- and microstructure transformations during processing, loading, and operating modern materials and composites under critical conditions, in aggressive media and complex physical and mechanical treatments). Practical and industrial needs require from modern devices and goods a very high accuracy, reliability, longevity, and extended possibilities to operate at broad temperature and pressure ranges. At the same time, the device characteristics are directly defined by used materials and composites, opening new possibilities in study of various physical processes.

This collection of 50 papers presents selected reports of the 2015 International Conference on “Physics, Mechanics of New Materials and Their Applications” (PHENMA-2015), which has taken place in Azov, Russia, May 19–22, 2015 (<http://phenma2015.math.sfedu.ru>) and is devoted to 100-year anniversary of the Southern Federal University. The conference was sponsored by the Russian Department of Education and Science, Russian Foundation for Basic Research, Ministry of Science and Technology of Taiwan, South Scientific Center of Russian Academy of Sciences, New Century Education Foundation (Taiwan), Ocean & Underwater Technology Association, Unity Opto Technology Co., EPOCH Energy Technology Corp., Fair Well Fishery Co., Formosa Plastics Co., Woen Jinn Harbor Engineering Co., Lorom Group, Longwell Co., Taiwan International Ports Co., Ltd., University

of 17 Agustus 1945 Surabaya (Indonesia), Khon-Kaen University (Thailand), Don State Technical University (Russia), and South Russian Regional Centre for preparation and implementation of international projects.

The thematic of the PHENMA-2015 continued ideas of previous international symposia: PMNM-2012 (<http://pnm.math.rsu.ru>), PHENMA-2013 (<http://phenma.math.sfedu.ru>), and PHENMA-2014 (<http://phenma2014.math.sfedu.ru>) whose results have been published in the edited books “Physics and Mechanics of New Materials and Their Applications”, Ivan A. Parinov, Shun-Hsyung Chang (Eds.), Nova Science Publishers, New York, 2013, 444 p. ISBN: 978-1-62618-535-7, “Advanced Materials—Physics, Mechanics and Applications”, Springer Proceedings in Physics. Vol. 152. Shun-Hsyung Chang, Ivan A. Parinov, Vitaly Yu. Topolov (Eds.), Springer, Heidelberg, New York, Dordrecht, London, 2014, 380 p. ISBN: 978-3319037486, and “Advanced Materials—Studies and Applications”, Ivan A. Parinov, Shun-Hsyung Chang, Somnuk Theerakulpisut (Eds.), Nova Science Publishers, New York, 2015, 527 p. ISBN: 978-1-63463-749-7, respectively.

The presented papers are divided into four scientific directions: (i) processing techniques of advanced materials, (ii) physics of advanced materials, (iii) mechanics of advanced materials, and (iv) applications of advanced materials.

In framework of the first theme, the structural modification of sulfide minerals irradiated by high-power nanosecond pulses; the magnetic nanoparticles and heterogeneous persulfate oxidation of the nanoparticles and organic compounds are considered. Then the microstructure optimization of Pt/C catalysts for PEMFC; the synthesis of titanium dioxide, polyacrylonitrile-based materials; and also features of phase formation in bismuth ferrite are considered. Moreover, this section contains investigations of growth of the strongly doped $\text{LiNbO}_3\text{:Zn}$ single crystals and features of crystallization of sapphire melt. The first section is finished by considering the lignin degradation and production of slow release fertilizer from waste materials.

The second direction is opened by the numerical study of dielectric resonant gratings; the method of equilibrium density matrix in theory of superconductivity; new investigations of 1–3-type composites based on relaxor-ferroelectrics single crystals and ZTS-19/clay composite. Novel results are present at the modeling and characterization of advanced functional materials. In this section, in particular the following are studied: diffusion of ferroelectric phase transition and glass-dipole state in the PZT-based solid solutions; the electromagnetic microwave radiation absorption by ferroelectric complex niobium oxides; and the structural ordering in ceramic ferroelectromagnets. Special attention is given to physical properties of the graphene materials; morphology, and atomic and electronic structure of metal oxide (CuO_x , SnO_x) nanocomposites and thin films; dispersion characteristics of zinc oxide nanorods organized in two-dimensional uniform arrays. Finally, new technical and technological solutions for measurement of displacements of the control object surfaces by laser interferometer and contactless method of temperature measurements are provided.

From viewpoint of mechanics the models for nanosized magnetoelectric bodies with surface effects and general theory of polarization of the ferroelectric materials are present. The surface SH-waves in the weakly inhomogeneous pre-stressed piezoelectric structures; elastic waves in layered phononic crystals with strip-like cracks; ultrasonic guided waves in laminated fiber-reinforced composite plates; low-frequency elastic waves penetrating the triple periodic array of cracks; and ultrasonic torsional guided waves in pipes with defects are studied. Then, why and how residual stress affects metal fatigue and also present the mathematical modeling dynamics of prismatic body of two- and three-component materials and numerical study of three-dimensional anisotropic viscoelastic solids are discussed. In the third section, the conclusion is brought by investigations of the thermo-physical processes in boundary layers of metal-polymeric systems; the antifriction fillers influencing the characteristics of the metal polymer tribosystems and carbon brake discs with frictionally induced thermoelastic instability.

On the whole, the presented applications are devoted to lot of modern devices based on novel approaches. In particular, the developments of new metamaterials for advanced element base of micro- and nanoelectronics; the radiation detector with sensitive elements on the base of array of multi-walled carbon nanotubes; and the magnetic field sensor with nanosized elements are discussed. Then the transducer designs for ultrasonic diagnostics and therapy, and also the electric power harvesting system based on the piezoelectric stack transducer and non-uniform polarization of multi-layered piezoelectric transducer are considered. Then, the multifrequency sonar equipment based on the self-action nonlinear effect is regarded. Finally, the singular nullor and mirror elements for circuit design; the usage of Markov chain model for wireless local area networks; and the time-frequency features in the Berardius Baird whistles are discussed.

The book is addressed to students, postgraduate students, scientists, and engineers taking part in research and development of nanomaterials, nanostructures, ferro-piezoelectrics and other advanced materials and composites, and also to manufacturing of the different devices based on novel materials having broad applications in various areas of modern science and techniques. The book include new studies and results in the fields of Processing Techniques and Engineering of Nanomaterials, Piezoelectrics, other Advanced Materials and Composites, Condensed Matter Physics, Mechanics of Deformable Solids, Materials Science, Physical and Mechanical Experiment, and Numerical Methods with various applications, in particular developed devices and goods.

Rostov-on-Don, Russia
Kaohsiung City, Taiwan
Rostov-on-Don, Russia

Ivan A. Parinov
Shun-Hsyung Chang
Vitaly Yu. Topolov

Contents

Part I Processing Techniques of Advanced Materials

1	Structural Modification of Sulfide Minerals Irradiated by High-Power Nanosecond Pulses	3
	I. Zh. Bunin, V.A. Chanturiya, M.V. Ryazantseva, I.A. Khabarova, E.V. Koporulina and A.T. Kovalev	
2	Magnetic Nanoparticles and Their Heterogeneous Persulfate Oxidation Organic Compound Applications.	23
	Cheng-Di Dong, Chiu-Wen Chen and Chang-Mao Hung	
3	Microstructure Optimization of Pt/C Catalysts for PEMFC	37
	A.A. Alekseenko, V.E. Guterman and V.A. Volochaev	
4	Synthesis of Titanium Dioxide: The Influence of Process Parameters on the Structural, Size and Photocatalytic Properties	51
	E.M. Bayan, T.G. Lupeiko, L.E. Pustovaya and A.G. Fedorenko	
5	Polyacrylonitrile-Based Materials: Properties, Methods and Applications	61
	T.V. Semenistaya	
6	Features of Phase Formation in the Preparation of Bismuth Ferrite	79
	L.A. Shilkina, I.A. Verbenko, A.G. Abubakarov, L.A. Reznichenko, O.N. Razumovskaya, T.N. Sorokun and V.A. Aleshin	

7	Research of Concentration Conditions for Growth of Strongly Doped LiNbO₃:Zn Single Crystals.	87
	M.N. Palatnikov, I.V. Biryukova, O.V. Makarova, N.V. Sidorov, V.V. Efremov, I.N. Efremov, N.A. Teplyakova and D.V. Manukovskaya	
8	Research of Gas Bubbles Interaction with Crystallization Front of Sapphire Melt.	101
	S.P. Malyukov, Yu. V. Klunnikova and M.V. Anikeev	
9	Investigation of Important Parameters for Lignin Degradation Using Fenton-Like Reaction via Cu Doped on Bagasses-MCM-41.	115
	Pongsert Sriprom, Chitsan Lin, Arthit Neramittagapong and Sutasinee Neramittagapong	
10	Production of Slow Release Fertilizer from Waste Materials	129
	Petchporn Chawakitchareon, Rewadee Anuwattana and Jitrera Buates	
Part II Physics of Advanced Materials		
11	Numerical Study of Dielectric Resonant Gratings	141
	A.M. Lerer, E.V. Golovacheva, P.E. Timoshenko, I.N. Ivanova, P.V. Makhno and E.A. Tsvetyansky	
12	Method of Equilibrium Density Matrix, Anisotropy and Superconductivity, Energy Gap	157
	B.V. Bondarev	
13	New Effects in 1–3-Type Composites Based on Relaxor-Ferroelectrics Single Crystals	179
	V. Yu. Topolov, C.R. Bowen and P. Bisegna	
14	Piezoelectric Properties of a Novel ZTS-19/Clay Composite	197
	S.E. Filippov, A.A. Vorontsov, V. Yu. Topolov, P. Bisegna, O.E. Brill and A.E. Panich	
15	Advanced Functional Materials: Modeling, Technology, Characterization, and Applications	211
	A.N. Rybyanets	
16	Diffusion of Ferroelectric Phase Transition and Glass-Dipole State in the PZT-Based Solid Solutions	229
	G.M. Konstantinov, A.N. Rybyanets, Y.B. Konstantinova, N.A. Shvetsova and N.O. Svetlichnaya	

17	Features of Electromagnetic Microwave Radiation Absorption by Ferroelectric Complex Niobium Oxides	245
	A.G. Abubakarov, I.A. Verbenko, L.A. Reznichenko, M.B. Manuilov, K.P. Andryushin, H.A. Sadykov, Y.M. Noykin, M.V. Talanov and M.S. Zakrieva	
18	Research of Structure Ordering in Ceramic Ferroelectromagnets Bi_{1-x}La_xFeO₃ by Raman Spectroscopy	259
	N.A. Teplyakova, S.V. Titov, I.A. Verbenko, N.V. Sidorov and L.A. Reznichenko	
19	A Multi-fractal Multi-permuted Multinomial Measurement for Unsupervised Image Segmentation	269
	Sung-Tsun Shih and Lui Kam	
20	Modulation the Band Structure and Physical Properties of the Graphene Materials with Electric Field and Semiconductor Substrate	279
	Victor V. Ilyasov, Besik C. Meshi, Nguyen V. Chuong, Igor V. Ershov, Inna G. Popova and Nguyen D. Chien	
21	Morphology, Atomic and Electronic Structure of Metal Oxide (CuO_x, SnO_x) Nanocomposites and Thin Films	299
	G.E. Yalovega, V.A. Shmatko, A.O. Funik and M.M. Brzhezinskaya	
22	Dispersion Characteristics of Zinc Oxide Nanorods Coated with Thin Silver Layer and Organized in Two-Dimensional Uniform Arrays	317
	A.M. Lerer, P.E. Timoshenko, E.M. Kaidashev, A.S. Puzanov and T.Y. Chernikova	
23	Effect of Electric Field on the EMF in the System “Electrode–Electrolyte–Capacitor Electrode”	329
	G. Ya. Karapetyan, V.G. Dneprovski, I.A. Parinov and G. Parchi	
24	Mathematical Models, Program Software, Technical and Technological Solutions for Measurement of Displacements of the Control Object Surfaces by Laser Interferometer	341
	I.P. Miroshnichenko, I.A. Parinov, E.V. Rozhkov and S.-H. Chang	
25	Material Temperature Measurement Using Non-contacting Method	357
	Muaffaq Achmad Jani	

26	Microstructure and Interface Bottom Ash Reinforced Aluminum Metal Matrix Composite	363
	Muslimin Abdulrahim and Harjo Seputro	
 Part III Mechanics of Advanced Materials		
27	Some Models for Nanosized Magnetolectric Bodies with Surface Effects	373
	A.V. Nasedkin and V.A. Eremeyev	
28	The General Theory of Polarization of Ferroelectric Materials	393
	Alexander Skaliukh and Guorong Li	
29	Peculiarities of the Surface SH-Waves Propagation in the Weakly Inhomogeneous Pre-stressed Piezoelectric Structures	413
	T.I. Belyankova, V.V. Kalinchuk and O.M. Tukodova	
30	Numerical Simulation of Elastic Wave Propagation in Layered Phononic Crystals with Strip-Like Cracks: Resonance Scattering and Wave Localization	431
	M.V. Golub and Ch. Zhang	
31	Ultrasonic Guided Wave Characterization and Inspection of Laminate Fiber-Reinforced Composite Plates	449
	E.V. Glushkov, N.V. Glushkova, A.A. Eremin, A.A. Evdokimov and R. Lammering	
32	Low Frequency Penetration of Elastic Waves Through a Triple Periodic Array of Cracks	459
	Mezhlum A. Sumbatyan and Michael Yu. Remizov	
33	Numerical Simulation of Ultrasonic Torsional Guided Wave Propagation for Pipes with Defects	475
	A.A. Nasedkina, A. Alexiev and J. Malachowski	
34	Why and How Residual Stress Affects Metal Fatigue	489
	R. Sunder	
35	Numerically Analytical Modeling the Dynamics of a Prismatic Body of Two- and Three-Component Materials	505
	L.A. Igumnov, S. Yu. Litvinchuk, A.N. Petrov and A.A. Ipatov	
36	Boundary-Element Modeling of Three-Dimensional Anisotropic Viscoelastic Solids	517
	L.A. Igumnov and I.P. Markov	

37 Thermo-physical Processes in Boundary Layers of Metal-Polymeric Systems 527
 V.I. Kolesnikov, M.I. Chebakov, I.V. Kolesnikov and A.A. Lyapin

38 The Influence of Antifriction Fillers on the Mechanical and Thermal Characteristics of Metal Polymer Tribosystems 539
 P.G. Ivanochkin and S.A. Danilchenko

39 Theoretical and Experimental Study of Carbon Brake Discs Frictionally Induced Thermoelastic Instability 551
 A.G. Shpenev, A.M. Kenigfest and A.K. Golubkov

Part IV Applications of Advanced Materials

40 Development of New Metamaterials for Advanced Element Base of Micro- and Nanoelectronics, and Microsystem Devices. 563
 O.A. Ageev, S.V. Balakirev, A.V. Bykov, E. Yu. Gusev, A.A. Fedotov, J.Y. Jityaeva, O.I. Il'in, M.V. Il'ina, A.S. Kolomiytsev, B.G. Konoplev, S.U. Krasnoborodko, V.V. Polyakov, V.A. Smirnov, M.S. Solodovnik and E.G. Zamburg

41 The Radiation Detector with Sensitive Elements on the Base of Array of Multi-walled Carbon Nanotubes 581
 E.V. Blagov, A.A. Pavlov, A.A. Dudin, A.P. Orlov, E.P. Kitsuk, Yu. Shaman, A. Yu. Gerasimenko, L.P. Ichkitidze and A.A. Polohin

42 Combined Magnetic Field Sensor with Nanosized Elements 591
 L.P. Ichkitidze, S.V. Selishchev and D.V. Telishev

43 New Methods and Transducer Designs for Ultrasonic Diagnostics and Therapy 603
 A.N. Rybyanets

44 Theoretical Modeling and Experimental Study of HIFU Transducers and Acoustic Fields. 621
 A.N. Rybyanets, A.A. Naumenko, N.A. Shvetsova, V.A. Khokhlova, O.A. Sapozhnikov and A.E. Berkovich

45 Optimization of the Electric Power Harvesting System Based on the Piezoelectric Stack Transducer 639
 S. Shevtsov, V. Akopyan, E. Rozhkov, V. Chebanenko, C.-C. Yang, C.-Y. Jenny Lee and C.-X. Kuo

46 Modeling of Non-uniform Polarization for Multi-layered Piezoelectric Transducer for Energy Harvesting Devices 651
 A.N. Soloviev, P.A. Oganesyanyan, T.G. Lupeiko, E.V. Kirillova, S.-H. Chang and C.-D. Yang

**47 The Multifrequency Sonar Equipment on the Self-action
Nonlinear Effect** 659
V.Y. Voloshchenko

48 Singular Nullor and Mirror Elements for Circuit Design 669
Quoc-Minh Nguyen, Huu-Duy Tran, Hung-Yu Wang
and Shun-Hsyung Chang

**49 The Performance Evaluation of IEEE 802.11 DCF
Using Markov Chain Model for Wireless LANs**. 675
Chien-Erh Weng

**50 HHT-Based Time-Frequency Features in the Berardius
Baird Whistles** 687
Chin-Feng Lin, Jin-De Zhu, Shun-Hsyung Chang, Chan-Chuan Wen,
Ivan A. Parinov and S.N. Shevtsov

Curriculum Vitae 695

Index 701

Contributors

Muslimin Abdulrahim Industrial Engineering Department, University of 17 Agustus 1945, Surabaya, Indonesia

A.G. Abubakarov Research Institute of Physics, Southern Federal University, Rostov-on-Don, Russia

O.A. Ageev Institute of Nanotechnologies, Electronics and Electronic Equipment Engineering, Southern Federal University, Taganrog, Russia

V. Akopyan Vorovich Mechanics and Applied Mathematics Research Institute, Southern Federal University, Rostov-on-Don, Russia

A.A. Alekseenko Faculty of Chemistry, Southern Federal University, Rostov-on-Don, Russia

V.A. Aleshin Research Institute of Physics, Southern Federal University, Rostov-on-Don, Russia

A. Alexiev Institute of Mechanics, Bulgarian Academy of Sciences, Sofia, Bulgaria

K.P. Andryushin Department of Physics, Southern Federal University, Rostov-on-Don, Russia

M.V. Anikeev Institute of Nanotechnology, Electronics and Electronic Equipment Engineering, Southern Federal University, Taganrog, Russia

Rewadee Anuwattana Thailand Institute of Scientific and Technological Research, Pathumthani, Thailand

S.V. Balakirev Institute of Nanotechnologies, Electronics and Electronic Equipment Engineering, Southern Federal University, Taganrog, Russia

E.M. Bayan Faculty of Chemistry, Southern Federal University, Rostov-on-Don, Russia

T.I. Belyankova Southern Scientific Center of the Russian Academy of Sciences, Rostov-on-Don, Russia

A.E. Berkovich Sankt-Petersburg Politechnical University, Sankt-Petersburg, Russia

I.V. Biryukova Institute of Chemistry and Technology of Rare Elements and Mineral Raw Materials, Akademgorodok, Apatity, Murmansk Region, Russia

P. Bisegna Department of Civil Engineering and Computer Science, University of Rome 'Tor Vergata', Rome, Italy

E.V. Blagov Institute of Nanotechnology of Microelectronics of the RAS, INME RAS, Moscow, Russian Federation

B.V. Bondarev Moscow Aviation Institute, Moscow, Russia

C.R. Bowen Department of Mechanical Engineering, University of Bath, Bath, UK

O.E. Brill Scientific Design & Technology Institute 'Piezopribor', Southern Federal University, Rostov-on-Don, Russia

M.M. Brzhezinskaya Helmholtz-Zentrum Berlin für Materialien Und Energie, Berlin, Germany

Jitrera Buates Faculty of Engineering, Department of Environmental Engineering, Chulalongkorn University, Bangkok, Thailand

I. Zh. Bunin Research Institute of Comprehensive Exploitation of Mineral Resources of the Russian Academy of Science (IPKON RAS), Moscow, Russia

A.V. Bykov Institute of Nanotechnologies, Electronics and Electronic Equipment Engineering, Southern Federal University, Taganrog, Russia

Shun-Hsyung Chang Department of Microelectronics Engineering, National Kaohsiung Marine University, Kaohsiung City, Taiwan

V.A. Chanturiya Research Institute of Comprehensive Exploitation of Mineral Resources of the Russian Academy of Science (IPKON RAS), Moscow, Russia

Petchporn Chawakitchareon Faculty of Engineering, Department of Environmental Engineering, Chulalongkorn University, Bangkok, Thailand

M.I. Chebakov Vorovich Mathematics, Mechanics and Computer Sciences Institute, Southern Federal University, Rostov-on-Don, Russia

V. Chebanenko Vorovich Mechanics and Applied Mathematics Research Institute, Southern Federal University, Rostov-on-Don, Russia

Chiu-Wen Chen Department of Marine Environmental Engineering, National Kaohsiung Marine University, Kaohsiung City, Taiwan

T.Y. Chernikova Department of Physics, Southern Federal University, Rostov-on-Don, Russia

Nguyen D. Chien Department of Electronic Materials, School of Engineering Physics, Hanoi University of Science and Technology, Hanoi, Vietnam

Nguyen V. Chuong Don State Technical University, Rostov-on-Don, Russia

S.A. Danilchenko Rostov State Transport University, Rostov-on-Don, Russia

V.G. Dneprovski Vorovich Mathematics, Mechanics and Computer Science Institute, Southern Federal University, Rostov-on-Don, Russia

Cheng-Di Dong Department of Marine Environmental Engineering, National Kaohsiung Marine University, Kaohsiung City, Taiwan

A.A. Dudin Institute of Nanotechnology of Microelectronics of the RAS, INME RAS, Moscow, Russian Federation

I.N. Efremov Institute of Chemistry and Technology of Rare Elements and Mineral Raw Materials, Akademgorodok, Apatity, Murmansk Region, Russia

V.V. Efremov Institute of Chemistry and Technology of Rare Elements and Mineral Raw Materials, Akademgorodok, Apatity, Murmansk Region, Russia

V.A. Eremeyev I.I. Vorovich Institute of Mathematics, Mechanics and Computer Sciences, Southern Federal University, Rostov-on-Don, Russia; Otto-von-Guericke-University, Magdeburg, Germany; Southern Scientific Center of Russian Academy of Sciences, Rostov-on-Don, Russia

A.A. Eremin Institute for Mathematics, Mechanics and Informatics, Kuban State University, Krasnodar, Russia

Igor V. Ershov Don State Technical University, Rostov-on-Don, Russia

A.A. Evdokimov Institute for Mathematics, Mechanics and Informatics, Kuban State University, Krasnodar, Russia

A.G. Fedorenko Faculty of Chemistry, Southern Federal University, Rostov-on-Don, Russia

A.A. Fedotov Institute of Nanotechnologies, Electronics and Electronic Equipment Engineering, Southern Federal University, Taganrog, Russia

S.E. Filippov Scientific Design & Technology Institute ‘Piezopribor’, Southern Federal University, Rostov-on-Don, Russia

A.O. Funik Faculty of Physics, Southern Federal University, Rostov-on-Don, Russia

A. Yu. Gerasimenko National Research University of Electronic Technology “MIET”, Zelenograd, Moscow, Russian Federation

E.V. Glushkov Institute for Mathematics, Mechanics and Informatics, Kuban State University, Krasnodar, Russia

N.V. Glushkova Institute for Mathematics, Mechanics and Informatics, Kuban State University, Krasnodar, Russia

E.V. Golovacheva Department of Physics, Southern Federal University, Rostov-on-Don, Russia

M.V. Golub Institute for Mathematics, Mechanics and Informatics, Kuban State University, Krasnodar, Russia

A.K. Golubkov JSC “Rubin”, Moscow, Russia

E. Yu. Gusev Institute of Nanotechnologies, Electronics and Electronic Equipment Engineering, Southern Federal University, Taganrog, Russia

V.E. Guterman Faculty of Chemistry, Southern Federal University, Rostov-on-Don, Russia

Chang-Mao Hung Department of Marine Environmental Engineering, National Kaohsiung Marine University, Kaohsiung City, Taiwan

L.P. Ichkitidze National Research University of Electronic Technology “MIET”, Zelenograd, Moscow, Russian Federation

L.A. Igumnov Research Institute for Mechanics, Lobachevsky State University of Nizhni Novgorod, Nizhny Novgorod, Russia

Victor V. Ilyasov Don State Technical University, Rostov-on-Don, Russia

O.I. Il'in Institute of Nanotechnologies, Electronics and Electronic Equipment Engineering, Southern Federal University, Taganrog, Russia

M.V. Il'ina Institute of Nanotechnologies, Electronics and Electronic Equipment Engineering, Southern Federal University, Taganrog, Russia

A.A. Ipatov Research Institute for Mechanics, Lobachevsky State University of Nizhni Novgorod, Nizhny Novgorod, Russia

P.G. Ivanochkin Rostov State Transport University, Rostov-on-Don, Russia

I.N. Ivanova Department of Physics, Southern Federal University, Rostov-on-Don, Russia

Muaffaq Achmad Jani Information Engineering Department, Faculty of Engineering, University of 17 Agustus 1945, Surabaya, Indonesia

C.-Y. Jenny Lee National Kaohsiung Marine University, Kaohsiung City, Taiwan, ROC

J.Y. Jityaeva Institute of Nanotechnologies, Electronics and Electronic Equipment Engineering, Southern Federal University, Taganrog, Russia

E.M. Kaidashev Laboratory of Nanomaterials, Southern Federal University, Rostov-on-Don, Russia

V.V. Kalinchuk Southern Scientific Center of the Russian Academy of Sciences, Rostov-on-Don, Russia

Lui Kam Department of Electronic Engineering, Cheng-Shiu University, Kaohsiung City, Taiwan

G. Ya. Karapetyan Vorovich Mathematics, Mechanics and Computer Science Institute, Southern Federal University, Rostov-on-Don, Russia

A.M. Kenigfest JSC “Rubin”, Moscow, Russia

I.A. Khabarova Research Institute of Comprehensive Exploitation of Mineral Resources of the Russian Academy of Science (IPKON RAS), Moscow, Russia

V.A. Khokhlova Faculty of Physics, Moscow State University, Moscow, Russia

E.V. Kirillova RheinMain University of Applied Sciences, Wiesbaden, Germany

E.P. Kitsuk Institute of Nanotechnology of Microelectronics of the RAS, INME RAS, Moscow, Russian Federation; Scientific-Manufacturing Complex “Technological Centre”, MIET, Zelenograd, Moscow, Russian Federation

Yu. V. Klunnikova Institute of Nanotechnology, Electronics and Electronic Equipment Engineering, Southern Federal University, Taganrog, Russia

I.V. Kolesnikov Rostov State Transport University, Rostov-on-Don, Russia

V.I. Kolesnikov Rostov State Transport University, Rostov-on-Don, Russia

A.S. Kolomiytsev Institute of Nanotechnologies, Electronics and Electronic Equipment Engineering, Southern Federal University, Taganrog, Russia

B.G. Konoplev Institute of Nanotechnologies, Electronics and Electronic Equipment Engineering, Southern Federal University, Taganrog, Russia

G.M. Konstantinov Research Institute of Physics, Southern Federal University, Rostov-on-Don, Russia

Y.B. Konstantinova Research Institute of Physics, Southern Federal University, Rostov-on-Don, Russia

E.V. Koporulina Research Institute of Comprehensive Exploitation of Mineral Resources of the Russian Academy of Science (IPKON RAS), Moscow, Russia

A.T. Kovalev Research Institute of Comprehensive Exploitation of Mineral Resources of the Russian Academy of Science (IPKON RAS), Moscow, Russia

S.U. Krasnoborodko Institute of Nanotechnologies, Electronics and Electronic Equipment Engineering, Southern Federal University, Taganrog, Russia

C.-X. Kuo National Kaohsiung Marine University, Kaohsiung City, Taiwan, ROC

R. Lammering Institute of Mechanics, Helmut-Schmidt-University/University of the Federal Armed Forces, Hamburg, Germany

A.M. Lerer Department of Physics, Southern Federal University, Rostov-on-Don, Russia

Guorong Li Shanghai Institute of Ceramics, Chinese Academy of Sciences, Shanghai, China

Chin-Feng Lin Department of Electrical Engineering, National Taiwan Ocean University, Keelung, Taiwan, R.O.C

Chitsan Lin Department of Marine Environmental Engineering, College of Ocean Engineering, National Kaohsiung Marine University, Kaohsiung City, Taiwan

S. Yu. Litvinchuk Research Institute for Mechanics, Lobachevsky State University of Nizhni Novgorod, Nizhny Novgorod, Russia

T.G. Lupeiko Faculty of Chemistry, Southern Federal University, Rostov-on-Don, Russia; Chemical Department, Southern Federal University, Rostov-on-Don, Russia

A.A. Lyapin Vorovich Mathematics, Mechanics and Computer Sciences Institute, Southern Federal University, Rostov-on-Don, Russia

O.V. Makarova Institute of Chemistry and Technology of Rare Elements and Mineral Raw Materials, Akademgorodok, Apatity, Murmansk Region, Russia

P.V. Makhno Department of Physics, Southern Federal University, Rostov-on-Don, Russia

J. Malachowski Faculty of Mechanical Engineering, Military University of Technology, Warsaw, Poland

S.P. Malyukov Institute of Nanotechnology, Electronics and Electronic Equipment Engineering, Southern Federal University, Taganrog, Russia

M.B. Manuilov Department of Physics, Southern Federal University, Rostov-on-Don, Russia

D.V. Manukovskaya Institute of Chemistry and Technology of Rare Elements and Mineral Raw Materials, Akademgorodok, Apatity, Murmansk Region, Russia

I.P. Markov Research Institute for Mechanics, Lobachevsky State University of Nizhni Novgorod, Nizhny Novgorod, Russia

Besik C. Meshi Don State Technical University, Rostov-on-Don, Russia

I.P. Miroshnichenko Don State Technical University, Rostov-on-Don, Russia

A.V. Nasedkin I.I. Vorovich Institute of Mathematics, Mechanics and Computer Sciences, Southern Federal University, Rostov-on-Don, Russia

A.A. Nasedkina I.I. Vorovich Institute of Mathematics, Mechanics and Computer Science, Southern Federal University, Rostov-on-Don, Russia

A.A. Naumenko Institute of Physics, Southern Federal University, Rostov-on-Don, Russia

Arthit Neramittagapong Faculty of Engineering, Department of Chemical Engineering, Khon Kaen University, Khon Kaen, Thailand

Sutasinee Neramittagapong Faculty of Engineering, Department of Chemical Engineering, Khon Kaen University, Khon Kaen, Thailand

Quoc-Minh Nguyen Department of Electronic Engineering, National Kaohsiung University of Applied Sciences, Kaohsiung City, Taiwan

Y.M. Noykin Department of Physics, Southern Federal University, Rostov-on-Don, Russia

P.A. Oganessian Department of Theoretical and Applied Mechanics, Don State Technical University, Rostov-on-Don, Russia; Department of Mechanics of Active Materials, South Scientific Centre of Russian Academy of Sciences, Rostov-on-Don, Russia

A.P. Orlov Institute of Nanotechnology of Microelectronics of the RAS, INME RAS, Moscow, Russian Federation; Kotel'nikov Institute of Radio-Engineering and Electronics of RAS, IRE RAS, Moscow, Russian Federation

M.N. Palatnikov Institute of Chemistry and Technology of Rare Elements and Mineral Raw Materials, Akademgorodok, Apatity, Murmansk Region, Russia

A.E. Panich Department of Physics, Southern Federal University, Rostov-on-Don, Russia

G. Parchi Prometeon SRL, Bologna, Italy

Ivan A. Parinov Vorovich Mathematics, Mechanics and Computer Sciences Institute, Southern Federal University, Rostov-on-Don, Russia

A.A. Pavlov Institute of Nanotechnology of Microelectronics of the RAS, INME RAS, Moscow, Russian Federation; Scientific-Manufacturing Complex "Technological Centre", MIET, Zelenograd, Moscow, Russian Federation

A.N. Petrov Research and Education Center "Materials", Don State Technical University, Rostov-on-Don, Russia

A.A. Polohin National Research University of Electronic Technology "MIET", MIET, Zelenograd, Moscow, Russian Federation

V.V. Polyakov Institute of Nanotechnologies, Electronics and Electronic Equipment Engineering, Southern Federal University, Taganrog, Russia

Inna G. Popova Don State Technical University, Rostov-on-Don, Russia

- L.E. Pustovaya** Don State Technical University, Rostov-on-Don, Russia
- A.S. Puzanov** Department of Physics, Southern Federal University, Rostov-on-Don, Russia
- O.N. Razumovskaya** Research Institute of Physics, Southern Federal University, Rostov-on-Don, Russia
- Michael Yu. Remizov** Rostov State University of Civil Engineering, Rostov-on-Don, Russia
- L.A. Reznichenko** Research Institute of Physics, Southern Federal University, Rostov-on-Don, Russia
- E. Rozhkov** Vorovich Mechanics and Applied Mathematics Research Institute, Southern Federal University, Rostov-on-Don, Russia
- E.V. Rozhkov** Vorovich Mathematics, Mechanics and Computer Science Institute, Southern Federal University, Rostov-on-Don, Russia
- M.V. Ryazantseva** Research Institute of Comprehensive Exploitation of Mineral Resources of the Russian Academy of Science (IPKON RAS), Moscow, Russia
- A.N. Rybyanets** Research Institute of Physics, Southern Federal University, Rostov-on-Don, Russia
- H.A. Sadykov** Research Institute of Physics, Southern Federal University, Rostov-on-Don, Russia
- O.A. Sapozhnikov** Faculty of Physics, Moscow State University, Moscow, Russia
- S.V. Selishchev** National Research University of Electronic Technology “MIET”, Moscow, Russian Federation
- T.V. Semenistaya** Engineering-Technological Academy, Southern Federal University, Taganrog, Russia
- Harjo Seputro** Mechanical Engineering Department, University of 17 Agustus 1945, Surabaya, Indonesia
- Yu. Shaman** Scientific-Manufacturing Complex “Technological Centre”, MIET, Zelenograd, Moscow, Russian Federation
- S. Shevtsov** South Center of Russian Academy, Rostov-on-Don, Russia; Vorovich Mechanics and Applied Mathematics Research Institute, Southern Federal University, Rostov-on-Don, Russia
- S.N. Shevtsov** South Scientific Center of Russian Academy of Sciences, Rostov-on-Don, Russia
- Sung-Tsun Shih** Department of Electronic Engineering, Cheng-Shiu University, Kaohsiung City, Taiwan

L.A. Shilkina Research Institute of Physics, Southern Federal University, Rostov-on-Don, Russia

V.A. Shmatko Faculty of Physics, Southern Federal University, Rostov-on-Don, Russia

A.G. Shpenev Institute for Problems in Mechanics, Russian Academy of Sciences, Moscow, Russia

N.A. Shvetsova Research Institute of Physics, Southern Federal University, Rostov-on-Don, Russia

N.V. Sidorov Institute of Chemistry and Technology of Rare Elements and Mineral Raw Materials, Akademgorodok, Apatity, Murmansk Region, Russia; Tananaev Institute of Chemistry and Technology of Rare Elements and Mineral Raw Materials of the Russian Academy of Sciences Kola Science Center, Apatity, Murmansk Region, Russia

Alexander Skaliukh Vorovich Mathematics, Mechanics and Computer Sciences Institute, Southern Federal University, Rostov-on-Don, Russia

V.A. Smirnov Institute of Nanotechnologies, Electronics and Electronic Equipment Engineering, Southern Federal University, Taganrog, Russia

M.S. Solodovnik Institute of Nanotechnologies, Electronics and Electronic Equipment Engineering, Southern Federal University, Taganrog, Russia

A.N. Soloviev Department of Theoretical and Applied Mechanics, Don State Technical University, Rostov-on-Don, Russia; Vorovich Mathematics, Mechanics and Computer Sciences Institute, Southern Federal University, Rostov-on-Don, Russia; Department of Mechanics of Active Materials, South Scientific Centre of Russian Academy of Sciences, Rostov-on-Don, Russia

T.N. Sorokun Research Institute of Physics, Southern Federal University, Rostov-on-Don, Russia

Pongsert Sriprom Faculty of Engineering, Department of Chemical Engineering, Khon Kaen University, Khon Kaen, Thailand

Mezhlum A. Sumbatyan Vorovich Institute of Mathematics, Mechanics and Computer Science, Southern Federal University, Rostov-on-Don, Russia

R. Sunder BiSS (P) Ltd, Bangalore, India

N.O. Svetlichnaya Research Institute of Physics, Southern Federal University, Rostov-on-Don, Russia

M.V. Talanov Research Institute of Physics, Southern Federal University, Rostov-on-Don, Russia

D.V. Telishev National Research University of Electronic Technology “MIET”, Moscow, Russian Federation

N.A. Teplyakova Tananaev Institute of Chemistry and Technology of Rare Elements and Mineral Raw Materials of the Russian Academy of Sciences Kola Science Center, Akademgorodok, Apatity, Murmansk Region, Russia

P.E. Timoshenko Department of Physics, Southern Federal University, Rostov-on-Don, Russia; Laboratory of Nanomaterials, Southern Federal University, Rostov-on-Don, Russia

S.V. Titov Research Institute of Physics, Southern Federal University, Rostov-on-Don, Russia

Vitaly Yu. Topolov Department of Physics, Southern Federal University, Rostov-on-Don, Russia

Huu-Duy Tran Department of Electronic Engineering, National Kaohsiung University of Applied Sciences, Kaohsiung City, Taiwan

E.A. Tsvetyansky Department of Physics, Southern Federal University, Rostov-on-Don, Russia

O.M. Tukodova Don State Technical University, Rostov-on-Don, Russia

I.A. Verbenko Research Institute of Physics, Southern Federal University, Rostov-on-Don, Russia

V.A. Volochaev Faculty of Chemistry, Southern Federal University, Rostov-on-Don, Russia

V.Y. Voloshchenko Engineering Technological Academy, Southern Federal University, Taganrog, Russia

A.A. Vorontsov Scientific Design & Technology Institute ‘Piezopribor’, Southern Federal University, Rostov-on-Don, Russia

Hung-Yu Wang Department of Electronic Engineering, National Kaohsiung University of Applied Sciences, Kaohsiung City, Taiwan

Chan-Chuan Wen Department of Shipping Technology, National Kaohsiung Marine University, Kaohsiung City, Taiwan, ROC

Chien-Erh Weng Department of Electronic Communication Engineering, National Kaohsiung Marine University, Kaohsiung, Taiwan, ROC

G.E. Yalovega Faculty of Physics, Southern Federal University, Rostov-on-Don, Russia

C.-C. Yang National Kaohsiung Marine University, Kaohsiung City, Taiwan, ROC

C.-D. Yang Department of Microelectronics Engineering, National Kaohsiung Marine University, Kaohsiung City, Taiwan

M.S. Zakrieva Research Institute of Physics, Southern Federal University, Rostov-on-Don, Russia

E.G. Zamburg Institute of Nanotechnologies, Electronics and Electronic Equipment Engineering, Southern Federal University, Taganrog, Russia

Ch. Zhang Chair of Structural Mechanics, Department of Civil Engineering, University of Siegen, Siegen, Germany

Jin-De Zhu Department of Electrical Engineering, National Taiwan Ocean University, Keelung, Taiwan, ROC

Part I
Processing Techniques of
Advanced Materials

Chapter 1

Structural Modification of Sulfide Minerals Irradiated by High-Power Nanosecond Pulses

I. Zh. Bunin, V.A. Chanturiya, M.V. Ryazantseva, I.A. Khabarova, E.V. Koporulina and A.T. Kovalev

Abstract The present work studies the effect of high-power (high-voltage) nanosecond pulses on the phase composition and chemical (quantum) state of atoms of surface layers of sulfide minerals with different semiconductor properties (galenite, chalcopyrite, pyrrhotite, pentlandite, molybdenite, and sphalerite) by means XPES and DRIFTS analysis, and analytical electron microscopy (SEM/EDX). Common patterns and main characteristic features of the structural phase transformations of sulfide surfaces under the pulsed energetic effect demonstrate: (i) formation and growth of a surface layer by the nonstoichiometric sulfur-enriched sulfide phase and metal (for example, Zn and Mo) oxides and hydroxides; (ii) the staged character of the transformation of sulfur atoms in the composition of galenite, pyrrhotite, pentlandite and sphalerite surface layers and (iii) the stability of the chemical state of sulfur in the molybdenite composition and lead atoms in the galenite composition. The increase of the electrode potential of sulfide minerals under pulsed effect provides favorable conditions for the adsorption of anion collector and, as a consequence, leads to the increase of galena, chalcopyrite and sphalerite floatability.

1.1 Introduction

The basic concept of application of energetic actions in processing of resistant noble-metal raw mineral materials with the purpose of selective disintegration of fine-disseminated mineral complexes and directed change in the physico-chemical surface properties of sulfides as main carriers of micro- and of noble metals provides conditions for maximally possible concentration of stress or energy. Thus, it

I.Zh. Bunin (✉) · V.A. Chanturiya · M.V. Ryazantseva · I.A. Khabarova · E.V. Koporulina · A.T. Kovalev
Research Institute of Comprehensive Exploitation of Mineral Resources of the Russian Academy of Science (IPKON RAS), Moscow, Russia
e-mail: bunin_i@mail.ru

facilitates disintegration of fine-grained mineral complexes that is sufficient for effective liberation of valuable components [1]. Different types of energy effects on minerals, mineral suspensions, and water are used to increase the contrast between the physicochemical and technological (flotation) properties of mineral raw materials: electrochemical, powerful microwave irradiation, electric pulse and magnetic pulse processing, and the effects of accelerated electron streams and high-power nanosecond electromagnetic pulses (HPEMP) [1–4].

In this chapter, we report the results of theoretical and experimental investigations of the development of electric discharges between particles of semiconducting sulfide minerals with sizes from 10 μm to 1 mm under the action of nanosecond high-power electromagnetic pulses with the field strength $E \sim 10^7 \text{ V m}^{-1}$. We take into account the technological conditions of electric-pulse processing of mineral raw materials. Mineral particles closely fill the interelectrode space in a high-voltage pulsed generator. High-voltage pulses may induce electric discharges between particles. Discharges between neighboring particles can form successive chains covering the entire discharge gap.

The effect of high-power (high-voltage) nanosecond pulses irradiation on phase composition and quantum (chemical) state of atoms in surface layers of sulfide minerals with different semiconducting properties (galenite, molybdenite, chalcopyrite and sphalerite) has been studied using X-ray photoelectron spectroscopy (XPS) analysis. The results of the SEM/EDX and SPM investigations of pyrrhotite and pentlandite testify about appearance of breakdown channels, microcracks and new micro- and nanophases on sulfide surface under the effect of the electro-pulse processing. In this chapter, we present the experimental data about the HPEMP effect on morphology, chemical and phase surface composition, electrochemical, sorption and flotation properties of sulfide minerals.

1.2 Experimental

1.2.1 *Materials and Research Technique*

We conducted experiments on monomineral samples of sulfide minerals (galenite, chalcopyrite and sphalerite from the Vtoroe Sovetskoe deposit in Dal'negorsk ore field of Primorskiy krai; molybdenite from the Sorsk copper-molybdenum deposit in Khakassia and the samples of pyrrhotite and pentlandite, extracted from copper-nickel pyrrhotite-bearing ore, from Norilsk region, Russia) with sizes of particles in the range 63–100 μm . By using simultaneously a Varian VistaCCD, ICP-AES device and inductively coupled plasma, we employed atomic emission spectroscopy to determine the gross contents of elements in each sample of the mineral (see Table 1.1; the content of minor impurities is not given).

Table 1.1 Chemical composition of sulfides samples, wt%

Specimen	Cu	Fe	Zn	S	Pb	Mo	Ni	Ca	Mn	Mg	As
PbS	0.09	1.41	8.75	15.6	56.71	<0.001	<0.001	0.24	0.06	0.01	0.45
CuFeS ₂	28.54	27.54	1.91	29.17	3.19	–	<0.001	0.70	0.04	0.01	0.01
ZnS	0.286	4.08	>50.00	29.30	6.61	–	0.002	0.19	0.13	0.02	0.15
MoS ₂	–	1.42	–	26.00	0.05	52.3	–	3.27	–	–	–
Fe _{1-x} S	0.04	59.75	–	39.15	–	–	0.03	–	–	–	–
(Fe, Ni) ₉ S ₈	4.71	32.92	–	33.67	–	–	18.30	–	–	–	–

1.2.2 The HPEMP Treatment Conditions

We conducted the treatment of powdered mineral samples with high-voltage nanosecond video pulses using the Laboratory Unit (Research Institute for the Comprehensive Exploitation of Mineral Resources, Russian Academy of Sciences, Moscow; Scientific-Production Enterprise FON, Ryazan'). Pulse duration was no longer than 10 ns, the strength of the electric component of the field was $\sim 10^7$ V/m, the energy in each pulse was 0.1 J, the pulse repetition frequency was 100 Hz, and the range of varying the treatment time t_{tr} was 5–100 s (the dose of the electromagnetic pulsed radiation was 5×10^2 – 10^4 pulses). Before treatment, the samples were wetted with distilled water in an S:L ratio of 5:1 to increase the efficiency of the electromagnetic pulse impact [5] and simulated conditions approaching those of actual production processes. After HPEMP treatment, the samples were dried in air under standard conditions and were kept in a rarefied atmosphere before performing the analysis.

1.2.3 Analysis Techniques

We used X-ray photoelectron spectroscopy (XPES) and Diffuse reflectance infrared Fourier transform spectroscopy (DRIFTS) to analyze the phase composition of the surfaces of mineral particles. To acquire the X-ray photoelectron (XPE) spectra, we used a Kratos Axis Ultra DLD spectrometer with a monochromatic AlK α X-ray radiation source. The IR-spectra of the diffuse reflection of mineral powders were recorded over a 400–4000 cm⁻¹ range of varying wave numbers with a resolution of 4 cm⁻¹ using an IRAffinity-1, IR spectrometer (Shimadzu) equipped with a DRS-8000 diffuse-reflection attachment. A detailed description of procedures for XPES and DRIFTS investigations of the surfaces of sulfide minerals was present in [6–8]. Potassium butyl xanthate (BX) sorption on mineral surface has been determined on residual concentration of collector by UV-spectrophotometry [9] on Shimadzu UV-1700 spectrophotometer.

We studied the morphology, sizes and elemental composition of neoformations on sulfide surfaces using analytical electron microscopy (SEM/EDX, LEO 1420

VP-INCA Oxford 350). Features of mineral surface relief on meso(nano)-scale (less than 100 nm) have been studied by scanning probe microscopy (SPM–AFM, INTEGRA Prima, NT-MDT) in semi-contact mode.

We determined electrochemical properties of sulfides (electrode potential; E , mV) using method of potentiometric titration with the simultaneous control of mineral potential and pH [10, 11]. pH-value has been changed by submission of a lime solution, interval of pH was 5.5–11.0. Working electrodes (approximately $10 \times 10 \times 5 \text{ mm}^3$) have been made of clean minerals. A comparison electrode was silver-chloride sated electrode. We investigated the dependence of electrode minerals potential from pH previously for the initial mineral samples, then the sulfides have been subjected to electromagnetic pulse processing and we conducted the measurements repeatedly.

We estimated flotation activity of sulfide minerals from a mineral yield in froth product in the presence of the following agents: potassium butyl xanthate (PBX, 30 g/t) and methylisobutylcarbinol (MIBC) frother at pH 9.5 (CaO). Flotation experiments were performed at a laboratory flotation machine with 20 ml cell, a 1 g mineral specimen with grade fineness particle 63–100 μm . Interaction time with reactants was 1 min, flotation time was 2.5 min. The mean-root-square error of measurements did not exceed 5 % in measurements.

1.3 Results and Discussions

1.3.1 *Nanosecond Electrical Discharges Between Semiconducting Sulphide Mineral Particles in Water*

Application of high-voltage nanosecond pulses to disperse mineral media containing particles (from 10 μm to 1 mm in size) of natural semiconducting sulfide minerals leads to electric field concentration at contacts or gaps between neighboring particles due to transient currents through the particles [12]. As a result, conditions form for developing electrical discharges between mineral particles [13]. When powder samples, previously moistened or placed in water, are subject to electric-pulse treatment, particle—particle discharges occur in water. The nature of these discharges differs from that for air gaps.

The mechanism of pulsed breakdown of water with microparticles (mineral suspensions, pulps) has barely been investigated. Electrical discharges in water have been most thoroughly studied for relatively large discharge gaps (from $\sim 1 \text{ mm}$ to several centimeters) under constantly applied voltage (dc voltage) or under voltage pulses with relatively long leading edges ($\sim 1 \mu\text{s}$ or more). For large particle—particle gaps, breakdowns from the positive electrode are most characteristic and likely. Their propagation is dominantly of bubble-streamer type, which implies formation of a plasma channel mainly in the gas bubbles formed during streamer propagation. If conditions for initiating a discharge from the negative

electrode form, the discharge development rate is several times below the discharge rate from a positive tip.

The main reason for the difference in the mechanisms of particle—particle discharges in water and air gaps is that the electron mobility and lifetime in liquids are very small. First, the frequency of electron elastic collisions is an order of magnitude higher than that in a gas of normal density. Second, inelastic collisions play a very important role: electrons become rapidly solvated or attached to water molecules or clusters. The mobility of such complexes is rather below the electron mobility and lower, than the mobility of hydroxyl and hydrogen ions.

In our previous works [13, 14], we demonstrated that discharges between sulfide particles may occur both from positive (anode streamer initiation) and negative (cathode initiation) tips, depending on the gap geometry. Let us consider, by analogy with [15], a system of discharges in gaps between semiconducting powder particles. The charge balance on the surfaces of the i -th particle in a linear chain of particles located between external electrodes is determined by the following equations:

$$\frac{\partial}{\partial t} Q_s^{(i)}(t) = j_s^{(i)} - j_a^{(i)} \frac{S_a}{S_0}, \quad \frac{\partial}{\partial t} Q_a^{(i)}(t) = j_a^{(i)} \frac{S_a}{S_0}, \quad (1.1)$$

$$\varepsilon_s \varepsilon_0 E_s^{(i)} = \varepsilon_a \varepsilon_0 E_a^{(i)} - Q_s^{(i)}, \quad \varepsilon_a \varepsilon_0 E_a^{(i+1)} = \varepsilon_s \varepsilon_0 E_s^{(i)} - Q_a^{(i+1)}. \quad (1.2)$$

Here $Q_s(t)$ is the charge per particle unit area; $Q_a(t)$ is the charge per particle unit area that is transferred to the surface of a neighboring particle; j_s and j_a are the current densities in a particle and between particles, respectively; S_s is the particle cross-section; S_a is the area of the region where the field-emission current generates; E_s and E_a are the field strengths in a particle and in the gap between particles; ε_s and ε_a are the permittivities of sulfide and aqueous medium (water).

Boundary conditions (1.2) are stated by the surface charge density $Q_s(t)$ on the electrodes and the charge source is the accumulating capacitor of the high-voltage pulse generator. Mineral particles $\sim 100 \mu\text{m}$ in size locate in the 0.5 cm inter-electrode gap, the voltage pulse amplitude is 50 kV, and the pulse width is 40 ns. We assumed that the gaps between particles are of the tip-plane type. The particle size and tip height were set with some spread. In the calculations, the tip radii for all particles were set to be $1 \mu\text{m}$; the breakdown channel radii were also chosen to be the same ($1 \mu\text{m}$).

The heating in breakdown channels calculates from the energy balance equation:

$$c_v dT/dt + \nabla_{\perp}(\kappa \nabla_{\perp} T) = \sigma E^2, \quad (1.3)$$

where ∇_{\perp} is the spatial derivative in the direction orthogonal to the channel axis, c_v is the specific heat at a constant volume, and κ is the thermal conductivity. The breakdown channel conductivity was calculated by using the Rompe–Weitzel relation:

$$d\sigma/dt = A_\sigma \sigma E^2 - \sigma/\tau_\sigma, \quad (1.4)$$

where A_σ , τ_σ are phenomenological parameters, responsible for the conductivity increase and relaxation in the channel.

The main results of analysis of equation set (1.1)–(1.4) are the following. Due to the spread of sizes and shapes of mineral (pyrite) particles in chains, breakdown in gaps does not occur simultaneously. During a voltage pulse, gaps between different particles are broken at different instants; in this case, the voltage across unbroken gaps increases. The breakdown pulses in later discharges are on average longer than in the previous ones, and more energy releases in them. Initiation of breakdowns from cathode and anode tips is approximately equiprobable.

We carried out an analysis of a set of superposed plots of discharge currents during a voltage pulse for pyrite particles with different conductivities ($\sigma \sim 1.0$, 0.1 , and $0.01 \text{ } \Omega^{-1} \text{ m}^{-1}$). At $\sigma \sim 0.1 \text{ } \Omega^{-1} \text{ m}^{-1}$ and for the specified calculation conditions, breakdowns occur in almost all gaps by the end of the voltage pulse. The characteristic current density in the breakdown channels is $2 \times 10^{12} \text{ A m}^{-2}$. With an increase in the pulse voltage, the gap breakdown time decreases.

For particles with a conductivity of $1.0 \text{ } \Omega^{-1} \text{ m}^{-1}$, breakdown occurs in all gaps during 7 ns. The current density in the breakdown channels increases by an order of magnitude. At a voltage pulse amplitude of 25 kV, all gaps are broken during 15 ns. At $\sigma \sim 0.01 \text{ } \Omega^{-1} \text{ m}^{-1}$, breakdowns in gaps between particles occur only after 25 ns, and less than a half of gaps are broken during the pulse. The current density in a breakdown channel decreases in this case by more than an order of magnitude.

The breakdown current density is somewhat overestimated because of neglect of the channel expansion. The estimated pressures in the shock wave, propagating from the breakdown channel, at a distance of 5 μm from the channel axis are 5.0, 0.6, and 0.08 MPa for particles with conductivities of 1.0, 0.1, and $0.01 \text{ } \Omega^{-1} \text{ m}^{-1}$, respectively.

Comparison with [15] shows that large voltages on discharge gaps are necessary to obtain discharges in water layers. In a dry powder, discharges in gaps between particles are of air type; the low initial density of the medium ensures a relatively low pressure at the front of the expanding discharge channel. The presence of a water leads to a higher energy release in the gaps between particles, which is caused by high water permittivity, and, respectively, to a higher pressure in the discharge channel. The shock wave from the expanding discharge channel is an additional destructive factor (electrohydraulic shock), which facilitates crack formation around the breakdown channel in sulfide mineral particles.

The results of our calculations indicate that the parameters of high-voltage pulses should be chosen such as to provide effective destruction of submillimeter particles of semiconducting minerals in water. To disintegrate particles with high conductivity, one has to use shorter pulses with a larger voltage amplitude and shorter leading edge, while low-conductive particles require longer pulses. Local heating of the surface of semiconductor mineral particles causes both selective disintegration of mineral complexes and formation of new surface micro- and nanophases [12–15].

1.3.2 Transformation of Morphological and Structural-Chemical Properties of Sulfide Mineral Surface Under HPEMP-Irradiation

1.3.2.1 Analysis of the SEM/EDX and AFM Data

The results of the SEM/EDX investigations of sulfides particles testify about appearance of breakdown channels, microcracks and new formations on mineral surface under the effect of nanosecond high-pulse processing. Simultaneously with the processes of disintegration within the localization of microcracks on the surface, formation of new phases, presumably, iron oxides and hydroxides takes place due to oxidation of sulfides surface, gas outflow from channel breakdown and other processes [16–18].

Figure 1.1a, b present the structural and morphological features of the surface of *pyrrhotite* exposed to HPEMP. Around the exit of the breakdown channel on mineral surfaces, typical coverage in the form of oxygen-containing amorphous

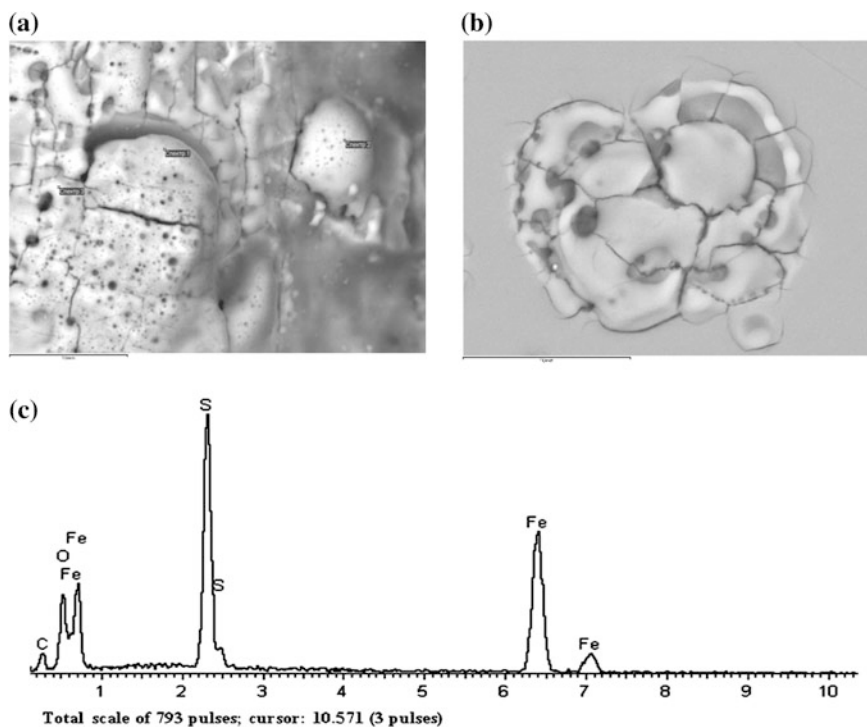


Fig. 1.1 SEM image (a, b) of microcracks, breakdown channels and new phases (namely, oxides of iron) on a surface of pyrrhotite, arisen due to HPEMP irradiation, and EDX-spectra from neoformations (c). Scale bars are 10 μm (a, b)

“scabs”, decorating the breakdown channel, formed. As the distance from the breakdown zone, the distribution of neophases becomes discrete, and they confine to the protruding parts of the mineral particles (edges and corners of crystals). Micro- and nanoformations are characterized by different (compared with the sulfide matrix) contrast, showing their different composition with a lower average atomic number. EDX-spectra (X-ray microanalysis, INCA Oxford 350) of the modified surface regions contain well-discernible peak of oxygen (Fig. 1.1c).

Due to the extreme thermodynamic non-equilibrium conditions of electropulse impact, numerous intermediate various on the composition oxide phases and chalcogenide semiconductor glasses can be formed during the oxidation of iron sulfides surface.

Three morphological types of neoformations, corresponding to the processes of structural and chemical transformations of the sulfide mineral surfaces due to the HPEMP effect (Fig. 1.2a–c), were revealed on *chalcopyrite* surface by means of analytical electron microscopy (SEM/EDX). The first of these form dense, extended ($\sim 100 \mu\text{m}$) coatings that are fractured and porous, with local swells of beadlike and irregular spherical shapes that, in some cases, decorate the breakdown channel openings (Fig. 1.2a, b). The second phase, represented by spherical formations with sizes of $3 \mu\text{m}$ and lower (Fig. 1.2c), is found mainly near the breakdown regions. Superthin ($Z \leq 100 \text{ nm}$) films of the third phase, which hypothetically consist of anhydrous sulfates of copper and can be diagnosed by scanning probe microscopy (SPM–AFM, Fig. 1.2c), uniformly cover the sulfide surface mainly in the regions

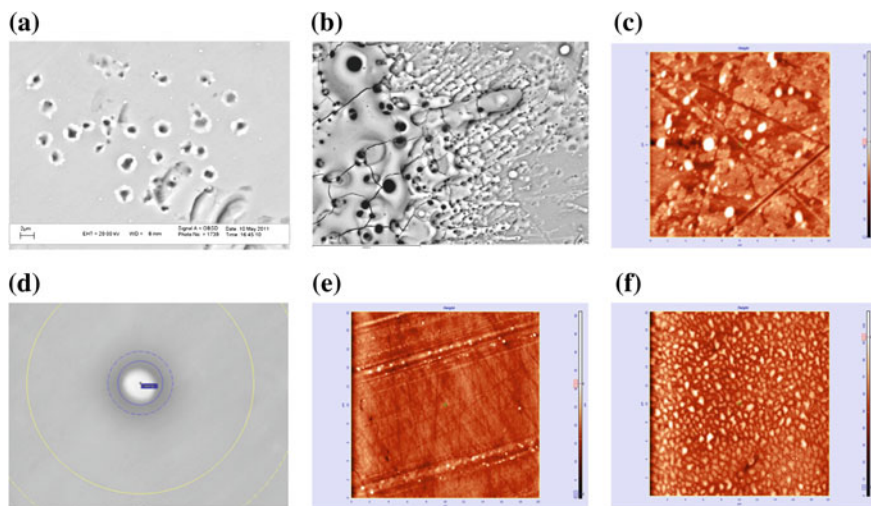


Fig. 1.2 Neoformations on chalcopyrite (a–c) and sphalerite (d–f) surface as a result of HPEMP-irradiation; SEM–EDX (a, b, d), scale bars— $2 \mu\text{m}$ (a), $30 \mu\text{m}$ (b), $4 \mu\text{m}$ (d); AFM (c, e, f), scanning fields: $10 \times 10 \mu\text{m}^2$, height $Z \sim 100 \text{ nm}$ (c); $10 \times 10 \text{ nm}^2$, height $Z \sim 40 \text{ nm}$ (e); $10 \times 10 \mu\text{m}^2$, height $Z \sim 90 \text{ nm}$ (f)

where the craters and erosion holes of breakdown channels (Fig. 1.2a) and microcracks localize.

As against chalcopyrite, essential transformations of *sphalerite* surface morphology (Fig. 1.2d–f) were marked only for samples subjected long electropulse treatment ($t_{tr} \geq 5 \times 10^3$ pulses). Breakdown microchannel openings and spherical formations (with sizes of 3 μm and lower, see Fig. 1.2d) located along surface defects (Fig. 1.2e) were revealed on the mineral surface. A pronounced peak corresponding to oxygen has been traced in the X-ray spectrum of a surface from these autonomous phases. With increase of duration of electropulse treatment up to approximately $t_{tr} \sim 2 \times 10^4$ pulses, the formation of dense (such as epitaxial) layer of new structured oxide phase (Fig. 1.2f), which hypothetically consists of copper sulfates and oxides (on the data obtained by IR-Fourier spectroscopy), was revealed on sphalerite surface.

According to analytical electron microscopy data, as a result of high-voltage nanosecond electromagnetic action for 10 s on galena surface, there appeared a thin film fragmented with fine fractures along the edges of crystal grains of mineral aggregate (Fig. 1.3a). As the size of the characteristic X-ray radiation generation area for light elements (oxygen, in particular) is 3–7 μm , energy dispersive spectra of areas covered by significantly thinner film mainly contain information on the elemental composition of sulfide carrying base. That is why the intensity of oxygen peak as the main distinctive element of oxide film is extremely insignificant (Fig. 1.3b). It is interesting to mention that while studying the topography of these areas of galena surface by methods of atomic force microscopy, fragmentation of the boundary layer was not found out. Apparently, this gives evidence of fracturing of a thin newly formed oxide layer on the part of massive sulfide carrying base (on the part of galena) caused by quasi-static (thermo-mechanical) stresses [15].

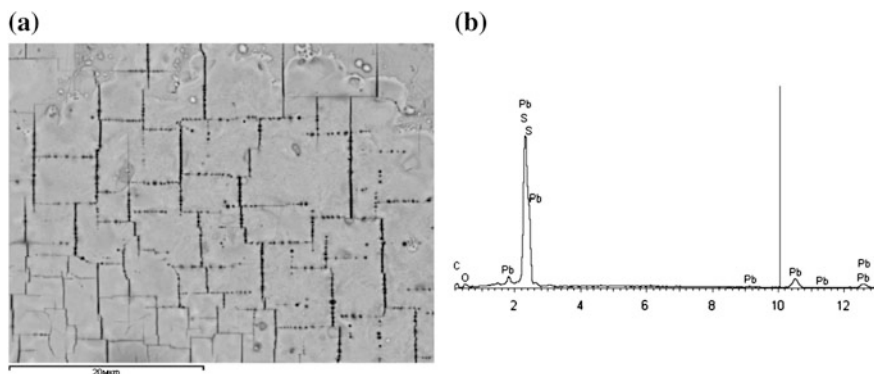


Fig. 1.3 **a** SEM image of galena surface changed by high-voltage nanosecond electromagnetic pulse treatment, the scale bar is 20 μm ; **b** EDX-spectra from modified surface areas

1.3.2.2 Analysis of the XPS Data

To analyze in detail the chemical (valent) state of atoms of lead, sulfur, oxygen, and carbon in the composition of galenite surface layers, we investigated the spectra of electron levels $Pb4f$, $S2p$, $O1s$, and $C1s$ for the atoms of zinc, sulfur, oxygen and carbon on the sphalerite surface ($Zn2p_{3/2}$, $S2p$, $O1s$, and $C1s$) and for the atoms of molybdenum, sulfur, and oxygen in the composition of the molybdenite surface layers ($Mo3d$, $S2p$, and $O1s$).

It should be noted, that galena, sphalerite and molybdenite have different semiconducting properties. Galenite PbS is a narrow-gap (direct-gap) ($E_g \sim 0.37\text{--}0.4$ eV) binary IV–VI semiconductor, molybdenite MoS_2 ($E_g = \sim 2.0$ eV) is a good (“ideln”) semiconductor, and sphalerite ZnS ($E_g = 3.68$ eV) is a wide-gap binary II–VI semiconductor.

1.3.2.3 Galenite

We showed [19] via XPS method, the structural-phase transformations of galenite surface layers after HEMP treatment were due mainly to variations in the chemical state of sulfur atoms. A metastable phase of lead thiosulfate (PbS_2O_3) formed in the surface of mineral particles in the result of pulsed treatment of the samples in first 5–10 s ($t_{tr} \leq 10$ s) and was reduced to the initial sulfide state as the duration of the pulsed effect increased to 30 s. The mineral surface then (at $t_{tr} \geq 30$ s) oxidized. The variation in the chemical composition of sulfur atoms accompanies by dehydration of the galenite surface at $t_{tr} \leq 10$ s.

According to the XPS data, the position and shape of the considered spectral bands of the $Pb4f$ level of lead did not differ appreciably after pulsed treatment, testifying to the stability of the chemical state of lead atoms in the composition of the galenite surface layers relative to the effect of nanosecond high-voltage pulses.

1.3.2.4 Sphalerite

The results of expanding the $2p$ spectrum of zinc show that there were two components with a chemical (energetic) shift on the order 1.3 eV in the $Zn2p_{3/2}$ spectra: the first component with a binding energy of ~ 1021 eV was attributed to ZnS [20–22], while the second with $E_{bind} = 1022$ eV was likely due to oxidized zinc compounds in the composition of the surface sphalerite layer ($\Sigma ZnSO_4 + ZnO + Zn(OH)_2$) [22].

Given the satisfactory coincidence between the experimental photoelectron $S2p$ spectrum and its full calculated envelope of the set of elementary components, it is possible that sulfur bound in zinc sulfide ($E_{bind} = 162.2\text{--}162.6$ eV) [23], elemental sulfur, and (or) its allotropic modifications of the type [20] were present on the sphalerite surface.

According to the XPES data, the electropulse effect led to variations in the chemical state of the sphalerite surface. Due to short-term ($t_{tr} \sim 5$ s) HPEMP treatment, a component with a binding energy of 166.8 eV and attributed to sulfite ions [24] was noted in the spectrum of $2p$ level of sulfur.

Two components with maxima $E_{bind} = 530.0$ – 530.5 eV and $E_{bind} = 532.0$ eV can distinguish in the spectra of $1s$ level of oxygen, both for the sample with no HPEMP treatment and for the treated sample, indicating the presence of ZnO oxide and Zn(OH)₂ hydroxide, respectively [25]. Prolonging the duration of the pulsed effect ($t_{tr} \geq 10$ s) led to variation in the shape of the spectra (asymmetric broadening with the emergence of a pronounced shoulder in the 533 eV region of binding energies), indicating that there was physically and/or chemically sorbed water in the composition of the sphalerite surface layer (48.5 at.%).

We can distinguish three components with binding energies of 285.0, 286.5, and 289.2 eV for all of our sphalerite samples in the spectra of the $1s$ level of carbon. The first two correspond to C–O and C=O bonds in the structure of hydrocarbon surface contaminations [26]; the last one attributes to the presence of zinc carbonate ZnCO₃ [27]. Analysis of the XPES data showed that the sulfide components in the spectra of the $2p$ level of zinc and sulfur were reduced by factors of 1.3 (from 69.8 to 53.7 at.%) and 1.8 (from 30.2 to 16.5 at.%) due to the pulsed effect for $t_{tr} \sim 5$ s. At the same time, the formation of the sulfite form of sulfur ($E_{bind} = 166.8$ eV) was observed, due apparently to sulfide and polysulfide sulfur bonding with oxygen. In addition, an increase in the concentration of carbon in zinc carbonate was established from the component with the binding energy (in the range of 288.5–289.2 eV) of spectrum $1s$ of carbon growing from 6.2 to 12.6 %.

Prolonging the duration of pulsed treatment to $t_{tr} \sim 10$ s reduced the fraction of zinc bound in the sulfide from 53.7 to 7.5 % and increased the surface concentration of zinc atoms corresponding to its oxidized forms. Variations in the profile of the spectrum of the $S2p$ level were also found, namely, the absence of the component with a binding energy of 166.8 eV, which corresponds to the state and increases in components of the spectrum, associated with sulfide and elemental sulfur by factors of 1.7 and 1.9, respectively. Electromagnetic pulsed treatment at $t_{tr} \sim 30$ s increased surface hydration by a factor of 1.6. It follows from the expansion of the Zn spectrum of the $2p$ level that the zinc in the region of collecting analytical information associates with oxides and hydroxides. Analysis of the spectrum of the $2p$ level of sulfur atoms showed a drop in the surface concentration of sulfur in state (from 71.6 to 51.2 %) due to its thermal removal and a simultaneous increase in the sulfide component of the spectrum (from 28.8 to 48.8 %).

Prolonging the duration of the pulsed effect to $t_{tr} \sim 50$ s led to the removal of sulfur from the surface of sphalerite particles, due apparently to a local increase in the temperature of surface non-uniformities of mineral particles [15]. This was confirmed by the XPES data, according to which sulfur and zinc (in amounts of 100 and 45.5 %, respectively) were in sulfide form. A reduction in the total hydration of the surface layer of mineral by a factor of 2.4 was observed, relative to the sample treated with HPEMP for 30 s.

On the results of SEM/EDX, AFM and IR-spectroscopy high-voltage nanosecond pulses in a range of electromagnetic effect doze N_{pulses} , 10^3 – 10^4 pulses result in formation and accumulation of copper sulfate CuSO_4 in superficial layer of chalcopyrite, and formation and accumulation of zinc sulfate ZnSO_4 and carbonate ZnCO_3 on sphalerite surface. The increase of HPEMP effect intensity up to $N_{\text{pulses}} \sim 1.5 \times 10^4$ pulses results in oxidation of sulfates and formation of copper (Cu_xO_y) and zinc (ZnO) oxides on sulfide surfaces. Formed micro- and nanophases locate mainly in the regions of sulfide surface heterogeneity (electrical breakdown craters, microdefects, edges and tops of crystals).

1.3.2.5 Molybdenite

In processing our XPES data, the spectrum of the $3d$ level of Mo atoms was approximated by two doublets, $\text{Mo}3d_{5/2-3/2}$ (binding energy with maxima $E_{\text{bind}} = 229.9$ – 235.8 eV and $E_{\text{bind}} = 232.9$ – 236.1 eV), the first of which associated with molybdenum disulfide MoS_2 and the second with molybdenum oxysulfides MoO_xS_y and oxides MoO_x [28, 29]. The results from expanding the $\text{S}2p$ level showed that the sulfur in the molybdenite surface layer (depth of analysis, ~ 1.2 nm) was in two chemical states: molybdenum disulfide itself (doublet 162.38–163.68 eV) and oxysulfide formations with the formula MoS_xO_y (doublet 163.53–164.83 eV) [28, 29].

The spectra of the $\text{O}1s$ states on the surfaces of molybdenite particles consisted of three lines, namely, the maxima of first two bands were due to oxides, hydroxides, and oxysulfides ($E_{\text{bind}} = 531.15$ eV), while the lines lying in the region of high binding energies 532.55 and 533.5 eV were associated with oxygen atoms (of water molecules) adsorbed on the mineral surfaces (molecularly adsorbed water) [30].

In a whole, a molybdenite surface oxidizes weakly both in the initial state and after treatment by nanosecond pulses: ~ 90 % of the molybdenum atoms and ~ 67 % of the sulfur atoms on the surfaces of mineral particles bound into molybdenum disulfide. The MoS_2 compound has a layered structure (a natural characteristic of two-dimensional structures) in which each layer consists of three atomic planes so that the layer (sheet) of hexagonally packed Mo atoms clamps between two hexagonally packed sheets of sulfur [31]. Molybdenite is characterized by strong anisotropy of its crystalline structure and chemical bonds, so the bonds of the atoms inside the layer are considerably stronger than those between the layers.

Data on the effect of high-voltage nanosecond pulses, obtained on the phase composition of the surfaces of molybdenite particles (according to which the chemical state of surface atoms of sulfur caused by pulsed treatment remained invariable), are presented in [33].

The main variations in the phase composition of the mineral surfaces under the high-voltage nanosecond pulses irradiation are due to the accumulation of molybdenum oxides and hydroxides, the surface concentrations of which rose by a factor of 1.2–1.9. For example, the fraction of molybdenum atoms associated with oxide and hydroxide phases grew from 6.2 % (reference sample) to 11.6 % after

pulsed treatment of the mineral samples for 30 s. The chemical state of surface atoms of sulfur caused by pulsed treatment remained invariable.

In addition, the HPEMP effect for $t_{ir} \sim 5$ s led to dehydration of the surface of mineral particles, or a reduction in the concentration of oxygen associated with molecules of water adsorbed on the mineral surfaces, compared to the reference sample. Prolonging the duration of pulsed treatment raised the concentration of surface water from 12.3 % ($t_{ir} \sim 5$ s) to 19.7 % (30 s). In this way, the main variations in the phase composition of molybdenite surfaces resulting from electromagnetic pulsed treatment associate with the accumulation of molybdenum oxides and hydroxides, and with the dehydration (hydration) of the mineral surfaces.

1.3.3 Effect of HPEMP-Irradiation on Electrochemical, Sorption and Flotation Properties of Sulfide Minerals

Structural phase transformations of the surfaces of sulfide minerals under the effect of high-voltage nanosecond pulses allowed targeted variations in the physico-chemical and manufacturing properties of sulfides: for example, the galenite, chalcopyrite and sphalerite electrode potential shifted to the region of increasing positive values, raised the sorption and flotation activity of sulfides. At the same time, we have shown via IRFS diffuse reflection that the HPEMP effect had no appreciable influence on the sorption activity of the molybdenite surfaces, relative to the anion collector (butyl xanthate); neither were the surface hydrophobicity and flotation properties of the mineral were subject to substantial variations.

1.3.3.1 Electrochemical Properties

We established the effect of nanosecond electromagnetic pulse processing on electrode potentials of sulfide minerals. The effect of HPEMP resulted in the increase of positive values of electrode chalcopyrite potential in the mean on 25 mV at pH 6–10. In alkaline environment at pH 10–11, electrode potential E of samples processed during 10 s (10^3 pulses) decreases in the mean on 20 mV. The maximal absolute difference in electrode potential values before and under HPEMP treatment ($\Delta E = E_{pulses} - E_0$) equals to -69 mV at pH 11. At increase of electropulse impact doze up to 10^4 pulses, the maximum ΔE becomes equal to 43 mV at pH 11.

Electrode potential of sphalerite got more positive values at electropulse processing, being increased in the mean on 35 mV. The absolute difference in values ΔE changed within limits of 12–70 mV, and the maximal value ($\Delta E = 70$ mV) was got at pH 6 as a result of preliminary HPEMP processing ($N \sim 10^4$ pulses).

Figure 1.4a shows the relation of galena electrode potential and pH before and after electromagnetic pulse processing ($N = 10^3$ and 5×10^3 pulses). Using potentiometric

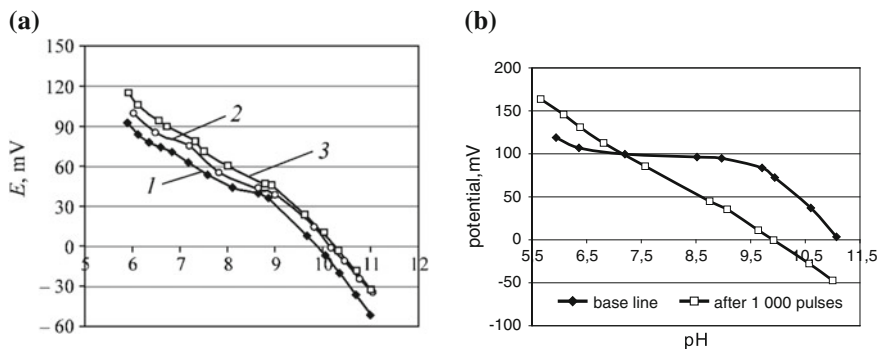


Fig. 1.4 Relation of galena (a) and pyrrhotite (b) electrode potential and pH: before high-voltage nanosecond electromagnetic pulse processing (1) and after processing for (2) 10 s and (3) 50 s

titration, it was found out that sulfide electrode potential after energy deposition increased in the region of positive values on average by 15 mV at pH 6–11. At the increase of the electromagnetic action up to 5×10^3 pulses, maximum ΔE was 22 mV at pH 6.

Electrode potential of pyrrhotite after HPEMP-irradiation ($N \sim 10^3$ pulses) decreases in alkaline medium owing to the increase of mineral surface hydrophilicity (Fig. 1.4b).

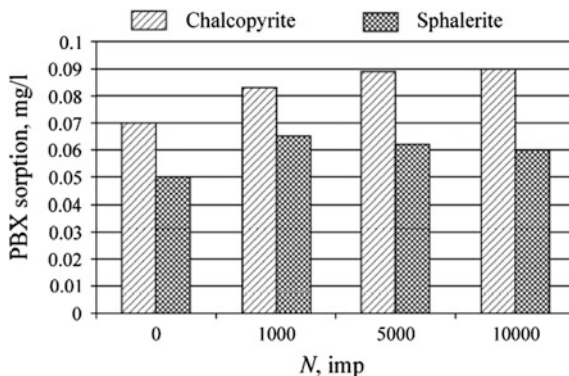
1.3.3.2 Sorption Properties of Minerals

UV-spectroscopy data show the improvement of potassium butyl xanthate (PBX) sorption at chalcopyrite and sphalerite surfaces, treated by HPEMP (Fig. 1.5). The maximum PBX sorption, higher by 22 % at chalcopyrite surface, is detected at HPEMP treatment mode of 10^4 pulses ($t_{tr} \sim 100$ s). The maximum PBX sorption, higher by 23 % at sphalerite surface, is detected at nanosecond pulses treatment mode of 10^3 pulses.

According to UV-spectroscopy data, the initial electromagnetic pulse processing of mineral specimens led to the increase of BX sorption on galena surface. Maximum BX sorption (increased by 6 %) on sulfide surface was found out for the specimens after HPEMP treatment electromagnetic pulse processing for $t_{tr} \sim 100$ s. The obtained results conform the data on the effect of high-voltage nanosecond electromagnetic pulses on electrochemical properties of the sulfide minerals (chalcopyrite, sphalerite, galenite and pentlandite): shift of the sulfides electrode potential to the region of positive values leads to the increase of anion collector sorption on the mineral surface.

We evaluated variation in PBX adsorption at mineral surfaces by comparing *IRF-spectra* of an initial specimen and specimens treated by the electromagnetic pulses. The main research target was to find the IR-spectral manifestation of any

Fig. 1.5 Influence of HPEMP treatment on the sorption activity of chalcopyrite and sphalerite surfaces at pH 9.5; UV-spectroscopy



atom groups or bonds, identifying an agent sorption at a mineral surface mainly from the spectra for butyl xanthate and butyl dixantogen (Kx_2) and taking into account the fact that the agent chemisorption can induce a shift of adsorption bands relative to positions, characterizing pure PBX or Kx_2 .

When treating chalcopyrite by HPEMP, it was detected in their-spectrum the growth of the intensity of the adsorption bands (671 cm^{-1}) which were present in the “virgin” specimen spectrum and related to the oscillations of the skeleton of an absorbed xanthate molecule (C–S bond), and a spring of new adsorption maxima (1157 cm^{-1} , C=S). All the above indicates the intensified sorption activity of the HPEMP-treated mineral surface.

Comparison of IR-spectra profiles for minerals treated by HPEMP ($t_{tr} \sim 50$; 100, and 150 s), with the spectrum for a specimen treated by HPEMP ($t_{tr} \sim 10$ s) revealed a certain reduction in the intensity of the absorption bands, responsible for valence vibrations of C–S bonds (671 cm^{-1}) and C=S (1157 cm^{-1}). Thus, it indicates the worsened sorption activity of chalcopyrite mineral surface in response of an increased duration of HPEMP treatment.

When treating sphalerite by HPEMP ($t_{tr} \sim 10$ s), it was detected a rise of a weakly intensive peak at 779 cm^{-1} , responsible for oscillations of C–S bond of an absorbed xanthate molecule and a wide weakly-intensive band with two maximums (1049 and 1126 cm^{-1}), corresponding to oscillations of C=S bond of a collecting agent. The above specific features were also typical of the spectra for specimens treated by HPEMP ($t_{tr} \sim 50$ and 100 s). This fact, no doubt, is an actual proof of the growth of the sphalerite sorption activity under the electromagnetic pulse effect.

The comparative analysis of profiles of differential infrared spectra of galenite after interaction with BX collector solution helped to find out the increase of sorption activity of the specimen mineral surface which was subjected to longer ($t_{tr} \geq 50$ s) electromagnetic pulse processing. The analysis of the spectral curve profiles of the specimens processed by high-voltage nanosecond electromagnetic pulses for $t_{tr} = 50$, 100 and 150 s, showed the presence of doublet ~ 1000 – 1107 cm^{-1} , corresponding to vibrations of C=S bond of the collector, and the increase of band intensity at 1269 and $\sim 1400\text{ cm}^{-1}$ referring to vibrations of

hydrocarbon frame of xanthate molecule. The obtained results in general correspond to UV spectroscopy data.

1.3.3.3 Flotation (Technological) Properties

The optimized electromagnetic pulse pre-treatment regime was experimentally proved in [6] for chalcopyrite and sphalerite: the HPEMP treatment duration from 5 to 30 s enhanced flotation ability of the minerals by 10–15 % on the average owing to the change of the surface phase composition, increase in the electrode potential and growth of the sorption activity.

Improvement of selectivity of flotation separation of chalcopyrite and sphalerite under the HPEMP treatment was studied in the presence of sphalerite depressing agent (zinc sulfate $ZnSO_4$) at $pH \approx 9.5$ (Fig. 1.6, curves 3 and 4). Floatability of sphalerite with zinc sulfate decreased in the result of the HPEMP pre-treatment. The maximum depression of sphalerite reaches after the short-term pulse treatment for 10 s: foam product yield reduced from 48 % (original sample) to 25.7 % after the HPEMP treatment.

Figure 1.6 shows the results of galena monomineral flotation before and after the high-voltage nanosecond pulse processing. In the low intensity region of pulse action (10^3 pulses, $t_{tr} \sim 10$ s), galena floatability increases from 76 to 85 % (Fig. 1.6, curve 1) in the result of structure phase transformations of sulfide surface, increased electrode potential (Fig. 1.4a) and higher collector quantity on the surface of mineral particles. As the number of pulses increases, the mineral yield in froth pulp reaches not less than 85 %.

After changing the flotation conditions (in test experiments), the increment of galena yield in froth pulp caused by preliminary pulse processing of specimens was from 12.2 to 19.3 %. The maximum yield increment from 72 to 91.3 % was obtained after the HPEMP treatment for $t_{tr} \sim 50$ s. Maximum sphalerite depression was obtained at short-term effect $t_{tr} \sim 10$ s (Fig. 1.6). In the same flotation conditions, galena floatability increased to ~ 8 –10 % (Fig. 1.6, curves 2, 4).

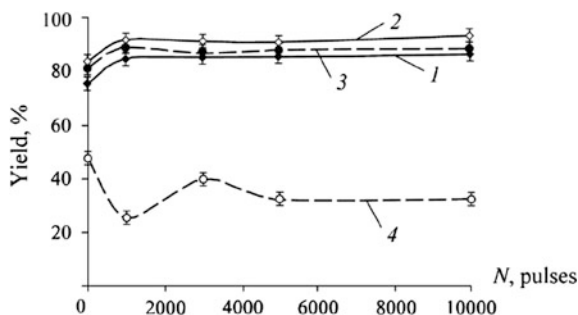


Fig. 1.6 The effect of high-voltage nanosecond electromagnetic pulses on flotation properties of galena (1, 2) and sphalerite (3, 4) at pH 10.2 (1) and 9.5 (2–4) in the presence of BX (1, 3) and its combination with $ZnSO_4$ (2, 4)

Flotation activity of pyrrhotite with BX changed nonlinearly at increase of pulses number [32]. In the field of low intensity of the pulse effect ($t_{tr} \sim 10$ s, $N_{pulses} \sim 10^3$ pulses), decrease of mineral flotability is observed. Floatability of pyrrhotite rises with increase of number of nanosecond pulses, owing to elevation of amount of elementary sulfur on its surface.

The maximal pentlandite yield in froth pulp reaches at $N_{pulses} \sim 10^3$ pulses owing to elevation of amount of elementary sulfur on its surface and increases of electrode potential. We have shown [32] that the preliminary nanosecond pulse treatment of pyrrhotite and pentlandite and introduction sodium dimethyldithiocarbamate (DMDC) at flotation results in increase of selectivity of flotation separation of minerals ($\Delta\varepsilon = 35$ % without HPEMP treatment, $\Delta\varepsilon = 55$ % at $N_{pulses} \sim 10^3$ pulses).

According to IRF-spectroscopy data [33], the HPEMP effect had no appreciable influence on the sorption activity of the molybdenite surfaces, relative to the anion collector (butyl xanthate); neither were the surface hydrophobicity and flotation properties of the mineral were subject to substantial variations.

1.4 Conclusions

The results of X-ray photoelectron spectroscopy (XPES) and DRIFTS analysis showed that structural phase transformations of chalcopyrite and sphalerite surfaces caused by high-voltage nanosecond electromagnetic pulses during the first 10 s period of treatment are mainly connected with formation of metal-deficient and sulfur-rich surface of sulfides ($\text{CuFe}_{1-x}\text{S}/\text{Zn}_{1-x}\text{S}$), Me oxides and hydroxides (Fe and Zn). The elongation of the HPEMP treatment period to 30–50 s results in chemical removal of elemental (polysulfide) sulfur and restoration of the sulfide mineral surface. The mechanisms of transformation of chalcopyrite and sphalerite surface under the HPEMP differ in terms of peculiar changes of chemical states of the surface sulfur atoms: (i) on chalcopyrite, there is origination of elemental sulfur in the result of the pulse treatment within 10 s and removal of the sulfur from the mineral surface under the longer treatment; (ii) on sphalerite, there is origination of metastable sulfite during the first 5 s of the HPEMP treatment and, then, formation of poly- and disulfide sulfur.

The structural modification of galena facial layer (~ 5 nm), caused by high-voltage nanosecond pulses, is mainly connected with the change of the chemical state of sulfur atoms, which determines the formation of metastable lead thiosulfate at the initial stage of the pulse treatment ($t_{tr} \sim 10$ s), thiosulfate reduction by products of water radiolytic decomposition up to the initial state at the increase of processing time up to 30 s and its oxidation at the late stages of action ($t_{tr} \geq 50$ s). We established the stability of the chemical state of sulfur in the molybdenite composition and lead atoms in the galenite composition under the action of nanosecond electromagnetic pulses. The increase of the electrode potential of sulfide minerals under HPEMP provides favorable conditions for the adsorption

of anion collector and, as a consequence, leads to the increase of galena, chalcopyrite and sphalerite floatability. The preliminary nanosecond pulse treatment of pyrrhotite and pentlandite and introduction of sodium dimethyldithiocarbamate (DMDC) at flotation result in increase of selectivity of flotation separation of these sulfides.

Acknowledgments This work was supported by the RF President's grant for the state support of leading scientific schools of the Russian Federation, Academician V.A. Chanturiya's School NSh-748.2014.5, and by the Russian Foundation for Basic Research, project No. 15-35-20 598 mol-a-ved.

References

1. V.A. Chanturiya, K.N. Trubetskoy, S.D. Viktorov, I.Zh. Bunin, *Nanoparticles in Geological Materials Destruction and Extraction Processes* (IPKON RAS, Moscow, 2006) (in Russian)
2. V.A. Chanturiya, Y.V. Gulyaev, I.Zh. Bunin et al., *J. Min. Sci.* **37**(4), 427 (2001)
3. I.Zh. Bunin, N.A. Bunina, V.A. Vdovin, P.S. Voronov, et al., *Bull. Russian Acad. Sci.: Phys.* **65**(12), 1788 (2001)
4. V.A. Chanturiya, I.Zh. Bunin, *J. Min. Sci.* **43**(3), 311 (2007)
5. V.A. Chanturiya, Y.V. Gulyaev, I.Zh. Bunin, V.A. Vdovin, et al., *Trans. (Doklady) Russian Acad. Sci.: Earth Sci. Section* **378**(3), 372 (2001)
6. V.A. Chanturiya, I.Zh. Bunin, M.V. Ryazantseva, I.A. Khabarova, *J. Min. Sci.* **48**(4), 732 (2012)
7. V.A. Chanturiya, I.Zh. Bunin, M.V. Ryazantseva, I.A. Khabarova, *J. Min. Sci.* **49**(3), 489 (2013)
8. V.A. Chanturiya, I.Zh. Bunin, M.V. Ryazantseva, I.A. Khabarova, *Bull. Russian Acad. Sci.: Phys.* **77**(9), 1096 (2013)
9. V.A. Chanturiya, V.E. Vigdergauz, *Electrochemistry of Sulfides. Theory and Practice of Flotation, Ore & Metals* (Moscow 2009) (in Russian)
10. V.A. Chanturiya, R.Sh. Shafeyev, *Surface Chemistry Under Flotation* (Nedra, Moscow, 1977) (in Russian)
11. R.Sh. Shafeyev, V.A. Chanturiya, V.P. Yakushkin, *Ionization Radiation Effect onto Flotation Process* (Nauka, Moscow, 1973) (in Russian)
12. V.A. Chanturiya, I.Zh. Bunin, A.T. Kovalev, *Bull. Russian Acad. Sci.: Physics*, **71**(5), 646 (2007)
13. V.A. Chanturiya, I.Zh. Bunin, A.T. Kovalev, in *Proceedings TMS 2008 137th Annual Meeting and Exhibition, Supplemental Proceeding: Materials Characterization, Computation and Modeling*, TMS, New Orleans, 2, 27 (2008)
14. V.A. Chanturiya, I.Zh. Bunin, A.T. Kovalev, *Bull. Russian Acad. Sci.: Phys.* **73**(5), 686 (2009)
15. V.A. Chanturiya, I.Zh. Bunin, A.T. Kovalev, *Bull. Russian Acad. Sci.: Phys.* **72**(8), 1053 (2008)
16. V.A. Chanturiya, I.Zh. Bunin, A.T. Kovalev, *Bull. Russian Acad. Sci.: Phys.* **74**(5), 663 (2010)
17. V.A. Chanturiya, I.Zh. Bunin, A.T. Kovalev, E.V. Koporulina, *Bull. Russian Acad. Sci.: Phys.* **75**(5), 593 (2011)
18. V.A. Chanturiya, I.Zh. Bunin, A.T. Kovalev, E.V. Koporulina, *Bull. Russian Acad. Sci.: Phys.* **76**(7), 757 (2012)
19. V.A. Chanturiya, I.Zh. Bunin, M.V. Ryazantseva, I.A. Khabarova, et al., *Bull. Russian Acad. Sci.: Phys.* **78**(4), 244 (2014)

20. C.D. Wagner, A.V. Naumkin, A. Kraut-Vass, et al., *NIST X-ray Photoelectron Spectroscopy Database*. <http://srdata.nist.gov/xps>
21. V.L. Tauson, D.N. Babkin, S.V. Lipko et al., *Geokhimiya* **1**, 101 (2010). (in Russian)
22. D. Brion, *Appl. Surf. Sci.* **5**, 133 (1980)
23. M.D. Veremeenko, P.M. Solozhenkin, V.I. Nefedov, et al., *Izv. Akad. Nauk Tadzh. SSR. Otd. Fiz.–Mat., Khim., Geol. Nauk*, No 2, 19 (1986) (in Russian)
24. M. Descostes, F. Mercier, N. Thomat et al., *Appl. Surf. Sci.* **165**(4), 288 (2000)
25. S.W. Knipe, J.R. Mycroft, A.R. Pratt et al., *Geochim. Cosmochim. Acta* **59**(6), 1079 (1995)
26. T.N. Khmeleva, T.V. Georgiev et al., *Surf. Interface Anal.* **37**(8), 699 (2005)
27. V.I. Nefedov, *X-Ray Spectroscopy for Chemical Compounds* (Handbook, Khimiya, Moscow, 1984). (In Russian)
28. N. Brown, N. Cui, A. McKinley, *Appl. Surf. Sci.* **134**(1), 11 (1998)
29. L. Benoist, D. Gonbeau, G. Pfister-Guillouzo et al., *Thin Solid Films* **258**(1), 110 (1995)
30. A. Galtayries, S. Wisniewski, J. Grimblot, *J. Electron. Spectroscopy Related Phenom.* **87**(1), 31 (1997)
31. E.F. Lazneva, I.V. Baryshev, *Zh. Tekh. Fiz.*, **61**(9), 167 (1991) (In Russian)
32. I.Zh. Bunin, V.A. Chanturiya, A.T. Kovalev, I.A. Khabarova et al., *Characterization of Minerals, Metals, and Materials*, vol. 89 (Wiley, New Jersey, 2012)
33. I.Zh. Bunin, V.A. Chanturiya, M.V. Ryazantseva, E.V. Koporulina, I.A. Khabarova, *Bull. Russian Acad. Sci.: Phys.* **79**(6), 723 (2015)

Chapter 2

Magnetic Nanoparticles and Their Heterogeneous Persulfate Oxidation Organic Compound Applications

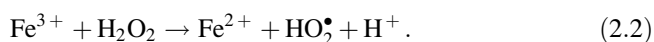
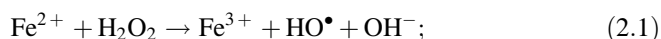
Cheng-Di Dong, Chiu-Wen Chen and Chang-Mao Hung

Abstract Nano-zero-valent iron (nZVI), Fe^0 , has been successfully used to transform and degrade contaminants in soils and water. Additionally, it has been used as a catalyst to heterogeneously activate persulfate ($\text{Na}_2\text{S}_2\text{O}_8$, PS) for the treatment of various contaminants. The nZVI-PS oxidation system has received increasing attention because of its successful use in the treatment of sediments contaminated with recalcitrant organic compounds; treated sediments have improved considerably to meet remediation goals, such as the remediation goal for polycyclic aromatic hydrocarbons (PAHs). The presence of PAHs in sediments is a major concern because of the risks posed to aquatic ecosystems through bioaccumulation in food chains. To minimize ecological risks posed by contaminated sediments, it is imperative to develop processes that can degrade the sorbed PAHs. Efforts have been focused on identifying the most effective PS oxidant for obtaining the maximum acceptable PAH compound concentration. Moreover, the oxidation of PAHs in sediments by PS along with the simultaneous activation of the PS by nZVI, which is a source of catalytic ferrous iron, has been investigated. The determination and quantification of PAHs in sediment samples were performed using gas chromatography coupled to mass spectrometry (GC-MS). An adequate amount of PS must be present because it is the source of sulfate radicals, which are responsible for the degradation of PAHs. Results have indicated that the addition of a larger amount of nZVI to a PS-slurry system can enhance the PS oxidation process, suggesting that nZVI assists PS in the ex-situ treatment of PAH-contaminated sediments. Thus, nZVI-assisted PS is a promising choice for organic compound treatment for environmental remediation. This paper presents a study on magnetic nanoparticles and the heterogeneous PS oxidation of the nanoparticles and organic compounds (PAH-contaminated sediment), conducted in our laboratory.

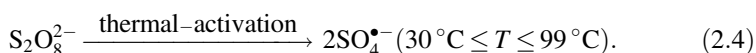
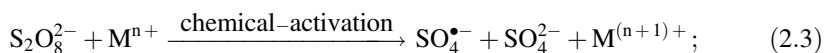
C.-D. Dong · C.-W. Chen · C.-M. Hung (✉)
Department of Marine Environmental Engineering,
National Kaohsiung Marine University, Kaohsiung City, Taiwan
e-mail: hungcm1031@gmail.com

2.1 Overview of Persulfate Oxidation Processes Used for Organic Compound Treatment

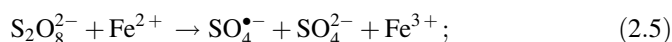
Advanced oxidation processes (AOPs) are chemical treatments used for removing organic (and sometimes inorganic) materials; they involve the use of highly reactive radicals generated from various combinations of reactants, such as O₃/UV, TiO₂/UV, H₂O₂/O₃, and transition metal/H₂O₂ [1, 2]. Among AOPs, those that involve the Fenton reagent and activated persulfate (Na₂S₂O₈, PS) are the most powerful, and they have been used for treating polluted wastewater in the last decade. In a regular Fenton process, ferrous ions (Fe²⁺) are used to catalyze hydrogen peroxide (H₂O₂), generating a highly reactive oxidizing species—hydroxyl radicals (HO•) that are strong nonspecific oxidants. These radicals are highly reactive and capable of decomposing organic compounds at high diffusion-controlled rates (10⁷–10¹⁰ M⁻¹ s⁻¹). Furthermore, HO• can effectively oxidize almost all organic compounds. The primary Fenton reactions include the following reactions [3]:



Typically, H₂O₂ reduces the ferric species, Fe(III), in catalytic reactions. The rates of ferrous consumption and ferrous regeneration differ appreciably. The rapidly exhausted ferrous ions terminate the Fenton reaction and shorten the period of efficient degradation of the target compounds. Recently, attention paid to the use of PS has been increasing because PS has been recognized as an emerging oxidizing agent that can be used for degrading a broad range of organic contaminants. PS has drawn considerable attention because of its unique characteristics [4, 5]. In general, subjecting PS to highly reactive sulfate radical (SO₄^{•-})-based AOPs can produce powerful oxidizing species, such as SO₄^{•-}, which can be potentially used for treating dye effluents [6, 7]. PS (S₂O₈²⁻) is used more frequently than H₂O₂ as an oxidant for in situ chemical oxidation remediation of environments contaminated with organic pollutants; the chemical oxidation is performed at room temperature, but the direct reaction of PS with most reductants is slow [8]. When appropriately activated, PS converts to SO₄^{•-} [9], which has an oxidation potential of 2.6 V. This value is greater than that of hydroxyl radicals (approximately 2.8 V), which are one-electron oxidants that can potentially remove contaminants. Numerous studies have been conducted to investigate the efficiency of activated PS for the chemical oxidation of pollutants. Generally, PS can be chemically activated by transition metal ions (Mⁿ⁺) or thermally activated to generate SO₄^{•-} [10].



Thermal activation of PS has been considered as a prominent method, particularly after intensive study and application in the detoxification of numerous organic pollutants at contaminated sites. The temperature required for the thermal activation has been experimentally shown to be in the range of 35–130 °C [11]. Zhao et al. found that thermal activation was one of the most effective methods of activating PS for the removal of PAHs in soil when the temperature was increased from 40 to 60 °C [12]. Cuypers et al. showed that the extent of PAH oxidation by persulfate increased with an increase in the temperature in the range of 20–70 °C (for oxidation durations up to 24 h) [4]. Furthermore, the thermally activated-PS-based oxidation of target compounds in soil slurries was strongly inhibited by the high organic carbon content in the soil [13]. Generally, oxidation involving thermally activated PS is energy-consuming. However, this crucial heterogeneous catalytic process has attracted considerable attention in materials chemistry, and the effectiveness of the chemical activation process has been improved using high-performance Fe(II), which generates $\text{SO}_4^{\bullet-}$ and HO^\bullet in a manner similar to that in the Fenton reaction in accordance with (2.5) and (2.6). If a sufficient quantity of Fe(II) ions, which act as electron donors, is present, PS anions can also be catalytically decomposed to form $\text{SO}_4^{\bullet-}$.

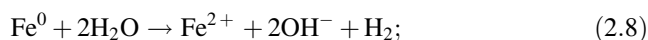
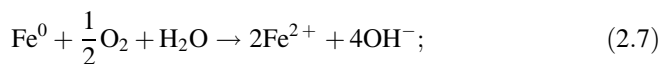


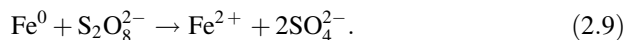
Generally, various types of catalysts have been widely used for the treatment of dye-contaminated wastewater. For example, Wang et al. prepared zero-valent iron (ZVI) catalysts for the degradation conversion of acid orange 7 (AO7); the degradation conversion involved PS activation through ultrasonic irradiation [14]. Nguyen et al. assessed the feasibility of using activated carbon as a supporting material for Fe_2MnO_4 catalysts in the oxidation of methyl orange at pH 3.0; they reported that treating activated carbon with HNO_3 can functionalize the carbon surface through the formation of carboxyl groups [15]. Additionally, a recent study described an efficient technique for the catalytic oxidation of the azo dye Orange G (OG) in an aqueous stream. The technique involved using a Fe^{2+} /PS reagent in the temperature range of 20–40 °C at pH 3.5. It was observed that the degradation of OG increased with both Fe^{2+} and PS doses [16]. Yang et al. discovered that PS oxidation can be used for degrading AO7 in the presence of suspended granular activated carbon (GAC); they observed a synergistic effect in a GAC/PS combined system [17]. The results of these studies showed the potential of PS to degrade organic contaminants.

Metal oxides, particularly iron oxides, are promising heterogeneous catalysts because of their natural abundance, low cost, and environmentally friendly properties, and they can be used as PS activators [18]. Iron oxides exist in the environment in different forms. The synthesis and use of iron oxide nanomaterials with novel properties and functions have been widely studied; their nanoscale size and superparamagnetism are responsible for their novel properties. Recently, there has

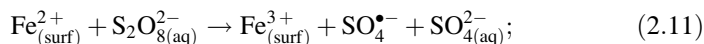
been considerable interest in the environmental applications of magnetite (Fe_3O_4) and ZVI, such as the oxidation of organic compounds in dye-contaminated wastewater [14, 19]. This compound improves the PS oxidation properties by accelerating the degradation rate through the formation of $\text{SO}_4^{\bullet-}$. Lin et al. investigated the substantial conversion of the azo dye AO7 to sodium sulfanilamide and 1-amino-2-naphthol by using a Fe_3O_4 catalyst activated by peroxydisulfate in an electro/ Fe_3O_4 /peroxydisulfate process, and they found that the Fe_3O_4 particles were stable and reusable [20]. Zhu et al. reported that core-shell Fe- Fe_2O_3 nanostructure (FN) materials can be used as catalysts in the catalytic oxidation of methyl orange in aqueous solution. They also found that the conversion of methyl orange reached 90 % in an FN/ $\text{Na}_2\text{S}_2\text{O}_8$ process after 10 min [21]. Yan et al. observed that complete treatment eliminated sulfamonomethoxine highly efficiently within 15 min when 2.4 mmol/L Fe_3O_4 magnetic nanoparticles were used as the heterogeneous activator of 1.2 mmol/L PS [22].

The nanoparticles (<100 nm) discussed in this chapter are ZVI particles, and they exhibit a typical core-shell structure. The core consists primarily of zero-valent or metallic iron, and the mixed-valent [i.e., Fe(II) and Fe(III)] oxide shell forms as a result of the oxidation of the metallic iron. Iron typically exists in the environment as Fe(II)- and Fe(III)-oxide, and therefore, ZVI is a manufactured material. Thus far, applications of ZVI have been based primarily on the electron-donating properties of ZVI. Under ambient conditions, ZVI is reactive in water and can serve as an excellent electron donor; these qualities make it a versatile remediation material. Moreover, ZVI is a highly reactive material and is used for remediating various pollutants. Because ZVI has a considerably low standard reduction potential ($\text{Fe}^{2+} + 2e^- = \text{Fe}^0$, $E_0 = -0.447$ V; $\text{Fe}^{3+} + 3e^- = \text{Fe}^0$, $E_0 = -0.037$), elemental iron is thermo-dynamically stable in oxide forms under normal conditions. The pathways for reducing contaminants involve (i) adsorption of contaminants on the surface of ZVI, (ii) direct reduction of the adsorbed contaminants, and (iii) catalytic reduction by Fe(II) at the interface of ZVI and target products. The nanoscale ZVI particles show high surface-to-volume ratios and high surface activity [23]. However, the use of nano-zero-valent iron (nZVI) has a drawback: the formation of aggregates with the passage of time reduces the activity of nZVI [24]. In the past few years, researchers have focused on stabilizing nZVI and reducing the cost, thereby increasing the use of nZVI in environmental technologies. As an Fe^{2+} source, ZVI has been widely used for activating PS to produce $\text{SO}_4^{\bullet-}$ under aerobic conditions, anaerobic conditions, or through the direct reaction between nZVI and PS in accordance with the following equations [25]:





In addition, heterogeneous activation of PS involving direct transfer of electrons or surface bound Fe^{2+} from ZVI to PS may be an alternative mechanism (2.10 and 2.11, respectively) [26]. An advantage of using ZVI is that the generation of ferrous iron and recycling of ferric iron at the ZVI surface can prevent the accumulation of excess ferrous iron and reduce the precipitation of iron hydroxides during the reaction (2.12) [27].



So far, numerous preliminary studies have reported the synergistic effect of ZVI on persulfate and the remediation of pollutants in aqueous solutions. The findings have suggested that the presence of ZVI in a PS-water system can considerably enhance the oxidation of pollutants [28]. In particular, nZVI shows a surface area reactivity that is approximately 100 times greater than that of micro-zero-valent iron powder. Moreover, nZVI has been found to exhibit the greatest capability to activate PS in the process of degradation of pollutants [29]. However, to the best of our knowledge, no study has been conducted on the simultaneous and synergistic nZVI activation of PS for the removal of PAHs in sediments. The nZVI obtained in the current study was characterized by using environmental scanning electron microscopy coupled with energy dispersive spectroscopy (ESEM-EDS), X-ray diffraction (XRD), and a vibration magnetometer. This chapter reports a study on nZVI activation of PS for the removal of PAHs from sediments, performed at the National Kaohsiung Marine University, with the removal performance and associated factors as major considerations.

2.2 Removal of PAHs from Sediments by Using Magnetic Nanoparticles

Polycyclic aromatic hydrocarbons (PAHs) are a ubiquitous group of several hundred chemically-related environmentally persistent organic compounds with various structures and varied toxicity. They tend to persist in the environment and are widely found in natural media, such as soils, sediments, water, and air. In particular, because of their hydrophobic nature and low water solubility, they can rapidly associate with sediments [30–32]. The effect of PAHs is usually widespread and permanent in environmental media, and thus, PAHs can be eventually deposited and persist in bed sediment (as a sink) in the aquatic system. Their presence in

environmental matrices is of grave concern because of their high toxicity, carcinogenic effects, and environmental persistence. Such contamination may pose a risk of indirect exposure to humans exposed to PAHs through the consumption of foods [33, 34]. Among the various remediation techniques for PAH removal, chemical oxidation is considered promising and can overcome many limitations of other methods for the remediation of aquatic matrices contaminated by recalcitrant PAHs. In other words, the strong sorption of PAHs to a solid phase reduces their availability for microbial attacks, and high-molecular-weight PAHs (with 5 or 6 aromatic rings) are more recalcitrant to biological degradation [35, 36]. Therefore, attention focused on the development of technologies for the control of PAHs in the environment has been increasing.

The use of chemical techniques for PAH remediation has generated considerable interest, because these methods can offer a rapid and aggressive alternative that is less sensitive to the type and concentration of contaminant compared with biological processes. Therefore, the activation of PS by ferrous ions is known to be effective for PAH removal. The use of $\text{SO}_4^{\bullet-}$ prevents the treatment from producing large amounts of slurry (which are produced in the Fenton process). Activated PS used for PAH oxidation can be effective for up to 24 h [3, 37]. Iron is a typical candidate transition metal for environmental applications, and ferric ions are easily precipitated as iron hydroxides at neutral pH [38]. Owing to the buffer capacity of geological materials such as clay and sediment, their ability to maintain a low pH in a solution of ferrous ions is limited in practice. Therefore, numerous chelating agents are employed to maximize the catalytic activity of ferrous ions by preventing the loss of Fe(II); the chelating agents bind the ferrous ions to the hydrophilic sites of natural organic matter [39, 40]. Moreover, the use of nZVI overcomes the disadvantages of losing Fe(II).

Contaminated sediments were collected from the industrial port of southern Kaohsiung, Taiwan. This area receives from a steel refinery effluent that is polluted by organic and inorganic compounds. Several sediment samples were taken from the first 15–20 cm layer at the bottom with following collection (using an Ekman Dredge Grab Sampler (6" × 6" × 6"), from Jae Sung International Co., Taiwan), samples were immediately scooped into glass bottles that had been pre-rinsed with *n*-hexane, and stored in a refrigerator until they were used. The samples were free-dried for 72 h and sieved through a 0.5 mm mesh to ensure uniformity and kept at $-20\text{ }^\circ\text{C}$ in amber glass bottles that had been pre-rinsed with *n*-hexane and covered with aluminum foil until further processing and analysis. Table 2.1 presents the initial concentrations of the PAHs in the sediment. According to the number of aromatic rings, the 16 PAHs were divided into three groups: (i) 2- and 3-ring, (ii) 4-ring, and (ii) 5- and 6-ring PAHs. The PAHs pollutant level classification was suggested by Baumardi et al. [41]: (i) low, 0–100 ng/g; (ii) moderate, 100–1000 ng/g; (iii) high, 1000–5000 ng/g; and (iv) very high, >5000 ng/g. Sediments from river mouth region can be characterized as moderate to high PAHs pollution. The results can be used for regular monitoring, and future pollution prevention and management should target the various industries in this region for reducing pollution. Moreover, the results of

Table 2.1 Initial concentration of PAHs in sediment

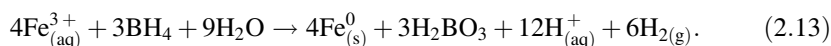
PAHs	Chemical formula	Concentration (ng/g)
<i>2-ring</i>		
1. Naphthalene (NA)	C ₁₀ H ₈	273
<i>3-ring</i>		
2. Acenaphthalene (ACY)	C ₁₂ H ₈	160
3. Acenaphthene (ACE)	C ₁₂ H ₁₀	265
4. Fluorene (FL)	C ₁₃ H ₁₀	238
5. Phenanthrene (PH)	C ₁₄ H ₁₀	392
6. Anthracene (AN)	C ₁₄ H ₁₀	230
<i>4-ring</i>		
7. Fluoranthene (FLU)	C ₁₆ H ₁₀	503
8. Pyrene (PY)	C ₁₆ H ₁₀	525
9. Benzo[a]anthracene (BaA)	C ₁₈ H ₁₂	235
10. Chrysene (CH)	C ₁₈ H ₁₂	245
<i>5-ring</i>		
11. Benzo[b]fluoranthene (BbF)	C ₂₀ H ₁₂	224
12. Benzo[k]fluoranthene (BkF)	C ₂₀ H ₁₂	197
13. Benzo[a]pyrene (BaP)	C ₂₀ H ₁₂	273
14. Dibenzo[a,h]anthracene (DA)	C ₂₂ H ₁₄	95
<i>6-ring</i>		
15. Indeno [1,2,3-cd]pyrene (IP)	C ₂₂ H ₁₂	193
16. Benzo[g,h,i]perylene (BP)	C ₂₂ H ₁₂	176
∑LPAHs: Total Light PAHs (1–7)	–	1559
∑HPAHs: Total Heavy PAHs (8–16)	–	2667
∑PAHs: Total PAHs	–	4226

previous studies carried out by the authors on the distribution of PAHs contained in the surface layers of harbor sediment show that sediment surface layers near river mouths have relatively higher PAHs concentrations [42]. This indicates that PAHs are borne by river flow and municipal runoffs to accumulate in the harbor sediment.

The concentration of PAHs (i.e., naphthalene (NA), acenaphthylene (ACE), acenaphthene (AC), fluorene (FL), phenanthrene (PH), anthracene (AN), fluoranthene (FLU), pyrene (PY), benzo[a]anthracene (BaA), chrysene (CH), benzo[b]fluoranthene (BbF), benzo[k]fluoranthene (BkF), benzo[a]pyrene (BaP), indeno [1,2,3-cd]pyrene (IP), dibenzo[a,h]anthracene (DBA), and benzo[g,h,i]perylene (BP)) in the extracts were analyzed using a GC (HP Agilent Technologies 6890 Gas Chromatography, USA), equipped with an Agilent 5975 mass selective detector (MSD). The GC was equipped with an Agilent 7683B split/splitless injector (splitless time: 1 min; flow: 60 mL/min); injector temperature was maintained at 300 °C. The transfer line and ion source temperature were 280 and 230 °C. Column being used to separate the PAH compounds was HP-5MS capillary column

(Hewlett-Packard, Palo Alto, CA, USA) with $30\text{ m} \times 0.25\text{ mm i.d} \times 0.25\text{ }\mu\text{m}$ film thickness. The carrier gas was helium at a constant flow rate of 1 mL/min . The column temperature was initially kept at $40\text{ }^\circ\text{C}$ for 1 min , gradually raised to $120\text{ }^\circ\text{C}$ at the rate of $25\text{ }^\circ\text{C/min}$, then increased to $160\text{ }^\circ\text{C}$ at the rate of $10\text{ }^\circ\text{C/min}$ and finally elevated to $300\text{ }^\circ\text{C}$ (final temperature was held for 15 min) at the rate of $5\text{ }^\circ\text{C/min}$. Mass spectrometer was operated in Selected Ion Monitoring (SIM) mode in the electron impact mode at 70 eV . The concentration of individual PAH in the solvent was quantified using the internal standard calibration method with 5-point standard curves ($r^2 = 0.99$). Figure 2.1 shows the total ion chromatogram for this analysis. The identities of 16 PAHs were confirmed by the retention time and abundance of quantification/confirmation ions in the authentic PAHs standards. A time sequence of PAH chromatographs showed that all of these peaks were found with respect to retention time of existing molecules.

nZVI particles were prepared by mixing equal volumes of 0.94 M NaBH_4 and 0.18 M FeCl_3 , following the reaction [43]:



The surface chemistry of magnetic nanoparticles is complex and plays a crucial role in various interactions. In this study, ESEM-EDS observations of the nanoparticles indicated that the nZVI formed small spherical particles, indicating a high degree of nanoparticle dispersion (Fig. 2.2). XRD spectra were used to characterize the phase structure of the nZVI nanostructures (Fig. 2.3). The broad peak reveals the existence of an amorphous phase of iron. The characteristic peak at $2\theta = 44.9^\circ$ confirmed the presence of fresh nZVI [44]. Figure 2.4 shows the magnetic hysteresis loops of fresh nZVI with a magnetic field cycle between -10

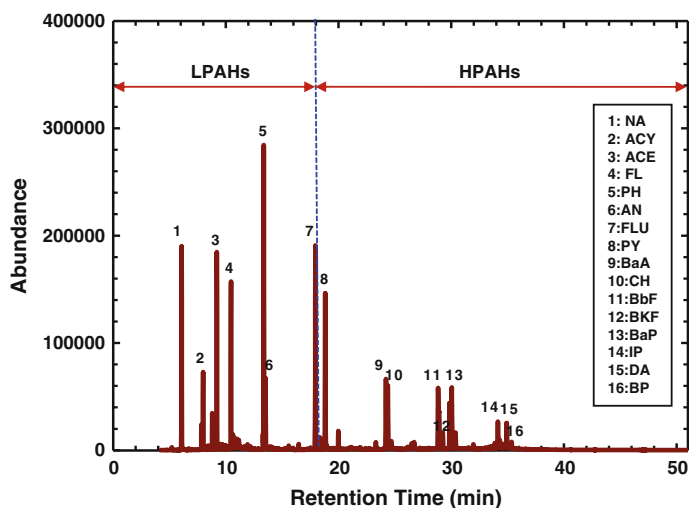


Fig. 2.1 Chromatograms of individual PAHs in slurry system are based on the measurements by GC-MS

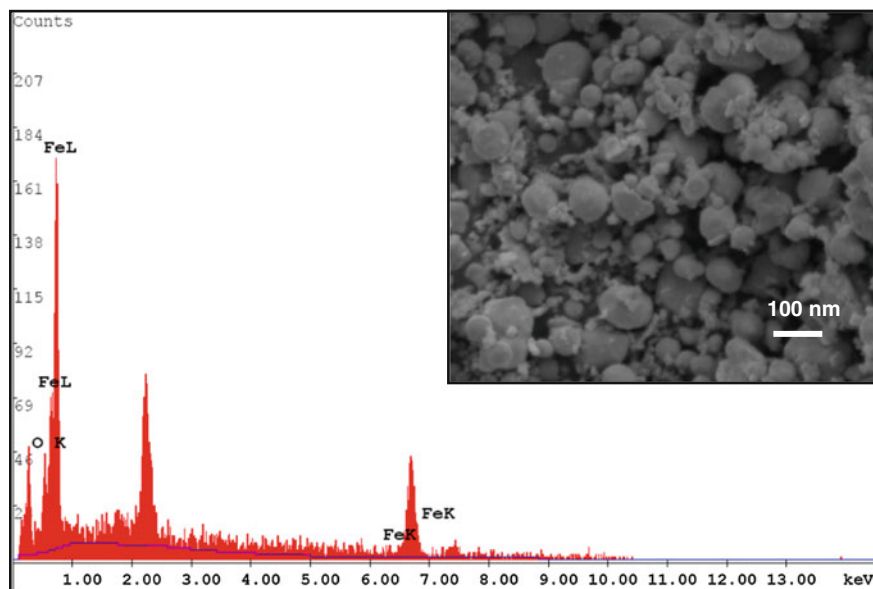
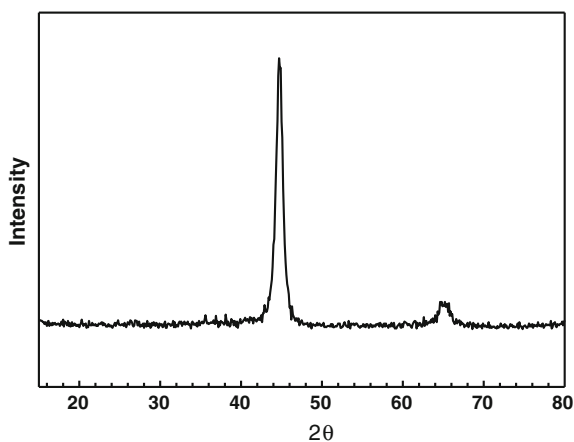


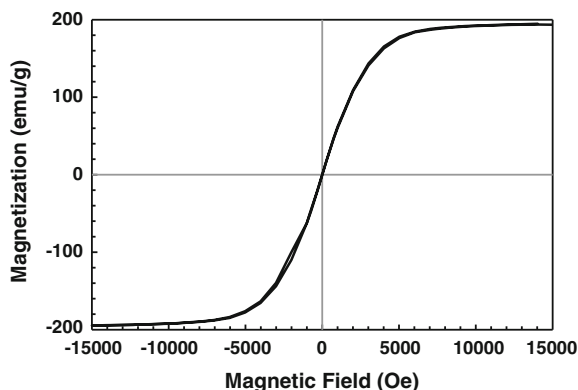
Fig. 2.2 ESEM-EDS photographs of nZVI particle at 10,000 \times in the PAH degradation reaction

Fig. 2.3 XRD pattern of nZVI particles used in the PAH degradation reaction



and +10 kOe at 300 K. The fresh nZVI showed strong magnetic properties at room temperature, and the $M-H$ hysteresis curves passed the original spot, revealing the super-paramagnetic nature of magnetite nZVI materials. The saturation magnetization of the fresh and used samples was 194 emu/g, suggesting that nZVI can be easily separated from an aqueous phase by applying an external magnetic field.

Fig. 2.4 Magnetic hysteresis loops (at 300 K) of the nZVI particles used in the PAH degradation reaction



The effectiveness of PS oxidation for the degradation of PAHs in sediments was evaluated through a series of batch experiments [45, 46]. The results revealed that a high degree of PAH oxidation occurred at high PS concentrations [45]. At the highest PS dose of 170 g/L, the PAHs removal efficiency was only 39.1 %. Similarities were observed between persulfate and permanganate in terms of the degradation of individual PAH compounds, namely the degradation rates of 3-ring and 4-ring PAH compounds were higher for a higher oxidant dose. It was found that the highest PS dose of 170 g/L can remove 3-ring (4-ring) PAH compounds with a maximum efficiency of 30.8 % (50.2 %).

These results and the results presented in the literature [45, 46] show that ZVI plays two roles in the oxidation of PAHs by PS in the PS/nZVI system. One role is as a Fe^{2+} source; it reacts with $\text{S}_2\text{O}_8^{2-}$ and other compounds and reduces Fe^{3+} to produce Fe^{2+} . To evaluate the effect of the initial nZVI concentration on the PAH removal efficiency, experiments were conducted by changing nZVI loading at a fixed initial PS concentration of 170 g/L. The range of the nZVI dose used was 0.01–1 g/L. The degradation efficiency was 70.2, 78.3, 86.3, and 78.0 % for nZVI doses of 0.01, 0.1, 0.5, and 1 g/L, respectively. These results demonstrated that a larger amount of nZVI resulted in the production of a larger amount of ferrous ions, resulted in higher PAH degradation. In addition, the consumption of PS was proportional to the amount of available Fe^{2+} , which was immediately consumed by PS to generate $\text{SO}_4^{\bullet-}$ for the degradation of PAHs. Similar to the thermal activation of PS, the decomposition of PS was characterized by an initial fast stage in the first 18 h, after which the PS decomposition leveled off. However, increasing the nZVI dose up to 1 g/L reduced the PAH degradation efficiency. The reason was likely that excessive Fe^{2+} could also act as a scavenger of $\text{SO}_4^{\bullet-}$ [14]. Similar to other studies, an optimal value of the ratio of persulfate to nZVI may exist for the slurry treatment system. For the conditions employed in our study (1 g of soil and 25 mL of solution), the optimal conditions to achieve the highest PAH degradation were found to be 0.5 g/L of nZVI and 170 g/L of PS, which correspond to a sediment/PS/nZVI weight ratio of 1/4.25/0.0125.

Moreover, the activation of PS to generate $\text{SO}_4^{\bullet-}$ is more effective when Fe^{2+} is supplied continuously compared with a one-time supply [45, 46]. In particular, the oxidation of sorbed organic compounds such as PAHs can be inhibited by high organic matter content in sediments. Thus, the remediation of hydrophobic compounds in sediments with high organic content requires high amounts of a strong oxidant, powerful oxidation conditions, and a long reaction time. Our results showed that nZVI is a long-lasting activating agent that can meet the requirements of sustained oxidation of PS. In addition, the final pH fluctuated in the range of 5.6–6.8 because of the formation of OH^- by iron corrosion after the pH rapidly decreased to the range of 3–4 at an early stage because of the formation of SO_4^{2-} . In general, $\text{SO}_4^{\bullet-}$ was more selective than HO^\bullet in oxidizing organic compounds. During the decomposition of organic compounds in the ZVI system, the corrosion of ZVI was strongly influenced by the H^+ concentration [14]. Therefore, the pH of the treated sediments was among the crucial variables, since treated sediments should exhibit optimal functions in a marine ecological system.

2.3 Conclusions

This study used magnetic nanoparticles and heterogeneous persulfate oxidation for degrading organic compounds. The oxidation of organic compounds such as PAHs sorbed on the surface of the nanoparticles could be inhibited by high organic matter content in the sediment. Thus, the remediation of hydrophobic compounds in sediments with high organic content requires a large amount of a stable oxidant. The use of PS eliminated PAH compounds, and PS was consumed by non-target compounds in sediments. In general, the degradation was limited, which can be explained by considering several parameters: PAH availability, PAH reactivity, and sediment characteristics. Moreover, the reaction of PS with PAHs is generally slow at ambient temperature, and activation of PS is necessary to accelerate the oxidation process. Therefore, nZVI was used to activate PS for the oxidation of representative PAHs in sediments. An adequate PS dose must be provided because it is the source of sulfate radicals, which are responsible for the degradation of PAHs. An increase in the nZVI dose resulted in an increase in the PAH degradation efficiency because of increased activation of PS. As a PS-activating agent, nZVI is more effective and longer-lasting than Fe^{2+} and potentially more suitable for ex situ treatment of hydrophobic compounds such as PAHs that are strongly absorbed on the sediment. Furthermore, according to the present experimental data, magnetic nZVI showed superior performance in environmental treatment applications for organic compounds, and it may therefore facilitate the improvement of industrial processes for meeting increasingly stringent regulations pertaining to sediment discharges containing other organic compounds and help achieve environmental sustainability. In the future, additional methods for activating PS should be studied, and nZVI-activated PS is expected to be widely used for the treatment of organic compounds for the remediation of sediments.

References

1. A.S. Bokare, W. Choi, *J. Hazard. Mater.* **275**, 121 (2014)
2. M. Sievers, *Treatise Water Sci.* **4**, 377 (2011)
3. S.G. Venny, H.K. Ng, *Chem. Eng. J.* **180**, 1 (2012)
4. C. Cuyppers, T. Grotenhuis, J. Joziassse, W. Rulkens, *Environ. Sci. Technol.* **34**, 2057 (2000)
5. H. Long, Y. Zhang, Y. Lei, *Sep. Purif. Technol.* **118**, 612 (2013)
6. A. Tsitonaki, B. Petri, M. Crimi, H. Mosbaek, R.L. Siegrist, P.L. Bjerg, *Critic. Rev. Environ. Sci. Tech.* **40**, 55 (2010)
7. X.R. Xu, S. Li, Q. Hao, J.L. Liu, Y.Y. Yu, H.B. Li, *Inter. J. Environ. Bioenergy* **1**, 60 (2012)
8. C.H. Yen, K.F. Chen, C.M. Kao, S.H. Liang, T.Y. Chen, *J. Hazard. Mater.* **186**, 2097 (2011)
9. S.H. Do, Y.J. Kwon, S.H. Kong, *J. Hazard. Mater.* **182**, 933 (2010)
10. A. Ghauch, A.M. Tuqan, N. Kibbi, S. Geryes, *Chem. Eng. J.* **213**, 259 (2012)
11. K.C. Huang, Z. Zhao, G.E. Hoag, A. Dahmani, P.A. Block, *Chemosphere* **61**, 551 (2005)
12. D. Zhao, X. Liao, X. Yan, S.G. Huling, T. Chai, H. Tao, *J. Hazard. Mater.* **254–255**, 228 (2013)
13. C.J. Liang, C.J. Bruell, M.C. Marley, K.L. Sperry, *Soil Sedim. Contam.* **12**, 207 (2003)
14. X. Wang, L. Wang, J. Li, J. Qiu, C. Cai, H. Zhang, *Sep. Purif. Technol.* **122**, 41 (2014)
15. T.D. Nguyen, N.H. Phan, M.H. Do, K.T. Ngo, *J. Hazard. Mater.* **185**, 653 (2011)
16. X.R. Xu, X.Z. Li, *Sep. Purif. Technol.* **72**, 105 (2010)
17. S.Y. Yang, X. Yang, X.T. Shao, R. Niu, L.L. Wang, *J. Hazard. Mater.* **186**, 659 (2011)
18. C. Tan, N. Gao, W. Chu, C. Li, *Sep. Purif. Technol.* **95**, 44 (2012)
19. S.C.N. Tang, I.M.C. Lo, *Water Res.* **47**, 2613 (2013)
20. H. Lin, H. Zhang, L. Hou, *J. Hazard. Mater.* **276**, 182 (2014)
21. L. Zhu, Z. Ai, W. Ho, L. Zhang, *Sep. Purif. Technol.* **108**, 159 (2013)
22. J. Yan, M. Lei, L. Zhu, M.N. Anjum, J. Zou, H. Tang, *J. Hazard. Mater.* **186**, 1398 (2011)
23. J. Cao, P. Clasen, W.X. Zhang, *J. Mater. Res.* **20**, 3238 (2005)
24. C. Noubactep, S. Caré, R. Crane, *Water Air Soil Pollut.* **223**, 1363 (2012)
25. Y. Furukawa, J.W. Kim, J. Watkins, R.T. Wilkin, *Environ. Sci. Technol.* **36**, 5469 (2002)
26. S.Y. Oh, D.S. Shin, *Soil Sedim. Contam.* **23**, 180 (2014)
27. D.H. Bremner, A.E. Burgess, D. Houlemare, K.C. Namkung, *Appl. Catal. B: Environ.* **63**, 15 (2006)
28. I. Hussain, Y. Zhang, S. Huang, *Appl. Catal. B: Environ.* **4**, 3502 (2014)
29. H. Li, J. Wan, Y. Ma, Y. Wang, M. Huang, *Chem. Eng. J.* **237**, 487 (2014)
30. C.C. Lin, S.J. Chen, K. Lin, M. Huang, *Environ. Sci. Technol.* **42**, 4229 (2008)
31. J.H. Tsai, S.J. Chen, K.L. Huang, Y.C. Lin, W.J. Lee, C.C. Lin, W.Y. Lin, *J. Mater. Res.* **179**, 237 (2010)
32. J.H. Tsai, S.J. Chen, K.L. Huang, W.Y. Lin, W.J. Lee, C.C. Lin, L.T. Hsieh, J.Y. Chiu, W.C. Kuo, *Sci. Total Environ.* **446–447**, 195 (2014)
33. M.M. O'Mahony, A.D.W. Dobson, J.D. Barnes, I. Singleton, *Chemosphere* **63**, 307 (2006)
34. B. Antizar-Ladislao, J. Lopez-Real, A.J. Beck, *Waste Manage.* **25**, 281 (2005)
35. P. Henner, M. Schiavon, J.L. Morel, E. Lichtfouse, *Analysis* **56**, 281 (1997)
36. P. Haapea, T. Tuhkanen, *J. Hazard. Mater.* **B136**, 244 (2006)
37. L.L. Johnson, T.K. Collier, J.E. Stein, *Aquat. Conserv. Mar. Freshw. Ecosyst.* **12**, 517 (2006)
38. P.K. Kakarla, T. Andrews, R.S. Greenberg, D. Zervas, *Remediat. J.* **12**, 23 (2002)
39. S. Tao, Y.H. Cui, J. Cao, F.L. Xu, R. Dawson, B.G. Li, *J. Environ. Sci. Health B* **37**, 141 (2002)
40. F. Vicente, J.M. Rosa, A. Santos, A. Romero, *Chem. Eng. J.* **172**, 689 (2011)
41. P. Baumar, H. Budzinski, P. Garrigues, *Environ. Toxicol. Chem.* **17**, 765 (1998)
42. C.D. Dong, C.F. Chen, C.W. Chen, *Mar. Pollut. Bull.* **85**, 665 (2014)

43. Y.P. Sung, X.Q. Li, W.X. Zhang, H.P. Wang, *Colloid. Surf. A: Physicochem. Eng. Aspects* **308**, 60 (2007)
44. Y.P. Sung, X.Q. Li, J. Cao, W.X. Zhang, H.P. Wang, *Adv. Colloid Interf. Sci.* **120**, 46 (2006)
45. C.F. Chen, N.T. Binh, C.W. Chen, C.D. Dong, *J. Air Waste Manage. Assoc.* **65**, 375 (2015)
46. C.W. Chen, N.T. Binh, C.M. Hung, C.F. Chen, C.D. Dong, *J. Adv. Oxid. Technol.* **18**, 15 (2015)

Chapter 3

Microstructure Optimization of Pt/C Catalysts for PEMFC

A.A. Alekseenko, V.E. Guterman and V.A. Volochaev

Abstract Development of optimal methods for the synthesis and for the control of multi-level microstructure of Pt/C materials is essential for the preparation of electrocatalysts, which have high activity and durability. Nucleation/growth of metallic nanoparticles could take place in the liquid phase, on the surface and in the pores of the carbon microparticles during the process of chemical reduction of Pt precursor in a liquid phase. These processes are sensitive to the composition of the medium, temperature, pH, mass transfer conditions, and other factors. On the one hand, that creates more opportunities to search the optimal conditions of synthesis. On the other hand, it makes difficult to control the reproducibility of the composition/structure of Pt/C. Pt/C materials with metal fraction from 10 to 20 wt% were obtained in this work. An average size of Pt crystallites was from 1.0 to 5.5 nm, depending on the method and conditions of synthesis. Electrochemically active surface area of catalysts measured by hydrogen electrodesorption method, was from 32 to 152 m²/g_{Pt}.

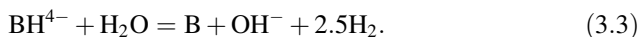
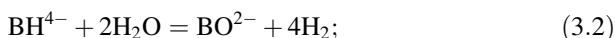
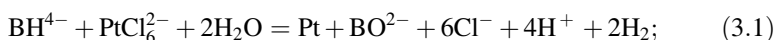
3.1 Introduction

Platinum carbon catalyst (Pt/C) is widely used for the manufacturing of catalytic layer in the low-temperature fuel cells. Supported Pt/C catalyst is a self-organized system, consisting of a variety of platinum or Pt-alloy nanoparticles (NPs), which are disposed on the surface and in the pores of carbon carrier microparticles, nanofibres or nanotubes [1]. Nanoparticles are characterized by certain dispersion in the size and in the spatial distribution [2]. The electrochemically active surface area (ECSA) of the Pt/C electrocatalyst is an important indicator that determines the mass activity of these materials [2]. Reduction of the average size of Pt nanoparticles can lead to increase in ECSA and, at the same time, to decrease in stability

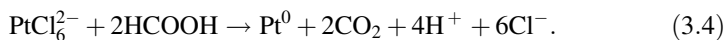
A.A. Alekseenko (✉) · V.E. Guterman · V.A. Volochaev
Chemistry Faculty, Southern Federal University, Rostov-on-Don, Russia
e-mail: an-an-alekseenko@yandex.ru

and specific activity of the catalyst during operation of the fuel cell. The causes of, so-called, “negative influence of the size effect” to the specific characteristics of Pt/C catalysts are actively discussed in the literature [1–3]. However, an actual scientific and technical problem is to find and optimize the methods for the synthesis of Pt/C catalysts, which demonstrate high mass activity in the reactions of hydrogen electrooxidation and oxygen electroreduction [1–4].

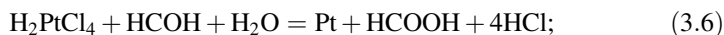
Methods of the chemical reduction of platinum precursors in a liquid phase, apparently, are the simplest way of Pt/C preparation. Different compounds could be used as a reducing agent for the synthesis of Pt/C: sodium borohydride [5–7], formaldehyde [6, 7], formic acid [8, 9], ethylene glycol [5, 10, 11], etc. Each of these reducing agents demands specific temperature, pH and synthesis conditions. That is the reason why it is very difficult to predict a key factor which affects the preparation of a catalyst with high activity or/and stability. Apparently, borohydride method of synthesis is the most simple to carry out the process, which proceeds at room temperature. Sodium borohydride is a highly reactive compound that is why the reduction of platinum passes quickly. The redox reaction between sodium borohydride and PtCl_6^{2-} may be expressed in several equations:

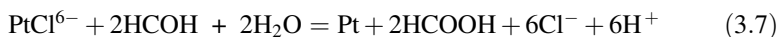


Unfortunately, the high reaction rate makes it difficult to control the processes of phase formation. A consequence of this is a problem of control the size and size distribution of nanoparticles. Use of formic acid as a reducing agent is interesting, too. This is due to the fact, that during redox reaction HCOOH does not form stable substances which pollute the surface of the Pt/C catalyst [8, 9].



Method of formaldehyde synthesis of Pt/C includes a two-stage reduction: $\text{Pt(IV)} \rightarrow \text{Pt(II)} \rightarrow \text{Pt}^0$ in an alkaline medium [12]. It is important that during the synthesis, heterogeneous and homogeneous (in solution) nucleations of platinum take place simultaneously, therefore necessary to add a strong electrolyte for the final deposition of nanoparticles on the surface of the carbon support. In [12], this method was used to obtain a catalyst with an average size of NPs Pt 2.6 nm. The redox reaction between PtCl_6^{2-} and formaldehyde can be expressed as follows:





Ethylene glycol is the solvent and reducing agent in the polyol synthesis method. In this case, some parameters such as the value of pH, temperature, the ratio of water and ethylene glycol in the solution influence on microstructure of the catalyst. Authors of [10] assume that the glycolate anions, adsorbed on the surface of the metal, act as a stabilizer and increase electrostatic repulsive forces between the metal particles. Change of pH can affect the concentration of the deprotonated form of glycolic acid and, therefore, influences on the size of the platinum nanoparticles:



Despite a large number of publications describing the use of a reducing agent (the method of chemical reduction) for Pt/C materials, definite optimal variant of the synthesis procedure is not selected (Table 3.1).

It is known that number and activity of centers at which nucleation occurs depend on the properties and the surface area of the support [13–17]. The literature describes the results of studies of the material microstructure in which the platinum nanoparticles fix on the surface of non-carbon carrier (such as, for example, oxides of iron and silica dioxide hydrate— $\text{Fe}(\text{OH})_2$ [15, 16] и $\text{H}_2\text{SiO}_3 \cdot n\text{H}_2\text{O}$ [17–19]). The use of such substrates (support, carrier) in electrocatalysis is impossible due to the low electronic conductivity, but these materials may be interesting as an intermediate support for the platinum nanoparticles deposition.

This conclusion is based, in particular, on works in which the freshly prepared sols and gels having high surface area with a large number of active centers were studied [19, 20]. Dissolving gel (sol) and reprecipitation of nanoparticles on the carbon support is the following step of the Pt/C catalyst synthesis.

Table 3.1 Some characteristics of the Pt/C catalysts obtained using different reducing agents

Pt fraction, wt%	Average diameter of crystallites, nm (XRD data)	ECSA, $\text{m}^2 \text{g}_{\text{Pt}}^{-1}$	Reducing agents	References
20	4.1	68	EG	[5]
20	4.8	58	NaBH_4	[5]
20	14.7	31.3	NaBH_4	[6]
20	17.8	16.4	HCHO	[6]
46	5.3	37.9	HCHO	[7]
46	6.1	35.6	NaBH_4	[7]
20	4.1	81	HCOOH	[8]
20	3.3	108	E-TEK	[8]
20	6.5	21	HCOOH	[9]
20	2.3	59	E-TEK	[10]
20	2.1	52	EG	[10]
19.7	2.3	63	EG	[11]
11.3	2.0	66	EG	[11]

It is known that various components of medium can easily and firmly adsorb on the surface of Pt [21, 22]. At the same time, there is practically no information in literature about influence of the atmosphere on the microstructure of Pt/C catalysts obtained in liquid-phase synthesis. We suppose that the adsorption of gas molecules dissolved in the solution (for example, O₂ or CO), or the lack of such gases (Ar) can be one of the factors that effect to the nucleation, growth and coalescence of Pt nuclei.

The aims of this work are to study:

- (i) the effect of the nature of the reducing agent and liquid-phase synthesis conditions on the composition and microstructure of Pt/C catalysts;
- (ii) the development of new approaches to obtain Pt/C catalyst by forming the metal nuclei on the active centers of the intermediate carrier (support) with its subsequent “transfer” on microparticles of carbon support;
- (iii) the effect of the nature of the gas atmosphere on the composition and microstructure characteristics of synthesized Pt/C material.

3.2 Experimental

In this work, four Pt/C catalysts containing 20 wt% Pt were prepared using formaldehyde, sodium borohydride, formic acid and ethylene glycol as reductant, respectively, and their properties were characterized by thermogravimetry, XRD, TEM and CV.

The Pt/C materials were prepared by chemically reducing the metal precursors (H₂PtCl₆ · 6H₂O, Aurat, Moscow, Russia) from a carbon suspension based on water-organic solvents. Vulcan XC-72 (specific surface area of 250–280 m²/g) was used as the carbon support. All catalyst was filtered, washed and dried in air at 80 °C.

3.2.1 Reducing Agent—Formaldehyde (Sample F)

As it demonstrated in Fig. 3.1, at first 0.1 g of Vulcan XC-72 carbon powder was suspended in an aqueous solution of the appropriate amount of chloroplatinic acid. Then 0.5 ml of 37 % formaldehyde with a mole ratio of HCHO:PtCl₆²⁻—20:1 was added into the suspension. Thereafter, a 1 mol/l NaOH solution (H₂O:EG—1:1) was gradually added to the suspended mixture until the pH of the mixed solution reached 11–12. Then, the mixture was heated for 2 h under vigorous stirring. Finally, a strong electrolyte such as HCl solution was added as sedimentation promoters.

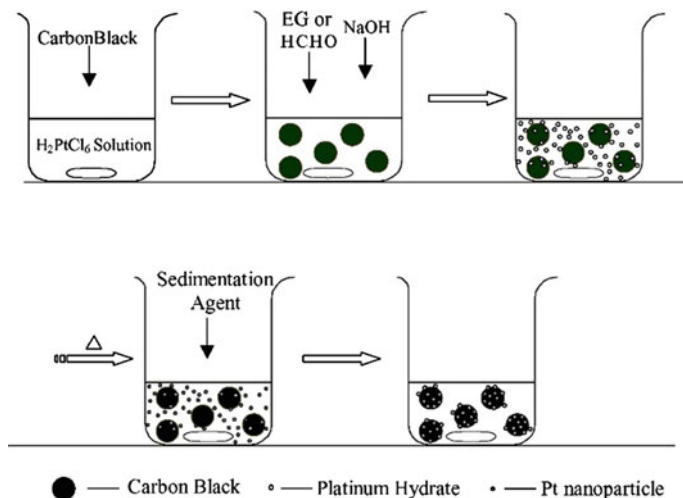


Fig. 3.1 Mechanism of chemical reduction of formaldehyde for Pt/C catalyst [12]

3.2.2 Reducing Agent—Sodium Borohydride (Sample BG)

The carbon carrier was mixed with 25 ml of ethylene glycol and 10 ml of bi-distilled water and then added the required amount of $H_2[PtCl_6] \cdot 6H_2O$. After ultrasonic homogenization of suspension and 30 min of magnetic stirring, pH was adjusted to 11 (concentrated NH_3), and within 5 min, 0.15 M solution of $NaBH_4$ was uniformly added. The suspension was maintained under constant stirring for 40 min.

3.2.3 Reducing Agent—Formic Acid (Sample FA)

A carbon support was mixed with 25 ml of 0.1 M solution of $HCOOH$, the suspension was homogenized by ultrasound. The suspension was heated to $90\text{ }^\circ\text{C}$ and a required amount of $H_2[PtCl_6] \cdot 6H_2O$ was added at constant stirring. The suspension was maintained 20 min at $90\text{ }^\circ\text{C}$ and 20 min without heating (constant stirring).

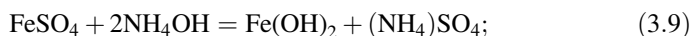
3.2.4 Reducing Agent—Ethylene Glycol (Sample EG)

A polyol method was used to prepare Pt/C electrocatalyst. Briefly, 100 mg of Vulcan were dispersed with solutions of H_2PtCl_6 in bi-distilled water and 8 vol% of 2-propanol. Then the pH of the mixture was set to a value of 6 using 0.5 M NaOH.

Suspension was mixed with 40 ml of ethylene glycol to initiate the reduction process. After that, the temperature of the mixture was kept constant at 80 °C for 2 h and then the heating was switched off and the solution was cooled down to room temperature.

3.2.5 *Preparation of Pt/C Materials Using Chemical Reduction with Following Reprecipitation*

An intermediate support was used initially for anchoring of Pt nanoparticles, High surface area of gels of $\text{Fe}(\text{OH})_2$ or $\text{H}_2\text{SiO}_3 \cdot n\text{H}_2\text{O}$ were initially formed in solution:



Then, at the appropriate pH, a solution containing Pt (IV) was added and, after 20 min of stirring, the excess of reductant HCOH (*Method 1*) or NaBH_4 (*Method 2*).

As a result, a significant proportion of Pt nanoparticles were formed (anchored) on the surface of non-carbon support. After the addition of carbon powder and 30 min of magnetic stirring, an excess of the reagent dissolving the hydroxide carrier was added. In the case of $\text{Fe}(\text{OH})_2$, it was 1 M solution of H_2SO_4 , and in the case of $\text{H}_2\text{SiO}_3 \cdot n\text{H}_2\text{O}$, it was 1 M NaOH. In the process of support dissolution, nanoparticles previously attached to the surface of hydroxide were sorbed by carbon surface (without ceasing mixing). Resulted Pt/C catalyst samples that were named as F' (reductant HCOH), BG' (intermediate carrier $\text{Fe}(\text{OH})_2$) and BG'' (intermediate carrier $\text{H}_2\text{SiO}_3 \cdot n\text{H}_2\text{O}$, reducing agent NaBH_4).

By implementing this method of synthesis, we thought that size and shape of the growing nanocrystals should depend on the properties of the carrier on which they form and on the character and intensity of the interaction between nanoparticle and support.

3.2.6 *Preparation of Pt/C Materials by Chemical Reduction in Different Gas Atmospheres*

To study the influence of the atmosphere composition (air, CO, Ar) on characteristics of Pt/C materials, the corresponding gas (CO or Ar) was bubbled into reaction mixture during 2 h in the course of the “formaldehyde” synthesis. Pt/C samples obtained in air, CO or Ar atmospheres were named F, F_{CO} and F_{Ar} , respectively.

Synthesis of the samples was repeated at least three times to assess the reproducibility of the characteristics obtained Pt/C catalyst.

The mass fraction of platinum (ω , Pt) in the Pt/C was determined by thermogravimetric mass residue (Pt) after combustion (800 °C, 40 min). The measurement accuracy is equal to ± 1.8 % (Table 3.2).

Optimization of the compositions and microstructures of catalysts requires appropriate experimental methods. X-ray diffraction (XRD) is one of the easiest and most commonly used methods for investigating the structural properties of Pt/C catalysts [23]. The average particle size was determined using the well-known Scherrer equation, as follows: $D = K\lambda/(\text{FWHM} \cdot \cos\theta)$, where λ is the wavelength, D is the volume-averaged particle size, $K = 0.89$ is a Scherrer constant, FWHM is the full width at half maximum, θ is the Bragg angle of the $[hkl]$ reflection [5, 8, 23]. The Scherrer equation is a simple method for calculating the average nanoparticle size using recently reported results [23], which revealed that more precise calculation methods do not have a significant effect on the value of D .

The XRD patterns of Pt/C materials supported on Vulcan XC-72 are shown in Figs. 3.2a, 3.3, and 3.4a. The peak around 25 corresponds to the (002) plane of graphitized carbon. Figures 3.2, 3.3, and 3.4 show the XRD patterns of Pt

Table 3.2 Characteristics of obtained Pt/C materials

Sample	Average diameter of crystallites, nm (XRD data)	Pt fraction, wt%	ECSA, $\text{m}^2 \text{g}^{-1}(\text{Pt})$
BG	5.5	19	37 ± 4
FA	4.9	17	54 ± 4
EG	2.0	19	99 ± 10
F	1.4	18	128 ± 13
F _{CO}	1.0	13	152 ± 15
F _{Ar}	1.1	20	110 ± 11
F'	4.2	19	32 ± 3
BG'	2.9	10	54 ± 5
BG''	4.5	10	35 ± 4

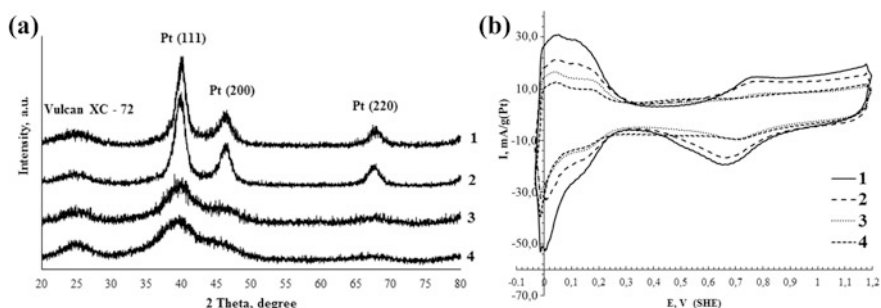


Fig. 3.2 **a** XRD patterns of samples Pt/C materials obtained using various reducing agents: 1 BG, 2 FA, 3 EG and 4 F; **b** cyclic voltammograms of Pt/C electrocatalysts obtained using various reducing agents: 1 F, 2 EG, 3 FA, 4 BG. Potential scan rate is 20 mV/s (2nd cycle)

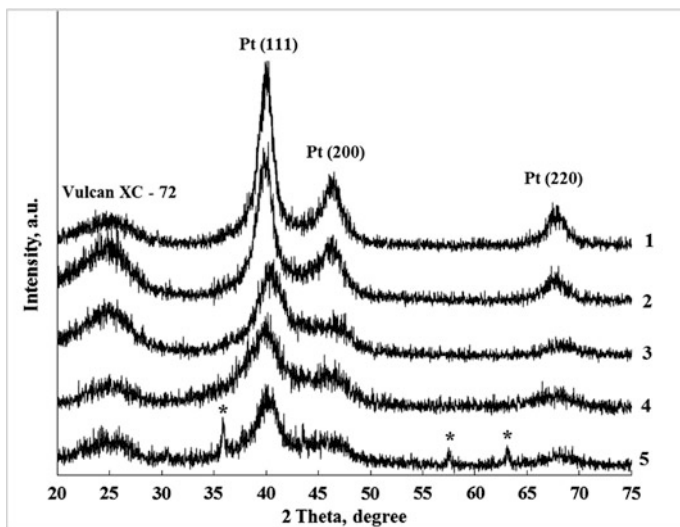


Fig. 3.3 XRD patterns of samples obtained in the reduction of Pt (IV) according to standard methods (1 BG, 4 F) by using as an intermediate support $\text{Fe}(\text{OH})_2$ (3 BG', 5 F') and $\text{H}_2\text{SiO}_3 \cdot n\text{H}_2\text{O}$ (2 BG''); asterisk marks the reflected phase Fe_3O_4

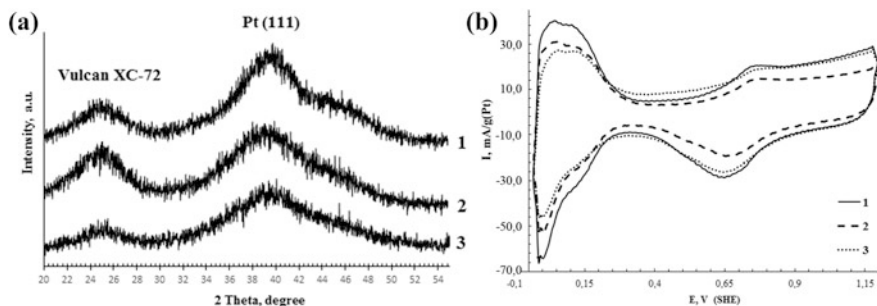


Fig. 3.4 a) X-ray diffractograms of Pt/C electrocatalysts: 1 F, 2 F_{CO} , 3 F_{Ar} ; b) cyclic voltammograms of Pt/C electrocatalysts obtained in different gas-atmospheres: 1 F_{CO} , 2 F, 3 F_{Ar} . Potential scan rate is 20 mV/s (2nd cycle)

crystalites on Vulcan XC-72. The diffraction peaks which locate at 2θ value of 39.6, 46.3 and 67.4 are assigned to (111), (200) and (220) planes, respectively, characteristic for FCC crystal structure of platinum.

The active surface area was determined on a stationary electrode using the cycling voltammetry method. Measurements were performed in three-electrode cells at room temperature; a saturated silver-chloride electrode was used as the reference electrode. All potentials in this work are referenced versus a standard hydrogen electrode (SHE). A 0.1 M HClO_4 solution saturated with Ar at atmospheric pressure was used as an electrolyte.

Typically, 6 mg of the electrocatalyst was ultrasonically suspended in 0.9 ml of isopropanol and 0.1 ml of Nafion solution (0.5 %) for 20 min to homogeneous ink. Then 6 μl of the ink was spread onto the surface of the GC electrode with a microdoser to form a uniform film on the GC. Then 7 μl of Nafion solution (0.05 %) was applied to fixing ink on carbon.

The working electrode potential was scanned 10 cycles between 0.0 and 1.0 V with scan rate of 200 mV/s. Then there were recorded 2 cycles between 0.0 and 0.9 V with scan rate of 20 mV/s to determine surface area (Figs. 3.2b, 3.4b).

3.3 Results and Discussion

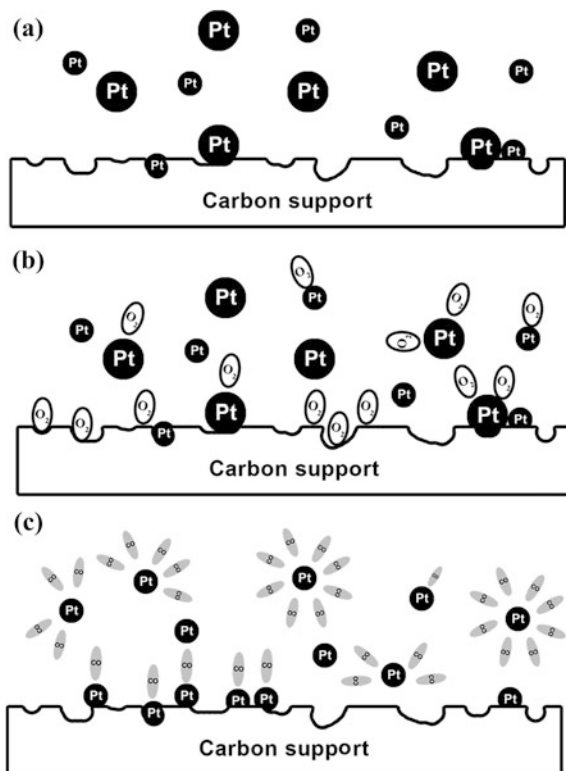
Prepared Pt/C materials contained from 10 to 20 wt% of the metal. An average crystallite size was from 1.0 to 5.5 nm, depending on the method and conditions of synthesis (Table 3.2). ECSA, measured by hydrogen electrodesorption method, was from 32 to 152 $\text{m}^2/\text{g}_{\text{Pt}}$. Therefore, an optimal value of Pt loading was determined as 20 wt%. The most appropriate method of obtaining the platinum catalyst is a method of chemical reduction with formaldehyde as a reducing agent.

For the Pt/C catalysts F and BG, obtained using standard techniques, actual and estimated values of the Pt loading are in a good agreement (Table 3.2). Modification of synthesis methods can lead to decrease of the mass fraction of platinum in the Pt/C (Table 3.2). The greatest degree characterized by samples BG' and BG'', which were obtained by using intermediate carrier, as well as during the synthesis with formaldehyde as a reducing agent in CO-atmosphere (sample F_{CO}) (Table 3.2) This result may be due to the difficulty of Pt NPs adsorption on the surface of carbon microparticles. The reason for this phenomenon may be in stabilization of the colloidal state of Pt nanoparticles in the respective solutions, and the change in the surface charge of carbon microparticles due to the change of adsorption conditions for components of the electrolyte and change the composition of the adsorptive layer.

In our opinion, the explanation of the experimental data on the effect of gas-atmosphere composition (dissolved gas) on the structural characteristics of Pt/C needs to take into account the possible effect of the adsorption of gases on the surface of the carbon support, and on the surface of growing Pt NPs.

CO molecules, which strongly adsorb on the surface of Pt, hinder growth and aggregation of nanoparticles. This causes a narrow particle size distribution and small size of NPs for the F_{CO} sample. On the other hand, the adsorption of CO on the NPs in solution can prevent their subsequent deposition and retention on the surface of the carbon support, resulting in a lower mass fraction of Pt in the F_{CO} sample. In carrying out the synthesis in an air atmosphere, O₂ molecule is weakly adsorbed on the surface Pt NPs and therefore cannot prevent their growth. Obviously, Ar is not an adsorbent (Fig. 3.5).

Fig. 3.5 Scheme of gas-atmosphere effect to the nucleation and growth of nanoparticles during synthesis



The specificity of the effect of oxygen may be associated with its adsorption on the surface of the carbon support, resulting to a decrease in the number of active centers of nucleation/growth of platinum NPs.

Changing nature (adsorption activity) and the number of active nucleation centers (adsorption NPs) of Pt, due to a change in the nature of the primary support, as was confirmed by the results of the study. Unfortunately, a variety of complex processes and phenomena occurring in the course of the multi-stage synthesis of Pt/C material does not allow one to predict the character of such an effect in this study.

The usage of an intermediate carrier and a change in the composition of the atmosphere leads to changes of the powder X-ray diffraction patterns. It occurs due to a change in a microstructure and, partly, a composition of the Pt/C material (see Figs. 3.3a and 3.4a). All diffractograms contains reflections of Pt (fcc, s.g. Fm-3 m). The peaks become broad due to a small crystallite size (Fig. 3.2a, curve 4, 5; Fig. 3.4a).

It should be noted, there is only one the most intense reflection of Pt $\langle 111 \rangle$ at the diffractogram of the sample F_{CO} (Fig. 3.4a, curve 2). It may be a result of least D for this material (Table 3.2).

There are visible reflection belonging phase Fe_3O_4 [16] (indicated with an asterisk) at the diffractogram of F' -sample (Fig. 3.3 curve 5). It could be explained by an incomplete removal of the intermediate support $Fe(OH)_2$ from Pt/C in the

case of formaldehyde synthesis. For the sample BG'' (which was obtained using $\text{H}_2\text{SiO}_3 \cdot n\text{H}_2\text{O}$ as intermediate support) the diffractogram does not have signs of SiO_2 .

Calculation of the average crystallite size which was held by the Scherrer equation revealed that the smallest value (about 1.0 nm) corresponds to the samples F, F_{CO} and F_{Ar} (obtained under an atmosphere of CO and Ar, respectively, as a result of synthesis with formaldehyde) (Table 3.2).

The cyclic voltammograms for the synthesized catalysts are typical for platinum dispersed on a carbon support (Figs. 3.2b, 3.4b). The calculation carried out on the results of cyclic voltammograms taking into account differences in the actual fraction of Pt, it showed that the values of ECSA generally correlated with size of NPs (Table 3.2). Among them, the highest ECSA value ($152 \text{ m}^2/\text{g}(\text{Pt})$) was found for the sample F_{CO} with minimal D . The lowest values of ECSA belong to the

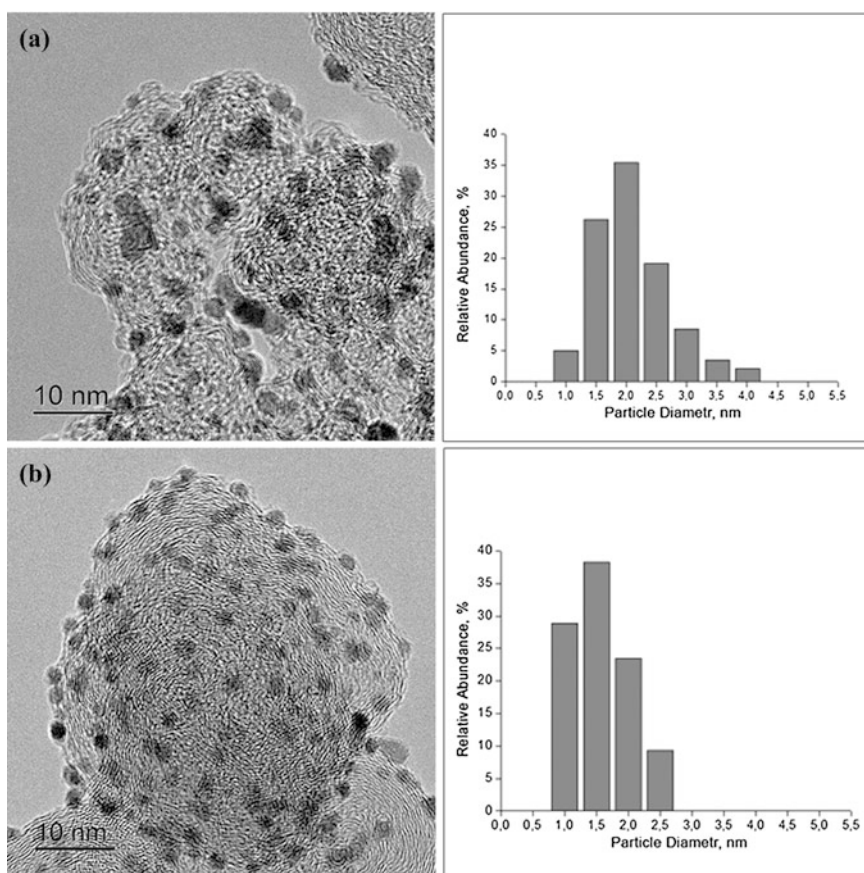


Fig. 3.6 TEM of Pt/C catalysts and the corresponding histograms of the distributions of nanoparticles in size: **a** sample F; **b** sample F_{CO}

samples BG and BG', containing larger crystallites ($D = 5.5$ and 4.5 nm, respectively).

Despite the small size of the crystallites in a sample, F_{Ar} values of ECSA are lower than samples F and F_{CO} . One can assume that during the synthesis in an inert (Ar) gas atmosphere an agglomeration of NPs is stronger than during the synthesis in air or CO.

Thus, the hypothesis that CO adsorbs on the surface of platinum nanoparticles and inhibits a growth and aggregation of nanoparticles was confirmed in this research. Consequently, platinum nanoparticles were uniformly distributed on the carbon surface. Such distribution increases the surface area of the electrocatalyst and a catalytic activity of the material (Fig. 3.6).

In this research, we have demonstrated in principle the possibility of Pt/C electrocatalysts synthesis using «an intermediate» support. As the intermediate carriers, sol of iron hydroxide (II) and silica gel were studied. Formation of nanoparticles of $Fe(OH)_2$ followed by reprecipitation of carbon can lead to both to increase (synthesis of borohydride) and to decrease (formaldehyde synthesis) the average crystallite size and the values of ECSA.

The experimental data indicate that changes in the composition of the atmosphere in the liquid phase synthesis of Pt/C, as well as the use of an intermediate carrier for nucleation (absorption) Pt nanoparticles, can be used as a method of regulation composition, microstructure and, consequently, electrochemically active surface area of the Pt/C materials.

Variety of options for the combination of the mentioned above methods of the synthesis with additional factors shows a wide field to create highly effective Pt/C electrocatalysts for low-temperature fuel cells.

Acknowledgments This work was supported by the Russian Foundation for Basic Research (grants 14-29-04041).

References

1. H.A. Gasteiger, S.S. Kocha, B. Sompalli et al., *Appl. Catalysis B: Environ.* **56**, 9 (2005)
2. Y. Shao-Horn, W.C. Sheng, S. Chen et al., *Top. Catal.* **46**, 285 (2007)
3. A.B. Yaroslavl'tsev, Yu.A. Dobrovolsky, N.S. Shaglaeva, et al., *Uspekhi Khimii*, **81**, 191 (2012) (In Russian)
4. M.R. Tarasevich, *Altern Energ Ecol* **85**(5), 135 (2010) (In Russian)
5. J. Zhang, X. Wang, C. Wu et al., *React. Kinet. Catal. Lett.* **83**(2), 229 (2004)
6. J. Chen, C. Jiang, X. Yang et al., *Electrochem. Comm.* **13**, 314 (2011)
7. H.-C. Ma, X.-Z. Xue, J.-H. Liao et al., *Appl. Surface Sci.* **252**, 8593 (2006)
8. J. Prabhuram, T.S. Zhao, C.W. Wong et al., *J. Power Sour.* **134**, 1 (2004)
9. F.J. Nores-Pondala, I.M. Vilellab, H. Troianic et al., *Int. J. Hydrogen Energy* **34**, 8193 (2009)
10. J. Qi, L.H. Jiang, M.Y. Jing et al., *Int. J. Hydrogen Energy* **36**, 10490 (2011)
11. P.C. Favilla, J.J. Acosta, C.E. Schvezov et al., *Chem. Eng. Sci.* **101**, 27 (2013)
12. Z. Zhou, S. Wang, W. Zhou et al., *Phys. Chem. Chem. Phys.* **5**, 5485 (2003)
13. B. Del'mon, *Kinetics of Heterogeneous Reactions* (Mir, Moscow, 1972) (In Russian)

14. A.B. Yaroslavtsev, Yu.A. Dobrovolsky, N.S. Shaglaeva, et al., *Uspekhi Khimii*, **81**, 191 (2012) (In Russian)
15. N. An, Q. Yu, G. Liu et al., *J. Hazard. Mater.* **186**, 1392 (2011)
16. N. Ana, P. Wua, S. Lia et al., *Appl. Surf. Sci.* **285**, 805 (2013)
17. Y. Cao, W. Zhai, X. Zhang, et al., *ISRN Nanomater.* 7p. (2013)
18. A.V. Arsatov, YuA Dobrovolsky, *Altern. Energ. Ecol.* **8**, 171 (2009). (In Russian)
19. M. Mohapatra, S. Anand, *Int. Eng. Sci. Technol.* **2**(8), 127 (2010)
20. N.A. Shakhbanova, *Sol-Gel Technologies. Nano-Dispersive Silica* (Binom, Moscow, 2012)
21. J.R.C. Salgado, J.J. Quintana, L. Calvillo et al., *Phys. Chem. Chem. Phys.* **10**, 6796 (2008)
22. W. Zhou, J. Wu, H. Yang, *Nano Lett.* **13**, 2870 (2013)
23. V.E. Guterman, A.Y. Pakharev, N.Y. Tabachkova, *Appl. Catal. A* **453**, 113 (2013)

Chapter 4

Synthesis of Titanium Dioxide: The Influence of Process Parameters on the Structural, Size and Photocatalytic Properties

E.M. Bayan, T.G. Lupeiko, L.E. Pustovaya and A.G. Fedorenko

Abstract The influence of various factors on the photocatalytic activity of titanium dioxide produced from different precursors by a gel and sonochemical methods was analyzed. Obtained nanosized titanium dioxide demonstrates an increased photocatalytic activity, which can be as high as that of the best commercial crystalline powders and even higher. The material with a high photocatalytic activity was prepared from the aqueous solution of titanium chloride by sonochemical method and calcined at 600 °C. The total surface area of the sample is about 50 m²/g, the phase composition is anatase with a minor proportion of rutile modification.

4.1 Introduction

Due to its low toxicity, chemical stability, low cost, high efficiency in the oxidation of organic and biological objects, nanosized titanium dioxide is the most promising material for photocatalysis, water treatment [1–12]. Parameters affecting the properties of catalysts are porosity, specific surface area, the degree of crystallinity and the ratio of the TiO₂-crystalline modifications (anatase, rutile, brookite). Among these modifications of titanium dioxide anatase is considered to be the most effective photocatalytic phase [13, 14]. However, as it is stated in the work of Zünic et al. [15], a small addition of rutile to anatase increases the photocatalytic activity of the material due to the synergistic effect between rutile and anatase, which increases the lifetime of the charge carriers. Titanium dioxide in various phase compositions can be produced by choosing the method of synthesis or through varying its parameters (precursor concentration, temperature, duration of process,

E.M. Bayan (✉) · T.G. Lupeiko · A.G. Fedorenko
Faculty of Chemistry, Southern Federal University, Rostov-on-Don, Russia
e-mail: ekbayan@sfedu.ru

L.E. Pustovaya
Don State Technical University, Rostov-on-Don, Russia

etc.) [16, 17]. Practical application of photocatalytic reactions requires the maintenance of light intensity in order to achieve sufficient energy rates that exceeds TiO_2 band gap energy (BGE). Anatase and brookite are known to have $\text{BGE} = 3.2 \text{ eV}$, $\text{BGE (rutile)} = 3.02 \text{ eV}$, the absorption thresholds corresponding to 380 and 410 nm, respectively [18]. Various methods to prepare TiO_2 -based photocatalysts are available including combustion titanium chloride in oxygen stream, vapor-phase or hydrothermal hydrolysis and others [19–22]. In recent years, sol-gel method, which allows one to obtain nanoparticles with desired properties has attracted close attention [23–28]. Sonochemical method is a relatively new method to prepare nanocrystalline materials [15, 29]. Compared with conventional synthetic methods, sonochemical synthesis yields materials with a high specific surface area and a better thermal stability [15].

The main objective of this study was to prepare nanosized titanium dioxide characterized by higher photocatalytic properties compared with existing analogues obtained via gel technology and sonochemistry from different precursors such as titanium chloride and titanyl nitrate. Different physical properties and photocatalytic activity of the synthesized materials were compared.

4.2 Experimental Methods

4.2.1 Materials

All reagents used were commercially obtained and used without any further purification. All solutions were prepared using deionized water.

4.2.2 Photocatalyst Preparation

TiO_2 nanocrystallites were synthesized from aqueous solutions of titanium chloride (pure TiCl_4 liquid was carefully diluted with ice water to a transparent colorless aqueous solution) or titanyl nitrate, $\text{TiO}(\text{NO}_3)_2$ with concentration $[\text{Ti}^{4+}] = 0.1 \text{ M}$. Ammonia solution (10 %) was added to these solutions drop wise until white precipitates (gel) were obtained and the $\text{pH} = 8$. The temperature of aqueous solutions varied from 0 to 100 °C. Some precipitates were obtained in the Ultrasonic Cleaning Units (Elma D-78224) under sonication (Ultrasonic power effective 280 W, frequency 50–60 Hz). The precipitates were washed with deionized water until chlorine or nitrate ions became undetectable. Then the gels were dried and calcined at the different temperature selected according DTA/TG-analysis (450, 600, 700 °C) for 30, 60, 120 min. Synthesis parameters are summarized in Table 4.1. Degussa P25 (P25) was applied as a reference for comparison.

Table 4.1 Conditions for the synthesis; characteristics of synthesized samples

Series of samples	Precursor	Synthesis temperature (°C)	Sonication	Calcined temperature (°C)	Sample after calcination	Crystallite size (nm)	Structure ^a
1	TiCl ₄	≤5	–	700	1.1	18	A
				600	1.2	13	A
				450	1.3	9	A
2	TiCl ₄	80	+	700	2.1	22	A + R
				600	2.2	18	A + R
				450	2.3	9	A + R
3	TiCl ₄	≤20	+	700	3.1	20	A
				600	3.2	14	A
				450	3.3	9	A
4	TiO (NO ₃) ₂	≤5	–	700	4.1	23	A
				600	4.2	12	A
				450	4.3	8	A
5	TiO (NO ₃) ₂	80	+	700	5.1	11	A
				600	5.2	9	A
				450	5.3	6	A

^a A anatase, R rutile

4.2.3 Materials Characterization

X-ray powder diffraction (XRD) analysis was carried out using an ARL X'TRA diffractometer equipped with a high-intensity K α 1 irradiation ($\lambda = 1.540562 \text{ \AA}$) operated at 40 kV and 30 mA. Typical scans were performed in a wide range of Bragg angle ($20^\circ \leq 2\theta \leq 60^\circ$). The XRD patterns were analyzed using the standard JCPDS files. Qualitative analysis of phase state was performed by using data PDF-2 data base and PCPDFWIN software.

The average particle size and total surface area of the samples were determined by sedimentation analysis in a CPS Disk Centrifuge Model DC24000.

Coherent scattering region was calculated from the X-ray line broadening, according to the Debye-Scherrer equation:

$$d = \lambda / (\beta \cos \theta), \quad (4.1)$$

where $\lambda = 0.1540562 \text{ nm}$ is the X-ray wave length, β is the full width at half maximum (FWHM) of the diffraction peak (101) for anatase and (110) for rutile, θ is the diffraction angle.

Thermogravimetry (TGA) and Differential Thermal Analysis (DTA) of the samples were carried out using a thermal analyzer (STA 449°S/4 G Jupiter Jupted) at a heating rate of $10 \text{ }^\circ\text{C}/\text{min}$ from 283 to 1000 K.

The morphological characteristics were analyzed with transmission electron microscopy utilizing a TEM Tecnai G² Spirit Bio TWIN operating at 120 kV.

4.2.4 Photocatalytic Activity Measurements

The photocatalytic activity of the prepared samples in the aqueous media was evaluated through monitoring of the discoloration of organic azo dye methylene blue (MB, $C_{16}H_{18}N_3SCl$) or methyl orange (MO, $C_{14}H_{14}N_3O_3SNa$). In a typical measurement, TiO_2 power (1 g/l) was suspended in MB (or MO) aqueous solution (20 mg/l) by stirring. Experiments were carried out at room temperature in quartz glass beakers. 125 W medium pressure mercury lamp was used as the UV light source. Residual concentration of the MB solutions was analyzed by mass spectrometry (Spectrophotometer UNICO 1201). Recycling test was subsequently performed three times.

4.3 Results and Discussion

4.3.1 DTA/TGA Measurements

Figure 4.1 demonstrates the removal of a large part of sample mass at temperatures up to 180 °C due to the release of water. The exothermic peak in the DTA pattern at 437 °C corresponds to degradation of titanium hydroxide along with formation of anatase crystalline phase. The exothermic peak at 500–700 °C at a constant mass of the sample is apparently associated with a new phase transition (presumably anatase-rutile). As a result, calcination temperatures of the samples were selected: 450, 600 and 700 °C.

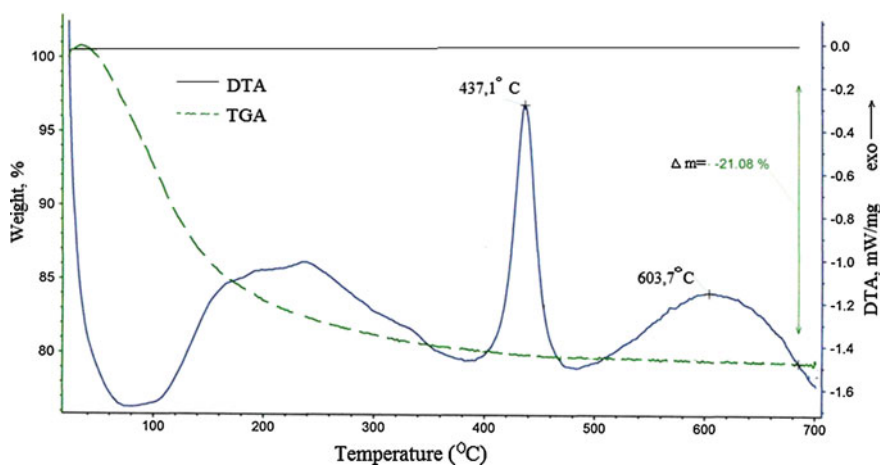


Fig. 4.1 DTA/TGA patterns of the sample prepared

4.3.2 Structural and Size Characterizations

According to XRD, the samples were found to preserve their amorphous structure after calcination for 30 min, after 60 min calcination the mixture of amorphous and crystallized phase was detected, after 120 min calcination the anatase phase was stated to be prevailing. Based on these data, the calcination was carried out for 120 min in further experiments. Longer calcination of the samples resulted in the formation of rutile phase and the increase of crystallite size.

XRD patterns demonstrated that all samples of 1, 3–5 series (Table 4.1) had anatase modification; the degree of their crystallinity grew with increasing temperature. Samples of series 2 (Fig. 4.2) had a mixture of anatase and rutile, the proportion of rutile in the mixture increased with increasing temperature. XRD data (Fig. 4.3) for samples synthesized from titanyl nitrate suggest stabilization of anatase modification under above-mentioned conditions of synthesis.

In assessing the coherent scattering regions by Scherrer method, it was found that the average crystallites size increases with increasing calcination temperature and equals 6–9 nm (450 °C), ~15 nm (600 °C), ~20 nm (700 °C). It could be explained by the processes of titanium dioxide crystallization.

TiO₂ synthesized via the gel-precipitation from titanium chloride consisted of particles with anatase sizes of 9–18 nm depending on the calcination temperature. The size of detected particles for the gel-precipitation samples obtained from titanyl nitrate solutions equals 8–23 nm. The smallest TiO₂ particles of 6–11 nm were prepared by sonochemical method from titanyl nitrate solutions.

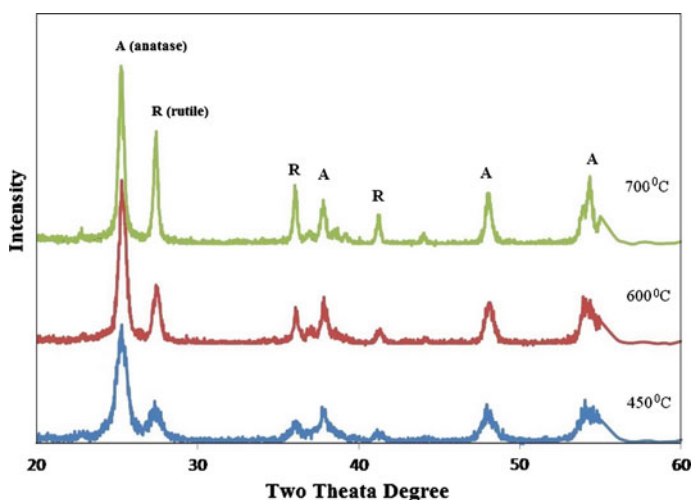


Fig. 4.2 XRD patterns of the samples prepared from titanium chloride and calcined at different temperatures

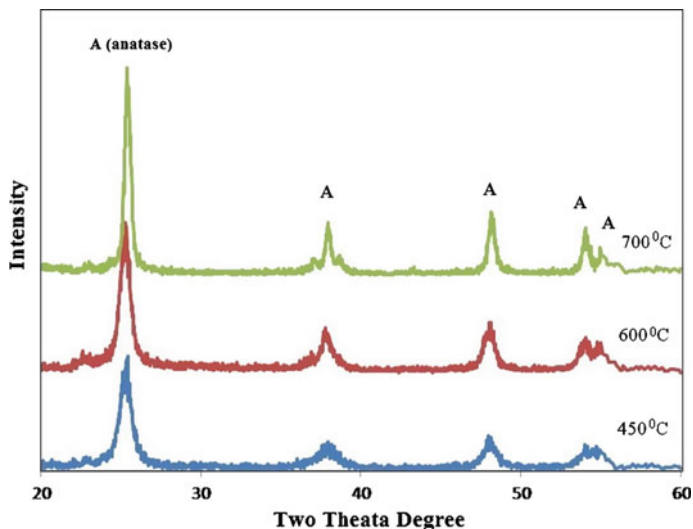


Fig. 4.3 XRD patterns of the samples prepared from titanyl nitrate and calcined at different temperatures

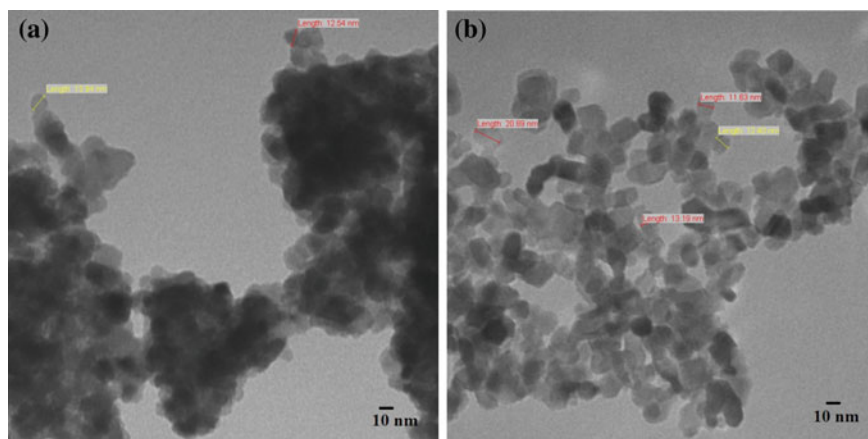


Fig. 4.4 TEM microphotographs of TiO_2 powders: the sample 1.1 (a), the sample 2.2 (b)

Figure 4.4 presents the TEM microphotographs of TiO_2 powders. The microphotographs emphasize that sizes of titanium dioxide grains increase with the sonochemical treatment.

Sedimentation analysis revealed that the total surface area of prepared samples was about $50 \text{ m}^2/\text{g}$.

4.3.3 Photocatalytic Performance

Photocatalytic activities of TiO_2 were evaluated by the degradation of MB and MO.

Figures 4.5 and 4.6 demonstrate that the samples prepared by sonochemical method are characterized by far better photocatalytic activities. However, the effect of calcination temperature is different for different sample series. The highest photocatalytic activity by MB from the 1 and 3 series is shown by samples 1.1 and 3.1, respectively, calcined at 700 °C. However, the highest photocatalytic activity from the 2-nd series is demonstrated by sample 2.2, which was calcined at 600 °C. It could be explained by the fact that sample 2.1, which was calcined at 700 °C contains considerable amount of rutile, which did not have photocatalytic activity.

Figure 4.7 demonstrates low photocatalytic activities for 1 and 2 series samples with respect to methyl orange which was the same or lower than that of Degussa P25. It should be noted that observed photocatalytic activity is lower with respect to the MO than that with respect to the MB for all series of samples (Figs. 4.5, 4.6 and 4.7).

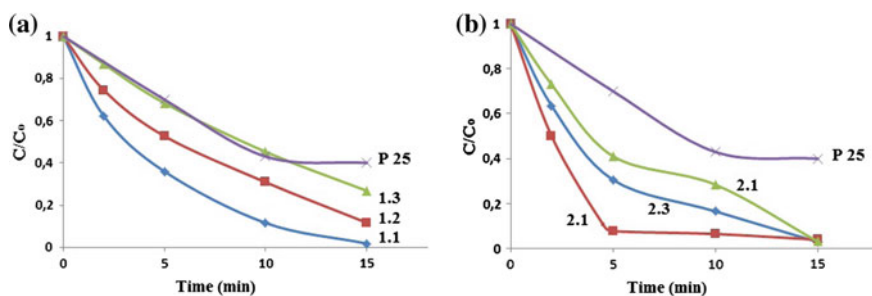


Fig. 4.5 Degradation profiles for TiO_2 samples of the 1 series (a) and the 2 series (b) with respect to methylene blue

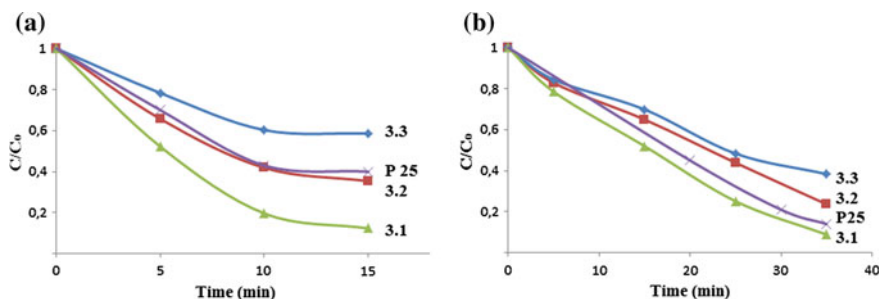


Fig. 4.6 Degradation profiles for TiO_2 samples of 3 series with respect to methylene blue (a) and methyl orange (b)

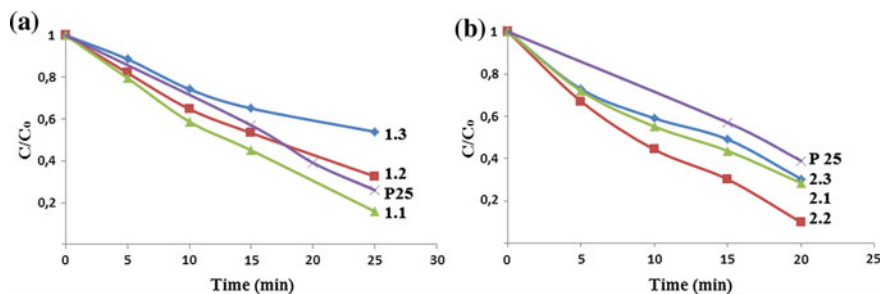


Fig. 4.7 Degradation profiles for TiO_2 samples of the 1 series (a) and the 2 series (b) with respect to methyl orange

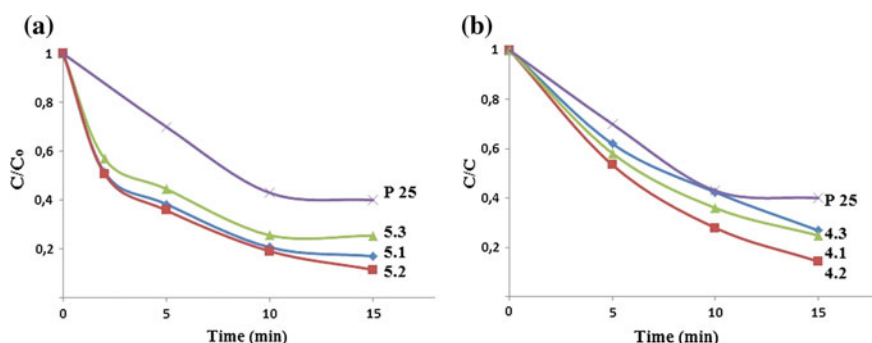


Fig. 4.8 Degradation profiles for TiO_2 samples of the 5 series (a) and the 4 series (b) with respect to methylene blue

Photocatalytic activities for 4 and 5 series samples obtained from titanium nitrate are lower than that for 1, 2 and 3 series samples which were synthesized from titanium chloride (Fig. 4.8).

4.4 Conclusions

We have found that the precursors (aqueous solutions of titanium chloride and titanium nitrate) do not demonstrate essential influence on the final value of photocatalytic activity but determine significantly the time of photodegradation process.

Thus, the samples synthesized from aqueous solution of titanium tetrachloride demonstrate higher rate of photodegradation process than the ones synthesized from nitrate solutions. It has been established that sonochemical method enables us to obtain samples with the best photocatalytic properties (the best sample is 2.2). High photocatalytic activity of the sample 2.2 can be explained by its structure (Fig. 4.2). When comparing XRD patterns for 2nd series samples, it was determined that these

samples had small proportion of rutile modification and significant amounts of anatase. This is probably due to the use of TiCl_4 as a precursor in combination of high temperature (80 °C) at the synthesis stage and ultrasonic treatment, which led to the formation of nanocrystalline anatase phase domains with inclusions of rutile phases and heterophase particles formation. The optimal values of quantum yield are known to be obtained on heterophase particles, because photogenerated charge of heterophase are particles spatially separated, recombination is also hindered [15]. So, photocatalytic activity of nanosized titanium dioxide obtained this way is higher than that of Degussa P25. The synthesis of produced titanium dioxide was performed from the aqueous solutions of titanium chloride at 80 °C by sonochemical method with calcination at 600 °C. The best sample was obtained with a total surface area of about 50 m²/g, the size was estimated to be 20 nm, its phase composition being anatase with a minor proportion of rutile. It is determined that the methods which enable us to obtain a biphasic system (anatase and rutile) are promising for further synthesis of materials with high photocatalytic activity.

Acknowledgments This research was supported by the Project Part of the State Assignment for Research (Ref. No. 4.2592.2014/K).

References

1. F. Han, V.S.R. Kambala, M. Srinivasan, D. Rajarathnam, R. Naidu, *Appl. Catal. A* **359**, 25 (2009)
2. H. Xu, S. Ouyang, L. Liu, P. Reunchan, N. Umezawa, J. Ye, *J. Mater. Chem. B*, **32**, 12642 (2014)
3. Y. Xie, O. Zhao, X.J. Zhao, Y. Li, *Catal. Lett.* **118**, 231 (2007)
4. H.U. Lee, G. Lee, J.C. Park, Y.-C. Lee, S.M. Lee, B. Son, S.Y. Park, C. Kim, S. Lee, S.C. Lee, *Chem. Eng. J.* **240**, 91 (2014)
5. H. Khan, Dimitrios Berk, *Catal. Lett.* **144**, 890 (2014)
6. J. Choi, H. Lee, Y. Choi, S. Kim, S. Lee, S. Lee, W. Choi, J. Lee, *Appl. Catal. B: Environ.* **147**, 8 (2014)
7. A.R. Khataee, M.B. Kasiri, *J. Mol. Catal. A: Chem.* **328**, 8 (2010)
8. A. Di Paola, E. García-López, G. Marci, L. Palmisano, *J. Hazard. Mater.* **211–212**, 3 (2012)
9. M.N. Chong, B. Jin, C.W.K. Chow, C. Saint, *Water Res.* **44**, 2997 (2010)
10. U.I. Gaya, A.H. Abdullah, *J. Photochem. Photobiol., C* **9**, 1 (2008)
11. K. Hashimoto, H. Irie, A. Fujishima, *Jpn. J. Appl. Phys. Part 1: Regul. Pap. Short Notes Rev. Pap.* **44**, 8269 (2005)
12. M. Răileanu, M. Crişan, I. Niţoi, A. Ianculescu, P. Oancea, D. Crişan, L. Todan, *Water. Air Soil Pollut* **224**, 1548 (2013)
13. D.C. Hurum, A.G. Agrios, K.A. Gray, T. Rajh, M.C. Thurnauer, *J. Phys. Chem. B* **107**, 4545 (2003)
14. C. Wu, Y. Yue, X. Deng, W. Hua, Z. Gao, *Catal. Today* **93–95**, 863 (2004)
15. V. Zünic, M. Vukomanović, S.D. Škapin, D. Suvorov, J. Kovac, *Ultrason. Sonochem.* **21**, 367 (2014)
16. M. Dawsot, G.B. Soares, C. Ribeiro, *J. Solid State Chem.* **215**, 211 (2014)
17. Z. Ismagilov, L.T. Tsikoza, N.V. Shikina, V.F. Zarytova, V.V. Zinovev, S.N. Zagrebely, *Usp.* **78**, 942 (2009)

18. M. Pelaeza, N.T. Nolanb, S.C. Pillaib, M.K. Seeryc, P. Falarasd, A.G. Kontosd, P.S.M. Dunlope, J.W.J. Hamilton, J.A. Byrne, K. O'Sheaf, M.H. Entezarig, D.D. Dionysiou, *Appl. Catal. B* **125**, 331 (2012)
19. J.Q. Qi, Y. Wang, W.P. Chen, H.Y. Tian, L.T. Li, H.L.W. Chan, *J Alloy Compd* **413**, 307 (2006)
20. T.K. Tseng, Y.S. Lin, Y.J. Chen, H. Chu, *Int. J. Mol. Sci.* **11**, 2336 (2010)
21. J. Lin, Y. Lin, P. Liu, J.M. Meziani, L.F. Allard, Y.P. Sun, *J. Am. Chem. Soc.* **124**, 11514 (2002)
22. F.A. Deorsola, D. Vallauri, *Powder Technol.* **190**, 304 (2009)
23. U.G. Akpan, B.H. Hameed, *Appl. Catal. A* **375**, 1 (2010)
24. M. Răileanu, M. Crișan, N. Drăgan, D. Crișan, A. Galtayries, A. Brăileanu, A. Ianculescu, V. S. Teodorescu, I. Nițoi, M. Anastasescu, *J. Sol-Gel. Sci. Technol.* **51**, 315 (2009)
25. T.K. Tseng, Y.S. Lin, Y.J. Chen, H. Chu, *Int. J. Mol. Sci.* **11**, 2336 (2010)
26. W.H. Ching, M. Leung, D.Y.C. Leung, *Sol. Energy* **77**, 129 (2004)
27. N. Arconada, A. Durán, S. Suárez, R. Portela, J.M. Coronado, B. Sánchez, Y. Castro, *Appl. Catal. B* **86**, 1 (2009)
28. J.H. Schattka, D.G. Schukin, J. Jia, M. Antonietti, R.A. Caruso, *Chem. Mater.* **14**, 5103 (2002)
29. B. Neppolian, Q. Wang, H. Jung, H. Choi, *Ultrason. Sonochem.* **15**, 649 (2008)

Chapter 5

Polyacrylonitrile-Based Materials: Properties, Methods and Applications

T.V. Semenistaya

Abstract Polyacrylonitrile (PAN) is extremely popular and attracts much attention due to its unique structure and ability to change the structure under heating. PAN and modifying additives (Cu(II), Ag(I), Co(II), Cr(III)) were dissolved in DMF and coated on polycor substrates and then the thin films were fabricated by pyrolysis method under the influence of incoherent IR-radiation under low vacuum conditions. Surface structure and morphology of the fabricated samples were investigated by X-ray photoelectronic spectroscopy (XPS), X-ray diffraction analysis (XPD), transmission electron microscopy (TEM), scanning electron microscopy (SEM), atomic force microscopy (AFM). The electrical resistance of the metal-containing PAN films was measured in the range from 10^2 to 10^{12} Ω . The fabricated films demonstrate gas-sensing properties to NO_2 , Cl_2 , NH_3 and gasoline vapors at room temperature.

5.1 Introduction

Currently, intensive researches have been conducted in the new promising area of science, which is called organic electronics. The advantage of organic materials over inorganic materials is in a wide range of physical and chemical properties. They have characteristics such as low-gas permeability and excellent flexibility, their electrical properties can be changed in various range of values, also they are technologically and economically more profitable. Their properties have its origin in the particular molecular structure. Therefore, the question of purposeful synthesis to control the desired properties in the preparation of organic material is relevant.

One of types of the organic materials, which has found plentiful kinds of application in electronics as molecular conductors, is conducting organic polymers [1–3].

T.V. Semenistaya (✉)

Engineering-Technological Academy, Southern Federal University, Taganrog, Russia
e-mail: semenistayatv@sfnedu.ru

Due to their molecular structure, they have specific properties: controlled electrical conductivity, simulated electrical properties through the tailoring of certain molecular structures, preparation of various nanostructured forms (film, nanoparticles, nanowires).

The subject of this research is the heat-treated polyacrylonitrile (PAN), which is a conducting polymer due to the formation of π -conjugated bonds occurring in the carbon chain owing to course of thermochemical reactions during the IR-annealing over the temperature range 250–500 °C [4, 5]. The heat-treated PAN is the organic semiconductor; values of its resistance are in the range from 10^2 to 10^{13} Ω , which we used to create the gas sensors of resistive type [6–9].

PAN has been the subject of numerous investigations for the last twenty years. There are four main forms of PAN that are of interest by researchers, namely films [10–21], membranes [22–28], composites [29–38] and carbon fibers or nanofibers [39–44].

PAN is used as a film forming matrix that prevents from aggregation of the dispersed nanoparticles [10], due to its ability to form very adherent organic coatings chemically grafted on the metallic substrate [11, 13], to improve the durability of a proton exchange membrane fuel cell [12], to form low-level electrical contacts [14].

There are particular methods and techniques for each type of PAN-based material. The conventional evaporation technique [10], electropolymerization [11, 13, 16, 18, 20], electrochemical adsorption [15], laser ablation [19] and a free radical polymerization technique [21] are used to obtain PAN films. The most widely used method in manufacturing PAN films is deposition by electropolymerization. Electropolymerization indeed gives very adherent organic coatings chemically grafted on the metallic substrate [13].

PAN has been successfully used in energy storage device [17, 28, 41] and sensor applications [15, 18] owing to its good mechanical and thermal properties and its low cost.

PAN is used for making membranes due to its good solvent resistance [22, 29], high porosity and excellent mechanical properties [26], surface area and antifouling property [25], its ability to form uniform polymeric interconnected structures that exhibit excellent mechanical properties along with high porosity, high electrolyte uptake and good relative absorption ratio [28].

PAN-based membranes are fabricated by phase inversion method [22, 24], via thermally induced phase separation [26] and by electrospinning [28].

In membrane materials PAN is used as a support [23, 25] or as a mid-layer to fabricate composite membranes [24].

The resulted membranes may be suitable for micro- or ultra-filtration processes in water treatments, prevaporation and bioproduct purification [22, 23, 26], for separating an oil/water emulsion [24], for humic acid removal [25], used as supports for enzyme immobilization [26].

The modifications of PAN membranes usually include plasma treatment, plasma-initiated graft polymerization, photoinduced grafting and hydrolysis. Among these methods, hydrolysis under alkaline condition is one of the most

important and most frequently used methods for PAN-based membranes. The hydrolysis with alkaline solution is based on the conversion of $-\text{CN}$ groups on the PAN membrane surface firstly into $-\text{CONH}_2$, then into $-\text{COO}^-$ groups [27].

PAN has been used as a precursor for composites [29, 30, 36, 37], as a matrix of nanocomposites [31, 33, 35, 38] and a substrate [34]. In a composite ion exchanger, inorganic materials are active components to which all the radionuclides are bound and organic materials are simply inert binders [30]. Its strong static electricity causes PAN to absorb dust and microbes easily [33]. Nano-Sn embedded by pyrolytic PAN is the spherical nano-tin encapsulated pyrolytic polyacrylonitrile composite: the pyrolyzed PAN becomes polymer matrix and acts as a buffer to relieve the morphological change of Sn, and as an inactive component to prevent the further aggregation of Sn during cycling [35]. The organic polymer may contribute to disaggregating the small metallic particles [38].

The PAN composite materials were prepared by using sequential process that may include polymerization, filtration, mixing, phase inversion process, pyrolysis, heating, soaking, electropolymerization etc. [29–38]. There is not universal method or technique that introduces PAN into a composite. PAN is performed under flowing N_2 (20 ml/min) on platinum crucible with a heating rate of $8\text{ }^\circ\text{C}/\text{min}$ from ambient temperature to $350\text{ }^\circ\text{C}$ [29]. A sulfur and PAN mixture was ball milled for 5 h with ethanol as the dispersant, then the resulting mixture was dried at $50\text{ }^\circ\text{C}$ for 3 h in a vacuum oven and after that annealed at $300\text{ }^\circ\text{C}$ in argon during 0.5–4.0 h [31]. PAN was dissolved in DMF and coated on a platinum electrode, and then was fabricated into porous membrane by phase inversion process [34]. The composite was obtained by the pyrolysis of the Sn/PAN mixture at $300\text{ }^\circ\text{C}$ for 5 h under the protection of N_2 [35]. Active nitrile groups present in PAN copolymers allow introducing new functional groups by special reactions [36]. The cobalt oxalates and PAN suspension was gently heated at $50\text{ }^\circ\text{C}$ in air atmosphere until solvent evaporation while continuous stirring, and further heating at $120\text{ }^\circ\text{C}$ was carried out in a Buchi oven under dynamic vacuum [38].

PAN-containing composites are applied widely in diverse spheres. Zr–Mn oxide/PAN composite adsorbent spheres were prepared to remove strontium ions from aqueous solution [30]. A composite consisting of sulfur/dehydrogenated polyacrylonitrile is one of the most promising cathode materials for use in rechargeable lithium-sulfur batteries [31, 32]. A new class of PAN/o-MMT/Ag nanocomposites [33] showed the most effectively inhibited growth of bacteria of Gram (+) *Staphylococcus aureus*, Gram (–) *Escherichia coli* and *Klebsiella pneumoniae* (o-MMT—organically modified montmorillonite). An enzyme PAN-PAN/PPO electrode [34] was applied for determination of benzoic acid (PAN—polyaniline, PPO—polyphenol oxidase). Spherical nano-Sn encapsulated pyrolytic polyacrylonitrile composite anode material was prepared for Li-ion batteries [35]. Aminated PAN resins were prepared for adsorption of Hg(II), Fe(III), Pb(II), Ag(I) and Zn(II) from aqueous solutions [36].

PAN is not only an important engineering polymer due to its high resistance to many chemicals, but also the main precursor of carbon fibers via deliberate

carbonization [39]. PAN has been widely used in producing carbon nanofibers because of its good stability [29].

PAN-based fibers mainly produced by the electrospinning method [39–42], but the PAN fibers doped with 2,3,5-triphenyltetrazolium chloride (TTC), 4,4',4''-tri-di- β -hydroxyethylaminotriphenylacetone nitrile (HHEVC) and 10,12-pentacosadiionic acid (PENTA) manufactured by a wet spinning method [44]. For carbonization, the CoFe_2O_4 /PAN fibers produced by electrospinning were placed in a tube furnace and stabilized via heating at 0.5 °C/min up to 250 °C, then incubating at 250 °C for 2 h in an air atmosphere. Carbonization was performed at 1000 °C for 4 h under an argon atmosphere at a heating rate of 5 °C/min [39]. PAN/CuS composite nanofibers with monodispersed CuS nanoparticles uniformly distributed on the surface of electrospun PAN fibers were fabricated via a simple hydrothermal method [43]. Electrospinning technique is currently a highly versatile method to fabricate continuously long fibers with controllable morphology [43].

S.K. Nataraj et al. made the excellent report about the advantage of PAN precursor to produce carbon nanofibers (CNFs) due to its high carbon yield and flexibility for tailoring the structure of the final CNFs as well as the ease of obtaining stabilized products due to the formation of a ladder structure via nitrile polymerization. In the work [40], the applications of PAN based carbon nanofibers were shown in such areas as electronics, tissue engineering, membrane filtration and high performance composites.

Thus, PAN is extremely popular and functional, applicative organic polymer.

In this work, PAN is the subject of interest due to its ability to become conjugated conducting polymer by low temperature pyrolysis.

Pyrolyzation conditions and resistivity are as follows: PAN as deposited and oxidized but not pyrolyzed— $10^{17} \Omega \cdot \text{cm}$, PAN pyrolyzed at 300 °C— $10^{14} \Omega \cdot \text{cm}$, at 400 °C— $10^{10} \Omega \cdot \text{cm}$, at 500 °C— $10^5 \Omega \cdot \text{cm}$ [17]. The electric conduction of conducting polymer is attributed to the participation of lone pairs of electrons on nitrogen atom with *s*-bond in the macrochain [29].

It is well known that pyrolysis of PAN induces a considerable transformation of its molecular structure as well as an increase of its electrical conductivity. However, the correlation between these two processes is not clearly established [45].

Understanding the modifications occurring in the chemical and physical structure of the films during thermal treatment is essential to establish the best set of parameters for the process and to control the polymer properties [13].

PAN, which is a polymer with a chain of carbon atoms, connected one to other, turns in a semiconductor material under pyrolysis without changing its basic structure. PAN subjected to carbonization under controlled conditions is known to transform in polymer with conjugated bonds and semiconductor properties.

Heat treated PAN is a polymer with conjugated bonds and semiconductor properties whose electrical conductivity can vary from dielectric to metallic during the transition of the chemical structure of the polymer from linear to polyaromatic [40].

The chemical transformations in PAN that result from thermal action can be represent by two types of reactions. At temperatures 200–220 °C in the air atmosphere, the intramolecular reaction of cyclization of nitrile groups occurs with the

breaking of ternary bonds of $C\equiv N$ registered in the nitrile groups and a system of conjugated $>C=N$ bonds formed after that. The formation of intermolecular bonds can occur with a methyleneimino group $>C=NH$ formed. This process exists due to a hydrogen atom of a tertiary carbon, which accelerates the process of cyclization of nitrile groups [46–48].

During the heat treatment in air above 220 °C, the processes of polymer destruction occur with weight losses and liberation of gaseous products of decomposition (allyl cyanide, vinyl cyanide, propylene, ethylene, hydrogen cyanide) H , H_2 , NH_3 , CNH , CO , and CO_2 .

Under IR-radiation at 200 °C, we can also observe changes in the polymer structure, namely, the hydrogen atom of a tertiary carbon migrates to the nitrile group with the formation of a methyleneimine group to form a hydrogen bond with the nitrile group. This ensures the formation of a cycle with the migration of a hydrogen atom along the forming system of conjugated $C=N$ bonds [49].

With a further increase in the temperature and in the duration of the heat treatment, the reaction of degradation of the main chain of the PAN macromolecule is found to occur with the formation of a system $-C=C-$ of conjugated bonds [46–48].

Introduction into PAN initial solution of modifying additives in the form of compounds of transition metals leads to the reduction of the heat treatment time and the temperature of cyclization starting at 140 °C. In this case, the reaction of complex formation is competitive with respect to the reaction of cyclization of nitrile groups [50].

Transformations in the chemical structure of a macromolecule of a linear polymer PAN at low temperatures (up to 250 °C) do not lead to diminution of the side groups. In the formation of a polyene structure, nitrile groups participate. The peculiarity of PAN is in that the chain of a polymer does not split into low-molecule products (depolymerization), and the changes occur in the basic chain of the macromolecule; i.e., intramolecule transformations are registered, which result in arising of a system with conjugated links in the polymer [51].

The method of fabrication of the electroconductive structure of PAN, hardware peculiarities and synthesis conditions ambiguously exert influence on the properties of the formed material. There are some methods of manufacturing the electroconductive structure of PAN such as: thermal pyrolysis and IR-radiation pyrolysis. Under the pyrolysis proceeding at temperatures higher than 300 °C, PAN transforms in a polymer with a cyclic structure, containing the conjugated double bonds. Due to the π -orbital overlap of the neighboring molecules of the conjugated structure, the π -electrons delocalize along the entire chain, which provides semi-conducting properties of PAN polymer. This method enables to manufacture films with a developed surface morphology and provides uniform distribution of modifying additives in a film. The presence of a transitional metal and its compounds completely excludes a stage of cyclization of PAN's nitrile groups. Formed in the result of dehydrogenation of the main polymeric chain, the sequence of conjugated bonds has greater length in comparison with the areas, fabricated in the absence of salts of transition metals, which increases the material conductivity.

A study of thin films of pyrolyzed PAN is of interest because of its applications in gas-sensing layers.

In order to increase the selectivity and adsorption activity of semiconductor organic materials the modifying with transition metals such as Pd, Pt, Au, Ag are carried out. Embedding of modifying additives into organic polymers opens up wide opportunities for changing the electrical and optical properties of the gained material. The atoms of metals, situated in an organic matrix, exert the electron transition in the polymer structure. There seems to be a strong relation between the dispersion of Au/Co alloy particles and the structural rearrangement of PAN caused by the heat treatment [10]. A presence of modifying additives in polymer matrix affects gas-sensitivity of the composite metal-containing organic materials. This could be explained by changing the mechanism of conductivity in polyconjugated polymer or by the metallic nanoparticles distributed in the polymer matrix.

Gas-sensing ability of metal-containing PAN films is complex owing to the numerous molecular and intermolecular interactions during forming the structure that control its spatial and temporal variability. There is a problem to choose the appropriate technological parameters to form the structure of best sensing properties. In order to examine how the annealing affects the structural and electric properties of the PAN-based materials, we fulfilled this investigation.

5.2 Experimental Details

The metal-containing PAN films were fabricated by pyrolysis method under the influence of incoherent IR-radiation under low vacuum conditions. The following components were used: PAN (Aldrich 181315) as a conductive polymer matrix, copper chloride (II) CuCl_2 , silver nitrate (I) AgNO_3 , chrome chloride (III) CrCl_3 and cobalt chloride (II) CoCl_2 as modifying additives for increasing the selectivity and adsorption activity of the films, dimethylformamide (DMF) as a solvent.

Initial solutions were prepared by dissolving 0.8 g PAN and a modifying additive in an amount of 0.2–10 wt% in 20 ml DMF under stirring at 90 °C. After being cooled down to room temperature, the initial solutions were deposited (centrifuged) onto polycor substrates and then were dried at 90 °C for 30 min.

There are some methods for deposition of initial solution on the surface of a substrate, namely dipping, coating and centrifugation. For sensor electronics purposes the most advantageous deposition method is the centrifugation, which was used for the fabrication of films based on PAN. The spin coating runs at 3,000 to 4,000 rpm for 30 to 60 s. This method makes it possible to produce a uniformly thick layer of 0.5–2 μm thickness. Substrates were degreased by boiling in isopropanol for 10 min beforehand.

Further, the samples were stored in air for 24 h at 22 °C to extract the solvent.

To establish the optimum temperature of drying the PAN films, the computer simulation was used [4]. The computer simulation of formation of a polymer PAN chain with the greatest possible number of the monomer links at three values of

temperatures: 80, 130 and 160 °C was done. It was established that drying the metal-containing PAN thin films at temperature 160 °C is expedient according to the results of computer simulation using the Monte-Carlo method. It has been shown the Monte-Carlo simulation technique is valid and effective through the experiment. It has an adequate application in the sphere of creation the functional material with defined properties.

IR-annealing of the films was performed in a vacuum chamber. Time-temperature modes of IR-annealing were selected experimentally, since the intensity and duration of infrared radiation provides an opportunity to control the properties of the material films by changing the molecular structure of the polymer. The radiation intensity at the first stage of IR-annealing corresponds to temperatures varying from 150 to 350 °C during a 5–60 min time period, and the intensity of radiation at the second stage of the IR-annealing corresponds to temperatures of 350–515 °C during a 2–60 min period.

The thickness of the films was measured by the interferential microscopy using Linnik interferometer MII-4.

Scanning electron microscopy (SEM) of the gained films was carried out using LEO 1560.

Energy-filtered TEM (EFTEM) microanalysis was done using LEO 912 AB OMEGA transmission electron microscope fitted with an in-column Omega energy filter, having such characteristic as an operating accelerating voltage of 100 kV; magnification: 80–500,000x; image resolution: 0.2–0.34 nm.

The XPS spectra were registered using a K-Alpha X-ray photoelectron spectrometer (Thermo Fisher Scientific Company). The source of the X-ray radiation was K α 12-line Al ($h\nu = 1,486.6$ eV). The vacuum in the analyzer chamber was $4.5 \cdot 10^{-9}$ mbar. The accuracy in determining the binding energy was ± 0.1 eV, and that of the element composition was ± 1.0 at.%. The binding energy scale was calibrated against the C 1s line of aliphatic carbon ($E_b = 285.0$ eV).

The XRD was performed using a DRON-6 device; the wavelength of the X-ray radiation of CuK α was 1.54051 Å.

The surface morphology was observed by atomic force microscopy (AFM) using scanning probe microscope Solver P-47 Pro (NT-MDT) in a semicontact mode across areas of $5 \times 5 \mu\text{m}^2$. The statistical parameters of the surface morphology were determined using the Image Analysis NT-MDT program.

The electrical characteristics of the fabricated samples were carried out in a setup equipped with heating element. The measurements of the resistance of the film samples were performed using an E6-13A teraohmmeter with a 10 % value of the relative error.

The steady-state gas distribution method was used for testing gas-sensing properties. A specially made setup equipped with a quartz chamber, sensor holder, gas and purge lines was used to maintain the desired level of detected gas concentration. Sensing characteristics were examined on base of the measurement of the film resistance. The quartz chamber volume was around 700 cm^3 so that the changes in gas concentration was immediate and measurements of the response time and the recovery time of the sensors were accurate.

The gas sensitivity (S) was defined as the following ratio [52]:

$$S = (R_o - R_g)/R_o, \text{ when } R_o > R_g, \quad (5.1)$$

where R_o is the resistance in air, R_g is the resistance in the atmosphere of the detected gas.

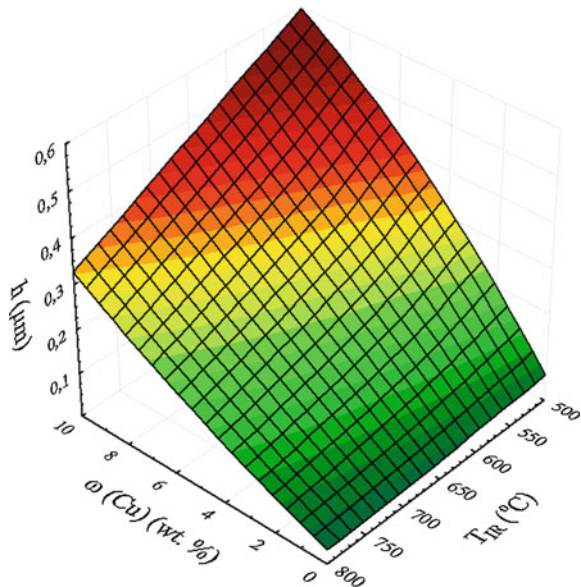
5.3 Results and Discussion

PAN has the ability to form thin films that demonstrate strong adhesive forces with inorganic material of polycor substrate and its solution in DMF turns into gel that is advantage for modifying additive's particles uniform distribution in the polymer organic matrix of PAN.

The thickness of the prepared films was measured by the method of the interferential microscopy (Fig. 5.1). The films growth was observed in accordance with the technological parameters and different weight concentration of a modifying additive in the initial solutions.

The PAN films thickness was up to 0.12 μm . The Cu-containing PAN films were of various thicknesses in the range from 0.04 to 0.6 μm ; the Co-containing PAN film's thickness was in the range from 0.03 to 0.28 μm ; the Ag-containing PAN film's thickness was between 0.22 and 0.68 μm .

Fig. 5.1 A 3D histogram showing the Cu-containing PAN films thickness dependence on the weight concentration of a modifying additive and IR-pyrolysis temperature



From SEM image (Fig. 5.2), it is revealed the information about the fabricated Co-containing PAN film sample including external morphology (texture) and crystalline structure and orientation of materials.

Topographic contrast allows one to observe existing in the sample phase, grain boundaries and to evaluate the morphology of the particles, their dispersion and other parameters. Figure 5.2 clearly shows the simultaneous presence of the particles, very different in size, e.g., particles having a radius of 0.2 and 1.0 μm . The SEM image is characterized by the particles of modifying additives dispersion in PAN matrix.

The transmission electron microscopy (TEM) was used to measure the size of the nanoparticles in the fabricated films. The microstructure of the Cu-containing PAN film obtained using EFTEM is shown in Fig. 5.3. The micrograph clearly indicates nanoparticles of the modifying additive (Cu, CuO and Cu₂O) and their size distribution. Transition metal chlorides convert into oxides during the heat treatment. The size of copper compounds nanoparticles changes from 3 to 19 nm. The modifying additive nanoparticles embedded into the polymer PAN matrix and it stabilized them to avoid the aggregation [10].

The corresponding selected-area electron diffraction pattern indicates the crystalline order regardless of the light-sized nanoparticles (Fig. 5.4). These TEM results were verified by XPD analysis.

The phase formation and surface crystallization were analyzed by the XRD. There are three main diffraction peaks: at $2\theta = 36.02^\circ$, 37.05° and 43.36° that match to CuO, Cu₂O and Cu crystalline inclusions in the composite films respectively in the XPD pattern [53].

There are three main sharp peaks of Cr, CrO₃ and Cr₂O₃, which observe at 34.88° , 57.38° and 76.62° on the XRD pattern of a Cr-containing PAN film (Fig. 5.5). Other peaks for the most part may be attributed to CrO₃, Cr(OH)₃, Cr₂O₃, Cr₂N, CrO.

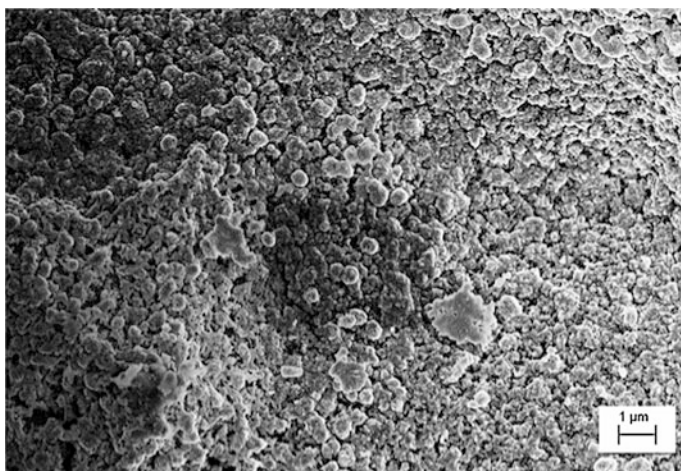


Fig. 5.2 SEM image of Co-containing PAN film

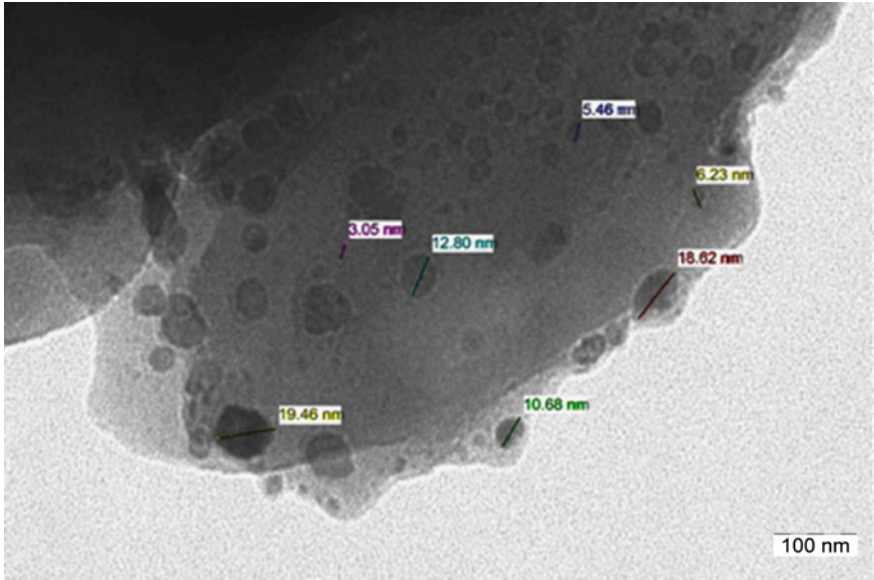
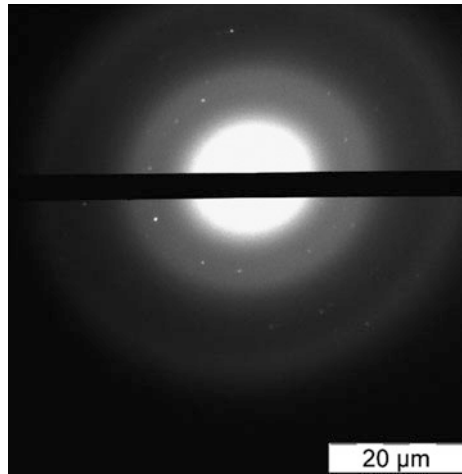


Fig. 5.3 TEM image of a Cu-containing PAN film

Fig. 5.4 Electron diffraction pattern of copper particles trapped in the PAN matrix that is typical nanosized phase



The XRD pattern of a Co-containing PAN film (Fig. 5.6) shows the cobalt state in the structure of the fabricated film. The crystalline structure and phase composition of the films were studied using the XRD method [54]. The X-ray phase analysis showed that the samples studied contain crystalline inclusions of CoO, Co₃O₄ and CoO(OH), whose average sizes were calculated using the Scherrer formula (Table 5.1) [52].

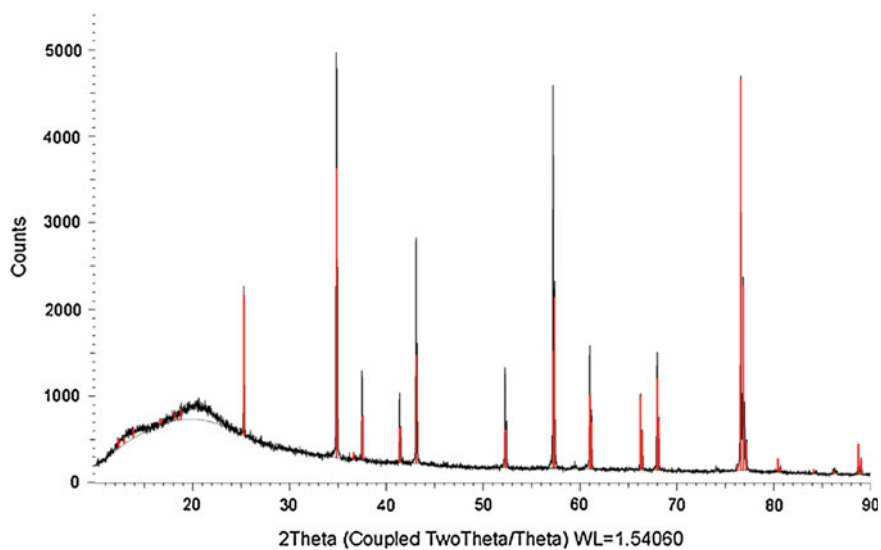


Fig. 5.5 XRD pattern of Cr-containing PAN film

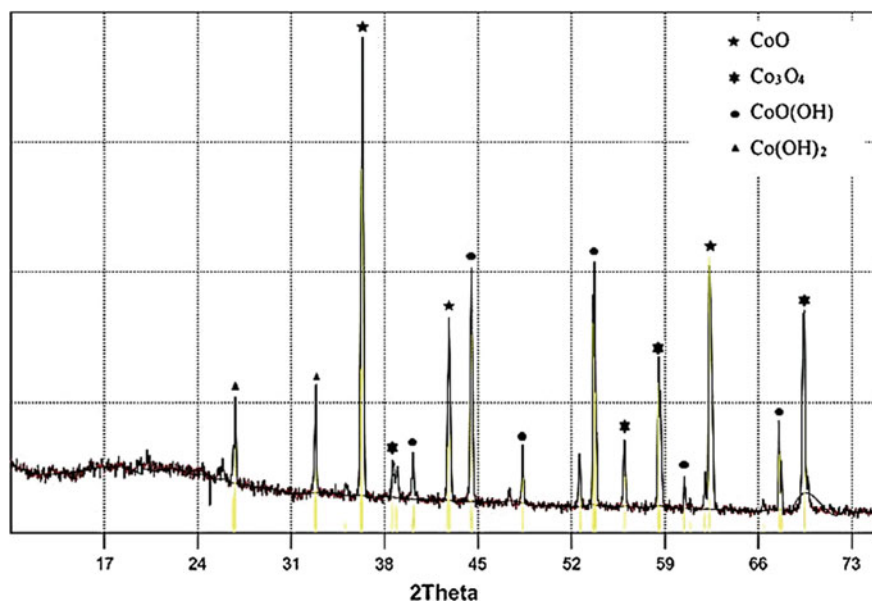
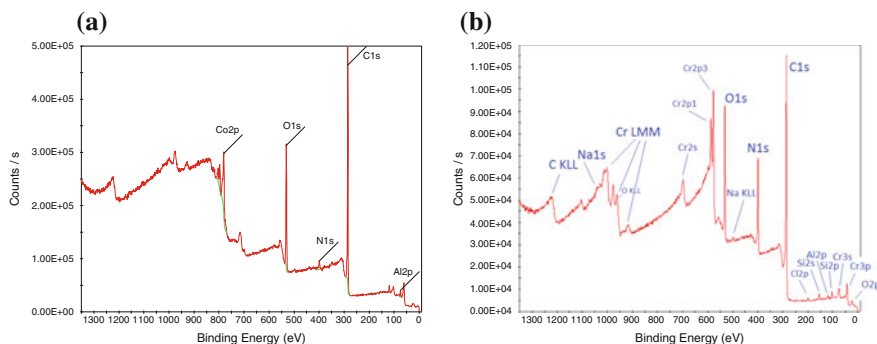


Fig. 5.6 XRD pattern of Co-containing PAN film

Table 5.1 Size of crystallites in the composition of the Co-containing PAN films

Compound	Size of crystallites, D (μm)
CoO	0.38–0.62
Co ₃ O ₄	0.46–0.70
CoO(OH)	0.64–1.07
Co(OH) ₂	0.13–0.67

**Fig. 5.7** X-ray photoelectron spectroscopy survey spectra of the Co-containing PAN film (a) and the Cr-containing PAN film (b)

In order to study the structure of the fabricated films, the XPS-investigations were fulfilled. The character of the chemical bonds in the structure of the organic matrix of the films, the concentration and chemical state of the modifying additive's metal in the near surface region of the samples were determined [55].

XPS survey and narrow scan data were taken for the obtained samples (Fig. 5.7). XPS survey spectra of the Co-containing PAN film showed that the main peaks referring to C 1s (~ 285.7 eV), N 1s (~ 399 eV), O 1s (~ 531 eV), and Co 2p (~ 781 eV) can be expanded into several components. XPS survey spectra, acquired for the Cu-containing PAN film, is present. The peaks located at about 933, 531, 400, and 285 eV corresponding to the electron states of Cu 2p, O 1s, N 1s and C 1s in the PAN molecule, respectively. XPS survey spectra of the Cr-containing PAN film showed the main peaks attributed to C 1s (~ 285.4 eV), N 1s (~ 399 eV), O 1s (~ 532 eV), and Cr 2p (~ 577 eV).

In Tables 5.2, 5.3, 5.4, the XPS elemental surface compositions of the studied metal-containing PAN films are present.

The IR-annealing temperature, time modes variation and different modifying additives allow processing the films with different surface properties, which along with other factors influence on their gas-sensing properties [6, 8, 9, 52].

The comparative analysis of AFM-images of the surface morphology of the metal-containing PAN films showed that the structure morphology of the composite film material and its surface roughness are connected with technological parameters of the films formation (Fig. 5.8).

Table 5.2 Assignments of main spectral bands based on their binding energies (BE) and atomic concentration (AC) of the Co-containing PAN films

Element	BE (eV)	AC (at.%)	Assignments
C 1s	284.68	68.93	Aromatic C=C, aliphatic C-H
	285.60		C(sp ²)-N
	288.20		C(sp ³)-N
N 1s	398.37	3.48	N-C (sp ³)
	399.80		N-C (sp ²)
	402.45		=N ⁺ H
O 1s	529.65	19.76	Co ₃ O ₄
	531.20		Adsorbed O ⁻ and/or OH ⁻
	532.12		C=O, O-C-O
Co 2p	779.94	4.58	Co ₂ O ₃ , Co ₃ O ₄
	781.76		Mixed Co(II, III)
	785.84		CoO
	788.44		CoO(OH), Co(OH) ₂

Table 5.3 Assignments of main spectral bands based on their binding energies (BE) and atomic concentration (AC) of the Cu-containing PAN films

Element	BE (eV)	AC (at.%)	Assignments
C 1s	283.8	81.1	Carbodic
	285.0		C-H
	285.8		C≡N
	287.3		C-O
N 1s	397.5	11.7	C=N-H
	399.5		C≡N
O 1s	530.0	6.4	CuO
	531.4		Adsorbed O ⁻ and/or OH ⁻
Cu 2p	931.6	0.7	Cu ⁰ , Cu ¹⁺
	933.9		Cu ²⁺

The study of structure and composition of the fabricated films gives an opportunity to explain their electrical and gas-sensing properties.

The thin films with resistance values in the range $4.0 \cdot 10^{2-2}$ to $7 \cdot 10^{11} \Omega$ were fabricated using various IR-annealing temperature and various weights of a modifying additive (see Fig. 5.9). As it is obvious from Fig. 5.9, the film conductivity improves significantly by the IR-annealing temperature growth and copper chloride (II) weight concentration increasing.

Table 5.5 and Fig. 5.8 demonstrate that the surfaces of films are uniform, dense and show rougher surface when higher temperatures of IR-annealing are used. The films with uniform surface structure have the resistance values of $10^6 \Omega$. The films with the resistance values about 10^8 – $10^{10} \Omega$ have the non-uniform developed surface. Percentage of the modifying additive in initial solutions and its type had impact on sensing properties of the fabricated nanostructured materials.

Table 5.4 Assignments of main spectral bands based on their binding energies (BE) and atomic concentration (AC) of the Cr-containing PAN films

Element	BE (eV)	AC (at.%)	Assignments
C 1s	284.61	62.51	C–C
	286.24	29.85	C–N
	289.55	7.64	O=C–O
N 1s	398.32	47.17	Nitrogen of pyridine type C ₅ H ₅ N
	398.93	52.83	Nitrogen of pyrrolidone type C ₄ H ₇ NO
O 1s	530.12	17.68	CrO
	531.37	72.64	Adsorbed O ⁻ and/or OH ⁻
	532.45	9.68	
Cr 2p3	576.15	65.17	Cr ₂ O ₃ , Cr ₂ N
	574.44	13.85	Cr
	580.97	9.17	Cr(OH) ₃
	578.48	11.81	CrO ₃

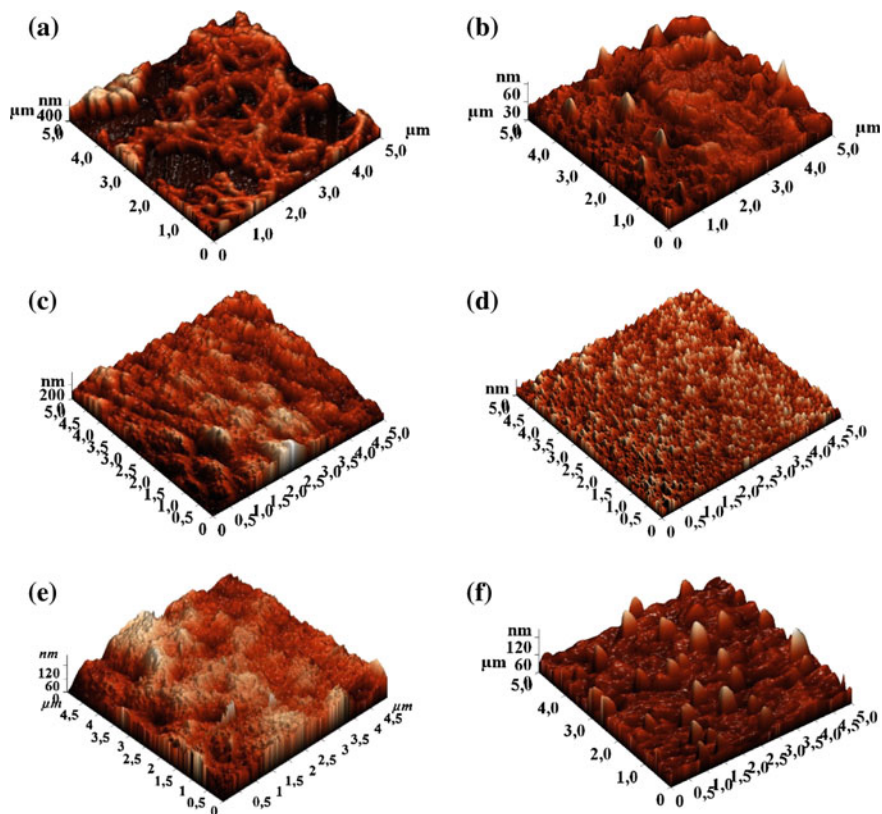


Fig. 5.8 AFM-images of the surface of metal-containing PAN films sensitive to different gases: **a** Cr/PAN on gasoline vapors ($S = 0.99$ r. u.); **b** Co/PAN on NO_2 and Cl_2 ($S = 0.88$ r. u. and $S = 0.87$ r. u., respectively); **c** Co/PAN on NO_2 and Cl_2 ($S = 0.62$ r. u. and $S = 0.09$ r. u., respectively); **d** Co/PAN on NO_2 and Cl_2 ($S = 0$ r. u. and $S = 0.13$ r. u., respectively); **e** Ag/PAN on Cl_2 ($S = 0.73$ r. u.); **f** Cu/PAN on NH_3 ($S = 0.53$ r. u.)

Fig. 5.9 A 3D histogram showing the Cu-containing PAN films resistance dependence on the weight concentration of a modifying additive and IR-pyrolysis temperature

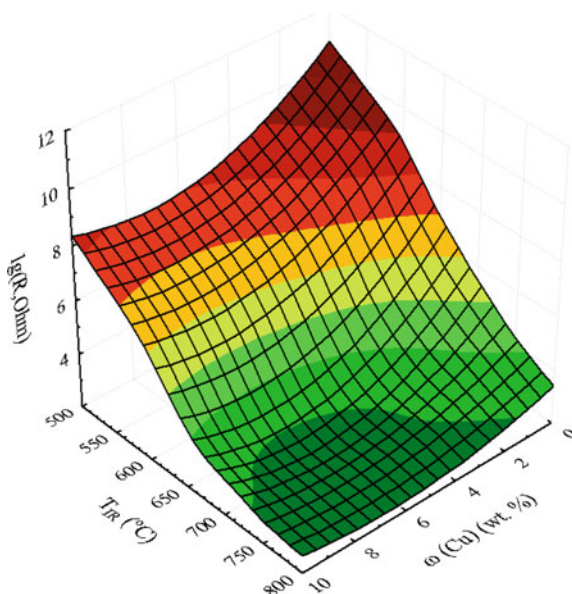


Table 5.5 Technological modes of the fabricated metal-containing PAN films, its resistance values R , the root-mean-square R_q and the gas sensitivity coefficient values S

No.	Modifying additive	ω (Me) (wt%)	T_1 (°C) – t_1 (min)	T_2 , °C – t_2 , min	R (Ω)	R_q (nm)	Detected gas	S , r. u.
1	Cr	0.75	350 – 5	400 – 5	$2.48 \cdot 10^{10}$	108.55	Gasoline vapors	0.99
2 ^a	Co	0.25	250 – 5	500 – 2	$9.2 \cdot 10^6$	8.32	NO ₂	0.88
							Cl ₂	0.87
3 ^a	Co	1	250 – 5	450 – 10	$9.5 \cdot 10^6$	55.30	NO ₂	0.62
							Cl ₂	0.09
4 ^a	Co	1	250 – 5	500 – 2	$2.9 \cdot 10^2$	12.90	NO ₂	0
							Cl ₂	0.13
5 ^a	Ag	0.05	300 – 10	400 – 2	$1.9 \cdot 10^6$	21.3	Cl ₂	0.73
6 ^a	Cu	0.25	300 – 20	350 – 10	$2.6 \cdot 10^8$	111.3	NH ₃	0.53

^a $T_{\text{drying}} = 160$ °C, $t_{\text{drying}} = 30$ min

5.4 Conclusions

The literature review of studies on PAN-based material has been done. It has been demonstrated that PAN exhibits four main structured forms that are interesting for researchers: films, membranes, composites and carbon fibers or nanofibers. Some of the methods of PAN-based material's fabrication and its applications have been discussed.

The new method of manufacturing the metal-containing PAN thin films has been proposed. A novel resistive type gas sensor, based on polyacrylonitrile composite matrix, was applied for determination of NO₂, Cl₂, NH₃ and gasoline vapors at room temperature.

The fabricated metal-containing PAN films are nanocomposites in which the particles of modifying additives are distributed in an amorphous polymer PAN matrix. The gas sensitivity of the fabricated semiconductor thin films based on metal-containing PAN depends on the composition of the initial solutions and on the process parameters of forming the film material. The fulfilled research inspires the idea that metal-containing PAN films can be good materials for high performance multisensory systems.

Acknowledgments This work was performed with the financial support of the Federal Targeted Program “Investigation and High Priority Branches of Development of Scientific Technological Complexes of Russia for the period of 2014–2020” of the Ministry of Education and Science of the Russian Federation (the unique project number RFMEFI57514X0103). The equipment of the Centre of Collective Use of Equipment “Nanotechnologies” and Multi-Access Center of Microsystem Engineering and Integral Sensor Technology of the Southern Federal University as well as the Kabardino-Balkarsky State University and the Helmholtz-Zentrum Berlin für Materialien und Energie was used for this study. The author is also grateful to M.M. Brzhezinskaya, Helmholtz-Zentrum Berlin für Materialien und Energie, Berlin, Germany; to Z. Kh. Kalazhokov and Kh.Kh. Kalazhokov, Kabardino-Balkarsky State University, Nalchik, Kabardino-Balkar Republic, Russia; to O.A. Ageev, Engineering-Technological Academy, Southern Federal University, Taganrog, Russia.

References

1. T.J. Dawidczyk, H. Kong, H.E. Katz, *Handb. Org. Mater. Opt. (Opto)electron. Devices* **20**, 577 (2013)
2. J.V. Yakhmi, V. Saxena, D.K. Aswal, *Funct. Mater.* **2**, 61 (2012)
3. X. Li, Y. Wang, X. Yang, J. Chen, H. Fu, T. Cheng, *Trends Anal. Chem.* **39**, 163 (2012)
4. T. Semenistaya, N. Plugotarenko, V. Petrov, *Appl. Mech. Mater.* **727–728**, 145 (2015)
5. A.N. Korolev, T.V. Semenistaya, I.S. Al-Hadrami, T.P. Loginova, M. Bruns, *Perspect. Mater.* **5**, 52 (2010). (In Russian)
6. P. Lu, V.A. Ivanets, T.V. Semenistaya, N.K. Plugotarenko, *Nano- Microsyst. Technics* **5**, 21 (2012). (In Russian)
7. T.V. Semenistaya, V.V. Petrov, P. Lu, *Adv. Mater. Res.* **804**, 135 (2013)
8. T.V. Semenistaya, V.V. Petrov, T.A. Bednaya, O.A. Zaruba, *Mater. Today: Proc.* **2**(1), 77 (2015)
9. V.V. Petrov, N.K. Plugotarenko, T.V. Semenistaya, *Chaotic Model Simul* **4**, 609 (2013)
10. Sh. Deki, H. Nabika, K. Akamatsu, M. Mizuhata, A. Kajinami, *Scripta Mater.* **44**, 1879 (2001)
11. C. Calberg, M. Mertens, R. Jérôme, X. Arys, A.M. Jonas, R. Legras, *Thin Solid Films* **310**, 148 (1997)
12. D.M. Yu, S.-W. Nam, S. Yoon, T.-H. Kim, J.Y. Lee, S.Y. Nam, Y.T. Hong, *J. Ind. Eng. Chem.* **28**, 190 (2015)
13. P. Newton, F. Houzé, S. Guessab, S. Noël, L. Boyer, G. Lécayon, P. Viel, *Thin Solid Films* **303**, 200 (1997)
14. S. Guessab, L. Boyer, F. Houzé, S. Noël, O. Schneegans, *Synth. Met.* **118**, 121 (2001)

15. H. Zheng, H. Xue, Y. Zhang, Z. Shen, *Biosens. Bioelectron.* **17**, 541 (2002)
16. C. Reynaud, C. Boiziau, C. Juret, S. Leroy, J. Perreau, G. Lecayon, *Synth. Met.* **11**, 159 (1985)
17. J.A. Meyers, *J. Non-Cryst. Solids* **63**, 425 (1984)
18. H. Xue, Z. Shen, Ch. Li, *Biosens. Bioelectron.* **20**, 2330 (2005)
19. S. Nishio, T. Chiba, A. Matsuzaki, H. Sato, *Appl. Surf. Sci.* **106**, 132 (1996)
20. S. Leroy, C. Boiziau, J. Perreau, C. Reynaud, G. Zalczer, G. Lécayon, C. Le Gressus, *J. Mol. Struct.* **128**, 269 (1985)
21. Q. Ouyang, L. Cheng, H. Wang, K. Li, *Polym. Degrad. Stab.* **93**, 1415 (2008)
22. B. Jung, *J. Membr. Sci.* **229**, 129 (2004)
23. M. Dalwani, N.E. Benes, G. Bargeman, D. Stamatialis, M. Wessling, *J. Membr. Sci.* **372**, 228 (2011)
24. M. Khamforoush, O. Pirouzram, T. Hatami, *Desalination* **359**, 14 (2015)
25. S.R. Panda, M. Mukherjee, S. De, *J. Water Process Eng.* **6**, 93 (2015)
26. Q.-Y. Wu, L.-Sh Wan, Z.-K. Xu, *J. Membr. Sci.* **409–410**, 355 (2012)
27. G. Zhang, H. Meng, Sh Ji, *Desalination* **242**, 313 (2009)
28. Q. Wang, W.-L. Song, L.-Z. Fan, Y. Song, *J. Membr. Sci.* **486**, 21 (2015)
29. N.A. El-Ghamaz, M.A. Diab, MSh Zoromba, A.Z. El-Sonbati, O. El-Shahat, *Solid State Sci.* **24**, 140 (2013)
30. S. İnan, Y.I Altaş, *Chem. Eng. J.* **168**, 1263 (2011)
31. T.N.L. Doan, M. Ghaznavi, Y. Zhao, Y. Zhang, A. Konarov, M. Sadhu, R. Tangirala, P. Chen, *J. Power Sources* **241**, 61 (2013)
32. J. Wang, J. Yang, C. Wan, K. Du, J. Xie, N. Xu, *Adv. Funct. Mater.* **13**, 487 (2003)
33. J.-J. Hwang, T.-W. Ma, *Mater. Chem. Phys.* **136**, 613 (2012)
34. D. Shan, Q. Shi, D. Zhu, H. Xue, *Talanta* **72**, 1767 (2007)
35. X. He, W. Pu, L. Wang, J. Ren, Ch. Jiang, Ch. Wan, *Solid State Ionics* **178**, 833 (2007)
36. G.R. Kiani, H. Sheikhoie, N. Arsalani, *Desalination* **269**, 266 (2011)
37. A.V. Korobeinyk, R.L.D. Whitby, S.V. Mikhailovsky, *Eur. Polymer J.* **48**, 97 (2012)
38. F. Nacimiento, R. Alcántara, J.L. Tirado, *J. Electroanal. Chem.* **642**, 143 (2010)
39. I.-H. Chen, Ch.-Ch. Wang, Ch.-Y. Chen, *Carbon* **48**, 604 (2010)
40. S.K. Nataraj, K.S. Yang, T.M. Aminabhavi, *Prog. Polym. Sci.* **37**, 487 (2012)
41. T. Evans, J.-H. Lee, V. Bhat, S.-H. Lee, *J. Power Sources* **292**, 1 (2015)
42. J.H. Lee, J. Manuel, H. Choi, W.H. Park, J.-H. Ahn, *Polymer* **68**, 335 (2015)
43. G. Nie, Z. Li, X. Lu, J. Lei, Ch. Zhang, C. Wang, *Appl. Surf. Sci.* **284**, 595 (2013)
44. M. Kozicki, E. Szaśiadek, I. Karbownik, W. Maniukiewicz, *Sensors and Actuators B* **213**, 234 (2015)
45. C. Reynaud, C. Boiziau, C. Juret, S. Leroy, J. Perreau, G. Lecayon, *Synth. Met.* **11**, 159 (1985)
46. M. Surianarayanan, R. Vijayaraghavan, K.V. Raghavan, *J. of Polymer Science* **36**, 2503 (1998)
47. N. Chatterjee, S. Basu, S.K. Palit, M.M. Maiti, *J. of Polymer Science: Part B: Polymer Physics* **33**, 1705 (1995)
48. M. Jing, C. Wang, Q. Wang, Y.-J. Bai, B. Zhu, *Polym. Degrad. Stab.* **92**, 1737 (2007)
49. Q. Ouyang, L. Cheng, H. Wang, K. Li, *Polym. Degrad. Stab.* **93**, 1415 (2008)
50. L.M. Zemtsov, G.P. Karpacheva, *High-molecular Compounds*, **36(6)**, 919 (1994). (In Russian)
51. L.M. Zemtsov, G.P. Karpacheva, O.N. Efimov, V.V. Kozlov, K.A. Bagdasarova, D.G. Muratov, *Chem. Technol.* **35(1)**, 25 (2005)
52. T.V. Semenistaya, V.V. Petrov, KhKh Kalazhokov, ZKh Kalazhokov, B.S. Karamurzov, KhV Kushkhov, S.P. Konovalenko, *Surf. Eng. Appl. Electrochem.* **51(1)**, 9 (2015)
53. Z.H. Liang, Y.J. Zhu, *Chem. Lett.* **34**, 214 (2005)
54. W. Li, H. Jung, N.D. Hoa, D. Kim, S.-K. Hong, H. Kim, *Sens Actuators B* **150**, 160 (2010)
55. C.R. Wu, W.R. Salaneck, J.J. Ritsko, *Synth. Met.* **16**, 147 (1986)

Chapter 6

Features of Phase Formation in the Preparation of Bismuth Ferrite

L.A. Shilkina, I.A. Verbenko, A.G. Abubakarov, L.A. Reznichenko,
O.N. Razumovskaya, T.N. Sorokun and V.A. Aleshin

Abstract Based on a series of experiments, features of BiFeO₃ phase formation in solid-phase synthesis and sintering without pressure were studied in detail. It was shown that processes caused by structural nonstoichiometry of objects play important role in the formation of real ceramics. We discuss probable causes of the structural nonstoichiometry occurrence. They are connected both with a high stability of intermediate phases, and with the losses of oxygen resulting from partial reduction of elements with variable oxidation states. Conclusions about the possible ways to optimize the technology of materials based on BiFeO₃ were taken.

6.1 Introduction

Multiferroics, which represent a class of materials exhibiting simultaneous ferroelectric, ferromagnetic, and ferroelastic ordering, are under intensive investigation nowadays due to the potential applications in new devices based on the mutual controls of magnetic and electric fields. The most famous and well-studied of multiferroics is bismuth ferrite (BiFeO₃).

Because of high temperatures of the ferroelectric (FE) ($T_C = 1083$ K) and magnetic ($T_N \sim 643$ K) ordering, BiFeO₃ is considered as a convenient target for magnetoelectric materials. However, its magnetoelectric properties are relatively small. This is because of the peculiarities of the magnetic and crystal structures, and due to a large difference in temperature between the magnetic and ferroelectric phase transition. Moreover, it was found that the BiFeO₃ is not thermodynamically stable at temperatures, required for the synthesis by solid-phase method [1–3].

L.A. Shilkina · I.A. Verbenko (✉) · A.G. Abubakarov · L.A. Reznichenko
O.N. Razumovskaya · T.N. Sorokun · V.A. Aleshin
Research Institute of Physics, Southern Federal University,
344090 Rostov-on-Don, Russia
e-mail: ilich001@yandex.ru

Despite numerous attempts to synthesize thermally stable powder, it was not possible at sintering of dense ceramics. For example, to stabilize the bismuth ferrite, it is necessary the addition of modifiers.

6.2 Objects and Methods

All samples were obtained by using solid-phase oxides Bi_2O_3 , Fe_2O_3 with quality no lower than “analytical grade”. The temperature was adjusted in the range of first synthesis $T_{\text{ sint}} = (400\text{--}800)^\circ\text{C}$, $\Delta T = (20\text{--}50)^\circ\text{C}$, during 10 h. Second synthesis was performed at $T_2 = (700\text{--}900)^\circ\text{C}$, $\Delta T = (20\text{--}50)^\circ\text{C}$, during 10 h and sintering was carried out at $T_s = (800\text{--}930)^\circ\text{C}$ for 2 h.

Phase composition and synthesis completeness were verified with help of X-ray diffraction analysis. Precise studies were performed on fine-grained ceramic powder by X-ray diffraction on a DRON 3.0, $\text{FeK}\alpha$ radiation. The linear (a), angular (α), and bulk (V , perovskite cell volume) parameters were calculated by standard technique.

The experimental (ρ_{exp}) sample density was found by hydrostatic weighing in octane; the X-ray density ($\rho_{\text{X-ray}}$) was calculated from the formula $\rho_{\text{X-ray}} = 1.66 \times M/V$, where M is the weight unit in grams and V is the perovskite cell volume in \AA ; relative density ρ_{rel} was calculated from the formula $\rho_{\text{rel}} = (\rho_{\text{exp}}/\rho_{\text{X-ray}}) \times 100\%$.

The polycrystalline (grain) structure of multiferroics was studied in reflected light using a Neophot 2 optical microscope and a Leica DMI 5000 M inverted microscope.

6.3 Results and Discussion

Based on a series of experiments, features of BiFeO_3 phase formation in solid-phase synthesis and sintering without pressure were studied in detail.

We discuss probable causes of BiFeO_3 phase formation occurrence, below. Comparison with reagents and possible reaction products was carried out:

Fe_2O_3 is the hematite of rhombohedral (Rh) symmetry, S.G. R-3c, $a = 5.035 \text{ \AA}$, $c = 13.749 \text{ \AA}$ [4];

$\alpha\text{-Bi}_2\text{O}_3$ demonstrates monoclinic (M) symmetry, S.G. P21/c, $a = 5.848 \text{ \AA}$, $b = 8.166 \text{ \AA}$, $c = 7.51 \text{ \AA}$, $\beta = 113^\circ$ [5];

$\text{Bi}_{25}\text{FeO}_{40}$ has cubic (C) symmetry, S.G. I23, $a = 10.181 \text{ \AA}$ [6];

$\text{Bi}_2\text{Fe}_4\text{O}_9$ shows rhombic (R) symmetry, S.G. Pbam, $a = 7.965 \text{ \AA}$, $b = 8.44 \text{ \AA}$, $c = 5.994 \text{ \AA}$ [7];

BiFeO_3 has rhombohedral (Rh) symmetry, S.G. R-3 m, $a = 5.58 \text{ \AA}$, $c = 6.93 \text{ \AA}$ [8].

These products and compounds are connected both with a high stability of intermediate phases, and with the losses of oxygen resulting from partial reduction of elements with variable oxidation states.

It was shown that processes caused by structural non-stoichiometry of objects play important role in the formation of real ceramics. Based on the X-ray diffraction analysis, we shows that the mechanism of formation of impurities in the solid phase synthesis and sintering of ceramics without the application of pressure is inextricably linked to the complex kinetics of processes occurring with the participation of intermediate phases ($\text{Bi}_{25}\text{FeO}_{40}$, $\text{Bi}_2\text{Fe}_4\text{O}_9$).

Table 6.1 shows that crystalline phase $\text{Bi}_{25}\text{FeO}_{40}$ forms even at 450 °C. Obviously, this compound is an intermediate in the synthesis of BiFeO_3 , and BiFeO_3 forms only at $T_1 = (500\text{--}550)$ °C. Phase $\text{Bi}_2\text{Fe}_4\text{O}_9$ was not detected at these temperatures.

Figure 6.1 shows the relative intensities of strong lines of BiFeO_3 , $\text{Bi}_{25}\text{FeO}_{40}$, $\text{Bi}_2\text{Fe}_4\text{O}_9$ and their mutual concentrations in mixtures. We can see that the line of $\text{Bi}_{25}\text{FeO}_{40}$ becomes the strongest in diffractogram at concentration 40 vol% in the mixture $\text{BiFeO}_3\text{--Bi}_{25}\text{FeO}_{40}$ (Fig. 6.1a), the line of $\text{Bi}_2\text{Fe}_4\text{O}_9$ becomes the strongest in diffractogram at concentration 70 vol% in mixture $\text{BiFeO}_3\text{--Bi}_2\text{Fe}_4\text{O}_9$ (Fig. 6.1b), the line of $\text{Bi}_2\text{Fe}_4\text{O}_9$ becomes maximum in diffractogram at concentration 80 vol% in mixture $\text{Bi}_{25}\text{FeO}_{40}\text{--Bi}_2\text{Fe}_4\text{O}_9$ (Fig. 6.1c).

The small quantities of this compound do not show itself in the diffraction patterns.

Figure 6.2 and Table 6.2 show the content (by vol%) of $\text{Bi}_2\text{Fe}_4\text{O}_9$ (1), BiFeO_3 (2), $\text{Bi}_{25}\text{FeO}_{40}$ (3) in the sample after 1 synthesis at different T_1 . Analysis of Fig. 6.2 shows that the active synthesis of $\text{Bi}_2\text{Fe}_4\text{O}_9$ occurs in temperature range ($650 < T_1 \leq 750$) °C. However, with increasing temperature up to $T_1 = 790$ °C, the bismuth ferrite becomes main phase.

This leads to violations of local stoichiometry. At the same time, the chemical bonds of Bi–O and Fe–O are broken at the synthesis temperatures and oxygen is partially lost. Point defects of the vacancy type form in a large amount and create

Table 6.1 Relative intensities of strong X-ray lines of source products and compounds, formed during the first synthesis of the BiFeO_3

T_1 (°C)	Relative intensities of X-ray lines				
	BiFeO_3	$\text{Bi}_{25}\text{FeO}_{40}$	$\text{Bi}_2\text{Fe}_4\text{O}_9$	Fe_2O_3	$\alpha\text{-Bi}_2\text{O}_3$
400	–	–	–	33	100
450	–	17	–	22	100
500	–	46	–	30	100
550	3	100	–	20	66
600	4	100	–	15	15
650	47	100	18	–	–
700	36	100	41	–	–
750	61	100	54	–	–
790	100	22	17	–	–
800	100	5	4	–	–

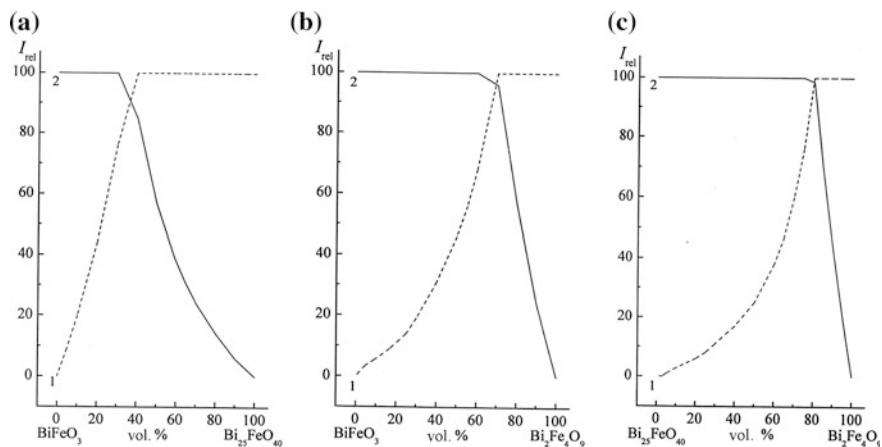
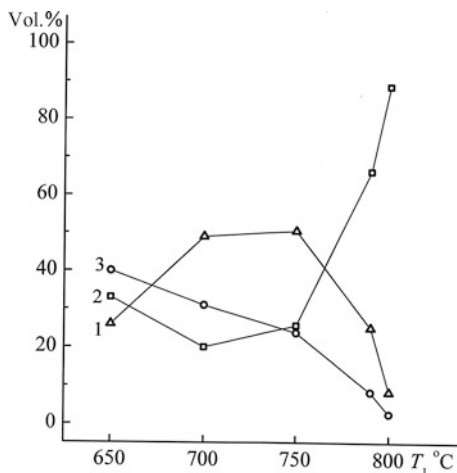


Fig. 6.1 Relative intensity of X-ray strong lines of BiFeO_3 , $\text{Bi}_{25}\text{FeO}_{40}$, $\text{Bi}_2\text{Fe}_4\text{O}_9$ on the diffraction patterns of these mixtures: **a** 1 $\text{Bi}_{25}\text{FeO}_{40}$, 2 BiFeO_3 ; **b** 1 $\text{Bi}_2\text{Fe}_4\text{O}_9$, 2 BiFeO_3 ; **c** 1 $\text{Bi}_2\text{Fe}_4\text{O}_9$, 2 $\text{Bi}_{25}\text{FeO}_{40}$

Fig. 6.2 Content of $\text{Bi}_2\text{Fe}_4\text{O}_9$ (1), BiFeO_3 (2), $\text{Bi}_{25}\text{FeO}_{40}$ (3) in the samples after first synthesis at different values of T_1



extended structures. Then crystallographic shear occurs at exception of the extended defects. A disadvantage of position arises in the structure of the compound. It reflects in all subsequent processes of phase formation and leads to the appearance of impurities.

We stated that bismuth ferrite with relatively low content of impurities formed even at low content of the main phase of the synthesized powders. The results of sintering ceramics (Table 6.3) show that the maximum density achieved at $T_s = 850$ °C. The minimum amount of the impurity phases reached at $T_s = (850-870)$ °C.

Table 6.2 The relative intensity of X-ray strong lines of $\text{Bi}_{25}\text{FeO}_{40}$, $\text{Bi}_2\text{Fe}_4\text{O}_9$, BiFeO_3 and cell parameters formed during the second synthesis of the BiFeO_3

$T_1, ^\circ\text{C}$	$T_2, ^\circ\text{C}$	Relative intensities of X-ray lines			Parameters of Rh-cell of BiFeO_3		
		BiFeO_3	$\text{Bi}_{25}\text{FeO}_{40}$	$\text{Bi}_2\text{Fe}_4\text{O}_9$	a (Å)	α (degrees)	V (Å ³)
500	700	27	100	37			
	750	100	20	12	3.9640	89.43	62.29
	800	100	8	3	3.9646	89.43	62.31
	850	100	8	8	3.9637	89.43	62.28
	900	100	12	5	3.9636	89.45	62.27
550	700	23	100	45			
	750	100	20	11	3.9637	89.43	62.28
	800	100	6	5	3.9651	89.44	62.34
	850	100	8	8	3.9641	89.43	62.29
	900	100	35	21	3.9641	89.43	62.29
600	700	42	100	44			
	750	100	15	11	3.9646	89.44	62.31
	800	100	7	6	3.9650	89.43	62.33
	850	100	10	6	3.9620	89.43	62.20
	900	100	36	29	3.9648	89.45	62.32

Figure 6.3 presents photographs of the bismuth ferrite microstructure sintered at different temperatures. Black areas of irregular shapes correspond to pores, distributed inhomogeneously over the surface. The boundaries of the crystallites, revealed by etching, are shown by dark lines around the lighter areas (ceramic grains). The bright grains present the main “light” phase and the darker grains demonstrate the second “gray” phase. Moreover, there is a certain amount of etching products. The grain size decreases with increasing temperature. Traces of melting appear at 900 °C.

Table 6.4 shows the results of X-ray diffraction and density of the ceramics sintered at 870 °C and synthesized in various conditions.

The clear relationship between the bulk of the unit cell and the temperature of the second synthesis was stated. It was shown that the maximum values of the unit cell bulk reaches at $T_2 = 800$ °C. We identify that amount of impurity phases and density of sintered ceramics did not depend almost of the temperature of the first synthesis. Minimal amount of impurities observed at $T_2 = 800$ °C, and the maximum density was at $T_2 = 750$ °C. Moreover, at higher temperatures the samples had traces of melting showing partial decomposition of BiFeO_3 .

The most precise X-ray reflections observed in the material with a temperature of the second synthesis equal to 800 °C. The splitting of the doublet α_1/α_2 is clearly seen. During sintering of ceramics synthesized at $T_2 \geq 800$ °C, the degradation of the diffraction pattern—X-ray lines are blurred, their width increases, and the intensities of maxima fall.

Table 6.3 Relative intensity of X-ray strong lines of $\text{Bi}_{25}\text{FeO}_{40}$, $\text{Bi}_2\text{Fe}_4\text{O}_9$, BiFeO_3 , cell parameters and density of ceramics: experimental, ρ_{exp} , X-ray, $\rho_{\text{X-ray}}$, relative, ρ_{rel} , after sintering at $T_s = (800\text{--}930)^\circ\text{C}$ for 2 h

T_1 ($^\circ\text{C}$)	T_s ($^\circ\text{C}$)	Cell parameters		α (degree)	V (\AA^3)	ρ_{exp} (g/cm^3)	$\rho_{\text{X-ray}}$ (g/cm^3)	ρ_{rel} (%)		
		$\text{Bi}_{25}\text{FeO}_{40}$	$\text{Bi}_2\text{Fe}_4\text{O}_9$							
650 (No. 1) ($T_2 = 800^\circ\text{C}$) 8—($\text{Bi}_{25}\text{FeO}_{40}$) 5—($\text{Bi}_2\text{Fe}_4\text{O}_9$) $a = 3.9656 \text{ \AA}$ $\alpha = 89.43^\circ$ $V = 62.364 \text{ \AA}^3$	800	8	6	3.9653	89.43	62.349	6.21	8.379	74.11	
	820	6	5	3.9654	89.44	62.354	7.35	8.378	87.73	
	840	8	7	3.9642	89.43	62.295	7.50	8.386	89.43	
	850	8	5	3.9647	89.42	62.320	7.52	8.383	89.71	
	870	15	9	3.9653	89.44	62.349	7.34	8.379	87.60	
	890	9	6	3.9652	89.44	62.344	7.50	8.379	89.50	
	910	15	13	3.9643	89.42	62.300	6.64	8.385	79.18	
	930	33	25	3.9652	89.41	62.345	6.57	8.379	78.41	
	800 (No. 2) ($T_2 = 800^\circ\text{C}$) 7—($\text{Bi}_{25}\text{FeO}_{40}$) 7—($\text{Bi}_2\text{Fe}_4\text{O}_9$) $a = 3.9642 \text{ \AA}$ $\alpha = 89.43^\circ$ $V = 62.295 \text{ \AA}^3$	800	6	6	3.9654	89.43	62.354	6.23	8.378	74.36
	820	8	7	3.9653	89.44	62.349	7.13	8.379	85.09	
	840	8	8	3.9647	89.42	62.320	7.50	8.383	89.47	
	850	10	6	3.9649	89.43	62.330	7.55	8.381	90.08	
	870	9	7	3.9654	89.42	62.355	7.29	8.378	87.01	
	890	9	6	3.9650	89.43	62.335	7.57	8.381	90.32	
	910	19	16	3.9649	89.43	62.330	6.77	8.381	80.77	
930	29	23	3.9653	89.43	62.349	6.64	87.379	79.25		
800 (No. 5) (only after T_1)	800	7	7	3.9648	89.44	62.327	6.08	8.382	72.54	
820	5	6	3.9650	89.43	62.335	6.94	8.381	82.81		
840	7	6	3.9650	89.44	62.334	7.44	8.381	88.77		
850	5	7	3.9648	89.43	62.325	7.55	8.382	90.07		
870	7	4	3.9648	89.44	62.325	7.34	8.382	87.57		
890	19	14	3.9650	89.44	62.334	6.80	8.381	81.14		
910	25	14.	3.9651	89.44	62.339	6.62	8.380	78.99		
930	33	27	3.9651	89.44	62.339	6.55	8.380	78.16		

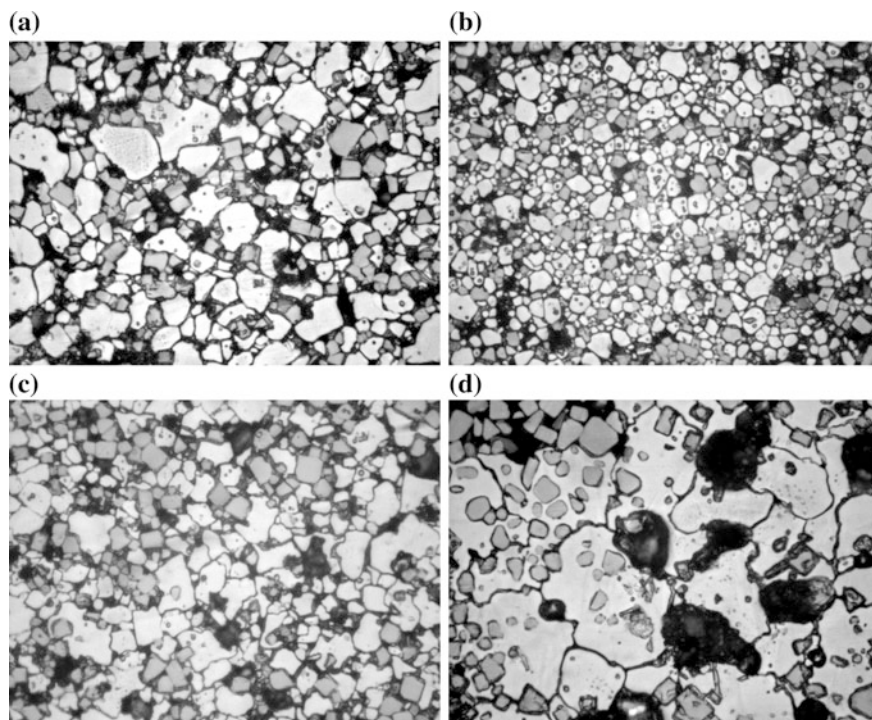


Fig. 6.3 Photographs of the bismuth ferrite microstructure sintered at different temperatures: **a** 850 °C; **b** 870 °C; **c** 890 °C; **d** 900 °C

Table 6.4 Relative intensity of X-ray strong lines of $\text{Bi}_{25}\text{FeO}_{40}$, $\text{Bi}_2\text{Fe}_4\text{O}_9$, BiFeO_3 , cell parameters and density of ceramics: experimental, ρ_{exp} , X-ray, $\rho_{\text{X-ray}}$, relative, ρ_{rel} , after sintering at $T_s = 870$ °C for 2 h

T_1 (°C)	T_2 (°C)			Cell parameters			ρ_{exp} (g/cm ³)	$\rho_{\text{X-ray}}$ (g/cm ³)	ρ_{rel} (%)
		$\text{Bi}_{25}\text{FeO}_{40}$	$\text{Bi}_2\text{Fe}_4\text{O}_9$	a (Å)	α	V (Å ³)			
500	700	8	8	3.9641	89.44	62.290	7.22	8.387	86.09
	750	8	8	3.9643	89.43	62.303	7.46	8.385	88.97
	800	4	5	3.9648	89.43	62.325	6.69	8.382	79.81
	850	9	12	3.9639	89.44	62.285	7.09	8.387	84.53
	900	23	15	3.9640	89.43	62.286	7.24	8.387	86.32
550	700	7	7	3.9643	89.42	62.300	7.24	8.385	86.34
	750	8	7	3.9647	89.44	62.320	7.71	8.383	91.97
	800	6	7	3.9649	89.44	62.332	7.16	8.381	85.43
	850	14	10	3.9649	89.43	62.330	7.15	8.381	85.31
	900	23	24	3.9635	89.43	62.266	7.02	8.390	83.67
600	700	6	6	3.9642	89.43	62.295	7.24	8.386	86.33
	750	9	9	3.9642	89.42	62.296	7.44	8.386	88.72
	800	5	6	3.9650	89.44	62.334	7.22	8.381	86.15
	850	16	15	3.9644	89.43	62.305	7.05	8.385	84.08
	900	29	25	3.9633	89.44	62.256	7.06	8.391	84.13

It is possible, the optimum sintering temperature of the second synthesis is caused by specific conditions of slow development of the BiFeO_3 decomposition processes, and increased activity of chemical bonds Bi-O in the temperature range considered. It evinces the existence of a phase transition in the corresponding simple oxides: for $\alpha\text{-Bi}_2\text{O}_3$ at 727°C in air partially loses oxygen and arises another modification $\delta\text{-Bi}_2\text{O}_3$, the cubic space group $\text{Pn}3\text{m}$. A similar phenomenon of “inheritance” of the anomalous behavior of properties has been previously observed. It was shown that the temperature ranges of the anomalous behavior of structural and electrical parameters existed in complex oxides with equal intervals of anomalies in the initial oxide containing transition metal ions occupying position B in the perovskite structure. In our case, the decrease in stability of the chemical bonds $A\text{-O}$ can also contribute to the loss of oxygen, accumulation and elimination of vacancies. It leads to shearing the crystalline structure and increasing the density of ceramics at 750°C . Ordering of vacancies at higher firing temperatures can lead to the emergence of strong diffuse scattering, and erosion of the main diffraction reflections.

Acknowledgments The work was supported by the Russian Ministry of Education into framework of Federal Target Program (Agreement No. 14.575.21.0007).

References

1. A. Maitre, M. Francois, J.C. Gachon, J. Phase Equilib. Diffus. **25**, 1 (2004)
2. T.T. Carvalho, P.B. Tavares, Mater. Let. **62**, 3984 (2008)
3. S. Phapale, R. Mishra, D. Das, J. Nucl. Mater. **373**, 137 (2008)
4. Powder Diffraction File. Data Card. Inorganic Section. Set 33, card 664. JCPDS. Swarthmore, PA, USA (1948)
5. Powder Diffraction File. Data Card. Inorganic Section. Set 27, card 53. JCPDS. Swarthmore, PA, USA (1948)
6. Powder Diffraction File. Data Card. Inorganic Section. Set 46, card 416. JCPDS. Swarthmore, PA, USA (1948)
7. Powder Diffraction File. Data Card. Inorganic Section. Set 25, card 90. JCPDS. Swarthmore, PA, USA (1948)
8. Powder Diffraction File. Data Card. Inorganic Section. Set 14, card 181. JCPDS. Swarthmore, PA, USA (1948)

Chapter 7

Research of Concentration Conditions for Growth of Strongly Doped $\text{LiNbO}_3\text{:Zn}$ Single Crystals

M.N. Palatnikov, I.V. Biryukova, O.V. Makarova, N.V. Sidorov,
V.V. Efremov, I.N. Efremov, N.A. Teplyakova
and D.V. Manukovskaya

Abstract In this chapter, the concentration conditions of $\text{LiNbO}_3\text{:Zn}$ single crystals growth are searched in concentration range $\sim 4.0\text{--}8.91$ mol% ZnO. We have shown that the area of concentrations $\sim 4\text{--}6.8$ mol% ZnO is suitable for obtaining of optically and compositionally homogeneous $\text{LiNbO}_3\text{:Zn}$ single crystals with high resistance to optical damage. During this research the best characteristics were revealed for $\text{LiNbO}_3\text{:Zn}$ single crystals grown from melt containing 6.12 mol% ZnO. If more than 20 % of the melt contains more than 6.8 mol% ZnO crystallizes, highly defective $\text{LiNbO}_3\text{:Zn}$ crystals grow. They contain two crystal phases: $\text{Li}_6\text{ZnNb}_4\text{O}_{14}$ and LiNbO_3 . The concentrations of ZnO in the melt that change conditions of $\text{LiNbO}_3\text{:Zn}$ crystals formation have been obtained from 5.4 up to 6.8 mol%.

7.1 Introduction

The active search of new materials resistant to optical damage carried out by doping with non-photorefractive impurities is reflected in papers about $\text{LiNbO}_3\text{:Zn}$ single crystals properties [1–7]. The results of such a research are often not consistent. One of the most important reasons of this is ignoring the genesis of the crystal, i.e. the charge synthesis method, the doping type, physical and chemical particularities of the melt and growth conditions. In the paper [8], we reported influence of doping type on structure and properties of $\text{LiNbO}_3\text{:Mg}$. The $\text{LiNbO}_3\text{:Mg}$ crystals doped by the same concentration of impurity but different methods showed big difference in properties.

M.N. Palatnikov (✉) · I.V. Biryukova · O.V. Makarova · N.V. Sidorov
V.V. Efremov · I.N. Efremov · N.A. Teplyakova · D.V. Manukovskaya
Institute of Chemistry and Technology of Rare Elements and Mineral Raw Materials,
26a, 184209 Akademgorodok, Apatity, Murmansk Region, Russia
e-mail: palat_mn@chemy.kolasc.net.ru

The most detailed research of influence of melt structure on properties of lithium niobate crystals was performed by Uda et al. [9, 10]. In the most other papers, only some technological parameters of crystals growth are mentioned. In the paper [9], some theoretical calculations of equilibrium coefficient for lithium niobate melt containing doping element were given and electromotive force (EMF) of crystallization was experimentally obtained by the micro-growing method. The data enabled calculating of optimal compound for growing of optically homogeneous $\text{LiNbO}_3:\text{Mg}$ single crystals [10]. The behavior of the doping element in the melt have been shown at quasi-triple diagram of the system $\text{Li}_2\text{O}-\text{ZnO}-\text{Nb}_2\text{O}_5$ [11, 12], but the $\text{Li}_{1-x}\text{NbO}_{3-\delta}$ homogeneity areas were approximate and the solidus temperature were not shown.

The influence of the doping element on the lithium niobate crystal properties are usually has jump-like character [1]. This is the “concentration threshold” type of dependence. In general, one impurity can have several concentration thresholds in lithium niobate crystals. At this the melt characteristics change and the properties of the crystal, grown from such a melt, change sharply, too.

In the paper [1], $\text{LiNbO}_3:\text{Zn}$ crystals were searched with ZnO concentration step ~ 1.5 mol%. In the papers [4, 10], the step was 2 mol%. In these cases, determination of exact concentration of the threshold is not possible. Moreover, some anomalies of the melt and crystals properties could be missed. To determine the concentrations of the threshold in $\text{LiNbO}_3:\text{Zn}$, we took the ZnO concentration step less than 1 mol%.

In this chapter, we researched concentration conditions of $\text{LiNbO}_3:\text{Zn}$ crystallization in ZnO range $\sim 4.0-9.0$ mol% with step 1 mol%. Around the threshold concentration, which is 6.8 mol%, we chose the step 0.1 mol%. The crystals were highly homogeneous optically and compositionally. The resistances to optical damage and optical homogeneity were evaluated due to photo-induced light scattering (PILS) analysis and by laser conoscope method, respectively.

7.2 Method

To grow lithium niobate crystals, we used granular congruous charge with high density (48.6 mol% Li_2O) [13]. The zinc oxide was added to the crucible. The chemical compounds used during the work, niobium oxide, lithium carbonate, zinc oxide had less than 10^{-4} wt% of admixtures. The cylindrical parts of $\text{LiNbO}_3:\text{Zn}$ crystals were 40 mm in diameter and 30 mm in length. The crystals were grown in (001) direction by Czochralski method from platinum crucibles of $\varnothing 75$ mm on air. The growth equipment was of induction type and had the system of crystal diameter control. The growth velocity was 1.1 mm per hour, the rotational speed 14 turns per minute. The axis temperature gradient was 1° per mm. To decrease the thermoelastic stresses, grown crystals were heated at $T = 1200^\circ\text{C}$ for 24 h. The Zn concentration was determined by analysis of the plates cut from the top (C_{top} , closest to the cone) and bottom (C_{bottom}) of the cylindrical part of the boule. The analysis was made by

atom-emission spectroscopy (spectrometer ICPS-9000 made by Shimadzu). The method error was $\sim 2\%$. $\text{LiNbO}_3:\text{Zn}$ crystals were put into single-domain state by high-temperature electro-diffusion annealing. The method is cooling samples from 1241 to 888 °C at speed 20° per hour at constant application of direct current. The level of single domain state was controlled by analysis of dependence of electrical impedance on frequency and by determination of static piezomodulus ($d_{33\text{stat}}$) of the boule.

The searched samples were in two shapes: (i) cuboids $7 \times 6 \times 5$ mm with thoroughly polished facets that coincided with crystallographic axes were used in experiments on PILS; (ii) Z-oriented polished plates with 40 mm in diameter and 4–5 mm thickness were used in experiments on laser conoscopy.

Photoinduced light scattering (PILS) in these experiments was excited by MLL-100 laser at Y:Al garnet ($\lambda_0 = 530$ nm). Laser beam was directed along the y -axis, while E , the electric field vector of the laser radiation, was parallel to z , the polar axis of the crystals. In this geometry ee -type PILS is the most bright and evident due to the biggest photorefraction effect (PE) value. The scattered light fell on a translucent screen located behind the crystal, and was fixed by the digital video-camera.

The optical homogeneity and structure distortions were controlled by the laser conoscope method. The method used in our researches enables observing conoscope picture of big size and high resolution. In this method, conoscope pictures are big enough to reveal all details in the center and on the edges of the picture and thus, find and describe structure distortions of crystals. The method is described in [14].

Physical and chemical characteristics were measured by differential thermal analysis at NETZSCH STA 409 PC/PG analyzer. The measurement of liquidus and solidus temperatures had error ± 2 K.

The approximate behavior of the system “melt–crystal” is evaluated by the distribution coefficient $K_{0\text{eff}}$. The effective distribution coefficient for single element crystal doped by small amount of impurity is calculated due to Burton-Prime-Slichter (BPS) or Pfann model [14]. Using of these models for the multi-component system is difficult. For example, the BPS model contains kinematic viscosity. This quantity should be obtained for each melt composition and each growing condition, which is highly laborious and is very long. Moreover, the data on equilibrium distribution coefficient are absent for $\text{LiNbO}_3:\text{Zn}$ system.

For BPS model, we have

$$k_{\text{eff}} = \frac{k_0}{k_0 + (1 - k_0)\exp\left(-\frac{V_{\text{crist}} \cdot \delta}{D}\right)} \quad (7.1)$$

where V is the velocity of crystal growth, k_0 is an equilibrium distribution coefficient, D is a diffusion coefficient ($\sim 10^{-5}$ – 10^{-4} cm²/s), δ is the thickness of impurity reach layer.

Using of the Pfann model is also difficult. It was developed for zone recrystallization method of compounds with very low impurity concentrations [15], when small melted zones are like dilute solution. For systems with high impurities concentrations, many Pfann's assumptions break and his model does not work.

Note that earlier lithium niobate crystals were widely grown with high growth speed at big temperature gradients. It was assumed that the big temperature gradient at the phase border was the condition for steady crystallization. As the growth technologies improved, growing of the crystals with low growth speed and at almost zero temperature gradients became possible. Such conditions are close to the thermodynamic equilibrium. Today the model that takes into consideration all growth conditions of the complicated multi-component systems does not exist despite on the development of crystal growth theory [15–17]. Therefore in the case of multi-component system such as $\text{LiNbO}_3\text{:Zn}$ crystals with dopant concentration $\sim 0.05\text{--}2.0$ wt%, empirical methods are more reliable for distribution coefficient evaluation.

We developed the method of evaluation of impurity behavior in complicated system “melt–impurity–crystal” with unknown state diagram and with unknown physicochemical parameters of the melt. The method is realized at growing of series of crystals with different impurity concentration from one crucible, i.e. during one technological cycle. Estimated effective distribution coefficient (K_{0eff}) is used for the numerical evaluation of the melt-crystal system. The coefficient is analogues to the effective distribution coefficient [15]. K_{0eff} is ratio between the impurity concentration in solid phase (C_{cryst}) and in liquid phase (C_{melt}). However, unlike [15], we take only the initial moment of crystallization, when the impurity concentration in the melt is the closest to the given one:

$$K_{\text{0eff}} = C_{\text{cryst}}/C_{\text{melt}}. \quad (7.2)$$

In a system as difficult as $\text{LiNbO}_3\text{:Zn}$, there is no possibility to determine all parameters that influence K_{0eff} , but it is possible to fix them many times and reproduce the experiment. Thus the necessary condition for evaluation of the coefficient is growing of series of crystals in identical conditions with the same temperature gradient, the melt amount in the crucible, the growth velocity, the percent of crystallized melt.

The calculation scheme for multiple growing of crystals with different impurity concentration from initial melt that we applied in this work is the following. First, crystal is grown from the charge with the minimal impurity concentration. This concentration is taken as minimal impurity concentration in the melt $C_{\text{melt}1}$. After the crystal is grown, it is weighted, thin plates are cut from the top (cone) and the bottom (cylinder) parts of the boule and impurity concentrations $C_{\text{top}1}$ and $C_{\text{bottom}1}$ are determined by chemical analysis.

To calculate $K_{0\text{eff}}$, the C_{cryst} is determined as C_{top1} . So the estimated effective coefficient is calculated by using formula (7.2) as

$$K_{0\text{eff}} = C_{\text{cryst}}/C_{\text{melt}} = C_{\text{top1}}/C_{\text{melt1}}. \quad (7.3)$$

Then the amount of the charge and impurity that will be added to crucible to grow the next crystal with higher impurity concentration is calculated on the base of material balance of the system and value of the average impurity concentration in the previous crystal C_{crystav} as

$$C_{\text{crystav}} = (C_{\text{top1}} + C_{\text{bottom1}})/2. \quad (7.4)$$

After definition of the charge and impurity addition, the melt has impurity concentration C_{melt2} . After growing of the second crystal, the calculations are repeated and $K_{0\text{eff2}}$ is obtained.

We have grown the series of $\text{LiNbO}_3:\text{Zn}$ crystals with different Zn concentrations by this method. Note that the concentration step in this growing method can be very small; it is restricted only by the weighting error and the concentration measurement error.

The series of lithium niobate crystals doped by magnesium and rare earth elements were grown in our laboratory by this method earlier [18, 19]. The experiments show that the method is efficient for evaluation of physicochemical characteristics of the multi-component system “melt–impurity–crystal”. This is very important for the development of new optical material due to the necessity to achieve absolute reproducibility of the experimental procedures for obtaining of competitive technology.

7.3 Results and Discussion

Uda [9] showed the complexity of ion compound of the melt even at growing of pure lithium niobate crystals. Addition of Zn raises the complexity. Growing in isothermal conditions means that ion complexes with the highest electrochemical activity have preferences at crystallization [10]. Thus, such ion complexes determine the melt $K_{0\text{eff}}$. If the melt compound changes, some other ion complexes become more active and the $K_{0\text{eff}}$ changes. The impurity concentration in crystals will be stable until particular complexes will be the most active in the melt. When the concentration of the complexes will get lower than the critical point, the physicochemical properties of the melt will change sharply, and the crystal compound, structure and properties will change, too.

The behavior of the melt-crystal system in this chapter is analyzed by estimated effective distribution coefficient $K_{0\text{eff}}$. This parameter enables comparison of different experiment series at growing of multi-component system in wide range of

impurity concentrations. The distribution of the impurity in the volume of the boule is evaluated due to the parameter $\Delta C = C_{\text{top}} - C_{\text{bottom}}$.

Table 7.1 contains zinc concentration in the melt C_{melt} , zinc concentration in the top, cone part of the boule C_{top} , parameter $\Delta C = C_{\text{top}} - C_{\text{bottom}}$, and estimated effective distribution coefficient K_{0eff} . Table 7.1 demonstrates that value of K_{0eff} is less than 1 for all searched impurity concentrations. The coefficient dependence of the impurity concentration is non-monotonic and mostly decreases with the rise in zinc concentration in the melt.

The data on distribution coefficient for $\text{LiNbO}_3\text{:Zn}$ are mostly few and conflicting. Papers [2, 20] show that $K_{\text{0eff}} = 1.2$, but paper [10] revealed that $K_{\text{0eff}} < 1$. The paper [10] contains data that generally are close to ours.

Figure 7.1a reveals dependence of K_{0eff} on zinc concentration in the melt. The plot contains three different areas. The first area is $4.0 < C_{\text{melt}} \leq 5.4 \text{ mol\%}$. K_{0eff} decreases sharply from 0.87 to 0.74 relative units. At the second area ($5.4 < C_{\text{melt}} \leq 6.8 \text{ mol\%}$), K_{0eff} increases from 0.74 to 0.77 relative units. At the beginning of the third area, at $C_{\text{melt}} \approx 6.8 \text{ mol\%}$, the coefficient decreases sharply to 0.68 relative units, and then for $C_{\text{melt}} \approx 6.88\text{--}8.91 \text{ mol\%}$, it continues to decrease, but more smoothly, to the value 0.66 relative units.

Figure 7.1b shows dependence of zinc concentration in crystal on zinc concentration in melt. In Fig. 7.1b, an anomaly around $C_{\text{melt}} \approx 6.8 \text{ mol\%}$ is observed. The anomaly reveals itself at the border between the II and the III concentration areas. After this point, the dependence is approximated with correlation 99 % by the line.

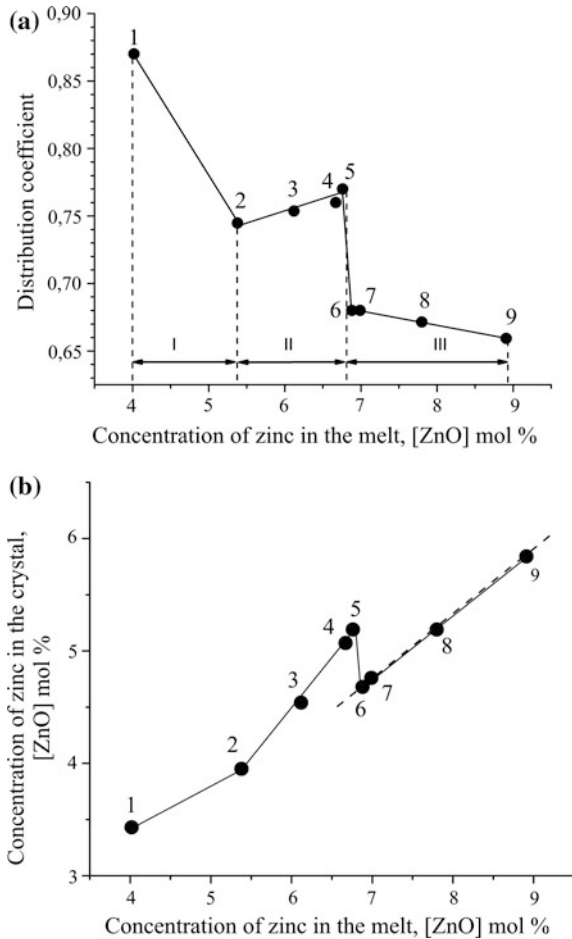
Table 7.1 demonstrates almost constant zinc concentration along the boule growth axis in the concentration areas I and II ($\Delta C = 0.03\text{--}0.1 \text{ mol\%}$). The value 0.1 mol% is close to the measurement error. The constant concentration of the impurity along the crystal boule (small ΔC) means high homogeneity that in classic case [15] is characteristic for melts with K_{0eff} close to 1. However, in our case K_{0eff} is 0.87–0.77 in this concentration areas ($\sim 4.0\text{--}6.8 \text{ mol\%}$).

The Pfann or BPS models [15] for effective distribution coefficient calculation are used at small impurity concentrations in the cases of zone melting or directed

Table 7.1 Zinc concentrations and effective distribution coefficient

Crystal no.	C_{melt} (mol%)	C_{top} (mol%)	$\Delta C = C_{\text{top}} - C_{\text{bottom}}$	K_{0eff}
1	4.02	3.43	0.1	0.87
2	5.38	3.95	-0.03	0.74
3	6.12	4.54	0.1	0.75
4	6.67	5.07	0.04	0.76
5	6.76	5.19	0.1	0.77
6	6.88	4.68	-0.5	0.68
7	6.99	4.76	-0.4	0.68
8	7.8	5.19	-0.3	0.67
9	8.91	5.84	-1.0	0.66

Fig. 7.1 Dependence of distribution coefficient $K_{0\text{eff}}$ (a) and concentration of Zn in the crystal (b) on the concentration of Zn in the melt



crystallization, when all melt is crystallized. In our case, impurity concentration is high and only some part of the melt becomes a crystal ($\sim 20\%$). Moreover, the models are able to show only linear dependencies of impurity concentration in crystal on the concentration in melt. Moreover, classic formula (7.1) means that at $K_{\text{eff}} < 1$, melting temperature decreases and the impurity concentration should rise from the cone to the bottom of the boule. However, the both conditions do not correspond to our case. The melting temperature stays stable within the error or slightly rises (Fig. 7.2). The impurity concentration is the same for the bulk of the boule in I and II areas and rises from the cone to the bottom at the III concentration area (Table 7.1). So the Pfann or BPS models are not applied to the complex multi-component melts with impurity concentrations larger than 1 mol% when $\leq 20\%$ of the melt becomes a crystal.

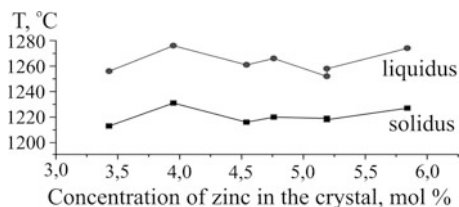


Fig. 7.2 Dependence of liquidus and solidus temperatures on the concentration of Zn in the crystal

The crystals, grown from melts corresponding to I and II concentration areas, were not only highly homogeneous (which is a property of melts with $K_{\text{eff}} \sim 1$), but also were resistant to optical damage, did not damage during growth, and were easily brought to single domain state. The best crystal judging by these properties was crystal sample 3 (see Table 7.1). Figure 7.3 shows time dynamics of PILS of sample 3 excited by laser radiation 2 and 160 mW ($\lambda_0 = 532$ nm). PILS picture of sample 3 is absolutely stable. As one can see, photorefractive response does not excite in this sample irradiated both by low-power and high-power laser radiation and only ideal round scattering is observed (Fig. 7.3). The PILS indicatrix angle opening does not exceed 3° . All crystals grown from melt with discussed ZnO concentrations (4–9 mol%) had qualitatively the same PILS pictures. Thus, the photorefractive effect in all searched crystals is suppressed.

Conoscope pictures of lithium niobate crystals consist of two isogyres of minimal intensity that cross perpendicularly and form a “Maltese Cross”. Isogyres coincide with the polarizer and analyzer transmission axes. The “Maltese Cross” on the conoscope pictures exists because in a divergent light beam there are always beams with perpendicular principal planes and parallel \mathbf{E} vectors. Such beams are either ordinary or unordinary ones. Appearance of the biaxiality reveals through distortion or break of the “Maltese Cross” in its center with appearance of the fair spot (brightening) at the cross of isogyres. Shift or break of the “Maltese Cross” is connected with direction of optic indicatrix deformation. Figure 7.4 shows conoscope pictures of samples 1 and 3 excited by laser beam 1 and 90 mW. The distortions of conoscope pictures excited by laser beam 1 mW occur due to the structure defect or optic inhomogeneity (for example, if impurity in growing crystal was distributed inhomogeneously). The distortions that reveal in conoscope pictures excited by laser beam 90 mW occur due to the crystal structure changes that occur under laser irradiation. Thus, such conoscope pictures reveal information about the optical damage value.

The conoscope pictures of sample 1 are given in Fig. 7.4(1). In conoscope picture of this sample, excited by laser beam 1 mW, one can see signs of optical biaxiality. In the center of the “Maltese Cross”, a vertical shift of the cross parts is observed. This direction corresponds to the direction of optical indicatrix deformation (Fig. 7.3). The brightening in the center of the “Maltese Cross” is also observed. The angle of isogyres crossing is not 90° . Isochromes are whole and have

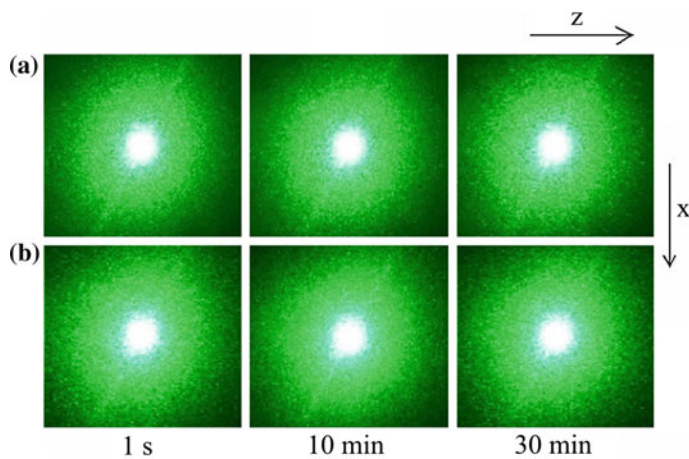


Fig. 7.3 Time dynamics of PILS of sample 3, excited by laser radiation $P = 2$ mW (a), $P = 160$ mW (b) at $\lambda_0 = 532$ nm

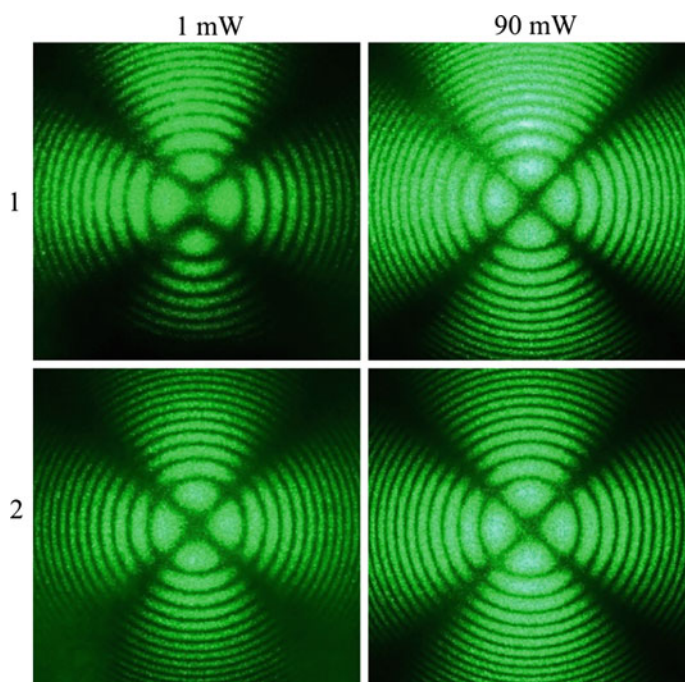


Fig. 7.4 Conoscope pictures of $\text{LiNbO}_3:\text{Zn}$ crystals: (1) sample 1, (2) sample 3; $\lambda_0 = 532$ nm, $P = 1$ and 90 mW

regular geometric shape, but they are stretched along the fragments shift and ellipse shaped. The image is a bit blurred and each “Maltese Cross” branch has visible anomalies. Such conoscope picture distortions are connected with structure defects and optical inhomogeneity of sample 1. At higher excitation power conoscope picture of sample 1 is closer to the standard. The picture is symmetrical; the “Maltese Cross” is whole and has no brightening in the center. Isochromes are circular and have center in the cross of the isogyres. At the left upper branch of the cross, the image is slightly blurred. However, this conoscope picture shows that the sample has good optical quality and high optical homogeneity. It is obvious that under more powerful laser radiation, crystal defects are “healed” by the radiation recombination of the charged defects.

The conoscope pictures of sample 3 are different. Excitation by radiation 1 mW reveals the picture usual for single axis crystals. Isochromes are regular concentric rings; “Maltese Cross” is whole and has no brightening in the center. The “Maltese Cross” is slightly stretched along the vertical direction, but the signs of biaxiality are absent (see Fig. 7.4). Thus, sample 3 is more optically homogeneous compared with sample 1. At rise of the excitation beam power, the standard conoscope picture of single-axis crystal appears for sample 3. The rise of excitation power does not reveal PE in crystals. This fact correlates with data on PILS study (Fig. 7.3).

Our research of PILS and conoscope pictures revealed absence of the photorefractive response for the investigated crystals. It means that ZnO concentration $C_{\text{melt}} = \sim 4.0\text{--}9.0$ mol% suppresses PE in $\text{LiNbO}_3\text{:Zn}$ crystals. However, for crystals with lower ZnO concentrations (less than 3.4 mol%), PE is strong [21]. Figure 7.5 shows PILS pictures of $\text{LiNbO}_3\text{:Zn}$ crystals with ZnO concentrations 1.5 and 2 mol%. Photorefractive response is very strong and PILS indicatrix opening is observed. For sample 3 only round light scattering is present (Fig. 7.3), and for

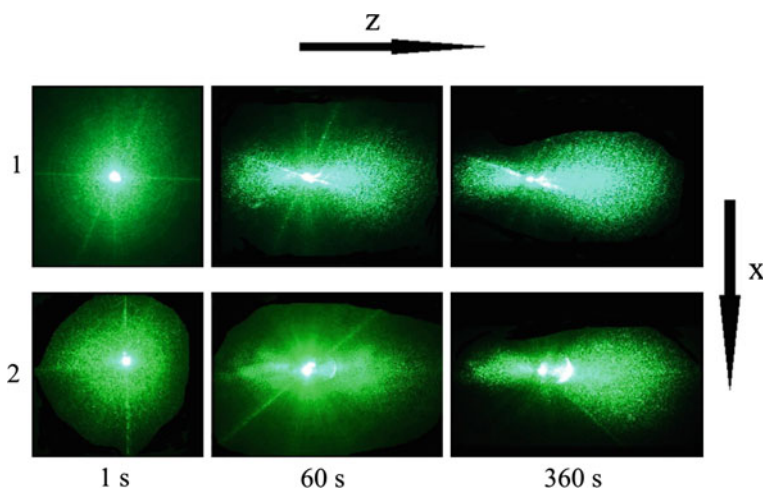


Fig. 7.5 PILS pictures of $\text{LiNbO}_3\text{:Zn}$ crystals with ZnO concentration 1.47 (1) and 2.01 (2) mol%

samples with low impurity concentration, scattering on laser-induced defects is observed. The refractive index changes in the area of scattering. The refractive index in the defects changes constantly or fluctuates. The pump beam interferes with scattered light and forms a complex picture of minima and maximums. The form and shape of the picture is determined by the crystal intrinsic and defect structure [22, 23]. The three-layer speckle structure of PILS picture was observed for $\text{LiNbO}_3\text{:Zn}$ crystals with ZnO concentrations 1.47 and 2.01 mol% before in [24]. The PILS pictures change during irradiation from round form to asymmetric form for sample 8. The biggest petal of sample 8 opens along the positive direction of polar axis (that coincides with spontaneous polarization vector), the smallest petal opens along the negative axis direction.

At the same time $\text{LiNbO}_3\text{:Zn}$ crystals were optically homogeneous and compositionally uniform in I and II concentration areas. In III concentration area, where PE was suppressed, crystals were defective and optically inhomogeneous.

Perhaps, due to the Uda assumption [10], the activity of the electrochemical complexes is maximal in I and II concentration areas. Such complexes provide the stability of the melt compound, which leads to optical homogeneity and structure perfection of the crystal at $K_{\text{0eff}} \neq 1$. At the rise of Zn concentration in the melt, the concentration of such complexes decreases below the critical one and other kinds of complexes appear. This leads to change of melt compound and physicochemical properties which means change of $\text{LiNbO}_3\text{:Zn}$ crystals compound, structure and properties in III concentration area.

$\text{LiNbO}_3\text{:Zn}$ crystals, grown in conditions of III concentration area, have K_{0eff} much less than 1. The impurity distribution in crystal is classic—the concentration increases from cone to top part of the boule (see Table 7.1). Due to this fact, the crystals are more defective and damage can arise more easily. The dependence of impurity concentration in the crystal on the concentration in the melt is linear with correlation coefficient 0.99 (Fig. 7.1b).

Note that due to the sharp change of K_{0eff} with change of impurity concentration in the melt there is a possibility to obtain $\text{LiNbO}_3\text{:Zn}$ crystals with the same impurity concentration. For example, samples 5 and 8 have the same concentration C_{top} . However, sample 5 belongs to II concentration area, and sample 8—to III area (Table 7.1, Fig. 7.1). Thus, the defectiveness and optical properties in these two crystals will be completely different. For example, sample 5 has homogeneous impurity distribution in the crystal, but impurity concentration increases in sample 8 from cone to bottom of the boule. Thus the inside structures of the crystals are completely different. It is quite possible that no one paid attention to the particularities of the crystals obtaining and the genesis of the charge. That is why the data on crystals with the same concentration of impurity could be so different in the literature.

Hence, in III concentration area when $C_{\text{melt}} \approx 7$ mol%, the melt structure changes very much which leads to change of $\text{LiNbO}_3\text{:Zn}$ crystals characteristics. Moreover, the X-ray diffraction analysis revealed in this boule two phases that crystallize after 20 % of the melt is crystallized. The phases are identified as $\text{Li}_6\text{ZnNb}_4\text{O}_{14}$ and LiNbO_3 . Existence of two phases is clearly visible at the bottom of the boule.

7.4 Conclusion

The system “melt–crystal” was searched for $\text{LiNbO}_3\text{:Zn}$ in the concentration area $4 \leq C_{\text{melt}} \leq 9$ mol%. The concentration added slowly and by small step. The concentration thresholds were determined as 5.4 and 6.8 mol%. Three concentration areas were revealed. Physicochemical properties of the melt were different at the different areas and, respectively, $\text{LiNbO}_3\text{:Zn}$ crystals characteristics were different, too. The best growing conditions for optically and structurally homogeneous crystals with high optical damage resistance is growing from the melt containing $5.4 \leq C_{\text{melt}} \leq 6.8$ mol% Zn. At $C_{\text{melt}} \geq 6.8$ mol% physicochemical properties and structure of the melt change. Thermodynamic conditions in this case do not allow obtaining of single-phase crystal. This is possible only if much less than 20 % of the melt crystallizes. $\text{LiNbO}_3\text{:Zn}$ crystals with the same impurity concentration, but with different inside structure could be obtained due to difference in physicochemical properties of the melt and sharp change of K_{0ef} . Thus, the system melt-crystal is very sensitive to the zinc concentration in the melt. This is the reason why the searched system is completely different from $\text{LiNbO}_3\text{:Mg}$ system [8, 18, 25]. Thus, the similarity in ion radii of Zn^{2+} and Mg^{2+} cations is not an important factor for the conclusions about the impurity behavior in melt-crystal system.

References

1. T.R. Volk, N.M. Rubinina, *Phys. Solid State* **33**, 1180 (1991)
2. U. Schlarb, M. Woehlecke, B. Gather, A. Reichert, K. Betzler, T. Volk, N. Rubinina, *Opt. Mater.* **4**, 791 (1995)
3. T.S. Chernaya, T.R. Volk, I.A. Verin, V.I. Simonov, *Cryst. Rep.* **53**, 573 (2008)
4. Y. Zhang, Y.H. Xu, M.H. Li, Y.Q. Zhao, *J. Cryst. Growth* **233**, 537 (2001)
5. F. Abdi, M. Aillerie, M. Fontana, P. Bourson, T. Volk, B. Maximov, S. Sulyanov, N. Rubinina, M. Wöhlecke, *Appl. Phys. B.* **68**, 795 (1999)
6. L. Zhao, X. Wang, B. Wang, W. Wen, T.-Y. Zhang, *Appl. Phys. B.* **78**, 769 (2004)
7. M. Aillerie, P. Bourson, M. Mostefa, F. Abdi, M.D. Fontana, *J. Phys.: Conf. Ser.* **416**, 012001 (2013)
8. M.N. Palatnikov, I.V. Biryukova, S.M. Masloboeva, O.V. Makarova, O.E. Kravchenko, A.A. Yanichev, N.V. Sidorov, *Inorg. Mater.* **49**, 715 (2013)
9. S. Uda, W.A. Tiller, *J. Cryst. Growth* **121**, 155 (1992)
10. H. Kimura, H. Koizumi, T. Uchidab, S. Uda, *J. Cryst. Growth* **311**, 1553 (2009)
11. V.V. Konovalova, V.V. Fomichev, D.V. Drobot, R.M. Zakalyukin, SYu. Stefanovich, *Rus. J. Inorg. Mater.* **54**, 1650 (2009)
12. V.B. Nalbandjan, B.S. Medvedev, V.I. Nalbandjan, A.V. Chunenova, *Dokl. Inorg. Mater.* **6**, 980 (1988)
13. M.N. Palatnikov, N.V. Sidorov, V.T. Kalinnikov, *Ferroelectric Solid Solutions Based on Oxide Compounds of Niobium and Tantalum: Synthesis (Search of Structure Order and Physical Characteristics*, Nauka, Saint-Petersburg, 2001). (In Russian)
14. O.Y. Picoul, N.V. Sidorov, O.V. Makarova, M.N. Palatnikov, *Inorg. Mater.: Appl. Res.*, **5**, 189 (2014)

15. Y.M. Tairov, V.P. Tscvetkov, *Technology of Ferroelectric and Dielectric Materials* (Vyshsaya Shkola, Moscow, 1983). (In Russian)
16. I.V. Mochalov, *Growth of Optical Crystals* (SPbSU ITMU, Saint-Petersburg, 2010). (In Russian)
17. N.A. Baldina, B.V. Vasekin, V.A. Goncharov, *Theor. Found. Chem. Eng.* **43**, 353 (2009)
18. M.N. Palatnikov, I.V. Biryukova, O.V. Makarova, N.V. Sidorov, O.E. Kravchenko, V.V. Efremov, *Inorg. Mater.* **49**, 288 (2013)
19. M.N. Palatnikov, I.V. Biryukova, N.V. Sidorov, A.V. Denisov, V.T. Kalinnikov, P.G.R. Smith, V. Shur, *Ya. J. Cryst. Growth* **291**, 390 (2006)
20. A. Rauber, in *Chemistry and Physics of Lithium Niobate*, ed. by E. Kaldis (North Holland Publishing Company, Holland, 1978)
21. N.V. Sidorov, A.A. Yanichev, M.N. Palatnikov, A.A. Gabain, *Opt. Spectrosc.* **116**, 281 (2014)
22. V.A. Maksimenko, A.V. Syui, YuM Karpets, *Photoinduced Processes in Lithium Niobate Crystals* (Fizmatlit, Moscow, 2008). (In Russian)
23. A.V. Syui, N.V. Sidorov, E.A. Antonycheva, *Photorefractive Properties and Peculiarities of the Structure of Optically Nonlinear Lithium Niobate Crystals* (DVGUPS, Khabarovsk, 2011). (In Russian)
24. N.V. Sidorov, A.V. Syui, M.N. Palatnikov, V.T. Kalinnikov, *Dokl. Phys. Chem.* **437**, 47 (2011)
25. M.N. Palatnikov, I.V. Birukova, S.M. Masloboeva, O.V. Makarova, D.V. Manukovskaya, N. V. Sidorov, *J. Cryst. Growth* **386**, 113 (2014)

Chapter 8

Research of Gas Bubbles Interaction with Crystallization Front of Sapphire Melt

S.P. Malyukov, Yu.V. Klunnikova and M.V. Anikeev

Abstract The temperature gradient for the sapphire crystals growth by the horizontal directed crystallization method was defined by mathematical simulation with the help of finite volume method in three-dimensional coordinates on the unstructured grid. The estimation of gas bubbles sizes near the liquid crystallization front was determined taking into account temperature gradients during sapphire growth. The results of simulation of sapphire crystals growth allows one to understand the physical nature of this process and to come nearer to solution of the main problem of processing such crystals with the reduced defect level.

8.1 Introduction

The big size crystals growth with improved structural characteristics became a priority of modern science and equipment. In the last decades, the Czochralsky's method, Kiropoulos's method, the horizontal directed crystallization (HDC) method and Stepanov's method were applied for studying growth of big size monocrystals. These crystals were widely used in electronic technique [1].

The sapphire crystal quality can be characterized by the crystallographic orientation, density of single dislocations, extension of blocks borders and their misorientation, the value of residual stresses, chemical purity, impurity heterogeneity, density and nature of dot defects distribution [2–13].

The impurity atoms placed in the lattice nodes and lattice interstices belong to the dot defects. The impurity atoms positions are defined by the energy of their insertion. The impurity atoms occupy the nodes closest to them in accordance with the chemical nature of atoms. The small size atoms as a rule locate in the lattice interstices. The insertion of big size atoms can be possible only in the case of defects like dislocations and block borders.

S.P. Malyukov (✉) · Yu.V. Klunnikova · M.V. Anikeev
Institute of Nanotechnology, Electronics and Electronic Equipment Engineering,
Southern Federal University, 347928 Taganrog, Russia
e-mail: spmalyukov@sfnu.ru

There are some mechanisms of dislocation formation during crystal growth from the melt [14]: (i) dislocation initiation from the fuse crystal, and also during crystal growth; (ii) plastic deformation caused by thermo-elastic stresses; (iii) impurity trapping by the growing crystal (the impurity mechanism); (iv) disk-like vacancies accumulation with subsequent formation of dislocation loops (the vacancy mechanism); (v) incoherent growth in the conditions of incomplete compliance of nuclei, growth layers, dendrite branches. The critical dislocations density in the plane (0001) for sapphire grown by the HDC method is $(2-3) \cdot 10^4 \text{ cm}^{-2}$.

The assumption on thermal stresses in the growing crystal as the main source of dislocations was already significantly confirmed. The theory of the thermal stresses formation during crystal growth was developed by Indenbom [15, 16]. The dislocations formation occurs under influence of internal (residual) stresses caused by nonlinearity of temperature distribution in the growing crystal. If value of thermal stress exceeds a certain critical value, the conditions for structure defect formation will be created in its volume.

The micro- and macroblocks are one of the most important defects in crystals. The analysis of blocks in various crystals allowed one to reveal the mechanisms of their formation, which are similar to principles of dislocations formation in sapphire crystals [17].

The common condition of pore formation (from submicronic sizes up to 3–5 mm) is the saturation of melt by the dissolved gases, the main source of the gas saturation is the melt dissociation and also melt interaction with impurity in powder, container or medium. At high concentration of pore (more than 10^5 cm^{-3}) the material becomes unsuitable for optical application. The bubble with the size less than the critical one is pushed off by the crystallization front. In dilute liquid mixture, the concentration consolidation [17] and increase in the sizes of bubbles lead to their contact with the front of crystallization and to their trapping by forces of superficial tension. As the crystal growth around of the bubble completes, a pore forms into solid phase.

It is difficult to avoid overheating some zones of the container during sapphire crystal growth by HDC method, and, hence, melting during sapphire growth by using the container. The propagating front can take colder microvolumes of the melt. In this case, voids form during crystallization of these microvolumes because of the difference between crystal and melt density. The melt dissociation is not only source of melt gas saturation. Such elements of technological process as initial raw materials, crucible, gas atmosphere, constructional materials of growth equipment have serious impact on the formation mechanism and structure of pores [18].

8.2 Research Results

Gas inclusions in the form of micropores are the main defects of sapphire crystals [19]. There are various and complex mechanisms of pores formation. However, the main condition of their arising is the liquid supersaturation by the dissolved gases.

It is a result of evaporation with dissociation of sapphire powder and processes of destruction of the molecular couples in liquid. Thus, the study of distribution, structure and the mechanism of bubbles formation assists to development of restricting methods of the bubble excess. It is very important task for big size sapphire crystals grown by HDC method.

As it has been noted in [20, 21] at different stages of the crystal growth, the location and shape of the excessive bubbles are various. The largest problem for removal of the excessive bubbles are the bubbles located in the benthonic zone beginning approximately at the distance of 250 mm from the fuse in the case of the container length of 320 mm. It is shown schematically in Fig. 8.1.

At trapping, the bubbles positions are defined by the propagation speed of crystallization front (Fig. 8.2) and its shape [7]. It is actual problem to define disposition and shape of the crystallization front during sapphire growth and to reveal the factors influencing on growth kinetics at various stages of crystal growth.

The gas-filled bubble enclosed in the melt moves in the same direction with an external force field [22]. At melt crystallization in the conditions of a temperature gradient, movement of a gas bubble may be caused by constantly operating Archimedean force F_a and the capillary force F_k , due to dependence of surface tension at the boundary 'gas-melt' on temperature. In the coordinate system coupled with the front of the growing crystal moving with speed V_f , the velocity of the gas bubble V_p will be equal to the vector sum of all velocities:

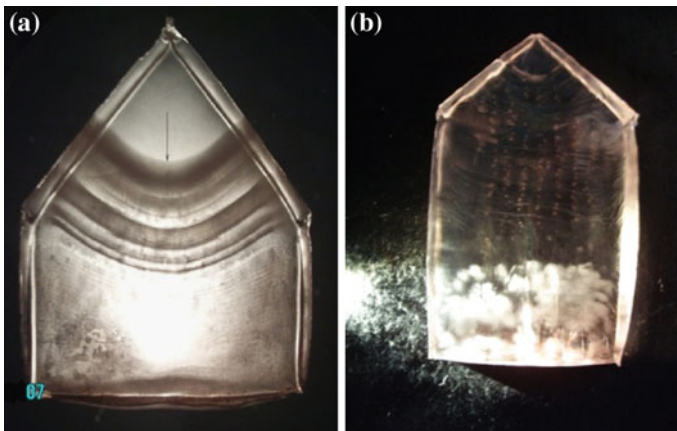


Fig. 8.1 Inclusions in sapphire crystals: **a** at the distance of 60 mm from the fuse, **b** at the distance of 250 mm from the fuse at the crystal length 320 mm



Fig. 8.2 Scheme of position of the crystallization front and excess of bubbles at various stages of crystal growth (the *arrow* shows the direction of crucible movement)

$$\vec{V}_p = \vec{V}_f + \vec{V}_a + \vec{V}_k, \quad (8.1)$$

where \vec{V}_a, \vec{V}_k are the components of the bubble velocity relatively to the melt caused by the influence of Archimedean and capillary forces, respectively. In the case of horizontal directed crystallization method, the projection of Archimedean velocity on the direction of front movement is zero, and the direction of the temperature gradient in the melt ∇T coincides with the direction of the growing front velocity. We shall take into account that the thermo-capillary force in the stationary mode [23]:

$$F_k = -2\pi r^2 \frac{\partial \alpha}{\partial T} \nabla T \quad (8.2)$$

must be equal to the force of the viscous medium resistance [24]:

$$F_c = 6\pi r \mu V_k. \quad (8.3)$$

Then the rate of bubble thermo-capillary movement relatively the liquid will be determined by the formula:

$$V_k = \frac{r}{3\mu} \frac{\partial \alpha}{\partial T} \nabla T, \quad (8.4)$$

where r is the radius of formed bubble, α and μ are the surface tension between gas and liquid boundary and dynamic viscosity of liquid, respectively. We also take into account that for the majority of liquids the derivative $\partial \alpha / \partial T < 0$. At the rate $V_a = 0$, it follows from expression (8.1), that the velocity of the bubble relatively the growing front is defined by the relationship:

$$V_p = \frac{r}{3\mu} \frac{\partial \alpha}{\partial T} \nabla T - V_f. \quad (8.5)$$

As we can see from (8.5) in the ensemble of bubbles in the melt there are bubbles of critical size r^* at which the bubble motion direction changes relatively the crystal growth surface. Gas bubbles with the size:

$$r > r^* = \frac{3\mu}{\nabla T} \frac{V_f}{\partial \alpha / \partial T} \quad (8.6)$$

will move in the direction from the front, but the bubbles with $r < r^*$ will move in the opposite direction.

The bubbles with radius $r < r^*$, appearing in surface of phase transformation during crystallization will be trapped by the growth front. So they create system of steady defects in the material volume.

It is necessary to calculate the temperature distribution in equipment for sapphire crystal growth by the HDC method for study of gas bubbles and crystallization front interaction. The temperature distribution in the “crystal–melt–crystal powder” system is defined by solution of the heat conductivity equations [25, 26]:

$$\begin{aligned} \frac{\partial T_i(x, y, z, \tau)}{\partial \tau} = & \left(\frac{\partial}{\partial x} a_i \frac{\partial T_i(x, y, z, \tau)}{\partial x} + \frac{\partial}{\partial y} a_i \frac{\partial T_i(x, y, z, \tau)}{\partial y} + \frac{\partial}{\partial z} a_i \frac{\partial T_i(x, y, z, \tau)}{\partial z} \right) \\ & - W \frac{\partial T_i(x, y, z, \tau)}{\partial x}, \\ & 0 < x < x_L, \quad 0 < y < y_L, \quad 0 < z < z_L, \end{aligned} \quad (8.7)$$

where $i = 1, 2, 3$ is the crystal, melt and crystal powder, respectively; a_i are the heat diffusivity coefficients: $a_i = \frac{\lambda_i}{\rho_i C_i}$, where λ_i is the thermal conductivity coefficient; ρ_i is the material density; C_i is the specific heat; W is the container movement speed.

The container movement speed is small enough (6–10 mm/h), so we can conclude that the process is in quasi-steady state and the temperature distribution can be found by the following formula [25, 26]:

$$\operatorname{div} [\lambda_i \operatorname{grad} T_i(x, y, z)] = 0. \quad (8.8)$$

The boundary conditions for set of (8.8), reflecting continuity of thermal fields and fluxes on boundaries of the considered sample, can be found by the following equations:

$$\lambda_1 \frac{\partial T_1(x_C, y, z)}{\partial x} = \lambda_2 \frac{\partial T_2(x_C, y, z)}{\partial x}, \quad (8.9)$$

$$\lambda_2 \frac{\partial T_2(x_C + \Delta x, y, z)}{\partial x} = \lambda_3 \frac{\partial T_3(x_C + \Delta x, y, z)}{\partial x}, \quad (8.10)$$

$$q_{s_1} = q_{s_2} = q_{s_3} = \sigma \beta (T^4 - T_{hot}^4), \quad (8.11)$$

where σ is the Stephan–Boltzmann constant; β is the radiation coefficient; T_{hot} is the function with the heat temperature distribution (Fig. 8.3).

There are both mechanisms of heat transfer in crystal: phonon and radiation. Their contribution is defined by optical properties of specific system. In this case, the coefficient of heat conductivity is understood as the sum of two components—phonon and radiation [27]:

$$\lambda_{com} = \lambda_{ph} + \lambda_{rad}, \quad (8.12)$$

$$\lambda_{rad} = \frac{16n^2 k T^3}{3\alpha}, \quad (8.13)$$

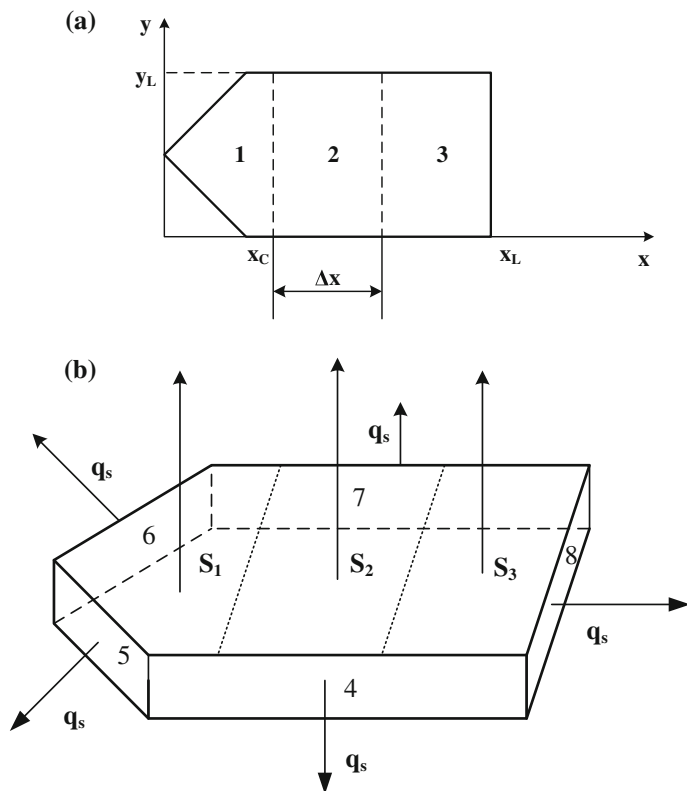


Fig. 8.3 Schemes for calculation of horizontal directed crystallization process: **a** 1 crystal, 2 melt, 3 powder; **b** 4, 5, 6, 7, 8 side surfaces of the crystal; S_1 , S_2 , S_3 are the upper and lower boundaries

where λ_{com} is the thermal conductivity; λ_{ph} is the phonon component of thermal conductivity coefficient; λ_{rad} is the radiation component of thermal conductivity coefficient; n is a coefficient of environment refraction; α is a coefficient of environment absorption; k is the Boltzmann constant.

The heat physical properties of aluminum oxide melt (sapphire monocrystal consists of 99.99 % of Al_2O_3), measured experimentally [27], have values, which are comparable with the heat physical properties of monocrystal: $\lambda_{rad} = 2.05$ W/(m K), $\lambda_{ph} = 3.4$ W/(m K). Thus, the contribution of heat transfer radiation component to the general heat exchange is very considerable for sapphire crystal growth.

Finally, the volume method on an unstructured grid was used for simulation. The discrete analogue of the heat conductivity equation for the finite volume (tetrahedron) is:

$$\sum_j \frac{\lambda(T_j - T_i)A_{ij}}{(x_j - x_i)n_{jx} + (y_j - y_i)n_{jy} + (z_j - z_i)n_{jz}} = 0, \tag{8.14}$$

where volume i is the volume for which the heat conductivity equation is solved; volume j is the volume following for volume i ; A_{ij} is the area of common face for i and j volumes; $\vec{n}_j(n_{jx}, n_{jy}, n_{jz})$ is the normal to the next i and j tetrahedrons; $\vec{l}_j(x_j - x_i, y_j - y_i, z_j - z_i)$ is the direction along which the thermal flow is defined.

The simulation program was developed in Microsoft Visual Studio 2008 in C++.

The results of temperature calculation in crystal-liquid-powder system are present in Figs. 8.4, 8.5, 8.6, 8.7, 8.8 and 8.9. The temperature fields in “crystal-liquid-powder” system are shown in Fig. 8.4. The temperature fields in horizontal and vertical crystal cuts are present in Fig. 8.5. In Fig. 8.6, distribution of temperature on the heater and crystallizers of equipment is shown.

The calculation results showed transparency of sapphire crystals in the crystal phase and opacity of the melt influenced directly by the radiation fluxes in the system. By considering their great influence on the common heat exchange, this factor affects also on the temperature field and the crystallization front location.

The temperature fields influence on the radiation heat transfer intensity. For estimation of this influence, the calculation with temperature increase on 300 K in the system “crystal-liquid-powder” was carried out. The calculations showed that the melt width increased and, in the result, the crystallization front location changed. Thus, we can conclude that we have possibility to control the crystallization front location by heat temperature increase.

The temperature gradients in sapphire crystals were calculated by the method of the smallest squares. The results of calculation are present in Fig. 8.7.

As we can see from (8.6), the obtained temperature gradients allow estimating the formed gas bubbles sizes. The results of the estimation are shown in Fig. 8.8.

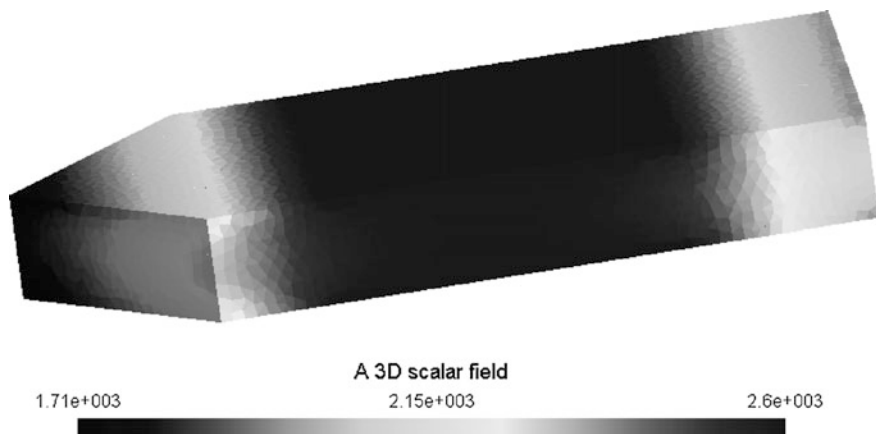


Fig. 8.4 Temperature distribution in “crystal-liquid-powder” system

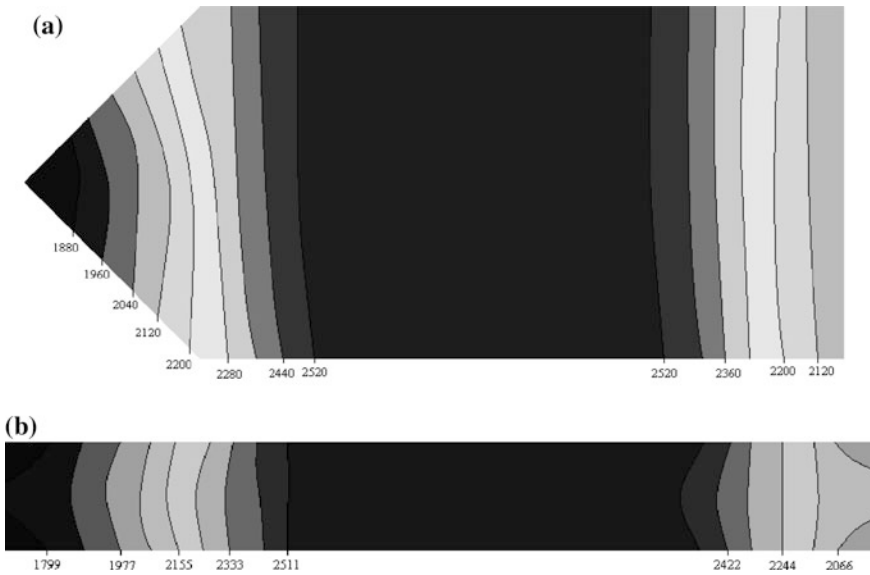


Fig. 8.5 Temperature distribution in horizontal (a) and vertical (b) crystal cut

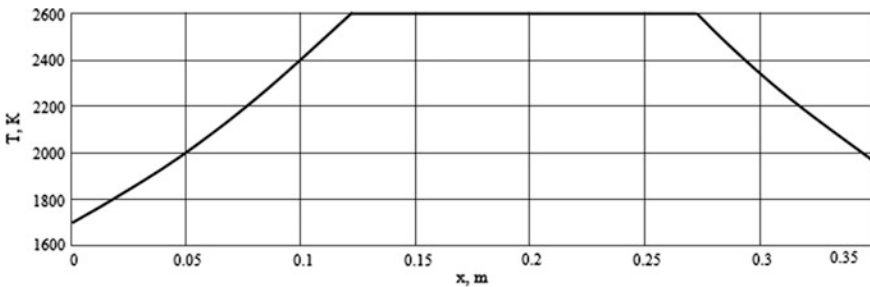


Fig. 8.6 Temperature distribution on the heater and crystallizers of equipment

The results of calculations showed that process of bubbles formation began at the melt bottom where maximum radius of the formed bubbles was about 0.16 mm at the growth rate of crystal equal to 6 mm/h.

At bubble trapping, the ratio of crystal growth and bubble rates defines a final form of inclusion. The obtained dependencies of the bubble average size on the growth speed can be explained (Fig. 8.9). At the given crystallization speed, the bubbles with certain radius which have the minimum gap with the front of growth are characterized by the greatest probability of capture. The increase in growth rate will lead to increase in probability of larger bubbles capture.

Thus, it is known that the crystal growth rate influences on the trapping of impurity and foreign inclusions by the front of crystallization. The dependence of

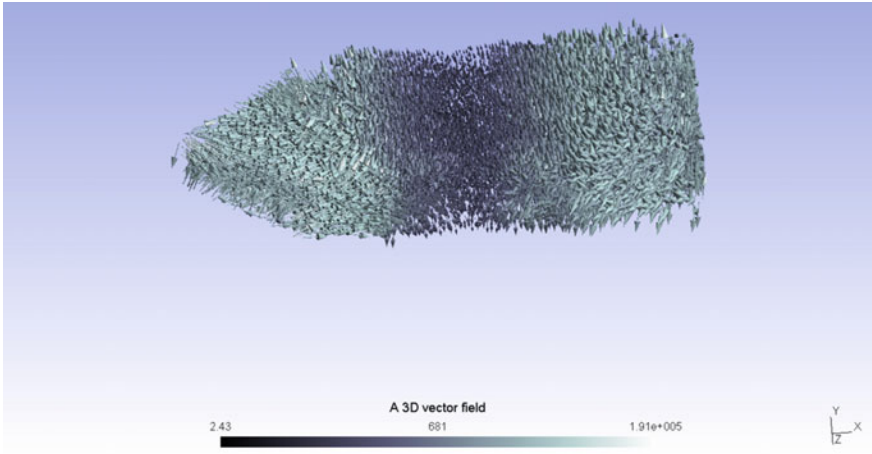
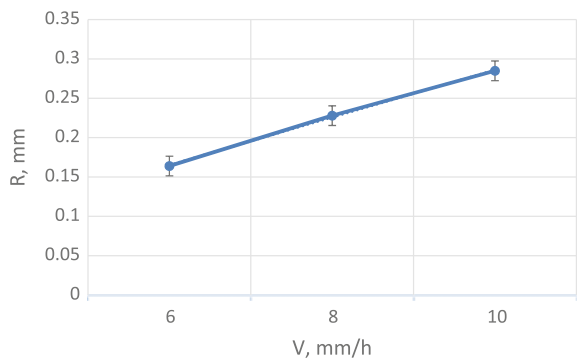


Fig. 8.7 Temperatures gradients in sapphire crystals in the “crystal–liquid–powder” system



Fig. 8.8 Dependence of temperature gradients on the gas bubbles size at the vertical crystal cut

Fig. 8.9 Dependence of sapphire crystal growth on average size of gas bubbles



segregation effective coefficient on the interface of phases on growth rate can be determined in the form [1, 18, 20]:

$$K_{\text{eff}} = \frac{K_0}{K_0 + (1 - K_0) \exp(-v\delta/D)}, \quad (8.15)$$

where K_0 is the equilibrium segregation coefficient, δ is the depth of the area with raised or lowered concentration of impurity at the crystallization front, D is the diffusion coefficient of impurity in melt, v is the crystal growth rate. At the intensive interdiffusion $\delta \rightarrow 0$ or at the small crystallization speed $v \rightarrow 0$, $K_{\text{eff}} \rightarrow K_0$, the impurities and bubbles are taking away in melt. When the growth speed $v \gg D/\delta$, i.e. $\exp(-v\delta/D) \rightarrow 0$, and $K_{\text{eff}} = 1$, it means that all bubbles and impurity are taken by crystal.

The growth rate depends on position of the container relatively the heater and increases throughout the process of sapphire crystal growth in the conditions of large temperature gradients [18, 20]. The effective coefficient dependence at the various stages of growth is shown in Fig. 8.10.

From Fig. 8.10, it is visible that only at the initial stage ($x = 0.1$ m) the effective coefficient of the segregation is close to equilibrium value. It is defined by small growth rate. Thus, the crystal grows without foreign inclusions. As we can see from the figure, the effective coefficient of segregation does not depend on temperature gradient in melt, practically.

The prediction algorithm of sapphire crystal quality is present in Fig. 8.11. The simulation results can help to define defect formation zones and can be used for recommendations on improvement of crystals quality. The defect level of sapphire crystal is considered as the main parameter for formation of the functional criterion.

Thus, the obtained results correlate completely with experimental data [28]. Numerical simulation of processes in sapphire crystals allows one to understand the

Fig. 8.10 Effective coefficient of segregation depending on the crucible position: 1 gradient in melt is 1000 K/m, 2 gradient in melt is 500 K/m

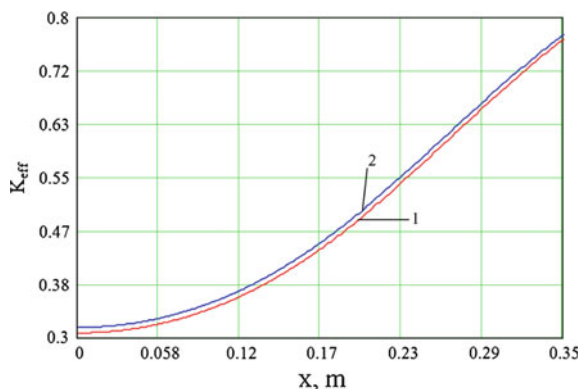
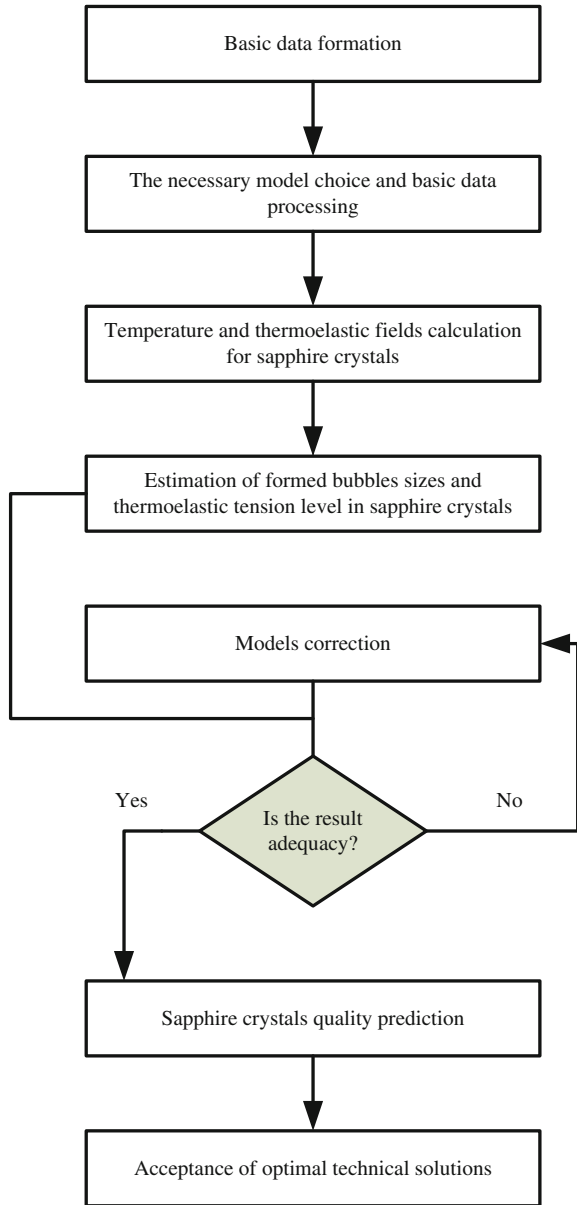


Fig. 8.11 Sapphire crystals quality prediction algorithm



nature of the physical phenomena and to find quantitative estimates of parameters (crystal growth velocity, heat power). The trapped inclusions in crystal from liquid define the main reasons of solid-phase defect formation.

Acknowledgments The results were obtained with use of the equipment of the Scientific and Educational Center “Laser Technologies”, Center of Collective Use and the Scientific and Educational Center “Nanotechnology” of the Institute of Nanotechnologies, Electronics and Electronic Equipment Engineering of Southern Federal University (Taganrog, Russia).

References

1. E.R. Dobrovinskaya, L.A. Lytvynov, V.V. Pishchik, *Sapphire. Material Manufacturing, Applications* (Springer, New York, 2009)
2. A.G. Shtukenberg, Yu.O. Punin, *Optical Anomalies in Crystals* (Science, St. Petersburg, 2004). (in Russian)
3. V.L. Indenbom, *J. Crystallogr.* **9**, 74 (1964)
4. V.L. Indenbom, *Proc. of the USSR Academy of Sciences. Physical Series*, **37**, 2258 (1973)
5. A.I. Belaya, E.R. Dobrovinskaya, L.A. Lytvynov, V.V. Pishchik, *J. Crystallogr.* **26**, 164 (1981)
6. A.I. Landay, *Proc. Cryst. Growth* **1**, 74 (1957)
7. P.I. Antonov, S.I. Baholdin, L.L. Kuandykov, Yu.K. Lingart, *J. Crystallogr.* **49**, 300 (2004)
8. T.S. Bessonova, A.L. Samsonov, L.A. Avvakumova, S.V. Bodyachevskiy, E.G. Shalfeev, *J. Inorg. Mater.* **26**, 2531 (1990)
9. S.P. Malyukov, S.N. Nelina, V.I. Zaitsev, in *Proceedings of the Nanotechnology, Nanomaterials and Nanodiagnosics*, vol. 42 (2008) (in Russian)
10. V.N. Popov, YuS Tsivinskaya, A.E. Koch, *J. Math. Model.* **17**, 77 (2005)
11. M.P. Marchenko, I.V. Fryazinov, *J. Crystallogr.* **50**, 1114 (2005)
12. S.C. Hannanov, S.P. Nikanorov, S.I. Baholdin, *J. Solids Phys.* **45**, 1020 (2003)
13. S.P. Malyukov, S.N. Nelina, in *Proceedings of the Microelectronics and Informatics*, vol. 190 (2007) (in Russian)
14. A.S. Dzyuba, I. Zu, *J. Crystallogr.* **30**, 1177 (1985)
15. V.L. Indenbom, G.N. Tomilevsky, *J. Crystallogr.* **1**, 593 (1957)
16. V.L. Indenbom, V.B. Osvensky, *J. Cryst. Growth* **13**, 240 (1980)
17. S.P. Malyukov, S.N. Nelina, D.I. Cherednichenko, in *Proceedings of the Solids Chemistry*, vol. 105 (2009) (in Russian)
18. S.P. Malyukov, Y.V. Klunnikova, I.A. Painov, in *Advanced Nano- and Piezoelectric Materials and Their Applications*, vol. 89, ed. by I.A. Parinov (Nova Science Publishers, New York, 2014)
19. A.V. Budnikov, A.E. Vorobev, V.N. Kanishev et al. in *Release of the Dissolved and Ion-introduced Gases at Fragile Destruction, Plastic Deformation and Heating Poly- and Monocrystals of Oxides of Aluminum, Magnesium, Zirconium, Aluminum-Yttrium Granate and Metals*, vol. 63 ASRI of Monocrystals, Kharkov, (1990)
20. S.P. Malyukov, S.N. Nelina, V.A. Stefanovich, *Physicotechnological Aspects of Sapphire Production* (Lap Lambert Academic Publishing, Germany, 2012)
21. D.I. Cherednichenko, S.P. Malyukov, Y.V. Klunnikova, in *Sapphire: Structure, Technology and Applications*, ed. by I. Tartaglia, (Nova Science Publishers, New York, 2013)
22. S.P. Malyukov, Yu.V. Klunnikova, In: *Advanced Materials—Studies and Applications*, vol. 65, eds. by I.A. Parinov, S.-H. Chang, S. Theerakulpisut (Nova Science Publishers, New York, 2015)
23. Y.E. Geguzin, A.S. Dzyuba, N.V. Kononenko, *J. Crystallogr.* **26**, 577 (1981)
24. Y.I. Frenkel, *Kinetic Theory of Liquids* (Science, Leningrad, 1975). (in Russian)
25. S.P. Malyukov, Y.V. Klunnikova, *J. SFedU News. Tech. Sci.* **4**, 86 (2011). (in Russian)

26. S.P. Malyukov, Y.V. Klunnikova, *Optimization of Sapphire Crystals Production for Electronic Technique* (Lap Lambert Academic Publishing, Germany, 2012)
27. C.S. Bagdasarov, *High-temperature Crystallization from Melt* (Phismathlit, Moscow, 2004). (in Russian)
28. S.N. Ryadnov, *PhD Thesis*, Institute of the Crystallography of A.B. Shubnikova, Moscow (1987) (in Russian)

Chapter 9

Investigation of Important Parameters for Lignin Degradation Using Fenton-Like Reaction via Cu Doped on Bagasses-MCM-41

Pongsert Sriprom, Chitsan Lin, Arthit Neramittagapong and Sutasinee Neramittagapong

Abstract Fenton-like's reaction using 5 wt% Cu-BG-MCM-41 catalyst was applied to lignin degradation. The 5 wt% Cu-BG-MCM-41 catalyst was prepared by hydrothermal and wetness impregnation method, and characterized by XRD and BET for surface areas. The results showed that the surface area and pore diameter are up to 621 m²/g and 2.62 nm, respectively. Plackett-Burman full factorial design was applied to identify the significant parameters in lignin degradation. Five factors (temperature, pH, catalyst loading, hydrogen peroxide concentration, and reaction time) influencing lignin degradation were investigated. The results show that the regression model for parameter screening was well-fitted with the experiment data, supported by the high R^2 of coefficient 0.9767. The results show that catalyst loading and reaction time were the significant effects ($P < 0.05$) rather than temperature, pH and H₂O₂ concentration. These results were reported by former researchers. The finding means a lot in engineering design involves with multifactor confounding together. The conclusion of this study indicates that Plackett-Burman Full Factorial Design is a useful tool for screening a large number of parameters, when complicate interactions of these parameters are involved. Therefore, key parameters can be identified and properly engineered thus treatment efficiency is warranted and cost minimized.

P. Sriprom · A. Neramittagapong · S. Neramittagapong (✉)
Department of Chemical Engineering, Faculty of Engineering,
Khon Kaen University, Khon Kaen 40002, Thailand
e-mail: sutasineene@kku.ac.th

C. Lin
Department of Marine Environmental Engineering, College of Ocean Engineering,
National Kaohsiung Marine University, Kaohsiung 81157, Taiwan

9.1 Introduction

Lignin is one of the major pollutants in black liquor, which is difficult to be degraded by traditional biological technology. However, it should be removed from the wastewater to meet the effluent discharge standard before being discharged to the environment. Among all methods, the polluted water treated with the help of catalysts has drawn much attention and research interest. Several catalytic processes have been reported as possible methods in resolving the organic pollution [21]. These processes are often referred to as advanced oxidation processes (AOPs). Several AOPs have been studied to improve efficiency and reduced cost for eliminating organic pollutant in air and wastewater such as photo-catalysis [8, 12, 37], wet oxidation [2, 9, 25] and Fenton's reaction [4, 11, 22].

Fenton oxidation reaction is one of the AOPs, which can effectively destroy the organic compounds in wastewater. The Fenton reaction uses Fenton's reagents (H_2O_2 and Fe^{2+}) to generate the hydroxyl radical, which is non-selective and highly oxidative to organic compounds [3, 4, 35, 36, 38]. However, the limitations of ferric iron in the Fenton reactions include that it is difficult to separate after the reaction, and works well only in a narrow pH range of 3–4 and ineffective at pH over 4. Thus, a copper catalyst was suggested to be used as Fenton's reagent and call it a Fenton-like catalyst, which works well at a pH range of 5–7. However, homogeneous copper in liquid phase oxidation process is hazardous to animals and humans, and is also difficult to remove after reaction. To overcome such limitation, copper was immobilized on another support such as zeolite, alumina, and MCM-41 [1, 10, 16, 19, 30]. MCM-41 is one of mesoporous materials, which has pore size ranging from 2 to 50 nm. MCM-41 has lot of applications such as adsorption and support catalyst. Owing to larger specific surface area and more active site available, MCM-41 was chosen as the support of copper which was reported in [7, 18]. Therefore, scanning experiments were employed aiming to classify significant factors that provide large effects on the response [6, 24]. However, these effects were evaluated by varying one factor at a time while keeping the others constant. Such experimental design was not only time consuming but also very costly. Moreover, it can only study the main effects of the reaction but the interaction effects. Therefore, experimental methods that can handle several factors and to optimize the system are warranted. Examples, such as central composite design (CCD) [27, 29, 33] or Box-Behnken design (BBD) [20, 28, 34] have been reported. Moreover, it was also suggested that full factorial design may be used to determine the important factor with the largest effect. Plackett-Burman [6] is one of the full factorial designs that is usually applied to evaluate the relative importance of the examining factors, in which there are no interaction effects between the different effective parameters in the range of consideration and each factor is tested at both high and low levels. In this situation, one or two relative important parameters are identified. However, this was seldom studied before. Therefore, in this research, we used Plackett-Burman Full Factorial Design to screen parameters influence the efficiency of the Fenton's reaction. In the Fenton reaction, many factors affect

organic removal efficiency including temperature [17, 22], pH [24], initial concentration of the sample [13, 26], catalyst loading [23], hydrogen peroxide [3, 36, 38], and reaction time [24]. These factors were optimized to increase the organic removal efficiency.

In this research, Fenton's reaction was applied to determine lignin degradation from lignin aqueous solution using 5 wt% Cu-BG-MCM-41 as catalyst. Under selected reaction conditions of temperature, pH, catalyst loading, hydrogen peroxide concentration, and reaction time, Plackett-Burman Full Factorial Design was applied to screen parameters.

9.2 Method and Experiment

9.2.1 Chemicals

Lignin was chosen as a probe of the pulp and paper wastewater model pollutant and purchased from Sigma Aldrich (Germany). The lignin solution was reproduced from the pulp and paper wastewater pre-treatment plant. The concentration of lignin solution 350 mg/L was prepared by dissolving lignin 0.35 g in distilled water at pH 10. The pH of lignin solution was adjusted using 1 M sodium hydroxide (NaOH) and nitric acid (5 % HNO₃) (Analytical grade, Ajax Laboratory Chemical, Australia). Hydrogen peroxide (30 % w/w) purchased from QREC, New Zealand was used as obtained. The 5 wt% Cu-BG-MCM-41 catalyst was used as the catalyst in Fenton-like reaction. The 5 wt% Cu-BG-MCM-41 was prepared by hydrothermal technique that all chemicals were purchased from UNILAB (Thailand) and LAB SCAN (Thailand).

9.2.2 Plackett-Burman Screening Designs

A Plackett-Burman screening design [6] is an adjusted fractional factorial design that assists experimenters to study a large number of factors with a significantly decreased number of runs. Plackett-Burman designs are often applied as a screening tool to identify statistically significant main effects for a large number of experimental factors. With such a design, 5–7 factors can be investigated in 12 runs, and 9–15 factors can be studied in as little as 16 runs. Owing to the reduced number of experimental runs, the design is only appropriate for identifying main effects. Frequently, once significant factors have been identified and insignificant ones excluded from the study, a smaller, more described fractional factorial or full factorial is performed to optimize the reduced set of factors. Thus, the Plackett-Burman Full factorial design (FFD) was applied to study the effect of parameter to lignin degradation using Fenton-like reaction over 5 wt% Cu-BG-MCM-41. The two-level

Plackett-Burman FFD with five factors was applied. Five factors were temperature (X_1), pH (X_2), catalyst loading (X_3), H_2O_2 (X_4) and Reaction time (X_5). The statistical significance of each factors and their arrangement at 95 % significance level were estimated using the MINITAB software (version 16.0, Minitab Inc., State College, PA). These parameters were screened for effects on percent lignin degradation. The percentage of lignin degradation was identified to be the response (Y , %), which can be calculated as

$$Y = \frac{(C_0 - C_t)}{C_0} \times 100 \%, \quad (9.1)$$

where C_0 and C_t are initial lignin concentration and lignin concentration at a certain time t , respectively. Total of 12 experimental runs as shown in Table 9.1 were performed to complete the designs.

A regression analysis was conducted on a regression model, which corresponded to the following first-order regression equation:

$$Y = \beta_0 + \sum \beta_i X_i, \quad (9.2)$$

where β_0 and β_i are the regression coefficients for the intercept and linear coefficients, respectively, Y is the response or dependent variable, X_i is the independent variables in coded units. The regression equation was used to predict the screen parameters. The adequacy of regression model was tested by the analysis of variance (ANOVA).

9.2.3 Fenton-Like Reaction Procedure

A stock lignin solution containing 350 mg/L was prepared. Following the arrangement shown in Table 9.1, the effects of the factors of initial solution were investigated. The oxidation reaction occurred in 500 mL of lignin solution. The solution was analyzed for lignin degradation by UV-vis spectroscopy (UV-vis, Agilent 8453) at 280 nm. The metal leached was analyzed by atomic adsorption spectroscopy (AAS, Perkin Elmer Analyst 100).

Table 9.1 Experimental design of Fenton-like reaction of lignin degradation using 5 wt % Cu-BG-MCM-41 catalyst

Independent variable	Code	Level minimum (-1)	Level maximum (+1)
Temperature (°C)	X_1	60	80
pH	X_2	3	9
Catalyst loading (mg/L)	X_3	0	1
H_2O_2 (mL)	X_4	0	1
Reaction time (min)	X_5	5	30

9.3 Results and Discussion

9.3.1 Characterization of Catalyst

The XRD pattern of BG-MCM-41 at low angle from 1.5° to 15° is shown in Fig. 9.1a. The results show that the synthesized BG-MCM-41 at three low angle reflections corresponding to d_{100} , d_{110} , and d_{200} , respectively, which are typical of the ordered mesoporous structure of hexagonal MCM-41. The decrease of corresponding d_{100} peak intensity and lack of d_{200} peak of 5 wt% Cu-BG-MCM-41 compared with BG-MCM-41 synthesized consider a less ordered hexagonal mesoporous structure. This result indicates that the decrease in the peak intensity is mainly related to metal species instead of the thermal instability of the support [14].

Figure 9.1b shows the higher-angle XRD pattern of 5 wt% Cu-BG-MCM-41. The result shows that the CuO phase was shown the peak at $2\theta = 35.5^\circ$, 38.7° , and 48.7° , respectively. On the other hand, CuO characteristic diffraction peaks appearing above $2\theta^\circ$ given to the 110 and 220 lattice planes were found by XRD for 5 wt% Cu as shown in Fig. 9.1b. Thus, suggesting that the formation of crystalline copper oxides occurs during the calcination. This formation may be caused by CuO sintering at a high calcination temperature (550°C), wherein the CuO was produced as large crystal particles on the catalyst surface [32]. The specific surface area and average pore diameter were analyzed by Nitrogen adsorption-desorption, which BET theory was used for calculating small pore diameter ($<5\text{ nm}$). The results were listed in Table 9.2 that shows the BET surface area and pore diameter of

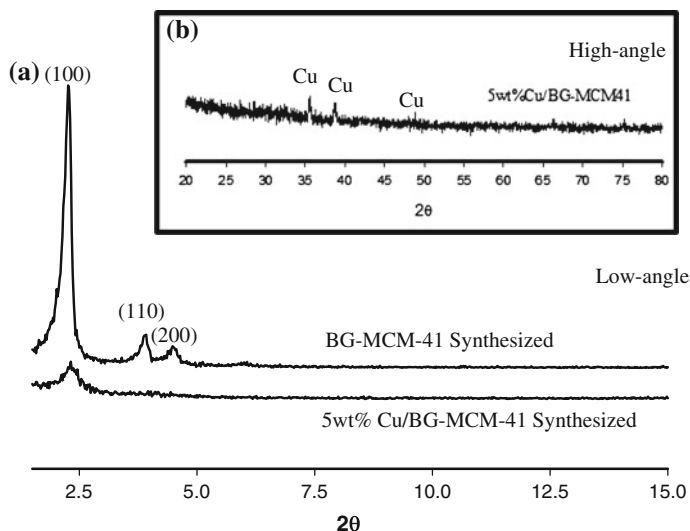


Fig. 9.1 XRD pattern of BG-MCM-41 and Cu on BG-MCM-41 catalyst **a** low-angle and **b** higher-angle

Table 9.2 BET surface area and pore diameter of the catalysts

Catalyst	Prepared method	Surface area (m ² /g)	Pore diameter (nm)
BG-MCM-41	Hydrothermal	1161	2.73
Cu-BG-MCM-41	Wetness impregnation	621	2.62

BG-MCM-41 and Cu-BG-MCM-41. The specific surface area reduction has two causes: the copper oxide is nano-particles within the mesopores reduces the mean pore diameter and, the introduction of metallic elements on BG-MCM-41 decreases the surface area can be also attributed to an increase in density of the composites after loading copper elements [14].

9.3.2 Parameter Screening

The 5 wt% Cu-BG-MCM-41 catalyst was chosen to be used in the Fenton-like reaction of lignin degradation. It was found that several parameters affecting the efficiency of the Fenton-like reaction are temperature, pH, H₂O₂ concentration, catalyst loading, and reaction time. The two-level Plackett-Burman FFD with five factors was used in order to prioritize the important factors. Five factors and two center points and a total of 12 experimental runs were carried out, shown in Table 9.3, with temperature, pH, catalyst loading, H₂O₂ concentration and reaction time as the selected factors to be studied. The response was chosen as the percentage of lignin degradation. The *Y*, % was found to range from 5.14 to 76.92 % and the significant effect of each factor on *Y*, % was assessed by a normal probability plot of standardized effects, a Pareto chart, main effects and interaction plots at 5 % significance level using the Minitab Version 16.0 software.

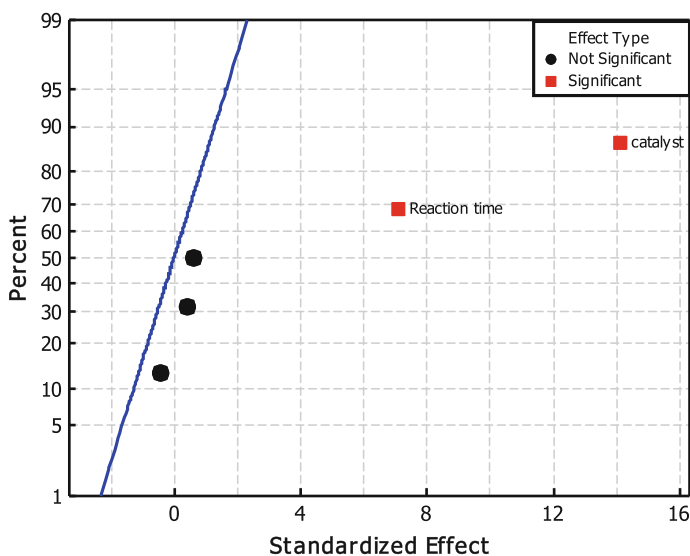
A normality probability plot of effect was generated from main effects of factors as shown in Fig. 9.2. The results show that temperature, pH and H₂O₂ concentration are insignificant, which are normally distributed with mean zero and variance, and tend to fall on the straight line in the plot. The effects of reaction time and catalyst loading are significant which are placed far away from the straight line, and have non-zero means.

The Pareto chart of effects is used to identifying the important factors. The estimated main effects plotted against the horizontal axis were shown in Fig. 9.3. The estimated main effects were ranked according to their significance, and showed that the most significant effect was catalyst loading, followed by reaction time. While the other three factors are insignificant includes H₂O₂ concentration, reaction temperature and pH at *P* = 0.05 as shown in Fig. 9.3. However, these factors were commonly applied in Fenton-like reaction.

The main effect plot explains the trend of all effects as shown in Fig. 9.4. It is clear that increase in catalyst loading and reaction time leads to increase in % of

Table 9.3 Plackett-Burman design for screening of the Fenton-like reaction parameters

Run order	Temperature	pH	Catalyst loading	H ₂ O ₂ (ml/L _{sample})	Reaction time (min)	% of lignin degradation	Predicted % of lignin degradation
1	60	3	0	0	5	8.27	4.12
2	80	3	1	0	5	40.39	45.98
3	60	9	1	1	5	47.76	50.48
4	60	9	1	0	30	66.83	70.28
5	80	9	0	1	5	8.41	6.00
6	60	3	1	1	30	72.77	70.95
7	60	9	0	0	5	5.14	5.38
8	80	9	0	1	30	23.79	27.73
9	80	3	0	0	30	21.73	24.54
10	80	9	1	0	30	76.92	68.97
11	60	3	0	1	30	28.22	27.78
12	80	3	1	1	5	49.89	47.90

**Fig. 9.2** Normal probability plot of standardized effects for % lignin degradation (Y, %)

lignin degradation, while increase in the other three parameters no significant change in lignin degradation was observed.

Again, the results show that % of lignin degradation was significantly affected by the reaction time and catalyst loading. In the experiments, the results indicate that catalyst loading increase from 0 to 1 g/L yield on higher lignin degradation. This is mainly ascribed to the availability of more catalyst active site that can accelerate the

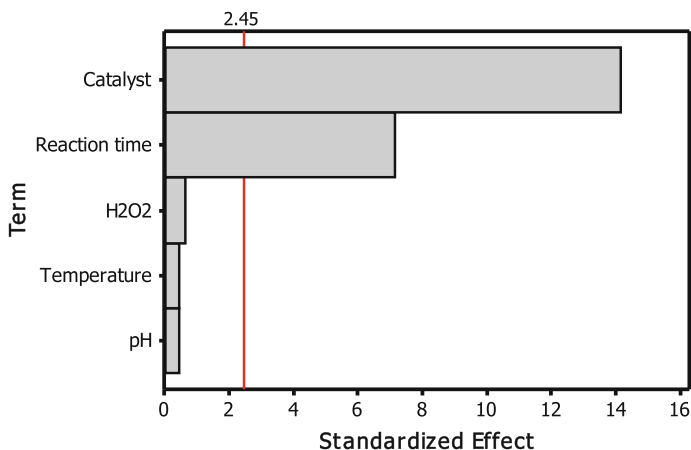


Fig. 9.3 Pareto charts for the main factors effect on lignin degradation using Fenton-like reaction. The vertical line shows the $P = 0.05$ level for statistical significant

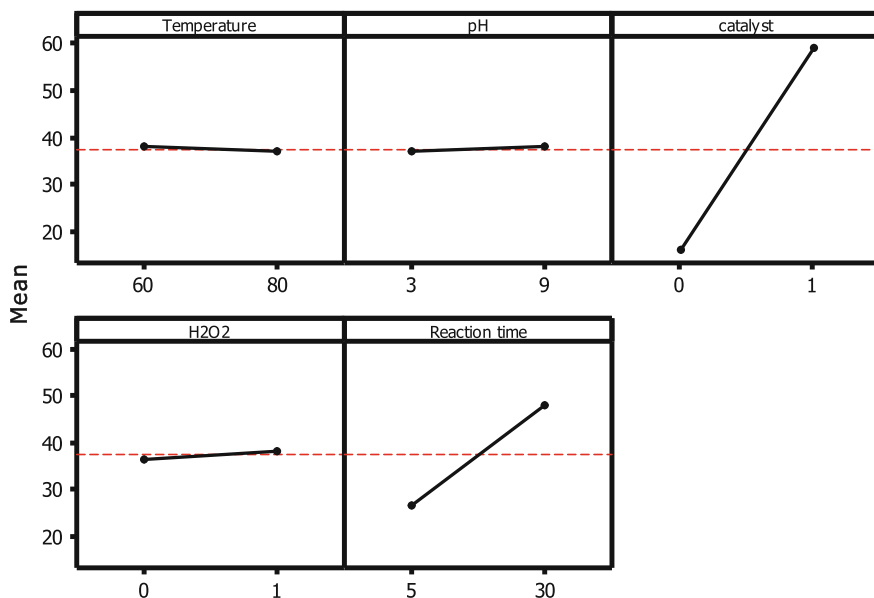
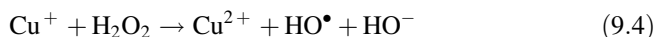
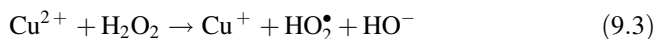


Fig. 9.4 Plots of main effects for % of lignin degradation

lignin degradation on the catalyst surface. Similar results were reported in [13], where reported the higher amount of near surface organic pollutant generated can attack the adsorbed pollutants and increased reaction rate. Nevertheless, indicating that Cu^{2+} used in Fenton-like reaction can be shown that strikingly similar redox

properties like iron, which oxidation states react easily with hydrogen peroxide as described [4] in the following equations:



Reference [15] reported that the high specific surface area, narrow pore size distribution, and well dispersion of Cu loaded on support could be the reasons for its high organic compound adsorption capacity. In this study, it was shown that the organic pollutants were first adsorbed on the surface of the catalyst and then the Fenton-like reaction also occurred on the surface of catalyst. However, the reaction time is one of significant effect on lignin degradation. The researcher reports that the reaction time was effect to generated rate of OH radical [22, 24]. From the interaction plots (Fig. 9.5) the interaction effects line was unparallelled for each parameter, implying that there was a very strong two-way interaction between each of the main effects. However, the interaction line for catalyst loading and reaction time were relatively weak due to the parallel interaction effects line. Reference [5] mentioned that the interaction effects would not be detected in multivariate statistical techniques. Therefore, temperature pH and H₂O₂ concentration do not significantly affect % of lignin degradation but, which cannot be ignored in the engineering design of Fenton-like reactions. Due to these, the parameters have interaction effects on lignin degradation in Fenton-like reactions as shown in Fig. 9.5. The results indicate that OH[•] radical was an important oxidizing agent to react with organic pollutants which was produced by H₂O₂ decomposition. More

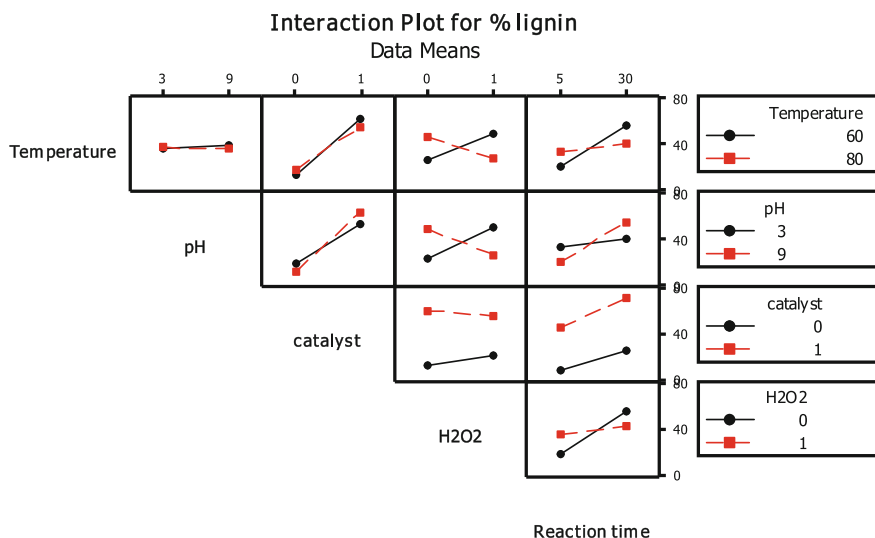


Fig. 9.5 Plots of interaction effects for % of lignin degradation

OH^\bullet radical were generated at increased H_2O_2 concentrations. However, due to the self-decomposition at high concentrations, increasing H_2O_2 concentrations did not improve removal efficiency. Additionally, pH, catalyst loading, and temperature affected the generation of OH^\bullet by H_2O_2 . Related results [31] reported that higher pH can cause the formation of an inactive hydrogen peroxide anion due to H_2O_2 dissociation leading to inhibition of degradation. So, H_2O_2 became unstable and decomposed to oxygen at high pH, also losing its oxidation ability. Nevertheless, [17] reported that at high temperatures, the oxidation reaction rate increased more than the hydrogen peroxide decomposition rate.

9.3.3 Regression Analysis

After the collection of 12 runs and the estimated response, the system is complete for analysis initiating with the calculation of the regression coefficients (Table 9.4). The regression coefficients are used to predict the response of each factor assisted by the linear regression equation as follows:

$$Y = 3.071 - 0.065X_1 + 0.211X_2 + 43.167X_3 + 1.927X_4 + 0.869X_5 \quad (9.5)$$

$(R^2 = 97.67\%, R^2_{adj} = 95.73\%)$,

where every regression coefficient was calculated by the least square method and the results are depicted in Table 9.4.

At 95 % significance level found that catalyst loading and reaction time were significant main effects, which were observed by P -value less than 0.05. However, in term of temperature, pH and H_2O_2 concentration were deemed insignificant main effect as P -values are higher than 0.05. In (9.5), the coefficients of X_2 , X_3 , X_4 and X_5 were positive show that their effects were synergic effect on Y , %. Nevertheless, the coefficient of X_1 was negative indicates an antagonistic effect on Y , %.

The predicted versus the observed values plot for % of lignin degradation was shown in Fig. 9.6. The observed points were distributed on the plot near the straight line indicates that it was highly satisfactory with R^2 of 0.9767. Imply that the

Table 9.4 ANOVA of the regression model for lignin degradation

Source	Coefficient	Adj MS	F	P
Constant	3.0717	1405.63	50.30	0.000
Temperature	-0.0650	5.15	0.18	0.683
pH	0.2105	4.79	0.17	0.693
Catalyst loading	43.1667	5590.08	200.02	0.000
H_2O_2	1.9267	11.14	0.40	0.551
Reaction time	0.8693	1417.01	50.70	0.000

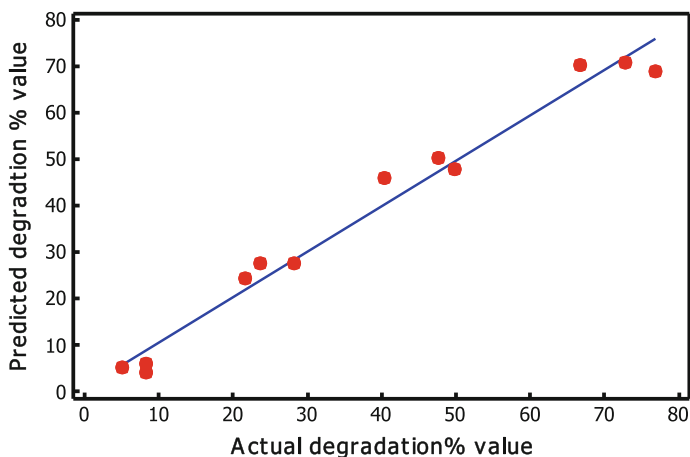


Fig. 9.6 Normal probability plot of standardized residuals

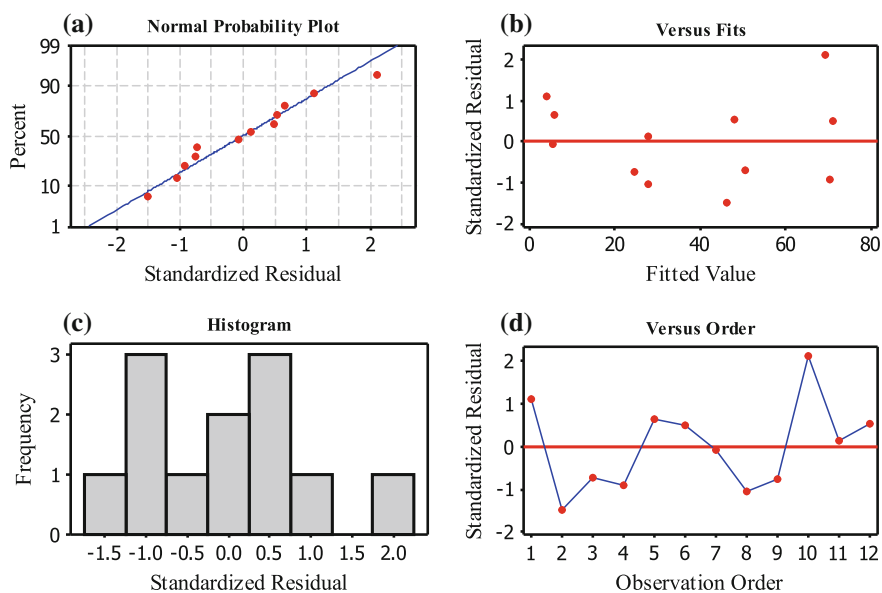


Fig. 9.7 Internal standardized residual plots versus a normal probability, b fits, c histogram and d observation order for % of lignin degradation

regression model (5) is appropriate for screening important parameter on % of lignin degradation efficiencies.

The adequacy of fit was checked by graphical analysis of residuals. The differences of the experimental and the predicted values were used for calculation of the residuals. The residual plots of this study for the quadratic regression model

are shown in Fig. 9.7. The normal probability plot of residuals (Fig. 9.7a) is approximately along the straight line indicating the normality assumption is satisfied. Figure 9.7b shows the standardized residual and fitted value (predicted response) scatters randomly, suggesting that the data seem to exhibit relatively constant variance across predicted values and there does not appear to have any outliers or influential observations. The histogram chart, shown in Fig. 9.7c, indicates that the frequency of standardized residual is distributed in the normal curve. Figure 9.7d shows a plot of the standardized residual versus run order, and the results present randomly scatters in the standard residual plots fluctuate around the center line (in the range of ± 2). These results show that the data is randomly distributed. It shows that the data has accuracy and reliability. It has been explained that all experiment orders have no abnormality in this study. Therefore, it was concluded that the regression model was useful for screening the important parameter as well.

9.4 Conclusion

Lignin was degraded by Fenton-like reaction using 5 wt% Cu-BG-MCM-41 as catalyst. The results show that 5 wt% Cu-BG-MCM-41 catalyst has the highest stability for Fenton-like reactions. The stability of catalyst can be observed on the metal leached from the support in the reaction. The pH and temperature affected the stability of Cu loading in which Cu was leached into the aqueous solution and that the reaction will occur in the aqueous solution more than on the surface of the catalyst. Hence, the reaction most likely occurred through a homogenous Fenton-like reaction than a heterogeneous one. Thus, this study, although is designed as heterogeneous Fenton-like reaction, the overall effect is compounded with homogeneous reaction mechanism. Therefore, the Plackett-Burman full factorial design was applied to identify the key parameters from a large number of parameters in this reaction. The parameters chosen to be studied were temperature, pH, catalyst loading, H_2O_2 concentration, and reaction time. The results show that catalyst loading and reaction time are statistically significant as the most influential parameters. Temperature, H_2O_2 concentration and pH, although, were statistically insignificant; however, they are non-negligible in the engineering design aspect of Fenton-like reactions. All parameters have significant contributions, which cannot be removed from engineering consideration. A regression model for % of lignin degradation has R^2 (97.67 %) and R^2_{adj} (95.73 %). The high value of R^2 shows that the model achieved is able provide reasonable estimate of response for the system in the variety studies. The results show that the Plackett-Burman full factorial design was suitable to identify variables which can be modified in further investigation, thus, save time and cost.

Acknowledgments This work was supported by the Higher Education Research Promotion and National Research University Project of Thailand, Office of the Higher Education Commission.

References

1. A. Angi, D. Sanli, C. Erkey, Ö. Birer, *Ultrason. Sonochem.* **21**, 854 (2014)
2. E. Arvaniti, A.B. Bjerre, J.E. Schmidt, *Biorefinery* **39**, 94 (2012)
3. E. Basturk, M. Karatas, *Ultrason. Sonochem.* **21**, 1881 (2014)
4. A.D. Bokare, W. Choi, *J. Hazard. Mater.* **275**, 121 (2014)
5. S.H. Chang, T.T. Teng, N. Ismail, *J. Environ. Manage.* **92**, 2580 (2011)
6. K. Chauhan, U. Trivedi, K.C. Patel, *Bioresour. Technol.* **98**, 98 (2007)
7. S. Chiarakorn, T. Areerob, N. Grisdanurak, *APNF Int. Symp. Nanotechnol. Environ. Prot. Pollut. ISNEPP2006.* **8**, 110 (2007)
8. J.H. Cho, T.G. Lee, Y. Eom, *J. Air Waste Manag. Assoc.* **62**, 1208 (2012)
9. B.J. Cox, S. Jia, Z.C. Zhang, J.G. Ekerdt, *Polym. Degrad. Stab.* **96**, 426 (2011)
10. G. Ersöz, S. Atalay, *J. Environ. Manage.* **113**, 244 (2012)
11. N. Ertugay, F.N. Acar, *Arab. J. Chem.* (2013). doi:[10.1016/j.arabjc.2013.02.009](https://doi.org/10.1016/j.arabjc.2013.02.009)
12. J. Fang, H. Zhang, N. Yang, L. Shao, P. He, *J. Air Waste Manag. Assoc.* **63**, 1287 (2013)
13. P.P. Gan, S.F.Y. Li, *Chem. Eng. J.* **229**, 351 (2013)
14. X.-Y. Hao, Y.-Q. Zhang, J.-W. Wang, W. Zhou, C. Zhang, S. Liu, *Microporous Mesoporous Mater.* **88**, 38 (2006)
15. J.-N. Hsu, H. Bai, S.-N. Li, C.-J. Tsai, *J. Air Waste Manag. Assoc.* **60**, 629 (2010)
16. L. Hua, H. Ma, L. Zhang, *Chemosphere* **90**, 143 (2013)
17. N. Inchaurredo, E. Contreras, P. Haure, *Chem. Eng. J.* **251**, 146 (2014)
18. S. Jin, K. Cui, H. Guan, M. Yang, L. Liu, C. Lan, *Appl. Clay Sci.* **56**, 1 (2012)
19. N. Khanikar, K.G. Bhattacharyya, *Chem. Eng. J.* **233**, 88 (2013)
20. H.-W. Kim, H.-S. Shin, S.-K. Han, S.-E. Oh, *J. Air Waste Manag. Assoc.* **57**, 309 (2007)
21. K.-H. Kim, S.-K. Ihm, *J. Hazard. Mater.* **186**, 16 (2011)
22. Y. Kuang, Q. Wang, Z. Chen, M. Megharaj, R. Naidu, *J. Colloid Interface Sci.* **410**, 67 (2013)
23. H.-J. Lee, H. Lee, C. Lee, *Chem. Eng. J.* **245**, 258 (2014)
24. Y. Li, A. Zhang, *Chemosphere* **105**, 24 (2014)
25. M. Luan, G. Jing, Y. Piao, D. Liu, L. Jin, *Arab. J. Chem.* (2012). doi:[10.1016/j.arabjc.2012.12.003](https://doi.org/10.1016/j.arabjc.2012.12.003)
26. J. Maekawa, K. Mae, H. Nakagawa, *J. Environ. Chem. Eng.* **2**, 1275 (2014)
27. E.E. Mitsika, C. Christophoridis, K. Fytianos, *Chemosphere* **93**, 1818 (2013)
28. K. Papadopoulou, I.M. Kalagona, A. Philippoussis, F. Rigas, *Int. Biodeterior. Biodegrad.* **77**, 31 (2013)
29. T.T.H. Pham, S.K. Brar, R.D. Tyagi, R.Y. Surampalli, *J. Environ. Manage.* **91**, 1657 (2010)
30. A. Santos, P. Yustos, A. Quintanilla, G. Ruiz, F. Garcia-Ochoa, *Appl. Catal. B Environ.* **61**, 323 (2005)
31. S.K. Singh, W.Z. Tang, *Waste Manag.* **33**, 81 (2013)
32. P. Sriprom, A. Neramittagapong, *Neramittagapong S.* **931–932**, 12 (2014)
33. Y. Wang, W. Li, A. Irini, C. Su, *Chem. Eng. J.* **252**, 22 (2014)
34. K. Wantala, E. Khongkasem, N. Khlongkarnpanich, S. Sthiannopkao, K.-W. Kim, *Recent Prog. Environ. Geochem.-Tribute Iain Thornton.* **27**, 1027 (2012)
35. X. Yin, W. Liu, J. Ni, *Chem. Eng. J.* **248**, 89 (2014)
36. L. Zhang, H. Zeng, Y. Zeng, Z. Zhang, X. Zhao, *J. Mol. Catal. Chem.* **392**, 202 (2014)
37. Q. Zhang, C.-F. Lin, Y.H. Jing, C.-T. Chang, *J. Air Waste Manag. Assoc.* **64**, 578 (2013)
38. S. Zha, Y. Cheng, Y. Gao, Z. Chen, M. Megharaj, R. Naidu, *Chem. Eng. J.* **255**, 141 (2014)

Chapter 10

Production of Slow Release Fertilizer from Waste Materials

Petchporn Chawakitchareon, Rewadee Anuwattana
and Jitrera Buates

Abstract This chapter aims to study the feasibility to produce slow release fertilizer from waste materials. Three waste materials i.e. leonardite, zeolite and rice straw were utilized. Four formulations of slow release fertilizer were prepared by using different compositions of leonardite, leonardite and zeolite, leonardite and rice straw and leonardite, zeolite and rice straw. The nutrient contents of each formulation were adjusted in order to relate to those of the N13:P13:K13 commercial slow release fertilizer by the addition of fertilizer materials. Bentonite was applied at 10 wt% to act as a binder. All four formulations of slow release fertilizer were coated with resin. Morphologies of the coated and uncoated formulation surfaces were revealed by scanning electron microscopy (SEM) and the N, P, K nutrients release contents were also determined. The results indicated that the uncoated formulations have the N, P, K release contents higher than the coated formulations and the commercial slow release fertilizer. The slow release fertilizer formulations without zeolite (sample 2) have N, P, K nutrient release contents slower than with zeolite (samples 1 and 3). However, the N, P, K nutrient release rates are still high comparing to the commercial slow release fertilizer. Moreover, the coated formulation has the nutrient release contents as well as the commercial slow release fertilizer especially for the formulation with zeolite (formulations 1 and 3). According to the morphologies revealed by Scanning Electron Microscopy, many pores were found on the uncoated formulations in contrast to the coated formulations and the commercial slow release fertilizer, which have smooth surfaces.

P. Chawakitchareon (✉) · J. Buates
Department of Environmental Engineering, Faculty of Engineering,
Chulalongkorn University, Bangkok 10330, Thailand
e-mail: petchporn.c@chula.ac.th

R. Anuwattana (✉)
Thailand Institute of Scientific and Technological Research, Technopolis,
Khlong 5, KhlongLuang, Pathumthani 12120, Thailand
e-mail: rewadee_a@tistr.or.th

10.1 Introduction

Fertilizers have been used extensively as nutrients for plant growth. The three major nutrients are nitrogen (N), phosphorus (P) and potassium (K). Nowadays, fertilizers are important for sustainable development of crop yield. However, large amount of fertilizers are lost from volatilization and leaching out to surface and ground water. The solution to reduce the nutrient losses is to use slow release fertilizers (SRFs). Slow release fertilizers design for gradually release fertilizers to plants at a rate to coincide with the nutrient requirement of a plant, while simultaneously reducing fertilizer loss [1]. Slow release fertilizers generally divide into one of several groups: palletized or matrix based, chemically altered, coated or infiltrated into zeolite reservoirs. Because nutrients release at a slower rate throughout the season with slow release fertilizer, plants are able to take up most of the nutrients without waste by leaching. Slow release fertilizer is also more convenient, since less frequent application is required [2]. The N13:P13:K13 slow releases fertilizer usually uses in planting and is very beneficial in enhancing plant growth with balanced nutrient contents. The N13:P13:K13 formulation is a longer term product ideal for perennials and slower growing flowering crops. It is most appropriate for hanging basket plants [3]. Leonardite is a special low rank coal. It is processed either from lignite that has undergone oxidation during surface exposure, or it represents sediments enriched in humic substance. Leonardite is a coal-like substance similar in structure to lignite, but significantly different in its oxygen and ash contents [4]. However, it contains large amounts of humic substances (20–70 %) which has a complex in properties from carboxylic and hydroxylic sites of functional groups in humic substances and various inorganic minerals. Lignite mines in Lampang province, which is in the northern region of Thailand, is mined in open pits and used for power generation of electricity. This leonardite is in the benches outcrop at the lignite open pits. In the mine, a low-grade leonardite was dumped on-site storage in lignite mine and made problem to the surrounding area and had a negative impact on aquatic and terrestrial systems through runoff. This low-grade leonardite identified to contain humic acid and mineral matter [5]. In many studies, humic acids preparations reported to increase the uptake of mineral elements, to promote the root length and to increase the fresh and dry weights of crop plants. Due to the positive effect of humic substances on the visible growth of plants, these chemicals have been widely used by the growers instead of other substances such as pesticides etc. [6]. Zeolites are a naturally occurring mineral group consisting of about 50 mineral types. They have a rigid three-dimensional crystal structure with voids and channels of molecular size and a high cation exchange capacity (CEC) arising from the substitution of Al for Si in the silicon oxide tetrahedral units that constitute the mineral structure [7]. Zeolites are important materials with very broad applications in refineries as catalysts, sorption and separation processes, and in agriculture and environmental engineering, too. It was found that incorporation of zeolite in soil increased tomato yield but had no positive effect on sweet corn. Other possible uses investigated include applications as a carrier of slow release fertilizers, insecticides, fungicides, and herbicides, and as

a trap for heavy metals in soils. Zeolites have potential applications in many ways in agriculture [8]. Rice straw is the most abundant agricultural by-product during the rice harvesting. The harvested rice straw to paddy ratio is approximately 1.0. Based on the data from the food and agriculture organization (FAO), the global production of rice straw is approximately 720 million tons per year [9]. Rice straw contains a large amount of nutrients: a ton of rice straw adds 6.16 kg of nitrogen (N), 0.83 kg of phosphorus (P), 22.5 kg of potassium (K), 4.16 kg of calcium (Ca), 2.33 kg of magnesium (Mg), and 0.83 kg of sulphur (S). These values confirm the importance of rice straw incorporation as a mean to return such nutrients in order to reduce the cost of fertilizers [10]. Moreover, a slow-release N source for rice formed effectively by blending rice straw, urea, and soil into balls [11].

10.2 Materials

The leonardite, used in this chapter, was present by Maneechan Industry Limited Company, Lampang, Thailand. Table 10.1 shows some of its physical and chemical characteristics.

Zeolite 4A was present by PQ Chemicals Limited Company, Bangkok, Thailand. Rice straw collected from the farm in Prathum Thani Province, Thailand. Fertilizer material (diammonium phosphate, urea and potassium chloride) was present by YVP fertilizer Company, Thailand. Bentonite was present by TCM Limited Company, China. The N13:P13:K13 commercial slow release fertilizer, used in this chapter, was Osmocote[®], provided by Sotus International Limited Company, Nonthaburi Province, Thailand.

10.3 Methods

10.3.1 Nutrient Contents Determination

The nutrient contents, nitrogen, phosphorous and potassium determined by Kjeldahl method, ammonium molybdate method, ammonium metavanadate method and Atomic Absorption Spectrometry method, respectively [12].

Table 10.1 Some physical and chemical properties of leonardite used in this chapter

Properties	Units	Value
pH	–	2.65
Ratio of carbon to nitrogen (C/N ratio)	–	63.46
Electrical conductivity (EC)	ds/m	10.71
Cations exchange capacity (CEC)	cmol/kg	53.35
Organic matter (OM)	%	25.23
Humic acid	%	35.65

Table 10.2 Samples of slow release fertilizer prepared in the present study

Formulations	Composition (%)		
	Leonardite	Zeolite	Rice straw
1	50	50	0
2	50	0	50
3	33.33	33.33	33.33

10.3.2 Preparation of the Slow Release Fertilizer

All components were prepared for homogeneous substance. First of all, the rice straw was dried at 80 °C for 24 h using an air-circulating oven and then grinded using a crumbling machine with 0.25 mm sieve. Other components, leonardite, zeolite and fertilizer material were also sieved to particles with a top cut of 0.25 mm. Three formulations were prepared with different compositions as shown in Table 10.2.

The nutrient contents of all samples adjusted to be relative to the nutrient contents of the N13:P13:K13 commercial slow release fertilizer (Osmocote[®]) by the addition of diammonium phosphate (18–46–0), urea (46–0–0) and potassium chloride (0–0–60). Moreover, 10 % by weight of bentonite were used in the formulations as a binder. The components of each sample mixed thoroughly sprayed over with water. Granules of slow release fertilizer with about 4 mm in diameter were prepared. All the slow release fertilizer granules were oven-dried at 105 °C for 1 h and then heated in the muffle furnace at 200 °C for 1 h. For coated sample, the granules were coated with resin and heated at 50 °C for 3 h.

10.3.3 Determination of Nutrient Release Rate

One gram of the fertilizer sample placed in a 125 ml flask containing 50 ml of distilled water. The flask then placed on an automatic shaker. The sample solution of each fertilizer sample collected at certain time, 1, 5, 24 and 48 h. The suspended solid separated from the solutions. Then, the nutrient contents were determined from each solution.

10.4 Results and Discussion

10.4.1 Nutrient Contents

Table 10.3 shows the nutrient contents in terms of nitrogen, phosphorus and potassium of leonardite, zeolite and rice straw prepared as slow release fertilizer in this chapter. Both leonardite and rice straw contained high primary plant nutrients.

Table 10.3 Nutrient contents of leonardite, zeolite and rice straw used in this chapter

Components	Sources	Nutrient contents (%)		
		Nitrogen	Phosphorus	Potassium
Leonardite	Maneechan Industry Limited Company	0.63	0.10	1.71
Zeolite	PQ Chemicals Limited Company	0.11	0.04	0.03
Rice straw	Prathum Thani	0.84	0.17	0.63

Leonardite comprised of nitrogen, phosphorus and potassium at 0.63, 0.10 and 1.71 %, respectively, while those of the rice straw were 0.84, 0.17 and 0.63 %, respectively. The potassium contents of leonardite and rice straw were higher than that of the organic fertilizer standard (more than 0.5 %) [13]. Therefore, leonardite and rice straw could be used to increase the nutrient and act as plant growth promoters stimulating plant development [14, 15]. Furthermore, the nutrient contents found in zeolite were less than those in leonardite and rice straw and also lower than those in the organic fertilizer standard (more than 0.5 %). Zeolite comprised of nitrogen, phosphorus and potassium at 0.11, 0.04 and 0.03 %, respectively. Although the nutrient contents of zeolite were very low, zeolite also contained secondary plant nutrients like sulfur, calcium, magnesium, iron, manganese and boron. Moreover, zeolite showed great potential for use in organic agriculture as it can improve plant growth and soil conditions in the long term [16].

10.4.2 Surface Morphology

The surface morphology of the N13:P13:K13 commercial slow release fertilizer and all the slow release fertilizer in the present study investigated by using scanning electron microscopy (SEM) as demonstrated in Figs. 10.1, 10.2 and 10.3.

The SEM images in Figs. 10.1, 10.2 and 10.3 showed that the uncoated and without zeolite component (formulation 2) had less number of pores with about 31–188 μm in size while the uncoated and with zeolite components (formulations 1 and 3) had many pores with about 31–750 μm in size. This might be referred that the formulation with zeolite had rougher surface. Moreover, many pores were found on the uncoated formulations in contrast to the coated formulations and the commercial slow release fertilizer, which have smooth surfaces.

10.4.3 NPK Nutrient Release Contents

The nitrogen, phosphorus and potassium released at various times for the N13:P13:K13 commercial slow release fertilizer (osmocote) and all the slow release fertilizer prepared in this chapter are plotted in Figs. 10.4, 10.5 and 10.6.

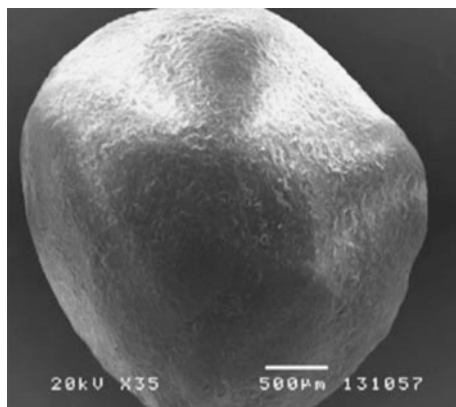


Fig. 10.1 SEM image of the N13:P13:K13 commercial slow release fertilizer

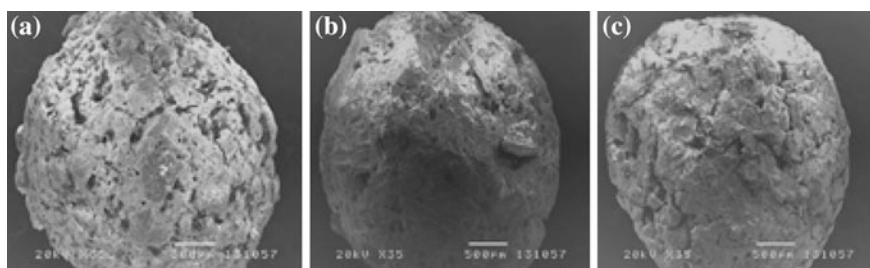


Fig. 10.2 SEM images of the uncoated slow release fertilizer: **a** Leonardite+Zeolite, **b** Leonardite+Rice straw and **c** Leonardite+Zeolite+Rice straw

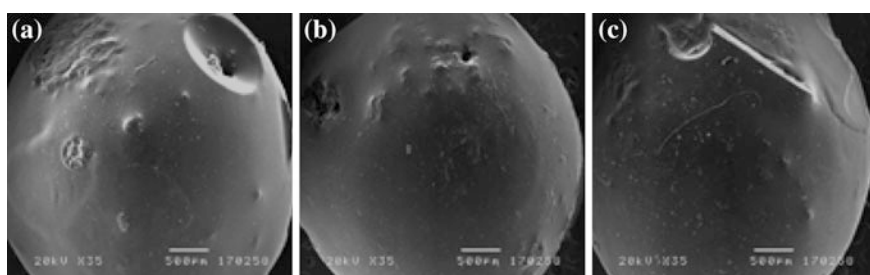


Fig. 10.3 SEM images of the coated slow release fertilizer: **a** Leonardite+Zeolite, **b** Leonardite+Rice straw and **c** Leonardite+Zeolite+rice straw

The uncoated formulations without zeolite (formulation 2) have greater potential to retain N, P, K nutrient release due to the less number of pores and smaller pore size than those uncoated formulations with zeolite (formulations 1 and 3).

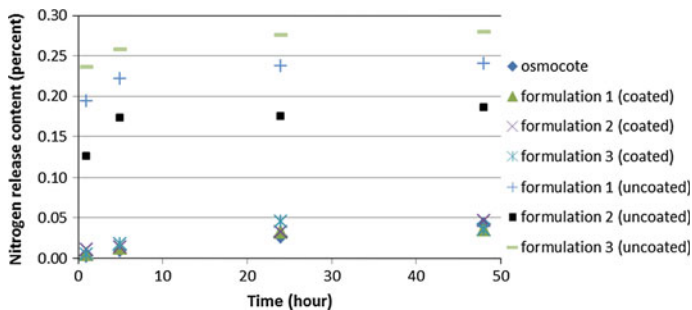


Fig. 10.4 Nitrogen release curves of osmocote, uncoated sample and coated sample

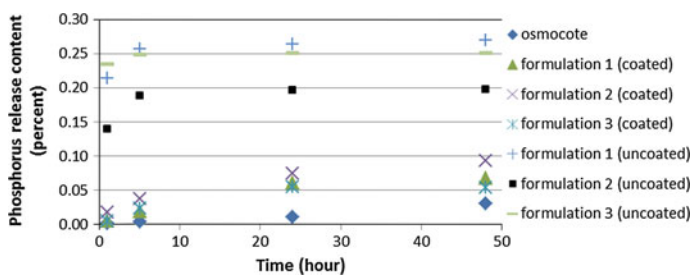


Fig. 10.5 Phosphorus release curves of osmocote, uncoated sample and coated sample

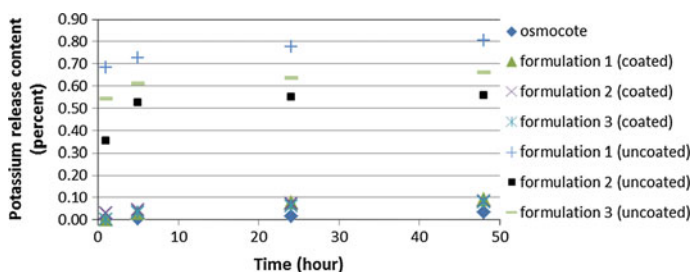


Fig. 10.6 Potassium release curves of osmocote, uncoated sample and coated sample

The uncoated formulations 1, 2 and 3 provide the accumulation of nitrogen release in 48 h as 0.2399, 0.1856 and 0.2797 %, respectively. For phosphorus, the uncoated formulations 1, 2 and 3 provide the accumulation of phosphorus release in 48 h as 0.2690, 0.1973 and 0.2513 %, respectively. For potassium, the uncoated formulations 1, 2 and 3 provide the accumulation of potassium release in 48 h as 0.8042, 0.5593 and 0.6624 %, respectively. Moreover, the porous structure of the uncoated formulations with zeolite caused by the preparation process could degrade the slow release fertilization for this experiment. These pores may occur in a result of the preparation process. Zeolite itself has a porous structure containing water within the

pores, once the water under heat, these pores became vacant [17]. In the experiment, the each slow release fertilizer prepared was soaked in water. Hence, water could penetrate into the granules, the loss of water upon heating could cause the structure to collapse from inside, allowing the nutrients to leach out. On the other hand, the smooth surface of formulation 2 (uncoated formulations without zeolite) could hold the penetrated water longer. In contrast, all the coated formulations have all nutrient release like the commercial slow release fertilizer (osmocote), especially, nitrogen. The osmocote and coated formulations 1, 2 and 3 provide the accumulation nitrogen release in 48 h as 0.0414, 0.0357, 0.0467 and 0.0356 %, respectively. Therefore, we can conclude that osmocote and coated formulations can retain their structures and nutrient releases with resin-coated. When the water absorbs into the granule to dissolve the fertilizer inside, but the nutrient cannot release until the granule expands sufficiently to allow the fertilizer to escape through the tiny cracks [18].

10.5 Conclusion

The uncoated formulations have the N, P, K release contents higher than that the coated formulations and the commercial slow release fertilizer. The slow release fertilizer formulations without zeolite (formulation 2) demonstrate N, P, K nutrient release contents slower than those with zeolite (formulations 1 and 3). However, the N, P, K nutrient release rates still high comparing to the commercial slow release fertilizer. Moreover, the coated formulation has the nutrient release contents as well as the commercial slow release fertilizer especially for the formulation with zeolite (formulation 1 and 3).

Acknowledgments The authors gratefully acknowledge the financial and other support received for this research from the TISTR funds for master's degree student program, which is established and supported under TISTR and financial support from the graduate school, Chulalongkorn University, Thailand. The authors would like to acknowledge the help and support received from Rochana Tangkoonboribun, PhD for the use of laboratory instruments.

References

1. A. Rashidzadeh, A. Olad, *Carbohydr. Polym.* **114**, 269 (2014)
2. P. Sharrock, M. Fiallo, A. Nzihou, M. Chkir, J. Hazard. Mater. **167**, 119 (2009)
3. *Fertilizers* (American Plant Products and Services Incorporation, 2010), <http://americanplant.com/fertilizers.pdf>
4. B. Kołodziej, D. Sugier, E. Bielińska, J. *Geochem. Explor.* **129**, 64 (2013)
5. Y. Chammui, P. Sooksamiti, W. Naksata, S. Thiansem, O. Arquerpanyo, *Chem. Eng. J.* **240**, 202 (2014)
6. H. Khaled, H.A. Fawy, *Soil Water Res.* **6**, 21 (2011)
7. H.W. Pickering, N.W. Menzies, M.N. Hunter, *Sci. Hortic.* **94**, 333 (2002)

8. K. Ramesh, D.D. Reddy, *Adv. Agron.* **113**, 219 (2011)
9. F. Duan, C.S. Chyang, L.H. Zhang, S.F. Yin, *Bioresour. Technol.* **183**, 195 (2015)
10. S.L. Ranamukhaarachchi, W.M. Ratnayake, *Sci. Asia* **32**, 151 (2006)
11. P.R. Hesse, *Potential of Organic Materials for Soil Improvement. Organic Matter and Rice* (1984)
12. *Guide to Laboratory Establishment for Nutrient Analysis of Fertilizer* (Agricultural Technology Department, Thailand Institute of Scientific and Technological Research, 2005)
13. *Fertilizer Analysis* (Department of Agriculture, Ministry of Agriculture and Cooperatives, Bangkok, 2005)
14. A. Sanli, T. Karadogan, M. Tonguc, *Turk. J. Field Crops* **18**, 20 (2012)
15. N.W. Pruitt, *Controlled Release Composition and Method of Manufacturing Same*. United States Patent No. 4,975,108 (1990)
16. H. Yolcu, H. Seker, M.K. Gullap, A. Lithourgidis, A. Gunes, *Aust. J. Crop Sci.* **5**, 926 (2011)
17. J. Szerement, A. Ambrozewicz-Nita, K. Kedziora, J. Piasek, *Use of Zeolite in Agriculture and Environmental Protection* (Institute of Agrophysics PAS, 2014)
18. Scotts Australia, *How Osmocote Works* (2015), <http://www.scottsaustralia.com.au>

Part II
Physics of Advanced Materials

Chapter 11

Numerical Study of Dielectric Resonant Gratings

A.M. Lerer, E.V. Golovacheva, P.E. Timoshenko, I.N. Ivanova,
P.V. Makhno and E.A. Tsvetyansky

Abstract In this chapter we have presented a review of plasmonic nanostructures investigations. A new design of optical antenna consisting of ZnO nanorod coated with a thin metal film is discussed. The solution of electromagnetic waves diffraction by a single metal-dielectric nanooscillator and two-dimensional uniform periodic grating of ones either located on the layered dielectric substrate was shown. Electrodynamics characteristics of one- and two-dimensional dielectric resonant gratings are considered in this chapter.

11.1 Introduction

To design new modern devices with significantly improved technical specifications compared to all previous models we should use new optic materials. Artificial composite structures with exotic electromagnetic properties emerged as a new frontier of science involving physics, material science, engineering and chemistry may be used as such materials. They usually comprise a basic element arranged in repeating patterns similar crystal lattice in solids, often at microscopic or smaller scales that are smaller than the wavelengths. One of the distinguishing features of some periodic structures often called metamaterials is that electromagnetic waves can propagate in them like the media with negative permittivity and permeability. Although this phenomenon is observed in a narrow band, it attracted the attention of a large number of researchers.

Sub long-wavelength periodic structures represent the metamaterial with a rather small spacing for suppression of the diffraction effect that emerges because of their

A.M. Lerer (✉) · E.V. Golovacheva · P.E. Timoshenko · I.N. Ivanova
P.V. Makhno · E.A. Tsvetyansky
Department of Physics, Southern Federal University, Rostov-on-Don, Russia
e-mail: lerer@sfnu.ru

P.E. Timoshenko
Laboratory of Nanomaterials, Southern Federal University, Rostov-on-Don, Russia

periodicity. Such structures gained the opportunity of wide practical application in photonics due to the recent silicon photonics studies and development of the highly precise lithography technology. The application range of such structures covers antireflection coating, polarization rotators, highly effective crystal fiber couplings, spectrometers, highly reflective mirrors, athremal waveguides up to the multiple mode interference couplings and ultra-band-wide waveguide couplers etc. [1].

The photonic and plasmonic nanostructures reveal the new unique opportunities to signal processing. In particular, the ability of plasmon nanostructures to manipulate with local density of the electromagnetic states has already been used in optical communication and biomedicine [2]. The ability of plasmon waveguides to conduct the light signal in the extents less than diffraction limit will allow one to significantly reduce the sizes and increase the efficiency of integrated circuits used in radioelectronics [3, 4]. In future, plasmon nanostructures will become a useful feature to explore the new physical phenomena in atom physics and quantum optics. The progress in development of the next generation of nanophotonic structures is determined by the new technologies of nanomaterial design and development of the theoretical methods allowing one to better understand physics and know to manipulate with collective phenomena emerging as a result of interaction of separate photonic, plasmonic, electronic and mechanic components.

The researches of the widely differing plasmon waveguide structures, for example, metal strips [5, 6], three-layered metal and dielectric structures [7, 8], metallic gaps filled with a dielectric [9, 10], V and W-shaped grooves in metal [11, 12, 13, 14] and Λ -shaped metallic wires [15] have been recently conducted with the purpose of using nano-waveguides as the conducting wires for signal transmitting.

The media with clustered discontinuities for the optical band were addressed to these studies in [16]. The availability of frequency band in which wave cannot propagate through the periodically structured electromagnetic media allows one to introduce the term of photonic crystals [17]. This is the electromagnetic analogue of an atomic lattice, where the latter acts on the electron wave function to produce the familiar band gaps of solid-state physics. Eventually, various one- and two-dimensional electromagnetic crystals mainly consisting of cylindrical discontinuities [18] have been studied. The attempts of elaboration of a simplified technology of the three-dimensional photonic crystals production consisting of finite-length cylinders placed in between two multilayered films [19] are made. The layered waveguides with thin metallic films in which boundaries of the plasmons located are used in the optical band.

The main issue of plasmon waveguides is their big losses because of substantial absorption in metal [20, 21]. In order to resolve the absorption issue, thin metallic films interchanging with dielectric films [22] have recently been used and the impressive results have been achieved. The signal began transmitting up to 2.5 cm [23] but at that, the wave did not localize in cross direction, because the crosswise size of the waveguide structure was exceeding much the diffraction limit.

Apart from the phenomenon of the intense light propagation through the perforated metallic grating discovered more than 10 years, the possibility to reach almost ideal optical wave attenuation by the similar structures has been recently

actively studied. One of the most recent suggestions [18] is the use of full absorption of the falling at the angle TM -polarized light of the metallic grating placed in asymmetric environment. It is believed that the abnormally high absorption is caused by full internal reflection at the grating's borders and Fabry-Perot resonance caused by the grating's elements. Under certain conditions (fill factor is less than 0.9) the intense abnormal absorption takes place only with glazing incidence at the angle of incidence of more than 85° . Under the other conditions (fill factor exceeds 0.9) the abnormal absorption is observed only if the full internal reflection takes place.

The theoretical investigation of various grating types of nanomaterials is rather popular. It is important to calculate the structures and gratings that allow reach this or that required electrodynamic characteristics. For example, the transmission and reflection coefficients of the terahertz range of the plane wave by the graphene grating have been studied in [19]. Excitation of the surface plasmon-polariton on every band in the case with H -polarization and the variations of penetration, absorption and reflection caused by Rayleigh abnormalities are observed for E -polarization. The development of such structures may be used when the filter devices are designing.

On the other hand, it is important to easily and cheaply investigate the currently produced materials. "The cloud" of randomly placed silver nanowires in the center of which there is the chain of the lined nanowires of the same type at the same distance between them, shows the frequency resonances caused by the periodic structure [20].

In the large spacing fiber grating, the fiber modes propagated in the core may lead to occurring the surface plasmon resonance (SPR) within the thin metallic film covering the cylindrical fiber surface. The review [24] bears evidence of the possibility of EH -mode relating to the surface plasmon modes. The slump in transmission coefficient caused by the SPR responsiveness to the refraction index of the media is observed within the certain frequency band. That may be used in the refraction index sensors and the application as a temperature and expansion sensors are possible together with the wave length shift at the resonant frequency with grating step alteration.

The optical fiber Bragg grating has also been actively studied for different applications including the terahertz range to create the distributed sensors that have the best properties of the fiber Bragg grating of the optical band and coaxial Bragg gratings of microwave band. One of the latest researches suggests this type of sensors having resolution close to 0.0017°C [25].

The gratings are also popular for application in the power supply systems of next generation including in organic solar elements with the back contact in the grating form [26]. The calculations demonstrate that the configuration used together with grating allows achieving about 15–20 % of the energy transformation performance increasing in comparison with the planar configuration of the solar element as grating guarantees increase both of the fault current and of filling factor.

In order to achieve the optimal parameters of the components for practical application including the solar batteries, various combinations of gratings have been

studied to provide highly efficient broadband absorption within the wide range of light incidence angles. The model of the metal and dielectric nano-meanders (dielectric grating which edges covered with a thin aluminum film) has been suggested [27]. The achieved good absorption coefficients are almost not changing over the wide range of the *TM*-polarized wave's incidence angles.

The researches to create the effective devices of various applications within terahertz range have been actively developing. The silicon two-dimensional photonic structures of terahertz range may also be used as the refraction index sensors [28].

The interaction of several various resonance types (the resonance of surface plasmon modes caused by the grating mode periodicity, and resonator's mode) at light dissemination by the finite ridge nanograting of silver bands is detected as Fano's curve of the total effective reflection area and effective capture cross-section [29, 30]. The resonances of grating's mode and resonator's mode within the optic band make a more significant contribution to the structure properties as a refraction index sensor and such sensor's Q-quality rather than the plasmon-polariton resonances.

The optical antennas (OA) of submicrometer (nano) dimension are used to increase the efficiency of energy transfer of the excitation electromagnetic field to the local field and vice versa. This OA's property may be used to increase the efficiency of the photophysical processes at the optically sensitive structures [31–33], at the DNA structure determination and separate molecules identification [34]. Within the microscopy objectives, the optical antennas replace the traditional focusing lens and objective lens allowing concentrate the emission in the dimensions smaller than the diffraction limit [35]. OA's properties are not similar to those of antennas in radio band with larger dimensions as the principal physics of the processes in them is different. It leads to the failure of the scalability principle at their physical description. Another theoretical method when returning to the submicrometer (nano) dimensions is caused by the dominance of the properties of the solid body's plasma over that of the metallic conductivity due to availability of the optical infrared range of the free electron gas responsive to excitation at the wavelength. The additional differences are caused by sort of the OA excitation methods. The carbon nanotubes [36], metallic and "metal-dielectric" cylinders and spheres [37] are usually used as OA.

Use of metamaterials is impossible or is technologically difficult without theoretical research of their electrodynamic properties. Calculation of three-dimensional metamaterials is a difficult electrodynamic issue caused not only by complexity of investigated structures, but also needs to deal with resonance frequencies region in which the sizes of low-level cells of periodic structure are commensurable with wavelength. Owing to this fact, application of approximates, for example, quasistatic or asymptotic methods is impossible. Therefore, calculation of such structures is one of the most effective methods of the solution of boundary value problems in resonance region by the method of integrable equations is actual.

The purpose of this chapter is review theoretical methods of resonant dielectric gratings calculation. In this article are partially used results published by us in [38–43].

The objects of the research are the planar structures formed by plane-parallel dielectric layers. In several layers, dielectric inhomogeneity locates. These periodic

inhomogeneities can be two-dimensional (the periods are D_x and D_y) and one-dimensional and periodic (the period is D_y). Dielectric layers are parallel to the $z = 0$ plane. Number of layers of structure, number of layers with inhomogeneities is arbitrary. The upper and lower layers are semi-infinite, thickness of remaining layers are equal to h_n . The layers are numbered from top to down.

The electromagnetic wave falls under angle φ to an axis x . Number of inhomogeneities in each layer and their layout are arbitrary. Therefore, calculation of gratings with almost any transverse section is possible. Dielectric constants of layers and inhomogeneities are complex that allows to model metal layers in optical band.

The diffraction of arbitrary polarized electromagnetic wave on two types of the nanorods with a metal film located on a SiO_2 substrate with ZnO thin film was studied theoretically for the single nanorod and the uniform two-dimensional periodic array of nanorods [43]. It is supposed, that nanocrystals would be cylindrical shape. Moreover, dispersion of a refraction index ZnO ($n = 1.95$) did not consider. The solution is obtained by the volume integro-differential equation method (VIDE). Remain unknowns in VIDE Cartesian components of electric field intensity $E(x, y, z)$ into dielectric inhomogeneity region. The method has a row of advantages: it is simpler than others; shape of dielectric does not complicate significantly the calculation process. As a simulation result, we obtain electric field in the investigated structure.

11.2 Theory

The problem of electromagnetic wave diffraction on a multi-layered two-dimensional periodic dielectric array are recommend to solve by VIDE method [37]. The method has a major advantages: (i) it is simpler than surface integro-differential equation method [5]; (ii) shape of dielectric does not complicate significantly the calculation process. As a simulation result, we obtain electric field in the investigated structure.

According to periodicity of the structure is possible to solve VIDE only in the volume V of single inhomogeneity. In relation to our problem, VIDE has an appearance

$$\frac{D_r(x, y, z)}{\tau} = E_r^e(x, y, z) + \sum_{p=-\infty}^{\infty} \sum_{q=-\infty}^{\infty} \sum_{s=1}^3 \int_V \exp[i(\alpha_p \bar{x} + \beta_q \bar{y})] \tilde{g}_{rs}(z, z') D_s(z') dv',$$

$$D_r(x, y, z) = E_r(x, y, z) \tau(x, y, z), \quad \tau(x, y, z) = \varepsilon_b(x, y, z) / \varepsilon_n(z) - 1,$$

$$\alpha_p = \frac{2p\pi}{d_x} + kn \cos \varphi, \quad \beta_q = \frac{2q\pi}{d_y} + kn \sin \varphi,$$

$$\bar{x} = x - x', \bar{y} = y - y', \quad r = 1, 2, 3, \quad x, y, z \in V,$$

(11.1)

where k is a wave number in free space, $n = c/v_p$ is the wave deceleration factor in structure, $\varepsilon_b(x, y, z)$ and $\varepsilon_n(z)$ are the dielectric permeability of inhomogeneity and the layer surrounding it in observation point (x, y, z) , respectively. The components of tensor function of Green \tilde{g}_{rs} are shown in [37].

The VIDE (11.1) is bisingular. The numerical methods shall take into account the singularity, so the integral representation of Green function uses in the method [36]. The kernel of VIDE singularity is appear in slow integral convergence in the matrix of the system of the linear algebraic equations (SLAE) obtained by Galerkin's method. It is simpler to improve convergence of integrals, than to regularize integro-differential equations in spatial representation. In this paper, this approach is used to solve VIDE by Galerkin's method. We find the solution in the form of

$$D_r(x, y, z) = \sum_{l=-N_\varphi}^{N_\varphi} \sum_{m=1}^{N_r} \sum_{n=1}^{N_z} X_{lmn}^r V_{lmn}(x, y, z), \quad (11.2)$$

where X_{lmn}^r are unknown coefficients and $V_{lmn}(x, y, z)$ are the basic functions (BF),

$$V_{lmn}(x, y, z) = \exp(il\varphi) J_l\left(\zeta_m^{(l)} r(z)\right) Z_n(z), \quad (11.3)$$

J_l are Bessel functions of the first kind, $\zeta_m^{(l)}$ are the zeroes of derivative of the Bessel function, i.e., $J_l'(\zeta_m^{(l)}) = 0$, coordinates r, φ express through x, y :

$$x = a_x(z)r \sin \varphi, \quad y = a_y(z)r \cos \varphi, \quad (11.4)$$

$2a_x(z), 2a_y(z)$ are the ellipse axes in a transverse direction with z coordinate, $Z_n(z)$ are the basis functions on coordinate. We used splines of first order $Z_n(z) = \sigma_n^{(1)}(z)$.

We substituted (11.2) and (11.3) into (11.1), then obtained equations we multiply on $V_{lmn}^*(x, y, z)$; ($l = 0, \pm 1, \dots$; $m = 1, 2, \dots$; $n = 1, 2, \dots$) and integrate them on the volume of the inhomogeneity. As a result, we will get SLAE rather unknown coefficients X_{lmn}^r . All integrals are in matrix of SLAE may be written analytically. The dispersion relation is obtained by calculating the determinant of the SLAE being equated to zero.

We expressed matrix components of SLAE through double series on p, q indexes (11.1). The main part of computer time leaves on their summing. The easy way of improving of their convergence is offered. In case of

$$\rho_{pq} = \sqrt{(a_x(z)\alpha_p)^2 + (a_y(z)\beta_q)^2} > R_{\max} \gg 1,$$

R_{\max} is the floating point number when terms of series are replaced with their asymptotic. The oscillating member of asymptotic is discarded. We use the lead term of Euler–Makloren formula for summing of residual members of series, i.e. summing on p and q are replaced with integration on p, q . Such easy way of accelerating convergence of series allowed us to reduce number of summable terms of a series at 16–25 times with maintaining accuracy. In the same time it was reduced a computing duration. For calculations with a error (on internal convergence) no more than 0.1 % it is enough to take 2–3 angular BF $\exp(il\varphi)$ and the same quantity of radial $J_l(\zeta_m^{(l)} r(z))$. The quantity of BF $Z_n(z)$ is defined by a shape profile of inhomogeneity and the relation of it general height to wavelength. The 6–8 functions on one wavelength along inhomogeneity there are enough to achieve the extra accuracy. For example, the calculation time of barrel-like inhomogeneity crossed three layers with four wavelengths height is about 10 s, when we used the i3-2100 CPU with 3.10 GHz for each core.

Let us consider a one-dimensional array of wave-guides. We suppose that the grid is regular in the x direction. In this case in (11.1), dependence of electric fields on x can be described by $\exp(-ik_x x)$ function, the series on p index is absent. The VIDE (11.1) can be divided into two parts when a wave propagates across array ($\varphi = \pi/2$). The first part describes TE-wave and second—TM-wave. In remaining cases, the wave is hybrid.

We find solution in the form of

$$D_r(y', z') = \sum_{\mu=0}^{N_y-1} \sum_{\nu=1}^{N_z} X_{\mu\nu}^r V_{\mu\nu}(y', z'),$$

where $X_{\mu\nu}^r$ are unknown coefficients, $V_{\mu\nu}(y, z)$ are the basis functions,

$$V_{\mu\nu}(y, z) = Y_{\mu\nu}(y) \sigma_v^{(1)}(z), \quad Y_{\mu\nu}(y) = C_{\mu\nu} P_\mu \left(\frac{y - \bar{y}_v}{l_v} \right),$$

where P_μ are Legendre polynomials, \bar{y}_v is the periodic inhomogeneity center coordinate, l_v is its half-width in section $z = z_v$, z_v is a node of spline $\sigma_v^{(1)}(z)$, a constant $C_{\mu\nu}$ is chosen so that the Fourier transform on $Y_{\mu\nu}(y)$ in (11.1) had an appearance of

$$\tilde{Y}_{\mu\nu}(\beta_q) = (-i)^\mu \frac{J_{\mu+1/2}(\beta_q l_v)}{(\beta_q l_v)^{1/2}} \exp(-i\beta_q \bar{y}_v).$$

For a one-dimensional array of nanorods, the asymptotic series are summed analytically.

11.3 Results and Discussions

First, we present results of dispersion curves calculation for the single nanorod. Dependence of a scattered field on wavelength has resonant character. The maximum of the power, which passed in a substrate, and therefore a maximum of losses in nanorods corresponds to a minimum in the wave dispersion curve in upper half plane (over a substrate). The resonant wavelengths are obtained experimentally: the first resonance is of 580 nm, the second resonance is about 845nm; the third resonance is of 1360 nm that is well coordinates with theoretically calculated data [42]. On theoretical characteristics for the nanooscillator array and in case of experiment for nanovibrator 0.7 μm long, the number of resonances are more, than a number of resonances of single one. Some resonant wavelengths of the nanooscillator array are close to resonances of single oscillator. These resonances can be interpreted as resonances of the waves propagating on nanovibrator and as resonances of the waves propagating along an array, perpendicular to nanovibrators. The resonant wavelengths of longitudinal resonances differ for single nanorod and a grid of nanorods because of interaction between nanorods. Moreover, electrodynamic model for nanooscillator is less strict, than that for an array. In short-wave band is present a large number of high-Q resonances. The quantity of resonances at the long rod is bigger, than at the short rod that is fair for all oscillators, including a radio-frequency range. During experiment, this feature does not observe. It can be caused by superimposing of the close resonances because of statistical distribution of the synthesized rods on lengths, diameters and the form of section.

In the paper [41] is offered and theoretically explored the new optical metal dielectric diffraction grating (DG) which in case of a resonance of the surface wave spreading on boundary “metal–dielectric”, absorbs nearly 100 % of the energy falling on it. In the present chapter, the effect of resonance absorption in the grids formed by the ZnO nanorods is studied. Two types of grids (Fig. 11.1) are investigated. In the first type (Fig. 11.1c) on a substrate of SiO_2 was applied first a metal layer–silver (Ag) then, on a metal layer was applied a ZnO, that is dielectric layer. In the article [40] dependence of resonant wavelength of absorption on a type of the metal used in DG is marked. Therefore, the assumption of receiving grids with broadband properties of absorption by use of two films from different metals was made. Therefore the grid of the second type was explored, namely layers of gold and silver were applied on a substrate from SiO_2 , and SiO_2 layer was also put between the metal layers, the layer of ZnO on which nanosized rods were synthesized, was applied on a film from gold. The sizes of rods remained constants.

The numerical results are given in Figs. 11.2, 11.3. The unit cell of a grid is square $d_x = d_y = d = 200$ nm. The height of the ZnO rods located in the air is equal to $h = 140$ nm. The ZnO film thickness, h_{add1} , is equal to 20 nm. The thickness of a metal silver coating t_m is 90 nm. The dielectric thickness between metals, h_{add2} , has 20 nm. The angle of incident wave varies from 0° to 40° . It was supposed that rods were in an air environment under normal conditions. The refraction index of the

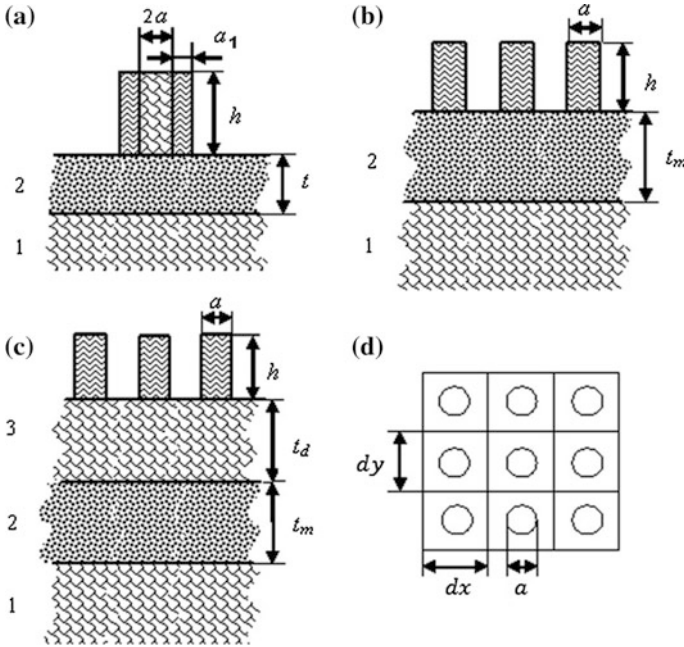


Fig. 11.1 Single nanooscillator covered by metal film (a) with l dielectric substrate, 2 metal film, 3 additional dielectric layer; two types of grids (b) and (c); view with upper (d)

substrate is $n_s = 1.495$. It is showed by numerical calculations the possibility of existence of effect of total resonance absorption in arrays with the ZnO nanorods. The resonant wavelength of absorption depends on incident wave angle only in case of p -polarization (Fig. 11.2). For s -polarization, the resonant wavelength has small dependence on incident angle (Fig. 11.3). This property is important in case of practical use of DG. The assumption confirms that use of two different metal films in one grid increases width of resonances. Absorption not least than 90 % is observed in a band about 100 nm.

The curves 1 in Fig. 11.2 are also computed by COMSOL Multiphysics™ platform of finite-element physics-based modeling and simulation. As the advantages of using the finite element method (FEM) for the numerical calculation of the optical layered structures properties, we may highlight the conservatism and high stability of the numerical method, the ability to solve problems with a complicated geometry and to reduce the mesh in those places where special care is not required. Comparing the data of curves, we can see that the results are in good agreement with the results of simulation in COMSOL Multiphysics™. The calculated by FEM results have minor differences in the waveband close to the critical wavelength.

Dependencies on wavelength of reflection coefficients (on power) of plane electromagnetic wave R (continuous curves), passing T (on power, shaped curves) and the relative losses P (dotted curves) are given in Fig. 11.4. A refraction index of

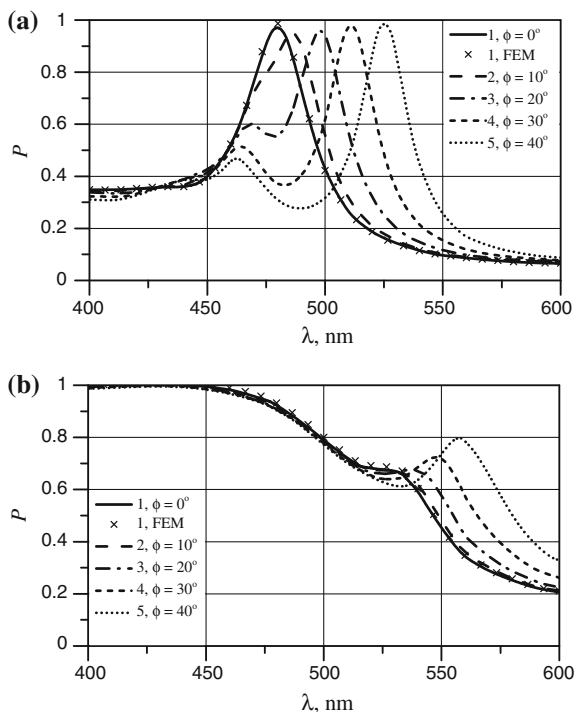


Fig. 11.2 Absorption coefficient dependence on incident wave angle in case of *p*-polarization and single metal layer (a) and two metal layers (b): 1-normal wave incidence ($\phi = 0^\circ$), 2- $\phi = 10^\circ$, 3- $\phi = 20^\circ$, 4- $\phi = 30^\circ$, 5- $\phi = 40^\circ$

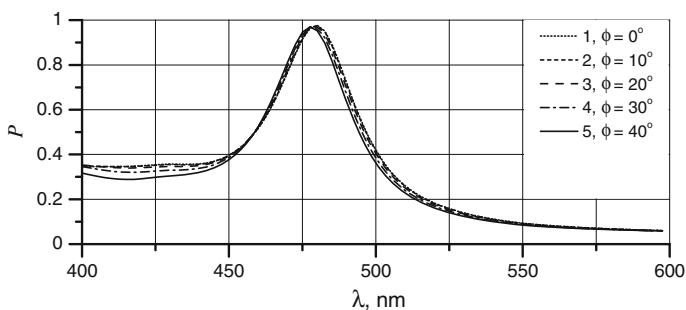


Fig. 11.3 Absorption coefficient dependence on incident wave angle in case of *s*-polarization: 1-normal wave incidence ($\phi = 0^\circ$), 2- $\phi = 10^\circ$, 3- $\phi = 20^\circ$, 4- $\phi = 30^\circ$, 5- $\phi = 40^\circ$

dielectric cylinders $n_b = 2.1$, substrates $n_s = 1.495$, a covering is from a silver film. The wave falls on a grid normally (descent angle $\phi = 0^\circ$). Unit cell of a grid is square. In calculations, parameters of the metals taken from the electronic reference manual [44, 45] were used. In the case of increasing in the period of a grid, as one

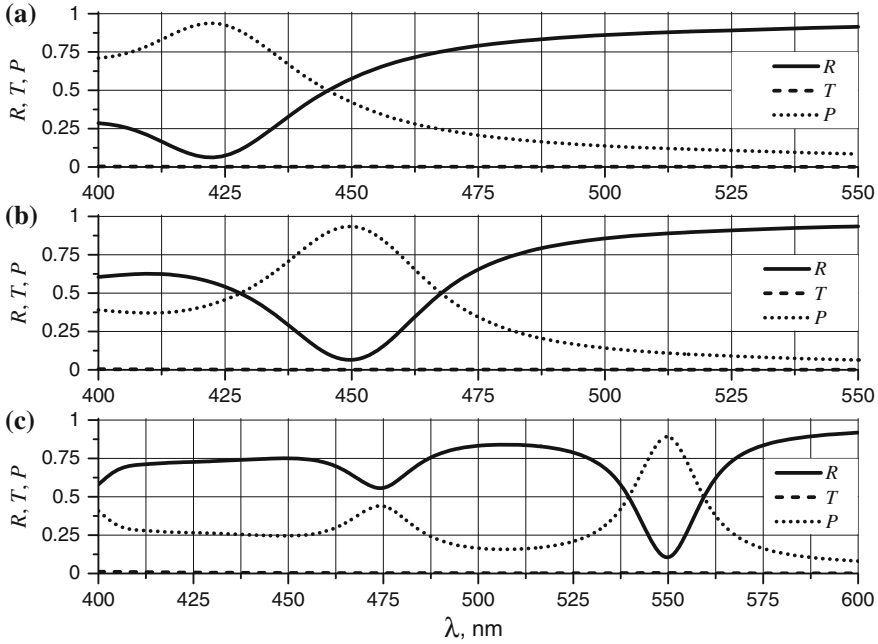
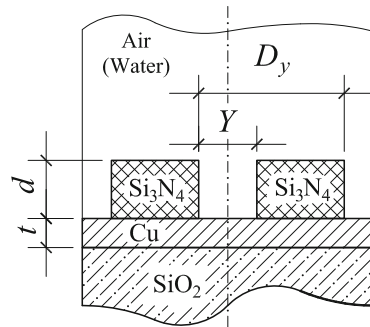


Fig. 11.4 Dependencies on wavelength of reflection coefficients (on power) of plane electromagnetic wave R (continuous curves), passing T (on power, shaped curves) and the relative losses P (dotted curves) with dielectric layer thickness $t_d = 18$ nm, refractive index $n_d = 2.1$, $t_m = 100$ nm and various unit cell size: **a**— $d = 140$ nm, $a = 100$ nm; **b**— $d = 250$ nm, $a = 100$ nm; **c**— $d = 400$ nm, $a = 120$ nm

Fig. 11.5 Geometry used in the modeling with $t = 80$ nm, $d = 160$ nm, $Y = 300$ nm, $D_y = 600$ nm



would expect, the result increases (Fig. 11.4a, b). Observation of two and more plasmonic resonances (Fig. 11.4c) is possible.

Reflection characteristics and propagation of optical waves in the range from 400 to 1300 nm for the structure shown in Fig. 11.5 are calculated. The structure represents a one-dimensional periodic multi-layered grid. The thin copper film of 80 m thick, on which periodic non-uniformity from nitride of silicon (Si_3N_4) with

160 nm thickness (refractive index of Si_3N_4 $n = 2.04$) and width of 300 nm is placed, is applied on a substrate from SiO_2 . The grid period is equal to 600 nm.

In Fig. 11.6 are given the numerical results of reflection coefficient of s - and p -polarized wave for such a structure in water and in air. It is visible that in water the pattern in general displaces on wavelength on ~ 100 nm (for s -polarization) and ~ 250 nm (for p -polarization) towards longer waves, thus the main resonance becomes less sharp, and an additional resonance, on the contrary, more sharper.

In Fig. 11.7 are given dependencies of calculation for reflection coefficient of s -polarized wave in the case of different periods of array (other parameters—as in Fig. 11.6).

It is possible to see offset of a resonance towards longer waves in case of increasing in the period of a grid, the main resonance thus becomes sharper, and there are present some additional resonances. It is necessary to mark that in the case

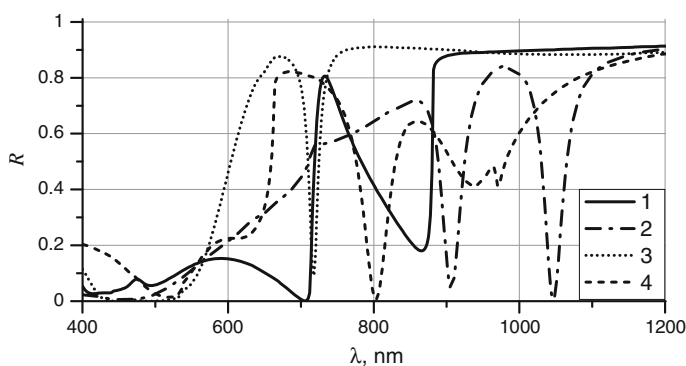


Fig. 11.6 Reflection coefficient of s - and p -polarized wave for the structure in water and in air: 1— s -wave, water; 2— p -wave, water; 3— s -wave, air; 4— p -wave, air

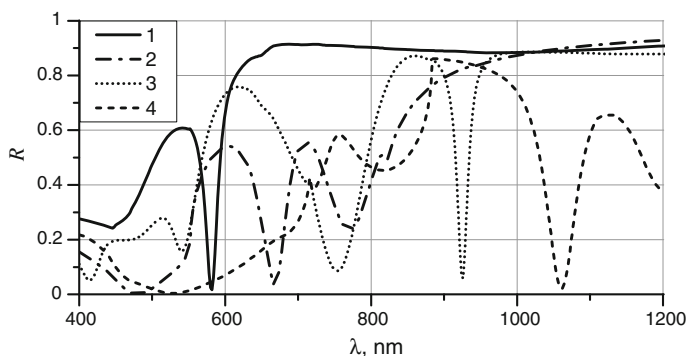


Fig. 11.7 Reflection coefficient dependence on wavelength with various periods along y-axis: 1—500 nm, s -wave; 2—500 nm, p -wave; 3—500 nm, s -wave; 4—500 nm, p -wave

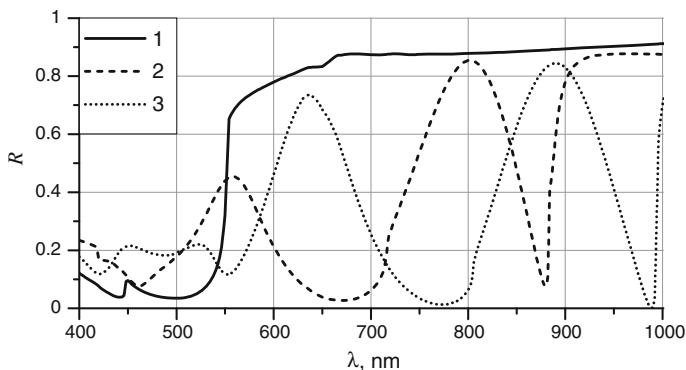


Fig. 11.8 Reflection coefficient dependence on wavelength for structures with different periods of grid, but with width of air gap between in homogeneties equal to $Y = 400$ nm: 1—500 nm, 2—800 nm, 3—900 nm

of the period 600 nm, the additional resonance shows in fact zero reflection in the range from ~ 430 to ~ 520 nm.

In Fig. 11.8 are given results for structures with different periods of a grid, but with a width of air gap between non-uniformities, equal to 400 nm (instead of 300 nm, as in the previous case), and, respectively, non-uniformity with a reduced width up to 200 nm.

It is visible that the increasing of the gap and reducing the width of non-uniformity affect on results in the same way, as well as the increasing of the period.

11.4 Conclusion

The theoretical investigation of the resonant absorbing optical “metal–dielectric” diffraction grating is discussed in this chapter. It is shown that the resonant frequency does not depend on height of dielectric cylinders and weakly depends on their diameters. The sizes of the cylinder depend on reflection, passages and losses coefficients. Thus, resonating characteristics of investigated grating are defined by a plasmonic resonance, but not by the resonance of dielectric cylinders. The resonant wavelength λ_r decreases with increasing of thickness of a thin metal film t_m . The wavelength λ_r does not depend on t_m , when $t_m > 90$ nm. This may be explained by the fact, that at small thickness of film, the surface waves propagate on opposite boundaries of the film and they are interacting among themselves. Therefore their speed, and so λ_r , depend on t_m . When $t_m > 90$ nm, the wave propagates on upper bound of the film. Its speed does not depend on permittivity of the substrate. Nearly full energy absorption at a plasmonic resonance shows us about the strong localization of an electromagnetic field near a metal film.

The calculated results of the resonance frequency displacement with various refraction indexes for the substance material filling the high semi-infinite layer allow considering this structure as a basis of gas or liquid sensors. The possibility of managing resonance frequencies by a variation of unit cell parameters allows us flexible tuning of sensor properties.

Acknowledgments The authors acknowledge the support of the Russian Ministry of Education and Science, provided by grant 16.219.2014/K, and the part of the Internal Grant project of Southern Federal University in 2014–2016, provided by grant 213.01.-07.2014/08PChVG, for carrying out this research study.

References

1. R. Halir, P.J. Bock, P. Cheben, M.A. Ortega, R.C. Alonso, J.H. Schmid, J. Lapointe, D.X. Xu, P.J. Wangüemert, F.I. Molina, S. Janz, *Laser Photonics Rev.* **9**(1), 25 (2015)
2. M.I. Stockman, *Opt. Express* **19**(22), 22029 (2011)
3. W.L. Barnes, A. Dereux, T.W. Ebbesen, *Nature* **424**, 824 (2003)
4. M. Hochberg, T.J. Baehr, C. Walker, A. Scherer, *Opt. Express* **12**(22), 54811 (2004)
5. P. Berini, *Phys. Rev. B* **61**(15), 10484 (2000)
6. J. Gosciniaik, V.S. Volkov, S.I. Bozhevolnyi, L. Markey, S. Massenet, A. Dereux, *Opt. Express* **18**(5), 5314 (2010)
7. L. Liu, Z. Han, S. He, *Opt. Express* **13**(17), 6645 (2005)
8. R. Zia, M.D. Selker, P.B. Catrysse, M.L. Brongersma, *J. Opt. Soc. Am. A. Opt Image Sci. Vis.* **21**(12), 2442 (2004)
9. S.I. Bozhevolnyi, V.S. Volkov, E. Devaux, T.W. Ebbesen, *Phys. Rev. Lett.* **95**(4), 046802 (2005)
10. T. Holmgaard, S.I. Bozhevolnyi, *Phys. Rev. B* **75**(24), 245405 (2007)
11. I.V. Novikov, A.A. Maradudin, *Phys. Rev. B* **66**, 035403 (2002)
12. D. Arbel, M. Orenstein, W-shaped plasmon waveguide for silicon based plasmonic modulator. *Proc. IEEE LEOS Ann. Meet. Conf.* **262**, (2006)
13. D.F. Pile, T. Ogawa, D.K. Gramotnev, Y. Matsuzaki, K.C. Vernon, K. Yamaguchi, T. Okamoto, M. Haraguchi, M. Fukui, *Appl. Phys. Lett.* **87**(26), 261114 (2005)
14. D.K. Gramotnev, D.F. Pile, *Appl. Phys. Lett.* **85**(26), 6323 (2004)
15. E. Moreno, S.G. Rodrigo, S.I. Bozhevolnyi, L. Martín-Moreno, F.J. García-Vidal, *Phys. Rev. Lett.* **100**(2), 023901 (2008)
16. E. Yablonovich, *Phys. Rev. Lett.* **58**(20), 2059 (1987)
17. J.D. Joannopoulos, S.G. Johnson, J.N. Winn, R.D. Meade, *Photonic Crystals: Molding the Flow of Light* (Princeton University Press, Princeton, 2008)
18. S.E. Bankov, *Electromagnetic Crystals* (PhysMatLit, Moscow, 2010). (In Russian)
19. C.O. Choa, Y.G. Roha, Y. Parka, J.S. Iaa, H. Jeona, B.S. Leeb, H.W. Kimb, Y.H. Choeb, M. Sunga, J.C. Wooa, *Curr. Appl. Phys.* **4**(2–4), 245 (2004)
20. A. Degiron, D.R. Smith, *Opt. Express* **14**(4), 1611 (2006)
21. J. Nie, H. Li, W. Liu, *IEEE Photonics J.* **6**(6), 2000208 (2014)
22. A.I. Nosich, T.L. Zinenko, Method of analytical regularization in terahertz wave scattering and absorption by infinite gratings of graphene strips. *IEEE Conf. Antenna Meas. Appl. CAMA-2014* **382**, (2014)
23. D.M. Natarov, M. Marciniak, R. Sauleau, A.I. Nosich, *Opt. Express* **22**(23), 28190 (2014)
24. H.F. Hu, Z.Q. Deng, Y. Zhao, J. Li, Q. Wang, *IEEE Photonics Technol. Lett.* **27**(1), 46 (2015)

25. C. Zhen, Y. Lei, G. Hefferman, W. Tao, *IEEE Photonics Technol. Lett.* **27**(10), 1084 (2015)
26. A.H. Fallahpour, G. Ulisse, M. Auf der Maur, A. Di Carlo, F. Brunetti, *IEEE J. Photovoltaics* **5**(2), 591 (2015)
27. S. Su, Q. Wen, Y. Yan, Z. Yun, C. Linsen, *Opt. Express* **23**(2), 963 (2015)
28. F. Fan, C. Sai, W. Xiang-Hui, W. Peng-Fei, C. Sheng-Jiang, *IEEE Photonics Technol. Lett.* **27**(5), 478 (2015)
29. S.M. Kamali, E. Arbabi, L.L. Goddard, *IEEE Photonics Technol. Lett.* **27**(7), 790 (2015)
30. O.V. Shapoval, *IEEE J. Quantum Electron.* **51**(4), 7200108 (2015)
31. N.M. Miskovsky, P.H. Cutler, A. Mayer, B.L. Weiss, B. Willis, T.E. Sullivan, P.B. Lerner, *J. Nanotechnol.* **512379**, 1 (2012)
32. D.P. Lyvers, J.M. Moon, A.V. Kildishev, V.M. Shalaev, *ACS Nano* **2**(12), 2569 (2008)
33. O. Imafidon, S. Georgakopoulos, P.K. Vabbina, P. Nezih, Multifunctional nanodevices for energy harvesting in unconventional spectral ranges. *Proc. SPIE 7679, Micro Nanotechnol. Sens. Syst. Appl. II 76792L* **5**(1), (2010)
34. F.J. Garcia-Vidal, J. Sanchez-Dehesa, A. Dechelette, E. Bustarret, T. Lopez-Rios, T. Fournier, B. Pannetier, *J. Lightwave Technol.* **17**(11), 2191 (1999)
35. V.V. Klimov, *Nanoplasmonics*, vol. 11422 (CRC Press, London, 2014)
36. F.J. Garcia-Vidal, L. Martin-Moreno, J.B. Pendry, *J. Opt. A* **7**, S97 (2005)
37. A.I. Zhmakin, *Phys. Rep.* **498**, 189 (2011)
38. E.V. Golovacheva, A.M. Lerer, N.G. Parkhomenko, *Mosc. Univ. Phys. Bull.* **66**(1), 5 (2011)
39. E.V. Golovacheva, A.M. Lerer, P.V. Makhno, G.P. Sinyavskiy, *Electromagn. Waves Electron. Syst.* **16**(5), 9 (2011). (In Russian)
40. A.M.J. Lerer, *Comm. Technol. Electr.* **57**(11), 1151 (2012)
41. A.M. Lerer, E.A. Tsvetyansky, *Technol. Electr.* **38**(11), 995 (2012)
42. E.M. Kaidashev, N.V. Lyanguzov, A.M. Lerer, E.A. Raspopova, *Technol. Phys. Lett.* **40**(4), 313 (2014)
43. E.M. Kaidashev, A.M. Lerer, E.V. Golovacheva, V.E. Kaidashev, N.V. Lyanguzov, E.A. Tsvetyansky, *J. Commun. Technol. Electr.* (2015) (in press)
44. G. Boisset, *Luxpop: Index of Refraction, Thin Film, Optical Simulation and Ray Tracing.* <http://www.luxpop.com>.
45. M. Polyanskiy, *RefractiveIndex.INFO: Refractive index database* <http://refractiveindex.info/>

Chapter 12

Method of Equilibrium Density Matrix, Anisotropy and Superconductivity, Energy Gap

B.V. Bondarev

Abstract A new variational method has been proposed for studying the equilibrium states of the interacting particle system to have been statistically described by using the density matrix. This method is used for describing conductivity electrons and their behavior in metals. The electron energy has been expressed by means of the density matrix. The interaction energy of two $\varepsilon_{\mathbf{k}\mathbf{k}'}$ electrons dependent on their wave vectors \mathbf{k} and \mathbf{k}' has been found. Energy $\varepsilon_{\mathbf{k}\mathbf{k}'}$ has two summands. The first energy I summand depends on the wave vectors to be equal in magnitude and opposite in direction. This summand describes the repulsion between electrons. Another energy J summand describes the attraction between the electrons of equal wave vectors. Thus, the equation of wave-vector electron distribution function has been obtained by using the variational method. Particular solutions of the equations have been found. It has been demonstrated that the electron distribution function exhibits some previously unknown features at low temperatures. Repulsion of the wave vectors \mathbf{k} and $-\mathbf{k}$ electrons results in anisotropy of the distribution function. This matter points to the electron superconductivity. Those electrons to have equal wave vectors are attracted thus producing pairs and creating an energy gap.

12.1 Introduction

Kamerlingh Onnes discovered the phenomenon of superconductivity at Leiden Laboratory, Holland, in 1911 [1]. While investigating dependence of Hg resistance on temperature, he could find that when the material is cooled down to about 4 K temperature the resistance drops abruptly to zero. The very phenomenon was called superconductivity. Shortly thereafter, other elements exhibiting similar properties were discovered.

B.V. Bondarev (✉)

Moscow Aviation Institute, Volokolamskoe Shosse, 4, 125871 Moscow, Russia
e-mail: bondarev.b@mail.ru

A superconductor is immersed in liquid helium. Initially, weak current is supplied. Then, temperature is reduced. When temperature falls below the defined value, the superconductor circuit is shorted. The superconductor circuit current sustains its steady state as long as it can. A magnetic needle provided as a detector finds some persistent current in the superconductor, thus indicating the magnetic field produced in the solenoid. Temperature T_c , below of which a test piece exhibits its superconducting properties, is called *critical temperature*.

Shortly thereafter, it was discovered that such superconductivity disappears when a test piece is placed in a relatively weak magnetic field. This phenomenon was discovered by Meissner and Ochsenfeld [2]. Value H_c of the magnetic field in which superconductivity disrupts is called a *critical field*. Superconductivity continuity disruption is caused by the substance-flowing current that exceeds a particular critical value (Selsby effect). Type-I and type-II superconductors of different properties have been discovered [3]. There are some other experimental superconductivity factors subjected to this description.

Brothers Fritz and Heinz London developed the first macroscopic theory of superconductivity in 1935 [4]. They mathematically formulated the theory based on principal experimental factors: absence of resistance and Meissner–Ochsenfeld effect:

$$\rho = 0, \quad \mathbf{B} = 0. \quad (12.1)$$

These facts were acknowledged a priori. For the superconductor magnetic field, the brothers obtained the following equation:

$$\Delta \mathbf{B} - \frac{1}{\lambda^2} \mathbf{B} = 0, \quad (12.2)$$

where

$$\lambda = \sqrt{\frac{mc^2}{4\pi ne^2}} \quad (12.3)$$

Value λ is called London length of the magnetic field penetration in a superconductor.

Superconductivity was theoretically explained by using the phenomenological expression of the Ginzburg-Landau theory [5] and 46 years later, upon discovery of the superconductivity phenomenon by Kamerlingh-Onnes, the microscopic theory of this phenomenon was framed by Bardeen, Cooper, and Schriffer [6]. However, many years after my student time, I cannot still understand by what means electrons are distributed over wave vectors \mathbf{k} , when the substance superconductivity occurs and where the attraction is coming from with the electrons travelling at equal speeds.

The answer provided is rather simple by its nature. The matter of concern is a density matrix. Electrons are the very particles that make for superconductivity.

As for electrons, they are classified as Fermi particles, in other words, defined by the antisymmetric functions. There are *pure* and *mixed* states specified by the quantum mechanics. Pure states are defined by the wave functions and mixed states —by the density matrix. When the quantum mechanical system is thermally coupled with a thermostat, the only correct statistical description of the system under analysis is to be considered the density matrix [7–14]. Kinetic density matrix equations, as applicable to superconductivity properties, are described in the author's papers [15–24].

Complete statistical description of the system consisting of the N identical particles is provided in the quantum mechanics by statistical operator $\hat{\rho}^{(N)}$ to satisfy the normalizing condition as follows:

$$\text{Tr}_{12\dots N}\hat{\rho}^{(N)} = N! \quad (12.4)$$

This operator can be used for making the hierarchical sequence of operators $\hat{\rho}^{(1)}$, $\hat{\rho}^{(2)}$, ..., defined by the following relation:

$$\hat{\rho}^{(n)} = \frac{1}{(N-n)!} \text{Tr}_{n+1\dots N}\hat{\rho}^{(N)}, \quad (12.5)$$

where $n = 1, 2, \dots, N-1$. In spite of the fact that statistical operators of the lowest order provide short description of the multi-particle system, only, they are indispensable for their simplicity, particularly when some useful formulae and expressions are virtually required. This kind of a short description makes it possible to express all observable physical quantities that characterize the macroscopic system state exactly or approximately by using operators $\hat{\rho}^{(1)}$ and $\hat{\rho}^{(2)}$, or one-particle operator $\hat{\rho}^{(1)}$, only. The one-particle statistical operator can be found by the following formula:

$$\hat{\rho}^{(1)} = \frac{1}{(N-1)!} \text{Tr}_{2\dots N}\hat{\rho}^{(N)}. \quad (12.6)$$

The one-particle matrix exposed to particular α -representation can be formulated as follows:

$$\rho_{\alpha\alpha'}^{(1)} = \int \varphi_{\alpha}^*(q)\hat{\rho}^{(1)}\varphi_{\alpha'}(q)dq, \quad (12.7)$$

where $\varphi_{\alpha}(q)$ is the wave function; α is the quantum number system under which the state of one particle is specified; $q \equiv \{\mathbf{r}, \sigma\}$, \mathbf{r} is the particle radius vector, σ is the spin variable.

As follows from some methods, one-particle statistical operator $\hat{\rho}^{(1)}$ can be found and applied for the equilibrium system, whether individually or together with

operator $\hat{\rho}^{(2)}$, by using the variational principle taking into account the properties of some thermodynamic quantities to possess an extreme value when the multi-particle system is in the static equilibrium state. The equation for the wave vector electron distribution function can be solved hereunder by using the variational method.

12.2 Internal Fermion System Energy

The system consisting of N -identical Fermi particles can be shortly described by using one- and two-particle density matrixes:

$$\rho_{11'} = \rho_{\alpha\alpha'}^{(1)}, \quad \rho_{12,1'2'} = \rho_{\alpha_1\alpha_2;\alpha'_1\alpha'_2}^{(2)}, \quad (12.8)$$

One-particle density matrix $\rho_{11'}$ satisfies the following normalizing condition:

$$\sum_{\alpha} \rho_{\alpha\alpha} = N, \quad (12.9)$$

where $\rho_{\alpha\alpha}$ is the probability of filling the state α .

The exact expression of the internal energy of the identical particle system can be written by using the density matrix (12.8) as follows:

$$E = \sum_{11'} H_{11'} \rho_{1'1} + \frac{1}{2} \sum_{12,1'2'} H_{12,1'2'} \rho_{1'2',12}. \quad (12.10)$$

Here $H_{11'}$ and $H_{12,1'2'}$ are matrix elements of one-particle Hamiltonian $\hat{H}^{(1)}$ and the Hamiltonian $\hat{H}^{(2)}$ of the interaction of two particles, respectively:

$$H_{11'} = H_{\alpha_1\alpha'_1}, \quad H_{12,1'2'} = H_{\alpha_1\alpha_2;\alpha'_1\alpha'_2}. \quad (12.11)$$

Density matrix $\rho_{12,1'2'}$ is antisymmetric, that is:

$$\rho_{12,1'2'} = -\rho_{21,1'2'} = -\rho_{12,2'1'} = \rho_{21,2'1'}. \quad (12.12)$$

Consequently, matrix elements $H_{12,1'2'}$ subject to the above expression (12.10), we also consider antisymmetric, that is:

$$H_{12,1'2'} = -H_{21,1'2'} = -H_{12,2'1'} = H_{21,2'1'} \quad (12.13)$$

The transition from the coordinate representation, in which Hamiltonians are usually defined, to particular α -representation is performed using the orthonormal system of wave functions $\varphi_\alpha(q)$. As referred to these functions, the matrix elements of the Hamiltonians (12.11) can be calculated by using well-known formulae as follows:

$$H_{\alpha\alpha'} = \int \varphi_\alpha^* \widehat{H}^{(1)} \varphi_{\alpha'} dq, \quad (12.14)$$

$$H_{12;1'2'} = \int \Phi_{12}^* \widehat{H}^{(2)} \Phi_{1'2'} dq_1 dq_2, \quad (12.15)$$

where the integral symbol points out integration over the coordinates and indicates summation over the spin variable; Φ_{12} is a Slater two-particle wave function:

$$\Phi_{12} = \frac{1}{2} \{ \varphi_{\alpha_1}(q_1) \varphi_{\alpha_2}(q_2) - \varphi_{\alpha_1}(q_2) \varphi_{\alpha_2}(q_1) \}. \quad (12.16)$$

Substituting this function into formula (12.15), we obtain the following antisymmetric matrix:

$$H_{12;1'2'} = \frac{1}{2} (V_{12;1'2'} - V_{21;1'2'} - V_{12;2'1'} + V_{21;2'1'}), \quad (12.17)$$

where

$$V_{12;1'2'} = \int \varphi_{\alpha_1}^*(q_1) \varphi_{\alpha_2}^*(q_2) U(q_1, q_2) \varphi_{\alpha'_1}(q_1) \varphi_{\alpha'_2}(q_2) dq_1 dq_2; \quad (12.18)$$

$U(q_1, q_2)$ is the potential energy of interaction between two fermions.

Provided that the two-particle density matrix applicable to the fermion system is antisymmetric, we can accept the following approximated expression:

$$\rho_{12;1'2'} = \rho_{11'} \rho_{22'} - \rho_{12'} \rho_{21'}. \quad (12.19)$$

Substituting this expression into formula (12.10), we can formulate the following expression:

$$E = \sum_{11'} H_{11'} \rho_{11'} + \sum_{12;1'2'} H_{12;1'2'} \rho_{11'} \rho_{22'}, \quad (12.20)$$

that meets the medium field approximation.

12.3 Entropy

There is a representation in which the single-party density matrix is diagonal, i.e. it has the form as follows:

$$\rho_{nn'} = w_n \delta_{nn'}, \quad (12.21)$$

where n is a set of quantum numbers, which determines the state of one particle under the new representation; w_n are the diagonal elements of the density matrix; $\delta_{nn'}$ is a Kronecker symbol. By definition, value w_n points to the probability of occupation of state n by one of the particles. Thus, the function w_n describes the distribution of particles over states and satisfies the normalization condition as follows:

$$\sum_n w_n = N \quad (12.22)$$

Transition from n -representation to α -representation that specifies the matrix elements (12.11) of Hamiltonians $\hat{H}^{(1)}$ and $\hat{H}^{(2)}$ is performed by using a unitary transformation approach:

$$\rho_{\alpha\alpha'} = \sum_n U_{\alpha n}^* w_n U_{\alpha' n}, \quad (12.23)$$

where $U_{\alpha n}$ is the unitary matrix;

$$\sum_\alpha U_{\alpha n}^* U_{\alpha n'} = \delta_{nn'} \quad (12.24)$$

Using the distribution function w_n we can write down the well-known approximated expression for the entropy of the fermion system:

$$S = -k_B \sum_n \{w_n \ln w_n + (1 - w_n) \ln(1 - w_n)\}. \quad (12.25)$$

12.4 Variational Principle

Referring to formulae (12.13) and (12.25), we can state that free energy $F = E - ST$, subject to the assumed approximation, is the w_n and $U_{\alpha n}$ dependent functional. Since the equilibrium state of the system corresponds to the minimum free energy value at fixed temperature T and volume V , functions w_n and $U_{\alpha n}$ can be found by minimizing the free energy subject to conditions (12.22) and (12.24). By this

means, we encounter the problem of the conditional extremum solved by employing the following auxiliary Langrange-method functional:

$$\Omega = E - ST - \mu \sum_n w_n - \sum_{n,n'} \sum_{\alpha} U_{nn'}^* v_{nn'} U_{nn'}, \quad (12.26)$$

where μ and $v_{nn'}$ are undetermined multipliers. Extremum conditions for the functional (12.27) lead to the following distribution function w_n and unitary matrix $U_{nn'}$ equations:

$$\ln \frac{1 - w_n}{w_n} = \beta(\bar{\varepsilon}_n - \mu), \quad (12.27)$$

$$w_n \sum_{\alpha'} H_{\alpha\alpha'}^{(\text{eff})} U_{\alpha'n} = \sum_{n'} v_{nn'} U_{nn'}, \quad (12.28)$$

where $\bar{\varepsilon}_n$ is the mean energy of one particle:

$$\bar{\varepsilon}_n = \varepsilon_n + \sum_n \varepsilon_{nn'} w_{n'}, \quad (12.29)$$

$$\varepsilon_n = \sum_{\alpha, \alpha'} U_{nn'}^* H_{\alpha\alpha'} U_{\alpha'n} \quad (12.30)$$

is the kinetic energy of a particle,

$$\varepsilon_{nn'} = 2 \sum_{1,2;1'2'} U_{\alpha_1 n}^* U_{\alpha_2 n'}^* H_{12,1'2'} U_{\alpha'_1 n} U_{\alpha'_2 n'}, \quad \varepsilon_{nn'} = \varepsilon_{n'n}; \quad (12.31)$$

$H_{\alpha\alpha'}^{(\text{eff})}$ is the effective one-particle Hamiltonian as defined in the mean-field approximation:

$$H_{\alpha\alpha'}^{(\text{eff})} = H_{\alpha\alpha'} + 2 \sum_{1,1'} H_{\alpha\alpha_1, \alpha'\alpha'_1} \rho_{\alpha'_1 \alpha_1}.$$

The solution is significantly easier in the case when the properties of the system under analysis make it possible to predict what representation is used to bring the density matrix to its diagonal pattern. As applies to this case, it is time to solve the (12.27). Any solutions sourced from the above equation can exhibit certain interesting features related to its nonlinearity and particular dependence of kernel $\varepsilon_{nn'}$ on quantum numbers n and n' . The aim of this chapter is to study such features and their physical effect.

12.5 Statistical Description of the Electrons in the Crystal Lattice

The arrangement of atoms within a given type of crystal can be described in terms of the Bravais lattice with location of the atoms in an isolated unit cell specified. We shall determine position of one of the atoms in the unit cell using vector \mathbf{R} and arrangement of all other atoms in the cell relative to the first one—using vector \mathbf{a} . Let s be a set of quantum numbers defining the wave function of one of the states of an electron located within the neighborhood of the atom, the position of which is determined by vector $\mathbf{R} + \mathbf{a}$. By using the available notations, we write the orthonormal system of wave functions that define localized electron states in the form as follows:

$$\varphi_\alpha(q) \equiv \varphi(\mathbf{r} - \mathbf{R} - \mathbf{a}, \sigma | \mathbf{a}, s),$$

where $\alpha = \{\mathbf{R}, \mathbf{a}, s\}$ is a set of quantum numbers that determine the state of the electron in the crystal lattice. In this case, the Vanier functions are preferable to use for these functions. Using these functions, we can calculate the matrix element of the Hamiltonians (12.14) and (12.15).

Using the method proposed in the previous section, the density matrix of equilibrium state of the system of electrons within a crystal can be found. Some of the simplest types of Hamiltonians only that simulate interaction and behavior of conduction electrons in real metals to the extent of a particular precision will be analyzed in this chapter.

We consider the cases when one atom ($\mathbf{a} = 0$) only is in the unit cell and assume that the valence electron matrixes (12.14) and (12.18) have the form as follows:

$$H_{\alpha\alpha'} = \varepsilon_{\mathbf{R}-\mathbf{R}'} \delta_{ss'}; \quad V_{12,1'2'} = V_{\mathbf{R}_1\mathbf{R}_2, \mathbf{R}'_1\mathbf{R}'_2} \delta_{s_1s'_1} \delta_{s_2s'_2}, \quad (12.32)$$

where parameter s takes on finite number G of different values;

$$V_{\mathbf{R}_1\mathbf{R}_2, \mathbf{R}'_1\mathbf{R}'_2} = \int \varphi(\mathbf{r}_1) \varphi(\mathbf{r}_1 + \mathbf{R}_1 - \mathbf{R}'_1) U(\mathbf{r}_1 - \mathbf{r}_2 + \mathbf{R}_1 - \mathbf{R}_2) \varphi(\mathbf{r}_2) \\ \times \varphi(\mathbf{r}_2 + \mathbf{R}_2 - \mathbf{R}'_2) d\mathbf{r}_1 d\mathbf{r}_2, \quad (12.33)$$

$\varphi(\mathbf{r} - \mathbf{R})$ is the averaged wave function that defines an electron located within the neighborhood of site \mathbf{R} ; $U(\mathbf{r}_1 - \mathbf{r}_2)$ is the potential Coulomb-based two electron repulsion energy. In this case, the density matrix describing conduction electrons is expressed as follows:

$$\rho_{\alpha\alpha'} \equiv \rho_{\mathbf{RR}'}^{ss'} = \rho_{\mathbf{RR}'} \delta_{ss'}. \quad (12.34)$$

Using formulae (12.32), (12.34) and making some simple transformations, the electron energy (12.20) can be expressed as follows:

$$E = G \left\{ \sum_{\mathbf{R}\mathbf{R}'} \varepsilon_{\mathbf{R}-\mathbf{R}'} \rho_{\mathbf{R}'\mathbf{R}} + \sum_{\{\mathbf{R}\}} \mathbf{H}_{\mathbf{R}_1\mathbf{R}_2, \mathbf{R}'_1\mathbf{R}'_2} \rho_{\mathbf{R}'_1\mathbf{R}_1} \rho_{\mathbf{R}'_2\mathbf{R}_2} \right\}, \quad (12.35)$$

where $\{\mathbf{R}\} = \mathbf{R}_1, \mathbf{R}_2, \mathbf{R}'_1, \mathbf{R}'_2$;

$$\mathbf{H}_{\mathbf{R}_1\mathbf{R}_2, \mathbf{R}'_1, \mathbf{R}'_2} = \frac{1}{4} \left[G \left(V_{\mathbf{R}_1\mathbf{R}_2, \mathbf{R}'_1, \mathbf{R}'_2} + V_{\mathbf{R}_2\mathbf{R}_1, \mathbf{R}'_2, \mathbf{R}'_1} \right) - V_{\mathbf{R}_2\mathbf{R}_1, \mathbf{R}'_1, \mathbf{R}'_2} - V_{\mathbf{R}_1\mathbf{R}_2, \mathbf{R}'_2, \mathbf{R}'_1} \right]. \quad (12.36)$$

If the electrons are distributed over the sites of the crystal lattice evenly, than the density matrix $\rho_{\mathbf{R}\mathbf{R}'}$ can be formulated as follows:

$$\rho_{\mathbf{R}\mathbf{R}'} = \frac{1}{N_L} \sum_{\mathbf{k}} w_{\mathbf{k}} e^{i\mathbf{k}(\mathbf{R}-\mathbf{R}')}, \quad (12.37)$$

where the summation is performed by using vectors \mathbf{k} of the first Brillouin zone; N_L is number of lattice sites; $w_{\mathbf{k}}$ is a wave vector electron distribution function that satisfies the following normalizing condition:

$$G \sum_{\mathbf{k}} w_{\mathbf{k}} = N \quad \text{or} \quad \frac{1}{N_L} \sum_{\mathbf{k}} w_{\mathbf{k}} = v; \quad (12.38)$$

v is the extent to which the zone is filled: $v = N/G N_L$.

With the expression (12.37) substituted in the formula (12.35), the following expression can be obtained:

$$E = G \left(\sum_{\mathbf{k}} \varepsilon_{\mathbf{k}} w_{\mathbf{k}} + \frac{1}{2} \sum_{\mathbf{k}, \mathbf{k}'} \varepsilon_{\mathbf{k}\mathbf{k}'} w_{\mathbf{k}} w_{\mathbf{k}'} \right), \quad (12.39)$$

where $\varepsilon_{\mathbf{k}}$ is the kinetic electron energy: $\varepsilon_{\mathbf{k}} = \sum_{\mathbf{R}} \varepsilon_{\mathbf{R}} e^{-i\mathbf{k}\mathbf{R}}$; $\varepsilon_{\mathbf{k}\mathbf{k}'}$ is the energy of interaction of two electrons with wave vectors \mathbf{k} and \mathbf{k}' :

$$\varepsilon_{\mathbf{k}\mathbf{k}'} = \frac{2}{N_L^2} \sum_{\{\mathbf{R}\}} \mathbf{H}_{\mathbf{R}_1\mathbf{R}_2, \mathbf{R}'_1\mathbf{R}'_2} \exp [i\mathbf{k}(\mathbf{R}'_1 - \mathbf{R}_1) + i\mathbf{k}'(\mathbf{R}'_2 - \mathbf{R}_2)] \quad (12.40)$$

The equality (12.37) is, in its essence, the unitary transformation that diagonalizes the density matrix. In this case, the formula (12.25) takes on the form as follows:

$$S = -Gk_B \sum_{\mathbf{k}} \{w_{\mathbf{k}} \ln w_{\mathbf{k}} + (1 - w_{\mathbf{k}}) \ln(1 - w_{\mathbf{k}})\}$$

While minimizing free energy subject to the normalizing condition (12.38), we can obtain the equation that makes it possible to find the wave vector conduction electron distribution function $w_{\mathbf{k}}$ that is of similar nature as the (12.27):

$$\ln \frac{1 - w_{\mathbf{k}}}{w_{\mathbf{k}}} = \beta(\bar{\varepsilon}_{\mathbf{k}} - \mu), \quad (12.41)$$

where $\bar{\varepsilon}_{\mathbf{k}}$ is the mean energy of one electron with wave vector \mathbf{k} :

$$\bar{\varepsilon}_{\mathbf{k}} = \varepsilon_{\mathbf{k}} + \sum_{\mathbf{k}'} \varepsilon_{\mathbf{k}\mathbf{k}'} w_{\mathbf{k}'}. \quad (12.42)$$

Now, we can refer to the formula (12.40) to determine the structure of the kernel $\varepsilon_{\mathbf{k}\mathbf{k}'}$ in the functionals (12.39) and (12.42). Since diagonal elements are the greatest ones of the matrix elements (12.40), as complies with $\mathbf{R}_1 = \mathbf{R}_1$ and $\mathbf{R}_2 = \mathbf{R}_2$, we can use an approximated formula as follows:

$$V_{\mathbf{R}_1 \mathbf{R}_2 \mathbf{R}'_1 \mathbf{R}'_2} = U_{\mathbf{R}_1 - \mathbf{R}_2} \delta_{\mathbf{R}_1 \mathbf{R}'_1} \delta_{\mathbf{R}_2 \mathbf{R}'_2} + U_{\mathbf{R}_1 - \mathbf{R}_2}^{(0)} \delta(\mathbf{R}_1 - \mathbf{R}'_1 - \mathbf{R}_2 + \mathbf{R}'_2), \quad (12.43)$$

where $U_{\mathbf{R}_1 - \mathbf{R}_2}$ is the mean energy of Coulomb interaction of two electrons localized at the sites $\mathbf{R}_1 - \mathbf{R}_2$ and the second summand approximates the off-diagonal elements. In the strict sense, the function $U^{(0)}$ in the formula (12.43) should depend not only on $\mathbf{R}_1 - \mathbf{R}_2$, but also on $\mathbf{R}_1 - \mathbf{R}'_1$. Using formulae (12.36), (12.39), (12.40), and (12.43) we obtain the following approximate expression for interaction energy of electrons:

$$E_{int} = \frac{1}{2} G \left(v U_0 N - \sum_{\mathbf{k}, \mathbf{k}'} J_{\mathbf{k}-\mathbf{k}'} w_{\mathbf{k}} w_{\mathbf{k}'} + \sum_{\mathbf{k}} I_{\mathbf{k}} w_{\mathbf{k}} w_{-\mathbf{k}} \right), \quad (12.44)$$

where

$$J_{\mathbf{k}-\mathbf{k}'} = \frac{1}{N_L} \sum_{\mathbf{R}} U_{\mathbf{R}} e^{i(\mathbf{k}-\mathbf{k}')\mathbf{R}}; \quad (12.45)$$

$$J_{\mathbf{k}} = \sum_{\mathbf{R}} U_{\mathbf{R}}^{(0)} (G - e^{-2i\mathbf{k}\mathbf{R}}); \quad (12.46)$$

The first summand expressed in the formula (12.44) is the energy of direct Coulomb electron interaction that does not depend on the distribution function $w_{\mathbf{k}}$. The following summand represents the exchange energy of electrons. The kernel $J_{\mathbf{k}-\mathbf{k}'}$ in the above sum is a positive function that takes on the largest value at $\mathbf{k}' = -\mathbf{k}$ and rapidly decreases against increase of the $[\mathbf{k}' - \mathbf{k}]$ as a result of long-range Coulomb interaction behavior. Since the exchange energy is negative, such behavior of the function $J_{\mathbf{k}-\mathbf{k}'}$ makes for effective attraction to occur between

electrons with the nearest wave vector values. As applies to the positive summands expressed in the formula (12.44) that contain values $I_{\mathbf{k}}$, they simulate effective repulsion of \mathbf{k} and $-\mathbf{k}$ wave vector electrons. The mean one-electron energy (12.42) that corresponds to the interaction energy (12.44) can be formulated as follows:

$$\bar{\varepsilon}_{\mathbf{k}} = \varepsilon_{\mathbf{k}} - \sum_{\mathbf{k}'} J_{\mathbf{k}-\mathbf{k}'} w_{\mathbf{k}'} + I_{\mathbf{k}} w_{-\mathbf{k}}, \quad (12.47)$$

Unfortunately, while using the formula (12.45) or (12.46), it is impossible not only to find any analytical solution of the (12.41), but also to study it in details. Therefore, we approximate the function (12.45) by using the following expression:

$$J_{\mathbf{k}-\mathbf{k}'} = J \delta_{\mathbf{k}\mathbf{k}'},$$

where J is a positive constant; and the value (12.46) can be considered as that does not depend on a wave vector:

$$J_{\mathbf{k}} = I > 0.$$

As applies to this case, the formula (12.47) takes on the following expression:

$$\bar{\varepsilon}_{\mathbf{k}} = \varepsilon_{\mathbf{k}} - J w_{\mathbf{k}} + I w_{-\mathbf{k}}. \quad (12.48)$$

and the energy of two electron interaction with wave vectors \mathbf{k} and \mathbf{k}' takes on the following expression:

$$\varepsilon_{\mathbf{k}\mathbf{k}'} = -J \delta_{\mathbf{k}-\mathbf{k}'} + I \delta_{\mathbf{k}+\mathbf{k}'}. \quad (12.49)$$

12.6 Electron Wave Vector Distribution Function

The formula (12.48) can be used for transforming the (12.41) as follows:

$$\ln \frac{1 - w_{\mathbf{k}}}{w_{\mathbf{k}}} = \beta(\varepsilon_{\mathbf{k}} + I w_{-\mathbf{k}} - J w_{\mathbf{k}} - \mu). \quad (12.50)$$

In this equation, we substitute \mathbf{k} for $-\mathbf{k}$. Since $\varepsilon_{-\mathbf{k}} = \varepsilon_{\mathbf{k}}$, we can obtain the following expression:

$$\ln \frac{1 - w_{-\mathbf{k}}}{w_{-\mathbf{k}}} = \beta(\varepsilon_{\mathbf{k}} + I w_{\mathbf{k}} - J w_{-\mathbf{k}} - \mu). \quad (12.51)$$

Equations (12.50) and (12.51) result in the following combined equations for two values $w_{\mathbf{k}}$ and $w_{-\mathbf{k}}$ of the electron distribution function:

$$\left. \begin{aligned} \ln \frac{1-w_{\mathbf{k}}}{w_{\mathbf{k}}} &= \beta(\varepsilon_{\mathbf{k}} + Iw_{-\mathbf{k}} - Jw_{\mathbf{k}} - \mu), \\ \ln \frac{1-w_{-\mathbf{k}}}{w_{-\mathbf{k}}} &= \beta(\varepsilon_{\mathbf{k}} + Iw_{\mathbf{k}} - Jw_{-\mathbf{k}} - \mu). \end{aligned} \right\} \quad (12.52)$$

We can demonstrate that this system admits two types of solutions. One of them describes isotropic wave vectors distribution of electrons and other—anisotropic wave vectors distribution of electrons. If

$$w_{-\mathbf{k}} = w_{\mathbf{k}} \quad (12.53)$$

then each of the (12.52) transformed can be formulated as follows:

$$\ln \frac{1-w_{\mathbf{k}}}{w_{\mathbf{k}}} = \beta(\varepsilon_{\mathbf{k}} + (I-J)w_{\mathbf{k}} - \mu). \quad (12.54)$$

If $I = J$, this equation is solvable as the Fermi–Dirac function.

The unknown functions $w_{\mathbf{k}}$ and $w_{-\mathbf{k}}$, expressed via (12.52), admit as combined functions where the kinetic electron energy $\varepsilon_{\mathbf{k}}$ acts as a intervening variable: $w_{-\mathbf{k}} = w_1(\varepsilon_{\mathbf{k}})$ and $w_{\mathbf{k}} = w_2(\varepsilon_{\mathbf{k}})$. The functions $w_1 = w_1(\varepsilon)$ and $w_2 = w_2(\varepsilon)$ are solvable as follows:

$$\left. \begin{aligned} \ln \frac{1-w_1}{w_1} &= \frac{2}{\tau}(2\epsilon + (1-f)w_2 - (1+f)w_1), \\ \ln \frac{1-w_2}{w_2} &= \frac{2}{\tau}(2\epsilon + (1-f)w_1 - (1+f)w_2). \end{aligned} \right\} \quad (12.55)$$

where

$$\epsilon = \frac{\varepsilon - \mu}{J+I}, \quad \tau = \frac{4\theta}{J+I}, \quad (12.56)$$

energy ratio I and J defined by the parameter

$$f = \frac{J-I}{J+I}. \quad (12.57)$$

In this chapter, we will study the case when the parameter $J = 3I$; in this case $f = 1/2$.

12.7 Anisotropy

We have prescribed function $f = f(\mathbf{a})$, i.e. value f depends on vector \mathbf{a} . If value f depends on modulus of this vector \mathbf{a} , only, the distribution concerned is called isotropic, i.e. it may be formulated as $f = f(a)$. We will depict a sphere of radius a centered in the origin of coordinates. So, value f will remain equal at any point of this sphere, providing that $f = f(a)$ is the isotropic function. Any other $f = f(\mathbf{a})$ function will be referred to the anisotropy one.

Now, we will consider the example of the anisotropic function. We will depict two vectors. One of them will be an arbitrary vector \mathbf{a} and the other one will be rated as equal, but opposite in its direction $-\mathbf{a}$. So, if it is appeared that function values fail matching in the points concerned, i.e.

$$f(\mathbf{a}) \neq f(-\mathbf{a}), \tag{12.58}$$

this function will be called the anisotropic one.

12.8 Isotropic Distribution of Electrons

We express the combined (12.55) regarding the case when no anisotropic condition is available, i.e. $w_1 = w_2 = w_0$. Now we can obtain the following equation:

$$\ln \frac{1 - w_0}{w_0} = \frac{4}{\tau} (\epsilon - f w_0). \tag{12.59}$$

This function is graphically represent in Fig. 12.1.

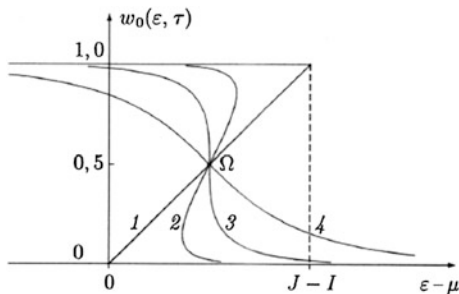


Fig. 12.1 Isotropic energy distribution of electrons regarding the case when $J = 3I$ and at various temperature values (τ): 1 $\tau = 0$; 2 $\tau = 0.25$; 3 $\tau = 0.5$; 4 $\tau = 1$

12.9 Anisotropic Distribution of Electrons

With the electrons being distributed over wave vectors in the anisotropic manner, we will introduce new variables d and s by means of the following relations:

$$w_2 - w_1 = d, \quad w_1 + w_2 = 1 + s \quad (12.60)$$

Without loss of generality, the difference d of two values w_1 and w_2 of the distribution function can be considered as a nonnegative value: $d \geq 0$,

$$w_1(\epsilon) \leq w_2(\epsilon) \quad (12.61)$$

In this case, the largest value d equals to one: $d \in [0, 1]$. Value s can take on those to be ranged from -1 to 1 : $s \in [-1, 1]$. Now, we solve (12.60) relative to the probabilities w_1 and w_2 :

$$w_1 = \frac{1}{2}(1 + s - d), \quad w_2 = \frac{1}{2}(1 + s + d). \quad (12.62)$$

Using the formulae (12.62), we transform the combined (12.55). For this purpose, we at first subtract one equation from other and then sum them up. As a result, we can obtain the following combination:

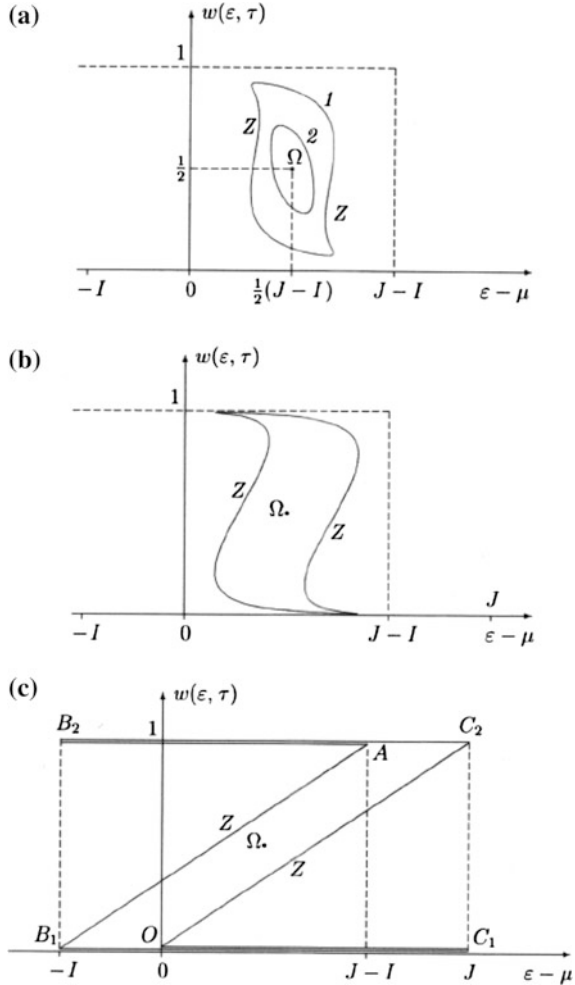
$$\left. \begin{aligned} \frac{(1+d)^2 - s^2}{(1-d)^2 - s^2} &= e^{Ad/\tau}, \\ \epsilon &= \frac{\tau}{8} \ln \frac{(1-s)^2 - d^2}{(1+s)^2 - d^2} + \frac{1}{2}(1+s)f. \end{aligned} \right\} \quad (12.63)$$

The first equation of the above combination is easily to solve in relation to s :

$$s(d) = \pm \sqrt{\frac{(1-d)^2 e^{Ad/\tau} - (1+d)^2}{e^{Ad/\tau} - 1}} \quad (12.64)$$

As provided by the relations (12.62) hereinabove, the probabilities w_1 and w_2 can be considered as the functions of parameter d : $w_1 = w_1(d)$, $w_2 = w_2(d)$. The second combined (12.63) makes it possible to express the electron energy ϵ by using parameter d . As based on the obtained dependencies, it is easy enough to plot the function graphs $w_1 = w_1(\epsilon)$ and $w_2(\epsilon)$ for various temperature values. Such anisotropic curve graphs are demonstrated in Fig. 12.2. Many-valuedness of the function $w = w(\epsilon)$ proves that various equilibrium states of conduction electrons in metals are possible at the same temperature. These macro-states are different from those represented by the Bloch electron distribution function. As a matter of the fact, it is the electron minimum energy macro-state that can be actually implemented provided, that this kind of state is rather stable and it is kept out of any disruption under external effects.

Fig. 12.2 Anisotropic energy distribution of conduction electrons regarding the cases when: **a** $J = 3I$, at various temperatures (τ): 1 $\tau = 0.75$, 2 $\tau = 0.95$; **b** $J = 3I$, $\tau = 0.5$; **c** $J = 3I$, $\tau = 0$



The plots, demonstrated in Figs. 12.1 and 12.2, provide a particular insight into electron state distribution pattern shaped up under various metal temperatures. When temperature $\tau \geq 1$, the isotropic electron wave vector distribution only is possible that is described by the function $w_{\mathbf{k}} = w_0(\epsilon_{\mathbf{k}})$. The function graph curve $w_0 = w_0(\epsilon)$ stated against all temperature values passes point Ω at the coordinates of $\epsilon = \mu + (J - I)/2$ and $w = 0.5$. When the temperature falls down ($\tau < 1$), the curve slope at this point is increased. When temperature drops down to rather low values, the dependency curve $w_0 = w_0(\epsilon)$ is bent so that it looks like letter Z.

A closed anisotropic curve originates at point Ω of the curve $w_0 = w_0(\epsilon)$ at $\tau = 1$ and its dimensions increase against the falling temperature. The curve shape also changes. The following critical temperature corresponds to value $\tau = 1$:

$$T_c = \frac{I+J}{4k} \quad (12.65)$$

If values $\tau \in (\tau', 1)$ are used, where τ' is a certain critical value, the vertical straight line meets an anisotropic curve maximum at two points (curve 2 in Fig. 12.2a). If $\tau < \tau'$, the anisotropic curve Z bends so that the vertical straight line cuts it at four points (curve 1 in Fig. 12.2a, b). The anisotropic curve Z transforms to a polygon at $\tau \rightarrow 0$. As a result, the $AB_1C_1OC_2B_2A$ polygon line resembles letter Z . This polygonal line is shown in Fig. 12.2c.

12.10 Electron Distribution at $T = 0$

Now, we consider the electron distribution function at $T = 0$ in details. Within the range of $\tau \rightarrow 0$, the isotropic distribution solvable by the (12.59) is expressed as follows:

$$w_0(\varepsilon) = \begin{cases} 1 & \text{at } \varepsilon \leq \mu + J - I, \\ \frac{\varepsilon - \mu}{J - I} & \text{at } \mu \leq \varepsilon \leq \mu + J - I, \\ 0 & \text{at } \varepsilon \geq \mu. \end{cases} \quad (12.66)$$

This dependence is graphically represent in Fig. 12.1.

Within the range of $\tau \rightarrow 0$, as stated by the (12.63), the following occupation probability dependence w of the kinetic electron energy ε that describes anisotropic electron wave vector distribution can be formulated:

$$w(\varepsilon) = \begin{cases} 1 & \text{at } \varepsilon \leq \mu - I, \\ w_i(\varepsilon) & \text{at } \mu - I \leq \varepsilon \leq \mu + J, \\ 0 & \text{at } \varepsilon \geq \mu + J. \end{cases} \quad (12.67)$$

where $i = 1$ or 2 . So, the values of functions $w_1 = w_1(\varepsilon)$ and $w_2 = w_2(\varepsilon)$ produce the following pairs:

$$w_1(\varepsilon) = 0 \quad \text{and} \quad w_2(\varepsilon) = 1 \quad (12.68)$$

$$\text{at } \mu - I \leq \varepsilon \leq \mu + J, \text{ or}$$

$$w_1(\varepsilon) = \frac{1}{J}(\varepsilon - \mu + I) \quad \text{and} \quad w_2(\varepsilon) = 1 \quad (12.69)$$

$$\text{at } \mu - I \leq \varepsilon \leq \mu + J - I, \text{ or}$$

$$w_1(\varepsilon) = 0 \quad \text{and} \quad w_2(\varepsilon) = \frac{1}{J}(\varepsilon - \mu) \quad (12.70)$$

at $0 \leq \varepsilon \leq \mu + J$. As demonstrated in Fig. 12.2c, the AB_1C_1O polygonal line meets the relationship

$$w_1 = w_1(\varepsilon) \text{ and the } AB_2C_2O \text{ polygonal line—the relationship } w_2 = w_2(\varepsilon).$$

12.11 Electron Energy Calculation at $T = 0$

Now, we calculate the energy of electrons distributed isotropically or anisotropically. For this purpose, we use the normalizing condition that can be expressed by the following equation:

$$G \sum_{\mathbf{k}} w_{\mathbf{k}} = \bar{N}. \quad (12.71)$$

The electron system energy, when approximated in the mean field, takes on the following expression:

$$\bar{E} = \frac{1}{2} G \sum_{\mathbf{k}} (2\varepsilon_{\mathbf{k}} w_{\mathbf{k}} + I w_{\mathbf{k}} w_{-\mathbf{k}} - J w_{\mathbf{k}}^2). \quad (12.72)$$

As the distribution function $w = w(\varepsilon)$ is known, we can find chemical potential and electron energy at $T = 0$. Such calculations are demonstrated in the previous papers [19–24]. In fact, it is macro-state of the electron energy minimum that can be actually implemented. The energy calculated at $T = 0$ is the lower-range one regarding the condition described by the following formula:

$$w_{\mathbf{k}} = \begin{cases} 1 & \text{at } \varepsilon_{\mathbf{k}} \leq \mu \\ 0 & \text{at } \varepsilon_{\mathbf{k}} > \mu - I \end{cases} \quad (12.73)$$

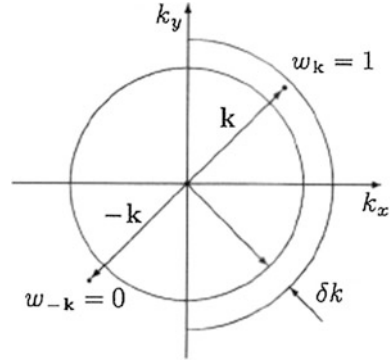
This function is anisotropic at $\mu - I < \varepsilon_{\mathbf{k}} \leq \mu$.

12.12 Superconducting Electron State

The distribution function is a single-valued one. This means that one value of the distribution function shall correspond to one value of the energy. As concerns the anisotropic distribution function, it is two-valued. It simultaneously determines two values of the wave vectors \mathbf{k} and $-\mathbf{k}$, to which two values of the distribution function $w_{-\mathbf{k}} = w_1(\varepsilon_{\mathbf{k}})$ and $w_{\mathbf{k}} = w_2(\varepsilon_{\mathbf{k}})$ are conformed. However, whether the values $w_{-\mathbf{k}} = w_2(\varepsilon_{\mathbf{k}})$ and $w_{\mathbf{k}} = w_1(\varepsilon_{\mathbf{k}})$ can be conformed to the above vectors. In this case, the superconductivity phenomenon is examined.

For detecting superconductivity, initially weak current is supplied to a conductor. Then, temperature is reduced. When temperature falls below the defined

Fig. 12.3 Electron distribution function with superconducting current flowing through the substance



value, the superconductor circuit is shorted. The superconductor circuit current sustains its steady state as long as it can. Let current flows along axis x . Than at $T = 0$, the following electron wave-vector space distribution function \mathbf{k} can be represented in Fig. 12.3.

12.13 Electron Mean Energy

Dependence $\bar{\varepsilon} = \bar{\varepsilon}(\varepsilon)$ of the electron mean energy $\bar{\varepsilon}$ against kinetic energy ε can be found by the formula (12.48):

$$\bar{\varepsilon}(\varepsilon) = \varepsilon - (J - I)w_0(\varepsilon) \quad \text{at} \quad \varepsilon \leq \varepsilon_1, \quad \varepsilon \geq \varepsilon_2 \quad (12.74)$$

$$\bar{\varepsilon}(\varepsilon) = \varepsilon + Iw_1(\varepsilon) - Jw_2(\varepsilon) \quad \text{at} \quad \varepsilon_1 < \varepsilon < \varepsilon_2 \quad (12.75)$$

This dependence, as rated at various temperatures τ , is graphically represented in Fig. 12.4. At $T < T_c$, each of the curves $\bar{\varepsilon} = \bar{\varepsilon}(\varepsilon)$ has a “well” conforming to values of the kinetic energy anisotropy ε , that satisfies the inequalities as follows:

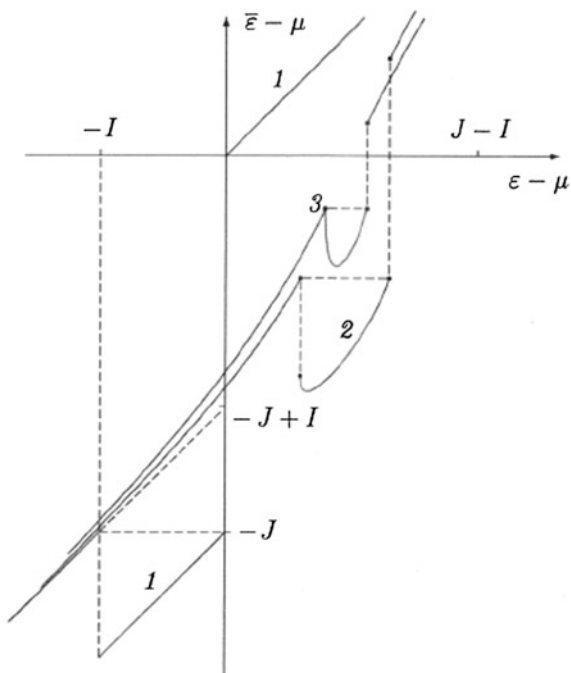
$$\varepsilon_1 < \varepsilon_{\mathbf{k}} < \varepsilon_2 \quad (12.76)$$

Value ε_1 is the lower-range value of the kinetic electron energy ε subject to functions $w_1(\varepsilon)$ and $w_2(\varepsilon)$. Value ε_2 satisfies the following condition:

$$\bar{\varepsilon}(\varepsilon_1) = \bar{\varepsilon}(\varepsilon_2), \quad (12.77)$$

according to which the “well” edges, represented by the graphic chart $\bar{\varepsilon} = \bar{\varepsilon}(\varepsilon)$, are shown at the same level. However, there is an opening on the well edge’s right. This means that there is a certain “gap” in the spectrum of values of the electron energy $\bar{\varepsilon}$. The energy gap width Δ extends from zero to value J , when temperature

Fig. 12.4 Dependence of the mean electron energy $\bar{\varepsilon}$ of the kinetic energy ε at various temperature values τ : 1 $\tau = 0$; 2 $\tau = 0.75$; 3 $\tau = 0.95$



falls down from T_c to zero. The well width $\delta\varepsilon = \varepsilon_2 - \varepsilon_1$ is also extended from zero to value I at $T = 0$.

12.14 Real-Valued Distribution Function

The lower-range electron energy corresponds to the real-valued equilibrium distribution function. The real-valued equilibrium distribution function follows from the electron energy calculated for various distribution functions. The function curve, as rated against $\tau = 0.75$, is shown in Fig. 12.5.

12.15 Type-I and Type-II Superconductors

For characterizing type of a superconductor, the following parameter value is involved:

Fig. 12.5 Real-valued conduction electron equilibrium distribution function at $\tau = 0.75$. Electron interaction energy values I and J are coupled by the $J = 3I$ relation

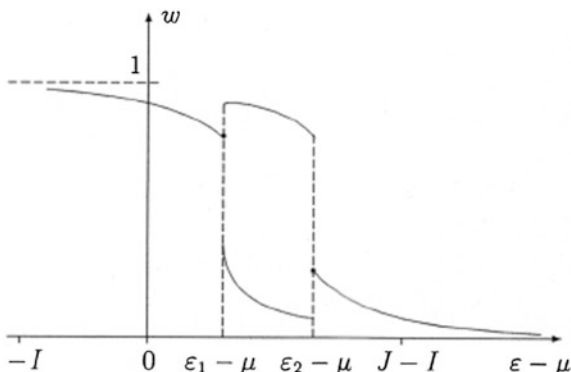
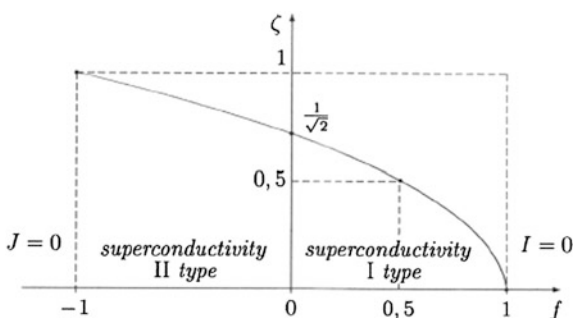


Fig. 12.6 Graph of function $\zeta = \zeta(f)$



$$\zeta = \sqrt{\frac{I}{I+J}}. \tag{12.78}$$

We express parameter ζ in terms of parameter f . Now, we can obtain the following formula:

$$\zeta = \sqrt{\frac{1-f}{2}}. \tag{12.79}$$

This function is graphically represented in Fig. 12.6. Using known inequalities, we can write the superconductor type condition. The condition $\zeta < 1/\sqrt{2}$ indicates to a type-I superconductor. And the condition $\zeta > 1/\sqrt{2}$ indicates to a type-II superconductor. These conditions have been originally gained by A.A. Abrikosov.

Parameter $f = -1$ shows that value of $J = 0$, that characterizes the gap width Δ , does not produce any pair. Consequently, the coherent length ζ (i.e. electron pair interaction length) equals zero, as well. As applies to this case, the condition $\zeta < \lambda$ satisfies where λ is the superconductor magnetic field penetration depth. This condition shows that the type-II superconductor is in the range of the f parameter-defined values.

12.16 Density Matrix

Now, when we find the probability $w_{\mathbf{k}}$, it is possible in principle to find the density matrix. Using a unitary transformation, we have

$$\rho_{\mathbf{R}\mathbf{R}'} = \frac{1}{N_L} \sum_{\mathbf{k}} w_{\mathbf{k}} e^{i\mathbf{k}(\mathbf{R}-\mathbf{R}')}. \quad (12.80)$$

Unfortunately, the calculations carried out at arbitrary temperatures are very complex. The density matrix can be calculated only for the probability of (12.73) at the temperature $T = 0$:

$$\rho_{\mathbf{R}\mathbf{R}'} = \frac{1}{N_L} \sum_{\mathbf{k}, 0 < \varepsilon_{\mathbf{k}} < \mu - I} e^{i\mathbf{k}(\mathbf{R}-\mathbf{R}')} + \frac{1}{N_L} \sum_{\mathbf{k}, k_x > 0, \mu - I < \varepsilon_{\mathbf{k}} < \mu} e^{i\mathbf{k}(\mathbf{R}-\mathbf{R}')}. \quad (12.81)$$

12.17 Conclusion

The model for electrons in metal, described in this paper, can be assumed as a basis of an alternative theory of superconductivity. This model significantly differs from those which have been applied in the contemporary theory of superconductivity. The superconductivity, described herein, is caused by repulsion of wave vector \mathbf{k} and $-\mathbf{k}$ electrons, but electron pairs and energy gap in the spectrum—by attraction between the electrons of equal wave vectors. Electrons are statistically described in terms of the density matrix formalism, featured with the simplicity representative by specific formulae and physical content. The problem examined demonstrates advantages of the density matrix method.

References

1. H. Kamerlingh-Onnes, *Comm. Phys. Leb. Univ. Leiden* **122**, 13 (1911)
2. W. Meissner, R. Ochsenfeld, *Naturwiss* **21**, 787 (1933)
3. A.A. Abrikosov, *Proc. Acad. Sci. USSR* **86**, 489 (1952), *UFN* **87**, 125 (1965)
4. H. London, F. London, *Proc. Roy. Soc. A* **149**, 71 (1935), *Physica* **2**, 341 (1935)
5. V.L. Ginszburg, L.D. Landau, *J. Exp. Theor. Phys.* **20**, 1064 (1950)
6. J. Bardeen, L.N. Cooper, J.R. Schrieffer, *Phys. Rev.* **106**(1), 162 (1957)
7. J. Von Neumann, *Mathematical Foundations of Quantum Mechanics* (Nauka, Moscow, 1964)
8. Y.R. Shen, *Phys. Rev.* **155**, 921 (1967)
9. M. Grover, R. Silbey, *Chem. Phys.* **52**, 2099 (1970); **54**, 4843 (1971)
10. A. Kossakowski, *Rep. Math. Phys.* **3**, 247 (1972)
11. V. Gorini, A. Kossakowski, E.C.G. Sudarshan, *J. Math. Phys.* **17**, 821 (1976)
12. G. Lindblad, *Commun. Math. Phys.* **48**, 119 (1976)

13. V. Gorini, A. Frigeio, N. Verri, A. Kossakowski, E.C.G. Sudarshan, Rep. Math. Phys. **13**, 149 (1978)
14. K. Blum, *Density Matrix Theory and Application* (Plenum, New York, 1981)
15. B.V. Bondarev, Phys. A **176**, 366 (1991)
16. B.V. Bondarev, Phys. A **183**, 159 (1992)
17. B.V. Bondarev, Phys. A **184**, 205 (1992)
18. B.V. Bondarev, Teor. Mat. Fiz. **100**, 33 (1994)
19. B.V. Bondarev, Vestnik MAI **3**, 56 (1996)
20. B.V. Bondarev, *Density Matrix Method in Cooperative Phenomena Quantum Theory*, 2nd edn. (Sputnik+, Moscow, 2013)
21. B.V. Bondarev, *New Theory of Superconductivity. Method of Equilibrium Density Matrix*, arxiv:1412.6008 (2013)
22. B.V. Bondarev, *Fermi–Dirac Function and Energy Gap*. arxiv:1412.6009 (2013)
23. B.V. Bondarev, *Anisotropy and Superconductivity*. arxiv:1302.5066 (2013)
24. B.V. Bondarev, *Matrix Density Method in Quantum Superconductivity Theory* (Sputnik+, Moscow, 2014)

Chapter 13

New Effects in 1–3-Type Composites Based on Relaxor-Ferroelectrics Single Crystals

V.Yu. Topolov, C.R. Bowen and P. Bisegna

Abstract Two effects of the matrix subsystem on the piezoelectric performance and hydrostatic parameters are first studied in novel 1–0–3 composites that contain relaxor-ferroelectric single-crystal rods surrounded by a ferroelectric ceramic/polymer matrix with 0–3 connectivity. First, the influence of the mutual orientation of the poling direction of the single-crystal and ceramic components on the properties of the 1–0–3 composite is discussed to demonstrate advantages concerned with the high hydrostatic piezoelectric performance and large anisotropy of squared figures of merit. In a 1–0–3 $0.67\text{Pb}(\text{Mg}_{1/3}\text{Nb}_{2/3})\text{O}_3 - 0.33\text{PbTiO}_3$ single crystal/ $(\text{Pb}_{1-x}\text{Ca}_x)\text{TiO}_3$ ceramic/araldite composite with $x = 0.20\text{--}0.25$, values of $\max g_h^* \sim 10^2 \text{ mV} \cdot \text{m/N}$ and $\max(d_h^* g_h^*) \sim 10^{-11} \text{ Pa}^{-1}$ are achieved at specific volume-fraction and rotation-angle ranges due to the new orientation effect in the presence of a highly anisotropic 0–3 matrix. Second, the influence of the aspect ratio of ceramic inclusions on the piezoelectric and hydrostatic parameters of the 1–0–3 composite based on relaxor-ferroelectric SCs is studied. In this case, the elastic anisotropy of the 0–3 matrix plays the key role in forming the large effective parameters of the composite. The studied composites can be used in piezoelectric sensor, energy-harvesting and hydrophone applications.

V.Yu. Topolov (✉)

Department of Physics, Southern Federal University, Rostov-on-Don, Russia
e-mail: vutopolov@sfedu.ru

C.R. Bowen

Department of Mechanical Engineering, University of Bath, Bath, UK

P. Bisegna

Department of Civil Engineering and Computer Science, University of Rome
'Tor Vergata', Rome, Italy

13.1 Introduction

Composites based on relaxor-ferroelectric single crystals (SCs) with high piezoelectric activity are an important group of advanced dielectric materials wherein the effective electromechanical properties and their anisotropy can be varied and tailored [1–4] in a wide range. Among the composite systems with a high piezoelectric activity and/or sensitivity [3–5], of particular interest are those based on domain-engineered relaxor-ferroelectric SCs such as $(1 - z)\text{Pb}(\text{Mg}_{1/3}\text{Nb}_{2/3})\text{O}_3 - z\text{PbTiO}_3$ (PMN- z PT) or $(1 - z)\text{Pb}(\text{Zn}_{1/3}\text{Nb}_{2/3})\text{O}_3 - z\text{PbTiO}_3$ (PZN- z PT) with compositions near the morphotropic phase boundary [6–9]. These composites are of interest due to the polarization orientation effect [4, 10–12] studied for a few connectivity patterns (e.g., 1–3, 2–2 and 0–3) in the last decade. This orientation effect depends not only on the connectivity of the composite system, but also on the electromechanical properties of the SC component, and this component can be poled along a specific crystallographic direction, for instance, along [001], [011] or [111] of the perovskite unit cell.

A potential method to increase the performance of the piezo-active composites is to modify their structure by introducing a third component [13–16]. Some modifications were studied for 1–3-type composites, and their parameters were compared to those of the conventional 1–3 ferroelectric ceramic (FC)/polymer composites. The presence of an anisotropic matrix in a 1–3-type composite structure opens up new and exciting possibilities of further tailoring the effective electromechanical properties of the composite and its hydrostatic parameters [14–16].

In this chapter, we show that the use of two ferroelectric components with distinct differences in their electromechanical properties leads to important effects that promote improving a few effective parameters of the three-component 1–3-type composite. Such a composite is of particular interest due to the complex inter-relationships in the fundamental triangle of ‘composition—structure—properties’ [17]. The aim of this chapter is to discuss advantages in effective parameters that are achieved by taking into account the new effects and the active role of the matrix subsystem in the 1–3-type SC/FC/polymer composites.

13.2 Orientation Effect in the 1–0–3 Composite with Two Polarization Directions

13.2.1 Model Concepts and Effective Parameters of the Composite

It is assumed that the composite consists of long SC rods embedded in a heterogeneous matrix (Fig. 13.1). The SC rods are in the form of the rectangular parallelepiped with a square base and square arrangement in the (X_1OX_2) plane. The main crystallographic axes X, Y and Z of each SC rod with the spontaneous

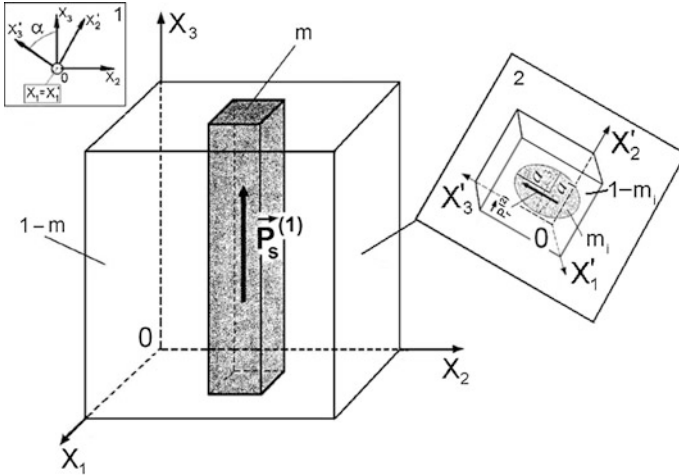


Fig. 13.1 Schematic of the 1–0–3 relaxor-ferroelectric SC/FC/polymer composite. m and $1 - m$ are volume fractions of the SC and surrounding 0–3 matrix, respectively. Rotation of co-ordinate axes $(X_1'X_2'X_3') \rightarrow (X_1X_2X_3)$ is shown in *inset 1*, the 0–3 matrix is shown in *inset 2*. In the 0–3 matrix, m_i and $1 - m_i$ are volume fractions of the FC and polymer, respectively (reprinted from Topolov et al. [14], with permission from Elsevier)

polarization $\mathbf{P}_s^{(1)}$ are oriented as follows: $X \parallel OX_1$, $Y \parallel OX_2$ and $Z \parallel \mathbf{P}_s^{(1)} \parallel OX_3$. Spheroidal FC inclusions are surrounded by a large polymer matrix. The shape of each FC inclusion obeys the equation

$$(x'_1/a_1)^2 + (x'_2/a_2)^2 + (x'_3/a_3)^2 = 1 \tag{13.1}$$

relative to the axes of the rectangular co-ordinate system $(X_1'X_2'X_3')$ rotated by an angle α with respect to $(X_1X_2X_3)$ (*inset 1* in Fig. 13.1). In (13.1), $a_1, a_2 = a_1$ and a_3 are semi-axes of the inclusion. To characterise its shape, we introduce the aspect ratio $\rho_i = a_1/a_3$. Centres of the inclusions occupy sites of a simple tetragonal lattice with unit-cell vectors parallel to the OX_k' axes. We assume that $0 < \rho_i < 1$, and the presence of prolate inclusions facilitates poling of the FC/polymer matrix due to a weaker depolarization effect. The remanent polarization vector of the FC inclusion is $\mathbf{P}_r^{(2)} \uparrow OX_3'$, and OX_3' is the poling axis of the matrix (*inset 2* in Fig. 13.1). The FC/polymer matrix represents a composite with 0–3 connectivity in terms of work [17, 18], and the three-component composite (Fig. 13.1) is described by 1–0–3 connectivity. Assuming that the linear sizes of each inclusion in the 0–3 matrix are much smaller than the length of the side of the square being intersected the rod in the (X_1OX_2) plane, we evaluate the effective properties of the 1–0–3 relaxor-ferroelectric SC/FC/polymer composite in two stages [14].

The first stage is related to the effective properties of the 0–3 composite matrix. Taking into account the electromechanical interaction between the piezo-active (poled FC) inclusions, the effective properties of the 0–3 composite matrix are

determined by either the effective field method (EFM) [4, 17] or finite element method (FEM) [17]. In the EFM, an electromechanical interaction in the FC/polymer matrix (see inset 2 in Fig. 13.1) is described using a local effective field. This effective field is determined by taking into account a system of interacting inclusions and boundary conditions based on inclusions with a spheroidal shape [4, 14, 15].

In terms of FEM modeling, COMSOL [19] is applied to obtain the volume-fraction dependence of the effective electromechanical properties of the 0–3 composite matrix. A representative unit cell, containing a spheroidal inclusion with a radius adjusted to yield the appropriate volume fraction m_i , is discretized using tetrahedral elements [4, 15]. The number of elements, depending on the aspect ratio ρ_i of the spheroidal inclusion, varies from 1,000,000 to 1,700,000. The unknown displacement and electric-potential fields are interpolated using linear Lagrangian shape functions. The corresponding number of degrees of freedom varies from 700,000 to 1,200,000. The following conditions are assumed at the inclusion—matrix interface: (i) perfect bonding (i.e., continuity of the displacement field) and (ii) continuity of the electric potential. Moreover, either Dirichlet or periodic boundary conditions are considered at the boundary of the parallelepiped representative unit cell ‘inclusion—matrix’ [14].

At the second stage, the effective electromechanical properties of the 1–0–3 composite are evaluated using the matrix method [4, 17]. The electromechanical properties of the SC rod and 0–3 composite matrix are averaged in the OX_1 and OX_2 directions, in which the periodic structure of the composite (Fig. 13.1) is observed, and take into account electromechanical interactions in a system of ‘piezo-active rods—piezo-active matrix’. The effective electromechanical properties of the 1–0–3 composite in the co-ordinate system $(X_1X_2X_3)$ are given by

$$\|C^*\| = \|C^*(m, m_i, \rho_i, \alpha)\| = \begin{pmatrix} \|s^{*E}\| & \|d^{*t}\| \\ \|d^*\| & \|\varepsilon^{*\sigma}\| \end{pmatrix}. \quad (13.2)$$

In (13.1), $\|s^{*E}\|$, $\|d^*\|$ and $\|\varepsilon^{*\sigma}\|$ are matrices of elastic compliances at electric field $E = \text{const}$, piezoelectric coefficients and dielectric permittivities at mechanical stress $\sigma = \text{const}$, respectively, and superscript ‘ t ’ denotes transposition.

Based on the $\|C^*\|$ matrix from (13.1), we determine the following effective parameters of the 1–0–3 composite: piezoelectric coefficients g_{jt}^* from equation $\|d^*\| = \|\varepsilon^{*\sigma}\| \|g^*\|$, squared strain–voltage figures of merit

$$(Q_{33}^*)^2 = d_{33}^* g_{33}^*, (Q_{32}^*)^2 = d_{32}^* g_{32}^* \text{ and } (Q_{31}^*)^2 = d_{31}^* g_{31}^*, \quad (13.3)$$

hydrostatic piezoelectric coefficients

$$d_h^* = d_{33}^* + d_{32}^* + d_{31}^* \text{ and } g_h^* = g_{33}^* + g_{32}^* + g_{31}^*, \quad (13.4)$$

and squared hydrostatic figure of merit

$$(Q_h^*)^2 = d_h^* g_h^* \quad (13.5)$$

It is assumed that electrodes applied to a composite sample (Fig. 13.1) are perpendicular to the OX_3 axis. The piezoelectric coefficients g_{β}^* characterise the piezoelectric sensitivity of the composite. Squared figures of merit $(Q_{\beta}^*)^2$ from (13.3) are used to characterise [4, 17] the piezoelectric sensor signal-to-noise ratio. The hydrostatic piezoelectric coefficients d_h^* and g_h^* from (13.4) describe [4, 17] the piezoelectric activity and sensitivity under hydrostatic loading of the composite sample for SONAR and hydrophone applications. The parameter $(Q_h^*)^2$ from (13.5) plays the role of the hydrostatic analog of $(Q_{31}^*)^2$ from (13.3) and is used [17] to characterize the piezoelectric sensitivity under hydrostatic loading.

13.2.2 Components of the Composite

Among the components of the 1–0–3 composite, we mention [001]-poled domain-engineered PMN–0.33PT and PZN–0.08PT SCs with high piezoelectric activity, poled $(\text{Pb}_{1-x}\text{Ca}_x)\text{TiO}_3$ and modified PbTiO_3 FCs with a large piezoelectric anisotropy but moderate piezoelectric activity, and piezo-passive polymers such as araldite and polyurethane (Table 13.1). The hydrostatic piezoelectric coefficient $d_h^{(1)}$ evaluated in accordance with (13.4) exhibits different signs: $d_h^{(1)} > 0$ for the PMN–0.33PT SC, but $d_h^{(1)} < 0$ for the PZN–0.08PT SC. Hereafter, we use superscript ‘(1)’ to denote the SC component and ‘(2)’ to denote the FC component.

As follows from experimental data [7, 24], the coercive fields $E_c^{(n)}$ of the PMN– x PT SC ($n = 1$) and $(\text{Pb}_{1-x}\text{Ca}_x)\text{TiO}_3$ FC ($n = 2$) obey the condition $E_c^{(1)} \ll E_c^{(2)}$. Such a condition enables initial poling of the 0–3 matrix under a strong electric field with a subsequent poling of the SC rods in the composite (Fig. 13.1) under a lower electric field. We add that $(\text{Pb}_{1-x}\text{Ca}_x)\text{TiO}_3$ and related highly anisotropic FCs were used to form some 0–3 FC/polymer composites [17, 20, 25, 26].

13.2.3 Volume-Fraction and Orientation Dependence of Hydrostatic Parameters

As seen from Fig. 13.2, a and b, $\max g_h^*$ and $\max[(Q_h^*)^2]$ of the PMN–0.33PT-based composite are achieved at a rotation angle $\alpha \approx 90^\circ$ with a volume fraction of FC $m_i = 0.12$. Local $\max g_h^*$ relates to the volume fraction of SC $0.01 < m < 0.12$, however, the fabrication of a composite sample at $m < 0.03$ may be problematic in terms of the manufacturing tolerance [1, 2, 4, 17, 25]. The largest value of g_h^* at

Table 13.1 Elastic compliances s_{ab}^E (in 10^{-12} Pa $^{-1}$), piezoelectric coefficients d_{ij} (in pC/N) and relative dielectric permittivities $\epsilon_{ij}^e/\epsilon_0$ of components at room temperature

Component	s_{11}^E	s_{12}^E	s_{13}^E	s_{33}^E	s_{44}^E	s_{66}^E	d_{31}	d_{33}	d_{15}	$\epsilon_{11}^e/\epsilon_0$	$\epsilon_{33}^e/\epsilon_0$
PMN-0.33PT SC, 4 mm symmetry [6]	69.0	-11.1	-55.7	119.6	14.5	15.2	-1330	2820	146	1600	8200
PZN-0.08PT SC, 4 mm symmetry [7]	87.0	-13.1	-70.0	141	15.8	15.4	-1455	2890	158	2900	7700
(Pb _{0.80} Ca _{0.20})TiO ₃ FC [20]	6.04	-1.24	-1.25	6.21	14.7	14.6	-1.33	24.6	26.1	131	135
(Pb _{0.75} Ca _{0.25})TiO ₃ FC [20]	6.00	-1.30	-1.30	6.18	14.8	14.6	-0.364	28.0	28.9	158	163
Modified PbTiO ₃ FC [21]	7.50	-1.51	-1.10	8.00	17.9	18.0	-4.40	51.0	53.0	228	177
Araldite [22]	216	-78	-78	216	588	588	0	0	0	4.0	4.0
Polyurethane [23]	405	-151	-151	405	1110	1110	0	0	0	3.5	3.5

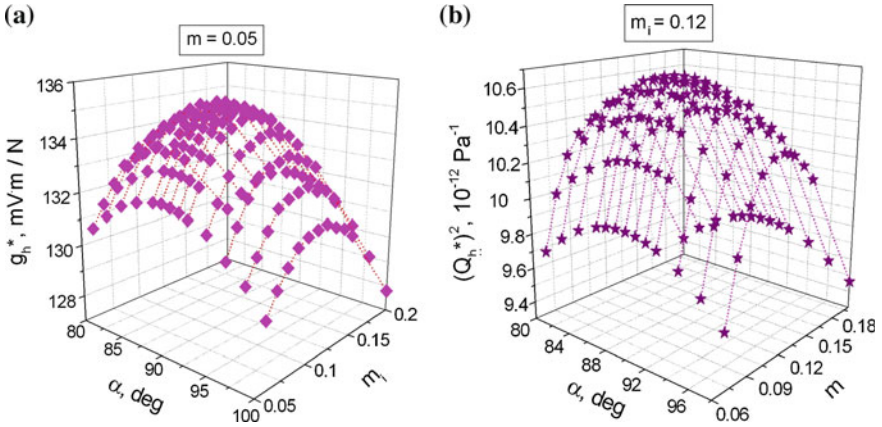


Fig. 13.2 Examples of the hydrostatic piezoelectric response of the 1–0–3 PMN–0.33PT SC/ (Pb_{0.75}Ca_{0.25})TiO₃ FC/araldite composite at $\rho_i = 0.1$: **a** near local max $g_h^*(0.05, m_i, 0.1, \alpha)$, **b** near absolute max $\{[Q_h^*(m, 0.12, 0.1, \alpha)]^2\}$. Electromechanical properties of the 0–3 matrix at the first stage of averaging were determined by means of the EFM (reprinted from Topolov et al. [14], with permission from Elsevier)

$0.1 \leq \rho_i \leq 0.5$ relates to $m_i \approx 0.12$ and $0.01 < m < 0.03$, and in this m range, a local max g_h^* is observed at various values of m_i, ρ_i and α [14]. Our evaluations based on the EFM (0–3 matrix) and matrix method (1–3-type composite) lead to absolute max $d_h^* = 305$ pC/N at $m = 0.532, m_i = 0.12, \rho_i = 0.1$, and $\alpha = 90^\circ$ [14].

Using the matrix method, we find for comparison, that the 1–3 PMN–0.33PT SC/araldite composite is characterized by absolute max $g_h^* = 158$ mV · m/N, absolute max $[(Q_h^*)^2] = 8.27 \cdot 10^{-12}$ Pa⁻¹ and absolute max $d_h^* = 274$ pC/N at $m = 0.016, 0.103$ and 0.509 , respectively [14]. At $m = 0.05$ for the 1–3 PMN–0.33PT SC/araldite composite, we obtain $g_h^* = 115$ mV·m/N, and this value is considerably smaller than g_h^* near the maximum point in Fig. 13.2a.

The large values of $(Q_h^*)^2$ (Fig. 13.2b) and d_h^* in the 1–0–3 composite are achieved due to the presence of a 0–3 matrix based on FC with piezoelectric coefficients $d_{3f}^{(2)}$ that obey the condition [20] $d_{33}^{(2)} / |d_{31}^{(2)}| \gg 1$. At $\alpha = 90^\circ$, the remanent polarization vector $\mathbf{P}_r^{(2)}$ of each FC inclusion (see inset 2 in Fig. 13.1) is parallel to OX_2 , and this $\mathbf{P}_r^{(2)}$ orientation leads to a decrease in $|d_{32}^*|$ with minor changes in d_{31}^* and d_{33}^* (or g_{31}^* and g_{33}^* , respectively) as a result of the weak lateral piezoelectric effect in the 0–3 matrix. As a consequence of the reduced $|d_{32}^*|$, we observe an increase in both d_h^* and g_h^* .

The elastic anisotropy of the 0–3 matrix with highly prolate inclusions is an additional factor in increasing the hydrostatic parameters from (13.4) and (13.5). Ratios of the elastic compliances in the 0–3 (Pb_{0.75}Ca_{0.25})TiO₃ FC/araldite composite matrix are represented as follows:

$s_{11,0-3}^E/s_{12,0-3}^E = -2.21$, $s_{11,0-3}^E/s_{13,0-3}^E = -6.52$ and $s_{11,0-3}^E/s_{33,0-3}^E = 1.95$ at $\rho_i = 0.1$ and $m_i = 0.10$,
and
 $s_{11,0-3}^E/s_{12,0-3}^E = -2.52$, $s_{11,0-3}^E/s_{13,0-3}^E = -3.51$ and $s_{11,0-3}^E/s_{33,0-3}^E = 1.25$ at $\rho_i = 0.3$ and $m_i = 0.10$.

This means that a significant decrease of $|s_{11,0-3}^E/s_{13,0-3}^E|$ and $|s_{11,0-3}^E/s_{33,0-3}^E|$ is observed with a weakening of the piezoelectric activity of the 0–3 composite.

The orientation effect considered in the 1–0–3 composite favours an increase in $(Q_h^*)^2$ and d_h^* near its maxima by approximately 29 % and 11 %, respectively, in comparison to a ‘traditional’ two-component 1–3 PMN–0.33PT SC/araldite composite [14]. The studied 1–0–3 composite is attractive due to large values of local maxima of d_h^* , g_h^* and $(Q_h^*)^2$ at $m_i = \text{const}$, especially at $m_i < 0.15$.

13.2.4 Anisotropy of Squared Figures of Merit

An important feature of the studied 1–0–3 composite consists in a large anisotropy of squared figures of merit from (13.3). For instance, the inequality

$$(Q_{33}^*)^2/(Q_{3j}^*)^2 \geq 10 \quad (j = 1 \text{ and } 2) \quad (13.6)$$

holds at volume fractions of SC $m_{Q1} \leq m \leq m_{Q2}$ which depend on the rotation angle α (Fig. 13.3). The validity of condition (13.6) is achieved due to the 0–3 FC/polymer matrix with a significant elastic and piezoelectric anisotropy at $m_i = 0.50$ and $\rho_i = 0.1$. The presence of prolate FC inclusions has a significant influence on the electromechanical properties of the 0–3 matrix, and the anisotropy of these properties promotes the validity of condition (13.6) for the 1–0–3 composite. Values of $m_{Q2} < 0.1$ may be a result of the high piezoelectric activity of the SC while $d_{33}^{(1)}/d_{33}^{(2)} \approx 100$. We note that for the PMN–0.33PT SC, condition $(Q_{33}^{(1)})^2/(Q_{31}^{(1)})^2 = (Q_{33}^{(1)})^2/(Q_{32}^{(1)})^2 = (d_{33}^{(1)}/d_{31}^{(1)})^2 \approx 4.5$ holds (see Table 13.1).

13.2.5 Comparison of Effective Parameters

The effective parameters obtained using different methods are given for comparison in Table 13.2. To predict the effective properties of the 0–3 composite matrix at the first stage of calculations, we use either the EFM or one of two FEM models. Either Dirichlet (FEM-1) or periodic (FEM-2) boundary conditions are enforced on the boundary of the representative unit cell of the 0–3 FC/polymer matrix. At the second stage of calculations, we use the matrix method that is applicable to the 1–3 composite structure with planar interfaces [14]. The use of Dirichlet boundary conditions gives rise to a higher piezoelectric activity of the 0–3 matrix, whereas

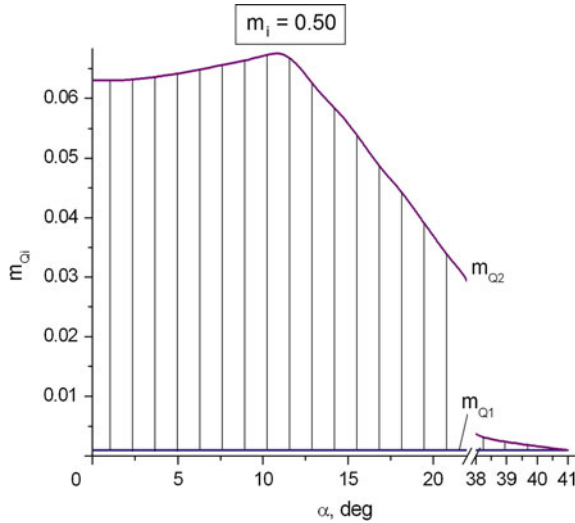


Fig. 13.3 Region of validity of condition (13.6) (hatched area) in the 1–0–3 PMN–0.33PT SC/(Pb_{0.75}Ca_{0.25})TiO₃ FC/araldite composite at $\rho_i = 0.1$ and $m_i = 0.50$. Electromechanical properties of the 0–3 matrix at the first stage of averaging were determined by means of the EFM (reprinted from Topolov et al. [14], with permission from Elsevier)

Table 13.2 Hydrostatic piezoelectric coefficient g_h^* (in mV · m/N) and squared hydrostatic figure of merit $(Q_h^*)^2$ (in 10^{-12} Pa⁻¹) of the 1–0–3 PMN–0.33PT SC/(Pb_{0.80}Ca_{0.20})TiO₃ FC/araldite composite at $\rho_i = 0.1$ and $\alpha = 90^\circ$

Methods	g_h^* at $m_i = 0.10, m = 0.05$	g_h^* at $m_i = 0.10, m = 0.06$	g_h^* at $m_i = 0.10, m = 0.10$	g_h^* at $m_i = 0.15, m = 0.05$	g_h^* at $m_i = 0.15, m = 0.06$	g_h^* at $m_i = 0.15, m = 0.10$
EFM	133	121	86.6	133	122	89.1
FEM-1 ^a	139	128	92.2	139	129	95.5
FEM-2 ^b	128	117	84.3	127	118	86.5
Methods	$(Q_h^*)^2$ at $m_i = 0.10, m = 0.10$	$(Q_h^*)^2$ at $m_i = 0.10, m = 0.12$	$(Q_h^*)^2$ at $m_i = 0.10, m = 0.15$	$(Q_h^*)^2$ at $m_i = 0.15, m = 0.10$	$(Q_h^*)^2$ at $m_i = 0.15, m = 0.12$	$(Q_h^*)^2$ at $m_i = 0.15, m = 0.15$
EFM	10.2	10.3	10.0	10.3	10.4	10.2
FEM-1 ^a	11.1	11.2	11.0	11.0	11.2	11.1
FEM-2 ^b	9.53	9.59	9.40	9.32	9.46	9.36

Methods for prediction of properties of the 0–3 FC/polymer matrix are listed in the 1st column (reprinted from Topolov et al. [14], with permission from Elsevier)

^aWith Dirichlet boundary conditions, leading to higher piezoelectric activity of the 0–3 matrix

^bWith periodic boundary conditions, leading to lower piezoelectric activity of the 0–3 matrix

periodic boundary conditions lead to a lower piezoelectric activity than that obtained using the EFM method. The EFM results are close to average values obtained from the FEM models. Relatively small differences between the

parameters obtained using the EFM, FEM-1 and FEM-2 (Table 13.2) are accounted for by the very high piezoelectric activity of the SC rod in comparison to the 0–3 matrix.

We add for a further comparison, that in a 1–3 PZT FC/epoxy composite with aligned FC rods [27], values of $\max d_h^* \approx 110$ pC/N and $\max[(Q_h^*)^2] = 6.0 \cdot 10^{-12}$ Pa⁻¹ are considerably lower than the maximum values of these parameters of the studied 1–0–3 composite (see, for instance, Fig. 13.2 and Table 13.2). According to data [17], a 1–3 PMN–0.33PT SC/araldite composite (a limiting case of the 1–0–3 composite at $m_i = 0$) is characterized by absolute $\max d_h^* = 274$ pC/N (at $m = 0.509$), absolute $\max g_h^* = 130$ mV · m/N (at $m = 0.016$) and absolute $\max [(Q_h^*)^2] = 7.45 \cdot 10^{-12}$ Pa⁻¹ (at $m = 0.115$). The aforementioned values are also smaller than those related to the 1–0–3 composite.

13.3 Aspect-Ratio Effect in the 1–0–3 Composite

13.3.1 Two Examples of the High Performance

In Sect. 13.3, we discuss the role of the aspect ratio ρ_i of FC inclusions in forming the large effective parameters of the 1–0–3 SC/FC/polymer composite. Hereafter, we consider the composite shown in Fig. 13.1 at $\alpha = 0^\circ$ and vary ρ_i in the 0–3 FC/polymer composite matrix to show its influence on the effective parameters of the 1–0–3 composite.

Our recent results suggest that large changes in the piezoelectric coefficient g_{33}^* and squared figures of merit $(Q_{3j}^*)^2$ are observed (Fig. 13.4) at

$$0.01 < \rho_i < 2. \quad (13.7)$$

In the range (13.7), the shape of the FC inclusions changes from highly prolate ($\rho_i \ll 1$) to oblate ($\rho_i > 1$). Such changes in the microgeometry of the 0–3 composite matrix give rise to significant changes in its elastic properties and ratios of elastic compliances $s_{1b}^{(m),E}/s_{pq}^{(m),E}$ that then have a strong influence on the piezoelectric properties and their anisotropy in the 1–0–3 composite even at the small volume fraction of FC $m_i = 0.05$ (Fig. 13.4).

The correlation between the elastic compliance $s_{33}^{(m),E}$ of the 0–3 matrix and the squared figure of merit $(Q_{33}^*)^2$ of the composite was recently studied in work [15]. This correlation stems from the important role of $s_{33}^{(m),E}$ in the formation of the piezoelectric response of a 1–3 composite along the poling axis OX_3 . In the case of the 1–0–3 composite (Fig. 13.1), the elastic anisotropy of its 0–3 matrix leads to a stronger link between $s_{33}^{(m),E}$ and $(Q_{33}^*)^2$, especially in the range (13.6).

Now we consider the hydrostatic piezoelectric coefficients of the 1–0–3 PZN–0.08PT SC/modified PbTiO₃/polyurethane composite (Fig. 13.5). Graphs in

Fig. 13.5 show the important role of the matrix subsystem in forming the hydrostatic response of the composite wherein the highly piezo-active SC component is characterized by $d_h^{(1)} = -20$ pC/N. Even at a relatively small volume fraction of the FC inclusions m_i , changes in the aspect ratio ρ_i give rise to considerable changes in the hydrostatic parameters, especially at $\rho_i > 1$. Moreover, $\max g_h^*$ (Fig. 13.5b) correlates with $\max d_h^*$ (Fig. 13.5a) because the relation [17] $g_h^* = d_h^*/\epsilon_{33}^*\sigma$ is valid. In Fig. 13.5b we show a restricted range of volume fractions of SC m due to the significant decreasing g_h^* at $m > 0.2$ irrespective of the FC content. Changes in $\text{sgn } d_h^*$ (Fig. 13.5a) take place at $m \approx 1$, when the SC rods play the dominating role in forming the piezoelectric properties of the composite. The use of the highly oblate FC inclusions ($\rho_i \gg 1$) leads to a lower dielectric permittivity of the 0–3 FC/polymer matrix at $m_i = \text{const}$ and to a larger piezoelectric coefficient g_h^* of the composite at $m = \text{const}$ (cf. curves 1 and 5 in Fig. 13.5b). We note that changes in the matrix elastic properties and their anisotropy become appreciable at aspect ratios $\rho_i > 1$.

13.3.2 Comparison of Data Obtained Using Different Methods

In Sect. 13.3.2, we consider a few effective parameters that were calculated for the 1–0–3 SC/FC/polymer composite by means of different methods. We also compare the effective parameters of the 1–0–3 composite to those known for related piezo-active composites.

First, for the PZN–0.08PT-based composite with oblate FC inclusions in the 0–3 matrix, we see good consistence between the hydrostatic piezoelectric coefficients calculated in two different ways (Table 13.3).

Second, we consider a specific case of a performance of a 1–0–3 SC/FC/polymer composite with a piezo-passive 0–3 matrix. It is assumed that the FC inclusions in the polymer matrix (Fig. 13.1) were not previously poled and, therefore, remain piezo-passive. By varying the aspect ratio ρ_i of these inclusions, we see changes in the effective parameters of the 1–0–3 composite (Table 13.4), however these parameters become larger than those in the case of the poled 0–3 matrix. This is a result of a decrease in the dielectric permittivity of the piezo-passive 0–3 matrix that leads to an appreciable decrease of the dielectric permittivity of the 1–0–3 composite $\epsilon_{33}^*\sigma$ at relatively small SC volume fractions m . Results shown in Table 13.4 suggest that the elastic anisotropy in achieving high piezoelectric performance for the 1–0–3 composite remains a dominant factor irrespective of the piezoelectric activity of its 0–3 matrix. Thus, during the manufacture of samples of the 1–0–3 composite at $\alpha = 0^\circ$ (Fig. 13.1), there is no need to pole the 0–3 FC/polymer matrix under a fairly strong electric field, as applied, for instance, to the PbTiO₃-type FC samples [24]. Changes in the volume fraction of FC, m_i , in the 0–3 matrix give rise to weaker changes in the effective parameters of the composite (Table 13.4) in

Table 13.3 Hydrostatic piezoelectric coefficients calculated for the 1–0–3 PZN–0.08PT SC/modified PbTiO₃ FC/polyurethane composite at $\rho_i = 100$

m_i	m	d_h^* , pC/N ^a	g_h^* , mV · m/N ^a	d_h^* , pC/N ^b	g_h^* , mV · m/N ^b
0.10	0.05	152	213	151	211
	0.10	266	146	262	145
	0.20	410	80.9	406	79.6
0.15	0.05	150	216	147	213
	0.10	260	151	254	148
	0.20	400	84.6	389	83.0
0.20	0.05	144	213	140	208
	0.10	250	151	241	147
	0.20	382	85.7	369	83.8
0.25	0.05	137	206	132	201
	0.10	237	148	227	144
	0.20	362	85.5	362	83.3

^aValues were calculated using the EFM and matrix method at the first and second stages of averaging, respectively

^bValues were calculated using the EFM and FEM at the first and second stages of averaging, respectively

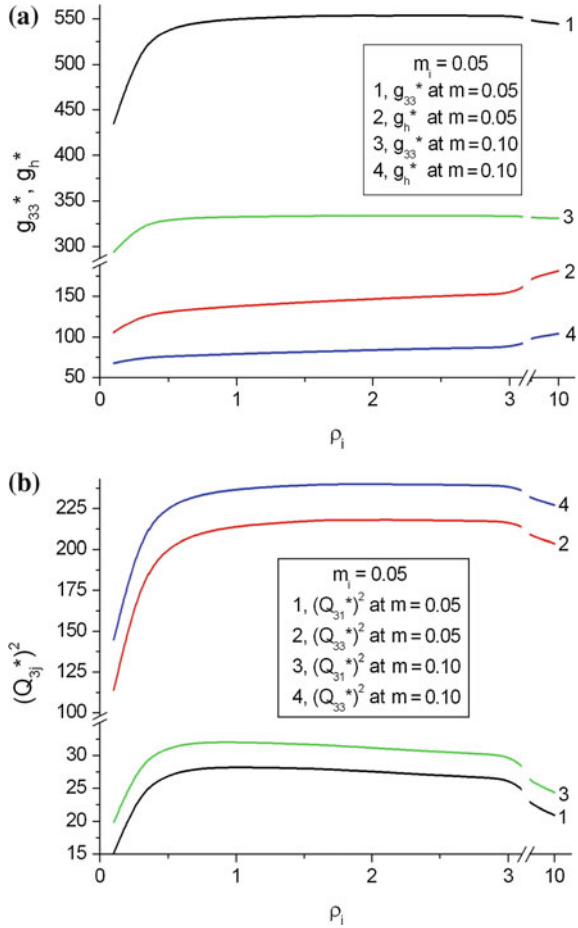
Table 13.4 Effective parameters of the 1–0–3 PMN–0.33PT SC/modified PbTiO₃ FC/polyurethane composite in a case of a piezo-passive 0–3 matrix^a (reprinted from Topolov et al. [15], with permission from Elsevier)

ρ_i	m_i	m	g_{33}^* , mV · m/N	$(Q_{33}^*)^2$, 10^{-12} , Pa ⁻¹	$(Q_{31}^*)^2$, 10^{-12} , Pa ⁻¹	d_h^* , pC/N	g_h^* , mV · m/N	$(Q_h^*)^2$, 10^{-12} , Pa ⁻¹
1.5	0.05	0.05	553	218	28.1	102	143	14.5
2.0	0.05	0.05	554	218	27.5	105	147	15.4
2.5	0.05	0.05	554	218	27.0	107	150	16.1
1.5	0.10	0.05	535	194	23.7	101	148	14.9
2.0	0.10	0.05	536	185	23.0	105	155	16.3
2.5	0.10	0.05	536	195	22.2	109	161	17.6
1.5	0.05	0.10	333	240	31.7	177	81.9	14.5
2.0	0.05	0.10	334	240	31.2	182	84.1	15.3
2.5	0.05	0.10	334	240	30.6	186	86.1	16.0
1.5	0.10	0.10	328	220	27.7	176	86.2	15.2
2.0	0.10	0.10	328	221	26.8	195	90.2	16.6
2.5	0.10	0.10	328	220	25.9	191	93.5	17.9

^aEffective properties of the 0–3 FC/polymer matrix were evaluated by means of the EFM

comparison to changes caused by the volume fraction of SC, m . These weaker changes are concerned with the high piezoelectric activity of the SC rods and their parallel orientation along the poling axis: at such an arrangement, even minor

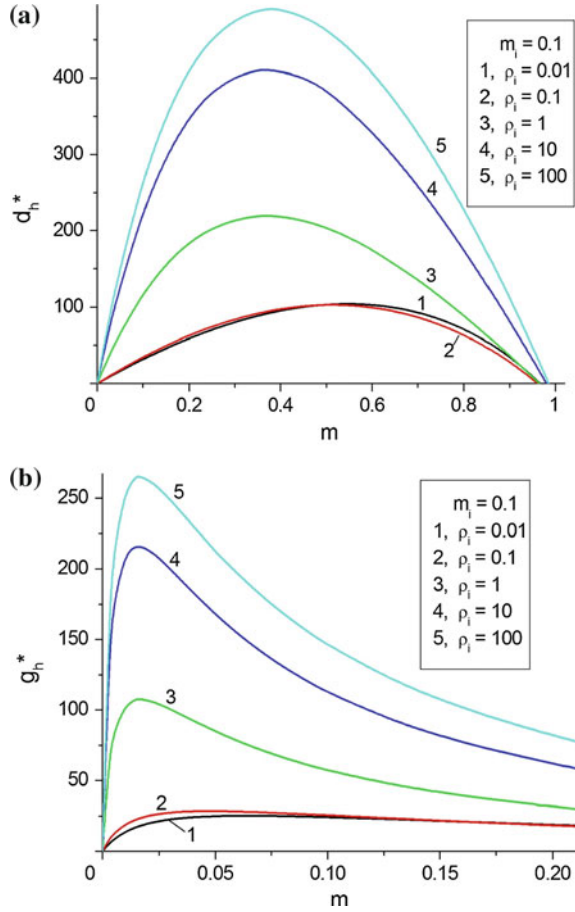
Fig. 13.4 Aspect-ratio (ρ_i) dependence of the piezoelectric coefficient g_{33}^* and hydrostatic piezoelectric coefficient g_h^* (a, in $\text{mV} \cdot \text{m/N}$), and squared figures of merit (Q_{3j}^*)² (b, in 10^{-12}Pa^{-1}) of the 1–0–3 PMN–0.33PT SC/modified PbTiO₃ FC/polyurethane composite at volume fractions $m_i = \text{const}$ (FC inclusions in the 0–3 matrix) and $m = \text{const}$ (SC rods in the composite). At the first stage of averaging, electromechanical properties of the 0–3 matrix were evaluated by EFM (reprinted from Topolov et al. [15], with permission from Elsevier)



changes in m at $m \ll 1$ give rise to considerable changes in the piezoelectric performance and figures of merit of the 1–0–3 composite [4, 15–17].

Third, our results on the performance of the 1–0–3 composites based on SCs are compared to literature data on the 1–3-type piezo-active composites. For instance, work [28] reports a piezoelectric performance of a 1–0–3 FC/FC/polyurethane composite, where the PCR-7 M FC (a PZT-type composition [17]) is the main component. The 1–0–3 PCR-7 M FC/PCR-7 M FC/polyurethane composite is characterized [28] by large piezoelectric coefficients, e.g., $g_{33}^* \approx 400 \text{ mV} \cdot \text{m/N}$, $g_h^* \approx 200 \text{ mV} \cdot \text{m/N}$ and $d_h^* \approx 350 \text{ pC/N}$. The aforementioned parameters are comparable to those given in Tables 13.3 and 13.4. According to data [2], $\max g_{33}^*$ related to a 1–3 PMN–0.30PT SC/epoxy composite is $440 \text{ mV} \cdot \text{m/N}$ (at the volume

Fig. 13.5 Volume-fraction (m) dependence of hydrostatic piezoelectric coefficients d_h^* (**a** in pC/N) and g_h^* (**b** in mV · m/N) of the 1–0–3 PZN–0.08PT SC/modified PbTiO₃ FC/polyurethane composite at $m_i = \text{const}$ (reprinted from Topolov et al. [16], with permission from World Scientific)



fraction of SC $m = 0.018$) and is comparable to values of g_{33}^* from Tables 13.3 and 13.4. However, a 1–3 PMN–zPT-based composite from work [29] is characterized by $d_h^* = 111$ pC/N, $g_h^* = 37$ mV · m/N and $(Q_h^*)^2 = 4.12 \cdot 10^{-12}$ Pa⁻¹, and these effective parameters are smaller than those shown in Tables 13.3 and 13.4.

Fourth, data on the squared hydrostatic figure of merit $(Q_h^*)^2 \sim 10^{-12}$ Pa⁻¹ (see Fig. 13.2b and Table 13.4) are to be compared to $(Q_h^*)^2$ of the 1–3-type FC-based composites. We note that the $(Q_h^*)^2$ values achieved at small volume fractions of the FC inclusions m_i (see Table 13.4) are approximately equal to $(Q_h^*)^2$ of a 1–3–0 PZT FC/foamed polymer composite [30].

13.4 Conclusions

In the present chapter, we have analyzed the new effects in the piezo-active 1–3-type composites. The first effect is the new orientation effect in the 1–0–3 SC/FC/polymer composite (Fig. 13.1) with two contrasting ferroelectric components (a highly piezo-active SC and highly anisotropic FC) poled on different directions. The second effect is concerned with the active role of the 0–3 matrix and the aspect ratio of its FC inclusions in forming the large hydrostatic parameters of the 1–0–3 SC/FC/polymer composite. Our main research results are concluded as follows.

1. Changes in the rotation angle $\alpha = (\mathbf{P}_s^{(1)} \wedge \mathbf{P}_r^{(2)})$ (Fig. 13.1) give rise to changes in the elastic and piezoelectric anisotropy of the 0–3 FC/polymer matrix. The $(\text{Pb}_{1-x}\text{Ca}_x)\text{TiO}_3$ FC component plays an important role in the orientation effect due to the large anisotropy of the piezoelectric coefficients $d_{3j}^{(2)}$ in comparison to the anisotropy of $d_{3j}^{(1)}$ of the PMN–0.33PT SC, and due to the high degree of the elastic anisotropy.
2. The orientation effect studied in this 1–0–3 composite leads to a considerable anisotropy of squared figures of merit (5) and a relatively high piezoelectric activity, and such characteristics are of significant interest for the design of high performance composite structures for hydroacoustic, piezoelectric energy harvesting and transducer applications.
3. An important feature of the studied 1–0–3 composite is that elastic properties of its 0–3 matrix considerably depend on the aspect ratio ρ_i of FC inclusions therein and influence the effective electromechanical properties of the 1–0–3 composite in wide aspect-ratio and volume-fraction ranges. This influence becomes important in the presence of two contrasting piezoelectric components. There is no need to pole the 0–3 matrix in a strong electric field, and the high piezoelectric sensitivity is achieved in the case of the non-poled 0–3 matrix with aligned FC inclusions.
4. The electromechanical interaction between the highly piezo-active SC component and the anisotropic 0–3 matrix leads to the creation of high-performance 1–0–3 composite structures. The large values of $g_{33}^* \sim 10^2 \text{ mV} \cdot \text{m/N}$ are of significant interest for sensor and receive-type transducer applications, and the large values of $d_h^* \sim 10^2 \text{ pC/N}$, $g_h^* \sim 10^2 \text{ mV} \cdot \text{m/N}$ and $(Q_h^*)^2 \sim 10^{-11} \text{ Pa}^{-1}$ are of value for hydrophone and related hydroacoustic applications. The large values of the squared figure of merit $(Q_{33}^*)^2 \sim 10^{-10} \text{ Pa}^{-1}$ and anisotropy $(Q_{33}^*)^2 / (Q_{31}^*)^2 \approx 8\text{--}9$ are important for piezoelectric energy-harvesting applications.
5. Calculations of effective parameters of the studied 1–0–3 composite were performed using the EFM, FEM and matrix method. Changes in the boundary conditions of the unit cell of the 0–3 matrix with spheroidal FC inclusions, i.e., either Dirichlet (FEM-1) or periodic (FEM-2) boundary conditions, do not give rise to considerable changes in g_h^* and $(Q_h^*)^2$ as predicted by means of the FEM. Results obtained by different ways of averaging the properties at the first and second stages are in agreement.

Acknowledgments The authors thank Prof. Dr. S.-H. Chang (National Kaohsiung Marine University, Taiwan, ROC), Prof. Dr. I.A. Parinov, Prof. Dr. A.E. Panich, Prof. Dr. A.A. Nesterov, and Dr. V.V. Eremkin (Southern Federal University, Russia), and Dr. A.V. Krivoruchko (Don State Technical University, Russia) for their continuing interest in the research problems. The research subject is concerned with the Programme Supporting the Research at the Southern Federal University (Russia). The results on the research work No. 1597 have been represented within the framework of the base part of the state task No. 2014/174 in the scientific activity area at the Southern Federal University (Russia). Prof. Dr. C. R. Bowen acknowledges funding from the European Research Council under the European Union's Seventh Framework Programme (FP/2007-2013)/ERC Grant Agreement No. 320963 on Novel Energy Materials, Engineering Science and Integrated Systems (NEMESIS).

References

1. K. Ren, Y. Liu, X. Geng, H.F. Hofmann, Q.M. Zhang, *IEEE Trans. Ultrason., Ferroelec., a. Freq. Contr.* **53**, 631 (2006)
2. F. Wang, C. He, Y. Tang, *Mater. Chem. Phys.* **105**, 273 (2007)
3. L. Li, S. Zhang, Z. Xu, X. Geng, F. Wen, J. Luo, T.R. Shrout, *Appl. Phys. Lett.* **104**, 032909 (2014)
4. V.Yu. Topolov, P. Bisegna, C.R. Bowen, *Piezo-active Composites* (Orientation Effects and Anisotropy Factors. Springer, Berlin, Heidelberg, 2014)
5. V.Yu. Topolov, V.R. Bowen, S.V. Glushanin, in *Piezoceramic Materials and Devices*, ed. by I.A. Parinov (Nova Science Publishers, New York, 2010), p. 71
6. R. Zhang, B. Jiang, W. Cao, *J. Appl. Phys.* **90**, 3471 (2001)
7. R. Zhang, B. Jiang, W. Cao, A. Amin, *J. Mater. Sci. Lett.* **21**, 1877 (2002)
8. G. Liu, W. Jiang, J. Zhu, W. Cao, *Appl. Phys. Lett.* **99**, 162901 (2011)
9. J. Yin, B. Jiang, W. Cao, *IEEE Trans. Ultrason., Ferroelec., a. Freq. Contr.* **47**, 285 (2000)
10. A.V. Krivoruchko, V.Yu. Topolov, *J. Phys. D Appl. Phys.* **40**, 7113 (2007)
11. V.Yu. Topolov, A.V. Krivoruchko, *J. Appl. Phys.* **105**, 074105 (2009)
12. V.Yu. Topolov, A.V. Krivoruchko, *Smart Mater. Struct.* **18**, 065011 (2009)
13. V.Yu. Topolov, C.R. Bowen, P. Bisegna, S.E. Filippov, in *Nano- and Piezoelectric Technologies, Materials and Devices*, ed. by I.A. Parinov (Nova Science Publishers, New York, 2013), p. 51
14. V.Yu. Topolov, C.R. Bowen, P. Bisegna, A.V. Krivoruchko, *Mater. Chem. Phys.* **151**, 187 (2015)
15. V.Yu. Topolov, C.R. Bowen, P. Bisegna, *Sens. a. Actuat. A Phys.* **229**, 94 (2015)
16. V.Yu. Topolov, C.R. Bowen, P. Bisegna, A.E. Panich, *Funct. Mater. Lett.* **8**, 1550049 (2015)
17. V.Yu. Topolov, C.R. Bowen, *Electromechanical Properties in Composites Based on Ferroelectrics* (Springer, London, 2009)
18. R.E. Newnham, D.P. Skinner, L.E. Cross, *Mater. Res. Bull.* **13**, 525 (1978)
19. COMSOL, Inc. COMSOLMultiphysics™ User's Guide (version 4.4, 2014), <http://www.comsol.com>
20. S.V. Glushanin, V.Yu. Topolov, A.V. Krivoruchko, *Mater. Chem. Phys.* **97**, 357 (2006)
21. S. Ikegami, I. Ueda, T. Nagata, *J. Acoust. Soc. Am.* **50**, 1060 (1971)
22. F. Levassort, M. Lethiecq, C. Millar, L. Pourcelot, *IEEE Trans. Ultrason., Ferroelec., a. Freq. Contr.* **45**, 1497 (1998)
23. L.V. Gibiansky, S. Torquato, *J. Mech. Phys. Solids* **45**, 689 (1997)
24. Y. Xu, *Ferroelectric Materials and Their Applications* (North-Holland, London, 1991)
25. K.H. Yoon, J.H. Yoo, W.S. Kim, E.S. Kim, *Ferroelectrics* **186**, 169 (1996)
26. S.A. Wilson, G.M. Maistros, R.W. Whatmore, *J. Phys. D Appl. Phys.* **38**, 175 (2005)

27. C.-W. Nan, L. Liu, D. Guo, L. Li, *J. Phys. D Appl. Phys.* **33**, 2977 (2000)
28. V.Yu. Topolov, C.R. Bowen, S.E. Filippov, *Ferroelectrics* **430**, 92 (2012)
29. S. Zhang, F. Li, *J. Appl. Phys.* **111**, 031301 (2012)
30. E.K. Akdogan, M. Allahverdi, A. Safari, *IEEE Trans. Ultrason., Ferroelec., a. Freq. Contr.* **52**, 746 (2005)

Chapter 14

Piezoelectric Properties of a Novel ZTS-19/Clay Composite

S.E. Filippov, A.A. Vorontsov, V. Yu. Topolov, P. Bisegna,
O.E. Brill and A.E. Panich

Abstract Results on the piezoelectric performance of the ZTS-19 ferroelectric ceramic/clay composite are reported. In this composite, clay is regarded as an elastically soft piezo-passive component that strongly influences effective electromechanical properties and related parameters of the composite even at small volume fractions of clay m_{cl} . Changes in the microgeometry of the composite are discussed, and its piezoelectric performance is interpreted in terms of models of the two- and three-component composites based on poled ferroelectric ceramics. Results of modeling are compared to experimental data. The studied composite is of interest as a piezoelectric material with relatively high piezoelectric sensitivity ($g_{33}^* > 50 \text{ mV} \cdot \text{m/N}$), large anisotropy of the piezoelectric coefficients d_{3j}^* ($5.4 < d_{33}^*/|d_{31}^*| < 8.2$ at $0.01 \leq m_{cl} \leq 0.05$), and with considerable variation of the sound velocity v_s .

14.1 Introduction

Effective electromechanical properties of piezo-active composites based on poled ferroelectric ceramics (FCs) depend [1–3] on the properties of components, microgeometry, connectivity patterns, poling and technological conditions, etc. Interrelations between the electromechanical properties of the composite and its piezoelectric components have been the important subject of research in the last

S.E. Filippov · A.A. Vorontsov · O.E. Brill
Scientific Design & Technology Institute ‘Piezopribor’, Southern Federal University,
Rostov-on-Don, Russia

V.Yu. Topolov (✉) · A.E. Panich
Department of Physics, Southern Federal University, Rostov-on-Don, Russia
e-mail: vutopolov@sfedu.ru

P. Bisegna
Department of Civil Engineering and Computer Science, University of Rome
‘Tor Vergata’, Rome, Italy

decade [3, 4]. The effective properties of the FC-based composites can be varied in wide ranges, as is known, for instance, from studies [1–4] on the piezoelectric coefficients d_{3j}^* , g_{3j}^* , their hydrostatic analogues

$$d_h^* = d_{33}^* + 2d_{31}^* \text{ and } g_h^* = g_{33}^* + 2g_{31}^*, \quad (14.1)$$

dielectric permittivity $\varepsilon_{33}^{*\sigma}$, and elastic moduli c_{ab}^{*E} . An electromechanical interaction between components at the specific microgeometry [1, 3] plays the key role in the formation of the piezoelectric performance of the composite.

As follows from literature data, various combinations of the components (FC and polymer, FC and FC, FC and relaxor-ferroelectric single crystal) were considered [1, 3, 4] to show the piezoelectric performance and related parameters. In a few papers, building materials (e.g., cement and silica fume cement) [5–8] were used to provide close matching of the components in the FC-based composite. Very recently, clay was first applied [9] as a component of a novel FC-based composite. However, relations between the microgeometry and effective piezoelectric properties of this composite were not yet discussed in detail. The aim of the present chapter is to analyze the piezoelectric performance of the novel FC/clay composite and to interpret experimental data on its piezoelectric performance in a wide range of volume fractions of clay m_{cl} .

14.2 Experimental

Samples of the clay-containing composite based on ZTS-19 FC were manufactured at the Scientific Design & Technology Institute ‘Piezopribor’ (Southern Federal University, Russia). ZTS-19 is a typical PZT-type FC composition near the morphotropic phase boundary, and the full set of electromechanical constants of this FC in the poled state is given in Table 14.1. Clay is a soft piezo-passive component with properties shown in Table 14.1. In the present study, we used clay from the Vladimirovsky open pit located in the Rostov region, Russia.

The sintered ZTS-19 powder with a size of particles $(3\text{--}12) \cdot 10^{-6}$ m and clay with a size of particles $(5\text{--}9) \cdot 10^{-6}$ m were mixed on previously calculated proportions. This mixture was put into a press-form, and pressing the sample was carried out at $5 \cdot 10^7$ Pa. Baking the composite sample was carried out at increasing temperature T with the ratio 25 K/min and then at $T = 1243$ K for 40 min.

The air poling of the composite samples was carried out under electric field $E = 3.5 - 4.0$ MV/m. Electrophysical measurements were performed on the poled disk-shaped sample. Like poled FCs, the studied composite is characterized by ∞mm symmetry. Table 14.2 contains experimental data on the diameter D and height h of the disk, its volume $V = \pi D^2 h / 4$, mass of the sample m , its density $\rho^* = m/V$, electric capacitance C_0 and tangent of dielectric loss $\text{tg}\delta$ at 1 kHz, sensitivity on voltage M_u and electric charge M_q , resonance frequency f_r ,

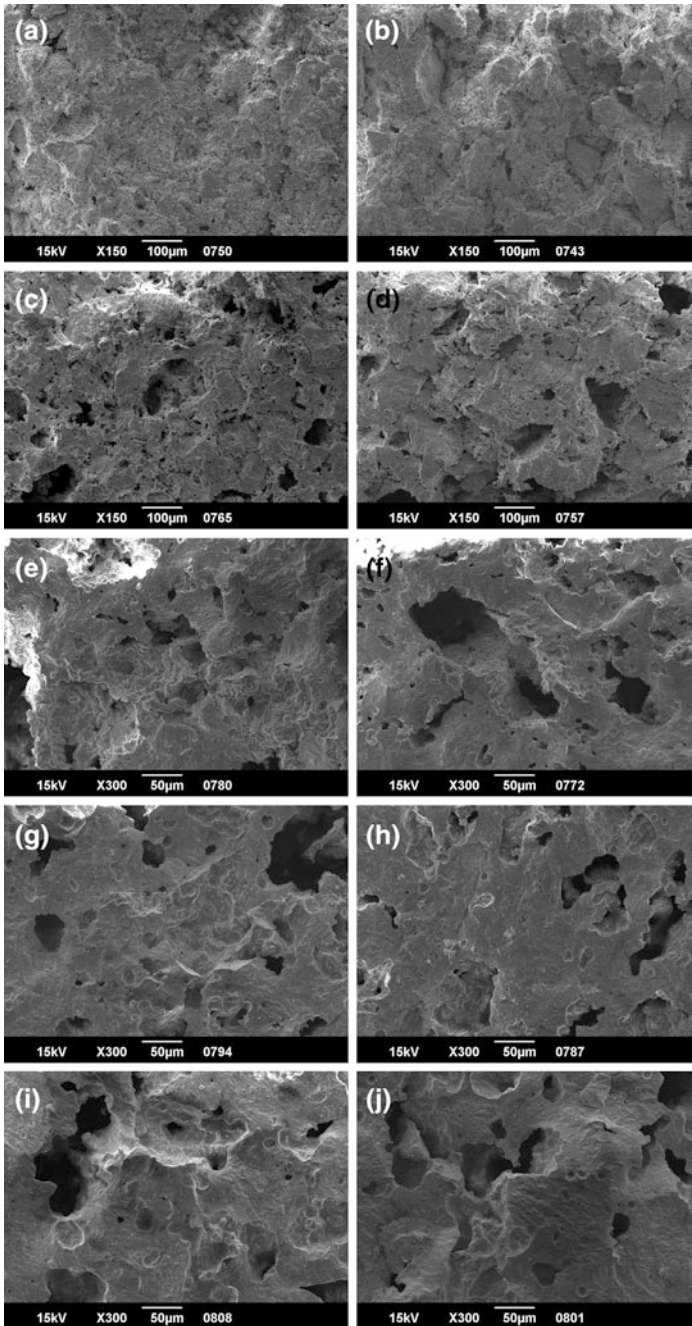


Fig. 14.1 Micrographs of the ZTS-19 FC/clay composite at $m_{cl} = 0.10$ (a, b), 0.20 (c, d), 0.30 (e, f), 0.40 (g, h), and 0.50 (i, j) at room temperature. Micrographs were taken on cuts being either perpendicular (a, c, e, g, and i) or parallel (b, d, f, h, and j) to the poling direction

Table 14.1 Room-temperature experimental values of elastic moduli $c_{db}^{(n),E}$ (in 10^{10} Pa), piezoelectric coefficients $e_{ij}^{(n)}$ (in C/m²) and dielectric permittivities $\epsilon_{pp}^{(n),\xi} / \epsilon_0$ of components

Component	$c_{11}^{(n),E}$	$c_{12}^{(n),E}$	$c_{13}^{(n),E}$	$c_{33}^{(n),E}$	$c_{44}^{(n),E}$	$e_{31}^{(n)}$	$e_{33}^{(n)}$	$e_{15}^{(n)}$	$\epsilon_{11}^{(n),\xi} / \epsilon_0$	$\epsilon_{33}^{(n),\xi} / \epsilon_0$
ZTS-19 FC [3]	10.9	6.1	5.4	9.3	2.4	-4.9	14.9	10.6	820	840
Clay [10, 11]	0.0445	0.0173	0.0173	0.0445	0.0136	0.0136	0	0	8.0	8.0

Table 14.2 Experimental data on ZTS-19 FC/clay composite samples

m_{cl}	$D, 10^{-3} \text{ m}$	$h, 10^{-3} \text{ m}$	$V, 10^{-6} \text{ m}^3$	$m, 10^{-3} \text{ kg}$	$\rho^*, 10^3 \text{ kg/m}^3$	$C_0, \text{ pF}$
0.05	22.87	7.77	3.19	17.5	5.48	88
0.10	22.80	7.65	3.12	16.7	5.35	73
0.15	22.88	7.48	3.07	16.0	5.21	62
0.20	22.80	7.34	3.00	15.1	5.03	52
0.25	22.81	7.22	2.95	14.6	4.95	43
0.30	22.76	7.06	2.87	13.8	4.81	38
0.35	22.68	6.94	2.80	13.1	4.68	30
0.40	22.60	6.70	2.68	12.4	4.63	27
0.45	22.73	6.73	2.73	11.8	4.32	22
0.50	22.60	6.56	2.63	11.1	4.22	19
m_{cl}	$\text{tg}\delta$	M_u	M_q	$f_r, \text{ kHz}$	$f_a, \text{ kHz}$	k_e
0.05	0.034	277.0	27.0	92.60	99.20	0.268
0.10	0.012	209.0	16.5	132.83	133.26	0.164
0.15	0.012	128.0	8.4	140.50	162.80	0.094
0.20	0.011	120.0	6.4	180.98	182.21	0.095
0.25	0.021	93.0	6.6	201.60	202.50	0.070
0.30	0.011	61.7.0	2.5	213.36	213.98	0.052
0.35	0.013	41.0	1.2	229.50	230.00	0.037
0.40	0.009	–	–	236.49	237.22	0.014
0.45	0.016	–	–	245.70	246.30	0.019
0.50	0.012	–	–	252.36	253.01	0.020

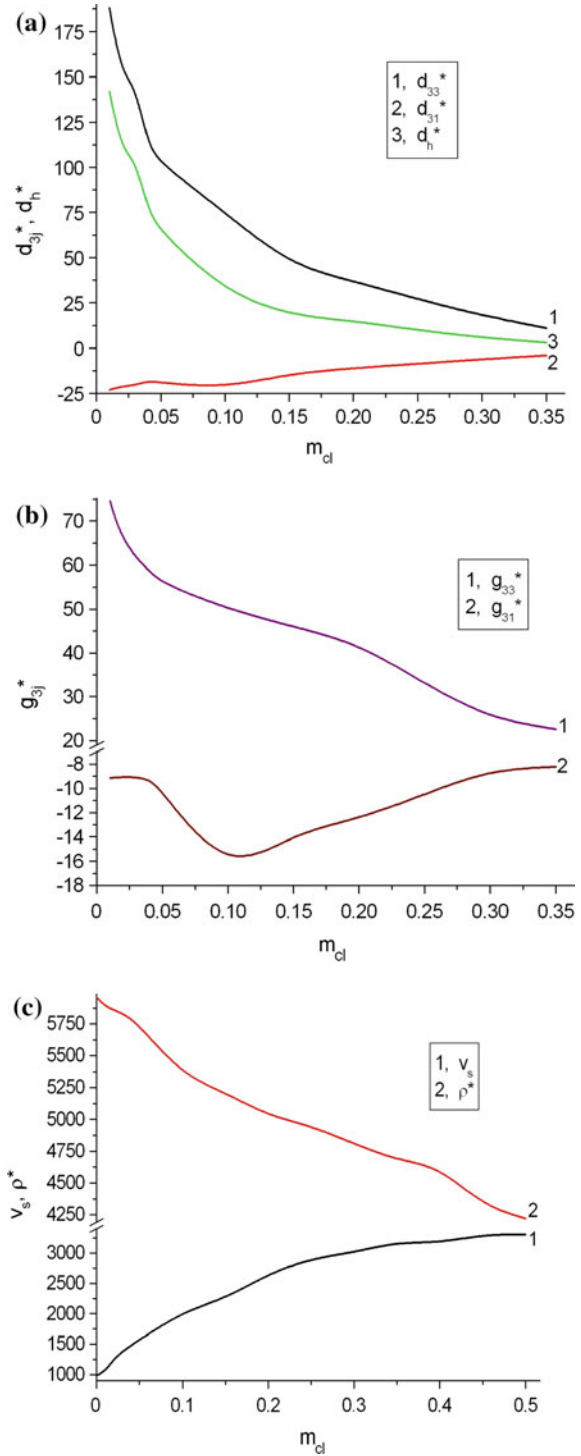
antiresonance frequency f_a , and effective electromechanical coupling factor k_e . It is seen that M_u , M_q and k_e decrease with increasing the volume fraction of clay m_{cl} .

Micrographs of the poled composite samples (Fig. 14.1) were taken using JEOL JSM-6390LA Analytical Electron Microscope. The micrographs shown in Fig. 14.1 suggest that an evolution of the microgeometry is observed, and at increasing m_{cl} , FC regions distributed continuously along the poling direction become rare. Pores are distributed over the samples fairly evenly. An interface separating the FC and clay components becomes less distinct at increasing the volume fraction m_{cl} .

Experimental data from Fig. 14.2a, b show that the longitudinal piezoelectric effect (d_{33}^* or g_{33}^* measured along the poling axis OX_3) strongly depends on the volume fraction of clay m_{cl} , and an unusual combination of the monotonic $d_{33}^*(m_{cl})$ and non-monotonic $d_{31}^*(m_{cl})$ dependencies is observed. This is due to considerable changes in the microgeometry of the composite at relatively small volume fractions m_{cl} . In our opinion, these changes would influence electromechanical interaction between the adjacent regions of the composite sample on the non-polar direction OX_1 .

The monotonic $g_{33}^*(m_{cl})$ and non-monotonic $g_{31}^*(m_{cl})$ dependencies (Fig. 14.2b) are mainly caused by changes in $d_{3j}^*(m_{cl})$ (Fig. 14.2a), while dielectric permittivity $\epsilon_{33}^{*\sigma}(m_{cl})$ remains monotonic. The $d_{33}^*(m_{cl})$ dependence (Fig. 14.2a) strongly influences the hydrostatic piezoelectric coefficient $d_h^*(m_{cl})$ from (14.1), and the large

Fig. 14.2 Experimental dependence of piezoelectric coefficients d_{3j}^* and d_h^* (**a** in pC/N), g_{3j}^* (**b** in mV · m/N), sound velocity v_s (in m/s) and density ρ^* (in kg/m³) on the volume fraction of clay m_{cl} in the composite based on ZTS-19 FC (reprinted from Filippov et al. [9], with permission from Taylor and Francis)



piezoelectric anisotropy of the composite (i.e., $5.4 < d_{33}^*/|d_{31}^*| < 8.2$) is observed at $0.01 \leq m_{cl} \leq 0.05$. Such a performance of the composite means, that changes in its microgeometry at small volume fractions m_{cl} lead to drastic changes in the piezoelectric effect. Incorporation of small portions of piezo-passive clay into the FC medium may impede the poling of the composite sample as a whole and lead to a considerable decrease of its piezoelectric coefficients $|d_{3j}^*|$. In graphs of Fig. 14.2a, b, we do not show parameters at $m_{cl} > 0.35$ because of the weak piezoelectric effect, i.e., inequalities $d_{33}^*(m_{cl}) < 10$ pC/N and $|d_{31}^*(m_{cl})| < 4$ pC/N are valid. The small values of $|d_{3j}^*|$ from Fig. 14.2, a correlate with small M_u , M_q and k_e from Table 14.2.

The sound velocity v_s measured on the poling direction increases by about three times while the density ρ^* decreases by about 1.4 times. For the disk-shaped composite sample with electrodes perpendicular to the poling axis OX_3 , the relation [2]:

$$v_s = (c_{33}^{*D}/\rho^*)^{1/2} \quad (14.2)$$

holds, and therefore, the elastic modulus $c_{33}^{*D}(m_{cl})$ related to the poling direction plays the key role in the formation of v_s .

As follows from our evaluations using (14.2) and Fig. 14.2c, $c_{33}^{*D}(m_{cl})$ increases by about seven times with increasing m_{cl} from 0.01 to 0.50 [9]. This performance of the composite is concerned with porosity of the FC component even at small values of m_{cl} and with the important role of a stiff FC framework at increasing m_{cl} . Moreover, relatively small values of $c_{33}^{*D}(m_{cl}) = (0.66-1.42) \cdot 10^{10}$ Pa at $0.01 < m_{cl} < 0.05$ and the value of $c_{33}^{(1),D} = 1.23 \cdot 10^{11}$ Pa (as evaluated using data from Table 14.1 on monolithic ZTS-19 FC and conventional formulae [12] for piezoelectric media) enable us to conclude that porosity of the composite is to be taken into consideration. The $c_{33}^{*D}(m_{cl})$ dependence increases relatively slowly: for example, $c_{33}^{*D}(0.50) = 4.63 \cdot 10^{10}$ Pa $< 0.4 c_{33}^{(1),D}$. This means that the effect of porosity may be appreciable even at large volume fractions of clay, for instance, at $m_{cl} \approx 0.5$. We add that various composite samples at $m_{cl} = 0.4$ and 0.5 contain pores, see, e.g., micrographs in Fig. 14.1g-j.

14.3 Prediction of Effective Parameters of the Composite

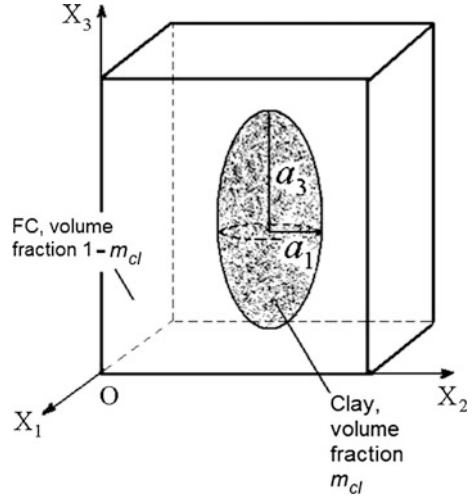
14.3.1 3-0 and 3-1 Connectivity Patterns

Table 14.3 shows examples of the volume-fraction dependence of the piezoelectric coefficients $d_{3j}^*(m_{cl})$ and $g_{3j}^*(m_{cl})$ that were calculated using the finite element method [4] and experimental constants from Table 14.1. The finite element method is applied to a composite comprising a system of aligned spheroidal clay inclusions in a large FC matrix (Fig. 14.3). It is assumed that these inclusions with the volume fraction m_{cl} are regularly distributed over the matrix. Centers of symmetry of the

Table 14.3 Piezoelectric coefficients d_{3j}^* (in pC/N) and g_{3j}^* (in mV · m/N) which have been calculated for the clay/ZTS-19 FC composite with spheroidal inclusions by means of the finite element method

m_{cl}	d_{31}^*	d_{33}^*	g_{31}^*	g_{33}^*
$\rho_i = 0$ (3-1 composite)				
0.01	-126	307	-9.63	23.4
0.03	-126	307	-9.83	23.9
0.05	-126	307	-10.0	24.4
0.10	-126	307	-10.6	25.7
0.15	-126	307	-11.2	27.2
0.20	-126	306	-11.9	28.9
0.30	-126	306	-13.5	33.0
0.40	-126	306	-15.7	38.4
0.50	-125	305	-18.8	45.9
$\rho_i = 0.1$ (3-0 composite)				
0.01	-126	307	-9.62	23.4
0.03	-125	307	-9.78	23.9
0.05	-124	306	-9.73	24.5
0.10	-121	305	-10.3	26.0
0.15	-117	303	-10.7	27.8
0.20	-113	302	-11.2	29.9
0.30	-106	300	-12.3	35.0
0.40	-93.9	295	-13.6	42.9
0.50	-87.8	294	-14.4	48.1
$\rho_i = 0.5$ (3-0 composite)				
0.01	-126	307	-9.61	23.5
0.03	-125	307	-9.76	24.1
0.05	-123	306	-9.91	24.7
0.10	-119	305	-10.3	26.4
0.15	-114	304	-10.7	28.3
0.20	-109	302	-11.1	30.6
0.30	-99.2	298	-12.1	36.2
0.40	-88.2	294	-13.3	44.2
0.50	-82.1	293	-13.9	49.6
$\rho_i = 1$ (3-0 composite)				
0.01	-125	307	-9.60	23.5
0.03	-123	306	-9.73	24.2
0.05	-121	306	-9.85	25.0
0.10	-115	305	-10.2	27.0
0.15	-109	303	-10.5	29.2
0.20	-104	301	-10.9	31.7
0.30	-92.9	297	-11.8	37.6
0.40	-82.1	292	-12.9	45.9
0.50	-69.5	288	-14.3	59.3

Fig. 14.3 Schematic of the 3–0 clay/FC composite with spheroidal inclusions. (X_1 X_2 X_3) is the rectangular co-ordinate system, a_i are semi-axes of the spheroid



inclusions occupy sites of a simple lattice with unit-cell vectors parallel to the OX_j axes shown in Fig. 14.3. Each inclusion is characterized by semi-axes a_1 , $a_2 = a_1$ and a_3 , and $\rho_i = a_1/a_3$ is the aspect ratio of the inclusion. The remanent polarization vector of the FC matrix is parallel to the OX_3 direction. The composite shown in Fig. 14.3 is described by 3–0 connectivity in terms of [3]. In a limiting case of $\rho_i = 0$, the composite is characterized by 3–1 connectivity.

The COMSOL package [13] is applied to obtain the volume-fraction dependence of the effective electromechanical properties of the 0–3 composite within the framework of the FEM. A representative unit cell, containing the spheroidal inclusion with $\rho_i = \text{const}$ and a radius adjusted to yield the appropriate volume fraction m_{cl} , is discretized using tetrahedral elements [4]. The unknown displacement and electric-potential fields are interpolated using linear Lagrangian shape functions. Periodic boundary conditions are enforced on the boundary of the representative unit cell. The matrix of effective constants of the composite is computed column-wise, performing calculations for diverse average strain and electric fields imposed to the structure. The Geometric Multigrid [14] iterative solver (V-cycle, successive over-relaxation pre- and post-smoother, direct coarse solver) is employed. After solving the electroelastic equilibrium problem, the effective electromechanical constants of the composite (Fig. 14.3) are computed, by averaging the resulting local stress and electric-displacement fields over the representative unit cell ‘inclusion—matrix’.

Data from Table 14.3 suggest that values of $|d_{3j}^*(m_{cl})|$ are a few times larger than those shown in Fig. 14.2, a for the same m_{cl} range. Values of the piezoelectric coefficient $g_{33}^*(m_{cl}) = d_{33}^*(m_{cl})/\epsilon_{33}^{*\sigma}(m_{cl})$ that describes the piezoelectric sensitivity along the poling axis, are larger than those measured for small volume fractions m_{cl} (see curve 1 in Fig. 14.2b). At the same time, values of the piezoelectric coefficient

$g_{31}^*(m_{cl}) = d_{31}^*(m_{cl})/e_{33}^{*\sigma}(m_{cl})$ are comparable to those shown in Fig. 14.2b (see curve 2). We add that the relation

$$d_{33}^*(m_{cl}) \approx d_{33}^{(1)} \tag{14.3}$$

is valid in a case [3], when a continuous distribution of the piezoelectric component along the poling axis OX_3 takes place.

As follows from Table 14.3, the piezoelectric coefficient $d_{31}^*(m_{cl})$ undergoes appreciable changes if to substitute the cylindrical clay inclusions ($\rho_i = 0$, composite with 3–1 connectivity) with the spherical clay inclusions ($\rho_i = 1$, composite with 3–0 connectivity). This is accounted for by the more active influence of the spherical clay inclusion on the transversal piezoelectric effect in comparison to the cylindrical inclusion. The internal mechanical and electric fields that appear in the presence of the spherical piezo-passive inclusion weaken the piezoelectric activity of the 3–0 composite along OX_1 and OX_2 more strongly than in the case of the related 3–1 composite. However, the continuous distribution of the FC component along OX_3 (see Fig. 14.3) promotes the large piezoelectric coefficient d_{33}^* that obeys (14.3) in the wide volume-fraction range for both the 3–0 and 3–1 composites.

14.3.2 Two Types of Layers in a Composite Sample

Changes in the piezoelectric activity and sensitivity of the two-component composite described in Sect. 14.3.1 give rise to a question on a role of clay interlayers that may appear in samples at various volume fractions m_{cl} . Now we consider a system of the clay/FC and air/clay layers (Fig. 14.4) which form the composite

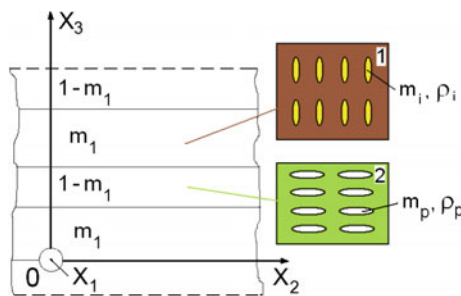


Fig. 14.4 Schematic of the composite with series-connected heterogeneous layers. m_1 is the volume fraction of FC/clay layers (layers of the 1st type), and $1 - m_1$ is the volume fraction of porous clay layers (layers of the 2nd type). In *inset 1*, m_i is the volume fraction of clay inclusions in the FC matrix, and $\rho_i = a_1/a_3$ is the aspect ratio of clay inclusions with semi-axes a_i . In *inset 2*, m_p is the volume fraction of air inclusions in the clay matrix, and $\rho_p = a_{1,p}/a_{3,p}$ is the aspect ratio of air inclusions with semi-axes $a_{i,p}$ (reprinted from Filippov et al. [9], with permission from Taylor and Francis)

sample. Herewith it is assumed that these layers (see insets 1 and 2 in Fig. 14.4) are elastically matched, and interfaces are perpendicular to the OX_3 axis. This axis is regarded as a poling axis for the composite sample as a whole. The presence of spheroidal inclusions in each layer enables us to vary the elastic and dielectric properties of the layers and composite.

Effective electromechanical properties of the composite are consecutively evaluated by means of the finite element method [4] (3–0 structure, see inset 1 in Fig. 14.4), dilute approach [3, 4] (3–0 structure, see inset 2 in Fig. 14.4) and matrix method [3] (2–2 structure of layers alternating along OX_3 , see Fig. 14.4) on assumption that the inclusions and layers are distributed regularly over the composite sample. The effective properties of the composite are considered as functions of ρ_i and m_i (from the clay inclusion), and ρ_p and m_p (from the air pore). An optimization of these properties may represent an independent task.

The presence of the FC matrix in the clay/FC layer promotes the high piezoelectric activity at various volume fractions m_i and aspect ratios ρ_i (Table 14.4). The piezo-passive porous clay layer with relatively low elastic moduli leads to considerable weakening the electromechanical interaction between the piezo-active clay/FC layers. As a result, the piezoelectric activity of the composite becomes lower, but its piezoelectric sensitivity remains relatively high due to relatively small dielectric permittivity $\epsilon_{33}^{*\sigma}$. We underline that even at fairly small volume fractions of the porous layers $1 - m_1 \approx 0.01$, the piezoelectric activity of the composite is restricted (see data on d_{3j}^* in Table 14.4) in comparison to that from Table 14.3.

Table 14.4 Calculated and experimental parameters of the composite based on ZTS-19 FC

m_i	m_{cl}	d_{33}^* , pC/N	d_{31}^* , pC/N	$\epsilon_{33}^{*\sigma}/\epsilon_0$	g_{33}^* , mV · m/N
At $\rho_i = 0.1$, $m_i = 0.40$, $\rho_p = 100$, and $m_p = 0.40$					
0.93	0.414	11.0	-3.66	30.4	41.0
0.95	0.410	15.4	-5.04	41.8	41.5
0.97	0.406	25.1	-8.11	67.3	42.1
Exp.	0.35	11	-4.0	58	21
At $\rho_i = 0.1$, $m_i = 0.30$, $\rho_p = 100$, and $m_p = 0.40$					
0.95	0.315	12.7	-4.61	42.3	34.0
0.97	0.309	20.8	-7.47	68.4	34.4
0.99	0.303	55.4	-19.6	180	34.8
Exp.	0.30	18	-6.1	75	27
Exp.	0.25	27	-8.6	86	36
At $\rho_i = 0.1$, $m_i = 0.20$, $\rho_p = 100$, and $m_p = 0.40$					
0.95	0.220	10.9	-4.21	42.5	29.1
0.97	0.212	18.0	-6.84	69.2	29.4
0.99	0.204	48.7	-18.3	185	29.7
Exp.	0.20	37	-11	106	39
Exp.	0.15	46	-14	128	41

Note that experimental values (in lines denoted 'Exp. ') are related to the volume fraction of clay m_{cl} given in the 2nd column (reprinted from Filippov et al. [9], with permission from Taylor and Francis)

The model shown in Fig. 14.4 and data from Table 14.4 enable us to emphasize the important role of clay interlayers in forming the piezoelectric effect in the studied composite. For example, small changes in the volume fraction m_1 (from 0.95 to 0.99) give rise to appreciable changes in d_{3j}^* and $e_{33}^{*\sigma}$, however these changes do not influence g_{33}^* considerably. Undoubtedly, such a performance is of interest for piezoelectric sensor applications.

Some differences between the predicted and experimental values shown in Table 14.4 may be concerned with specifics of the orientation of the above-considered layers and their complicated microgeometry in real composite samples as well with an incomplete poling of the composite sample because of the presence of the piezo-passive clay-containing layers with low dielectric permittivity. Moreover, technological factors concerned with mixing the components and temperature regimes at manufacturing the composite sample are also taken into consideration.

The studied composite shows an advantage over the well-known highly anisotropic PbTiO₃-type FCs [3, 15]. For instance, at volume fractions of clay $m_{cl} < 0.15$, the larger values of the piezoelectric coefficients d_{33}^* and d_h^* are achieved in comparison to the PbTiO₃-type FCs, and values of the piezoelectric coefficient g_{33}^* of the studied composite are comparable to g_{33} of these FCs. We remind that this performance of the composite is achieved at relatively small volume fractions of clay m_{cl} therein.

14.4 Conclusions

The novel clay-containing piezo-active composite is characterized as a material with the high piezoelectric sensitivity ($g_{33}^* > 50 \text{ mV} \cdot \text{m/N}$), the large anisotropy of the piezoelectric coefficients d_{3j}^* ($5.4 < d_{33}^*/|d_{31}^*| < 8.2$) at $0.01 \leq m_{cl} \leq 0.05$, and with the considerable variation of the sound velocity v_s (Fig. 14.2) measured along the poling direction OX_3 . The composite microgeometry (Fig. 14.1) is complicated and puzzling, however one can emphasize the effect of clay-containing layers on the electromechanical interaction between piezoelectric regions in the composite sample and on its effective piezoelectric properties. This effect becomes pronounced with increasing the volume fraction m_{cl} , and the aforementioned layers can weaken the piezoelectric activity of the composite. Moreover, results of our calculations performed using a few methods in the wide m_{cl} range are consistent with this conclusion.

Of interest is the volume-fraction range $0.01 \leq m_{cl} \leq 0.05$ where considerable changes in the piezoelectric activity and sensitivity are observed. Our experimental data show that the piezoelectric effect remains appreciable in samples at $0.01 \leq m_{cl} \leq 0.35$. The influence of the porous structure and clay component on the piezoelectric performance of the studied composite at $m_{cl} < 0.15$ leads to a set of its effective parameters that have an advantage over the well-known highly anisotropic PbTiO₃-type FCs. First of all, it concerns the larger values of d_{33}^* and d_h^* , while g_{33}^*

is comparable to g_{33} related to the PbTiO_3 -type FCs. The set of the studied effective parameters of the composite can promote its use in sensor, hydroacoustic and other piezo technical applications.

Acknowledgments The authors thank Prof. Dr. C.R. Bowen (University of Bath, UK), Prof. Dr. S.-H. Chang (National Kaohsiung Marine University, Taiwan, ROC), Prof. Dr. I.A. Parinov, Prof. Dr. A.A. Nesterov, and Dr. V.V. Eremkin (Southern Federal University, Russia) for their continuing interest in the research problems. The research subject is concerned with the Programme Supporting the Research at the Southern Federal University (Russia). In the present chapters, the results on the research work No. 11.1302.2014/K have been represented within the framework of the project part of the state task in the scientific activity area at the Southern Federal University.

References

1. E.K. Akdogan, M. Allahverdi, A. Safari, IEEE Trans. Ultrason. Ferroelec. Freq. Contr. **52**, 746 (2005)
2. H. Taunamang, I.L. Guy, H.L.W. Chan, J. Appl. Phys. **76**, 484 (1994)
3. V.Yu. Topolov, C.R. Bowen, *Electromechanical Properties in Composites Based on Ferroelectrics* (Springer, London, 2009)
4. V.Yu. Topolov, P. Bisegna, C.R. Bowen, Ferroelectrics **413**, 176 (2011)
5. A. Chaipanich, Curr. Appl. Phys. **7**, 532 (2007)
6. Z. Li, D. Zhang, K. Wu, J. Am. Ceram. Soc. **85**, 305 (2002)
7. S. Huang, J. Chang, R. Xu, F. Liu, L. Lu, Z. Ye, X. Cheng, Smart Mater. Struct. **13**, 270 (2004)
8. B. Dong, Z. Li, Comp. Sci. Tech. **65**, 1363 (2005)
9. S.E. Filippov, A.A. Vorontsov, V.Yu. Topolov, O.E. Brill, P. Bisegna, A.E. Panich, Ferroelectrics Lett. Sec. **41** (4–6), 82 (2014)
10. J.E. Bowles, *Foundation Analysis and Design* (McGraw-Hill, New York, 1996)
11. V.L. Balkevich, *Technical Ceramics* (Stroyizdat, Moscow, 1996, in Russian)
12. T. Ikeda, *Fundamentals of Piezoelectricity* (Oxford University Press, Oxford, New York, and Toronto, 1990)
13. COMSOL, Inc. COMSOLMultiphysics™ User's Guide (version 4.4, 2014), <http://www.comsol.com>
14. W. Hacksbusch, *Multi-grid Methods and Applications* (Springer, Springer, Berlin, 1985)
15. S. Ikegami, I. Ueda, T. Nagata, J. Acoust. Soc. Am. **50**, 1060 (1971)

Chapter 15

Advanced Functional Materials: Modeling, Technology, Characterization, and Applications

A.N. Rybyanets

Abstract A review of microstructure peculiarities, mathematical models, methods of fabrication and measurements, as well as systematic experimental data for different types of ceramic matrix piezocomposites is present. New families of polymer-free ceramic matrix piezocomposites (porous piezoceramics, composites ceramics/ceramics and ceramics/crystals) with properties combining better parameters of PZT and PN type ceramics, and 1–3 composites are introduced. Experimental results for different porous piezoceramics with various connectivity types are present. New “damped by scattering” ceramic matrix piezocomposites, characterized by previously unachievable parameter combinations are described. New material designing concept and methods of fabrication for ceramic matrix piezocomposites are considered. Piezoelectric resonance analysis methods for automatic iterative evaluation of complex material parameters, together with the full sets of complex constants for different ceramic matrix piezocomposites are present. Critical comparison of FEM calculations of effective constants for the ceramic piezocomposites with the results of various mathematical models, approximated formulae, unit cell models and experimental data are carried out.

15.1 Introduction

Limited transducer materials are currently available for use in ultrasonic transducer design in non destructive testing (NDT) and medical diagnostics systems, considering combinations of high sensitivity (efficiency), resolution (bandwidth) and operational requirements (working temperature). There are currently no commercially available piezoceramic materials that offer high piezoelectric properties together with low Q , low acoustic impedance, electromechanical anisotropy and

A.N. Rybyanets (✉)
Institute of Physics, Southern Federal University, 194 Stachky Ave.,
Rostov-on-Don 344090, Russia
e-mail: arybyanets@gmail.com

high operating temperatures ($>250\text{ }^{\circ}\text{C}$) [1]. Those that are available offer either high piezoelectric properties (lead zirconate titanate—PZT, lead magnesium and zinc niobates—PMN, PZN) or high electromechanical anisotropy (lead titanate—PT) and low Q , low acoustic impedance (lead metaniobate—PN) [2].

To date, practically all broadband transducers are based on strongly externally damped PZT or lead metaniobate (PN) ceramics. PN ceramics show the better properties ($Q'_M \sim 8$, $Z_A \sim 18$) and are widely used at high temperatures, but the piezoelectric properties of PN are weak. In addition, PN is very difficult for mass production, and it reflects in its relatively high cost. Therefore, efforts have been made to replace lead metaniobate by 1–3 piezocomposite materials. However, to date the production costs of these components well exceeds the common price of a complete standard transducer. Moreover, there are considerable technical limitations with this type of transducer, in particular, with respect to the maximum allowable ambient temperature and pressure [1].

Porous piezoceramics based on different piezoceramic compositions were proposed as a promising candidate for PN replacement in wide-band ultrasonic transducers [3, 4]. Despite their long history and unique characteristics, so far porous piezoelectric ceramics have not been commercialized and their application in transducers and devices is limited [2–4]. Intensive research and technological work, as well as improvements in fabrication methods, have allowed large-scale manufacture of porous piezoelectric ceramics with reproducible and controllable porosity and properties [2, 5]. To date, PZT-type compositions are mainly used as initial materials for porous piezoelectric ceramics manufacturing [2, 3]. Other ceramic systems were not investigated as porous piezoelectric ceramics owing to high initial anisotropy, low piezoelectric activity and other technological difficulties inherent for ceramic compositions of these systems. With growing demand for piezoceramics for advanced piezoelectric applications alongside with increasing operational requirements [1], PT and PN porous piezoelectric ceramics are of considerable interest in both scientific research and practical applications. Recently [2, 6], the manufacturing technology for PT and PN porous piezoelectric ceramics with reproducible properties was developed.

Over the past years, considerable advances have been made to improve the mechanical properties of ceramics using ceramic composite approaches. Numerous technologies based on incorporation of functional ceramics into structural ones and vice versa have been developed, and novel design ideas have applied in the field of functional ferroelectric ceramics [7, 8]. However, the problem of property trade-off, i.e., the deterioration of electromechanical properties, remains unsolved. Commercialization of composite materials has lead also to the development of new concepts of material and ultrasonic transducers designing [9]. Meanwhile, demands on medical and NDT ultrasonic transducer performance have increased in recent years. Meeting these market demands requires the development of new piezoelectric materials and improved manufacturing methods.

This chapter presents a review and critical comparison of different mathematical models, methods of measurements and fabrication technologies, as well as

systematic experimental data for different types of new, polymer-free ceramic matrix piezocomposites (porous piezoceramics, composites ceramics/ceramics and ceramics/crystals).

15.2 Microstructural Design Concept for Polycrystalline Composite Materials

The original microstructural design concept (MSD) for these materials was proposed in [9]. The MSD concept offers a brand-new range of polymer-free polycrystalline piezocomposite materials with parameters that are adjustable over a wide range. The MSD concept is based on controllable substitution during composite formation of separate crystallites or crystallite groups making a polycrystal by pores, crystallites with other composition and/or structure, or amorphous substances, all with preliminary choice of chemically, thermally and technologically compatible components and with FEM modeling of polycrystalline composite properties. The distinctive peculiarities of the MSD concept is the transition to a microscale level of separate crystallites and the use of the full set of technological approaches at particular stages of synthesis, preparation of initial materials (powders, solutions, suspensions, gels), granulation and compacting of a green bodies, sintering and the-post sintering treatment of a composites.

The MSD concept offers an innovative range of polymer-free polycrystalline piezocomposite materials with properties combining better parameters for PZT, PMN, PN and PT type ceramics and 1–3 composites. The developed MSD technology is suitable for large-scale production and characterized by low cost for produced polycrystalline composites. Preliminary validation of the MSD concept was carried out over several years. Initially, a line of small-scale production technologies and polycrystalline composites with unique and reproducible properties (micro-, meso- and macroporous ferroelectric ceramics, ferroelectric ceramics/ceramics and ceramic/crystal composites, ferroelectric/engineering ceramics composites etc.) was developed and systematically studied as precursors to the actual piezocomposite materials.

The following polycrystalline composites were fabricated and tested:

- i. PZT/BeO ceramic/ceramic composites with extremely high thermoconductivity for high-intensity ultrasonic applications;
- ii. PZT/ α -Al₂O₃ ceramic/monocrystal composites with high wear resistance, mechanical strength and excellent electromechanical properties for high frequency (NDT) applications;
- iii. (Na, Li)NbO₃/LiNbO₃ ceramic/monocrystal composites with low density and high ultrasound velocity for high frequency ultrasonic applications;
- iv. PZT/PZT ceramic/ceramic composites with changeable parameters for a diverse range of piezo- and ultrasonic applications;

- v. PZT/BaTiO₃ insulator/semiconductor ceramics composites with giant dielectric permittivity for condenser applications;
- vi. micro-, meza- and macro- porous piezoceramics (PZT, lead metaniobate, lead titanate, bismuth titanate, lead magnezium niobate, lithium niobate, etc.) with continuously changeable parameters for ultrasonic transducer applications.

Figure 15.1 shows typical optical micrographs of polished and thermally etched surfaces of different types of polycrystalline composites fabricated using MSD technology. The results of elastic, dielectric and piezoelectric constants measurement for several kinds of polycrystalline composites are summarized in Table 15.1.

The full-scale use of the MSD concept will results in a new generation of polycrystalline piezocomposite materials derived from more technologically simple processing, whilst offering preferable properties along with a lower manufacturing cost. At the same time, new types of polycrystalline composites made from electronic, industrial (engineering) and semiconductor ceramics for thermal insulation, filtration, sensing, biomedical and catalyst applications, and also “smart” composite materials for advanced piezoelectric applications will be developed on the base of MSD [10].

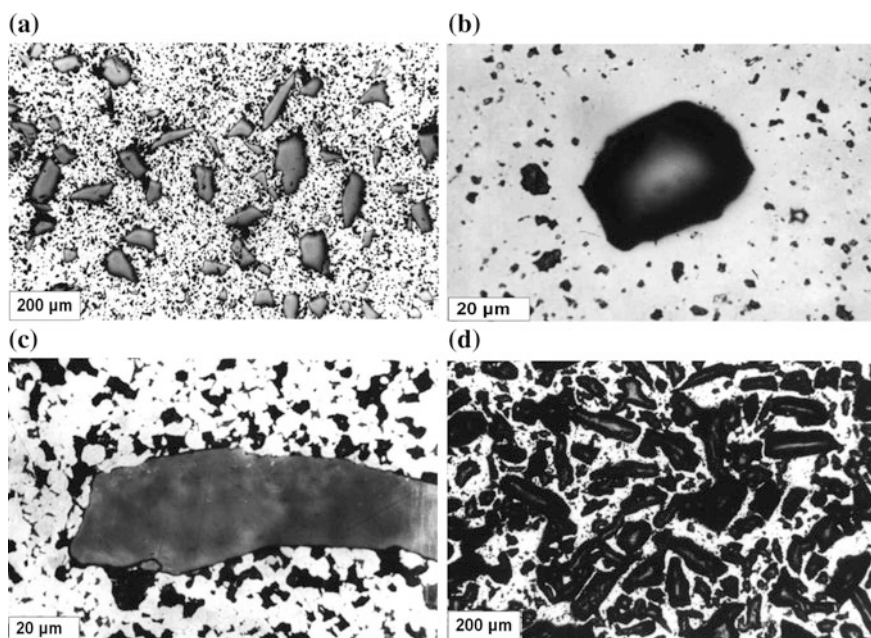


Fig. 15.1 Optical micrographs of polished and thermally etched surfaces of different polycrystalline composites: **a** microporous ceramic/crystal (PZT/ α -Al₂O₃) composites; **b** (Na, Li)NbO₃/LiNbO₃ ceramic/monocrystal composites; **c** mesoporous ceramic/crystal (PZT/coarse α -Al₂O₃) composites; **d** porous PZT ceramics with mixed macro and mesa porosity (relative porosity 60 %)

Table 15.1 Piezoelectric and physical properties of polycrystalline composite materials fabricated using MSD technology

Parameter/material	PbNb ₂ O ₆ (porosity 15 %)	PZT/ α - Al ₂ O ₃	(Na, Li)NbO ₃ / LiNbO ₃	PZT porous piezoceramics
k_p	0	0	0.2	0–0.2
k_t	0.4	0.54	0.58	0.55–65
d_{33} (10^{-12}), C/N	65	240	100	100–700
$\varepsilon_{33}^T/\varepsilon_0$	160	400	120	100–6,000
$\tan\delta$, %	0.6	2	2	0.2–3
Q_M^T	<10	2–3	30	5–20
ρ (10^3), g/cm ³	5.7	6	4.5	3–7
T_C , °C	560	340	350	150–350
N_r , kHz mm	1,300	1,500	2,500	500–1,600

15.3 Impedance Spectroscopy Characterization of Highly Attenuating Piezocomposites

Demands on medical and NDT ultrasonic transducer performance have increased in recent years. Low- Q piezoceramics and piezocomposite materials are widely used for wide-band NDT ultrasonic transducers with high sensitivity and resolution. Some of these advanced materials are lossy, and direct use of IEEE Standards for material constant determination leads to significant errors. The modeling and design of piezoelectric devices by finite element methods, among others, rely on the accuracy of the dielectric, piezoelectric and elastic coefficients of the active material used which is, commonly, an anisotropic ferroelectric polycrystal. The accurate description of piezoceramics must include the evaluation of the dielectric, piezoelectric and mechanical losses, accounting for the out-of-phase material response to the input signal.

The basic techniques for finding material constants of piezoelectric materials are outlined in the IEEE Standard on Piezoelectricity (1987) [11]. These methods work for many of the most widely used commercial piezoceramics based on lead-titanate-zirconate (PZT) compositions that are high- Q_M and high-coupling coefficient piezoelectric materials. However, there is a general agreement that their use in many new piezoelectric materials such as porous piezoceramics, piezoelectric polymers or piezoelectric composites may lead to significant errors. Furthermore, the current IEEE Standard does not comprehensively account for the complex nature of material coefficients, as it uses only the dielectric loss factor ($\tan \delta$) and the mechanical quality factor (Q_M) to account for loss.

Numerous techniques using complex material constants have been proposed to take into account losses in low- Q_M materials and to overcome limitations in the IEEE Standard [12–15]. Iterative methods [14] provide a means to accurately determine the complex coefficients in the linear range of poled piezoceramics from complex

impedance resonance measurements. The piezoelectric resonance analysis program (PRAP) automatic iterative method [16] has been applied [17–19] to the full set of standard geometries and resonance modes needed to complete complex characterization in a wide range of materials with very high and moderate loss factors.

15.4 Porous Piezoceramics

The microstructure of porous ceramics is unequivocally defined by the fabrication method and by the initial chemical composition of the piezoceramic phase [2, 4]. It is necessary also to note a qualitative structural aspect that distinguishes porous piezoceramics from other commixture and periodic composites, namely, the presence of a rigid three-dimensional ceramic skeleton persisting up to relative porosity values of 75–95 %, depending on manufacturing technology.

Figure 15.2 shows micrographs illustrating a micro-structural variety of porous ceramic materials. The resulting elastic, dielectric, and piezoelectric properties of

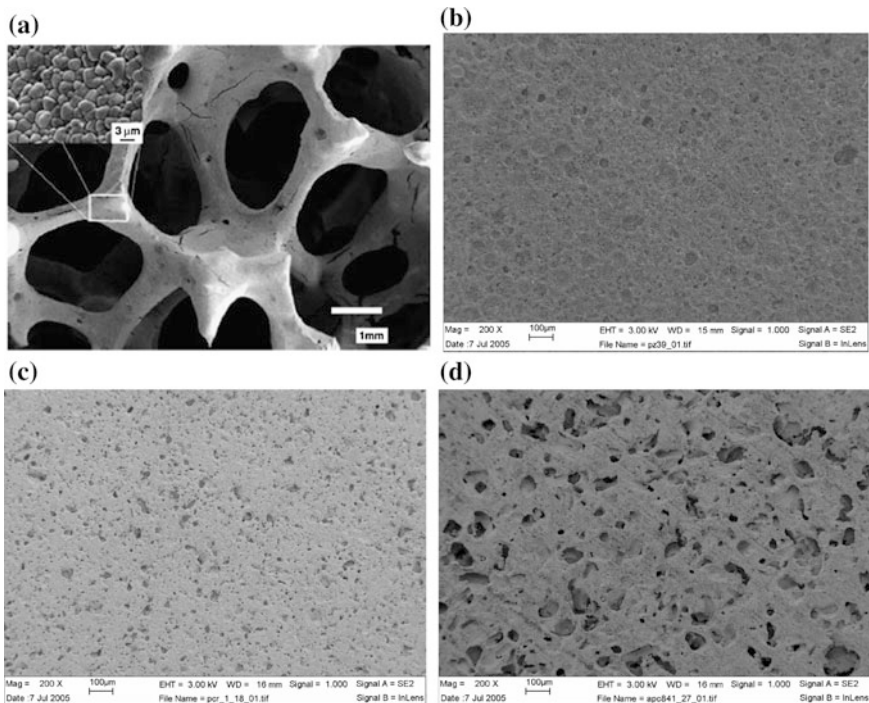


Fig. 15.2 SEM micrographs of different porous piezoceramics structures: **a** open cell PZT ceramics, fabricated by polymer foam method [21]; **b** closed cell PZT ceramics, obtained by burning out polymer granules, **c** ground surface of “soft” PZT ceramics, relative porosity 18 %, **d** ground surface of “hard” PZT ceramics, relative porosity 21 %

porous piezoceramics are defined by the properties of its piezoceramic matrix: that is, the porosity, type of connectivity, shape, and size of pores (and, in the case of irregular shaped pores, by the degree of their primary orientation and arising anisotropy) [2, 20, 21].

All existing methods of porous piezoceramics fabrication can be divided into two basic approaches: subtractive processes and processing limitations. In subtractive processes, certain elements of an original structure are selectively removed to create pores. In processing limitations, technological processing regimes are modified to form porous structures.

A series of technological process for the preparation of porous piezoceramics and composites with 3–0, 3–3 connectivity were subsequently introduced [2–5, 22, 23]: (i) method of burning out of plastic spheres; (ii) method based on washing-out of water-soluble granules; (iii) preparation of hole spheres of PZT by spray drying of alcoxides; (iv) polymer foam method; (v) reaction synthesis method; (vi) cryochemical method; (vii) thermal decomposition of carbonates, nitrates or oxalates, as well as chemical etching and carbon activation; (viii) methods based on differences in shrinkage coefficients of ceramic components, special sintering and pressing regimes, excessing of plasticiser and other processing limiters.

Intensive research and technological works as well as improvements of fabrication methods [2, 5–9] have allowed large-scale manufacture of porous piezoelectric ceramics with reproducible and controllable porosity and properties.

For more than a century, scientists have been seeking ways and means of calculating the permittivity and other material constants of composite bodies from their constituents. Modern statistical theories for calculating the constants of heterogeneous materials that go back to Brown [24] use ensemble averages and postulate that these ensemble averages can be substituted by volume averages (ergodic hypothesis) [4].

Different mathematical models and approximated formulae based on the effective medium approximation were proposed for porous ceramic modeling [2, 4, 24–27]. However, most of them clearly fail to describe important practical application parameters of porous piezoceramics, such as electromechanical coupling factors k_t^* and k_{33}^* , piezoelectric modulus d_{33}^* , and elastic constants C_{33}^{D*} , S_{33}^{D*} . The reason for this is that the formulae derived from isotropic materials, satisfactorily describe only the isotropic and quasi-isotropic properties of porous piezoceramics. At the same time, effective medium approximation presupposes the dimensions of the sample to be very large compared to the microstructure of the ceramics. This requirement is fully met for the radial mode, but obviously fails for thickness and shear vibration modes of porous piezoceramic elements.

Various updates of the effective medium approximation, as well as modern powerful mathematical models were suggested recently for the description of composites and porous piezoceramics [2, 22, 28–30]: unit cell models, models of local stress-strain, minimum solid area (MSA) models, percolation models, fractal analysis, and finite element method (FEM).

Different types of PZT type porous piezoelectric ceramics with 3–0/3–3 connectivity based on ferroelectrically “soft” and “hard” PZT compositions were systematically studied [2, 5–10].

Figures 15.3 compares measured porosity dependencies of piezomoduli d_{33}^* (quasistatic), d_{31}^* and electromechanical coupling factors k_t^* , k_{31}^* and k_{33}^* with the results of FEM modeling, as well as with theoretical results obtained on the base of Marutake’s effective medium approximation, Bruggeman’s formulae and unit-cell models [2, 25, 26]. These experimental data include averages for different types of PZT porous piezoceramics with the same porosity and average pore size (30 μm). Parameters were normalized to corresponding values for dense PZT piezoceramics. The piezoelectric modulus d_{33}^* for porous PZT piezoceramics in porosity range 0–70 % has a minor alteration caused by the continuity of the rigid “quasi-rod” ceramic skeleton in the polarization direction (sample thickness). An increase in measured d_{33}^* are caused by the more complete polarization of porous piezoceramics in comparison with analogous dense piezoceramics. Changes in mechanical stress conditions for a portion of the grains located on pore surfaces can lead to full realization of 90° domain rotations and subsequent freezing in soft PZT porous piezoceramics.

Figure 15.3 clearly shows that FEM calculations taking into account real microstructure of porous piezoelectric ceramics, give the most adequate results, which well agree with the experiment. On the other hand, in view of the matrix structure of porous piezoelectric ceramics, the application of self-consistent methods such as effective medium approximation for porous piezoelectric ceramics calculation, does not satisfactorily describe experimental data.

Figure 15.4 shows domain structure of porous piezoceramics grains in the volume of the sample (a) and inside a pore (b) after polarization and etching [2]. It is obvious, that the grains inside a pore are polarized more completely and a single domain wall variant appears apparently.

A manufacturing technology of porous piezoelectric ceramics, based on pure and modified PT and PN compositions, was developed in [6]. It was also shown [2, 6],

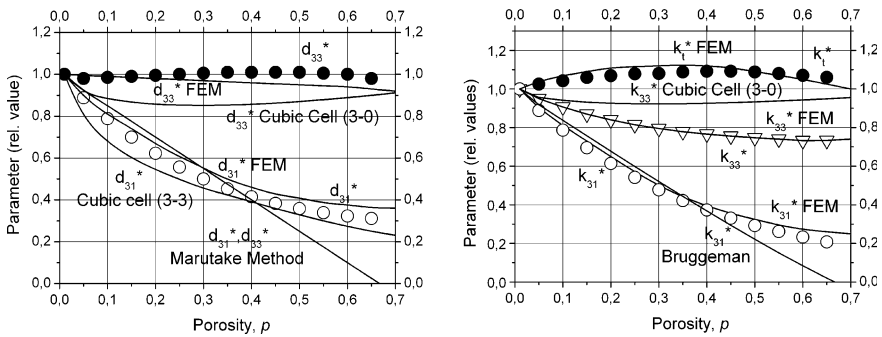


Fig. 15.3 Experimental and calculated piezomoduli and electromechanical coupling factors versus relative porosity for PZT porous piezoceramics

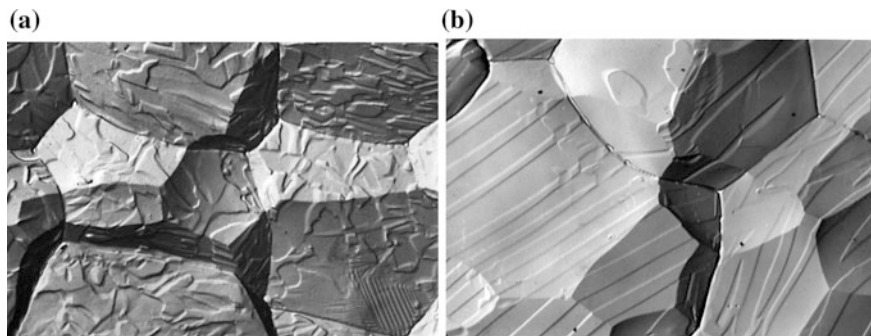


Fig. 15.4 SEM photograph of etched grain structure in the volume of the sample and inside a pore for soft porous PZT ceramics

that the porous piezoceramics technology results in increase of piezoelectric anisotropy and mechanical durability, removal of internal mechanical stress, prevention of cracking and finally, allows production of stable in time elements with excellent and reproducible properties for such “technologically difficult” ceramics as lead titanate and lead metaniobate.

Figure 15.5 shows a typical optical micrograph of polished and thermally etched surfaces of explored porous piezoceramics with different types of porosity. The elastic, dielectric and piezoelectric constants measured for PT and PN porous piezoceramics with optimal porosities are summarized in Table 15.2. It was found that for PT and PN porous piezoceramics (in contrast to PZT-based porous piezoceramics [2, 5]), piezoelectric constant d_{33} and electromechanical coupling factor k_t decrease insignificantly with relative porosity grows.

Lead-free porous piezoceramics based on sodium-potassium niobates $\text{Na}(\text{K}_x, \text{Nb}_{1-x})\text{O}_3$ solid solutions (PCR-34) were also prepared and tested [2, 9]. The porous piezoceramics were prepared by burning out of organic powders. Table 15.3 summarizes the results of elastic, dielectric and piezoelectric constants measurement for lead-free porous piezoceramics with two different relative porosities.

15.5 Ceramic Piezocomposites $\text{PZT}/\alpha\text{-Al}_2\text{O}_3$

New polymer-free ceramic piezocomposites with properties combining better parameters of PZT, PN type ceramics and 1–3 composites for wide-band NDT ultrasonic transducer applications were developed and studied in [5, 7]. These new “damped by scattering” ceramic piezocomposites $\text{PZT}/\alpha\text{-Al}_2\text{O}_3$ were developed based on the original microstructural design concept [9]. They are characterized by previously unachievable low Q_M ($Q_M^f = 2\text{--}3$), combined with high piezoelectric ($d_{33} = 250\text{--}350$) and electromechanical ($k_t = 0.45\text{--}0.5$) parameters, high Curie point ($340\text{ }^\circ\text{C}$), and low acoustic impedance ($15\text{--}20\text{ MRayl}$) in a wide working frequency

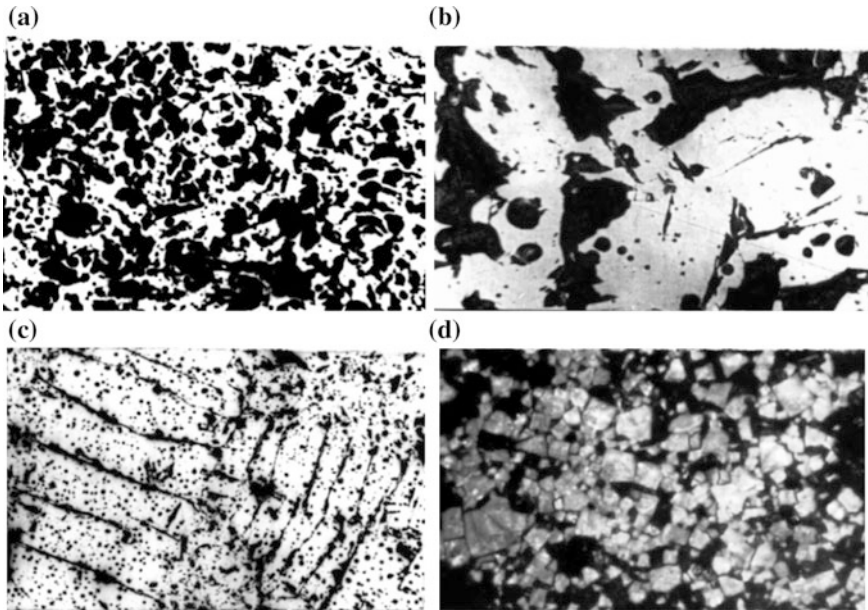


Fig. 15.5 Optical micrographs of polished and thermally etched surfaces of different porous piezoceramics: **a** PbNb_2O_6 porous piezoceramics with mixed macro-, mesa- and micro-porosity ($p = 15\%$); **b** PbNb_2O_6 porous piezoceramics with mixed micro- and mesa-porosity ($p = 15\%$); **c** $(\text{Pb}, \text{K})\text{Nb}_2\text{O}_6$ porous piezoceramics with optimized micro-porosity ($p = 15\%$); **d** PbTiO_3 porous piezoceramics with mixed macro- and mesa-porosity ($p = 25\%$)

Table 15.2 Piezoelectric and dielectric properties of PN and PT based porous piezoceramics

Parameter/material	PbNb_2O_6 , porosity 15 %	$(\text{Pb}, \text{K})\text{Nb}_2\text{O}_6$, porosity 15 %	PbTiO_3 , porosity 25 %	$(\text{Pb}, \text{Ca})\text{TiO}_3$, porosity 25 %
k_p	0	0	0	0
k_t	0.4	0.42	0.50	0.56
d_{33} (10^{-12}), C/N	65	70	50	75
$\varepsilon_{33}^T/\varepsilon_0$	160	160	150	80
$\tan\delta$, %	0.6	0.8	2	2
Q_M^*	<10	<10	<10	<10
ρ (10^3), g/cm^3	5.7	5.6	6	5.6
T_C , °C	560	550	490	325
N_t , kHz mm	1,300	1,380	1,400	1,300

range (0.5–10 MHz). These composites were used to develop a line of wide-band NDT and medical diagnostic ultrasonic transducers with high sensitivity and resolution, which were manufactured and tested [5, 30].

Table 15.3 Piezoelectric and dielectric properties of lead-free porous piezoceramics

Material/parameter	$\frac{T}{\epsilon_{33}/\epsilon_0}$	$\text{tg}\delta$, %	d_{33} , pC/N	$ d_{31} $, pC/N	k_t	k_p	V_t , m/s	Q_M^L	ρ , g/cm ³	Z_A , Mrayl
PCR-34*	310	2.5	102	32	0.52	0.09	3,250	20	2.75	8.93
PCR-34**	200	2.75	98	56	0.51	0.13	4,500	35	3.5	15.75

Note * relative porosity $p = 0.4$; **relative porosity $p = 0.2$

The MSD concept offers a brand-new range of polymer-free polycrystalline piezocomposite materials with parameters that are adjustable over a wide range [9]. Starting from this point, a novel “damping by scattering” approach was proposed in [5, 30] for the development of a new family of low- Q ceramic piezocomposites for wide-band ultrasonic transducer applications. The main idea of the damping by scattering approach is introducing the scattering particles as a secondary phase into the porous piezoceramics matrix during the same technological process. Preliminary optimization of composite properties are fulfilled using the results of single and multiple scattering theories, composite micromechanics and effective medium models, as well as FEM models [5, 7, 30]. Acoustic properties of materials, along with the shape, size, and size distribution, as well as volume fraction of the scattering particles are the main optimization parameters. Different kinds of PZT type piezoceramic powders and stabilized α -Al₂O₃ powders were used as initial components for ceramic composite preparation. Methods of powder preparation, composite sintering and piezocomposite samples fabrication and measurements, as well as technological regimes are described in details in [5, 7].

The composite samples composed of the “soft” PZT matrix and randomly distributed α -Al₂O₃ particles with a mean size ~ 200 μm and volume fraction from 9 up to 26 vol% were chosen for detailed measurements. Optical micrographs of polished surface of PZT/ α -Al₂O₃ sample with 10 and 20 % volume fractions of α -Al₂O₃ particles are shown in Fig. 15.6.

Figure 15.7 shows impedance spectra and PRAP approximations for thickness modes of PZT/ α -Al₂O₃ composite disks at 10 and 20 % volume fraction of α -Al₂O₃ particles, respectively. It shows clearly that at low concentrations of scattering particles, the measured impedance spectrum is modulated by individual scattering events with the period corresponding to the average diameter of scattering particles N . Increase in scattering particles fraction up to 20 vol% leads to smoothing of impedance spectra as a result of multiple scattering averaging.

Complex constants of PZT/20 vol% α -Al₂O₃ composite disk obtained using PRAP analysis for thickness extensional and radial modes as well as corresponding IEEE Standard results, are summarized in Tables 15.4 and 15.5. Additional physical parameters of PZT/20 vol% α -Al₂O₃ composite are as follows: $Z_A = 22.8$ Mrayl, $\rho = 6.4$ g/cm³, $V_t = 3,568$ m/s, $d_{33}^{quasi} = 300$ pC/N, $T_C = 340$ °C. We can summarize the results as follows: optimal materials for extreme damping at reasonable electromechanical parameters are ceramic composites with 15–25 vol% of α -Al₂O₃ particles in soft PZT matrix at λ/D ratio ~ 10 .

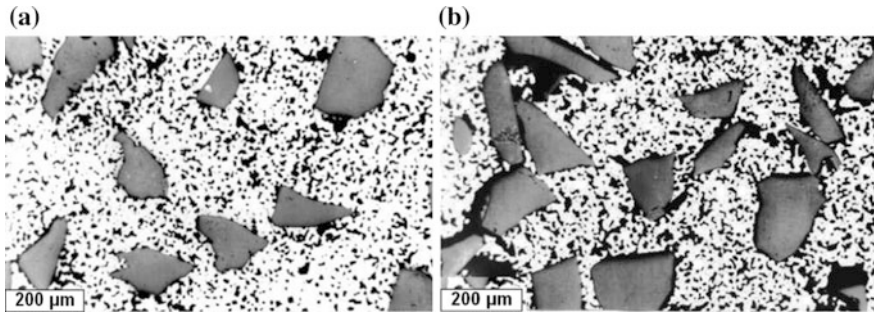


Fig. 15.6 Optical micrographs of polished surface of composite sample with 10 vol% (a) and 20 vol% (b) of α -Al₂O₃ particles

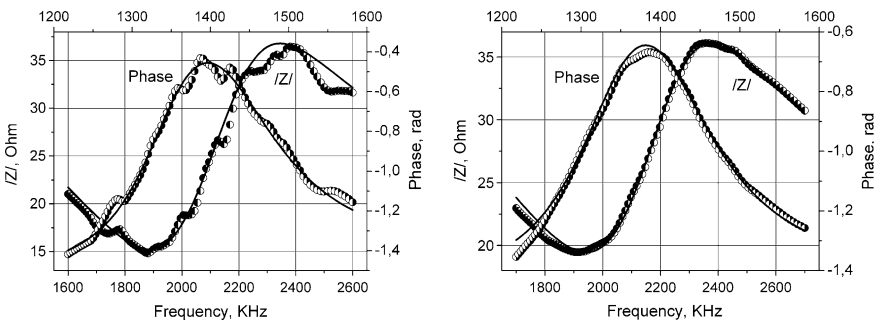


Fig. 15.7 Impedance spectra and PRAP approximations for thickness extensional mode of composite disk ($\varnothing 19.95 \times 0.8 \text{ mm}^2$) with 10 and 20 vol% α -Al₂O₃

Table 15.4 PRAP analysis results for TE mode of PZT/20 vol% α -Al₂O₃ composite disk

PRAP parameter	Real	Imaginary	IEEE standard	% Error
f_p (Hz)	$2.26 \cdot 10^6$	340,289	$2.29 \cdot 10^6$	1.3
f_s (Hz)	$2.01 \cdot 10^6$	304,601	$2.01 \cdot 10^6$	0.0
k_t	0.492734	-0.00138	0.513653	4.3
c_{33}^D (N/m ²)	$8.15 \cdot 10^{10}$	$2.52 \cdot 10^{10}$	$8.58 \cdot 10^{10}$	5.3
c_{33}^E (N/m ²)	$6.17 \cdot 10^{10}$	$1.92 \cdot 10^{10}$	$6.31 \cdot 10^{10}$	2.3
e_{33} (C/m ²)	10.6185	1.31335	-	
h_{33} (V/m)	$1.91 \cdot 10^9$	$3.29 \cdot 10^8$	-	
ϵ_{33}^S (F/m)	$5.52 \cdot 10^{-9}$	$-2.64 \cdot 10^{-10}$	-	

In conclusion, the advantages of ceramic composites are demonstrated with reference to implemented ultrasonic transducers. Figure 15.8 shows pulse echo and transmit-mode characteristics (hydrophone signal) of PZT/ α -Al₂O₃ elements and

Table 15.5 PRAP analysis results for radial mode A850L-20 disk

PRAP parameter	Real	Imaginary	IEEE standard	% Error
f_s^A (Hz)	105,834	1,737.27	106,037	0.2
f_p^A (Hz)	110,947	1,623.38	111,192	0.2
f_s^B (Hz)	275,536	4,522.35	275,194	0.1
S_{11}^E (m ² /N)	$1.72 \cdot 10^{-11}$	$-5.66 \cdot 10^{-13}$	$1.75 \cdot 10^{-11}$	1.7
S_{12}^E (m ² /N)	$-5.84 \cdot 10^{-12}$	$1.92 \cdot 10^{-13}$	$-6.14 \cdot 10^{-12}$	5.1
$-d_{31}$ (C/N)	$7.35 \cdot 10^{-11}$	$-3.59 \cdot 10^{-12}$	$7.38 \cdot 10^{-11}$	0.4
ϵ_{33}^T (F/m)	$8.27 \cdot 10^{-9}$	$-2.38 \cdot 10^{-10}$	$8.29 \cdot 10^{-9}$	0.2
k_p	0.339052	-0.00613	0.340468	0.4
σ^p	0.339174	$8.34 \cdot 10^{-6}$	0.351532	3.6
e_{31} (C/m ²)	6.46184	-0.10351	6.51219	0.8
S_{66}^E (m ² /N)	$4.61 \cdot 10^{-11}$	$-1.51 \cdot 10^{-12}$	$4.72 \cdot 10^{-11}$	2.4
C_{66}^E (N/m ²)	$2.16 \cdot 10^{10}$	$7.10 \cdot 10^8$	$2.12 \cdot 10^{10}$	1.9

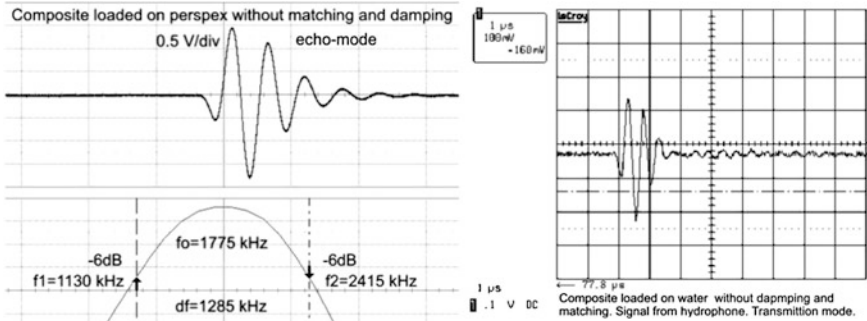


Fig. 15.8 Pulse-echo and transmit characteristics with corresponding FFT for PZT/20 vol% α -Al₂O₃ composite elements

ultrasonic transducer loaded on water and Perspex. Piezoelements were excited by spike pulses. Echo signals in water were received from Perspex reflector.

Figure 15.8 shows that a low- Q and low- Z_A composite element demonstrates high-damped and high amplitude signals even without matching and damper. Notice also that the transducer made of new ceramic composites exhibits a smaller ripple, a larger bandwidth and is free of harmonics, i.e., the spatial resolution is higher and its dynamic range broader. Keeping the optimal scatterers size-to-wavelength ratio, we manufactured and tested a line of wide-band NDT ultrasonic transducers made from new ceramic composites with high sensitivity and resolution in frequency range 0.2–10 MHz.

15.6 PZT/PZT Ceramic Matrix Composites

A new method of low- Q PZT/PZT ceramic piezocomposites fabrication is proposed in [5, 7]. Different types of PZT type piezoceramics powders and milled PZT piezoceramic particles, as well as pre-sintered piezoceramic granules were used as matrix and filling components, respectively. Samples of piezocomposites with the volume fraction of components 0–100 % were manufactured and tested. Complex sets of elastic, dielectric, and piezoelectric parameters of piezocomposites were measured by impedance spectroscopy method using piezoelectric resonance analysis (PRAP) software.

At first, a line of chemically, thermally, and technologically compatible ceramic matrix and scattering phase materials were chosen. Different types of raw PZT powders and milled PZT piezoceramic particles as well as pre-sintered PZT granules were used as initial components for ceramic composite preparations. Special pressing and firing regimes and porosifiers were used for the formation of microporous piezoceramic matrices. Sintering of the green bodies was carried out at special thermal profiles to prevent cracking caused by difference in shrinkage and thermal expansion coefficients of the composite components. Figure 15.9 shows two examples of ceramic composite microstructures.

PZT/PZT ceramic piezocomposites composed by the hard PZT matrix with randomly distributed pre-sintered PZT granules with a mean particle diameter $\sim 30 \mu\text{m}$ and volume fraction from 0 up to 100 $m\%$ were chosen as model samples for illustration of the “damping by scattering” approach.

Figure 15.10 shows shrinkage coefficient K_{sh}^{diam} , theoretical ρ^{theor} and measured ρ^{exper} density, as well as relative porosity $P\%$ of ceramic composite as a function of concentration of pre-sintered ceramic granules $m\%$ fabricated at the same sintering regimes.

It is readily seen in Fig. 15.10 that K_{sh}^{diam} decreases drastically with $m\%$ caused by the increase of the non-shrinking phase concentration (pre-sintered ceramic

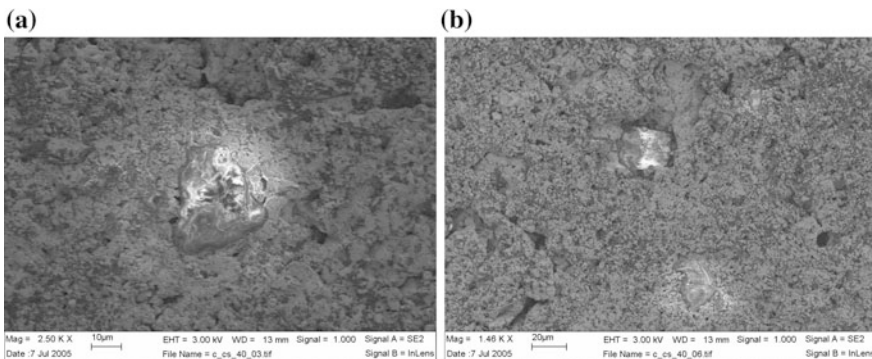


Fig. 15.9 SEM micrographs of ceramic composite structures: **a** pre-sintered PZT granules in porous PZT matrix; **b** milled dense PZT particles in porous PZT matrix

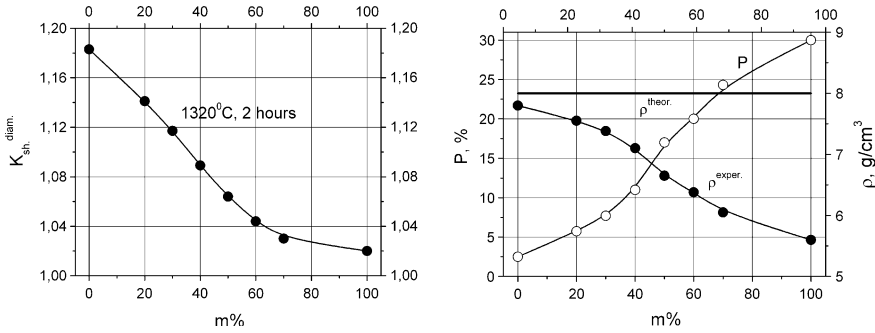


Fig. 15.10 Dependence of shrinkage coefficient $K_{sh}^{diam.}$, theoretical ρ^{theor} and measured ρ^{exper} density, as well as relative porosity $P\%$ of composite elements on concentration of pre-sintered ceramic granules $m\%$

granules), which prevents shrinkage of ceramics matrix and leads to microporosity appearance. It is also observed in Fig. 15.10 that the density of the ceramic composite drops and relative porosity grows rapidly with concentration $m\%$, which corresponds well to shrinkage coefficient behavior.

The dielectric constant of the composite $\epsilon_{33}^T/\epsilon_0$ decreases drastically with $m\%$ because porosity grows (i.e., the dielectric constant of air is much less than for PZT ceramics). The piezoelectric modulus d_{33} for ceramic composite has minor changes in all $m\%$ range caused by continuity of rigid “quasi-rod” ceramic skeleton in the polarization direction (sample thickness). Reduction in $|d_{31}|$ with $m\%$ is obvious and is caused by alteration of quasi-rod ceramic skeleton continuity in a lateral direction (i.e., the lateral size of elements usually twenty times more than the thickness).

The main reason for the decrease of k_p and k_{31} is above-mentioned alteration of piezoceramics skeleton continuity in a lateral direction and, as the consequence, an increase in corresponding elastic compliances of porous piezoceramics. The electromechanical coupling factor k_t slightly increases with $m\%$ due to partial removal of mechanical clamping of a porous piezoceramic structure in lateral direction (electromechanical coupling factor for piezoceramic rods equal to k_{33} , and mechanical clamping of porous piezoceramic skeleton by air is negligible).

Figure 15.11 shows piezoelectric moduli d_{33} , d_{31} , relative dielectric constant $\epsilon_{33}^T/\epsilon_0$ and electromechanical coupling factors for thickness k_t , transverse k_{31} and radial k_p vibration modes of ceramic composites as a function of concentration of pre-sintered ceramic granules $m\%$.

The full complex set of measured complex parameters for ceramic composites PZT/PZT is present in Table 15.6.

PZT/PZT ceramic piezocomposites are characterized by a unique spectrum of the electrophysical properties unachievable for standard PZT ceramic compositions fabricated by standard methods and can be useful for wide-band ultrasonic transducer applications.

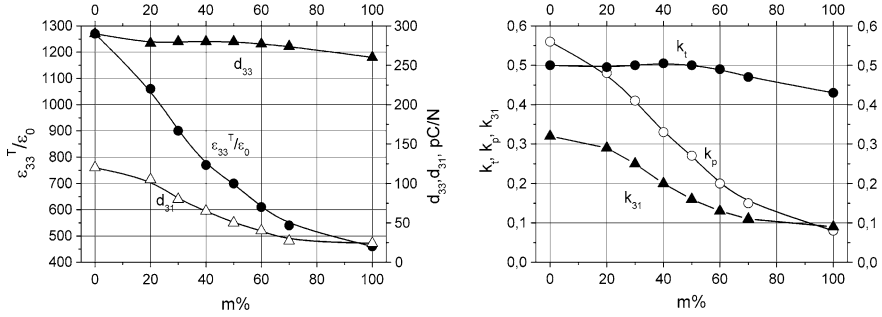


Fig. 15.11 Dependencies of piezoelectric moduli d_{33} , d_{31} , relative dielectric constant $\epsilon_{33}^T/\epsilon_0$ and electromechanical coupling factors k_t , k_{31} and k_p on concentration of pre-sintered ceramic granules $m\%$ for ceramic composites PZT/PZT

Table 15.6 Complex set of parameters measured for thickness and radial extension modes of PZT/PZT composite disks for different concentrations of pre-sintered ceramic granules $m\%$

Parameter/mass%	0	20	60	100
Porosity, vol%	2.5	5.75	20	30
d_{33} quasistatic (pC/N)	290	280	280	260
f_s radial (kHz)	113.4	109	84.4	70.3
$S_{11}^r E$, 10^{-11} (m ² /N)	1.17	1.33	2.60	4.48
$S_{11}^n E$, 10^{-14} (m ² /N)	-1.25	-2.33	-19.44	-56.73
$S_{12}^r E$, 10^{-12} (m ² /N)	-3.49	-4.09	-7.77	-13.22
$S_{12}^n E$, 10^{-14} (m ² /N)	0.485	9.61	32.06	43.21
$-d'_{31}$ (pC/N)	120	98	45	20
$-d''_{31}$ (pC/N)	-0.0974	-1.4713	-1.7495	-2.0596
ϵ_{33}^T , 10^{-9} (F/m)	11.20	9.35	5.86	4.05
ϵ_{33}^n , 10^{-12} (F/m)	-3.93	-56.32	-32.52	-23.81
k'_p	0.561	0.473	0.201	0.109
k''_p	-0.0002	-0.0056	-0.0015	-0.0073
$-e'_{31}$ (C/m ²)	14.7	10.8	2.6	0.8
$-e''_{31}$ (C/m ²)	-0.0038	-0.1480	-0.0088	-0.0430
f_s^{thick} (kHz)	2,010	1,789	1,076	941
k'_t	0.498	0.498	0.516	0.440
k''_t	-0.00899	-0.01842	-0.02829	-0.03118
C_{33}^D , 10^{10} (N/m ²)	17.2	12.48	4.04	2.33
C_{33}^m , 10^8 (N/m ²)	7.71	12.24	15.99	19.89
C_{33}^E , 10^{10} (N/m ²)	13.01	10.19	2.99	1.91
C_{33}^n , 10^8 (N/m ²)	21.2	21.9208	23.552	25.3558
e'_{33} (C/m ²)	19.6	14.2	6.6	3.5
e''_{33} (C/m ²)	-0.1	-0.15	-0.30	-0.50
ϵ_{33}^S , 10^{-9} (F/m)	7.62	6.59	4.41	3.22
ϵ_{33}^n , 10^{-9} (F/m)	-0.81	-1.75	-0.23	-0.43

15.7 Conclusions

This chapter presents a review of microstructure peculiarities, mathematical models, methods of fabrication and measurements, as well as systematical experimental data for different types of ceramic piezocomposites.

New families of polymer-free ceramic piezocomposites (porous piezoceramics, composites of types ceramics/ceramics and ceramics/crystals), are considered with properties that improve the combining of parameters of PZT, PN type ceramics and 1–3 composites.

A line of proprietary porous piezoelectric ceramics was systematically studied. Complex sets of elastic, dielectric, and piezoelectric coefficients measured by piezoelectric resonance analysis methods were present. It was shown that, for any connectivity type and porosity up to 70 %, the real structures of porous piezoelectric ceramics are close to the matrix medium structure with continuous piezoelectric ceramic skeleton. A critical comparison of numerical FEM calculations was carried out to provide the results of various approximated formulae and experimental data for different porous piezoelectric ceramics. It was shown that FEM calculations based on effective moduli methods give the most adequate results and agree well with the experiment in a wide porosity range.

New low- Q ceramic piezocomposites technology based on the original microstructural design concept (MSD) using “damping by scattering” approach was described. Complex sets of elastic, dielectric, and piezoelectric parameters of the ceramic piezocomposites were systematically studied using impedance spectroscopy and ultrasonic method. A line of wide-band NDT ultrasonic transducers with high sensitivity and resolution was manufactured and tested.

The main advantages of the new PZT/ α -Al₂O₃ piezocomposites are high acoustic efficiency, low crosstalk, and low mechanical Q , and especially high acoustic sensitivity combined with well-damped signals. Additional advantages of the developed piezocomposites include the possibility of executing controllable changes in the main properties within a wide range, compatibility with standard fabrication technologies and processing flexibility.

New ceramics and ceramic piezocomposites composed by pre-sintered piezoceramic granules embedded in porous piezoceramic matrix are described. PZT/PZT ceramic piezocomposites are characterized by a unique spectrum of the electro-physical properties, unachievable in standard PZT ceramic compositions, by novel fabrication methods and potential for use in wide-band ultrasonic transducer applications.

Acknowledgments Work supported by the RSF grant No. 15-12-00023.

References

1. W. Wersing, in *Piezoelectric Materials in Devices*, ed. by N. Setter (Swiss Federal Institute of Technology, Lausanne, Switzerland, 2002)
2. A.N. Rybyanets, *IEEE Trans. UFFC* **58**, 1492 (2011)
3. S.S. Lopatin, T.G. Lupeiko, *Izv. AN USSR. Ser. Neorg. Mat.* **27**, 1948 (1991)
4. W. Wersing, K. Lubitz, J.T.G. Moliaupt, *Ferroelectrics* **68**, 77 (1986)
5. A.N. Rybyanets, in *Piezoceramic Materials and Devices*, ed. by I.A. Parinov (Nova Science Publishers, New York, 2010), p. 113. (Chapter 3)
6. A.N. Rybyanets, O.N. Razumovskaja, L.A. Reznitchenko, V.D. Komarov, A.V. Turik, *Integr. Ferroelectr.* **63**, 197 (2004)
7. A.N. Rybyanets, A.A. Rybyanets, *IEEE Trans. UFFC* **58**, 1757 (2011)
8. A.N. Rybyanets, *Ferroelectrics* **419**, 90 (2011)
9. A.N. Rybyanets, A.V. Nasedkin, A.V. Turik, *Integr. Ferroelectr.* **63**, 179 (2004)
10. A.N. Rybyanets, *Ferroelectrics* **360**, 84 (2007)
11. *IEEE Standard on Piezoelectricity*. ANSI/IEEE Std. 176 (1987)
12. R. Holland, *IEEE Trans. Sonics Ultrason.* **SU-14**, 18 (1967)
13. S. Sherrit, H.D. Wiederick, B.K. Mukherjee, *Ferroelectrics* **134**, 111 (1992)
14. C. Alemany, L. Pardo, B. Jimenez, F. Carmona, J. Mendiola, A.M. Gonzalez, *J. Phys. D: Appl. Phys.* **27**, 148 (1994)
15. J.G. Smits, *IEEE Trans. Sonics Ultrason.* **SU-23**, 393 (1976)
16. *PRAP (Piezoelectric Resonance Analysis Program)*. TASI Technical Software Inc. www.tasitechnical.com
17. A. Rybyanets, A.V. Nasedkin, *Ferroelectrics* **360**, 57 (2007)
18. A.N. Rybyanets, A.A. Naumenko, N.A. Shvetsova, in *Nano- and Piezoelectric Technologies, Materials and Devices*, ed. by I.A. Parinov (Nova Science Publishers, New York, 2013), p. 275. (Chapter 1)
19. A.N. Rybyanets, R. Tasker, *Ferroelectrics* **360**, 90 (2007)
20. H. Kara, R. Ramesh, R. Stevens, C.R. Bowen, *IEEE Trans. UFFC*, **50**, 289 (2003)
21. R. Ramesh, H. Kara, C.R. Bowen, *Ultrasonics* **43**, 173 (2005)
22. R.W. Rice, in *Key Engineering Materials*, ed. by D.-M. Liu (Trans. Tech. Publications, Switzerland, 1996), p. 115, 1
23. T.R. Shrout, W.A. Shulze, J.V. Biggers, *Mater. Res. Bull.* **14**, 1553 (1979)
24. W.F. Brown, *Trans. Soc. Rheol.* **9**, 357 (1965)
25. D.A.G. Bruggeman, *Ann. Phys.* **24**, 636 (1935)
26. M. Marutake, *J. Phys. Soc. Jap.* **11**, 807 (1956)
27. Nan Ce-We, *J. Appl. Phys.* **76**, 1155 (1994)
28. VYu. Topolov, C.R. Bowen, *Electromechanical Properties in Composites Based on Ferroelectrics* (Springer, London, 2009)
29. D. Avnir, D. Farin, P. Pfeifer, *J. Chem. Phys.* **79**, 3566 (1983)
30. A. Nasedkin, A. Rybyanets, L. Kushkuley, Y. Eshel, *IEEE Ultrason. Symp. Proc.* 1648 (2005)

Chapter 16

Diffusion of Ferroelectric Phase Transition and Glass-Dipole State in the PZT-Based Solid Solutions

G.M. Konstantinov, A.N. Rybyanets, Y.B. Konstantinova,
N.A. Shvetsova and N.O. Svetlichnaya

Abstract The chapter covers the structural features and physical properties of ferroelectric ceramics solid solutions based on lead zirconate-titanate with an abnormally strong diffuse ferroelectric phase transition. It is found out that in the solid solution in a wide range of temperature the relaxor-like non-paraelectric cubic phase coexists along with the ferroelectric tetragonal, and rhombohedral phases. Discussion of the experimental results is based on the existence of glass-dipole state in the solid solutions that is typical for compounds like lead magno-niobate.

16.1 Introduction

Studies of ferroelectrics with perovskite structure having a diffuse phase transition (PT) have been widely discussed. The properties of such ferroelectrics under different thermodynamic conditions as well as the reasons for diffuse phase transitions (PT) are the subject of public debates [1–22].

It was found out that the peak width of dielectric permittivity depending on the temperature $\varepsilon(T)$ is influenced by the existence of different ferroelectric atoms having identical positions in the crystalline structure, and the presence of different kinds of defects, and the domain and interphases boundaries. It is believed that in both cases, a sample (crystal, ceramics) can be represented as a statistical set of elementary subsystems—microdomains with different properties (in particular, different Curie-Weiss temperatures). Distribution of properties to such microdomains is

G.M. Konstantinov (✉) · A.N. Rybyanets · Y.B. Konstantinova
N.A. Shvetsova · N.O. Svetlichnaya
Research Institute of Physics, Southern Federal University,
344090 Rostov-on-Don, Russia
e-mail: georgy.konstantinov@yandex.ru

generally considered to be a Gaussian one [21]. It is assumed that in a number of clusters, the Curie point is below the maximum temperature of dielectric permittivity T_m , and in some others, it is above. It is logical to assume that near T_m , there is a temperature range in which both the paraelectric cubic (K) and ferroelectric phases are present. However, one could not observe such coexistence of different phases using direct X-ray methods. There are only some indirect evidences (presence of hysteresis loop, possibility of polarization for the samples at temperatures above T_m [2, 4], nonlinear refractive index [23], and others), proving the presence of the ferroelectric phase in such objects at the temperature above T_m . The cubic phase is below T_m or it does not detect at all, or vice versa, it exists in the temperature range coming to that of liquid nitrogen, as in the case of lead magno-niobate. The complexity of X-ray detecting the region of coexistence of ferro- and para-phases with a diffuse phase transition is primarily explained by the choice of objects to be studied. In most cases, such object was lead magno-niobate or similar compounds, in which the polar phase clusters have a very small size and therefore cannot be detected by X-ray analysis. The small size of the polar phase clusters are primarily related to the fact that the base of their formation is a disordered arrangement of the Mg^{2+} and Nb^{5+} ions in the *B*-nodes of the perovskite lattice (ABO_3). As mentioned before [24] the sizes of the polar phase clusters in the lead magno-niobate do not exceed a few unit cells. This division is due to local fields with the partially ordered ions of Mg^{2+} and Nb^{5+} . Such clusters are too small to be detected by direct X-ray methods, so in experiments they are recorded as a usual cubic phase with a higher concentration of defects.

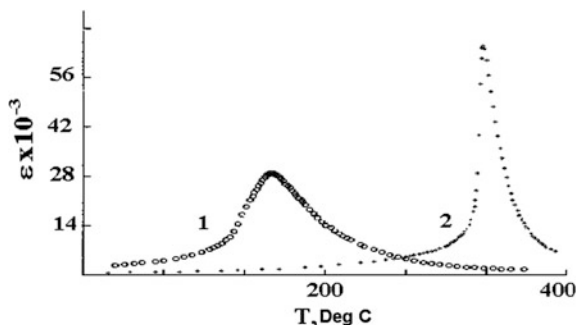
We succeeded to choose a material that does not have such disadvantages at the X-ray investigation, but at the same time, it has a strongly diffuse phase transition. We are talking about PKR-7M ferroelectric ceramics. Based on this material, we noted some regularities in the structural parameters changes of the ferroelectric and paraelectric phases coexisting in a wide temperature range near T_m .

16.2 Main Features of PKR-7M Ferroelectric Ceramics

Most used in industry ceramic materials, based on lead-zirconate-titanate (PZT), have a slightly diffuse PT. This refers to the materials, which compositions can exhibit a morphotropic transition (MT) at room temperature [25–28]. Typically, such materials are solid solutions, and their main components are $PbZrO_3$ and $PbTiO_3$. Their compositions usually include a number of modifiers in an amount of not more than several percents. In these cases, the light diffuse ferroelectric phase transition characteristic to the pure PZT solid solution is maintained.

PKR-7M material studied in this chapter is a six-component solid solution $PbZrO_3$ – $PbTiO_3$ – $SrTiO_3$ – $PbW_{1/2}Cd_{1/2}O_3$ – $PbW_{1/2}Mg_{1/2}O_3$ – $PbSb_{3/4}Li_{1/4}O_3$. According to the research objectives of this work, our interest in this material is primarily caused by the anomalous characteristics of the ferroelectric phase transition. Figure 16.1 shows a comparison of the temperature dependence of the

Fig. 16.1 Dependence of the dielectric permittivity on the temperature in PKR-7M (1) and PKR-1 (2) materials



dielectric permittivity of this material (curve 1) and the PKR-1 material, which is a three-component solid solution $\text{PbZrO}_3\text{-PbTiO}_3\text{-PbW}_{1/2}\text{Cd}_{1/2}\text{O}_3$ (curve 2). Experiments were performed with the help of the bridge P-5010 at the frequency of 1 kHz. One can see that width of the peak 1 exceeds several times the width of the peak 2, while the value of the Curie point and the value of ϵ at the Curie point of the PKR-7M material are significantly less. The width of the peak 1 characteristic to the PKR-7M material is close to the peak width $\epsilon(T)$ observed in lead magnoniobate, a typical representative of the ferroelectrics with a diffuse phase transition.

The main reason for the anomalous diffuse PT observed in the PKR-7M material is a greater, than in other PZT-based materials, amount of additional components. Incomplete solubility of various compounds in each other inevitably leads to the segregation of groups of atoms. Consequently, microdomains of a rather large size form, where the concentrations of the solid solution components greatly differ from the specified macroscopic concentrations. As the content and range of the Curie temperatures of additional components of the solid solutions are very large (from minus 263 °C in SrTiO_3 to 400 °C in $\text{PbW}_{1/2}\text{Cd}_{1/2}\text{O}_3$), fluctuations of concentration in microdomains inevitably lead to fluctuations of local Curie temperatures. This is one of the main causes of diffuse PT [22, 24, 25]. Furthermore, the presence of the ions of different valences ($\text{W}^{6+}\text{-Sb}^{5+}$, $\text{Mg}^{2+}\text{-Li}^{1+}$, etc.) in the perovskite structure in the state *B* causes its distortion at heterovalent substitutions, in particular, formation of vacancies. As discussed in [29], this fact results to an interruption of polarization chains and decreasing the spontaneous polarization and hence increasing the ferroelectric softness. Increasing ferroelectric softness and the presence of the compounds in solid solution with extremely low Curie temperatures lead to a significant reduce of the Curie temperature of the studied material (by 180 °C if compared to PKR-1).

According to the content of the main components of the solid solution, the PKR-7M material is in the middle of MT. This situation is atypical for most industrial piezoceramics. States of microdomains in crystallites with rhombohedral (Rh) and tetragonal (T) phases are very close. In order to have a phase different from the surrounding microdomains, it is necessary for a microdomain to have a small difference of its state from the states of other microdomains (in comparison with compositions being close to the border of MT). Such difference can be a slight

change in the concentrations of the components or the number of structural defects. This results in reduce of the sizes of microdomains of different phases, which, in turn, reduces the ferroelectric rigidity of the material and increases the dispersion of properties to microdomains.

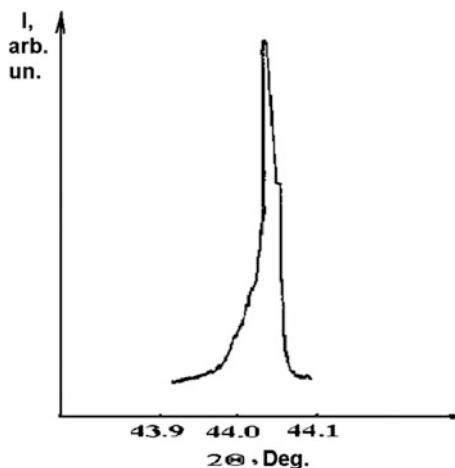
Thus, the PKR-7M piezoceramic material has the following advantages: (i) strong diffuse ferroelectric PT; (ii) temperatures conditions of PT accessible for studies; (iii) an other mechanism, different from the PMN, forming domains with different properties (mainly content fluctuations in microdomains). This explains the existence of rather large (for X-ray investigation) clusters of different phases.

In this chapter we present the results of studies of changes in the phase composition and properties under the influence of temperature in the PKR-7M ferroelectric in diffuse ferroelectric phase transition.

16.3 Features of the Diffraction Peaks at Temperature Changes in the Field of the Diffuse Phase Transition in the PKR-7M Ferroelectric Ceramics

Initial structural studied of the PKR-7M material at high temperatures were carried out on a DRON-2.0 diffractometer in a continuous scan mode using radiation $\text{CuK}\alpha$. The experiments were made in the temperature range of 20–600 °C in a special attachment to the diffractometer, which allows one to maintain the temperature of the sample with an accuracy of $\pm 1^\circ$. Such types of diffraction profiles as 200, 222 and 400 were shot at the counter speed of $1/8^\circ$ per minute. It was found out that at temperatures higher than the maximum temperature of the dielectric permittivity T_m by a few tens of degrees, these profiles could not be described by a single symmetrical peak, that should be detected in the sample in the presence of only one cubic phase. Figure 16.2, for example, represents a 200 diffractive profile, obtained

Fig. 16.2 Diffraction profile of reflections 200 of the PKR-7M ferroelectric ceramics obtained by continuous scanning at the temperature of 200 °C



at the temperature of 200 °C. Although the temperature of the experiment conducted is higher than T_m by 25 °C, in the figure the asymmetry can be seen in the field of small-angle diffraction. A similar diffusion of the diffraction reflections profiles observed in all other reflections typical for the cubic phase of perovskite structure. As a result, in the work [30] we concluded that in the PKR-7M material in a temperature range higher than the temperature T_m besides the basic cubic phase there is an additional perovskite phase with a high concentration of structural defects. At the increasing temperature, the content of the additional phase gradually decreases, that is recorded by reducing the asymmetry of the diffraction reflections. Moreover, we established that the PKR-7M ferroelectric ceramics had a piezoelectricity after polarization at temperatures exceeding the temperature T_m by 25 °C, and also in a short circuited state when cooled down to room temperature. The electromechanical coupling coefficient k_p of the ceramics, polarized this way, is 50–70 % of k_p achieved during polarization to saturation at $T < T_m$. Under this influence of field, at $T < T_m$, piezomodulus was 30–50 % of the maximum achievable value (Table 16.1).

Because of the fact that diffraction patterns obtained in the continuous scan mode do not allow one to separate the diffraction reflexes corresponding to different phases, a further more thorough study of structural parameters in the field of the diffuse PT in the PKR-7M material was conducted in a discrete scanning mode. Shooting of 200, 222 and 400 diffraction profiles of the PKR-7M ferroelectric ceramics was carried out on a DRON-3 M diffractometer with the exposure time at the points of 50, 90 and 120 s, respectively. When shooting the radiation CuK_α was used, the size of the movement of the detector was 0.01° in the corners 2θ . In the temperature range of 20–320 °C, measurements were taken every 20 °C; at further heating, the step of change of the temperature between shoots was slightly increased. Decomposition of the obtained diffraction profiles to peaks corresponding to different perovskite phases was made on computer with the program described in [31].

Figure 16.3 shows the diffraction profile 200 obtained at the temperature of 110 °C. In this case, description of the profile is based on the assumption that it consists of four distinct peaks. To compare, Fig. 16.4 shows how one can describe

Table 16.1 Dependencies of $\varepsilon/\varepsilon_0$, k_p and d_{31} on the amplitude of the polarizing electric field and the time of its action at the temperature exceeding the temperature T_m by 25 °C in the PKR-7M material

E , kV/cm	t , min	$\varepsilon/\varepsilon_0$	K_p	$d_{31} \cdot 10^{12}$, C/N
15	30	2,800	0.30	100
15	60	3,070	0.36	120
15	120	3,100	0.40	140
20	30	3,200	0.47	160
20	60	3,400	0.48	174
30	30	2,960	0.39	130
30	60	3,230	0.45	142
30	90	3,360	0.49	180
30	120	3,320	0.50	180

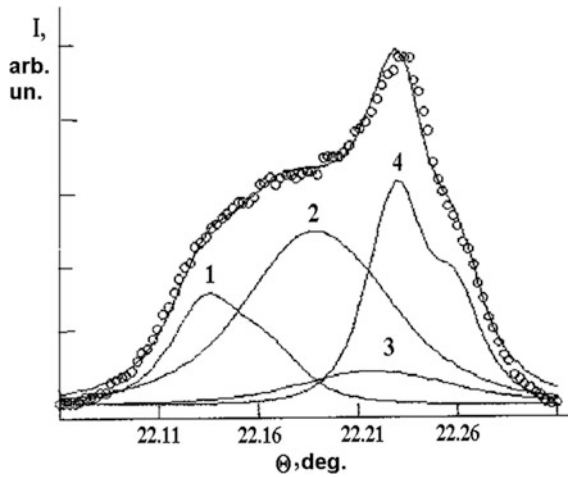
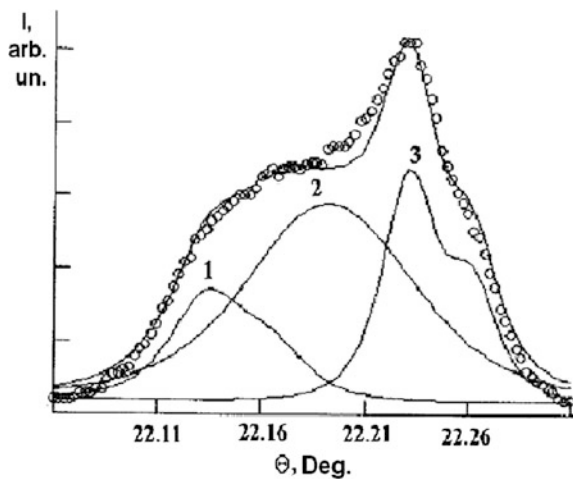


Fig. 16.3 The diffraction profile of reflections 200 in PKR-7M ferroelectric ceramics shot at the temperature of 110 °C. Circles are experimental intensities. The lines are obtained by means of an approximation when dividing the diffraction profile to 4 peaks

Fig. 16.4 The diffraction profile of reflections 200 in PKR-7M ferroelectric ceramics shot at the temperature of 110 °C. An approximation with three peaks



this profile with the assumption of three diffraction peaks composing the profile. Figures 16.3 and 16.4 illustrate the best of possible approximation options (the mean-square deviation from the experimentally obtained points is minimum).

A comparative analysis of Figs. 16.3 and 16.4 shows that in this case the use of three diffraction peaks 1 (002T), 3 (200R) and 4 (200T) typical for PZT-based solid solutions in MT does not provide a good description of the total diffraction profile. To do this, it is necessary to enter a new maximum (the 2 maximum in Fig. 16.3). Next, we determine the perovskite phase to which this peak belongs. Assume that

this is the type of diffraction reflection 200 of an additional tetragonal phase (reflection 002 coincides with the reflection of the main tetragonal phase). Figure 16.5 shows the position of the diffraction peak 222 calculated on the base of this assumption. As we can see, it does not match the experimental results, and goes beyond the profile 222. Let the peak 2 (Fig. 16.3) be a reflection 200 of the additional rhombohedral phase.

Figure 16.6 illustrates what location could have the diffraction peaks 222_R and $22\bar{2}_R$ in this case, if the peak 200 corresponds to their positions. As in the case with the additional T-phase, the received reflection (in this case, the reflection 222) surpasses the boundaries of the experimental profile. The most acceptable interpretation is the presentation of peak 2 as a reflection 200 of the cubic (K-) phase. Figure 16.7 shows the position of the diffraction peak 222. It matches well (with accuracy of $2\theta < 0.02$) one of the three peaks obtained at computer decomposition

Fig. 16.5 Position of the diffraction reflection 222 of T-phase, calculated on peaks 2 and 4 in Fig. 16.3 (line) and the experimental profile 222 (circles)

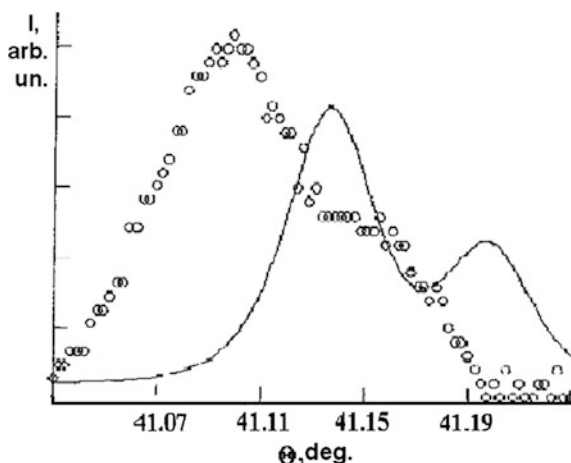


Fig. 16.6 Positions of the diffraction reflections 222_R (1) and $22\bar{2}_R$ (2) calculated with the assumption that the peak 2 (Fig. 16.3) is a reflection of Rh-phase, and the experimental diffraction profile (circles)

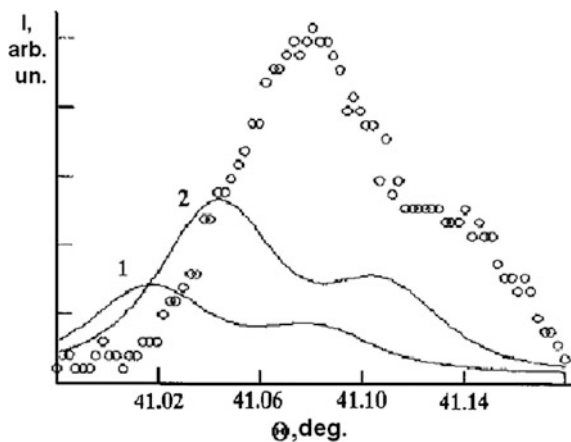
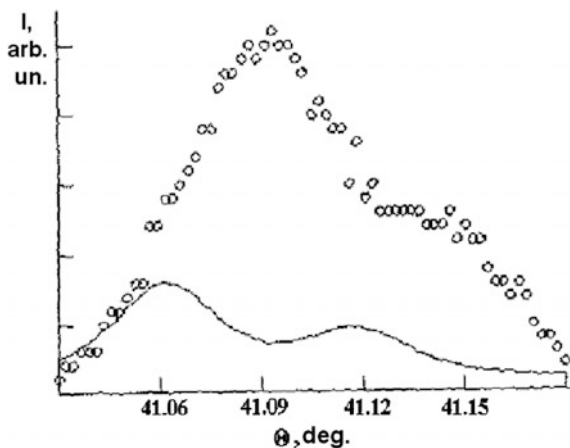


Fig. 16.7 Position of diffraction reflection 222_K calculated with the assumption that the peak 2 is the reflection of K-phase (line), and the experimental diffraction profile (circles)



of the profile 222 to the components. We did not consider more complex cases of monoclinic distortion of the perovskite lattice. It is evident that in this case the character of the profile 222 would be more complicated because of the presence of two peaks 222 and $22\bar{2}$ of equal intensity.

Thus, for the first time in the solid solution based on PZT, we could observe the coexistence of the cubic perovskite phase with the ferroelectric phases in diffuse phase transition at temperatures are below T_m .

When the temperature increased to $150\text{ }^\circ\text{C}$, the intensity of the diffraction peak 3 (Fig. 16.3) was gradually decreasing, while at the temperature of $150\text{ }^\circ\text{C}$ the diffraction profile was well described by three peaks: 1, 2 and 4. This goes with the gradual disappearance of the Rh-phase in the ceramic sample. It should be noted that the existence of T-phase at temperatures above T_m (which will be discussed below), is proved by the analysis of the diffraction profile 200 obtained at such temperatures. Figure 16.8 shows the result of the decomposition of the diffraction reflections profile of type 200 obtained at $190\text{ }^\circ\text{C}$ that is above T_m . Here as well as in the case of analysis of X-ray patterns in a continuous scan mode (Fig. 16.1), we observed the diffraction profile not described by a single peak that is expected when there is one cubic paraelectric phase in the sample. At computer processing, two additional peaks 1 and 3 appear (Fig. 16.8). These peaks are the peaks 1 and 4 changed by heating (Fig. 16.3), they correspond to the tetragonal phase. The angular positions of reflections 1 and 3 are accorded by a square shape of T-phase with the position of the corresponding diffraction reflection, obtained after the decomposition of the peak 222.

It should be noted that by calculating percentage of T- and K-phases according to the diffraction profiles obtained at $T > T_m$, the distortion of the diffraction pattern was taken into account. The distortion was caused by a vertical divergence of the X-ray beam. This distortion is manifested by an additional broadening of diffraction peaks at small angles θ that correspond to small values of the amount of $h^2 + k^2 + l^2$. Figure 16.9 shows the profile of the diffraction peak 200 of a reference sample. The

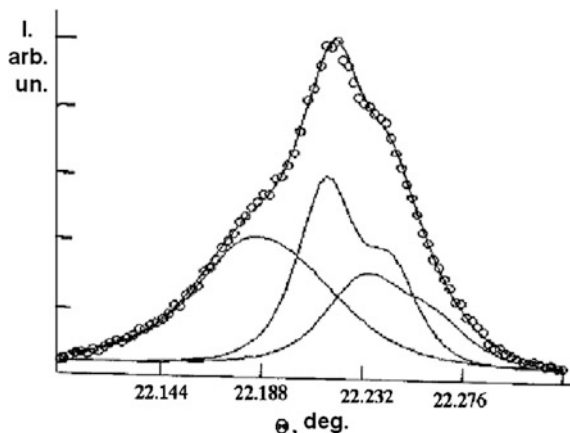
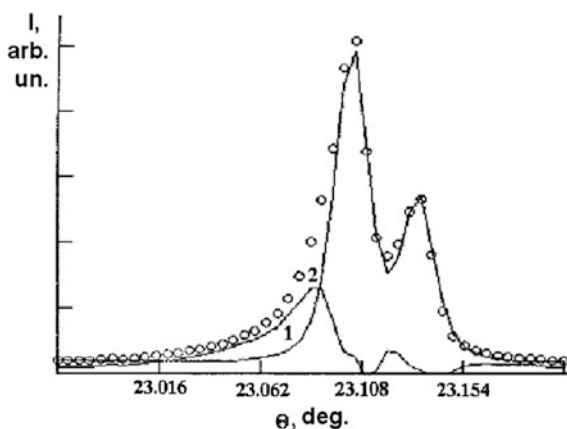


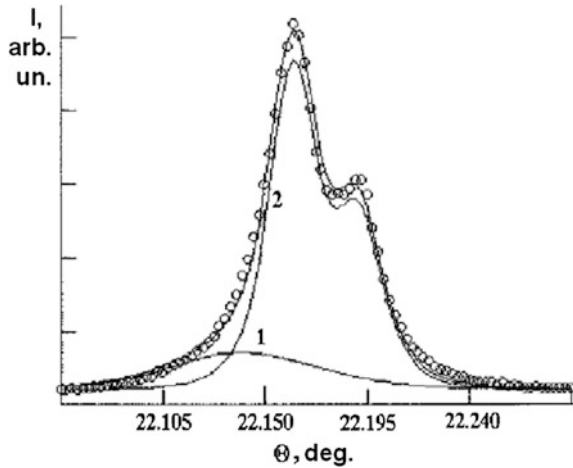
Fig. 16.8 The diffraction profile of reflections 200 in PKR-7M ferroelectric ceramics shot at the temperature of 190 °C. Circles are experimental intensities. The lines are obtained by means of the approximation when dividing the profile to 3 peaks

Fig. 16.9 The diffraction profile of reflections 200 of the SrTiO₃ reference sample shot at room temperature. Circles are the experimental intensity, (1) approximation with a single peak, (2) the difference of the experimental and calculated results



sample of SrTiO₃ ceramics with a polished surface served the reference sample. It was annealed for 3 h at a temperature of 600 °C and then slowly cooled down. It is well known that strontium titanate has a cubic crystal lattice at room temperature. Therefore, each diffraction peak, obtained from the samples of this compound, should be present by a single line. The curve 2 in Fig. 16.9 represents the best calculated approximation with one peak; the curve 1 is the difference between experimental values of the intensity and the intensities corresponding to the curve 2. As it can be seen in the figure, a deviation from the calculated approximation, which in this case is characterized only by a vertical divergence of the X-ray beam, is an asymmetric peak. Therefore, it is quite logical to take into account this deviation, using an additional peak in computer calculations.

Fig. 16.10 Diffraction profile of reflections 200 of PKR-7M ferroelectric shot at the temperature of 600 °C. Circles are experimental intensity. Lines are obtained by approximating the two peaks (1) and (2)



In the PKR-7M material this peak is applied to the peak 1 in the experimental profile of reflection 200 (Figs. 16.3, 16.8), this corresponds to the T-phase. At temperatures over 320 °C the peak 3 did not appear (Fig. 16.10), while the intensity and half-width of the peak 1 remained unchanged at the increasing temperature. As the broadening of the diffraction peaks caused by the vertical divergence of the X-ray beam cannot depend on the temperature, we interpreted this fact as disappearance of T-phase at temperatures close to 320 °C. The percentage of T-phase at temperatures below 320 °C was calculated by the formula:

$$X = \frac{I_1 B_1 + I_3 B_3}{I_1 B_1 + I_2 B_2 + I_3 B_3} - \frac{I'_1 B'_1}{I'_1 B'_1 + I'_2 B'_2}, \quad (16.1)$$

where I_i and B_i are intensities and half-widths of the lines 1, 2 and 3 at the shooting temperature, I'_i and B'_i are intensities and half-widths of the lines 1 and 2 at the temperature $T = 600$ °C.

The diffraction reflections 400 began to be recorded at the temperature $T > 190$ °C. According to the half-widths of peaks 200 and 400 the values of microdeformations and coherent scattering regions were calculated.

16.4 Specific Points of Temperature and the Glass-Dipole State in the Material with a Diffuse Phase Transition

The dependence of the dielectric permittivity on the temperature of PKR-7M material is shown in Fig. 16.11. At the temperature of about 150 °C one can observe an abrupt change ε of the polarized sample (curve 2). The Curie-Weiss law starts realizing at the temperatures exceeding the peak temperature by 140 °C. A sharp

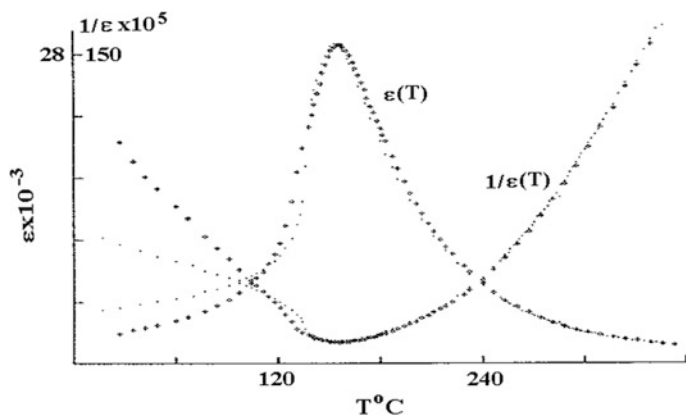


Fig. 16.11 Dependence $\varepsilon(T)$ and $1/\varepsilon(T)$ of PKR-7M ferroelectric ceramics. Points represent the previously polarized sample. Circles represent the unpolarized sample

bend can be seen on the dependence $1/\varepsilon(T)$ that corresponds to the beginning of the Curie-Weiss law implementation.

In the unpolarized sample besides ferroelectric Rh- and T-phases, we found a considerable amount (about 50 %) of the cubic phase at room temperature. In the polarized sample, K-phase is missing. As the temperature increases up to 150 °C, the content of K-phase practically does not change; Rh-phase is gradually transformed into the T-phase, which corresponds to the previously well-studied bend MT in the phase x , T -diagram [31–33].

Parameters c and a of T-phase gradually converge, with spontaneous deformations of the unit cells of the Rh- and T-phases (δ_R and δ_T) monotonically decreasing at increasing temperature (Fig. 16.12). At the temperature of about 150 °C, R-phase disappears. The parameter a of K-phase decreases in the temperature range from room temperature to 150 °C. In the interval 150–210 °C, \bar{a} does not change, whereas c_T and a_T continue to converge. The contents of K- and T-phases in this temperature range are constant. T-phase is still registered at the temperature over 210 °C up to 320 °C; lattice parameters a_K and δ_T do not depend on the temperature. The content of the T-phase gradually decreases to zero at continuous heating. At the temperature of 320 °C, a sharp bend can be observed in the dependence $a_K(T)$; at the temperature over 320 °C, the parameter a_K increases linearly with increasing T . Note that at the temperature $T_m = 180$ °C, sudden changes in the behavior of the structural parameters were not found. However, after 180 °C, we can observe a sharp (twice) decrease in the half-widths of the diffraction peaks corresponding to the K-phase, and an increase of their intensity. Along with this, the width of the diffraction peaks increases by 1.5 times with decreasing intensity that corresponds to T-phase. Calculations show (Table 16.2) that such changes of half-widths associate with a decrease of coherent scattering regions (CSR) of T-phase at the temperature T_m , increase of CSR, and decrease of microdeformations of K-phase.

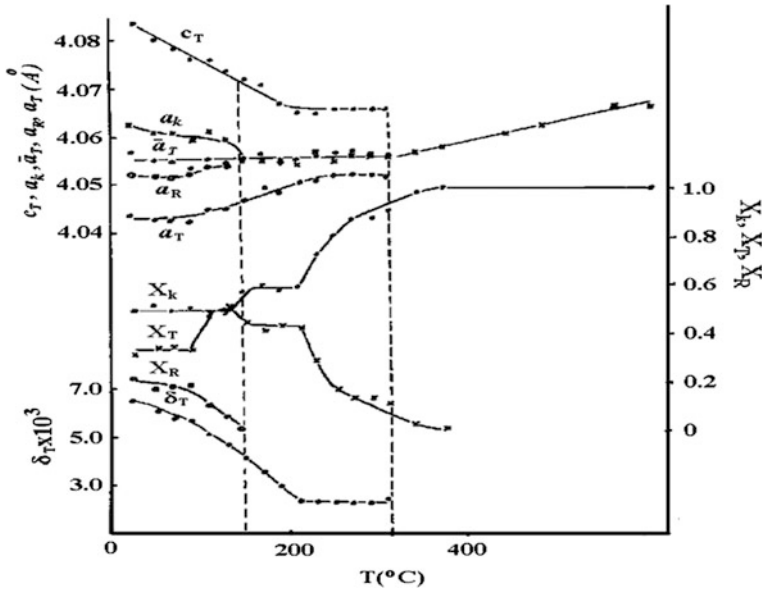


Fig. 16.12 Temperature dependence of structural parameters of PKR-7M material

Table 16.2 Values of microdeformations and dimensions of CSR of K- and T-phases in the PKR-7M material

Temperature	Microdeformations of K-phase	CSR (Å) of K-phase	Microdeformations of T-phase	CSR (Å) of T-phase
$T < T_m$	1.5×10^{-3}	400	1.7×10^{-4}	>1000
$T > T_m$	7×10^{-5}	>1000	3×10^{-4}	800

Thus, according to the results of studies of phase transitions in the PKR-7M material, we can define four specific temperature points: 150, 180, 210 and 320 °C. Let us discuss the physical significance of each of them.

The width of the diffraction reflections of K-phase at $T < 180$ °C is very high. This allows one to suppose that at these temperatures, the K-phase has a higher concentration of structural defects, and its CSR is small. Probably, the observed cubic phase, as well as the cubic phase at $T < T_m$ in PMN, has no paraelectric nature. Apparently the space occupied by K-phase at 20 °C $< T < 180$ °C consists of very small, spontaneously polarized clusters. This state of the ferroelectric structure is called the dipole glass state [24, 34]. In this state, the direction of polarization in spontaneously polarized clusters is not constant with time. Because of thermal fluctuations, it is continuously changing. As a result, in the X-ray diffraction experiments, there is an “averaged” diffraction pattern characteristic to the K-phase. On the base of these arguments, the possibility of transition of K-phase

microregions to the ferroelectric microregions under the influence of an electric field (polarization) can be explained. In the presence of the electric field, microscopic spontaneously polarized clusters forming K-phase reorient their polarization vectors to one direction. Some domains form, which are not capable any more to change the direction of the spontaneous polarization vector \vec{P}_s under the influence of thermal fluctuations. In this case, only ferroelectric phase must be found by means of X-ray methods. Our studies of polarization in patterns confirm the correctness of our reasoning. Thus, in the temperature range of 20–150 °C in an unpolarized sample of PKR-7M material, there exist rather large domains of Rh- and T-phases, along with K-phase domains consisting of microscopic clusters with alternating polarization. In this temperature range, there is a decrease of the spontaneous ferroelectric deformation and gradual transition from T- to Rh-phase at increasing temperature. At the temperature 150 °C, Rh-phase disappears completely, volumes of unit cells of K- and T-phases are equalized. Under conditions of the same temperatures, the observed gain ε of polarized sample (Fig. 16.11) indicates the destruction of the domain structure created by the electric field. The temperature of 150 °C is an analog of the temperature discussed in works [9, 35–41], the temperature of “defrosting” domains T_g .

At the temperature corresponding to the peak of dependence $\varepsilon(T)$ (180 °C), the K-phase previously representing a set of microscopic clusters with variable polarization direction becomes a paraelectric cubic phase. In the result of this transition, the number of K-phase structural defects reduces, the size of the CSR increases that is confirmed by narrowing the respective diffraction reflections. The observed broadening of diffraction reflections of T-phase at this temperature associates with a decrease of size of spontaneously polarized clusters of T-phase.

The estimation of the CSR sizes shows that starting with this temperature, the possible size of the regions of homogeneous polarization of T-phase is not more than 800 Å. It seems that in the temperature range 180–210 °C the value of T-phase spontaneous deformation is not yet small enough to let T-phase clusters make a transition to the K-phase. At the temperature up to 210 °C, there occurs a continuous reducing of δ_T , the concentrations of K- and T-phases were maintained. In the temperature range 210–320 °C, not only the values of unit cells of K- and T-phases retain their magnitudes, but also the values of parameters c_T , a_T and δ_T do this. The reason of this is probably the proximity of free energies of the K- and T-phases. Due to this fact, clusters of ferroelectric phase can turn into K-phase clusters at any moment because of thermal fluctuations. At the same time, some inverse transformations may take place. Coexistence of K- and T-phases makes the system unstable. In the case with dipole glass, only spontaneously polarized clusters exist, which, due to their small size, can change the direction of the spontaneous polarization, but in the present case, the change of direction P_s in the large enough microregions of T-phase is facilitated by the existence of a nearby space filled with K-phase.

The state existing in the temperature range 210–320 °C can be regarded as an analogue of the dipole glass state. The zero coefficient of thermal expansion (fixed volume of unit cells of phases at increasing temperature) found in the PKR-7M at

PT, is usually regarded as one of the characteristic features of this state [35]. Unlike PMN, in PKR-7M at these temperatures T-phase clusters can be recorded by X-ray methods. Their sizes (800 Å) enable transitions from T-phase to K-phase and back, and at the same time they do not impede observation of the independent diffraction reflections of the T-phase. The difference from the glass-dipole state is limited only by the size of the clusters. Qualitative differences in the properties were not found.

The content of the T-phase gradually decreases and becomes zero at the temperature of 320 °C. At the same temperature, processes, associated with the ferroelectric phase transition, complete, but at increasing temperature, there is a linear expansion of the unit cell. It should be noted that since $T = 320$ °C, the behavior $\varepsilon(T)$ obeys the Curie-Weiss law.

16.5 Conclusions

1. The PKR-7M ferroelectric ceramics have an abnormally strong diffusion of the ferroelectric phase transition in solid solutions based on PZT.
2. By means of X-ray methods in the samples of PKR-7M ferroelectric ceramics in the field of the diffuse phase transition, we found out the existence of a relaxor-type non-paraelectric cubic phase at the temperature below the dielectric permittivity peak, and the presence of the tetragonal ferroelectric phase at the temperature over that one.
3. The cubic non-paraelectric phase existing at the temperature below 180 °C is similar on its characteristics to the glass-dipole state in lead magnesium niobate. The presence of small clusters of the T-phase along with the paraelectric cubic phase in the temperature range 210–320 °C can be considered as an analogue of the glass-dipole state.
4. Detection of several temperature points at PT in the PKR-7M, at which some qualitative changes in the structure and properties of the material take place, indicates a very significant role of the interaction between the microregions in crystallites. Therefore, consideration of a ferroelectric with a diffuse phase transition as a statistical set of elementary non-interacting subsystems—microregions with different properties [21] is not quite correct.

Acknowledgments Work supported by the Ministry of Education and Science of RF (base and project parts of state order themes Nos. 213.01-11/2014-21 and 3.1246.2014/K), Southern Federal University (internal grant No. 213.01-2014/012-BT) and FCP (TK No. 14.575.21.0007).

References

1. G.A. Smolenskiy, V.A. Isupov, *Tech. Phys.* **24**(8), 1375 (1954) (in Russian)
2. V.A. Isupov, *Tech. Phys.* **24**(9), 1913 (1956) (in Russian)
3. G.A. Smolenskiy, V.A. Isupov, A.I. Agranovskaya, S.N. Popov, *Phys. Solid State* **2**(11), 2906 (1960) (in Russian)
4. V.A. Isupov, *Phys. Solid State* **5**(1), 187 (1963) (in Russian)
5. V.Y. Frizberg, B.N. Rolov, *Izv. AN USSR. Ser. Phys.* **28**(4), 649 (1964) (in Russian)
6. G.A. Smolenskiy, V.A. Bokov, V.A. Isupov, et al., in *The Physics of Ferroelectric Phenomenon*, ed. by G.A. Smolenskiy (Nauka, Moscow, 1985) (in Russian)
7. S.N. Dorogovzev, in *Proc. XII Russ. Conf. Phys. Ferroelectr.* **1**(1), 29 (1989) (in Russian)
8. A.A. Bokov, M.A. Malizkaya, I.P. Raevski, V.Y. Shonov, *Phys. Solid State* **32**(8), 2488 (1990) (in Russian)
9. A.A. Bokov, I.P. Raevski, V.Y. Shonov, *Izv. AN USSR. Ser. Neorg. Mater.* **26**(11), 2371 (1990) (in Russian)
10. A.A. Bokov, I.P. Raevski, in *Proceedings of the III International Conference on Preparation, Investigation and Application of Transparent Ferroelectric Ceramics*. Riga **2**, 235 (1988) (in Russian)
11. A.A. Bokov, *Bull. Russ. Acad. Sci.: Phys.* **57**(6), 25 (1993) (in Russian)
12. S.G.F. Stenger, A.J. Burgraaf, *Phys. Stat. Sol. (a)* **61**(11), 989 (1980)
13. C.A. Randall, D.J. Barber, P. Groves, R.W. Whatmore, *J. Mater. Sci.* **23**(1), 3678 (1988)
14. S.G. Kirillov, I.P. Raevski, A.A. Bokov, V.Y. Shonov, in: *Proceedings of the III International Conference on Preparation, Investigation and Application of Transparent Ferroelectric Ceramics*. Riga **2**, 212 (1988) (in Russian)
15. V.V. Laguta, M.D. Glinchuk, I.P. Bokov, A.N. Titov, E.M. Andreev, *Phys. Solid State* **32**(10), 3132 (1990) (in Russian)
16. Chen Zhili, N. Setter, L.E. Cross, *Ferroelectrics* **37**(1–4), 619 (1981)
17. C.G.F. Stenger, F.L. Scholten, A.J. Burgraaf, *Solid State Commun.* **32**(11), 989 (1979)
18. L.S. Kamzina, N.N. Kraynik, L.M. Sapoznikova, in: *Proceedings of the III International Conference on Preparation, Investigation and Application of transparent ferroelectric ceramics*. Riga **2**, 176 (1988) (in Russian)
19. N.N. Kraynik, L.A. Markova, A.A. Karamyan, *Phys. Solid State* **34**(6), 1789 (1992) (in Russian)
20. A.A. Bokov, I.P. Raevski, V.G. Smotrakov, *Phys. Solid State* **25**(7), 2025 (1983) (in Russian)
21. V.E. Yurkevich, *The Physics of Phase Transitions in Ferroelectric Solid Solutions* (Rostov University Press, Rostov-on-Don, 1983). (in Russian)
22. I.N. Zakcharchenko, Y.S. Dudek, M.G. Radchenko, et al., in *About the Reasons of Phase Transition Diffusion in Ferroelectrics* (Rostov University Press, Rostov-on-Don, 1988) (in Russian)
23. G. Burns, F.N. Dacol, *Phys. Rev.* **28**, 2527 (1983)
24. G. Burns, B.A. Scott, *Solid State Commun.* **13**(3), 423 (1973)
25. V.A. Isupov, *Phys. Solid State* **28**(7), 2235 (1986) (in Russian)
26. M.F. Kupriyanov, G.M. Konstantinov, in *Proceedings of Internation Conference on Electronic Ceramics—Production and Properties*. Riga **1**, 36 (1990)
27. G.M. Konstantinov, *Structural Peculiarities of Perovskite Structure of Ferroelectric Solid Solutions in Morphotropic Transition Regions*, *PhD Thesis*, Rostov-on-Don (1989) (in Russian)
28. G.M. Konstantinov, M.F. Kupriyanov, in *Proceedings of International Conference on Electronic Ceramics—Production and Properties*. Riga **1**, 114 (1990)
29. E.G. Fesenko, A.Y. Danziger, O.N. Razumovskaya, *New Piezoelectric Materials* (Rostov University Press, Rostov-on-Don, 1983) (in Russian)

30. G.M. Konstantinov, V.A. Servuli, Y.B. Ponomarenko, M.F. Kupriyanov, A.D. Feronov, in *Proceedings of Russ. Conference on Real Structure and Properties Acentric Crystals*, ed. by Aleksandrov (VIAMS, Moscow, 1990) (in Russian)
31. M.F. Kupriyanov, G.M. Konstantinov, A.E. Panich, *Ferroelectric Morphotropic Transitions* (Rostov University Press, Rostov-on-Don, 1992). (in Russian)
32. Y.Y. Kruchan, V.A. Freimanis, *Physical Properties of Ferroelectric Materials* (Latv. University, Riga, 1981), p. 56
33. R. Shyker, R.W. Gammon, *Phys. Rev. Lett.* **25**(4), 222 (1970)
34. P. Bonneau, P. Garnier, G. Calvarin, *J. Solid State Chem.* **31**, 350 (1991)
35. V.A. Isupov, *Izv. AN USSR* **54**, 6 (1990). (in Russian)
36. F.I. Savenko, L.P. Panchenko, B.V. Fedanov, in *Proceedings of Russ. Conference on Real Structure and Properties Acentric Crystals*, ed. by Aleksandrov **1**, 274 (1990) (in Russian)
37. N.N. Krainik, L.A. Markova, in: *Proceedings of Russ. Conference on Real Structure and Properties Acentric Crystals*, ed. by Aleksandrov **1**, 356 (1990) (in Russian)
38. V.A. Isupov, *Phys. Solid State* **34**(7), 2025 (1992) (in Russian)
39. V.A. Isupov, I.P. Pronin, T.A. Yazbaev, T.A. Shapligina, *Bull. Russ. Acad. Sci.: Phys.* **57**(3), 23 (1993) (in Russian)
40. V.A. Isupov, I.P. Pronin, V.I. Sizich, in *Proceedings of the III International Conference on Preparation, Investigation and Application of Transparent Ferroelectric Ceramics*. Riga **2**, 232 (1988)
41. G. Burns, F.N. Dacol, *Solid State Commun.* **58**(9), 567 (1986)

Chapter 17

Features of Electromagnetic Microwave Radiation Absorption by Ferroelectric Complex Niobium Oxides

A.G. Abubakarov, I.A. Verbenko, L.A. Reznichenko,
M.B. Manuilov, K.P. Andryushin, H.A. Sadykov, Y.M. Noykin,
M.V. Talanov and M.S. Zakrieva

Abstract The solid solutions of the niobium oxides were prepared using two-stage solid-phase synthesis and sintering by conventional ceramic technology. The dissipative characteristics of the solutions were studied experimentally in the microwave frequency range 1.0–11.0 GHz. It is shown that the maximum of microwave power absorption is observed usually near the phase boundaries in the systems of solid solutions, containing phase transitions of different nature. It is suggested that this behavior is connected with development of the defective structures in the corresponding media due to breaking of chemical bonds during the structure adjustments, accumulation of vacancies and impurity phases and increasing the number of interfaces. The obtained results open a possibility for development of new functional materials, which may be used in a variety of industrial applications operating within microwave frequency band. In particular, these materials may be employed to solve the problem of electromagnetic compatibility (EMC) of different radio-electronic systems, as well as the problem of protection against electromagnetic interference and development of passive microwave components including integrated circuit components.

17.1 Introduction

The dramatically fast growth and expansion of modern radio frequency (RF) and microwave wireless communications state the problem of electromagnetic safety. The long exposure under RF/microwave energy may lead to the various negative

A.G. Abubakarov (✉) · I.A. Verbenko · L.A. Reznichenko · H.A. Sadykov · M.V. Talanov
M.S. Zakrieva
Research Institute of Physics, Southern Federal University, 344090 Rostov-on-Don, Russia
e-mail: abubakarov12@mail.ru

M.B. Manuilov · K.P. Andryushin · Y.M. Noykin
Department of Physics, Southern Federal University, 344090 Rostov-on-Don, Russia

biological effects and diseases for human. Since the biological effects of RF/microwave radiation, associated with wireless devices, were studied still tentative, the precautionary approach currently is most appropriate. It means that the human exposure under RF/microwave energy should be reduced to acceptable level.

The efficient way to meet the electromagnetic safety standards as well as to reduce acceptable level of the electromagnetic interference by simultaneous operation of the different radio-electronic systems is based on utilizing the radio absorbing materials (RAM), the radio absorbing covers (RAC) and shields.

The radio absorbing materials may be used for protection of computer information processing systems against the unauthorized access as well as in the space applications and for electromagnetic radiation absorption in the absorbing screens, covers and in the measuring anechoic chambers.

The other important problem is the electromagnetic compatibility (EMC) of various radio electronic systems by their simultaneous operation. To eliminate the effects of electromagnetic interference, the radio absorbing materials may be considered as a promising candidate for the protection of radio electronic systems against the electromagnetic radiation.

The presented paper is devoted to the investigation of dissipative characteristics of the solid solutions ceramics based on niobium oxides.

17.2 Subjects Under Consideration. Methods of Samples Fabrication and Investigation of Samples

The subjects under consideration are the solid solutions of the stoichiometric and non-stoichiometric combinations, binary and triple systems as follow: Na_xNbO_3 , $\text{Na}_{1-x}\text{Li}_x\text{NbO}_3$, $(1-x)\text{NaNbO}_3-x\text{Ca}_2\text{Nb}_2\text{O}_7$, $(1-x)\text{NaNbO}_3-x\text{Sr}_2\text{Nb}_2\text{O}_7$, $(1-x)\text{BaNb}_2\text{O}_6-x\text{SrNb}_2\text{O}_6$, $\text{NaNbO}_3-\text{CuNb}_2\text{O}_6$, $(1-x-y)\text{NaNbO}_3-x\text{KNbO}_3-y\text{Cd}_{0.5}\text{NbO}_3$, $x\text{NaNbO}_3-y\text{KNbO}_3-z\text{CuNb}_2\text{O}_6$. The solid solutions have been synthesized by solid-state reaction method on the base of the corresponding oxides and carbonates. We used the two-stage firing with the intermediate grinding. The ceramic samples were sintered by the temperature 1190–1200 °C during the time interval up to 2 h depending on the composition. In the next step, all ceramic columns were cutted and polished to obtain the samples in the form of discs with a diameter 10 mm and a thickness 1 mm.

To test experimentally the fabricated ferroelectric samples, we used the vector network analyzer Agilent PNA E8363 V (operational frequency band $f = 10 \text{ kHz} - 40 \text{ GHz}$) with a measuring cell based on micro-strip line. In Figs. 17.1 and 17.2 the measurement set and the micro-strip line based measuring cell are schematically depicted. The tested sample is placed on the micro-strip line with the 50Ω —wave impedance. The two-port structure in Fig. 17.2 is linear mutual symmetrical quadripole in terms of the circuit theory.

Fig. 17.1 Measurement set based on agilent PNA E8363B

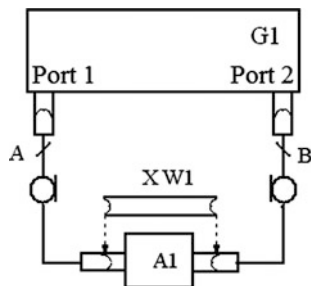
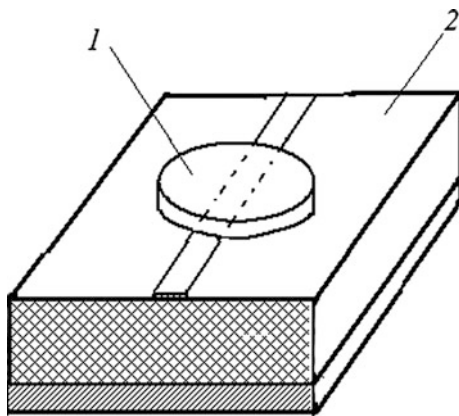


Fig. 17.2 Placement of the sample by measurements (1—ferroelectric sample, 2—microstrip line)



To characterize the microwave absorption of the ceramic samples we used the scattering matrix of two-port structure in Fig. 17.1 [1, 2]:

$$(S) = \begin{pmatrix} S_{11} & S_{12} \\ S_{21} & S_{22} \end{pmatrix} \tag{17.1}$$

Here, the complex parameter $S_{21} = |S_{21}|e^{j\varphi_{21}}$ is the transmission coefficient at the port 2 by the excitation of two-port device from the port 1; the element $S_{11} = |S_{11}|e^{j\varphi_{11}}$ is the reflection coefficient by excitation of the port 1. The matrix elements S_{12} and S_{22} in (17.1) correspond to the excitation of the two-port structure from the port 2 and they have the same physical interpretation. In the case of linear mutual symmetrical quadripole we can write

$$|S_{12}| = |S_{21}|, \quad \arg S_{12} = \arg S_{21}$$

. In the first step of the experiment the frequency characteristics of module S_{21} (in dB) and phase φ_{21} (in degrees) are measured for the micro-strip line without the ferroelectric sample. In the next step, we measured the frequency characteristics of two-port device with the ferroelectric sample placed on the micro-strip line. The difference between the respective characteristics is the frequency dependence of the

module and phase on the transmission coefficient of the test sample. So we obtained the evaluation of the microwave absorption (insertion loss) associated with the ferroelectric sample.

17.3 Experimental Results and Discussion

Figure 17.3 shows the electromagnetic energy absorption spectra for the following compositions: 1— BaNb_2O_6 ; 2— NaNbO_3 ; 3— AgNbO_3 ; 4— $\text{Sr}_2\text{Nb}_2\text{O}_7$; 5— $\text{Ca}_2\text{Nb}_2\text{O}_7$; 6— SrNb_2O_6 —which are the base compositions for binary and triple systems.

The analysis of the experimental results demonstrates that in all examined systems of solid solutions, the deep resonant absorption peaks (up to 30–40 dB) may be observed. First of all, it is associated with the presence of the ferroelectric states in the examined matters (including anti-ferrielectric NaNbO_3 , AgNbO_3). It means that the crystallite grains have the specific domain structure.

Some elements of the structure may be in the resonance by the incidence of electromagnetic waves. Thus, it leads to the efficient absorption of the microwave energy. The features of the crystal structures of the examined combinations play a role of the additional causes of the considerable absorption.

The friability of the structure of natrium niobate and argentum niobate connects with the discrepancy of the crystal-chemical parameters to the structure of perovskite (the own dimensions of cations Na^+ and Ag^+ are considerably lesser than the dimensions of the interoctahedral hollows where they are placed). Thus, the friability provides the high sensitivity of their properties, including the domain wall mobility by the external exposure. Moreover, these combinations have the block structure in which the presence of the ordered extensive defects (unfilled interblock channels) is observed.

The change of domain structure is possible under the influence of mechanical stresses in the areas of their origins. On the other hand, the conditions appear for the redistribution of the polarized nanoclusters of the ferrielectric state.

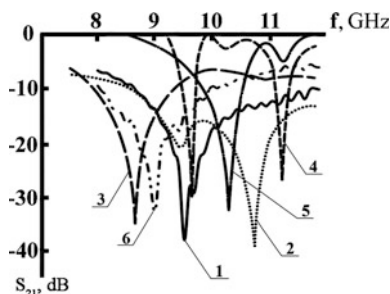


Fig. 17.3 The absorption spectra of the energy of electromagnetic radiation connections: 1— BaNb_2O_6 ; 2— NaNbO_3 ; 3— AgNbO_3 ; 4— $\text{Sr}_2\text{Nb}_2\text{O}_7$; 5— $\text{Ca}_2\text{Nb}_2\text{O}_7$; 6— SrNb_2O_6

Probably, the deep absorption peaks in the spectra of BaNb_2O_6 and SrNb_2O_6 are caused by the presence of unfilled interoctahedral hollows in the triangular, quadrangular, pentagonal channels of their structure. In the cases of $\text{Sr}_2\text{Nb}_2\text{O}_7$ and $\text{Ca}_2\text{Nb}_2\text{O}_7$, it may be caused by stratified structure of these compositions.

The electromagnetic radiation absorption spectra of compositions Na_xNbO_3 are present in Fig. 17.4 and the dependence $S_{21}(x)$ is depicted in Fig. 17.5. We can see in Fig. 17.4a–c that the characteristics of $S_{21}(f)$ have absorption peaks (~ 30 – 40 dB) in the frequency range $f = 6$ – 9 GHz. In the cation-deficit ($0.80 \leq x < 1.00$) and in the cation-excessive ($1.00 < x \leq 1.20$) sodium niobat, we observe the change of the multiplicity of the monocline (M) subcell of the rhombic (RII) cell of NaNbO_3 from quadruple one (M4) (which corresponds to stoichiometric composition) to doubled one (M2). In these ranges, the considerable absorption has been registered (Figs. 17.4 and 17.5). Undoubtedly, this effect is connected with the increased defectiveness of the examined compositions.

Figures 17.6 and 17.7 show the electromagnetic radiation absorption spectra of the compositions $\text{Na}_{1-x}\text{Li}_x\text{NbO}_3$ and the phase diagrams of systems with the dependencies of $S_{21}(x)$ for the samples with the different thermodynamic prehistory of solid solutions of the system (the phase diagram of $(\text{Na}, \text{Li})\text{NbO}_3$ is given in accordance with [3]). As we can see, the presented spectra are non-monotonous and they have resonant absorption maxima within the frequency band 6–10.5 GHz. The extremum values of S_{21} are typical for HP (hot-pressing) samples, which are disposed on the phase diagram in the vicinity of the structure instability of the various

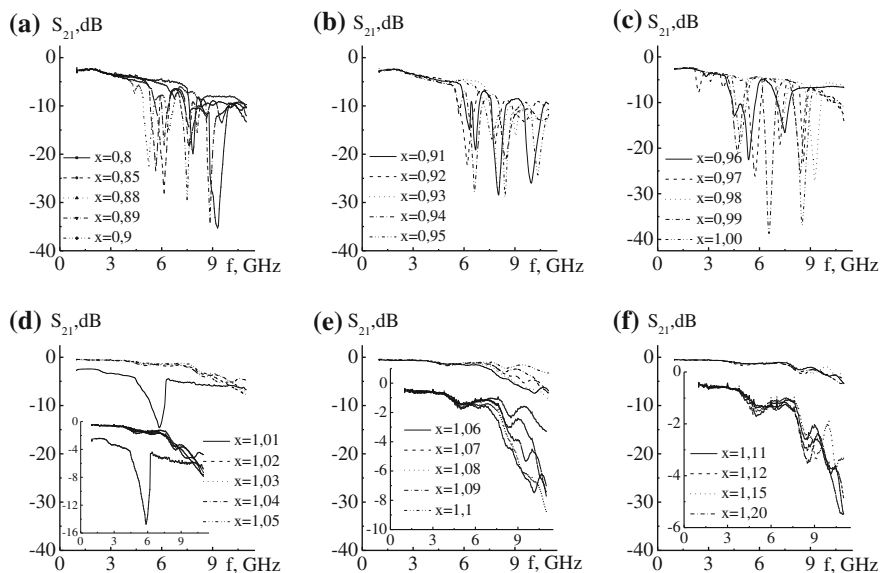


Fig. 17.4 Electromagnetic radiation absorption spectra of compositions Na_xNbO_3 ($0.80 < x \leq 1.20$)

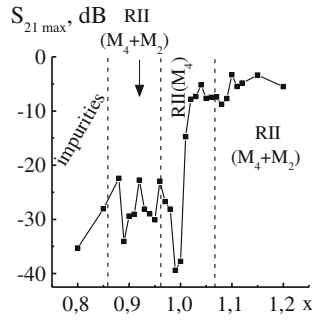


Fig. 17.5 Dependence of the maximum values of the microwave absorption on index of non-stoichiometry x for compositions Na_xNbO_3 ($0.80 < x \leq 1.20$)

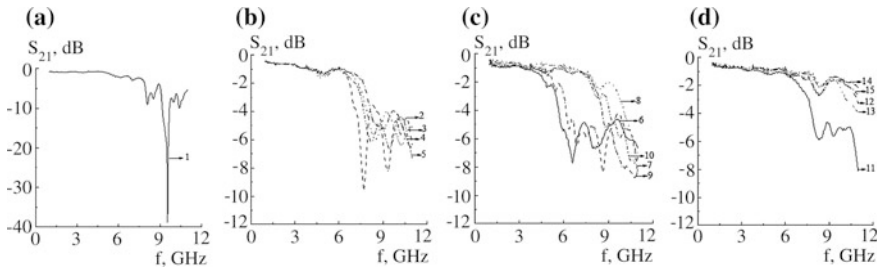


Fig. 17.6 Electromagnetic radiation absorption spectra of the compositions $\text{Na}_{1-x}\text{Li}_x\text{NbO}_3$: **a–d** $x = 0$ (1); 0.01 (2); 0.02 (3); 0.03 (4); 0.04 (5); 0.05 (6); 0.06 (7); 0.07 (8); 0.08 (9); 0.09 (10); 0.10 (11); 0.11 (12); 0.12 (13); 0.13 (14); 0.14 (15)

nature (with the exception of CCT (conventional ceramic technology) NaNbO_3 which has the record value of S_{21} (~ 40 dB) in conventional sintered ceramics). These values are accompanied with the anti-ferrielectric—ferrielectric transition (it corresponds to transition $1 \rightarrow 7$ in Fig. 17.8), the change of the cell multiplicity (it is the transition $3 \rightarrow 8$ in Fig. 17.7), the cell symmetry (it is the complex transition $10 \rightarrow 11 \rightarrow 12$ in Fig. 17.7) and the isomorphous types of the solid solutions (introduction-substitution, there are the transitions $5 \rightarrow 9 \rightarrow 14 \rightarrow 15$ in Fig. 17.7).

The absorption spectra, $S_{21}(f)$, of the investigated samples of the system $(1-x)\text{NaNbO}_3-x\text{Ca}_2\text{Nb}_2\text{O}_7$, $(1-x)\text{NaNbO}_3-x\text{Sr}_2\text{Nb}_2\text{O}_7$ are present in Figs. 17.8, 17.9, 17.10 and 17.11a–f as well as the dependencies of $S_{21}(x)$ for these systems with the phase diagrams. The solid solutions of perovskite type arise in these systems at $0 \leq x \leq 0.2$. The symmetry of the solutions changes by increasing x from rhombic (R) phase with the quadruple monocline subcell (M4) to cubic one with the superstructure (K2) and further without of superstructure (K). We can mark out two areas with the mixed type of structures, including the structures with the monocline cells of the different multiplicity. By the penetrating deep into the system, the perovskite structure changes to the stratified structure (c) with the various values of n . The alternative to the stratified structure be the phases, which crystallize as the

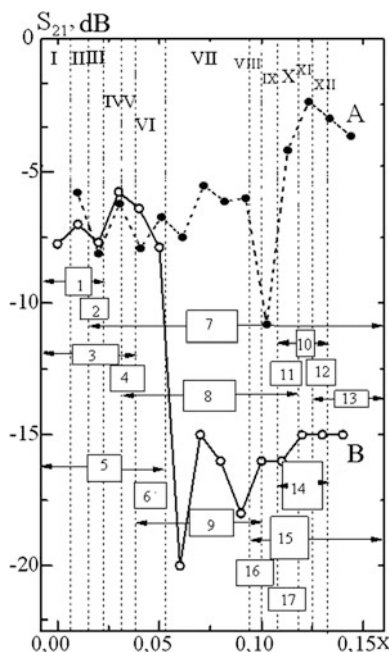


Fig. 17.7 Phase diagram of the system $\text{Na}_{1-x}\text{Li}_x\text{NbO}_3$: 1—antiferroelectric phase; 2, 4, 6, 11, 12, 16, 17—morphotropic regions; 3—rhombohedral (R) cell with the quadruple monocline subcell (M4); 8, 13—R-cell with double monocline subcell (M2); 5—SS introduction (T_{in}); 7—ferroelectric phase; 9, 14, 15—SS substitution (SS_{sb}) of various types; 10—rhombohedral (Rh) phase with dependencies of $S_{21}(x)$ for samples with different thermodynamic prehistory (A—CCT unpolarized specimens B—HP unpolarized samples)

independent forms at $x = 0.33$ (C(1), $\text{Na}_4\text{Ca}(\text{Sr})_2\text{Nb}_5\text{O}_{19}$, $b = 60.14\text{--}60.85 \text{ \AA}$, $n = 12$); $x = 0.40$ (C(2), $\text{Na}_3\text{Ca}(\text{Sr})_2\text{Nb}_5\text{O}_{11}$, $b = 52.24\text{--}53.3 \text{ \AA}$, $n = 10$); $x = 0.67$ (C(3), $\text{NaCa}(\text{Sr})_2\text{Nb}_5\text{O}_{10}$, $b = 37.7 \text{ \AA}$, $n = 6$); $x = 0.80$ (C(4), $\text{NaCa}(\text{Sr})_4\text{Nb}_5\text{O}_{17}$, $b = 32.1\text{--}32.8 \text{ \AA}$, $n = 5$); $x = 0.89$ (C(5), $\text{NaCa}(\text{Sr})_8\text{Nb}_9\text{O}_{31}$, $b = 58.8\text{--}59.5 \text{ \AA}$, $n = 4.5$), $x = 1.0$ (C(6), $\text{NaCa}(\text{Sr})_2\text{Nb}_2\text{O}_7$, $b = 26.0\text{--}26.9 \text{ \AA}$, $n = 4$), that is accompanied by decreasing n .

Generally, the pictures of the phase states are nearly identical in the both systems. The exception is that in the system with $\text{Ca}_2\text{Nb}_2\text{O}_7$ the structures C(1) and C(2) coexist with the other structures and they produce the multi-phase areas. Moreover, in the system with $\text{Sr}_2\text{Nb}_2\text{O}_7$, the phase of the variable composition forms in the range $0.6 < x < 0.85$, which is based on the compositions C(3) and C(4). Figures 17.8, 17.9, 17.10, 17.11, 17.12 and 17.13 show that the absorption peaks are observed at $x \approx 0.3, 0.8, 0.9, 0.95, 1.0$. The peak positions and the peak shapes depend on the frequency: at $f = 3 \text{ GHz}$, the maximal absorption is approximately constant within the considered interval of x ; at $f = 6 \text{ GHz}$ the maximal absorption registers at $x \approx 0.85, 0.92, 0.97$; at $f = 9 \text{ GHz}$, the maximal absorption corresponds to $x \approx 0.8, 0.9, 0.98, 0.6$.

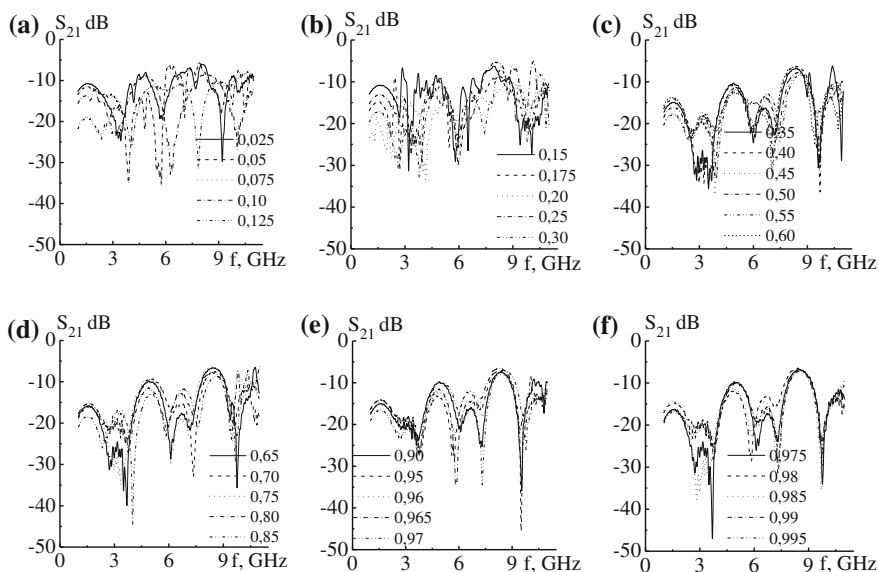
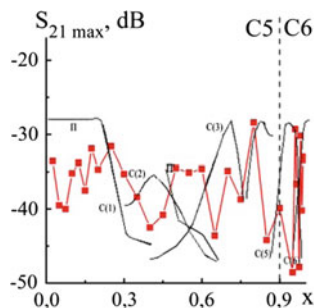


Fig. 17.8 Absorption spectra of microwave power of solid solutions $(1-x)\text{NaNbO}_3-x\text{Ca}_2\text{Nb}_2\text{O}_7$

Fig. 17.9 Dependence of $S_{21}(x)$ in $(1-x)\text{NaNbO}_3-x\text{Ca}_2\text{Nb}_2\text{O}_7$ superimposed phase diagram



Thus, in these systems with the stratified structures, the maximal absorption ($\sim 35\text{--}40$ dB, ~ 60 dB) is observed near the edge components. The moderate values of $|S_{21}|$ correspond to the middle (principal) part of the systems. These values are greater in the system with $(1-x)\text{NaNbO}_3-x\text{Ca}_2\text{Nb}_2\text{O}_7$ (~ 30 dB) (~ 40 dB).

The microwave absorption spectra, $S_{21}(f)$ for binary system $(1-x)\text{BaNb}_2\text{O}_6-x\text{SrNb}_2\text{O}_6$ ($x = 0.00\text{--}0.10$) are present in Fig. 17.12a, b and the dependence $S_{21}(x)$ with phased diagram is shown in Fig. 17.13. The high values of the absorption achieve near the morphotropic areas (in Fig. 17.13— MO_1 , MO_2).

Figure 17.14a, b shows the microwave absorption spectra, $S_{21}(f)$, of the binary system $\text{NaNbO}_3\text{--CuNb}_2\text{O}_6$. In this system, the maximal microwave absorption achieves in the frequency band $f = 3\text{--}5$ GHz and it corresponds to $x \sim 0.15$ within morphotropic area (T + Psc) (Fig. 17.15).

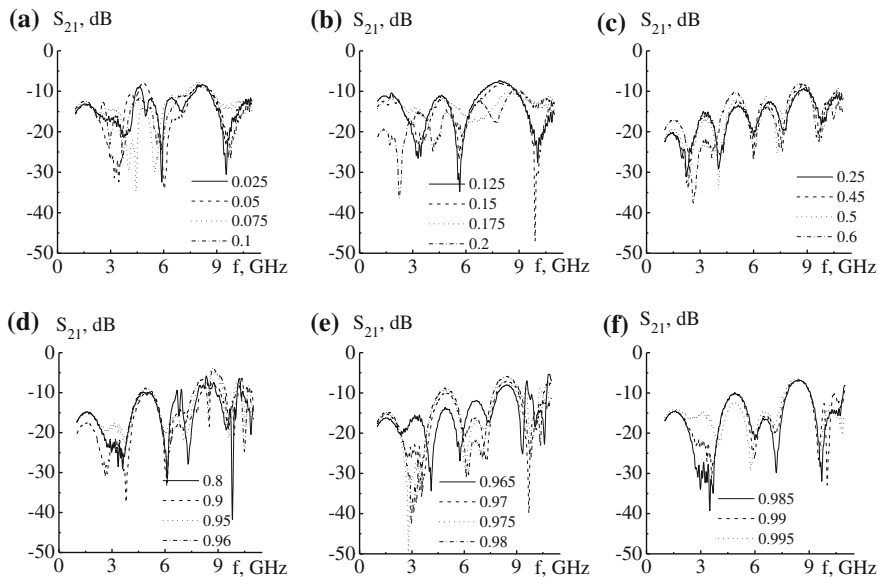


Fig. 17.10 Absorption spectra of microwave power of solid solutions $(1 - x)\text{NaNbO}_3 - x\text{Sr}_2\text{Nb}_2\text{O}_7$

Fig. 17.11 Dependence of $S_{21}(x)$ in $(1 - x)\text{NaNbO}_3 - x\text{Sr}_2\text{Nb}_2\text{O}_7$ superimposed phase diagram

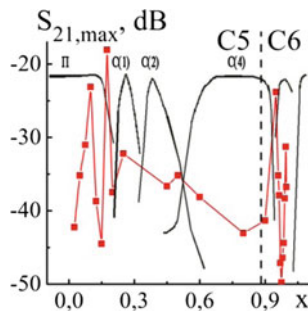


Fig. 17.12 Absorption spectra of microwave power of solid solutions $(1 - x)\text{BaNb}_2\text{O}_6 - x\text{SrNb}_2\text{O}_6$

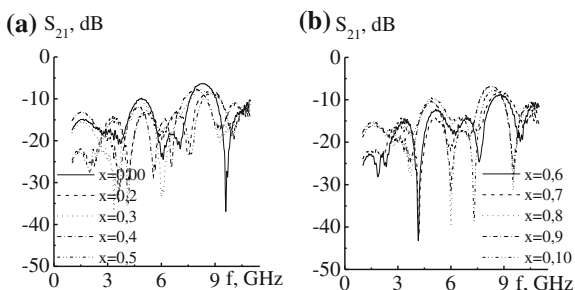


Fig. 17.13 Dependence of $S_{21}(x)$ in $(1-x)\text{BaNb}_2\text{O}_6-x\text{SrNb}_2\text{O}_6$ superimposed phase diagram

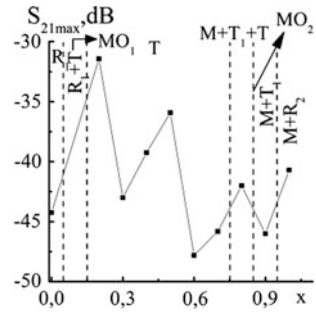


Fig. 17.14 The absorption spectra of microwave power for solid solutions of $\text{NaNbO}_3\text{-CuNb}_2\text{O}_6$ system

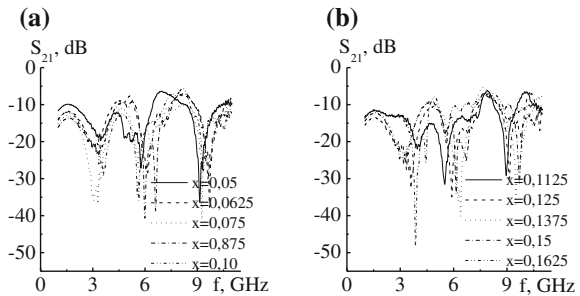
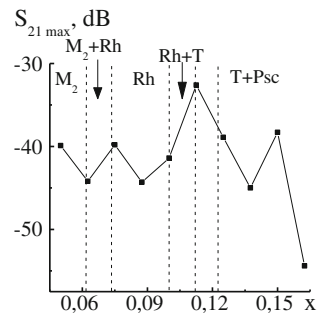


Fig. 17.15 Dependence of $S_{21}(x)$ in $\text{NaNbO}_3\text{-CuNb}_2\text{O}_6$; overlay of the phase diagram



The absorption spectra for the solid solutions of $\text{Na}_x\text{K}_y\text{Cu}_{0.5}\text{NbO}_3$ system are present in Fig. 17.16a–f for three sections (I section: $y = 0.05\text{--}0.50$; $\Delta y = 0.05$) (II section: $y = 0.05\text{--}0.45$; $\Delta y = 0.05$) (III section: $y = 0.05\text{--}0.40$; $\Delta y = 0.05$) as well as the dependencies $S_{21}(x)$ for these sections with the phase diagrams (i–l). In all sections, the maximal absorption takes place in the areas of the phase transitions of the various nature or in the vicinities of the phase transitions.

In Fig. 17.17a–k, the microwave absorption spectra for the solid solutions of $(1-x-y)\text{NaNbO}_3-x\text{KNbO}_3-y\text{Cd}_{0.5}\text{NbO}_3$ system, are present for seven sections, corresponding to the following compositions: I section with $y = 0.05$, $x = 0.05\text{--}0.65$, $\Delta x = 0.05$; II section with $y = 0.10$, $x = 0.05\text{--}0.50$, $\Delta x = 0.05$; III section with

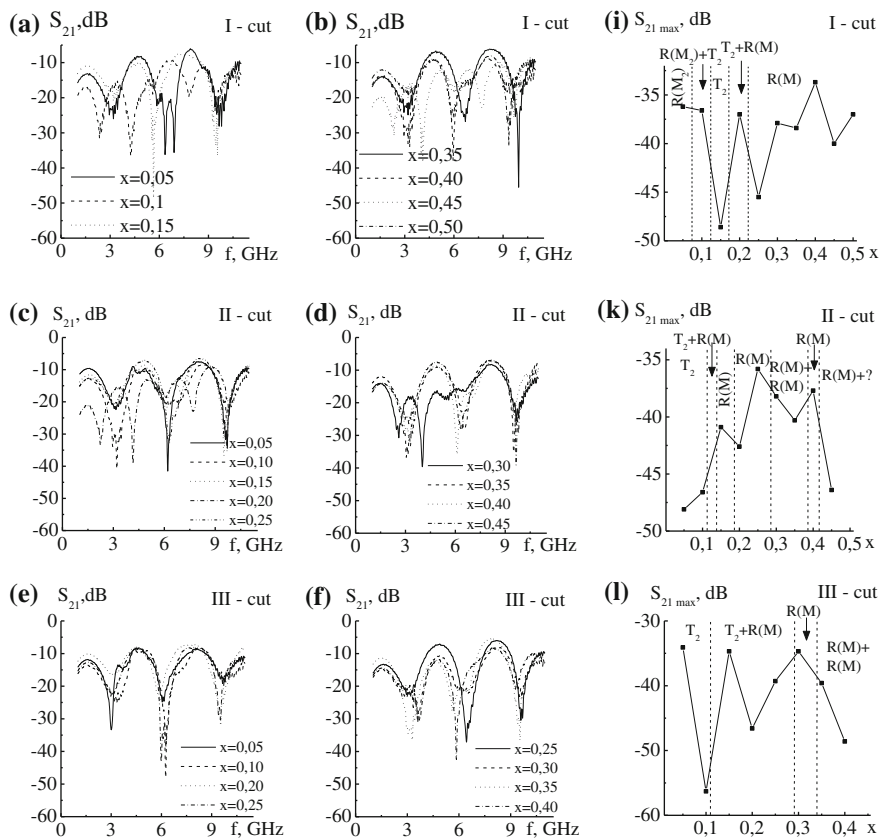


Fig. 17.16 Absorption spectra of microwave power for solid solutions of $\text{Na}_x\text{K}_y\text{Cu}_{0.025}\text{NbO}_3$ system (a–f) and dependencies $S_{21}(x)$ for these sections with phase diagrams (i–l)

$y = 0.15, x = 0.05\text{--}0.30, \Delta x = 0.05$; IV section with $y = 0.20, x = 0.05\text{--}0.20, \Delta x = 0.025$; V section with $y = 0.25, x = 0.05\text{--}0.20, \Delta x = 0.025$; VI section with $y = 0.30, x = 0.05\text{--}0.20, \Delta x = 0.025$; VII section with $y = 0.025\text{--}0.150, x = 0.45, \Delta y = 0.025$.

We can see that in all figures, the maximal loss ($|S_{21}|$) achieves near the phase edges.

Thus, it is the common fact for all examined samples that the largest values of the insertion loss are observed in the areas of the structural instabilities of the different nature. These results are accompanied in the various systems with the change of the cell multiplicity [4], cell symmetry, types of the shaped structures (Fig. 17.5: M4–quadruple, M2–doubled monocline subcell of the rhombic cell of Na_xNbO_3 ; Fig. 17.13: T–P–tetragonal–rhombic transition in the system (Ba, Sr) Nb_2O_6 ; Fig. 17.9, 11: C5, C6—stratified phases in the $[\text{Na}, \text{Ca}(\text{Sr})]_2\text{Nb}_2\text{O}_7$ systems with the stratified perovskite-like structure of $A_nB_nO_{3n+2}$ type in which $n = 4$ (C6)

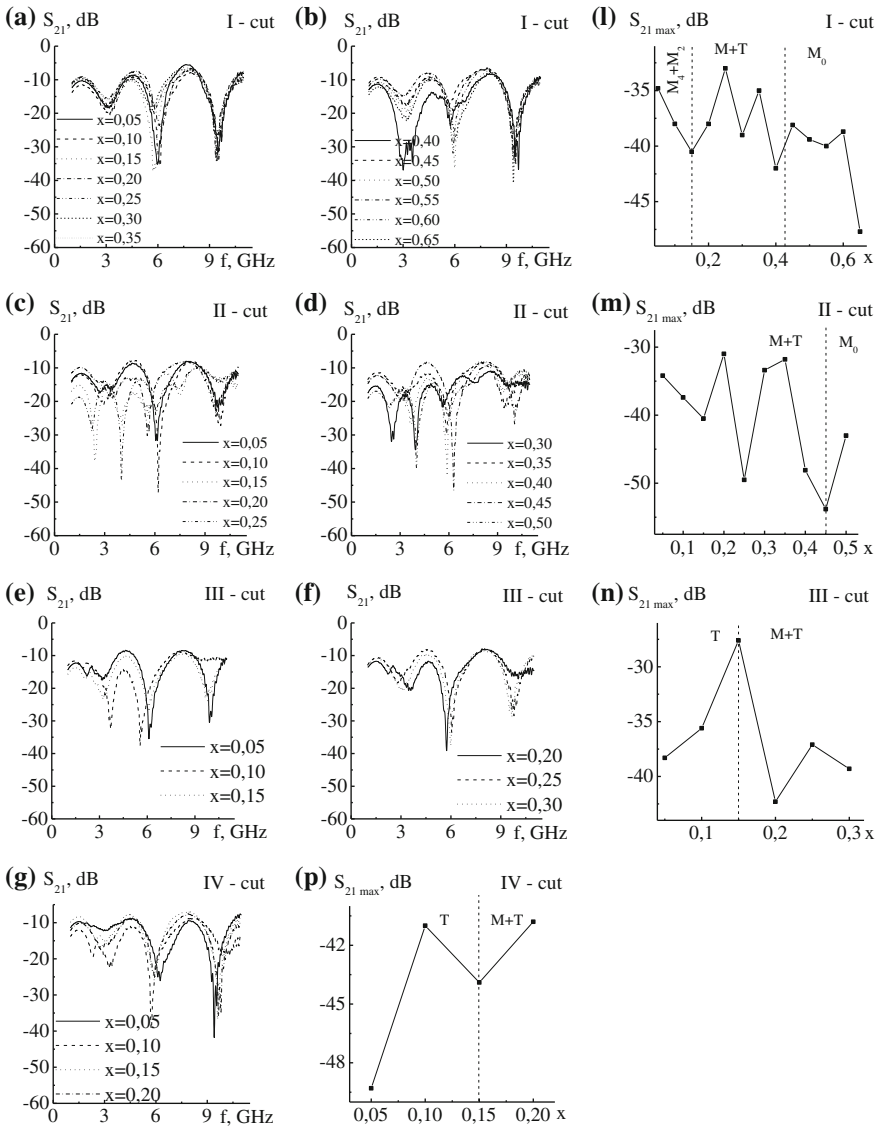


Fig. 17.17 Absorption spectra of microwave power for solid solution of $(1 - x - y)\text{NaNbO}_3 - x\text{KNbO}_3 - y\text{Cd}_{0.5}\text{NbO}_3$ system (a–k) and dependencies $S_{21}(x)$ for these sections with phase diagrams (e–t)

and 4.5 (C5)). These solid solutions have the increased defectiveness providing the high microwave absorption (at the expense of the break of the chemical links by rebuilding of the structure, accumulation of the vacancies, impurity phases [5], increase of the number of interfaces).

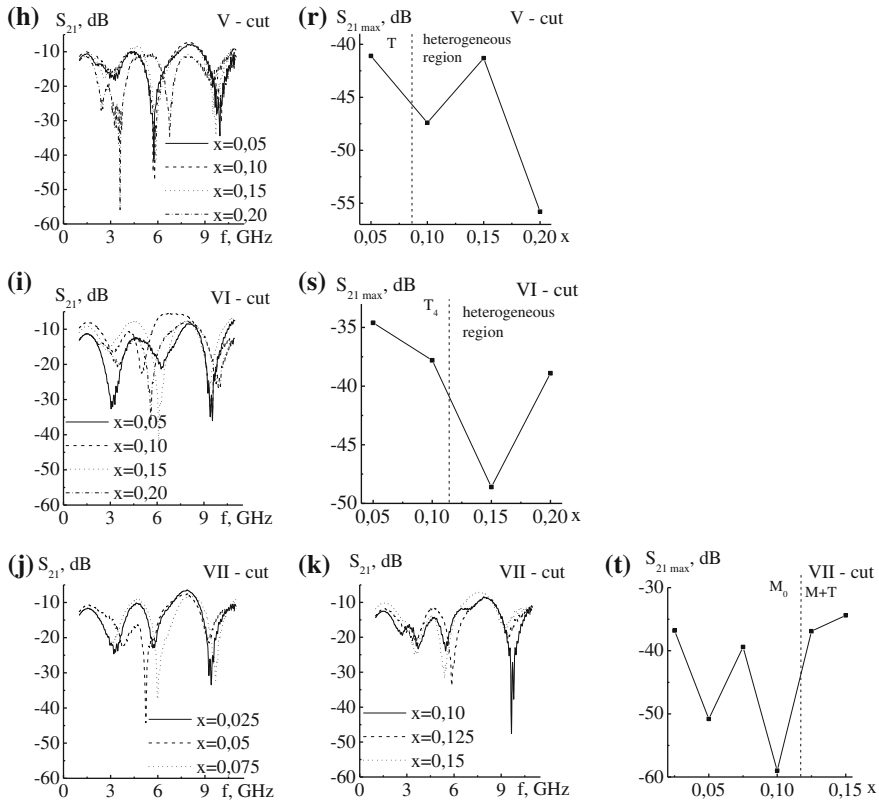


Fig. 17.17 (continued)

17.4 Conclusions

1. It is proven, that in the systems of the solid solutions based on the examined niobium compositions, the maximal values of $|S_{21}|$ achieve in the vicinity of the structural instabilities of the different nature. It is coupled with development of the defect state in the corresponding media at expense of the break of the chemical links by rebuilding of structure, accumulation of vacancies and impurity phases, increase of the number of interfaces.
2. The detected principle of forming the dissipative properties of the investigated complex niobium compositions provides the foundations for the choice of the prospective media for development of the materials with high absorption of electromagnetic radiation within the wide frequency band.

Acknowledgments This work was financially supported by the Ministry of Education and Science of the Russian Federation: Agreement No. 14.575.21.0007 (Federal Target Program).

References

1. A.S. Elizarov, *Automation of Measurements of Parameters of Linear Non-reciprocal Microwave Four-poles* (Soviet Radio, Moscow, 1978). (In Russian)
2. A. Vaysfloh, in *Theory of Circuits and Measurement Technique in the Decimeter and Centimeter bands*. ed. by M.A. Silaeva. Soviet Radio, Moscow (1961) (In Russian)
3. L.A. Reznichenko, L.A. Shilkina, O.N. Razumovskaya, S.I. Dudkina, E.S. Gagarina, A.V. Borodin, *Neorgan. Mater.* **39**(2), 187 (2003)
4. E.M. Kuznetsova, L.A. Reznichenko, I.P. Rajewski, in *International Symposium Streamlining of minerals and alloys (OMA-2000)*, Rostov-on-Don, pp. 59 (2000) (In Russian)
5. L.A. Reznichenko, I.N. Andryushina, I.A. Verbenko, O.Y. Kravchenko, A.I. Miller, A.A. Pavelko, in *XIV National Conference on Crystal Growth, IV International Conference Crystal Physics of the XXI Century in the memory of M. P. Shaskolskaya (NKRK 2010)*. Moscow. vol. 1, pp. 437 (2010)

Chapter 18

Research of Structure Ordering in Ceramic Ferroelectromagnets $\text{Bi}_{1-x}\text{La}_x\text{FeO}_3$ by Raman Spectroscopy

N.A. Teplyakova, S.V. Titov, I.A. Verbenko, N.V. Sidorov
and L.A. Reznichenko

Abstract The ordering processes in structures of ceramic ferroelectromagnets $\text{Bi}_{1-x}\text{La}_x\text{FeO}_3$ ($x=0.075-0.20$) is researched by Raman spectra. It was discovered that $\text{Bi}_{1-x}\text{La}_x\text{FeO}_3$ structure is close to the one of BiFeO_3 . However, bands in Raman spectra of $\text{Bi}_{1-x}\text{La}_x\text{FeO}_3$ were much wider than bands of single crystal BiFeO_3 which means that in ceramics solid solutions, structure is more disordered than in single crystals. In Raman spectra of $\text{Bi}_{1-x}\text{La}_x\text{FeO}_3$ in the area of oxygen octahedrons librations ($50-90\text{ cm}^{-1}$) several groups of bands with frequencies $59-69$, $72-77$, $86-92\text{ cm}^{-1}$ were observed in dependence of solid solution compound. This result confirms XRD data that researched solid solutions are not single phase. At La ($x=0.120$) low-frequency bands in Raman spectra narrowed which indicates ordering of structure units in cation sublattices. At increase of La concentration in $\text{Bi}_{1-x}\text{La}_x\text{FeO}_3$ structure, unambiguous dependence of spectral bands parameters was not observed. Perhaps this could be explained by the fact that at increase of x value, character of La integration to the solid solution structure changes.

18.1 Introduction

Bismuth ferrite (BiFeO_3) is a ferroelectromagnetic with high Curie temperature (1123 K) and high antiferromagnetic Neel point (643 K). It is a perspective base for creation of highly effective magnetoelectric materials. Partial substitution of bismuth ions by ions of rare earth elements in the structure possibly leads to the destruction of the spatially modulated spin structure of BiFeO_3 that prevents the emergence of the

N.A. Teplyakova (✉) · N.V. Sidorov

Tananaev Institute of Chemistry and Technology of Rare Elements and Mineral Raw Materials of the Russian Academy of Sciences Kola Science Center, Apatity, Murmansk Region, Russia
e-mail: tepl_na@chemy.kolasc.net.ru

S.V. Titov · I.A. Verbenko · L.A. Reznichenko

Research Institute of Physics, Southern Federal University, Rostov-on-Don, Russia

magnetoelectric effect in BiFeO_3 [1]. Lanthanum ions are among the most technological and perspective modifiers. Analysis of publications on the topic of structure researches of $\text{Bi}_{1-x}\text{La}_x\text{FeO}_3$ solid solutions revealed absence of consensus about the structural phase transitions sequence and intervals of phases existence, especially the close to BiFeO_3 ones [2–7]. Common among these opinions is that with La/Bi ratio growth, solid solutions form continuously and rhombohedral (Rh) phase transforms, usually to rhombic (R) phase. La-concentration of this transition is varying in papers of different researches. This chapter presents the results of a study of ordering processes in structure of ceramic $\text{Bi}_{1-x}\text{La}_x\text{FeO}_3$ solid solutions at change of lanthanum amount ($x = 0.075\text{--}0.20$) by Raman spectra. In the literature, as far as we aware of, there are no studies of the Raman spectra of $\text{Bi}_{1-x}\text{La}_x\text{FeO}_3$ ($x = 0.075\text{--}0.20$) solid solutions. Such researches are important at development of new ferroelectric materials based on modified bismuth ferrite.

18.2 Method

Ceramic $\text{Bi}_{1-x}\text{La}_x\text{FeO}_3$ solid solutions were created by solid phase synthesis with subsequent annealing by usual ceramic technology. Annealing regimes were chosen to obtain the densest ceramic samples. Annealing lasted in $0.00 \leq x \leq 0.10$ (910 °C) and $0.11 \leq x \leq 0.20$ (930 °C) ranges for the same time (2 h). Solid solutions samples of series of $\text{Bi}_{1-x}\text{La}_x\text{FeO}_3$ compound were obtained with different concentration step (Δx) for different x areas: $\Delta x = 0.025$ (in areas $0.000 \leq x \leq 0.075$ and $0.150 \leq x \leq 0.200$) and $\Delta x = 0.010$ (in area $0.090 < x \leq 0.150$).

Joint analysis of parameters of crystalline and grain structures of $\text{Bi}_{1-x}\text{La}_x\text{FeO}_3$ ceramic solid solutions at nominal La-concentration growth revealed that phase and mezostructure reorganization occurs simultaneously in the area $0.09 \leq x < 0.20$. Stepped character of solid solution formation is observed. After that, phases with high and low content of La co-exist in solid solutions. X-ray phase analysis showed that impurity-free samples could be obtained only for La-concentration $0.09 < x \leq 0.12$. There were standard admixtures of $\text{Bi}_{25}\text{FeO}_{40}$ and $\text{Bi}_2\text{Fe}_4\text{O}_9$ in samples with $x \leq 0.090$. In samples with $0.120 < x \leq 0.175$ appeared grains with compound corresponding to $\text{Bi}_{0.6}\text{La}_{0.4}\text{FeO}_3$. X-ray studies [8] revealed that single-phase Rh-area locates in the range $0.00 \leq x < 0.75$ and range $0.075 \leq x < 0.20$ contains wide morphotropic region. Ratio of R- and Rh-phases in this area varies significantly. Multifractal parameters of solid solutions reveal that these phase changes influence grain structure. Thus, clear picture of phase diagram with single-phase areas was impossible to obtain. We presented more detailed research of $\text{Bi}_{1-x}\text{La}_x\text{FeO}_3$ phase diagram in area $0.00 \leq x \leq 0.20$ by a complex of methods in [8].

Raman spectra were excited by 514.5 nm line of argon laser Spectra Physics (model 2018-RM) and were registered by spectrograph T64000 by Horiba Jobin Yvon with use of confocal microscope. Spectra were excited by low-power radiation ($P < 3$ mW). All spectra were registered with a resolution of 1.0 cm^{-1} at room temperature.

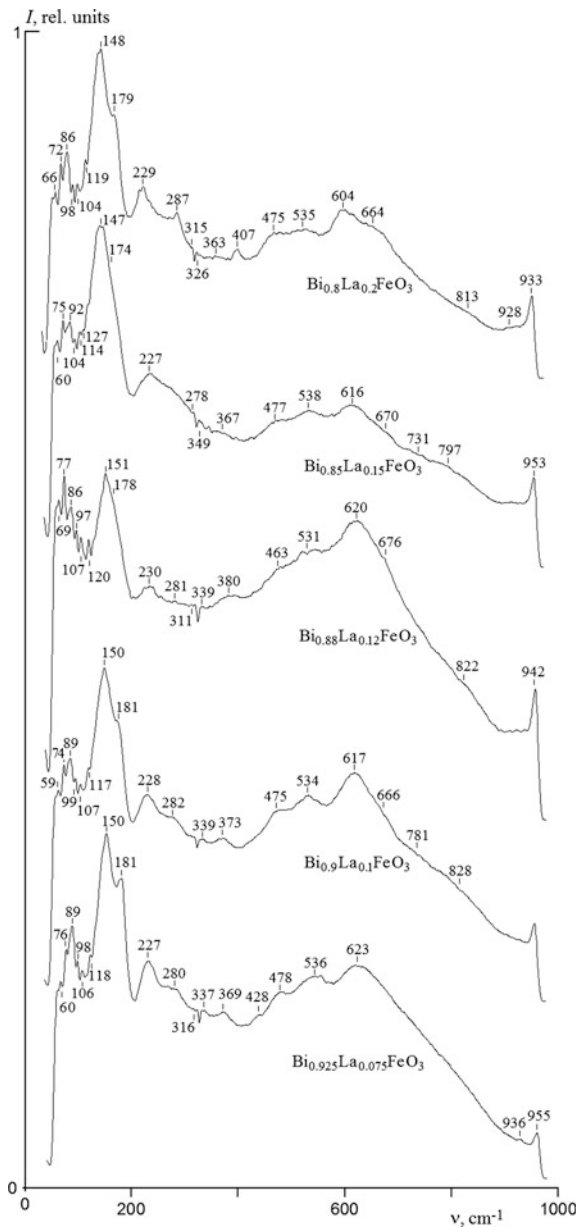
18.3 Results and Discussion

Crystal structure of BiFeO_3 single crystal at temperatures below ferroelectric transition ($T_C = 1083$ K) belongs to perovskite type ABO_3 and is described by spatial group $R3c$. Rhombohedral unit cell contains two formulae units and has parameters $a = 0.562$ nm and $\alpha = 59.35^\circ$ at room temperature. Octahedrons FeO_6 are antiphase deployed around the threefold axis. The crystal is characterized by complex domain structure. Due to factor-group analysis in IR and Raman spectra of rhombohedral BiFeO_3 crystal, $4A_1 + 9E$ modes are expected [9, 10]. The Raman spectra in polarized light in geometry “back” (180°) were compared in papers [9–14] in attempt to assign the Raman spectra bands of BiFeO_3 to the certain symmetry type vibrations (LO or TO). However, literature does not contain unambiguous assignment of LO and TO phonon modes of BiFeO_3 crystals. Raman spectra of BiFeO_3 crystals and films were searched by authors of [11–14]. Due to numerous experimental [9–13] and theoretical [15–17] researches, frequencies of Raman spectra of BiFeO_3 single crystals that are caused by optical phonons of first order belong to area of frequencies lower than 600 cm^{-1} and observed high-frequency bands are caused by two-particle processes.

Ceramic samples of $\text{Bi}_{1-x}\text{La}_x\text{FeO}_3$ solid solutions belong to complex perovskites $(A'_{1-x}A''_x)(B'_{1-y}B''_y)\text{O}_3$. In structure of complex perovskite apart from octahedral gaps BO_6 , there are much bigger gaps—coordination polyhedrons AO_x ($x \leq 12$). In system BiFeO_3 – LaFeO_3 in the area $x = (0.00\text{--}0.30)$, continuous row of solid solutions does not exist and obtained ceramics are many-phase composites with complex irregular structures. The structure and properties of these ceramics strongly depend on obtaining conditions. Due to co-existence of additional phases close to each other in composition, $\text{Bi}_{1-x}\text{La}_x\text{FeO}_3$ solid solutions structure cannot be correctly described by diffraction analysis methods. This is why correct interpretation of Raman spectra of $\text{Bi}_{1-x}\text{La}_x\text{FeO}_3$ solid solutions based on the calculations of the lattice dynamics is almost impossible. Interpretation of Raman spectrum could be clearer at calculations of structures and spectra ab initio.

Figure 18.1 demonstrates Raman spectra ($0\text{--}1000 \text{ cm}^{-1}$) of ceramic solid solutions $\text{Bi}_{1-x}\text{La}_x\text{FeO}_3$ ($x = 0.075\text{--}0.20$). Basic parameters of the spectral bands are shown in Table 18.1. In the $\text{Bi}_{1-x}\text{La}_x\text{FeO}_3$ ($x = 0.075\text{--}0.20$) solid solutions Raman spectra were observed almost the same bands as in crystal BiFeO_3 spectra [15] with slight changes in frequencies. This means that structure of solid solutions $\text{Bi}_{1-x}\text{La}_x\text{FeO}_3$ ($x = 0.075\text{--}0.20$) is close to structure of BiFeO_3 crystal. However, bands of Raman spectra of $\text{Bi}_{1-x}\text{La}_x\text{FeO}_3$ ($x = 0.075\text{--}0.20$) solid solutions are wider than the ones of the BiFeO_3 single crystal, that means much disorder of $\text{Bi}_{1-x}\text{La}_x\text{FeO}_3$ ($x = 0.075\text{--}0.20$) solid solutions structure. In paper [14], at research of BiFeO_3 film, it was revealed that in $Y(\text{XX})\bar{Y}$ geometry 71, 141, 172 and 221 cm^{-1} bands were the most intense. For $\text{Bi}_{1-x}\text{La}_x\text{FeO}_3$ solid solutions, the most intense were Raman bands with frequencies 89, 150, 181, 227, 623 cm^{-1} ($x = 0.075$) (see Fig. 18.1). Band 610 cm^{-1} is absent in spectra of BiFeO_3 single crystal [11, 13] but it was observed in Raman spectrum of BiFeO_3 film [14]. Authors assumed that this band corresponds to

Fig. 18.1 Raman spectra of solid solution $\text{Bi}_{1-x}\text{La}_x\text{FeO}_3$ ($x = 0.075\text{--}0.20$); $T = 273\text{ K}$



magnon from the Brillouin zone boundary that is activated in this spectrum due to violations of wave-vector selection that occurs in violation of the translational symmetry of crystal structure of films and ceramics because they contain a lot of substitutional defects, oxygen vacancies, dislocations, etc. In paper [17] a significant increase was discovered in $610\text{--}620\text{ cm}^{-1}$ band intensity of films of solid solutions

$\text{BiFeO}_3\text{-RMnO}_3$ ($R = \text{La, Eu, Gd, Tb, Dy}$), where the translational symmetry was violated due to both Fe and Bi substitution in BiFeO_3 structure. It is obvious that appearance of bands with frequencies $\sim 620 \text{ cm}^{-1}$ in Raman spectra of solid solutions $\text{Bi}_{1-x}\text{La}_x\text{FeO}_3$ ($x = 0.075\text{-}0.20$) that is forbidden by selection rules and the bands of high intensity are caused by significant disorder in solid solution structure. However, parameters of $\sim 620 \text{ cm}^{-1}$ band in Raman spectra of solid solutions $\text{Bi}_{1-x}\text{La}_x\text{FeO}_3$ ($x = 0.075\text{-}0.20$) depend on La concentration ambiguous (see Table 18.1). Width of this band increases with increase of La to $x = 0.120$ but then it decreases at La rise to $x = 0.20$. By this, intensity of the $\sim 620 \text{ cm}^{-1}$ band decreases monotonously with La rise.

Due to [9, 12, 14] the band with the lowest frequency ($71\text{-}74 \text{ cm}^{-1}$) in BiFeO_3 single crystals and films spectra corresponds to soft mode. This soft mode appears in Raman spectra of single crystals, ceramics, films of perovskite type [9, 12, 15, 18–21]. Its frequency varies from 40 to 90 cm^{-1} ($T = 273 \text{ K}$). Thus, in ceramic samples, soft mode frequency shifts into high-frequency area in comparison with single crystal samples [21]. For nano-crystal powders, the soft mode frequency depends on the powder particles size: at decrease of the particles size, the soft mode frequency shifts to low-frequency area [21]. Such behavior suggests decrease of T_C at decrease of powder particles size [21]. In the literature, low-frequency mode is usually connected with shift of cations, located in octahedral gaps, towards the

Table 18.1 Basic parameters of Raman bands of solid solution system $\text{Bi}_{1-x}\text{La}_x\text{FeO}_3$ ($x = 0.075\text{-}0.20$)

$x = 0.075$			$x = 0.1$			$x = 0.12$			$x = 0.15$			$x = 0.2$		
ν	S	I	ν	S	I	ν	S	I	ν	S	I	ν	S	I
60	14	5412	59	12	3683	69	6	2676	60	11	3371	66	20	2946
76	18	6121	74	24	5592	77	6	3512	75	25	4537	72	25	160
89	12	4779	89	13	3205	86	10	2863	92	17	3001	86	12	2790
98	8	2827	99	10	2389	97	8	1672	104	16	2024	98	18	2041
106	12	2478	107	9	1449	107	10	1106	114	22	1654	104	–	261
118	33	3971	117	33	3685	120	24	1525	127	33	2773	119	26	2087
150	38	7976	150	39	6518	151	30	3452	147	34	4737	148	34	5346
181	26	5549	181	32	4065	178	44	2926	174	42	3620	179	27	3159
227	54	3737	228	60	2656	230	65	2751	227	78	2282	229	58	2085
280	71	2384	282	89	1882	281	67	1664	278	92	1427	287	64	1166
316	19	405	339	38	401	311	39	766	349	3	76	315	55	–
337	27	794	373	38	499	339	59	990	367	199	1238	326	2	–
369	42	821	475	82	1101	380	85	1681	477	54	389	363	66	–
428	23	101	534	77	1396	463	94	1658	538	80	994	475	95	1151
478	48	1050	617	92	2014	531	97	1704	616	74	1209	535	87	1106
536	43	959	666	128	1188	620	98	2007	670	73	753	604	68	1267
623	66	2846	781	104	525	676	105	1000	731	68	401	664	133	1649
936	–	–	828	449	1470	822	–	394	797	97	643	928	41	673
955	–	–	–	–	–	942	26	400	953	22	462	933	51	710

oxygen octahedrons. For example, in SrTiO₃ it corresponds to Ti-cation shift in respect to the oxygen octahedrons [21].

In Raman spectra of potassium niobate (NaNbO₃) that also belongs to perovskite type, two low-frequency bands 60 and 74 cm⁻¹ are observed. They are connected with Na⁺ ions vibrations in NbO₆ octahedrons [22]. These peaks correspond to Na (1) and Na(2) cations that occupy different sites in NaNbO₃ structure in antiferroelectric phase [23]. At transition to ferroelectric state, this doublet converts into a single band. At research of Raman spectra of ferroelectric perovskite-type solid solutions Pb_{1-x}Sr_xTiO₃, it was revealed in paper [21] that complex structure and splitting of the soft mode for all solid solutions compounds is caused by the type of the bond (ionic or covalent) Pb(Sr)—O and difference in Pb and Sr cations weights. Earlier we researched Raman spectra of series of ceramic solid solutions Li_xNa_{1-x}Ta_yNb_{1-y}O₃ with structure of potassium niobate NaNbO₃ of complex perovskite type [19]. In the result of this research and after comparison of Raman spectra of solid solutions Li_xNa_{1-x}Ta_yNb_{1-y}O₃ with NaNbO₃ and LiNbO₃ crystals, we concluded that in the 50–80 cm⁻¹ area bands that correspond to librations (torsional oscillations) of oxygen octahedrons O₆ as whole are located. These vibrations exist only in perovskite structure where octahedrons are labile as a whole because they are connected through vertices. In pseudoilmenite structure to which LiNbO₃ crystals correspond, the octahedrons are rigidly connected by sides and torsional oscillations of oxygen octahedrons as a whole are impossible. At rise of the temperature and at change of y-component concentration, the Raman band of solid solution Li_xNa_{1-x}Ta_yNb_{1-y}O₃ in the area 50–80 cm⁻¹ considerably softens. We observed such softening at rise of tantalum to y = 0.5 in solid solution Li_xNa_{1-x}Ta_yNb_{1-y}O₃, when niobium and tantalum sub-lattice completely disordered and correlation of oxygen octahedrons librations distorted [19]. These arguments can obviously be applied to other compounds with oxygen octahedrons structure of perovskite type, i.e. to Bi_{1-x}La_xFeO₃ solid solution searched in this chapter. Thus, we assume that bands in area ~80 cm⁻¹ corresponds to totally symmetrical librations of oxygen octahedrons as a whole of A_J-type of symmetry that are unharmonically associated with Bi and La atoms vibrations. Interpretation of the spectra and bands attribution could be clearer at calculations ab initio.

Figure 18.1 also shows that Raman spectra of solid solutions Bi_{1-x}La_xFeO₃ (x = 0.075–0.20) in the area of oxygen octahedrons librations contains several bands with frequencies 59–69, 72–77, 86–92 cm⁻¹ in dependence of the solid solution compound. This could mean that the searched solid solutions Bi_{1-x}La_xFeO₃ are not single phases, which is confirmed by X-ray phase analysis [10]. At increase of La-concentration to x = 0.120, widths of low-frequency bands decrease (Table 18.1), but at continuing rise of x, the widths rise. Such behavior could be explained by partial rise of ordering of sub-lattices structures of solid solution Bi_{1-x}La_xFeO₃ (x = 0.120).

At research of solid solution Li_xNa_{1-x}Ta_yNb_{1-y}O₃, we noted that at x = 0.12 (Na:Li = 7:1, special concentration point) some ordering of the structure occurs. By this, solid solution Li_xNa_{1-x}Ta_yNb_{1-y}O₃ (x = 0.12) shows new properties that are absent when x ≠ 0.12. Namely, at temperatures ~400–460 °C, phase transition to

super-ion state was observed in solid solution $\text{Li}_x\text{Na}_{1-x}\text{Ta}_y\text{Nb}_{1-y}\text{O}_3$ ($x = 0.12$, $y = 0-0.5$). The transition was accompanied by intense transport of Li^+ ions and “melting” of alkali metal sub-lattice [18, 19, 24, 25]. Thus, the phase transition temperature, its degree of fuzziness and spontaneous polarization value could be varied by changing of Nb^{5+} and Ta^{5+} sub-lattices structure units order [19]. It is obvious that in solid solution $\text{Li}_x\text{Na}_{1-x}\text{Ta}_y\text{Nb}_{1-y}\text{O}_3$ at $x = 0.12$, polyhedrons AO_x deform and alkali metal sub-lattice orders so that in structure sites of free Na^+ create kind of conductivity channels and light Li^+ ions can move along them [18, 24]. In solid solutions $\text{Bi}_{1-x}\text{La}_x\text{FeO}_3$ at La concentration close to $x = 0.12-0.13$, sharp decrease of elastic characteristics of the ceramic grains is observed [8]. These data and results of X-ray and multifractal analysis [8] allowed us to conclude that in this point ($x = 0.12-0.13$) occurs percolation of P_2 phase nanoclusters.

At increase of La-concentration from $x = 0.075$ to $x = 0.2$ in $\text{Bi}_{1-x}\text{La}_x\text{FeO}_3$ solid solution structure, unambiguous dependence of the parameters of the spectral bands are not observed, Table 18.1. Frequencies of all Raman bands of solid solutions $\text{Bi}_{1-x}\text{La}_x\text{FeO}_3$ ($x = 0.075-0.20$) change slightly at rise in x , but widths and intensities of Raman bands vary in a wide range for different $\text{Bi}_{1-x}\text{La}_x\text{FeO}_3$ solid solutions compounds. However, general trend is not observed. This could be explained by the fact that at increase of x , character of entering of lanthanum into the solid solution structure changes. At $x \leq 0.09$, lanthanum takes part in formation of the material structure that decreases its defectiveness and stops distortions of stoichiometry. This is due to both decrease of A-sites vacancies concentration and decrease of possible oxygen loss [8, 26]. In Raman spectra of the solid solutions at $x \leq 0.09$, bands in area $180-623 \text{ cm}^{-1}$ are much more narrow and more intense than the same bands of solid solutions at $x = 0.1$, see Fig. 18.1. At the same time, low-frequency part of the Raman spectra does not show such changes. The continuing increase of lanthanum concentration $x = (0.09-0.14)$ probably leads to appearance of the compound that contains $\sim 7 \text{ mol\%}$ lanthanum and has a very narrow area of homogeneity. As a result, non-regular solid solutions with this compound appear. At ongoing increase of lanthanum concentration, solid solutions decompose and grains of compounds with variable ratio of elements close to $\text{Bi}_{0.93}\text{La}_{0.07}\text{FeO}_3$ and $\text{Bi}_{0.75}\text{La}_{0.25}\text{FeO}_3$ appear [8]. In Raman spectra, it reveals as general decrease of bands intensities (see Fig. 18.1, Table 18.1). At $x > 0.13$, unit cell value changes which is probably connected with the fact that “extra” lanthanum ions at accumulation concentrate in the areas of planar defects and partially occupy oxygen octahedrons [8]. By this, width of the low-frequency bands in Raman spectra considerably rises (see Table 18.1).

18.4 Conclusions

It was discovered that in Raman spectra of solid solutions $\text{Bi}_{1-x}\text{La}_x\text{FeO}_3$ ($x = 0.075-0.20$) were observed almost the same bands as for crystal BiFeO_3 but with some differences in frequencies. This means that structure of searched solid

solutions is close to structure of the crystal BiFeO_3 . However, Raman bands of $\text{Bi}_{1-x}\text{La}_x\text{FeO}_3$ solid solutions were considerably wider than bands of BiFeO_3 single crystal that indicates disordering in ceramic solid solutions structure.

We believe that bands $\sim 80 \text{ cm}^{-1}$ of Raman spectrum of $\text{Bi}_{1-x}\text{La}_x\text{FeO}_3$ solid solutions correspond to totally symmetrical libration of oxygen octahedrons as whole of A_1 -type of symmetry that are unharmonically associated with Bi and La atoms vibrations. Librations of oxygen octahedrons as a whole exist only in perovskite structure, where octahedrons are connected through vertices. In pseudoilmenite structure, the octahedrons are rigidly connected by sides and librations of oxygen octahedrons as a whole are absent. Bands $\sim 80 \text{ cm}^{-1}$ appear only in Raman spectra of single crystals, ceramics, films of perovskite type, that is why one could assume that this band in Raman spectrum is a characteristic feature of compounds with perovskite structure. It should be noted that in Raman spectra of solid solutions $\text{Bi}_{1-x}\text{La}_x\text{FeO}_3$ ($x = 0.075\text{--}0.20$) in the area of librational vibrations of oxygen octahedrons as a whole, several bands with frequencies $59\text{--}69$, $72\text{--}77$, $86\text{--}92 \text{ cm}^{-1}$ are observed in dependence of compound. This could mean that the searched solid solutions are not single phases, which is confirmed by X-ray phase analysis [8]. At La-concentration $x = 0.12$, decrease of widths of low-frequency bands of Raman spectrum is observed, which could mean ordering of structure units in cation sub-lattices of the structure. Perhaps for solid solutions $\text{Bi}_{1-x}\text{La}_x\text{FeO}_3$ ($x = 0.12$) different properties should be expected in comparison with other solid solutions. Results of X-ray and multifractal analysis allowed us to conclude that in the point $x = 0.12\text{--}0.13$ occurs percolation of P_2 phase nanoclusters. Moreover, in this solid solution with $x = 0.12\text{--}0.13$, sharp decrease of strength and elastic characteristics of the ceramic grains is observed [8].

At increase of La-concentration from $x = 0.075$ to $x = 0.2$ in $\text{Bi}_{1-x}\text{La}_x\text{FeO}_3$ solid solution structure, there is no unambiguous dependence of the parameters of the spectral bands. Frequencies of all Raman bands of solid solutions change slightly with the rise of x , but widths and intensities of bands in Raman spectra sometimes vary in a wide range for different compounds of $\text{Bi}_{1-x}\text{La}_x\text{FeO}_3$ solid solutions. However, general trend is not observed. This could be explained by the fact that at increase of x , character of entering of La into the solid solution structure changes.

References

1. A.K. Zvezdin, A.P. Pjatakov, *Uspekhi Fizicheskikh Nauk* **174**(4), 465 (1991) (in Russian)
2. Y.E. Roginskaya, Y.N. Venetsev, S.A. Fedoulov, G.S. Zhdanov, *Kristallographija* **8**(4), 610 (1963) (in Russian)
3. G.L. Yuan, W.O. Siu, L.H. Wa Chan, *J. Phys. D: Appl. Phys.* **40**, 1196 (2007)
4. I.O. Troyanchuk, M.V. Bushinsky, D.V. Karpinsky, O.S. Mantytskaya, V.V. Fedotova, O.I. Proknenko, *Phys. Status Solidi. B: Basic Solid State Phys.* **246**(8), 1901 (2009)
5. D. Rusakov, A.M. Abakumov, K. Yamaura, A.A. Belik, G. Tendeloo, E. Takayama-Muromachi, *Chem. Mater.* **23**(2), 285 (2011)

6. D.V. Karpinsky, I.O. Troyanchuk, O.S. Mantytskaya, V.A. Khomchenko, A.L. Kholkin, *Solid State Commun.* **151**, 1686 (2011)
7. I.A. Verbenko, Yu.M. Goofan, S.P. Koubrin, A.A. Amirov, A.A. Pavelko, V.A. Aljoshin, L.A. Shilkina, O.N. Razoumovskaya, L.A. Reznichenko, I.A. Osipenko, D.A. Sarychev, A.B. Batdalov, *Izvestiya RAS. Seriya Fizicheskaya* **74**(8), 1192 (2010). (in Russian)
8. S.V. Titov, I. A. Verbenko, L.A. Shilkina, V.A. Aljoshin, S.I. Shevtsova, N.A. Teplyakova, N. V. Sidorov, K.S. Kravchuk, V.M. Shabanov, V.V. Titov, S.V. Hasboulatov, L.A. Reznichenko, in: *Proceedings of the III International Youth Interdisciplinary Symposium "Physics of Lead-Free Piezoelectric and Relative Matters (Analysis of Current State and Prospects of Development)". LFPM-2014*, Rostov-on-Don, **2**, 318 (2014) (in Russian)
9. H. Fukumura, H. Harima, K. Kisoda, M. Tamada, Y. Noguchi, M. Miyavama, J. Magn. Magn. Mater. **310**, e367 (2007)
10. H. Fukumura, S. Matsui, H. Harima, T. Takahashi, T. Itoh, K. Kisoda, M. Tamada, Y. Noguchi, M. Miyavama, *J. Phys.: Condensed Matter* **19**, 365224 (2007)
11. R. Palai, H. Schmid, J.F. Scott, R.S. Katiyar, *Phys. Rev. B* **81**, 064110 (2010)
12. J. Hlinka, J. Pokorny, S. Karimi, I.M. Reaney, *Phys. Rev. B* **83**, 020101 (2011)
13. C. Beekman, A.A. Reijnders, Y.S. Oh, S.W. Cheong, K.S. Burch, *Phys. Rev. B* **86**, 020403 (R) (2012)
14. G. Khabiri, A.S. Anokhin, A.G. Razoumnaya, YuI Yuzyuk, I. Gueye, B. Carcan, H. Bouyanfif, J. Wolfman, C. Autret-Lambert, M. Marssi, *El. Fizika Tverdogo Tela* **56**(12), 2420 (2014). (In Russian)
15. M.N. Iliiev, M.V. Abrashev, D. Mazumdar, V. Shelke, A. Gupta, *Phys. Rev. B* **81**, 014107 (2010)
16. A.F. Revinskij, V.V. Trigook, I.I. Makojed, *Fizika Tverdogo Tela* **56**(10), 1740 (2014) (in Russian)
17. A. Lahmar, S. Habouti, M. Dietze, C.-H. Solterbeck, M. Es-Souni, *Appl. Phys. Lett.* **94**, 012903 (2009)
18. M.N. Palatnikov, N.V. Sidorov, V.T. Kalinnikov, *Ferroelectrical Solid Solutions Based on Oxyde Compounds of Niobium and Tantalum: Synthesis, Research of Structure Order and Physical Characteristics* (Nauka, Saint-Petersburg, 2001). (in Russian)
19. N.A. Teplyakova, *Structure Phase Transitions in Ferroelectric Solid Solutions $Li_{0.12}Na_{0.88}Ta_yNb_{1-y}O_3$ and Their Manifestations in Raman Spectra*, PhD Thesis, Petrozavodsk (2012) (in Russian)
20. L.A. Reznichenko, L.A. Shilkina, E.S. Gagarina, Y.I. Yuzyuk, O.N. Razoumnaya, A.V. Kozinkin, *Kristallografiya* **49**(5), 909 (2004) (in Russian)
21. Y.I. Yuzyuk *Fizika Tverdogo Tela* **54**(5), 963 (2012) (in Russian)
22. Z.X. Shen, X.B. Wang, M.N. Kuok, S.H. Tang, *J. Raman Spectrosc.* **29**, 379 (1998)
23. A.C. Sakowski-Cowley, K. Lukaszewicz, H.D. Megaw, *Acta Crystallogr. B* **25**, 851 (1969)
24. M.N. Palatnikov, *Materials of Electronical Technics Based on Ferroelectric Single Crystals and Ceramic Solid Solutions on Niobates-Tantalates of Alkali Metals with Micro-and Nanostructures*, PhD Thesis, Apatity (2010) (in Russian)
25. N.V. Sidorov, M.N. Palatnikov, N.A. Teplyakova, E.Y. Obrjadina, V.V. Efremov, *Neorganicheskije Materialy* **49**(6), 635 (2013) (in Russian)
26. L.A. Shilkina, I.A. Verbenko, A.G. Abubakarov, L.A. Reznichenko, O.N. Razoumnaya, T.N. Sorokun, in *Proceedings of the III International Youth Interdisciplinary Symposium "Physics of Lead-Free Piezoelectric and Relative Matter (Analysis of Current State and Prospects of Development)". LFPM-2014*, Rostov-on-Don, **1**, 336 (2014) (in Russian)

Chapter 19

A Multi-fractal Multi-permuted Multinomial Measurement for Unsupervised Image Segmentation

Sung-Tsun Shih and Lui Kam

Abstract By extending multinomial measures, a new class of self-similar multi-fractal measures is developed for texture representation. Two multi-fractal features have been shown to be suitable for texture discrimination and classification. Their use within a supervised segmentation framework provides us with satisfactory results. In this chapter, we complete the survey on these features by showing their rotation invariant property and their scaling behavior. Both properties are particularly important for analyzing aerial images because the geographical elements can appear in different orientations and scales. Then, an automatic clustering algorithm based on a watershed technique is used for the segmentation of real world images. The experimental results are encouraging. Through this study of the multi-fractal measures, we demonstrated a relevant characterization of natural textures by only two attributes. They are rotation invariant and that possess a good behavior with respect to the scaling ratio. These properties reinforce the reliability of these two attributes for aerial or satellite image characterization.

19.1 Introduction

Analyzing and interpreting images by means of texture attributes is a widespread method including many approaches like statistical characterization [1, 2], filtering techniques [3, 4], geometric models [5, 6], fractal geometry [7–9], or multifractal analysis [10–12]. Each of them is well adapted only to a specific application.

In a previous work [13], the use of co-occurrence statistics [2] gave poor segmentation results on aerial images. A straightforward application of fractal features (fractal dimension, lacunarity) proves them inappropriate for this purpose. Nevertheless, each geographical element exhibits a kind of statistical self-similarity

S.-T. Shih (✉) · L. Kam
Department of Electronic Engineering, Cheng-Shiu University,
Kaohsiung City, Taiwan
e-mail: stshih@gcloud.csu.edu.tw

in its own way. Several works [14, 15] suggested computing local fractal dimension for the improvement of the segmentation results. Hence, the multifractal analysis, which is a generalization of the fractal geometry, is well adapted to the description of the aerial and satellite images.

The former works of Lévy-Véhel [10, 16] introduced a multifractal approach for image segmentation. The analysis of an image is based on local Holder exponents (with respect to a measure or a Choquet capacity) and the multifractal spectrum (global information). Although these mathematical tools can provide relevant information for image analysis, we must emphasize on the fact that we do not know which measure or capacity to choose in practice. Furthermore, the computation of the local Holder exponents and the multifractal spectrum must rely on estimators and is time consuming in most of cases.

A multifractal measure is developed in [13] for segmenting real world images. The theoretical background and some useful properties of this model are reviewed briefly in the next section, and an estimator for the inverse problem of parameters identification is defined. The use of this estimator on several natural textures provides us with meaningful results. In Section 19.3, we first recall the main results related to the texture characterization by using two multifractal features. As the aerial scenes are shaped by man-made objects (urban areas, open countries) and natural elements (water-courses, vegetation) which can occur at different scales and orientations, this survey is completed by studying the scaling behavior and the rotation invariance of both texture descriptors. Then, after a short review of the classical methods of data clustering, we describe the unsupervised algorithm we proposed for the segmentation of images. Experimental results are given in Sect. 4.3. The limits of our model and future investigations are detailed as a conclusion.

19.2 Multifractal Texture Model

The multinomial measures are well studied self-similar measures [17]. They can be generated as the limit of multiplicative cascaded processes. By introducing spatial permutations into each stage of the underlying processes, we extended the multinomial measures to, so-called, Multi-permuted Multinomial Measures (or MMM).

19.2.1 Definitions and Properties

More formally, let $N_p(n)$ be the set of the first p^n non-negative integers and $C_0 = [0, 1]^2$ be the support of the measure. Given p^2 masses $P_{i,j}$ ($i, j \in N_p(1)$) whose total sum is 1, the pyramidal construction of a MMM (denoted by $\mu\Pi_p$) is based on an iterative splitting of C_0 associated with a multiplicative rule between successive stages.

At the first stage, $C_0 = [0, 1]^2$ (with measure 1) is partitioned regularly into p^2 subsets $C_{i,j}^1$ whose measure is $P_{i,j}$. The same splitting procedure is carried out on

these subsets at the next stage, yielding $(p^2)^2$ new subsets C_{k_i,l_j}^2 with a measure defined by a multiplicative rule:

$$\forall n \geq 1, \quad \mu_{\Pi p}(C_{k_i,l_j}^{n+1}) = P_{\pi_{ij}^n}(k,l)\mu_{\Pi p}(C_{i,j}^n) \tag{19.1}$$

with $k_i = [(i + 1)/p] + k$ and $l_j = [(j + 1)/p] + l$ (where $[x]$ is the integer part of x), π_{ij}^n is a permutation related to $C_{i,j}^n$ at the stage n , acting on the position of the masses $P_{i,j}$ for the multiplicative rule involved at the stage $n + 1$. By iterating this process *ad infinitum*, one gets a MMM.

Figure 19.1 displays two first steps of the cascaded process of a MMM with $p = 3$ and $\pi_{1,1}^1(k, l) = (l, k)$. One can notice that the limit measure is a multinomial measure, if all the permutations are equal to the identity function.

Its multifractality can be determined through a repartition function [18] defined at stage n as

$$\Gamma_n(q, \tau) = \sum_{i,j \in N_p(n)} \frac{[\mu_{\Pi p}(C_{i,j}^n)]^q}{p^{-2n\tau}}. \tag{19.2}$$

There exists a unique function $\tau(q)$, called Rényi exponent, such that $\Gamma_n(q, \tau(q)) = 1$. It characterizes the multifractal behavior of a singular measure. Since the permutations operate only on the position of the masses $P_{i,j}$ at each stage, the set of measures $\mu_{\Pi p}(C_{i,j}^n)$ remains invariant.

Thus, the Rényi exponent of a MMM and its corresponding multinomial measure are identical. Moreover, the MMMs are self-similar (modulo permutations) by construction. The set of the local Holder exponents and the multifractal spectrum simply relate to the Rényi exponent by the Legendre transform (see [17]). This remark is very important for the computation of the multi-fractal features because they can be determined analytically once the parameters of the model are identified.

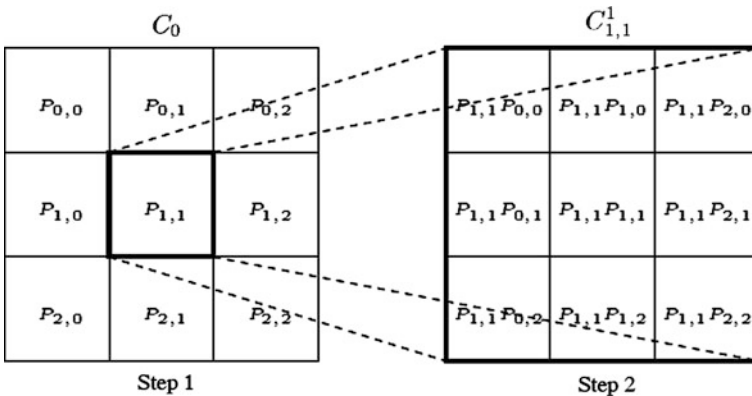


Fig. 19.1 Steps 1 and 2 of MMM's cascade

19.2.2 Inverse Problem

A MMM is completely defined by the knowledge of the integer p , the p^2 masses $P_{i,j}$ and the permutations. A fast algorithm is developed in [13] for the masses estimation:

$$\tilde{P}_{i,j} = \frac{1}{1 + N_\pi(p, n_0)} \sum_{n=0}^{n_0-1} \sum \tilde{P}_{\pi_{i,j}^n}(k, l). \quad (19.3)$$

The values $\tilde{P}_{\pi_{i,j}^n}(k, l)$ correspond to the estimates of the permuted masses observed at iteration n . They can be computed according to the (19.1). $N_\pi(p, n_0)$ is the number of permutations achieved after n_0 iterations:

$$N_\pi(p, n_0) = \sum_{n=2}^{n_0} (p^2)^{n-1} = \frac{p^{2n_0} - p^2}{p^2 - 1}. \quad (19.4)$$

The permutations can be determined at the same time as the estimation of the permuted masses. Indeed, the sorting of the estimates $\tilde{P}_{\pi_{i,j}^n}(k, l)$ yields a mapping between the initial and the permuted positions of the masses.

The method described above is applicable if p and n_0 are known a priori. Their choice depends both on the intrinsic characteristics of the images and on the application considered. In order to avoid texture mixing within an analyzing window, we suggested to take small values of p and n_0 (3 and 2, respectively) for an accurate segmentation [13].

19.2.3 Approximating Textures

Our first goal was to find a relevant multifractal representation for texture characterization. In order to evaluate the relevance of the MMM model for texture approximation, several natural textures—drawn from the Brodatz album and the image database of SIPI (Signal and Image Processing Institute) of the USC—are used as testing images. Figure 19.2 shows a sample of four original textured images (grass, bark, wool and rough wall) and their corresponding approximation computed by $\mu\Pi_3$ with $n_0 = 5$ iterations.

Some artifacts (square blocks) can be observed on the synthesized images. They are due to the regular iterated splitting of C_0 . However, as well as micro-textures (grass, wool) or macro-textures (bark, rough wall), the MMM approximations preserve quite correctly their geometric structures thanks to the effect of the permutations.

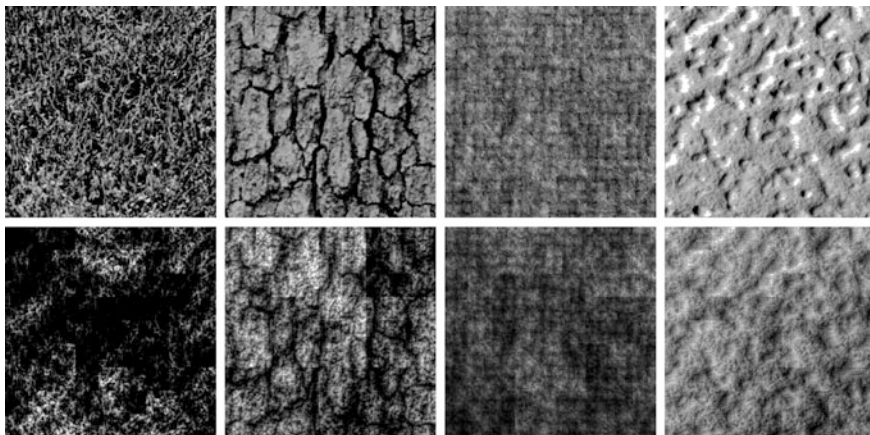


Fig. 19.2 Four natural textures (D9, D12, D19, T3) and their approximations by $\mu\Pi_3$

19.3 Texture Attributes

The multifractal analysis of a MMM can also be achieved by means of the multifractal spectrum approach (see Sect. 19.2.1) which gives both local and global information.

19.3.1 Previous Results

This huge amount of information has been largely reduced as only two attributes are extracted, namely the extreme of the local Hölder exponents [17]:

$$\alpha_{\min} = -\log(\max_{i,j} P_{i,j})/2 \log p, \quad (19.5)$$

$$\alpha_{\max} = -\log(\min_{i,j} P_{i,j})/2 \log p. \quad (19.6)$$

They relate directly to the parameters of the model and should give a good characterization of the model.

In [13], these texture attributes are computed (with $p = 3$ and $n_0 = 5$) on 100 sub-images (of size 243^2) extracted from each of the 13 Brodatz textures: grass, bark, straw, textile, wool, pressed calf leather, sand, water, wood, raffia, pigskin, wall bricks and bubbles. Here, we add 3 more textures (called T1, T2, T3) retrieved from the image database of the SIPI: hexagonal holes, gravels and rough wall.

The $(\alpha_{\min}, \alpha_{\max})$ plot of these textures is displayed in Figure 19.3. Most of the clusters are separated from the others, except those of the textures D19 and D84

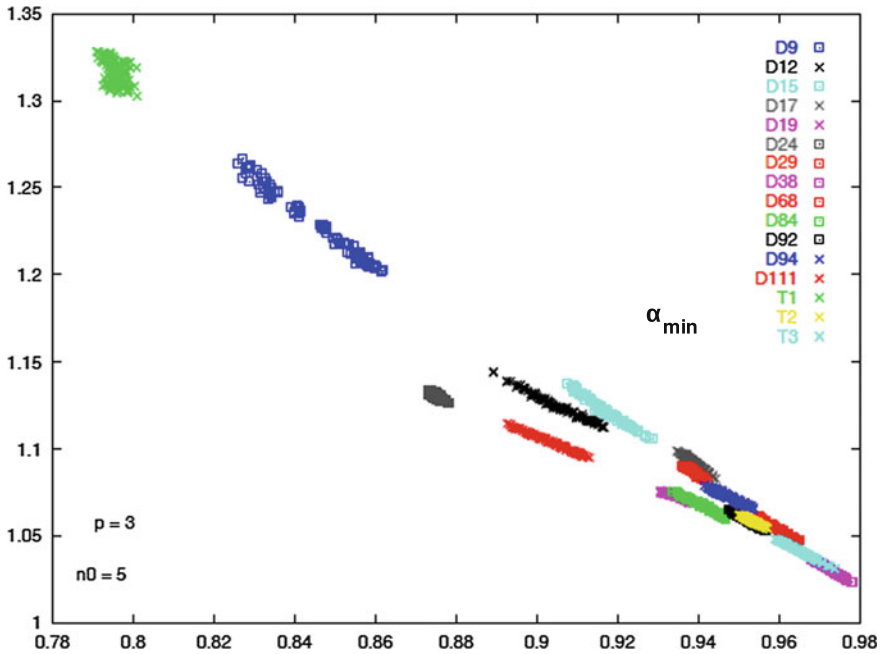


Fig. 19.3 $(\alpha_{\min}, \alpha_{\max})$ plot computed for each of the 16 Brodatz and Brodatz-like textures

(D92 and T2, respectively). In fact, if one examines these pairs of textures, their patterns look similar. For instance, D19 and D84 are both structured micro-textures whose patterns are about the same size. As for D92 and T2, they are non-structured macro-textures also with equivalent pattern size.

Furthermore, the spatial arrangement of the clusters directly relates to the visual irregularities of the textures. Indeed, the most irregular (D9) or contrasted (T1) textures have their clusters located on the top left corner of the $(\alpha_{\min}, \alpha_{\max})$ plot. Whereas the clusters of the smoother textures (D38) are located near the right bottom corner. This phenomenon can be explained by the fact that irregular or contrasted textures have a wide range of local irregularities (i.e. small α_{\min} and large α_{\max} values). The opposite behavior is observed for the smoother textures.

19.3.2 Scaling Behavior

Our multifractal attributes should be scale invariant according to the theory. For each textured image, we studied this behavior over a set of 5 images with size 243^2 , 365^2 , 486^2 , 608^2 and 729^2 zoomed in or out from the original 512^2 sized image by a bi-cubic interpolation. The ratio between the largest image and the smallest one is 3.

Again, min and max are computed from sub-images of size 243^2 for each zoomed images. The plots shown in Figure 19.4 reveal the representative (only 6 textures are considered for clarity) scaling behavior of the mean values of the attributes. When the scaling ratio increases, the two attributes are not as stable as predicted by the theory, but their variation does not exceed a few percent. Hence, we can assume that both attributes are relevant enough for texture characterization whatever the scale of observation is (in practice, a range of scales).

19.3.3 Rotation Invariance

The Hölder exponents characterize the local irregularities of a measure. If the support of the image is rotated, the irregularities should remain unchanged. This invariance property is investigated by testing images drawn from the SIPI image database in which the 13 Brodatz textures are scanned under seven different angles: 0° , 30° , 60° , 90° , 120° , 150° and 200° . For the three other textures (T1, T2 and T3), the rotated images are generated by a bi cubic interpolation.

The attributes are estimated for each rotated texture in the same manner as we do in the previous sections. Each cluster is modeled by a 2D Gaussian distribution whose means and covariance matrices are determined from the data. Whatever the rotated texture is, the coefficients of the covariance matrices are very small (10^{-4} to 10^{-6}): the clusters are compact and can be represented by the means.

For almost every texture (13 over 16), the variation of the two attributes with respect to the rotation angles does not exceed 10^{-2} . The less favorable case we can observe is that of the grass texture, but the variations are not excessive (maximum difference is about 0.06). According to these experimental results, we can conclude that α_{\min} and α_{\max} are stable enough under the rotation transformation (Fig. 19.5).

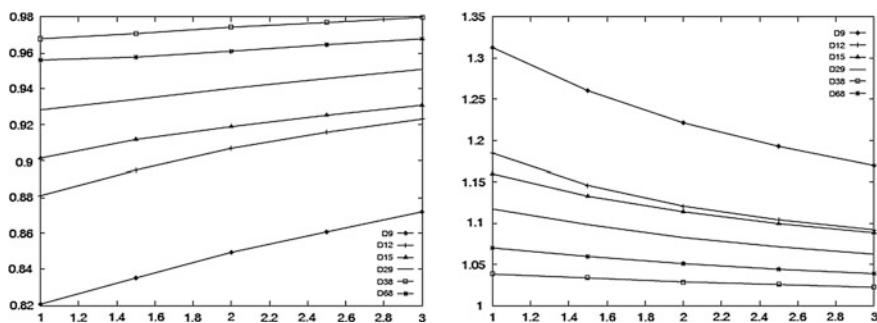


Fig. 19.4 Scaling behavior of the mean values of min (left) and max (right) for six textures



Fig. 19.5 *Left* Histogram of $(\alpha_{\min}, \alpha_{\max})$ related to the aerial photograph of Toride. *Middle and Right* Original and segmented aerial photograph of Toride

19.4 Conclusions

Through this study of the multifractal measures, we demonstrated a relevant characterization of natural textures by only two attributes. They are rotation invariant and possess a good behavior with respect to the scaling ratio. These properties reinforce the reliability of these two attributes for aerial or satellite image characterization.

The two multifractal attributes are also used for segmenting simulated SPOT5 images and other non-aerial textured images with outstanding results [19]. Of course, our method is ill-adapted, if the local maxima of the histogram are too close or unbalanced. In that case, the coarse density estimation may not take into account the smaller ones, which may lead to a poor segmentation result.

Although the two attributes implicitly relate to the permutations, we have to extend the study related to the effect of the permutations on the texture patterns. As the number of iterations is generally limited, a Markovian analysis cannot be considered. Thus, we shall define empirically a certain distance, which is a very difficult task so as to reveal the geometric information carried by the permutations.

References

1. A. Gagalowicz, C. Toumier-Lasserve, in *IEEE ICIP*. Third order model for non-homogeneous natural textures, p. 409 (1986)
2. R.M. Haralick, K. Shanmugam, I. Dinstein, *IEEE Trans. SMC* **3**(6), 610 (1973)
3. K. Deguchi, I. Morishita, *IEEE Trans. Comput.* **C-27**(8), 739 (1978)
4. K.I. Laws, Rapid texture identification. in *Proceedings of SPIE Conference on Missile Guidance*, p. 376 (1980)
5. F.G. Peet, T.S. Sahota, *IEEE Trans. PAMI* **7**(6), 734 (1985)
6. S. Philipp, M. Smadja, *Pattern Recognition* **27**(8), 1051 (1994)
7. B. Chaudhuri, N. Sarkar, *IEEE Trans. PAMI* **17**(1), 72 (1995)
8. J.M. Keller, S. Chen, R.M. Crownover, *CVGIP* **45**, 150 (1989)

9. A.P. Pentland, IEEE Trans. PAMI **6**(6), 661 (1984)
10. J. Lévy-Véhel, P. Mignot, Fractals **2**(3), 371 (1994)
11. P. Martinez, D. Schertzer, K. Pham, in *IGARSS'96*. Texture analysis by universal multifractal features in a polarimetric SAR image, vol. 1, p. 27 (1996)
12. N. Sarkar, B. Chaudhuri, Sig. Process. **42**, 181 (1995)
13. L. Kam, J. Blanc-Talon, in *Advanced Concepts for Intelligent Vision Systems*. Multifractal texture characterization for real world image segmentation, p. 45 (1999)
14. J.M. Keller, Y.B. Seo, Int. J. Imaging Syst. Technol. **2**, 267 (1990)
15. J. Maeda, V.V. Anh, T. Ishizaka, Y. Suzuki, in *IEEE ICIP*. Integration of local fractal dimension and boundary edge in segmenting natural images, p. 845 (1996)
16. J. Lévy-Véhel, P. Mignot, J.P. Berroir, *Texture and Multifractals: New Tools for Image Analysis*. Technical Report 1706, INRIA, France, June (1992)
17. K.J. Falconer, *Techniques in Fractal Geometry* (Wiley & Sons, Chichester, 1997)
18. J. Hakansson, G. Russberg, Phys. Rev. A, **41**(4), 1855 (1990)
19. L. Kam, J. Blanc-Talon, *Intelligent Systems: Theory and Applications, Chapter Multifractal Texture Segmentation for Off-Road Robot Vision* (IOS Press, Netherlands, 2000)

Chapter 20

Modulation the Band Structure and Physical Properties of the Graphene Materials with Electric Field and Semiconductor Substrate

Victor V. Ilyasov, Besik C. Meshi, Nguyen V. Chuong, Igor V. Ershov, Inna G. Popova and Nguyen D. Chien

Abstract The results of ab initio study of the opportunities for tuning the band structure, magnetic and transport properties of graphene materials on semiconductor substrates by transverse electric field (E_{ext}) are present. This study was performed within the framework of the density functional theory (DFT) using Grimme's (DFT-D2) scheme. We determined the effect of low E_{ext} applied to the graphene semiconductor heterostructure on the preserved local magnetic moment ($0.3 \mu_B$) of edge carbon atoms. The transport properties of the 8-ZGNR/h-BN(0001) semiconductor heterostructure can be controlled using E_{ext} . In particular, at a critical value of the positive potential, the electron mobility can increase to $7 \cdot 10^5 \text{ cm}^2/(\text{V s})$ or remain zero in the spin-up and spin-down electron subsystems, respectively. We established that magnetic moments, band gaps and carrier mobility can be altered using E_{ext} . These abilities enable the use of 8-ZGNR/h-BN(0001) semiconductor heterostructure in spintronics.

20.1 Physics of New Graphene Materials

One of the fundamental scientific problems connected with graphene (SLG) discovered in 2004 and with its practical use in spintronics devices consists in an existence of stationary and quasi-stationary surface states at the graphene-oxide

V.V. Ilyasov (✉) · B.C. Meshi · N.V. Chuong (✉) · I.V. Ershov · I.G. Popova
Don State Technical University, Rostov-on-Don, Russia
e-mail: viily@mail.ru

N.V. Chuong
e-mail: chuongnguyen11@gmail.com

N.D. Chien
Department of Electronic Materials, School of Engineering Physics,
Hanoi University of Science and Technology, Hanoi, Vietnam

(SLG/MeO) interface as well as in a control of the interface surface state [1, 2]. The mentioned surface states in particular can appear in non-equilibrium processes of optical absorption. Actually through the spectra study of Raman scattering in SLG/ R ($R = \text{SiO}_2/\text{Si}$, GaAs, Al_2O_3 , SiC, quartz, glass, etc.) interfaces a different shift values of Raman spectroscopy peaks such as G and 2D have been ascertained [3–7].

Hereby characteristics of surface states and a chemical bond mechanism in such a interface can be determined by its both atom and electron structures. Interfaces of types such as metal-oxide ($Me/\text{Al}_2\text{O}_3$, $Me = \text{Ag}$, Au, Al, Cu, etc.) [8–10] and graphene-semiconductor (SLG/SiC) [11] have been mostly studied by means of ab initio and experimental methods. The electron structure of the interfaces has been studied with use of band structure methods within the bounds of the both density functional theory (DFT) and generalized gradient approximation (GGA) of the exchange-correlation functional. It is known that oxides with the corundum structure ($\alpha\text{-Al}_2\text{O}_3$, $\alpha\text{-Fe}_2\text{O}_3$, Cr_2O_3 , Ti_2O_3 , V_2O_3) are of most technologically important class of metal oxides. In particular, sapphire $\alpha\text{-Al}_2\text{O}_3$ is one of the most extensively used substrate materials for growth of thin films of metals, semiconductor and dielectrics intended for microelectronics and fundamental investigations.

From the point of view of microelectronics SLG/ Al_2O_3 interface can be used as a part of a MOS field-effect transistor or in heterostructures for various purposes. In particular, in $\text{Co}/\text{Al}_2\text{O}_3/\text{SLG}/\text{SiO}_2/n\text{-Si}$ heterostructure a possibility of both electron spin transport and spin procession at the room temperature has been experimentally. In specimens of graphene/ Al_2O_3 synthesized with the method of the chemical vapor deposition (CVD) of carbon onto sapphire a high mobility of carriers and a negative magnetoresistance in the temperature range from 2 to 300 K have been experimentally ascertained. A comparison of these measurements [12] with analogous ones for graphene obtained by mechanical peeling does enable an assumption of different mechanisms of carriers scattering for graphene materials obtained with different methods. It is obvious that in strong electric fields electrons can be brought onto levels of surface states that also can affect the surface mobility of charge carriers [13]. Therefore, for every interface, it is necessary to study features of both atom and electron structures as well as a physicochemical nature of surface states.

Zigzag graphene nanoribbons (8-ZGNR) represent a suitable 1D carbon nanostructure for electronic devices, sensors, solar cells, and energy accumulation because of their high carrier mobility at room temperature [14–16]. We have demonstrated [17] that ZGNR deposition on hexagonal boron nitride (h-BN(0001)) preserves localized states in the proximity of the Fermi level, which are responsible for edge ferromagnetism. The energy gap in the low-energy spectrum of π -electrons in 8-ZGNR on h-BN substrate is 550 meV [17]. Due to the quantum confinement effect, band gap in ZGNRs increases with decreasing nanoribbon width [14, 18], while for armchair graphene nanoribbons (AGNRs) a band gap oscillations as a function of the width were predicted [19, 20]. Significant progress has been achieved in the producing of high-quality 1D graphene channels, such as graphene nanoribbons (GNRs) [16, 21]. ZGNRs are known [16, 22] to allow implementation of high magnetoresistance and spin-polarized carrier transport. However, it should be noted that ZGNRs exhibit antiferromagnetically ordered edge states subject to a

semi-metallic spin polarization under transverse electric field (E_{ext}); it has been recently called into question in some papers due to a limited treatment of electron correlation [23, 24]. At ground state, spin moments of two ZGNR edges exhibit antiferromagnetic (AF) ordering; ferromagnetic and non-magnetic ordering are the metastable and excited states, respectively [14, 25]. The quantum confinement effect and the inter-edge superexchange interaction in ZGNRs offer an opportunity to alter (tune) their remarkable properties (such as band gap, magnetic moment (MMs), electronic stability and transport) depending on the nanoribbon width [26]. ZGNR band structure with AF ordering (AF-ZGNRs) corresponds to the semiconductor type [16, 27–29]. Selection of h-BN as substrate is determined by its ability to ensure high carrier mobility ($125,000 \text{ cm}^2 \text{ V}^{-1} \text{ s}^{-1}$, at room temperature) in graphene [30]. High carrier mobility is attributed to the smooth surface, low density of charged impurities, lack of dangling bonds, and relative inertness of h-BN [31]. The mismatch between the atom lattices of graphene and h-BN is only 1.7 %. These properties make h-BN a potential material for graphene-based nanoelectronic devices. In a previous study [32], h-BN was used not only as a ZGNR substrate consisting of six carbon dimers, but also as the means employed to achieve new properties in the G-BN-NR (graphene—boron nitride—nanoribbon) system. However, the maximum energy gap opening accomplished in the low-energy spectrum of π -electrons is only 0.32 eV for the spin-down electron subsystem. AF-8-ZGNR placement on an infinite h-BN(0001) plane provided for 1.4 times larger gap size [28].

Bilayer zigzag graphene nanoribbons (BZGNRs) represent an essential 1D carbon nanostructure for creation of spintronic devices due to their remarkable physical properties [14–16]. Bernal-stacked BZGNRs (AB) represent a gapless semiconductor, in which the energy gap may be induced by the interaction with the substrate [17, 33, 34], external force [35, 36] and transverse electric fields [37, 38]. There are two possibilities for AB stacking of BZGNR: the so-called AB_α and AB_β schemes [17]. Stacking method AB_α has typical structural instability resulting in deformation of nanoribbon edges, in stacking method AB_β there is no structural deformation so that nanoribbon layers are flat [38]. Therefore, further we shall only discuss the stacking. Four magnetic spin configurations of the edge states can potentially exist in the BZGNR model [39]. We have demonstrated that electronic properties of spin-polarized AF-BZGNRs are very sensitive to the interlayer distance between ZGNRs. The effect of transverse electric field applied to suspended AF-BZGNR facilitates the semiconductor-semimetal transition for the spin down electron subsystem. When the AF-BZGNR/h-BN(0001) heterostructure is used, the effects of transverse electric field and uniaxial (nanomechanical) compression are supplemented with interaction with the substrate. In a number of recent theoretical references, interaction with dielectric substrate assumed weak and thus excluded from the scope of the research task, which therefore became much simpler. However, modulation of the energy gap in GNRs is strongly affected by the modification of electron self-energy owing to dielectric screening [40]. The nature of the effect relates to the electron energy modification by nonlocal dielectric

screening of the electron-electron interaction in GNRs due to polarization of the substrate surface.

Studies on magnetic characteristics in 8-ZGNR/h-BN(0001) heterostructures have revealed that edge C atoms exhibit the highest local magnetic moments (LMM) among C atoms [17, 28]. For the ZGNRs on metal substrates (such as Au, Pt, Ni, Cu, Al, Ag, Pd), MMs in ZGNR on *s*-dominated metal surfaces can be reordered using E_{ext} [41] because of the prevalence of electrostatic interaction between ZGNR and *s*-dominated surfaces. For ZGNRs on *p*- and *d*-dominated metal surfaces, tuning with E_{ext} is less efficient because of strong interaction between carbon π -orbitals and metal substrate during chemical adsorption. Based on ab initio density functional theory (DFT) calculations [29], application of E_{ext} across the width of ZGNRs effectively cancels energy degeneracy of two edges, resulting in spin-selective ZGNRs. The E_{ext} effect can be employed to control and regulate carrier transport through spin-polarized ZGNRs, such as a spin filter or a field-effect transistor [36].

It should be noted that the role of known effects, namely force (nanomechanical compression) and electric fields, edge geometry and nanoribbon width, and GNR interaction with the substrate in the modulation of the energy gap in semiconductor heterostructures like AF-BZGNR/h-BN(0001) is insufficiently studied so far in cases, when the effects are combined. Therefore, we used the density functional theory to examine the potential for modulation of spin-polarized electron spectrum of the AF-BZGNR/h-BN(0001) semiconductor heterostructure with the using the effects of force field, transverse electric field, substrate interaction, edge geometry and nanoribbon width. Thus, in our opinion an investigation of regularities of forming the both surface states and chemical bond in the interface of SLG/Al₂O₃ type is far from being complete. The incompleteness of data on a nature of interaction between graphene coatings and various ultrathin layers as well as on features of both electron states in valence band, at Fermi level and interatomic interaction in two-dimensional structures has motivated us to theoretically study electron structure features and properties in SLG/Al₂O₃ (0001) interface.

The effects of E_{ext} on energy gap width, magnetism and transport properties of ZGNR/h-BN(0001) and AF-BZGNR/h-BN(0001) heterostructures have not been thoroughly investigated. Therefore, we used the DFT ab initio to examine the possibility for tuning spin-polarized electron structure, magnetic and transport properties of 8-ZGNR/h-BN(0001) and AF-BZGNR/h-BN(0001) heterostructures with the use of E_{ext} .

20.2 Models of Graphene Heterostructures and Method

The theoretical model of the studied SLG/Al₂O₃(0001) system is built according to the scheme where one layer repeats itself in the [0001]-direction alternating with vacuum ‘layers’. A surface of Al₂O₃ layer does not have a tendency to the reconstruction even at significant temperatures. Therefore we have used the *p*

(1×1) -superlattice. The Al_2O_3 -layer consists of 18 nonequivalent planes in the $[0001]$ -direction (12 planes of aluminum and 6 ones of oxygen). The vacuum layer amounted about 15–17 Å. The vacuum volume selected in this way aids to prevent partly an artificial electrostatic field appearance in a space between the layers. Our preliminary calculations have shown that at the distance 15 Å between the graphene layer and the next layer of aluminum their wave functions do not sustain a mutual influence practically.

The graphene heterostructure consisted of a ZGNR placed on a h-BN(0001) substrate. 8-ZGNR was the basic cell of the atomic structure used in the calculations. The ZGNR located in the x - y plane. ZGNR width was made up of eight dimers of C atoms along the x -axis. Dangling bonds of the edge atoms were passivated with H atoms. The model is shown in Fig. 20.1, which also shows two non-contact electrodes and the direction of E_{ext} . The h-BN was characterized by weak interaction between the layers, interchange of B and N atoms from one layer to another in the $[0001]$ direction, and their location above each other. C atoms in the first graphene sublattice located immediately above B atoms on the surface, whereas C atoms in the second sublattice projected over the center of B-N lattice hexagons of the substrate surface. Total energy calculations showed that this configuration is the most stable.

The 8-ZGNR/h-BN(0001) heterostructure model was based on 3D periodic slab scheme (Fig. 20.1b, d). To simulate a system consisting of substrate and 8-ZGNR, we used a supercell containing unit cells of (4×4) h-BN and (4×4) graphene arranged within a plane (0001). The supercell parameter was selected divisible by

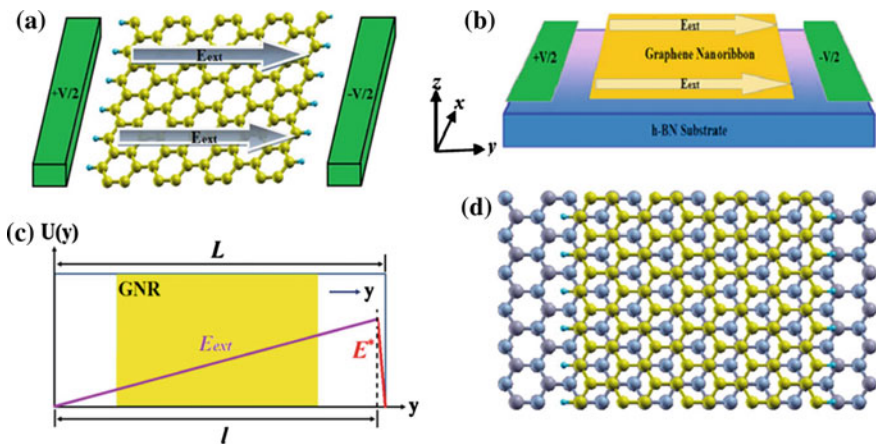


Fig. 20.1 Schematic representation of the systems considered [26]: **a** diagram of 8-ZGNR with E_{ext} ; E_{ext} has been applied along the cross-ribbon width, which is the y -axis direction; **b** schematics of ZGNR deposited on h-BN substrate with E_{ext} along y -axis direction (*top*) and (**d**) atomistic schematics of h-BN supported 8-ZGNR (*bottom*); **c** schematics of how to arrange saw-tooth potential; the shaded yellow area represents the system under investigation and the empty white space is the vacuum; the purple and red solid lines denote the linear external electric potential and its counterpart; L is the size of the periodic cell along y -direction

the equilibrium value of the graphene unit cell parameter. Graphene cells were used to build an 8-ZGNR. Figure 20.1b demonstrates a fragment of the 8-ZGNR/h-BN (0001) slab. The surface and the 8-ZGNR/h-BN interface were simulated as a slab consisting of three atomic layers of h-BN and a monolayer of 8-ZGNR. Each slab was isolated from others by 25 Å vacuum space.

Atomic and band structure calculations were performed using Quantum Espresso software suite [42] based on DFT [43–45]. Plane wave and pseudo-potentials were used in the basic calculations. The influence of core electrons was considered using ultrasoft pseudopotentials. Nonlocal exchange correlation functional was used in Perdew-Burke-Ernzerhof (PBE, PBEsol) parametrization [46]. The energy cutoff of plane waves for self-consistent field calculation was 410 eV. The accomplished total cell energy convergence was at least 10^{-4} Ry/cell. In all our calculations, spin-restricted wave functions and calculation upon singlet ground state were considered. Symmetry breaking in spin-densities yielded overestimated band gap and an exact treatment of the electron correlation in singlet wave functions necessary restored and symmetry breaking in spin density.

Local density (LDA) and semilocal approximations used for describing the exchange and correlation energy (LDA, GGA, including PBEsol) within the DFT framework are incapable correctly describing dispersion (van-der-Waals) interaction in layered structures, including the present system. Given that the dispersion interaction is determined exclusively by nonlocal dynamic correlations, the use of hybrid exchange-correlation functionals in DFT calculations is also unreasonable because they consider only the local (HF) exchange. In the current study, we considered van-der-Waals interaction in our system within the DFT framework using semi-empirical potential introduced in the total energy functional (DFT-D2) in accordance with [47]: $E_{\text{DFT-D2}} = E_{\text{DFT}} + E_{\text{disp}}$. In DFT-D2 calculations, we used PBE exchange correlation functional with dispersion correction (PBE-D2).

The interaction of electrons with external electrostatic field along the y -axis is determined by the following expression, which similarly to [26] has the form:

$$U_{\text{ext}}(r) = |e|E \cdot r,$$

where U is used to distinguish the potential energy in electrostatic field from all other potential terms of the Kohn-Sham equation:

$$\left(V_{\text{KS}}(\mathbf{r}) = \int d\mathbf{r}' \frac{n(\mathbf{r}')}{|\mathbf{r} - \mathbf{r}'|} + V_{\text{ion}}(\mathbf{r}) + V_{\text{xc}}(\mathbf{r}) \right).$$

Considering E_{ext} , the Kohn-Sham equations can be interpreted as

$$\left(-\frac{\hbar^2}{2m} \nabla^2 + V_{\text{KS}} + U_{\text{ext}} \right) \psi_i(\mathbf{r}) = \varepsilon_i \psi_i(\mathbf{r}).$$

Applied electrostatic potential changes linearly along the entire unit cell. Therefore, to observe the periodic boundary conditions, the original value should be

restored at the cell boundary. Thus, the saw-tooth potential shape with period equal to the unit cell period along the y -axis is most suitable (Fig. 20.1). The scheme of relative placement of the slab and external electrostatic potential is shown in Fig. 20.1. If E_{ext} exists in the interval from 0 to l and the simulated cell size is L along the y -axis, then the gauge field E^* is defined as: $E^* = -E_{\text{ext}} \frac{1}{L}$, the sign of minus indicates that E^* -direction is always opposite E_{ext} -direction.

For transport properties calculations, the carrier mobility tensor components are evaluated in the relaxation time approximation, based on the ratio: $\mu \approx e \cdot \tau / m^*$, where τ is the relaxation time in the system, m^* is the effective carrier mass. Our quantitative assessments of the tensor components of electron and hole effective masses are based on the ratio: $\frac{1}{m^*(k)_{ij}} = \frac{1}{\hbar^2} \frac{\partial^2 E}{\partial k_i \partial k_j}$ where \hbar is the Planck's constant, k is the wave vector. Experimental values of relaxation time $\tau = 20$ ps [1, 2] and $\tau = 4$ ps [3] are used in the calculations for electrons and holes, respectively.

20.3 Atomic and Magnetic Structures of 8-ZGNR/H-BN (0001) Heterostructure

To study the atomic structure of the 8-ZGNR/h-BN(0001) interface, relaxation of ZGNR and one upper h-BN atomic plane of the slab was performed. Two lower layers of the h-BN(0001) substrate were “frozen”. The relaxation was conducted until the sum total of all the forces in the system was reduced to 0.0001 eV/Å. We established equilibrium parameter values for the lattices, atomic positions of the nanoribbon and the upper layer of h-BN, and the bond length $d = 3.39$ Å between the nanoribbon and substrate atomic layers. The obtained results correlate well with known data [22]. For the highlighted 8-ZGNR/h-BN(0001) heterostructure fragment, shown in Fig. 20.1d, the obtained total energy values are $E_{\text{tot}} = -1130.6441$ Ry/cell. DFT calculation results also demonstrated that the lengths of σ -bonds in planar (0001) can be described well using PBE-D2 functional. In the 8-ZGNR/h-BN(0001) heterostructure, the length of the C-C bond for internal atoms reaches 1.4177 Å. The bond length between two edge C atoms is 1.4047 Å, indicating its deformation. This deformation cause sharp peaks corresponding to the electron density states in the proximity of the Fermi level and induces local magnetic moments at the ZGNR edges [35].

We used DFT calculations to establish the dependence of the local magnetic moment at the GNRs edges upon the strength and direction of an E_{ext} applied perpendicularly to the nanoribbon width. Figure 20.2 demonstrates local magnetic moment of the edge C atoms in 8-ZGNR without substrate (a) and on the h-BN(0001) substrate (b) depending on E_{ext} . The dependence exhibits a dome-like shape. Based on Fig. 20.2, the induced local magnetic moment of the edge C atoms decreases with the increase in E_{ext} strength, independent of the field direction. However, the present heterostructure is magnetic. Remarkably, the effect of preserved local magnetic

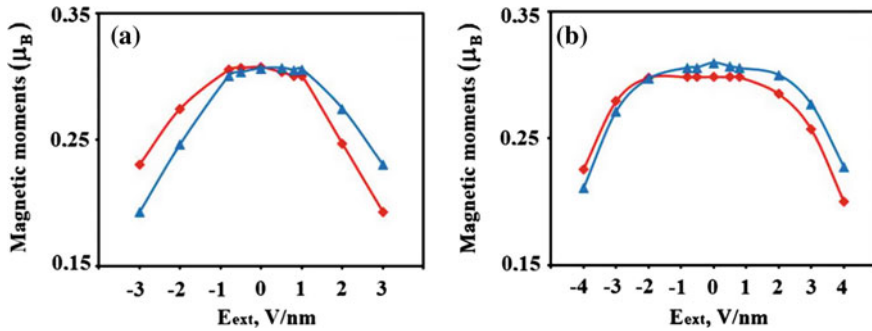


Fig. 20.2 Magnetic moments of two edge C atoms (*red* left edge C atom, *blue* right edge C atom) in the suspended 8-ZGNR (a) and in 8-ZGNR/h-BN (b) subject to E_{ext} [26]

moment ($0.3\mu_B$) is observed when low E_{ext} ($-2 \div 1$ V/nm) is applied to the 8-ZGNR/h-BN(0001) semiconductor heterostructure. The nature of the effect that cause stability of the magnetic properties is unclear. This phenomenon can be associated with the domination of exchange splitting in the edge states of C atoms (according to the Stoner model [48]) over the tendency of valence band and conduction band contraction. Weaker influence of E_{ext} on magnetism can also be caused by another mechanism, which can be explained by strong interaction between p_z -orbitals of C and p -substrate during chemical adsorption [41]. However, the adsorption energy in the 8-ZGNR/h-BN(0001) heterostructure is 74 meV/atom, indicating the physical adsorption mechanism. Physical adsorption mechanism is characterized by weak interaction making the chemical mechanism impossible in practice. When E_{ext} strength increases to critical values (4 V/nm), the adhesive binding energy decreases to 54 meV/atom. Magnetism tuning in this heterostructure with low E_{ext} , can also be considered, inefficient. The presence of a dielectric substrate increases the effect of conservation of local magnetic moment on C atom in the interval ranges ($-1 \div 1$ V/nm) in the absence of the substrate (Fig. 20.2a). This expansion of the range of E_{ext} values could be attributed to the modification of electron energy owing to dielectric screening of electron-electron interaction in 8-ZGNR/h-BN(0001) [40].

20.4 Electronic Structure of the Graphene Heterostructures

The band structure of SLG/ $\text{Al}_2\text{O}_3(0001)$ -H two-dimensional system interface for model A is present in Fig. 20.3b in comparison with both band structure of $\text{Al}_2\text{O}_3(0001)$ -H ultrathin layer (a) and graphene (c) for special points of the first Brillouin band. First of all, it is noteworthy that dispersive curves of $E(k)$ energy for two-dimensional systems in particular for 2D $\text{Al}_2\text{O}_3(0001)$ -H with adsorbed hydrogen atoms on single torn bond of aluminum (Fig. 20.3a) and both surfaces

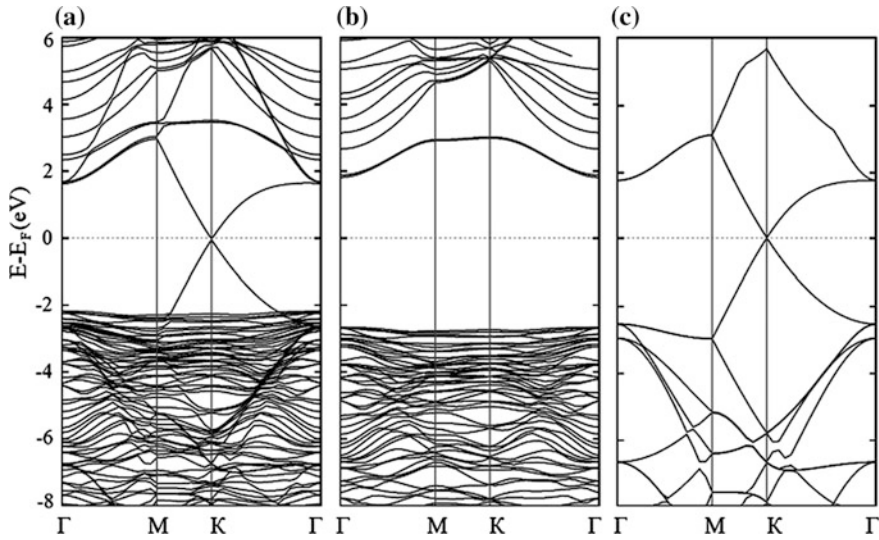


Fig. 20.3 Band structure of 2D-systems: **a** $\text{Al}_2\text{O}_3(0001)\text{-H}$; **b** $\text{SLG}/\text{Al}_2\text{O}_3\text{-H}$; **c** graphene

comprising aluminum atoms essentially differ from $E(k)$ for 3D Al_2O_3 crystal. The band structure of 2D $\text{Al}_2\text{O}_3(0001)\text{-H}$ substrate layer (with single torn bond of Al atom) is characterized by a presence of an unfilled band of surface aluminum s -, p -states. This band has a low dispersion and localizes in the energy range of 4.3–5.7 eV. The 2D $\text{SLG}/\text{Al}_2\text{O}_3(0001)\text{-H}$ system interface is characterized by the presence of unfilled s -, p - hybrid bands in the M - K direction of the Brillouin zone for the energy of 4.9 eV (Fig. 20.3b). These zones appear in the result of interaction between unfilled s -, p -hybrid band of aluminum and unfilled band of graphene carbon atoms with s -, p_z -symmetry.

Thus, the band structure of Al_2O_3 substrate demonstrates the presence of an unfilled aluminum acceptor-like surface states band. The band shows little dispersion being localized in the 4.3–5.7 eV interval (Fig. 20.3a). In the presence of graphene, redistribution of surface electron states is observed in the 2D $\text{SLG}/\text{Al}_2\text{O}_3(0001)\text{-H}$ system. We should note the shift down in energy of the surface states band and the highest-energy filled state by 1 eV. We should also note splitting of the mentioned Al_2O_3 surface states band into four interface bands (Fig. 20.3b). It is necessary to mention that the interval of energies from the Fermi level to -1 eV includes surface states of the substrate surface opposite to the interface, which are practically unable to affect the interface states. Energy bands in the region are mostly determined by the states of hydrogen and subsurface oxygen with a small contribution from aluminum. Substrate presence causes little variation in carbon states. Modification of the substrate surface states in the presence of a graphene layer may be caused by redistribution of subsurface space charge, which specifically affects the behavior of surface states in the band gap. Indeed, a graphene layer can alter the configuration of electric field in the proximity of the

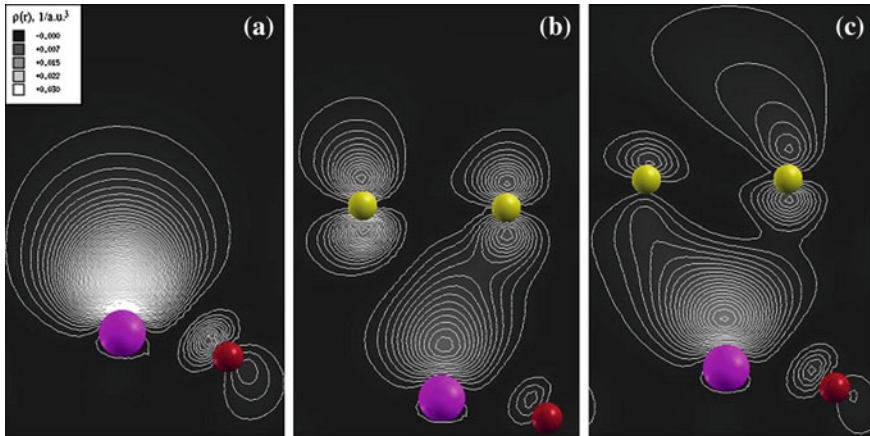


Fig. 20.4 Partial charge density maps: **a** sapphire surface and **(b, c)** SLG/ Al_2O_3 -H interface orbitals

substrate surface. As it has been shown in [49], it is possible to use adsorbed atoms and layers to alter not only the value but also the direction of electric field strength for polarized surfaces. The same paper demonstrated the opportunity to employ the same effect for changing the doping level from n -type to p -type and vice versa.

To study the character of graphene interaction with the substrate, we additionally examined the behavior of partial densities of electron states on clear Al_2O_3 substrate surface (Fig. 20.4a) and in the SLG/ $\text{Al}_2\text{O}_3(0001)$ -H interface (Fig. 20.4b, c). Wave functions (squares) of the above-mentioned unoccupied band of Al_2O_3 substrate in the 4.3–5.7 eV interval of energies are localized exclusively on the surface, mainly close to the Al atom and slightly in the proximity of the O atom (Fig. 20.4a). The shape of examined orbitals is practically independent from the wave vector, it elongates in the direction perpendicular to the interface surface. The area should be recognized as a surface states band. In the SLG/ $\text{Al}_2\text{O}_3(0001)$ -H system interface, it mixes with unoccupied π -regions of carbon creating interface states bands in the conduction band (Fig. 20.3b). Figure 20.4b, c contains the partial density maps of electron states of two interface orbitals for the \mathbf{k} -vector in the middle of the M - K segment. We should note binding character of these orbitals forming shared electron densities with two different carbon atoms; however, they are quite far (~ 4.5 eV) in terms of energy from the last filled level.

Band structure of the 8-ZGNR/h-BN(0001) heterostructure shows correlation with applied E_{ext} (Fig. 20.5). The band structure of 8-ZGNR without substrate is also shown for comparison, which is in good agreement with that in other studies [32, 36, 50, 51].

In the absence of E_{ext} , the band structure of the 8-ZGNR/h-BN(0001) heterostructure and the 8-ZGNR without substrate show that their band gap are $E_g = 0.50$ and 0.60 eV, respectively. With the increase in E_{ext} , the heterostructure and nanoribbon show an increase in energy gap for the spin-up electron subsystem.

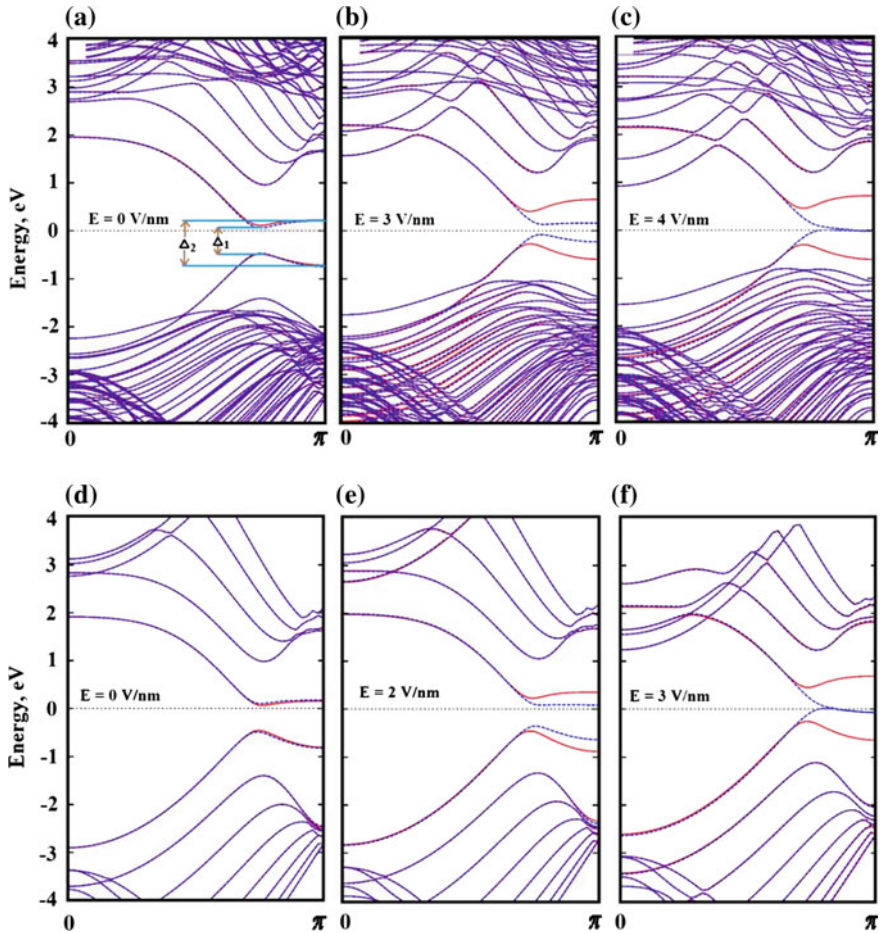


Fig. 20.5 DFT-D2 spin-polarized calculation of the band structure (**a, b, c**) for the 8-ZGNR/h-BN (0001) heterostructure and (**d, e, f**) for suspended 8-ZGNR with various E_{ext} values (from left to right: red spin-up, blue spin-down) [26]

For the spin-down electron subsystem, we observe a decrease of the band gap. In addition, closure of the band gap occurs at a certain critical value of E_{ext} . Figure 20.5c, f show the overlapping bands of edge C atoms for the spin-down electron subsystem. The effect of E_{ext} essentially manifests itself as the cancellation of energy degeneracy for localized edge states (both spins). Such an effect becomes possible because the energy of edge states shifts in the reverse directions for two spins. Semi-metallic character for the spin-down electron subsystem is accomplished in the 8-ZGNR/h-BN(0001) heterostructure when the critical field value of 4 V/nm is applied. For 8-ZGNR without substrate, semi-metallic character is achieved at lower values of E_{ext} (3 V/nm, Fig. 20.5f).

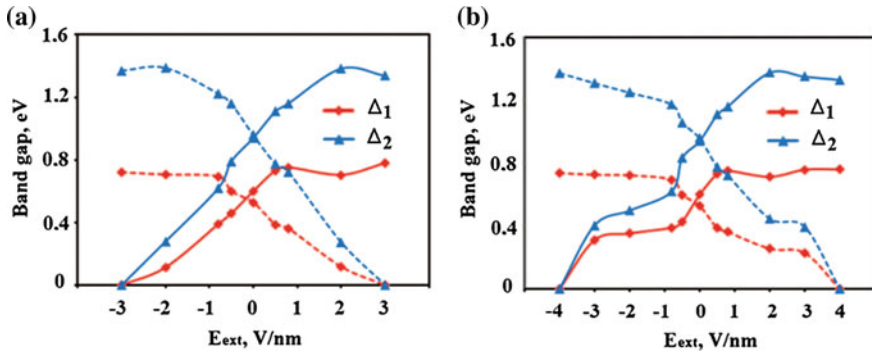


Fig. 20.6 Variations of band gaps of the suspended 8-ZGNR (a) and 8-ZGNR/h-BN interface (b) with various spins configuration (*dark line* spin-up, *dashed line* spin-down) [26]

DFT calculations were used to establish critical values of E_{ext} for the 8-ZGNR/h-BN(0001) heterostructure providing for semiconductor-semimetal transition for one of spin electron configurations. At the critical value of the positive potential (4 V/nm, Fig. 20.5), the spin-down electron subsystem in the heterostructure undergoes semiconductor-semimetal transition. For the spin-up electron subsystem, we observed an increase of the band gap to 0.8 and 1.2 eV for the Dirac points $k = 2\pi/3$ and $k = \pi$, respectively. If the sign of the external potential changes, then the semiconductor-semimetal transition is observed in the spin-up subsystem, whereas the spin-down subsystem retains its semiconductor properties. Figure 20.6 demonstrates the relationship between the change in E_g and the value and sign of the E_{ext} .

The influence of E_{ext} on partial electron states of edge and central atoms of C, B, and N in the 8-ZGNR/h-BN(0001) heterostructure exhibits considerable distinctions, although they are identical to a certain extent. For edge C atoms, the size of peaks of the partial densities of states (PDOS) in the proximity of the Fermi level depends on the strength of E_{ext} for the spin-up and spin-down electron configurations. In the absence of E_{ext} , the shift of localized edge states in the proximity of the Fermi level is 0.83 eV. The shift decreases 1.7 times at critical field values. At the same time, local magnetic moments of the edge C atoms in ZGNR decrease 1.5 times for both spins. The response of edge magnetism to E_{ext} in the 8-ZGNR/h-BN(0001) heterostructure can be caused by partial suppression of spin exchange interaction at the nanoribbon edges with increasing E_{ext} .

The effect of E_{ext} is clearly illustrated by the maps of partial electron density for C, B, and N atoms in the 8-ZGNR/h-BN(0001) heterostructure shown in Fig. 20.7. The maps of partial electron density for spin-up edge states of C atoms in the heterostructure are calculated using the DFT-D2 method for 0.002 electron/bohr³ isosurface in the points: $k = 2\pi/3$ and $k = \pi$.

Based on Fig. 20.7, spatial localization of spin density of C atoms in the 8-ZGNR/h-BN(0001) heterostructure can be estimated for the k -vector at $2\pi/3$ and

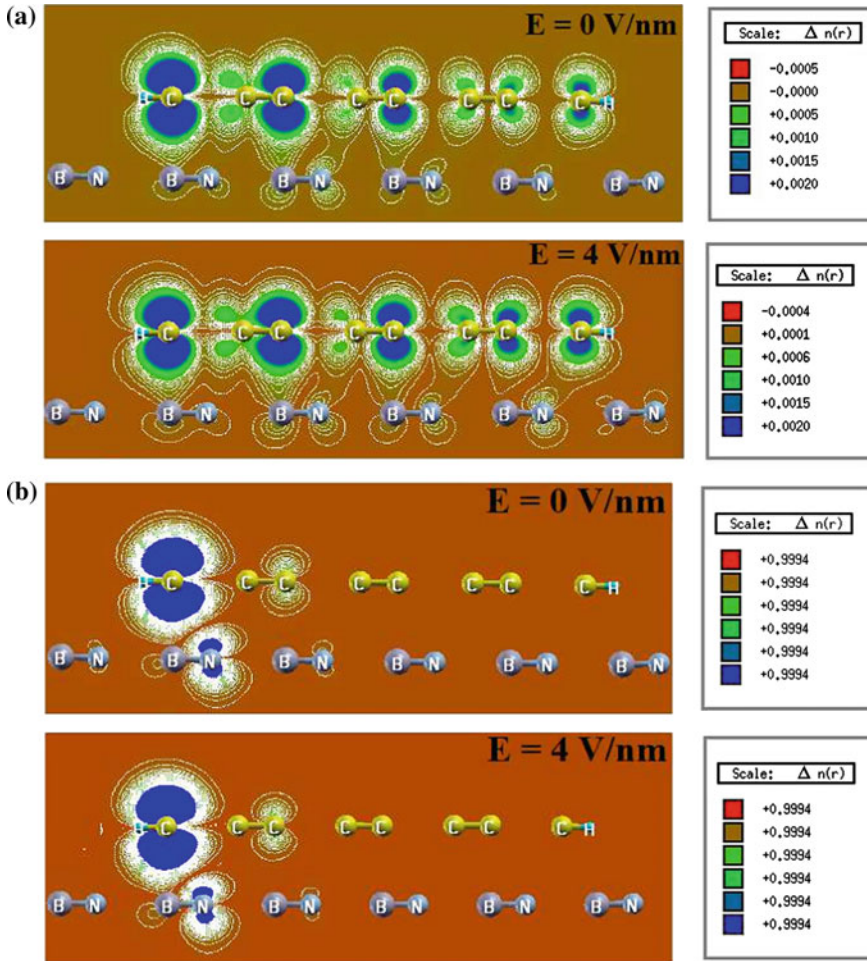


Fig. 20.7 PDOS maps of $2p_z$ -orbitals of C in the 8-ZGNR/h-BN(0001) heterostructure for spin-up (with $E_{\text{ext}} = 0$ V/nm and with $E_{\text{ext}} = 4$ V/nm). Calculation is performed using the DFT-D2 method for the 0.002 electron/bohr³ isosurface at the points: $k = 2\pi/3$ (a) and $k = \pi$ (b)

π . In the absence of E_{ext} , wave functions (squares) of occupied bands, of partial electron states of C for the $(-0.6 \div 0)$ eV energy interval localize exclusively at C atoms (Fig. 20.7a). The shape of these orbitals is practically independent of the wave vector; it elongates in the direction perpendicular to the interface surface. When E_{ext} is applied, the bands mix with the bands of B and N in the 8-ZGNR/h-BN(0001) interface, creating interface-state bands (Fig. 20.7b). These orbitals show binding characteristics.

We used DFT calculations to study the responses of the band structure and edge magnetism to the effect of electric field in two cases: AF-8-BZGNR without

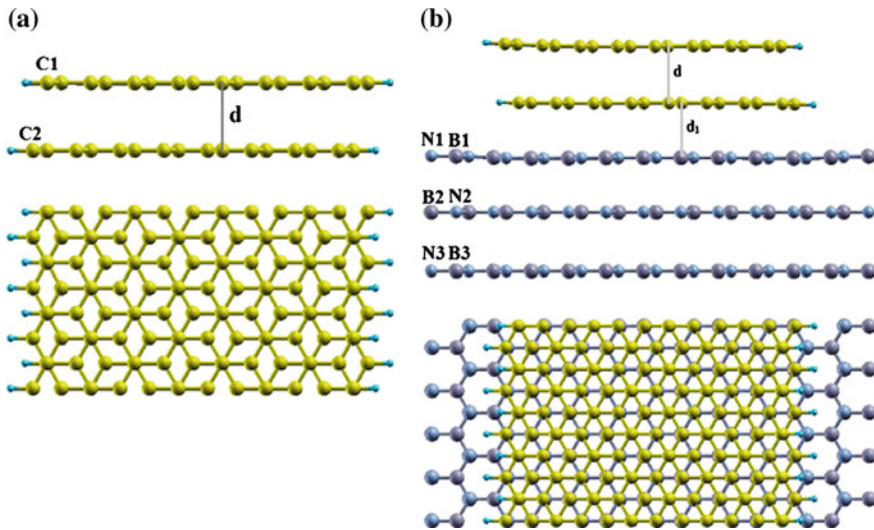


Fig. 20.8 Relaxed atomic structure of 8-BZGNR (a) and 8-BZGNR/h-BN(0001) (b) using DFT with vdW, where *top, front* view and *bottom, top* view are shown

substrate and the same on hexagonal boron nitride. For the highlighted AF-8-BZGNR/h-BN(0001) heterostructure fragment, shown in Fig. 20.8b, we obtained in DFT calculations the total energy values as a function of interlayer distance in graphene bilayer. As follows from the analysis [39], the equilibrium state of the AF-8-BZGNR/h-BN(0001) system corresponds to the minimum total energy at the interlayer distance $d = 0.327$ nm. Uniaxial compression or extension of the system makes its state metastable.

Early ab initio DFT calculations established [52] that electric field applied across the width of suspended 8-ZBGNR bilayer induces in it the semiconductor-semimetal transition at the critical electric field value over 3 V/nm. Our DFT calculations have demonstrated that band spectrum in the AF-8-BZGNR/h-BN(0001) heterostructure, similarly to the 8-BZGNR system without substrate, exhibit dependence on the applied external electric field as shown in Fig. 20.9. DFT calculations of total energy for a heterostructure fragment (Fig. 20.8b) in this magnetic configuration have shown that in the examined interval of electric fields the total energy value increases insignificantly (0.02 %). As we have noted above, in the absence of electric field and uniaxial compression, band spectrum of the AF-8-BZGNR/h-BN(0001) heterostructure exhibits band gap 0.54 and 0.35 eV for the spin-up and spin-down electron subsystems, respectively. With the increase of the external electric field, the AF-8-BZGNR/h-BN(0001) heterostructure shows an increase of the energy gap for the spin-up electron subsystem. At the same time, for the spin-down electron subsystem, we observe a decrease of the said gap and at a certain critical value of the electric field, closure of the band gap takes place. The

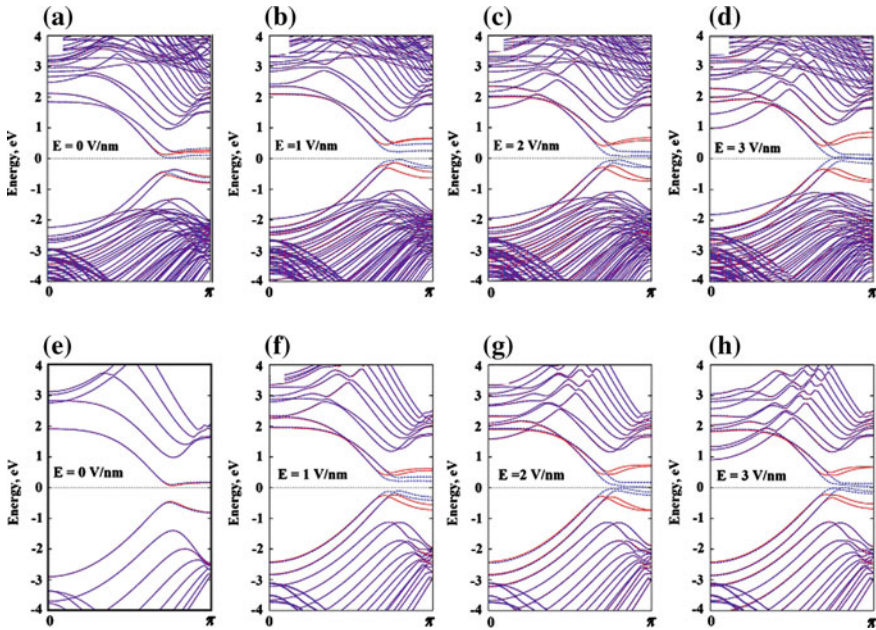


Fig. 20.9 DFT-D2 spin-polarized calculation of the band spectrum (a–d) for the AF-8-BZGNR/h-BN(0001) heterostructure and (e–h) for suspended AF-8-BZGNR with various values of E_{ext} from left to right: *red* spin-up, *blue* spin-down

effect is shown in Fig. 20.9d demonstrating overlapping bands of edge carbon atoms for the spin down electron subsystem.

It should be noted that the effect of transverse electric field essentially manifests itself as cancellation of energy degeneracy for localized edge states (both spins). An effect like that becomes possible because the energy of edge states shifts in the reverse directions for two spins. Addition of the substrate effect to the external electric field effect results in an increase of the noted splitting evidently illustrated in Fig. 20.9b, f. Semimetallic character for the spin-down electron subsystem is accomplished in the AF-8-BZGNR/h-BN(0001) heterostructure when the critical field value of 3 V/nm is applied (Fig. 20.9d). For suspended AF-8-BZGNR bilayer, semimetallic character is not achieved yet at values $E_{\text{ext}} = 3$ V/nm (Fig. 20.9h).

20.5 Transport Properties of the 8-ZGNR/H-BN(0001) Semiconductor Heterostructure

In this section, we study the influence of E_{ext} applied across ZGNR on the transport properties of the 8-ZGNR/h-BN(0001) spin-polarized semiconductor heterostructure [26]. Channel conductivity can be controlled by the applied voltage and the

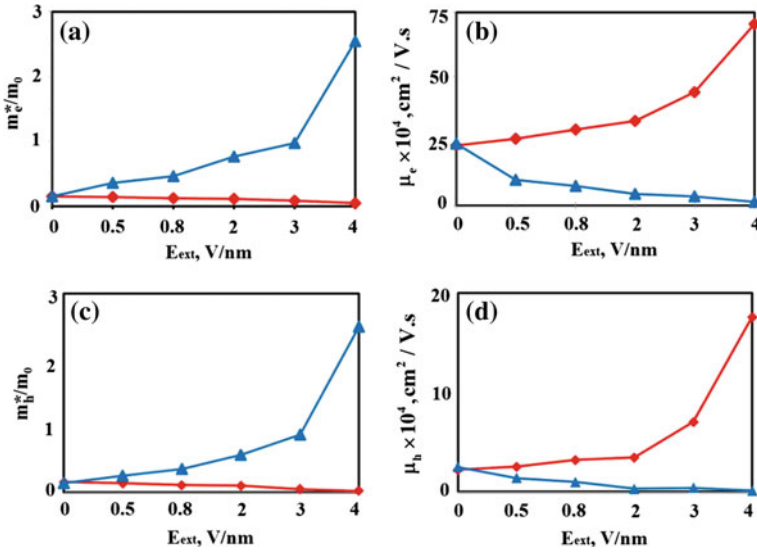


Fig. 20.10 Dependence of effective masses of electrons (a), holes (b), with electron mobility $\mu_e \times 10^4, \text{cm}^2/(\text{V}\cdot\text{s})$ (c) and hole mobility $\mu_h \times 10^4, \text{cm}^2/(\text{V}\cdot\text{s})$ (d) on E_{ext} for two spins: red line spin-up, blue line spin-down [26]

alternating polarity charge of the carriers in the Dirac point. Therefore, fundamental study of carrier mobility in the 1D 8-ZGNR-AF/h-BN(0001) interface affected by applied E_{ext} can open the possibilities for controlling the transport properties of charge carriers. The results of DFT calculations of effective carrier mass and carrier mobility in the 8-ZGNR/h-BN(0001) spin-polarized semiconductor heterostructure show their dependence on E_{ext} (Fig. 20.10).

The DFT calculations for the heterostructure provide effective masses (Fig. 20.10a, c) and carrier mobilities (Fig. 20.10b, d) that are comparable with the data in [30, 53, 54]. However, unlike those of previous studies, the current results provide estimates of carrier mobility in 1D graphene channel of the 8-ZGNR/h-BN(0001) heterostructure. Figures 20.10b, d show that transport properties of the 8-ZGNR/h-BN(0001) semiconductor heterostructure can be controlled using E_{ext} . In particular, at critical value of the positive potential, electron mobility can increase thrice or stay at zero in the spin-up and spin-down electron subsystems, respectively. Within the relaxation time approximation, the electron mobility for the spin-up subsystem can be regulated from $23.3 \cdot 10^4$ to $7 \cdot 10^5 \text{ cm}^2/(\text{V}\cdot\text{s})$ using E_{ext} . The predicted high electron mobility in the 8-ZGNR/h-BN(0001) heterostructure can serve as a good foundation in fabricating graphene-based electronic components.

The variation in electron mobility within the relaxation time approximation frame can be caused by the characteristic of change in the effective carrier mass (Fig. 20.10a) when the E_{ext} increases from zero to critical value (4 V/nm). The effective mass of spin-up electrons can decrease by four times with the increase in

E_{ext} , which increases the electron mobility of the spin-up subsystem (Fig. 20.10b). Moreover, the electron effective mass increases by an order of magnitude because of the 18 times decreasing electron mobility. This phenomenon can be related to partial closure of graphene channel for the spin-down electron subsystem. The hole mobility in 1D graphene channel in the absence of E_{ext} is lower than electron mobility by an order of magnitude (Fig. 20.10b, d). However, when E_{ext} is applied (up to the critical value), the character of hole mobility variation is similar for both spins. The only difference is that spin-up hole mobility increases by 8 times, where spin-down hole mobility decreases by a factor of 125.

20.6 Conclusion

We have used the pseudopotential method ab initio to study within the DFT framework the equilibrium geometry and band structure of the (0001) Al_2O_3 surface and the SLG/ Al_2O_3 (0001) interface. Several possible variants of graphene monolayer arrangement on (0001) sapphire surface were examined, with a subsequent study of two main models. Despite the known problem of describing the van der Waals forces using DFT, a satisfactory correlation was obtained between the results calculated within the GGA framework and experimental estimates of the distance between Al_2O_3 surface and graphene in the SLG/ Al_2O_3 (0001) interface. Analysis of the band structure and interatomic spacing in the interface for both models allows one to speak about physical graphene adsorption on the (0001) sapphire surface constrained by aluminum atoms. Analysis of effective atomic charge in the interface revealed surface charge fluctuations on the substrate in the presence of graphene, which can be explained by a decrease of the energy of occupied subsurface Al_2O_3 states relatively to the Fermi level.

We used first-principles calculations based on the DFT to study the band structure, magnetic and transport properties of a 1D graphene channel on h-BN functioning as a part of the 8-ZGNR/h-BN(0001) magnetic semiconductor heterostructure, in relation with E_{ext} . We have noted that, the substrate significantly varies magnetic and transport properties of ZGNRs. In particular, it was also shown that the influence of the substrate on electronic properties of the heterostructure increases with decreasing GNR width. In this study, we showed that the degeneration in energy of the edge-localized states removes when E_{ext} is applied. In ZGNR/h-BN(0001) heterostructure, value of this splitting energy was higher than one in ZGNRs without substrate. We established the critical values of E_{ext} for the 8-ZGNR/h-BN(0001) heterostructure providing for semiconductor-semimetal transition for one of the spin electron configurations. When the sign of the external field potential changes, the semiconductor-semimetal transition is observed in the spin-up subsystem, whereas the spin-down subsystem retains its semiconductor properties. The E_{ext} does not disrupt the magnetism of 1D graphene channel in the 8-ZGNR/h-BN(0001) heterostructure. Thus, the magnetic semiconductor heterostructure of 8-ZGNR/h-BN(0001) should be studied further. This study

showed that the transport properties of the 8-ZGNR/h-BN(0001) magnetic semiconductor heterostructure can be successfully varied by regulating E_{ext} . These abilities enable the use of 8-ZGNR/h-BN(0001) semiconductor heterostructure in spintronics.

We used first-principles calculations based on the density functional theory (DFT) to study the band spectrum and magnetic properties of a 1D graphene channel on hexagonal boron nitride functioning as a part of the AF-8-BZGNR/h-BN(0001) magnetic semiconductor heterostructure, in relation to three effects: uniaxial interlayer compression, external transverse electric field and interaction with the substrate. We established critical values of uniaxial nanomechanical compression and external electric fields for the AF-8-BZGNR/h-BN(0001) heterostructure providing for semiconductor-semimetal phase transition for one of spin electron configurations. As an important note, uniaxial interlayer compression and external transverse electric field does not disrupt the magnetism of 1D graphene channel in the AF-8-BZGNR/h-BN(0001) heterostructure. Thus, we should speak about the magnetic semiconductor heterostructure of AF-8-BZGNR/h-BN(0001). The study has shown that magnetic properties of the AF-8-BZGNR/h-BN(0001) semiconductor heterostructure can be successfully varied in a wide range using their regulation with uniaxial interlayer compression and external transverse electric field.

References

1. K.S. Novoselov, A.K. Geim, S. Morozov, D. Jiang, Y. Zhang, S. Dubonos, I. Grigorieva, A. Firsov, *Science* **306**, 666 (2004)
2. S. Ereemeev, S. Tsirkin, E.V. Chulkov, *Phys. Solid State* **52**, 1768 (2010)
3. I. Calizo, S. Ghosh, W. Bao, F. Miao, C.N. Lau, A.A. Balandin, *Solid State Commun.* **149**, 1132 (2009)
4. S. Ghosh, W. Bao, D.L. Nika, S. Subrina, E.P. Pokatilov, C.N. Lau, A.A. Balandin, *Nat. Mater.* **9**, 555 (2010)
5. C. Faugeras, A. Nèrière, M. Potemski, A. Mahmood, E. Dujardin, C. Berger, W. De Heer, *Appl. Phys. Lett.* **92**, 011914 (2008)
6. Y.Y. Wang, Z.H. Ni, T. Yu, Z.X. Shen, H.M. Wang, Y.H. Wu, W. Chen, A.T. Shen Wee, *J. Phys. Chem. C* **112**, 10637 (2008)
7. S. Akcöltekin, M. El Kharrazi, B. Köhler, A. Lorke, M. Schleberger, *Nanotechnology* **20**, 155601 (2009)
8. J. Feng, W. Zhang, W. Jiang, *Phys. Rev. B* **72**, 115423 (2005)
9. S. Ereemeev, S. Schmauder, S. Hocker, S. Kulkova, *Phys. B* **404**, 2065 (2009)
10. L. Han, S. Qing-Qing, C. Lin, X. Yan, D. Shi-Jin, Z. Wei, Z. Shi-Li, *Chin. Phys. Lett.* **27**, 077201 (2010)
11. A. Ramasubramaniam, D. Naveh, *Phys. Rev. B* **84**, 075405 (2011)
12. Y.S. Dedkov, A. Shikin, V. Adamchuk, S. Molodtsov, C. Laubschat, A. Bauer, G. Kaindl, *Phys. Rev. B* **64**, 035405 (2001)
13. A. Chaplik, A. Karpushin, *Soviet. J. Exp. Theor. Phys. Lett.* **12**, 34 (1970)
14. L.F. Huang, G.R. Zhang, X.H. Zheng, P.L. Gong, T.F. Cao, Z. Zeng, *J. Phys.: Condens. Matter* **25**, 055304 (2013)
15. Q. Tang, Z. Zhou, Z. Chen, *Nanoscale* **5**, 4541 (2013)
16. Q. Tang, Z. Zhou, *Prog. Mater. Sci.* **58**, 1244 (2013)

17. V. Ilyasov, B. Meshi, V. Nguyen, I. Ershov, D. Nguyen, *AIP Adv.* **3**, 092105 (2013)
18. K. Wakabayashi, S. Dutta, *Solid State Commun.* **152**, 1420 (2012)
19. O. Hod, V. Barone, J.E. Peralta, G.E. Scuseria, *Nano Lett.* **7**, 2295 (2007)
20. F.J. Martín-Martínez, S. Fias, G. Van Lier, F. De Proft, P. Geerlings, *Chemistry-A. Eur. J.* **18**, 6183 (2012)
21. I.-S. Byun, D. Yoon, J.S. Choi, I. Hwang, D.H. Lee, M.J. Lee, T. Kawai, Y.-W. Son, Q. Jia, H. Cheong, *ACS Nano* **5**, 6417 (2011)
22. G. Giovannetti, P.A. Khomyakov, G. Brocks, P.J. Kelly, J. van den Brink, *Phys. Rev. B* **76**, 073103 (2007)
23. M. Huzak, M.S. Deleuze, B. Hajgato, *J. Chem. Phys.* **135**, 104704 (2011)
24. B. Hajgató, M. Huzak, M.S. Deleuze, *J. Phys. Chem. A* **115**, 9282 (2011)
25. F. Withers, T.H. Bointon, M. Dubois, S. Russo, M.F. Craciun, *Nano Lett.* **11**, 3912 (2011)
26. V.V. Ilyasov, B.C. Meshi, V.C. Nguyen, I.V. Ershov, D.C. Nguyen, *J. Chem. Phys.* **141** (2014)
27. R. Qin, J. Lu, L. Lai, J. Zhou, H. Li, Q. Liu, G. Luo, L. Zhao, Z. Gao, W.N. Mei, *Phys. Rev. B* **81**, 233403 (2010)
28. V.V. Ilyasov, V.C. Nguyen, I.V. Ershov, D.C. Nguyen, *J. Struct. Chem.* **55**, 191 (2014)
29. Y.-W. Son, M.L. Cohen, S.G. Louie, *Nature* **444**, 347 (2006)
30. P. Zomer, S. Dash, N. Tombros, B. Van Wees, *Appl. Phys. Lett.* **99**, 232104 (2011)
31. C.R. Dean, A.F. Young, I. Meric, C. Lee, L. Wang, S. Sorgenfrei, K. Watanabe, T. Taniguchi, P. Kim, K.L. Shepard, J. Hone, *Nat. Nano* **5**, 722 (2010)
32. J. Yu, Z. Zhang, W. Guo, *J. Appl. Phys.* **113**, 133701 (2013)
33. J.B. Oostinga, H.B. Heersche, X. Liu, A.F. Morpurgo, L.M.K. Vandersypen, *Nat. Mater.* **7**, 151 (2008)
34. A. Mattausch, O. Pankratov, *Phys. Rev. Lett.* **99**, 076802 (2007)
35. V. Ilyasov, B. Meshi, V. Nguyen, I. Ershov, D. Nguyen, *J. Appl. Phys.* **115**, 053708 (2014)
36. J. Guo, D. Gunlycke, C. White, *Appl. Phys. Lett.* **92**, 163109 (2008)
37. Z. Zhang, C. Chen, X.C. Zeng, W. Guo, *Phys. Rev. B* **81**, 155428 (2010)
38. Y. Zhang, X.-L. Lu, Y. Jiang, B. Teng, J.-Q. Lu, *J. Comput. Theor. Nanosci.* **8**, 2448 (2011)
39. V.V. Ilyasov, B.C. Meshi, V.C. Nguyen, I.V. Ershov, D.C. Nguyen, *Solid State Commun.* **199**, 1 (2014)
40. X. Jiang, N. Kharche, P. Kohl, T.B. Boykin, G. Klimeck, M. Luisier, P.M. Ajayan, S.K. Nayak, *Appl. Phys. Lett.* **103**, 133107 (2013)
41. J. Chen, M. Vanin, Y. Hu, H. Guo, *Phys. Rev. B* **86**, 075146 (2012)
42. P. Giannozzi, S. Baroni, N. Bonini, M. Calandra, R. Car, C. Cavazzoni, D. Ceresoli, G.L. Chiarotti, M. Cococcioni, I. Dabo, *J. Phys.: Condens. Matter* **21**, 395502 (2009)
43. P. Hohenberg, W. Kohn, *Phys. Rev.* **136**, B864 (1964)
44. W. Kohn, L.J. Sham, *Phys. Rev.* **140**, A1133 (1965)
45. A. Dal Corso, A. Pasquarello, A. Baldereschi, *Phys. Rev. B* **56**, R11369 (1997)
46. K. Burke, J.P. Perdew, M. Ernzerhof, *Int. J. Quantum Chem.* **61**, 287 (1997)
47. S. Grimme, *J. Comput. Chem.* **25**, 1463 (2004)
48. E.C. Stoner, *Proc. R. Soc. Lond. Ser. A Math. Phys. Sci.* **372** (1938)
49. S. Gong, W. Sheng, Z. Yang, J. Chu, *J. Phys.: Condens. Matter* **22**, 245502 (2010)
50. X. Zheng, L. Song, R. Wang, H. Hao, L. Guo, Z. Zeng, *Appl. Phys. Lett.* **97**, 153129 (2010)
51. E.-J. Kan, Z. Li, J. Yang, J. Hou, *Appl. Phys. Lett.* **91**, 243116 (2007)
52. Y. Guo, W. Guo, C. Chen, *J. Phys. Chem. C* **114**, 13098 (2010)
53. P. Neugebauer, M. Orlita, C. Faugeras, A.-L. Barra, M. Potemski, *Phys. Rev. Lett.* **103**, 136403 (2009)
54. K.I. Bolotin, K. Sikes, Z. Jiang, M. Klima, G. Fudenberg, J. Hone, P. Kim, H. Stormer, *Solid State Commun.* **146**, 351 (2008)

Chapter 21

Morphology, Atomic and Electronic Structure of Metal Oxide (CuO_x , SnO_x) Nanocomposites and Thin Films

G.E. Yalovega, V.A. Shmatko, A.O. Funik and M.M. Brzhezinskaya

Abstract We investigated the surface morphology, oxidation state, local and electronic structure of a number of metal oxide (CuO_x , SnO_x) nanoparticles, nanocomposites and thin films based on them, synthesized by electrochemical deposition and sol-gel techniques. Surface morphological studies were carried out using a SEM (scanning electron microscopy). The bonding structure with element sensitivity to Cu and Sn, local environment and electronic structure were studied by the XPS (X-ray photoelectron spectroscopy) and the XANES (X-ray absorption near edge structure) spectroscopy. The changes in local and electronic structure, oxidation state and the surface morphology of nanocomposites in the interaction of metal oxide nanoparticles with CNT (carbon nanotubes) and SiO_2 (silicon oxide) matrices were observed. We discovered that the shape and size of metal oxide nanoparticles depend on metal oxidation state as well as parameters of synthesis and, moreover, kind of matrix affect in direction of the nano-unit nucleation and subsequent organization of metal oxide nanoparticles/microcrystals.

21.1 Introduction

In recent years, developing ways of tuning the structure of materials on specific morphologies have been one of the most important goals of materials science. One of the main problems in the synthesis of sorbent and catalytically active nanocomposites is increase and development of surface of active sorbent centre [1–5]. Sorption activity of these centers depends on the size, shape, structure and

G.E. Yalovega (✉) · V.A. Shmatko · A.O. Funik
Faculty of Physics, Southern Federal University, Zorge 5,
Rostov-on-Don 344090, Russia
e-mail: yalovega1968@mail.ru

M.M. Brzhezinskaya
Helmholtz-Zentrum Berlin Für Materialien Und Energie,
Albert-Einstein-Strasse 15, Berlin 12489, Germany

the oxidation state of inorganic nanoparticles component [6–10]. Composite materials based on metal oxide nanoparticles in/on different matrices attracted increasing attention thanks to the possibility of tailoring their chemico-physical properties as a function of particle size, shape, composition and structure [11–15]. It is well known fact, that morphology and structure of nanoparticles as well as composition and morphological details of matrix have great effects on electrical, catalytic, adsorption etc. properties of the resulting composites and films based on them [16–19]. The influence kind of matrix in direction of the nano-unit nucleation and subsequent organization of metal oxide nanoparticles is observed. The reason of this phenomenon is the interaction between the matrix and metal oxide nanoparticles, that leads to changes in local atomic and electronic structure of the both components of the resulting composite and, as a result, changes in the properties of the whole composite. Controlled synthesis of inorganic nanostructures in terms of size and shape strongly motivated by their size and shape dependent gas adsorption properties [20, 21].

Silicon is the basic material of modern electronics. Moreover, new possibilities have opened up for using silicon dioxide as a matrix in the fabrication of nanocomposite for gas sensors [22, 23]. Doping of silicon dioxide with transition metal oxides and tin dioxide makes it possible to produce materials with desired properties. Recent investigations have demonstrated that the best gas sensitive properties are exhibited by many materials based on tin, zinc, indium, tungsten, titanium and silicon oxides; lead sulfide; complexes based on potassium and chromium [24, 25].

Nowadays a lot of publications are devoted to studies of the influence of synthesis parameters to changes in local atomic and electronic structure as well as properties of nanocomposites based on multi-walled nanotubes (MWNT) and CuO, Cu₂O, Cu, ZnO, MnO₂, Co₃O₄, NiO, Fe_xO_y metal oxide nanoparticles. In particular, Xiuying Wang et al. [26] studied controlled modification of the structure and morphology of Cu/CNT nanocomposites by modification of MWNT with CuO, Cu₂O and Cu nanoparticles and changing in synthesis process (the amount of precursor, soaking time and calcination temperature). Encapsulation of CuO and ZnO nanoparticles into internal diameter CNT leads to the reducing of active surface area of particles due to interaction between each one of them and walls of CNT [27].

Composites based on Fe₂O₃-out-CNT have amorphed carbon outside the tube, at the same time Fe₂O₃-in-CNT do not have the one [28]. In the synthesis of a number of nanocomposites based on transition metal oxides and CNT, it was established that the metal oxides dispersed on a surface of functionalized CNT. The combination of metal oxide nanoparticles and CNT into the one composite makes it possible to control the morphology of functionalized CNT and the area of surface of the nanocomposite [29]. Thus, the metal oxide nanoparticles in matrixes of carbon nanotubes and silicon oxides may play a role of the active adsorption centers.

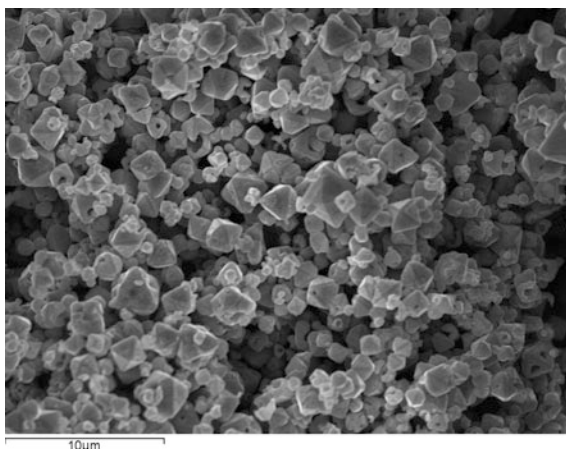
We investigated the surface morphology, oxidation state, local and electronic structure of CuO_x, SnO_x nanocomposites based on carbon nanotubes and silicon oxides by means of SEM, XANES and XPS technique. The samples were synthesized by electrochemical deposition and sol-gel techniques with different parameters.

21.2 $\text{CuO}_x/\text{SnO}_x$ Nanocomposites and Thin Films

The morphology, structure and size of nanomaterials as it is known to correlate with a method of preparation. Here, we present results of our investigation of correlation between morphology, structure, oxide states of CuO_x , SnO_x nanoparticles and synthesis techniques with various parameters. The formation of one or other crystalline phase of copper depends on the method and technological features of the synthesis. In [8, 9], it was reported study of the synthesis of copper(I) and copper (II) oxide nanoparticles with different structural and physical characteristics due to stoichiometric deviations associated with technological parameters of the synthesis [30]. There are several methods for the preparation of CuO_x and SnO_x rich nanocomposites and based on them thin films, such as hydrothermal method [31], chemical reduction of copper salts with selected reducing agent [30], sonochemical synthesis [32], seed mediated synthesis [33], chemical vapor deposition method [34], electrochemical deposition [35], atomic layer deposition [36], sol-gel technique [37]. We study changes in morphology and structure of copper-based nanocomposites and thin films, based on them, synthesized by electrochemical deposition and sol-gel technique. Recently, there have been great efforts in controlled synthesis of copper oxides nano-crystals since shape, as it is known to be an important factor in determining the structural, physical, and chemical properties of nanoparticles. It has turned out that copper oxides are promising for use in the fabrication of gas-sensitive and catalytically active materials, because they possess a chemical resistance and provide the stability of the gas-sensitive and electro-physical characteristics over time in a wide range of operating temperatures [38, 39]. It is known that copper oxides can exist in two *p*-type semiconducting phases: copper oxide (CuO) with a monoclinic crystal structure and copper oxide (Cu_2O) with a cubic crystal structure. It has been previously found that Cu_2O octahedra shows better photocatalytic activity than cubes, because the {111} facets are more active than {100} facets due to the dangling bonds of {111} surfaces, while {100} facets have saturated chemical bonds and no dangling bonds exist [40]. The octahedral Cu_2O nanoparticles were synthesized by a simple electrochemical route for the controlled synthesis of a CuO_x ($0 < x < 1$) micro/nanocrystals from hollow to monodisperse core-shell $\text{Cu}_2\text{O}@\text{CuO}$ spheres via control of the current density [41]. We examined the morphology of synthesized samples by electron microscopy. As one can see (Fig. 21.1), the shape of the CuO_x particles is octahedral enclosed by the lowest energy {111} facets with an average edge length of 700–1200 nm.

The local atomic structure around Cu in the synthesized sample was characterized with XANES spectroscopy, which contains stereo-chemical information [42]. The copper K-edge X-ray absorption spectra were recorded at the Dutch-Belgian beamline (DUBBLE, 26A) of the European Synchrotron Radiation Facility (ESRF, Grenoble, France) in transmission mode using double crystal Si (111) monochromator. The XANES spectra of nanoparticles CuO_x and reference compounds in the energy range from 8970 to 9035 eV are shown in Fig. 21.2. The

Fig. 21.1 SEM images of the synthesized sample prepared by the electrochemical route



intensity of main spectrum peak between 8991 and 8997 eV for copper (I) oxide and Cu-foil as well as between 8995 and 8999 eV for copper (II) is known as a “white line”. The changes in the white line intensity relate to empty *d*-states indicating the changes in the oxidation state of the copper. Reduced white line intensity indicates a lower oxidation state because of a decrease in the density of empty *d*-states [43]. Besides, the exact energy position of the Cu K-edge XANES depends on the oxidation number of the target element Cu. Comparison of the normalized XANES spectra of synthesized nanocrystals with spectra of the standard compounds shows that all spectral features (A, B, C) are closer to those of Cu_2O , rather than those of Cu metal and CuO (Fig. 21.2). We can conclude, that spectrum of the CuO_x sample is most similar to Cu_2O spectrum, reflecting presence practically pure Cu_2O .

As we noted, influence of kind of matrix in direction of the nano-unit nucleation and subsequent organization of metal oxide nanoparticles is observed. We studied changes in the morphology, structure and oxidation state of nanoparticles in the nanocomposites based on CNT. Synthesis of the nanocomposite was the same to pure nanoparticles by the identical electrochemical deposition method as described above.

Scanning electron microscopy was used to study the microstructure of the surface morphology, size and shape of particles in the nanocomposite CuO_x/CNT . An image obtained by the SEM microscope LEO 1560 VP ZEISS firms. Figure 21.3 reveals flake-like copper nanoparticles with the size about 500 nm. One can see the nanoparticles attached to the outer surface of the nanotube. We used XANES spectroscopy to determine the oxidation state of copper in nanocomposite CuO_x/CNT . The copper K-edge X-ray absorption spectra were recorded in fluorescence mode at 300 K at the KMC-2 beam-line at BESSY II (Berlin, Germany).

Changes in the electronic and the local structure of the absorbing atom leads to changes in the XANES spectrum. In Fig. 21.4 the Cu K-edge XANES spectra of pure nanoparticles CuO_x and nanocomposite CuO_x/CNT in the energy range from

Fig. 21.2 Normalized copper K-edge XANES spectra of CuO_x nanoparticles in comparison with standard compounds (Cu metal foil, CuO, Cu_2O)

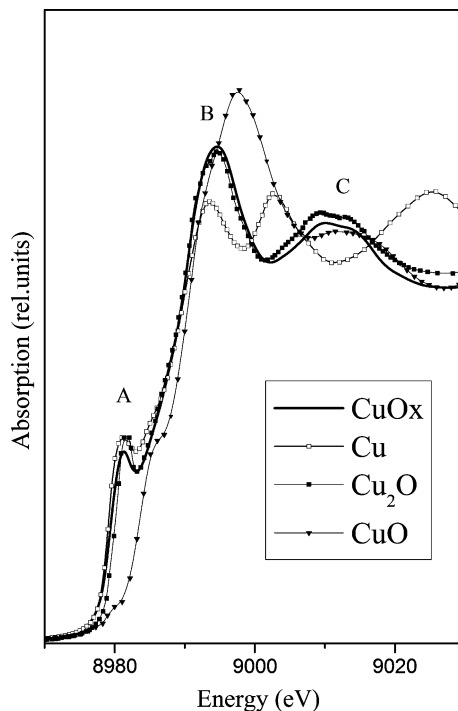
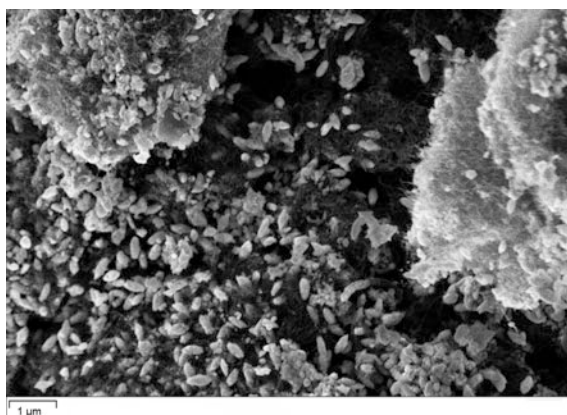


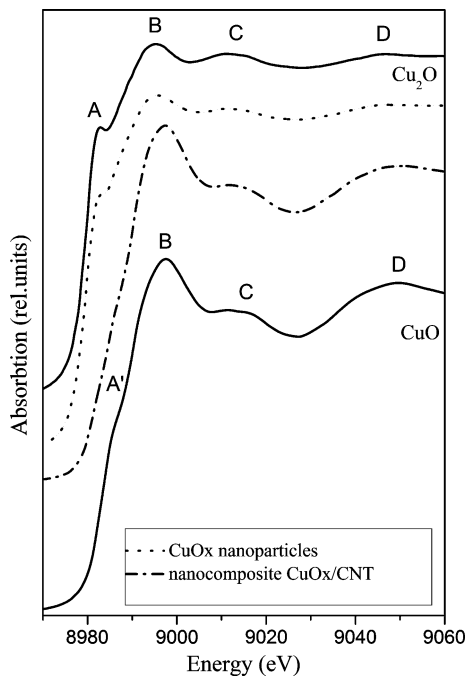
Fig. 21.3 SEM images of CuO_x/CNT nanocomposite prepared by the electrochemical deposition under the current densities 0.5 A cm^{-2}



8970 to 9060 eV are shown. Bulk CuO and Cu_2O were used as the reference compounds.

The XANES spectra were obtained by subtracting a smooth background from the XAS after selecting energy points in the pre-edge and main edge region of the XAS. The formation of A, A' peaks in XANES spectra just behind the absorption edge is a result of the transitions of 1 s electrons to the band of free states $4p\pi$, at the

Fig. 21.4 XANES spectra Cu K-edge of CuO_x nanoparticles and nanocomposite CuO_x/CNT compared with reference (CuO and Cu_2O)



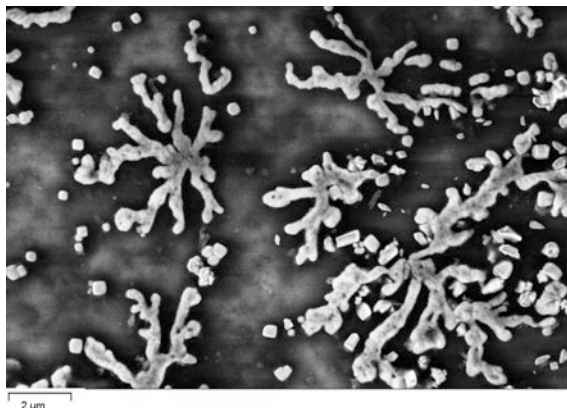
same time the B peak could be explained as a result of the transitions of 1 s electrons to $4p\sigma$ band [44, 45]. Both determination of the energy position of the absorption edge and comparing the spectra with reference samples indicate that the local and electronic structure of copper nanoparticles and nanocomposite based them is different. Increasing the oxidation state of the copper occurs during the transition from nanoparticle to nanocomposite. This process increases adsorption properties of the same nanocomposite. The spectra of nanoparticles and of nanocomposite have a less intense peaks A and A', indicating a lower $4p\pi$ density of states in comparison with CuO crystal structure [46]. This slight smearing features XANES spectrum is a characteristic of nanostructured materials [47].

Our next task was to study morphology, local atomic and electronic structure of the thin films, synthesized with sol-gel method based on copper oxide and copper oxide in the silicon matrix. All details of the synthesis are published in [48]. The films samples with total thickness equal $4.3 \mu\text{m}$ including silicon substrate with thickness of order $3 \mu\text{m}$, SiO sublayer with thickness equal $1 \mu\text{m}$ and Cu layer of order $0.3 \mu\text{m}$ were investigated.

SEM micrographs reveal the formation of copper based structures on the film surface with different shapes and sizes (see Fig. 21.5). It seems appropriate to consider that the particles, which appear in SEM images are, in fact, grain agglomerates with fractal structure of the random nature.

The copper K-edge X-ray absorption spectra were recorded at the KMC-2 beam-line in fluorescence mode at 300 K at BESSY II (Berlin, Germany). In order

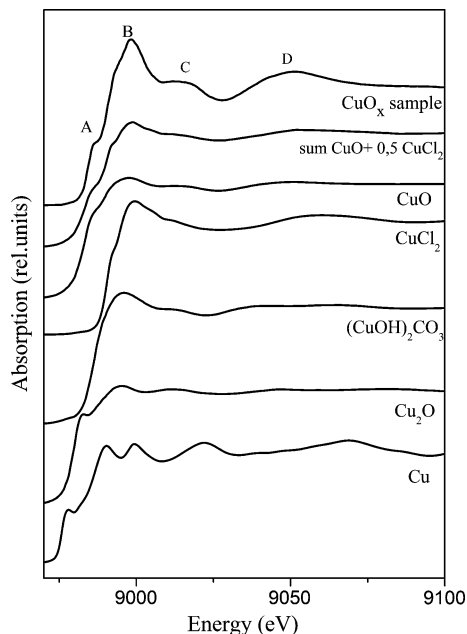
Fig. 21.5 SEM images of CuO_x films annealed at 500°C



to determine oxidation state and local structure copper oxide nanoparticles, Fig. 21.6 presents the Cu K-edge XANES spectra for the CuO_x thin films. The spectra of reference samples, viz. Cu foil, CuO, Cu_2O , CuCl_2 and $\text{Cu}(\text{OH})_2\text{CO}_3$, are also present for comparison. From comparison of the spectra sample under investigation and measured reference compounds, it is perfectly clear formation of CuO oxide. However, the origin of the high-energy shoulder A is not so understandable. Therefore, the XANES signal from a thin film can be considered resulting from a linear combination of signals from Cu atoms with neighborhood similar to that found in CuO and CuCl_2 . The results of fitting the model spectra to the experimental spectra in the near-edge region are shown in Fig. 21.6 along with the obtained best fit values, which describe the contribution due to the various Cu phases. The fit is not always satisfactory (especially in the range around 9040 eV). This may be due to the fact that the electronic and geometric structures of thin films prepared by sol-gel method are more complex than the results of a simple combination of two phases. Many types of oxide phases must be taken into account in order to precisely reconstruct the Cu electronic structure. However, the values presented in Fig. 21.6 can be used as a good first estimate of the contribution from a Cu-like local neighborhood.

Then we examined the effect of the matrix of silicon dioxide on the morphology and structure of the copper oxide active gas-adsorption centers, also synthesized with sol-gel method. We investigated the structural characteristics of a gas sensitive layer in SiO_2CuO_x thin films for different copper concentrations in the initial solution. The purpose of this study was an investigation of the relationship between the surface morphology and structure of SiO_2CuO_x nanocomposite films synthesized by the sol-gel method under different conditions. The SiO_2CuO_x films were prepared according to the original technology based on the sol-gel method. This technology allow the synthesis of films that were sensitive to molecules of ammonia (NH_3) and nitrogen dioxide (NO_2) [49]. A series of samples were synthesized by varying the concentration of copper nitrate in the initial solution (1, 3, 5 and 7 wt%), calculated in terms of metal.

Fig. 21.6 Comparison Cu K-edge XANES spectra of CuO_x thin films with reference samples



The surface morphology of the films was examined using scanning electron microscopy (SEM) on a LEO 1560 microscope. The SEM investigations have demonstrated that the copper concentration in the initial solution significantly affects the character of the distribution of copper oxide crystallites over the surface of the films. At the copper concentration of 1 wt% (Fig. 21.7a), there is a uniform distribution of copper oxides over the all surface of the sample. As the copper concentration increases, the surface of the films covers by crater-like pores of different diameters, located in the amorphous silicon dioxide matrix. Note that the formation of copper crystallites occurs in these pores. Thus, for sample prepared from the solution containing 7 wt% Cu the formation of copper oxide crystallites is observed only in large pores with a diameter of more than 30 μm . The size of copper oxide crystallites in all the studied samples lie in the range from 100 to 500 nm. Information about other concentrations is published in the paper [50].

We used the X-ray absorption spectroscopy and X-ray photoelectron spectroscopy to answer the question: which copper compounds form in the surface layers of thin film nanocomposites. The experimental Cu $L_{2,3}$ XANES spectra and X-ray photoelectron spectra of the SiO_2CuO_x films with copper concentrations of 1, 3, 5, 7 wt% in the initial solution were measured by the RGBL station at BESSY II (HZB, Berlin, Germany). Figure 21.8 shows the Cu $L_{2,3}$ XANES spectra of thin film nanocomposites deposited from the solutions containing 1, 3 and 7 wt% Cu in comparison with the spectra of reference compounds CuO and Cu_2O .

The $L_{2,3}$ XANES spectrum reflects the distribution of s - and p - local partial density of states. The Cu $L_{2,3}$ XANES spectrum consists of two absorption edges

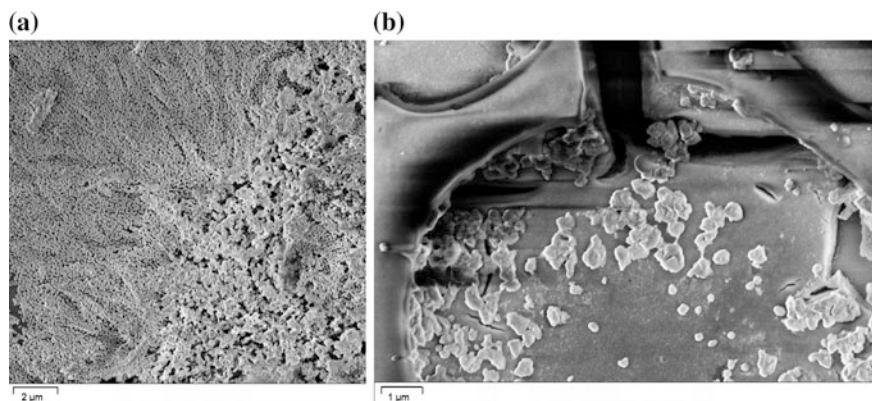
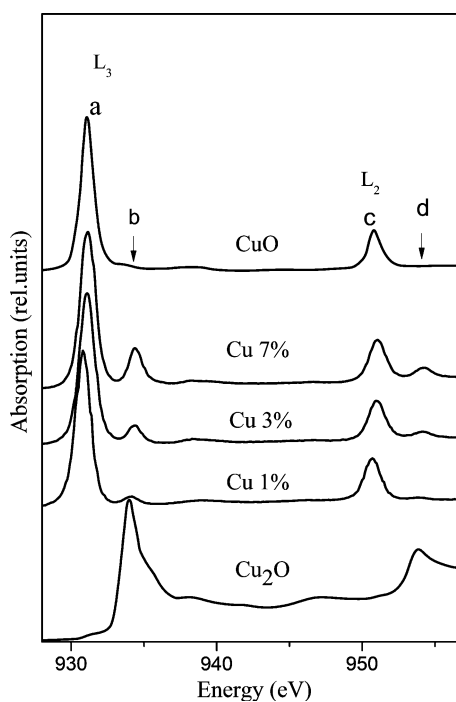


Fig. 21.7 SEM images of the surfaces of the films with copper concentrations of 1 wt% (a) and 7 wt% (b)

Fig. 21.8 Cu $L_{2,3}$ -edge XANES spectra of the SiO_2CuO_x nanocomposite films with copper concentrations of 1, 3 and 7 wt% in comparison with the spectra of the reference samples CuO and Cu_2O



(L_3 and L_2) separated by the spin-orbit splitting of the core Cu $2p$ state into the $2p_{3/2}$ and $2p_{1/2}$ states. Figure 21.8 shows the spectra of Cu $L_{2,3}$ XANES nanocomposite thin films consisting of two L_3 and L_2 edges, separated on energy (about 20 eV) of spin-orbit interaction. The Cu L_3 and Cu L_2 absorption edges of the thin film

nanocomposites demonstrate fine structure with details a, b in the case of L_3 and c, d in the case of L_2 edges. In [51], Tanaka et al. showed that the concentration ratio of monovalent and divalent copper ions in the sample can be estimated from the ratio of the intensities of peaks a and b in the spectrum. We carried out analysis of the intensity ratio of the peaks a and b in the spectra. All details of this procedure are published in our previous paper [50]. The analysis allows us to conclude that, in all nanocomposite films under investigation, the copper atoms form mainly divalent copper oxide. An increase in the copper concentration leads to a systematic increase in the intensity of resonance peaks b and d, whose energy positions correspond to the L_3 and L_2 absorption edges of monovalent copper oxide Cu_2O . This indicates an increase in the content of Cu_2O in the films. A comparison of the results obtained from the scanning electron microscopy and X-ray absorption spectroscopy investigation suggests that an increase in the concentration of monovalent copper in the composite affects the formation of pores on the surface of the films.

The chemical state of copper on the surface of films was investigated by analyzing the X-ray photoelectron spectra. Figure 21.9 shows the analytical lines of the Cu $2p$ level for the SiO_2CuO_x thin films synthesized from the solutions containing 1, 3 and 7 wt% Cu in comparison with the spectra of the reference samples Cu metal foil, Cu_2O and CuO .

Fig. 21.9 Cu $2p$ XPS of the thin films SiO_2CuO_x nanocomposite materials with copper concentrations of 1, 3 and 7 wt% in comparison with the spectra of the reference samples of Cu metal foil, Cu_2O and CuO

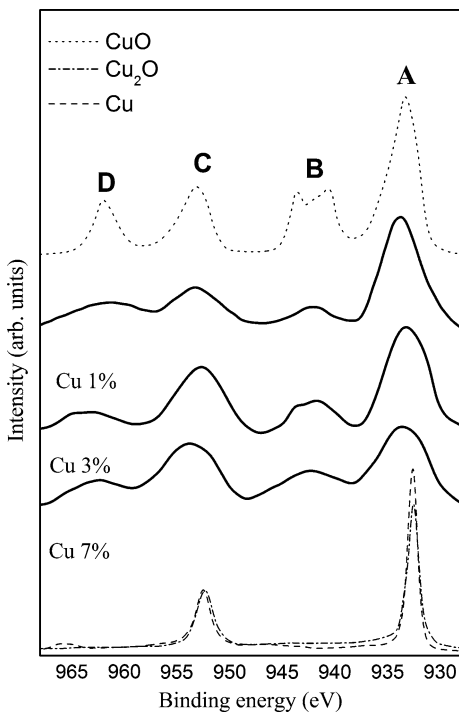


Figure 21.9 demonstrates the Cu 2*p* X-ray photoelectron spectra of all the studied samples. They have a spin-doublet character, i.e. in these spectra, there is a 2*p*-splitting into features A and C. Taking into account the energy position of the main lines (933.4–933.9 eV for the Cu 2*p*_{3/2} states), the shape and energy position of the satellite structures (942.1–942.6 eV), it can be concluded that all the studied samples have a predominant content of divalent copper, which is consistent with the XANES data. However, the low intensity of peak B and the lack of its clear splitting in the spectra of the nanocomposites, in contrast to the spectrum of copper oxide CuO, indicate that surface layers of the films contain different compounds of divalent copper oxide. Moreover, the broadening of all spectral features in the spectra of the samples under study, as compared with those observed in the spectrum of the reference compound CuO, associates with changes in the chemical state of copper atoms. The energy position and shape of features A and C as well as the presence of satellite lines in the spectrum of the sample prepared from the solution containing 1 wt% Cu indicate the presence of divalent copper oxides on the surface of the film. However, the low intensity of peak B and the lack of its clear splitting, indicates that on the surface of the film, there are divalent copper oxides other than CuO [52]. We can assume the formation of divalent copper oxides Cu(OH)₂ and CuSiO₃, which is in agreement with the results of the SEM investigations. According to them, the film has a smooth surface with small copper crystallites, which embedded in the silicon dioxide matrix. As the copper concentration increases to 3 wt%, there appear signs of the splitting of satellite B and its shape is more consistent with the shape of the spectrum of CuO. At the same time, the spectra of both samples are characterized by a small shift in the binding energy of the main peaks A and C and contain broad peaks with shoulders in the low-energy region, which indicate the presence of several oxide states in the studied samples [53]. In the spectra of the studied samples, the spin-doublet splitting between peaks A and C is equal to ~20 eV, and the splitting between peaks A, B and C, D is ~9 eV. These values can indicate the presence of the CuO (Cu²⁺) phase with a low content of monovalent copper oxide Cu₂O (Cu¹⁺) [54]. From the SEM results, it follows that these concentrations are characterized by the formation of a large amount of pores on the surface of the sample with the simultaneous formation of copper crystallites therein. On the other hand, the analysis of the XANES spectra revealed an increase in the content of the Cu₂O phase along with the main crystalline phase CuO. The XPS spectra are consistent with the SEM and XANES data for the samples with copper concentrations of 3 %. This suggests that the main content of copper is concentrated in crystallites formed in the pores, because the content of divalent copper compounds Cu(OH)₂ and CuSiO₃ is less than that for the samples with 1 wt% Cu (peak B). The composition of the crystallites includes divalent copper oxide CuO with a small admixture of Cu₂O (low energy shoulders on the main lines of the spectra). An increase in the copper concentration to 7 wt% leads to the “erosion” of the surface by the chemically unstable oxide Cu₂O and to the formation of a small amount of larger sized pores with a minor amount of copper crystallites. The disappearance of the splitting of peak B and the broadening of all features in the X-ray photoelectron spectra indicate an increase in the content

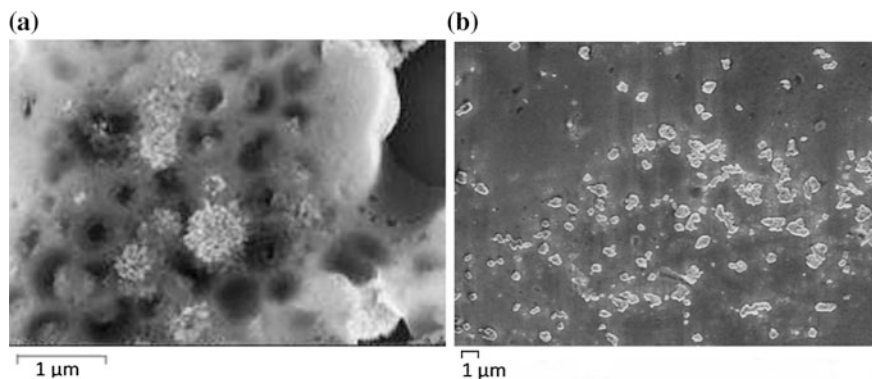


Fig. 21.10 SEM images of the surface morphology of the SiO_2CuO_x (a) and $\text{SiO}_2\text{CuO}_x\text{SnO}_y$ (b) thin films

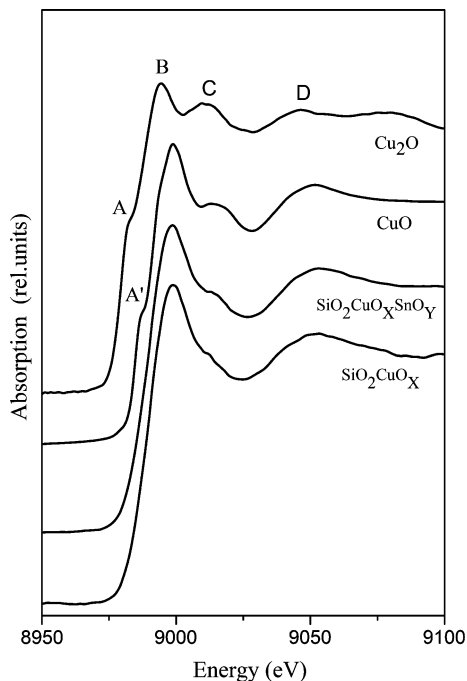
of divalent copper oxide compounds ($\text{Cu}(\text{OH})_2$, CuSiO_3) and Cu_2O on the surface of the sample as compared to the samples with 3 wt% Cu.

In the next stage of our research, we studied the effect of adding Sn precursor to the initial sol-gel solution on the morphology and structure of the active centers of SiO_2CuO_x nanocomposite. Description of the preparation of sol for fabrication of the SiO_2CuO_x thin film with 5 % copper content is given in [49]. Sol of the Cu/Sn precursor was obtained by the adding of SnCl_4 in an amount of 3 wt% of Sn to previous copper-rich solution.

Surface morphological study of the deposited film samples was carried out using a scanning electron microscopy (microscope LEO 1560, ZEISS). Figure 21.10 shows some examples of SEM photomicrographs. The formations of the copper oxide agglomerates are observed on the surface of the silica matrix (Fig. 21.10a). The agglomerates have spherical shape flower-like structure with diameter in the range of 0.7–1 μm . The films deposited from $\text{SiO}_2\text{CuO}_x\text{SnO}_y$ sol reveal well-separated grains with different sizes and grain boundaries. The grain size is found to be in the range of 150 to 500 nm. A large number of well-defined grains with good crystalline nature are observed as shown in Fig. 21.10b. Formed crystallites mainly accumulated inside of the pores as compared to the SiO_2CuO_x films.

In order to determine oxidation states and local surrounding of Cu ions for both SiO_2CuO_x and $\text{SiO}_2\text{CuO}_x\text{SnO}_y$ thin films, XANES spectroscopy has been applied at the Cu K-edge. The experimental spectra were recorded at the KMC-2 beamline in fluorescence mode at BESSY II (Berlin, Germany). Figure 21.11 compares the Cu K-edge XANES spectra of SiO_2CuO_x and $\text{SiO}_2\text{CuO}_x\text{SnO}_y$ to those of reference compounds, namely single crystalline CuO (formally Cu^{2+}) and Cu_2O (formally Cu^+). This comparison reveals that the most of the Cu ions are divalent as indicated by the edge energy position and shape of spectrum of both thin films under study. At the same time, there are some differences in the shape of spectra of the test and reference samples. First of all, there is a lack of typical for CuO (peak A') and Cu_2O (peak A) spectra low-energy shoulder in the spectra of both films. It is a sign of the

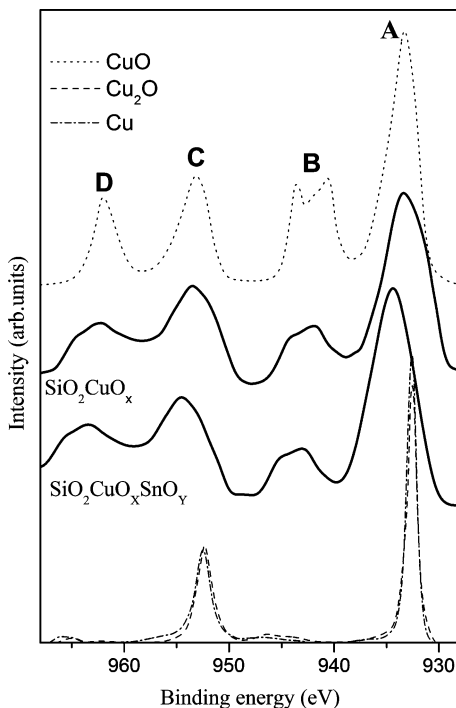
Fig. 21.11 Cu K-edge XANES spectra of SiO_2CuO_x and $\text{SiO}_2\text{CuO}_x\text{SnO}_y$ thin films compared with a reference compounds Cu_2O and CuO



presence of the some additional phases of copper. Based on the results obtained for SiO_2CuO_x with 1, 3, 7 wt% copper content, the most probable is the presence of CuSiO_3 and $\text{Cu}(\text{OH})_2$. From the other hand, difference between SiO_2CuO_x and $\text{SiO}_2\text{CuO}_x\text{SnO}_y$ spectra is observed. Peak C is less intense in SiO_2CuO_x than in $\text{SiO}_2\text{CuO}_x\text{SnO}_y$. This indicates that a difference in the local environment of copper for both films is present.

In order to investigate the chemical species formed as result of addition of the Sn to copper containing solution, XPS profiles were obtained by scanning the Cu $2p$ regions. The results are depicted in Fig. 21.12. The interpretation of the spectra was made in the same way with described above for SiO_2CuO_x with 1, 3, 7 wt% concentration. In accordance with referenced data, the observation of obvious shake-up satellites (peaks B, D) can be attributed to the Cu^{2+} oxidation state in both samples before and after the Sn addition [54–56]. The maximal peak energy corresponds to the CuO , but the broader $2p_{3/2}$ (A) and $\text{Cu } 2p_{1/2}$ (C) peaks, absence of clear peak B splitting (in comparison with the spectrum of CuO) indicates an availability of the mixed oxidation Cu state [53, 57]. Therefore, in the analyzed films the presence of copper in Cu^{2+} and Cu^+ state is quite possible, namely: divalent copper oxides CuO , with a mixture of divalent double oxide CuSiO_3 , monovalent oxide Cu_2O and hydroxide $\text{Cu}(\text{OH})_2$ [58, 59]. The Cu $2p$ peak for $\text{SiO}_2\text{CuO}_x\text{SnO}_y$ shifts by 0.7 eV towards higher energy from its value for SiO_2CuO_x and CuO . After the addition of tin to the sample, the concentration of Cu^+ ions decreases, that is consistent with XANES investigations.

Fig. 21.12 Cu 2*p* XPS spectra of the SiO₂CuO_x and SiO₂CuO_xSnO_y thin films



21.3 Conclusions

We studied the morphology and structure CuO_x and CuO_x/SnO_x nanocomposites and thin films based on them, synthesized by sol-gel and electrochemical deposition methods. Carbon nanotubes and silicon dioxide were used as a base for inorganic component matrixes.

Here, we give some examples when the shape of copper oxide crystallites varies and depends on parameters of the synthesis and matrix type. Thus, octahedral Cu₂O nanoparticles with size about 5 μm were synthesized by a electrochemical methods. The formation of CuO_x/CNT nanocomposite leads to creation of flake-like copper nanoparticles with the size about 500 nm, attached to the outer surface of the nanotube. Both the energy position of the absorption edges and comparing the spectra with reference samples indicate that the local and electronic structure of copper nanoparticles and nanocomposite is different. Increasing the oxidation state of the copper occurs during the transition from nanoparticle to nanocomposite.

In case of thin films, synthesized by sol-gel technique, an increase in the copper concentrations results in the formation of crater-like pores of different diameters, which, in turn, leads to the formation of local crystallization centers of copper oxides. All studied samples predominantly contain copper in the form of divalent

copper oxide (CuO). However, an increase in the copper concentration leads to a systematic increase in the content of the Cu₂O phase, which affects the character of the formation of pores and the distribution of copper crystallites on the surface of the films. The addition of SnCl₄ precursor in copper-bearing sol affects on surface morphology and size of nanoparticles in SiO₂CuO_x and SiO₂CuO_xSnO_y thin films. Transformation of flower-like copper oxide agglomerates to regular shaped copper/tin grains with smaller size is observed. The tin adding prevents the formation and growth of the flower-like nanoparticles. After the addition of tin to the sample, the concentration of Cu⁺ ions decreases.

Acknowledgments The research leading to these results received funding from the Ministry of Education and Science of the Russian Federation under grant agreement No 11.2432.2014/K. We thank HZB (Berlin, Germany) for the allocation of synchrotron radiation beam-time (RGLB at BESSY II) and the Institute for Nanometre Optics and Technology (HZB) for the provided opportunity of SEM measurements. We thank ESRF (Grenoble, France) for the allocation of synchrotron radiation beam-time (Dutch-Belgian Beam Lines, DUBBLE 26A). The DUBBLE staffs are acknowledged for technical support. We would like to thank N.V. Smirnova and T.N. Myasoedova for provided samples and I.N. Leontyev for the provided SEM measurement of CuO_x nanoparticles.

References

1. D. Barreca, E. Comini, A. Gasparotto, C. Maccato, C. Sada, G. Sberveglieri, E. Tondello, *Sens. Actuators B: Chem.* **141**, 270 (2009)
2. N.D. Hoa, S.Y. An, N.Q. Dung, N. Van Quy, D. Kim, *Sens. Actuators B: Chem.* **146**, 239 (2010)
3. M. Yang, J. He, *J. Colloid Interface Sci.* **368**, 41 (2012)
4. M. Yang, J. He, *J. Colloid Interface Sci.* **144**, 229 (2012)
5. S. Singh, B.C. Yadava, R. Prakash, B. Bajaj, J. Rocklee, *Appl. Surf. Sci.* **257**, 10763 (2011)
6. Y. Hames, S. San Eren, *Sol. Energy* **77**, 291 (2004)
7. H. Yang, J. Ouyang, A. Tang, Y. Xiao, X. Li, X. Dong, Y. Yu, *Mater. Res. Bull.* **41**(7), 1310 (2006)
8. J. Wang, L. Li, D. Xiong, R. Wang, D. Zhao, C. Min, Y. Yu, L. Ma, *Nanotechnology* **18**, 075705 (2007)
9. Z.Q. Yu, C.M. Wang, M.H. Engelhard, P. Nachimuthu, D.E. Mc Cready, I.V. Lyubinetsky, S. Thevuthasan, *Nanotechnology* **18**, 115601 (2007)
10. O. Akhavan, H. Tohidi, A.Z. Moshfegh, *Thin Solid Films* **517**, 6700 (2009)
11. K.E. Drexler, *Nanosystems: Molecular Machinery, Manufacturing, and Computation* (Wiley, New York, 1992)
12. L. Armelao, D. Barreca, G. Bottaro, A. Gasparotto, S. Gross, C. Maragno, E. Tondello, *Coord. Chem. Rev.* **250**, 1294 (2006)
13. A. Sakly, J. Costa, B. Trindade, J.V. Fernandes, T. Benameur, *J. Alloy. Compd.* **502**, 480 (2010)
14. Y. Zhao, Y. Liang, X. Zhao, Q. Jia, L. Hs, *Progr. Nat. Sci.: Mater. Int.* **21**(4), 330 (2011)
15. M.C. López, L. Pedro, G.F. Ortiz, L. José, *Electrochem. Commun.* **27**, 152 (2013)
16. J.W. Fergus, *Sens. Actuators B: Chem.* **121**, 652 (2007)
17. S. Zhuiyikova, D. Marneyb, E. Katsa, K. Kalantar-Zadehc, *Sens. Actuators B: Chem.* **153**, 312 (2011)
18. G. Korotcenkova, B.K. Cho, *Sens. Actuators B: Chem.* **156**, 527 (2011)

19. G. Korotcenkova, B.K. Cho, *Sens. Actuators B: Chem.* **161**, 28 (2012)
20. B. Liu, H.C. Zeng, *J. Am. Chem. Soc.* **126**, 8124 (2004)
21. X.M. Lin, A.C.S. Samia, *J. Magn. Magn. Mater.* **305**, 100 (2006)
22. G. Korotcenkov, *Sens. Actuators B: Chem.* **107**, 209 (2005)
23. A.A. Eliseev, K.S. Napolskii, A.V. Lukashin, Y.D. Tretyakov, *J. Magn. Magn. Mater.* **1609**, 227 (2004)
24. R. Wanbayor, V. Ruangpornvisuti, *Mater. Chem. Phys.* **124**, 720 (2010)
25. T. Fu, *Mater. Chem. Phys.* **140**, 116 (2009)
26. X. Wang, F. Zhang, B. Xia, X. Zhu, J. Chen, S. Qiu, P. Zhang, J. Li, *Solid State Sci.* **11**, 655 (2009)
27. D. Großmanna, A. Dreierb, C.W. Lehmannb, W. Grünert, *Microporous Mesoporous Mater.* **202**, 189 (2015)
28. Y. Nie, L. Bai, J. Gao, J. Liu, G. Zhao, T. Xie, X.-H. Sun, J. Zhong, *Appl. Surf. Sci.* **273**, 386 (2013)
29. N.I. Media, S.A. Andersen, A. Plamen, *Appl. Catal. B: Environ.* **163**, 623 (2015)
30. B. Li, Y. Li, Y. Zhao, L. Sun, *J. Phys. Chem. Solids* **74**, 1842 (2013)
31. C.H. Wang, Y.X. Ye, B. Tao, B.Y. Geng, *CrystEngComm* **14**, 3677 (2012)
32. X. L. P. Li, J. Zhu, *Nanotechnology* **20**, 045605 (2009)
33. C.-H. Kuo, C.-H. Chen, M.H. Huang, *Adv. Funct. Mater.* **17**, 3773 (2007)
34. P.R. Markworth, X. Liu, J.Y. Dai, W. Fan, T.J. Marks, R.P.H. Chang, *Mater. Res. Bull.* **8**, 16 (2001)
35. V. Dhanasekaran, T. Mahalingam, R. Chandramohan, J.K. Rhee, J.P. Chu, *Thin Solid Films* **520**, 6608 (2012)
36. A.P. Alekhin, S.A. Gudkova, A.M. Markeev, A.S. Mitiaev, A.A. Sigarev, V.F. Toknova, *Appl. Surf. Sci.* **257**, 186 (2010)
37. E.V. Skorb, A.G. Skirtach, D.V. Sviridov, D.G. Shchukin, H. Műhlwad, *ACS Nano* **3**, 1753 (2009)
38. W. Fergus, *Sens. Actuators B: Chem.* **134**, 1034 (2008)
39. T. Hubert, L. Boon_Brett, G. Black, U. Banach, *Sens. Actuators, B* **157**, 329 (2011)
40. J.Y. Ho, M.H.J. Huang, *Phys. Chem.* **10**, 21 (2009)
41. D.V. Leontyeva, I.N. Leontyev, M.V. Avramenko, Y. Yuzyuk, Y. Kukushkina, N.V. Smirnova, *Electrochim. Acta* **114**, 356 (2013)
42. G. Bunker, *Introduction to XAFS: A Practical Guide to X-ray Absorption Fine Structure Spectroscopy* (Cambridge University Press, New York, 2010)
43. W.C.M. Gomes, A.de O.W. Neto, P.M. Pimentel, D.M.de A. Melo, F.R. Gonçalves, *Colloids Surf., A* **426**, 18 (2013)
44. R.P. Wijesundera, M. Hidaka, K. Koga, J.-Y. Choi, N. Eeon, *Ceramics-Silikáty* **54**(1), 19 (2010)
45. A. Gaur, B.D. Shrivastava, *Acta Phys. Pol.* **3**, 647 (2012)
46. G. Silversmita, H. Poelmana, V. Balcaenb, P.M. Heynderickxb, M. Oleab, S. Nikitenkoc, W. Brasc, P.F. Smeta, D. Poelmana, R. De Grysea, M.-F. Reniersb, G.B. Marinb, *J. Phys. Chem. Solids* **9**, 1274 (2009)
47. M. Fröba, R. Köhn, G. Bouffaud, O. Richard, G. Tendeloo, *Chem. Mater.* **11**, 2858 (1999)
48. T.N. Myasoedova, G.E. Yalovega, N.K. Plugotorenko, M. Brzhezinskaya, V.V. Petrov, T.A. Moiseeva, V.A. Shmatko, *Appl. Mech. Mater.* **481**, 133 (2014)
49. N.K. Plugotarenko, A.N. Korolev, V.V. Petrov, T.N. Nazarova, *Inorg. Mater.* **43**, 1010 (2007)
50. V.A. Shmatko, G.E. Yalovega, T.N. Myasoedova, M.M. Brzhezinskaya, I.E. Shtekhin, V.V. Petrov, *Phys. Solid State*, **2**, 399 (2015) (in Russian)
51. Y. Tanaka, M. Karppinen, J.M. Lee, R.S. Liu, J.M. Chen, H. Yamauchia, *Solid State Commun.* **147**, 370 (2008)
52. C.D. Wanger, W.M. Riggs, L.E. Davis, J.F. Moulder, G.E. Muilenberg, *Handbook of X-Ray Photoelectron Spectroscopy* (Perkin-Elmer, Physical Electronics Division, Waltham, 1979)
53. R.J. Park, K. Lim, R.D. Ramsier, Y.-C. Kang, *Bull. Korean Chem. Soc.* **32**, 3395 (2011)
54. S.S. Chang, H.J. Lee, H.J. Park, *Ceram. Int.* **31**(3), 411 (2005)

55. J. Morales, A. Caballero, J.P. Holgado, J.P. Espinós, A.R. González-Elipe, *J. Phys. Chem. B* **106**, 10185 (2002)
56. J. Chastain, R.C. King, *Handbook of X-Ray Photoelectron Spectroscopy, Physical Electronics* (Eden Prairie, 1995)
57. T. Ghodselahi, M.A. Vesaghi, A. Shafiekhani, A. Baghizadeh, M. Lameii, *Appl. Surf. Sci.* **255**, 2730 (2008)
58. C.D. Wagner, A.V. Naumkin, A. Kraut-Vass, J.W. Allison, C.J. Powell, J.R. Rumble (Jr.), *NIST X-Ray Photoelectron Spectroscopy Database*, <http://srdata.nist.gov/xps/Default.aspx>
59. N.S. McIntyre, S. Sunder, D.W. Shoesmith, F.W. Stanchell, *J. Vac. Sci. Technol.* **18**, 714 (1981)

Chapter 22

Dispersion Characteristics of Zinc Oxide Nanorods Coated with Thin Silver Layer and Organized in Two-Dimensional Uniform Arrays

A.M. Lerer, P.E. Timoshenko, E.M. Kaidashev, A.S. Puzanov
and T.Y. Chernikova

Abstract The problem on electromagnetic waves propagation in a two-dimensional periodic array of zinc oxide nano-waveguides covered with a thin metal film is solved by the method of variables separation in cylindrical coordinates. The numerical results obtained by the method are in good agreement with the results computed by the commercial software COMSOL MultiphysicsTM over all optical range and have minor deviations for the wavelength range close to the critical wavelength. Resonances located at the amplitude-frequency characteristics of optical nano-antennas may be interpreted as resonances of circular bilayer nano-wave-guide segments with the ZnO core covered with thin metal shell. The results may also be used to predict the resonance wavelength of two-dimensional periodic arrays of ZnO nanorods, coated with a thin metal layer and grown on a dielectric substrate.

22.1 Introduction

The new design of optical antennas based on the ZnO nanorods coated with a thin metal film is discussed in the paper [1]. The diffraction of electromagnetic waves by a single metal-dielectric nano-oscillator and array of nano-oscillators, placed at the interface between dielectric layers, has been studied. The dependencies of electrodynamic characteristics of optical antennas on the geometrical parameters have been compared with the experimental data. Resonances, located at the amplitude-frequency characteristics of optical nano-antennas, may be interpreted as

A.M. Lerer (✉) · P.E. Timoshenko · A.S. Puzanov · T.Y. Chernikova
Department of Physics, Southern Federal University, Rostov-on-Don, Russia
e-mail: Lerer@sfedu.ru

P.E. Timoshenko · E.M. Kaidashev
Laboratory of Nanomaterials, Southern Federal University, Rostov-on-Don, Russia

resonances of circular bilayer nano-wave-guide segments with the ZnO core covered with thin metal shell. In this regard, it is of interest to investigate the range of the optical characteristics of similar waveguides.

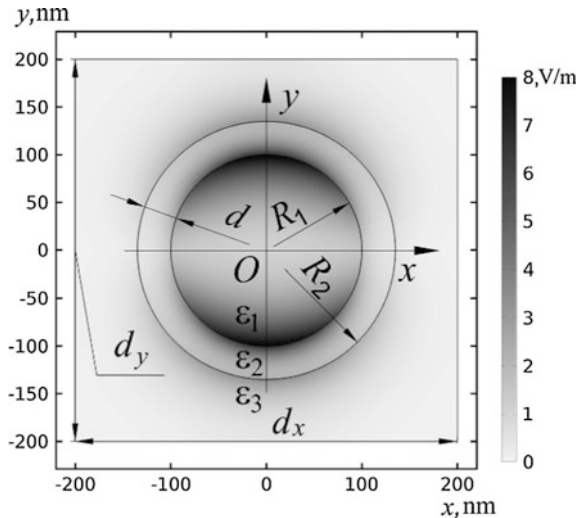
The calculated dispersion characteristics of single waveguide and two-dimensional periodic arrays of the waveguides are discussed in this chapter. The dielectric constant dispersion of ZnO [2] and metal [3] were taken into account. The metals are known to have a finite complex dielectric constant in the optical range.

22.2 Statement of the Problem

Figure 22.1 shows the geometry of optical waveguide composed of a core covered by a thin metal shell. The core has a radius R_1 and a dielectric constant ϵ_1 . The shell with a dielectric constant ϵ_2 has a radius R_2 . The thickness of the shell is $d = R_2 - R_1$. We assume that the dielectric constant ϵ_3 outside of the waveguide is equal to free space permittivity. The magnetic permeability μ is equal to free-space permeability everywhere. The geometry of optical waveguide, shown in Fig. 22.1, is described by the Cartesian rectangular coordinate system. The x - and y -axis are the longitudinal coordinate. The z -axis is directed along the waveguide being unlimited in this direction. The parameters d_x and d_y are periods of the array along x - and y -axes, respectively.

The method of variables separation in cylindrical coordinate system (r, φ, z) is applied to determine the frequency dependence of the complex propagation constant $\gamma(\omega)$ in the nano-antennas.

Fig. 22.1 The electric field of the cylindrical nano-waveguide with $\lambda = 450$ nm, $R_1 = 100$ nm, $\epsilon_1 = 4.0397 + 0.002i$ (ZnO), $R_2 = 135$ nm, $\epsilon_2 = 6.0830 + 0.7462i$ (Ag), $\epsilon_3 = 1$, $d_x = d_y = 400$ nm



The electromagnetic field in the waveguide can be described by the longitudinal components of the electric $P^e(r, \varphi)\exp(-i\gamma z)$ and magnetic $P^\mu(r, \varphi)\exp(-i\gamma z)$ vector of Hertz. The solution of Helmholtz equation for waveguide arrays is assumed in the form:

$$P^e(r, \varphi) = \sum_{m=1}^{\infty} \hat{P}_m^e(r) \sin m\varphi, \quad P^\mu(r, \varphi) = \sum_{m=0}^{\infty} \hat{P}_m^\mu(r) \cos m\varphi. \quad (22.1)$$

where m is the azimuthal wave mode number. The summing symbol in (22.1) should be omitted in case of a single waveguide. The function $\hat{P}_m^{e,\mu}(r)$ may be written:

- in the core of the waveguide ($r \leq R_1$) as

$$\hat{P}_m^{e,\mu}(r) = A_m^{e,\mu} \frac{\hat{J}_m(r)}{\eta_1^2 \hat{J}_m(R_1)}, \quad (22.2)$$

- in the shell ($R_1 \leq r \leq R_2$) as

$$\hat{P}_m^{e,\mu}(r) = \frac{1}{\eta_2^2 \Phi_m^{(2)}(R_1, R_2)} \left[A_m^{e,\mu} \Phi_m^{(2)}(r, R_2) - C_m^{e,\mu} \Phi_m^{(2)}(r, R_1) \right], \quad (22.3)$$

- in free space ($r \geq R_2$) in the case of a single waveguide as

$$\hat{P}_m^{e,\mu}(r) = C_m^{e,\mu} \frac{\hat{K}_m(r)}{\eta_3^2 \hat{K}_m(R_2)}, \quad (22.4)$$

- in free space ($r \geq R_2$) in the case of a periodic waveguide array as

$$\hat{P}_m^{e,\mu}(r) = \frac{1}{\eta_3^2 \Phi_m^{(2)}(R_2, R_3)} \left[C_m^{e,\mu} \Phi_m^{(2)}(r, R_3) - B_m^{e,\mu} \Phi_m^{(3)}(r, R_2) \right], \quad (22.5)$$

where R_3 is an arbitrary radius, satisfying the condition: $R_3 > \sqrt{d_x^2 + d_y^2}/2$. In (22.2)–(22.5), we use the representations:

$$\hat{J}_m(r) = \begin{cases} J_m(\eta_1 r), & \eta_1^2 \geq 0, \\ I_m(\hat{\eta}_1 r), & \eta_1^2 = -\hat{\eta}_1^2 < 0, \end{cases}$$

$$\hat{K}_m(r) = \begin{cases} N_m(\eta_3 r), & \eta_3^2 \geq 0, \\ K_m(\hat{\eta}_3 r), & \eta_3^2 = -\hat{\eta}_3^2 < 0, \end{cases}$$

$$\Phi_m^{(j)}(r, d) = \begin{cases} J_m(\eta_j r)N_m(\eta_j d) - N_m(\eta_j r)J_m(\eta_j d), & \eta_j^2 \geq 0, \\ I_m(\hat{\eta}_j r)K_m(\hat{\eta}_j d) - K_m(\hat{\eta}_j r)I_m(\hat{\eta}_j d), & \eta_j^2 < 0, \end{cases}$$

$A_m^{e,\mu} = \left\{ \begin{matrix} E_{z,m}(R_1) \\ H_{z,m}(R_1) \end{matrix} \right\}$, $C_m^{e,\mu} = \left\{ \begin{matrix} E_{z,m}(R_2) \\ H_{z,m}(R_2) \end{matrix} \right\}$, $B_m^{e,\mu} = \left\{ \begin{matrix} E_{z,m}(R_3) \\ H_{z,m}(R_3) \end{matrix} \right\}$ are the unknown coefficients, $E_{z,m}$, and $H_{z,m}$ are the longitudinal components of the electromagnetic field, $\eta_j^2 = k^2 \varepsilon_j - \gamma^2$, k is a wavenumber, J_m is the Bessel function, I_m is the modified Bessel function, N_m is the Neumann function, K_m is the Macdonald function.

Let us find the components of the electromagnetic field in the waveguide using the potentials:

$$E_\varphi(r, \varphi) = \sum_{m=0}^\infty \hat{E}_{\varphi,n}(r) \cos n\varphi, E_z(r, \varphi) = \sum_{m=0}^\infty \hat{E}_{z,n}(r) \sin n\varphi,$$

$$H_\varphi(r, \varphi) = \sum_{m=0}^\infty \hat{H}_{\varphi,n}(r) \sin n\varphi, H_z(r, \varphi) = \sum_{m=0}^\infty \hat{H}_{z,n}(r) \cos n\varphi,$$

where

$$E_{\varphi,n} = -i \left(\beta \frac{n}{r} P_n^e + \tau^m \frac{\partial P_n^m}{\partial r} \right), \quad H_{\varphi,n} = i \left(\beta \frac{n}{r} P_n^m + \tau^e \frac{\partial P_n^e}{\partial r} \right),$$

$$E_{z,n} = (k^2 \varepsilon \mu - \beta^2) P_n^e, \quad H_{z,n} = (k^2 \varepsilon \mu - \beta^2) P_n^m.$$

Satisfying the continuity condition of E_φ, H_φ on edge $r = R$ and the cell boundary conditions on $x = \pm d_x/2$ (magnetic walls), $y = \pm d_y/2$ (electric walls) for each modes, we obtain a set of linear algebraic equations (SLAE). The unknown coefficients $\hat{A}_n^e, \hat{A}_n^m, \hat{B}_n^e, \hat{B}_n^m$ depended on $\hat{C}_n^{e,m}$ may be calculated by the SLAE solving.

The solution is ordinary in the case of a single waveguide except the Hertz vector that can be written in form of (22.2)–(22.5) satisfying the continuity condition of the longitudinal component of the electromagnetic field at boundaries $r = R_{1,2}$. The components $E_{\varphi, m}(r), H_{\varphi, m}(r)$ should be found in each waveguide region considering boundary conditions. The solution may be written as system of linear algebraic equations for the four unknown coefficients. The dispersion relation is obtained by calculating the determinant of the SLAE being equated to zero.

In (22.5) we use an arbitrary radius R_3 and additional unknown coefficients $B_m^{e,\mu}$ in the case of two-dimensional periodic array of zinc oxide nano-waveguides. The

unknown coefficients $A_m^{e,\mu}$, and $B_m^{e,\mu}$ may be omitted by using the continuity condition of azimuthal components $E_{\phi, m}(r)$, $H_{\phi, m}(r)$ on boundaries $r = R_{1,2}$. Let us take the sum in (22.1) for $m \leq M$ values and require satisfaction the boundary conditions of $H_z(r, \varphi) = 0$ for M values on the side of the cell $x = d_x/2$ and $E_z(r, \varphi) = 0$ for M values on the top side of the cell $y = d_y/2$. These conditions are valid for waves in the array of waveguides excited by a normal incidence plane wave with polarization along the y -axis. The dispersion relation is also obtained by finding the determinant of the SLAE being equated to zero for unknown coefficients $C_m^{e,\mu}$.

The surface E -wave (surface plasmon polariton, SPP) [4] may travel along metal-dielectric interface with:

$$n = \frac{\gamma}{k} = \sqrt{\frac{\epsilon_d \epsilon_p}{\epsilon_d + \epsilon_p}},$$

where ϵ_p and ϵ_d are the permittivity of plasma and dielectric, respectively. The domain of existence this wave depends on $\text{Re } \epsilon_p < 0$ and $\epsilon_d + \text{Re } \epsilon_p < 0$. The two surface waves localized near the interface can propagate in the planar waveguide “dielectric–metal film–dielectric”. These waves have weak interaction in the case of the film thickness is about 30–40 nm. We also have two types of waves in a circular waveguide. The electromagnetic field of the first type waves (EH_{11}) localizes near “ZnO nanorods–silver” interface. The second type field (EH_{12}) localizes near “silver film–air” interface.

The propagation constant in waveguides with complex permittivity has a complex value. It is very difficult to locate complex roots of a complex function at the complex plane. To solve this problem, we use the Cauchy’s argument principle [5].

Only waves with low losses have a wide range of practical applications. In this case, we may simplify the finding complex roots method [6, 7]. The propagation constant may be assumed as $\gamma(\epsilon' - i\epsilon'')$. Let us expand it in a Taylor series and take three terms of the series:

$$\gamma(\epsilon' - i\epsilon'') \approx \gamma(\epsilon') - i\epsilon''\gamma'(\epsilon') - (\epsilon'')^2\gamma''(\epsilon')/2$$

The derivatives do not depend on the direction, because the function $\gamma(\epsilon)$ is an analytic. Therefore, we replace derivatives by finite differences:

$$\begin{aligned} \epsilon''\gamma'(\epsilon'') &\approx \gamma(\epsilon') - \gamma(\epsilon' - \epsilon''), \\ (\epsilon'')^2\gamma''(\epsilon') &\approx \gamma(\epsilon' + \epsilon'') + \gamma(\epsilon' - \epsilon'') - 2\gamma(\epsilon'). \end{aligned}$$

Hence

$$\gamma(\epsilon' - i\epsilon'') \approx \gamma(\epsilon') - i[\gamma(\epsilon') - \gamma(\epsilon' - \epsilon'')] - [\gamma(\epsilon' + \epsilon'') + \gamma(\epsilon' - \epsilon'') - 2\gamma(\epsilon')]. \quad (22.6)$$

Using this approach, the three real propagation constants of waveguide with a real permittivity should be found and applied the expression (22.6) to them to

determine the complex propagation constant. The detailed analysis and verification of the numerical method described in this paper are shown in [6, 7]. The calculation error increases sharply when $n''/n' > 0.1$, where $\gamma/k = n' - in''$. So if we use the silver as a coating film, the fairly large errors are in the wavelength range 400–440 nm.

The dispersion characteristics of electromagnetic wave (light) can be also modeled using the RF or Wave Optics modules from the COMSOL Multiphysics™, which involves dividing the simulation domain into smaller sub-domains forming a mesh. In this study, the standard physics-controlled mesh was used and the size set of elements to “extremely fine”. The field equations discretized into an SLAE and solved for their characteristic eigen-values. The implementation of the FEM in COMSOL enhances an insight into the numerical methodology and analyses factors that affect its performance.

We use “Electromagnetic Waves, Frequency Domain” module with standard preset parameters. The boundary conditions of perfect magnetic and electric conductors were applied on edges of $x = \pm d_x/2$ and $y = \pm d_y/2$, respectively. For our investigation, we apply “Mode Analysis” solver. The mode analysis study may be used to compute the complex propagation constants for a given frequency.

22.3 Results and Discussions

The numerical results for EH_{11} mode of the waveguide with radius $R_1 = 100$ nm covered by silver thin film having different thicknesses close to 40 nm are present in this chapter. These geometrical parameters are typical for ZnO nanorods [1, 8, 9].

Figure 22.2 shows the dispersion curves of the wave mode EH_{11} of a single waveguide with the various shell thicknesses d . It also displays the refractive index

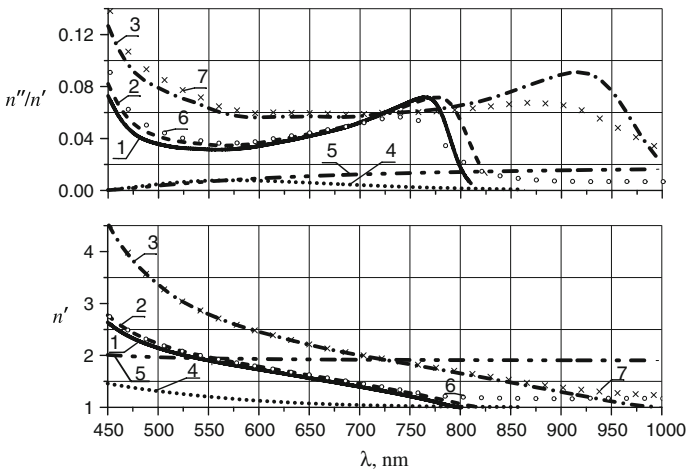


Fig. 22.2 Dispersion curves of the optical waveguide with different shell thicknesses d : 1—45 nm, 2—35 nm, 3—15 nm, 4—0, 5—ZnO, 6—35 nm (FEM), 7—15 nm (FEM)

of ZnO, n_{ZnO} (curve 5). The surface plasmon-polaritons (E -waves) localized near the boundary of ZnO–Ag can be excited in wavelength range, where $n > n_{\text{ZnO}}$. When the refractive index $n < n_{\text{ZnO}}$, the volume wave localizes in the waveguide and decreases exponentially outside it. The waveguide properties do not depend on thickness of the silver shell d , when the thickness d is greater than 30 nm. The properties of the metal in optical waveband will close to microwave waveband, when the wavelength increases. Therefore, the fundamental wave mode in the bilayered waveguide ZnO–Ag in contrast to a dielectric waveguide has a limited critical wavelength.

The dispersion curves in Fig. 22.2 with a shell thickness $d = 35$ nm (curve 6) and 15 nm (curve 7) are computed by COMSOL Multiphysics™ platform of finite-element physics-based modeling and simulation. As the advantages of using the finite element method (FEM) for the numerical calculation of the optical layered structures properties [10], we may highlight the conservatism and high stability of the numerical method, the ability to solve problems with a complicated geometry and to reduce the mesh in those places where special care is not required. Comparing the data of curves 2 and 3, 6 and 7, we can see that the results are in good agreement with the results of simulation in COMSOL Multiphysics™. Dispersion characteristics calculated by FEM have minor differences in the waveband close to the critical wavelength.

If we increase waveguide radius as shown in Fig. 22.3, the wave retardation coefficient will increase too and the losses will become considerably lower.

The wave mode EH_{11} has strong field localization in the waveguide in optical wavelength range, thus the dispersion properties of a periodic waveguide array as shown in Fig. 22.4 have a very weak dependence on the distance between nanorods.

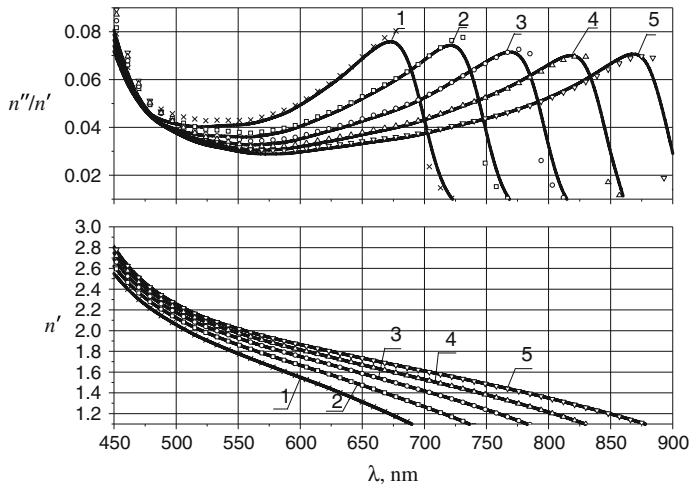


Fig. 22.3 Dispersion curves of the waveguide with fixed shell thickness $d = 40$ nm and different core radiuses R_1 : 1—80 nm, 2—90 nm, 3—100 nm, 4—110 nm, 5—120 nm. The results, obtained by FEM in COMSOL Multiphysics™, are marked by symbols

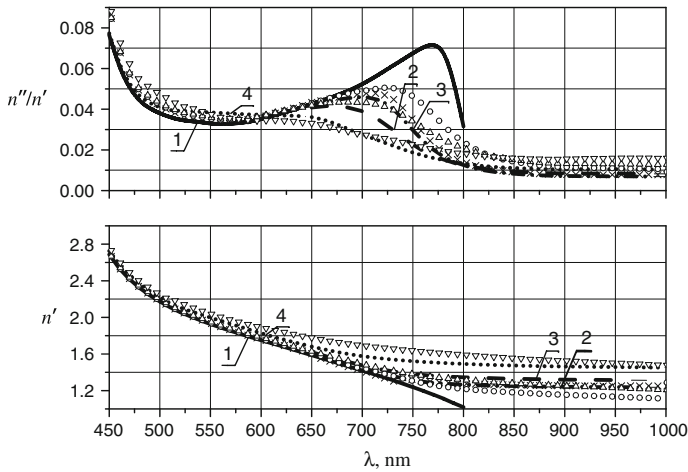


Fig. 22.4 Dispersion curves of the array of waveguides with $R_1 = 100$ nm, $R_2 = 140$ nm and various unit cell size: 1—single waveguide, 2—array of waveguides with $d_x = d_y = 350$ nm, 3—325 nm, 4—300 nm. The results obtained by FEM are marked by symbols

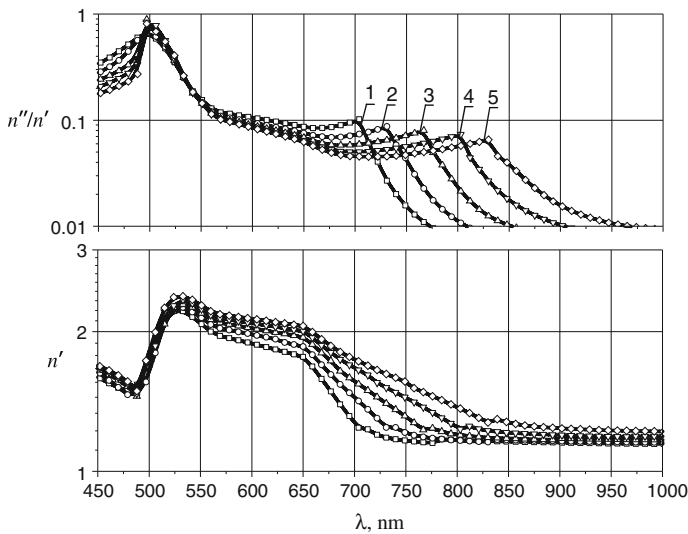


Fig. 22.5 Dispersion curves of the mode EH_{11} of the waveguide calculated by FEM with gold shell thickness $d = 40$ nm and different core radiuses R_1 : 1—80 nm, 2—90 nm, 3—100 nm, 4—110 nm, 5—120 nm

Figure 22.5 shows the dispersion curves have significant differences compared with similar characteristics depicted in Fig. 22.3 for waveguides with a silver shell, because the complex dielectric constant of gold and silver are essentially different.

Figure 22.6 shows the dispersion characteristics of the higher modes. They have a rather narrow waveband of the SPP excitation compared with the main mode.

The wave EH_{11} has a strong localization of the field in the waveguide. Therefore, the dispersion characteristics are essentially independent of the distance between nanorods (Fig. 22.4) in the SPP wavelength range.

The wave EH_{12} is SPP localized at the “metallic film–vacuum” interface with parameters having dependence on the film thickness up to $d < 50$ nm (Fig. 22.7). The field outside the waveguide for EH_{12} wave is much larger than EH_{11} . Therefore, the interaction between the waveguides of the lattice is significantly stronger (Fig. 22.8).

Fig. 22.6 Dispersion curves of the single waveguide with $R_1 = 100$ nm and $R_2 = 140$ nm: 1— EH_{01} , 2— EH_{11} , 3— EH_{21}

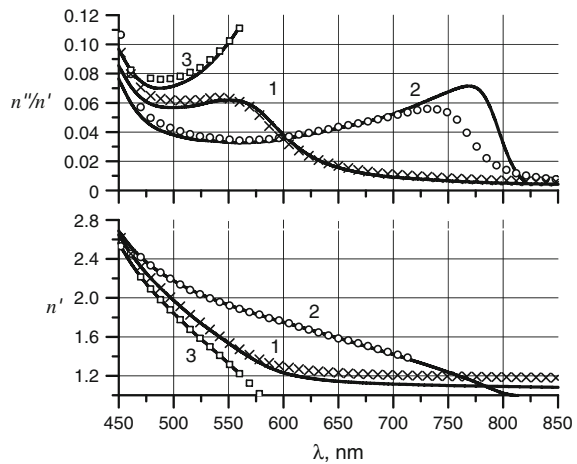


Fig. 22.7 Dispersion curves of the mode EH_{12} of the waveguide with core radius $R_1 = 100$ nm and various shell thicknesses: 1— $d = 45$ nm, 2— $d = 35$ nm, 3— $d = 25$ nm

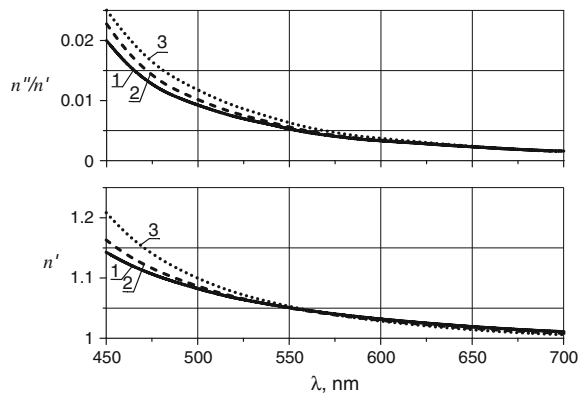
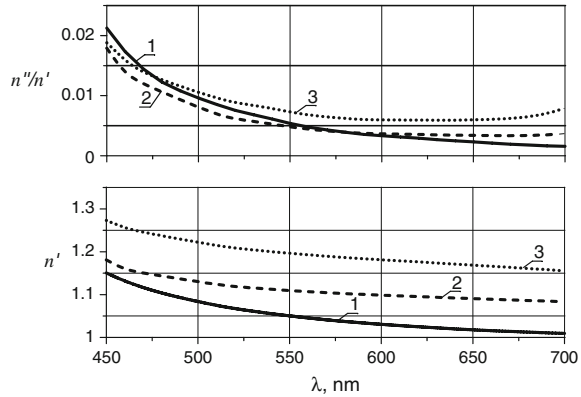


Fig. 22.8 Dispersion curves of the array of waveguides with $R_1 = 100$ nm, $R_2 = 140$ nm and various unit cell sizes: 1—single waveguide, 2— $d_x = d_y = 500$ nm, 3—400 nm



22.4 Conclusions

For a quantitative estimation the resonant wavelengths of optical nanoantennas, they should be interpreted as resonances of double-layer nano-waveguide segments composed of the ZnO core and the thin metal shell excited an integer number of half wavelengths of the waveguide.

The resonances of a periodic waveguide array with average distance between adjacent nanorods 700 nm were present in paper [1] on wavelengths: 550, 650, 890 and 1,340 nm. The quantitative estimates, calculated by the method described in this chapter and by the COMSOL MultiphysicsTM, give values of 500–550, 600–670, 780–800 and 1,400–1,420 nm.

The results discussed in this paper may be used to predict the resonant wavelengths of two-dimensional periodic array of ZnO nanorods grown on a dielectric substrate.

Acknowledgments The authors acknowledge the support of the Russian Ministry of Education and Science, provided by grant 16.219.2014/K, and the part of the Internal Grant project of the Southern Federal University in 2014–2016, provided by grant 213.01.-07.2014/08PCHVG, for carrying out this research study.

References

1. E.M. Kaidashev, N.V. Lyanguzov, A.M. Lerer, E.A. Raspopova, *Tech. Phys. Lett.* **40**(7), 79 (2014)
2. A.D. Rakic, A.B. Djurusic, J.M. Elazar, M.L. Majewski, *Appl. Opt.* **37**(22), 5271 (1998)
3. Z.H. Dai, R.J. Zhang, J. Shao, Y.M. Chen, Y.X. Zheng, J.D. Wu, L.Y. Chen, *J. Korean Phys. Soc.* **55**(3), 1227 (2009)
4. S.A. Mayer, Springer, New York (2007)
5. M.A. Lavrentiev, B.V. Shabbat, Nauka, Moscow, 1965 (In Russian)

6. A.M. Lerer, I.V. Donets, G.A. Kalinchenko, P.V. Makhno, *Electromagnet. Waves Electron. Syst.* **18**(9), 5 (2013). (In Russian)
7. A.M. Lerer, I.V. Donets, G.A. Kalinchenko, P.V. Makhno, *Photon. Res.* **2**(1), 31 (2014)
8. M. Lorenz, A. Rahm, B. Cao, Z.P. Jesus, E.M. Kaidashev, N. Zhakarov, G. Wagner, Th Nobis, C. Czekalla, G. Zimmermann, M. Grundmann, *Phys. Status Solidi B* **247**(6), 1265 (2010)
9. N.V. Lyanguzov, V.E. Kaydashev, I.N. Zakharchenko, YuA Kuprina, O.A. Bunina, YuI Yuzyuk, A.P. Kiselev, E.M. Kaidashev, *Tech. Phys.* **57**(4), 534 (2012)
10. J. Hoffmann, C. Hafner, P. Leidenberger, J. Hesselbarth, S. Burger, in *Proceedings of SPIE7390, Modeling Aspects in Optical Metrology II*, vol. 3790, p. 73900J. Munich, Germany, 2009

Chapter 23

Effect of Electric Field on the EMF in the System “Electrode–Electrolyte– Capacitor Electrode”

G.Ya. Karapetyan, V.G. Dneprovski, I.A. Parinov and G. Parchi

Abstract We investigate a dependence of the electromotive force (EMF) on electric field in the system “electrode–electrolyte–capacitor electrode”. The capacitor electrode is a plate of ferroelectric ceramics, on one of the surfaces of which the solid electrode is deposited and there is a mesh electrode on the other surface. When a voltage is applied to these electrodes, EMF changes or appears, if it was not before, due to changes in the concentration of ions near the mesh electrode. Shorting of the electrodes in the electrolyte through resistor R leads to arising the flow of electric current and also absorbing and emitting Peltier heat in electrodes contacting with electrolyte. In this case, greater heat absorbs compared with the emitted heat, supporting EMF, i.e. ambient heat converts into electrical energy. We also show that similar phenomenon of creating EMF takes place in structure “metal–insulator–semiconductor–metal” (MISM).

23.1 Introduction

The technology of converting environmental energy into electric energy considers as “without battery” technology providing an electric power of systems in which application of batteries is complicated (Technology of Energy Harvesting) [1]. This technology is perspective for a powering of devices, which should work continuously without replacement of the power source within decades, and also for wireless sensors, switches, various electronic devices—from gadgets to portable computers and printed electronic schemes (Fig. 23.1).

At the same time, electric schemes using energy of environment can carry out functions of the additional power source operating together with micro-batteries and

G.Ya. Karapetyan (✉) · V.G. Dneprovski · I.A. Parinov
Vorovich Mathematics, Mechanics and Computer Science Institute,
Southern Federal University, Rostov-on-Don, Russia
e-mail: jorichkaka@yandex.ru

G. Parchi
Prometeon SRL, Bologna, Italy

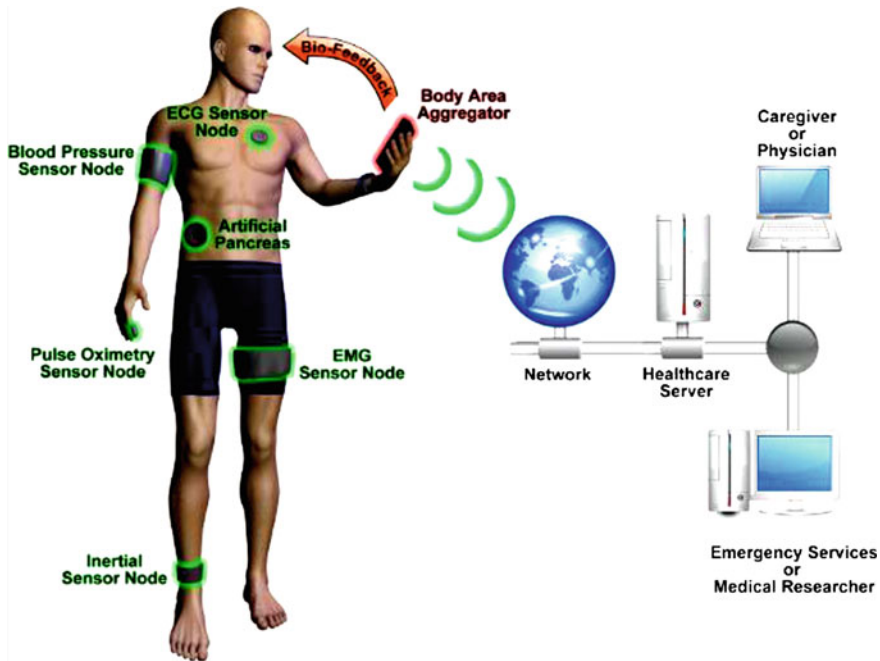


Fig. 23.1 Energy harvesting device

allowing one to accumulate energy for powering of the system from the batteries and to give it if necessary. Technology of energy harvesting is developed some years, but only now, a possibility appeared of its commercial realization.

Thermoelectric devices, used in the technology of energy harvesting, work only if exists a definite temperature difference, which does not always convenient, since the ambient temperature may be close to the temperature of human body or lifeless objects have a temperature equal to the ambient temperature. Therefore, it would be useful to have such thermoelectric generators that work without the presence of a temperature difference. Discussion of this thermoelectric generator is the aim of the present chapter.

23.2 System of Electrolyte and Two Electrodes

Let us consider a system containing electrolyte and two copper electrodes (Fig. 23.2). One of the electrodes represents solid electrode and the other electrode is mesh. The mesh electrode locates on the surface of the ferroelectric plate of copper film. The solid electrode is deposited on the opposite side of the ferroelectric plate. The mesh electrode contacts with the electrolyte, but the solid electrode is outside of the electrolyte. Between the electrodes in the electrolyte, a resistor $R = 390 \text{ k}\Omega$ and voltmeter dispose.

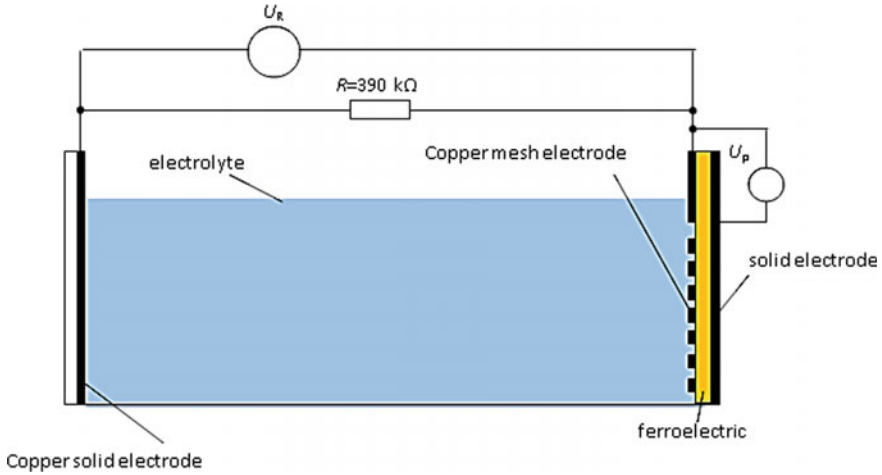


Fig. 23.2 Experimental setup

A voltage source U_p is connected to the mesh and solid electrodes situated on opposite surfaces of ferroelectric plate. Thus, since the mesh electrode is in contact with the electrolyte, the electrolyte has an electric potential equal or close to the potential of the mesh electrode. Therefore, we can assume that between the electrolyte and the solid electrode on opposite side of the ferroelectric plate outside electrolyte there is a potential difference equal to a voltage of the voltage source U_p . In this case, the penetration depth of the electric field can determine by the formula [2]:

$$L_D = \sqrt{\frac{\varepsilon\varepsilon_0kT}{e^2n_0}}, \tag{23.1}$$

where ε is the permittivity, k is the Boltzmann constant, $\varepsilon_0 = 8.85 \cdot 10^{-12}$ F/m is the permittivity of vacuum, e is the electron charge, n_0 is the concentration of ions.

Since as the electrolyte, it is used a polar liquid (water, alcohol, glycerin), then ε can be taken equal to 50 F/m. At room temperature ($T = 300$ K), we have

$$L_D = 8.459/\sqrt{n_0}. \tag{23.2}$$

From this formula (23.2), it is seen that when the concentration of ions $n_0 = 10^{12}$ 1/cm³, the depth of penetration of the electric field $L_D \approx 100$ nm, which is quite a significant value, since the thickness of the deposited metallic electrodes usually does not exceed of 1 μm. For ferroelectric plate with thickness 0.5 mm, we can get a capacity up to 1 μF/cm² and at a voltage 100 V, the charge on the capacitor plates can reach 10⁻⁴ C, i.e. from the side of the electrolyte on 1 cm² will be accumulated 6.25 · 10¹⁴ ions of the electrolyte. Since the penetration depth of charge is equal to 0.1 μm, the concentration will increase from $n_0 = 10^{12}$ to $n = 10^{19}$ 1/cm³, i.e., by seven orders of magnitude.

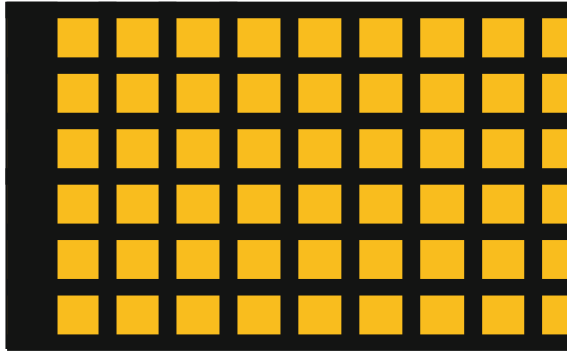


Fig. 23.3 Mesh electrode

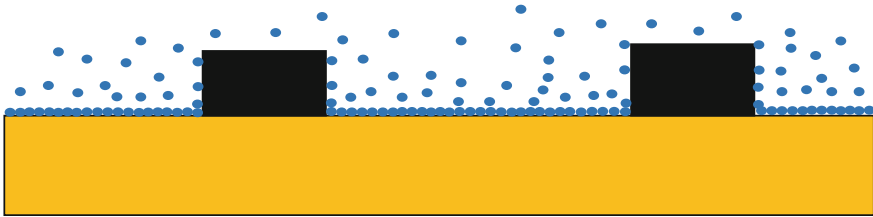


Fig. 23.4 Distribution of ions around mesh electrode

The mesh electrode has a cell size $5 \times 5 \text{ mm}^2$ (Fig. 23.3). The thickness of the film from which this electrode is made equal to $1 \text{ }\mu\text{m}$. Since the thickness of the surface layer of ions is much lesser, than thickness of the electrodes, the average concentration of ions in near-electrode area will not differ from the concentration of ions in the electrolyte bulk (Fig. 23.4). To increase the concentration, it is necessary to reduce thickness of the electrodes, so that it will be close to thickness of the ion layer on the wafer surface. Moreover, it is required to significantly reduce the cell size of the mesh electrode down to $5 \times 5 \text{ nm}^2$. In this case, the concentration of ions in near-electrode regions will increase significantly, that lead to a change of a potential difference at the contact between the electrode and electrolyte. In this case, between the solid electrode in an electrolyte and mesh electrode will arise EMF or change its value, if it existed before application of voltage.

23.3 Electromotive Force in the System

Figure 23.5 shows dependence of the voltage U_R on resistor R on the voltage between mesh and solid electrodes on ferroelectric plate. As we can see, at zero voltage across the electrodes of the plate, this dependence has a non-zero EMF that

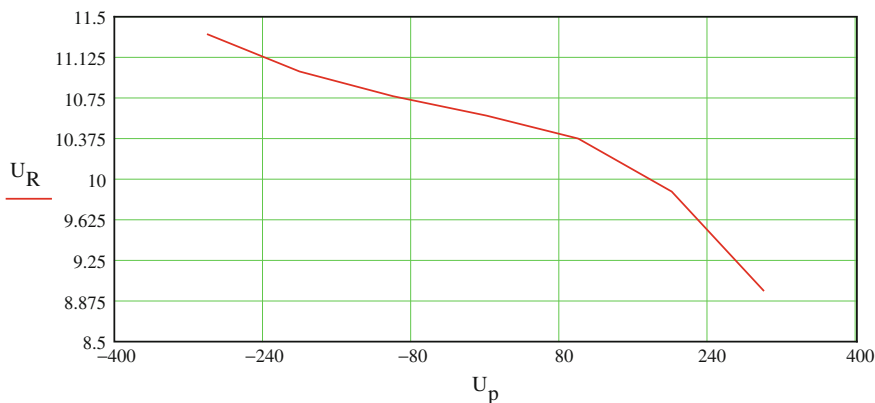


Fig. 23.5 Dependence of voltage on resistor R on voltage between both electrodes on the plate

can be explained by a slightly different chemical composition of the electrodes, connected to the resistor R . From this figure, it is clear that EMF increases at growth of negative voltage, and EMF decreases at growth of positive voltage.

Since EMF in this case is caused by change in the concentration of ions near the electrodes, such systems call the concentration of circuits of the second kind [2]. This concentration of circuits comprises two identical electrodes immersed in solutions of the same electrolyte with different concentrations. The process that causes EMF in circuits of this kind consists in transformation of electrolyte from a concentrated solution to diluted one. Therefore, the concentration of circuits of the second kind calls also circuit with mass transport.

Between two solutions, there is a border, arising due to the transfer of localized ions, caused by the diffusion potential that allows one to determine the systems as circuits with a liquid border. For the concentration of circuits, general thermodynamic equation that determines a reversible EMF of electrochemical systems is simplified. It excludes the value of standard EMF E_0 and remains only the term describing an influence of the electrochemical reactions at existence of EMF (see below).

Figure 23.6 shows that between electrolyte and electrode in dependence on the electrode material and composition of the electrolyte there is a jump of Fermi level and an electric potential difference arises at contact. For different electrodes, these jumps of the Fermi level are various, leading to the difference of Fermi levels between electrodes, i.e. to occurrence of EMF. Various jumps of the Fermi level occur, when identical electrodes be in the electrolyte with different concentration of ions, i.e. EMF occurs also in the systems, where identical electrodes contact with electrolyte of different concentration [2].

As we can see from the dependence of voltage across the resistor, it depends on the polarity of the application voltage. This is understandable, because when voltage is applied to electrodes of the plate, the concentration of ions at the plate surface changes, leading to change in EMF. If the electrodes are the same, then the

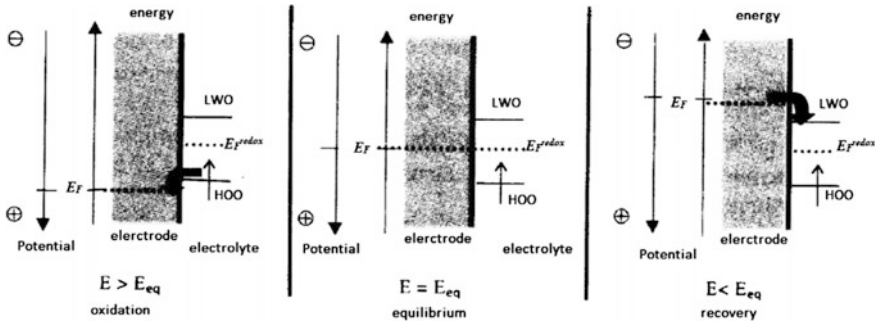


Fig. 23.6 Energy diagram for the boundary “metal–electrolyte”; *LWO* is the lowest vacant orbital, *HOO* is the highest occupied orbital

EMF will be equal to zero, when the voltage does not apply to the mesh electrode and will change its sign depending on the polarity of the voltage. For example, when passing a current, one of the electrodes will decrease (gives ions) and the other one increase (accepts ions). If we now reverse the polarity of the voltage, the decreasing electrode becomes to accept ions, and the increasing electrode, will give ions. Thus, it is possible to perform this cycle an unlimited number of times, i.e., the electrodes will not be dissolved. So at each electrode will occur reversible chemical reaction and an energy effect of this reaction will be equal to zero.

The source voltage after transient charging-discharging does not consume energy, because the current through the ferroelectric plate in this case is zero. We can always prolong the switching period so that the energy, deposited on resistor, became greater than the energy required to change a polarity of the voltage source. Due to the switching period can be made much longer for switching the polarity of the voltage. Since in this system, the electrodes do not dissolve, and the energy, deposited on resistor, is greater than energy, consumed for switching polarity of the voltage, applied to electrodes on the ferroelectric plate, then only source of energy to create EMF will be environmental heat. It will absorb at the contact of one of the electrodes with electrolyte and emit to the contact place of the other electrode with the electrolyte. However, a heat will absorb in more degree than emit, so that the heat absorbs during the passage of the current through resistor. Then we can assume that $dE/dT > 0$, where E is the magnitude of EMF. Since $dE/dT > 0$, then the system will convert into electrical energy not only the heat corresponding to the heat effect of reaction (which in this case is zero), but additionally the Peltier heat, absorbed from the environment. In an adiabatic system, i.e. in terms of thermal insulation, when an exchange of heat with environment is impossible, the temperature of the system decreases.

By changing the voltage between the mesh and solid electrodes in the range: $-300 \text{ V} < U_p < 300 \text{ V}$, the voltage across the resistor varies into range: $11.2 \text{ mV} > U_R > 8.9 \text{ mV}$, i.e. on the value of $\Delta U = 2.3 \text{ mV}$. This behavior can

explain by the dependence of EMF in galvanic cells on concentration of ions at the electrodes [2]:

$$E = E_0 + \frac{0.059}{q} \lg \frac{\gamma_{ox}}{\gamma_{red}},$$

where E_0 is the standard electric potential of the redox-system, γ_{ox} and γ_{red} are the ion concentrations of the oxidizing and reducing forms, respectively, q is the ion charge in the electron charges. Since by varying the concentration, E_0 does not vary, then the electric potential change of the electrode due to changes in the concentration is defined by the formula (at $q = 1$):

$$E = 0.059 \lg \frac{\gamma_{ox}}{\gamma_{red}}.$$

As it mentioned above, for the given parameters of the mesh electrode, the change in the electric potential difference at contact on mesh electrode will be negligible as Fig. 23.5 shows. By decreasing the film thickness of the mesh electrode down to 50 nm, the cell size to $5 \times 5 \mu\text{m}^2$ and change of the ion concentration on 7 orders of magnitude, we can obtain EMF, $E = 0.059 \cdot 7 = 0.413$ V. This concentration change may be in only high-resistive electrolytes. Therefore, as the electrolyte, we used a mixture of distilled water and glycerin in a ratio of 50:50.

Since the voltage $U_R \neq 0$, then an electric current passes through resistor R . This current flows through the contacts of electrolyte and the metallic electrodes. Then, one of the contacts will emit Peltier heat, but other contact absorbs it. If $U_p = 0$ (what can be performed properly selecting the electrode material), then EMF will be equal to 0. At non-zero voltage, the ion concentration on the mesh electrode will differ from the concentration of ions in the electrolyte bulk in accordance with formula (23.2). This will lead to the different Peltier coefficients on the electrodes, by this, it will be greater where heat absorbs, i.e., absorption of the heat will exceed a return of the heat. In this case, the energy to create EMF is caused by the absorption of heat from environment that is environmental heat will convert into electrical energy. Therefore, no necessity for creation of preliminary temperature difference, since at flowing current through contacts of electrolyte with metallic electrodes, the absorption of heat in these contacts will be larger, than its emitting.

23.4 Thermoelectric Generator Based on MISM-Structure

If to compare the proposed structure with the metal–insulator–semiconductor–metal (MISM) structure, shown in Fig. 23.7 [3], we can say that they are similar. Only in the later case, instead of the ion charge carriers, electrons operate. Metallic electrodes 3 replace mesh electrode in this structure. Instead of the ferroelectric plate, it is used thin dielectric layer 4, and solid electrode plate is a gate. In addition, similar to the

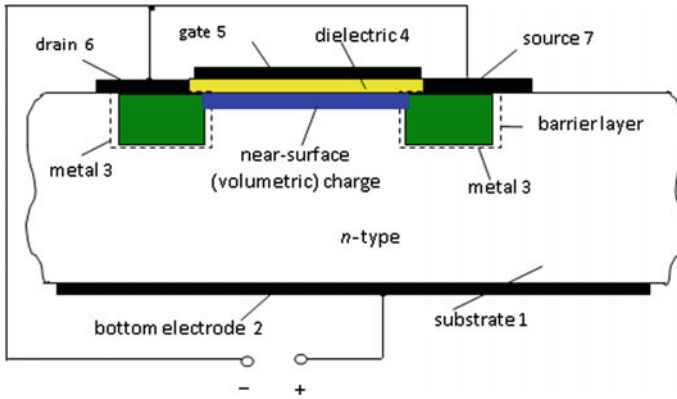


Fig. 23.7 MISM-structure

case with the electrolyte, when a voltage is applied between the mesh and solid electrodes, the carrier concentration significantly increases under dielectric, forming the near-surface charge. This should result to a change in the potential difference at the contact between the metallic electrodes 3 and the near-surface charge.

At the same time, between substrate 1 and bottom electrode 2, contact difference does not change. Therefore, EMF arises between the bottom electrode, the drain connected in parallel and source, connected to the metallic electrode 3. So current flows in such a direction that heat will absorb at the junction of the bottom electrode with the substrate and it will emit at the junction of the metallic electrode with near-surface charge. However, heat emitting will be less, because of electric potential difference at the junction, and, therefore, the Peltier coefficient will smaller than at the bottom electrode junction with the substrate. As a result, similar to the case of electrolyte, electromotive force is caused by the absorption of heat from the environment.

Further, let us consider a plate of the n -type semiconductor with electrode on the plate bottom surface, and other electrode, located above of the plate at some distance from it [4]. This structure forms a capacitor, whose one plate is the electrode, which does not connect to the plate, and other electrode is the plate itself (see Fig. 23.8). The square of surface of these electrodes is much lesser than square of the plate surface. The plate thickness is chosen much thicker than the screening length of surface charge, i.e. charge on the upper surface does not influence on the junction of the lower electrode with the plate.

The charging of the capacitor is carried out from battery with voltage U_0 . The battery connect in such a way that the positive pole of the battery connect to the electrode, which does not connect with the semiconductor plate. The concentration of electrons on the semiconductor surface, located under upper electrode can exceed significantly the electron concentration in the bulk of semiconductor and on its surface outside of the electrode. It takes place due to the electrons are attracted to the semiconductor surface by positively charged electrode. However, according to the laws of electrostatics for conducting bodies, a whole surface of the plate should

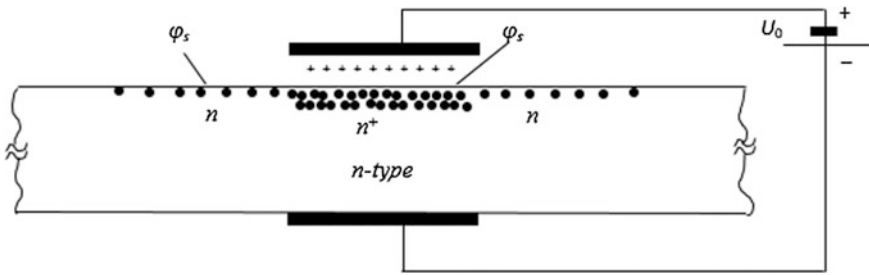


Fig. 23.8 Semiconductor plate with electrodes

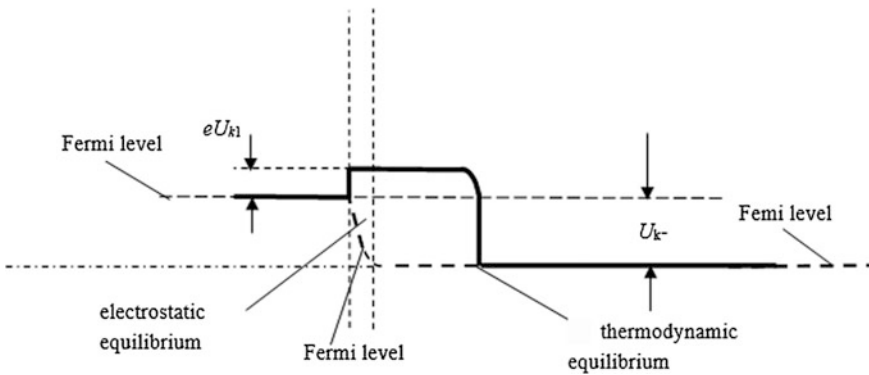


Fig. 23.9 Chart of energy for lower plate of the capacitor, presented in Fig. 23.7

be an equipotential surface. Therefore, the electric potential on the surface (including area, located under upper electrode), as we assume, is equal to ϕ_s . Moreover, note that the electric potentials of the conducting bodies are the same, when the electric field equals zero in its bulk. Thus, we can choose the electric potential ϕ_s for a whole plate. However, the equality of the electric potentials at the body surface and in its bulk means that bottom of the conduction band has the same level. Consequently, the Fermi level changes in area of near-surface charge under upper electrode, because the electron concentration depends on the difference between the Fermi level and bottom of the conduction band, but electron concentration in the near-surface charge differs from electron concentration into bulk of the plate.

Figure 23.9 shows chart of electric potentials for the charged capacitor, depicted in Fig. 23.7. As we can see in this chart, electric potential of the near-surface charge is equal to the electric potential of semiconductor plate, and voltage on capacitor is greater than voltage on battery on the value of U_k . This occurs, as shown in [4], because heat energy absorbs during charging the capacitor in the junction of bottom electrode (see Fig. 23.7) with the semiconductor plate (i.e. the junction cools in this case). The heat (kinetic) energy transforms into potential energy of the charged

capacitor. Thus, electric potential in the near-surface charge equals φ_s , and concentration of electrons in it is much higher than in the bulk semiconductor. We carry out calculations from bottom of the conduction band. Then the difference of potentials at the junction between the near-surface charge and metallic electrode connected with it, necessary to calculate from bottom of the conduction band. It leads to the conclusion that the Fermi level of the electrode does not coincide with the Fermi level of bottom electrode and semiconductor (see Fig. 23.9).

Since concentration of electrons in the near-surface charge is much higher than in the bulk of semiconductor and taking into account that calculation is performed from bottom of the conduction band, then it should lead to a distortion of the Fermi level (see Fig. 23.9). Thus electric potential difference forms between electrode, connected to the near-surface charge and electrode, connected to the semiconductor plate, which is equal to $\Delta U_k = U_k - U_{k1}$ (see Fig. 23.9). If to assume that the Fermi level does not curve, we should suppose that the near-surface charge has electric potential, which is equal to the electric potential of lower electrode. Then the energy, absorbed in the process of charging, does not transform into potential energy of the charged capacitor and disappears in unknown direction that violates the law of energy conservation. The fact that surface of the semiconductor plate is an equipotential surface shows that an electrostatic equilibrium arises, at which a charge distribution exists on the surface in absence of currents. At the junction between bottom electrode and semiconductor plate, the thermodynamic equilibrium creates, in which the Fermi levels coincide in the metal and semiconductor. This occurred due to that bottom electrode was connected before charging the capacitor, when this equilibrium only was possible.

Since the Fermi levels of the lower electrode and upper electrode, connected to the near-surface charge, are different, then we can speak on that the difference of electric potentials at the junction between lower electrode and semiconductor plate is the electromotive force, in which non-electric force, driving charges against the forces of the electric field, is a heat of environment. Thus, similar to the case of junction of the metallic electrode with electrolyte (see Fig. 23.6), change of the Fermi level occurs in this case at the junction of metallic electrode with semiconductor.

Figure 23.10 explains how the environmental heat transforms into electric energy in the MISM structure. As it is shown above, the electric potential difference $\Delta U_k = U_k - U_{k1}$ is created between lower electrode and the parallel connected drain and source, which connected to the near-surface charge. Therefore, if we connect resistor r to these electrodes then the current flows through it along the direction, at which electrons should overcome the potential barrier. These electrons, reaching the near-surface charge, give its energy to the electric field, maintaining the attained potential difference in each moment of time. The electrons that move from the near-surface charge take away this amount of energy. Thus, the energy of the charged capacitor remains constant in each moment, and the energy, absorbed at overcoming the potential barrier, evolves on the resistor r .

Air molecules influence on the MISM-structure (see Fig. 23.9), interacting with the surface of the metallic electrode. The air molecules influence on atoms in the

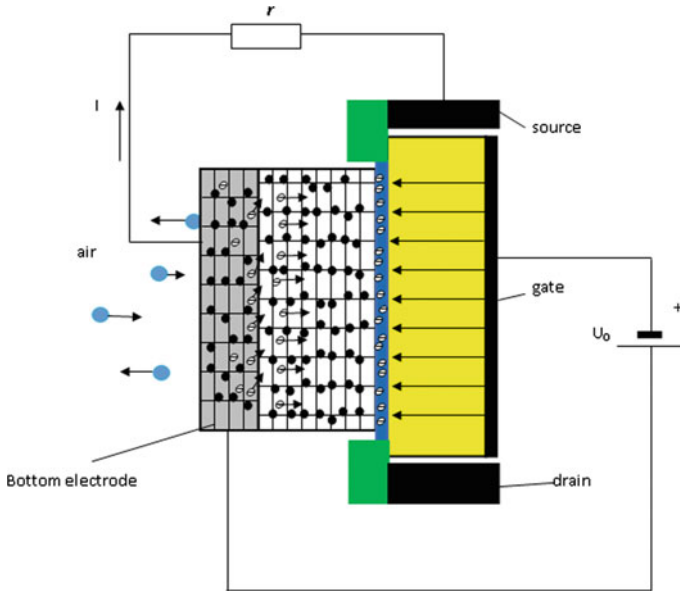


Fig. 23.10 Explanation of heat absorption from environment by MISFET structure

crystalline lattice. Then the atoms interact with electrons, causing their distribution on energies. This process allows the electrons to overcome the potential barrier. The electrons with lesser energy, which cannot overcome the potential barrier, take away the energy from atoms of the crystalline lattice in the result of interaction with them. At the same time, the atoms of the crystalline lattice interact with the molecules of air and also take away their energy. However, the energy of the air molecules recovers in each moment of time, owing to the solar radiation, which is provided by energy of these molecules (sun warms air, water, land). This process leads to transformation of the solar energy into electrical one. If structure is insulate from heat, then it begins to cool and the energy distribution starts to decrease and aspires to zero in the end of the process.

We also performed experiments with field effect transistors [3], which had a similar structure, but with barrier layer between the near-surface charge and the substrate. Measurements in the mode of charging-discharging the gate capacitor showed that there is excess of power on the resistors R and r to the power consumption by an average of 10 %, because of absorbing heat from the environment.

Acknowledgments This work was supported in part by the Southern Federal University (No. 213.01-2014/03VG), Russian Foundation for Basic Research (grant No. 13-08-00754) and the Russian Education and Science Ministry (the project No. 16.219.2014/K “Development of synthesis methods, theoretical and experimental study of zinc oxide based nanostructures to create elements of photodetectors, optical nanoantennas, piezosensors and chemosensors”. I.A. Parinov acknowledges financial support from Ministry of Education and Sciences of Russia in the framework of “Organization of Scientific Research” Government Assignment (grant No. 654).

References

1. V. Mayskaya, *Electron: Sci Technol Bus* **8**, 72 (2009). (In Russian)
2. L.I. Antropov, *Theoretical Electrochemistry: Textbook for Chemical and Technological Speciality of Higher Education*, 4th edn. (Higher School, Moscow, 1984). (In Russian)
3. G.Y. Karapetyan, V.G. Dneprovski, Research of opportunity to use MISM structures for cooling of light-emitting diodes, in *Physics and Mechanics of New Materials and their Applications*, ed. by I.A. Parinov, S.H. Chang (Nova Science Publishers, New York, 2013), Chapter 29, p. 405
4. G.Y. Karapetyan, V.G. Dneprovski, I.A. Parinov, Change of fermi level in area of near-surface charge in MISM structures, in *Advanced Materials. Studies and Applications*, ed. by I.A. Parinov, S.H. Chang, S. Theeraculpisut (Nova Science Publishers, New York, 2015), Chapter 14, p. 209

Chapter 24

Mathematical Models, Program Software, Technical and Technological Solutions for Measurement of Displacements of the Control Object Surfaces by Laser Interferometer

I.P. Miroshnichenko, I.A. Parinov, E.V. Rozhkov and S.-H. Chang

Abstract The chapter presents results of development and scientific (calculations and experiments) grounds of perspective methods and means of contactless measurement of displacements of the control object surfaces, directed to creation of novel high-accuracy optic measurement technologies and corresponding technical means for state diagnostics of construction materials and goods during all stages of their lifetime (in manufacture and operation) by acoustic methods of non-destructive testing based on the modern methods of laser interferometry.

24.1 Introduction

In present, one of the actual and most perspective directions for solution of scientific and applied problems of state diagnostics of construction materials and goods during their lifetime is the laser interferometry. Its methods allow one to study damage processes in novel materials and composites and register displacements of the control object surfaces by using high-accuracy contactless measurement means. This approach increase significantly a quality (accuracy) and information of analysis of the elastic wave fields at ultrasound defectoscopy, state

I.P. Miroshnichenko (✉)
Don State Technical University, Rostov-on-Don, Russia
e-mail: ipmir@rambler.ru

I.A. Parinov · E.V. Rozhkov
Vorovich Mathematics, Mechanics and Computer Science Institute, Southern Federal University, Rostov-on-Don, Russia

S.-H. Chang
Department of Microelectronic Engineering, National Kaohsiung Marine University, Kaohsiung, Taiwan

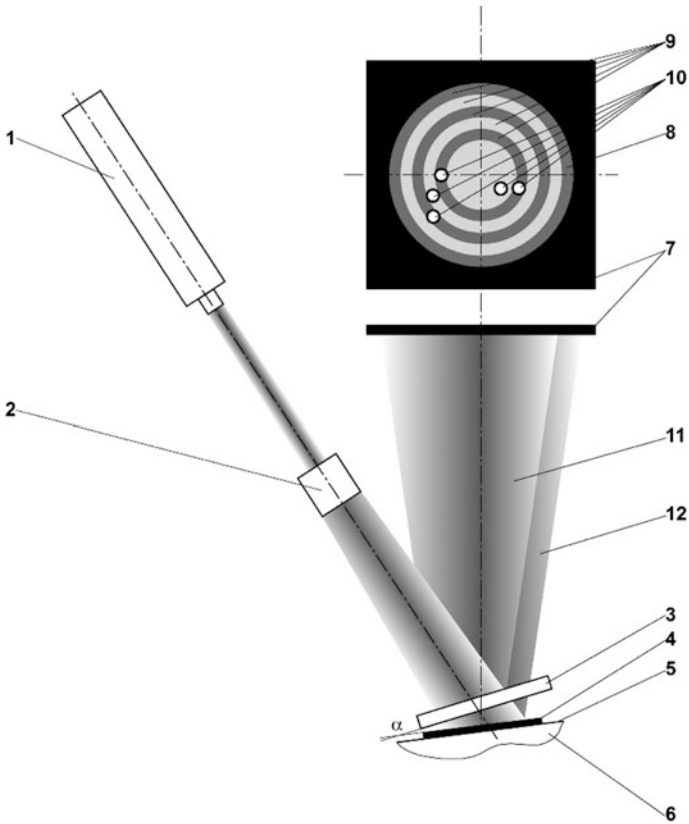


Fig. 24.1 Typical schematic of two-way laser interferometer with combined branches

diagnostics of materials and goods by using acoustic emission methods, etc., that improve a quality and reliability of different machines and equipment.

The aim of this chapter is the development and scientific (calculations and experiments) grounds of perspective methods and means of contactless measurement of displacements of the control object surfaces. The results are directed to R&D of novel high-accuracy optic measurement technologies and corresponding technical means for state diagnostics of construction materials and goods during all stages of their lifetime (in manufacture and operation). These results are reached by using active and passive methods of non-destructive testing on the base of modern methods of the laser interferometry.

As a base device for solution the pointed problems, we select the two-way laser interferometer with combined branches (see Fig. 24.1). This interferometer includes optically coupled and consecutively located source 1 of coherent optical radiation, optical system 2, beam-splitter 3, reflector 4 fastened at surface 5 of a control object 6, and screen 7 on which are stated photo-detectors 10. The beam-splitter 3 and reflector 4 are situated one from other under angle α . Obtained in combination of

reference beam 11 and object beam 12 the interference picture 8 presenting itself the set of rings 9 with various intensities projects on the screen 7, and the photo-detectors 10 are located into rings 9 of interference picture 8.

The main directions for improvement of above two-way laser interferometer with combined branches were extension of its functional possibilities and using for solution of applied problems in the structure of mobile diagnostic systems.

24.2 Models, Methods and Measurement Means

24.2.1 Modeling Intensity of Optic Radiation in Interference Pictures

We have developed new mathematical models and program software for modeling intensity of optic radiation in interference pictures. These pictures are created by optic meter of displacements on the base of two-way laser interferometer with combined branches. In this case, it takes into account features of an optic measurement scheme and kind of beam-splitter, and also a technical solution (measurement device), ensuring the meter application at solution of scientific-technical problems.

Above results allow us to numerically model different optical schemes (defined by specific problem) of interference meters for contactless measurement of small displacements of the control object surfaces by using two-way laser interferometer with combined branches. This technical solution increases an accuracy of the measurement results during diagnostics of construction materials by acoustic non-destructive testing methods up to 30 % in dependence on used method of processing information, obtained from interference picture. It attains taking into account heterogeneities of distribution of the interference picture optical field.

Based on the proposed models and program software, we performed numerical modeling of intensity distributions of the interference picture optical fields. These results (see Figs. 24.2, 24.3, 24.4 and 24.5) have been obtained at registration of small displacements of the control object surfaces for various versions of optical

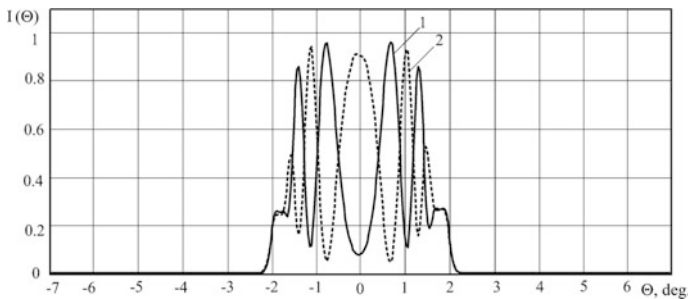


Fig. 24.2 Distribution of intensity in horizontal section of interference picture (beam-splitter is the amplitude sinusoidal grid with parallel polarization)

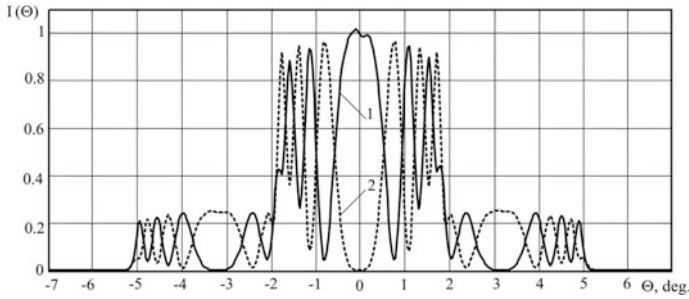


Fig. 24.3 Distribution of intensity in horizontal section of interference picture (beam-splitter is the amplitude sinusoidal grid with perpendicular polarization)

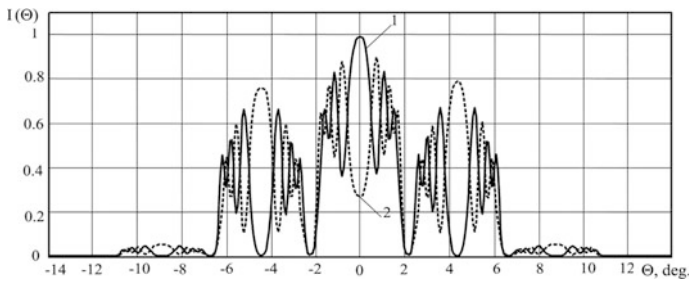


Fig. 24.4 Distribution of intensity in horizontal section of interference picture (beam-splitter is the phase sinusoidal grid)

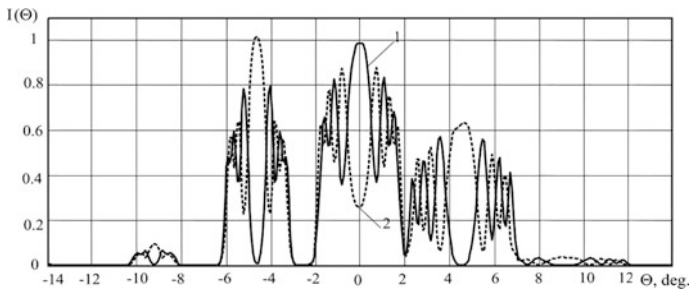
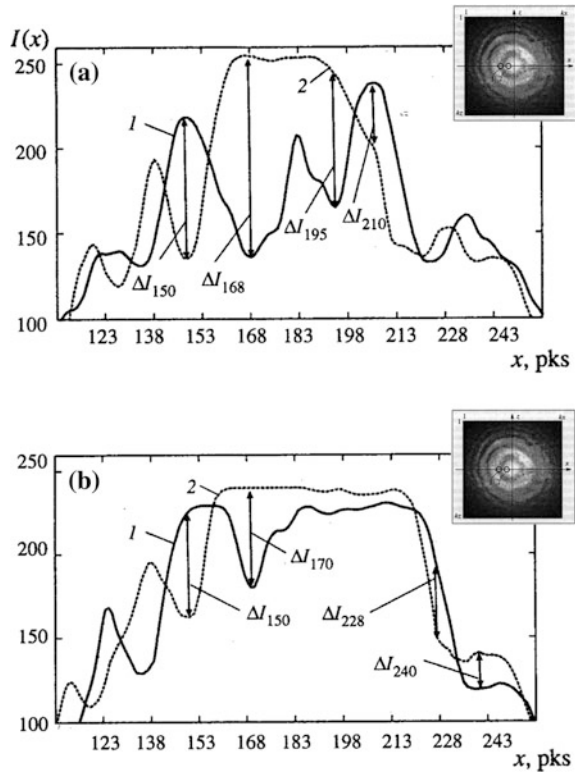


Fig. 24.5 Distribution of intensity in horizontal section of interference picture (beam-splitter is the phase zone plate)

measurement schemes and kinds of beam-splitters. As the beam-splitters, we considered a semitransparent mirror, amplitude sinusoidal grid, amplitude zone plate, phase sinusoidal grid, phase zone plate and amplitude holographic diffraction grid.

The computer simulation results agree well with the test results and operation data.

Fig. 24.6 Distribution of intensity in horizontal section of interference picture (beam-splitter is the phase zone plate)



As an example, Fig. 24.6 presents the computer simulation results of dependencies of variation of the optic field intensity for interference picture in horizontal section for displacements $h = 0$ (curve 1) and $h = \lambda/4$ (curve 2) (where λ is the wavelength of optical radiation of the used laser) for beam-splitter in the form of diffraction grid displayed in contrary beams (a), and for beam-splitter in the form of semitransparent mirror (b). Figure 24.7 presents a scheme of meter of the small displacements with pointed area 11 for registration of optic field intensity of the interference picture.

Above results have been published in necessary details in [1–17].

24.2.2 Method of Contactless Measurement of Small Linear and Angular Displacements

We have developed a novel method of contactless measurement of small linear and angular displacements of the control object surfaces, its theoretical and experimental grounds (mathematical model, program software, results of computer simulation,

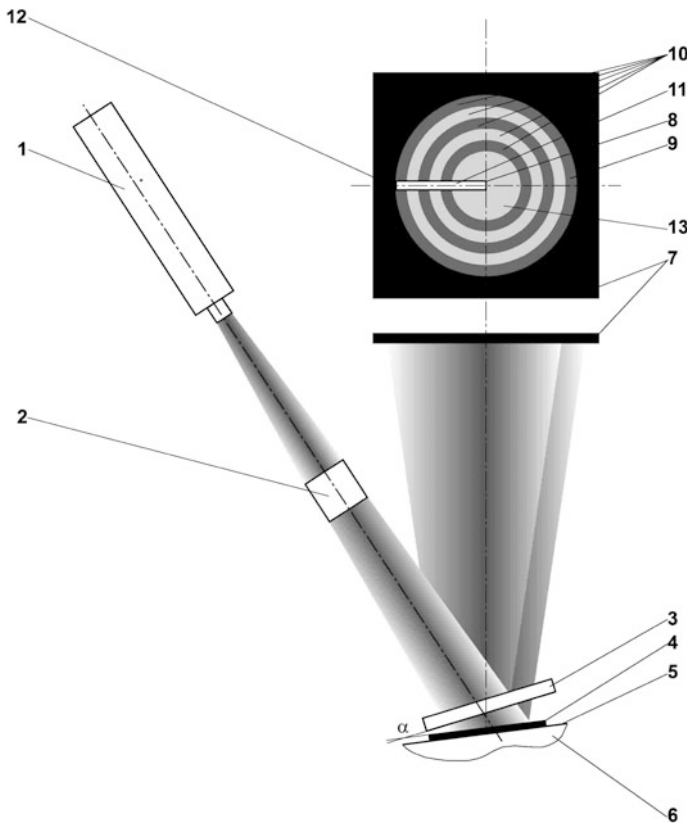


Fig. 24.7 Scheme of meter of small displacements

experimental means, test results, etc.) and technological solution (measurement method), ensuring its realization in solution of scientific-technical problems.

Essence of the proposed solutions consists in that as beam-splitter, it is used sinusoidal diffraction grid; maxima of +1 and -1 orders of interference picture are projected at the screen; the photo-detectors are divided into two groups and placed in areas of the maxima of +1 and -1 orders of the interference picture. The components of small displacement are defined on the base of two values of intensity, measured by using the photo-detector groups, applying dependencies known for each of the maximum. These dependencies couple the intensity with linear and angular displacements. As a result, there are used the values of linear and angular components of displacement, which satisfy simultaneously to the measured intensity at the maxima of +1 and -1 orders.

Significant difference of the technological solution, compared with known analogues, consists in ensuring of possibility of the simultaneous contactless registration of small linear and angular displacements of the control object surface by using only one optical meter. This allows one to extend considerably its functional possibilities.

Figure 24.8 presents optical scheme of the proposed technological solution, and Fig. 24.9 shows dependencies of intensity on linear and angular displacements of the control object surface at -1 (a) and $+1$ (b) maxima of interference picture (solid lines correspond to results of computer simulation and dotted lines show experimental results).

Above results have been published in necessary details in [1, 13, 14, 16–22].

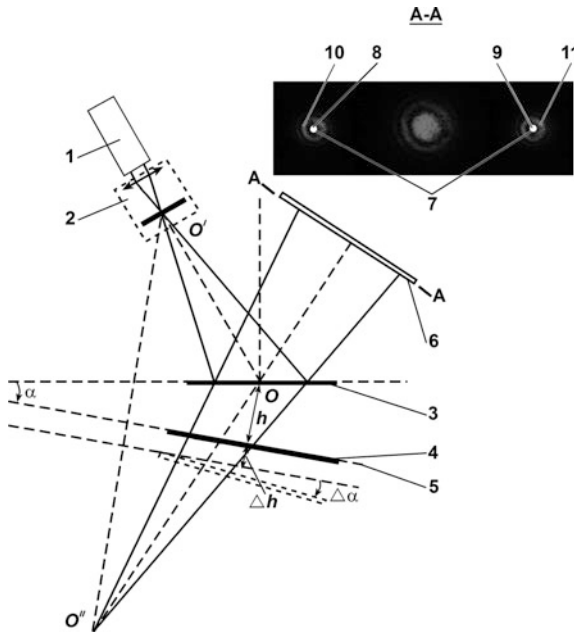


Fig. 24.8 Optical scheme of the proposed technological solution

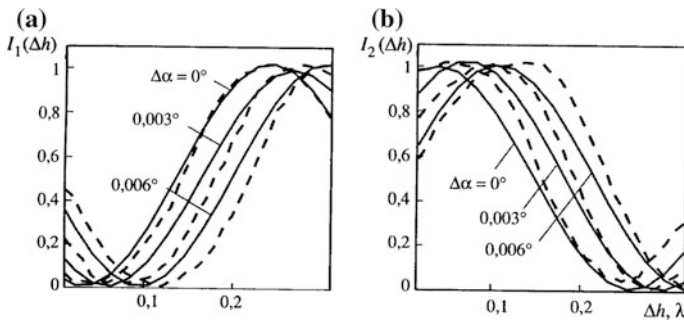


Fig. 24.9 Dependencies of intensity on linear and angular displacements of the control object surface at -1 (a) and $+1$ (b) maxima of interference picture (solid lines correspond to results of computer simulation and dotted lines show experimental results)

24.2.3 Under-Shining Method of Control Object Surface by Laser Interferometer

We have developed a novel method of contactless measurement of displacements of the control object surfaces, consisting in under-shining these surfaces by laser interferometer, its scientific theoretical and experimental grounds (mathematical model, program software, results of computer simulation, experimental means, test results, etc.) and technical solution (measurement device), ensuring its realization in solution of scientific-technical problems.

Essence of the proposed results consists in that the control object is placed after optical scheme, focusing optical radiation on the object surface in the form of a lighting point; beam-splitter, reflector and photo-detector are rigidly fasten on common base, supplied by the displacement mechanism. This mechanism is made with a possibility to increase (decrease) distance between the control object surface and external surface of beam-splitter at increasing (decreasing) a range of measured displacements.

Significant difference of the proposed solution from known analogues is a possibility to change a range of measured values of displacements of the control object surface during experiment without change a measurement scheme by way of alteration of the wave front curvature of the optical radiation reflected from the control object surface. This allows one to extend functional possibilities of the optical interference meter of displacements.

Figure 24.10 presents scheme of the proposed measurement device, and Fig. 24.11 demonstrate the obtained experimental dependence of sensitivity alteration on distance between surfaces of the control object and beam-splitter.

Above results have been published in necessary details in [1, 23–28].

24.2.4 Method of Complex Correction of the Measurement Results of Displacements

We have developed a novel method of complex correction of the measurement results of displacements by using optical interference means, its scientific theoretical and experimental grounds (mathematical model, program software, results of computer simulation, experimental means, test results, etc.) and technical solution (measurement method), ensuring its realization in solution of scientific-technical problems.

The proposed results differ from known analogues that during measurement of displacements of the control object surface, it is registered simultaneously and continuously a summary intensity of optical field by using a square of interference picture, value of which introduces a correction to the measurement results. This allows one to carry out a correction of the measurement results, immediately during

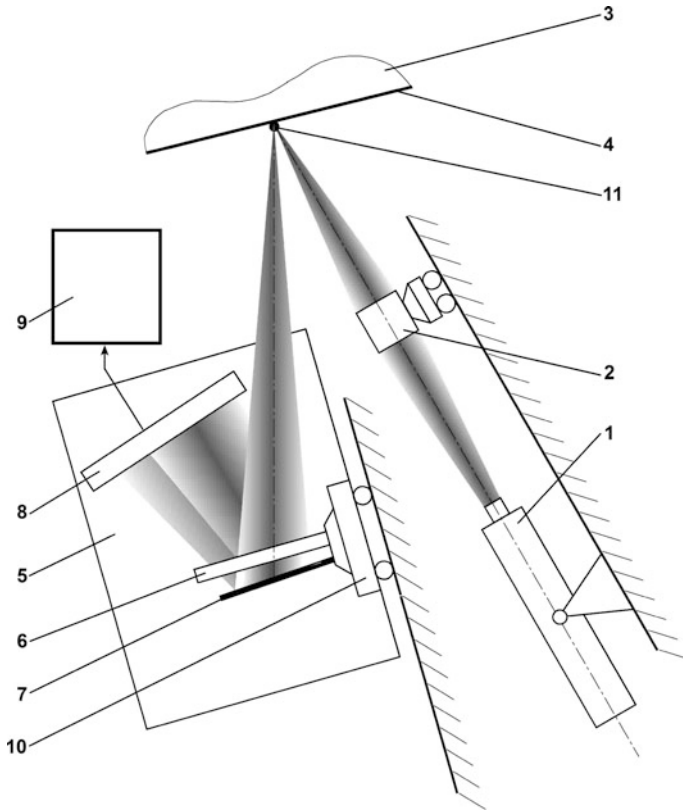
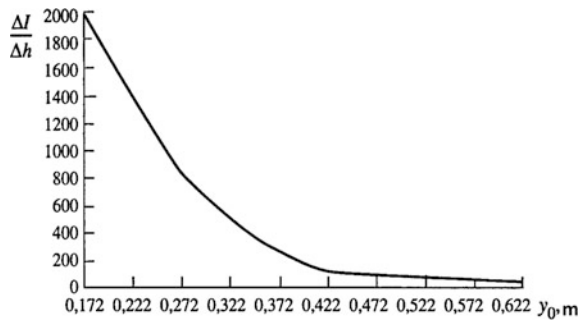


Fig. 24.10 Scheme of the proposed measurement device

Fig. 24.11 Dependence of sensitivity on distance between surfaces of control object and beam-splitter



controlling process (in the same time scale) and increase an accuracy of the measurement results up to 20 % in dependence on excitation amplitude.

Figure 24.12 shows a device scheme realizing the proposed technological solution. Figure 24.13 demonstrates an experimental dependence of summary intensity of optical field of the interference picture during measurement of

displacement of the control object surface (a) and results of direct measurement of displacement of the control object surface (b). The dotted line shows measurement results, and solid line corresponds to measurements after introducing the correction.

Above results have been published in necessary details in [1, 29, 30].

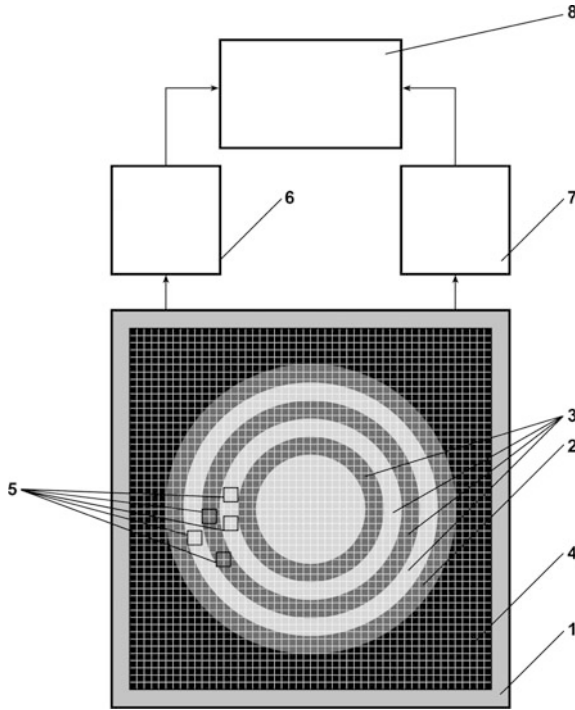


Fig. 24.12 Scheme of device realizing the proposed method

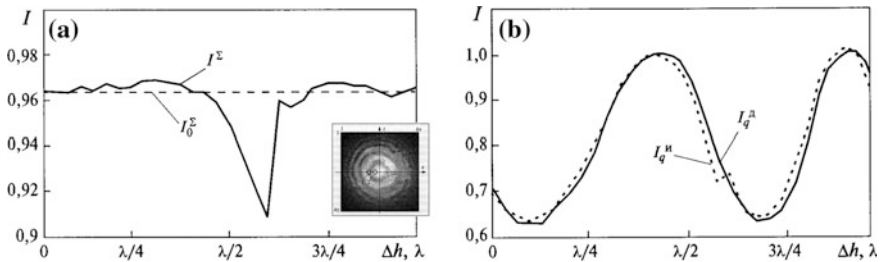


Fig. 24.13 Results of measurements and processing

24.2.5 Method of Increasing Vibro-stability of the Optical Interference Meter

We have developed a novel method of increasing vibro-stability of the optical interference meter based on using its own measurement possibilities, its scientific theoretical and experimental grounds (experimental means, test results, etc.) and technical solution (measurement ground device), ensuring its realization in solution of scientific-technical problems.

The proposed results differ from known analogues by continuous during measurement of displacements of the control object surface, the registration and compensation of influence of the external destabilizing effect (vibrations, impacts, etc.) on the measurement results. They allow increasing an accuracy of the measurement results up to 40 % in dependence of kind of the destabilizing influence.

Figure 24.14 presents a scheme of the proposed technical solution.

Above results have been published in necessary details in [1, 31–33].

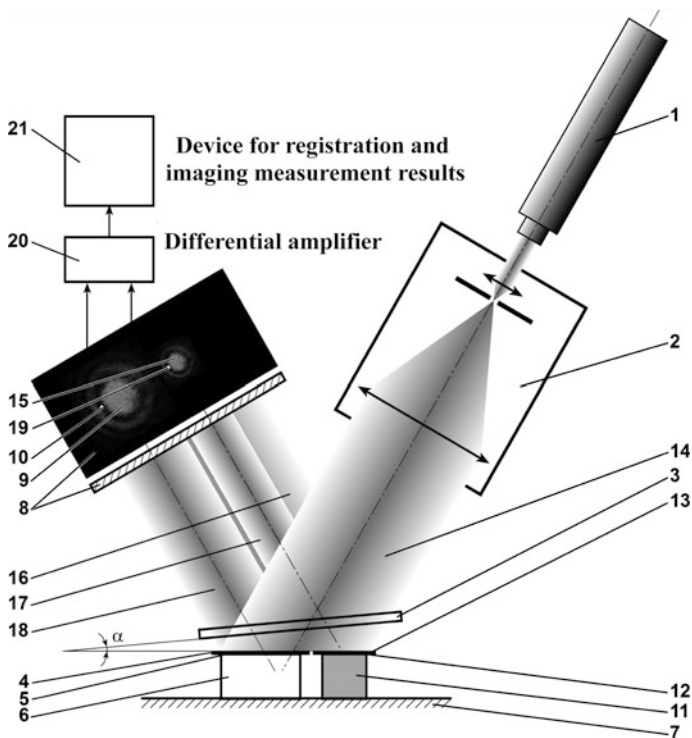


Fig. 24.14 Scheme of device for measurement of small displacements of the control object surfaces, protected of external destabilizing influences

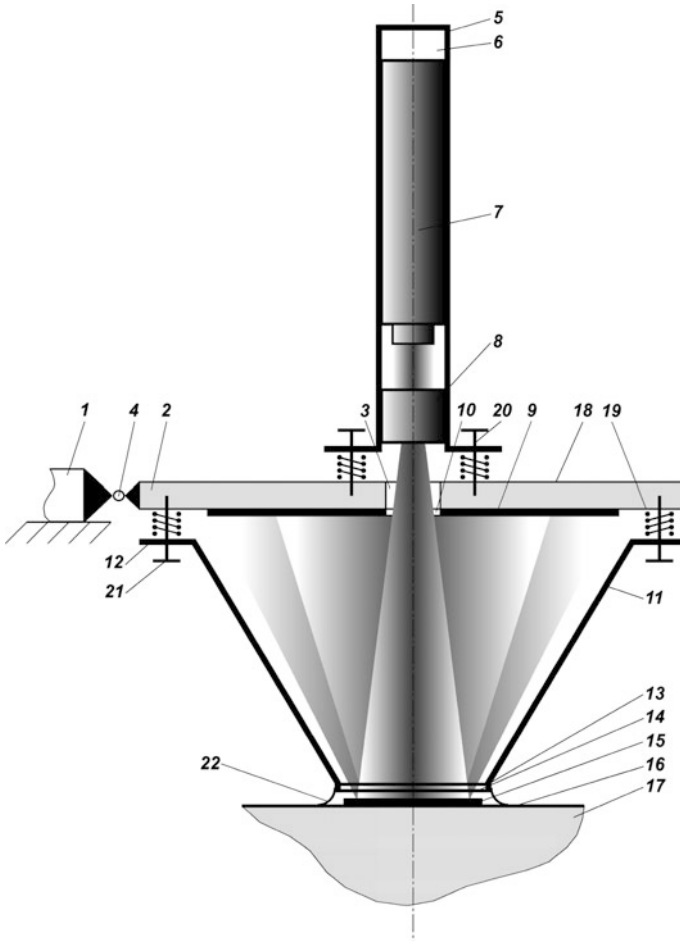


Fig. 24.15 Scheme of device for measurement of small displacements of the control object surfaces for mobile diagnostic complexes

24.2.6 Measurement Devices Realizing the Optical Interference Measurement Methods

We have developed new scientific-grounded technical solutions (measurement devices), realizing the optical interference measurement methods of displacements of the control object surfaces (see Sects. 24.2.1–24.2.5), adapted for using in the structure of stationary and mobile diagnostic complexes.

These measurement devices allow us to ensure solution of measurement problems both as in laboratory conditions, as in “wild” conditions (mobile diagnostic complexes). By this, we reach complete preservation of functional possibilities of

the methods, presented in Sects. 24.2.1–24.2.5, decreasing labor and time expenses on mounting and tuning at preparation of measurements and also during testing.

Figure 24.15 presents scheme of device for measurement of small displacements of the control object surfaces for mobile diagnostic complexes. Figure 24.16 shows

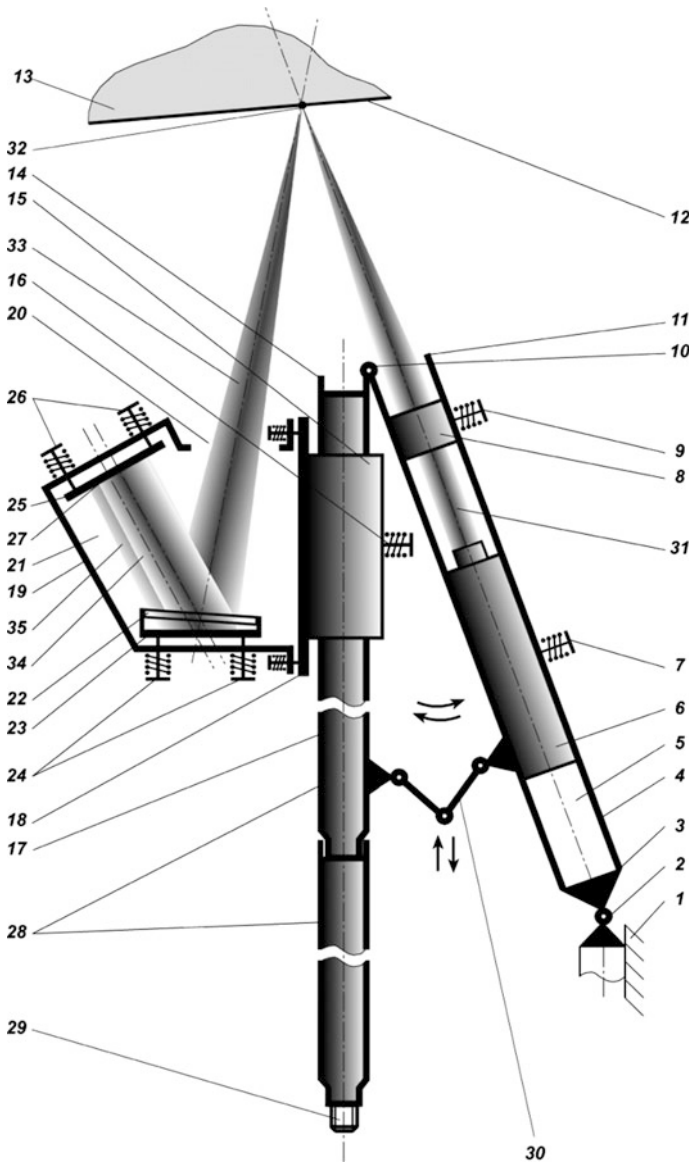
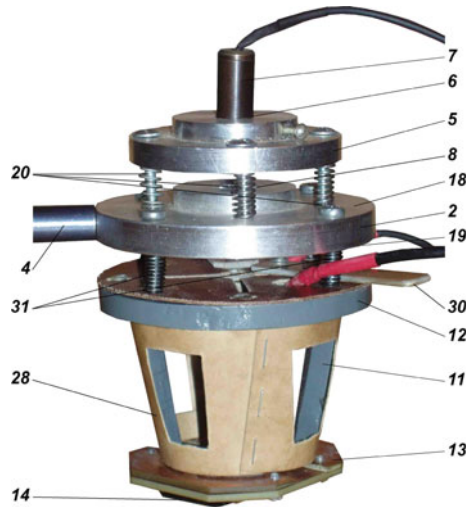


Fig. 24.16 Scheme of device for measurement of small displacements of the control object surfaces for mobile diagnostic complexes with regulated range

Fig. 24.17 Common form of experimental sample of measurement device



scheme of device for measurement of small displacements of the control object surfaces for mobile diagnostic complexes with regulated range. Figure 24.17 demonstrates common form of experimental sample for measurement of small displacements of the control object surfaces.

Above results have been published in necessary details in [9, 10, 31, 34–37].

24.3 Conclusions

The technical and technological solutions have been manufactured in the form of full-scale measurement means, experimental-measurement laboratory devices, demonstration models and used in solution of actual scientific and industrial problems for study of strength characteristics of construction materials, developments of novel methods for quality control of construction materials and goods. Moreover, the obtained results have been used for study of damage processes in high-temperature superconductive tapes [38–41].

These technical and technological solutions and also program software, presented in the chapter, have been awarded by 13 medals and main prizes of the following international salons and exhibitions: “Concours Lepine International Paris 2014”, “Inventions Geneva—2014”, “INVENTICA 2013–2015”, “TunisInnov—2014”, “Tesla Fest—2014”, “Archemede 2013–2014”.

Scientific novelty and significance of the obtained results are confirmed by the Russian patents and certificates on Russian state registration of programs for computer. Reliability of the obtained results is based on the performed modeling and study of functional characteristics of the technical and technological solutions, compared with known analogues.

The obtained results may be applied in high-accuracy measurements of small linear and angular displacements of the control object surfaces at experimental studies of perspective constructions, estimation of their state and diagnostics, investigation of acoustic-emission processes in solids, research of damage in novel materials, consideration of wave processes in layered constructions and anisotropic materials applied in different branches of industry.

Acknowledgments This work was supported in part by the Southern Federal University (No. 213.01-2014/03VG) and Russian Foundation for Basic Research (grant No. 13-08-00754). I.A. Parinov acknowledges financial support from Ministry of Education and Sciences of Russia in the framework of “Organization of Scientific Research” Government Assignment (grant No. 654).

References

1. I.P. Miroshnichenko, I.A. Parinov, E.V. Rozhkov, A.G. Serkin, V.P. Sizov, in *Piezoelectrics and Related Materials: Investigations and Applications*, vol. 238, ed. by Ivan A. Parinov (Nova Science Publishers, New York, 2012)
2. I.P. Miroshnichenko, A.G. Serkin, *Meas. Tech.* **49**(5), 22 (2006)
3. I.P. Miroshnichenko, A.G. Serkin, V.P. Sizov, *Meas. Tech.* **50**(1), 9 (2007)
4. I.P. Miroshnichenko, A.G. Serkin, *Russ. J. Nondestr. Test.* **43**(4), 234 (2007)
5. I.P. Miroshnichenko, A.G. Serkin, V.P. Sizov, *Izv. VUZov. Priborostroenie* **12**, 34 (2007). (In Russian)
6. I.P. Miroshnichenko, A.G. Serkin, V.P. Sizov, *J. Opt. Technol.* **75**(7), 437 (2008)
7. I.P. Miroshnichenko, A.G. Serkin, V.P. Sizov, *Nanotekhnika* **4**, 56 (2008). (In Russian)
8. I.P. Miroshnichenko, A.G. Serkin, V.P. Sizov, in *Common Issues of Radio-electronics* (RNIRS, Rostov-on-Don, 2009), p. 155
9. I.P. Miroshnichenko, *Mod. Sci. Res.* **2** (2014). <http://e-koncept.ru/2014/55188.htm>. (In Russian)
10. Miroshnichenko I., *DOAJ—Lund University: Concept: Sci. Methodological e-magazine, Lund*, **4** (2014). <http://www.doaj.net/2846/>
11. I.P. Miroshnichenko, I.A. Parinov, E.V. Rozhkov, A.G. Serkin, Optical device for measurement of displacements. Russian Patent No. 2373492, 11.20.2009 (In Russian)
12. I.P. Miroshnichenko, A.G. Serkin, Program for calculation of optical field intensity of the interference picture. Certificate on Russian State Registration of Program for Computer No. 2008614831(2008) (In Russian)
13. I.P. Miroshnichenko, Program for Calculation of optical field intensity of the interference picture (Case of Perpendicular Polarization). Certificate on Russian State Registration of Program for Computer No. 2014614501 (2014) (In Russian)
14. I.P. Miroshnichenko, Program for calculation of optical field intensity of the interference picture (Case of Parallel Polarization). Certificate on Russian State Registration of Program for Computer No. 2014614502 (2014) (In Russian)
15. I.P. Miroshnichenko, V.A. Shevtsov, Program for calculation of optical field intensity of the interference picture, created by laser two-way interferometer with combined branches. Certificate on Russian State Registration of Program for Computer No. 2014662261 (2014) (In Russian)
16. I.P. Miroshnichenko, I.A. Parinov, Definition of optical field intensity of interference picture, created by laser interferometer, for beam-splitter in the form of phase sinusoidal grid with uniform period. Certificate on Russian State Registration of Program for Computer No. 2015610921 (2015) (In Russian)

17. I.P. Miroshnichenko, I.A. Parinov, Definition of optical field intensity of interference picture, created by laser interferometer, for beam-splitter in the form of phase zone plate. Certificate on Russian State Registration of Program for Computer No. 2015611078 (2015) (In Russian)
18. I.P. Miroshnichenko, A.G. Serkin, *Russ. J. Nondestr. Test.* **44**(5), 318 (2008)
19. I.P. Miroshnichenko, *Control. Diagnostics* **1**, 45 (2010). (In Russian)
20. I.P. Miroshnichenko, A.G. Serkin, *Control. Diagnostics* **7**, 46 (2011). (In Russian)
21. I.P. Miroshnichenko, *South-Siberian Scientific Vestnik* **2**, 149 (2014). (In Russian)
22. I.P. Miroshnichenko, A.G. Serkin, V.P. Sizov, Method of measurement of the linear and angle displacements. Russian Patent No. 2388994, 05.10.2010 (In Russian)
23. I.P. Miroshnichenko, I.A. Parinov, S.H. Chang, in *Advanced Materials—Studies and Applications*, vol. 437, ed. by Ivan A. Parinov, Chang Shun-Hsyung, Somnuk Theerakulpisit (Nova Science Publisher, New York, 2015)
24. V.E. Alekhin, I.P. Miroshnichenko, V.P. Sizov, *Russ. J. Nondestr. Test.* **43**(2), 113 (2007)
25. V.E. Alekhin, I.P. Miroshnichenko, V.A. Nesterov, V.P. Sizov, *Russ. J. Nondestr. Test.* **43**(9), 592 (2007)
26. V.E. Alekhin, I.P. Miroshnichenko, A.G. Serkin, *Meas. Tech.* **51**(10), 26 (2008)
27. I.P. Miroshnichenko, *Control. Diagnostics* **2**, 34 (2010). (In Russian)
28. V.E. Alekhin, I.P. Miroshnichenko, A.G. Serkin, V.P. Sizov, Optical device for measurement of displacements of the control object surfaces. Russian Patent No. 2343402, 01.10.2009 (In Russian)
29. I.P. Miroshnichenko, A.G. Serkin, *Sens. Syst.* **3**, 28 (2008). (In Russian)
30. V.E. Alekhin V. E., Miroshnichenko I. P., Serkin A. G., Sizov V. P., *Registration Method of Displacements by Optical Transducers*. Russian Patent No. 2343403, 01.10.2009 (In Russian)
31. I.P. Miroshnichenko, I.A. Parinov, E.V. Rozhkov, V.P. Sizov, V.A. Shevtsov, in *Physics and Mechanics of New Materials and Their Applications*, vol. 145, ed. by Ivan A. Parinov, Chang Shun-Hsyung (Nova Science Publishers, New York, 2013)
32. I.P. Miroshnichenko, V.A. Shevtsov, *Polzunov Vestnik* **2**, 66 (2014). (In Russian)
33. I.P. Miroshnichenko, V.A. Nesterov, A.G. Serkin, V.P. Sizov, V.A. Shevtsov, Interference meter of small displacements. Russian Patent No. 2410642, 01.27.2011
34. I.P. Miroshnichenko, *Polzunov Vestnik* **2**, 95 (2014). (In Russian)
35. I.P. Miroshnichenko, I.A. Parinov, E.V. Rozhkov, A.G. Serkin, Device for testing thin specimens on bending. Russian Patent No. 2376567, 12.20.2009 (In Russian)
36. I.P. Miroshnichenko, I.A. Parinov, E.V. Rozhkov, A.G. Serkin, Device for measurement of displacements. Russian Patent No. 2407988, 2010 (In Russian)
37. I.P. Miroshnichenko, I.A. Parinov, E.V. Rozhkov, Optical interference device for measurement of displacements of control object surfaces. Russian Patent No. 2512697 (2014) (In Russian)
38. I.P. Miroshnichenko, I.A. Parinov, E.V. Rozhkov, A.G. Serkin, *Metallurgist* **50**(7–8), 408 (2006)
39. I.P. Miroshnichenko, A.G. Serkin, *Metallurgist* **54**(3–4), 189 (2010)
40. I.P. Miroshnichenko, *Mod. Sci. Res.* **3** (2015). <http://e-koncept.ru/2015/85842.htm>. (In Russian)
41. I.P. Miroshnichenko, DOAJ—Lund University: Concept: Scientific and Methodological e-magazine, Lund, **7** (2015). <http://www.doaj.net/5062/>

Chapter 25

Material Temperature Measurement Using Non-contacting Method

Muaffaq Achmad Jani

Abstract It is necessary for setting up and controlling the substrate temperature during the plasma process. The temperature of the substrate material during the process will affect the quality of equipment produced. The measurements, using laser interferometry being a non-contacting method, can be carried out to overcome the problems that exist during the material temperature measurement of substrate surface changes and plasma conditions. The result of measurement was average temperature of material. The material, used for this experiment, was LiNbO_3 with a thickness of several millimeters. Average temperature changes over a certain period of time were measured. Temperature change is measured during a plasma process using argon gas and the RF input mounted ~ 100 W. The temperature equilibrium is affected by the heat transfer coefficient and the input power of plasma Q . From this, it can be determined the relationship between ΔT_{\max} and Q , and from calculations using values $h = 28 \text{ W/m}^2 \text{ }^\circ\text{C}$ and $Q = 10 \text{ W}$, we obtained the value of the equilibrium temperature is $30 \text{ }^\circ\text{C}$.

25.1 Introduction

In the plasma process, a temperature of substrate material will affect the quality of the equipment produced during the process [1]. It is necessary for the setting and control of the substrate temperature during the plasma processing [2, 3]. Measurements with contact methods such as thermocouple lead to problems such as changes in the substrate surface and the plasma conditions. In this case, the required measurements use indirect contact method to solve the existing problem during the measurement [4, 5]. The method of observations, based on thermal expansion, can be used by applying laser interferometry to measure the temperature of a substrate [6, 7]. According to recent research, there are different methods to measure sub-

M.A. Jani (✉)

Information Engineering Department, Faculty of Engineering,
University of 17 Agustus 1945, Surabaya, Indonesia
e-mail: muaffaqjani@gmail.com; muaffaq@untag-sby.ac.id

strate material during plasma processing. The measurements using He–Ne laser interferometry, being a non-contacting method, can be carried out to overcome the problems that exist during the material temperature measurement of substrate surface changes and plasma conditions. Transparent material such as poly(methyl methacrylate), more often called PMMA, is a commonly thermoplastic polymer, has been used experimentally for measurements by Fujiwara et al. [5]. The beam of He–Ne laser is delivered through a glass material such as PMMA, during plasma processing. The substrate thickness d (in mm), will be affected by change of temperature ΔT , and will have expansion of length on Δd . The thickness change of an object is one of the more obvious thing, which depends on temperature as

$$\Delta d = d_0 \alpha \Delta T, \tag{25.1}$$

where α is the coefficient of thermal expansion, d_0 is the initial length of material, Δd is the change of material thickness, ΔT is the change of material temperature.

Method of laser measurement is present in Fig. 25.1. By using a concept on dependence of material expansion on the change of temperature, the temperature change during the experiment can be calculate on the base of (25.1).

The output change of material expansion is measured by using change of thickness d affected by change of temperature T , which in its turn recorded by using xy -recorder during plasma processing. A result of this recording is present in Fig. 25.2.

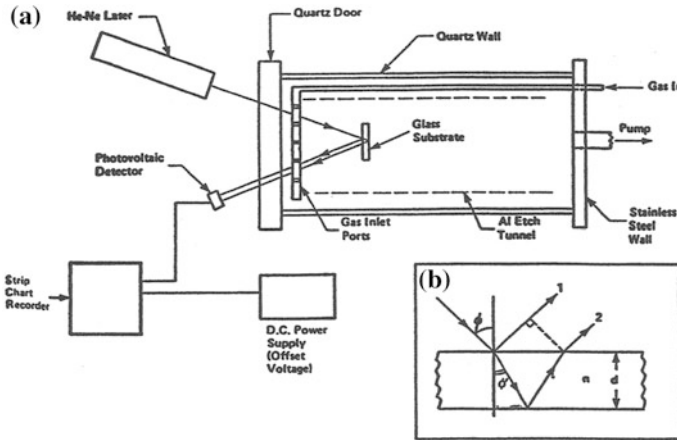


Fig. 25.1 Method of laser beam measurement

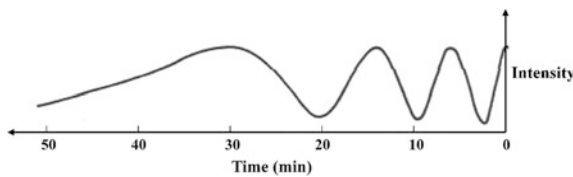


Fig. 25.2 Output of recorder

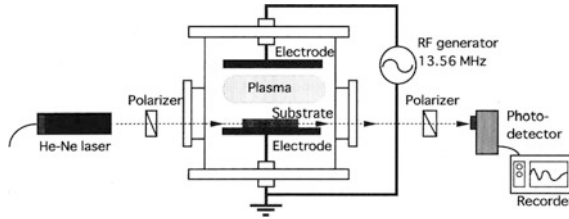


Fig. 25.3 Experimental set up

25.2 Experimental Set Up

The experimental set up, shown in Fig. 25.3, allows one to generate Radio Frequency (RF) glow discharge plasma by using argon gas in the reactor chamber.

Power of RF with frequency of 13.56 MHz has electrodes connected to the top of the reactor. The material is a LiNbO_3 crystal, used as the substrate and placed on bottom of electrode, and a water cooler is connected to ground. He-Ne laser beam with a diameter of 1 mm polarized by a polarizer is passed to the substrate. Retardation δ of phase difference, caused by light coming out of the chamber, is recorded and calculated as

$$\delta = \frac{2\pi \cdot \Delta n \cdot l}{\lambda}, \tag{25.2}$$

where λ is the laser beam wave length, Δn is the birefringence index, l is the substrate length.

The results of measurements by a recorder of the obtained interference output laser beam in the average of period equivalent to $T = 0.74 \text{ }^\circ\text{C}$.

25.3 Experimental Results

The experimental results for the obtained function of temperature change with time can be defined in the form:

$$\Delta T = \Delta T_{\max} \{1 - \exp(-t/\tau)\}, \tag{25.3}$$

where ΔT_{\max} is the maximum temperature rise and τ is a time constant.

Figure 25.4 shows the dependence of phase on temperature, which is defined as the linear temperature increase with the phase change.

Figure 25.5 demonstrates the substrate temperature changes over time. From the experimental results, electron density measured by a probe, will increase if the gas pressure increases, affected by change of substrate temperature. In the plasma process, the substrate surface temperature is very important information, while the

Fig. 25.4 Change of phase versus change of material temperature

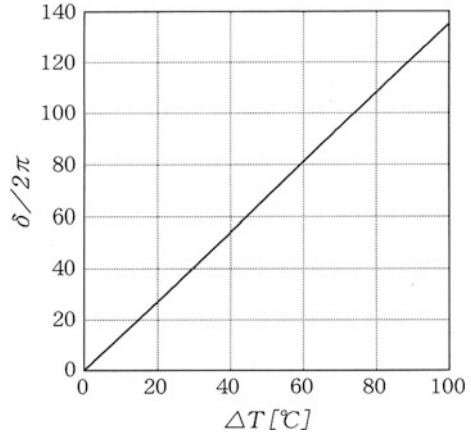
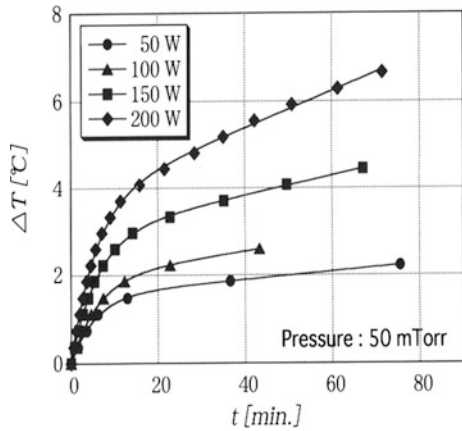


Fig. 25.5 Substrate temperature changes over time



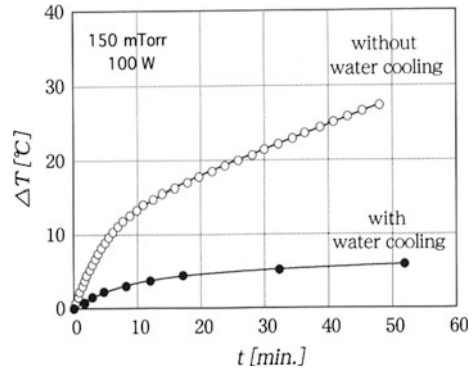
measurement results in this method shows the average temperature in the substrate. By using the numerical method of analysis [8], the temperature distribution of the substrate thickness can be calculated by using the following heat conduction equation for solids:

$$c\rho \frac{\partial T}{\partial t} - k \frac{\partial^2 T}{\partial x^2} = 0, \tag{25.4}$$

where $T = T(x, t)$ is the temperature, c is the specific heat, ρ is the mass density, k is the thermal conductivity, x is the thickness coordinate.

Let, an initial condition has the form: $T(d_0, 0) = T_0$.

Fig. 25.6 Change of temperature with a water cooler



The boundary condition on the upper surface of the substrate ($x = 0$) is defined as

$$k \frac{\partial T}{\partial x} = -Q/A. \tag{25.5}$$

At the bottom of the substrate ($x = d_0$), we have

$$k \frac{\partial T}{\partial x} = -h\{T(d_0, T) - T_0\}, \tag{25.6}$$

where Q is the input power from the plasma, A is the surface area of substrate, h is the heat transfer coefficient.

Figure 25.6 shows the change in the substrate temperature at 100 mTorr and 100 W; by using such changes, we obtained heat transfer coefficient (h) as a parameter to $Q = 10$ W. From the simulation results, we find a change in the coefficient of heat transfer, resulting at changes in the temperature of the substrate and time constants. Analysis of the experimental results, showed that by using a water-cooling, the water heat transfer coefficient was $h = 30 \text{ W/m}^2 \text{ }^\circ\text{C}$, and free air heat transfer coefficient was $6 \text{ W/m}^2 \text{ }^\circ\text{C}$. The temperature equilibrium is affected by the coefficient of heat transfer and input power of plasma Q . It can be determined by the relationship between ΔT_{max} and Q . Then by using the values of $h = 30 \text{ W/m}^2 \text{ }^\circ\text{C}$ and $Q = 10$ W, we obtain the value of the equilibrium temperature equal to $30 \text{ }^\circ\text{C}$.

25.4 Conclusions

The temperature of anisotropic substrate can be measured using laser interferometry. Change of bias voltage can be used to adjust the heat flux of plasma to the substrate surface. The calculation results showed that only 10 % of the installed power affects the substrate (heat flux value of $Q \sim 10 \%$ of power). The time constant of the substrate temperature rise in the case of water cooler is smaller than in the case of air cooler.

References

1. R.A. Bond, S. Dzioba, H.M. Naguib, *J. Vac. Sci. Technol.* **18**, 335 (1981)
2. T. Fujiwara, H. Yamada, *Rev. Sci. Instrum.* **65**, 267 (1994)
3. S. Yoges, S. Eckehard, in *Seventh International Conference on CFD in the Minerals and Process Industries CSIRO*, Melbourne, Australia (2009)
4. M.A. Jani, in *IEE-Tohoku Region Conference*, 2H14 (1994)
5. T. Fujiwara, M.A. Jani, M. Itagaki, H. Yamada, *Jap. Soc. Appl. Phys. Proc. IIC17*, **253** (1995)
6. K. Takaki, K. Sayama, A. Takahashi, T. Fujiwara, M. Nagata, M. Ono, M.A. Jani, *Electr. Eng. Jpn.* **127**(4) (1999)
7. T. Griniys, S. Tamulevicius, M. Zadvydas, *Mater. Sci.* **10**(3) (2004)
8. M.A. Jani, *J. Adv. Mater. Res.* **931–932**, 397 (2014)

Chapter 26

Microstructure and Interface Bottom Ash Reinforced Aluminum Metal Matrix Composite

Muslimin Abdulrahim and Harjo Seputro

Abstract Composites are one kind of new materials that continue constantly to develop. As a new composite material, we propose a solution overcoming the limitations of existing material, namely a composite structure consisting of two or more components with different material properties. In this composite, one component acts as reinforcement and the other as binder. They form a structure with combined properties are better than corresponding composite materials demonstrating several advantages such as light weight, strength, good rigidity and low production cost. T6 heat treatment process ensures the dissolving solution treatment in which the specimen heats at a temperature of 580 °C and held for 6 h in state of rapidly cooled specimen with water down to room temperature. Furthermore, we study the process of aging at which the specimen heats again with various temperatures determined for first sampling of nine specimens as a temperature 160 °C during 3, 5, and 7 h. Then second sampling of nine specimens heated under temperature 180 °C during 3, 5, and 7 h, and third nine specimens was at temperature 180 °C during 3, 5, and 7 h, and then slowly cooled to room temperature. From the analysis of the reaction product by EDX testing, the microstructure formed at the interface between matrix and reinforcement before T6 heating and then was treated by the T6 heat treatment at a temperature 200 °C with holding time for 3, 5, and 7 h. The result remained the same, namely a new compound, that is, $\text{Al}_2\text{MgSiO}_4$ formed, moreover formed additional element having different concentrations for various holding time.

M. Abdulrahim (✉)

Industrial Engineering Department, University of 17 Agustus 1945,
Surabaya, Indonesia

e-mail: musliminabdulrahim@untag-sby.ac.id

H. Seputro

Mechanical Engineering Department, University of 17 Agustus 1945,
Surabaya, Indonesia

e-mail: harjoseputra@untag-sby.ac.id

26.1 Introduction

26.1.1 Background

Into framework of the study, the composite of matrix—reinforcement type produced a combination of different mechanical characteristics in comparison with each basic characteristic of both matrix and reinforcement, considered separately, because of the existence of an interface between the two components. The interface was a planar area of a micron thickness with infinitely small volume. Classically, an interface is the surface between matrix and reinforcing component, presenting a contact of two coupled components. Interface could be in the form of simple atom or in the form of a reaction occurring in the layer between matrix and reinforcing component. In the study, the matrix had good mechanical characteristics, so that it could serve as a couple. It coupled other structures inside the composite. Reinforcing component inside the composite was the main material for the composite to serve as reinforcement to make the composite light and stiff. This phenomenon was influenced by the interface, which existed between the matrix and reinforcement. The interface of the composite influenced the composite characteristics as well. Because the interface contributed in the process of transferring load between matrix and reinforcement, the strong interface intensified force and vice versa [1].

26.1.2 Objective of the Research

This research aims to discovering influence of various temperatures and aging time of T6 heating on microstructure of interface existing between matrix and reinforcement made of coal ash-aluminum composite.

26.2 Review of Related Results

26.2.1 Composite Characteristics and Features

Characteristics and features of the composites determined by the following factors [2]:

- (i) *Materials composing the composite*: the composite characteristics determined by its composing materials. Theoretically, it could be determined so that they would be proportionally comparable.
- (ii) *Shape and structure of the composite components*: sizes of the components and boundary of the composite influenced on the characteristics of the composite.
- (iii) *Interaction between the components*: when there was an interaction between the components, the properties of the composite improved.

26.2.2 Wettability

Wettability is the matrix liquid capacity spreads on the surface of solid. If the liquid has good wettability, this liquid is capable to cover all of the holes and contours of a rough surface, in the result intensifying and providing airlessness. The capacity of soaking and reactivating determines the quality of the structure of both materials because, in turn, it will effect on the final characteristics of the composite. Several methods are applied to improve compatibility of the two materials, such as adding two mixed elements covering ceramic reinforcement. The capacity of soaking is estimated at the contact point of metal and ceramic.

26.2.3 Interface

Interface is the surface between matrix and reinforcing component and matrix determines the process of transformation of the matrix and reinforcing component tension. The separate area of the interface is the plane with only some atomic thickness and the transformation occurs in this area. Concerning the characteristics of the matrix in respect to reinforcement, note the interface has a natural chemical discontinuity of structural and molecular properties, mechanical characteristics and so on.

One of the functions of matrix is transferring to the reinforcement the loads applied to the composite. This process of transferring load in the composite is caused in main by the interface between the matrix and reinforcement. The fracture behavior of the composite depends on the interface, as well.

26.2.4 SEM-EDX

Energy dispersive spectroscopy-X (EDX) is used to identify the types of atoms on the surface containing multiple atoms. Most of SEM tools are equipped with this capacity, but no all SEM setups have this addition. EDX produces information obtained from X-ray radiation in the result of the process when electron, disposed outside surface migrates in depth of the surface, whenever an atomic surface contains energy. This is required condition for the electron located outside surface to release a part of its energy in order to be capable to move in depth of the surface. The released energy radiates in the form of X-rays.

The energy, released by electron in the form of X-rays, is detected and counted by EDX, in the result, demonstrating some graphic peaks, corresponding to the contained substances. EDX is also able to perform elemental mapping providing different color for each of the substances on the material surface. EDX can also be used to analyze quantitatively the fraction percentage of each element [3].

The distinction of the description of the secondary electronic signal from backscattered are following:

- (i) the topography of the analyzed sample shows a brighter color for a higher surface and a darker color for a lower surface,
- (ii) the electronic backscattered provides different weights of atomic molecules located at surface; heavier atomic molecules will have brighter color than lighter atomic molecules.

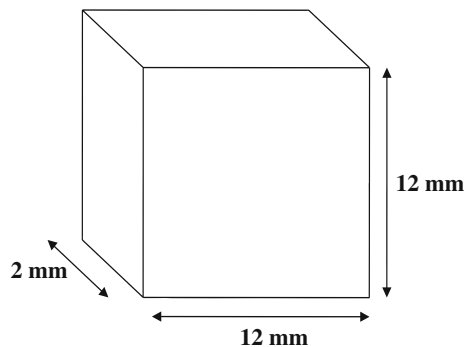
26.3 Research Method

This research was conducted in several stages. First, we prepared the materials and tools. Using a saw, the composites were cut into small pieces for fulfilling the standard SEM-EDX experiments. They had the following sizes: 2 mm thick, 12 mm long, 12 mm wide, and a whole sampling consisted of 27 specimens. Second, we refined the specimens using sandpaper moving in turn direction from 400, 800, 1000 to 1200 mesh.

The next stage was to conduct a SEM-EDX test in which Zeiss-Bruker tool was used to carry out the test. The steps of the test were the following:

- (i) The preparation stage before conducting the SEM-EDX test included:
 - preparing pins in the same amount as the number of tested specimens
 - preparing carbon tape
 - preparing specimen
 - standard sizes of the specimens in SEM-EDX tests: $2 \times 12 \times 12 \text{ mm}^3$, see Fig. 26.1
 - attaching the carbon tape on the pins (the carbon tape applied in the tool to stick the specimen on the pin)
 - sticking the specimens on the carbon tape pins

Fig. 26.1 Standard sizes of the specimens in SEM-EDX tests



- (ii) Putting the specimens into testing tool by using the following steps:
- open the nitrogen regulator until it points 0.1 bar in order to let out the air that enables to open the chamber
 - open the chamber (the door of the testing tool)
 - put the specimens inside the chamber
 - close the chamber
 - press the pump existing in a tool namely adixen in order to keep vacuum inside the testing tool
- (iii) Next stage is the study:
- search the image that has been obtained by SEM using an analog
 - mark the image that be taken
 - if next image has the same result as previous, press *equal*, for example: first, the thing we are looking is morphology, and the next specimen is morphology, then we do not need to look it again and again, at pressing the *equal*, the program will find it automatically
 - in order to conduct EDX test, we mark the area that will be studied by EDX, and then press EDX
 - saving and insertion of the image in CD
 - examination process.

The examination process aims to know which microstructure exists at interface between matrix and reinforcing component before fulfillment of the T6 heat treatment process. This microstructure compares with the specimen heated by T6 being Thermolyne Furnace Type 30400. The steps of the T6 heating process consist in carrying out dissolution with treatment of solution, which is the specimen, heated at the temperature of 580 °C for 6 h, and then quenched; the specimen cools down with water to room temperature.

After that, the next process was aging; samples reheated with various temperatures: first sampling of 9 specimens hold during 3, 5, 7 h at temperature 160 °C, second sampling of 9 specimens hold during 3, 5, 7 h at temperature 180 °C, and third sampling of 9 specimens hold during 3, 5, 7 h at temperature 200 °C.

After that, we carried out the SEM-EDX test, in which Zeiss-Bruker tool was used to conduct the test. This test was aimed to know which kind of microstructure arose inside interface between matrix and reinforcing component after T6 heat treatment at the variation of temperature and aging time. Moreover, we compared the obtained data with results for other specimens that did not heat preliminary by the T6. We related the data analysis of T6 heat treatment to microstructure and reaction product at interface between matrix and reinforcement, made of aluminum composite, namely the basic ash from coal.

26.4 Data and Discussion

26.4.1 Testing Results

Observations of the interface between matrix and reinforcement obtained its SEM-image and EDX results, presented in Figs. 26.2, 26.3, 26.4 and 26.5.

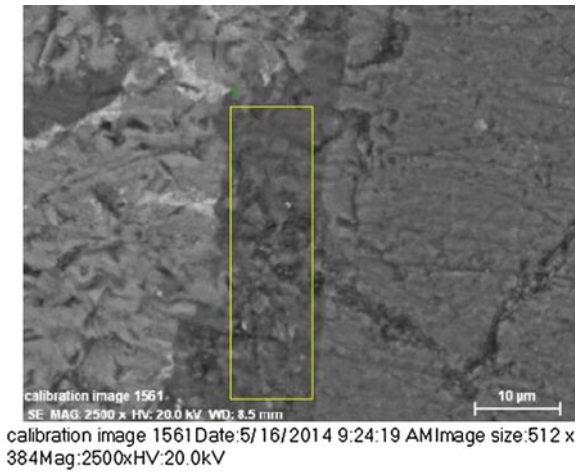


Fig. 26.2 SEM testing result of interface between matrix and reinforcement

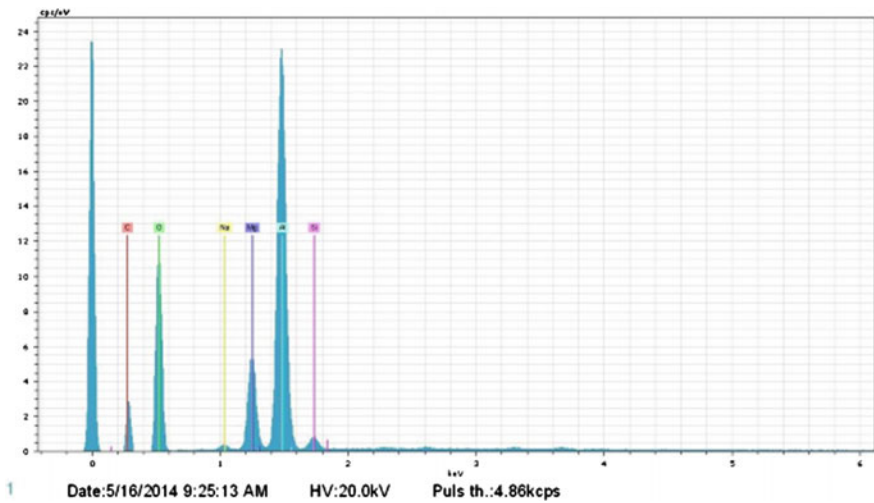


Fig. 26.3 EDX peaks, corresponding to the new compound (Al_2MgSiO_4) at the interface

El	AN	Series	unn. C [wt.%]	norm. C [wt.%]	Atom. C [at.%]	Error [%]
C	6	K-series	8.51	7.87	12.18	1.1
O	8	K-series	54.32	50.25	58.39	6.2
Na	11	K-series	0.29	0.27	0.22	0.0
Mg	12	K-series	8.11	7.50	5.74	0.5
Al	13	K-series	35.78	33.09	22.80	1.7
Si	14	K-series	1.10	1.01	0.67	0.1
Total:			108.10	100.00	100.00	

Fig. 26.4 Test data showing formation of Al_2MgSiO_4 compound at interface

calibration image 21 1204Date:5/16/2014 9:29:59 AMImage size:72 x 260Mag:2500xHV:20.0kV



Fig. 26.5 Color image of Al_2MgSiO_4 compound at the interface

26.4.2 Discussion

From the SEM testing result, we found that in the scale of interface between matrix and reinforcement takes place a reaction (a new compound— Al_2MgSiO_4 arises). EDX-analysis confirmed existence of this compound.

26.5 Conclusion

EDX analysis confirmed that the reaction product is the microstructure, formed at the interface between matrix and reinforcement, before T6 heating in the result of the T6 heat treatment at a temperature of 200 °C. At the holding time of 3, 5, 7 h, the results remain the same, and the new compound— $\text{Al}_2\text{MgSiO}_4$ creates at the interface. Moreover, it is formed the element having different concentrations at various holding times. The highest concentration of oxygen (maximum value) arises at the holding time of 3 h and at holding time of 7 h, we obtained the lowest oxygen concentration (minimum value).

References

1. H.J. Dudek, *Frezeniusus Zeitschrift fur Analytische Chemie* **333**, 422 (1989)
2. D. Huang, L. Froyen, M. Wevers, *Quality Control and Nondestructive Tests. MMC-Assess Thematic Network* **5** (2004)
3. P. Merle et al., *Metallographic Preparation of Metal Matrix Composites. MMC-Assess Thematic Network* **3** (2009)

Part III
Mechanics of Advanced Materials

Chapter 27

Some Models for Nanosized Magnetolectric Bodies with Surface Effects

A.V. Nasedkin and V.A. Eremeyev

Abstract The dynamic problems for piezomagnetolectric nanosized bodies with account for damping and surface effects are considered. For these problems, we propose the new mathematical model, which generalizes the models of the elastic medium with damping in sense of the Rayleigh approach and with surface effects for the cases of piezoelectric and magnetolectric materials. For solving these problems, the finite element approximations are discussed. A set of effective finite element schemes is examined for finding numerical solutions of weak statements for transient, harmonic, modal and static problems within the framework of modeling the piezomagnetolectric nanosized materials with surface effects.

27.1 Introduction

Recently, it is well established that nanostructured materials have abnormal but promising properties, which may entirely different from conventional macromaterials. One of the reasons responsible for such a behavior of nanomaterials is the surface-related phenomena. Surface-enhanced models of continua for modeling of material behavior at the nanoscale are discussed in [1–3] where almost the Gurtin–Murdoch model of surface elasticity is used which was originally introduced in [4]. From the physical point of view, the model [4] can be interpreted as a model of deformation of elastic solids with attached on its surface elastic film which properties are described by additional constitutive equations for surface strains and

A.V. Nasedkin (✉) · V.A. Eremeyev

I.I. Vorovich Institute of Mathematics, Mechanics and Computer Sciences,
Southern Federal University, Rostov-on-Don, Russia
e-mail: nasedkin@math.sfedu.ru

V.A. Eremeyev
Otto-Von-Guericke-University at Magdeburg, Magdeburg, Germany

V.A. Eremeyev
Southern Scientific Center of Russian Academy of Sciences, Rostov-on-Don, Russia

stresses. For the bodies of submicro- and nanosizes the surface stresses play an important role and influence the deformation of the bodies in general. For example, it changes the behavior of solutions near crack tips, holes, notches, see [5]. In particular, the Gurtin–Murdoch model predicts the size-effects observed in the case of nanomaterials, see [1, 6–8] and reference therein. Mathematical studies of the boundary-value problems of the linear elasticity with surface stresses are provided through various methods in [9–11], see also [12], where the general framework of weak solutions of problems with boundary reinforcements is discussed.

Recently, in several works, the pure mechanical theory of elasticity with surface stresses was extended for piezoelectric and flexoelectric solids, see [13–16] among others. This extension is important since many nanostructured materials exhibit coupling between electromagnetic field and elastic strains, see for example [17, 18]. As a result, one can apply classic methods used for example for control and vibrations damping [19–21] to construct NEMS [22, 23]. In the one of the first papers concerned surface effects for active materials [13], it was proposed the new model of a nanosized piezoelectric solid with introduction into the functional of energy surface integrals depending on the surface stresses and strains. Later coupled constitutive relations for surface mechanical, electric and magnetic fields were proposed in [24] for magnetoelectric nanosized bodies in order to model the bending of nanobilayers. Nevertheless, the rigorous theory of nanosized piezoelectric and magnetoelectric solids is still under development.

The main goal of our investigation is to present the mathematical study of the dynamic boundary-value problems for magnetoelectric solids with damping, surface stresses, surface electric fields and surface magnetic fields. In the chapter, we propose the new models for nanosized magnetoelectric (piezomagneto-electric or electromagnetoelastic) bodies with surface effects in accordance with corresponding investigations of piezoelectric solids earlier presented in [24, 25]. We assume that magnetoelectric composite body can be considered as homogeneous material with appropriate effective material properties, see for example [26–29]. Here we assume that the surface piezoelectric, piezomagnetic and magnetoelectric coupling effects are absent. In other words, we assume that the tensor of surface stresses depends only on the surface strains, while the surface electric displacement vector relates with the surface electric field intensity vector and the surface magnetic flux density vector relates with the surface magnetic field. Obviously, due to coupling in the three-dimensional constitutive relations the surface stresses tensor, the surface electric displacement vector and the surface magnetic flux density vector depend each of others. Using these assumptions, we formulate the system of differential equations with damping properties, the special boundary conditions taking into account the surface effects and the initial conditions for magnetoelectric nanosized body.

For numerical solution of the dynamic problems for magnetoelectric bodies with surface effects, we propose the finite element approximations and the corresponding generalized matrix problems. Here standard finite element software could be used with additional introduction of surface membrane elements and surface dielectric and magnetic films in the computation models.

We note that the finite element systems for coupled problems for magneto-electric nanosized bodies can be represent in the form of a system of linear algebraic equations with symmetric saddle point quasi-definite matrices [30]. We also describe special efficient approaches to solve the resulting finite element equations for transient, harmonic, modal and static problems.

27.2 Boundary Problems for Magnetolectric Bodies

Let $\Omega \in \mathbb{R}^3$ is the region occupied by a magnetolectric (piezomagnetolectric) material; $\Gamma = \partial\Omega$ is the boundary of Ω ; \mathbf{n} is the external unit normal to Γ ; $\mathbf{x} = \{x_1, x_2, x_3\}$; t is the time; $\mathbf{u} = \mathbf{u}(\mathbf{x}, t)$ is the vector of mechanical displacements; $\varphi = \varphi(\mathbf{x}, t)$ is the function of electric potential; $\phi = \phi(\mathbf{x}, t)$ is the function of magnetic potential. The set of differential equations for magnetolectric body occupying Ω considering damping effects take the following form:

$$\nabla \cdot \boldsymbol{\sigma} + \rho \mathbf{f} = \rho(\ddot{\mathbf{u}} + \alpha_d \dot{\mathbf{u}}), \quad \nabla \cdot \mathbf{D} = \sigma_\Omega, \quad \nabla \cdot \mathbf{B} = 0, \quad (27.1)$$

$$\boldsymbol{\sigma} = \mathbf{c} : (\boldsymbol{\varepsilon} + \beta_d \dot{\boldsymbol{\varepsilon}}) - \mathbf{e}^T \cdot \mathbf{E} - \mathbf{h}^T \cdot \mathbf{H}, \quad (27.2)$$

$$\mathbf{D} + \zeta_d \dot{\mathbf{D}} = \mathbf{e} : (\boldsymbol{\varepsilon} + \zeta_d \dot{\boldsymbol{\varepsilon}}) + \boldsymbol{\kappa} \cdot \mathbf{E} + \boldsymbol{\alpha} \cdot \mathbf{H}, \quad (27.3)$$

$$\mathbf{B} + \gamma_d \dot{\mathbf{B}} = \mathbf{h} : (\boldsymbol{\varepsilon} + \gamma_d \dot{\boldsymbol{\varepsilon}}) + \boldsymbol{\alpha}^T \cdot \mathbf{E} + \boldsymbol{\mu} \cdot \mathbf{H}. \quad (27.4)$$

$$\boldsymbol{\varepsilon} = (\nabla \mathbf{u} + (\nabla \mathbf{u})^T)/2, \quad \mathbf{E} = -\nabla \varphi, \quad \mathbf{H} = -\nabla \phi, \quad (27.5)$$

Here $\boldsymbol{\sigma}$ and $\boldsymbol{\varepsilon}$ are the second-order stress and strain tensors; \mathbf{D} and \mathbf{E} are the electric flux density vector called also the electric displacement vector and the electric field vector, respectively; \mathbf{B} and \mathbf{H} are the magnetic flux density vector and the magnetic field vector, respectively; $\mathbf{c} = \mathbf{c}^{E,H}$ is the fourth-order tensor of elastic stiffness moduli; $\mathbf{e} = \mathbf{e}^H$ is the third-order tensor of piezoelectric moduli; $\mathbf{h} = \mathbf{h}^E$ is the third-order tensor of magnetostriction moduli (piezomagnetic moduli); $\boldsymbol{\kappa} = \boldsymbol{\kappa}^{S,H} = \boldsymbol{\varepsilon}^{S,H}$ is the second-order tensor of dielectric permittivity moduli; $\boldsymbol{\alpha} = \boldsymbol{\alpha}^S$ is the second-order tensor of magnetolectric coupling coefficients; $\boldsymbol{\mu} = \boldsymbol{\mu}^{S,E}$ is the second-order tensor of magnetic permeability moduli. The upper indexes indicate the constant fields under which these moduli are calculated. So S denotes the strains, E denotes the electric field, H denotes the magnetic field. $\alpha_d, \beta_d, \zeta_d, \gamma_d$ are the damping coefficients; \mathbf{f} is the vector of mass forces; σ_Ω is the density of free electric charges (usually, $\sigma_\Omega = 0$); $(\dots)^T$ is the transpose operation, and $(\dots) : (\dots)$ is the double scalar product operation.

We suppose that the material moduli have the usual symmetry properties: $c_{ijkl} = c_{jikl} = c_{klij}$, $e_{ikl} = e_{ilk}$, $h_{ikl} = h_{ilk}$, $\kappa_{kl} = \kappa_{lk}$, $\mu_{kl} = \mu_{lk}$. In addition to the latter

the requirement of positive definiteness of intrinsic energy of the magnetoelectric medium leads to the following equalities valid for $\boldsymbol{\varepsilon} = \boldsymbol{\varepsilon}^T$, \mathbf{E} and \mathbf{H} :

$$\boldsymbol{\varepsilon}^T : \mathbf{c} : \boldsymbol{\varepsilon} + \mathbf{E}^T \cdot \boldsymbol{\kappa} \cdot \mathbf{E} + 2\mathbf{E}^T \cdot \boldsymbol{\alpha} \cdot \mathbf{H} + \mathbf{H}^T \cdot \boldsymbol{\mu} \cdot \mathbf{H} = c_{vU}(\boldsymbol{\varepsilon}^T : \boldsymbol{\varepsilon} + \mathbf{E}^T \cdot \mathbf{E} + \mathbf{H}^T \cdot \mathbf{H}),$$

where $c_{vU} > 0$ is a positive constant.

In models (27.1)–(27.5) for the magnetoelectric material, we use a generalized Rayleigh method of damping evaluation, see [31, 32] for the case of piezoelectric material, which is admissible for many practical applications. When $\zeta_d = \gamma_d = 0$ in (27.3) and (27.4), we have the model taking into account the mechanical damping in magnetoelectric media, which is adopted in the case of elastic and piezoelectric materials in several well-known finite element packages. More complicated model (27.3) and (27.4) extends Kelvin's model to the case of magnetoelectric media. It has been shown that the model (27.1)–(27.5) with $\beta_d = \zeta_d = \gamma_d$ satisfies the conditions of the energy dissipation and has the possibility of splitting the finite element system into independent equations for the separate modes in the case of piezomagnetolectric media (see Sects. 27.4.5 and 27.4.6).

For completeness, the boundary and the initial conditions should be added to the system of differential (27.1)–(27.5). The boundary conditions are of three types: mechanical, electric and magnetic.

To formulate the mechanical boundary conditions, we assume that the boundary $\Gamma = \partial\Omega$ is divided into two subsets Γ_σ and Γ_u ($\Gamma = \Gamma_\sigma \cup \Gamma_u$) for dynamic and kinematic boundary conditions, respectively. The dynamic boundary conditions given at Γ_σ take the form:

$$\mathbf{n} \cdot \boldsymbol{\sigma} = \nabla^s \cdot \boldsymbol{\tau}^s + \mathbf{p}_\Gamma, \quad \mathbf{x} \in \Gamma_\sigma, \quad (27.6)$$

where ∇^s is the surface gradient operator, associated with nabla-operator by the formula $\nabla^s = \nabla - \mathbf{n}(\partial/\partial r)$, r is the coordinate, measured along the direction of normal \mathbf{n} to Γ_σ ; $\boldsymbol{\tau}^s$ is the second-order tensor of surface stresses, and \mathbf{p}_Γ are the external surface loads.

As for purely elastic body, by taking into account the surface stresses and the Kelvin's damping model, we adopt that the surface stresses $\boldsymbol{\tau}^s$ are related to the surface strains $\boldsymbol{\varepsilon}^s$ by the formula $\boldsymbol{\tau}^s = \mathbf{c}^s : (\boldsymbol{\varepsilon}^s + \beta_d \dot{\boldsymbol{\varepsilon}}^s)$, where $\boldsymbol{\varepsilon}^s = (\nabla^s \mathbf{u} \cdot \mathbf{A} + \mathbf{A} \cdot (\nabla^s \mathbf{u})^T)/2$; \mathbf{c}^s is the fourth-order tensor of surface elastic moduli; $\mathbf{A} = \mathbf{I} - \mathbf{n} \otimes \mathbf{n}$; \mathbf{I} is the unit tensor in \mathbb{R}^3 .

Here the properties of the tensor of surface elastic moduli \mathbf{c}^s are similar to the corresponding properties of the tensor \mathbf{c} , i.e. $c_{ijkl}^s = c_{jikl}^s = c_{klij}^s$,

$$\exists c_{sU} > 0, \quad \forall \boldsymbol{\varepsilon}^s = \boldsymbol{\varepsilon}^{sT} \quad U(\boldsymbol{\varepsilon}^s) = \frac{1}{2} \boldsymbol{\varepsilon}^{sT} : \mathbf{c}^s : \boldsymbol{\varepsilon}^s \geq c_{sU} \boldsymbol{\varepsilon}^{sT} : \boldsymbol{\varepsilon}^s,$$

that follow from the condition of the positive definiteness of the surface energy density $U(\boldsymbol{\varepsilon}^s)$ which is required for well-posedness of the problem [9].

On the remaining part Γ_u of the boundary Γ , we pose known the mechanical displacements vector \mathbf{u}_Γ as

$$\mathbf{u} = \mathbf{u}_\Gamma, \quad \mathbf{x} \in \Gamma_u. \quad (27.7)$$

To set the electric boundary conditions we assume that the surface Γ is also subdivided into two subsets: Γ_D and Γ_φ ($\Gamma = \Gamma_D \cup \Gamma_\varphi$).

The region Γ_D does not contain electrodes, so the following conditions hold:

$$\mathbf{n} \cdot \mathbf{D} = \nabla^s \cdot \mathbf{d}^s - \sigma_\Gamma, \quad \mathbf{x} \in \Gamma_D, \quad (27.8)$$

where the surface electric flux density vector \mathbf{d}^s joins with the surface electric field vector $\mathbf{E}^s = -\nabla^s \varphi$ by the constitutive equation $\mathbf{d}^s + \zeta_d \dot{\mathbf{d}}^s = \mathbf{A} \cdot \boldsymbol{\kappa}^s \cdot \mathbf{A} \cdot \mathbf{E}^s$; $\boldsymbol{\kappa}^s$ is the second-order dielectric surface permittivity tensor that is symmetric positive definite relatively to the vectors \mathbf{E}^s ; σ_Γ is the given surface density of electric charge, and usually, $\sigma_\Gamma = 0$.

The subset Γ_φ is the union of $M + 1$ regions $\Gamma_{\varphi j}$ ($j \in J_Q \cup J_V$, $J_Q = \{1, 2, \dots, m\}$, $J_V = \{0, m, m + 1, \dots, M\}$), that does not border on each other and are covered with infinitely thin electrodes. At these regions, we set the following boundary conditions:

$$\varphi = \Phi_j, \quad \mathbf{x} \in \Gamma_{\varphi j}, \quad j \in J_Q, \quad (27.9)$$

$$\int_{\Gamma_{\varphi j}} \mathbf{n} \cdot \mathbf{D} d\Gamma = -Q_j, \quad I_j = \pm \dot{Q}_j, \quad \mathbf{x} \in \Gamma_{\varphi j}, \quad j \in J_Q, \quad (27.10)$$

$$\varphi = V_j, \quad \mathbf{x} \in \Gamma_{\varphi j}, \quad \Gamma_{\varphi 0} \neq \Lambda, \quad j \in J_V, \quad (27.11)$$

where the variables Φ_j, V_j do not depend on \mathbf{x} ; Q_j is the overall electric charge on $\Gamma_{\varphi j}$, and the sign “ \pm ” in (27.10) is chosen in accordance with the accepted direction of the current I_j in the electric circuit.

For magnetic boundary condition, we suppose that the following condition hold on the boundary Γ :

$$\mathbf{n} \cdot \mathbf{B} = \nabla^s \cdot \mathbf{b}^s, \quad \mathbf{x} \in \Gamma, \quad (27.12)$$

where the surface magnetic flux density vector \mathbf{b}^s depends from the surface magnetic field vector $\mathbf{H}^s = -\nabla^s \phi$ by the constitutive equation $\mathbf{b}^s + \gamma_d \dot{\mathbf{b}}^s = \mathbf{A} \cdot \boldsymbol{\mu}^s \cdot \mathbf{A} \cdot \mathbf{H}^s$; $\boldsymbol{\mu}^s$ is the second-order magnetic surface permittivity tensor that is symmetric positive definite relatively to the vectors \mathbf{H}^s .

For transient problems, it is also necessary to pose initial conditions, which are given by

$$\mathbf{u} = \mathbf{u}_*(\mathbf{x}), \quad \dot{\mathbf{u}} = \dot{\mathbf{r}}_*(\mathbf{x}), \quad t = 0, \quad \mathbf{x} \in \Omega, \quad (27.13)$$

where $\mathbf{u}_*(\mathbf{x})$ and $\dot{\mathbf{r}}_*(\mathbf{x})$ are the known initial values of the corresponding fields.

Formulae (27.1)–(27.13) represent the statement of the transient problem for magnetoelectric body with the generalized Rayleigh damping and with account for surface effects for mechanical, electric and magnetic fields. From (27.1)–(27.13), we can also obtain the formulations of static, modal and harmonic problems for magnetoelectric media with surface effects by standard methods.

We can also consider the particular cases of this model without taking into account the connectivity between some physical fields, and without the surface mechanical stresses ($\boldsymbol{\tau}^s = 0$), surface electric fields ($\mathbf{d}^s = 0$), or surface magnetic fields ($\mathbf{b}^s = 0$).

For example, we can obtain the model of piezoelectric material with damping properties and with surface effects, if we assume $\mathbf{h} = 0$ in (27.2) and if we ignore the equations for magnetic fields.

27.3 Generalized Formulations for Dynamic Problems

In order to formulate the weak or generalized statement of dynamic problem for magnetoelectric solid with surface effects we scalar multiply (27.1) by some sufficiently differentiable vector-function $\mathbf{v}(\mathbf{x})$ and functions $\chi(\mathbf{x})$ and $\eta(\mathbf{x})$, which satisfy homogeneous principal boundary conditions, i.e.

$$\mathbf{v} = 0, \quad \mathbf{x} \in \Gamma_u. \quad (27.14)$$

$$\chi = X_j, \quad \mathbf{x} \in \Gamma_{\varphi j}, \quad j \in J_Q, \quad (27.15)$$

$$\chi = 0, \quad \mathbf{x} \in \Gamma_{\varphi j}, \quad j \in J_V, \quad (27.16)$$

where X_j are the arbitrary constant values on $\Gamma_{\varphi j}$, $j \in J_Q$. Further we describe the mathematical restrictions imposed on the functions $\mathbf{v}(\mathbf{x})$, $\chi(\mathbf{x})$ and $\eta(\mathbf{x})$ more precisely.

By integrating the obtained equations over Ω and by using the standard technique of the integration by parts, with (27.2)–(27.12), (27.14)–(27.16) and with the relations for surface fields, we obtain

$$\rho(\mathbf{v}, \ddot{\mathbf{u}}) + d(\mathbf{v}, \dot{\mathbf{u}}) + c(\mathbf{v}, \mathbf{u}) + e(\varphi, \mathbf{v}) + h(\phi, \mathbf{v}) = \tilde{L}_u(\mathbf{v}), \quad (27.17)$$

$$-e(\chi, \mathbf{u} + \varsigma_d \dot{\mathbf{u}}) + \kappa(\chi, \varphi) + \alpha(\chi, \phi) = \tilde{L}_\varphi(\chi) + \varsigma_d \frac{\partial}{\partial t} \tilde{L}_\varphi(\chi), \quad (27.18)$$

$$-h(\eta, \mathbf{u} + \gamma_d \dot{\mathbf{u}}) + \alpha(\varphi, \eta) + \mu(\eta, \phi) = 0, \quad (27.19)$$

where

$$\rho(\mathbf{v}, \mathbf{u}) = \int_{\Omega} \rho \mathbf{v}^T \cdot \mathbf{u} d\Omega, \quad d(\mathbf{v}, \mathbf{u}) = \alpha_d \rho(\mathbf{v}, \mathbf{u}) + \beta_d c(\mathbf{v}, \mathbf{u}), \quad (27.20)$$

$$c(\mathbf{v}, \mathbf{u}) = c_{\Omega}(\mathbf{v}, \mathbf{u}) + c_{\Gamma}(\mathbf{v}, \mathbf{u}), \quad (27.21)$$

$$\kappa(\chi, \varphi) = \kappa_{\Omega}(\chi, \varphi) + \kappa_{\Gamma}(\chi, \varphi), \quad \mu(\eta, \phi) = \mu_{\Omega}(\eta, \phi) + \mu_{\Gamma}(\eta, \phi), \quad (27.22)$$

$$c_{\Omega}(\mathbf{v}, \mathbf{u}) = \int_{\Omega} \boldsymbol{\varepsilon}(\mathbf{v}) : \mathbf{c} : \boldsymbol{\varepsilon}(\mathbf{u}) d\Omega, \quad c_{\Gamma}(\mathbf{v}, \mathbf{u}) = \int_{\Gamma_{\sigma}} \boldsymbol{\varepsilon}^s(\mathbf{v}) : \mathbf{c}^s : \boldsymbol{\varepsilon}^s(\mathbf{u}) d\Gamma, \quad (27.23)$$

$$\kappa_{\Omega}(\chi, \varphi) = \int_{\Omega} \nabla^T \chi \cdot \boldsymbol{\kappa} \cdot \nabla \varphi d\Omega, \quad \kappa_{\Gamma}(\chi, \varphi) = \int_{\Gamma_D} \nabla^{sT} \chi \cdot \boldsymbol{\kappa}^s \cdot \nabla^s \varphi d\Gamma, \quad (27.24)$$

$$\mu_{\Omega}(\eta, \phi) = \int_{\Omega} \nabla^T \eta \cdot \boldsymbol{\mu} \cdot \nabla \phi d\Omega, \quad \mu_{\Gamma}(\eta, \phi) = \int_{\Gamma} \nabla^{sT} \eta \cdot \boldsymbol{\mu}^s \cdot \nabla^s \phi d\Gamma, \quad (27.25)$$

$$e(\varphi, \mathbf{v}) = \int_{\Omega} \nabla^T \varphi \cdot \mathbf{e} : \boldsymbol{\varepsilon}(\mathbf{v}) d\Omega, \quad h(\phi, \mathbf{v}) = \int_{\Omega} \nabla^T \phi \cdot \mathbf{h} : \boldsymbol{\varepsilon}(\mathbf{v}) d\Omega, \quad (27.26)$$

$$\alpha(\chi, \phi) = \int_{\Omega} \nabla^T \chi \cdot \boldsymbol{\alpha} \cdot \nabla \phi d\Omega, \quad (27.27)$$

$$\tilde{L}_u(\mathbf{v}) = \int_{\Omega} \mathbf{v}^T \cdot \boldsymbol{\rho} \mathbf{f} d\Omega + \int_{\Gamma_{\sigma}} \mathbf{v}^T \cdot \mathbf{p}_{\Gamma} d\Gamma, \quad (27.28)$$

$$\tilde{L}_{\varphi}(\chi) = \int_{\Omega} \chi \sigma_{\Omega} d\Omega + \int_{\Gamma_D} \chi \sigma_{\Gamma} d\Gamma + \sum_{j \in J_Q} X_j Q_j. \quad (27.29)$$

The weak form of the initial conditions (27.13) results in

$$\rho(\mathbf{v}, \mathbf{u}) = \rho(\mathbf{v}, \mathbf{u}_*), \quad \rho(\mathbf{v}, \dot{\mathbf{u}}) = \rho(\mathbf{v}, \mathbf{r}_*), \quad t = 0. \quad (27.30)$$

Further we present the functions \mathbf{u} and φ as

$$\mathbf{u} = \mathbf{u}_0 + \mathbf{u}_b, \quad \varphi = \varphi_0 + \varphi_b, \quad (27.31)$$

where \mathbf{u}_0, φ_0 satisfy homogeneous boundary mechanical and electric conditions and \mathbf{u}_b, φ_b are the given functions satisfying the inhomogeneous boundary conditions, i.e.

$$\mathbf{u}_0 = 0, \quad \mathbf{u}_b = \mathbf{u}_\Gamma, \quad \mathbf{x} \in \Gamma_u. \quad (27.32)$$

$$\varphi_0 = \Phi_{0j}, \quad \varphi_b = \Phi_{bj}, \quad \Phi_{0j} + \Phi_{bj} = \Phi_j, \quad \mathbf{x} \in \Gamma_{\varphi j}, \quad j \in J_Q, \quad (27.33)$$

$$\varphi_0 = 0, \quad \varphi_b = V_j, \quad \mathbf{x} \in \Gamma_{\varphi j}, \quad j \in J_V. \quad (27.34)$$

Using representations (27.31), we modify the system (27.17)–(27.19) into the form;

$$\rho(\mathbf{v}, \ddot{\mathbf{u}}_0) + d(\mathbf{v}, \dot{\mathbf{u}}_0) + c(\mathbf{v}, \mathbf{u}_0) + e(\varphi_0, \mathbf{v}) + h(\phi, \mathbf{v}) = L_u(\mathbf{v}), \quad (27.35)$$

$$-e(\chi, \mathbf{u}_0 + \varsigma_d \dot{\mathbf{u}}_0) + \kappa(\chi, \varphi_0) + \alpha(\chi, \phi) = L_\varphi(\chi), \quad (27.36)$$

$$-h(\eta, \mathbf{u}_0 + \gamma_d \dot{\mathbf{u}}_0) + \alpha(\varphi_0, \eta) + \mu(\eta, \phi) = L_\phi(\eta), \quad (27.37)$$

where

$$L_u(\mathbf{v}) = \tilde{L}_u(\mathbf{v}) - \rho(\mathbf{v}, \ddot{\mathbf{u}}_b) - d(\mathbf{v}, \dot{\mathbf{u}}_b) - c(\mathbf{v}, \mathbf{u}_b) - e(\varphi_b, \mathbf{v}). \quad (27.38)$$

$$L_\varphi(\chi) = \tilde{L}_\varphi(\chi) + \varsigma_d \frac{\partial}{\partial t} \tilde{L}_\varphi(\chi) + e(\chi, \mathbf{u}_b + \varsigma_d \dot{\mathbf{u}}_b) - \kappa(\chi, \varphi_b), \quad (27.39)$$

$$L_\phi(\eta) = h(\eta, \mathbf{u}_b + \gamma_d \dot{\mathbf{u}}_b) - \alpha(\varphi_b, \eta). \quad (27.40)$$

We denote with the Hilbert vector space H_u the closure of the set of vector functions $\mathbf{v} \in C^1$, satisfying homogeneous principal boundary condition (27.14), with the norm generated by bilinear form $c(\mathbf{v}, \mathbf{u})$ defined in (27.21) and (27.23).

We also denote with the Hilbert space H_φ the closure of the set of function $\chi \in C^1$, satisfying boundary condition (27.15), (27.16), in the norm generated by scalar production $\kappa(\chi, \varphi)$ from (27.22), (27.24), and with the Hilbert space H_ϕ the closure of the set of function $\eta \in C^1$ in the norm generated by scalar production $\mu(\eta, \phi)$ from (27.22) and (27.25).

Then, we introduce the functional spaces $Q_u = L^2(0, T; H_u)$, $Q_\varphi = L^2(0, T; H_\varphi)$ and $Q_\phi = L^2(0, T; H_\phi)$, where for Banach space X with norm $\|\cdot\|_X$, the space $L^2(0, T; X)$ is the space of (class) functions $t \rightarrow f(t)$ from $[0, T]$ into X , which satisfy the condition:

$$\left(\int_0^T \|f(t)\|_X^2 dt \right)^{1/2} = \|f\|_{L^2(0, T; X)} < \infty.$$

Now we are ready to define generalized or weak solution of dynamic problem (27.1)–(27.13) using these functional spaces.

Definition The functions $\mathbf{u} = \mathbf{u}_0 + \mathbf{u}_b$, $\mathbf{u}_0 \in Q_u$; $\varphi = \varphi_0 + \varphi_b$, $\varphi_0 \in Q_\varphi$; $\phi_0 \in Q_\phi$ are the weak solution of dynamic problem for the magnetoelectric body with damping and surface effects, if (27.35)–(27.37) with (27.38)–(27.40), (27.20)–(27.29) are

satisfied for $\forall t \in [0, T]$; $\mathbf{v} \in H_u, \chi \in H_\varphi, \eta \in H_\phi$, and the initial conditions (27.30) are also hold.

27.4 Finite Element Approximations

27.4.1 Transient Problems

For solving the problems (27.35)–(27.37), (27.30), we shall use the classical finite element approximation techniques [33, 34]. Let Ω_h be the region of the corresponding finite element mesh: $\Omega_h \subseteq \Omega, \Omega_h = \cup_m \Omega^{em}$, where Ω^{em} is a separate finite element with number m . On this mesh, we shall find the approximation to the weak solution $\{\mathbf{u}_{0h}, \varphi_{0h}, \phi_h\}$ in the form:

$$\mathbf{u}_h(\mathbf{x}, t) = \mathbf{N}_u^T(\mathbf{x}) \cdot \mathbf{U}(t), \quad \varphi_h(\mathbf{x}, t) = \mathbf{N}_\varphi^T(\mathbf{x}) \cdot \Phi(t), \quad \phi_h(\mathbf{x}, t) = \mathbf{N}_\phi^T(\mathbf{x}) \cdot \Psi(t), \quad (27.41)$$

where \mathbf{N}_u^T is the matrix of the shape functions for displacements, \mathbf{N}_φ^T is the row vector of the shape functions for electric potential, \mathbf{N}_ϕ^T is the row vector of the shape functions for magnetic potential, $\mathbf{U}(t), \Phi(t), \Psi(t)$ are the global vectors of nodal displacements, electric potential and magnetic potential, respectively.

We represent the projecting functions \mathbf{v}, χ and η in finite-dimensional spaces by the formulae:

$$\mathbf{v}(\mathbf{x}) = \mathbf{N}_u^T(\mathbf{x}) \cdot \delta \mathbf{U}, \quad \chi(\mathbf{x}) = \mathbf{N}_\varphi^T(\mathbf{x}) \cdot \delta \Phi, \quad \eta(\mathbf{x}) = \mathbf{N}_\phi^T(\mathbf{x}) \cdot \delta \Psi, \quad (27.42)$$

In accordance with standard finite element technique, we approximate the weak formulation (27.35)–(27.37) by the problem in finite-dimensional spaces. Substituting (27.41) and (27.42) into the problem (27.35)–(27.37) with (27.38)–(27.40), (27.20)–(27.29) for $\Omega_h, \Gamma_h = \partial\Omega_h, \Gamma_{\sigma h}, \Gamma_{Dh}$, we obtain

$$\mathbf{M}_{uu} \cdot \ddot{\mathbf{U}} + \mathbf{C}_{uu} \cdot \dot{\mathbf{U}} + \mathbf{K}_{uu} \cdot \mathbf{U} + \mathbf{K}_{u\varphi} \cdot \Phi + \mathbf{K}_{u\phi} \cdot \Psi = \mathbf{F}_u, \quad (27.43)$$

$$-\mathbf{K}_{u\varphi}^T \cdot (\mathbf{U} + \zeta_d \dot{\mathbf{U}}) + \mathbf{K}_{\varphi\varphi} \cdot \Phi + \mathbf{K}_{\varphi\phi} \cdot \Psi = \mathbf{F}_\varphi, \quad (27.44)$$

$$-\mathbf{K}_{u\phi}^* \cdot (\mathbf{U} + \gamma_d \dot{\mathbf{U}}) + \mathbf{K}_{\phi\phi}^* \cdot \Phi + \mathbf{K}_{\phi\phi} \cdot \Psi = \mathbf{F}_\phi, \quad (27.45)$$

with the initial conditions:

$$\mathbf{U}(0) = \mathbf{U}_*, \quad \dot{\mathbf{U}}(0) = \mathbf{R}_*, \quad (27.46)$$

which are derived from the corresponding instantaneous conditions (27.13) or (27.30).

Here, $\mathbf{M}_{uu} = \sum^a \mathbf{M}_{uu}^{ek}$, $\mathbf{C}_{uu} = \sum^a \mathbf{C}_{uu}^{ek}$, $\mathbf{K}_{uu} = \sum^a \mathbf{K}_{uu}^{ek}$, $\mathbf{K}_{u\varphi} = \sum^a \mathbf{K}_{u\varphi}^{ek}$, etc., are the global matrices, obtained from the corresponding element matrices ensemble (Σ^a).

According to (27.20)–(27.29) the element matrices have the form:

$$\mathbf{M}_{uu}^{ek} = \int_{\Omega^{ek}} \rho \mathbf{N}_u^e \cdot \mathbf{N}_u^{eT} d\Omega, \quad \mathbf{C}_{uu}^{ek} = \alpha_d \mathbf{M}_{uu}^{ek} + \beta_d \mathbf{K}_{uu}^{ek}, \quad (27.47)$$

$$\mathbf{K}_{uu}^{ek} = \mathbf{K}_{\Omega uu}^{ek} + \mathbf{K}_{\Gamma uu}^{ek}, \quad \mathbf{K}_{\varphi\varphi}^{ek} = \mathbf{K}_{\Omega\varphi\varphi}^{ek} + \mathbf{K}_{\Gamma\varphi\varphi}^{ek}, \quad \mathbf{K}_{\phi\phi}^{ek} = \mathbf{K}_{\Omega\phi\phi}^{ek} + \mathbf{K}_{\Gamma\phi\phi}^{ek}, \quad (27.48)$$

$$\mathbf{K}_{\Omega uu}^{ek} = \int_{\Omega^{ek}} \mathbf{B}_u^{eT} : \mathbf{c} : \mathbf{B}_u^e d\Omega, \quad \mathbf{K}_{\Gamma uu}^{ek} = \int_{\Gamma_\sigma^{ek}} \mathbf{B}_{su}^{eT} : \mathbf{c}^s : \mathbf{B}_{su}^e d\Gamma, \quad (27.49)$$

$$\mathbf{K}_{\Omega\varphi\varphi}^{ek} = \int_{\Omega^{ek}} \mathbf{B}_\varphi^{eT} \cdot \mathbf{k} \cdot \mathbf{B}_\varphi^e d\Omega, \quad \mathbf{K}_{\Gamma\varphi\varphi}^{ek} = \int_{\Gamma_D^{ek}} \mathbf{B}_{s\varphi}^{eT} \cdot \mathbf{k}^s \cdot \mathbf{B}_{s\varphi}^e d\Gamma, \quad (27.50)$$

$$\mathbf{K}_{\Omega\phi\phi}^{ek} = \int_{\Omega^{ek}} \mathbf{B}_\phi^{eT} \cdot \boldsymbol{\mu} \cdot \mathbf{B}_\phi^e d\Omega, \quad \mathbf{K}_{\Gamma\phi\phi}^{ek} = \int_{\Gamma^{ek}} \mathbf{B}_{s\phi}^{eT} \cdot \boldsymbol{\mu}^s \cdot \mathbf{B}_{s\phi}^e d\Gamma \quad (27.51)$$

$$\mathbf{K}_{u\varphi}^{ek} = \int_{\Omega^{ek}} \mathbf{B}_u^{eT} : \mathbf{e}^T \cdot \mathbf{B}_\varphi^e d\Omega, \quad \mathbf{K}_{u\phi}^{ek} = \int_{\Omega^{ek}} \mathbf{B}_u^{eT} : \mathbf{h}^T \cdot \mathbf{B}_\phi^e d\Omega, \quad (27.52)$$

$$\mathbf{K}_{\varphi\phi}^{ek} = \int_{\Omega^{ek}} \mathbf{B}_\varphi^{eT} : \boldsymbol{\alpha} \cdot \mathbf{B}_\phi^e d\Omega, \quad (27.53)$$

$$\mathbf{B}_{(s)u}^e = \mathbf{L}(\nabla^{(s)}) \mathbf{N}_u^{eT}, \quad \mathbf{B}_{(s)\varphi}^e = \nabla^{(s)} \mathbf{N}_\varphi^{eT}, \quad \mathbf{B}_{(s)\phi}^e = \nabla^{(s)} \mathbf{N}_\phi^{eT}, \quad (27.54)$$

$$\mathbf{L}^T(\nabla^{(s)}) = \begin{bmatrix} \partial_1^{(s)} & 0 & 0 & 0 & \partial_3^{(s)} & \partial_2^{(s)} \\ 0 & \partial_2^{(s)} & 0 & \partial_3^{(s)} & 0 & \partial_1^{(s)} \\ 0 & 0 & \partial_3^{(s)} & \partial_2^{(s)} & \partial_1^{(s)} & 0 \end{bmatrix}, \quad (27.55)$$

where Γ^{ek} , Γ_σ^{ek} , Γ_D^{ek} , are the edges of finite elements facing the regions $\Gamma_h, \Gamma_{h\sigma}, \Gamma_{hD}$, that approximate the corresponding boundaries $\Gamma, \Gamma_\sigma, \Gamma_D$, $\mathbf{N}_u^{eT}, \mathbf{N}_\varphi^{eT}, \mathbf{N}_\phi^{eT}$ are the matrix and the row vectors of approximating basis functions, respectively, defined at separate finite elements. The vectors $\mathbf{F}_u, \mathbf{F}_\varphi, \mathbf{F}_\phi$ in (27.43)–(27.45) are obtained from the corresponding right parts of the weak statements (27.35)–(27.37) with (27.38)–(27.40), (27.20), (27.28), (27.29) and the finite element representations (27.42).

In (27.48)–(27.55), we use vector-matrix forms for the moduli [35]: c is the 6×6 matrix of elastic moduli, $c_{\alpha\beta}^{(s)} = c_{ijkl}^{(s)}$; $\alpha, \beta = 1, 2, \dots, 6$; $i, j, k, l = 1, 2, 3$ with the correspondence law $\alpha \leftrightarrow (ij), \beta \leftrightarrow (kl), 1 \leftrightarrow (11), 2 \leftrightarrow (22), 3 \leftrightarrow (33), 4 \leftrightarrow (23) \sim (32), 5 \leftrightarrow (13) \sim (31), 6 \leftrightarrow (12) \sim (21)$; \mathbf{e} is the 3×6 matrix of piezoelectric moduli ($e_{i\beta} = e_{ikl}$); and \mathbf{h} is the 3×6 matrix of piezomagnetic moduli ($h_{i\beta} = h_{ikl}$).

27.4.2 Static Problems

In the case of static problems, all dependencies on time t are absent, and the finite element system (27.43)–(27.45) reduces to the form;

$$\mathbf{K} \cdot \mathbf{a} = \mathbf{F}, \tag{27.56}$$

where

$$\mathbf{K} = \begin{bmatrix} \mathbf{K}_{uu} & \mathbf{K}_{ub} \\ \mathbf{K}_{ub}^T & -\mathbf{K}_{bb} \end{bmatrix}, \quad \mathbf{a} = \begin{Bmatrix} \mathbf{U} \\ \mathbf{b} \end{Bmatrix}, \quad \mathbf{F} = \begin{Bmatrix} \mathbf{F}_u \\ -\mathbf{F}_b \end{Bmatrix}, \tag{27.57}$$

$$\mathbf{K}_{bb} = \begin{bmatrix} \mathbf{K}_{\phi\phi} & \mathbf{K}_{\phi\psi} \\ \mathbf{K}_{\phi\psi}^T & \mathbf{K}_{\psi\psi} \end{bmatrix}, \quad \mathbf{K}_{ub}^T = \begin{Bmatrix} \mathbf{K}_{u\phi}^T \\ \mathbf{K}_{u\psi}^T \end{Bmatrix}, \quad \mathbf{b} = \begin{Bmatrix} \mathbf{\Phi} \\ \mathbf{\Psi} \end{Bmatrix}, \quad \mathbf{F}_b = \begin{Bmatrix} \mathbf{F}_\phi \\ \mathbf{F}_\psi \end{Bmatrix}. \tag{27.58}$$

The matrix \mathbf{K} in (27.56)–(27.58) is symmetric and quasi-definite. Thus, problem (27.56) possesses the main calculating properties of finite element matrices for the theory of piezoelectricity. Therefore, it can be solved by using the same effective algorithms as the similar problems for ordinary piezoelectric media. For example, we can use the set of algorithms for finite element analysis with symmetric and quasi-definite matrices represented in ACELAN package [36]: the degree of freedom rotations, boundary condition settings, LDL^T -factorization or Cholesky method for solving the system of linear algebraic equations, and others.

27.4.3 Harmonic Problems

When all external volumetric and surface loads vary with the same harmonic law: $\exp[j\omega t]$ (i.e. $\mathbf{F}_u = \tilde{\mathbf{F}}_u \exp[j\omega t], \mathbf{F}_b = \tilde{\mathbf{F}}_b \exp[j\omega t]$), we have the behavior of steady-state oscillations ($\mathbf{U} = \tilde{\mathbf{U}} \exp[j\omega t], \mathbf{b} = \tilde{\mathbf{b}} \exp[j\omega t]$). In this case for $\zeta_d = \gamma_d$, as it is obvious from (27.43)–(27.45), we have a system of linear algebraic (27.55) for the amplitude values $\mathbf{a} = \{\tilde{\mathbf{U}}, \tilde{\mathbf{b}}\}$ with

$$\mathbf{K} = \begin{bmatrix} -\omega^2 \mathbf{M}_{uu} + j\omega \mathbf{C}_{uu} + \mathbf{K}_{uu} & \mathbf{K}_{ub} \\ \mathbf{K}_{ub}^T & -q \mathbf{K}_{bb} \end{bmatrix}, \quad \mathbf{F} = \begin{Bmatrix} \tilde{\mathbf{F}}_u \\ -q \tilde{\mathbf{F}}_b \end{Bmatrix}, \quad (27.59)$$

where $q = (1 + j\omega\varsigma_d)^{-1}$.

Then, the well-known algorithm for large symmetric complex matrices can be applied for solution of (27.56) and (27.59). Often we have solved these equations for generating the necessary frequency response functions. In this situation, because the matrix \mathbf{K} depends on ω and changes every step of iteration, the mode superposition method discussed in Sect. 27.4.5 is preferential.

27.4.4 Modal Problems

The resonance frequencies $f_k = \omega_k / (2\pi)$ for magnetoelectric can be found using the finite element method from the solution of the generalized eigenvalue problem, obtained from (27.56) and (27.59) with $\mathbf{C}_{uu} = 0$, $\varsigma_d = 0$, $\mathbf{F}_u = 0$, $\mathbf{F}_b = 0$ given by

$$\mathbf{K}_{uu} \cdot \tilde{\mathbf{U}} + \mathbf{K}_{ub} \cdot \tilde{\mathbf{b}} = \omega^2 \mathbf{M}_{uu} \cdot \tilde{\mathbf{U}}, \quad (27.60)$$

$$\mathbf{K}_{ub}^T \cdot \tilde{\mathbf{U}} - \mathbf{K}_{bb} \cdot \tilde{\mathbf{b}} = 0. \quad (27.61)$$

Eigenvalue problem (27.60) and (27.61) can be represented in the form:

$$\bar{\mathbf{K}}_{uu} \cdot \tilde{\mathbf{U}} = \lambda \mathbf{M}_{uu} \cdot \tilde{\mathbf{U}}, \quad \lambda = \omega^2, \quad (27.62)$$

where

$$\bar{\mathbf{K}}_{uu} = \mathbf{K}_{uu} + \mathbf{K}_{ub} \cdot \mathbf{K}_{bb}^{-1} \cdot \mathbf{K}_{ub}^T, \quad \tilde{\mathbf{b}} = \mathbf{K}_{bb}^{-1} \cdot \mathbf{K}_{ub}^T \cdot \tilde{\mathbf{U}}, \quad (27.63)$$

By virtue of positive definiteness of the intrinsic bulk and surface energies, the generalized stiffness matrix $\bar{\mathbf{K}}_{uu}$ is nonnegative definite ($\bar{\mathbf{K}}_{uu} \geq 0$), and mass matrix \mathbf{M}_{uu} is positive definite ($\mathbf{M}_{uu} > 0$), because $\rho(\mathbf{x}) \geq \rho_0 > 0$. Then, by analogy with the eigenvalue problems for elastic body, the eigenvalues $\lambda_k = \omega_k^2$ ($k = 1, 2, \dots, n$; n is the order of matrices \mathbf{M}_{uu} and $\bar{\mathbf{K}}_{uu}$) are real and non-negative. The eigenvectors, corresponding to them, which we will denote by \mathbf{W}_k , form basis in \mathbb{R}^n . The system of these eigenvectors \mathbf{W}_k can be chosen orthonormal with respect to the mass matrix \mathbf{M}_{uu} and orthogonal with respect to the extended stiffness matrix $\bar{\mathbf{K}}_{uu}$:

$$\langle \mathbf{W}_k, \mathbf{W}_m \rangle = \mathbf{W}_k^T \cdot \mathbf{M}_{uu} \cdot \mathbf{W}_m = \delta_{km}, \quad \mathbf{W}_k^T \cdot \bar{\mathbf{K}}_{uu} \cdot \mathbf{W}_m = \omega_m^2 \delta_{km}. \quad (27.64)$$

Thus, the coupled eigenvalue problems (27.60), (27.61) with respect to the triple of unknowns $\{\omega, \tilde{\mathbf{U}}, \tilde{\mathbf{b}}\}$ are the generalized eigenvalue problems (27.62), (27.63) with respect to the pair $\{\omega, \tilde{\mathbf{U}}\}$. Let us note that several effective block algorithms

for these finite element eigenvalue problems with partial coupling similar algorithms for piezoelectric modal problems are described in [37].

27.4.5 Mode Superposition Method for Harmonic Analysis

In the case of harmonic problem with $\beta_d = \zeta_d = \gamma_d$ for solution of (27.56) with (27.59), we obtain

$$(-\omega^2 \mathbf{M}_{uu} + j\omega \bar{\mathbf{C}}_{uu} + \bar{\mathbf{K}}_{uu}) \cdot \tilde{\mathbf{U}} = \bar{\mathbf{F}}_u, \quad (27.65)$$

$$\bar{\mathbf{C}}_{uu} = \alpha_d \mathbf{M}_{uu} + \beta_d \bar{\mathbf{K}}_{uu}, \quad \bar{\mathbf{F}}_u = \tilde{\mathbf{F}}_u - \mathbf{K}_{ub} \cdot \mathbf{K}_{bb}^{-1} \cdot \tilde{\mathbf{F}}_b, \quad (27.66)$$

$$\mathbf{b} = \mathbf{K}_{bb}^{-1} \cdot (\tilde{\mathbf{F}}_b + (1 + j\omega\beta_d) \mathbf{K}_{ub}^T \cdot \tilde{\mathbf{U}}). \quad (27.67)$$

If $\mathbf{u}_\Gamma = 0$ in (27.7), we find the solution of problem (27.65) in the form of an expansion in eigenvectors (modes) \mathbf{W}_k of eigenvalue problem (27.62) with the same homogeneous principal boundary conditions:

$$\tilde{\mathbf{U}} = \sum_{k=1}^n Z_k \mathbf{W}_k. \quad (27.68)$$

Substituting (27.68) into (27.65) and scalar multiplying the obtained equation by \mathbf{W}_m^T and taking into account the orthogonality relations (27.64) and (27.66), we obtain;

$$Z_k = \frac{1}{\omega_k^2 - \omega^2 + 2j\zeta_k \omega \omega_k} P_k, \quad P_k = \mathbf{W}_k^T \cdot \bar{\mathbf{F}}_u, \quad \zeta_k = \alpha_d \frac{1}{2\omega_k} + \beta_d \frac{\omega_k}{2}. \quad (27.69)$$

Thus, using the method of mode superposition, the solutions of the harmonic problems are determined by (27.68), (27.69) and (27.67).

27.4.6 Mode Superposition Method for Transient Analysis

For transient problems with homogeneous principal boundary conditions and $\beta_d = \zeta_d = \gamma_d$, we can also apply the method of mode expansion. Having solved (27.44) and (27.45) for $\mathbf{b} = \{\Phi, \Psi\}$ and converted (27.43), we obtain

$$\mathbf{M}_{uu} \cdot \ddot{\mathbf{U}} + \bar{\mathbf{C}}_{uu} \cdot \dot{\mathbf{U}} + \bar{\mathbf{K}}_{uu} \cdot \mathbf{U} = \mathbf{F}_u - \mathbf{K}_{ub} \cdot \mathbf{K}_{bb}^{-1} \cdot \mathbf{b}, \quad (27.70)$$

$$\mathbf{b} = \mathbf{K}_{bb}^{-1} \cdot (\mathbf{F}_b + \mathbf{K}_{ub}^T \cdot (\mathbf{U} + \beta_d \dot{\mathbf{U}})). \quad (27.71)$$

We will find the solution \mathbf{U} of problem (27.70) in the form of an expansion in modes (27.68), where $Z_k = Z_k(t)$. Substituting this expansion into (27.70), scalar multiplying the resulting equality by \mathbf{W}_m^T , and using the relation of orthogonality of the eigenvectors, we derive scalar differential equations for the individual functions $Z_k(t)$. Solving these equations with corresponding initial conditions, we obtain

$$Z_k = \frac{1}{\bar{\omega}_k} \int_0^t P_k(\tau) e^{-\xi_k \omega_k (t-\tau)} \sin[\bar{\omega}_k (t-\tau)] d\tau + A_k(0) e^{-\xi_k \omega_k t} \sin(\bar{\omega}_k t + \delta_k), \quad (27.72)$$

$$P_k = \mathbf{W}_k^T \cdot (\mathbf{F}_u - \mathbf{K}_{ub} \cdot \mathbf{K}_{bb}^{-1} \cdot \mathbf{b}), \quad \bar{\omega}_k = \omega_k \sqrt{1 - \xi_k^2}. \quad (27.73)$$

$$A_k(0) = \sqrt{Z_k^2(0) + \frac{(Z_k'(0) + \xi_k \omega_k Z_k(0))^2}{\bar{\omega}_k^2}}, \quad \delta_k = \arctg \frac{Z_k(0) \bar{\omega}_k}{Z_k'(0) + \xi_k \omega_k Z_k(0)}, \quad (27.74)$$

$$Z_k(0) = \mathbf{W}_k^T \cdot \mathbf{M}_{uu} \cdot \mathbf{U}_0, \quad Z_k'(0) = \mathbf{W}_k^T \cdot \mathbf{M}_{uu} \cdot \dot{\mathbf{U}}_0. \quad (27.75)$$

Hence, using the mode superposition method, the solution of problem (27.43)–(27.46) with homogeneous principal boundary conditions and $\beta_d = \zeta_d = \gamma_d$, is given by (27.68), (27.72)–(27.75) for \mathbf{U} and by (27.71) for \mathbf{b} .

27.4.7 The Newmark Scheme for Solving Transient Problems

The mode superposition method requires the equality of the damping parameters for different media and the homogeneity of the principal boundary conditions. Methods of direct integration with respect to time are more general. We will use the Newmark method for integrating Cauchy problem (27.43)–(27.46) in a formulation of which the velocities and accelerations in the time layers are not explicitly given [31, 32, 34].

The conventional Newmark scheme is based on the expansions of the vector functions $\mathbf{a}_{i+1} = \mathbf{a}(t_{i+1})$, $\dot{\mathbf{a}}_{i+1} = \dot{\mathbf{a}}(t_{i+1})$, $\mathbf{a} = \{\mathbf{U}, \Phi, \Psi\}$ ($t_i = i\tau$, $\tau = \Delta t$ is the time step size):

$$\mathbf{a}_{i+1}^p = \mathbf{a}_i + \tau \dot{\mathbf{a}}_i + \left(\frac{1}{2} - \beta\right) \tau^2 \ddot{\mathbf{a}}_i, \quad \mathbf{a}_{i+1} = \mathbf{a}_{i+1}^p + \beta \tau^2 \ddot{\mathbf{a}}_{i+1}, \quad (27.76)$$

$$\dot{\mathbf{a}}_{i+1}^p = \dot{\mathbf{a}}_i + (1 - \gamma) \tau \ddot{\mathbf{a}}_i, \quad \dot{\mathbf{a}}_{i+1} = \dot{\mathbf{a}}_{i+1}^p + \gamma \tau \ddot{\mathbf{a}}_{i+1}, \quad (27.77)$$

where β and γ are the parameters of the Newmark method.

We introduce the averaging operator Y_i :

$$Y_i \mathbf{a} = \sum_{k=0}^2 \beta_k \mathbf{a}_{i+1-k}, \quad (27.78)$$

where

$$\beta_0 = \beta, \quad \beta_1 = \gamma_1 - 2\beta, \quad \beta_2 = \gamma_2 + \beta, \quad \gamma_1 = 1/2 + \gamma, \quad \gamma_2 = 1/2 - \gamma.$$

As is shown in [31, 32], if the quantities $\mathbf{a}_i, \dot{\mathbf{a}}_i, \ddot{\mathbf{a}}_i, \mathbf{a}_i^p$ and $\dot{\mathbf{a}}_i^p$ are coupled by relations (27.76)–(27.78) for all $i \in \mathbb{N}$, then the following relations hold:

$$Y_i \mathbf{a}^p = \gamma_1 \mathbf{a}_i + \gamma_2 \mathbf{a}_{i-1}, \quad Y_i \dot{\mathbf{a}}^p = (\mathbf{a}_i - \mathbf{a}_{i-1})/\tau, \quad (27.79)$$

$$Y_i \dot{\mathbf{a}} = (\gamma \mathbf{a}_{i+1} - (2\gamma - 1)\mathbf{a}_i - (1 - \gamma)\mathbf{a}_{i-1})/\tau, \quad (27.80)$$

$$Y_i \ddot{\mathbf{a}} = (\mathbf{a}_{i+1} - 2\mathbf{a}_i + \mathbf{a}_{i-1})/\tau^2, \quad (27.81)$$

It is also easy to establish that the quantities $Y_i \ddot{\mathbf{a}}$ and $Y_i \dot{\mathbf{a}}$ can be expressed in terms of $Y_i \mathbf{a}^p, Y_i \dot{\mathbf{a}}^p$ and $Y_i \mathbf{a}$ using the formulae:

$$Y_i \ddot{\mathbf{a}} = \frac{1}{\beta\tau^2} (Y_i \mathbf{a} - Y_i \mathbf{a}^p), \quad Y_i \dot{\mathbf{a}} = \frac{\gamma}{\beta\tau} (Y_i \mathbf{a} - Y_i \mathbf{a}^p) + Y_i \dot{\mathbf{a}}^p. \quad (27.82)$$

We apply the averaging operator Y_i defined by (27.78) to (27.43)–(27.45), written for the instants of time t_i . Taking expressions (27.82) into account we obtain the systems of linear algebraic equations for each time layer:

$$\mathbf{K}^{eff} \cdot Y_i \mathbf{a} = \mathbf{F}_i^{eff}, \quad (27.83)$$

where

$$\mathbf{K}^{eff} = \begin{bmatrix} \mathbf{K}_{uu}^{eff} & \mathbf{K}_{u\varphi} & \mathbf{K}_{u\phi} \\ \mathbf{K}_{u\varphi}^{eff\Gamma} & -\mathbf{K}_{\varphi\varphi} & -\mathbf{K}_{\varphi\phi} \\ \mathbf{K}_{u\phi}^{eff\Gamma} & -\mathbf{K}_{\varphi\phi}^\Gamma & -\mathbf{K}_{\phi\phi} \end{bmatrix}, \quad (27.84)$$

$$\mathbf{K}_{uu}^{eff} = \frac{1}{\beta\tau^2} \mathbf{M}_{uu} + \frac{\gamma}{\beta\tau} \mathbf{C}_{uu} + \mathbf{K}_{uu}, \quad (27.85)$$

$$\mathbf{K}_{u\varphi}^{eff\Gamma} = (1 + \frac{\zeta_d \gamma}{\beta\tau}) \mathbf{K}_{u\varphi}^\Gamma, \quad \mathbf{K}_{u\phi}^{eff\Gamma} = (1 + \frac{\gamma_d \gamma}{\beta\tau}) \mathbf{K}_{u\phi}^\Gamma. \quad (27.86)$$

Here the vector $\mathbf{F}_i^{eff} = \mathbf{F}_i^{eff}(Y_i \mathbf{F}, Y_i \mathbf{F}^p, Y_i \mathbf{a}^p, Y_i \dot{\mathbf{a}}^p)$ has the intricate form, and the further formula is required for the transition to the next time layer:

$$\mathbf{a}_{i+1} = (Y_i \mathbf{a} - \beta_1 \mathbf{a}_i - \beta_2 \mathbf{a}_{i-1}) / \beta, \quad (27.87)$$

which follows from (27.78).

The system of (27.83)–(27.86) with respect to the vector of the averaged of nodal unknowns $\{Y_i \mathbf{U}, Y_i \Phi, Y_i \Psi\}$ can be rewritten in the symmetric form with the quasi-definite matrix \mathbf{K}^{eff} for the case $\varsigma_d = \gamma_d$ as

$$\mathbf{K}^{eff} = \begin{bmatrix} \mathbf{K}_{uu}^{eff} & \mathbf{K}_{u\varphi} & \mathbf{K}_{u\phi} \\ \mathbf{K}_{u\varphi}^T & -p\mathbf{K}_{\varphi\varphi} & -p\mathbf{K}_{\varphi\phi} \\ \mathbf{K}_{u\phi}^T & -p\mathbf{K}_{\varphi\phi}^T & -p\mathbf{K}_{\phi\phi} \end{bmatrix},$$

where $p = (1 + \frac{\varsigma_d \gamma}{\beta \tau})^{-1}$.

This matrix can be factorized using the LDL^T -factorization method, and only the systems of linear algebraic equations with lower and upper triangular matrices can be solved in each time layer.

According to (27.79)–(27.81), the Newmark scheme presented here is mathematically equivalent to the usual Newmark scheme with velocities and accelerations [33]. Consequently, it is absolutely stable, when $\beta \geq (1/2 + \gamma)^2/4$; $\gamma \geq 1/2$, and, when $\beta \geq 1/4$; $\gamma = 1/2$, it does not have an viscosity approximation. However, Newmark scheme (27.83)–(27.87) does not explicitly use velocities and accelerations, and this makes it preferable in the case of the transient problems for piezomagnetolectric nanosized solids with account for damping and surface effects.

27.5 Concluding Remarks

Thus, we have proposed a new model that describes the behavior of the magnetolectric material, taking into account the damping properties and surface effects at the nanoscale. Magnetolectric material here is understood as a composite consisting of piezoelectric and piezomagnetic phases, and is used to describe the theory of coupled piezomagnetolectric medium with effective properties. In the particular case, when we neglect the coupling with magnetic fields, this model describes the behavior of a well-known piezoelectric material with damping properties and nanoscale effects.

We consider dynamic problems in quasistatic approximation for the electric and magnetic fields. The novelty of the model consists in taking into account the damping properties, as well as surface phenomena, which are important at the nanoscale.

To describe the size effects, we use recently popular theory of surface stresses and its generalization to piezomagnetolectric media. Under this generalization, we also consider the surface electric and magnetic fields.

Another new feature is the account for the damping properties in the sense of a generalization of the conventional for the structural analysis Rayleigh damping

method for the electric and magnetic fields. We also added the terms, describing the attenuation, in the constitutive equations for the surface mechanic, electric and magnetic fields. By taking into account the damping, the basic idea was that for some relation between the damping coefficients, the method of mode superposition can be applied for transient and harmonic problems.

After the initial-boundary value problem setting for the magnetoelectric bodies, we have obtained a weak or generalized formulation of this problem in terms of energy functional spaces. We note that the basic mathematical properties of this problem are quite close to the particular case of the relevant problems for piezoelectric media. Therefore, most of the previously established results, valid for piezoelectric media, can be extended to the more general case of magnetoelectric media.

Thus, it can be shown as in [25, 38] that the magnetoelectric bodies of limited dimensions with surface effects without damping have a real countable spectrum of eigenvalues (resonant frequencies) with accumulation point at infinity, and the corresponding eigenvectors (modes of vibration) are orthogonal in the energy space associated with the operator of the problem. In addition, we can establish the theorems on the change of the natural frequencies under the change material moduli, including surface properties, and the change of the boundary conditions types, similar to [10]. Thus, the same type changes in the mechanical and electrical or magnetic properties and the boundary conditions will lead to opposite changes in the natural frequencies. In addition, the natural frequencies with the same numbers for the medium with the surface stresses are greater than the natural frequencies for the medium without surface stresses. However, the natural frequencies for the medium with the surface electric or magnetic films, on the contrary, are lesser than those values for the medium without these films.

In order to solve the formulated problems numerically, we use the finite element approaches. Based on the weak formulations of the problems, we derive the finite element equations for transient, harmonic, modal and static problems for magnetoelectric media. As we can see from the finite element systems, the account for the surface mechanical, electrical and magnetic effects gives the additional components in the stiffness matrix, the permittivity and permeability, which are formed by the diaphragm and the film elements at the respective borders. Therefore, for the computer analysis of nanoscale magnetoelectric bodies (as well as piezoelectric, piezomagnetic and elastic nanosized bodies) one can use the well-known finite element software with added membrane and film elements in finite element models.

We also demonstrate that for the dynamic problems, our models with the same damping coefficients allow one to use the method of mode superposition, which is efficient tool for the analysis of the influence of individual modes and for the analysis of the same model under various external loads.

In all cases, we show that the resulting finite element systems can be reduced to finite element problems with symmetric quasi-definite matrices typical for problems with a saddle point.

Examples of the finite element calculations for the case of piezoelectric bodies with surface effects previously appeared in [25, 38]. For calculations of

magnetolectric bodies, the developed technology can be extended within the same type of approaches. However, nowadays these approaches cannot be used in practice, as there is not enough experimental data on the surface properties of nanosized magnetolectric bodies.

Acknowledgments This work was supported by the Russian Science Foundation (Grant No. 15-19-10008).

References

1. H.L. Duan, J. Wang, B.L. Karihaloo, *Adv. Appl. Mech. Elsevier*, **42**, 1 (2008)
2. J. Wang, Z. Huang, H. Duan, S. Yu, X. Feng, G. Wang, W. Zhang, T. Wang, *Acta Mech. Solida Sin.* **24**, 52 (2011)
3. A. Javili, A. McBride, P. Steinmann, *Appl. Mech. Rev.* **65**, 010802 (2012)
4. M.E. Gurtin, A.I. Murdoch, *Arch. Ration. Mech. Analysis* **57**(4), 291 (1975)
5. C. Kim, C. Ru, P. Schiavone, *Math. Mech. Solids* **18**(1), 59 (2013)
6. H.L. Duan, J. Wang, Z.P. Huang, B.L. Karihaloo, *J. Mech. Phys. Solids* **53**, 1574 (2005)
7. H.L. Duan, J. Wang, B.L. Karihaloo, Z.P. Huang, *Acta Mater.* **54**, 2983 (2006)
8. V. Eremeyev, N. Morozov, *Dokl. Phys.* **55**(6), 279 (2010)
9. H. Altenbach, V.A. Eremeyev, L.P. Lebedev, *ZAMM* **90**(3), 231 (2010)
10. H. Altenbach, V.A. Eremeyev, L.P. Lebedev, *ZAMM* **91**(9), 699 (2011)
11. P. Schiavone, C.Q. Ru, *Int. J. Eng. Sci.* **47**(11), 1331 (2009)
12. V.A. Eremeyev, L.P. Lebedev, *Math. Mech. Solids* **18**(2), 204 (2013)
13. G.Y. Huang, S.W. Yu, *Phys. Status Solidi B* **243**(4), R22 (2006)
14. X.H. Pan, S.W. Yu, X.Q. Feng, *Sci. China: Phys. Mech. Astron.* **54**(4), 564 (2011)
15. Z. Yan, L.Y. Jiang, *J. Phys. D Appl. Phys.* **44**(36), 365301 (2011)
16. Z. Yan, L.Y. Jiang, *J. Phys. D Appl. Phys.* **45**(25), 255401 (2012)
17. X. Wang, X. Wang, J. Zhou, J. Song, J. Liu, N. Xu, Z.L. Wang, *Nano Lett.* **6**(12), 2768 (2006)
18. Z.L. Wang, J. Song, *Science* **312**(5771), 242 (2006)
19. U. Andreaus, F. dell'Isola, M. Porfiri, *J. Vib. Control* **10**(5), 625 (2004)
20. F. dell'Isola, M. Porfiri, S. Vidoli, *Comptes Rendus—Mecanique* **331**(1), 69 (2003)
21. C. Maurini, F. dell'Isola, D.D. Vescovo, *Mech. Syst. Signal Process.* **18**(5), 1243 (2004)
22. H.G. Craighead, *Science* **290**(5496), 1532 (2000)
23. K.L. Ekinci, M.L. Roukes, *Rev. Sci. Instrum.* **76**(6), 061101 (2005)
24. F. Hao, D. Fang, *J. Appl. Phys.* **113**(10), 104103 (2013)
25. A.V. Nasedkin, V.A. Eremeyev, *Advanced Structured Materials, 30, Surface Effects in Solid Mechanics—Models, Simulations and Applications*, vol. 105, eds. by H. Altenbach, N.F. Morozov (Springer-Verlag, Berlin Heidelberg, 2013)
26. K.S. Challagulla, A.V. Georgiades, *Int. J. Eng. Sci.* **49**, 85 (2011)
27. X.Y. Lu, H. Li, B. Wang, *J. Mech. Phys. Solids* **59**, 1966 (2011)
28. C.-W. Nan, M.I. Bichurin, S. Dong, D. Viehland, G. Srinivasan, *J. Appl. Phys.* **103**, 031101 (2008)
29. Z.K. Zhang, A.K. Soh, *Europ. J. Mech. A/Solids* **24**, 1054 (2005)
30. M. Benzi, G.H. Golub, J. Liesen, *Acta Numerica* **14**, 1 (2005)
31. A.V. Belokon, A.V. Nasedkin, A.N. Soloviev, *J. Applied Math. Mech. (PMM)* **66**(3), 481 (2002)
32. A.V. Nasedkin, in *Piezoceramic Materials and Devices*, vol. 177, ed. by I.A. Parinov (Nova Science Publishers, New York, 2010)
33. K.J. Bathe, E.L. Wilson, *Numerical Methods in Finite Elements Analysis* (Prentice-Hall, Englewood Cliffs, New Jersey, 1976)

34. O.C. Zienkewicz, K. Morgan, *Finite Elements and Approximation* (Wiley, New York, 1983)
35. D.A. Berlincourt, D.R. Curran, H. Jaffe, *Physical Acoustics, Part A, I*, vol. 233 (Academic Press, New York, 1964)
36. O.N. Akopov, A.V. Belokon, K.A. Nadolin, A.V. Nasedkin, A.S. Skaliukh, A.N. Soloviev, *Math. Model.* **13**(2), 51 (2001)
37. A.V. Belokon, V.A. Eremeyev, A.V. Nasedkin, A.N. Soloviev, *J. Appl. Math. Mech. (PMM)* **64**, 367 (2000)
38. A.V. Nasedkin, V.A. Eremeyev, *ZAMM* **94**(10), 878 (2014)

Chapter 28

The General Theory of Polarization of Ferroelectric Materials

Alexander Skaliukh and Guorong Li

Abstract In the frame of a quasi-static process, was built the general theory of polarization and deformation of polycrystalline ferroelectric materials, subject to the simultaneous action of an electric field and mechanical stresses. Constitutive relations were obtained for induced and residual increments of polarizing vector and strain tensor. Distinctive features of present theory from the previous theory are the introduction of the energy criterion of switching domains, the study of anisotropy of the partially polarized representative volume, the introduction of the functional dependence of physical characteristics on the residual polarization and deformation. The proposed model is founded for the three-dimensional case.

28.1 Introduction

Among the numerous applications of ferroelectric polycrystalline materials, leading place takes their using as sensors and actuators in various applicable devices. When we create work samples of such converters, the first and most important step in terms of technology is the process of polarization. In the process of polarization of polycrystalline ferroelectrics frequently encountered the situations when the electric field is non-uniform, i.e. its direction and intensity change from point to point of the bulk sample. Such a field generates an inhomogeneous field of the residual polarization and deformation inside the bulk sample. Moreover, during the operation, these residual fields have a significant impact on the distribution of the electrical and mechanical fields in the ceramic elements that are fundamentally different from the

A. Skaliukh (✉)

Vorovich Mathematics, Mechanics and Computer Sciences Institute,
Southern Federal University, 344090 Rostov-on-Don, Russia
e-mail: a.s.kaliukh@gmail.com

G. Li

Shanghai Institute of Ceramics, Chinese Academy of Sciences,
1295 Dingxi Road, Shanghai 200050, China

situation of homogeneous polarization fields. Therefore, the theoretical calculation of the field of residual polarization and deformation is important in terms of modeling of converter as a whole. On the other hand, the presence of pores and inclusions within the ceramic samples, as well as the edges of the electrodes on the surfaces where there is a change of type of boundary conditions can significantly alter the field of remnant polarization, even with applying the external electrical or mechanical load of low intensity. All these factors require creating effective mathematical models allowing, on the one hand, to compute the internal fields of residual polarization and strain and, on the other hand, to define the corresponding physical characteristics of the converter, such as eigen-frequencies, eigen-forms of vibration, amplitude-frequency characteristics, transfer function, etc.

The difficulty in modeling such problems mainly associated with the polycrystalline structure of the material and the ferroelectric domain structure of the crystallites. At the macroscopic level, the relationships between the mechanical and electrical parameters are described by nonlinear dependencies of the dielectric and strain hysteresis loops [1–4]. Such dependencies are the direct result of irreversible processes, what are also reflected in a selection and construction of models and methods for solving of arising mathematical problems. If at solving the linear problems of electrodynamics or the theory of elasticity is sufficient to know the characteristics of the material, i.e., the components of the dielectric tensor and components of elastic tensor, then in non-linear problems these features are already functions of residual polarization vector and strain tensor. In the linear problems, the coefficients of corresponding tensors are determined experimentally with a certain degree of accuracy. The distinction of one material from other is determined only by the various components of those tensors, which, nevertheless, are always constants. In nonlinear problems, describing the irreversible processes, functional hysteresis dependencies quite significantly differ during the transition from one material to other. Therefore, before using this or that model as a calculated model, it is necessary to “adjust” it to appropriate material. This means that it must adequately reflect the very specific dependencies of the hysteresis of the quite certain material.

Review of existing mathematical models polarization of polycrystalline ferroelectric materials and methods of their solutions can be found in [5, 6]. In the present study, it was done the attempt to build a complete system of equations and present methods of numerical solutions with viewpoint of common unified energy positions and new researches. Obviously, the complete system of equations can be obtained using the basic laws of continuum mechanics, electrodynamics and thermodynamics. The key issue in these tasks, related to irreversible processes, is the problem of the statement of constitutive relations, which complement the equations up to the full system. Since in such problems appear not only the induced but also a residual parameters, the constitutive relations should be formulated for them separately. Induced parameters are parameters of state, so they depend and completely determined by the internal energy of a thermodynamic system. The remnant parameters are the parameters of the process, therefore, they are determined by the dissipative properties of system which are necessary to determine their rates of change. For

quasi-static processes, it is possible to determine the increments of these parameters. The latter circumstance predetermines the choice of methods for solving the problem in the form of incremental theory. From a mathematical point of view, the incremental theory is a kind of finite difference method, and as shown by numerical calculations, it can be successfully used to solve this class of problems.

Regarding the induced parameters, we can say that they generally are defined as linear functions linking the conjugate parameters. The linearity of the relationship is defined by the energy relations, when the internal energy of the thermodynamic system is selected as a quadratic function.

With the irreversible parameters, the situation is much more complicated. Dissipative properties of the system should be determined from the energy positions, which associate with the construction of dissipative flows. If in systems with irreversible processes, there is little deviation from thermodynamic equilibrium, such flows can be built as a linear function of the thermodynamic forces (a typical example is the model of viscous liquid). In the problems of plasticity of continuum, polarization of ferroelectric, magnetization of ferromagnetic material, etc., such approaches are ineffective. Various situations are possible in these problems, including such of them when the internal structure of the material changes. For example, in the problems of the polarization by electric field of polycrystalline ferroelectrics, the material gets the piezoelectric properties and changes its elastic and dielectric properties, due to the transition to a different class of anisotropy. If besides the electric field, it is also applied the mechanical stress, and/or the principal axis of the stress tensor does not coincide with the direction of the electric field, the situation becomes even more complicated. Using linear decompositions of dissipative flows by the thermodynamic forces leads to this case. Therefore, in such cases, it is required to take into account an additional information about changing of the material structure. For example, in the problems of the plasticity, the surface polarization is introduced, which, together with the associated law of plastic flow, allows us to build relationships for determining the rate of irreversible parameters.

In our case, we have also attracted additional research of changes the domain structure of the material; we have built a balanced ratio of energy in which used the energy criterion of switching domains. Constitutive relations for the irreversible parameters of remnant strain and polarization were obtained in the form of equations in differentials, which can also be regarded as finite-difference equations.

All above-mentioned discussion dictated the method of solving the problem in a whole: namely, the incremental theory was used and the whole process was represented as a sequence of equilibrium states. All increments of unknown parameters at the transition from one state to other are determined by the increments of external mechanical stress and electric potential. After definition all of the increments of required parameters on the current state, we make the transition to the next state. Solution of the problem will be finished when all the external loads vanish.

Thus, in this chapter we proposed a general method for solving three-dimensional problems with the effects of polarization and depolarization by the electric field and mechanical stresses of polycrystalline ferroelectric materials of arbitrary geometry. Constitutive relations are constructed in three-dimensional case

in increments between required and defining parameters based on the use of additional models of locked walls. The whole algorithm for solving was inserted in the finite-element package ACELAN.

28.2 Physical Problem. Hypothesis and Assumptions

Let an arbitrary volume of thermally depolarized ceramics is subject to mechanical and electrical impacts, as shown in Fig. 28.1.

The main goal of the research is to derive a complete system of equations describing the irreversible process of polarization, i.e. the effect of influence on polycrystalline ferroelectrics (ceramics) the external mechanical and electrical factors of varying intensity. In other words, is required for any values of boundary functions, such as the displacement vector, vector of stress and electric potential \mathbf{u}_* , \mathbf{p}_* , φ_* to determine the full displacements, stresses, electric fields, and arising fields of residual polarization and residual strain in the bulk material.

Taking into account the factor that the processes occurring in ferroelectrics depend on the intensity of the external fields and the speed of the process, as well as a complex structure and changing structure of the material itself, we introduce a number of supposition and assumptions that will be used in the future.

- (1) *Particles.* We take the conditions $\text{mes } \Omega_{cr} \ll \text{mes } \Omega_* \ll \text{mes } \Omega$, where Ω , Ω_* , Ω_{cr} are the total volume of the body, a representative volume and the volume of the atomic cell, respectively. Figure 28.2 shows the material structure of the ferroelectric perovskite structure. As it follows from the general provisions [1], the representative volume, comprising a multiplicity of crystallites, is taken as a particle.
- (2) *Dynamics of the process.* We will study the processes that satisfy the conditions of quasi-static, i.e. the conditions where the rate of changing of external influences much less the rate of changing the internal parameters. By virtue of this, the inertial terms are vanish, and we can neglect a dynamics of switching domains (the independent variable of time t falls out from our consideration). In this approach, instead of rates of changing of external function is taken a

Fig. 28.1 Problem statement

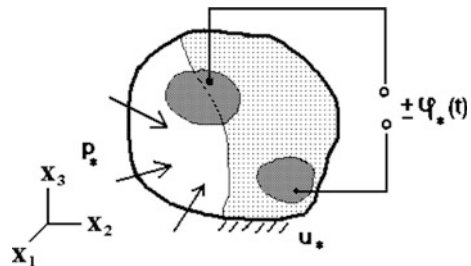
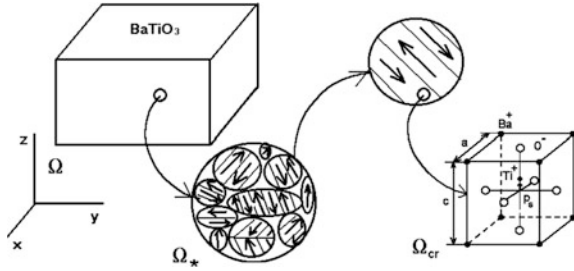


Fig. 28.2 Ferroelectric perovskite structure



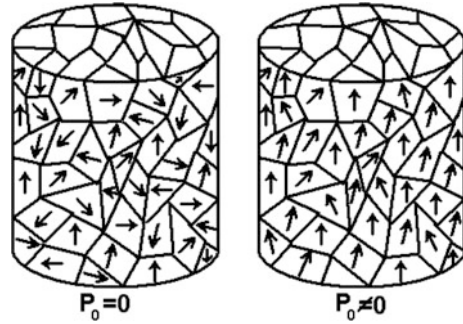
sequence of increments. For example, for an electrical potential $\varphi_* = \varphi_*(t)$, it is chosen the sequence of increments $\Delta\varphi_* = \varphi_*(t_{i+1}) - \varphi_*(t_i)$.

- (3) *Temperature.* It is considered the isothermal process with a temperature $T \ll T_C$, where T_C is the Curie temperature.
- (4) *Irreversibility.* Intensive external loads change the material structure. There is a nonlinear electromechanical response, which illustrate also the irreversible internal processes in them and showing self through hysteresis curves. Therefore, in general case, on a pair with external parameters of our system, we input the internal parameters that associate with the irreversibility of the process. They also describe the residual characteristics, which change the material structure. For external parameters is convenient to take a vector of electric field \mathbf{E} and a tensor of the stress $\boldsymbol{\sigma}$. The conjugating parameters to them will be a reversible parameters, namely the induced polarization vector \mathbf{P}_e and elastic tensor of strain $\boldsymbol{\varepsilon}_e$. The selection as independent parameters the mechanical stress and electric field is dictated by the results of numerous experiments, in which these parameters are principal and arbitrarily changeable.

When they reach the threshold values, the switching processes occur in the domains of the ferroelectric crystallites. For representative volume, the total effect of these switching is expressed in the appearance of the internal characteristics: the residual polarization vector \mathbf{P}_0 , and the residual strain tensor $\boldsymbol{\varepsilon}_0$. The vector of residual polarization is an average value of the spontaneous polarization vectors \mathbf{p}_s of all N cells within the particles $\mathbf{P}_0 = \frac{1}{N} \sum_{i=1}^N \mathbf{p}_s$, as it demonstrated in Fig. 28.3. Thus the total polarization and total strain are defined by the following relations $\mathbf{P} = \mathbf{P}_e + \mathbf{P}_0$, $\boldsymbol{\varepsilon} = \boldsymbol{\varepsilon}_e + \boldsymbol{\varepsilon}_0$ and the total deformation satisfy the physical conditions of compatibility of strains and the strain $\boldsymbol{\varepsilon}_0$ satisfy the conditions of incompressibility established by experimentally [7, 8].

- (5) *Phase transition.* During the switching of 180°- or 90°-domains in each crystal cell only the direction of the spontaneous polarization vector changes, but the cell remains in the same polar class. From the position of model of the continuum mechanics, the situation in the particle changes dramatically: unpolarized material goes into a state in which there are residual polarization and deformation. Anisotropy class of the material changes: continuous medium

Fig. 28.3 Polarization of the sample in dependence on the residual polarization vector \mathbf{P}_0



- undergoes a phase transition of type “body–body”, moving from one class of isotropy to another changing both of the mechanical and electrical properties.
- (6) *Geometrically linear theory.* Experiments have shown [9] that the total deformation in polycrystalline ferroelectric materials do not exceed 1–2 % even with creep long-time test. It allows one to apply the hypothesis of geometrically linear mechanics, and use the Lagrange coordinates, the integration carries out over the volume and surface of the initial configuration and we use the Cauchy linear tensor of strain and Euler tensor of stress.
 - (7) *Order of magnitudes.* On a par with the reversible part of the polarization, we introduce the non-reversible part of the electric displacement. Note that value of the residual polarization almost on order of the magnitude greater than value of a reversible part of polarization or reversible part of the electric displacement. This statement is made on the base of the experimental results by using the pictures of small dielectric hysteresis loops [2]. Similar experimental results with the strain hysteresis loops indicate that the order of value of the residual strain is approximately equal to the value of elastic strain.
 - (8) *Admissibility of fields.* Considered an intense, but the allowable values of mechanical stress and electric fields which mechanically does not destroy ceramics and does not cause electrical breakdown.
 - (9) *Membrane theory.* The question of existence in ceramics (strong dielectrics) the distributed volume or surface mechanical moments is now open, so we neglect these factors. For this reason, we take the classical theory without moments.

28.3 Mathematical Formulation of Problem

Let $\Omega \subset R^3$ is the volume filled with pure (thermally depolarized) ceramics, assigned to the coordinate system $Ox_1x_2x_3$, as shown in Fig. 28.1. Let \mathbf{u} is the displacement vector, φ is the electrical potential, $\boldsymbol{\sigma}$ is the stress tensor and \mathbf{D} is the

electric displacement vector (vector and tensor quantities are indicated in bold, scalar as usual).

As the main equations, we take the balanced equations of momentum, of angular momentum, Gauss's law, Faraday's law, the energy balance equation and the equation of the balance of entropy, which in differential form can be written as the following field equations:

- (i) equilibrium equation solid mechanics:

$$\nabla \cdot \boldsymbol{\sigma} + \rho \mathbf{f} = 0, \quad \boldsymbol{\sigma} = \boldsymbol{\sigma}^T; \quad (28.1)$$

- (ii) Maxwell's equations, the equations of electrostatics non-conducting dielectrics:

$$\nabla \cdot \mathbf{D} = 0, \quad \nabla \times \mathbf{E} = 0; \quad (28.2)$$

- (iii) the energy equation:

$$\rho \dot{u} = \boldsymbol{\sigma} : \dot{\boldsymbol{\varepsilon}} + \mathbf{E} \cdot \dot{\mathbf{D}} - \nabla \cdot \mathbf{q} + \rho \omega; \quad (28.3)$$

- (iv) the entropy inequality:

$$\rho \dot{s} \geq \frac{\rho \omega}{T} - \frac{\nabla \cdot \mathbf{q}}{T} - \mathbf{q} \cdot \nabla \left(\frac{1}{T} \right) \quad (28.4)$$

Here, on a par with the above parameters, are additionally introduced the field characteristics: ρ , \mathbf{f} , u , \mathbf{q} , ω , s , T , which are the mass density, density of the mass forces, mass density of the internal energy, the vector of the heat flow, internal heat sources per unit mass, mass density of entropy and absolute temperature, respectively. The top point, as usually designs the substantial (the complete) time derivative; ∇ , $\nabla \cdot$, $\nabla \times$ are the operations of gradient, divergence and curl, respectively.

To these equations, we add the geometric relationships connecting the electric potential and the displacement vector with the vector of the electric field and strain tensor:

$$\mathbf{E} = -\nabla \phi, \quad \boldsymbol{\varepsilon} = \frac{1}{2}(\nabla \mathbf{u} + \nabla \mathbf{u}^T); \quad (28.5)$$

the second relation in (28.2) satisfies identically in this case. Furthermore, in (28.1), inertial forces are neglected due to the assumption of quasi-static process.

To complete the task, we must add the constitutive relations for reversible components of the polarization and deformation, as well as to formulate a law to determine the rate of changing of the residual components of the polarization and deformation. Such dependencies in general case can be represented by the following operator relationships:

$$\boldsymbol{\varepsilon}_e = \mathbf{f}_\sigma(\boldsymbol{\sigma}, \mathbf{E}; \mathbf{P}_0, \boldsymbol{\varepsilon}_0), \quad \mathbf{P}_e = \mathbf{f}_P(\boldsymbol{\sigma}, \mathbf{E}; \mathbf{P}_0, \boldsymbol{\varepsilon}_0); \quad (28.6)$$

$$\dot{\boldsymbol{\varepsilon}}_0 = \mathbf{F}_1(\boldsymbol{\sigma}, \mathbf{E}; \boldsymbol{\varepsilon}_0, \mathbf{P}_0, E_c, \sigma_c, \dots), \quad \dot{\mathbf{P}}_0 = \mathbf{F}_2(\boldsymbol{\sigma}, \mathbf{E}; \boldsymbol{\varepsilon}_0, \mathbf{P}_0, E_c, \sigma_c, \dots); \quad (28.7)$$

in which there are some threshold values (coercive values) of the electric field and mechanical stress (E_c, σ_c, \dots) , that determine the beginning of an irreversible process, and moreover

$$\boldsymbol{\varepsilon} = \boldsymbol{\varepsilon}_e + \boldsymbol{\varepsilon}_0, \quad \mathbf{D} = \varepsilon_0 \mathbf{E} + \mathbf{P}_e + \mathbf{P}_0. \quad (28.8)$$

One way to solve this problem is concrete definition of the functional relations (28.6), (28.7), i.e. the construction of two thermodynamic functions of internal and external parameters, which include the function of the internal energy and the function of rate of dissipation, which depends on the generalized dissipative forces. However, proper formulation of these functions is possible only for simple environments, but only with the followed experimental determination of contained parameters. In more complex situations, as it takes place in the considered problem it is impossible for every process. Therefore, below on a par with the thermodynamic equations, we shall consider the auxiliary model of the polarization and deformation processes and comment the conditions by which they may be used instead of the thermodynamic relations.

Note that the parameters \mathbf{P}_e , $\boldsymbol{\varepsilon}_e$ are the variables of state, therefore they are determined by the current values of the mechanical stress and the electric field, but the internal parameters \mathbf{P}_0 , $\boldsymbol{\varepsilon}_0$ are the variables of the process, therefore the current values of the electric fields and mechanical stress can be identified by only the rate of their changes.

To formulate the boundary conditions, we assume that the boundary S has a two unrelated divisions: $S = S_\sigma \cup S_u = S_D \cup S_\varphi$, moreover, $S_\sigma \cap S_u = 0$ and $S_D \cap S_\varphi = 0$. The displacement vector and stress vector relate to a mechanical conditions, which are defined on S_u and S_σ , respectively. Electric potential and the normal component of the electric displacement belong to electrical conditions which are defined on S_φ and S_D , what can be written as

$$\mathbf{u} = \mathbf{u}_*(t) \text{ on } S_u; \quad \mathbf{n} \cdot \boldsymbol{\sigma} = \mathbf{p}_*(t) \text{ on } S_\sigma; \quad \varphi = \varphi_*(t) \text{ on } S_\varphi; \quad \mathbf{n} \cdot \mathbf{D} = \mathbf{0} \text{ on } S_D. \quad (28.9)$$

Additionally we must set the initial conditions for irreversible components. For example, in the case of an unpolarized ceramics, we have

$$\mathbf{P}_0|_{t=0} = 0, \quad \boldsymbol{\varepsilon}_0|_{t=0} = 0. \quad (28.10)$$

If initially, ceramic was polarized in some way, it is necessary to specify the field of the residual polarization and the residual strain in the initial time.

To solve the problem, we define the solutions of (28.1)–(28.7) satisfying (28.9), (28.10).

28.4 Constitutive Equations

As it follows from (28.1)–(28.10), the main goal of the research is to establish the constitutive relations (28.6), (28.7) for the process of polarization and deformation. For this purpose, we will use the first and second laws of thermodynamics (28.3), (28.4). We introduce the function of Gibbs:

$$G = u - Ts - \frac{1}{\rho} \boldsymbol{\sigma} : \boldsymbol{\varepsilon} - \frac{1}{\rho} \mathbf{E} \cdot \mathbf{D}. \quad (28.11)$$

Using the standard scheme, we exclude the density of internal heat sources from previous relationships and get dissipative inequality:

$$-\rho \dot{G} - \rho \dot{T}s - \dot{\boldsymbol{\sigma}} : \boldsymbol{\varepsilon} - \dot{\mathbf{E}} \cdot \mathbf{D} - \frac{\mathbf{q} \cdot \nabla T}{T} \geq 0. \quad (28.12)$$

By keeping a sufficient commonality, and considering only a finite number of parameters of state, we study the continuum of differential type and we can select minimal set of state parameters as

$$\boldsymbol{\sigma}, \mathbf{E}, T, \boldsymbol{\varepsilon}_0, \mathbf{P}_0.$$

Inequality (28.12) simplifies and takes the form, called the inequality of rate of dissipation:

$$\begin{aligned} -\rho(G_{,T} + s)\dot{T} - (\rho G_{,\boldsymbol{\sigma}} + \boldsymbol{\varepsilon}) : \dot{\boldsymbol{\sigma}} - (\rho G_{,\mathbf{E}} + \mathbf{D}) \cdot \dot{\mathbf{E}} - \frac{\mathbf{q} \cdot \nabla T}{T} - \rho G_{,\boldsymbol{\varepsilon}_0} \\ : \dot{\boldsymbol{\varepsilon}}_0 - \rho G_{,\mathbf{P}_0} \cdot \dot{\mathbf{P}}_0 \geq 0. \end{aligned}$$

Here we used the standard notations $G_{,T}$; $G_{,\boldsymbol{\sigma}}$; $G_{,\mathbf{E}}$; $G_{,\boldsymbol{\varepsilon}_0}$; $G_{,\mathbf{P}_0}$, that are the derivative of the Gibbs function with respect to scalar, vector and tensor fields specified after the comma.

We introduce the function of the dissipation rate S_i as

$$\begin{aligned} -\rho(G_{,T} + s)\dot{T} - (\rho G_{,\boldsymbol{\sigma}} + \boldsymbol{\varepsilon}) : \dot{\boldsymbol{\sigma}} - (\rho G_{,\mathbf{E}} + \mathbf{D}) \cdot \dot{\mathbf{E}} - \frac{\mathbf{q} \cdot \nabla T}{T} - \rho G_{,\boldsymbol{\varepsilon}_0} \\ : \dot{\boldsymbol{\varepsilon}}_0 - \rho G_{,\mathbf{P}_0} \cdot \dot{\mathbf{P}}_0 = S_i \geq 0. \end{aligned} \quad (28.13)$$

At thermodynamic equilibrium, this function is zero. In the non-equilibrium thermodynamic processes where there are small deviations from equilibrium, the entropy production S_i can be represented as a linear approximation over the velocities of independent parameters and the temperature gradient in the next form of linear kinematic combinations:

$$S_i = \chi_s^S \dot{T} + \chi_\varepsilon^S : \dot{\sigma} + \chi_D^S \cdot \dot{\mathbf{E}} + \chi_{\varepsilon_0}^S : \dot{\varepsilon}_0 + \chi_{P_0}^S \cdot \dot{\mathbf{P}}_0 + \frac{\chi_q^S \cdot \nabla T}{T}. \quad (28.14)$$

The generalized dissipative forces $\chi_s^S, \chi_\varepsilon^S, \dots$, in a general case, are functions that depend from the aforementioned parameter set as well as the velocities of these parameters and the temperature gradient, i.e. $\boldsymbol{\sigma}, \mathbf{E}, T, \varepsilon_0, \mathbf{P}_0, \dot{\sigma}, \dot{\mathbf{E}}, \dot{T}, \dot{\varepsilon}_0, \dot{\mathbf{P}}_0, \nabla T$. Most importantly, they must provide the fulfillment of inequality of dissipation rate (28.13). In general, we take into consideration the dependence of Gibbs function from following main parameters of the our task $G = G(\boldsymbol{\sigma}, \mathbf{E}, T, \varepsilon_0, \mathbf{P}_0)$, then on the base of (28.13), (28.14), we obtain the following equalities:

$$\begin{aligned} \boldsymbol{\varepsilon} &= -\rho G_{,\boldsymbol{\sigma}} - \chi_\varepsilon^S(\boldsymbol{\sigma}, \mathbf{E}, T, \varepsilon_0, \mathbf{P}_0, \dot{\sigma}, \dot{\mathbf{E}}, \dot{\varepsilon}_0, \dot{\mathbf{P}}_0), \\ \mathbf{D} &= -\rho G_{,\mathbf{E}} - \chi_D^S(\boldsymbol{\sigma}, \mathbf{E}, T, \varepsilon_0, \mathbf{P}_0, \dot{\sigma}, \dot{\mathbf{E}}, \dot{\varepsilon}_0, \dot{\mathbf{P}}_0), \\ s &= -G_{,T} - \chi_s^S(\boldsymbol{\sigma}, \mathbf{E}, T, \varepsilon_0, \mathbf{P}_0, \dot{\sigma}, \dot{\mathbf{E}}, \dot{\varepsilon}_0, \dot{\mathbf{P}}_0) \\ -\rho G_{,\varepsilon_0} &= \chi_{\varepsilon_0}^S(\boldsymbol{\sigma}, \mathbf{E}, T, \varepsilon_0, \mathbf{P}_0, \dot{\sigma}, \dot{\mathbf{E}}, \dot{\varepsilon}_0, \dot{\mathbf{P}}_0), \\ -\rho G_{,\mathbf{P}_0} &= \chi_{P_0}^S(\boldsymbol{\sigma}, \mathbf{E}, T, \varepsilon_0, \mathbf{P}_0, \dot{\sigma}, \dot{\mathbf{E}}, \dot{\varepsilon}_0, \dot{\mathbf{P}}_0), \\ \mathbf{q} &= -\chi_{P_0}^S(\boldsymbol{\sigma}, \mathbf{E}, T, \varepsilon_0, \mathbf{P}_0, \dot{\sigma}, \dot{\mathbf{E}}, \dot{\varepsilon}_0, \dot{\mathbf{P}}_0) \cdot \nabla T. \end{aligned} \quad (28.15)$$

Further studies in this area require the specification of the Gibbs function and dissipative forces.

Considering the processes of “cold” polarization, as it mentioned in assumption 3, we get that $G = G(\boldsymbol{\sigma}, \mathbf{E}, \varepsilon_0, \mathbf{P}_0)$. The function of the dissipation rate (28.14) and the dissipative inequality (28.13) can be written as

$$S_i = \chi_s^S : \dot{\sigma} + \chi_D^S \cdot \dot{\mathbf{E}} + \chi_{\varepsilon_0}^S : \dot{\varepsilon}_0 + \chi_{P_0}^S \cdot \dot{\mathbf{P}}_0, \quad (28.16)$$

$$-(\rho G_{,\boldsymbol{\sigma}} + \boldsymbol{\varepsilon}) : \dot{\sigma} - (\rho G_{,\mathbf{E}} + \mathbf{D}) \cdot \dot{\mathbf{E}} - \rho G_{,\varepsilon_0} : \dot{\varepsilon}_0 - \rho G_{,\mathbf{P}_0} \cdot \dot{\mathbf{P}}_0 = S_i \geq 0 \quad (28.17)$$

and from (28.15), we obtain the relations:

$$\begin{aligned} \boldsymbol{\varepsilon} &= -\rho G_{,\boldsymbol{\sigma}} - \chi_\varepsilon^S(\boldsymbol{\sigma}, \mathbf{E}, \varepsilon_0, \mathbf{P}_0, \dot{\sigma}, \dot{\mathbf{E}}, \dot{\varepsilon}_0, \dot{\mathbf{P}}_0), \\ \mathbf{D} &= -\rho G_{,\mathbf{E}} - \chi_D^S(\boldsymbol{\sigma}, \mathbf{E}, \varepsilon_0, \mathbf{P}_0, \dot{\sigma}, \dot{\mathbf{E}}, \dot{\varepsilon}_0, \dot{\mathbf{P}}_0), \\ -\rho G_{,\varepsilon_0} &= \chi_{\varepsilon_0}^S(\boldsymbol{\sigma}, \mathbf{E}, \varepsilon_0, \mathbf{P}_0, \dot{\sigma}, \dot{\mathbf{E}}, \dot{\varepsilon}_0, \dot{\mathbf{P}}_0), \\ -\rho G_{,\mathbf{P}_0} &= \chi_{P_0}^S(\boldsymbol{\sigma}, \mathbf{E}, \varepsilon_0, \mathbf{P}_0, \dot{\sigma}, \dot{\mathbf{E}}, \dot{\varepsilon}_0, \dot{\mathbf{P}}_0). \end{aligned} \quad (28.18)$$

Relying once more on assumptions 6 and 7, we state that the induced parts of deformation and polarization $\boldsymbol{\varepsilon}_e, \mathbf{P}_e$ are small, whereby it is sufficient to choose the function of the internal energy as a quadratic form, depending on the parts of the reversible deformation and polarization $u = u(\boldsymbol{\varepsilon}_e, \mathbf{P}_e, \varepsilon_0, \mathbf{P}_0)$. In this case, the state of representative volume completely determined by mechanical stresses and electric

field and the residual parts of strain and polarization as well as linear piezoelectric properties of such a continuum. Turning to the electrical function Gibbs, we can see that it is defined by the following expression:

$$G = -\frac{1}{\rho}(\boldsymbol{\sigma} : \boldsymbol{\varepsilon}_0 + \mathbf{E} \cdot \mathbf{P}_0) - \frac{1}{2\rho}[\boldsymbol{\sigma} : \mathbf{S}(\boldsymbol{\varepsilon}_0, \mathbf{P}_0) : \boldsymbol{\sigma} + 2\mathbf{E} \cdot \mathbf{d}(\boldsymbol{\varepsilon}_0, \mathbf{P}_0) : \boldsymbol{\sigma} + \mathbf{E} \cdot \boldsymbol{\varepsilon}(\boldsymbol{\varepsilon}_0, \mathbf{P}_0) \cdot \mathbf{E}]. \quad (28.19)$$

The included here elastic compliances, piezoelectric moduli and dielectric constants are continuously differentiable functions of the residual parameters. In the future, they also must be determined from additional physical representations of class anisotropy of partially polarized ceramics.

The next step is the choice of generalized dissipative forces so that, on the one hand, would be fulfilled the inequality of dissipation rate, and on the other hand, would be reflected the physics of process in strong electrical and mechanical fields. Desiring do not complicate the model and at the same time reflect all the basic properties of the system we will ignore the viscoelastic properties of reversible components. This assumption suggests that $\chi_{\varepsilon}^S = \chi_{\mathbf{D}}^S = 0$.

Then from (28.17) and (28.18), we obtain the equalities:

$$\begin{aligned} \boldsymbol{\varepsilon} &= -\rho G_{,\boldsymbol{\sigma}} = \boldsymbol{\varepsilon}_0 + \mathbf{S}(\boldsymbol{\varepsilon}_0, \mathbf{P}_0) : \boldsymbol{\sigma} + \mathbf{d}^T(\boldsymbol{\varepsilon}_0, \mathbf{P}_0) \cdot \mathbf{E}, \\ \mathbf{D} &= -\rho G_{,\mathbf{E}} = \mathbf{P}_0 + \mathbf{d}(\boldsymbol{\varepsilon}_0, \mathbf{P}_0) : \boldsymbol{\sigma} + \boldsymbol{\varepsilon}(\boldsymbol{\varepsilon}_0, \mathbf{P}_0) \cdot \mathbf{E}, \end{aligned} \quad (28.20)$$

Here, the elastic compliance tensor $\mathbf{S}(\boldsymbol{\varepsilon}_0, \mathbf{P}_0)$, the tensor of piezoelectric modules $\mathbf{d}(\boldsymbol{\varepsilon}_0, \mathbf{P}_0)$, and the permittivity tensor $\boldsymbol{\varepsilon}(\boldsymbol{\varepsilon}_0, \mathbf{P}_0)$ are the tensor functions of the tensor arguments, namely, residual strain and residual polarization $\boldsymbol{\varepsilon}_0, \mathbf{P}_0$, by this $\mathbf{d}^T = \mathbf{d}^{T(1,(23))}$. It is easy to see that when the plastic deformations and residual polarization are changing the elasticity tensor, piezoelectric and dielectric constants also changing, but the form of linear dependence is determined by relations (28.20) for reversible parameters and is conserved. In addition, the existence of the thermodynamic functions G imposes symmetric conditions for the tensors:

$$\mathbf{S} = \mathbf{S}^{T(1,2)} = \mathbf{S}^{T(3,4)} = \mathbf{S}^{T((12),(34))}; \quad \mathbf{d} = \mathbf{d}^{T(2,3)}; \quad \boldsymbol{\varepsilon} = \boldsymbol{\varepsilon}^{T(1,2)}.$$

28.5 Definition of Anisotropy Class of Partially Polarized Ceramic

One of the main issues, when we examine ceramics with the partial polarization, is the issue about a class of anisotropy of representative volume, when the mechanical stresses and electric field are applied to the volume simultaneously. To this end, we have built a supporting model, in which the arising due to the application of

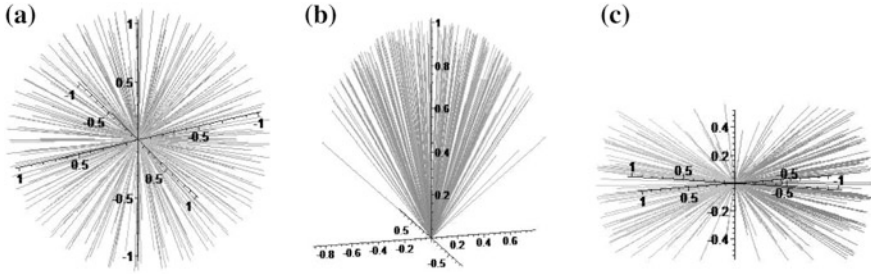


Fig. 28.4 **a** Axes of spontaneous polarization in the unpolarized state; **b** axes of spontaneous polarization under polarization at electric field; **c** axes of spontaneous polarization at the simultaneous influence of electric field and mechanical stresses

external loads residual polarization and residual strain are estimated. We have calculated also the elastic, piezoelectric and dielectric constants of the representative volume. Based on the results of these data, we infer about the class of anisotropy of the partially polarized ceramics. In our studies, we took into account only the process of dipoles switching at the electric field and mechanical stresses, but did not consider the effect of switching of neighboring domains on each other.

Briefly, an auxiliary model can be described as follows. We consider a representative volume, which contains lot of domains and take any point as a point of bringing the vectors. We associate with each vector of spontaneous polarization the unit vector having a direction of the vector spontaneous polarization and beginning at the selected point. Then, in the unpolarized state, a huge set of unit vectors in space will occupy the positions shown in Fig. 28.4a.

After application of an electric field, according to [10], we get a picture of their distribution, as shown in Fig. 28.4b. If a par with an electric field also the compressive stress is applied, then the distribution pattern of domains is shown in Fig. 28.4c. To build and evaluate the new position of the axes of each of a spontaneous polarization vector, we need to specify, first, the direction of the crystallographic axes of each of the domains, and, secondly, the criterion according which a new direction of spontaneous polarization vector is defined for given electrical and mechanical fields. Thereafter we implement averaging by all vectors of a spontaneous polarization and calculate the elastic, piezoelectric and dielectric constants of the representative volume. To be specific, the study was carried for the ferroelectrics of perovskite type.

Let a representative volume related to the Cartesian system has unit vectors $\mathbf{i}_1, \mathbf{i}_2, \mathbf{i}_3$. Suppose that process of applying the electric field and mechanical stresses is present as a series of equilibrium states $C^{(i)}$. The transition from one state $C^{(i)}$ to other $C^{(i+1)}$ occurs when acting loads acquire some increments $\boldsymbol{\sigma}^{(i+1)} = \boldsymbol{\sigma}^{(i)} + \Delta\boldsymbol{\sigma}^{(i)}$, $\mathbf{E}^{(i+1)} = \mathbf{E}^{(i)} + \Delta\mathbf{E}^{(i)}$. Note that the crystallographic axis of an individual domain in the representative volume for the current state can be uniquely determined by three angles of rotation ϕ_k, ψ_k, ω_k , $k = 1, \dots, N$. Denote the unit

vectors of this axes as $\mathbf{e}_1^{(i)}, \mathbf{e}_2^{(i)}, \mathbf{e}_3^{(i)}$, then the spontaneous polarization and spontaneous deformation are determined as follows $\mathbf{p}_s^{(i)} = p_s^{(i)} \mathbf{e}_1^{(i)}$, $\boldsymbol{\varepsilon}_s^{(i)} = \varepsilon_s^{(i)} (\mathbf{e}_1^{(i)} \mathbf{e}_1^{(i)} - \frac{1}{2} \mathbf{e}_2^{(i)} \mathbf{e}_2^{(i)} - \frac{1}{2} \mathbf{e}_3^{(i)} \mathbf{e}_3^{(i)})$. We believe that for all domains of representative volume the mechanical stresses and the electric field are the same. In the transition from one state to other, domain can switch to the new direction. The switching process is not arbitrary, and takes place only according to certain rules. First, the switching will be occurred only in the frame of the existing crystallographic axis, and only to such a direction where its energy in the loading fields is smallest. Secondly, switching will be possible only when the external load reach the threshold value. Without dwelling on the review of the various criteria of switching, we use the energy criterion. According to this criterion, the switching in the current state will take place only if the difference between the energy of domain current position and the energy of domain in a new position will exceed a certain threshold value. This criterion determines also the calculation algorithm. Namely, initially for each domain, we compute all possible values of its energy in predetermined fields. After that, we select the minimum value and determine the direction to which will be the switching according to the proposed criteria. Mathematically, this means that the unit vectors of local coordinate system are interchanged. Other words, we can say that we have identified the new crystallographic axis $\mathbf{e}_1^{(i+1)}_k$, $\mathbf{e}_2^{(i+1)}_k$, $\mathbf{e}_3^{(i+1)}_k$ of the domain with number k . Having done this for each domains of a representative volume, we can calculate the residual polarization and residual strain for this state:

$$\mathbf{P}_0^{(i+1)} = \frac{1}{N} \sum_{k=1}^N \mathbf{p}_s^{(i+1)}_k, \quad \boldsymbol{\varepsilon}_0^{(i+1)} = \frac{1}{N} \sum_{k=1}^N \boldsymbol{\varepsilon}_s^{(i+1)}_k$$

The new crystallographic axis of each domain allows us to compute the matrices $R_k^{(i+1)}$, $L_k^{(i+1)}$ of transition from these axes to the axes of the main system $\mathbf{i}_1, \mathbf{i}_2, \mathbf{i}_3$ of the representative volume. Because of the bulkiness, these matrices are not written out, but can be found in [5, 6]. Considering constitutive relations (28.20) and the condition of invariability of mechanical stress and an electric field for the considered representative volume, we can make averaging and obtain

$$\begin{aligned} \varepsilon_e^{(i+1)} &= \langle \varepsilon_e^{(i+1)}_k \rangle = \left(\frac{1}{N} \sum_{k=1}^N R_k^{(i+1)T} \cdot S \cdot R_k^{(i+1)} \right) \cdot \sigma^{(i+1)} + \left(\frac{1}{N} \sum_{k=1}^N R_k^{(i+1)T} \cdot d \cdot L_k^{(i+1)} \right) \cdot \mathbf{E}^{(i+1)}, \\ D_e^{(i+1)} &= \langle D_e^{(i+1)}_k \rangle = \left(\frac{1}{N} \sum_{k=1}^N L_k^{(i+1)T} \cdot d \cdot R_k^{(i+1)} \right) \cdot \sigma^{(i+1)} + \left(\frac{1}{N} \sum_{k=1}^N L_k^{(i+1)T} \cdot \ni \cdot L_k^{(i+1)} \right) \cdot \mathbf{E}^{(i+1)}. \end{aligned}$$

Here the matrix of compliances, matrices of piezoelectric and dielectric constants were been taken as appropriate matrices of the ferroelectric single crystal. The last step in this algorithm is to select local axes associated with the polarization of the

representative volume. There are three main situations: (i) polarization is implemented by the electric field with zero mechanical stresses; (ii) depolarization is implemented by the mechanical stresses with zero electric field (for short-circuited electrodes); (iii) polarization of ceramics is implemented with simultaneous exposure of the electric field and mechanical stresses. In the first case, we select a one axis $\mathbf{e}_\zeta^{(i+1)}$ along the direction of remnant polarization, while the other two axes $\mathbf{e}_\eta^{(i+1)}$, $\mathbf{e}_\xi^{(i+1)}$ are in the plane perpendicular to the first axis. In the second case, when the vector of the residual polarization is zero, we select two axes $\mathbf{e}_\eta^{(i+1)}$, $\mathbf{e}_\xi^{(i+1)}$ so that they are directed along the principal axes of the residual strain tensor. The third axis $\mathbf{e}_\zeta^{(i+1)}$ is orthogonal to the previous two. The third case is insufficiently investigated. Such selected axis allow one to determine the matrices of transition to the main coordinate system and calculate the corresponding matrix of compliances, matrices of piezoelectric coefficients and dielectric permittivities in the local axes of partly polarized ceramics.

$$\begin{aligned} \tilde{S} &= (RR)^T \cdot \langle S^{(i+1)} \rangle \cdot (RR), & S^{(i+1)} &= \frac{1}{N} \sum_{k=1}^N R_k^{(i+1)T} \cdot S \cdot R_k^{(i+1)}, \\ \tilde{d} &= (LL)^T \cdot \langle d^{(i+1)} \rangle \cdot (RR), & d^{(i+1)} &= \frac{1}{N} \sum_{k=1}^N L_k^{(i+1)T} \cdot d \cdot R_k^{(i+1)}, \\ \tilde{\ni} &= (LL)^T \cdot \langle \ni^{(i+1)} \rangle \cdot (LL), & \ni^{(i+1)} &= \frac{1}{N} \sum_{k=1}^N L_k^{(i+1)T} \cdot \ni \cdot L_k^{(i+1)}. \end{aligned}$$

The proposed studies allow us to assert that the partly polarized by electric field or depolarized by mechanical stresses ceramic belongs to the class of transversely isotropic body. All these results allow us to select the functional dependencies of the elastic compliances, piezoelectric moduli and dielectric constants in the form of a function of the residual parameters.

In the case when the polarization is executed by an electric field with zero mechanical stresses, we proceed as follows. A polarized to saturation state ceramic has polarization $|\mathbf{P}_0| = p_{sat}$ and refers to a class of transversely isotropic bodies, with the axis of isotropy directed along the polarization vector. Suppose that in the unpolarized state, these tensors accept the values:

$$\mathbf{S} = \mathbf{S}_0, \quad \mathbf{d} = 0, \quad \ni = \ni_0.$$

In the state of polarization up to saturation, we have

$$\mathbf{S} = \mathbf{S}_{sat}^E, \quad \mathbf{d} = \mathbf{d}_{sat}^E, \quad \ni = \ni_{sat}^E$$

We introduce the correcting tensors:

$$\mathbf{S}_1 = \mathbf{S}_{sat}^E - \mathbf{S}_0, \quad \mathbf{d}_1 = \mathbf{d}_{sat}^E, \quad \vartheta_1 = \vartheta_{sat}^E - \vartheta_0$$

Then we can construct the following linear function of the residual polarization

$$\mathbf{S}^{(E)} = \mathbf{S}_0 + \frac{|\mathbf{P}_0|}{P_{sat}} \mathbf{S}_1, \quad \mathbf{d}^{(E)} = \frac{|\mathbf{P}_0|}{P_{sat}} \mathbf{d}_1, \quad \vartheta^{(E)} = \vartheta_0 + \frac{|\mathbf{P}_0|}{P_{sat}} \vartheta_1. \quad (28.21)$$

Index “E” means that the physical moduli calculate only for the case of polarization by electric field.

For the case when depolarization performs by mechanical stresses with zero electric field, we find the principal values and direction of the principal axes of the residual strain tensor. Two of principal values are equal, but third ε_{III} will be different from these two. As this third axis we choose an axis of isotropy, while the other two axes will be in the perpendicular plane. In a state of maximum deformation, all vectors of spontaneous polarization will be placed in a symmetric shape; the residual polarization is zero, and, as a consequence, the tensor of piezoelectric moduli will be zero, that is

$$\mathbf{S} = \mathbf{S}_{sat}^\sigma, \quad \vartheta = \vartheta_{sat}^\sigma.$$

We introduce the correcting tensors:

$$\mathbf{S}_1 = \mathbf{S}_{sat}^\sigma - \mathbf{S}_0, \quad \vartheta_1 = \vartheta_{sat}^\sigma - \vartheta_0.$$

Then we can construct the following linear function of the residual strain:

$$\mathbf{S}^{(\sigma)} = \mathbf{S}_0 + \frac{|\varepsilon_{III}|}{\varepsilon_{sat}} \mathbf{S}_1, \quad \mathbf{d}^{(\sigma)} = 0, \quad \vartheta^{(\sigma)} = \vartheta_0 + \frac{|\varepsilon_{III}|}{\varepsilon_{sat}} \vartheta_1. \quad (28.22)$$

28.6 Constitutive Relations for Residual Components

A model of locked wall is present in [5], which allows one to find a residual polarization and a full polarization in one-dimensional case. In [6] this model was extended to three-dimensional case. The main shortcomings of the discussed models were as follows: (i) the position of each domain is defined by direction of one vector, while the directions of other two axes are not taken into account; (ii) there was used a basic model of locked wall in which it is impossible to consider the simultaneous effect of an electric field and mechanical stresses in three-dimensional case. To overcome these shortcomings, we proposed to characterize each domain by three unit vectors and to use the model of the locked walls. Detail choice of the axes has been described in Sect. 28.5 of this chapter, where we

investigated the anisotropy of the partially polarized ceramics. To determine the conditions of switching of domain and identify new directions of its axes, we proposed to use energy criterion of switching domains as discussed in Sect. 28.5 of this chapter, which can be mathematically represented as follows:

$$U - U_{\min} \geq U_c, \quad \begin{aligned} & -\mathbf{p}_S \cdot (\mathbf{E} + \alpha \mathbf{P}_0) - \mathbf{p}_S^{\min} \cdot (\mathbf{E} + \alpha \mathbf{P}_0) - \\ & -\boldsymbol{\varepsilon}_S : (\boldsymbol{\sigma} + \beta \boldsymbol{\varepsilon}_0) - \boldsymbol{\varepsilon}_S^{\min} : (\boldsymbol{\sigma} + \beta \boldsymbol{\varepsilon}_0) \geq U_c. \end{aligned} \quad (28.23)$$

Here \mathbf{E} , $\boldsymbol{\sigma}$, \mathbf{P}_0 , $\boldsymbol{\varepsilon}_0$ are the electric field, mechanical stress, the residual polarization and the residual strain, respectively; \mathbf{p}_S , $\boldsymbol{\varepsilon}_S$ are the spontaneous polarization and spontaneous strain of domain before switching, respectively; \mathbf{p}_S^{\min} , $\boldsymbol{\varepsilon}_S^{\min}$ are the position of the spontaneous polarization vector and tensor of spontaneous strain in a state where domain's energy is minimal, respectively; α , β are constants to be determined thereafter; U_c is the critical energy at which the switching domain occurs. After switching at the current state, the residual polarization and the residual strain are defined as follows:

$$\mathbf{P}_{\infty}^{(i+1)} = \frac{1}{N} \sum_{k=1}^N \mathbf{p}_s^{(i+1)}{}_k, \quad \boldsymbol{\varepsilon}_{\infty}^{(i+1)} = \frac{1}{N} \sum_{k=1}^N \boldsymbol{\varepsilon}_s^{(i+1)}{}_k \quad (28.24)$$

Note, these values will be maximum possible; they were obtained under the condition that the switching of adjacent domains does not affect on the process of switching each other. Therefore, they are marked with “ ∞ ” and represent the maximum possible values. These improvements have allowed the fullest use of the physics of the problem and at the same time to construct acceptable algorithm for calculating the residual parts of polarization and deformation of polycrystalline ceramics. Note, that the basic algorithm remains the same as in the case of model of locked wall. This algorithm has been described in detail in [5, 6]. Here we only indicate the basic steps in the derivation of the relevant equations. We must perform the following steps:

- (i) introduce an energy criterion of switching domains;
- (ii) determine the limiting residual polarization and limiting residual strain for current values of an electric field and mechanical stress;
- (iii) determine the energy required for breaking locking mechanisms of the domain wall;
- (iv) calculate the work of the electric fields and mechanical stresses in the polarization process;
- (v) determine the energy losses in the ideal and the real processes of polarization;
- (vi) derive the energy balance, including the energy losses in the ideal and the actual processes of polarizations, and the energy needed for breaking the locked mechanisms of domain walls;

- (vii) obtain the system of equations in differentials, linking the increments of residual polarization vector and residual strain tensor with the increments of electric field and mechanical stresses:

$$\begin{aligned} -\mathbf{P}_0 &= -\mathbf{P}_\infty + k_2 \frac{d\mathbf{P}_0}{|d\mathbf{E}^{ef}|}, \\ -\boldsymbol{\varepsilon}_0 &= -\boldsymbol{\varepsilon}_\infty + k_1 \frac{d\boldsymbol{\varepsilon}_0}{d\sigma_3^{ef} - \sigma_1^{ef}}. \end{aligned} \quad (28.25)$$

28.7 Method of Solving the Problem

Since we are considering the irreversible process, it is natural to use such an algorithm, which should take into account the increment of external loads, and through them find the increments of the unknown parameters of the problem, as it was mentioned in the assumption 2. The most appropriate method in this regard is the increment theory. Let the sequence of equilibrium states is $C^{(0)}, C^{(1)}, \dots, C^{(i)}, C^{(i+1)}, \dots, C^{(n)}$. We use the principle of possible work, where the increments of variables are varied in the transition from one equilibrium state to other:

$$\begin{aligned} \sum_m \int_{\Omega_m} (\Delta \boldsymbol{\sigma}^{(i)} : \delta(\Delta \boldsymbol{\varepsilon}^{(i)}) - \Delta \mathbf{f}^{(i)} \cdot \delta(\Delta \mathbf{u}^{(i)}) - \Delta \mathbf{D}^{(i)} \cdot \delta(\Delta \mathbf{E}^{(i)})) d\Omega - \\ \sum_n \int_{S_\sigma} \Delta \mathbf{p}_*^{(i)} \cdot \delta(\Delta \mathbf{u}^{(i)}) dS - \sum_q \int_{S_D} \Delta D_n^{(i)} \delta(\Delta \phi^{(i)}) dS = 0 \end{aligned} \quad (28.26)$$

It is necessary to add the constitutive relations for reversible and irreversible components of polarization and strain represented in increments. For reversible components, such relations obtain from (28.20). After appropriate mathematical transformations of these equations with use (28.21) or (28.22), we obtain the working relations for increments in the form:

$$\begin{aligned} \Delta \boldsymbol{\varepsilon}_e^{(i)} &= \mathbf{S}(\mathbf{P}_0^{(i)}) : \Delta \boldsymbol{\sigma}^{(i)} + \mathbf{d}^T(\mathbf{P}_0^{(i)}) \cdot \Delta \mathbf{E}^{(i)} + \frac{\Delta |\mathbf{P}_0^{(i-1)}|}{P_{sat}} \mathbf{S}_1 : \boldsymbol{\sigma}^{(i)} + \frac{\Delta |\mathbf{P}_0^{(i-1)}|}{P_{sat}} \mathbf{d}_1^T \cdot \mathbf{E}^{(i)}, \\ \Delta \mathbf{D}_e^{(i)} &= \mathbf{d}(\mathbf{P}_0^{(i)}) : \Delta \boldsymbol{\sigma}^{(i)} + \ni (\mathbf{P}_0^{(i)}) \cdot \Delta \mathbf{E}^{(i)} + \frac{\Delta |\mathbf{P}_0^{(i-1)}|}{P_{sat}} \mathbf{d}_1 : \boldsymbol{\sigma}^{(i)} + \frac{\Delta |\mathbf{P}_0^{(i-1)}|}{P_{sat}} \ni_1 \cdot \mathbf{E}^{(i)}. \end{aligned} \quad (28.27)$$

For irreversible components, we used the (28.25), which we can submit as the equations in a finite differences and resolve them by using the method of successive approximations:

$$\begin{aligned}
(\Delta \mathbf{P}_0^{(k)})_j &= \frac{\mathbf{P}_\infty[(\mathbf{P}_0^{(k)})_j] - (\mathbf{P}_0^{(k)})_j}{m} |\Delta \mathbf{E}^{(k)} + \alpha (\Delta \mathbf{P}_0^{(k)})_{j-1}|, \\
(\mathbf{P}_0^{(k)})_j &= (\mathbf{P}_0^{(k)})_{j-1} + (\Delta \mathbf{P}_0^{(k)})_j \\
(\Delta \boldsymbol{\varepsilon}_0^{(k)})_j &= \frac{\boldsymbol{\varepsilon}_\infty[(\boldsymbol{\varepsilon}_0^{(k)})_j] - (\boldsymbol{\varepsilon}_0^{(k)})_j}{m} |\Delta \boldsymbol{\sigma}^{(k)} + \beta (\Delta \boldsymbol{\varepsilon}_0^{(k)})_{j-1}|, \\
(\boldsymbol{\varepsilon}_0^{(k)})_j &= (\boldsymbol{\varepsilon}_0^{(k)})_{j-1} + (\Delta \boldsymbol{\varepsilon}_0^{(k)})_j
\end{aligned} \tag{28.28}$$

The integral (28.26), together with the constitutive relations (28.27) and (28.28) allow use of finite element method, as it was discussed in detail in [5, 6].

$$\begin{aligned}
\mathbf{K}_{\mathbf{uu}}^{(i)} \cdot \mathbf{U}^{(i)} + \mathbf{K}_{\mathbf{u}\phi}^{(i)} \cdot \Phi^{(i)} &= \mathbf{f}_1^{(i)} + \mathbf{f}_\varepsilon^{(i)}, \\
\mathbf{K}_{\mathbf{u}\phi}^{(i)\text{T}} \cdot \mathbf{U}^{(i)} - \mathbf{K}_{\phi\phi}^{(i)} \cdot \Phi^{(i)} &= \mathbf{f}_2^{(i)} + \mathbf{f}_\phi^{(i)}, \\
\mathbf{K}_{\mathbf{uu}}^{(i)} &= \int_{\Omega_m} \mathbf{B}_1^{\text{T}} \cdot \mathbf{C}^{(i)} \cdot \mathbf{B}_1 d\Omega, \quad \mathbf{K}_{\mathbf{u}\phi}^{(i)} = \int_{\Omega_m} \mathbf{B}_1^{\text{T}} \cdot \mathbf{e}^{(i)\text{T}} \cdot \mathbf{B}_0 d\Omega, \quad \mathbf{K}_{\phi\phi}^{(i)} = \int_{\Omega_m} \mathbf{B}_0^{\text{T}} \cdot \mathfrak{D}^{(i)} \cdot \mathbf{B}_0 d\Omega, \\
\mathbf{f}_1^{(i)} &= \int_{S_\sigma} \mathbf{N}_u \cdot \Delta \mathbf{p}^{(i)} dS + \int_{\Omega_m} \mathbf{N}_u \cdot \Delta \mathbf{f}^{(i)} d\Omega, \quad \mathbf{f}_\varepsilon^{(i)} = \int_{\Omega_m} \mathbf{B}_1^{\text{T}} \cdot \mathbf{C}^{(i)} \cdot \Delta \varepsilon_0^{(i-1)} d\Omega, \\
\mathbf{f}_2^{(i)} &= \int_{S_D} \mathbf{N}_\phi \Delta \mathbf{D}_n^{(i)} dS, \quad \mathbf{f}_\phi^{(i)} = \int_{\Omega_m} \mathbf{B}_0^{\text{T}} \cdot \mathbf{e}^{(i)} \cdot \Delta \varepsilon_0^{(i-1)} d\Omega - \int_{\Omega_m} \mathbf{B}_0^{\text{T}} \cdot \Delta \mathbf{P}_0^{(i-1)} d\Omega, \\
\mathbf{U}^{(i)} &= \{u_1 \quad v_1 \quad \dots \quad u_6 \quad v_6\}^T, \quad \Phi^{(i)} = \{\phi_1 \quad \phi_2 \quad \dots \quad \phi_6\}^T.
\end{aligned}$$

The principal feature of this method is that the set of algebraic equations contains additional terms in right parts, including the increment of the residual polarization and residual strain. The stiffness matrix is changed by changing the elastic constants, piezoelectric moduli and the dielectric permittivity which are also changing due to changes of residual polarization and deformation.

28.8 Conclusions

The chapter is devoted to general theory of irreversible processes of polarization by the electrical and mechanical fields in polycrystalline ferroelectric materials for quasi-static processes. The constitutive relations for reversible parts of the polarization vector and strain tensor are obtained on the base of the thermodynamics of irreversible processes, when the function of the internal energy is chosen in the quadratic form of the variables with coefficients depending on the remaining parts

of the polarization and the strain. For the construction constitutive relations of irreversible components of polarization and strain we used the theory of locked walls of the ferroelectric material. To take into account the simultaneous influence of the electric field and mechanical stress on switching of domains, it was used energy criterion. As a result, we constructed the hysteresis operators for definition of increments of the polarization vector and strain tensor in the form of equations in differentials. Considering the irreversible nature of the polarization processes, we used incremental theory and obtained the full system of equations necessary for the application of the finite element method in problems with irreversible processes. The fundamental difference of this work from the previous ones is the use of energy criterion for switching domains, which allowed us to take into account completely the simultaneous impact of electrical and mechanical fields on the polarization processes in three-dimensional case. The developed formulae and algorithms can be implemented in the finite-element programs for solving complex problems of polarization and depolarization of polycrystalline ferroelectric materials.

Acknowledgments The work was supported by the Russian Foundation for Basic Research (Grant No. 13-08-01094-a).

References

1. C.S. Lynch, *Acta Metall. Mater.* **44**(10), 4137 (1996)
2. M. Selten, G.A. Schneider, V. Knoblauch, R.M. McMeeking, *Int. J. Solids Struct.* **42**, 3953 (2005)
3. D. Zhou, M. Kamlah, *J. Eur. Ceram. Soc.* **25**, 2415 (2005)
4. D. Zhou, M. Kamlah, D. Munz, *J. Mater. Res.* **19**(3), 834 (2004)
5. A.V. Belokon, A.S. Skaliukh, *Mathematical Modeling of Irreversible Processes of Polarization* (Fizmatlit, Moscow, 2010). (In Russian)
6. A.S. Skaliukh, *Piezoelectric Materials and Devices*, vol. 50, ed. by I.A. Parinov (Nova Science Publishers, New York, 2012)
7. P.J. Chen, *Acta Mech.* **47**, 95 (1983)
8. P.J. Chen, T.J. Tucker, *Acta Mech.* **38**, 209 (1981)
9. T. Fett, G. Thun, *J. Mater. Sci. Lett.* **17**, 1929 (1998)
10. A.V. Belokon, M.Y. Radchenko, A.S. Skaliukh, Using an orientation model and a model of locked wall for the formulation of constitutive relations of polycrystalline ferroelectrics. *Proceedings of the XVI International Conference "Modern Problems of Continuum Mechanics"*, SFedU Press, Rostov-on-Don, vol. 2, p. 36 (2012)

Chapter 29

Peculiarities of the Surface SH-Waves Propagation in the Weakly Inhomogeneous Pre-stressed Piezoelectric Structures

T.I. Belyankova, V.V. Kalinchuk and O.M. Tukodova

Abstract A model of a pre-stressed structure consisting of a pre-stressed homogeneous half-space with a pre-stressed inhomogeneous coating, which is either a layer or a packet of both homogeneous and inhomogeneous layers, is suggested. The investigation is carried out in the Lagrangian coordinate system; the linearized constitutive relations and the equations of motion are used. The influence of the value, character and type of the initial stresses on the peculiarities of the propagation of surface waves in piezoelectric structures is studied. The conditions, under which the action of the initial mechanical stresses leads to the increase of the velocity of the Bleustein–Gulyaev wave with respect to the velocity of the original material, and the conditions, under which a pre-stressed piezoelectric structure ceases to be weakly inhomogeneous, are established.

29.1 The Problem Formulation

We consider the problem on propagation of the horizontally polarized shear waves moving in the x_1 -direction over the surface of the composite pre-stressed piezoelectric medium. We assume that the oscillations of the medium are caused by the action of a distant source of harmonic oscillations, the medium is a homogeneous pre-stressed half-space $x_2 \leq 0$, $|x_1|, |x_3| \leq \infty$ with a pre-stressed coating (Fig. 29.1a, b).

The coating is modeled either by one layer $0 \leq x_2 \leq h = H$ (Fig. 29.1b), or by a packet $|x_1|, |x_3| \leq \infty$, $h_{k+1} \leq x_2 \leq h_k$, $k = 1, 2, \dots, M - 1$ of both homogeneous and inhomogeneous layers from the functionally graded material. As the structure original material, we use the piezoelectric of 6 mm hexagonal crystal system, the

T.I. Belyankova (✉) · V.V. Kalinchuk
Southern Scientific Center of the Russian Academy of Sciences, Rostov-on-Don, Russia
e-mail: tbelen415@mail.ru

O.M. Tukodova
Don State Technical University, Rostov-on-Don, Russia

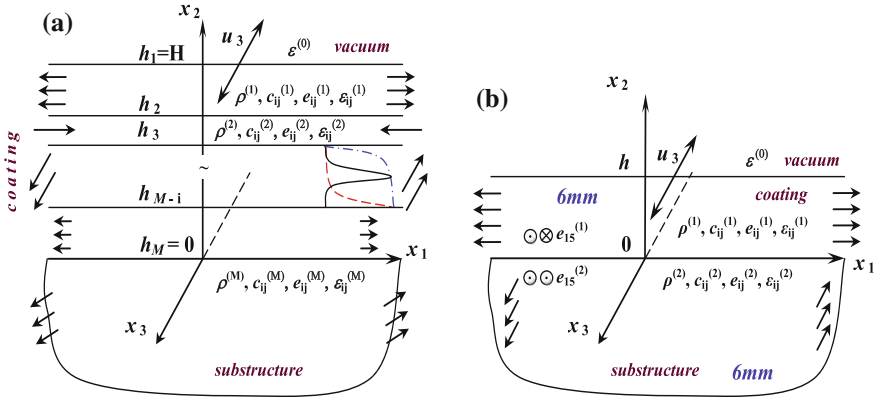


Fig. 29.1 Geometry of the problem

symmetry axis of which in the natural state (NS) coincides with the x_3 -axis, the polarization vectors of the components of the coating and of the half-space either coincide or are oppositely directed. The initially deformed state (IDS) of each component of the structure is homogeneous and is induced by means of action of the initial mechanical stresses, the external initial electrical actions are absent [1–4]:

$$\mathbf{R} = \mathbf{r} \cdot \mathbf{\Lambda}, \quad \mathbf{G} = \mathbf{\Lambda} \cdot \mathbf{\Lambda}^T, \quad \mathbf{\Lambda} = \delta_{ij} v_i \mathbf{r}_i \mathbf{r}_j, \quad v_i = \text{const}, \quad (29.1)$$

where \mathbf{R}, \mathbf{r} are the radius-vectors of the medium point in the initially deformed state and in the natural state, respectively, $v_i = 1 + \delta_i$, δ_i are relative lengthening of the fibers directed in the natural configuration along the axes coinciding with the Cartesian coordinates, δ_{ij} is the Kronecker delta. The non-homogeneity of the initially stressed state of the structure components is caused only by the non-homogeneity of the physical properties. The investigations are carried out in the Lagrangian coordinate system coinciding with the Cartesian coordinate system, the mode of oscillations is assumed to be steady-state, the dynamic process satisfies the conditions:

$$u_1^{(n)} = u_2^{(n)} = 0, \quad \frac{\partial}{\partial x_3} = 0, \quad u_k^{(n)} = u_k^{(n)}(x_1, x_2), \quad u_3^{(0)} = 0, \quad k = 3, 4, \quad n = 0, 1, 2, \dots, M. \quad (29.2)$$

Thus, for the weakly inhomogeneous piezoelectric structure (Fig. 29.1a, b) in NS, the following relations are correct:

(i) for the homogeneous components [5–8]:

$$\rho_0^{(n)} = \rho_0^{(M)}, \quad c_{ij}^{0(n)} = c_{ij}^{0(M)}, \quad e_{ij}^{0(n)} = e_{ij}^{0(M)}, \quad \varepsilon_{ij}^{0(n)} = \varepsilon_{ij}^{0(M)} \text{ or } e_{15}^{0(n)} = -e_{15}^{0(M)} \quad (29.3)$$

(ii) for the inhomogeneous components [2, 9]:

$$\begin{aligned} \rho^{(n)} &= \rho_0^{(M)} f_\rho^{(n)}(x_2), & c_{ij}^{(n)} &= c_{ij}^{0(M)} f_c^{(n)}(x_2), & e_{ij}^{(n)} &= e_{ij}^{0(M)} f_e^{(n)}(x_2), \\ \varepsilon_{ij}^{(n)} &= \varepsilon_{ij}^{0(M)} f_\varepsilon^{(n)}(x_2). \end{aligned} \quad (29.4)$$

Further, we use dimensionless parameters: the linear parameters are related to the characteristic thickness of k layer $l = l(h_0^{(k)})^{-1}$, the density is related to the half-space density $\rho^{l(n)} = \rho^{(n)}/\rho_0^{(M)}$, the elastic parameters are related to the shear modulus of the underlying half-space $c_{ij}^{l(n)} = c_{ij}^{(n)}/c_{44}^{0(M)}$. When we pass to the dimensionless parameters of the piezoelectric and dielectric constants, we use the factor $\zeta = 10^{10}$ V/m, in this case, $e_{ij}^{l(n)} = e_{ij}^{(n)}\zeta/c_{44}^{0(M)}$, $\varepsilon_{ij}^{l(n)} = \varepsilon_{ij}^{(n)}\varepsilon^{(0)}\zeta^2/c_{44}^{0(M)}$ (where $\varepsilon^{(0)}$ is the vacuum permittivity). Further, the primes are omitted.

As a dimensionless frequency, we use either the parameter $\kappa_2 = \omega h/V_S^{(M)}$, or $\kappa_2^e = \omega h/V_{Se}^{(M)}$ (where $V_S^{(M)} = \sqrt{c_{44}^{0(M)}/\rho_0^{(M)}}$ is the velocity of the shear wave of the half-space, and $V_{Se}^{(M)} = \sqrt{(c_{44}^{0(M)} + e_{15}^{0(M)2}/\varepsilon_{11}^{0(M)})/\rho_0^{(M)}}$ is the velocity of the shear wave of the half-space with regard to the piezoelectric properties in NS).

In the context of the accepted assumptions, the boundary problem on the oscillations of the pre-stressed electroelastic medium $x_2 \leq H$ is described by the linearized equations [1–3, 6]:

$$\nabla_0 \cdot \Theta^{(n)} = \rho_0^{(n)} \ddot{\mathbf{u}}^{(n)} \quad (29.5)$$

$$\nabla_0 \cdot \Delta^{(n)} = 0 \quad (29.6)$$

for the vacuum $x_2 > H$

$$\Delta\varphi^{(0)} = 0 \quad (29.7)$$

with the boundary conditions *on the surface*:

(i) the absence of the mechanical actions:

$$\mathbf{n} \cdot \Theta^{(1)}|_{x_2=H} = 0 \quad (29.8)$$

(ii) the electrically free surface:

$$\mathbf{n} \cdot \Delta^{(1)}|_{x_2=H} = \mathbf{n} \cdot \Delta^{(0)}|_{x_2=H}, \quad \varphi^{(1)}|_{x_2=H} = \varphi^{(0)}|_{x_2=H} \quad (29.9)$$

(iii) the metallized surface:

$$\varphi^{(1)}|_{x_2=H} = 0 \tag{29.10}$$

at the interface boundary ($i = 2, 3, \dots, M - 1$)

$$\begin{aligned} \mathbf{u}^{e(i)}|_{x_2=h_i} &= \mathbf{u}^{e(i+1)}|_{x_2=h_i}, & \mathbf{n} \cdot \Theta^{(i)}|_{x_2=h_i} &= \mathbf{n} \cdot \Theta^{(i+1)}|_{x_2=h_i}, \\ \mathbf{n} \cdot \Delta^{(i)}|_{x_2=h_i} &= \mathbf{n} \cdot \Delta^{(i+1)}|_{x_2=h_i} \end{aligned} \tag{29.11}$$

at the infinity:

$$\mathbf{u}^{e(M)}|_{x_2 \rightarrow -\infty} \downarrow \mathbf{0}, \mathbf{u}^{e(0)}|_{x_2 \rightarrow \infty} \downarrow \mathbf{0} \tag{29.12}$$

here ∇_0 is the Hamilton operator, $\mathbf{u}^{e(n)} = \{u_3^{(n)}, u_4^{(n)} = \varphi^{(n)}\}$ is the augmented vector of displacements, \mathbf{n} is the vector of the external normal to the medium surface, they are determined in the coordinate system connected with the natural state (NS); $\rho_0^{(n)}$ is the density of the material of the n ' component in NS; $\Delta = \frac{\partial^2}{\partial x_1^2} + \frac{\partial^2}{\partial x_2^2}$ is the Laplace operator. The upper index (n) corresponds to the number of the medium, that constitutes the structure ($n = 0$ corresponds to vacuum, $n = 1$ —the surface layer, $n = M$ —the half-space). The linearized tensor of stresses $\Theta^{(n)}$ and the linearized vector of induction $\Delta^{(n)}$ with regard to (29.1) are present in the form [1–3, 6]:

$$\theta_{lk}^{(n)} = c_{lksp}^{(n)*} u_{s,p}^{(n)} + e_{lkp}^{(n)*} \varphi_{,p}^{(n)}, \quad \Delta_l^{(n)} = e_{lsp}^{(n)*} u_{s,p}^{(n)} - \varepsilon_{lp}^{(n)*} \varphi_{,p}^{(n)} \tag{29.13}$$

where

$$\begin{aligned} c_{lksp}^{(n)*} &= P_{lp}^{(n)} \delta_{ks} + v_k^{(n)} v_s^{(n)} c_{lksp}^{(n)\times}, & e_{lsp}^{(n)*} &= v_s^{(n)} e_{lsp}^{(n)}, \varepsilon_{lp}^{(n)*} \\ &= \varepsilon_0 v_1^{(n)} v_2^{(n)} v_3^{(n)} \left(v_l^{(n)}\right)^{-2} \delta_{lp} + \beta_{lp}^{(n)} \end{aligned} \tag{29.14}$$

The components of the Kirchhoff tensor $P_{lp}^{(n)}$, as well as the elastic constants $c_{lksp}^{(n)\times}$ in (29.14), depend both on the properties of the material and on the type of the initial stressed state of the medium [1–3, 10–13]:

$$\begin{aligned} P_{lp} &= \frac{1}{2} c_{qjlp} \delta_{qj} (v_q^2 - 1) - e_{jlp} W_j + \frac{1}{8} \delta_{mn} \delta_{qj} c_{mnnqjlp} (v_q^2 - 1) (v_m^2 - 1) \\ c_{qjlp}^\times &= \frac{\partial^2 \chi}{\partial S_{lp} \partial S_{ij}} = c_{qjlp} + \frac{1}{2} c_{mnnqjlp} S_{mn} = c_{qjlp} + \frac{1}{4} \delta_{mn} c_{mnnqjlp} (v_m^2 - 1) \end{aligned} \tag{29.15}$$

Here the simplified representation of the thermodynamic potential χ [1, 10] is used:

$$\chi^{(n)} = \frac{1}{2} c_{qjkl}^{(n)} S_{qj}^{(n)} S_{kl}^{(n)} - e_{jkl}^{(n)} W_j^{(n)} S_{kl}^{(n)} - \frac{1}{2} \beta_{aj}^{(n)} W_q^{(n)} W_j^{(n)} + \frac{1}{6} c_{mnajkl}^{(n)} S_{mn}^{(n)} S_{qj}^{(n)} S_{kl}^{(n)}.$$

$S_{kj}^{(n)}$ are the components of the Cauchy deformation tensor in the case of the homogeneous deformation (29.1), which are determined by the formulae:

$$S_{ij}^{(n)} = 1/2 \delta_{ij} \left(\left(v_i^{(n)} \right)^2 - 1 \right)$$

$W_j^{(n)}$ are the components of the material vector of the electrical induction, $c_{qjkl}^{(n)}$ and $c_{mnajkl}^{(n)}$ are the elastic constants of the II and III order, $\beta_{kp}^{(n)}$ are the constants of the dielectric susceptibility, which are connected with the constants of the permittivity by the relations:

$$\varepsilon_{kp}^{(n)} = \varepsilon_0 \delta_{kp} + \beta_{kp}^{(n)}$$

For the sake of convenience of the further presentation, we introduce the notations:

$$\theta_{lksp} = c_{lksp}^*, \quad \theta_{lk4p} = v_k e_{plk}, \quad \theta_{l4sp} = v_s e_{lsp}, \quad \theta_{l44p} = -\varepsilon_{lp}^*, \quad k, l, s, p = 1, 2, 3. \quad (29.16)$$

Substituting the expressions of the components of the tensor of stresses and of the vector of induction (29.13) with regard to (29.2), the properties (29.3), (29.4), and the notations (29.16) in (29.5)–(29.12) for the pre-stressed homogeneous components of the structure, we obtain (the indices after the comma mark the derivatives with respect to the corresponding coordinates):

$$\begin{aligned} \theta_{1331}^{(n)} u_{3,11}^{(n)} + \theta_{2332}^{(n)} u_{3,22}^{(n)} + \theta_{1341}^{(n)} u_{4,11}^{(n)} + \theta_{2342}^{(n)} u_{4,22}^{(n)} &= \rho_0^{(n)} \frac{\partial^2 u_3^{(n)}}{\partial t^2} \\ \theta_{1431}^{(n)} u_{3,11}^{(n)} + \theta_{2432}^{(n)} u_{3,22}^{(n)} + \theta_{1441}^{(n)} u_{4,11}^{(n)} + \theta_{2442}^{(n)} u_{4,22}^{(n)} &= 0 \end{aligned} \quad (29.17)$$

for the pre-stressed functionally graded components

$$\begin{aligned} \theta_{1331}^{(n)} u_{3,11}^{(n)} + \theta_{2332}^{(n)} u_{3,22}^{(n)} + \theta_{1341}^{(n)} u_{4,11}^{(n)} + \theta_{2342}^{(n)} u_{4,22}^{(n)} + \theta_{2332,2}^{(n)} u_{3,2}^{(n)} + \theta_{2342,2}^{(n)} u_{4,2}^{(n)} &= \rho_0^{(n)} \frac{\partial^2 u_3^{(n)}}{\partial t^2} \\ \theta_{1431}^{(n)} u_{3,11}^{(n)} + \theta_{2432}^{(n)} u_{3,22}^{(n)} + \theta_{1441}^{(n)} u_{4,11}^{(n)} + \theta_{2442}^{(n)} u_{4,22}^{(n)} + \theta_{2432,2}^{(n)} u_{3,2}^{(n)} + \theta_{2442,2}^{(n)} u_{4,2}^{(n)} &= 0 \end{aligned} \quad (29.18)$$

for the vacuum:

$$u_{4,11}^{(0)} + u_{4,22}^{(0)} = 0 \quad (29.19)$$

with the boundary conditions ($m = 2, 3, \dots, M-1$):

$$\Theta_{23}^{(1)} \Big|_{x_2=H} = \left[\theta_{2332}^{(1)} u_{3,2}^{(1)} + \theta_{2342}^{(1)} u_{4,2}^{(1)} \right]_{x_2=H} \Big| = 0 \quad (29.20)$$

$$\begin{aligned} D_2^{(1)} \Big|_{x_2=H} &= \left[\theta_{2432}^{(1)} u_{3,2}^{(1)} + \theta_{2442}^{(1)} u_{4,2}^{(1)} \right]_{x_2=H} = D_2^{(0)} \Big|_{x_2=H} = \left[\theta_{2442}^{(0)} u_{4,2}^{(0)} \right]_{x_2=H}, \quad u_4^{(1)} \Big|_{x_2=H} \\ &= u_4^{(0)} \Big|_{x_2=H} \end{aligned} \quad (29.21)$$

$$u_4^{(1)} \Big|_{x_2=H} = 0 \quad (29.22)$$

$$\mathbf{u}^{e(m)} \Big|_{x_2=h_m} = \mathbf{u}^{e(m+1)} \Big|_{x_2=h_m}, \quad \Theta_{23}^{(m)} \Big|_{x_2=h_m} = \Theta_{23}^{(m+1)} \Big|_{x_2=h_m}, \quad D_2^{(m)} \Big|_{x_2=h_m} = D_2^{(m+1)} \Big|_{x_2=h_m} \quad (29.23)$$

$$\mathbf{u}^{e(M)} \Big|_{x_2 \rightarrow -\infty} \downarrow 0, \quad \varphi^{(0)} \Big|_{x_2 \rightarrow \infty} \downarrow 0 \quad (29.24)$$

In the context of the present chapter, we investigate two boundary problems on the propagation of the horizontally polarized surface waves in the pre-stressed piezoelectrics with the coating [1, 2, 5, 10–14]:

- (i) Problem I is the problem with the free surface, which is described by the motion equations (29.17)–(29.19) with the boundary conditions (29.20), (29.21), (29.23), (29.24);
- (ii) Problem II is the problem with the metallized surface, which is described by the motion equations (29.17)–(29.18) with the boundary conditions (29.20), (29.22)–(29.24).

29.2 The Boundary Problem Solution. The Dispersion Equation for the Pre-stressed Piezoactive Half-Space with the Pre-stressed Coating

Solving boundary Problems I and II, we use the Fourier transform with respect to the coordinate x_1 , α is a transform parameter. The motion of the piezoelectric structure in the transforms is of the form:

for the pre-stressed homogeneous components

$$\begin{aligned} \theta_{2332}^{(n)} U_3^{(n)''} - \left(\alpha^2 \theta_{1331}^{(n)} - \rho^{(n)} \kappa_2^2 \right) U_3^{(n)} + \theta_{2342}^{(n)} U_4^{(n)''} - \alpha^2 \theta_{1341}^{(n)} U_4^{(n)} &= 0 \\ \theta_{2432}^{(n)} U_3^{(n)''} - \alpha^2 \theta_{1431}^{(n)} U_3^{(n)} + \theta_{2442}^{(n)} U_4^{(n)''} - \alpha^2 \theta_{1441}^{(n)} U_4^{(n)} &= 0 \end{aligned} \quad (29.25)$$

for the pre-stressed functionally graded components

$$\begin{aligned} \theta_{2332}^{(n)} U_3^{(n)''} - \left(\alpha^2 \theta_{1331}^{(n)} - \rho^{(n)} \kappa_2^2 \right) U_3^{(n)} + \theta_{2342}^{(n)} U_3^{(n)''} - \alpha^2 \theta_{1341}^{(n)} U_4^{(n)} + \theta_{2332}^{(n)'} U_3^{(n)'} + \theta_{2342}^{(n)'} U_4^{(n)'} &= 0 \\ \theta_{2432}^{(n)} U_3^{(n)''} - \alpha^2 \theta_{1431}^{(n)} U_3^{(n)} + \theta_{2442}^{(n)} U_4^{(n)''} - \alpha^2 \theta_{1441}^{(n)} U_4^{(n)} + \theta_{2432}^{(n)'} U_3^{(n)'} + \theta_{2442}^{(n)'} U_4^{(n)'} &= 0 \end{aligned} \quad (29.26)$$

for the vacuum:

$$U_4^{(0)''} - \alpha^2 U_4^{(0)} = 0 \quad (29.27)$$

with the boundary conditions ($m = 2, 3, \dots, M-1$):

$$\Theta_{23}^{F(1)}|_{x_2=H} = \left[\theta_{2332}^{(1)} U_3^{(1)'} + \theta_{2342}^{(1)} U_4^{(1)'} \right] |_{x_2=H} = 0 \quad (29.28)$$

$$\begin{aligned} D_2^{F(1)}|_{x_2=H} &= \left[\theta_{2432}^{(1)} U_3^{(1)'} + \theta_{2442}^{(1)} U_4^{(1)'} \right] |_{x_2=H} = D_2^{F(0)}|_{x_2=H} = \left[\theta_{2442}^{(0)} U_4^{(0)'} \right] |_{x_2=H}, \\ U_4^{(1)}|_{x_2=H} &= U_4^{(0)}|_{x_2=H} \end{aligned} \quad (29.29)$$

$$U_4^{(1)}|_{x_2=H} = 0, \quad (29.30)$$

$$\begin{aligned} \mathbf{U}^{e(m)}|_{x_2=h_m} &= \mathbf{U}^{e(m+1)}|_{x_2=h_m}, \Theta_{23}^{F(m)}|_{x_2=h_m} = \Theta_{23}^{F(m+1)}|_{x_2=h_m}, D_2^{F(m)}|_{x_2=h_m} \\ &= D_2^{F(m+1)}|_{x_2=h_m} \end{aligned} \quad (29.31)$$

$$\mathbf{U}^{e(M)}|_{x_2 \rightarrow -\infty} \downarrow 0, U_4^{(0)}|_{x_2 \rightarrow \infty} \downarrow 0 \quad (29.32)$$

The solution of the problems (29.25)–(29.27) with the boundary conditions (29.28)–(29.32) in the Fourier transforms for the homogeneous components of the coating is obtained in the form ($p = 3, 4, \quad n = 1, 2, \dots, M-1$) [1, 2]:

$$U_p^{(n)}(\alpha, x_2) = \sum_{k=1}^2 f_{pk}^{(n)} [c_k^{(n)} ch\sigma_k^{(n)} x_2 + c_{k+2}^{(n)} sh\sigma_k^{(n)} x_2] \quad (29.33)$$

for the inhomogeneous components

$$U_p^{(n)}(\alpha, x_2) = \sum_{k=1}^4 c_k^{(n)} y_{kp}^{(n)}(\alpha, x_2), \tag{29.34}$$

for the half-space and vacuum

$$U_p^{(M)}(\alpha, x_2) = \sum_{k=1}^2 f_{pk}^{(M)} c_k^{(M)} e^{\sigma_k^{(M)} x_2}, \quad U_4^{(0)}(\alpha, x_2) = c_1^{(0)} e^{-\alpha x_2} \tag{29.35}$$

$\sigma_k^{(n)}$ in (29.33), (29.35) satisfy the characteristic equation: $\det \mathbf{M}_\sigma^{(n)}(\sigma^{(n)}) = 0$,

$$\mathbf{M}_\sigma^{(n)}(\sigma^{(n)}) = \begin{pmatrix} \theta_{2332}^{(n)}(\sigma^{(n)})^2 - (\alpha^2 \theta_{1331}^{(n)} - \rho^{(n)} \kappa_2^2) & \theta_{2342}^{(n)}(\sigma^{(n)})^2 - \alpha^2 \theta_{1341}^{(n)} \\ \theta_{2432}^{(n)}(\sigma^{(n)})^2 - \alpha^2 \theta_{1431}^{(n)} & \theta_{2442}^{(n)}(\sigma^{(n)})^2 - \alpha^2 \theta_{1441}^{(n)} \end{pmatrix} \tag{29.36}$$

coefficients $f_{pk}^{(n)}$ are determined from the solution of the homogeneous system of the linear equations with the matrix of the coefficients $\mathbf{M}_\sigma^{(n)}(\sigma_k^{(n)}) \cdot y_{kp}^{(n)}(\alpha, x_2)$ in (29.34) are the linearly independent solutions of the Cauchy problem with the initial conditions $y_{kp}^{(n)}(\alpha_1, \alpha_2, 0) = \delta_{kp}$ for the equation:

$$\mathbf{Y}^{(n)'} = \mathbf{M}^{(n)}(\alpha_2, x_2) \mathbf{Y}^{(n)} \tag{29.37}$$

with the notations:

$$\mathbf{Y}^{(n)} = \begin{pmatrix} \mathbf{Y}_\Sigma^n \\ \mathbf{Y}_u^n \end{pmatrix}, \quad \mathbf{Y}_\Sigma^n = \left\| \begin{matrix} \Theta_{23}^{F(n)} \\ D_2^{F(n)} \end{matrix} \right\|, \quad \mathbf{Y}_u^n = \left\| \begin{matrix} U_3^{(n)} \\ U_4^{(n)} \end{matrix} \right\|$$

$$\mathbf{M}^{(n)} = \begin{pmatrix} 0 & 0 & \alpha^2 \theta_{1331}^{(n)} - \rho^{(n)} \kappa_2^2 & \alpha^2 \theta_{1431}^{(n)} \\ 0 & 0 & \alpha^2 \theta_{1431}^{(n)} & \alpha^2 \theta_{1441}^{(n)} \\ -\theta_{2442}^{(n)}(g_0)^{-1} & \theta_{2432}^{(n)}(g_0)^{-1} & 0 & 0 \\ \theta_{2432}^{(n)}(g_0)^{-1} & -\theta_{2332}^{(n)}(g_0)^{-1} & 0 & 0 \end{pmatrix} \tag{29.38}$$

$$g_0 = \theta_{2442}^{(n)} \theta_{2332}^{(n)} - \left(\theta_{2432}^{(n)} \right)^2$$

It should be pointed out, that for the solution of the system (29.37) with the notations (29.38) in [2, 6, 9, 15], it is recommended to use the Runge-Kutta numerical method with the Merson's modification.

The unknowns $c_k^{(n)}$ in (29.33)–(29.35) are determined by means of satisfying the boundary conditions (29.28), (29.29), (29.31), (29.32) for Problem I or (29.28), (29.30)–(29.32) for Problem II. Using the approach [12], we present the dispersion equation of the problems in the form:

$$\det \mathbf{A} = 0 \quad (29.39)$$

$$\mathbf{A} = \begin{pmatrix} \mathbf{B}^{(1)}(h_1) & \mathbf{G}^{(1)}(h_1) \\ \mathbf{A}^{(1)}(h_{2,\dots,M}) & \mathbf{B}^{(M)}(h_M) \end{pmatrix} \quad (29.40)$$

the orders of matrix \mathbf{A} and of the matrices, which constitute it are determined by the problem geometry and by the conditions on the surface.

Problem I Matrices \mathbf{A} and $\mathbf{A}^{(1)}(h_{2,\dots,M})$ are square ones, their order is determined by the problem geometry and is equal to $4(M-1)+3$ and $4(M-1)$, respectively. $\mathbf{B}^{(1)}(h_1)$, $\mathbf{B}^{(M)}(h_M)$ and $\mathbf{G}^{(1)}(h_1)$ are the matrices of 3×4 , 4×3 and 3×3 orders. Their type is completely determined by the properties of the upper layer, of the underlying half-space and by the vacuum permittivity, respectively, and does not depend on the properties and on the number of the possible interfacial layers.

$$\mathbf{G}^{(1)}(h_1) = \begin{pmatrix} 0 & 0 & 0 \\ 0 & 0 & -\varepsilon^{(0)}\alpha \\ 0 & 0 & -1 \end{pmatrix}, \mathbf{B}^{(M)}(h_M) = \begin{pmatrix} -l_{11}^M & -l_{12}^M & 0 \\ -l_{21}^M & -l_{22}^M & 0 \\ -f_{31}^M & -f_{32}^M & 0 \\ -f_{41}^M & -f_{42}^M & 0 \end{pmatrix} \quad (29.41)$$

for the pre-stressed homogeneous surface layer:

$$\mathbf{B}^{(1)}(h_1) = \begin{pmatrix} l_{11}^{1*} s_{11}^{1*} & l_{12}^{1*} s_{21}^{1*} & l_{11}^{1*} c_{11}^1 & l_{12}^{1*} c_{21}^1 \\ l_{21}^{1*} s_{11}^{1*} \gamma & l_{22}^{1*} s_{21}^{1*} \gamma & l_{21}^{1*} c_{11}^1 \gamma & l_{22}^{1*} c_{21}^1 \gamma \\ f_{41}^1 c_{11}^1 \gamma & f_{42}^1 c_{21}^1 \gamma & f_{41}^1 s_{11}^{10} \gamma & f_{42}^1 s_{21}^{10} \gamma \end{pmatrix} \quad (29.42)$$

for the pre-stressed functionally graded surface layer:

$$\mathbf{B}^{(1)}(h_1) = \begin{pmatrix} y_{11}^{(1)} & y_{12}^{(1)} & y_{13}^{(1)} & y_{14}^{(1)} \\ y_{21}^{(1)} \gamma & y_{22}^{(1)} \gamma & y_{23}^{(1)} \gamma & y_{24}^{(1)} \gamma \\ y_{41}^{(1)} \gamma & y_{42}^{(1)} \gamma & y_{43}^{(1)} \gamma & y_{44}^{(1)} \gamma \end{pmatrix} \quad (29.43)$$

The following notations are used:

$$\begin{aligned}
 s_{pk}^{n0} &= sh^0 \sigma_p^{(n)} h_k, sh^0 \sigma_p^{(n)} h_k = \sigma_p^{(n)-1} sh \sigma_p^{(n)} h_k, \\
 s_{pk}^{n*} &= \sigma_p^{(n)} sh \sigma_p^{(n)} h_k, c_{pk}^n = ch \sigma_p^{(n)} h_k, \gamma = e^{xh}, f_{pk}^n = f_{pk}^{(n)}, \quad p, k = 1, 2 \quad (29.44) \\
 l_{pk}^n &= \sigma_k^{(n)} l_{pk}^{n*}, \quad l_{1k}^{n*} = \theta_{2332}^{(n)} f_{3k}^{(n)} + \theta_{2342}^{(n)} f_{4k}^{(n)}, \quad l_{2k}^{n*} = \theta_{2432}^{(n)} f_{3k}^{(n)} + \theta_{2442}^{(n)} f_{4k}^{(n)}
 \end{aligned}$$

In the case of $M = 2$, i.e. in the case of two-layer half-space (Fig. 29.1b), the type of matrix $\mathbf{A}^{(1)}(h_M)$ is determined by properties of the layer, and for the pre-stressed homogeneous layer:

$$\mathbf{A}^{(1)}(h_M) = \begin{pmatrix} 0 & 0 & l_{11}^* & l_{12}^* \\ 0 & 0 & l_{21}^* & l_{22}^* \\ f_{31}^1 & f_{32}^1 & 0 & 0 \\ f_{41}^1 & f_{42}^1 & 0 & 0 \end{pmatrix} \quad (29.45)$$

for the pre-stressed functionally graded layer $\mathbf{A}^{(1)}(h_M) = \mathbf{E}$, i.e. it coincides with the diagonal unit matrix of 4×4 order.

In the case of $M > 2$, i.e. in the case of the half-space with the layered coating, matrices $\mathbf{A}^{(1)}(h_{2,\dots,M})$ and \mathbf{A} have the forms:

$$\mathbf{A}^{(1)}(h_{2,\dots,M}) = \begin{pmatrix} \mathbf{B}^1(h_2) & \mathbf{P}^2(h_2) & 0 & 0 & \vdots & 0 & 0 \\ 0 & \mathbf{B}^2(h_3) & \mathbf{P}^3(h_3) & 0 & \vdots & 0 & 0 \\ 0 & 0 & \mathbf{B}^3(h_4) & \mathbf{P}^4(h_4) & \vdots & 0 & 0 \\ \dots & \dots & \dots & \dots & \dots & \dots & \dots \\ 0 & 0 & 0 & 0 & \vdots & \mathbf{B}^{M-2}(h_{M-1}) & \mathbf{P}^{M-1}(h_{M-1}) \\ 0 & 0 & 0 & 0 & \vdots & 0 & \mathbf{B}^{M-1}(h_M) \end{pmatrix} \quad (29.46)$$

$$\mathbf{A} = \begin{pmatrix} \mathbf{B}^1(h_1) & 0 & 0 & 0 & \vdots & 0 & 0 & \mathbf{G}^1(h_1) \\ \mathbf{B}^1(h_2) & \mathbf{P}^2(h_2) & 0 & 0 & \vdots & 0 & 0 & 0 \\ 0 & \mathbf{B}^2(h_3) & \mathbf{P}^3(h_3) & 0 & \vdots & 0 & 0 & 0 \\ 0 & 0 & \mathbf{B}^3(h_4) & \mathbf{P}^4(h_4) & \vdots & 0 & 0 & 0 \\ \dots & \dots & \dots & \dots & \vdots & \dots & \dots & \dots \\ 0 & 0 & 0 & 0 & \vdots & \mathbf{B}^{M-2}(h_{M-1}) & \mathbf{P}^{M-1}(h_{M-1}) & 0 \\ 0 & 0 & 0 & 0 & \vdots & 0 & \mathbf{B}^{M-1}(h_M) & \mathbf{B}^M(h_M) \end{pmatrix} \quad (29.47)$$

Matrices $\mathbf{B}^n(h_k)$ and $\mathbf{P}^n(h_k) = -\mathbf{B}^n(h_k)$ in (29.46), which are determined by the properties of the layers with the common boundary h_k , are of 4×4 order. The upper index corresponds to the layer number, the argument corresponds to the interface boundary (Fig. 29.1a). For the pre-stressed homogeneous layer with regard to the notations (29.44), matrix $\mathbf{B}^n(h_k)$ is determined by the formula:

$$\mathbf{B}^n(h_k) = \begin{pmatrix} l_{11}^{n*} s_{1k}^{n*} & l_{12}^{n*} s_{2k}^{n*} & l_{11}^{n*} c_{1k}^n & l_{12}^{n*} c_{2k}^n \\ l_{21}^{n*} s_{1k}^{n*} & l_{22}^{n*} s_{2k}^{n*} & l_{21}^{n*} c_{1k}^n & l_{22}^{n*} c_{2k}^n \\ f_{31}^n c_{1k}^n & f_{32}^n c_{2k}^n & f_{31}^n s_{1k}^{n0} & f_{32}^n s_{2k}^{n0} \\ f_{41}^n c_{1k}^n & f_{42}^n c_{2k}^n & f_{41}^n s_{1k}^{n0} & f_{42}^n s_{2k}^{n0} \end{pmatrix} \quad (29.48)$$

for the pre-stressed functionally graded layer

$$\mathbf{B}^n(h_k) = \left\| y_{mp}^{(n)}(h_k) \right\|_{m,p=1}^4. \quad (29.49)$$

Problem II The order of matrix \mathbf{A} is $4(M - 1) + 2$, which may be represented by the expressions (29.40) and (29.47) depending on the problem geometry. The order and type of matrix $\mathbf{A}^{(1)}(h_{2,\dots,M})$ coincide with the order and type of the corresponding matrix of the Problem I, and are determined by the formulae (29.45) and (29.46). Matrices $\mathbf{B}^{(1)}(h_1)$, $\mathbf{B}^{(M)}(h_M)$ and $\mathbf{G}^{(1)}(h_1)$, in (29.40) are of the 2×4 , 4×2 and 2×2 orders. The type of matrices is determined from the representations (29.41)–(29.43) by means of deleting the 2-nd line and the 3-rd column in the expression $\mathbf{G}^{(1)}(h_1)$. In this case, the matrix becomes a zero one. After deleting the 3-rd column in the representation $\mathbf{B}^{(M)}(h_M)$ and the 2-nd column in the representations $\mathbf{B}^{(1)}(h_1)$ (29.42), (29.43) the order and type of matrices $\mathbf{B}^n(h_k)$ and $\mathbf{P}^n(h_k)$ completely coincide with the order and type of the corresponding matrices of the Problem I (29.48), (29.49).

29.3 IDS Formulation

In the context of the presented assumptions, the initially deformed state in each component of the structure is homogeneous (29.1) and can differ depending on the character and value of the initial deformations. The inhomogeneity of the initial stressed state of the components is caused only by the inhomogeneity of their physical properties. The character of the initial stressed state is determined by the Kirchhoff tensor, the components $P_{lp}^{(n)}$ (29.15) of which, with regard to the material properties and assumptions about the IDS homogeneity induced by means of the mechanical actions in the absence of the external initial electrostatic fields are determined by the formulae [1, 2]:

$$\begin{aligned}
P_{11}^{(n)} &= c_{11}^{(n)} S_{11}^{(n)} + c_{12}^{(n)} S_{22}^{(n)} + c_{13}^{(n)} S_{33}^{(n)} - e_{31}^{(n)} W_3^{(n)} + H_1^{(n)}, \\
P_{22}^{(n)} &= c_{12}^{(n)} S_{11}^{(n)} + c_{11}^{(n)} S_{22}^{(n)} + c_{13}^{(n)} S_{33}^{(n)} - e_{31}^{(n)} W_3^{(n)} + H_2^{(n)}, \\
P_{33}^{(n)} &= c_{13}^{(n)} S_{11}^{(n)} + c_{13}^{(n)} S_{22}^{(n)} + c_{33}^{(n)} S_{33}^{(n)} - e_{33}^{(n)} W_3^{(n)} + H_3^{(n)}, \\
d_1^{(n)} &= \varepsilon_{11}^{(n)} W_0^{(n)}, d_2^{(n)} = \varepsilon_{11}^{(n)} W_2^{(n)}, \\
d_3^{(n)} &= e_{31}^{(n)} S_{11}^{(n)} + e_{31}^{(n)} S_{22}^{(n)} + e_{33}^{(n)} S_{33}^{(n)} + \varepsilon_{33}^{(n)} W_3^{(n)}
\end{aligned} \tag{29.50}$$

where the coefficients $H_i^{(n)}$ make it possible to take into account the influence of the moduli of elasticity of the III order (summing over the umbral indices):

$$H_i = \frac{1}{8} c_{mmqqii} (v_q^2 - 1)(v_m^2 - 1)$$

According to the assumptions about the absence of the initial external electrical actions, $d_i = 0$, and so, depending on the method of formulating IDS, the unknowns can be either $S_{11}^{(n)}, S_{22}^{(n)}, S_{33}^{(n)}, W_1^{(n)}, W_2^{(n)}, W_3^{(n)}$, or, for example, $P_{11}^{(n)}, S_{22}^{(n)}, S_{33}^{(n)}, W_1^{(n)}, W_2^{(n)}, W_3^{(n)}$ obtained from the solution of the system (29.50). In the chapter influence of the

uniaxial IDS: $1x_i \Rightarrow P_{ii}^{(n)} = P, P_{jj \neq ii}^{(n)} = P_{kk \neq jj \neq ii}^{(n)} = 0, k, j, i = 1, 2, 3,$

biaxial IDS: $2x_i \Rightarrow P_{ii}^{(n)} = 0, P_{jj \neq ii}^{(n)} = P_{kk \neq jj \neq ii}^{(n)} = P, k, j, i = 1, 2, 3,$

and hydrostatic IDS: $3x \Rightarrow P_{11}^{(n)} = P_{22}^{(n)} = P_{33}^{(n)} = P$ is investigated.

As the structure material, we consider ZnO with the parameters [16]:

$$\begin{aligned}
\rho &= 5680 \text{ kg/m}^3, c_{11} = 2.09718 \cdot 10^{11} \text{ N/m}^2, c_{12} = 1.2114 \cdot 10^{11} \text{ N/m}^2, c_{13} = 1.0513 \cdot 10^{11} \text{ N/m}^2, \\
c_{33} &= 2.10941 \cdot 10^{11} \text{ N/m}^2, c_{44} = 4.2449 \cdot 10^{10} \text{ N/m}^2, e_{15} = -0.59 \text{ C/m}^2, e_{31} = -0.61 \text{ C/m}^2, \\
e_{33} &= 1.14 \text{ C/m}^2, \varepsilon_{11}/\varepsilon^{(0)} = 8.3, \varepsilon_{33}/\varepsilon^{(0)} = 8.8, \varepsilon^{(0)} = 8.85 \cdot 10^{-12} \text{ F/m}, \\
V_P &= 6097 \text{ m/s}, V_S = 2743 \text{ m/s}, V_{Se} = 2892 \text{ m/s}.
\end{aligned}$$

Calculated for ZnO without regard for the moduli of elasticity of the III order, the relative velocities of the Bleustein–Gulyaev wave (BGW) for the half-space with the free surface and for the half-space with the metallization are $V_{GB}^f/V_{Se} = 0.9999417$ and $V_{GB}^m/V_{Se} = 0.99494441$, respectively.

Figures 29.2a, b present the dependencies of the initial stresses $P_{ii}(v_i)$ and of the non-zero component $W_3(v_i)$ for the material vector of electrical induction on value of the relative lengthening for the considered above types of IDS. The figures demonstrate the dependence of $P(v_1)$ in the case of hydrostatic IDS.

The dots (Fig. 29.2a) mark the maximum admissible values of the deformations, which can be realized at the appropriate initial stressed state. Figure 29.2b illustrates the presence of the piezo-effect in the material, the maximum values of the electrical induction are reached at IDS $2x_3$, whereas at the hydrostatic IDS ($3x$), the piezo-effect is absent.

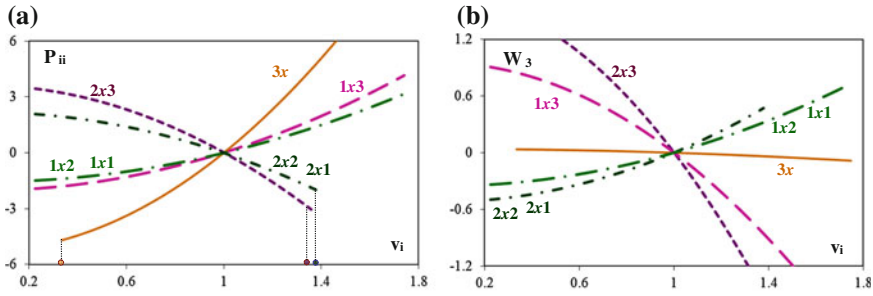


Fig. 29.2 Dependencies of initial stresses $P_{ii}(v_i)$ and $W_3(v_i)$ on initial deformations

29.4 The Numerical Results

For detailed study of the influence of value of the induced deformation, type and character of the pre-stresses in the structure components on peculiarities of behavior and velocity of the propagation of the horizontally polarized surface waves, we consider the simplest case of the pre-stressed piezoelectric half-space with the pre-stressed one-layer coating ($M = 2$, Fig. 29.1b). As the structure material (the coating and base), we use ZnO [16] without regarding the moduli of elasticity of the III order. We assume that the symmetry axis of the material in NS coincides with the x_3 -axis, the polarization vectors of the components of the coating and of the half-space either coincide, or are opposite in direction (29.3).

Figures 29.3, 29.4, 29.5 and 29.6 demonstrate influence of the character and value of the initial mechanical actions on the relative phase velocities of the surface waves ($V_F^{(1)}/V_{Se}^{(2)}$, where $V_F = \kappa_2/\zeta$, ζ is the solution of the dispersion equation (29.39) with the matrix (29.40), or (29.47), depending on the problem geometry in the notations (29.41)–(29.46), (29.48)–(29.49)). Numbers 0, 1, 2, ..., 10 in the figures mark the combination of the induced deformations $v_i^{(1)}/v_i^{(2)} = 1/1, 0.97/1, 1.03/1, 0.95/0.97, 0.97/0.97, 1/0.97, 1.03/0.97, 0.97/1.03, 1/1.03, 1.03/1.03, 1.06/1.03$, respectively. In this case, inferior indices f and m denote the free and metallized surface, the upper index e denotes the case of $e_{15}^{(1)} = -e_{15}^{(2)}$.

Figures 29.3a–d present influence of the polarization direction of the coating and base (Fig. 29.3a), of the value, of the character of induced deformations (Fig. 29.3b) and of the type of initial stresses (Fig. 29.3c, d) on change of BGW velocity for free and metallized surfaces. Figure 29.3a demonstrates the characteristic behavior of BGW velocity in NS at $e_{15}^{(1)} = e_{15}^{(2)}$ and $e_{15}^{(1)} = -e_{15}^{(2)}$, in the case of IDS 1x1 with the deformations $v_1^{(1)}/v_1^{(2)} = 1.03/1.03$ (curves 9 in Fig. 29.3b), $V_{GB}^{1.03f}/V_{Se}^{(2)} = 1.0356454$ and $V_{GB}^{1.03m}/V_{Se}^{(2)} = 1.30791675$. Figure 29.3c, d demonstrate the influence of uniaxial and biaxial IDS, the combination of induced deformations in the biaxial IDS corresponding to 0.97/0.97.

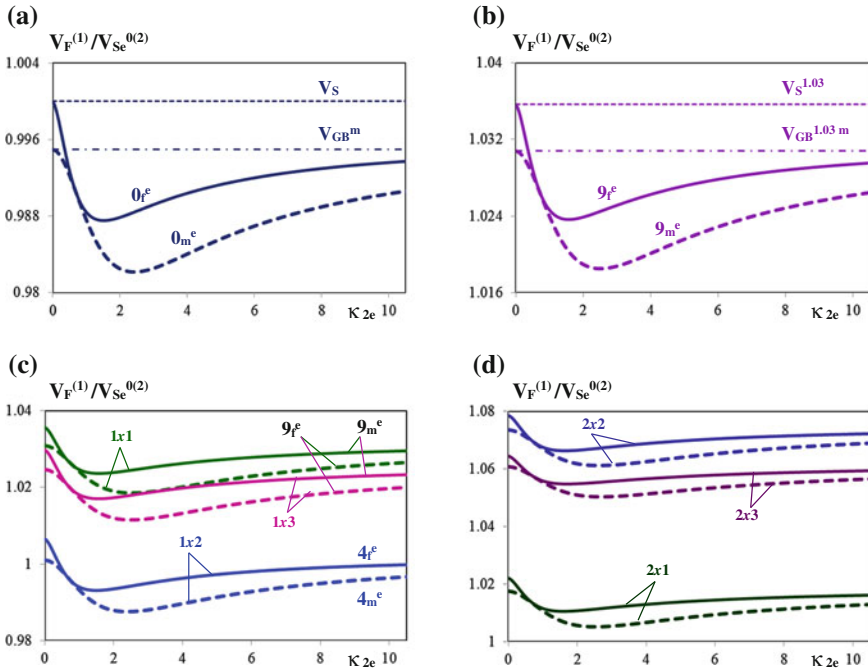


Fig. 29.3 Influence of the value, character and type of initial actions on relative BGW velocities in the case of free and metallized surface

The figures demonstrate that the greatest values of velocities V_{GB}^f and V_{GB}^m are reached, when IDS 1x1 ($v_1^{(1)}/v_1^{(2)} = 1.03/1.03$, Fig. 29.3b, c) and IDS 2x2 ($v_1^{(1)}/v_1^{(2)} = 0.97/0.97$, Fig. 29.3d).

Figures 29.4a–d and 29.5a–d demonstrate influence of the value and character of the initial stresses acting on the coating and base within framework of one type of IDS 1x1 (Fig. 29.4) and 2x1 (Fig. 29.5), on relative phase velocities of the surface acoustic waves (SAW). The numbers in the figures mark the combination of deformations induced by the action of the initial stresses in the case, when polarization in the layer and polarization in the half-space coincide (Figs. 29.4 and 29.5a, b) and when they are opposite in direction (Figs. 29.4 and 29.5c, d).

The comparisons of Figs. 29.4 and 29.5b with c and d show that certain combinations of the induced deformations (for example, IDS 1x1: 1.06/1.03, 1.03/1, 1/0.97, curves 10, 2, 5 in Fig. 29.4b) and IDS 2x1: 0.95/0.97, 0.97/1, 1/1.03, curves 3, 1, 8 in Fig. 29.5b) result in increasing a rigidity of the coating. In this case the velocity of SAW increases from the value of BGW velocity of the pre-stressed half-space with free or metallized surface (V_{GB}^{of} or V_{GB}^{om}) to the value of shear velocity V_S^σ . The frequency range of SAW is restricted; in the case of $e_{15}^{(1)} = -e_{15}^{(2)}$ (Figs. 29.4 and 29.5 c, d) the frequency range is much wider in comparison with

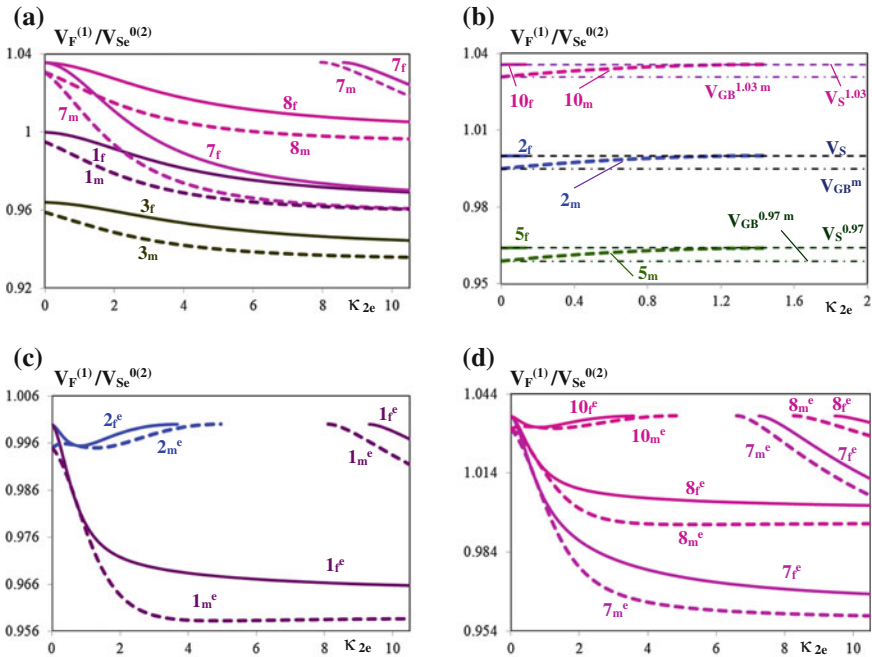


Fig. 29.4 Influence of value and character of the initial stresses acting on the coating and base in the framework of IDS 1x1 on the relative phase velocities of SAW

$e_{15}^{(1)} = e_{15}^{(2)}$ (Figs. 29.4 and 29.5b); the character of the curves behavior changes. The comparisons of Figs. 29.4 and 29.5a with c and d show, that at certain combinations of the induced deformations, the piezoelectric structure ceases to be weakly inhomogeneous. In the considered frequency range, there appear the second modes of SAW (curves 7 in Fig. 29.4a, and curves 6, 10 in Fig. 29.5a), and in some cases there appear the third modes of SAW and in the case of $e_{15}^{(1)} = -e_{15}^{(2)}$ (Figs. 29.4 and 29.5c, d) the effect increases.

Figures 29.6a, b demonstrate influence of the initial stresses inducing IDS of different types in the coating and base on the phase velocities of SAW. To make the comparison clear, IDS 2x2 is used as the IDS of the base, uniaxial IDSs 1x1, 1x2, 1x3 (Fig. 29.6a) are used as IDS of the coating. Figure 29.6b shows the comparison between uniaxial 1x1 IDS coating and biaxial 2x1 IDS coating. The relation of the induced deformations in the figures corresponds to the case 1.03/0.97, the polarization vectors of the coating and base are opposite in direction.

The figures demonstrate that at the considered relation of deformations regardless of IDS of the coating in the considered frequency range, there are the second modes of SAW. The minimum change of velocity is achieved at IDS 1x1/2x2

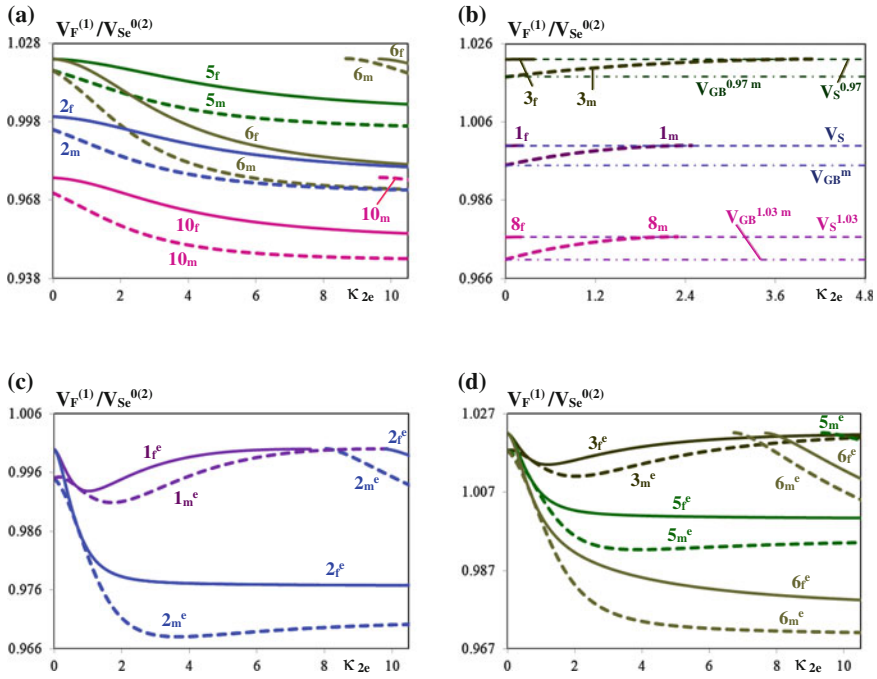


Fig. 29.5 Influence of value and character of the initial stresses in the framework of IDS 2x1 on the relative phase velocities of SAW

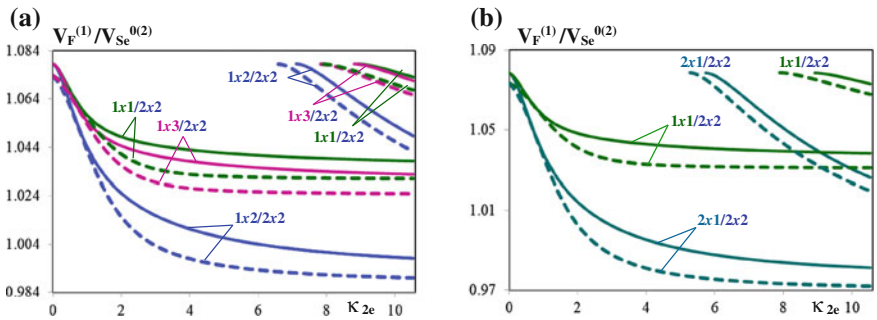


Fig. 29.6 Influence of IDS types of the coating and base on the phase velocities of SAW

(Fig. 29.6a), the maximum change of the velocity is achieved at IDS 2x1/2x2 (Fig. 29.6b). The comparisons of Fig. 29.6a, b with Fig. 29.3c, d show the possibility of increasing the velocity of SAW due to the differences in the initial mechanical actions on the components of the piezoelectric structure.

Acknowledgments This work was performed with the financial support of the Russian Science Foundation (Project No. 14-19-01676).

References

1. V.V. Kalinchuk, T.I. Belyankova, *Dynamic Contact Problems for Prestressed Electroelastic Media* (Fizmatlit, Moscow, 2006). (in Russian)
2. V.V. Kalinchuk, T.I. Belyankova, *Dynamic of the Surface of Inhomogeneous Media* (Fizmatlit, Moscow, 2009). (in Russian)
3. V.V. Kalinchuk, T.I. Belyankova, O.V. Evdokimova, *Vestnik SSC RAS Nauka, Moscow* **2** (1), 16 (2006). (In Russian)
4. A.I. Lurie, *Nonlinear Theory of Elasticity* (Nauka, Moscow, 1980). (In Russian)
5. S.V. Biryukov, Y.V. Gulyaev, V.V. Krylov, V.P. Plessky, *Surface Acoustic Waves in Inhomogeneous Media* (Springer-Verlag, New York, 1995)
6. T.I. Belyankova, V.A. Lyzhov, *Vestnik SSC RAS Nauka, Moscow* **6**(2), 3 (2010). (In Russian)
7. V.V. Kalinchuk, T.I. Belyankova, in *Proceedings of the 4th International Conference on Structural Dynamics. Structural Dynamics: EUROLYN 2002*, vol. 2 (Balkema, The Netherlands, 2002), p. 1309
8. V.V. Kalinchuk, T.I. Belyankova, Tosecky, in *Proceedings of the 6th European Conference on Structural Dynamics. Structural Dynamics: EUROLYN 2005*, vol. 2 (MillPress, Rotterdam, The Netherlands, 2005), p. 1309
9. V.V. Kalinchuk, T.I. Belyankova, A.S. Bogomolov, *Ecol. Bull. Res. Centers Black Sea Econ. Cooper.* **2**, 26 (2006). (In Russian)
10. G.A. Maugin, *Continuum Mechanics of Electromagnetic Solids* (Elsevier science publishers Amsterdam, New York, Oxford, Tokyo, 1988).
11. H. Liu, Z.K. Wang, T.J. Wang, *Int. J. Eng. Sci.* **38**, 37 (2001)
12. H. Liu, Z.B. Kuang, Z.M. Cai, *Ultrasonics* **41**, 397 (2003)
13. Z. Qian, F. Jin, Z. Wang, X. China, K. Kishimoto, *Acta Mech.* **171**, 41 (2004)
14. Feng Jin, Zikun Wang, Tiejun Wang, *Int. J. Eng. Sci.* **39**, 1271 (2001)
15. T.I. Belyankova, V.V. Kalinchuk, *Acoust. Phys.* **60**(5), 530 (2014)
16. M.P. Shaskolskaya (eds.), *Acoustic Crystals: Handbook* (Nauka, Moscow, 1982) (In Russian)

Chapter 30

Numerical Simulation of Elastic Wave Propagation in Layered Phononic Crystals with Strip-Like Cracks: Resonance Scattering and Wave Localization

M.V. Golub and Ch. Zhang

Abstract The periodicity violation due to single or distributed cracks may change the wave reflection and transmission properties of periodically layered composites or one-dimensional phononic crystals. Numerical models for in-plane wave motion in layered phononic crystals with strip-like cracks are developed and the related wave propagation phenomena are investigated. For a prescribed incident wave field, the transfer matrix method is applied to calculate the reflected and the transmitted wave fields and to estimate the elastic wave band-gaps. The cracks are dealt with by using the integral approach, which represents the scattered wave field by a boundary integral containing the convolution of the Fourier-transform of the Green's matrix of the corresponding layered structures and the crack-opening displacements. These unknown displacement jumps are calculated by applying the Bubnov-Galerkin scheme in conjunction with the boundary integral equation method. The typical wave characteristics describing the wave propagation phenomena related to the elastic wave scattering by cracks are analysed. Resonance wave scattering by interior or interface strip-like cracks (delaminations) is investigated, and the corresponding streamlines of the wave energy flow are demonstrated and discussed. Wave localization and focusing by cracks is also analysed and discussed.

M.V. Golub (✉)
Institute for Mathematics, Mechanics and Informatics,
Kuban State University, Krasnodar, Russia
e-mail: m_golub@inbox.ru

Ch. Zhang
Chair of Structural Mechanics, Department of Civil Engineering,
University of Siegen, Siegen, Germany

30.1 Phononic Crystals or Periodic Elastic Composites

Phononic crystals or acoustic/elastic metamaterials are artificial elastic composites consisting of two or more materials with a periodic arrangement and different mechanical properties and mass densities. Phononic crystals represent a class of functional composite materials capable for manipulating the energy transfer of acoustic/elastic waves and have many promising applications. In recent decades, elastic periodic composites have received a great deal of attention and some innovative acoustic devices based on such periodic composites have been already developed and applied. Phononic crystals are the acoustic/elastic equivalent of photonic crystals, where a periodic arrangement of the material components causes certain frequency ranges (band-gaps) in which waves cannot propagate in the structures. They can also exhibit several special properties such as the negative refraction, focusing, resonances, cloaking etc. [1], especially when a local disorder is introduced [2].

The periodicity of phononic crystals can be disturbed by the introduction of artificial inhomogeneities or if they have been imperfectly manufactured or damaged during their exploitation. Inhomogeneities like inclusions, voids or cracks can be considered as disorders in periodic structures. Their presence may lead to the focusing of the wave energy [2], wave localization and resonance phenomena [3–7]. In addition, the periodicity violation may also change the wave transmission properties of phononic crystals. Near the crack-tips, the linear elastic stress field shows a singular behaviour which may lead to fatal failure of the structures. Indeed, layered structures with cracks may result in wave localization and resonances in the region between the stress-free crack-faces and the neighbouring interfaces, which were experimentally observed [7]. A good agreement of the band structures calculated and experimentally observed was demonstrated for one-dimensional porous silicon-based optical Bragg mirrors [8]. Defects in one-dimensional phononic crystals were analysed to reveal the sensitivity of the hybrid superlattices to periodicity perturbations due to defect layers [9].

The present chapter is devoted to the numerical modelling and analysis of wave propagation phenomena in layered phononic crystals with defects such as single, multiple and periodic strip-like cracks. A great deal of studies on wave motion in periodic composite structures was performed during last two decades. Many methods were developed in order to simulate the wave propagation in phononic crystals, and experimental studies were also conducted [1]. Several approaches including analytical, semi-analytical and numerical methods can be applied for this purpose. In particular, many numerical methods have been developed and applied so far including the plane wave expansion method, the transfer matrix method, the multiple scattering theory, the finite difference time domain method, the spectral element method, the finite element method, the boundary element method etc.

This analysis concentrates on the numerical simulation and investigation of the wave resonance, localization and focusing phenomena due to the crack-like defects in elastic layered periodic composites or one-dimensional phononic crystals.

The transfer matrix method [10] is chosen in order to simulate the wave motion in layered uncracked phononic crystals. The presence of cracks in periodic structures leads to extra computational efforts due to the large number of layers, which demands modifications of the traditional methods such as the boundary integral equation method based on the integral representations expressed as the integral transforms of the convolution of the Fourier symbols of the Green's matrix and the crack-opening displacements (CODs) [11]. In the case of a periodic array of cracks, the Bloch-Floquet theorem relates the CODs for all the cracks. The CODs are expressed in terms of orthogonal Chebyshev polynomials, and the Bubnov-Galerkin method is used in order to calculate the expansion coefficients. Non-resonant and resonant wave propagation and transmission are illustrated via the power density vector and the energy streamlines, which provide a better understanding of the physics of the wave resonance, localization and focusing phenomena. Some of the results presented in this chapter have been published in our previous papers [4–6], where more attention was paid to the wave band-gaps as well as the influences of the defects and the material properties on the wave transmission characteristics.

30.2 Governing Equations and Wave Fields in Phononic Crystals Without Cracks

Let us consider the propagation of plane elastic waves in a multi-layered periodic elastic structure consisting of N elastic unit-cells composed of two sublayers between two identical half-planes without cracks as shown in Fig. 30.1. The Cartesian coordinate system $\mathbf{x} = \{x_1, x_2\}$ is introduced on the left boundary of the layered structure, where the x_1 -axis is assumed to be parallel to the boundaries of the layers. The j th layer ($j = 1, 2, \dots, 2N$) of the thickness h_j occupying the domain $a_{j-1} \leq x_2 \leq a_j$, $|x_1| < \infty$ is made of the material A_j with the Lamé elastic constants λ_j , μ_j and the mass density ρ_j . The material and geometrical properties of the layers are

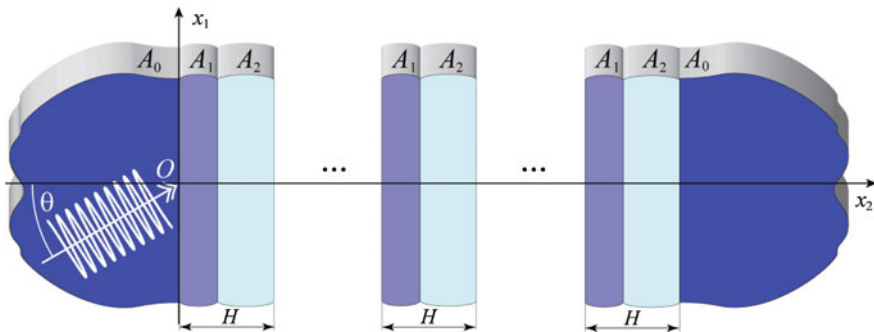


Fig. 30.1 Layered phononic crystal without cracks

repeated periodically in the phononic crystal, i.e., $A_j = A_{j+2}$ and $h_j = h_{j+2}$ ($j = 1, 2, \dots, 2N - 2$). The subscripts $j = 0$ and $j = 2N + 1$ correspond to the two half-planes surrounding the layered structure, and the thickness of the unit-cell is $H = h_1 + h_2$. In the present study, the two half-planes are assumed to be of the same material ($A_0 = A_{2N+1}$).

The governing elastodynamic equations in a homogeneous and linear elastic material are given by

$$\frac{\partial \sigma_{ij}}{\partial x_j} = \rho \frac{\partial^2 u_i}{\partial t^2}, \quad i = 1, 2. \quad (30.1)$$

Here, ρ is the mass density, and the stress tensor σ_{ij} can be written in terms of the displacements u_i via the Lamé's elastic constants λ_j and μ_j according to the Hooke's law. If a time-harmonic motion with the circular frequency ω is considered, then the governing (30.1) can be written as

$$(\lambda_j + \mu_j) \nabla \operatorname{div} \mathbf{u}_j + \mu_j \Delta \mathbf{u}_j + \rho_j \omega^2 \mathbf{u}_j = 0, \quad (30.2)$$

where the subscript "j" denotes the jth sublayer of the composite structure. Let us consider the motion of the layered periodic structure excited by time-harmonic plane waves incident from the plane $x_2 < 0$ at an angle θ to the boundary $x_2 = 0$ with the wave number k_0 . The displacements u_i^{in} and the stresses σ_{ij}^{in} in the absence of any cracks are continuous everywhere within the structure. The wave field can be described by the transfer matrix (**T**-matrix) that gives a simple expression describing the elastic wave motion in a homogeneous elastic sublayer. Thus, the generalized state vector $\mathbf{v} = \{u_1, u_2, \sigma_{12}, \sigma_{22}\}$ is introduced. The generalized state vectors at the boundaries of the jth sub-layer can be expressed in terms of the transfer matrix as

$$\mathbf{v}(h_j) = \mathbf{T}(h_j, h_{j-1}) \mathbf{v}(h_{j-1}). \quad (30.3)$$

The transfer matrix $\mathbf{T}(x_2, h_k)$ can be expressed explicitly in terms of the coordinate x_2 , the elastic constants, the circular frequency and the angle of the wave incidence θ [12].

The transfer matrix for P- and SV-waves propagating through a unit-cell of the layered phononic crystal is determined from the continuity conditions of the stresses and displacements at the interfaces of the sublayers. The total **T**-matrix for the whole layered periodic structure is a product $\mathbf{T} = (\mathbf{T}_{\text{unit-cell}})^N$ of the N transfer matrices for a unit-cell $\mathbf{T}_{\text{unit-cell}}$. In the case of two sublayers in a unit-cell, the 4×4 transfer matrix is a composition of the **T**-matrices for each of the two sublayers, i.e., $\mathbf{T}_{\text{unit-cell}} = \mathbf{T}(h_1, 0) \cdot \mathbf{T}(h_2, h_1)$.

30.3 Scattered Wave Fields in Phononic Crystals with Multiple Cracks

In this section, two problems are studied and compared, namely, one for K strip-like cracks and other for an array of periodic cracks. All the cracks are parallel to the interfaces of the layers of the phononic crystal. The geometry of the problem for a phononic crystal with K cracks is demonstrated in Fig. 30.2. The k th crack has a length $2l_k$, it is located in the B_k th sublayer within the M_k th unit-cell on the line d_k , and the centre of the crack is located at the distance b_k from the $x_1 = 0$ axis. In other words, the k th crack is an infinitesimal cut defined by $\Omega_k = \{|x_1 - b_k| \leq l_k, x_2 = d_k\}$ with stress-free faces, i.e.

$$\sigma_{i2}|_{\Omega_k} = 0, \quad k = \overline{1, K}. \tag{30.4}$$

The scattered wave field by a set of cracks satisfies the governing (30.2) and the boundary conditions on all the crack-faces. The total wave field in the cracked phononic crystal is a sum of the incident field \mathbf{u}^{in} and the scattered field \mathbf{u}^{sc} , which is a superposition of the fields scattered by all the cracks, i.e., $\mathbf{u}^{\text{sc}} = \sum_{k=1}^K \mathbf{u}_k$. The continuity of the scattered displacement fields \mathbf{u}^{sc} is violated on the stress-free crack-faces, where the displacements have a jump defined by

$$\Delta \mathbf{u}_k(x_1) = \mathbf{u}(x_1, d_k - 0) - \mathbf{u}(x_1, d_k + 0). \tag{30.5}$$

The integral approach [11] has been applied to the wave scattering analysis by multiple cracks in an elastic layer in [13], and a similar notation and scheme is used here. In order to apply the integral approach the structure is virtually divided along the line $x_2 = d_k$ into two half-planes for each crack. The scattered displacement field by the k th crack can be separately written in both multi-layered half-planes as

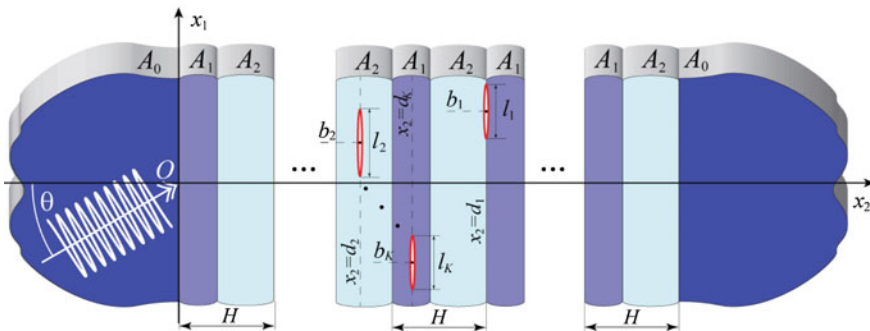
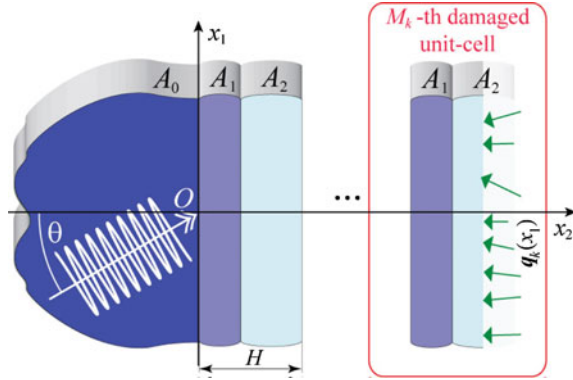


Fig. 30.2 Layered phononic crystal with multiple strip-like cracks

Fig. 30.3 Left multi-layered half-plane with the considered k th crack



$$u_k(x_1, x_2) = \begin{cases} u_k^+(x_1, x_2), & x_2 \geq d_k, \\ u_k^-(x_1, x_2), & x_2 < d_k. \end{cases} \quad (30.6)$$

Then an unknown traction vector $q_k(x_1)$ is introduced for the k th crack at the interface $x_2 = d_k$ as shown in Fig. 30.3. The integral representation for the scattered displacement field by the k th crack can be written as follows

$$u_k^\pm(x_1, x_2) = \frac{1}{2\pi} \int_{-\infty}^{\infty} \mathbf{K}_k^\pm(\alpha, x_2) \mathbf{Q}_k(\alpha) e^{-i\alpha x_1} d\alpha, \quad k = \overline{1, K}. \quad (30.7)$$

Here, $\mathbf{Q}_k(\alpha)$ is the Fourier-transform of the unknown traction vector $q_k(x_1)$, α is the Fourier-transform parameter, and $\mathbf{K}_k^\pm(\alpha, x_2)$ are the Fourier-transformed Green's matrices for the multi-layered half-planes $x_2 \leq d_k$ and $x_2 \geq d_k$ [14]. The crack-opening displacements (CODs) for the k th crack are also related to the traction vector $q_k(x_1)$. After applying the Fourier-transform to the integral representation (30.7) the relation between the stresses on the interface and the CODs can be written in terms of the Fourier symbols as

$$\mathbf{Q}_k(\alpha) = [\mathbf{K}_k^-(\alpha, d_k) - \mathbf{K}_k^+(\alpha, d_k)]^{-1} \Delta \mathbf{U}_k(\alpha) = \mathbf{L}_k(\alpha) \Delta \mathbf{U}_k(\alpha),$$

where $\Delta \mathbf{U}_k$ denotes the Fourier-transform of the CODs Δu_k . After applying the stress operator to the integral representation (30.7), the stresses of the scattered wave field can be written as

$$\tau_k(x_1, x_2) = \frac{1}{2\pi} \int_{-\infty}^{\infty} \mathbf{S}_k^\pm(\alpha, x_2) \Delta \mathbf{U}_k(\alpha) e^{-i\alpha x_1} d\alpha, \quad k = \overline{1, K}. \quad (30.8)$$

Substitution of the integral representation (30.8) into the boundary conditions (30.4) on all crack-faces leads to the following set of integral equations for the unknown CODs:

$$\frac{1}{2\pi} \sum_{j=1}^K \int_{-\infty}^{\infty} \mathbf{S}_j^{\pm}(\alpha, d_k) \Delta \mathbf{U}_j(\alpha) e^{-i\alpha x_1} d\alpha = \mathbf{f}_k(x), \quad |x_1 - b_k| \leq l_k, \quad k = \overline{1, K},$$

$$\mathbf{f}_k(x_1) = -\boldsymbol{\tau}^{\text{in}}(x_1, d_k) = -\boldsymbol{\tau}^{\text{in}}(0, d_k) \exp(ik_0 \sin \theta x_1). \quad (30.9)$$

The CODs are expanded then into the series

$$\Delta \mathbf{u}_k(x_1) = \sum_{n=1}^{\infty} \mathbf{c}_{kn} \phi_n \left(\frac{x_1 - b_k}{l_k} \right), \quad (30.10)$$

where ϕ_j are the orthogonal Chebyshev polynomials of the second kind. The Chebyshev polynomials form a complete set of functions in the interval $[-1, 1]$ and give the correct square-root behaviour of the CODs at the crack-tips [15]. In order to solve the integral (30.9), the boundary integral equation method and the Bubnov-Galerkin method are applied. This can be done by substituting the series expansion of the CODs (30.10) into (30.9) and then projecting on the space of the Chebyshev polynomials, which gives the following discretized form of the integral equations:

$$\sum_{k'=1}^K \sum_{n'=1}^N \mathbf{Q}_{kk'nn'} \mathbf{c}_{k'n'} = \mathbf{f}_{kn}, \quad k = \overline{1, K}, n = \overline{1, N_r},$$

$$\mathbf{Q}_{kk'nn'} = \begin{cases} \frac{1}{2\pi} \int_{-\infty}^{\infty} \mathbf{L}_k(\alpha) \Phi_n(\alpha l_k) \Phi_{n'}(\alpha l_k) d\alpha, & k = k', \\ \frac{1}{2\pi} \int_{-\infty}^{\infty} \mathbf{S}_k(\alpha, d_k) \Phi_n(\alpha l_k) \Phi_{n'}(\alpha l_{k'}) e^{-i\alpha(b_k - b_{k'})} d\alpha, & k \neq k', \end{cases}$$

$$\mathbf{f}_{kn} = -\boldsymbol{\tau}^{\text{in}}(0, d_k) \Phi_n(l_k k_0 \sin \theta) \quad (30.11)$$

Here, $\Phi_n(\alpha l_k) = J_n(\alpha l_k) / \alpha$ is the Fourier-transform of the Chebyshev polynomials $\phi_n(x)$, N_r is the number of terms kept in the expansion (30.10) in the numerical computation. The coefficients on the left-hand side of (30.11) are integrals along the real axis in the α complex plane bypassing the poles of the kernel $\mathbf{S}_k(\alpha, d_k)$ and $\mathbf{L}_k(\alpha) = \mathbf{S}_k(\alpha, d_k)$.

30.4 Scattered Wave Fields in Phononic Crystals with Periodic Cracks

The cracked domain with a periodic array of cracks is a set of cracks of the length $2l$ at the distance s from each other (Fig. 30.4). The periodic cracks are assumed to be located in the B th sublayer within the M th unit-cell at the distance d from the interface $x_2 = 0$, i.e. the periodic array of cracks is determined by $\Omega_k = \{|x_1 - ks| \leq l, x_2 = d\}$. The boundary conditions (30.4) are still valid, but k is now an integer number because the periodic array has an infinite number of terms along the x_1 -axis. The integral representations (30.7) and (30.8) can be used in this case by assuming that the cracks are situated at $x_2 = d$. Due to the periodicity of the crack spacing and according to the Bloch-Floquet theorem, the CODs can be expressed as

$$\Delta U_j(\alpha) = \sum_{k=-\infty}^{\infty} \Delta U_j(\alpha), \quad \Delta U_j(\alpha) = \Delta U_0(\alpha) e^{iz(k_0 \sin \theta + ks)}.$$

Thus, the following integral equation is obtained

$$\frac{1}{2\pi} \sum_{k=-\infty}^{\infty} \int_{-\infty}^{\infty} \mathbf{L}(\alpha) \Delta U_j(\alpha) e^{-izx_1} d\alpha = \mathbf{f}_k(x), \quad |x_1| \leq l, \tag{30.12}$$

$$[\mathbf{K}^-(\alpha, d) - \mathbf{K}^+(\alpha, d)]^{-1} = \mathbf{L}(\alpha)$$

in terms of the Green's matrices $\mathbf{K}^{\pm}(\alpha, d)$ for the half-planes $x_2 \leq d$ and $x_2 \geq d$. Here the left-hand side of the integral (30.12) can be rewritten as the infinite sum:

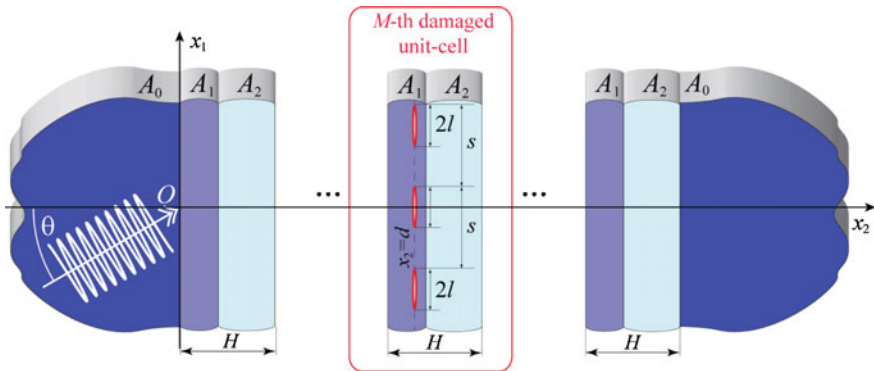


Fig. 30.4 Layered phononic crystal with a periodic array of strip-like cracks

$$\begin{aligned} & \frac{1}{2\pi} \int_{-\infty}^{\infty} \mathbf{L}(\alpha) \Delta U_0(\alpha) \sum_{j=-\infty}^{\infty} e^{i(\alpha + k_0 \sin \theta)js - i\alpha x_1} d\alpha \\ &= \frac{1}{s} \sum_{j=-\infty}^{\infty} \mathbf{L}(\alpha_j) \Delta U_0(\alpha_j) e^{-i\alpha_j x_1} \Big|_{\alpha_j = 2\pi j/s + k_0 \sin \theta} \end{aligned}$$

In order to solve the boundary value problem, the CODs of the reference crack ($|x_1| \leq l$) is approximated by Chebyshev polynomials in the same manner as for (30.10) in the case of the non-periodic multiple cracks. The boundary integral (30.12) is solved by applying the Bubnov-Galerkin method, resulting in the following system of algebraic equations for the unknown expansion coefficients $\mathbf{c}_{n'}$

$$\begin{aligned} \sum_{n'=1}^{N_r} \mathbf{Q}_{nn'} \mathbf{c}_{n'} &= \mathbf{f}_n, \quad n = \overline{1, N_r}, \\ \mathbf{Q}_{nn'} &= \frac{1}{s} \sum_{k=-\infty}^{\infty} \mathbf{L}(\alpha_k) \Phi_n(\alpha_k l) \Phi_{n'}(-\alpha_k l), \quad \mathbf{f}_n = -\boldsymbol{\tau}^{\text{in}}(0, d) \Phi_n(lk_0 \sin \theta). \end{aligned} \tag{30.13}$$

30.5 Wave Propagation Characterization

The developed mathematical and computational models are applied in this analysis in order to investigate the wave propagation phenomena in layered phononic crystals with cracks parallel to the interfaces. The verification of the models for some special cases can be found in [4–6, 12]. Lead and epoxy are selected because of their high contrast in material properties, see Table 30.1. For convenience, dimensionless parameters are introduced by using the mass density ρ_1 and the wave speed c_1 in the first layer A_1 as well as the unit-cell thickness H . For simplicity, only the case with $h_1/h_2 = 1$ and 12 unit-cells is considered.

The transport of the wave energy in the time-harmonic wave motion can be visualized by the energy streamlines, which are the trajectories of the time-averaged energy flow in the elastic media [16, 17]. The energy streamlines are tangential to

Table 30.1 Properties of the sublayers composing the phononic crystal

No.	Material	λ (Pa)	μ (Pa)	ρ (kg m ⁻³)
1	Epoxy	$6.38 \cdot 10^9$	$1.61 \cdot 10^9$	1200
2	Lead	$36.32 \cdot 10^9$	$8.4 \cdot 10^9$	3800

the power density vector $\mathbf{e} = \{e_1, e_2\}$ introduced by Umov. Their components in the time-harmonic case are expressed via the displacements \mathbf{u} and the stresses $\boldsymbol{\tau}_n$ as

$$\mathbf{e}_n(\mathbf{x}) = -\frac{\omega}{2} \text{Im}(\mathbf{u}, \boldsymbol{\tau}_n),$$

where $\boldsymbol{\tau}_n$ is the stress vector at an elementary area orthogonal to the \mathbf{n} vector. The energy transmission coefficient $\kappa^+ = E^+/E^0$ is used in the present analysis, which is defined as the ratio of the time-averaged energy flow transmitted through the phononic crystal E^+ to the energy transferable by the incident plane waves E^0 . Analogously, for the reflected wave field the reflection coefficient $\kappa^- = E^-/E^0$ is introduced. Due to the energy conservation law we have $\kappa^+ + \kappa^- = 1$, which is used in order to check the correctness of the numerical solution. Using the eigenvalues of the transfer matrix for the sublayers, the asymptotics of the transmission coefficient for a large number of unit-cells can be derived. It provides us simple conditions to distinguish band-gaps and pass-bands [12].

The COD vectors $\Delta \mathbf{u}_k(x_1)$ characterize the behavior of multiple cracks, but they depend on the x_1 -coordinate, so it is convenient to introduce and analyse the average CODs \overline{v}_k^j and the normalized average CODs v_k^j , which are defined by

$$v_k^j = \overline{v}_k^j / \overline{u}^{\text{in}}, \quad j = 1, 2$$

$$\overline{v}_k^j = \frac{1}{2l_k} \left| \int_{-l_k}^{l_k} \Delta u_{kj}(x_1) dx_1 \right|, \quad \overline{u}^{\text{in}} = \frac{1}{H} \left| \int_{(M_k-1)H}^{M_k H} \mathbf{u}(0, x_2) dx_2 \right|.$$

The average CODs \overline{v}_k^j provide sufficient information at frequencies being within the pass-bands, but within the band-gaps the value of \overline{v}_k^j is very small and depends on the incident waves due to the properties of the integral equations (30.9) and (30.12). In order to perform a detailed parametrical analysis of the wave motion, the normalized average CODs v_k^j are more preferable as they can show the resonance peaks within the band-gaps. On the other hand, the stress intensity factors (SIFs) are frequently used in linear elastic fracture mechanics to describe the stress state near the crack-tips and estimate the possibility of an eventual crack growth in the structure, see [4–6, 12].

30.6 Wave Resonances, Localization and Focusing in Layered Phononic Crystals with Cracks

In order to study the physical nature of the wave scattering phenomena by strip-like cracks a parametric analysis can be performed by using the \overline{v}_k^j and v_k^j values, for more details and results see, for instance, [4–6]. Wave resonances are accompanied

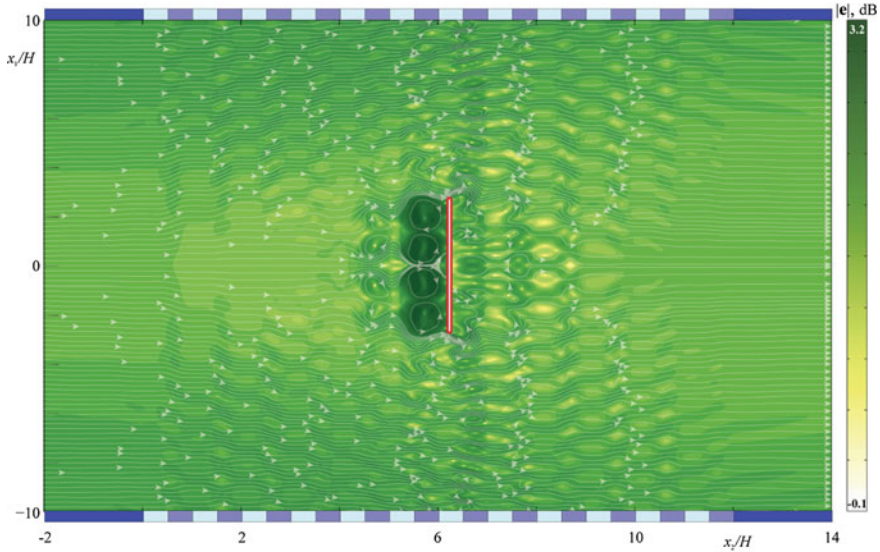


Fig. 30.5 Power density vector $|e(\mathbf{x})|$ in logarithmic scale and the related energy streamlines for normally incident P-wave scattering by single crack at $\omega H/c_0 = 7.6$, $l_1/H = 2.74$, $d_1/H = 6.25$ and $b_1/H = 0.0$ (non-resonant case)

by larger amplitudes of the wave motion in the vicinity of cracks and correspondingly, the values of the CODs and SIFs are larger as well. This has been used during the search of the combinations of the problem parameters for wave resonances. The results depicted in Figs. 30.5, 30.6, 30.7, 30.8, 30.9, 30.10, 30.11 and 30.12 for the power density vector $|e(\mathbf{x})|$ in logarithmic scale, i.e. $\log_{10}|e(\mathbf{x})|$ in dB, are used (note: the logarithmic scale provides a better visualization). The corresponding energy streamlines are given over the contour plots of $|e(\mathbf{x})|$. The figures have been obtained for incident P-waves only, because very similar effects can be observed for incident SV-waves. In order to reveal the wave localization and focusing phenomenon, resonant and non-resonant situations were considered and compared for a single crack, multiple cracks and periodic cracks.

First, a single crack in the phononic crystal is considered. It is clearly seen in Fig. 30.5, demonstrating the non-resonant wave scattering by a crack, that the energy flow does not change significantly by the crack at the distance equal to the length of the crack. The energy flow goes around the crack, and the maxima of the displacements and the power density are arising in the zone before the crack, where four energy vortices (closed energy streamlines) are observed. A shadow zone occurs in this case, but its size and strength is quite small.

Resonance wave scattering by a single strip-like crack is depicted in Fig. 30.6. Here, the energy flow deviates much more compared to the non-resonant case. Accordingly, the distribution of the power density is much more complicated and additional energy vortices occur, where the energy captures as in the non-resonant

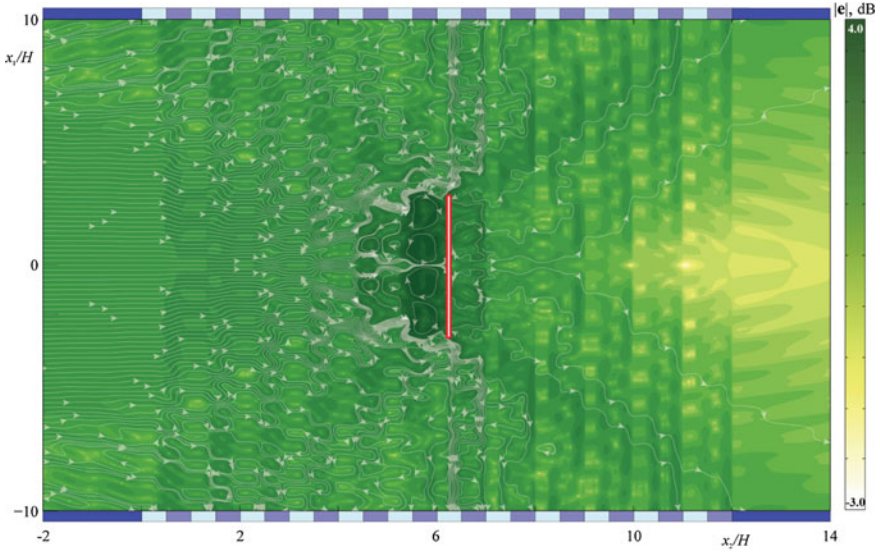


Fig. 30.6 Power density vector $|e(x)|$ in logarithmic scale and the related energy streamlines for normally incident P-wave scattering by single crack at $\omega H/c_0 = 7.5$, $l_1/H = 2.9$, $d_1/H = 6.25$ and $b_1/H = 0.0$ (resonant case)

case shown in Fig. 30.5. The resonance wave motion affects the energy flow and the wave field in the cracked phononic crystal much stronger. The crack scatters and bends the energy flow of the incident wave in a rather strong manner, and it reflects the incident wave backward and forward, while the forward energy flow is not orthogonal to the interfaces. Thus, a single crack can act as an energy pump, while the amount of the energy captures increases, when the parameters of the structure with a crack approach that of the resonant case.

Figures 30.7 and 30.8 depict the plane wave scattering by two cracks. The non-resonant wave scattering pattern (Fig. 30.7) shows some energy vortices of a small intensity. On the other hand, the resonant wave scattering leads to a larger amount of the energy captured with larger vortices formed between the cracks. A larger shadow zone occurs behind the cracked zone compared to the case of a single crack, which can be identified by comparing Figs. 30.5 and 30.6 with Figs. 30.7 and 30.8. Accordingly, an obvious conclusion can be made here that the addition of an extra crack will change the energy flow through the phononic crystal, which can be used in order to manipulate the wave energy flow.

Now, we consider periodic cracks as shown in Figs. 30.9 and 30.10. Owing to the periodicity of the crack spacing, only the region surrounding a reference crack in the centre of the Cartesian coordinate system needs to be considered. Wave resonances are usually related to the wave energy capturing and localization, which show also resonance blocking or, in some cases, wave transmission [7]. A typical pattern of the wave resonance is observed here, namely, the vortices exist between

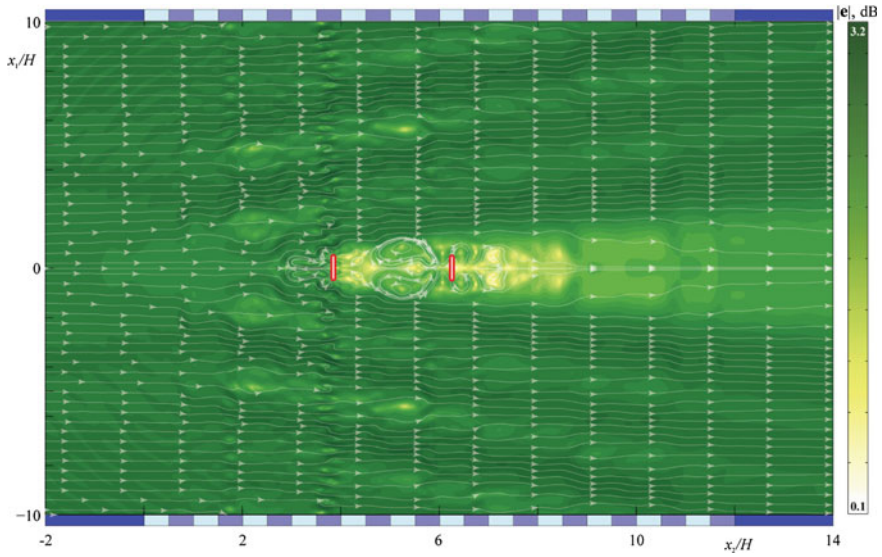


Fig. 30.7 Power density vector $|e(\mathbf{x})|$ in logarithmic scale and the related energy streamlines for normally incident P-wave scattering by two cracks at $\omega H/c_0 = 10.679$, $l_{1,2}/H = 0.5$, $d_1/H = 6.25$, $d_2/H = 3.84$ and $b_{1,2}/H = 0.0$ (non-resonant case)

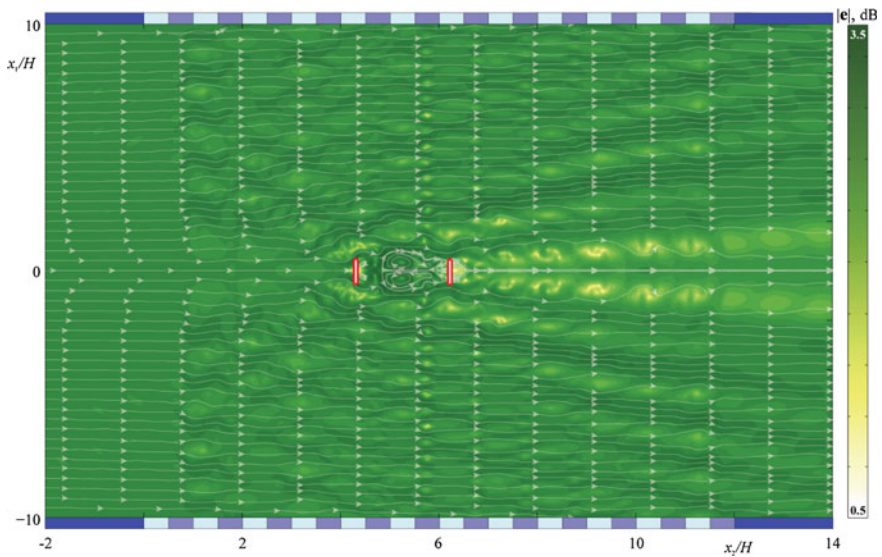


Fig. 30.8 Power density vector $|e(\mathbf{x})|$ in logarithmic scale and the related energy streamlines for normally incident P-wave scattering by two cracks at $\omega H/c_0 = 11.472$, $l_{1,2}/H = 0.5$, $d_1/H = 6.25$, $d_2/H = 4.32$ and $b_{1,2}/H = 0.0$ (resonant case)

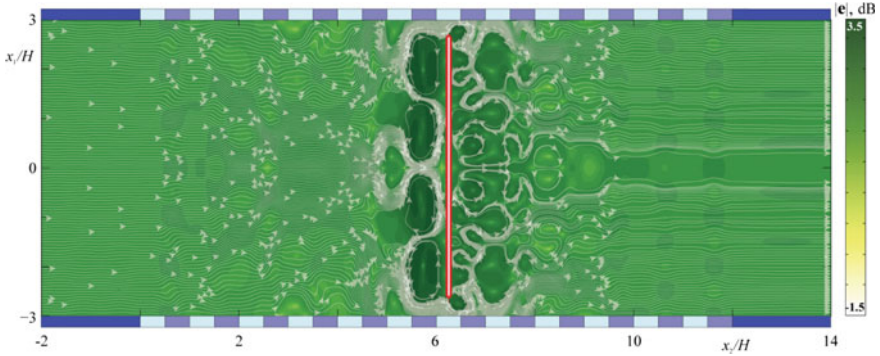


Fig. 30.9 Power density vector $|e(x)|$ in logarithmic scale and the related energy streamlines for normally incident P-wave scattering by periodic cracks at $\omega H/c_0 = 7.77$, $l/H = 2.65$, $d/H = 6.25$ and $s/H = 6.0$ (non-resonant case)

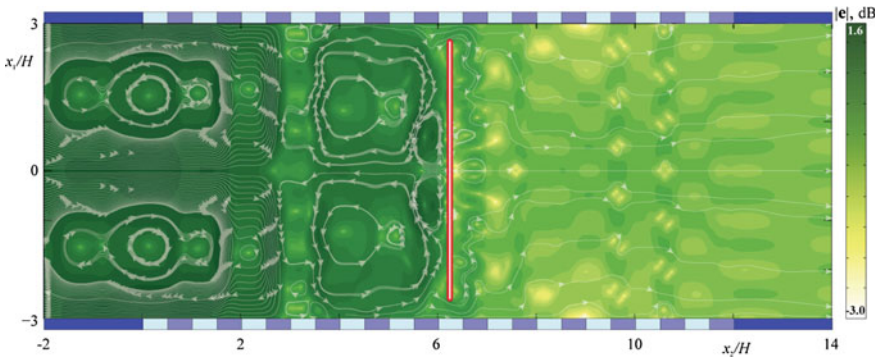


Fig. 30.10 The power density vector $|e(x)|$ in logarithmic scale and the related energy streamlines for normally incident P-wave scattering by periodic cracks at $\omega H/c_0 = 7.77$, $l/H = 2.65$, $d/H = 6.25$ and $s/H = 6.0$ (resonant case)

the crack-tips and the largest ones appear in front of the crack-line, where the localization of the wave energy is strong (in a few unit-cells before the crack-line). However, the wave resonance in this example can be classified as a weak resonance, because the energy vortices do not distribute in the whole layered structure and a part of the wave energy flows around the cracks. The corresponding examples are depicted in Fig. 30.9 (non-resonant case) and Fig. 30.10 (resonant case).

If the location or the size of the cracks shifts from the resonance depth and length, then a usual wave scattering is observed. The energy vortices then do not close the waveguide for the energy flow and bend around them, so the energy flow of the elastic waves can thus pass all the vortices and the cracks. Here, numerical examples for the wave scattering by cracks at frequencies lying within the band-gaps are not demonstrated for the sake of brevity, but several such examples and a detailed discussion on the subject can be found in our previous papers [4–6].

Finally, the possibility of the wave energy focusing due to cracks is studied for certain frequencies. Elastic wave focusing may help to capture the wave energy and it has a number of potential applications in transducers, sensors, etc. Flat lens focusing of elastic waves has been predicted in the time-harmonic case [18], and recently the focusing of Lamb waves has also been recognized numerically and experimentally in structured plates [19]. Figure 30.11 demonstrates an example of the wave-guiding energy flow by positioning six cracks in three rows. The presence of six cracks allows one to form shadow zones behind the cracks that leads to an energy flow increase in two elongated zones marked by the black dashed rectangles in Fig. 30.11. The energy vortices occur between the three crack pairs standing behind each other, and they enforce the energy flow to the focusing zones as mentioned above.

Periodic cracks may exhibit the wave focusing effect in different manner. Figure 30.12 shows the power density vector in logarithmic scale and the related energy streamlines for periodic cracks almost fully covering the crack-line. The cracks ($l/H = 2.98$, $d/H = 6.83$, $s/H = 6.0$) bend the energy flow in such a way that the vortices occur at $x = s/2$, so the energy flow is captured by the energy vortices and focused in two zones behind the cracks, near the border of the phononic crystal and between the right half-plane and the periodic cracks.

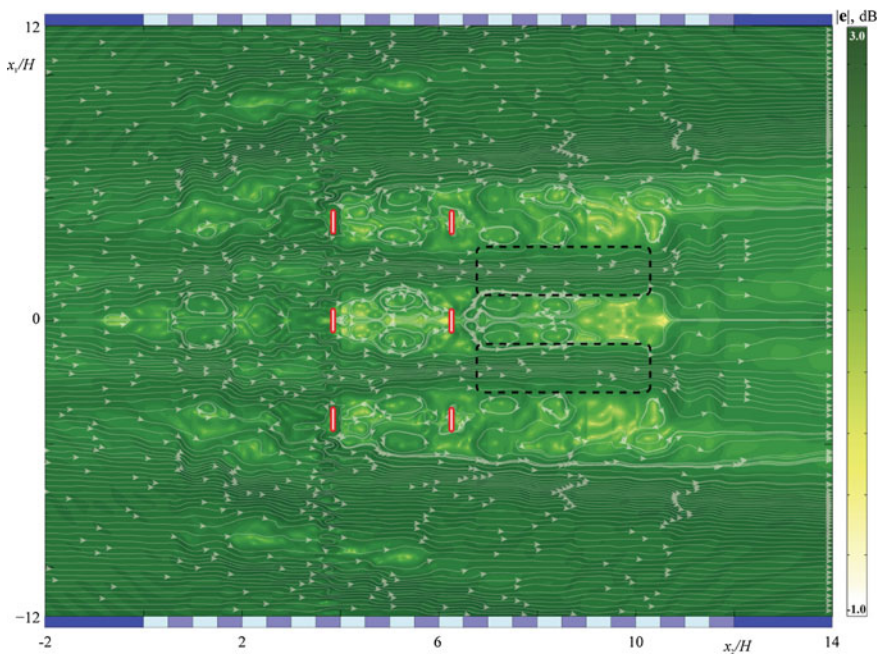


Fig. 30.11 The power density vector $|e(x)|$ in logarithmic scale and the related energy streamlines for normally incident P-wave scattering by six cracks at $\omega H/c_0 = 11.472$, $d_{1,2,3}/H = 6.25$, $d_{4,5,6}/H = 3.84$, $l_k/H = 0.5$, $k = \overline{1,6}$, $b_{1,4}/H = -4.0$, $b_{2,5}/H = 0.0$ and $b_{3,6}/H = 4.0$ (focusing case)

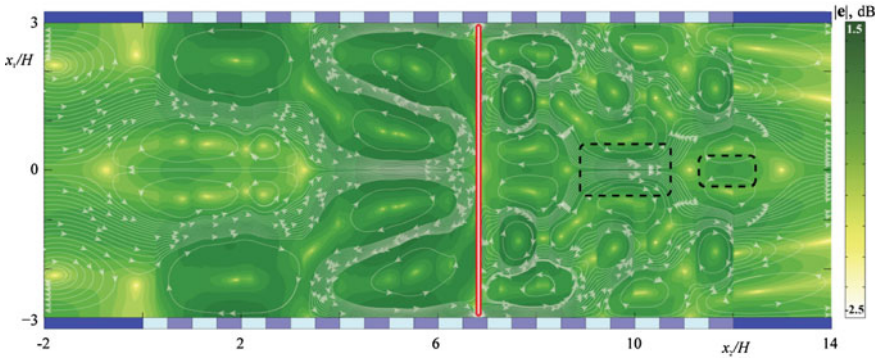


Fig. 30.12 The power density vector $|e(x)|$ in logarithmic scale and the related energy streamlines for normally incident P-wave scattering by periodic cracks at $\omega H/c_0 = 1.3$, $l/H = 2.98$, $d/H = 6.83$ and $s/H = 6.0$ (focusing case)

Finally, the situation of the oblique wave incidence should be mentioned. In this case, the formation of the energy flow vortices is hampered because the direction of the wave propagation is not perpendicular to the crack-faces and the interfaces of the phononic crystals. Although the wave localization and focusing near the cracks is still possible in this case, but the corresponding region is rather small.

30.7 Conclusions

Mathematical and computational models for wave propagation simulation in phononic crystals with single, multiple and periodic cracks as defects or disorders are developed and applied. The wave vector of energy flow and the corresponding energy streamlines are visualized to obtain a better and deeper understanding of the wave propagation, resonance, localization and focusing phenomena in layered phononic crystals with interior or interface cracks. Numerical examples are presented and discussed to show the effects of the wave frequency, crack size, crack number, crack spacing and location, as well as other material and structural parameters on the wave propagation characteristics in layered phononic crystals.

References

1. P.A. Deymier, *Acoustic Metamaterials and Phononic Crystals* (Springer-Verlag, Berlin Heidelberg, 2013)
2. M.I. Hussein, M.J. Leamy, M. Ruzzene, *ASME Appl. Mech. Rev.* **66**(4), 040802 (2014)
3. Y. Wang, F. Li, Y.-S. Wang, K. Kishimoto, W. Huang, *Acta. Mech. Sin.* **25**, 65 (2008)
4. M.V. Golub, Ch. Zhang, *Wave Motion* **54**(2), 308 (2014)

5. M.V. Golub, Ch. Zhang, *J. Acoust. Soc. Am.* **137**(1), 238 (2015)
6. M.V. Golub, *Comput. Continuum Mech.* **8**(2), 136 (2015). (in Russian)
7. E. Glushkov, N. Glushkova, M.V. Golub, J. Moll, C.-P. Fritzen, *Smart Mater. Struct.* **21**, 125001 (2012)
8. L.C. Parsons, G.T. Andrews, *J. Appl. Phys.* **111**(12), 123521 (2012)
9. D. Schneider, F. Liaqat, H. El Boudouti, O. El Abouti, W. Tremel, H.-J. Butt, B. Djafari-Rouhani, G. Fytas, *Phys. Rev. Lett.* **111**, 164301 (2013)
10. W. Thomson, *J. Appl. Phys.* **21**, 89 (1950)
11. E.V. Glushkov, N.V. Glushkova, *J. Comput. Acoust.* **9**(3), 889 (2001)
12. S.I. Fomenko, M.V. Golub, T.Q. Bui, Ch. Zhang, Y.-S. Wang, *Int. J. Solids Struct.* **51**(13), 2491 (2014)
13. E.V. Glushkov, N.V. Glushkova, M.V. Golub, Ch. Zhang, *Acoust. Phys.* **55**, 8 (2009)
14. E.V. Glushkov, N.V. Glushkova, A.A. Eremin, *J. Acoust. Soc. Am.* **129**(12), 2923 (2011)
15. A. Bostrom, *Appl. Mech. Rev.* **56**, 383 (2003)
16. A.P. Kiselev, *J. Sov. Math.* **19**, 1372 (1982)
17. E.V. Glushkov, N.V. Glushkova, *J. Acoust. Soc. Am.* **102**, 1356 (1997)
18. M. Farhat, S. Guenneau, S. Enoch, A.B. Movchan, G.G. Petursson, *Appl. Phys. Lett.* **96**, 081909 (2010)
19. M. Dubois, M. Farhat, E. Bossy, S. Enoch, S. Guenneau, P. Sebbah, *Appl. Phys. Lett.* **103**, 071915 (2013)

Chapter 31

Ultrasonic Guided Wave Characterization and Inspection of Laminate Fiber-Reinforced Composite Plates

E.V. Glushkov, N.V. Glushkova, A.A. Eremin, A.A. Evdokimov and R. Lammering

Abstract Computer simulation of wave processes in composite structures is a challenging task due to complicate waveguide properties induced by their anisotropy and lamination. In the present contribution, recent advances in analytically based guided wave (GW) simulation within 3D anisotropic elasticity are present. The wave fields generated in anisotropic laminate structures by surface or buried sources are explicitly expressed via integral and asymptotic expressions in terms of Green's matrix of the structure considered and the source load. On this basis, a set of low-cost computer models for a reliable quantitative near- and far-field analysis has been developed and experimentally validated. Their abilities are illustrated with several examples: (i) the evaluation of structural frequency response and radiation pattern diagrams for GWs generated by piezoelectric wafer active sensors (PWAS); (ii) the reconstruction of effective elastic moduli of fiber-reinforced composite plates based on laser vibrometer measurements; (iii) PWAS frequency tuning with accounting for the wave energy supplied by the source and the radiation directivity caused by the plate's anisotropy.

31.1 Introduction

In present, laminate composite materials are extensively utilized in aeronautical structures because of their high performance and reliability due to high strength-to-weight and stiffness-to-weight ratios, excellent fatigue strength, and design flexibility. The increasing role of composites has led to extensive research

E.V. Glushkov (✉) · N.V. Glushkova · A.A. Eremin · A.A. Evdokimov
Institute for Mathematics, Mechanics and Informatics, Kuban State University,
Krasnodar, Russia
e-mail: evg@math.kubsu.ru

R. Lammering
Institute of Mechanics, Helmut-Schmidt-University/University of the Federal
Armed Forces, Hamburg, Germany

activities in the development and implementation of non-destructive testing (NDT) and structural health monitoring (SHM) techniques for their integrity assessment during the structure service life. Among the promising solutions, we note the utilization of elastic guided waves (GWs) that travel for long distances covering large cross-sectional areas of the specimen and providing information regarding the presence of defects. Thus, the GWs are capable for long-range inspection of thin-walled composite structures. The active diagnostics widely utilizes piezoelectric wafer active sensors (PWAS) for transient GW generation and damage detection [1]. The complex characteristics of GWs in composite laminates, e.g., frequency and spatial directivity of dispersion characteristic and amplitudes are thoroughly studied. Thus, the development of reliable analytical and numerical tools for the simulation and analysis of wave propagation in healthy and damaged composites is evidently required.

A convenient approach to the simulation of GW phenomena is in the use of various mesh-based techniques such as a finite difference method, finite element method (FEM), etc. The undoubted benefits of these approaches are their high flexibility to simulate engineering structures of complex geometry and relative simplicity of realization. However, when high frequencies and wave numbers are involved and/or lengthy structures are considered, traditional FEM codes require fine spatial and temporal discretization to ensure numerical stability that requires excessive computational resources. Recently several novel mesh-based techniques have been successfully adopted for GW simulation, e.g. local interaction simulation approach (LISA) [2] or time-domain spectral FEM [3]. While the former enjoys the parallelism of modern computers, the latter relies on high-order polynomial shape functions in FE approximation.

With domains of simpler classical form, e.g., for laminate plates, which are widely used in construction units, analytically based methods are suitable [4, 5]. Semi-analytical GW simulation for 3D anisotropic laminate structures is based on the convolution-type integral representations via the Green's matrix of the structure considered and the load vectors of surface or buried sources [6]. Explicit analytical representations for GWs, derived from these integrals using the residue theory and stationary phase method, do not require any spatial discretization, and so they remain practically costless irrespective of the sample's size.

In the present contribution, we summarize the recent advances of our research team in the application of the aforementioned semi-analytical representations to theoretical and experimental investigation of GW phenomena in layered fiber-reinforced composite structures [7, 8]. The examples given below concentrate on the reconstruction of effective elastic moduli of fiber-reinforced composite plates based on laser vibrometer measurements as well as on the simulation of the structural frequency response and radiation pattern diagrams for PWAS generated GWs.

31.2 Mathematical Model

Time-harmonic oscillation $\mathbf{u}(\mathbf{x}, \omega)e^{-i\omega t}$, $\mathbf{u} = (u_x, u_y, u_z) = (u_1, u_2, u_3)$, $\mathbf{x} = (x, y, z) = (x_1, x_2, x_3)$, of a laminate structure $D = \cup_{m=1}^M D_m = \{(x, y, z) : |x|, |y| < \infty, -H < z < 0\}$ of thickness H is investigated (Fig. 31.1). Each sublayer D_m is considered as a linear anisotropic material, characterized by a stiffness matrix $C_{ij}^{(m)}$, $m = 1, 2, \dots, M$. The oscillation is excited by a surface load $\mathbf{q}(\mathbf{x}, \omega)e^{-i\omega t}$, $\mathbf{q} = (q_x, q_y, q_z) = (q_1, q_2, q_3)$, localized in area Ω at the top surface $z = 0$ (the time-harmonic factor $e^{-i\omega t}$ is further omitted).

The geometry of the problem allows one to apply the integral Fourier transform F_{xy} over the horizontal spatial variables x, y and to obtain the explicit solution in terms of inverse Fourier two-fold path integral. With the polar coordinates (r, φ) and (α, γ) : $x = r \cos \varphi$, $y = r \sin \varphi$ and $\alpha_1 = \alpha \cos \varphi$, $\alpha_2 = \alpha \sin \varphi$, it takes the form

$$\mathbf{u}(\mathbf{x}) = \frac{1}{4\pi^2} \int_{\Gamma_+} \int_0^{2\pi} K(\alpha, \gamma, z) \mathbf{Q}(\alpha, \gamma) e^{-i\alpha r \cos(\gamma - \varphi)} d\gamma \alpha d\alpha, \tag{31.1}$$

where $K = F_{xy}[k]$ and $\mathbf{Q} = F_{xy}[\mathbf{q}]$ are Fourier symbols of the Green's matrix $k(\mathbf{x})$ and the contact stress vector $\mathbf{q}(x, y)$ (here and below, we adhere to the notations of [6]). The integration path Γ_+ goes in the complex plane α along the real semi-axis $\text{Re } \alpha \geq 0, \text{Im } \alpha = 0$, bypassing real poles $\zeta_n = \zeta_n(\gamma) > 0$ of the matrix K elements according to the principle of limiting absorption. Using the residue technique and the stationary phase method, integral representation (31.1) is brought to the asymptotic expansion in terms of guided waves \mathbf{u}_n :

$$\begin{aligned} \mathbf{u}(\mathbf{x}) &= \sum_{n=1}^{N_r} \mathbf{u}_n(\mathbf{x}) + O((\zeta_n r)^{-1}), \quad \zeta_n r \rightarrow \infty \\ \mathbf{u}_n(\mathbf{x}) &= \sum_{m=1}^{M_n} \mathbf{a}_{nm}(\varphi, z) e^{i s_{nm} r} / \sqrt{\zeta_n r} \end{aligned} \tag{31.2}$$

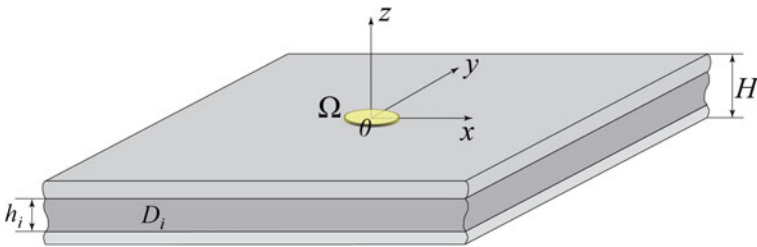


Fig. 31.1 Geometry of the problem

The amplitude factors \mathbf{a}_{nm} are expressed via the residues of the product $K\mathbf{Q}$ from the real poles ζ_n ; $s_{nm} = s_n(\gamma_{nm})$ are wave numbers of the GWs \mathbf{u}_n ; γ_{nm} are the stationary points of the phase functions $s_n(\gamma) = \zeta_n(\gamma + \varphi + \pi/2) \sin \gamma$; $s'_n(\gamma_{nm}) = 0$; N_r is the number of real poles ζ_n ; M_n is the number of stationary points γ_{nm} of the n th phase function s_n . Each term in the second sum of the (31.2) is a cylindrical guided wave (CGW), specified in the radial observation direction φ by the wave number $s_{nm}(\varphi)$, wave length $\lambda_{nm} = 2\pi/s_{nm}$ and group velocity

$$c_{g,nm}(\varphi) = [ds_{nm}/d\omega]^{-1} \quad (31.3)$$

In contrast to the conventional plane wave approach for group velocity evaluation [9], representations (31.2) and (31.3) provide a straightforward calculation procedure of the GW amplitudes and group velocities calculation in a prescribed observation direction φ , since they explicitly depend on this angle [7]. More details on the derivation of the expressions (31.1)–(31.3) can be found in [6, 7].

31.3 Estimation of Effective Elastic Properties

One of the promising non-destructive approaches to the identification of material elastic properties is to utilize the ultrasonic GWs, which amplitude and dispersion characteristics strongly depend on the mechanical properties of the host structure. The reconstruction is based on the minimization of discrepancies between the theoretically calculated and experimentally measured GW characteristics. In this process, it is more convenient to use GW dispersion curves since their numerical evaluation does not require to take into consideration the devices used for GW excitation/sensing and thus reduces the computational costs.

While the described technique is applicable to any laminate elastic waveguide with arbitrary anisotropy and thickness of each sublayer, below it is assumed that the specimen is fabricated from M identical transversely isotropic prepregs ideally bonded to each other. This assumption is typical for a wide range of composite materials utilized in real aeronautical applications. Thus, the composite mechanical properties are specified by the prepreg's stiffness matrix C_{ij} , density ρ and lamination scheme. Along with five independent elastic moduli, five engineering constants, namely, two Young's moduli E_x , E_y , two shear moduli G_{yz} , G_{xy} and the Poisson's ratio ν_{xy} are used. The benefit of these parameters is that they can be directly acquired from conventional tensile tests. It is also assumed that the direction of the axis $x = x_1$ coincides with the fiber alignment orientation in the first sublayer.

As a preliminary problem, it is worthy to study how the variation of elastic moduli affects the dispersion curves. For this purpose, the sensitivity of group velocities of the fundamental symmetric and antisymmetric S_0 and A_0 modes to the variation of individual elastic moduli in unidirectional $[0^\circ]$ and cross-ply $[0^\circ, 90^\circ]_s$ symmetric laminates fabricated from identical prepregs with the properties specified

in [9] has been considered for the directions coinciding with the material symmetry principal axes. Below, the uni-directional and cross-ply specimens are referred to as UD and CP plates, respectively.

In both cases, the A_0 mode group velocity is sensitive to four of five elastic constants though in different frequency ranges. At low frequencies, it is mainly affected by Young's moduli E_x and E_y , while at middle and higher ones—by shear moduli G_{yz} and G_{xy} . For the plates considered, it might be quite possible to use the A_0 mode alone for the moduli estimation. The symmetrical mode S_0 is sensitive only to E_x and E_y parameters. In the UD plate, impact of their variation on S_0 group velocity is sufficiently stronger than for the anti-symmetric mode and almost does not depend on frequency. Therefore, the S_0 dispersion curves can be used for the refinement of these Young's moduli. However, in the case of a CP laminate, the sensitivity of S_0 mode to E_y values is even smaller than that for the A_0 mode, which is also rather moderate. Therefore, its reliable reconstruction in cross-ply laminates may be complicated. In the frequency range considered, Poisson's ratio ν_{xy} has almost no effect on either A_0 or S_0 mode. Thus, its value cannot be trustworthy estimated.

Based on the obtained results the proposed algorithm for UD and CP laminates consists of the following steps:

- (i) Guided waves are generated by the adhesively bonded PWAS excited with the windowed tone-bursts of varying central frequencies; a non-contact device (e.g., laser vibrometer) is used to measure propagating wave fields at the points located along the laminate principal axes.
- (ii) Measured signals are processed with a continuous wavelet transform; then, the time of flight (ToF) of the wave package at each local frequency is extracted by using the corresponding magnitude peaks of the wavelet coefficients [10]. The corresponding GW group velocities are approximated by the ratio of distances between the measurement points to the ToFs between these points.
- (iii) As soon as the experimental group velocity dispersion curves are obtained for the principal axes directions, the elastic modulus reconstruction procedure is reduced to a minimization problem for the ravine objective function

$$E(C) = \sum_{j=1}^N (1 - c_{g,j}^c / c_{g,j}^m)^2, \quad (31.4)$$

where C is the candidate matrix of material constants (a varied input of the optimization problem), $c_{g,j}^c$ and $c_{g,j}^m$ are the computed and measured group velocities for the propagation directions considered, N is the total amount of measured velocities.

- (iv) The objective function (31.4) is minimized using a real coded microgenetic algorithm with a simulated binary crossover [11]. Every individual chromosome represents a candidate solution (matrix C), while its genes are specific elastic moduli.

Table 31.1 Effective elastic properties of the transversely isotropic prepreg evaluated with the proposed approach (all the values, except ν_{xy} , are given in GPa)

Plate type	E_x	E_y	G_{yz}	G_{xy}	ν_{xy}
Unidirectional laminate/ A_0 and S_0 group velocities	116.2	8.52	2.85	3.69	0.28
Cross-ply laminate/ A_0 and S_0 group velocities	111.7	7.14	2.47	3.89	0.20
Unidirectional laminate/tensile test	114.1	7.69	–	3.38	0.34

After extensive numerical testing of this approach, it has been adopted for experimental carbon fiber-reinforced plastic composite samples with unidirectional $[0^\circ]_4$ and cross-ply $[0^\circ, 90^\circ]_s$ lay-ups. The specimens' dimensions are $1000 \times 1000 \times 1.13 \text{ mm}^3$, and the prepreg's density is 1482 kg/m^3 ; the fiber volume fraction is about 52 %. Out-of-plane surface velocities of PWAS generated GWs are acquired with the 1D scanning laser Doppler vibrometer Polytec PSV-400. The results obtained for both unidirectional and cross-ply laminates after the averaging over eight genetic algorithm runs are summarized in Table 31.1. To verify the obtained results, standard tensile tests have been performed on the coupons cut from the unidirectional sample (last row). These values are in good agreement with the restored effective elastic moduli specified in the first two rows.

31.4 Frequency Response Simulation

The active elements of SHM systems are often made of flexible and thin vertically-polarized piezoelectric patches that are bonded to the inspected structure. Therefore, the longitudinal patch deformation caused by a driving electric field E due to piezoelectric effect results in a predominant shear contact stresses at the patch-structure interface. The corresponding traction $\mathbf{q}(\mathbf{x}, \omega)$ applied to the sub-structure generates traveling elastic waves described by the GW expansion in (31.2). In general, vector-function $\mathbf{q}(\mathbf{x}, \omega)$ is unknown and has to be obtained from a coupled contact problem accounting for both patch and plate deformation under the bonding condition in the contact area Ω .

In widely used simplified uncoupled models, the PWAS action is approximated by tangential point forces uniformly distributed along the patch edges [1]. It yields reasonably good results at low frequencies. However, they become worse with increasing frequency, especially when higher Lamb modes appear in addition to the fundamental symmetric and antisymmetric modes S_0 and A_0 . To improve the results, the contact problem arising in the coupled model, which accounts for the PWAS dynamics relying on the classical plate theory, is brought to the Wiener-Hopf type integral equation and solved via reducing it to a stably truncated

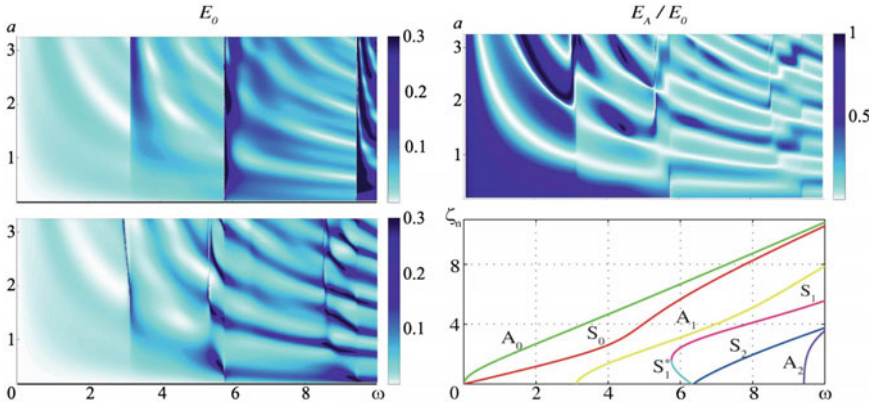


Fig. 31.2 Simulated within coupled (*top*) and uncoupled (*bottom-left*) models source energy E_0 and the part of A_0 energy E_A/E_0 as functions of ω and a ; substructure’s dispersion properties (*bottom-right*)

infinite algebraic system [12]. As an example, for the plane-strain case (a rectangular patch of semi-width a exciting GWs in an elastic aluminum strip), Fig. 31.2 depicts the time-averaged energy E_0 supplied by PWAS. Moreover, it is shown the part of the A_0 mode energy E_A in the total source power E_0 obtained as functions of frequency $\omega = 2\pi f/H/\nu_s$ and semi-width a within the coupled and uncoupled models (where f (Hz) is the dimensional frequency, $H = 1$ mm is the plate thickness and $\nu_s = 3,122$ m/s stands for the velocity unit). The plots confirm that in the low-frequency range simplified pin-force model adequately predict GW energy characteristics.

With the reconstructed elastic moduli, it becomes possible to predict the influence of material anisotropy on PWAS generated GW directivity in the investigated composite plates. The plots of the normalized out-of-plane velocity magnitude $|v_z| = \omega|u_z|$ versus frequency measured and computed at the points C_1-C_4 on the upper surface of the unidirectional plate are shown in Fig. 31.3. These points are located 30 mm away from the origin; $\varphi = 0, \pi/6, \pi/3$ and $\pi/2$ for C_1-C_4 , respectively. Left subplots correspond to the circular PWAS excitation (actuator radius $a = 8$ mm) while the right ones are for the square piezoactuator (square side $a = 10$ mm). The theoretical results depicted by the dashed lines are obtained using (31.2) with the simplified pin-force model for the PWAS- induce load function $\mathbf{q}(\mathbf{x}, \omega)$. The curves exhibit typical for dimensional sources alternations of minima and maxima, which are adequately predicted by the developed mathematical model. In contrast to the isotropic case [13], the local minima and maxima of the curves do not occur simultaneously due to the difference in wavelengths along various propagation directions.

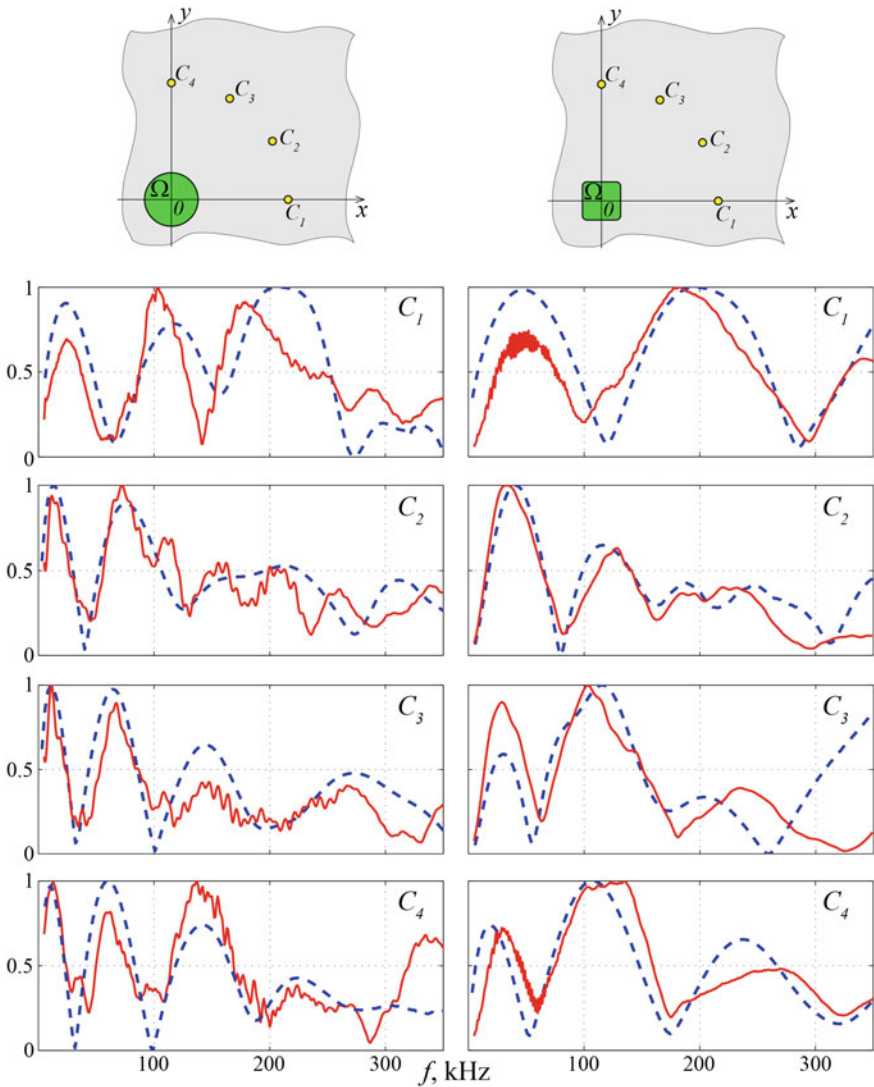


Fig. 31.3 Frequency spectrum of the out-of-plane velocity amplitudes at the points A and B (experimental measurements)

31.5 Conclusions

A method of non-destructive evaluation of effective elastic moduli of fiber-reinforced laminate composite plates based on experimentally obtained group velocity dispersion curves of the fundamental antisymmetric and symmetric Lamb modes has been developed. Its efficiency has been confirmed by conventional

tensile test results. The strong frequency dependence of GW directivity in anisotropic layered composites, actuated by a sized source, has been theoretically predicted and experimentally validated. It should be taken into account for a proper frequency tuning of Lamb wave based SHM and defect detection and localization in composite plates.

Acknowledgments This work is partly funded by the Russian Foundation for Basic Research (project No. 13-01-96516) and the Ministry of Education and Science of the Russian Federation (agreements No. 1.189.2014 K). The authors highly acknowledge the support of T. Fedorkova and S. Föll (Helmut Schmidt University, Hamburg) in laser vibrometry experiments.

References

1. V. Giurgiutiu, *Structural Health Monitoring with Piezoelectric Wafer Active Sensors*, 2nd edn. (Elsevier Academic Press, New York, 2014)
2. P. Kijanka, R. Radecki, P. Packo, W.J. Staszewski, T. Uhl, *Smart Mater. Struct.* **22**, 035014 (2013)
3. W. Ostachowicz, P. Kudela, M. Krawczuk, A. Zak, *Guided Waves in Structures for SHM: The Time-Domain Spectral Element Method* (Wiley, Chichester, 2012)
4. A.K Mal, S.-S Lih, *Trans ASME*, **59** (1992)
5. A. Velichko, P.D Wilcox, *J. Acoust. Soc. Am.* **121**(1) (2007)
6. E. Glushkov, N. Glushkova, A. Eremin, *J. Acoust. Soc. Am.* **129**(5) (2011)
7. E. Glushkov, N. Glushkova, A. Eremin, R. Lammering, *J. Acoust. Soc. Am.* **135**(1) (2014)
8. A.A. Eremin, E.V. Glushkov, N.V. Glushkova, R. Lammering, *Compos. Struct.* **125** (2015)
9. L. Wang, F.G. Yuan, *Compos. Sci. Technol.* **67** (2007)
10. K. Kishimoto, H. Inoue, M. Hamada, T. Shibuya, *J Appl Mech*, **62**(4) (1995)
11. K. Deb, R.B. Agrawal, *Complex Syst.* **9**(2) (1995)
12. E. Glushkov, N. Glushkova, O. Kvasha, W. Seemann, *Smart Mater. Struct.* **16** (2007)
13. E. Glushkov, N. Glushkova, R. Lammering, A. Eremin, M.-N. Neumann, *Smart Mater. Struct.* **20**, 015020 (2011)

Chapter 32

Low Frequency Penetration of Elastic Waves Through a Triple Periodic Array of Cracks

Mezhlum A. Sumbatyan and Michael Yu. Remizov

Abstract The chapter is devoted to the calculation of the reflection and transmission coefficients, when a plane wave is incident on a three-dimensional grating with a periodic array of rectangular cracks in the elastic material. In the one-mode frequency range the problem is reduced to a system of dual integral equations, which can be solved for various sizes of the cracks to give an explicit representation for the wave field inside the cracked structure.

32.1 Introduction

The investigation of elastic waves penetration through periodic gratings is an important problem in the fields of ultrasonic quantitative evaluation of materials, sound propagation and electromagnetic waveguides with diaphragms. Various numerical methods have been applied in two-dimensional problems for periodic arbitrary shaped apertures [1–3]. Despite high computer accuracy of the results, there are only few analytical theories. In practice, analytical results can be obtained under assumption of low frequency, with a weak interaction regime, where some approximated results can be established in an analytical form. Thus, the analytical methods, providing explicit formulae for the relevant scattering parameters, give as a rule only a certain low-frequency limit. For the normal incidence case, Lamb [4] obtained analytical formulae for the reflection and transmission coefficients in the low-frequency limit. Miles [5] studied the case of inclined plates in the one-mode

M.A. Sumbatyan (✉)

Vorovich Institute of Mathematics, Mechanics and Computer Science,
Southern Federal University, 8a Milchakova Street, Rostov-on-Don 344090, Russia
e-mail: sumbat@math.rsu.ru

M.Yu. Remizov

Rostov State University of Civil Engineering, 162, Socialisticheskaya Street,
Rostov-on-Don 344000, Russia
e-mail: remizov72@mail.ru

approximation for small screens. Achenbach and Li [3] have developed an exact method suitable for arbitrary incidence and frequency, utilizing a periodic Green's function which reduced the problem to a singular integral equation, whose solution was constructed by expanding the unknown function in Chebyshev polynomials. The coefficients of the expansion are taken from a linear set of algebraic equations after using a Galerkin-type approach. The papers of Scarpetta, Sumbatyan and Tibullo [6–9] provided explicit analytical formulae for reflection and transmission coefficients in the one-mode case for acoustic waves penetrating through a doubly and triple-periodic arrays of arbitrary shapes of apertures and volumetric obstacles, in two-dimensional wave propagation problems through a periodic array of screens in elastic solids. The influence of the viscosity on the reflection and transmission of an acoustic wave by a periodic array of screens both for 2-D and 3-D problems have been considered in [10, 11].

In the present chapter, we continue to study a triple periodic structure, consisting of a cascading system of screens in the 3-D case. In the same way as in [3–9], we follow two assumptions:

- (i) Only one-mode propagation (with normal incidence) is considered, $ak_1 < \pi$, ($a > c$); $ck_1 < \pi$, ($c > a$), where k_1 is the wave number of the longitudinal incident wave e^{ik_1x} .
- (ii) The vertical screen planes are sufficiently distant from each other so that ratios D/a , $a > c$ and D/c , $a < c$ are large enough.

According to these assumptions, a plane incident acoustic wave is reflected and transmitted by each vertical array $x = (m - 1)D$, $m = 1, \dots, N$. The inhomogeneous standing waves decay with distance from plane to plane. In the present work the propagation through the described structure with the two assumptions (1) and (2) above for arbitrary number N (>2) of screens is studied.

The aim of the present work is to extend some explicit analytical expressions for the reflection and transmission coefficients and for the wave inside the structure, in the case of the three-dimensional propagation problem in elastic media.

32.2 Mathematical Formulation of the Problem

Let us consider a medium, which consists of N identical infinite planes, located at $x = 0, D, \dots, (N - 1)D$, each of them containing a two-dimensional infinite periodic array of co-planar cracks, with the periods along axes y and z . The period of the grating along y -axis is $2a$, and along z -axis is $2c$. The distance between the plane screens is D , (see Fig. 32.1). If we study the incidence of a plane wave upon the grating along the positive direction of x -axis, then the problem is obviously equivalent (due to a symmetry) to a single waveguide of width $2a$ along y -axis and $2c$ along z -axis. Hence, if the plane screens are located at $x = (m - 1)D$, $m = 1, \dots, N$ and the incident wave of a unit amplitude is assumed to propagate normally to the planes

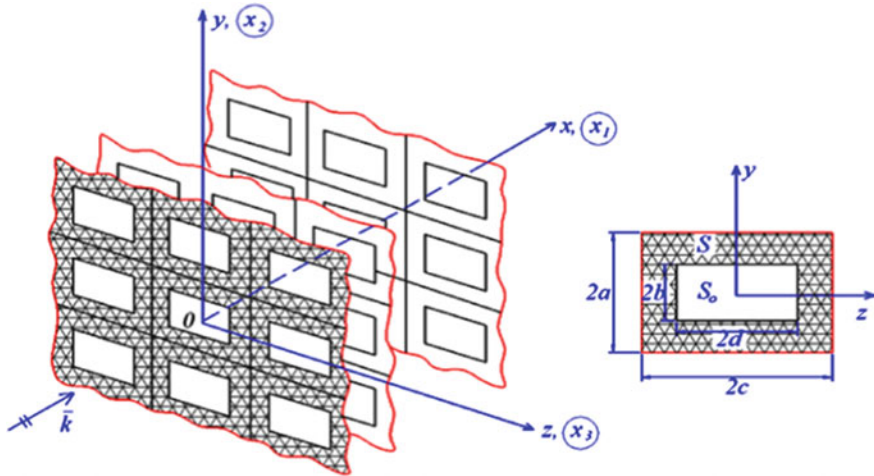


Fig. 32.1 Propagation of incident wave through a triple periodic array of cracks

along x -axis, then the Lamb potentials in the various regions, satisfying the Helmholtz equation, are:

$$\begin{aligned}
 \varphi^{left} &= e^{ik_1x} + Re^{-ik_1x} + \sum_{n+j>1}^{\infty} A_{nj}e^{q_{nj}x} \cos\left(\frac{\pi ny}{a}\right) \cos\left(\frac{\pi jz}{c}\right); \\
 \psi_1^{left} &= \sum_{n+j>1}^{\infty} B_{nj}^1 e^{r_{nj}x} \sin\left(\frac{\pi ny}{a}\right) \sin\left(\frac{\pi jz}{c}\right); \\
 \psi_2^{left} &= \sum_{n+j>1}^{\infty} B_{nj}^2 e^{r_{nj}x} \cos\left(\frac{\pi ny}{a}\right) \sin\left(\frac{\pi jz}{c}\right); \\
 \psi_3^{left} &= \sum_{n+j>1}^{\infty} B_{nj}^3 e^{r_{nj}x} \sin\left(\frac{\pi ny}{a}\right) \cos\left(\frac{\pi jz}{c}\right), \quad x < 0
 \end{aligned} \tag{32.1a}$$

$$\begin{aligned}
 \varphi_s &= F_0^s \cos k_1[x - (s-1)D] + H_0^s \cos k_1(x - sD) \\
 &+ \sum_{n+j>1}^{\infty} \left(F_{nj}^s \operatorname{ch}[q_{nj}(x - (s-1)D)] + H_{nj}^s \operatorname{ch}[q_{nj}(x - sD)] \right) \cos\left(\frac{\pi ny}{a}\right) \cos\left(\frac{\pi jz}{c}\right), \\
 \psi_1^s &= \sum_{n+j>1}^{\infty} \left(G_{nj}^s \operatorname{ch}[r_{nj}(x - (s-1)D)] + P_{nj}^s \operatorname{ch}[q_{nj}(x - sD)] \right) \sin\left(\frac{\pi ny}{a}\right) \sin\left(\frac{\pi jz}{c}\right); \\
 \psi_2^s &= \sum_{n+j>1}^{\infty} \left(V_{nj}^s \operatorname{sh}[r_{nj}(x - (s-1)D)] + Q_{nj}^s \operatorname{sh}[q_{nj}(x - sD)] \right) \cos\left(\frac{\pi ny}{a}\right) \sin\left(\frac{\pi jz}{c}\right); \\
 \psi_3^s &= \sum_{n+j>1}^{\infty} \left(W_{nj}^s \operatorname{sh}[r_{nj}(x - (s-1)D)] + Y_{nj}^s \operatorname{sh}[q_{nj}(x - sD)] \right) \sin\left(\frac{\pi ny}{a}\right) \cos\left(\frac{\pi jz}{c}\right), \\
 (s-1)D &< x < sD, \quad s = 2, \dots, N-1
 \end{aligned} \tag{32.1b}$$

$$\begin{aligned}
\varphi^{right} &= T e^{ik_1(x-(s-1)D)} + \sum_{n+j>1}^{\infty} C_{nj} e^{-q_{nj}(x-(s-1)D)} \cos\left(\frac{\pi n y}{a}\right) \cos\left(\frac{\pi j z}{c}\right); \\
\psi_1^{right} &= \sum_{n+j>1}^{\infty} D_{nj}^1 e^{-r_{nj}(x-(s-1)D)} \sin\left(\frac{\pi n y}{a}\right) \sin\left(\frac{\pi j z}{c}\right); \\
\psi_2^{right} &= \sum_{n+j>1}^{\infty} D_{nj}^2 e^{-r_{nj}(x-(s-1)D)} \cos\left(\frac{\pi n y}{a}\right) \sin\left(\frac{\pi j z}{c}\right); \\
\psi_3^{right} &= \sum_{n+j>1}^{\infty} D_{nj}^3 e^{-r_{nj}(x-(s-1)D)} \sin\left(\frac{\pi n y}{a}\right) \cos\left(\frac{\pi j z}{c}\right), \quad x > (N-1)D
\end{aligned} \tag{32.1c}$$

All capital letters are some unknown constants and

$$q_{nj} = \left[(\pi n/a)^2 + (\pi j/c)^2 - k_1^2 \right]^{1/2}, \quad r_{nj} = \left[(\pi n/a)^2 + (\pi j/c)^2 - k_2^2 \right]^{1/2}.$$

The time-harmonic dependence is taken as $e^{-i\omega t}$, k_1, k_2 are the longitudinal and transverse wave numbers, R and T are the reflection and transmission coefficients, respectively. Let the consideration be restricted to the one-mode case: $0 < k_1 a < \pi$; $0 < k_1 c < \pi$, then $q_{nj} > 0$, $r_{nj} > 0$ for all $n, j = 1, 2, \dots$. Moreover, we assume that the cracks arrays are sufficiently distant from each other, this involves $D/a \ll 1$, $D/c \ll 1$. The components of the stress tensor can be expressed in terms of the Lamb wave potentials, three of them are represented in the following forms:

$$\sigma_{xx}/\mu = k_1^2 \varphi \left(2 - \frac{c_1^2}{c_2^2} \right) + 2 \left(\frac{\partial^2 \varphi}{\partial x^2} + \frac{\partial^2 \psi_3}{\partial y \partial x} - \frac{\partial^2 \psi_2}{\partial z \partial x} \right); \tag{32.2a}$$

$$\sigma_{xy}/\mu = k_2^2 \psi_3 + 2 \left(\frac{\partial^2 \varphi}{\partial x \partial y} + \frac{\partial^2 \psi_3}{\partial y^2} - \frac{\partial^2 \psi_2}{\partial z \partial y} \right); \tag{32.2b}$$

$$\sigma_{xz}/\mu = -k_2^2 \psi_2 + 2 \left(\frac{\partial^2 \varphi}{\partial x \partial z} - \frac{\partial^2 \psi_2}{\partial y^2} + \frac{\partial^2 \psi_3}{\partial z \partial y} \right). \tag{32.2c}$$

The displacement field u_x, u_y, u_z is given by a representation of the Green-Lamb type, as follows:

$$\begin{aligned}
u_x &= \frac{\partial \varphi}{\partial x} + \frac{\partial \psi_3}{\partial y} - \frac{\partial \psi_2}{\partial z}; & u_y &= \frac{\partial \varphi}{\partial y} + \frac{\partial \psi_1}{\partial z} - \frac{\partial \psi_3}{\partial x}; \\
u_z &= \frac{\partial \varphi}{\partial z} + \frac{\partial \psi_2}{\partial x} - \frac{\partial \psi_1}{\partial y}
\end{aligned} \tag{32.3a}$$

The potentials $\psi^{(s)}(y, z)$, $s = 1, \dots, N$ should be considered with the additional condition for each region:

$$\operatorname{div} \psi^{(s)}(y, z) = 0, \quad s = 1, \dots, N. \quad (32.3b)$$

In the considered structure, a longitudinal plane wave of the form: $\varphi_0 = e^{ik_1x}$, $\psi = 0$ is entering from $-\infty$, rising to the scattered fields in the left ($x < 0$), central ($(s-1)D < x < sD$, $s = 2, \dots, N-1$) and right ($x > (N-1)D$) regions. Accepting the continuity of the displacement field u_x, u_y, u_z outside crack's domains, at each vertical plane with $\forall s$, we introduce the following $3N$ new unknown functions $g_x^{(s)}(y, z)$, $g_y^{(s)}(y, z)$, $g_z^{(s)}(y, z)$, $s = 1, \dots, N$ by

$$u_x^{(l)} - u_x^{(1)} = \begin{cases} g_x^{(1)}(y, z); & (y, z) \in \text{crack}, \\ 0; & (y, z) \notin \text{crack}, \end{cases} \quad (32.4a)$$

$$u_y^{(l)} - u_y^{(1)} = \begin{cases} g_y^{(1)}(y, z); & (y, z) \in \text{crack}, \\ 0; & (y, z) \notin \text{crack}, \end{cases} \quad (32.4b)$$

$$u_z^{(l)} - u_z^{(1)} = \begin{cases} g_z^{(1)}(y, z); & (y, z) \in \text{crack}, \\ 0; & (y, z) \notin \text{crack}, \end{cases} \quad (32.4c)$$

$$x = 0,$$

$$u_x^{(s-1)} - u_x^{(s)} = \begin{cases} g_x^{(s)}(y, z); & (y, z) \in \text{crack}, \\ 0; & (y, z) \notin \text{crack}, \end{cases} \quad (32.5a)$$

$$u_y^{(s-1)} - u_y^{(s)} = \begin{cases} g_y^{(s)}(y, z); & (y, z) \in \text{crack}, \\ 0; & (y, z) \notin \text{crack}, \end{cases} \quad (32.5b)$$

$$u_z^{(s-1)} - u_z^{(s)} = \begin{cases} g_z^{(s)}(y, z); & (y, z) \in \text{crack}, \\ 0; & (y, z) \notin \text{crack}, \end{cases} \quad (32.5c)$$

$$x = (s-1)D,$$

$$u_x^{(N-1)} - u_x^{(r)} = \begin{cases} g_x^{(N)}(y, z); & (y, z) \in \text{crack}, \\ 0; & (y, z) \notin \text{crack}, \end{cases} \quad (32.6a)$$

$$u_y^{(N-1)} - u_y^{(r)} = \begin{cases} g_y^{(N)}(y, z); & (y, z) \in \text{crack}, \\ 0; & (y, z) \notin \text{crack}, \end{cases} \quad (32.6b)$$

$$u_z^{(N-1)} - u_z^{(r)} = \begin{cases} g_z^{(N)}(y, z); & (y, z) \in \text{crack}, \\ 0; & (y, z) \notin \text{crack}, \end{cases} \quad (32.6c)$$

$$x = (N - 1)D.$$

These new introduced functions are to be even in view of geometrical symmetry.

Now we use (32.1a, b, c), (32.3a, b) in order to obtain expressions for all constants appearing in potentials (32.1a, b, c) in terms of $g_x^{(s)}(y, z)$, $g_y^{(s)}(y, z)$, $g_z^{(s)}(y, z)$, $s = 1, \dots, N$. By integration of (32.4a, b, c), (32.5a, b, c), (32.6a, b, c) over $(y, z) : |y| < a, |z| < c$, we obtain

$$ik_1(1 - R) - H_0^{(1)}k_1 \sin(k_1D) = \frac{1}{4ac} \iint_S g_x^{(1)}(\eta, \zeta) d\eta d\zeta; \quad (32.7a)$$

$$-F_0^{(s-1)}k_1 \sin(k_1D) - H_0^{(s)}k_1 \sin(k_1D) = \frac{1}{4ac} \iint_S g_x^{(s)}(\eta, \zeta) d\eta d\zeta; \quad (32.7b)$$

$$-F_0^{(N-1)}k_1 \sin(k_1D) - ik_1T = \frac{1}{4ac} \iint_S g_x^{(N)}(\eta, \zeta) d\eta d\zeta, \quad (32.7c)$$

where $S = \{(y, z) : |y| < b, |z| < d\}$. The orthogonality of the trigonometric functions reduces (32.4a, b, c), (32.5a, b, c), (32.6a, b, c) to the following relations:

$$\begin{aligned} & \left[A_{nj}/sh(q_{nj}D) + H_{nj}^{(1)} \right] \alpha q_{nj} + \left[B_{nj}^{(3)}/sh(r_{nj}D) + Y_{nj}^{(1)} \right] \frac{\pi n}{a} \\ & - \left[B_{nj}^{(2)}/sh(r_{nj}D) + Q_{nj}^{(1)} \right] \frac{\pi j}{c} \\ & = \frac{4}{ac sh(r_{nj}D)} \iint_S g_x^{(1)}(\eta, \zeta) \cos\left(\frac{\pi n \eta}{a}\right) \cos\left(\frac{\pi j \zeta}{c}\right) d\eta d\zeta; \end{aligned} \quad (32.8a)$$

$$\begin{aligned} & - \left[A_{nj}/ch(q_{nj}D) - H_{nj}^{(1)} \right] \beta \frac{\pi n}{a} + \left[B_{nj}^{(1)}/ch(r_{nj}D) - P_{nj}^{(1)} \right] \frac{\pi j}{c} \\ & - \left[B_{nj}^{(3)}/ch(r_{nj}D) - Y_{nj}^{(1)} \right] r_{nj} \\ & = \frac{4}{ac ch(r_{nj}D)} \iint_S g_y^{(1)}(\eta, \zeta) \cos\left(\frac{\pi n \eta}{a}\right) \cos\left(\frac{\pi j \zeta}{c}\right) d\eta d\zeta; \end{aligned} \quad (32.8b)$$

$$\begin{aligned} & - \left[A_{nj}/ch(q_{nj}D) - H_{nj}^{(1)} \right] \beta \frac{\pi j}{c} + \left[B_{nj}^{(2)}/ch(r_{nj}D) - Q_{nj}^{(1)} \right] r_{nj} \\ & - \left[B_{nj}^{(1)}/ch(r_{nj}D) - P_{nj}^{(1)} \right] \frac{\pi n}{a} \\ & = \frac{4}{ac ch(r_{nj}D)} \iint_S g_z^{(1)}(\eta, \zeta) \cos\left(\frac{\pi n \eta}{a}\right) \cos\left(\frac{\pi j \zeta}{c}\right) d\eta d\zeta; \end{aligned} \quad (32.8c)$$

$$\begin{aligned} & \left[F_{nj}^{(s-1)} + H_{nj}^{(s)} \right] \alpha q_{nj} + \left[W_{nj}^{(s-1)} + Y_{nj}^{(s)} \right] \frac{\pi n}{a} - \left[V_{nj}^{(s-1)} + Q_{nj}^{(s)} \right] \frac{\pi j}{c} \\ & = \frac{4}{ac \operatorname{sh}(r_{nj}D)} \iint_S g_x^{(s)}(\eta, \zeta) \cos\left(\frac{\pi n \eta}{a}\right) \cos\left(\frac{\pi j \zeta}{c}\right) d\eta d\zeta; \end{aligned} \quad (32.9a)$$

$$\begin{aligned} & \left[-F_{nj}^{(s-1)} + H_{nj}^{(s)} \right] \beta \frac{\pi n}{a} + \left[G_{nj}^{(s-1)} - P_{nj}^{(s)} \right] \frac{\pi j}{c} + \left[-W_{nj}^{(s-1)} + Y_{nj}^{(s)} \right] r_{nj} \\ & = \frac{4}{ac \operatorname{ch}(r_{nj}D)} \iint_S g_y^{(s)}(\eta, \zeta) \cos\left(\frac{\pi n \eta}{a}\right) \cos\left(\frac{\pi j \zeta}{c}\right) d\eta d\zeta; \end{aligned} \quad (32.9b)$$

$$\begin{aligned} & \left[-F_{nj}^{(s-1)} + H_{nj}^{(s)} \right] \beta \frac{\pi j}{c} + \left[V_{nj}^{(s-1)} - Q_{nj}^{(s)} \right] r_{nj}D + \left[-G_{nj}^{(s-1)} + P_{nj}^{(s)} \right] \frac{\pi n}{a} \\ & = \frac{4}{ac \operatorname{ch}(r_{nj}D)} \iint_S g_z^{(s)}(\eta, \zeta) \cos\left(\frac{\pi n \eta}{a}\right) \cos\left(\frac{\pi j \zeta}{c}\right) d\eta d\zeta; \end{aligned} \quad (32.9c)$$

$$\begin{aligned} & \left[C_{nj}/\operatorname{sh}(q_{nj}D) + F_{nj}^{(N-1)} \right] \alpha q_{nj} + \left[-D_{nj}^{(3)}/\operatorname{sh}(r_{nj}D) + W_{nj}^{(N-1)} \right] \frac{\pi n}{a} \\ & + \left[D_{nj}^{(2)}/\operatorname{sh}(r_{nj}D) - V_{nj}^{(N-1)} \right] \frac{\pi j}{c} \\ & = \frac{4}{ac \operatorname{sh}(r_{nj}D)} \iint_S g_x^{(N-1)}(\eta, \zeta) \cos\left(\frac{\pi n \eta}{a}\right) \cos\left(\frac{\pi j \zeta}{c}\right) d\eta d\zeta; \end{aligned} \quad (32.10a)$$

$$\begin{aligned} & \left[C_{nj}/\operatorname{ch}(q_{nj}D) - F_{nj}^{(N-1)} \right] \beta \frac{\pi n}{a} + \left[-D_{nj}^{(1)}/\operatorname{ch}(r_{nj}D) + G_{nj}^{(N-1)} \right] \frac{\pi j}{c} \\ & - \left[D_{nj}^{(2)}/\operatorname{ch}(r_{nj}D) + W_{nj}^{(N-1)} \right] r_{nj} \\ & = \frac{4}{ac \operatorname{ch}(r_{nj}D)} \iint_S g_y^{(N-1)}(\eta, \zeta) \cos\left(\frac{\pi n \eta}{a}\right) \cos\left(\frac{\pi j \zeta}{c}\right) d\eta d\zeta; \end{aligned} \quad (32.10b)$$

$$\begin{aligned} & \left[C_{nj}/\operatorname{ch}(q_{nj}D) - F_{nj}^{(N-1)} \right] \beta \frac{\pi j}{c} + \left[D_{nj}^{(2)}/\operatorname{ch}(r_{nj}D) + V_{nj}^{(N-1)} \right] r_{nj} \\ & + \left[D_{nj}^{(1)}/\operatorname{ch}(r_{nj}D) - G_{nj}^{(N-1)} \right] \frac{\pi n}{a} \\ & = \frac{4}{ac \operatorname{ch}(r_{nj}D)} \iint_S g_z^{(N-1)}(\eta, \zeta) \cos\left(\frac{\pi n \eta}{a}\right) \cos\left(\frac{\pi j \zeta}{c}\right) d\eta d\zeta, \end{aligned} \quad (32.10c)$$

where

$$\alpha = \operatorname{sh}(q_{nj}D)/\operatorname{sh}(r_{nj}D), \quad \beta = \operatorname{ch}(q_{nj}D)/\operatorname{ch}(q_{nj}D).$$

The continuity assumption for the stress fields through the openings inside every plane screen

$$\sigma_{xx}^{(l)} = \sigma_{xx}^{(1)}; \quad \sigma_{xy}^{(l)} = \sigma_{xy}^{(1)}; \quad \sigma_{xz}^{(l)} = \sigma_{xz}^{(1)}, \quad x = 0; \quad (32.11a)$$

$$\sigma_{xx}^{(s-1)} = \sigma_{xx}^{(s)}; \quad \sigma_{xy}^{(s-1)} = \sigma_{xy}^{(s)}; \quad \sigma_{xz}^{(s-1)} = \sigma_{xz}^{(s)}, \quad x = (s-1)D; \quad (32.11b)$$

$$\sigma_{xx}^{(N-1)} = \sigma_{xx}^{(r)}; \quad \sigma_{xy}^{(N-1)} = \sigma_{xy}^{(r)}; \quad \sigma_{xz}^{(N-1)} = \sigma_{xz}^{(r)}, \quad x = (N-1)D. \quad (32.11c)$$

$\forall(y, z)$, implies the following equalities with the main assumptions (i), (ii) of Sect. 32.1 (here, to be more specific, we give the transformations for the central area, with $x = (s-1)D$, $s = 1, \dots, N$):

$$\begin{aligned} & -k_1^2(c_1^2/c_2^2) \left[F_0^{(s-1)} \cos(k_1D) + H_0^{(s-1)} \right] \\ & + \sum_{n+j>1}^{\infty} \left\{ k_1^2(2 - c_1^2/c_2^2) F_{nj}^{(s-1)} ch(q_{nj}D). \right. \\ & \quad + 2 \left[F_{nj}^{(s-1)} q_{nj}^2 ch(q_{nj}D) + W_{nj}^{(s-1)} r_{nj} \frac{\pi n}{a} ch(r_{nj}D). \right. \\ & \quad \left. \left. - V_{nj}^{(s-1)} r_{nj} \frac{\pi j}{c} ch(r_{nj}D) \right] \right\} \cos\left(\frac{\pi n y}{a}\right) \cos\left(\frac{\pi j z}{c}\right) \\ & = -k_1^2(c_1^2/c_2^2) \left[H_0^{(s)} \cos(k_1D) + F_0^{(s)} \right] \end{aligned} \quad (32.12a)$$

$$\begin{aligned} & + \sum_{n+j>1}^{\infty} \left\{ k_1^2(2 - c_1^2/c_2^2) H_{nj}^{(s)} ch(q_{nj}D). \right. \\ & \quad + 2 \left[H_{nj}^{(s-1)} q_{nj}^2 ch(q_{nj}D) + W_{nj}^{(s)} r_{nj} \frac{\pi n}{a} ch(r_{nj}D). \right. \\ & \quad \left. \left. - Q_{nj}^{(s)} r_{nj} \frac{\pi j}{c} ch(r_{nj}D) \right] \right\} \cos\left(\frac{\pi n y}{a}\right) \cos\left(\frac{\pi j z}{c}\right); \\ & \sum_{n+j>1}^{\infty} \left\{ -a_n F_{nj}^{(s-1)} q_{nj} \alpha + W_{nj}^{(s-1)} (-a_n^2) + \frac{k_2^2}{2} W_{nj}^{(s-1)} + V_{nj}^{(s-1)} a_n c_j \right\} \\ & \quad \sin\left(\frac{\pi n y}{a}\right) \cos\left(\frac{\pi j z}{c}\right); \\ & = \sum_{n+j>1}^{\infty} \left\{ a_n H_{nj}^{(s)} q_{nj} \alpha + Y_{nj}^{(s)} a_n^2 - \frac{k_2^2}{2} Y_{nj}^{(s)} - Q_{nj}^{(s)} a_n c_j \right\} \\ & \quad \sin\left(\frac{\pi n y}{a}\right) \cos\left(\frac{\pi j z}{c}\right); \end{aligned} \quad (32.12b)$$

$$\begin{aligned}
& \sum_{n+j>1}^{\infty} \left\{ -c_j F_{nj}^{(s-1)} q_{nj} \alpha + V_{nj}^{(s-1)} (c_j^2) - \frac{k_2^2}{2} V_{nj}^{(s-1)} - W_{nj}^{(s-1)} a_n c_j \right\} \\
& \quad \cos\left(\frac{\pi n y}{a}\right) \sin\left(\frac{\pi j z}{c}\right); \\
& = \sum_{n+j>1}^{\infty} \left\{ c_j H_{nj}^{(s)} q_{nj} \alpha - Q_{nj}^{(s)} c_j^2 + \frac{k_2^2}{2} Q_{nj}^{(s)} + Y_{nj}^{(s)} a_n c_j \right\} \\
& \quad \cos\left(\frac{\pi n y}{a}\right) \sin\left(\frac{\pi j z}{c}\right);
\end{aligned} \tag{32.12c}$$

The orthogonality of the trigonometric functions reduces (32.12a, b, c) to the following equalities:

$$E_2 \frac{k_1^2}{2} (2 - c_1^2/c_2^2 + q_{nj}^2) \beta + E_6 a_n r_{nj} - E_5 c_j r_{nj} = 0; \tag{32.13a}$$

$$E_1 q_{nj} a_n \alpha + E_7 \left(a_n^2 - \frac{k_2^2}{2} \right) - E_4 c_j a_n = 0; \tag{32.13b}$$

$$E_1 q_{nj} c_j \alpha - E_4 \left(c_j^2 - \frac{k_2^2}{2} \right) + E_7 c_j a_n = 0; \tag{32.13c}$$

$$\begin{aligned}
E_1 q_{nj} \alpha + E_7 a_n - E_4 c_j &= \frac{4}{ac \operatorname{sh}(r_{nj} D)} \\
& \iint_S g_x^{(s)}(\eta, \zeta) \cos\left(\frac{\pi n \eta}{a}\right) \cos\left(\frac{\pi j \zeta}{c}\right) d\eta d\zeta;
\end{aligned} \tag{32.14a}$$

$$\begin{aligned}
-E_2 a_n \beta + E_3 c_j - E_6 r_{nj} &= \frac{4}{ac \operatorname{ch}(r_{nj} D)} \\
& \iint_S g_y^{(s)}(\eta, \zeta) \cos\left(\frac{\pi n \eta}{a}\right) \cos\left(\frac{\pi j \zeta}{c}\right) d\eta d\zeta;
\end{aligned} \tag{32.14b}$$

$$\begin{aligned}
-E_2 c_j \beta - E_3 a_n + E_5 r_{nj} &= \frac{4}{ac \operatorname{ch}(r_{nj} D)} \\
& \iint_S g_z^{(s)}(\eta, \zeta) \cos\left(\frac{\pi n \eta}{a}\right) \cos\left(\frac{\pi j \zeta}{c}\right) d\eta d\zeta,
\end{aligned} \tag{32.14c}$$

$$E_5 a_n + E_6 c_j - E_3 r_{nj} = 0, \tag{32.14d}$$

while introducing the variables E_m , $m = 1 - 7$, we put $a_n = \pi n/a$; $c_j = \pi j/c$. Equations (32.14a, b, c, d), (32.9a, b, c), (32.3b) and (32.12a, b, c) now imply:

$$\begin{aligned}
 E_1 &= F_{nj}^{(s-1)} + H_{nj}^{(s)}; & E_2 &= F_{nj}^{(s-1)} - H_{nj}^{(s)}; \\
 E_3 &= G_{nj}^{(s-1)} - P_{nj}^{(s)}; & E_4 &= V_{nj}^{(s-1)} + Q_{nj}^{(s)}; \\
 E_5 &= V_{nj}^{(s-1)} - Q_{nj}^{(s)}; & E_6 &= W_{nj}^{(s-1)} - Y_{nj}^{(s)}; \\
 E_7 &= W_{nj}^{(s-1)} + Y_{nj}^{(s)}.
 \end{aligned}
 \tag{32.15}$$

By analogy, one obtains for $E_m^{(l)}, E_m^{(r)}$, $m = 1 - 7$:

$$\begin{aligned}
 E_1^{(l)} &= A_{nj}/sh(q_{nj}D) + H_{nj}^{(1)}; & E_2^{(l)} &= A_{nj}/ch(q_{nj}D) - H_{nj}^{(1)}; \\
 E_3^{(l)} &= B_{nj}^{(1)}/ch(q_{nj}D) - P_{nj}^{(1)}; & E_4^{(l)} &= B_{nj}^{(2)}/sh(q_{nj}D) + Q_{nj}^{(1)}; \\
 E_5^{(l)} &= B_{nj}^{(2)}/ch(q_{nj}D) - Q_{nj}^{(1)}; & E_6^{(l)} &= B_{nj}^{(3)}/ch(q_{nj}D) - Y_{nj}^{(1)}; \\
 E_7^{(l)} &= B_{nj}^{(3)}/sh(q_{nj}D) + Y_{nj}^{(1)};
 \end{aligned}
 \tag{32.16}$$

$$\begin{aligned}
 E_1^{(r)} &= C_{nj}/sh(q_{nj}D) + F_{nj}^{(N-1)}; & E_2^{(r)} &= -C_{nj}/ch(q_{nj}D) + F_{nj}^{(N-1)}; \\
 E_3^{(r)} &= -D_{nj}^{(1)}/ch(r_{nj}D) + G_{nj}^{(N-1)}; & E_4^{(r)} &= -D_{nj}^{(2)}/sh(r_{nj}D) + V_{nj}^{(N-1)}; \\
 E_5^{(r)} &= D_{nj}^{(2)}/ch(r_{nj}D) + V_{nj}^{(N-1)}; & E_6^{(r)} &= D_{nj}^{(3)}/ch(r_{nj}D) + W_{nj}^{(N-1)}; \\
 E_7^{(r)} &= -D_{nj}^{(3)}/sh(r_{nj}D) + W_{nj}^{(N-1)}.
 \end{aligned}
 \tag{32.17}$$

The linear algebraic sets based on (32.11a), (32.8a, b, c) and (32.11c), (32.10a, b, c) should be obtained from the set (32.13a, b, c), (32.14a, b, c, d) by substitution of unknown variables $E_m \Leftrightarrow E_m^{(l)}$ and $E_m \Leftrightarrow E_m^{(r)}$, $m = 1 - 7$, respectively. The right-hand sides of (32.14a, b, c, d) have been taken with $s = 1$ and $s = N$.

The solution E_m , $m = 1 - 7$ of the main set (32.13a, b, c), (32.14a, b, c, d), corresponding to $x = (s - 1) D$, $s = 2, \dots, N - 1$ has the form:

$$\begin{aligned}
E_1 &= \frac{\left(\frac{k_2^2}{2} - a_n^2 - c_j^2\right)}{q_{nj} \alpha k_2^2} \frac{4}{ac \operatorname{sh}(r_{nj}D)} \iint_S g_x^{(1)}(\eta, \zeta) \cos\left(\frac{\pi n \eta}{a}\right) \cos\left(\frac{\pi j \zeta}{c}\right) d\eta d\zeta; \\
E_2 &= \frac{4}{\Delta_0 ac \operatorname{ch}(r_{nj}D)} \iint_S g_y^{(s)}(\eta, \zeta) \cos\left(\frac{\pi n \eta}{a}\right) \cos\left(\frac{\pi j \zeta}{c}\right) d\eta d\zeta \\
&\quad + \frac{4c_j}{\Delta_0 a_n ac \operatorname{ch}(r_{nj}D)} \iint_S g_z^{(s)}(\eta, \zeta) \cos\left(\frac{\pi n \eta}{a}\right) \cos\left(\frac{\pi j \zeta}{c}\right) d\eta d\zeta; \\
E_3 &= \frac{4c_j}{k_2^2 ac \operatorname{ch}(r_{nj}D)} \iint_S g_y^{(s)}(\eta, \zeta) \cos\left(\frac{\pi n \eta}{a}\right) \cos\left(\frac{\pi j \zeta}{c}\right) d\eta d\zeta \\
&\quad - \frac{4a_n c_j}{k_2^2 ac \operatorname{ch}(r_{nj}D)} \iint_S g_z^{(s)}(\eta, \zeta) \cos\left(\frac{\pi n \eta}{a}\right) \cos\left(\frac{\pi j \zeta}{c}\right) d\eta d\zeta; \\
E_4 &= -\frac{8c_j}{k_2^2 ac \operatorname{sh}(r_{nj}D)} \iint_S g_x^{(s)}(\eta, \zeta) \cos\left(\frac{\pi n \eta}{a}\right) \cos\left(\frac{\pi j \zeta}{c}\right) d\eta d\zeta; \\
E_5 &= \frac{r_{nj}}{a_n} E_3 - \frac{c_j}{a_n} E_6; \\
E_6 &= \frac{-\beta}{a_n \Delta_0} \left[\frac{c_j^2 r_{nj}}{k_2^2} + \frac{\gamma_0}{r_{nj}} - \frac{c_j^2 \gamma_0}{r_{nj} k_2^2} \right] \frac{4}{ac \operatorname{ch}(r_{nj}D)} \iint_S g_y^{(s)}(\eta, \zeta) \cos\left(\frac{\pi n \eta}{a}\right) \cos\left(\frac{\pi j \zeta}{c}\right) d\eta d\zeta \\
&\quad - \frac{\beta c_j}{\Delta_0 k_2^2} \left(r_{nj} - \frac{\gamma_0}{r_{nj}} \right) \frac{4}{ac \operatorname{ch}(r_{nj}D)} \iint_S g_z^{(s)}(\eta, \zeta) \cos\left(\frac{\pi n \eta}{a}\right) \cos\left(\frac{\pi j \zeta}{c}\right) d\eta d\zeta, \\
E_7 &= -\frac{8a_n}{k_2^2 ac \operatorname{sh}(r_{nj}D)} \iint_S g_x^{(s)}(\eta, \zeta) \cos\left(\frac{\pi n \eta}{a}\right) \cos\left(\frac{\pi j \zeta}{c}\right) d\eta d\zeta, \\
\gamma_0 &= \frac{k_1^2}{2} (2 - c_1^2/c_2^2 + a_{nj}^2); \quad \Delta_0 = -\beta \frac{a_n^2 + c_j^2 - \gamma_0}{a_n}.
\end{aligned} \tag{32.18}$$

Now we can obtain all the unknown constants, taken from (32.13a, b, c)–(32.17) and substitute these values to the continuity conditions for the stress components (32.11a, b, c). Here we should take into consideration that in every region there is only one nontrivial function of cracks opening, $g_x^{(s)}(y, z)$; $|y| < b$; $|z| < d$, $s = 1, \dots, N$ involved in the remaining three equations.

$$\sigma_{xx}^{(l)} = \sigma_{xx}^{(1)}; \quad x = 0; \tag{32.19a}$$

$$\sigma_{xx}^{(s-1)} = \sigma_{xx}^{(s)}; \quad x = (s-1)D; \tag{32.19b}$$

$$\sigma_{xx}^{(N-1)} = \sigma_{xx}^{(r)}; \quad x = (N-1)D. \quad (32.19c)$$

Omitting some routine mathematical transformations, one finally obtains the following system of integral equations for the unknown functions $g_x^{(s)}(y, z)$:

$$\begin{aligned} & \iint_{S_0} g_x^{(1)}(\eta, \zeta) \left\{ (8acik_1)^{-1} - \frac{e^{-ik_1D}}{ack_1 \sin(k_1D)} \right. \\ & \quad \left. - \sum_{n+j>0}^{\infty} \frac{R_{nj}}{ack_2^4 q_{nj}} \cos \left[\frac{\pi n(y-\eta)}{a} \right] \cos \left[\frac{\pi j(z-\zeta)}{c} \right] \right\} d\eta d\zeta \\ & - [ack_1 \sin(k_1D)]^{-1} \iint_{S_0} g_x^{(2)}(\eta, \zeta) d\eta d\zeta = 1; \end{aligned} \quad (32.20a)$$

$$\begin{aligned} & \iint_S g_x^{(s)}(\eta, \zeta) \sum_{n+j>0}^{\infty} \frac{R_{nj}}{ack_2^4 q_{nj}} \cos \left[\frac{\pi n(y-\eta)}{a} \right] \cos \left[\frac{\pi j(z-\zeta)}{c} \right] d\eta d\zeta \\ & + [ack_1 \sin(k_1D)]^{-1} \iint_S [g_x^{(s+1)}(\eta, \zeta) + g_x^{(s-1)}(\eta, \zeta)] d\eta d\zeta = 0; \end{aligned} \quad (32.20b)$$

$$\begin{aligned} & \iint_S g_x^{(N)}(\eta, \zeta) \left\{ (8acik_1)^{-1} - \frac{e^{-ik_1D}}{ack_1 \sin(k_1D)} \right. \\ & \quad \left. - \sum_{n+j>0}^{\infty} \frac{R_{nj}}{ack_2^4 q_{nj} sh(q_{nj}D)} \cos \left[\frac{\pi n(y-\eta)}{a} \right] \cos \left[\frac{\pi j(z-\zeta)}{c} \right] \right\} d\eta d\zeta \\ & - [ack_1 \sin(k_1D)]^{-1} \iint_S g_x^{(N-1)}(\eta, \zeta) d\eta d\zeta = 1; \end{aligned} \quad (32.20c)$$

where $S = (y, z) : |y| < b, |z| < d; s = 2, \dots, N-1$ and the function in the numerator of the kernel takes the form of Rayleigh function:

$$R_{nj} = [2(a_n^2 + c_j^2) - k_2^2]^2 - 4r_{nj}q_{nj}(a_n^2 + c_j^2). \quad (32.21)$$

Similarly to [6], let us consider the auxiliary equation:

$$\frac{1}{ack_2^4} \iint_S h(\eta, \zeta) \left\{ \sum_{n+j>0}^{\infty} \frac{R_{nj}}{q_{nj}} \cos \left[\frac{\pi n(y-\eta)}{a} \right] \cos \left[\frac{\pi j(z-\zeta)}{c} \right] \right\} d\eta d\zeta = 1, \quad (32.22)$$

and set

$$H = \iint_S h(\eta, \zeta) d\eta d\zeta. \quad (32.23)$$

In terms of the even function $h(y, z)$, we deduce from system (32.7a, b, c):

$$g_x^{(1)}(y, z) = \left\{ \left[(8acik_1)^{-1} - \frac{e^{-ik_1D}}{ack_1 \sin(k_1D)} \right] J_1 - [8ack_1 \sin(kD)]^{-1} J_2 - 1 \right\} h(y, z); \quad (32.24a)$$

$$g_x^{(s)}(y, z) = \left\{ [ack_1 \sin(kD)]^{-1} (J_{m-1} + J_{m+1}) \right\} h(y, z); \quad (32.24b)$$

$$g_x^{(N)}(y, z) = \left\{ \left[(8acik_1)^{-1} - \frac{e^{-ik_1D}}{ack_1 \sin(k_1D)} \right] J_N - [8ack_1 \sin(kD)]^{-1} J_{N-1} \right\} h(y, z), \quad (32.24c)$$

where we put

$$J_s = \iint_S g_x^{(s)}(\eta, \zeta) d\eta d\zeta; \quad s = 1, \dots, N. \quad (32.25)$$

After integration of (32.24a, b, c) over S , we obtain the following set of linear algebraic equations for the unknown quantities J_1, J_2, \dots, J_N :

$$\left\{ 1 - \left[(8acik_1)^{-1} - \frac{e^{-ik_1D}}{ack_1 \sin(k_1D)} \right] H \right\} J_1 + \left\{ [ack_1 \sin(k_1D)]^{-1} H \right\} J_2 = -H; \quad (32.26a)$$

$$\left\{ [ack \sin(k_1D)]^{-1} H \right\} J_{s-1} + J_s + \left\{ [ack \sin(k_1D)]^{-1} H \right\} J_{s+1} = 0; \quad (32.26b)$$

$$\begin{aligned} & \left\{ [ack_1 \sin(k_1D)]^{-1} H \right\} J_{N-1} \\ & + \left\{ 1 - \left[(8acik_1)^{-1} - \frac{e^{-ik_1D}}{ack_1 \sin(k_1D)} \right] H \right\} J_N = 0. \end{aligned} \quad (32.26c)$$

As soon as (32.12a, b, c) is solved, all necessary constants and the wave field can be found. The reflection and transmissions coefficients can be obtained as follows

$$R = 1 - [9/4iack_1]J_1; \tag{32.27a}$$

$$T = [9/4iack_1]J_N. \tag{32.27b}$$

32.3 Explicit Formulae for the Wave Characteristics

Set of (32.26a, b, c) has a specific form:

$$\begin{pmatrix} p & \delta & 0 & \cdots & f \\ \delta & \beta & \delta & \cdots & 0 \\ \vdots & \vdots & \vdots & \cdots & 0 \\ 0 & \delta & \beta & \delta & 0 \\ 0 & 0 & \delta & p & 0 \end{pmatrix} \tag{32.28}$$

$$f = -H; \quad \beta = 1; \quad p = 1 - \left[(8ack_1)^{-1} - \frac{e^{-ik_1D}}{ack_1 \sin(k_1D)} \right] H;$$

$$\delta = [ack_1 \sin(k_1D)]^{-1} H$$

with the following solution:

$$\begin{aligned} J_1 &= (f/L_N)(pI_{M-2} - \delta^2 I_{M-3}); & J_N &= (f/L_N)(-\delta)^{N-1}; \\ J_s &= (f/L_N)(pI_{N-s-1} - \delta^2 I_{N-s-2})(-\delta)^{s-1}; & s &= 2, 3, \dots, N-1, \end{aligned} \tag{32.29}$$

where

$$L_N = p^2 I_{N-2} - 2p\delta^2 I_{N-3} + \delta^4 I_{N-4}; \tag{32.30}$$

$$L_N = \beta I_{N-1} - \delta^2 I_{N-2} \tag{32.31}$$

are the full determinant and the N -th order determinant of Equations set (32.28), respectively.

Here we use also the representation for I_N :

$$I_N = (X_1^{N+1} - X_2^{N+1}) / (X_1 - X_2), \tag{32.32}$$

where

$$X_{1,2} = 1/2 \pm (1/4 - [H/ack_1 \sin(k_1D)]^2)^{1/2}. \tag{32.33}$$

Later the roots (32.33) will be used in the form:

$$\begin{aligned} X_1 &= -re^{i\theta}; & X_2 &= -re^{-i\theta}; \\ r &= \delta = H/(ack \sin(k_1 D)); & \cos(\theta) &= -ack_1 \sin(k_1 D)/2H. \end{aligned} \quad (32.34)$$

The reflection coefficient R , which is given by the first equation of (32.27a, b), after some transformations, including (32.30), (32.31), takes the form:

$$R = I_{N-1}/L_N \quad (32.35)$$

Also L_N , by using (32.31), can be represented as follows

$$L_N = [(p - \beta)^2 - \delta^2]I_{N-2} - (\beta - 2p)I_{N-1}. \quad (32.36)$$

Since (32.32), (32.34) imply that

$$I_{N-2}/I_{N-1} = -[\cos(\theta) - \sin(\theta)ctg(N\theta)]/c, \quad (32.37)$$

the reflection coefficient is finally obtained in the explicit form:

$$\begin{aligned} R &= \left\{ [(p - \beta)^2 - \delta^2]I_{N-2}/I_{N-1} - (\beta - 2p) \right\}^{-1} \\ &= \left\{ -c[(p - \beta)^2 - \delta^2][\cos(\theta) - \sin(\theta)ctg(N\theta)] - (\beta - 2p) \right\}^{-1} \end{aligned} \quad (32.38)$$

An explicit formula for the transmission coefficient can be deduced on the base of the second equation in (32.13a, b, c), the second one in (32.29), (32.32) and (32.35):

$$T = 9J_N/(4iack_1) = 9f(-\delta)^{N-1}/(L_N 4iack_1) = 9(-\delta)^{N-1}R/(I_{N-1} 4iack_1) \quad (32.39)$$

After using (32.32) for I_{N-1} , one obtains

$$I_{N-1} = (-\delta)^{N-1} \sin(\theta N)/\sin(\theta), \quad (32.40)$$

that finally turns to the following explicit expression:

$$T = 9R \sin(\theta)/[4ack_1 \sin(\theta N)]. \quad (32.41)$$

The explicit expressions developed above for the reflection and transmission coefficients show the possibilities to choose the values of frequency, in order to provide a particular regime, when, for instance, $|R| = 0$ and $|T| = 1$ or when $|R|$ reaches a maximum and $|T|$ —minimum.

It can be shown that the well-known property of energy balance automatically works, independently on what is the value of the constant H . When the expression

under square root in (32.33) is positive, quantity θ is real, otherwise, θ is imaginary. If the ratio d/a is fixed, a variation of other one b/a allows one to attain the regime when, say, $|R| \approx |T|$. The reflection tends to $|R| = 1$ and transmission to $|T| = 0$ exponentially with the frequency growth, when the value of θ becomes imaginary. According to (32.41), $|T|$ is a periodic function of N , when θ is real, that is equivalent to a periodicity of the attenuation with distance. The coefficient $|R|$ is also a periodic function of N .

Acknowledgments The first author is grateful to the Russian Scientific Foundation (RSCF), for its support by Project 15-19-10008.

References

1. E.L. Shenderov, *Sov. Phys. Acoust.* **16**(2) (1970)
2. Y.-L. Kok Jr, N.C. Galagher, R.V. Ziolkovski, *IEEE Trans. Antennas and Propagation AP* **37**, 901 (1989)
3. J.D. Achenbach, Z.L. Li, *Wave Motion* **8**, 225 (1986)
4. H. Lamb, *Hydrodynamics*, 6th ed. (Cambridge University Press, London, 1975)
5. J.W. Miles, *Wave Motion* **4**, 285 (1982)
6. E. Scarpetta, M.A. Sumbatyan, *IMA J. Appl. Math.* **56**, 109 (1996)
7. E. Scarpetta, M.A. Sumbatyan, *Wave Motion* **22**, 133 (1995)
8. E. Scarpetta, M.A. Sumbatyan, *Wave Motion* **25**, 61 (1997)
9. E. Scarpetta, V. Tibullo, *Int. J. Eng. Sci.* **46**, 105 (2008)
10. J.W. Homentcovschi, Miles. *Journal of Acoustical Society of America* **117**(5), 2761 (2005)
11. Ch. Zhang, D. Gross, *Int. J. Eng. Sci.* **31**, 841 (1993)

Chapter 33

Numerical Simulation of Ultrasonic Torsional Guided Wave Propagation for Pipes with Defects

A.A. Nasedkina, A. Alexiev and J. Malachowski

Abstract Long-range ultrasonic guided waves are widely used for the detection of defect founded in the long distance pipeline. Numerical simulation of guided wave propagation is considered for an experimental pipe with various forms of defects. The pipe is subjected to the propagation of the torsional guided wave. Numerical models are constructed for a sample pipe without defect and two sample pipes with two different types of defects: a notch and a notch with a hole. The desired $T(0, 1)$ guided wave is simulated by a special excitation pressure function applied to one end of the pipe, which spreads via shearing motion parallel to the circumferential direction. Finite element software ANSYS is used to build 3D solid and finite element models of the sample pipes and perform full transient analysis. The simulation results allow obtaining information on the amplitude and the transit time of the impulse reflected from the defect and from the end of the pipe. The results also include the investigation of influence of the length and depth of the notch on the stress-strain state of the pipe.

33.1 Introduction

The inspection process of pipeline is necessary in the oil-chemical industry where the pipelines, used to transport oil and chemical products, are subjected to corrosion. Inner surface and even outer surface corrosion is especially difficult to detect when the pipelines are located underground.

A.A. Nasedkina (✉)

I.I. Vorovich Institute of Mathematics, Mechanics and Computer Science,
Southern Federal University, Rostov-on-Don, Russia
e-mail: nasedkina@math.sfedu.ru

A. Alexiev

Institute of Mechanics, Bulgarian Academy of Sciences, Sofia, Bulgaria

J. Malachowski

Faculty of Mechanical Engineering, Military University of Technology,
Warsaw, Poland

Ultrasonic methods of diagnostics are effective non-destructive testing methods. Conventional non-destructive testing method consists of a series of point-to-point tests from the outside surface of the pipe. The major disadvantage of this technique is that it can be expensive and time-consuming when a coating covers the pipe, because an access to the outside surface requires removal of the coating to perform the test, and further re-installation of the coating when the testing is complete. Moreover, for long-distance pipeline, this method becomes difficult and inefficient.

Unlike conventional method, the method of damage detection by guided waves is more effective technique for a long-range diagnostics of pipes, which has attracted considerable attention in the recent years. Compared to the ordinary point-by-point testing, for long pipelines ultrasonic guided wave method largely reduces inspection time and costs. This technique enables one to inspect the pipelines for a long distance from a single position and facilitates the defect detection. Equipment with guided waves is installed at one location of a pipe and reflection echoes indicate the presence of corrosion or other defects [1].

There are three possible modes of guided waves, which can propagate along the pipe: longitudinal, torsional and flexural. Interaction of guided waves with geometrical discontinuities in structures has been investigated in several works. A number of studies examined efficiency of the defect detection using longitudinal and torsional modes [2–5]. Guided waves of the longitudinal mode $L(0, 2)$ are sensitive to defects and do not disperse from cut-off frequency. The torsional waves $T(0, 1)$ also have attractive advantages in defect detection due to their constant speed and propagation through the pipes filled with liquid without much leakage [6].

Numerical simulation of guided wave propagation is a valuable tool to investigate the behavior of the longitudinal and torsional wave modes. It is an important step in the process of development and optimization of nondestructive-testing procedures based on structural waves. Appropriate simulations can replace physical tests. A 3D model is required to simulate wave propagation phenomena with the wavelength magnitude compared with a thickness of the structure [7].

In the present study, two test pipes with different forms of defects (a notch and a notch with a hole) are considered by using finite element simulation in order to study the process of ultrasonic guided torsional wave propagation. In numerical simulation, only a part of the pipe (1 m long) around of the defect is taken into account. The guided wave reflects from the defect and from end of the pipe. Numerical simulation of the ultrasonic guided wave propagation in the pipe with a defect should give information on the amplitude and the transit time of the impulse reflected from the defect and from the end of the pipe.

Problem statement and mathematical model are present in Sect. 33.2. Section 33.3 describes numerical models for the pipes with defects. Three-dimensional solid and finite element models of the sample pipes are constructed with the help of ANSYS finite element package. Torsional guided waves are simulated by a special excitation pressure function applied to one edge of the pipe. The results are provided in Sect. 33.4. Full transient analysis is performed to simulate ultrasonic torsional guided wave propagation through the pipe with and without defect. The time period for the computations is such that the guided waves

would travel till the right end of the pipe, reflect from it, then go back and reflect from the left end of the pipe. The monitoring plane is located at the distance of 0.25 m from the left end at halfway to the defect location. The results for the nodes in this location would give opportunity to verify the excitation signal and to investigate its reflection from the defect. Additional analysis has been carried out to study an influence of the defect on the stress-strain state of the pipe with a defect in the shape of a notch for various values of depth and length of the notch. Concluding remarks are presented in Sect. 33.5.

33.2 Problem Statement and Mathematical Model

We consider torsional ultrasonic guided wave, which propagates in a steel pipe. We assume that a pipe is made of homogeneous isotropic material. Then a transient dynamic problem of the elasticity theory for isotropic body that occupies a region V in three-dimensional space can be described by the following equations:

$$\nabla \cdot \boldsymbol{\sigma} = \rho \ddot{\mathbf{u}} \quad (33.1)$$

$$\boldsymbol{\sigma} = \mathbf{c} \cdot \boldsymbol{\varepsilon} \quad (33.2)$$

$$\boldsymbol{\varepsilon} = \frac{1}{2}(\nabla \mathbf{u} + \nabla \mathbf{u}^T), \quad (33.3)$$

where $\boldsymbol{\sigma}$ is the second rank stress tensor, \mathbf{c} is the fourth rank tensor of elastic stiffness, $\boldsymbol{\varepsilon}$ is the second rank strain tensor, ρ is the density, $\mathbf{u} = \mathbf{u}(\mathbf{x}, t)$ is the displacement vector, $\mathbf{x} = (x, y, z) \in V$.

In vector-matrix notation, set of (33.1)–(33.3) can present in the form:

$$\mathbf{L}^T(\nabla) \cdot \mathbf{T} = \rho \ddot{\mathbf{u}}, \quad \mathbf{T} = \mathbf{C} \cdot \mathbf{S}, \quad \mathbf{S} = \mathbf{L}(\nabla) \cdot \mathbf{u}, \quad (33.4)$$

where

$$\mathbf{L}^T(\nabla) = \begin{bmatrix} \partial/\partial x & 0 & 0 & \partial/\partial y & 0 & \partial/\partial z \\ 0 & \partial/\partial y & 0 & \partial/\partial x & \partial/\partial z & 0 \\ 0 & 0 & \partial/\partial z & 0 & \partial/\partial y & \partial/\partial x \end{bmatrix}, \quad \nabla = \begin{bmatrix} \partial/\partial x \\ \partial/\partial y \\ \partial/\partial z \end{bmatrix} \quad (33.5)$$

$\mathbf{T} = [\sigma_{xx}, \sigma_{yy}, \sigma_{zz}, \sigma_{xy}, \sigma_{yz}, \sigma_{xz}]$ is the stress pseudo-vector, \mathbf{C} is the 6×6 matrix of elastic stiffness, $\mathbf{S} = [\varepsilon_{xx}, \varepsilon_{yy}, \varepsilon_{zz}, 2\varepsilon_{xy}, 2\varepsilon_{yz}, 2\varepsilon_{xz}]$ is the strain pseudo-vector. Here the correspondence law $(ij) \leftrightarrow \alpha$ is used between the indices ij , $i, j = x, y, z$, and one-dimensional array $\alpha = 1, 2, 3, 4, 5, 6$: $(xx) \leftrightarrow (1)$; $(yy) \leftrightarrow (2)$; $(zz) \leftrightarrow (3)$; $(xy), (yx) \leftrightarrow (4)$; $(yz), (zy) \leftrightarrow (5)$; $(xz), (zx) \leftrightarrow (6)$.

For isotropic medium, the matrix \mathbf{C} has the form:

$$\mathbf{C} = \frac{E}{(1+\nu)(1-2\nu)} \begin{bmatrix} 1-\nu & \nu & \nu & 0 & 0 & 0 \\ & 1-\nu & \nu & 0 & 0 & 0 \\ & & 1-\nu & 0 & 0 & 0 \\ & & & \frac{1-2\nu}{2} & 0 & 0 \\ & sym & & & \frac{1-2\nu}{2} & 0 \\ & & & & & \frac{1-2\nu}{2} \end{bmatrix},$$

where E is the Young's modulus, ν is the Poisson's ratio.

On the boundaries $\Gamma = \partial V$ of the volume V , we impose the boundary conditions. The right end Γ_r of the pipe is considered to be rigidly fixed:

$$\mathbf{u} = \mathbf{0}, \mathbf{x} \in \Gamma_r. \quad (33.6)$$

On the left end of the pipe Γ_l , the stress vector satisfies the relationship:

$$L^T(\mathbf{n}) \cdot \mathbf{T} = \mathbf{p}, \mathbf{x} \in \Gamma_l, \quad (33.7)$$

where \mathbf{n} is the external unit normal vector, $\mathbf{p} = \mathbf{p}(\mathbf{x}, t)$ is the pressure vector. The rest of the boundary $\Gamma_s = \Gamma \setminus (\Gamma_r \cup \Gamma_l)$ is considered to be free from stresses:

$$L^T(\mathbf{n}) \cdot \mathbf{T} = \mathbf{0}, \mathbf{x} \in \Gamma_s. \quad (33.8)$$

To complete the formulation of the transient dynamic elastic problem, we introduce the initial conditions:

$$\mathbf{u}(\mathbf{x}, 0) = \mathbf{0}, \mathbf{x} \in V. \quad (33.9)$$

In order to solve the problem (33.4)–(33.9) by the finite element method, we formulate the weak statement of this problem and apply a well-known technique of finite element approximations.

Let $V_h \subset V$ be the region occupied by the finite element mesh; $V_h = \cup_m V^{em}$, where V^{em} is a finite element with the number m . The approximate solution $\mathbf{u}_h \approx \mathbf{u}$ can be sought in the form of semi-discrete approximations:

$$\mathbf{u}_h = \mathbf{N}^T(\mathbf{x}) \cdot \mathbf{U}(t), \quad (33.10)$$

where \mathbf{N}^T is the matrix of basis functions, \mathbf{U} is the vector of the nodal degrees of freedom (nodal displacements).

According to the conventional finite-element technique, we approximate the weak problem statement in a finite dimensional space related to the basis functions $\mathbf{N}^T(\mathbf{x})$. Using (33.10) and similar representations for the projection functions for the weak problem statement in V_h , we obtain the system of finite-element equations with respect to the nodal displacements \mathbf{U} :

$$\mathbf{M} \cdot \ddot{\mathbf{U}} + \mathbf{K} \cdot \mathbf{U} = \mathbf{F}, \quad (33.11)$$

where $\mathbf{M} = \sum_m^a \mathbf{M}^{em}$, $\mathbf{K} = \sum_m^a \mathbf{K}^{em}$ are the global matrices obtained from the corresponding element matrices, $\mathbf{F} = \sum_m^a \mathbf{F}^{em}$ is the global vector of external influences obtained from the element vectors \mathbf{F}^{em} given by formulae:

$$\begin{aligned} \mathbf{M}^{em} &= \int_{V^{em}} \mathbf{N}^{em} \cdot (\mathbf{N}^{em})^T dV, \mathbf{K}^{em} \\ &= \int_{V^{em}} (\mathbf{L}(\nabla) \cdot (\mathbf{N}^{em})^T)^T \cdot \mathbf{c} \cdot \mathbf{L}(\nabla) \cdot (\mathbf{N}^{em})^T dV, \mathbf{F}^{em} = \int_{\Gamma_l^{em}} \mathbf{N}^{em} \cdot \mathbf{p} d\Gamma \end{aligned} \quad (33.12)$$

where \mathbf{N}^{em} is the matrix of approximate basis functions, defined for each finite element, Γ_l^{em} is a boundary that approximates the boundary Γ_l .

33.3 Numerical Models

The test pipe was constructed in the Paton Electric Welding Institute, Ukraine. Several types of defects were made on the pipe for experimental purposes.

The diameter of the pipe is $D = 114$ mm and the thickness of its walls is $a = 6$ mm. Two types of defects are considered for numerical simulation. The first type of defect is a notch with a length of $s = 180$ mm, depth of $d = 2$ mm and width of $w = 2$ mm (Fig. 33.1a). The second type of defect is a notch with a round hole, where the length of the notch is $s = 200$ mm, depth of the notch is $d = 2$ mm and width of the notch is $w = 2$ mm. The radius of the round hole is $r_h = 5$ mm (see Fig. 33.1b). The first type of the defect will be further referred to as defect I, and the second type of the defect will be referred to as defect II.

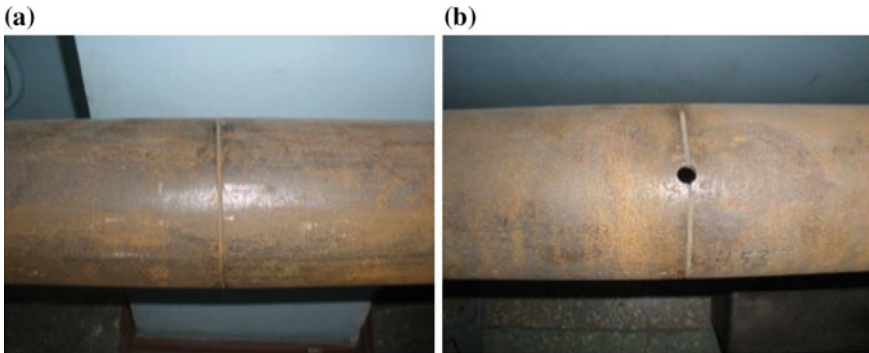


Fig. 33.1 Two types of defects on the sample pipe: notch (a) and notch with hole (b)

For numerical simulation of ultrasonic guided wave propagation through the pipe, it is sufficient to consider a part of the pipe around the defect. Solid and finite-element modeling was done with the help of ANSYS finite-element software.

Three-dimensional solid models were constructed for a pipe without defect, a pipe with defect I, and a pipe with defect II. The solid model of the part of the pipe under consideration is represented by a hollow cylinder of the length l and the distance l_{def} from the defect to the end of the pipe, where the waves are excited (further referred to as left end). The monitoring plane then will then be placed at halfway from the left end to the defect location (see Fig. 33.2).

An auxiliary volume was built at the left end of the pipe with aim to set boundary condition, and auxiliary volumes around the defects were built for the meshing purposes.

Solid models were meshed with 3-D 8-node brick elements Solid185 (Fig. 33.3). This element has three degrees of freedom at each node: displacements in nodal x -, y - and z -directions. The shape functions are given by the formulae [8]:

Fig. 33.2 Solid model of the pipe

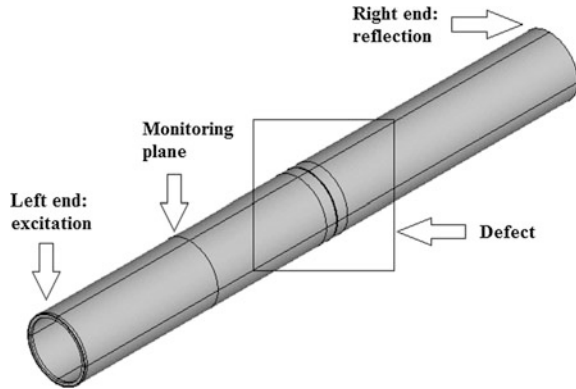
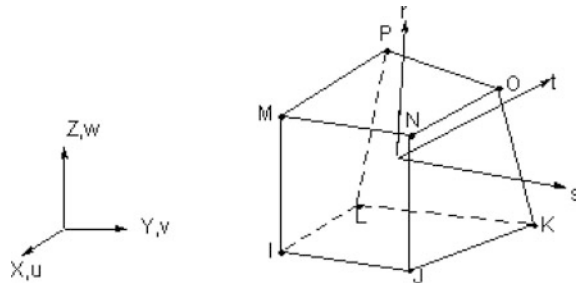


Fig. 33.3 Structural finite-element Solid185 with 8 nodes



$$\begin{aligned}
 u &= \frac{1}{8} (u_I(1-s)(1-t)(1-r) + u_J(1+s)(1-t)(1-r) + u_K(1+s)(1+t)(1-r) \\
 &\quad + u_L(1-s)(1+t)(1-r) + u_M(1-s)(1-t)(1+r) + u_N(1+s)(1-t)(1+r) \\
 &\quad + u_O(1+s)(1+t)(1+r) + u_P(1-s)(1+t)(1+r)); \\
 v &= \frac{1}{8} (v_I(1-s)(1-t)(1-r) + v_J(1+s)(1-t)(1-r) + v_K(1+s)(1+t)(1-r) \\
 &\quad + v_L(1-s)(1+t)(1-r) + v_M(1-s)(1-t)(1+r) + v_N(1+s)(1-t)(1+r) \\
 &\quad + v_O(1+s)(1+t)(1+r) + v_P(1-s)(1+t)(1+r)); \\
 w &= \frac{1}{8} (w_I(1-s)(1-t)(1-r) + w_J(1+s)(1-t)(1-r) + w_K(1+s)(1+t)(1-r) \\
 &\quad + w_L(1-s)(1+t)(1-r) + w_M(1-s)(1-t)(1+r) + w_N(1+s)(1-t)(1+r) \\
 &\quad + w_O(1+s)(1+t)(1+r) + w_P(1-s)(1+t)(1+r)).
 \end{aligned}$$

where s , t , r are the local coordinates for the canonical cube $\{-1 \leq s \leq 1; -1 \leq t \leq 1; -1 \leq r \leq 1\}$.

ANSYS documentation [8] suggests that 20 elements should be used in the length per one wavelength in order to guarantee high-precision calculation. For finite element models of the pipe, the number of elements along the wall thickness direction is 6, and the aspect ratio of the elements in the longitudinal direction is 5/1, which will ensure good accuracy. Finite element meshes of defect I and defect II are shown in Fig. 33.4.

In order to simulate the emission of the desired guided wave into the pipe, a special excitation function was applied at the left end of the pipe. The form of this excitation function was taken from [7]:

$$F(t) = \begin{cases} 0.5(1 - \cos \frac{2\pi ft}{n}) \sin(2\pi ft), & 0 < t \leq \tau; \\ 0, & t > \tau \end{cases}$$

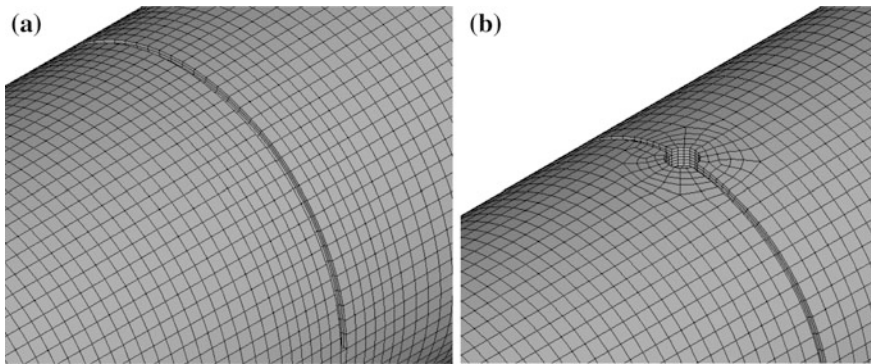
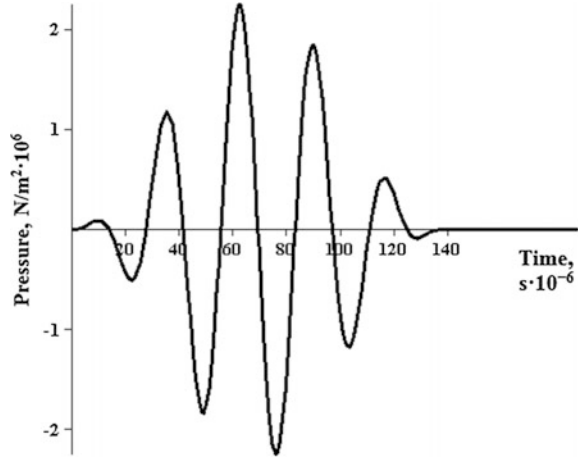


Fig. 33.4 Finite element meshes of defects: defect I—notch (a) and defect II—notch with a round hole (b)

Fig. 33.5 Graph of pulse-time signal: 5 cycles at 36 kHz



where n is the number of pulse cycles, f is the central frequency, $\tau = n/f$ is the signal impulse time. According to [7], with such a signal, the energy of the force function can effectively concentrate within a finite interval in both the time domain and frequency domain. For torsional guided waves $T(0, 1)$, which spread via shearing motion parallel to the circumferential direction $\mathbf{e}_\theta(\mathbf{x})$, where \mathbf{e}_θ is a unit vector in cylindrical coordinate system, the orientation of the load is around the circumference of the left end of the pipe. For simulation in ANSYS, a tangent pressure function $\mathbf{p} = P(t)\mathbf{e}_\theta(\mathbf{x})$, $P(t) = F_0F(t)/S$ was applied to the outer surface of the first row of elements at the left end of the pipe, where S is the area of the outer surface with applied load, F_0 is the value of the force. The graph of the pulse-time signal of the pressure function is shown in Fig. 33.5. Special surface finite elements Surf154 were used to apply tangential pressure around the circumferential area.

In ANSYS [8], the time integration of the transient system (33.11) is done according to the Newmark scheme with time step Δt , which has the form:

$$\begin{aligned}\dot{\mathbf{u}}_{n+1} &= \dot{\mathbf{u}}_n + [(1 - \delta)\ddot{\mathbf{u}}_n + \delta\ddot{\mathbf{u}}_{n+1}]\Delta t, \\ \mathbf{u}_{n+1} &= \mathbf{u}_n + \dot{\mathbf{u}}_n\Delta t + \left[\left(\frac{1}{2} - \alpha \right) \ddot{\mathbf{u}}_n + \alpha\ddot{\mathbf{u}}_{n+1} \right] \Delta t^2,\end{aligned}\quad (33.13)$$

where α and δ are Newmark integration parameters, \mathbf{u}_k is the nodal displacement at time t_k , $k = n, n + 1$. Then by using (33.13), set of (33.11) can be present as a set of algebraic equations with respect to \mathbf{u}_{n+1} for each time moment t_{n+1} :

$$\left(\frac{1}{\alpha\Delta t^2} \mathbf{M} + \mathbf{K} \right) \cdot \mathbf{u}_{n+1} = \mathbf{F} + \frac{1}{\alpha\Delta t^2} \mathbf{M} \cdot \mathbf{u}_n + \frac{1}{\alpha\Delta t} \mathbf{M} \cdot \dot{\mathbf{u}}_n + \left(\frac{1}{2\alpha} - 1 \right) \mathbf{M} \cdot \ddot{\mathbf{u}}_n.$$

The solution of (33.11) is unconditionally stable, when

$$\alpha \geq \frac{1}{4} \left(\frac{1}{2} + \delta \right)^2, \delta \geq \frac{1}{2}, \frac{1}{2} + \delta + \alpha > 0.$$

The Newmark parameters relate to input as $\alpha = \frac{1}{4}(1 + \gamma)^2$, $\delta = \frac{1}{2} + \gamma$, where γ is the amplitude decay factor which default value is 0.005.

33.4 Results of Numerical Simulation

Full transient analysis was performed to simulate ultrasonic guide wave propagation through the pipe with and without defect. The time period for the computations was equal to $t_{end} = 3l/c$, where l is the length of the pipe, c is the wave speed. During this time period, the guided waves would travel till the right end of the pipe, reflect from it, then go back and reflect from the left end of the pipe. Damping was not taken into account in this simulation.

The computations were performed for the central frequency $f = 36,000$ Hz, number of pulse cycles $n = 5$, force value $F_0 = 100$ N, and wave speed $c = 3,200$ m/s. The calculated signal impulse time was $\tau = 138 \mu\text{s}$, and the time period for the computations was $t_{end} = 937 \mu\text{s}$. The time step was $\Delta t = 2 \mu\text{s}$. The material (steel) was modeled as a linear isotropic material with elastic modulus $E = 205$ GPa, Poisson's ratio $\nu = 0.28$ and density $\rho = 7,800$ kg/m³.

The length of the pipe was $l = 1$ m and the defect was located at $l_{def} = 0.5$ m from the left edge of the pipe. The monitoring plane was located at the distance of 0.25 m from the left end at halfway to the defect location. The monitoring plane is characterized by six nodes (Fig. 33.6). Nodes 1, 2 and 3 are situated in the upper part of the pipe, where the defect is located, and nodes 4, 5 and 6 are situated in the lower part of the pipe. The results for these nodes can be extracted in order to compare the cases of the pipe without defect and the pipe with defect I and defect II. The results for the nodes in this location give opportunity to verify the excitation signal and investigate its reflection from the defect.

Fig. 33.6 Location of nodes at the monitoring plane

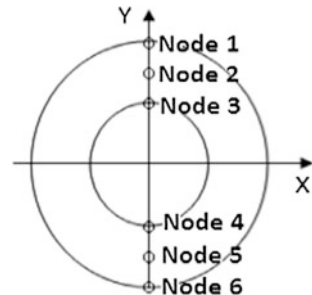


Fig. 33.7 Von Mises stresses for pipe without defect in node 1 versus time for the period of 937 μs

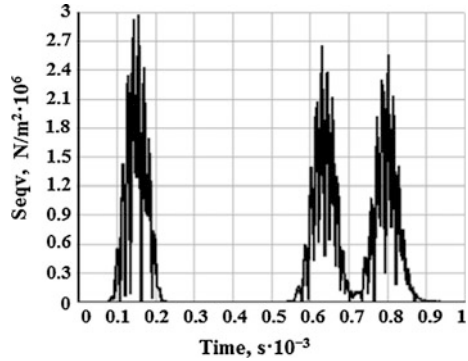
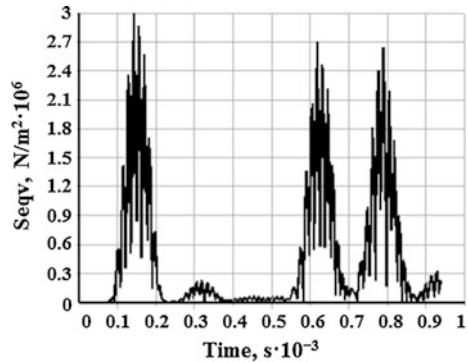


Fig. 33.8 Von Mises stresses in node 1 versus time for the period of 937 μs for pipe with defect I



As the torsional guided wave is excited by the load pressure function, the von Mises stresses can be considered as a qualitative characteristic of the computation results. Let us compare the distribution of the von Mises stresses in Node 1 for the cases without and with defects. Figure 33.7 shows the plots of the von Mises stresses for the pipe without defect for the whole monitoring period (937 μs). We can see that the incident wave has passed the monitoring plane three times. It was reflected first from the left end of the pipe and then from the right end of the pipe. The presence of defect causes the incident wave to reflect from it, which can be seen from Fig. 33.8 (defect I) and Fig. 33.9 (defect II). The comparison of these figures shows that defect II (notch with a hole) causes larger amplitudes of the von Mises stresses in the reflected wave than defect I.

The guided wave spreads through the pipe via shearing motion in z -direction. We note that at the monitoring plane with $x = 0$, the displacements $u_\theta = u_x$ for the nodes with $y > 0$ and $u_\theta = -u_x$ for the nodes with $y < 0$. The computations show that in both cases for the pipes with and without defects, the values of displacement u_x have the order of magnitude 10^{-7} m. At the same time, the displacements u_y and u_z have much smaller values: 10^{-20} m for the pipe without defect and 10^{-12} – 10^{-13} m for the

Fig. 33.9 Von Mises stresses in node 1 versus time for the period of 937 μs for pipe with defect II

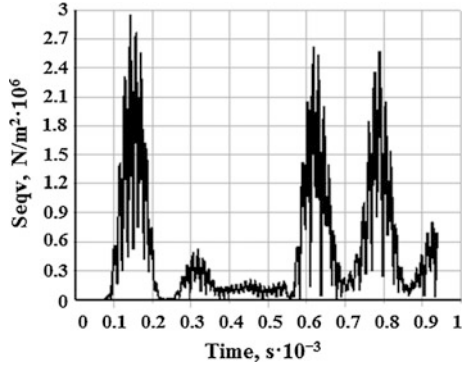
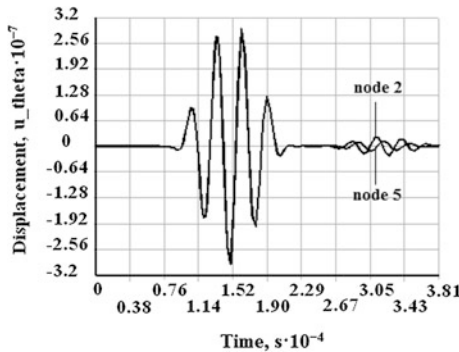


Fig. 33.10 Displacements u_θ in nodes 2 and 5 versus time for the period of 381 μs for a pipe with defect I



pipe with defect I and 10^{-10} m for the pipe with defect II. These results prove that the excited wave has torsional mode in numerical simulation.

Figure 33.10 shows the plots of displacement u_θ for the pipe with defect I for internal nodes 2 and 5 of the monitoring plane. Here the amplitude of the incident wave is slightly smaller, compared to that of the external node 1. It is easy to note that the form of the wave is very close to the waveform of the load pressure function. It can be seen that the defect generates the reflected wave of the same shape but with much smaller amplitude. The amplitude of the wave reflected from defect in node 2 is slightly larger than in node 5, which is expected as the defect is located in the upper part of the pipe. The same result for the pipe with defect II can be observed in Fig. 33.11. We can see that for defect II the difference between the wave amplitudes in nodes 2 and 5 is more significant. Moreover, defect II (notch with a hole) causes larger amplitudes of the displacements in the reflected wave than defect I.

It is of interest to analyze the influence of the defect size on the stress-strain state of the pipe. The investigation of the effect of depth and length of the defect has been carried out for the pipe with defect I (notch). The depth d of defect I was varied from 2 mm to 6 mm (equal to the thickness of the pipe) with the step of 1 mm. The length of the defect was equal to $s = 180$ mm for all cases. The comparison of the von Mises

Fig. 33.11 Displacements u_θ in nodes 2 and 5 versus time for the period of 381 μ s for pipe with defect II

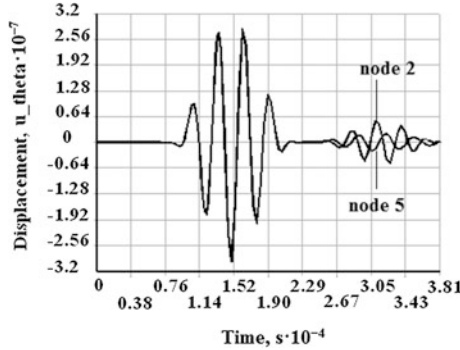
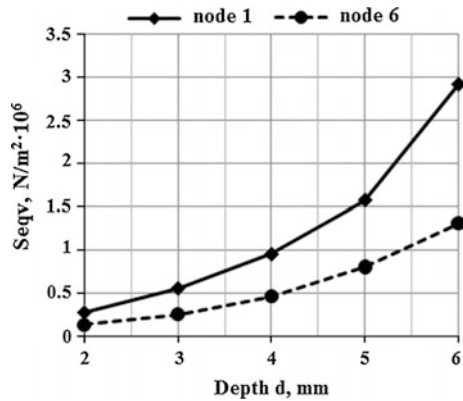


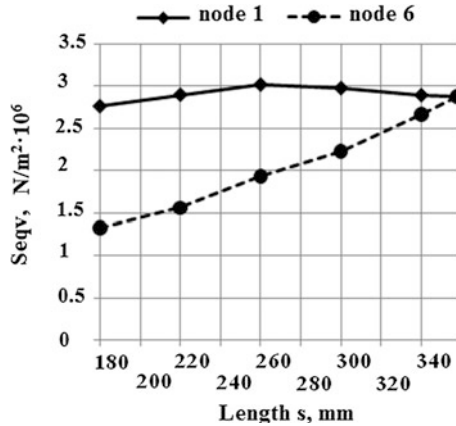
Fig. 33.12 Maximal von Mises stresses in nodes 1 and 6 versus depth of defect I for the reflected wave



stress distribution for the different cases of the defect depth for the nodes 1 and 6 has shown that the amplitude of the wave, reflected from defect, increased with increasing the defect depth. Again, for node 1, the amplitude of the reflected wave equals the amplitude of the incident wave for the case of $d = 6$ mm. The dependence of the maximal value of the von Mises stress on the defect depth is shown in Fig. 33.12. From Fig. 33.12, we can see that with increasing the defect depth, the von Mises stresses increase more significantly for node 1 than for node 6. Moreover, the maximal amplitude of the von Mises stresses for the case of $d = 6$ mm is twice larger in node 1 compared to that in node 6.

In order to analyze the influence of the defect length, the length s of defect I was varied from 180 mm to 358 mm (equal to the length of circumference of the pipe) with the step of 40 mm. The depth $d = 2$ mm of defect II remained constant for all cases. The dependence of the maximal value of the von Mises stress on the defect length is shown in Fig. 33.13. Here from the plot for node 6, we can see that an increase of the defect length leads to an increase of the von Mises stresses. The von Mises stresses in node 1 do not change considerably. Their values slightly increase at first when the length of the defect changes from 180 to 260 mm and then

Fig. 33.13 Maximal von Mises stresses in nodes 1 and 6 versus length of defect I for the reflected wave



slightly decrease with the further increase of the defect length. For the case of the full notch on a whole perimeter of the pipe ($s = 358$ mm), the values of the von Mises stresses are almost equal for nodes 1 and 6.

The comparison of Figs. 33.12 and 33.13 allows one to conclude that the change of the notch depth has more significant impact on the values of the von Mises stresses than the change of the notch length.

33.5 Concluding Remarks

Numerical simulation of ultrasonic torsional guided waves propagation was performed for a sample pipe without defect and two sample pipes with two different types of defect, a notch (defect I) and a notch with a hole (defect II). Finite element software ANSYS was used to build solid and finite element models of the pipe, simulate the applied pressure function for generating the desired guided waves and perform transient analysis.

The results of numerical simulation enable us to obtain information on the amplitude and the transit time of the impulse reflected from the defect and from the end of the pipe. The plots of the von Mises stress and displacement distribution versus time were depicted for several nodes of the monitoring plane. The comparison of numerical results for the pipes with two different forms of defects has shown that the amplitude of the wave reflected from defect is significantly larger for a notch with a hole.

The influence of the defect on the stress-strain state of the pipe was analyzed for a pipe with a notch. The comparison of results for various values of the depth and length of the notch has led to a conclusion that defect depth has more significant impact than the defect length.

Acknowledgments The work was supported by the European Commission, Marie Curie Programme, contract No. PIRSES-GA-2012-318874, Project “Innovative Nondestructive Testing and Advanced Composite Repair of Pipelines with Volumetric Surface Defects (INNOPIPES)”.

References

1. M.N. Karmanov, V.M. Gorbik, Possibilities of practical application of low-frequency ultrasonic methods for defect detection in long-size objects by guided waves, in *7th National Scientific-Technical Conference and Exhibition*. Kiev, p. 112 (2013) (In Russian)
2. M.J.S. Lowe, D.N. Alleyne, P. Cawley, Defect detection in pipes using guided waves. *Ultrasonics* **36**(1–5), 147 (1998)
3. J. Li, On circumferential disposition of pipe defects by Long-range ultrasonic guided waves. *J. Pressure Vessel Technol.* **127**(4), 530 (2005)
4. W. Zhu, An FEM simulation for guided elastic wave generation and reflection in hollow cylinders with corrosion defects. *J. Pressure Vessel Technol.* **124**(1), 108 (2002)
5. A. Demma, The reflection of guided waves from notches in pipes: a guide for interpreting corrosion measurements. *NDT E Int.* **37**(3), 167 (2004)
6. M. Kharrat, W. Zhou, O. Bareille, M. Ichchou, Defect detection in pipes by torsional guided-waves: a tool of recognition and decision-making for the inspection of pipelines, in ed. by G. De Roeck, G. Degrande, G. Lombaert, G. Müller, *Proceedings of the 8th International Conference on Structural Dynamics, EUROLYN 2011*. Leuven, Belgium, 4–6 July 2011
7. M.-F. Zheng, Chao Lua. Guo-zhu Chenb, Ping Men, Modeling three-dimensional ultrasonic guided wave propagation and scattering in circular cylindrical structures using finite element approach. *Physics Procedia* **22**, 112 (2011)
8. *ANSYS Mechanical APDL Theory Reference*. ANSYS Rel. 14.5—Canonsburg: ANSYS Inc., 2012

Chapter 34

Why and How Residual Stress Affects Metal Fatigue

R. Sunder

Abstract Understanding of the residual stress effect in metal fatigue has been largely correlative. This study summarizes the sequence of research that established why and how residual stress affects the process of metal fatigue. The residual stress effect manifests itself in two synergistic ways, through the well-known crack closure phenomenon that moderates the mechanics of fatigue crack growth and through the less known environmental mechanism controlling crack-tip surface layer resistance to fracture. The latter is associated with crack-tip surface diffusion kinetics of active species that induces premature fracture of crack tip atomic surface layers leading to reduced threshold stress intensity range. Further research established a governing relationship between near-tip residual stress, σ^* , and instantaneous threshold stress intensity, ΔK_{th} . σ^* can be modeled analytically as a function of prior load history, opening the way to account for stress history on the metal fatigue process. The influence of residual stress through crack closure extends over the entire duration of fatigue crack growth. However, its influence through ΔK_{th} is highest in the early stages of crack growth and at lower growth rates and diminishes to vanishing proportions into the Paris regime. In this may be its significance for high-cycle fatigue and to the fatigue limit.

34.1 Introduction

Unlike other engineering disciplines such as stress analysis, fluid flow, heat transfer and vibration, metal fatigue has largely remained an empirical science. If durability and structural integrity have advanced over the years, much of the credit may be due to advances in material and surface engineering and computational software related to assurance of uniformity in stressing across a structure.

R. Sunder (✉)
BiSS (P) Ltd, 497E 14th Cross, 4th Phase, Peenya Industrial Area,
Bangalore 560058, India
e-mail: rs@biss.in

A notable example of inevitable correlative approach is handling of the residual stress effect. For lack of scientific rationale behind the effect, the overwhelming majority of publications related to residual stress is restricted to its measurement and at best, computation. It is interesting that over all these years little effort was devoted to address the question as to *why* residual stress may be affecting the fatigue process.

The reasons for metal fatigue remaining a largely empirical science may lie in its nature. It is a two-stage process attributed to the formation and growth of fatigue cracks with both processes being influenced by a number of mechanisms involving both material response as well as environmental action.

The objective of this study is to consolidate the underlying science behind the residual stress effect based on irrefutable empirical evidence that cannot serve any alternate interpretation. The results of the study are likely to serve the advancement of targeted future research and improved analytical modeling of the fatigue process, particularly under load sequences of practical relevance.

34.2 Two Approaches to Fatigue Analyses

Conventional fatigue analyses serve two different practical requirements in designing metallic structures and machines. These are assurance of a given life to failure in order to determine when to retire (discard) the object and assignment of time between inspections for health monitoring purposes in order to operate the object as long as is economically viable without adversely affecting operational safety. The two requirements are addressed using two entirely different approaches to analysis even though the same phenomenon of metal fatigue is involved.

Life to failure is determined from the so-called S–N curve that describes the relationship between fatigue life expressed as number of load cycles to failure, N , and stress amplitude, σ_a , or strain amplitude, ε_a . The form of this relationship was established by Wohler in the mid-nineteenth century [1]. Wohler defined a certain stress amplitude called the fatigue limit, below which the material is unlikely to fail. This is associated with the asymptotic nature of the curve at fatigue life approaching 10^7 cycles, particularly in railway steels that were the object of Wohler's study.

Wohler and Bauschinger [2] also established the sensitivity of fatigue limit to mean stress. Thus, as mean stress tends towards ultimate stress, fatigue limit tends towards zero. This finding is extremely important from the standpoint of practical application. Most service loading spectra involve load cycles that are asymmetric. Moreover, manufacturing processes leave behind residual stress that is superposed onto loads experienced in service, causing resultant effective mean stress that can be very different from zero. If the offset is in tension, fatigue limit will reduce. If the offset is into compression, it will increase.

The sensitivity of fatigue limit to mean or residual stress plays a significant role in determining fatigue response in high-cycle fatigue (HCF). The fatigue response of most metals may be described by the schematic shown in Fig. 34.1. Note that the

horizontal axis is in the log scale. The left half of the curve falls into the category of low-cycle fatigue (LCF), while the right half is HCF. Most of the literature on metal fatigue is devoted to the interpretation of metal fatigue as a consequence of irreversible cyclic-slip. By definition, cyclic-slip is associated with cyclic plastic deformation that in turn, is known to control LCF. Obviously, as life extends into the HCF region, the plastic (or, inelastic) component of deformation will diminish to vanishing proportions. As seen in Fig. 34.1, in this region, the mean (residual) stress component progressively assumes increasing significance.

The significance of residual stress in HCF is accentuated by the asymptotic nature of the S–N curve in this region. As service life tends to higher values, a small change in residual stress can significantly impact overall fatigue life, even making the difference between finite and infinite life. Clearly, in the HCF domain, the significance of mean or residual stress overshadows that of irreversible slip. Incidentally, there is no known connection between irreversible slip and mean stress. Available analytical relationships such as the Ramberg-Osgood equation treat plastic strain amplitude as a unique function of stress amplitude [3].

For fatigue critical structures and machine components, service life between inspections is assigned based on the consideration that a detectable fatigue crack should not grow to critical proportions over two inspection periods [4], a timeframe, that may also be referred to as residual fatigue life. The approach used to estimate it involves integration of the crack growth rate (da/dN) curve over the interval from detectable to critical crack size.

A schematic of the da/dN curve appears in Fig. 34.2. It describes the relationship between da/dN and stress intensity range, ΔK . ΔK is a fracture mechanics parameter that essentially describes the intensity of the near-tip elastic stress field for a given crack size, crack geometry and applied remote stress level. A cursory comparison of

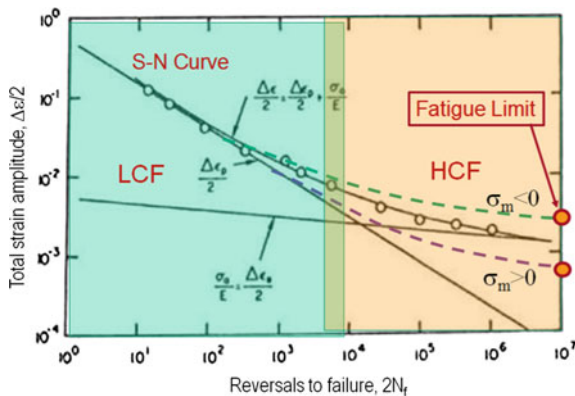
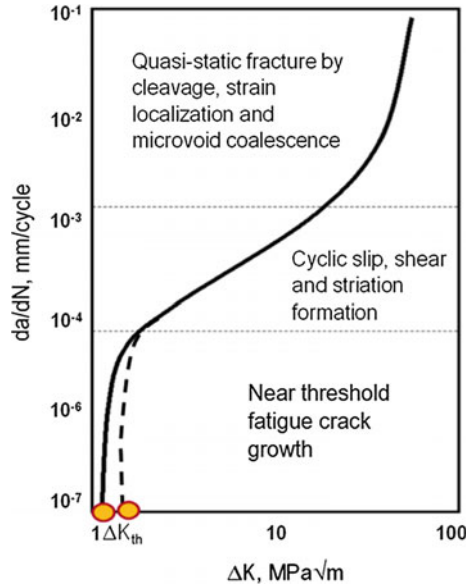


Fig. 34.1 Typical S–N curve for structural steel expressed in terms of fatigue life versus strain amplitude given by strain range by two. The dashed lines have been added to schematically describe the mean stress effect. Note how sensitive fatigue limit (circles) can be related to mean stress

Fig. 34.2 Schematic of da/dN curve with three characteristic segments. Note that just as fatigue limit varies with mean stress, ΔK_{th} also varies with stress ratio



this curve with the S–N curve in Fig. 34.1 reveals similar trends as would be more obvious if the S–N curve were to be rotated clockwise.

As indicated by Fig. 34.2, the da/dN versus ΔK curve may be broadly divided into three regions. The first region commencing below 10^{-4} mm/cycle and leading down towards 10^{-7} mm/cycle is the near threshold regime of crack growth. In this region, progressive decrease in ΔK leads to crack growth rate rapidly and asymptotically diminishing towards no growth conditions. The next region extending up towards 10^{-2} mm/cycle is the so-called Paris regime where, da/dN follows a log-linear function of ΔK . Above this region, with K_{max} approaching K_c associated with static fracture, crack growth rate rapidly accelerates towards the asymptotic boundary characterized by fracture toughness associated with static fracture.

34.3 Fatigue Limit, Threshold Stress Intensity and Crack Closure

It was noted earlier that fatigue limit, below which fatigue damage is unlikely to occur is sensitive to mean stress. In the same manner, certain threshold stress intensity, ΔK_{th} , exists, below which fatigue crack extension is unlikely to occur. ASTM E647 describes a standard practice to estimate this parameter and associates it with a crack growth rate of 10^{-7} mm/cycle.

Just as fatigue limit is sensitive to mean stress, ΔK_{th} is sensitive to applied stress ratio (see Fig. 34.2). The discovery of crack closure [5] led to the possibility that the

dependence of ΔK_{th} on stress ratio is closure related, leading to the conclusion of a certain $\Delta K_{th,eff}$ that may be treated as a material constant. However, crack closure becomes increasingly difficult to determine as ΔK tends towards ΔK_{th} , leaving the suggestion of a $\Delta K_{th,eff}$ as a material constant to be rather speculative. Some authors largely disregard closure and suggest, that fatigue crack growth rate is driven by two parameters: K_{max} and ΔK [6].

The crack closure phenomenon was discovered about 45 years ago by Elber [5]. In experiments on thin specimens with cracks, Elber discovered that the fatigue crack could close even under tensile load. This is attributed to the tensile stretch left in the wake of the crack as it grows through the monotonic plastic zone. The stretched wake can make contact well before the specimen is fully unloaded. Contact stresses developed in the process effectively truncate the lower bound of applied stress intensity given the wedge action of the closed wake. As a consequence, only a portion of the applied load cycle drives the crack in fatigue. Elber showed that crack closure is sensitive to applied stress ratio. The higher the stress ratio, the greater the fraction of the applied load cycle over which the crack will remain open.

Residual fatigue life from detectable crack size may be a small fraction of total fatigue life. However, much fatigue life may be consumed in crack growth *before* the crack assumes detectable proportions. Moreover, considering that crack growth rate would be much lower at smaller size, it would follow that substantial fraction of fatigue life may in fact be consumed by the process of fatigue crack growth. One may therefore expect that the mechanism and phenomenon that cause the mean stress (or residual stress) effect on fatigue limit must also be responsible for the sensitivity to mean stress of ΔK_{th} as indicated in the trends shown in Fig. 34.2.

34.4 Marker Loads to Characterize Near Threshold Fatigue

Fatigue life characterizes an *event* (failure) associated with conclusion of the *process* of fatigue crack growth. The *process* itself can be studied at the microscopic level by means of high-resolution electron fractography of the fracture surface, left behind by a growing fatigue crack. By introducing specially designed marker load cycles that do not noticeably grow the crack, but leave behind unmistakable footprints of the instantaneous position of the crack front, one can determine, how much exactly, the crack grew between marker cycles.

Figure 34.3a shows a typical fractograph of the initial stages of fatigue. At left, there is a secondary particulate on the notch surface where a crack commenced growth from an initial size of about 0.005 mm. The test was performed under three-step programmed loading as shown in Fig. 34.3b. The three steps of 2,000 cycles each were interspersed with 10 marker cycles that left behind traces of the extending crack front as clearly seen in the figure. The fractograph is obtained from

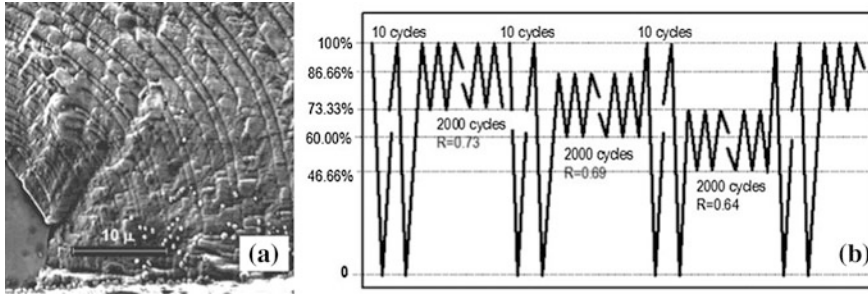


Fig. 34.3 **a** Surface crack growing out of a secondary particulate (*bottom left*) in a notched coupon cut from 2014-T6511 Al-alloy. **b** Programmed block loading used in the test that produced the fracture shown in **(a)**

tests on edge notched coupon cut from 2014-T511 Al–Cu alloy. Note, that the region covered by this picture is less than 50 μ but accounts for over 100,000 cycles of fatigue life. Al–Cu alloys are extremely conducive to the formation of discernible markers. They serve as ideal materials to study and understand the fatigue process from fractography. Thus, average crack growth rate, da/dN , in any individual step at a given point can be readily determined by dividing marker band spacing by the number of cycles in the step, i.e. 2,000.

Even though the material in question is extremely conducive to striation formation, still, striations as a rule, form only over a very narrow growth rate bandwidth, typically between 10^{-4} and 10^{-3} mm/cycle. At growth rates above 10^{-3} , a sizeable component of quasi-static crack extension may also occur, rendering occasional striations rather unrepresentative of process. At growth rates below 10^{-4} , formation of individual striations becomes exceedingly unlikely. The use of marker cycles allows reproducible measurements of crack growth rate even if striations do not form, as long as the occasional marker cycle, itself, leaves behind a discernible signature as seen in Fig. 34.3. Thus, marker cycles allow us to study growth rates even as low as 10^{-7} – 10^{-9} mm/cycle.

34.5 Sensitivity of Near Threshold Fatigue to Local Mean Stress

Conventional non-destructive testing (NDT) techniques in structural health monitoring cannot detect cracks much smaller than a few mm. Judging from Fig. 34.3, several million cycles can pass before a growing fatigue crack can assume detectable size. This appears to support the suggestion made earlier, that fatigue crack growth may occupy a decisive portion of fatigue life. A better understanding of metal fatigue may be therefore obtained through fractography of small crack growth at near-threshold growth rates. The marker loads in Fig. 34.3 carried low

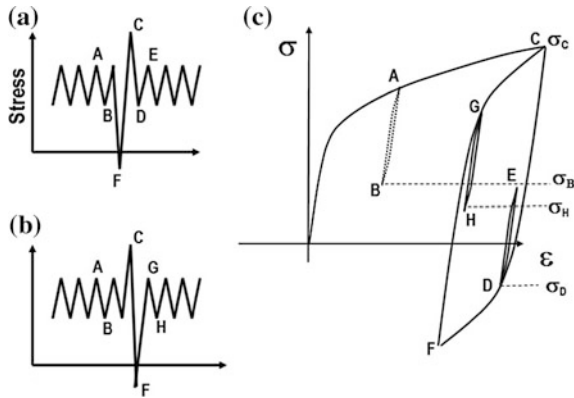


Fig. 34.4 **a, b** Two different load sequences showing identical overload cycle superposed onto baseline cycling but with reversed peak-valley sequence for the overload; **c** computed near-tip stress-strain response to sequences in **(a, b)**. Note how sensitive local stress in baseline cycles is to the introduction of the overload cycle and also to its peak-valley sequence

minimum loads that were designed to squeeze the wake and keep the crack fully open. Therefore, the vast difference in crack extension in individual steps cannot be attributed to closure. The stress ratio over the three steps varied over a small range from 0.73 down to 0.64. Yet, the growth rate in the first step was initially, as much as five times more than in the third step. This difference gradually evens out with increasing crack size. The reasons for such variation may be explained by the schematic in Fig. 34.4 that describes near-tip stress strain response under simple variable amplitude loading.

Two different peak-valley sequences of the major cycle and minor cycles are described in Fig. 34.4a, b and near-tip stress-strain response to these appears in Fig. 34.4c. The size of the major hysteresis loop CF in Fig. 34.4c will depend on the magnitude of loading and crack size. The schematic shows reasonable inelasticity as indicated by the significant sequence-sensitive hysteresis as induced shift in near-tip mean stress for the identical applied cycles AB, ED and GH. We see that introduction of the overload cycle CF causes significant drop in local mean stress in the baseline cycles that follow it, provided the baseline cycles lie on the falling half-cycle CF rather than in the rising half-cycle FC. The difference between the two will diminish with reducing width of the major loop CF. On the other hand, with increasing width of the CF hysteresis loop, baseline cycles lying on the rising half FC will gradually lose the benefit of the tensile overload C. The load sequence in Fig. 34.3b falls into this category and may explain why with increasing crack size, the difference in growth rate between the three steps gradually evens out.

Note that Fig. 34.4 describes crack-tip rather than notch root response. In the event, a tensile overload induces yield at the notch root it will cause a reduction in local (notch root) stress ratio, leading to increased closure [7]. This will also lead to

retarded crack extension until the crack tip grows out of the notch root area. The load sequence in Fig. 34.3b *did not* cause notch root yield.

The data in Fig. 34.4 appear to support the possibility that conditions inducing sensitivity in fatigue limit to mean stress may be the same, as those that induce sequence driven differences in near-threshold crack growth rates. Several other tests involving naturally forming notch root cracks initially growing at near-threshold growth rates yielded evidence similar to the one in Fig. 34.3 [8–10]. This leads to the possibility that the science behind the mean stress effect on fatigue limit may unravel through understanding the effect in near-threshold fatigue crack growth behavior.

34.6 Interfacial Fatigue Cracking Around Secondary Particulates

An unexpected input to this study comes from another work describing how secondary particulates separate from the matrix by interfacial cracking [11, 12]. Figure 34.5 shows typical fractographs from this study that were also obtained under 3-step programmed loading described earlier (see Fig. 34.3b). As secondary particulate separation must have occurred prior to the main fatigue crack approaching their location, the main fatigue crack obviously dissected individual particulate locations, with the by now separated particulate falling out to expose the cavity seen on the fatigue fracture. Reference [12] carries a detailed description of the nature and appearance of these voids.

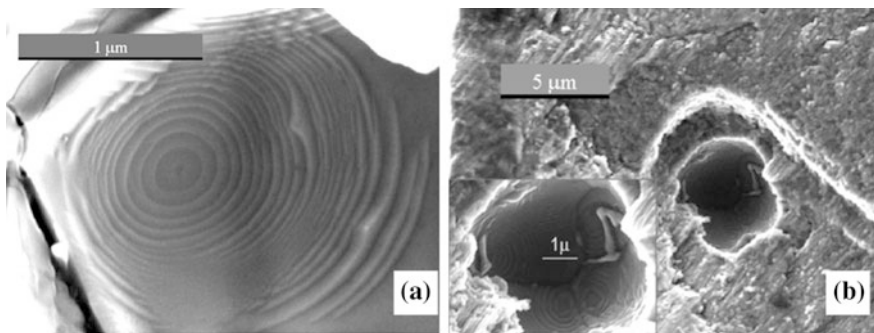


Fig. 34.5 Interfacial cracking of secondary particulates from the matrix under the load sequence shown in Fig. 34.3b. **a** Evenly spaced concentric circles mark the growth of the penny shaped from an initial size of about $0.125\ \mu$ diameter. **b** As the main crack approaches the particulate area, the thin wall separates the two shears along a lower plane causing a step as seen. *Inset* shows zoomed-in view of a number of interfacial cracks that had already separated the particulate from the matrix at the point of merger of void with main crack

Secondary particulates carry the same composition as the matrix but during solidification do not form part of the grain structure. Rather, they precipitate as particulates, typically along grain boundaries. During the rolling process of sheets, these secondary particulates break down into smaller ones and therefore often end up in clusters. The size of the particulates is around $5\ \mu$ while grains can be tens of times larger. Unlike nonmetallic inclusions that are not bonded to the base material, secondary particulates being of the same composition as the matrix are effectively fused with the matrix. During fatigue cycling, regions close to stress concentration as well as those ahead of the crack tip fall into areas of stress gradient. Stress gradient brings with it, inevitable plane strain conditions that in turn effectively impose local hydrostatic stressing. Thus, even if applied cyclic loading is tensile and uniaxial, individual secondary particulates will see cyclic hydrostatic tensile stress. This possibility is supported by the manner the particulates appear to separate from the matrix through interfacial cracking. As seen from Fig. 34.5, the process commences with the formation of penny shaped cracks all around the particulate-matrix interface. Thus, if the particulate was near-cubical in shape, one would see six such cracks. Figure 34.5b shows three. Most secondary particulates appear to segregate along grain boundaries. This is seen from the lines in some cavities demarcating individual grains (see inset in Fig. 34.5b).

Interfacial cracks appear to form almost immediately at the onset of cyclic loading as evident from their large initial size by comparison to the extension in each following programmed step of fatigue cycling. Of interest is their even spacing with increasing crack size, suggesting a fairly constant stress intensity that should not come as a surprise given stress relaxation with increasing crack size under conditions of constant strain (local displacement). The first marker showing growth of penny shaped cracks can be as small as 125 nm in diameter. The systematic and highly reproducible nature of their growth suggests applicability of Fracture Mechanics concepts down to this scale. The marker spacing of this and even smaller magnitude suggests that fatigue crack growth can occur in average increments down to 10^{-9} mm/cycle or less, and do so in a reproducible manner.

Of particular interest is what appears to be remarkably even spacing of the marker bands across the three steps of loading in each programmed block. Apparently, interfacial cracking inside the material is insensitive to change in mean stress of applied cycles! This is in stark contrast with the patterns seen in Fig. 34.3a for a small part-through surface crack. In that case, the difference in growth rates between steps rose with decrease in growth rates. One would have expected that the growth rates of interfacial cracks being even lower, the difference in growth rates between individual steps should be even more striking. There may be two possible explanations for this anomaly. One is the nature of the crack, i.e., interfacial versus surface, and, the other is the total absence of environment in case of the interfacial cracks. The more plausible reason may be that these interfacial cracks grow in ideal vacuum, while surface cracks growing through the matrix are exposed to the atmosphere.

One may note that secondary particulates even if fused with the matrix show a propensity to separate from the matrix when exposed to the environment. Thus, the

well-known mechanism of pitting corrosion in Al–Cu alloys is associated with interfacial environmental cracking leading to the exposed particulate foaling out and leaving behind a pit from which a fatigue crack may initiate.

34.7 Residual Stress—Moderator of Crack-Tip Surface Diffusion Kinetics

It is well known that environment accelerates fatigue crack growth. This is attributed to surface diffusion of hydrogen released by oxidation or hydroxide formation of fresh surface created by crack-tip deformation and extension [13, 14]. However, none of these authors noted the significant role of near-tip stress in moderating crack-tip diffusion kinetics and particularly, the sensitivity of this stress to load history. In unrelated work related to surface diffusion of active species onto ruthenium monolayers, Gsell et al. [15] observed the propensity of active species to congregate at regions of tensile strain and be practically repelled from regions of compressive strain. This underscores the possibility that surface diffusion kinetics of active species is extremely sensitive to elastic stress.

The fatigue crack tip represents the highest possible stress concentration. Obviously, it will also serve as the largest sink for hydrogen atoms potentially released in each rising load half cycle as the crack tip stretches in tension or extends. If indeed at this point, hydrogen atoms can get into crack-tip surface layers of crystalline metals, they may be embrittling the material by inhibiting slip. The crack tip stress-strain response will be largely displacement driven. If surface layers are unable to yield, they will fracture, causing instantaneous microscopic quasi-static crack extension.

34.8 Brittle Micro-fracture (BMF) Model of Near-Threshold Fatigue Crack Growth

Several important possibilities emerge from this model of atmospheric crack extension, some of which were highlighted in earlier work [16]:

- (i) This is a case of surface diffusion. Most metals and alloys are extremely resistant to interstitial diffusion of active species. Therefore, however intense the process may be, surface diffusion will not extend beyond a few atomic layers. This means that with growth rate extending beyond several atomic layers, i.e., say, 10^{-4} mm/cycle, the significance of this phenomenon will recede to vanishing proportions. The operation of this mechanism is effectively restricted to near-threshold fatigue crack growth and to HCF. This possibility is strongly supported by empirical data obtained at different growth rates both from Al-alloy [10] as well as a nickel-base superalloy at elevated

temperature [17]. Both studies indicated that the effect of hysteresis induced near-tip residual stress fades away as crack growth rate increases into the Paris regime.

- (ii) Diffusion kinetics being sensitive to surface strain, will be extremely sensitive to near-tip mean stress along with superposed residual stress. This may well be the most plausible reason why metal fatigue is sensitive to mean stress including residual stress. As was seen in the case of interfacial cracks separating secondary particulates from the matrix inside the material, mean stress and residual stress sensitivity of metal fatigue must recede to vanishing proportions in the absence of environment.
- (iii) Once hydrogen atoms are trapped within surface layers, they cannot be repelled easily. Therefore, the process renders itself to cumulative action. If the surface layers do not fracture in the next rising load half cycle, the probability of them doing so over subsequent cycles keeps increasing. This aspect provides for two important aspects of near-threshold fatigue crack growth. First, the crack need not extend all across the crack front in each cycle. Secondly, the crack front will always tend to stabilize into a smooth and stable shape given the propensity of lagging portions of the front to catch up given their continued embrittlement by diffusion when stationary. And thirdly, diffusion being a cumulative phenomenon, there may be no lower limit on crack growth rate given the possibility that the probability of crack extension in the next cycle is bound to increase with each successive cycle of no-growth, due to progressive, even if slow, crack-tip embrittlement with each successive cycle with no extension.
- (iv) The process of surface diffusion occurs with extremely high speed and can saturate within tens of microseconds. Assuming this must occur during the rising load half cycle, one may expect that the phenomenon in question will operate at cycling frequencies running to hundreds of hertz. However, it is also likely, that at frequencies exceeding several kilohertz, diffusion processes may begin to fall behind the cycling rate, slowly rendering the fatigue process less sensitive or even immune to atmospheric action with frequency increasing into the ultrasonic range. This possibility raises questions about the efficacy of fatigue crack growth testing at very high frequencies in the kilohertz range, such as typical ultrasonic apparatus used in Giga-cycle fatigue (GCF) studies.

The considerations listed above form the basis for the brittle Micro fracture (BMF) model of near-threshold fatigue crack extension [18]. The proposition of this model is rather controversial, given the classical understanding of fatigue crack growth as a slip driven process and the associated suggestion by the well-known Laird model that the fatigue crack extends during the unloading, rather than loading half cycle. The BMF model in contrast pre-supposes initial microscopic crack extension by BMF in Mode I (opening) followed by further crack extension in Mode II (shear). The sequential occurrence of these two in each loading half cycle may in fact serve as the model for striation formation [16].

34.9 Proof by Falsification of BMF Model

Conclusive evidence in support of the suggestion that environmental action may be the root cause for the residual stress effect demands proof by falsification. In search of such evidence, a specially designed experiment was performed using the same three-step programmed load sequence on the same type of test coupon and material as described earlier, but on a test system equipped with a vacuum chamber capable of evacuation down to 10^{-8} torr. The test involved cycling the specimen for a predetermined number of blocks in air, followed by subsequent cycling for another set of blocks in vacuum. This sequence was repeated until the specimen failed. The test took several weeks to complete because evacuation to high vacuum required about 50 h.

The results of the test performed in alternating air-vacuum-air sequence appear to provide conclusive evidence in support of the BMF model (see Fig. 34.6). We can see the expected variation in crack growth rate in air. However, upon switching to vacuum, there is an immediate change in response, leaving crack growth rate constant and insensitive to change in mean stress level. The switch in response being instantaneous rules out the possibility of other mechanisms such as closure playing a role. Any increase in closure would demand crack extension that in turn would have shown up as transitional response. Transient effects are clearly absent in both air-vacuum as well as vacuum-air transition underscoring the possibility that

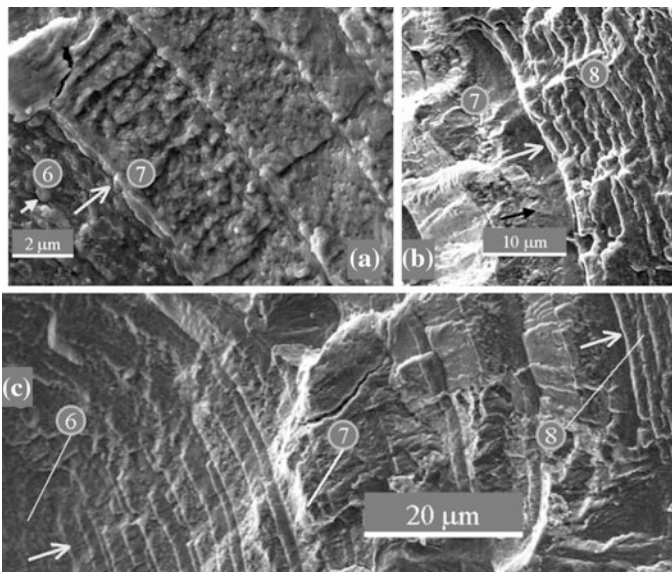


Fig. 34.6 Crack extension under three-step loading in air (7) and in vacuum (6, 8). Equal spacing of bands in vacuum indicates fatigue is insensitive to mean/residual stress due to the absence of active species and appears to represent proof by falsification of the BMF model

one is indeed dealing with crack-tip surface layer effects. By serving as a case of true falsification of a single parameter, namely environment, while keeping all other factors identical including material, specimen and load sequence, this experiment lays to rest any doubts that may have lingered from conclusions emerging from comparison of surface crack data with those of interfacial cracks in the same material.

34.10 Relationship Between ΔK_{th} and Near-Tip Residual Stress

The most significant outcome of the research described above is that (closure free) threshold stress intensity is not a material constant. Rather, it is closely linked to near-tip residual stress. The search for such a relationship required the development of two new methodologies. One is an experimental technique to reproducibly create different near-tip residual stress values and determine the threshold stress intensity associated with the given residual stress values. The second is a technique to analytically determine those near-tip residual stress values. Then, by plotting one against the other, one may be able to arrive at the desired relationship. Such a relationship would carry the prospect of engineering application because service load spectra are typically random in nature, rendering near tip residual stress sensitive to load history. The availability of a relationship between ΔK_{th} and near-tip residual stress, σ^* , would assist estimates of near-threshold crack growth rates under variable-amplitude loading including service load conditions.

Reference [19] describes a study that resulted in the establishment of the relationship between ΔK_{th} and σ^* for 2024-T351 Al-alloy sheet material. The methodology described in the paper may be implemented for any other material and appears to represent the framework for a future ASTM Standard Practice to determine ΔK_{th} that would be useful in engineering application. Figure 34.7a shows the relationship obtained. A set of analytical equations is solved to determine σ^* for each case of loading. ΔK_{th} is determined experimentally through progressive reduction of load range, maintaining constant maximum load. Each data point requires about two million cycles of loading. Testing was performed on a BISS high-frequency test system with specially developed software enabling cycling at 150 Hz to apply one million cycles in about three hours. The control hardware and software permit accurate cyclic loading to within better than 1 % of assigned amplitude with pre-programmed intermittent overloads and underloads of specified number, magnitude and sequence.

There are three distinct regions in Fig. 34.7a. Region I presents relatively low values of ΔK_{th} , associated with high values of local tensile residual stress, σ^* , typical of constant amplitude high stress ratio cycling. The reduced slope of this region may be due to “near saturation” of near-tip diffusion kinetics. Region II is characteristic of ΔK_{th} being very sensitive to change in σ^* , i.e., rate of active species

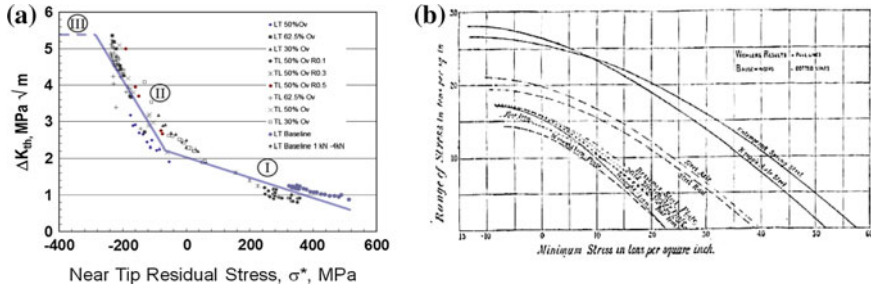


Fig. 34.7 a Relationship between threshold stress intensity and near-tip minimum stress [19]. b Relationship between fatigue limit and minimum stress established by Wohler and Bauschinger [1, 2]

diffusion affecting degree of near-tip embrittlement. Region III characterizes high enough compressive residual stress, σ^* , resulting near total absence of near-tip diffusion. The crack tip in this region behaves the same way as it would in high vacuum.

The relationship between ΔK_{th} and σ^* can be used to explain the fractographic observations made earlier. Thus, the computed values of near-tip residual (minimum) stress for individual baseline cycles in Fig. 34.4 can help explain how fatigue crack extension is affected in these cycles through change in ΔK_{th} as shown schematically by the shift in near-threshold $daldN$ curve in Fig. 34.2. Moreover, the relationship explains the fractographic data in Fig. 34.3.

Figure 34.7b shows the relationship obtained almost 150 years ago between minimum stress and fatigue limit. The curves in Fig. 34.7a, b appear to be similar at least in terms of trends to be expected, suggesting that indeed, the mean stress and residual stress effects in metal fatigue can now be explained using scientific rationale. This is not to suggest that the residual stress effect is entirely environment related. Crack closure is the other mechanism by which residual stress affects the fatigue process. The crack tip stress field is predominantly influenced by stress distribution in the specimen across the immediate vicinity of its tip. Therefore, crack closure for a crack growing out of a notch will be influenced by notch root, rather than applied stress ratio. In the event, a tensile overload is applied on the notched coupon before fatigue cycling, tensile yield at the notch root will result in compressive residual stress upon unloading. During subsequent fatigue cycling under elastic stress, the residual compressive stress will be superposed on the applied mean stress, leading to reduced *effective* stress ratio seen by the fatigue crack and therefore, increased closure. This effect has been demonstrated through electron fractography of fatigue failures of notched coupons subject to prior overloads causing notch root residual stress [7]. Residual stresses can also be left behind by technological processes such as cold hole expansion and shot and now, laser peening which are designed to leave behind beneficial compressive stress and therefore considerably extend fatigue life through reduced effective stress ratio.

Change in effective stress ratio demands distribution of residual stress over a substantial area around the crack tip, to an extent, sufficient to offset the stress field around the crack tip. This will affect fatigue crack growth rate in a manner, similar to that observed by varying stress ratio in a laboratory fatigue crack growth test on a standard coupon. The effect is mechanistic, through moderation of effective crack driving force, ΔK_{eff} , and will be constant and sustained for as long as the residual stresses remain so and can affect the crack tip stress field. This is fundamentally different from near-tip residual stress that is a superposition of three different stresses, any residual stress left in the area prior to the appearance of the crack, stress accruing from the applied load cycle and most significantly, the residual stress from hysteretic near-tip stress-strain response to prior cyclic loading. The last is the most significant because the crack-tip being a singularity will always see cyclic inelastic response even under extremely small applied load excursions.

Hysteresis will be absent in notch root stress-strain response unless local elastic stress excursion exceeds twice the yield stress of the material. Engineering practice seldom permits such large variation in applied loads. Experience shows however, that notch fatigue response is load sequence sensitive, even under fully elastic conditions. This paradox is readily addressed by considering notch root *crack-tip* response that will be *always* cyclic inelastic. This may underscore the significance of understanding the science behind the residual stress effect in metal fatigue and its synergy with the better-known crack closure phenomenon. The new understanding opens up the possibility of embedding into analytical models, the combined action of the two independent and vastly different mechanisms, crack closure that moderates crack tip driving force and near-tip residual stress that moderates crack-tip resistance to environment enhanced micro-fracture.

34.11 Concluding Remarks

The phenomenon of surface diffusion of active species is common to all engineering metals and metallic alloys. By virtue of the very nature of the phenomenon, this applies to practically all applications that involve cyclic loading conditions including structures, machines and transducers including miniaturized solutions such as MEMS. Any such detail is likely to be restricted in service lifetime by a number of variables, of which, metal fatigue is of major concern. Given the very nature of the phenomenon of surface diffusion and of metal fatigue including fatigue crack growth, it is very likely that for each material and operational environment, there will exist a relationship whose shape will be similar to the one in Fig. 34.7a. Future work is recommended leading to the adoption of a standard laboratory practice to obtain the relationship between ΔK_{th} and σ^* .

References

1. Anon., Wohler's Experiments on the "Fatigue" of Metals, Engineering, 199–441 (1871)
2. J. Bauschinger, On the change of the elastic limit and strength of iron and steel by tension and compression, by heating and cooling and by often repeated loading. Technical Report, Munich Technical University, Munich, Germany (1886). (in German)
3. W. Ramberg, W.R. Osgood, Description of stress-strain curves by three parameters. Technical Report No. 902, National Advisory Committee for Aeronautics, Washington, D.C. (1943)
4. *Aircraft Structural Integrity Program, Department of Defense Design Handbook*, MIL-HDBK-1530A(USAF) 24 Jan 2002, WPAFB, OH, USA (2002)
5. W. Elber, *The Significance of Fatigue Crack Closure, ASTM STP 486* (ASTM International, Philadelphia, PA, 1971), pp. 230–242
6. A.K. Vasudevan, K. Sadananda, N. Louat, Mater. Sci. Eng. **188**(1–2), 1 (1994)
7. K. Anandan, R. Sunder, Int. J. Fatigue **9**, 217 (1987)
8. R. Sunder, Effect of periodic overloads on fatigue thresholds in Al-Alloys, in *Fatigue and Fracture Mechanics: 34th Volume, ASTM STP 1461*, ed. by S.R. Daniewicz, J.C. Newman, K.H. Schwalbe, ASTM International, West Conshohocken, PA, 557 (2005)
9. R. Sunder, Fractographic reassessment of the significance of fatigue crack closure. *Fatigue and Fracture Mechanics: 34th Volume, ASTM STP 1461*, ed. by S.R. Daniewicz, J.C. Newman, K.-H. Schwalbe, ASTM International, West Conshohocken, PA, 22 (2005)
10. R. Sunder, Int. J. Fatigue **27**, 1494 (2005)
11. R. Sunder, Adv. Mater. Processes **159**(4), 41 (2001)
12. R. Sunder, W.J. Porter, N.E. Ashbaugh, Fatigue Fract. Eng. Mater. Struct. **25**, 1015 (2002)
13. C.Q. Bowles, The Role of Environment, Frequency and Wave Shape during Fatigue Crack Growth of Aluminum Alloys, Ph.D. thesis, Report No. LR-270. Delft University of Technology, Delft, The Netherlands (1978)
14. J. Petit, G. Henaff, C. Sarrazin-Baudoux, Mechanisms and modeling of near-threshold fatigue crack propagation, fatigue crack growth thresholds, endurance limits and design. *ASTM Spec. Tech. Publ.*; J. C. Newman, Jr., R. S. Piascik (eds.), **1372**, American Society for Testing and Materials, West Conshohocken, PA, 2000
15. M. Gsell, P. Jakob, D. Menzel, Science **280**, 717 (1998)
16. R. Sunder, J. ASTM Int. **9**(1), Paper ID JAI103940 (2012)
17. N.E. Ashbaugh, W.J. Porter, A.H. Rosenberger, R. Sunder, Environment-related load history effects in elevated temperature fatigue of a nickel-base super-alloy. Proc., Fatigue 2002, Stockholm, June 2–7, EMAS (2002)
18. R. Sunder, Fatigue Fract. Eng. Mater. Struct. **28**(3), 289 (2005)
19. R. Sunder, ASTM J. **4**(2), 105 (2015)

Chapter 35

Numerically Analytical Modeling the Dynamics of a Prismatic Body of Two- and Three-Component Materials

L.A. Igumnov, S.Yu. Litvinchuk, A.N. Petrov and A.A. Ipatov

Abstract Wave propagation in fully and partially saturated porous media is studied, using the example of the problem of two-component and three-component media having, respectively, four and five base functions for describing the wave process. The arising system of partial differential equations and the boundary conditions are written in terms of Laplace transforms for a time variable. To construct the original of the analytical solution, a stepped method of numerically inverting Laplace transform is used. Computations were done for various values of the saturation coefficients. To solve the problem of the effect of an axial force in the form of Heaviside function in time upon the end of a prismatic poroelastic cantilever beam in 3-D formulation, the boundary-element method is used. Boundary integral equations of the direct approach are written in explicit time. The boundary-element model is constructed using a time-step procedure. Along boundary elements, correlated approximation is applied. Discrete analogues are obtained by applying the collocation method to a regularized boundary integral equation. A specific feature of a wave process in saturated porous media is the presence of three types of waves: in contrast with the elastic case, there appears a slow wave, which can considerably change the wave picture. To demonstrate the effect of a slow wave arising, variation of the permeability coefficient is used. The appearance of the slow wave effect is observed on the pore pressure curves: for the pore pressure of a liquid filling two peaks of the amplitude are observed.

L.A. Igumnov · S.Yu. Litvinchuk · A.A. Ipatov
Research Institute for Mechanics, Lobachevsky State University of Nizhni Novgorod,
Nizhny Novgorod, Russia

A.N. Petrov (✉)
Research and Education Center “Materials”, Don State Technical University,
Rostov-on-Don, Russia
e-mail: andrey.petrov@mech.unn.ru

35.1 Introduction

Research of wave propagation processes in saturated porous continua began from the works of Y.I. Frenkel and M. Biot . L.Y. Kosachevsky in 1959 showed that Frenkel's and Biot's models rely on the same stress-strain relations but the latter is of a greater generality. After that waves in saturated porous continua have been studied by C. Zwikker and C.W. Kosten, J. Geertsma and D.C. Smith, P. P. Zolotaryov, V.N. Nikolayevsky, V.P. Stepanov, L.M. Doroginitskaya, C. McCann and D.M. McCann, S.H. Yakubov, A.A. Gubaydullin etc., but two classical Biot's works are considered the most influential. Common state of the art can be found in works of R. de Boer , M. Schanz, V.N. Nikolayevsky . Works of T.I. Belyankova, V.V. Kalinchuk, S. Diebels, W. Ehlers contain an overview of Biot's theory as well as other approaches to porous continua modeling.

Biot's model is based on the description of how two phases—porous elastic skeleton and gas or liquid filler—interact. Historically Biot's theory was the first model to predict all three possible types of waves in porous continuum: fast shear wave, fast and slow compression waves. Both fast waves are in their nature close to the ones of elastic continuum, and slow compression wave presence is the principal difference between elastic and poroelastic continua. This wave is caused by transfer of pore filler particles with respect to the skeleton. Ignoring the slow wave leads to serious inaccuracies in estimation of fast waves damping.

There are two major approaches to dynamic processes modeling by means of BEM: solving BIE system directly in time domain [1] or in Laplace or Fourier domain followed by the respective transform inversion [2]. Traditional stepping schemes with spline approximation in scope of the first approach require fundamental solutions in time what severely restricts their usage. Often, it is only possible to construct fundamental solution matrices in Laplace or Fourier domain. Thus first BEM formulations for Biot's poroelastodynamics, published by G.D. Manolis and D.E. Beskos, employ Laplace transform.

Formulation in time domain has been developed in [3] basing on analytical inversion of Laplace transform for fundamental solutions. The main shortcoming of the approach is again the demand of fundamental solutions in time. They exist for quasi-static problems of poro- and visco-elasticity, but are quite cumbersome; damping effects cannot be accounted at all. Moreover, the methodology is characterized by significant computing costs and low stability rate. In 1988, C. Lubich introduced brand of new Convolution Quadrature Method (CQM) [4, 5]. Now it is widely applied in construction of time-step boundary element schemes on the base of fundamental solutions in Laplace domain [6, 7]. In this chapter, a boundary element scheme based on the stepping method for Laplace transform numerical inversion is considered.

35.2 Problem Formulation

Biot’s saturated poroelastic material model is used for description of porous materials [6]. Saturated poroelastic continuum assumes to be a two-phase continuum consisting of an elastic skeleton and compressible fluid or gas filler. Saturation means $V = V^f + V^s$ where V is the overall volume of the considered body, V^f is the summary pore (filler) volume, V^s is the volume of the elastic skeleton. The filler can seep through the pores freely; closed pores are assumed to be a part of the skeleton.

There are several Biot’s theory formulations distinguished by the number of unknowns: three skeleton displacements plus pore pressure or three filler displacements along with the skeleton ones [8, 9]. However, in 1987 G. Bonnet showed that four components are sufficient for saturated porous continuum description [14]. Boundary-value problem for full Biot’s model of linear saturated poroelastic continuum in Laplace domain in terms of four unknowns (skeleton displacements \bar{u}_i and pore pressure \bar{p}) takes the following form [6]:

$$\begin{aligned}
 G\bar{u}_{i,jj} + \left(K + \frac{G}{3} \right) \bar{u}_{j,ij} - (\alpha - \beta)\bar{p}_{,i} - s^2(\rho - \beta\rho_f)\bar{u}_i &= -\bar{F}_i, \\
 \frac{\beta}{s\rho_f}\bar{p}_{,ii} - \frac{\phi^2 s}{R}\bar{p} - (\alpha - \beta)s\bar{u}_{i,i} &= -\bar{a}, \quad x \in \Omega, \\
 \bar{u}'(x, s) = \bar{u}', \quad x \in \Gamma^u, \quad \bar{u}' &= (\bar{u}_1, \bar{u}_2, \bar{u}_3, \bar{p}), \\
 \bar{t}'_n(x, s) = \bar{t}'_n, \quad x \in \Gamma^\sigma, \quad \bar{t}' &= (\bar{t}_1, \bar{t}_2, \bar{t}_3, \bar{q}),
 \end{aligned}
 \tag{35.1}$$

where Γ^u denotes Dirichlet boundary and Γ^σ denotes Neumann boundary, G, K are the elastic moduli, $\phi = V^f/V$ is the porosity, \bar{F}_i, \bar{a} are the bulk body forces,

$$\beta = \frac{\kappa\rho_f\phi^2 s}{\phi^2 + s\kappa(\rho_a + \phi\rho_f)}, \alpha = 1 - \frac{K}{K_s} \text{ and } R = \frac{\phi^2 K_f K_s^2}{K_f(K_s - K) + \phi K_s(K_s - K_f)}$$

are constants reflecting interaction between the skeleton and filler, κ is the permeability, ρ, ρ_a, ρ_f are the material density, apparent mass density and filler density, respectively, K_s, K_f are the elastic bulk moduli of the skeleton and filler, respectively; $\rho_a = C\phi\rho_f$, presenting the apparent mass density, is an imaginary mass density introduced in [8] to describe dynamic interaction between the skeleton and filler phases. The coefficient C depends on the pores geometry and excitation frequency. G. Bonnet and J.-L. Auriault measured $C = 0.66$ for low-frequency excitation and a system of spherical pores distributed right up to each other [10].

BIE system in terms of elastic skeleton displacements and pore pressure can be represented in time domain only in conditions of $\kappa \rightarrow \infty$. This model corresponds to the filler passing through pores without friction. Sometimes incompressible Biot’s model implying $\alpha = 1$ and $R \rightarrow \infty$ is applied; in this case pore pressure is completely defined by elastic skeleton deformations and makes no degree of freedom anymore.

The governing equations of partially saturated poroelasticity in the Laplace domain with five unknowns (solid displacements u_i , the pore wetting fluid pressure p^w , and the pore non-wetting fluid pressure p^a) are given by [11]

$$\begin{aligned}
 G\bar{u}_{i,jj} + \left(K + \frac{G}{3}\right)\bar{u}_{j,ij} - (\rho - \beta S_w \rho_w - \gamma S_a \rho_a) s^2 \bar{u}_i - (\alpha - \beta) S_w \bar{p}_{,i}^w + (\alpha - \gamma) S_a \bar{p}_{,i}^a &= -\bar{F}_i, \\
 -(\alpha - \beta) S_w s \bar{u}_{i,i} - (\zeta - S_{aa} S_w + S_u) s \bar{p}^a + \frac{\beta S_w}{\rho_w s} \bar{p}_{,ii}^w - (\zeta S_{ww} S_w + \frac{\phi}{K_w} S_w - S_u) s \bar{p}^w &= -\bar{I}^w, \\
 -(\alpha - \gamma) S_a s \bar{u}_{i,i} - (\zeta S_{ww} + S_u) s \bar{p}^w + \frac{\gamma S_a}{\rho_a s} \bar{p}_{,ii}^a - (\zeta S_{aa} + \frac{\phi}{K_a} S_a - S_u) s \bar{p}^a &= -\bar{I}^a, \quad x \in \Omega \\
 \bar{u}'(x, s) = \bar{u}', \quad x \in \Gamma^u, \quad \bar{u}' = (\bar{u}_1, \bar{u}_2, \bar{u}_3, \bar{p}^a, \bar{p}^w), \\
 \bar{t}'_n(x, s) = \bar{t}'_n, \quad x \in \Gamma^\sigma, \quad \bar{t}' = (\bar{t}_1, \bar{t}_2, \bar{t}_3, \bar{q}^a, \bar{q}^w),
 \end{aligned} \tag{35.2}$$

where K_w and K_a are the bulk moduli of the fluid, ϕ is the porosity, \bar{F}_i , \bar{I}^w , \bar{I}^a are the bulk body forces. The bulk density is denoted by $\rho = (1 - \phi)\rho_s + \phi S_w \rho_w + \phi S_a \rho_a$, where ρ_s is the density of the solid, ρ_w is the wetting fluid density, ρ_a is the non-wetting fluid density. The saturation degrees are defined as the ratios of the volume occupied by the fluid V_w or V_a to the void volume, i.e. it holds

$$S_w = \frac{V_w}{V_{void}}, \quad S_a = \frac{V_a}{V_{void}}, \quad S_w + S_a = 1.$$

The following abbreviations:

$$\begin{aligned}
 \zeta &= \frac{\alpha - \phi}{K_s}, \quad S_{ww} = S_w - \vartheta(S_w - S_{rw}), \\
 S_{aa} &= S_a + \vartheta(S_w - S_{rw}), \\
 S_u &= -\frac{\vartheta(S_{ra} - S_{rw})}{p^d} \left(\frac{S_w - S_{rw}}{S_{ra} - S_{rw}} \right)^{\frac{\vartheta+1}{\vartheta}}
 \end{aligned}$$

are introduced, where S_{rw} is the residual wetting fluid saturation and S_{ra} is the non-wetting fluid entry saturation. The symbol p^d means the non-wetting fluid entry pressure, ϑ is the pore distribution index while the value of ϑ lies between 0.2 and 3, usually. The symbols β and γ are the Laplace parameter dependent variables expressed as

$$\beta = \frac{\kappa_w \phi \rho_w s}{\phi S_w + \kappa_w \rho_w s}, \quad \gamma = \frac{\kappa_a \phi \rho_a s}{\phi S_a + \kappa_a \rho_a s},$$

here κ_w and κ_a the phase permeability of the wetting and the non-wetting fluid given by $\kappa_w = K_{rw} k / \eta_w$ and $\kappa_a = K_{ra} k / \eta_a$, respectively, where K_{rw} and K_{ra} denote the relative values of fluid phase permeability, k denotes the intrinsic fluid permeability, η_w and η_a are the viscosities of the fluid. To evaluate relative values of

phase permeability, the following equations are used $K_{rw} = S_e^{(2+3\vartheta)/\vartheta}$ and $K_{ra} = (1 - S_e)^2 [1 - S_e^{(2+\vartheta)/\vartheta}]$, where S_e denotes the effective wetting fluid saturation degree given by

$$S_e = \begin{cases} 0, & S_w \leq S_{rw}; \\ \frac{S_w - S_{rw}}{S_{ra} - S_{rw}}, & S_{rw} < S_w < S_{ra}; \\ 1, & S_w \geq S_{ra}. \end{cases}$$

For the extreme case $S_w = 0$, (35.2) turn out to state simple elasticity problem, and for the extreme case $S_w = 1$ —saturated poroelasticity problem.

35.3 BEM Application

Boundary-value problem (35.1) can be reduced to the following BIE [6, 12, 13]:

$$\alpha_\Omega \bar{u}_k(x, s) + \int_\Gamma (\tilde{T}_{ik}(x, y, s) \bar{u}_i(y, s) - \tilde{T}_{ik}^0(x, y, s) \bar{u}_i(x, s) - \tilde{U}_{ik}(x, y, s) \bar{t}_i(y, s)) d\Gamma = 0,$$

$$(x \in \Gamma), \quad \bar{t} = (\bar{t}_1, \bar{t}_2, \bar{t}_3, \bar{q})^T, \quad \bar{u} = (\bar{u}_1, \bar{u}_2, \bar{u}_3, \bar{p})^T,$$

where $\tilde{U}(x, s)$, $\tilde{T}(x, s)$ are the fundamental and singular solutions, respectively, $\tilde{T}^0(x, s)$ contains isolated singularities.

To approximate boundary of a piecewise homogeneous body, a set of quadrangular and triangular elements is used, where triangular elements are considered singular quadrangular. Quadrangular elements help to obtain a higher precision as compared to fully triangular approximation. Every boundary element is mapped to a reference one (canonical square $\xi = (\xi_1, \xi_2) \in [-1, 1]^2$ or triangle $0 \leq \xi_1 + \xi_2 \leq 1, \xi_1 \geq 0, \xi_2 \geq 0$) with the help of the formula:

$$y_i(\xi) = \sum_{l=1}^8 N^l(\xi) y_i^{\beta(k,l)}, \quad i = 1, 2, 3,$$

where $\beta(k, l)$ is the global node number, l is the local node number in element k , $N^l(\xi)$ are the shape functions. Boundary functions are interpolated by a subset of geometrical grid nodes. Local approximation of generalized boundary displacements and tractions follows the Goldshteyn’s displacement-stress matched model [13]. This means that generalized displacements are approximated by bilinear element and constant tractions.

After applying collocation method on the set of boundary functions approximation nodes, the following system of linear equations is obtained per each homogeneous region of the considered compound body:

$$\frac{1 - \alpha_\Omega}{2} u_i^m + \sum_{k=1}^N \sum_{l=1}^4 A_{ij}^{m,k,l} u_j^{\gamma(k,l)} = \sum_{k=1}^{N_1} B_{ij}^{m,k} t_j^k - \sum_{k=1}^{N_2} \sum_{l=1}^4 D_{ij}^{m,k,l} (u_j^{\gamma(k,l)} - u_j^{\bar{\gamma}(\bar{k},l)}),$$

$$\frac{1 - \alpha_\Omega}{8} u_i^m + \sum_{k=1}^N \sum_{l=1}^4 A_{ij}^{m,k,l} u_j^{\gamma(k,l)} = \sum_{k=1}^{N_1} B_{ij}^{m,k} t_j^k - \sum_{k=1}^{N_2} \sum_{l=1}^4 D_{ij}^{m,k,l} (u_j^{\gamma(k,l)} - u_j^{\bar{\gamma}(\bar{k},l)}),$$

$N = N_1 + N_2.$

The first equation here is written in generalized displacements approximation nodes, the second one—in generalized tractions approximation nodes. The first right-side term in the both equations relates to boundary elements with no contact, the second one satisfies the conditions of contact between elements k and \bar{k} belonging to different regions; coefficients A , B and D compute with the help of the following formulae:

$$A_{ij}^{m,k,l} = \int_{-1}^1 \int_{-1}^1 \left[R^l(\xi) T_{ij}(x^m, y^k(\xi), s) - \delta_{\gamma(k,l)} T_{ij}^0(x^m, y^k(\xi)) \right] J^k(\xi) d\xi_1 d\xi_2,$$

$$B_{ij}^{m,k} = \int_{-1}^1 \int_{-1}^1 U_{ij}(x^m, y^k(\xi), s) J_k(\xi) d\xi_1 d\xi_2,$$

$$D_{ij}^{m,k,l} = \int_{-1}^1 \int_{-1}^1 R^l(\xi) U_{ij}(x^m, y^k(\xi), s) J_k(\xi) \alpha_j^{\bar{\gamma}}(y^k(\xi)) d\xi_1 d\xi_2,$$

where s is the Laplace transform parameter. The integrals are calculated using Gaussian quadrature on the elements containing no singularities. Once an element contains singularity, the singularity decreasing or eliminating algorithm is used [14]. An adaptive integration algorithm is used: the order of Gaussian quadrature in an element is chosen by the satisfaction of the prescribed precision if possible, otherwise the element is recursively subdivided to smaller elements for integration.

35.4 Laplace Transform Inversion

Time-step method for Laplace transform numerical inversion is similar to CQM, but whereas CQM is based on the convolution theorem. It is based on the integration theorem, hence dedicated to the calculation of the original function integral.

In order to get as a result the original function $f(t)$ such as $f(0) = 0$ from $\bar{f}(s)$, we need to apply the theorem to its derivative:

$$f(t) = \int_0^t f'(\tau)d\tau = \frac{1}{2\pi i} \lim_{R \rightarrow \infty} \int_{c-iR}^{c+iR} \bar{f}(s)s \int_0^t e^{s\tau} d\tau ds = \dots$$

Following the theorem, the integral can be found as (basing on [4–6, 15]):

$$f(0) = 0, \quad f(n\Delta t) = \sum_{k=1}^n \omega_k(\Delta t), \quad n = 1, \dots, N,$$

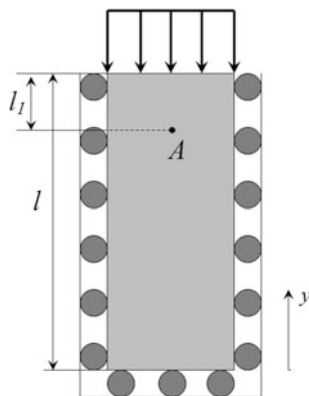
$$\omega_n(\Delta t) = \frac{R^{-n}}{L} \sum_{l=0}^{L-1} \bar{f}(s) s e^{-in\varphi}, \quad s = \frac{\gamma(z)}{\Delta t}, \quad z = \text{Re}^{i\varphi}, \quad \varphi = 2\pi \frac{l}{L}.$$

Here R is the radius of the analyticity region for $\bar{f}(\gamma(z)/\Delta t)$ and $\gamma(z)$ is the characteristic function for the linear multistep method applied to the Cauchy problem arising within the integral evaluation. Backward differentiation (BDF) based methods of order ≤ 6 are applicable in scope of this solution scheme. For BDF-2 we have $\gamma(z) = 3/2 - 2z + z^2/2$. Several modifications of the method can be derived from different ways to calculate $\omega_n(\Delta t)$.

35.5 Slow Compression Wave in 1d Case

An effect of slow compression wave appearance in poroelastic 1d column of length $l = 9$ m under axial thrust $F = 1$ N/m² is considered (Fig. 35.1). Material properties of the column are $K = 4.8 \cdot 10^9$ N/m², $G = 7.2 \cdot 10^9$ N/m², $\rho = 2,458$ kg/m³, $\phi = 0.19$, $K_s = 3.6 \cdot 10^{10}$ N/m², $\rho_f = 1,000$ kg/m³, $K_f = 3.3 \cdot 10^9$ N/m². The

Fig. 35.1 1d column



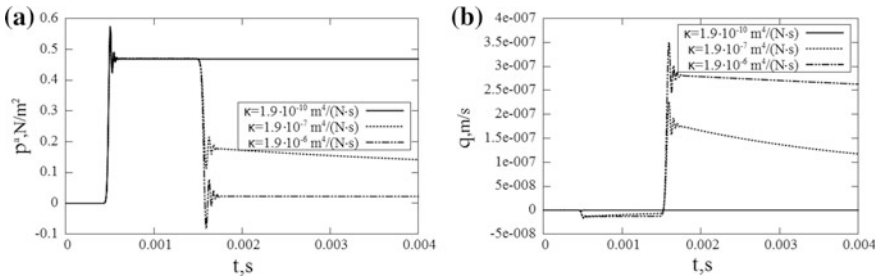


Fig. 35.2 Pore pressure (a) and pore flux (b) at point A

parameters $L = 20,000$, $N = 2,000$, $\Delta t = 2 \cdot 10^{-6}$ s and $R = 0.997$ are used in calculations. The results for pore pressure and flux responses at point A ($l_1 = 1.5$ m) in a time domain are shown in Fig. 35.2.

Figures 35.2 and 35.3 demonstrate the effect of slow wave appearance in porous continuum for large permeability coefficient value (0.00155 s). As compared to the study [6, 16], here the effect is shown by pore flux as well as pore pressure.

35.6 Slow Compression Wave in 3d Case

A problem of frontal thrust $f(t) = 1 \text{ N/m}^2$ to 3d poroelastic column $3 \text{ m} \times 1 \text{ m} \times 1 \text{ m}$ with other fixed front is considered (Fig. 35.6). The lateral faces are traction-free but as well transverse displacements u_1 and u_2 are prohibited. Pore flux vanishes everywhere except the loaded front where zero pore pressure is assumed. Axial displacement u_3 and pore pressure p are observed at points A and B, and due to an imaginary boundary at the center of the column. The problem is analogous to one-dimensional, so 1d analytical solutions are applicable here. Material properties are the same as for the previous problem. The problem is solved with the help of time-step method with $L = 1000$, $N = 250$; a mesh of 504 boundary elements is chosen. Figures 35.3, 35.4, 35.5 and 35.6 show the results of slow compression wave appearance modeling, depending on the permeability coefficient.

An influence of the porous permeability on the slow compression wave appearance ($t = 0$ and $t \approx 0.0062$ s for point A, $t \approx 0.0031$ s and $t \approx 0.0093$ s for point B, and $t \approx 0.00155$ s, $t \approx 0.00465$ s and $t \approx 0.00775$ s for the central point) is shown subsequent to [6, 16]. Whereas works [6, 16] only account for 1d analytical solution for displacements and pore pressure, here pore pressure and responses are numerically built for 3d case. Corresponding 1d numerical-analytical solutions are also added for comparison.

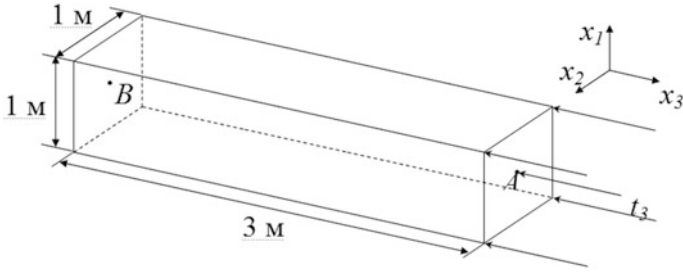


Fig. 35.3 3d column

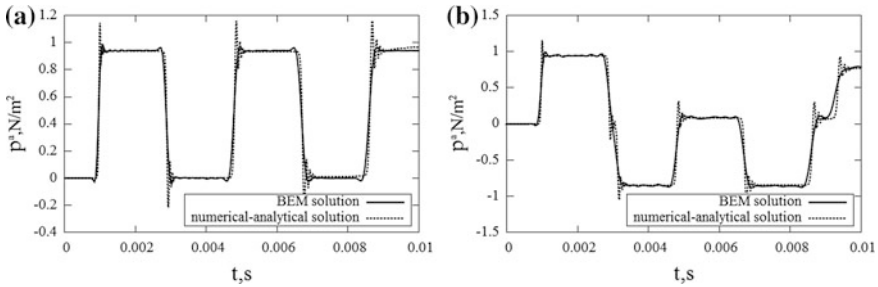


Fig. 35.4 Pore pressure at point B for case $\kappa = 1.9 \cdot 10^{-10} \text{m}^4/(\text{Ns})$ (a) and $\kappa = 1.9 \cdot 10^{-6} \text{m}^4/(\text{Ns})$ (b)

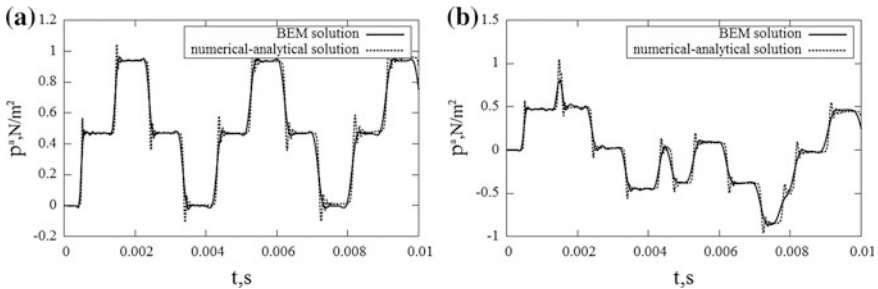


Fig. 35.5 Pore pressure at central point for case $\kappa = 1.9 \cdot 10^{-10} \text{m}^4/(\text{Ns})$ (a) and $\kappa = 1.9 \cdot 10^{-6} \text{m}^4/(\text{Ns})$ (b)

35.7 1d Partially Saturated Poroelastic Column

Assuming the values $F = 1 \text{ N/m}^2$ and $l = 10 \text{ m}$, the pore pressures p^w , p^a at the clamped end and displacement u_y at the other end are calculated with varying saturation degree (Fig. 35.1). The pore size distribution index ϑ is equal to 1.5, the

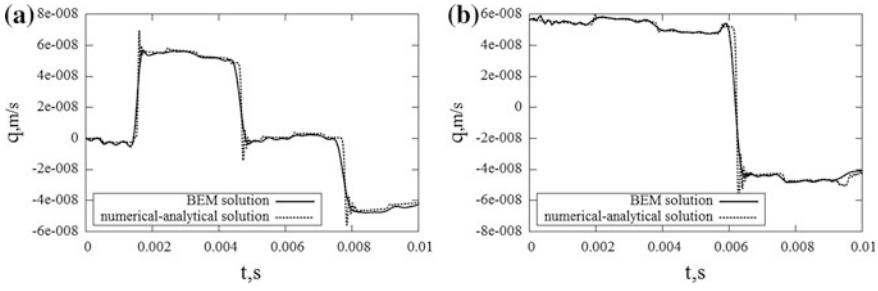
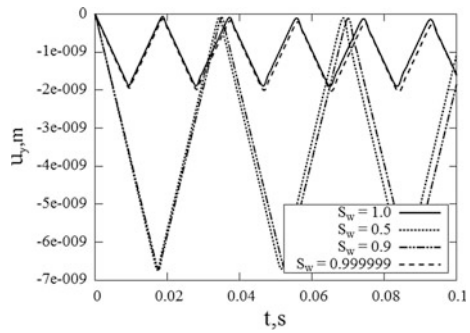


Fig. 35.6 Pore flux at the central point (a) and point A (b) for case $\kappa = 1.9 \cdot 10^{-6} \text{ m}^4/(\text{Ns})$

Fig. 35.7 Displacement at the top of the column for different water saturation



residual water saturation S_{rw} is equal to 0, and the air entry saturation S_{ra} is equal to 1. The column is made of Massilon sandstone with the following properties: $K = 1.02 \cdot 10^9 \text{ N/m}^2$, $G = 1.44 \cdot 10^9 \text{ N/m}^2$, $\phi = 0.23$, $\rho_s = 2,650 \text{ kg/m}^3$, $\rho_w = 997 \text{ kg/m}^3$, $\rho_a = 1.10 \text{ kg/m}^3$, $K_s = 3.55 \cdot 10^{10} \text{ N/m}^2$, $K_w = 2.25 \cdot 10^9 \text{ N/m}^2$, $K_a = 1.10 \cdot 10^5 \text{ N/m}^2$, $\kappa = 2.5 \cdot 10^{-12} \text{ m}^2$, $\eta_w = 1.0 \cdot 10^{-3} \text{ N s/m}^2$, $\eta_a = 1.8 \cdot 10^{-5} \text{ N s/m}^2$.

The parameters $L = 20,000$, $N = 2,000$, $\Delta t = 5 \cdot 10^{-6} \text{ s}$ and $R = 0.997$ are used in calculations. The displacement at the top of the column is displayed in Fig. 35.7 for different water saturation. For the nearly saturated case, $S_w = 0.99999$, the results are in good agreement with those of the saturated case. For smaller water saturation, larger displacements and slower wave speed are observed. The pore water pressure of the nearly saturated case $S_w = 0.99999$ is very close to that saturated case as displayed in Fig. 35.8. For smaller water saturation, the pore water pressure is very low. Similar results are found for the pore air pressure. By decreasing the saturation degree, the pore air pressure increases (Fig. 35.9).

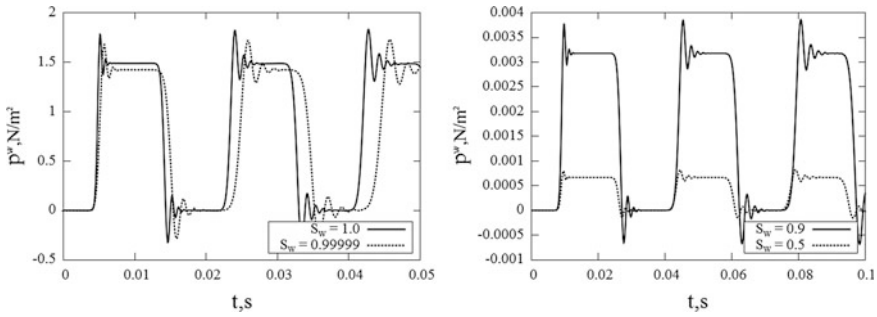


Fig. 35.8 Pore water pressure at the bottom of the column for different water saturation

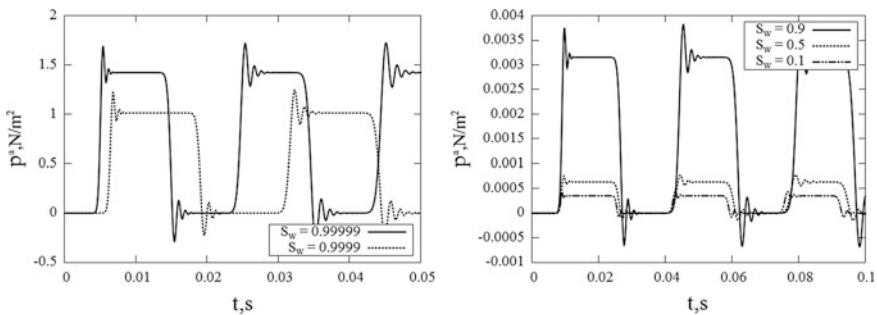


Fig. 35.9 Pore air pressure at the bottom of the column for different water saturation

35.8 Conclusions

In this chapter, the equation system of poroelasticity is written, and boundary-value problem is considered in Laplace domain. The full Biot’s model is chosen to describe poroelastic material properties. The boundary integral equations of poroelasticity with boundary element approach are present, and numerical inversion of Laplace transform, based on step method is used. The problem of poroelastic rod with applied axial force is solved by numerically analytical approach, and an effect of slow dilatational wave in porous media is demonstrated. The problem of poroelastic prismatic solid with one clamped end and applied load to other end is solved. An effect of slow dilatational wave is shown in case of poroelastic prismatic solid. The results obtained by numerical modeling are compared with numerically analytical solutions. The problem of axial force action on partly-saturated poroelastic rod is considered; displacement and pore pressure responses in cases of different values of media saturation coefficient are obtained.

Acknowledgments The work was supported by RSCF under grant 15-19-10056.

References

1. W.J. Mansur, A time-stepping technique to solve wave propagation problems using the boundary element method, PhD thesis, University of Southampton (1983)
2. T.A. Cruze, F.J. Rizzo, *J. Math. Anal. Appl.* **22**(1), 244 (1968)
3. J. Chen, G.F. Dargush, *Int. J. Solids Struct.* **32**(15), 2257 (1995)
4. C. Lubich, *Numer. Math.* **52**, 129 (1988)
5. C. Lubich, *Numer. Math.* **52**, 413 (1988)
6. M. Schanz, *Wave Propagation in Viscoelastic and Poroelastic Continua* (Springer, Berlin, 2001)
7. M. Schanz, H. Antes, *Porous Media: Theory, Experiments and Numerical Applications*, ed. by W. Ehlers, J. Bluhm (Springer, Berlin, 2002), p. 383
8. C. Lubich, A. Ostermann, *Math. Comput.* **60**, 105 (1993)
9. M.P. Calvo, E. Cuesta, C. Palencia, *Numer. Math.* **107**, 589 (2007)
10. L. Banjai, M. Messner, M. Schanz, *Comput. Methods Appl. Mech. Eng.* **245–246**, 90 (2012)
11. L. Banjai, M. Schanz, *Fast Boundary Element Methods in Engineering and Industrial Applications*, ed. by U. Langer (Springer, Berlin, 2012), p. 145
12. L. Banjai, C. Lubich, J.M. Melenk, *Numer. Math.* **119**, 1 (2011)
13. M.A. Biot, *J. Acoust. Soc. Am.* **28**(2), 168 (1956)
14. G. Bonnet, *J. Acoust. Soc. Am.* **82**(5), 1758 (1987)
15. G. Bonnet, J.-L. Auriault, *Physics of Finely Divided Matter*, ed. by N. Boccara, M. Daoud (Springer, Berlin, 1985), p. 306
16. P. Li, M. Schanz, *Geophys. J. Int.* **53** (2011)

Chapter 36

Boundary-Element Modeling of Three-Dimensional Anisotropic Viscoelastic Solids

L.A. Igumnov and I.P. Markov

Abstract On the base of the elastic-viscoelastic correspondence principle, the Laplace domain direct boundary element approach for the three-dimensional transient problems of the anisotropic viscoelasticity is present in this chapter, and its validity and accuracy is shown through numerical examples. Considered materials can have arbitrary degree of anisotropy. The anisotropic fundamental solutions cannot be expressed in an explicit closed form and in the most general case require a numerical evaluation of a double integral. To improve the efficiency of the formulation a special approximation technique is employed.

36.1 Introduction

Since the pioneering works of Rizzo [1], Cruse [2], Rizzo and Shippy [3], Cruse and Rizzo [4] the Boundary Element Method (BEM) has become a well-recognized and highly accurate numerical method for solving static and dynamic boundary value problems of linear elasticity.

Ever-growing use of new materials that exhibit anisotropic behavior of mechanical properties (e.g. in composites) called for developing an effective boundary element techniques for transient analysis of the problems which involve such materials [5, 6]. In the recent decades, several boundary element formulations that take into account viscoelastic behavior of materials were proposed: BEM in Laplace domain [7, 8], time-domain BEM [9] and Convolution Quadrature BEM (CQ-BEM) [10].

Implementation of the conventional direct BEM formulation requires the dynamic fundamental solutions (Green's functions) and their spatial derivatives. For the general anisotropic elastic and viscoelastic materials, Green's functions are

L.A. Igumnov · I.P. Markov (✉)

Research Institute for Mechanics, Lobachevsky State University of Nizhni Novgorod, Nizhny Novgorod, Russia
e-mail: teanku@gmail.com

not available in an explicit closed form. Wang and Achenbach [11, 12] used integral Radon transform to derive three-dimensional general anisotropic elastodynamics fundamental solutions in time and frequency domains. Their representation requires integration over a unit sphere for dynamic part and integration over a unit radius circumference for static part. During the numerical integration over the boundary elements, values of the fundamental solutions must be calculated at every integration point. Various techniques related to the evaluation of the fundamental solutions were proposed to accelerate the integration process, e.g., neglecting the far-field waves [5], interpolation of the fundamental solutions over the boundary elements [13].

As an extension of our previous works [14, 15], we present in this chapter Laplace transformed direct BEM formulation for three-dimensional anisotropic viscoelastodynamics based on the elastic-viscoelastic correspondence principle. Time domain solutions are obtained by modified Durbin's method for the numerical inversion of the Laplace transform [16]. Numerical modeling of dynamic elastic and viscoelastic problems is carried out to investigate the validity and efficiency of the proposed boundary element formulation.

36.2 Governing Equations

First, we consider a domain $\Omega \subset R^3$ with boundary $\Gamma = \partial\Omega$ occupied by linear elastic homogeneous continuum. The differential equations of motion in the absence of body forces are given as follows

$$\sigma_{ij,j}(\mathbf{x}, t) - \rho \ddot{u}_i(\mathbf{x}, t) = 0, \quad \mathbf{x} \in \Omega, \quad i, j = \overline{1, 3}, \quad (36.1)$$

where $\sigma_{ij}(\mathbf{x}, t)$ is the Cauchy stress tensor, $u_i(\mathbf{x}, t)$ is the displacement vector and ρ is the mass density.

Linear strain tensor is expressed as

$$\varepsilon_{ij}(\mathbf{x}, t) = \frac{1}{2} (u_{i,j}(\mathbf{x}, t) + u_{j,i}(\mathbf{x}, t)). \quad (36.2)$$

The stresses and strains for an anisotropic linear elastic material relate through the generalized Hooke's law:

$$\sigma_{ij}(\mathbf{x}, t) = C_{ijkl} \varepsilon_{kl}(\mathbf{x}, t), \quad i, j, k, l = \overline{1, 3}, \quad (36.3)$$

where C_{ijkl} is the fourth order elastic stiffness tensor with up to 21 independent components.

By combining (36.1)–(36.3), the equations of motion of an anisotropic elastic body can be rewritten in terms of displacements:

$$C_{ijkl}u_{k,lj}(\mathbf{x}, t) - \rho\ddot{u}_i(\mathbf{x}, t) = 0, \quad \mathbf{x} \in \Omega. \quad (36.4)$$

To complete the problem description, appropriate boundary and initial conditions must be prescribed:

$$u_i(\mathbf{x}, t) = u_i^*(\mathbf{x}, t), \quad \mathbf{x} \in \Gamma_u, \quad (36.5)$$

$$t_i(\mathbf{x}, t) = t_i^*(\mathbf{x}, t), \quad \mathbf{x} \in \Gamma_t, \quad (36.6)$$

$$u_i(\mathbf{x}, 0) = 0, \quad \mathbf{x} \in \Omega, \quad (36.7)$$

$$\dot{u}_i(\mathbf{x}, 0) = 0, \quad \mathbf{x} \in \Omega, \quad (36.8)$$

where $t_i(\mathbf{x}, s)$ represents tractions, $u_i^*(\mathbf{x}, t)$ and $t_i^*(\mathbf{x}, t)$ denote prescribed values on Dirichlet and Neumann boundaries Γ_u and Γ_t , respectively. Initial displacements and velocities are assumed to vanish.

The Laplace transform of a function $f(\mathbf{x}, t)$ is defined as follows

$$\bar{f}(\mathbf{x}, s) = L\{f(\mathbf{x}, t)\} = \int_0^{\infty} f(\mathbf{x}, t) \exp(-st) dt, \quad (36.9)$$

where s is the transform variable and a superposed bar denotes a transformed function.

Keeping in mind zero initial conditions (36.7) and (36.8), we now take Laplace transform of (36.4)–(36.6):

$$C_{ijkl}\bar{u}_{k,lj}(\mathbf{x}, s) - \rho s^2\bar{u}_i(\mathbf{x}, s) = 0, \quad \mathbf{x} \in \Omega, \quad (36.10)$$

$$\bar{u}_i(\mathbf{x}, s) = \bar{u}_i^*(\mathbf{x}, s), \quad \mathbf{x} \in \Gamma_u, \quad (36.11)$$

$$\bar{t}_i(\mathbf{x}, s) = \bar{t}_i^*(\mathbf{x}, s), \quad \mathbf{x} \in \Gamma_t. \quad (36.12)$$

36.2.1 Viscoelastic Governing Equations

The constitutive equations of an anisotropic linear viscoelastic material are given by

$$\sigma_{ij}(\mathbf{x}, t) = G_{ijkl}(t)\varepsilon_{kl}(\mathbf{x}, 0) + \int_0^t G_{ijkl}(t-\tau) \frac{d\varepsilon_{kl}(\mathbf{x}, \tau)}{d\tau} d\tau, \quad (36.13)$$

where G_{ijkl} is the fourth order relaxation tensor.

Applying the Laplace transform to the dynamic equilibrium equations (36.1), kinematic relations (36.2) and constitutive law (36.13) leads to

$$\bar{\sigma}_{ijj}(\mathbf{x}, s) - s^2 \rho \bar{u}_i(\mathbf{x}, s) = 0, \quad (36.14)$$

$$\bar{\varepsilon}_{ij}(\mathbf{x}, s) = \frac{1}{2} (\bar{u}_{ij}(\mathbf{x}, s) + \bar{u}_{ji}(\mathbf{x}, s)), \quad (36.15)$$

$$\bar{\sigma}_{ij}(\mathbf{x}, s) = s \bar{G}_{ijkl}(s) \bar{\varepsilon}_{kl}(\mathbf{x}, s). \quad (36.16)$$

Comparing the generalized Hooke's law (36.3) with the viscoelastic constitutive equations (36.16), we can formulate the so-called *elastic-viscoelastic correspondence principle*. The viscoelastodynamic solution of a particular problem can be obtained from the solution of the corresponding elastic problem by replacing elastic moduli with the complex viscoelastic moduli in Laplace domain:

$$C_{ijkl} \leftrightarrow s \bar{G}_{ijkl}(s). \quad (36.17)$$

36.3 Boundary Element Formulation

Here and in what follows, without loss of generality we consider problems of anisotropic elasticity governed by (36.10)–(36.12), starting with the boundary integral equations in the Laplace domain.

The displacements at any internal point in the domain Ω are represent by

$$\bar{u}_i(\mathbf{x}, s) = \int_{\Gamma} (\bar{g}_{ij}(\mathbf{r}, s) \bar{t}_j(\mathbf{y}, s) - \bar{h}_{ij}(\mathbf{r}, s) \bar{u}_j(\mathbf{y}, s)) d\Gamma(\mathbf{y}), \quad (36.18)$$

where $\mathbf{r} = \mathbf{y} - \mathbf{x}$, \bar{u}_i and \bar{t}_i are the displacement and traction on the boundary Γ , respectively. \bar{g}_{ij} and \bar{h}_{ij} are the displacement and traction fundamental solutions in the Laplace domain.

Employing standard boundary element techniques to (36.18), we obtain the displacement boundary integral equation:

$$c_{ij} \bar{u}_j(\mathbf{x}, s) = \int_{\Gamma} \bar{g}_{ij}(\mathbf{r}, s) \bar{t}_j(\mathbf{y}, s) d\Gamma(\mathbf{y}) - \text{p.v.} \int_{\Gamma} \bar{h}_{ij}(\mathbf{r}, s) \bar{u}_j(\mathbf{y}, s) d\Gamma(\mathbf{y}), \quad \mathbf{x} \in \Gamma, \quad (36.19)$$

where p.v. denotes the Cauchy principal value integral, c_{ij} are the integral free terms.

The numerical implementation of (36.19) is based on the idea of mixed boundary elements, which is to split nodal points of displacements and tractions. This allows maintaining continuous approximation of the displacements and to model properly discontinuous tractions, at the same time. Hence, we adopt the simplest possible discretization: continuous displacements \bar{u}_i and discontinuous tractions \bar{t}_i are approximated by linear and constant interpolation functions, respectively. The boundary Γ is approximated by eight-node quadrilateral elements with quadratic shape functions.

After solving the resulting system of linear equations that is parametrized by Laplace transform parameter, we employ modified Durbin’s method [16, 17] to obtain time domain solutions.

36.4 Laplace Domain Fundamental Solutions

Wang and Achenbach [11, 12] derived three-dimensional fundamental solutions in time and frequency domains for general anisotropic elastic medium by using the Radon transform. These fundamental solutions can be represented as a sum of static and dynamic parts:

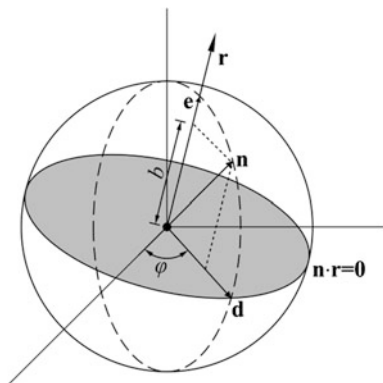
$$\bar{g}_{ij}(\mathbf{r}, s) = \bar{g}_{ij}^S(\mathbf{r}) + \bar{g}_{ij}^D(\mathbf{r}, s), \tag{36.20}$$

$$\bar{h}_{ij}(\mathbf{r}, s) = \bar{h}_{ij}^S(\mathbf{r}) + \bar{h}_{ij}^D(\mathbf{r}, s), \tag{36.21}$$

where superscripts S and D denote the static and dynamic parts, respectively.

The Laplace transform of Wang and Achenbach time domain solutions yields (see also Fig. 36.1)

Fig. 36.1 Geometrical representation of some variables required for integration of the fundamental solutions



$$\bar{g}_{ij}^S(\mathbf{r}) = \frac{1}{8\pi^2 r} \int_{|\mathbf{d}|=1} \Gamma_{ij}^{-1}(\mathbf{d}) dL(\mathbf{d}), \quad (36.22)$$

$$\bar{g}_{ij}^D(\mathbf{r}, s) = -\frac{1}{8\pi^2} \int_{\substack{|\mathbf{n}|=1 \\ \mathbf{n} \cdot \mathbf{r} > 0}} \sum_{m=1}^3 \frac{k_m E_{im} E_{jm}}{\rho c_m^2} \exp(-k_m |\mathbf{n} \cdot \mathbf{r}|) dS(\mathbf{n}), \quad (36.23)$$

$$c_m = \sqrt{\lambda_m / \rho}, \quad k_m = s / c_m, \quad (36.24)$$

$$\mathbf{n} = \sqrt{1 - b^2} \mathbf{d} + b \mathbf{e}, \quad r = |\mathbf{r}|, \quad \mathbf{e} = \mathbf{r} / r, \quad (36.25)$$

$$\mathbf{e} \cdot \mathbf{d} = 0, \mathbf{d}$$

$$= (e_2 \cos \varphi + e_1 e_3 \sin \varphi, -e_1 \cos \varphi + e_2 e_3 \sin \varphi, -(1 - e_3^2) \sin \varphi) / \sqrt{1 - e_3^2}, \quad (36.26)$$

$$dS(\mathbf{n}) \in \{0 \leq b \leq 1; 0 \leq \varphi \leq 2\pi\}, \quad (36.27)$$

$$dL(\mathbf{d}) \in \{0 \leq \varphi \leq 2\pi\}, \quad (36.28)$$

where c_m and k_m are the phase velocities and wave numbers; λ_m , E_{jm} are eigenvalues and the corresponding eigenvectors of Christoffel tensor $\Gamma_{jk}(\mathbf{n}) = C_{ijkl} n_j n_l$.

The expression of the traction fundamental solution can be written as

$$\bar{h}_{mj}(\mathbf{r}, s) = C_{ijkl} \bar{g}_{mk,ln}(\mathbf{x}), \quad (36.29)$$

where $n_i(\mathbf{x})$ is unit normal to the boundary Γ at the point \mathbf{x} .

Viscoelastic fundamental solutions are obtained from the elastic ones by employing the correspondence principle.

The evaluation of the anisotropic fundamental solution requires two-dimensional numerical integration of the double integral over a unit half sphere appearing in the dynamic part. Such integrations need to be performed for each pair of collocation point-field point in the process of evaluating the boundary integrals, which greatly increase overall computation time. In order to calculate boundary integrals more efficiently, we employ the technique proposed by Matsumoto et al. in [13]. The values of dynamic part of the displacement fundamental solution (36.23) and its derivatives at each integration point are approximated inside the boundary element, in analogy to approximation of the field variables, by

$$p_{ij}(\xi_1, \xi_2) = \sum_{n=1}^N F_n(\xi_1, \xi_2) p_{ij}^{(n)} \quad (36.30)$$

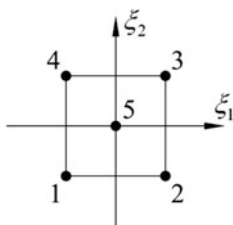


Fig. 36.2 Five-node element in reference coordinates

where p_{ij} represents the values of \bar{g}_{ij} or $\bar{g}_{ij,k}$ and $p_{ij}^{(n)}$ is their corresponding nodal value at the node n of the reference element. In addition, F_n are the shape functions, which might be different from those we used for the interpolation of the geometry and field variables.

Particularly, besides the four-node linear and eight-node quadratic elements, we consider a five-node quadrilateral element. A reference domain $\Gamma_\xi = [-1, 1] \times [-1, 1]$ has four corner nodes and a fifth node located at the center of the element as shown in Fig. 36.2. The shape functions for five-node element are expressed as follows

$$F_m(\xi_1, \xi_2) = \frac{1}{4} \left(1 + \xi_1^{(m)} \xi_1 \right) \left(1 + \xi_2^{(m)} \xi_2 \right) - \frac{1}{4} F_5, \quad m = \overline{1, 4}, \tag{36.31}$$

$$F_5(\xi_1, \xi_2) = (1 - \xi_1^2)(1 - \xi_2^2), \tag{36.32}$$

where $\xi_i^{(m)}$ are the coordinates of the corresponding corner nodes (see Fig. 36.2).

The approximation, defined by (36.30), is employed, when $R/l > k$ with R being the minimum distance from the collocation point to the current boundary element, l is the average length of edges of all the boundary elements and k is a fixed value.

36.5 Numerical Examples

36.5.1 Accuracy and Efficiency of the Proposed Formulation

In order to assess the accuracy of the proposed boundary element formulation and efficiency of the technique for approximate evaluation of the fundamental solutions and their spatial derivatives, we consider an anisotropic elastic problem: three-dimensional prismatic solid is clamped at its left end, and subjected to uniaxial and uniform impact loading $t_2 = t_2^* H(t)$, $t_2^* = -1 \text{ N/m}^2$ at the right end as shown in Fig. 36.3. The remaining surfaces are traction free. The density of the

Fig. 36.3 Analyzed model

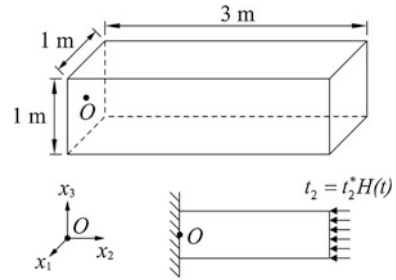
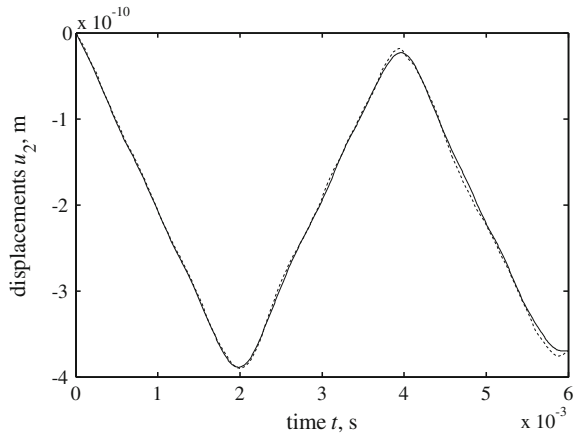


Fig. 36.4 Displacement $u_2(t)$ at the point (0, 3, 0) m; Solid curve BEM. Dashed curve FEM



material is $\rho = 1,600 \text{ kg/m}^3$ and the stiffness tensor in Voigt notation is given as follows

$$\mathbf{C} = \begin{bmatrix} 60.23 & 18.67 & 18.96 & -7.69 & 15.60 & -25.28 \\ & 21.26 & 9.36 & -3.74 & 4.21 & -8.47 \\ & & 47.04 & -8.82 & 15.28 & -8.31 \\ & & & 10.18 & -9.54 & 5.69 \\ & \text{sym.} & & & 21.19 & -8.54 \\ & & & & & 20.75 \end{bmatrix} \text{ GPa.} \quad (36.33)$$

We have conducted extensive analysis to determine the influence of parameters of the fundamental solutions approximation scheme. We considered three different types of elements (four, five and eight-node) and four different values of ratio k , namely $k = 0.0, 1.0, 2.0$ and 5.0 . Most suitable correlation between computational time and accuracy of the solution was attained with five-node element and $k = 0.0$. The total CPU time using five-node element approximation was only 53 % compared to the CPU time needed for the calculations without fundamental solutions approximation and the maximum relative error was 2.1 %. Figure 36.4 shows obtained BEM solution for the displacement response $u_2(t)$ at the point (0, 3, 0) m,

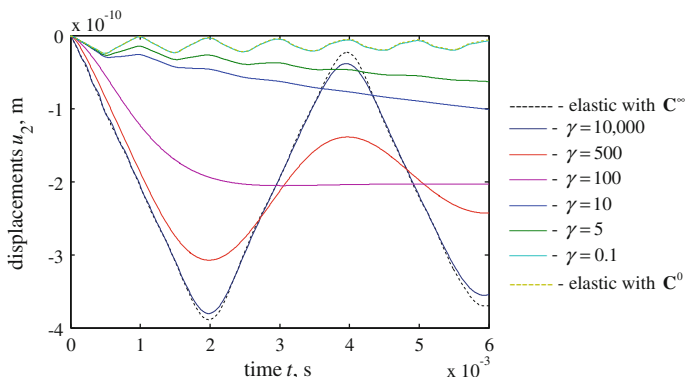


Fig. 36.5 Displacement $u_2(t)$ at the point (0, 3, 0) m for the transient viscoelastic problem

where a good correspondence with FEM results can be observed. In all further calculations, the fundamental solutions are approximated using five-node element.

36.5.2 Transient Response of an Anisotropic Viscoelastic Prismatic Solid

For the anisotropic transient viscoelastic problem, we use the same analyzed model as in Sect. 36.5.1 (see also Fig. 36.3). To describe the mechanical behavior of anisotropic viscoelastic material the standard linear solid model is employed:

$$s\bar{G}_{ijkl}(s) \rightarrow C_{ijkl}^\infty \left[(\beta - 1) \frac{s}{s + \gamma} + 1 \right], \tag{36.34}$$

$$\beta = C_{ijkl}^0 / C_{ijkl}^\infty, \tag{36.35}$$

where C_{ijkl}^0 is the stiffness tensor at the instantaneous state and C_{ijkl}^∞ is the equilibrium stiffness tensor given in (36.33); $\beta = 16$ and $\gamma = 0.1; 5; 10; 100; 500; 10,000$. Figure 36.5 shows the transient response of the axial displacements $u_2(t)$ at the nodal point (0, 3, 0) m located at the center of the loaded end.

36.6 Conclusions

In this chapter, it has been shown that conventional direct boundary element approach in Laplace domain can be successfully used to model transient three-dimensional problems of anisotropic elasticity and viscoelasticity. The

viscoelastic solution procedure is based on the elastic-viscoelastic correspondence principle.

In the boundary integrals calculation process, we used a simple and yet efficient technique for approximation of the fundamental solutions and their spatial derivatives over the boundary element, gaining almost 50 % reduction in computational time when using five–node element and keeping relative error just under 2.1 %. For the process of spatial discretization, the mixed boundary elements were employed.

The validity and accuracy of the proposed formulation was confirmed by comparing obtained solutions for transient anisotropic elastic problem with the corresponding finite element results. Applicability for transient problems of anisotropic viscoelasticity was demonstrated through the test example with the standard linear solid model used as viscoelastic constitutive model.

Acknowledgments The work is financially supported by the Ministry of Education and Science of the Russian Federation in the frame of the main part of the governmental task under project No. 2014/134 2226 and also by the Russian Foundation for Basic Research (RFBR) under grants No. 14-08-31410, No. 15-38-50827, No. 15-08-02814 and No. 15-48-02333.

References

1. F.J. Rizzo, Q. Appl. Math. **25**, 83 (1967)
2. T.A. Cruse, Int. J. Solids Struct. **5**, 1259 (1969)
3. F.J. Rizzo, D. Shippy, J. Compos. Mater. **4**, 36 (1970)
4. T. Cruse, F.J. Rizzo, Int. J. Math. Anal. Appl. **22**, 244 (1968)
5. A. Furukawa, T. Saitoh, S. Hirose, Eng. Anal. Boundary Elem. **39**, 64 (2014)
6. A. Milazzo, I. Benedetti, M.H. Aliabadi, Comput. Struct. **96–97**, 9 (2012)
7. A. Carini, G. Gioda, Int. J. Numer. Anal. Meth. Geomech. **10**, 585 (1986)
8. C. Hwu, Y.C. Chen, Procedia Eng. **10**, 3038 (2011)
9. W.J. Sim, B.M. Kwak, Comput. Struct. **29**, 531 (1988)
10. M. Schanz, *Wave Propagation in Viscoelastic and Poroelastic Continua* (Springer-Verlag, Berlin Heidelberg, 2001)
11. C.Y. Wang, J.D. Achenbach, Geophys. J. Int. **118**, 384 (1994)
12. C.Y. Wang, J.D. Achenbach, Proc. R. Soc Lond. A **449**, 441 (1995)
13. T. Matsumoto, M. Tanaka, Y. Ogawa, in *Proceedings Second MIT Conference on Computational Fluid and Solid Mechanics*, Elsevier, 2071 (2003)
14. L.A. Igumnov, I.P. Markov, Y.Y. Rataushko, Adv. Mater. Res. **1040**, 633 (2014)
15. L.A. Igumnov, I.P. Markov, A.A. Belov, Appl. Mech. Mater. **709**, 113 (2015)
16. X. Zhao, Int. J. Solids Struct. **41**, 3653 (2004)
17. L.A. Igumnov, A.V. Amenitskii, A.A. Belov, S.Y. Litvinchuk, A.N. Petrov, J. Appl. Mech. Tech. Phys. **55**, 89 (2014)

Chapter 37

Thermo-physical Processes in Boundary Layers of Metal-Polymeric Systems

V.I. Kolesnikov, M.I. Chebakov, I.V. Kolesnikov and A.A. Lyapin

Abstract The calculation of temperature field for metal-polymeric tribosystem like “wheel-brake pad” of railway unit is performed. One of the methods used for calculation of temperature distribution in boundary layers is regularization of singularly perturbed problems. As a tool for simulation of problem for disc braking systems the finite element method is used. In the both cases, the fact of temperature maximum located under frictional surface is demonstrated. The experimental study confirms this fact, too. Such negative temperature gradient acts on physical, mechanical and tribological properties of metal-polymeric frictional units. This influence is studied and demonstrated.

37.1 Introduction

One of the most important problems in tribo-techniques is establishing the features of behavior of boundary layers at metal-polymeric tribo-contact. Therefore, for more detailed studying the contact processes, it is necessary to develop both diagnostics test methods and more accurate theoretical models. Such models should be specific and consider changes that occur in the sample bulk and boundary layers but also lead to simple engineering calculations.

It is marked by many specialists that there is no one common description of micromechanical processes in boundary layers due to the volumes of bodies operating in frictional processes are very small.

Currently, there is common understanding that the most important factor during exploitation of metal-polymeric tribo-contact is the thermal stress in frictional unit.

V.I. Kolesnikov · I.V. Kolesnikov
Rostov State Transport University, Rostov-on-Don, Russia

M.I. Chebakov · A.A. Lyapin (✉)
Vorovich Mathematics, Mechanics and Computer Sciences Institute,
Southern Federal University, Rostov-on-Don, Russia
e-mail: lyapin@sfedu.ru

It is well known that external friction followed by heat generation due to irreversibility of the deformation processes and shear of adhesion bond. One part of heat due to thermal conductivity moves into volume of contacting bodies creating temperature field, another part scatters in environment. Under thermal loading, physical and mechanical properties of bodies change that leads to alteration of frictional connections and rate of wear.

However, the corresponding information about temperature field in frictional unit and its influence on physical and mechanical properties of plastics is not still sufficient studied for industry and researchers working in tribology area. We need to determine the mechanics of processes and to find physically correct model or approximate engineering data of elementary frictional phenomena caused by, first, specific properties of polymeric materials, their ability to generate products of destruction providing friction and accumulation of electric charges.

Therefore, the first stage of our study is to develop the methodic for calculation and analysis of temperature fields in boundary layers of frictional contact. Theoretical understanding of mechanical nature of temperature gradients clarifies the influence mechanisms on triboelectric, diffusion and segregation processes at frictional contacts.

According to traditional methods, the thermal problems with friction could be divided into two types:

- (i) problems solvable by analytical methods;
- (ii) problems solvable by numerical methods.

Among the analytical methods, we note the Fourier method and integral transformations method.

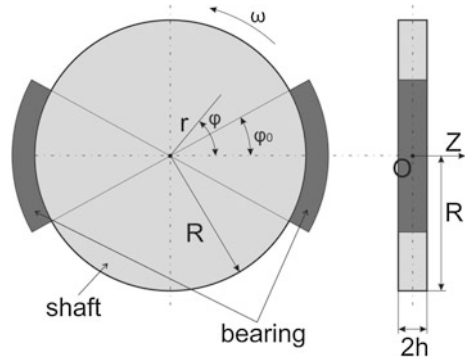
The Fourier method (or method of splitting variables) and the integral transformations method are classical for mathematical analysis and solution of partial-differential equations.

Among the most popular numerical methods for solution of partial-differential equations, we note the finite-element method.

The need to describe features of behavior for boundary layers at tribo-contact leads to problem of solving the boundary singularly perturbed problems, namely the problems with a small parameter at the highest derivative [1, 2]. For an asymptotical solution of the singularly perturbed problems, it is usually used Vishik-Lyusternik method or multiscale methods of matched expansions [3]. We were the first [4] who used method, developed by Lomov [5], for regularization of singular perturbed problems for calculating of temperature field in the boundary layers for tribosystem. This method combines ideas of both methods described above and has number of advantages compared with each of them individually, and is, therefore, more prospective. The aim is the regularization of singular perturbed problems by moving to resonance less solutions in space, induced by original problem. This induced space is determined by spectral characteristics of initial operator that gives opportunity to use the spectral theory of operators. The singularity of initial problem leads to appearance of zero kernel for main operator of the induced problem.

We calculate temperature field for the junction “wheel-braking pad” of railway unit as the most popular tribosystem “shaft-parted bearing” (see Fig. 37.1).

Fig. 37.1 Scheme of metal-polymeric system



Many researchers have studied the temperature mode of slippery contact during braking process of railway unit. All of them confirmed that the process of heating for the band is harder than for pads. Any part of frictional surface places under braking pad or cools away from it. Solution of such a problem is very difficult due to changing boundary conditions during time. Therefore, we shall state the problem for determination of temperature field for band during changing of boundary conditions.

37.2 Determination of Temperature Field for Band During Changing of Boundary Conditions

We assume that the wheel is a disk with radius R and thickness $2h$ (Fig. 37.1). We introduce a cylindrical coordinate system (r, φ, z) and denote by $T(r, \varphi, z, t)$ the temperature of the wheel point with coordinates (r, φ, z) at time t .

Let us consider the case of steady-state process: the wheel rotates with constant angular velocity ω , and the force pressing the pads to a wheel during braking process does not change. Under these assumptions, the function $T(r, \varphi, z, t)$ is periodic with a period π/ω (two pads). We can also assume that the wheel is motionless and the pads rotate with the same speed ω in the counter-clockwise direction.

Let us assume that we operate with classical principles, formulated by researchers in the field of thermal tribo-contact. Under the condition of isotropy for material of wheel the equations of heat transfer could be represented as [6]:

$$\frac{1}{r} \frac{\partial}{\partial r} \left(r \frac{\partial T}{\partial r} \right) + \frac{1}{r^2} \frac{\partial^2 T}{\partial \varphi^2} + \frac{\partial^2 T}{\partial z^2} = \frac{C\rho}{\lambda} \frac{\partial T}{\partial t}, \tag{37.1}$$

where C is the specific heat of the wheel material, λ is the thermal conductivity, ρ is the density. We assume that C, λ, ρ are constants.

We need to formulate corresponding boundary conditions. On the upper and lower edges ($z = \pm h$), the following convection conditions satisfy with coefficient of α_z :

$$\pm \lambda \frac{\partial T}{\partial z} + \alpha_z(T - T_c) = 0, \quad \text{at } z = \pm h, \quad (37.2)$$

where T_c is the temperature of environment.

The heat generation on the cylindrical surface ($r = R$) could be described as

$$\lambda \frac{\partial T}{\partial z} = Q, \quad \text{at } r = R, \quad (37.3)$$

$$\varphi \in [-\varphi_0 + \omega t, \varphi_0 + \omega t] \cup [\pi - \varphi_0 + \omega t, \pi + \varphi_0 + \omega t],$$

here $Q = k_{fr} P v K$ (where k_{fr} is the coefficient of friction, P is the specific load for pad, v is the linear rotational speed for wheel, K is a coefficient of thermal flux proportionality).

For other parts of cylindrical surface, we define free heat exchange with the convection coefficient α_r :

$$\lambda \frac{\partial T}{\partial r} + \alpha_r(T - T_c) = 0, \quad \text{at } r = R, \quad (37.4)$$

$$\varphi \notin [-\varphi_0 + \omega t, \varphi_0 + \omega t] \cup [\pi - \varphi_0 + \omega t, \pi + \varphi_0 + \omega t].$$

In the result of calculations, we find that almost from the beginning of frictional process, after moment when point of wheel outer surface leaves contact zone with pad, there arises maximum of temperature in undersurface layer that moves in depth of the wheel bulk. The maximum change in temperature observed in the range from $-2\pi/5$ to $-\pi/5$. Thus, the temperature maximum was at a distance 200–1000 mm from the tread surface. Today there is modern braking system used for speed railway units and based on disc brakes. Taking into account that analytical solution is difficult to realize for complex geometry of disc braking systems, we performed finite-element modeling to simulate coupled temperature-displacement process. We conducted coupled analysis for non-stationary thermoelastic problem of contact interaction for rotating braking disc and braking pads, pressed one to other with some load.

37.3 Non-stationary Thermoelastic Problem of Contact Interaction for Rotating Braking Disc and Braking Pads

As a model problem, we consider non-stationary contact coupled thermoelastic problem of the rotation brake disk of outer radius $R_1 = 30$ cm and inner radius $R_2 = 20$ cm that contains air channels, with the brake pads pressed to them with a predetermined force P . Schematic representation of the problem is present in Fig. 37.2. The brake disc rotates in the counter-clockwise direction with the speed V during time $t \in [0, T]$. In addition to the Cartesian coordinate system with the

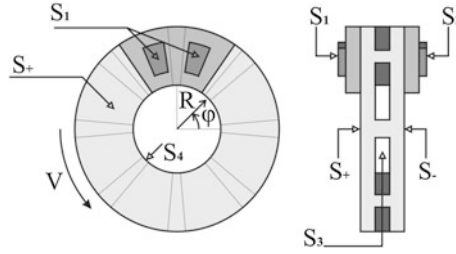


Fig. 37.2 Schematic representation of the studied system

origin at the center of the brake disc let us consider the cylindrical coordinate system (R, φ, Z) with respect to the same center (Z -axis is perpendicular to the plane of the disc). We denote the brake disc and pad by upper indices (1 corresponds to the brake disc, and 2, 3 define front and rear brake pads, respectively). Let us consider in the $S_{cont}^{+/-}$ the contact area of pads and disc with friction coefficient k and a heat arising due to the friction and thermal conductivity coefficient k_{cont} of the contact area.

The behavior of the system is described by the classical equations of motion of a thermoelastic medium [7]:

$$\begin{aligned}
 &(\lambda^{(i)} + 2\mu^{(i)})\nabla\nabla \cdot \mathbf{u}^{(i)} - (\lambda^{(i)} + \mu^{(i)})\nabla \times \nabla \times \mathbf{u}^{(i)} - \gamma^{(i)}\nabla\theta^{(i)} - \rho^{(i)}\ddot{\mathbf{u}}^{(i)} = 0, \\
 &\Lambda^{(i)}\nabla \cdot \nabla\theta^{(i)} - C_\epsilon^{(i)}\dot{\theta}^{(i)} - T_0\gamma^{(i)}\frac{\partial}{\partial t}\nabla \cdot \mathbf{u}^{(i)} = 0, i = 1, 3;
 \end{aligned}
 \tag{37.5}$$

Boundary conditions have the forms:

$$\left\{ \begin{array}{l}
 u_R^{(1)} = u_Z^{(1)} = 0, \mathbf{x} \in S_4, \\
 u_R^{(2,3)} = u_\varphi^{(2,3)} = 0, \mathbf{x} \in S_1 \cup S_2, \\
 \frac{1}{\|S_1\|} \int_{S_1} \sigma_{ZZ}^{(2)} dS = P, \\
 \frac{1}{\|S_2\|} \int_{S_2} \sigma_{ZZ}^{(3)} dS = -P, \\
 \tau_{\varphi Z}^+ = k^{1,2} \cdot \sigma_{ZZ}^+, \mathbf{x} \in S_{cont}^+, \\
 \tau_{\varphi Z}^- = k^{1,3} \cdot \sigma_{ZZ}^-, \mathbf{x} \in S_{cont}^-,
 \end{array} \right. \left\{ \begin{array}{l}
 q^{(1)} = a(\theta_{env} - \theta^{(1)}), \mathbf{x} \in S_+ \cup S_- \cup S_3, \\
 q_{cont}^{1,2} = k_{cont}^{1,2}(\theta^{(1)} - \theta^{(2)}), \mathbf{x} \in S_{cont}^+, \\
 q_{cont}^{1,3} = k_{cont}^{1,3}(\theta^{(1)} - \theta^{(3)}), \mathbf{x} \in S_{cont}^-, \\
 q_{cont}^{(1)gen+} = k_{en}^+ k_p^+ E_{fr}^+, \mathbf{x} \in S_{cont}^+, \\
 q_{cont}^{(2)gen} = k_{en}^+(1 - k_p^+) E_{fr}^+, \mathbf{x} \in S_{cont}^+, \\
 q_{cont}^{(1)gen-} = k_{en}^- k_p^- E_{fr}^-, \mathbf{x} \in S_{cont}^-, \\
 q_{cont}^{(3)gen} = k_{en}^-(1 - k_p^-) E_{fr}^-, \mathbf{x} \in S_{cont}^-, \\
 \theta^{(1)} = \theta^{(2)} = \theta^{(3)} = 0, t = 0, \\
 \dot{u}_\varphi^{(1)} = V(t), t \in [0, T];
 \end{array} \right.
 \tag{37.6}$$

Constitutive equations of coupled linear thermoelasticity are present as [7]

$$\begin{aligned}\sigma_{11}^{(i)} &= (2\mu^{(i)} + \lambda)\varepsilon_{11}^{(i)} + \lambda^{(i)}(\varepsilon_{22}^{(i)} + \varepsilon_{33}^{(i)}) - \gamma^{(i)}\theta^{(i)}, \quad \sigma_{12}^{(i)} = 2\mu^{(i)}\varepsilon_{12}^{(i)}, \\ \sigma_{22}^{(i)} &= (2\mu^{(i)} + \lambda)\varepsilon_{22}^{(i)} + \lambda^{(i)}(\varepsilon_{11}^{(i)} + \varepsilon_{33}^{(i)}) - \gamma^{(i)}\theta^{(i)}, \quad \sigma_{23}^{(i)} = 2\mu^{(i)}\varepsilon_{23}^{(i)}, \\ \sigma_{33}^{(i)} &= (2\mu^{(i)} + \lambda)\varepsilon_{33}^{(i)} + \lambda^{(i)}(\varepsilon_{11}^{(i)} + \varepsilon_{22}^{(i)}) - \gamma^{(i)}\theta^{(i)}, \quad \sigma_{31}^{(i)} = 2\mu^{(i)}\varepsilon_{31}^{(i)};\end{aligned}\quad (37.7)$$

where $\lambda^{(i)}, \mu^{(i)}$ are the respective elastic moduli of materials, $\gamma^{(i)} = (3\lambda^{(i)} + 2\mu^{(i)})\alpha_T^{(i)}$, $\alpha_T^{(i)}$ are the coefficients of thermal expansion, $\alpha^{(i)}$ are the coefficients of heat transfer, θ_{env} is the temperature of environment, $\Lambda^{(i)}$ are the thermal conductivities, $C_\varepsilon^{(i)}$ —are the specific heats of the bodies, T_0 is the absolute temperature of initial state of the bodies, $\rho^{(i)}$ are the densities of bodies, $\mathbf{u}^{(i)}$ is the displacement vector of the medium, $\theta^{(i)}$ are the temperatures of each of the bodies.

Let us describe in more detail each of boundary conditions (37.6). On the surface S_4 , it is considered a restriction on the movement in the direction R and z of the brake disc; it gives a possibility to study only rotational movements. Similarly, on the surfaces S_1, S_2 , there is a restriction on the movement in the directions R and φ to determine the motion of the brake pads only in the perpendicular direction to the braking surface of the disc. The loading conditions in the problem are present by distributed loads on surfaces S_1, S_2 that provide lower force for the brake system of value P . In the area of contact, the corresponding shear stress $\tau_{z\varphi}^{+/-}$ is proportional to the normal stress $\sigma_{zz}^{+/-}$ at friction with friction coefficient $k^{1,2/1,3}$. An important factor in describing the temperature behavior of the brake system is the convective heat transfer to environment, due to the air blowing the brake disc. The conditions, presented in the convection problem, are expressed by proportional magnitudes of the heat flux $q^{(1)}$ on the surfaces of the brake disc S_+, S_-, S_3 , corresponding to the right and left brake surfaces and the inner surface of the ventilation ducts, respectively, to the temperature difference between the brake disc $\theta^{(1)}$ and the ambient temperature θ_{env} with a factor a . A prerequisite for solving the contact problems with temperature field is the thermal contact conductivity condition at the contact zone. In the case of the described problem, such a condition requires for modeling the heat transfer from one body to other in contacting pair. It is expressed as a proportionality of heat flow $q_{cont}^{1,2/1,3}$ and temperature difference in the contact pair $\theta^{(1)}, \theta^{(2,3)}$ with a coefficient of thermal conductivity $k_{cont}^{1,2/1,3}$ of the contact. The condition of heat generation due to friction is expressed in adding the additional heat fluxes at the boundaries of the bodies in contact with intensities proportional to coefficient $k_{en}^{+/-}$ and the amount of mechanical energy $E_{fr}^{+/-}$ transforming due to friction into heat; the weighting factor $k_p^{+/-}$ denotes a distribution of heat between two surfaces. Since this problem is non-stationary, it is necessary to state the corresponding initial conditions, which describe the initial temperatures of the

bodies $\theta^{(1)}, \theta^{(2)}, \theta^{(3)}$ that are equal to zero in this case, as well as the initial speed of rotation of the brake disc, $\dot{u}_\phi^{(1)} = V(0)$.

Let us describe physical parameters used in the problem. As a material for all components, we selected steel with the following parameters: Young’s modulus $E = 2 \cdot 10^{11}$ Pa, Poisson’s ratio $\nu = 0.3$, density $\rho = 7.850$ kg/m³, thermal conductivity $\Lambda = 48$ Wt/(m K), specific heat $C_e = 452$ J/kg °C, coefficient of thermal expansion $\gamma = 1.1 \cdot 10^{-5}$ 1/°C.

The complexity of geometry and thermoelastic behavior of the system does not allow one to get the solution analytically. In such a case, an effective method is the using of appropriate finite-element packages. To solve this problem, we used the ABAQUS package. For constructing the finite-element mesh of bodies, there was used C3D8T finite element, allowing one to calculate both elastic and temperature fields; finite-element matrix equations are of the form:

$$\begin{bmatrix} [M] & [0] \\ [0] & [0] \end{bmatrix} \begin{Bmatrix} \{\ddot{u}\} \\ \{\dot{T}\} \end{Bmatrix} + \begin{bmatrix} [C] & [0] \\ [0] & [C^t] \end{bmatrix} \begin{Bmatrix} \{\dot{u}\} \\ \{T\} \end{Bmatrix} + \begin{bmatrix} [K] & [K^u] \\ [0] & [K^t] \end{bmatrix} \begin{Bmatrix} \{u\} \\ \{T\} \end{Bmatrix} = \begin{Bmatrix} \{F\} \\ \{Q\} \end{Bmatrix}, \tag{37.8}$$

where M is the mass matrix; C is the damping matrix; K is the stiffness matrix; u is the displacement vector; F are the total nodal forces and pressures applied to the elements; C^t is the specific heat capacity; K^t is the matrix of diffusion conductivity; T is the temperature vector; K^u is the thermoelastic stiffness matrix.

The finite-element analysis for a correct convergence has been divided into two stages. The first stage corresponded to solution of the problem on static transferring a force P of pads to brake disc. In the next stage a dynamic transient problem was solved with given rotation speed of brake disc.

The general character of heating can be expressed by three possible modes:

- (i) in the case of low-speed rotation, small clamping force, as well as significant heat transfer to environment, a point of the disk may take an initial value of temperature and after a certain time returns to the initial temperature state, due to the quantity of heat, emitted into the environment, is greater than the heat, generated by friction in the contact zone (Fig. 37.3, curve I);

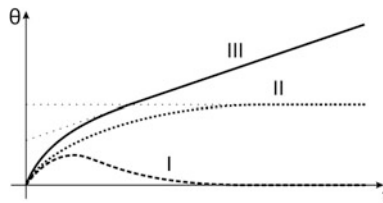


Fig. 37.3 Possible modes for temperature behavior of system

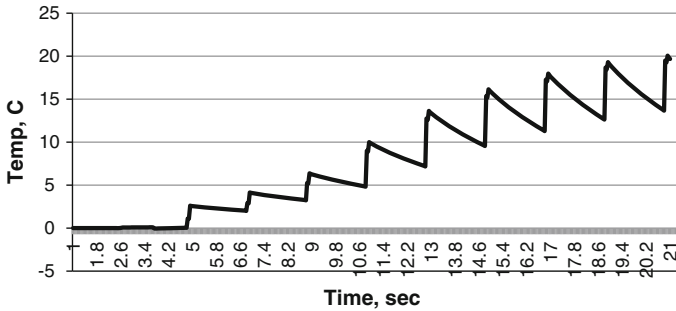


Fig. 37.4 Dynamic characteristic of temperature for a point of disc

- (ii) at high speed of rotation, but small clamping force, the temperature of the point may reach a certain steady state (Fig. 37.3, curve II);
- (iii) in the case of high speed of rotation and large clamping force, the temperature of the point after some moment will grow linearly (Fig. 37.3, curve III).

Let us represent some of the main results of the simulation. Figure 37.4 is a graph of the temperature rising of the brake disc at the point $(\frac{R_1+R_2}{2}, \frac{\pi}{2})$ under pad (at speed 10 rev/s and clamping force 8 kN). As it can be seen from the obtained results, the temperature growth degenerates into a cyclical increasing in temperature by a certain amount. The temperature reduces due to redistribution of the volume of the brake disc and convective heat exchange with environment. It is worth noting several properties corresponding to heating process. Temperature variations for each cycle become more and more with time. It is occurred because in the interval of movement at passing under the pad, temperature at the considered point is defined by the temperature, generated by friction, as well as by heat exchange with the pad. The temperature of the brake pad, unlike disk increases continuously, that leads to that more and more heat transfers to the point during each revolution.

Figure 37.5 demonstrates the temperature distribution on the brake disc after 20 revolutions at speed 1 rev/s. As expected, after a certain number of revolutions the temperature distributes uniformly along the angular coordinate of the disc. This fact allows one to display some simplified correlation to describe the warm process of brake disc for a particular geometry of the problem and inputs in the form of material constants, the values of lower force and speed of rotation for the disc.

Figure 37.6 demonstrates the temperature distributions for disc and brake pad. As it is expected, the temperature of brake pad is significantly higher than the temperature of brake disc. Moreover, holes of brake disc, providing a ventilation system, contribute significantly to the heating process and the temperature distribution.

An important result of the simulation consists in demonstration of the effect that maximum temperature of the disc disposes at a distance from the contact area and does not locate on the surface. In reality, the depth of this effect is of approximately 200–500 μ . In the finite-element statement, the value of temperature gradient

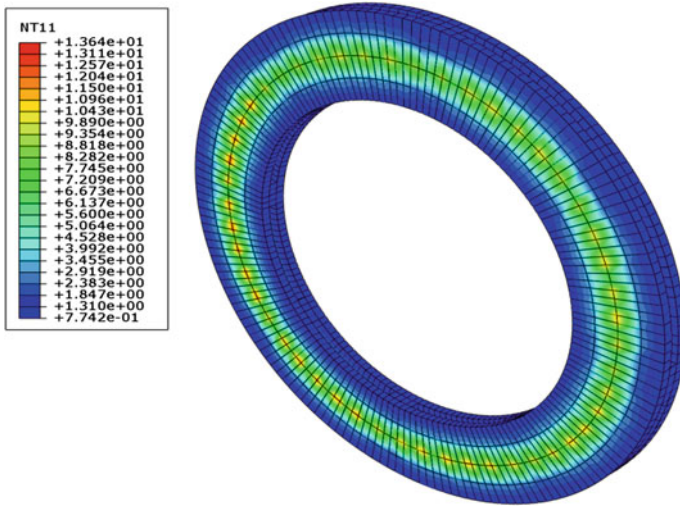


Fig. 37.5 Temperature gradient of the disc

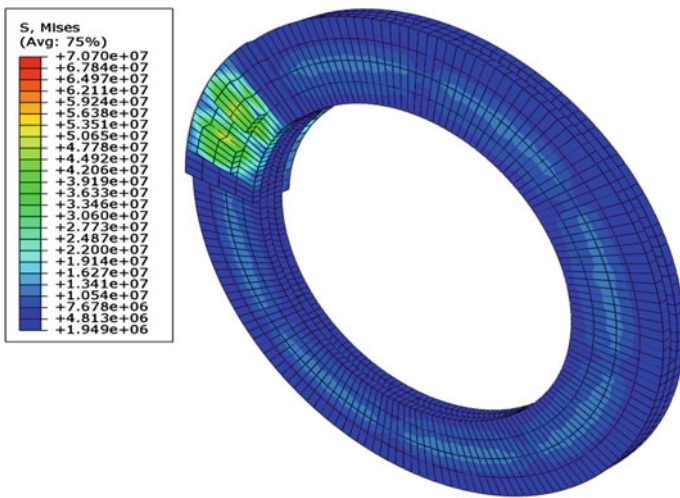


Fig. 37.6 Effective stresses on the disc and pad (irregular stress distribution on the disc is caused by partitions of ducts)

increases with the heat convection. Figure 37.7 demonstrates the temperature distribution in depth of the disc.

Likewise, it is possible to observe this effect in area of high-localized light color (see, Fig. 37.8).

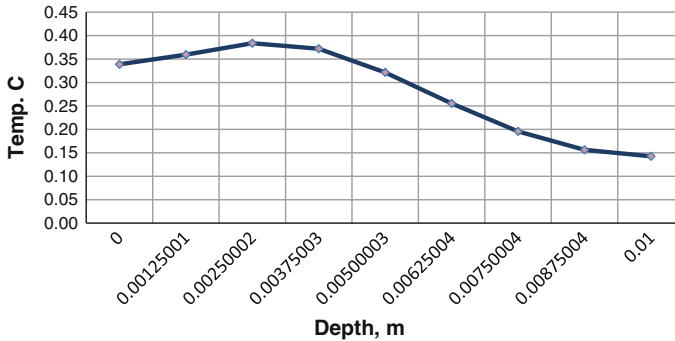


Fig. 37.7 Temperature gradient in depth of the disc

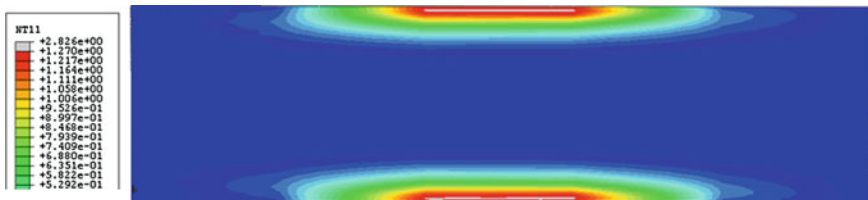


Fig. 37.8 Temperature gradient on cross-section of the disc

We verified the obtained results for undersurface maximum by using the experimental temperature defined by the method based on Rayleigh waves [8]. Further research will be devoted to analysis of influence of temperature field and temperature gradient, calculated using simulation described above, on the physical-mechanical (hardness, elastic modulus) and frictional properties (tribo-EMF, diffusion, friction transfer film) for tribo-connections.

To establish dependence of hardness and elastic modulus on temperature, we developed laboratory setup of thermo cryo-chamber and added it to hardness-meter and tension machine [8–10]. Temperature level and accuracy of measurement for specimen and environment guaranteed automatically by regulation and turning of heating element. The cooling of chamber is conducted by carbon dioxide passing through a tube cooler, supplied with gear.

By using the mathematical modeling methods and planning experiment, we demonstrated separate and common influence of temperature gradient on physical, mechanical and tribological characteristics of plastics [10].

The regression equations and equivalent surfaces were constructed by authors for tribo-characteristics allowing one to optimize the values of thermal gradients that led to minimal and steady values for friction and wear rate. We proved that common effect from action of temperature gradient deviates significantly from the additive rule. At the same time, temperature range, characterizing specific type of

wear and transfer, can be displaced to the increasing or decreasing of surface temperature in accordance with level and sign of temperature gradient.

We also analyzed the influence of load value, slippery speed rate, coefficient of mutual overlapping, temperature of friction surface and temperature gradient on the friction coefficient and wear rate.

Surface temperature for polymeric specimen was regulated by changing the temperature of second body. At the same time, the temperature gradient for polymer body was stabilized by changing the bulk temperature. The experimental study was performed by using frictional machine.

We determined dependencies for temperature gradient influence on value and polarity of triboelectrization [10]. In particular, we demonstrated that for polar polymers, the increasing of temperature leads to decreasing of positive tribocharging, but for nonpolar—to increasing of one due to corresponding changes in the level of the chemical potential. By using traditional scheme of measuring the tribo-EMF, the use of brush-collector qualitatively distorts the results, since the brush itself forms an extra pair of friction. We developed brushless methodology for measuring tribo-EMF in wide range of temperature for direct and inverse friction pairs.

We established the regularities of the influence for temperature gradient on the diffusion processes taking place in the area of metal-tribocontact [11]. In addition, we demonstrated the fact that changing of diffusive hydrogen concentration in steel specimen generated from polymer tribodestruction products significantly nonlinear and based on value and direction of temperature gradient. Wherein, maximal hydrogen concentration in steel specimen can be seen in the zone of maximum temperature.

We studied the dependence of triboelectric and diffusive processes with mechanism of hydrogen wear for metal-polymeric triboconnections [10, 12]. In particular, we establish that increasing of temperature gradient and negative potential on metal surface leads to decreasing of wear resistance, both for polymer and metal due to intensive hydrogenation.

In the result of using modern physical methods for studying of surface phenomena, we stated basic dependencies of temperature gradient influence on forming of friction transfer film (FTF) for polymeric materials [13]. Another result is description of processes in metal-polymer tribo-connection of frictional separation for components and demonstration of the fact that kinetics for process of FTF is determined by value and direction of thermal and electrical fields on contact and can be described effectively by the double layer model.

37.4 Conclusions

On the base of the established dependencies of temperature gradient influence on tribomechanical, triboelectrical and tribochemical processes in polymer-metal contact, we can formulate common recommendations for choosing fillers and reinforcing materials:

- (i) for antifriction composite polymeric materials, the main criterion for providing minimal friction coefficient and high wear resistivity is ability to create spontaneously double layer film on the surface of friction, including lubrication properties and high adhesion rate due to different polar charging of composites;
- (ii) for frictional materials, the most important criterion of high wear rate exclusion and metal moving to plastic surface is decreasing of hydrogenation rate for metallic body by creating optimal temperature gradient and positive tribocharging.

Acknowledgments The research was carried out with support of the Russian Science Foundation (project No. 14-29-00116).

References

1. N. De Bruijn, *Asymptotic Methods in Analysis* (North-Holland, Amsterdam, 1958)
2. H.A. Yaryshev, *Heat Mass Transf.* **10**, 561 (1974). (In Russian)
3. M. Vishik, L.A. Lusternik, *Russ. Math. Surv.* **15**, 4 (1960)
4. V.I. Kolesnikov, A.I. Zadorozhniy, V.E. Kovalchuk, *Herald Eng.* **12** (1986). (In Russian)
5. S.A. Lomov, *Introduction to the General Theory of Singular Perturbations* (Nauka, Moscow, 1981). (in Russian)
6. A.N. Tikhonov, A.A. Samarski, *Equations of Mathematical Physics* (Nauka, Moscow, 1977). (in Russian)
7. W. Novacki, *Dynamic Problems of Thermoelasticity* (Springer, Berlin, 1975)
8. V.I. Kolesnikov, *Thermal-Physical Processes in Metal-Polymeric Tribo-Systems* (Nauka, Moscow, 2003). (in Russian)
9. Y.A. Evdokimov, V.I. Kolesnikov, *Fr. RRIRT*, 103 (1974). (In Russian)
10. V.I. Kolesnikov, A.I. Teterin, *Fr. RRIRT*, 105 (1974). (In Russian)
11. Y.A. Evdokimov, V.I. Kolesnikov, A.V. Chelohyan, *Izv. SKNCVS, Technical Sci.* **1** (1987). (in Russian)
12. D.N. Garkunov, V.I. Kolesnikov, A.V. Chelohyan, *Friction Wear* **4**, 5 (1983)
13. V.N. Kravchenko, V.I. Kolesnikov, A.P. Sichev, *Friction Wear* **35**, 6 (2014)

Chapter 38

The Influence of Antifriction Fillers on the Mechanical and Thermal Characteristics of Metal Polymer Tribosystems

P.G. Ivanochkin and S.A. Danilchenko

Abstract In order to study the effect of antifriction fillers on the mechanical and thermal characteristics of composite materials, the theory of efficient modules was applied. In the given chapter, this approach is used to calculate the thermo-elastic moduli and coefficients of thermal conductivity of the two-phase composite material with a matrix based on aliphatic polyamide-6 and with different percentages of filler as rayon-based carbon fiber. The package ANSYS is used as a tool to simulate the composite representative volume and the finite-element analysis of its effective thermo-elastic properties. The two-phase composite with randomly placed dispersed inclusions was considered in the chapter as well. The simple random method of a representative volume generating was applied to obtain the structure of such a composite. The calculation of effective characteristics was carried out at the various parameters of the filler fraction, which ranges from 5 to 40 % in increments of 5 %. The obtained data showed that the values of the density, elastic modulus, Poisson's ratio, coefficient of linear thermal expansion and the thermal conductivity increases with the increasing of filler concentration. To confirm the obtained results, the experimental investigations were conducted to determine elastic modulus in NanoTest 600, the setup for definition of physical and mechanical characteristics in submicron and nano-volumes. The gotten as an experiment result the modulus was compared with the corresponding calculated value. Errors of results do not exceed 3 %. In order to assess the filler effect on the friction processes the test problem of rectangular composite stamp sliding on steel bars was considered. The model of this contact interaction was implemented in ANSYS. The results indicate that when the stamp has the properties of PA6, the heating temperature is much higher than the using UPA6-30 values. Based on these data, we can make preliminary conclusion that the addition of RCF into PA6 leads to the improvement of its thermal characteristics.

P.G. Ivanochkin (✉) · S.A. Danilchenko
Rostov State Transport University, Rostov-on-Don, Russia
e-mail: ivanochkin_p_g@mail.ru

38.1 Introduction

The widespread usage of composite materials with dispersed fillers in tribotechnology leads to the necessity of determining the physical and mechanical properties of these materials.

The conduction of appropriate tests appears to be the most preferred option to determine the required characteristics of the composite. However, resource-intensiveness, investment ratio and in some cases impossibility to carry out such tests are limiting factors for their fulfillment.

The usage of reference data about materials can be another potential option. However, this method allows obtaining adequate results only if the ready-made composite with known measured properties is used, while for creating a new material, which must meet certain requirements in accordance with its intended application area, tabular data simply do not exist.

The theory of efficient moduli seems to be a compromise between these two approaches. It allows determining the characteristics of the material based on the properties of its structure components.

In the given chapter, this approach is used to calculate the thermo-elastic moduli and coefficients of thermal conductivity of the two-phase composite material with a matrix of aliphatic polyamide-6 with different fractions of filler from rayon-based carbon fibers. The package ANSYS is used as a tool to simulate the composite representative volume and finite element analysis for definition of its effective thermo-elastic properties. To confirm the obtained results the experimental investigations were conducted to determine elastic modulus in NanoTest 600, the setup for definition of physical and mechanical characteristics in submicron and nano-volumes. In order to assess the filler effect on the friction processes the heat dissipation by friction test problem was considered.

38.2 Theory of Effective Moduli

The research of the mechanical behavior of composite materials includes an analytical study on the macro- and micro levels. In micromechanics material is regarded as non-uniform structure consisting of inclusions (fibers, particles, crystals) and a matrix, where these inclusions are disposed [1, 2].

One of the most important results by solving the problems in their micromechanical formulation is calculation of effective moduli that are coefficients relating the volume-averaged values of the tension tensor components and deformation under certain boundary conditions. These conditions are of two types: the conditions for the movement on the boundary (38.1) and the condition for the tension on the boundary (38.2):

$$u_i(S) = \varepsilon_{ij}^0 x_j \quad (38.1)$$

$$T_i(S) = \sigma_{ij}^0 n_j \quad (38.2)$$

where n_j are the components of unit vector of the outer normal to the boundary surface, S , x_j are the Cartesian coordinates of points of the surface, ε_{ij}^0 and σ_{ij}^0 correspond to constant tensors. For heterogeneous body under condition (38.1), the averaged volume strain is ε_{ij}^0 . Under condition (38.2), averaged volume stress is σ_{ij}^0 . If conditions (38.1) or (38.2) are stated, the effective moduli C_{ijkl} are defined with the following equation.

$$\langle \sigma_{ij} \rangle = C_{ijkl} \langle \varepsilon_{kl} \rangle \quad (38.3)$$

$\langle \rangle$ denotes averaging operation.

This method is based on the concept of a representative element of the volume, for which the average values of all components of the stress tensor and strain tensor are equal to those of a whole composite.

There are various approaches to solving the described problem. In the given chapter, the algorithm based on [3] was applied. It was assumed that the composite is characterized by a weak anisotropy. This assumption allows us to simplify the task, since in this case for finding a complete set of effective moduli is sufficient to solve 4 problems: (i) the problem of tension along one of the axes, (ii) the problem of a shift in one of the planes, (iii) the problem of thermal expansion and (iv) thermal conductivity problem.

38.3 Methods of Generation of Representative Volumes

The two-phase composite with randomly placed dispersed inclusions was considered in the chapter as well. The simple random method of generating a representative volume was applied to obtain the structure of such a composite.

This method is based on the Monte Carlo method [4], which solves the problems by means of random sequences. Since the observable composite is a binary one, thus each of its particles may be a material (matrix), or filler. From a mathematical point of view this means the following: there is a matrix of $N \times N \times N$ size, consisting of 0 and 1, only. In this case, 0 indicates that the cell contains a material, while 1 corresponds to filler.

The essence of the simple random method of generating a representative volume is as follows. In the first step some of the filler concentrations ρ_n is given and then, according to the formula $N_n = [N^3 \rho_n]$ (where $[.]$ is the integral part), the number of cells being filler is determined. Further, with the help of a special program, using a random number generator, the coordinates of the filler cells x_n, y_n, z_n are defined, and a binary composite is generated with the found coordinates.

38.4 Calculation Results of Efficient Characteristics of the Composite Material with Matrix Based on Aliphatic Polyamide-6 and with Different Percentages of Rayon-Based Carbon Fiber

In accordance with the procedures described in Sects. 38.2 and 38.3, in the finite-element package ANSYS, there were established the programs at the command language ANSYS APLD, allowing calculating of the effective thermo-elastic moduli and thermal conductivity of a two-phase composite. The parameter N was set equal to 15. In the simulation of a representative volume (see Fig. 38.1) for solving thermo-elasticity problems, we used 20-nodal finite element in the form of hexahedron SOLID226 with options for thermo-elastic analysis.

For the problem of the thermal conductivity, we also used 20-nodal finite element in the form of hexahedron SOLID90. Both elements provide a quadratic in the canonical variables approximating displacement and temperature fields.

The taken test samples are composites based on aliphatic polyamide-6 (PA6) with different percentages of rayon-based carbon fiber (RCF). Table 38.1 shows some properties of the components making up the composite. They were used as input data in the problems.

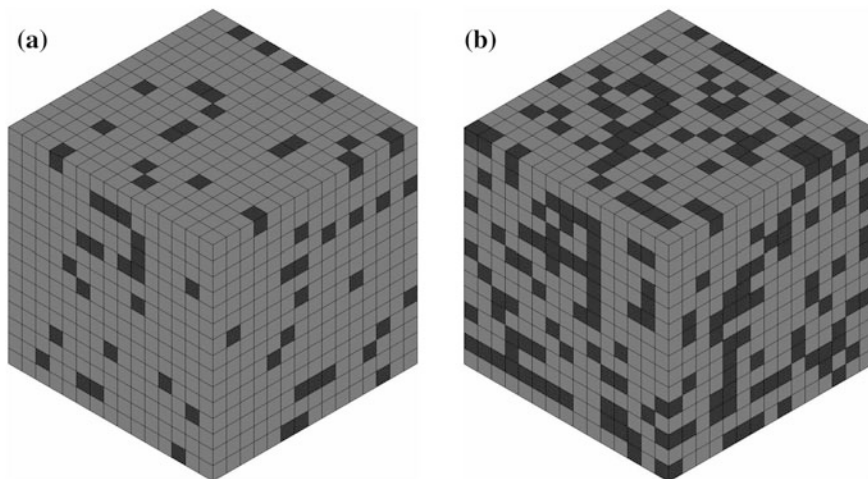


Fig. 38.1 Model of representative volume in ANSYS: **a** 10 % of filler, **b** 30 % of filler

Table 38.1 Properties of aliphatic polyamide-6 and rayon-based carbon fiber

Material/properties	PA6	RCF
Density ρ , kg/cm ³	1135	1535
Modulus of elasticity E , GPa	0.065	25
Poisson ratio ν	0.49	0.25
Coefficient of thermal expansion $\alpha \cdot 10^{-6}$, 1/K	80	1
Coefficient of thermal conductivity k , W/(m K)	0.32	24

The calculation of effective characteristics was carried out at the various percentage parameters of the filler, ranging from 5 to 40 % in increments of 5 %. The obtained results are summarized in Table 38.2.

Finite-element analysis allows one to investigate the stress-strain state and evaluate local stress concentration in simulated representative volume. As an example, Fig. 38.2 shows the results of calculations for the problem of uniaxial tension along x -axis.

Table 38.2 The value of effective characteristics of the composite with a matrix based on PA-6 and RCF at different percentages of the filler

Material/properties	UPA6-5	UPA6-10	UPA6-15	UPA6-20	UPA6-25	UPA6-30	UPA6-35	UPA6-40
ρ , kg/cm ³	1155	1175	1195	1215	1235	1255	1275	1295
E , GPa	0.210	0.415	0.728	1.125	1.655	2.382	3.264	4.182
ν	0.372	0.317	0.28	0.256	0.248	0.24	0.234	0.231
$\alpha \cdot 10^{-6}$, 1/K	58.4	42.2	28.9	20.6	14.5	10.3	7.6	6.0
k , W/(m K)	0.597	0.99	1.54	2.253	3.221	4.213	5.394	6.619

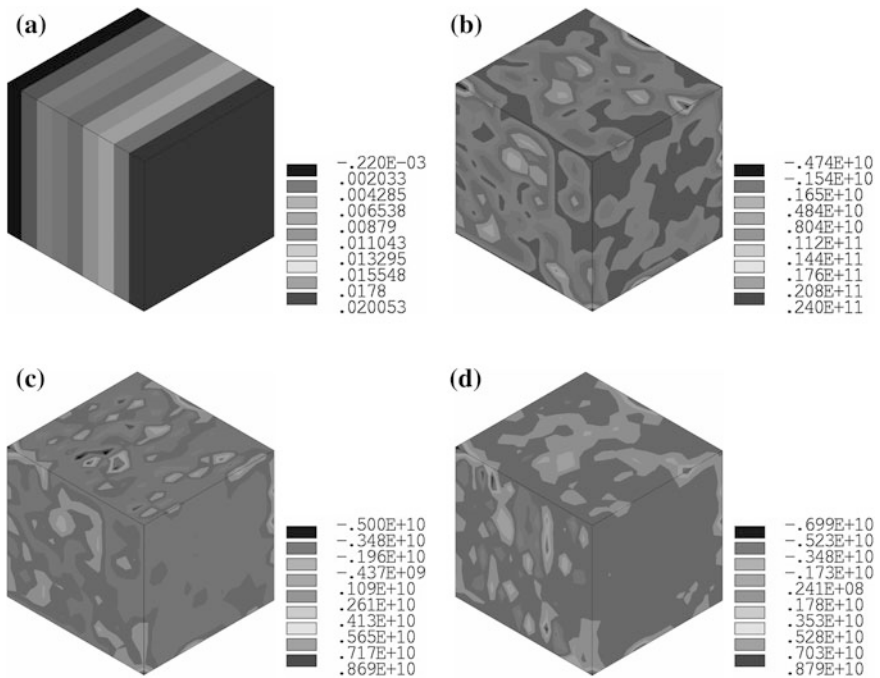


Fig. 38.2 Numerical results for the problem of uniaxial tension along x -axis. **a** ϵ_x , m; **b** σ_x , Pa; **c** σ_y , Pa; **d** σ_z , Pa

38.5 Determination of Physical and Mechanical Properties of Composites by Micro- and Nanoindentation Method

Based on the tribological considerations and results of calculation of the effective characteristics, the composite material UPA6-30 was tested as a sample. Determination of physical and mechanical properties of the material was implemented with micro- and nanoindentation method, using NanoTest 600 setup. The composite sample subjected to repeated indenting of spherical shape diamond indenter. As a result, we obtain a number of superimposed hysteresis curves “load—depth of penetration”.

Then, the values of microhardness, reduced elastic modulus, and elastic recovery are calculated from the obtained data, on the base of spherical analysis [5].

The essence of the spherical analysis is as follows. According to Hertz theory, for the applied load P , we have the following expression:

$$P = \frac{4}{3} E_r R^{1/2} h_e^{3/2}. \quad (38.4)$$

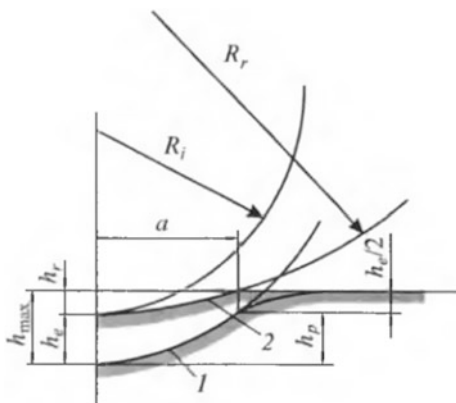
In common case, R does not mean the initial radius of the sphere, but some effective value R^* determined by the relation:

$$\frac{1}{R^*} = \frac{1}{R_i} - \frac{1}{R_r}, \quad (38.5)$$

where R_i is the radius of the indenter; R_r is the radius of profile of the reduced imprint after complete unloading. Geometric correlations at indentation with a spherical indenter are shown in Fig. 38.3.

Considering the elastic deflection of the surface, the depth of unreduced imprint is equal to

Fig. 38.3 Geometric correlations at indentation with spherical indenter



$$h_{\max} = h_r - h_s. \quad (38.6)$$

By assuming that at elastic recovery during unloading the imprint pin radius remains the same (since it is close to reality), the elasticity theory predicts that $h_s = h_e/2$, where h_e is the value of elastic recovery of the imprint. Then

$$h_p = h_{\max} - h_e/2. \quad (38.7)$$

In accordance with the known value of h_p the projection of the contact area is calculated as $A_c = \pi a^2 = \pi(2Rh_p - h_p^2)$, and then the hardness H is calculated with the ratio $H = P/A_c$. The obtained value H is equal to an average contact stress at the penetration of rigid sphere into elastic half-space.

Oliver-Pharr method [6] is used to determine modulus of elasticity and hardness in the case of elastic-plastic deformation.

Unloading leads to elastic recovery of the imprint, which is calculated considering the principles of the theory of elasticity, and then the derivative of h of the expression (38.4) defines relationship for rigidity.

$$S = \frac{dP}{dh} = 2E_r R^{1/2} h_e^{1/2} = 2E_r R^{1/2} (h_{\max} - h_p)^{1/2}. \quad (38.8)$$

By comparing formulae (38.4) and (38.8), we obtain

$$P = \frac{2}{3} \frac{dP}{dh} h_e \quad (38.9)$$

or

$$h_e = \frac{3}{2} P \frac{dh}{dP}. \quad (38.10)$$

Due to in the elastic case $h_s = h_e/2$, we have

$$h_s = \frac{3}{4} P \frac{dh}{dP} \quad (38.11)$$

and

$$h_p = h - h_s = h - \frac{3}{4} P \frac{dh}{dP}. \quad (38.12)$$

Based on the known value of h_p , we find a contact radius, a , as

$$a = \sqrt{2R_i h_p - h_p^2} \approx \sqrt{2R_i h_p}. \quad (38.13)$$

Last approximate equality is valid for $h_p \ll a$. Knowing the contact radius, we can calculate the projection of the contact pad and define rigidity.

We have for rigid indenter $h_e = a^2/R$, then together with (38.8) this gives

$$S \approx \frac{dP}{dh} = 2E_r R^{1/2} (a/R^{1/2}) = 2E_r a, \quad (38.14)$$

where the modulus of elasticity is

$$E_r = \frac{dP}{dh \cdot 2a} = \frac{1}{2} \frac{dP}{dh} \sqrt{\frac{\pi}{A_c}}. \quad (38.15)$$

For the given modulus E_r , we can define expression between it and elastic moduli of the tested material and indenter in the form:

$$\frac{1}{E_r} = \frac{1 - \nu_1^2}{E_1} + \frac{1 - \nu_2^2}{E_2} \quad (38.16)$$

where E_1, ν_1 are the elastic modulus and Poisson's ratio of the indenter, and E_2, ν_2 are the elastic modulus and Poisson's ratio of the tested material.

During indentation, we used diamond cone indenter with a spherical tip. The radius of curvature of the tip was $R = 25 \mu\text{m}$. The diamond had a set of standard values of the elastic modulus and Poisson ratio. The first of them was equal to $E_1 = 1141 \text{ GPa}$, and the second was equal to $\nu_1 = 0.07$, respectively. We performed 10 cycles of 'loading—unloading' with increments of $25 \mu\text{m}$ and applied load $P = 150 \text{ mN}$. The indentation results for UPA6-30 sample are present in Table 38.3.

Table 38.3 The indentation results for UPA6-30 sample

Test no.	Max depth of penetration, nm	Rigidity H , GPa	Reduced elastic modulus E_r , GPa
1	5990.42	0.239	2.486
2	6168.95	0.231	2.410
3	5237.71	0.288	2.630
4	5410.1	0.270	2.689
5	6460.62	0.219	2.373
6	6509.03	0.217	2.326
7	5577.98	0.266	2.496
8	5731.72	0.247	2.696
9	5420.53	0.268	2.715
10	5657.22	0.257	2.554

Fig. 38.4 Hysteresis curve for ‘loading—unloading’ cycle of UPA6-30 sample

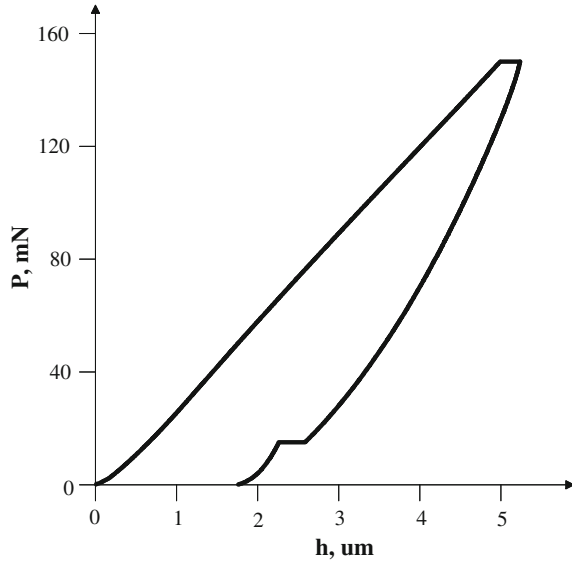


Table 38.4 Comparison of elastic moduli obtained experimentally (1) and calculated efficient modules (2) for UPA6-30 sample

	1	2
Elastic modulus E , GPa	2.451	2.382

Figure 38.4 shows a hysteresis curve for a single step of ‘loading—unloading’ cycle for the UPA6-30 sample.

We take the average value of the reduced elastic modulus from the obtained data and in accordance with formula (38.16) recalculated the elastic modulus of the composite. The obtained modulus compared with the modulus from Table 38.2 (see Table 38.4).

As we can see from Table 38.4, the calculation error does not exceed of 3 %. This fact leads to the conclusion that the proposed method for the determination of effective moduli can be used for assessment of thermo-elastic characteristics of composite materials.

38.6 Influence of Filler Fraction on Heating Temperature of Composite as Friction Result

Since the test material is intended for use in node details of tribomating, the significant interest arises to the process of its heating in the result of tribocontact, and influence of the filler fraction on this process. To investigate such an influence, we

considered the test problem on rectangular composite stamp sliding on steel bars. In this problem, all elastic and thermal characteristics, as well as the friction coefficient assumed temperature-independent. Under these assumptions, there is a heat flux between the contacting bodies. The density of the heat flux calculated as

$$q = f_{HTG}\tau v, \quad (38.17)$$

where f_{HTG} is the coefficient of energy dissipation, τ is the friction stress, v is the friction speed. The heat distribution between the bodies depends on the weighting coefficient of heat distribution f_{WTG} . Its values range from 0 to 1 and allow determining what proportion of the heat transfers into the first body (see formula (38.18)) and what proportion of the heat transfers into the second body (see formula (38.19)). In this problem f_{WTG} was set equal to 0.5.

$$q_1 = f_{WTG}q; \quad (38.18)$$

$$q_2 = (1 - f_{WTG})q. \quad (38.19)$$

The numerical model of this contact interaction was realized in ANSYS using the methodology described in [7]. In order to simplify the calculations, the problem was solved in a two-dimensional statement. In the simulation of stamp and bars, the plane finite elements PLANE13 with the option of a thermo-elastic analysis were applied. Contacting couples were represented with the finite elements CONTA171 and TARGE169, which were selected at the respective boundaries of the bodies.

Since the problem is dynamic, such type of analysis as TRANSIENT with one time step $t_{STEP} = 30$ s was used. The amount of substeps was determined at the assumption on ensuring continuous convergence of the algorithm, and was equal to 3000.

The calculations were performed for the stamp of two materials (PA6 and manufactured UPA6-30). Their properties selected from Tables 38.1 and 38.2, respectively. In both cases, the upper boundary of the stamp was subject to pressure $P = 1$ MPa, which compressed it to the bar. The speed of the stamp and the coefficient of friction was equal to $v = 0.5$ m/c and $f_{friction} = 0.2$, respectively. The initial temperature was $T_0 = 20^\circ\text{C}$.

The obtained results indicate that when the stamp had PA6 properties, the heating temperature was much higher than the temperature obtained by using UPA6-30 properties. Figures 38.5 and 38.6 show graphs of the temperature distribution along the bottom boundary of the stamp for PA6 and UPA6-30, respectively, at the time $t = 30$ s.

Based on the obtained data, we can make preliminary conclusion that the addition of RCF into PA6 leads to the improvement of the physical and thermal characteristics of later. In the future, we plan to consider the problem, where the properties of the material will depend on temperature.

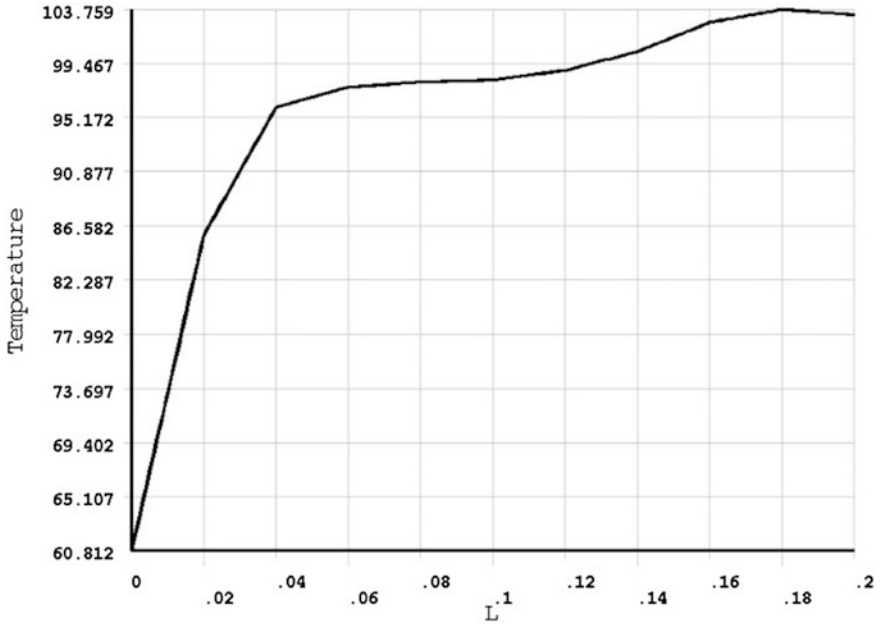


Fig. 38.5 Graphs of the temperature distribution for PA6

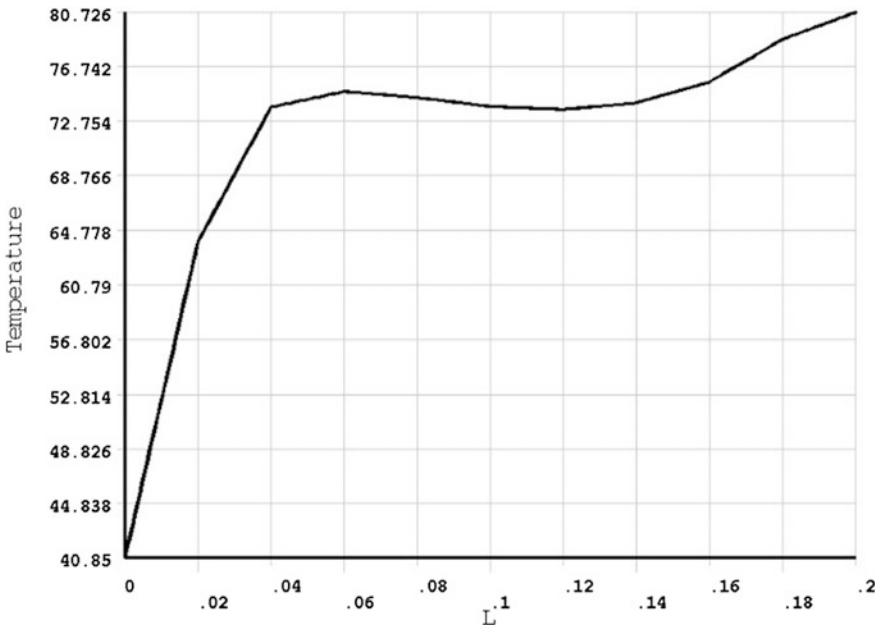


Fig. 38.6 Graphs of the temperature distribution for UPA6-30

38.7 Conclusion

This chapter presents the results of calculations of effective thermo-elastic moduli of composite materials with a matrix of aliphatic polyamide-6 with different fraction of rayon-based carbon fibers. The package ANSYS was used as a tool for implementation the finite-element models of representative volume of the test materials. The obtained data showed that the values of the density, elastic modulus, Poisson's ratio, coefficient of linear thermal expansion and thermal conductivity increase with the increasing of filler concentration.

Some experiments were conducted to determine the elastic characteristics for the selected model material UPA6-30 by using NanoTest 600 setup for determining the physical and mechanical characteristics. The comparison of the elastic modulus found numerically and experimentally, did not reveal any serious differences. This fact indicates that applied numerical methods can be used to estimate the effective characteristics of the composite materials.

The test problem of heat generation by friction was solved in the FEM package ANSYS. Based on the obtained results, the preliminary conclusions show that the increase of the filler concentration reduces the intensity of heating the composite.

Acknowledgments This study was supported by the Russian Science Foundation (grant number 14-29-00116).

References

1. *Mechanics of Composite Materials*, ed. by J. Sendetsky (Mir, Moscow, 1978) (in Russian)
2. B.E. Pobedrya, *Mechanics of Composite Materials* (Moscow State University Press, Moscow, 1984). (in Russian)
3. A.V. Nasedkin, A.A. Nasedkina, V.V. Remizov, *Comput. Continuum Mech.* **7**(1), 100 (2014) (in Russian)
4. N. Metropolis, S. Ulam, *J. Am. Stat. Assoc.* **44**(247), 335 (1949)
5. Y.I. Golovin, *Nanoindentation and Its Possibilities* (Mashinostroenie, Moscow, 2009). (in Russian)
6. W.C. Oliver, G.M. Pharr, *J. Mater. Res.* **7**(6), 1564 (1992)
7. P. Wiggers, C. Miede, *Comput. Methods Appl. Mech. Eng.* **113**, 301 (1994)

Chapter 39

Theoretical and Experimental Study of Carbon Brake Discs Frictionally Induced Thermoelastic Instability

A.G. Shpenev, A.M. Kenigfest and A.K. Golubkov

Abstract Frictionally induced thermoelastic instability (TEI) arises when the positive feedback between the contact pressures and temperatures become more than negative one. The first one exists due to thermal expansion of the material, and the second one due to the surface wear. TEI is typical mainly for brake systems, because of their high thermal load (Afferrante et al. *Wear* 254:136 (2003) [1]; Zagrodzki *Int. J. Solids Struct.* 46:2463 (2009) [2]). Usually TEI leads to vibrations, noise and increased wear in brake systems. In this chapter, we examine the connection between TEI and wear resistance for two composite materials based on carbon fibers (graphite and carbonated) and pitch carbon matrix. Composite, based on graphite fibers (TERMAR ADF-OS), has long been used in industry as a material for aircraft brake discs (JSC “Rubin”), and has stable characteristics and high wear resistance. The material on the base of carbonized fiber (TERMAR ADF-KV) is new and be in process of testing.

39.1 Testing Conditions

Materials were tested with friction machine IM-58 and experimental bench. The machine IM-58 uses friction samples with a diameter of 7 cm, the experimental bench uses full-size aircraft brake discs (40–50 cm in diameter) (Fig. 39.1).

Testing machines represent inertial friction machines in which the inertial masses are connected to the movable composite discs and accelerated to a certain speed. Afterwards the masses are braked by compression of movable and fixed discs. After the series of braking, the average wear is measured as disc thinning (Fig. 39.2).

A.G. Shpenev (✉)
Institute for Problems in Mechanics, Russian Academy of Sciences,
Moscow, Russia
e-mail: kel-a-kris@list.ru

A.M. Kenigfest · A.K. Golubkov
JSC “Rubin”, Moscow, Russia



Fig. 39.1 Experimental samples (*left*) and full-size brake discs (*right*)

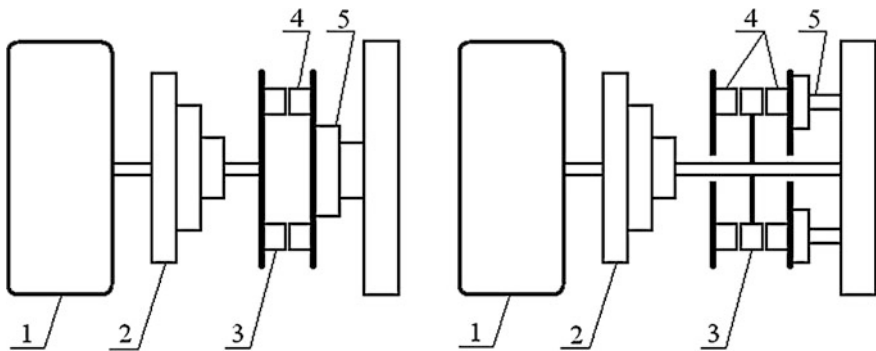


Fig. 39.2 Scheme of inertial tribological tests of carbon composites; *left* is the friction machine IM-58, *right* are the three-disc experimental bench for testing full-size brake discs: 1 motor, 2 inertial masses, 3 movable discs, 4 fixed discs, 5 clamping system

During the test of material ADF-KV, a paradoxical situation has arisen: the test results for wear on the IM-58 and experimental bench differed several times at specially selected equivalent conditions, while the material of AD-OS was running stable and gave the same results for all tests:

Material	Wear $\mu\text{m}/\text{braking}$	
	IM-58	Experimental bench
TERMAR ADF-OS	0.5–1.5	0.1–1.0
TERMAR ADF-KV	1.0–2.5	4.0–6.0

At the initial stage, there was a hypothesis of overheating in new material large discs because of worse heat exchange. To investigate this hypothesis, a study was conducted of the temperature test conditions by setting of the thermocouples in the thickness of fixed disc. The measurement results for the samples on the machine

IM-58 are in good agreement with the simulation. Results on the experimental bench had the following features: temperature varied from braking to braking, the results could be roughly divided into “cold” and “hot”, which succeeded each other with a good periodicity. Figure 39.3 shows the typical “cold” and “hot” testing and layout of thermocouples. Based on these data, we concluded presence of TEI during friction of full-size ADF-KV brake discs, and the circular nature of instability (temperature is evenly distributed along the sliding direction and varies in the transverse direction). This explains the absence of additional vibration and roar when testing new material.

39.2 Thermal Conduction Problem

To confirm the hypothesis of ring-shape TEI, we formulated and solved the problem of non-stationary frictional heating of composite brake discs on the three-disc experimental bench. Let us consider the section of extreme disc and half of the adjoined disc of the three-disc brake (Fig. 39.4). The cross-section has the shape of a rectangle with $3h$ height and $R_2 - R_1$ width. The insulation mode is performed on upper and lower bounds. Convection cooling $a(T)$ takes place on the sidewalls.

In parallel to the base line passing at the height h , the heat flux $q(r, t)$ is attached:

$$q(r, t) = 2Q_{br} \left(\frac{1}{t_{br}} - \frac{t}{t_{br}^2} \right) \left(1 + \sin \left[2\pi \left(\frac{r}{\Delta R} \pm 0.25 \right) \right] \right),$$

here the sign of plus corresponds to the cold braking (Fig. 39.5, right), the sign of minus corresponds to hot braking (Fig. 39.5, left); t_{br} is the braking time; Q_{br} is the average braking energy density:

$$Q_{br} = \frac{I\varphi_0^2}{2S},$$

where S is the contact surface square, I is the spinning masses moment of inertia, φ_0 is the initial rotational speed.

Simulation of temperature field in friction discs is carried out by solving the non-stationary heat conduction problem:

$$\lambda_r \frac{1}{r} \frac{\partial}{\partial r} \left(r \frac{\partial T}{\partial r} \right) + \lambda_z \frac{\partial^2 T}{\partial z^2} = c\rho \frac{\partial T}{\partial t}.$$

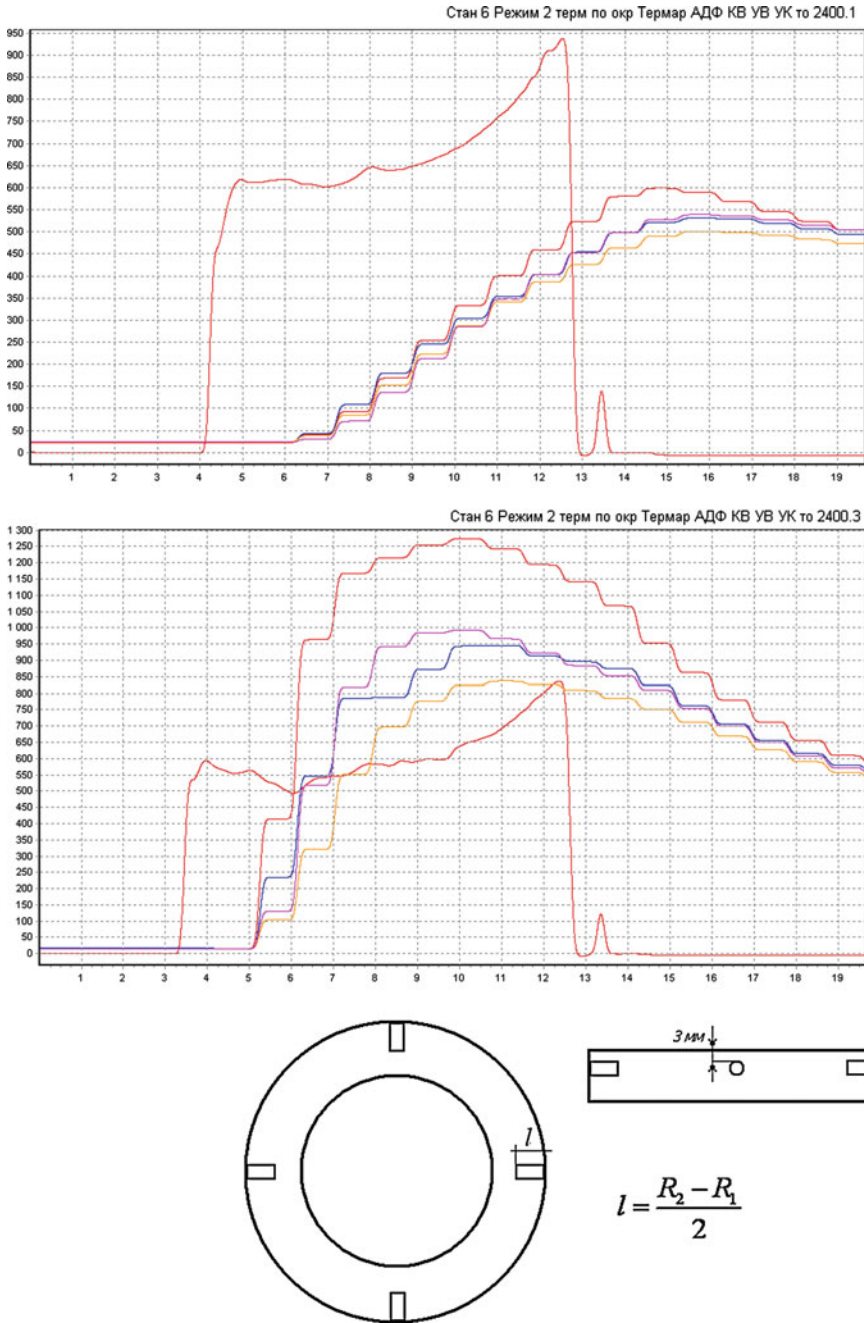


Fig. 39.3 Arrangement of thermocouples (*downwards*) and test results for different brakings (*upwards*)

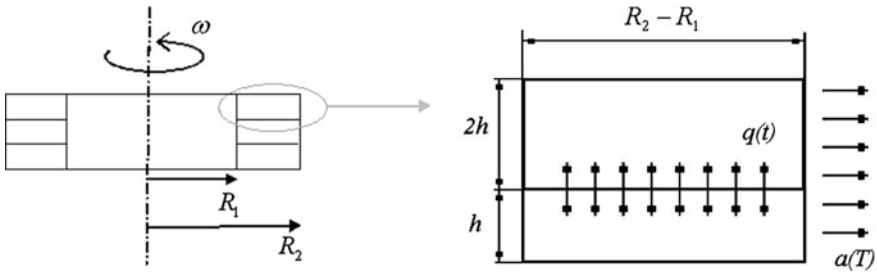


Fig. 39.4 Thermal conducting problem formulation

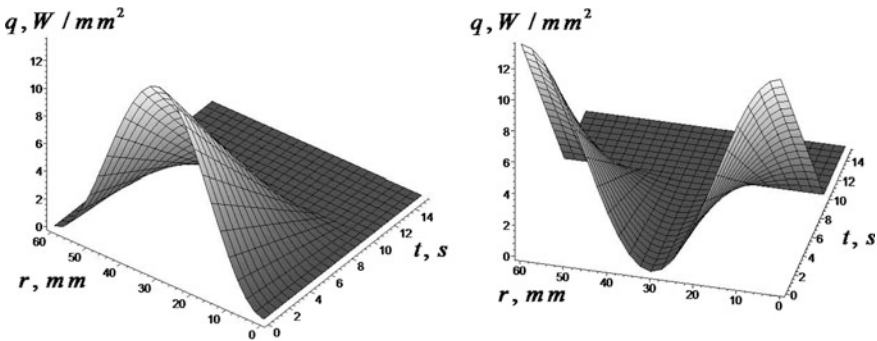


Fig. 39.5 Friction heat flux versus time and radius

If $R_1 \gg R_2 - R_1$, we can consider $r \approx \text{const}$:

$$\lambda_r \frac{\partial^2 T}{\partial r^2} + \lambda_z \frac{\partial^2 T}{\partial z^2} = c\rho \frac{\partial T}{\partial t},$$

λ_r and λ_z are the coefficients of disc thermal conductivity in the directions r and z , c is the heat capacity, ρ is the density of the composite.

Test parameters are the following:

$$I = 410 \text{ kg m}^2, \varphi_0 = 147 \text{ rad/s}, t_{br} = 10 \text{ s}, S = 2.66 \cdot 10^3 \text{ mm}^2, a = 4 \text{ J/(K m}^2\text{)}.$$

The solution was found by finite difference method using the explicit difference scheme. The calculated temperature versus time at the point located at a depth of 3 mm in the middle of the friction track (where the temperature was measured with thermocouples in the experiment) is shown in Fig. 39.6 on the left. Red color corresponds to the distribution in Fig. 39.5 on the left, and green color corresponds to the distribution in Fig. 39.5 on the right). The calculated dependence shows good agreement with the experimental curves in Fig. 39.3.

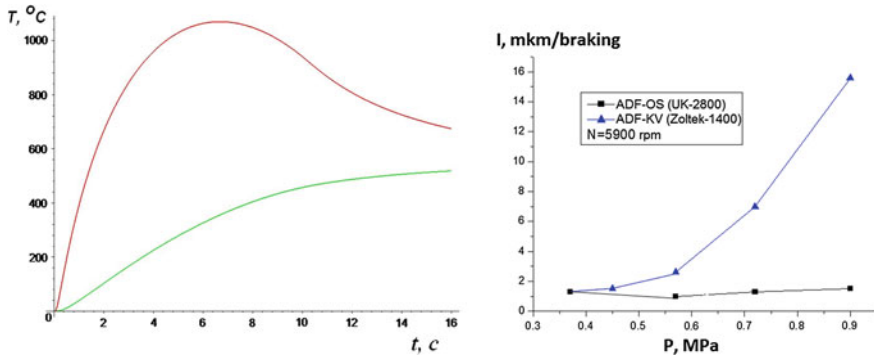


Fig. 39.6 Theoretical temperature versus time in the measurement point (left) and experimental dependence of wear from average contact pressure (right)

39.3 Composite Wear Rate

However, studies [3, 4] show that dependence of the wear from temperature of carbon composites has weak and non-monotonous character, so changing the temperature itself cannot cause a catastrophic increase of wear observed in the experiments. Let us consider the law of wear of composite material in the form: $\dot{l} = \dot{l}(p, T, v, \mu)$, where i is the wear rate, p is the contact pressure, T is the contact temperature, v is the sliding velocity, μ is the friction coefficient.

Based on the above and the fact that the friction coefficients of the considered materials vary slightly, wear law can be rewritten as $\dot{l} = Cp^n v$.

Then the average wear of the sample in a single braking (measured in the experiment) will be equal to

$$\tilde{l} = \frac{Cv_0 t_{br}}{2S} \int_s p^n dr \quad \int_s p dr = P.$$

Its form is mainly determined by the n : when $n = 1$, the average wear is:

$$\tilde{l} = \frac{CQ_{br}}{\mu} \tag{39.1}$$

It is important that in this case average wear does not depend on the total contact pressure or the distribution of the contact pressures. In the case of $n > 1$, average wear will be minimal at a uniform contact pressure distribution and will increase with the appearance of uneven contact pressure distribution (TEI). If the pressure distribution is uniform: $p = P/S$, then average wear will be equal to:

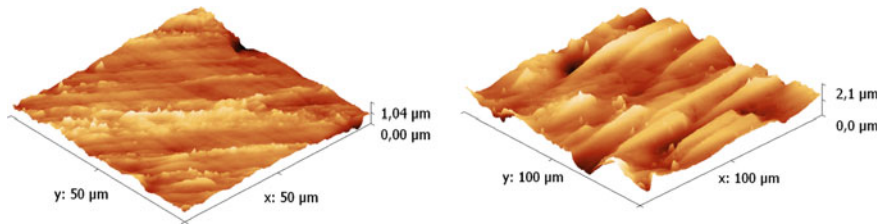


Fig. 39.7 Micro profilograms of friction surfaces of ADF-OS (*left*) and ADF-KV (*right*)

$$\tilde{l} = \frac{CQ_{br}P^{n-1}}{\mu S^{n-1}}. \quad (39.2)$$

Figure 39.6 on the right shows the average wear versus the average contact pressure for the considered materials, other conditions being equal on the friction machine IM-58, that is, with a uniform distribution of contact pressure (no TEI). At the material ADF-OS, wear is independent from the pressure, and the material ADF-KV has quadratic dependence of wear from pressure. Hence, in accordance with the formula (39.2), we can conclude that $n \approx 1$ for the ADF-OS, but $n \approx 3$ for ADF-KV. Such a difference in the influence of the contact pressure on the wear rate for similar materials can be explained by differences in the structure of their friction surfaces. Figure 39.7 shows micro profilograms of friction surfaces of these materials, made by scanning probe microscopy. The surface of ADF-KV is much rougher due to protruding fibers and hence by increasing the contact pressure, its abrasive properties are playing more significant role in the destruction of the surface layers by friction than for the material of ADF-OS.

From the formulae (39.1), (39.2), we obtain that the wear of material ADF-OS is not affected by TEI, while ADF-OS material shows much greater wear during braking in presence of TEI. For example, for the contact pressure distribution corresponding to the distribution of the heat flow in Fig. 39.5 (presence of TEI) the material of ADF-KV ($n = 3$) will have 2.5 times higher wear then in the case of constant contact pressure (no TEI) (that is in good agreement with experiment). Thus after braking in the places of contact pressures and temperature concentrations, wear will increase. Figure 39.8 shows the profiles of the full-size ADV-KV brake disc surface in the direction perpendicular to the sliding direction. They are in good agreement with the distribution of surface pressures and temperatures according to Fig. 39.5, right.

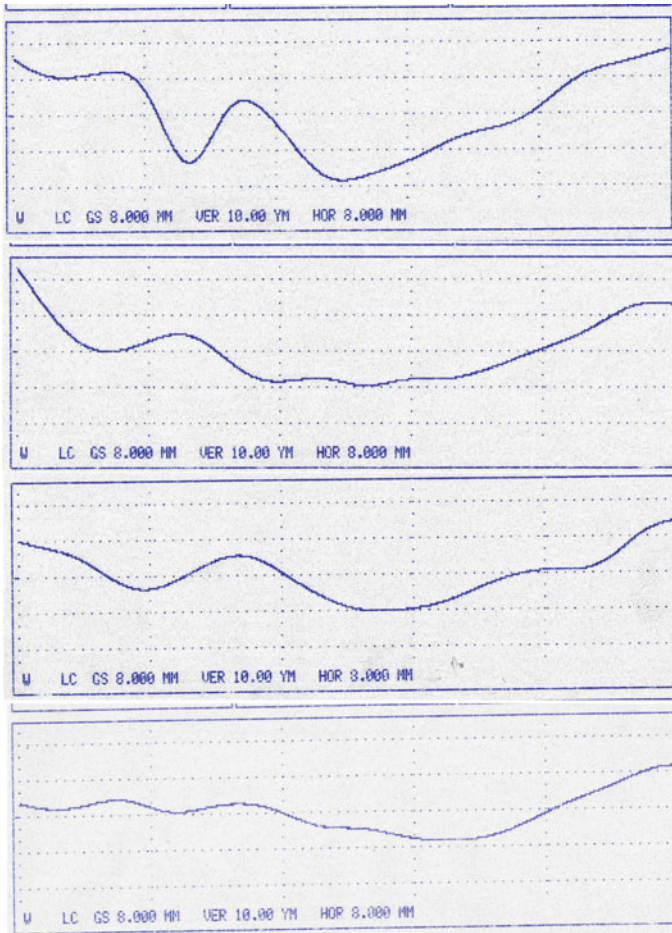


Fig. 39.8 Profiles of the full-size ADV-KV brake disc friction surface in the radial direction

39.4 Conclusions

We have found that during work of full-size carbon-based composite brake discs may occur frictionally induced thermoelastic instability. This phenomenon can lead to increased wear of the brake discs and mismatch results for different test specimens of the same material. However, there are conditions under which this phenomenon is safe. These conditions are determined by the dependence of the wear rate of the material from the contact pressure, which in turn is determined by the structure of the friction surface and the material itself. The obtained results can be used to optimize the tribological properties of carbon composites.

Acknowledgments This research was supported by the Russian Foundation for Basic Research, project No. 14-01-00372-a.

References

1. L. Afferrante, M. Ciavarella, P. Decuzzi, G. Demelio, *Wear* **254**, 136 (2003)
2. P. Zagrodzki, *Int. J. Solids Struct.* **46**, 2463 (2009)
3. C. Byrne, Z. Wang, *Carbon* **39**, 1789 (2001)
4. H.-K. Shin, H.-B. Lee, K.-S. Kim, *Carbon* **39**, 959 (2001)

Part IV
Applications of Advanced Materials

Chapter 40

Development of New Metamaterials for Advanced Element Base of Micro- and Nanoelectronics, and Microsystem Devices

O.A. Ageev, S.V. Balakirev, A.V. Bykov, E. Yu. Gusev, A.A. Fedotov,
J.Y. Jityaeva, O.I. Il'in, M.V. Il'ina, A.S. Kolomiytsev, B.G. Konoplev,
S.U. Krasnoborodko, V.V. Polyakov, V.A. Smirnov, M.S. Solodovnik
and E.G. Zamburg

Abstract The results of experimental researches of the geometrical parameters of vertically aligned carbon nanotubes (VACNTs) are present by atomic force microscopy. The analysis of the applicability of the different AFM modes to determine the geometrical parameters of VACNTs array was carried out and based on this analysis the rapid-technique for determination of the length of the nanotubes in VACNTs array was developed. Unified two-layer polysilicon surface micro-machining process for manufacture of biaxial micromechanical gyroscope, triaxial micromechanical accelerometer and biaxial nanomechanical accelerometer was proposed. Polysilicon inertial masses were fabricated by optical lithography, dry etching under different masks and wet etching of sacrificial layer. We developed AFM-technique for determination of electrical parameters GaAs nanowires (NWs), which does not require additional operations of NW fixation and allows one to estimate the resistivity and conductivity type of NW material. The obtained results can use to develop of the nanodiagnostic methods and the processes of formation of micro- and nanoelectronic elements based.

O.A. Ageev (✉) · S.V. Balakirev · A.V. Bykov · E.Yu.Gusev · A.A. Fedotov · J.Y. Jityaeva
O.I. Il'in · M.V. Il'ina · A.S. Kolomiytsev · B.G. Konoplev · S.U. Krasnoborodko
V.V. Polyakov · V.A. Smirnov · M.S. Solodovnik · E.G. Zamburg
Institute of Nanotechnologies, Electronics and Electronic Equipment Engineering,
Southern Federal University, Taganrog, Russia
e-mail: ageev@sfedu.ru

40.1 Introduction

The use of new carbon nanomaterials helps to achieve significant progress both in prospective nanoelectronic component technology and synthesis of nanomaterials with unique properties [1].

Carbon nanotubes (CNT) are one of the most promising objects studied by nanotechnology [2]. They have a number of unique properties, such as high aspect ratio, good conductivity, striking emission characteristics and high chemical stability, which means there are vast prospects for their use [3].

Hybrid carbon nanostructures (HCNs) are carbon nanotubes modified in order to obtain desirable properties of a future product. They combine all the advantages of CNTs and provide new opportunities for their use in various fields of science and industry [4].

Due to unique geometrical and electrical properties the vertically aligned carbon nanotubes (VACNTs) are the most promising materials for the formation of the modern nano- and microelectronic devices (emitter structures, elements of random-access memory, interconnections, etc.) [1–5]. However, for the VACNTs array application as basic components of such devices is necessary to make detailed researches of their properties, both electrical and geometrical.

One of the promising methods for the nanoscale structures research is the method of atomic force microscopy (AFM), which allows one to determine the parameters of the substrate surface without special sample preparation, as well as to make its modification by tip nanolithography [6, 7]. Additionally, the AFM method allows statistical processing of the measured parameters and one to determine their quantitative value. Therefore, the determination of the geometrical parameters of the VACNTs by the AFM is an actual task. However, in the investigation of the VACNTs array, the each mode of the AFM method has scanning artifacts, which should be taken into account by determining the parameters of VACNTs. This chapter describes the features of the VACNTs array study using a contact, semi-contact and noncontact modes of AFM.

Polysilicon processes for use it as the structural material in surface-micromachined devices such as gyroscope accelerometers and cantilevers have been reported (see e.g. [8–11]). Two, three and five polysilicon layers processes for manufacture of individual devices are described. Distinct approaches have been developed in order to reduce the number of layers and process steps. Surface micromachining offers the possibility of producing micromechanical devices using standard IC processing techniques [8, 9]. One of the main problems of micro- and nanosystems is a fabrication gyroscope simultaneous with accelerometer on a chip. It could be solved by development of the unified fabrication technology.

ZnO is widely used in nanoelectronics, spintronics, sensing, MEMS, optoelectronics and acoustoelectronics [12]. It has a high melting point and thermal conductivity, photosensitivity, piezoelectric and pyroelectric effects, anisotropic crystal structure, semiconductor properties with a large band gap, high integration with silicon technology, biocompatibility, chemical resistance and high sensitivity to

atmospheric concentrations of toxic and hazardous gases due to its ability to reversible chemisorption [12, 13].

To increase the gas sensitivity of the films made of oxide materials, surface nanostructuring technology has been actively used, including nano-profiling and creating nanopores and nano-sized grains [13], with the formation of nanostructured materials with controlled parameters being highly important. The grain size and resistivity are the most important parameters of nanostructured films when used as detecting elements of gas sensors, depending on methods and modes of formation.

One of the promising methods of the formation of nanostructured ZnO films is pulsed laser deposition (PLD), which allows controlling a large number of process parameters, enabling a wide range of controlled changes in the electrical, physical, chemical, mechanical and structural parameters of ZnO films [13, 14].

The dopant in GaAs NW forming by molecular beam epitaxy (MBE) may behave differently from the bulk material. This is due to possible changes in the NW crystal structure as well as features of vapor-liquid-solid growth mechanism [15–18]. Therefore, the development of a rapid method for NW doping level and conductivity type estimation is an urgent task today.

The above micro- and nanostructures are new metamaterials for advanced element base of micro- and nanoelectronics and microsystem devices.

40.2 Hybrid Carbon Nanotube-Based Nanostructures Used in Nanostructured Materials: Investigation of Process Parameters

This work is aimed to studying the influence of process parameters on HCNs formation performed by a multifunctional cluster-type UVH nanotechnology platform NANOFAB NTK-9.

To carry out CNT modification, we formed three samples where a vertically oriented CNT array was synthesized on a silicon substrate. CNT diameter and height were about 30–70 nm and 5–6 μm , respectively, and tip growth prevailed. We used acetylene (C_2H_2) as reaction gas.

Sample 1 was subjected to ion-beam etching (Fig. 40.1a) for 2 min at a beam current of 0.1 nA and an ion gun accelerating voltage of 30 keV. Thus we removed the catalyst particles from the tops of nanotube array.

CNTs grown on Sample 2 (Fig. 40.1b) were functionalized by carbon using ion beam-induced deposition. The result we obtained was mushroom-shaped HCNs. So, such a modification of CNT apexes leads to an increase in the active area of CNTs used as sensitive elements of micro- and nanosystem technology, e.g. gas sensors and nanowhiskers.

CNTs grown on Sample 3 were functionalized by tungsten using ion beam-induced deposition in order to form new catalytic centers different from the original one (nickel). This coating provides an opportunity to deposit a metal layer

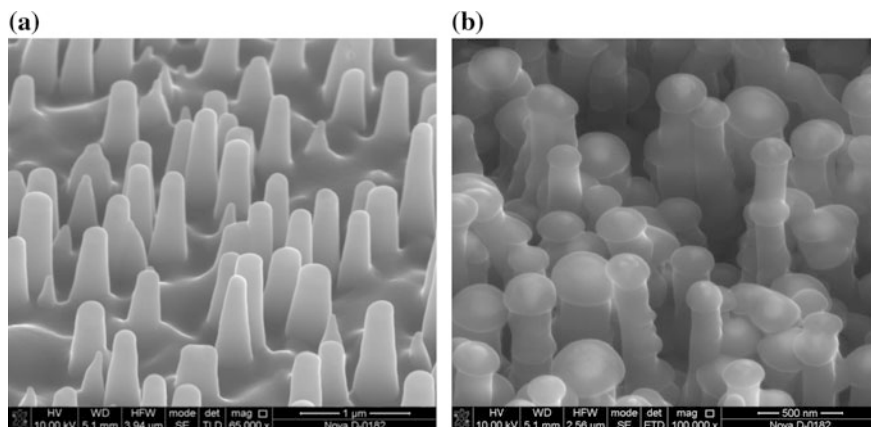


Fig. 40.1 Modified CNTs: **a** Sample 1, **b** Sample 2

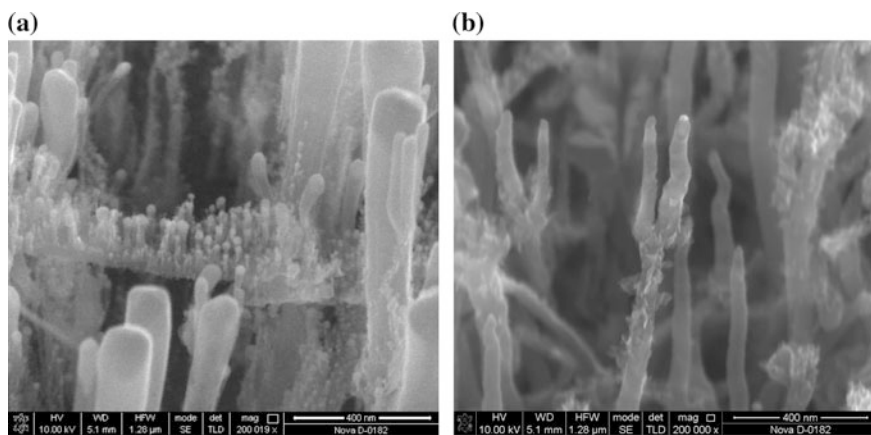


Fig. 40.2 Modified CNTs: **a** Sample 2, **b** Sample 3

onto semiconductor CNTs and thus increase the number of conductive nanotubes used as emitters in CNT-based displays and ionized gas sensors.

Having prepared the substrates with modified CNTs, we started to synthesize HCNs by putting the modified substrates into plasma enhanced chemical vapour deposition (PECVD) module and repeating CNTs growth there. The structures obtained were studied by using SEM (Nova NanoLab 600).

The studies showed that the shortened CNTs on Sample 1 were opened and further growth did not occur because of the lack of catalyst particles.

We discovered that thinner nanotubes with graphite flakes were formed on Sample 2 (Fig. 40.2a). There was some extra growth on the tops of CNTs coated

with tungsten (Sample 3). This led to HCNs formation, notably Y-shaped ones (Fig. 40.2b). Such HCNs can be used in nanoelectronics, e.g. as transistor elements in nanoelectronic devices.

Having analyzed the results, we identified the main parameters that influence HCN formation. We noticed the growth of extra lateral nanotubes on CNTs coated with carbon, and the direction of this growth was determined by the position of original nanotubes relative to the vector of the electric field generated by induced plasma. Since the materials of the nanotubes and the deposited film were identical, we decided to synthesize HCNs without carbon film deposition. In order to maximize the growth area we formed CNT arrays without a clear vertical orientation. During the first phase CNTs were grown at a pressure of 4.5 torr. Then the CNT array was subjected to extra growth with increased chamber pressure (3.5 torr).

Finally, we obtained HCNs coated with graphite flakes (Fig. 40.3). Having the same properties as nanotubes, these HCNs can be characterized by larger surface development and more complex geometric shapes, which means they have better adsorption capacity and can be dispersed in polymers more easily forming more stable dispersions. Therefore such HCNs can be used as fillers in various compounds.

In this work we used and studied different process parameters of CNT modification and HCNs synthesis. We obtained modified Y-shaped hybrid carbon nanostructures that can be used as elements of nanoelectronics. We successfully grew HCNs coated with graphite flakes which are characterized by more developed surface and complex geometric shapes and can be used as compound fillers and hydrogen accumulators.

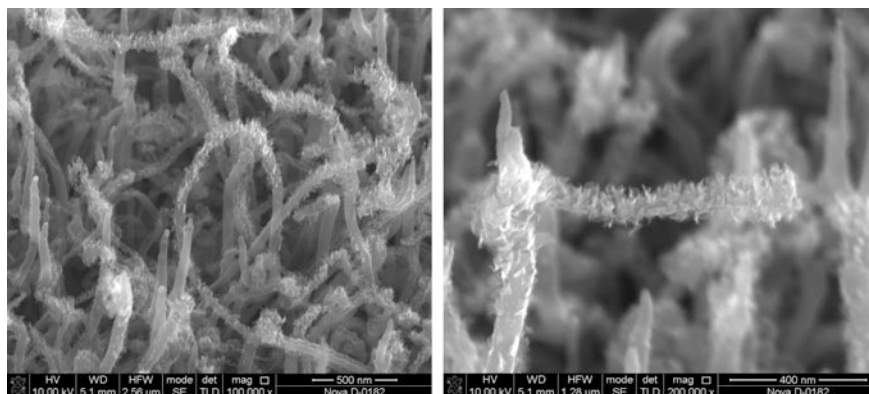


Fig. 40.3 HCNs covered with graphite flakes

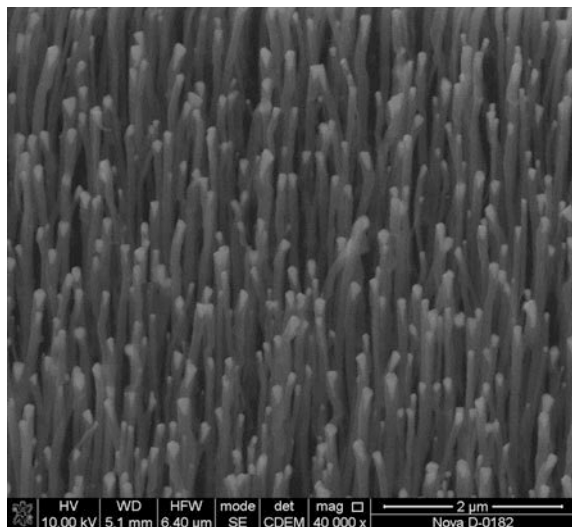
40.3 Determination of Geometrical Parameters of Vertically Aligned Carbon Nanotubes by Atomic Force Microscopy

The array of vertically aligned carbon nanotubes was deposited by plasma enhanced chemical vapour deposition (PECVD). The investigations of the surface of the obtained VACNTs array were carried out by using a scanning electron microscope Nova Nanolab 600 (FEI, Netherlands). The results are present in Fig. 40.4. The analysis of the obtained SEM image allowed us to estimate the diameter equal 80 nm, the length of nanotubes equal $2\ \mu\text{m}$ as well as the density of the nanotubes in the VACNTs array equal $30\ \mu\text{m}^{-2}$.

The more detailed study of the VACNTs array surface was carried out by using NanoLaboratory Ntegra (NT-MDT Co, Russia) in the contact, semicontact and noncontact AFM modes. The tip was a silicon cantilever NSG 20. The software package ImageAnalysis 3.5 was used for the experimental data processing. For the identification the most optimal scanning mode of the VACNTs array surface, the investigations of the VACNTs array were carried out in the each mode of the AFM method. The results of scanning the VACNTs array are present in Fig. 40.5.

The analysis of the AFM images, obtained in the contact mode, showed that during the scanning process of the VACNTs array surface, the tip “tore” the carbon nanotubes from the substrate surface, and by the way break sometimes occurred at 40–160 nm height from the bottom of the nanotube (Fig. 40.5a). Thus, the contact AFM mode cannot be used for the research and definition of geometrical parameters of the VACNTs.

Fig. 40.4 SEM image of vertically aligned carbon nanotubes array



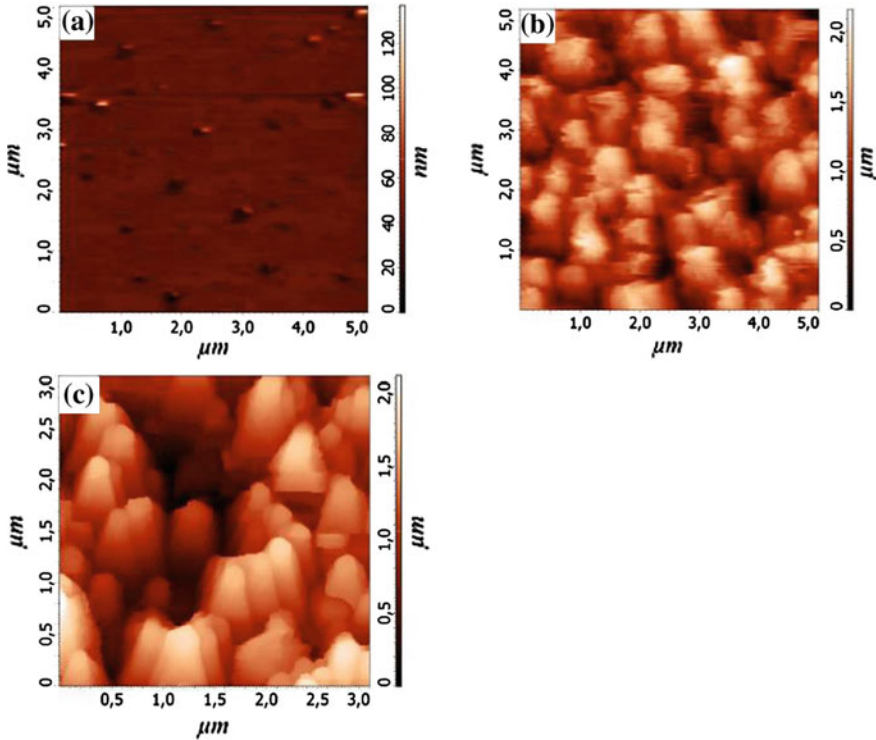


Fig. 40.5 AFM images of the VACNTs array surface obtained in: **a** contact mode, **b** semicontact mode, **c** noncontact mode

As result of the study of the VACNTs array surface by semicontact AFM mode, the AFM image was obtained and shown in Fig. 40.5b. The analysis of the AFM image showed that the individual nanotubes formed bundles under the influence of the tip. Statistical processing of the AFM images allowed one to determine the average length of the VACNTs bundle, which is equaled to $1.03 \pm 0.31 \mu\text{m}$, the maximum length was equal to $2.29 \mu\text{m}$ and the density of the bundles in the VACNTs array was equaled to about $1.49 \mu\text{m}^{-2}$.

The main shortcoming of the AFM images of the VACNTs array obtained by semicontact mode is a lot of artifacts of scanning, due to high mobility of the nanotubes by the mechanical contact with the tip and as a consequence the relatively low resolution of this AFM mode (Fig. 40.5b).

Using the noncontact AFM mode, in which the tip interacted with the surface of the array only due to van der Waals forces, allowed to obtain AFM images of the vertically aligned carbon nanotubes bundles with a higher resolution, without apparent artifacts (Fig. 40.5c). The statistical data processing of the AFM images showed that the maximum length of the bundle was $2.52 \mu\text{m}$, the average length

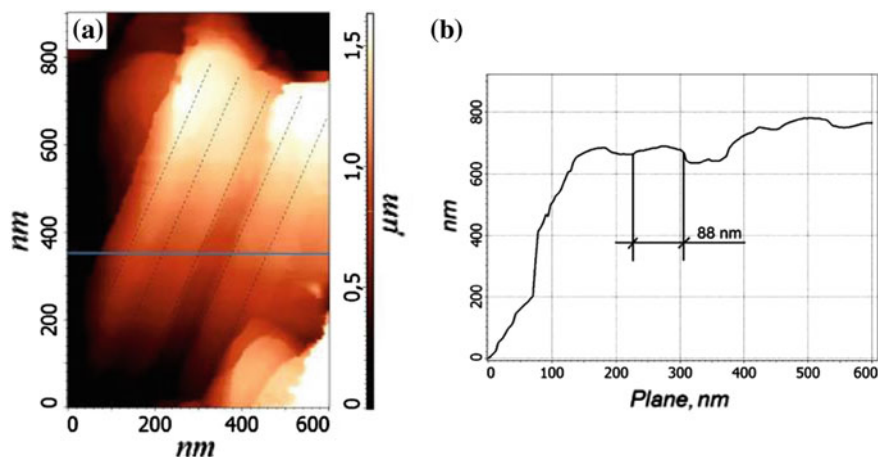


Fig. 40.6 AFM image of the bundle of the vertically aligned carbon nanotubes obtained in the noncontact mode of AFM: **a** surface topology, **b** profile along the *line*

was $1.27 \pm 0.35 \mu\text{m}$ and the density of the bundles in the VACNTs array was $1.68 \mu\text{m}^{-2}$.

While studying the VACNT array by the noncontact AFM mode, the individual nanotubes were also collected in bundles with a diameter of about 300 nm (Fig. 40.5c). During scanning by the noncontact AFM mode, the mechanical impact of the tip on the VACNTs array was absent, thus the causes of the “coalescence” of individual tubes in bundles could be the result of the influence of the van der Waals forces [19].

The analysis of AFM images of individual bundles obtained by the noncontact mode (Fig. 40.6) allowed us to evaluate the average diameter of the nanotubes in the VACNTs array as equal to $88 \pm 10 \text{ nm}$. So it is possible to suppose about the multilayer structure of the CNTs. The number of the individual nanotubes in the bundle was about 18, and the density of nanotubes in the VACNTs array was about $31 \mu\text{m}^{-2}$.

Thus, for the research of the surface and for determination of the geometric parameters of vertically aligned carbon nanotubes by the optimum AFM mode is the noncontact mode, as this mode allows one to obtain AFM images of the VACNTs array with a higher resolution, without destroying the structure of nanotubes. The results obtained by noncontact AFM mode are well correlate with the values of the VACNTs geometrical parameters determined by scanning electron microscopy.

These results were used for development of technique for determining the VACNTs array height based on sequential scanning in the contact, and then in semicontact or noncontact mode of the VACNTs array surface with different squares. In this work, the areas of VACNTs array with squares $10 \times 10 \mu\text{m}^2$, and then $30 \times 30 \mu\text{m}^2$ were scanned (Fig. 40.7a). The analysis of the profile of scanned

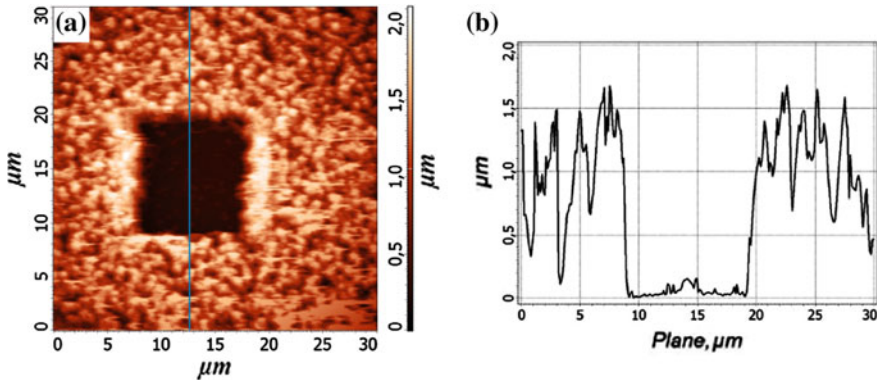


Fig. 40.7 AFM image of the VACNTs array obtained by the developed rapid-technique: **a** surface topology, **b** profile along the *line*

areas by the contact and tapping AFM mode (Fig. 40.7b) allowed one to determine the maximum height of the VACNTs array, which was equal to $1.98 \mu\text{m}$ and the average length of the nanotubes in the VACNTs array was equal to $1.12 \pm 0.45 \mu\text{m}$.

The developed rapid-technique for determining the VACNTs array height allows one to determine the length of the nanotubes with higher reliability than a direct scanning since the measurement of this parameter is carried out relatively to the substrate surface rather than to the greatest penetration depth of AFM probe in the VACNTs array.

In the result of the work, the geometric properties of carbon nanotubes in VACNTs array were investigated. The analysis of the applicability of AFM mode to study the VACNTs arrays was carried out and on the base of this analysis, the rapid-technique was developed for determination of the nanotubes length in the VACNTs array by sequential scanning in the contact, in tapping or noncontact AFM mode of the VACNTs array surface with different squares. It was shown that the optimum AFM mode for determining the diameters and the density of nanotubes in the VACNTs array is noncontact mode, as it allowed us to scan the surface of the VACNTs array without mechanical contact with it.

40.4 Development of Technology for Manufacturing of Polysilicon Inertial Masses of Micro- and Nanomechanical Gyroscopes and Accelerometers

We propose integrated two-layer polysilicon surface micromachining process for manufacture of micro- and nanomechanical gyroscope and accelerometers (Fig. 40.8). An important advantage of it is that only two polysilicon layers are

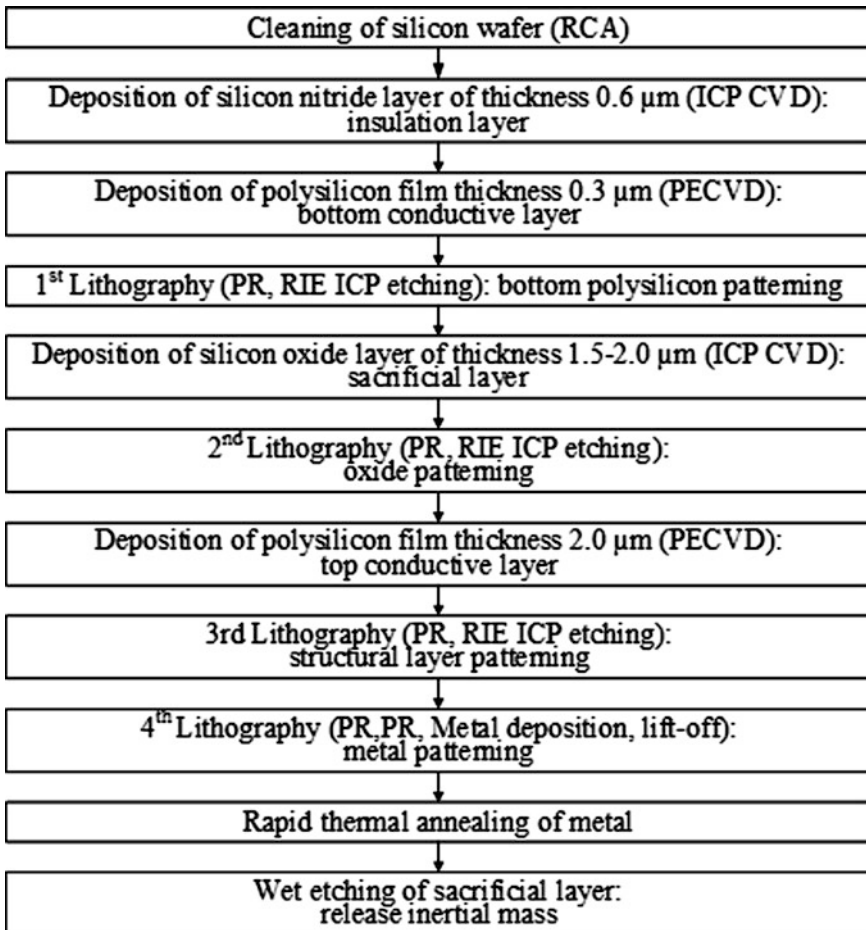


Fig. 40.8 Scheme of unified process

required to fabricate the biaxial micromechanical gyroscope, triaxial micromechanical accelerometer and biaxial nanomechanical accelerometer at one process. The process of manufacture of the nanomechanical accelerometer should include a high aspect ratio etch step by focused ion beams (not shown) [20, 21].

We fabricate polysilicon inertial masses according the following process scheme. The substrate was 100 mm *n*-type silicon wafer Si (100). Insulator film of silicon nitride of 0.6 μm thickness was grown on the substrate using inductively coupled plasma CVD (SemiTEq ICPd81). Then sandwich-like structures of bottom polycrystalline silicon, sacrificial silicon oxide and top polysilicon layers of 0.3, 1.5 and 1.5–2.0 μm were prepared by plasma enhanced (PlasmaLab 100 Oxford Instruments) [22, 23] and ICP CVD.

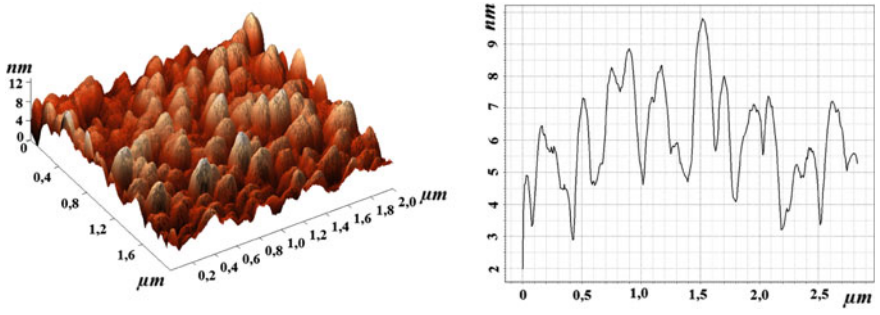


Fig. 40.9 AFM image and cross-section of the Si film deposited at 700 °C

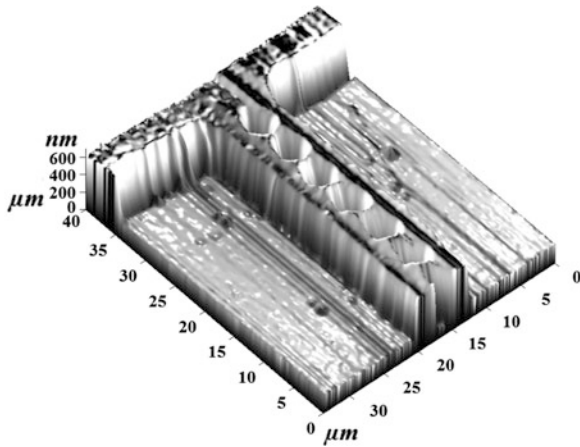
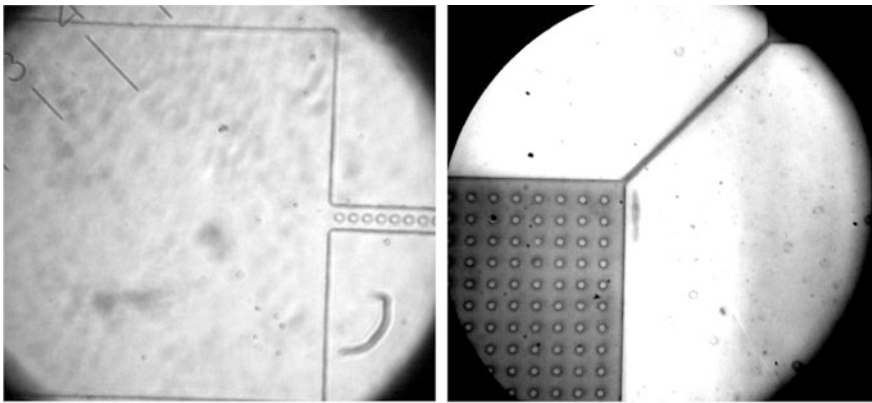


Fig. 40.10 Polysilicon inertial mass structure: optical (*top*) and AFM (*bottom*) images

In our experiments, we investigated the influence of deposition parameters on properties of polysilicon films [20–23]. We showed that structure, refractive index, grain size and surface roughness of polysilicon films depended on temperature, rf-power and chamber pressure of PECVD. They could be well controlled to obtain the polysilicon films with refractive index 4.0–5.0, the grain size and RMS roughness in the range 40–250 nm and 1.1–3.5 nm, respectively, the microhardness 14.66–19.33 GPa and Young modulus 147.03–253.61 GPa (Fig. 40.9) [20–23].

The polycrystalline silicon films were doped using the liquid PCl_3 diffusant (SD. OM-3 M) to $2 \cdot 10^{20} \text{ cm}^{-3}$, $30 \text{ cm}^2/(\text{V s})$ and $9.6 \cdot 10^{-4} \Omega \text{ cm}$ according to Hall/van-der-Pauw measurements. It was observed a decreasing of microhardness and Young modulus of the doped films.

Polysilicon inertial masses were fabricated by optical lithography (SUSS MJB4), dry etching under masks of photoresist, aluminum and nickel (SemiTEq ICPe68), and wet etching of sacrificial layer (Fig. 40.10) [21, 23].

The obtained results could be used to develop process flows for fabrication of micro- and nanomechanical gyroscopes and accelerometers by surface micromachining.

40.5 Development of Technology for Manufacturing of Nanostructured ZnO Films for Gas Sensors

Specialists of REC “Nanotechnology”, SFedU have conducted theoretical and experimental research of the formation of nanostructured ZnO films by pulsed laser deposition. Special measuring benches were designed and manufactured. Modes of formation of nanostructured ZnO films by PLD, stable during thermal cycling, were determined.

It was shown that by changing the substrate-target distance, the pressure, temperature, energy density of laser emission, the duration and temperature of annealing can be controlled. We obtained nanostructured ZnO film with resistivity from $1.7 \cdot 10^{-3}$ to $7.13 \cdot 10^4 \Omega \text{ cm}$, surface roughness from 0.75 to 22 nm, grain diameter from 40 to $1.4 \cdot 10^2 \text{ nm}$, carrier concentration from $8.9 \cdot 10^{12}$ to $8.5 \cdot 10^{19} \text{ cm}^{-3}$, and carrier mobility from 2.36 to $27 \text{ cm}^2/(\text{V s})$ [13, 24, 25].

Figure 40.11 shows the SEM and AFM images of a nanostructured ZnO film, obtained by PLD.

Evaluation of width of the spatial charge region, W , during the adsorption of CO , NO_2 , NH_3 at the concentration of 5 ppm on ZnO surface and also gas sensors based on it was conducted. It allowed us to obtain criteria for the grain diameter, d , film thickness, h , and operating temperature of gas sensor on the base of nanostructured ZnO films, necessary for high gas detection sensitivity.

If a nanostructured ZnO film is considered as consisting of a layer of columnar grains, then the maximum gas detection will be achieved with the full depletion of the charge carriers of the grain volume, i.e., at satisfying the criteria: $d \leq 2W$, $h \leq W$.

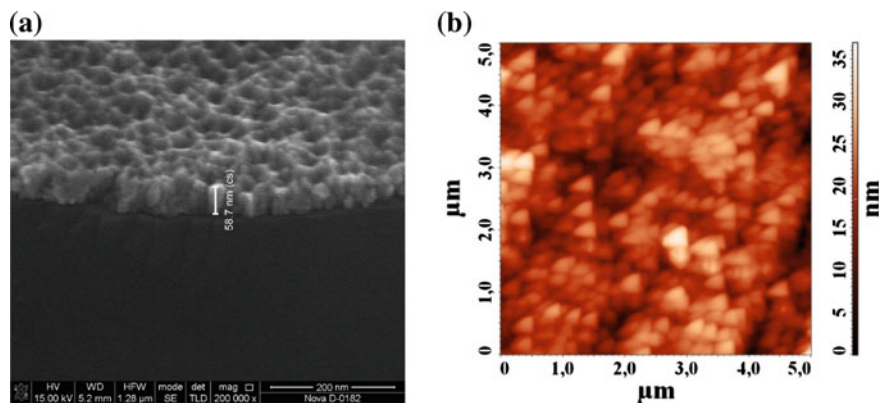


Fig. 40.11 SEM (a) and AFM (b) image of nanostructured ZnO film, obtained by PLD

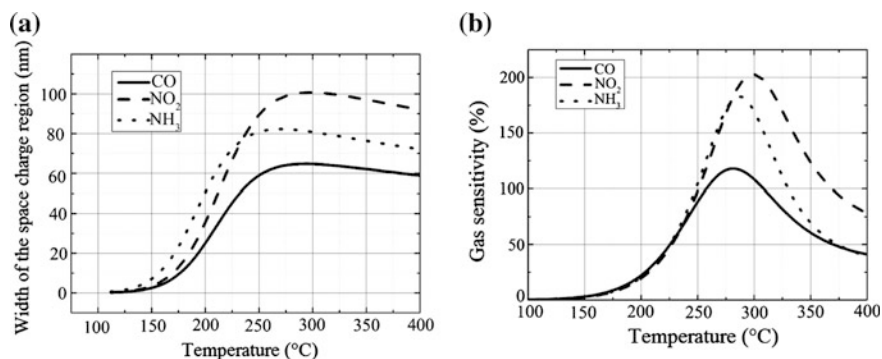


Fig. 40.12 Dependencies of width of the spatial charge (a) and gas sensitivity (b) of ZnO on the temperature during adsorption of gas molecules CO, NO₂, NH₃

Dependence of the width of the spatial charge and gas sensitivity of ZnO on the temperature during adsorption of gas molecules CO, NO₂, NH₃ at the concentration of 5 ppm are shown in Fig. 40.12.

The increase in the width of the spatial charge region in ZnO with the increase of temperature can be explained by the increase in the surface concentration of adsorbed particles and, as a consequence, by the increase in the surface charge. The increase in surface concentration with the increase of temperature may relate to a decrease of surface potential, thereby increasing the probability of interaction of gas molecules with the surface of ZnO. At a temperature of >300 °C, the width of the spatial charge region in ZnO diminishes, which may be associated with the predominance of desorption of the particles over their adsorption on the surface of ZnO.

With the increase in the temperature to 280–300 °C, gas sensitivity of ZnO also increases, which can be attributed to increased mobility and carrier concentration, and a decrease in resistance of ZnO. From the chemical point of view, the increase in gas sensitivity may be due to the increase in the concentration of free radicals at the surface of ZnO, which increases the probability of interaction of gas molecules with surface radicals.

Thus, to maximize the detection of gases, it is necessary that nanostructured ZnO films satisfy the criteria: $d \leq 100$, $h \leq 50$ nm, with the operating temperature of ~ 300 °C.

Based on the above-mentioned results, we developed gas sensors on the base of nanostructured ZnO films, obtained by PLD (Fig. 40.13).

The detection of gases by sensors based on nanostructured ZnO films with CO concentration of 5 ppm at the temperature 300 °C is shown in Fig. 40.14. The sensitivity of gas sensor at 5 ppm was 304 %, response time—39.6 s, and recovery time—42 s.

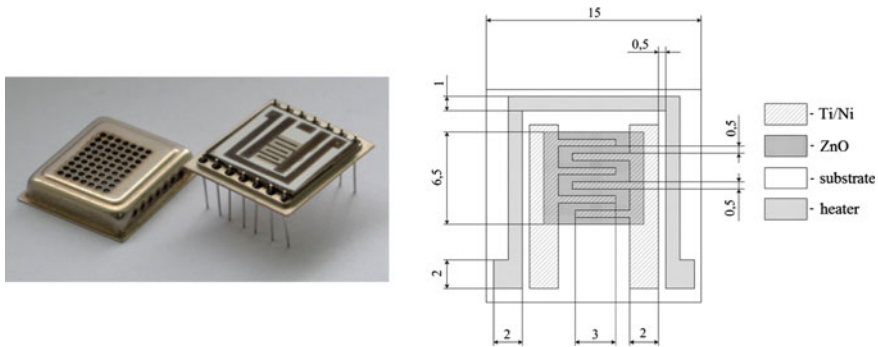
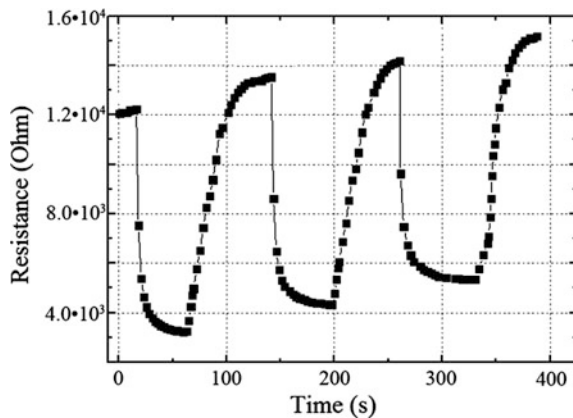


Fig. 40.13 Gas sensors based on nanostructured ZnO films

Fig. 40.14 Detection of gases by sensors based on nanostructured ZnO films with CO concentration of 5 ppm at the temperature 300 °C



The results can be used to develop the design and technology of sensor devices, nanoelectronic and microelectronic devices.

40.6 Development of AFM Analysis Techniques of Electrical Properties of GaAs NWs

To develop our technique, we have used samples with undoped GaAs NWs. Self-catalytic GaAs NWs were grown on GaAs (100) substrate by MBE. The NWs were 1–6 μm in length and 60–200 nm in diameter with aspect ratio of 20–50 (Fig. 40.15). The density of NWs array was $5 \cdot 10^8 \text{ cm}^{-2}$ [17].

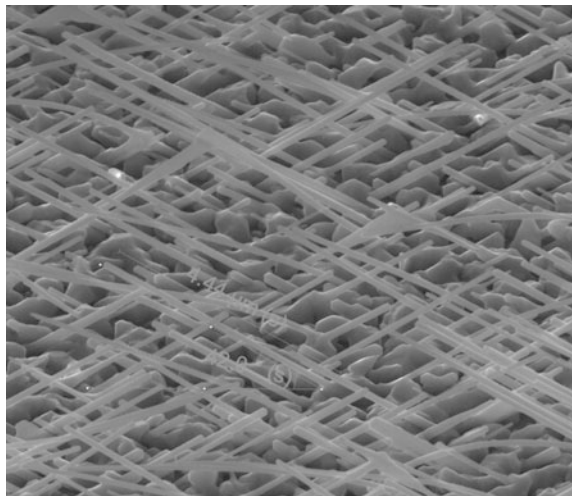
For studies of GaAs NWs electrical characteristics, we used cantilevers with conductive coating NSG 11/Pt. A radius of curvature of this cantilever tip was 35 nm.

The AFM-probe contact with nanowire leads to vibration of nanocrystal that distorts information about the topology of the sample [18]. Therefore, to obtain an AFM image of GaAs NWs array morphology, we scanned the samples in contactless mode. Then the supply of the probe was carried to a separate nanowire and *IV*-spectroscopy was performed.

To estimate the resistivity of GaAs NWs according to *IV*-spectroscopy we used modified model presented in [26, 27], where the sample resistivity depended on the parameters of the probe-sample system as

$$\rho_s = \left[\frac{U}{I} CF - R_b - \rho_p \left(\frac{2\lambda_p}{3\pi a^2} + \frac{L_p}{A_p} \right) \right] / \left(\frac{2\lambda_s}{3\pi a^2} + \frac{L_s}{A_s} \right).$$

Fig. 40.15 SEM image of GaAs NWs



The estimate of the GaAs NWs resistivity using this formula gives values in the range of 1–2.5 k Ω cm. This value correlates with the data obtained during the calibration of MBE system sources. The epitaxial undoped GaAs layer had a p -type conductivity and resistivity of 2.5 k Ω cm, which corresponded to the doping level $1.23 \cdot 10^{14}$ cm $^{-3}$.

In order to clearly determinate the NWs conductivity type, we must compare the current-voltage (I – V) characteristics, which were obtained for GaAs NW and for bulk material in single growth processes. For this, we carried out the AFM-scanning the same sample region in contact mode. Under AFM-probe pressure, GaAs NWs were broken and removed from the scanning area, allowing us to explore the structure of the sample surface (Fig. 40.16). Profilograms of relief and spreading current, obtained in the area, are shown in Fig. 40.17.

Comparative analysis of the AFM images and profilograms shows that in most cases spreading current is registered in the intergranular area. This corresponds to a surface current of the epitaxial GaAs layer, which also forms during the growth of the NWs. At the tops of the relief corresponding submicron GaAs crystal, the current does not register with the given voltage values (± 2 V).

Fig. 40.16 Scheme of AFM after NW removal

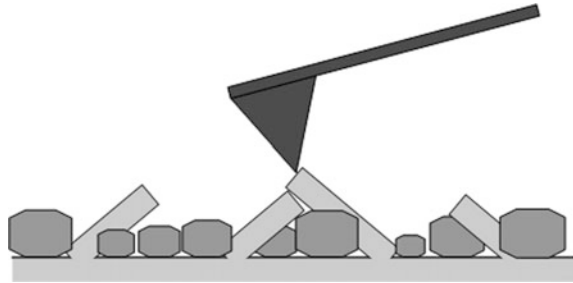


Fig. 40.17 AFM surface analysis of the sample after the GaAs NWs removal: profilograms of relief (*solid line*) and the spreading current (*dashed line*)

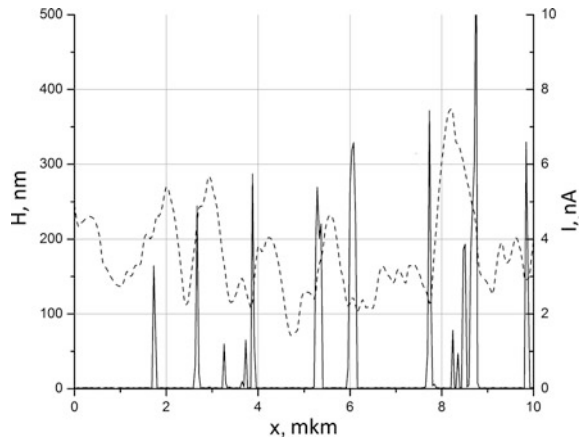
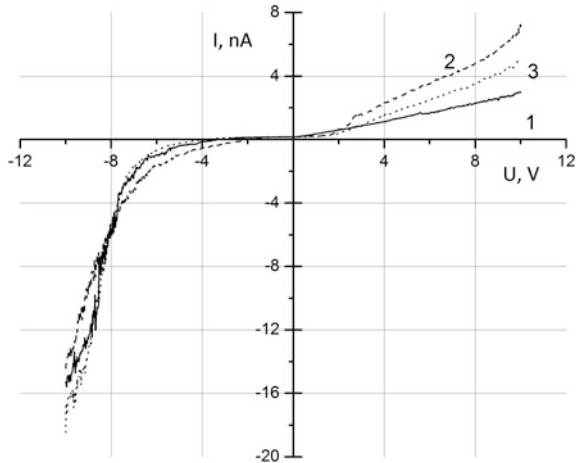


Fig. 40.18 AFM (I - V)-characteristics of NW (curve 1), NW cleavages (curve 2) and the epitaxial GaAs layer (curve 3)



However, in some cases, peaks in the spreading current profilogram match to peaks in the relief profilogram. There are cleavages of GaAs NWs, which structurally relate to the substrate, in these points. This is confirmed by comparing the (I - V)-characteristics of GaAs NWs and (I - V)-characteristics at various points on the surface of the sample (Fig. 40.18).

As can be seen from Fig. 40.18, the NW (I - V)-characteristic (curve 1) and (I - V)-characteristics at points corresponding to NW cleavages (curve 2) and the epitaxial GaAs layer (curve 3) have the same form. All of them have direct (I - V)-branches at the negative bias and flat sections at the beginning of the I - V - I . It clearly identifies the type of GaAs NW conductivity, because epitaxial layer conductivity type was determined during the formation of test structures. Furthermore, p -type of undoped self-catalytic GaAs NWs is indirect evidence about their zinc blendance crystal structure. It is because of in MBE, unintentional dopant is usually carbon (C), which occupies the As-sublattice sites in cubic crystal (bulk material).

Thus, in this work we developed the AFM-technique for determining the electrical parameters of GaAs NWs. This technique does not require additional operations of NWs fixation and allows one to determine the conductivity type and resistivity of NWs material. It has been shown that the undoped self-catalytic GaAs NWs had p -type and a resistivity of about 2 k Ω cm.

Acknowledgments This research was financially supported by the Ministry of Education and Science of Russian Federation: projects Nos. 1936, 16.1154.2014/K (items 40.2 and 40.3), project 14.575.21.0045 unique identifier RFMEFI57514X0045 (item 40.4); by the Russian Foundation for Basic Research: project Nos. 14-07-31322_mol_a, 14-07-31162_mol_a, 14-08-90010-Bel_a (items 40.2, 40.3 and 40.5); by the Russian Science Foundation: grant No. 15-19-10006 (item 40.6). The experimental results were obtained on the equipment of the Research and Educational Center and Centre of Collective Use "Nanotechnologies" of the Southern Federal University.

References

1. Z. Ren, Y. Lan, Y. Wang, *Aligned Carbon Nanotubes: Physics, Concepts* (Fabrication and Devices. Springer, Heidelberg, 2013)
2. M. Shakir, M. Nadeem, S. Shahid, N. Mohamed, *Nanotechnology* **17**(6), R41 (2006)
3. O.A. Ageev, Y.F. Blinov, O.I. Il'in, A.S. Kolomiitsev, B.G. Konoplev, M.V. Rubashkina, V.A. Smirnov, A.A. Fedotov, *Tech. Phys.* **58**, 1831 (2013)
4. O.A. Ageev, Y.F. Blinov, O.I. Il'in, B.G. Konoplev, M.V. Rubashkina, V.A. Smirnov, A.A. Fedotov, *Phys. Solid State* **57**(4), 825 (2015)
5. H. Li, K. Banerjee, *IEEE Trans. Electron Devices* **56**, 2202 (2009)
6. V.I. Avilov, O.A. Ageev, A.S. Kolomiitsev, B.G. Konoplev, V.A. Smirnov, *Semiconductors* **48**(13), 1757 (2014)
7. O.A. Ageev, B.G. Konoplev, V.A. Smirnov, *Semiconductors* **44**(13), 1703 (2010)
8. B. Bhushan, *Springer Handbook of Nanotechnology*, 3rd edn. (Springer, Heidelberg, 2010)
9. P.J. French, *Sens. Actuators, A* **99**, 3 (2002)
10. J. Fricke, E. Obermeier, *Sens. Actuators, A* **54**, 651 (1996)
11. T. Tsuchiya, Y. Kageyama, H. Funabashi, J. Sakata, *Sens. Actuators, A* **82**, 114 (2000)
12. H. Morkoc, *Zinc Oxide. Fundamentals, Materials and Device Technology* (Wiley-VCH, 2009)
13. O.A. Ageev, E.G. Zamburg, E.Y. Gusev, D.E. Vakulov, Z.E. Vakulov, A.V. Shumov, M.N. Ivonin, *Appl. Mech. Mater.* **475–476**, 446 (2014)
14. O.A. Ageev, E.G. Zamburg, E.Y. Gusev, A.V. Michailichenko, V.A. Gamaleev, V.V. Tkachuk, *Appl. Mech. Mater.* **475–476**, 1266 (2014)
15. J. Johansson et al., *Nanotechnology* **17**, 355 (2006)
16. K.A. Dick et al., *Semicond. Sci. Technol.* **25**, 1 (2010)
17. O.A. Ageev et al., Autocatalytic growth of whiskers on GaAs(100) by MBE. in *Russian–Taiwanese Symposium on “Physics and Mechanics of New Materials and Their Applications”* (SFedU Press, Rostov-on-Don, 2012), p. 2
18. O.A. Ageev et al., *Nanotechnol. Russ.* **8**, 23 (2013). (in Russian)
19. L. Liu, G. Cao, X. Chen, *J. Nanomater.* ID 271763 (2008)
20. O.A. Ageev, A.S. Kolomiitsev, A.V. Mikhaylichenko, V.A. Smirnov, V.V. Ptashnik, M.S. Solodovnik, A.A. Fedotov, E.G. Zamburg, V.S. Klimin, O.I. Ilin, A.L. Gromov, A.V. Rukomoykin, *News South. Fed. Univ.: Tech. Sci.* **1**, 109 (2011). (in Russian)
21. E.Y. Gusev, J.Y. Jityaeva, A.S. Kolomiitsev, V.A. Gamaleev, I.N. Kots, A.V. Bykov, Wet etching of silicon dioxide sacrificial layer for mems structures forming, in *International Conference on “Physics and Mechanics of New Materials and Their Applications” (PHENMA-2015)* (SFedU Press, Rostov-on-Don, 2015), p. 100
22. R.V. Velichko, E.Y. Gusev, V.A. Gamaleev, A.S. Mikhno, A.S. Bychkova, *Fundam. Res.* **11** (5), 1176 (2012) (in Russian)
23. E.Y. Gusev, J.Y. Jityaeva, V.A. Gamaleev, A.S. Kolomiitsev, I.N. Kots, A.V. Bykov, *News South. Fed. Univ.: Tech. Sci.* **2**, 236 (2015). (in Russian)
24. O.A. Ageev, E.G. Zamburg, D.A. Golosov, A.M. Alexeev, D.E. Vakulov, Z.E. Vakulov, A.V. Shumov, M.N. Ivonin, *Appl. Mech. Mater.* **481**, 55 (2014)
25. A.P. Dostanko, O.A. Ageev, D.A. Golosov, S.M. Zavadski, E.G. Zamburg, D.E. Vakulov, Z.E. Vakulov, *Semiconductors* **48**(9), 1242 (2014)
26. T. Clarysse et al., *Mater. Sci. Eng. R.* **47**, 123 (2004)
27. W. Frammelsberger et al., *Appl. Surf. Sci.* **253**, 3615 (2007)

Chapter 41

The Radiation Detector with Sensitive Elements on the Base of Array of Multi-walled Carbon Nanotubes

E.V. Blagov, A.A. Pavlov, A.A. Dudin, A.P. Orlov, E.P. Kitsuk,
Yu. Shaman, A.Yu. Gerasimenko, L.P. Ichkitidze and A.A. Polohin

Abstract The detector of the visible and infrared radiation on a multi-walled carbon nanotubes has been studied. The sensitive element was represented by a two-electron square-shaped matrix with linear dimension of 2 mm containing numerous cells (2 μm diameter, 2.3 μm depth, 6 μm distance between cells) in which arrays of multi-walled carbon nanotubes are synthesized. All measurements have been realized at the room temperature. Maximum photo-emf of ~ 100 mV was reached in the visible and short-range IR of 500–1500 nm and minimum photo-emf of ~ 0.1 mV in range of 1500–8000 nm. Maximum photosensitivity ~ 12.2 mA/W was realized at 1100 nm emission wavelength and its capacity of 50 μW . Speed capability was equal to ~ 30 μs and efficiency factor of energy transformation of infrared radiation into electric—0.13 %. It is expected that the optimization of the parameters of the sensitive element and the mode of operating temperature, characteristics of IR radiation detector on the arrays of multi-walled nanotubes will significantly improve. In particular, the operating range of wavelength, photoconductivity, speed capability and efficiency of energy transformation of IR radiation into electric will increase.

E.V. Blagov · A.A. Pavlov · A.A. Dudin · A.P. Orlov · E.P. Kitsuk
Institute of Nanotechnology of Microelectronics of the RAS, INME RAS,
Moscow 119991, Russian Federation

A.A. Pavlov · E.P. Kitsuk · Yu. Shaman
Scientific-Manufacturing Complex “Technological Centre”,
MIET, Zelenograd, Moscow 124498, Russian Federation

A.Yu. Gerasimenko · L.P. Ichkitidze (✉) · A.A. Polohin
National Research University of Electronic Technology “MIET”,
MIET, Zelenograd, Moscow 124498, Russian Federation
e-mail: leo852@inbox.ru

A.P. Orlov
Kotel'nikov Institute of Radio-Engineering and Electronics of RAS, IRE RAS,
Moscow 125009, Russian Federation

41.1 Introduction

The wide application of optical instruments in science, industry and medicine caused need for inspection of characteristics of the used radiation. As a result, developments of sensitive elements of radiation detectors are underway since 1930. Sensitive elements of radiation detectors are divided into two fundamental types, depending on its mode of operation: photothermal and photoemissive. In the first type of detectors, mechanism of transformation light energy into thermal is realized, and then into electric. Application of such a type of detectors is widely used in optoelectronic devices exploitable in different fields of human activity. However, photothermal radiation detectors are a subject to exposure, since it reacts even to a minimum heat source, located at immediate vicinity from sensitive element. Also, majority of such a type of detectors is peculiar to have relatively high persistence (from units to hundreds of milliseconds) [1, 2].

The second type of detectors works based on the mechanism of immediate transformation of energy of incident radiation on the surface of sensitive element into electric energy. Absolute photosensitivity value of photoemissive sensitive elements is determined by a quantity of nonequilibrium carriers, which arise as a result of photonic excitation. Such an effect is only possible in the case of usage semiconductor material as sensitive elements. Formation of free carriers occurs under the influence of radiation on semiconductors that is connected to transfer of electrons from valence band to conduction band. For realization of such a transfer, electron should receive energy, sufficient for overcoming forbidden band or energy barrier, linking electron on recombination center. The main disadvantage of such a type of detectors is a low operating range of wavelengths [3]. There are radiation detectors on the base of GaInAsSb/GaAlAsSb structures with upper bound of wavelength's operating range of 2550 nm but it is not serially issuing nowadays [4].

Semiconducting type of multi-walled carbon nanotubes (MWCNT) can be used as semiconductor materials of sensitive elements of semiconductor materials. Because of its unique structure and characteristics, MWCNT are perspective for many applications in nanoelectronics and nanoequipment, as well as in composition of sensitive element of wide-band receiver of infrared radiation [5].

Structural sensitive elements on the base of CNT can be divided into three main kinds (Fig. 41.1): (a) on the base of one carbon nanotube [6, 7], (b) on the base of CNT film [8, 9], (c) on the base of CNT array [10, 11].

For the creation of the first kind (see Fig. 41.1a) of a construction of a sensitive elements of radiation detectors, single-walled CNT (SWCNT) is used. Since CNT synthesis with the same parameters (length, diameter, defectiveness) is impossible, it is interesting to study photosensitivity of one CNT. The construction of a sensitive element (SE) on the base of one SWCNT is represented by pair of electrodes connected by one SWCNT. By using the method of an optic lithography, electrodes are made. Further, a drop of SWCNT suspension is applied on a substrate and using alternating current structurization is realized, thus, edges of few SWCNTs are connected by two electrodes. It attains due to the appearance of dielectrophoresis

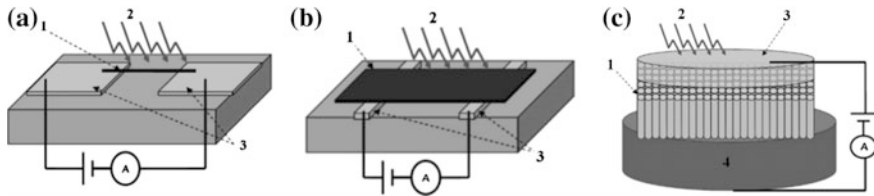


Fig. 41.1 Types of constructions of photodetectors on the base of CNT: **a** 1 single CNT, 2 radiation, 3 electrode; **b** 1 CNT film, 2 radiation, 3 electrode; **c** 1 CNT array, 2 radiation, 3 electrode, 4 silicon substrate

force around electrodes, which affects on neutral solids in inhomogeneous electric fields. In the end, one SWCNT is chosen and located between electrodes using nanorobot system of controlling atomic-force microscope. Researchers have shown that photoconductivity of separate SWCNT is much better than MWCNT films. Nowadays, the process of the production of radiation detectors on the base of one SWCNT is impossible in practice [10].

Practical production of construction of sensitive elements of radiation detectors using MWCNT film is more likely (see Fig. 41.1b). Infrared MWCNT photosensitivity harshly intensifies by building it, e.g. in polycarbonate matrix [8].

However, there are some difficulties regarding getting homogeneous structure of MWCNT film between two electrodes and getting uniform electrical conduction along the full area. In fact, the important characteristics for infrared detectors on the base of MWCNT films are already measured: absorption factor up to 10^5 cm^{-1} , reflection coefficient $\leq 0.04 \%$ in wide band of wavelengths (0.2–200 μm). Thereby, films of nanotubes are very similar to characteristics of black body [12–14].

The disadvantages are typical for both types of infrared sensors (see Fig. 41.1a, b) such as horizontal location of nanotubes on substrate. When nanotubes threads locate horizontally (parallel with surface of substrate), the radiation mainly falls on CNT lateral surface and its absorbing capacity is slender [15, 16]. Apparently, it is one of the reasons of very low transformation efficiency (transformation coefficient $C_F \leq 0.01 \%$) of infrared radiation energy registered by MWCNT film into electric energy [17].

Disadvantages of the first two types of SE constructions can be partially avoided by synthesis of a structured MWCNT array between two electrodes. In the study [10], SWCNT array was grown by using precipitation from gas phase (CVD) on monocrystalline quartz. Then, it was transplanted on a silicon wafer coated with 500 nm layer of SiO_2 , derived by thermal method. After the transplantation, SWCNT density was about 2–3 tubes/ μm . SWCNT arrays were slit by stripes with width $w = 20 \mu\text{m}$ (perpendicularly to nanotubes) by using the electron-beam lithography and plasma etching O_2 . All electrodes were located using the electron-beam lithography and sawn by using the electron-beam evaporation.

The third type of the construction of a sensitive element, shown in Fig. 41.1c, has vertical CNT orientation regarding substrate. By using such a construction, IR

radiation falls on the CNT edges and it absorbs almost 100 % of radiation. Consequently, high coefficient of energy transformation of IR radiation into electric is attained [18].

In this study, it is a question of a technology of the creation of an emissive detector with sensitive elements on the base of multi-walled carbon nanotubes (MWCNTs) array and analysis of its optic characteristics.

41.2 Materials and Methods

Two-electrode system, representing a matrix of cells with synthesized MWCNT arrays, was chosen as a main operating topology of sensitive element on the base of MWCNT structures (SE MWCNT) (Fig. 41.2).

Apertures, moulding the form of the cells of experimental sample, had 2 μm diameter, and 2.3 μm depth. An upper electrode in the used scheme was represented by a metal layer with 0.5 μm thickness, sprayed by using the magnetron sputtering method of a pure aluminum target (99.9999 %) with a non-uniformity less than 5 % on the surface of $\varnothing 100$ mm plate. Lithography on this layer moulded metallization and bonding area. A lower electrode (substrate) was represented by silicon wafer on which all structure had been moulded. Silicon of KEF 4.5 Ω/cm brand and KEM 0.001–0.002 Ω/cm brand with electric mode of conductivity (*n*-type) was used as a substrate. The silicon oxide layer (SiO_2) with 0.5 μm thickness, formed by the method of silicon thermal oxidation, was represented in a structure by dielectric.

SE MWCNT was presented by square-shaped matrix with 2 mm dimension in which distance between separated cells was equal to 6 μm .

Formation of cells matrix was performed by selective plasma-chemical etching of aluminum and silicon oxide, it had high anisotropy and selectivity. For that, experimental facility “Platran-100” with high-density plasma reactor on the base of high-frequency source with inductive excitation of plasma was used.

Further, cells etching in silicon took place on the BOSCH-etching machine, and etching of SiO_2 layer at 0.2 μm depth using gas-phase etching method. The process of Bosch-etching was used in order to provide contact between silicon and

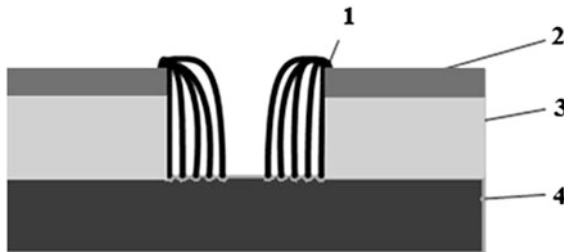


Fig. 41.2 Cell topology of experimental sample of sensitive elements: 1 SE MWCNT, 2 metal, 3 silicon oxide, 4 silicon

MWCNT array, and also for embedding MWCNT array inside the structure. Cluster installation IonFab 300 + ICP PECVD of Oxford Instruments brand was used in order to form the structure by reactive-ionic etching method. On the final stage, silicon plate was divided into crystals on which synthesis of MWCNT arrays realizes.

Capitalist pair Al/Ni was chosen by the experimental method, at which maximum response to IR radiation is observed. The selection of Al links to its burn in silicon and formation of MWCNT-silicon hetero-junction. Direct MWCNT-silicon contact forms because of Al dissolution in silicon and due to Ni spending during MWCNT growth. Taking into account requirements of radiation transmission to MWCNT-silicon joint, such synthesis parameters as height and array density were defined. Layers of capitalist metals were applied by dispersion of metals targets by magnetron at reactive ion-plasma dispersion installation URM 3,279,026 with non-uniformity of applied film density not more than 10 % on the surface of Ø100 mm plate. Removal of the catalytic layer from the surface of a plate was realized by using reactive-ionic etching methods. Its usage is caused by Ni stability to plasma-chemical etching processes.

The temperature of MWCNT array synthesis did not exceed 500 °C in order to avoid a damage of an aluminum metallization. In this connection, the method of a plasma stimulated chemical vapor-phase precipitation was used for a synthesis, in which additional plasma assistance allowed one to decrease a process temperature lower than 500 °C with preservation of a specified morphology of synthesized MWCNT array. A MWCNT growth rate did not exceed 5 µm/min that allowed us to mould nanotubes with a height from 0.3 µm up to 30 µm with a high degree of homogeneity on the substrate. Control of array density was realized by using an electric field influence.

In the study of MWCNT array synthesis the “Oxford PlasmaLab System 100 (Nanofab 800 Agile)” installation was used. The usage of ultra purity gases during MWCNT synthesis allowed us to achieve a high stability of processes, and also provided with a low defectiveness of moulding multi-walled carbon nanotubes.

The analysis of synthesized structure of sensitive element using scanning electronic-ionic microscope FEI Helios NanoLab 650 showed that by using the same synthesis parameters, it was observed more intensive growth of MWCNT array from horizontal walls of cells, mainly in horizontal direction, in comparison with vertical array, which synthesizes only upward. It may be bound up with a difficulty of reagents penetration inside the cell as well as influence of an electric field, which contributes to the synthesis of arrays at horizontal projection. Preliminary studies of responses to IR radiation showed that the effect is observed not only at vertical tubes orientation but also at horizontal, when MWCNT synthesis mainly passes on lateral elements surface. In this case, by a lesser density of MWCNT array, the length of separated nanotubes may amount to big values (see Fig. 41.2).

The ionic etching, used at removal of capitalistic layer from the structure surface, introduced the effect of reprecipitation of pulverizable materials that in turn affects the morphology of the synthesized MWCNT array. Exactly in such a way, horizontal direction of MWCNT arrays was moulded (Fig. 41.3).

Fig. 41.3 Image of scanning electronic microscopy of the SE MWCNT cell, mainly with lateral synthesis

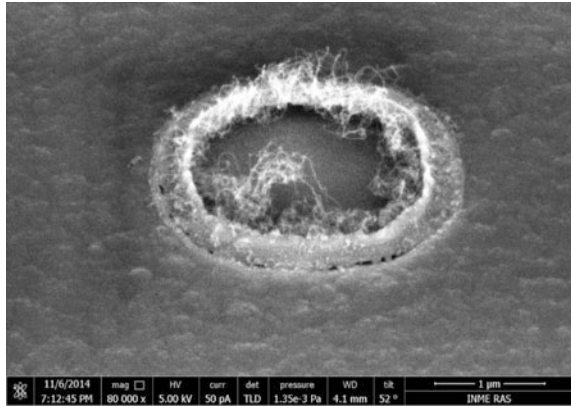
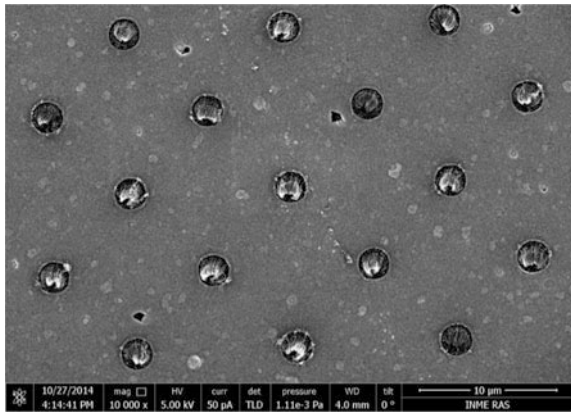


Fig. 41.4 Image of scanning electronic microscopy of the SE MWCNT with the synthesized MWCNT arrays



During the studies, it was explored an array synthesized in such a way, at a processing immediately after the synthesis process in an oxygen atmosphere (O_2 —100 cm/min, Ar—100 cm/min), under a pressure of 1.5 Torr, at an applied power of $RF = 100$ W, $T = 280$ °C during 5 min. It gives a noticeable increase of observed response effect to IR radiation, in some cases, the response increased by approximately an order. This effect relates to a cleaning of structure surface from undesirable carbon transplanting and removal of defective layers of multi-walled carbon nanotubes that increases a quality of array and enlarges light penetration to a MWCNT-silicon contact.

Automated control processing system of the SE MWCNT production guaranteed the repetition of processes and absence of parameters, introduced by oscillation operator.

The ionic etching, used at removal of capitalistic layer from the structure surface, introduced the effect of reprecipitation of pulverizable materials that in turn affects the morphology of the synthesized MWCNT array. Exactly in such a way, horizontal direction of MWCNT arrays was moulded (Fig. 41.4).

41.3 Results and Discussion

As a result, such optic parameters characterizing the SE MWCNT as an operating wavelengths range, sensitivity and speed capability were studied. For the studies, experimental facility operational units, which synchronously were controlled by a program developed in the programming environment LabVIEW, were used.

By the operating wavelengths range radiation wavelengths are understood, which when falling on SE MWCNT, photo-emf appears on the outlets. The study of operating range of SE MWCNT wavelengths was realized by using spectrometric complex on the base of monochromator MDR-41 (LOMO, Saint-Petersburg). The complex contained two sources of light on the base of halogen lamp (with wavelength of 370–2500 nm) and black body (2000–2500 nm). The forming of input radiation into monochromator's body provided the first mirror condenser and turret with color filters, and the image of output radiation was formed due to monochromator's aperture and the second condenser.

All measurements were realized at the room temperature. During the experiments, the dependence of the photo-emf of the SE MWCNT sample on the wavelength of the incident radiation was found (Fig. 41.4). As can be seen from the diagram, maximum photo-emf reached in the visible and short-range infrared range of 500–1500 nm and equaled to 110 mV. Probably, it was due to cells' size ratio (greater diameter and smaller depth) of the synthesized MWCNT array in the sample, which acted as electric conductors connecting two electrodes. In the range from 1500 to 8000 nm photo-voltage value was about 0.1 mV (Fig. 41.5).

Under the SE MWCNT sensitivity, the ratio of the current strength flowing through the SE MWCNT to the power of incident radiation was studied. Three radiation wavelengths (500, 800, 1100 nm) were chosen for the study of the SE MWCNT sensitivity. The measurement of radiation power at the selected wavelengths was realized by using attenuator with a set of neutral optical filters 10MWA168 (Standa, Lithuania), and the measurement of the radiation power by

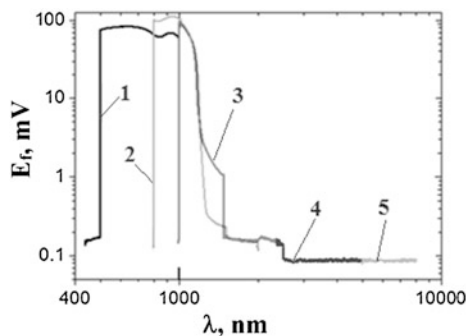


Fig. 41.5 The dependence of the photo-emf (E_p) of the sample on the radiation wavelength (λ) incident on SE MWCNT, diffraction grating: 1 1500 lines/mm, 2 750 lines/mm, 3 600 lines/mm, 4 300 lines/mm, 5 150 lines/mm

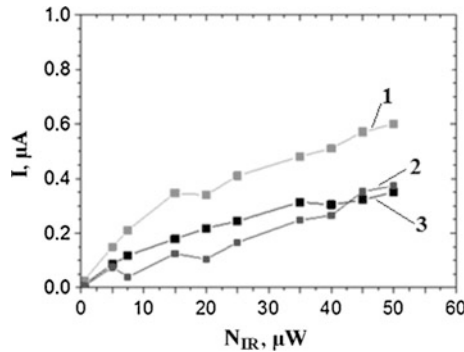


Fig. 41.6 Dependence of the current strength flowing through the SE MWCNT (I) on power of incident radiation (N_{IR}) of different wavelengths: *curve 1 800 nm, curve 2 1100 nm, curve 3 500 nm*

using an instrument 3A-FS (Ophir, Israel). As a result, by using multimeter 2634B (Keithley, USA) values of current strength passing through the SE MWCNT sample were measured. Thus, dependencies of current strength of sample on radiation power for the selected wavelength was found (Fig. 41.6). As can be seen from the diagram, the value of sensitivity for the SE MWCNT at a wavelength of 500 nm (curve 3) reached the value of 7.1 mA/W at a radiation power of 50 μW . For the radiation wavelength of 800 nm (curve 1) and 1100 nm (curve 2), the same sample showed the sensitivity of 7.4 and 12.2 mA/W, respectively. Thus, the maximum sensitivity reached at a wavelength of 1100 nm.

Studies of the SE MWCNT speed capability were conducted in the following way. The signal generator pulsed at a high-speed LED SFH 4205 (OSRAM Opto Semiconductors Inc, USA) which radiation hit the SE MWCNT. The signal generator 33250A (Agilent, USA) and the SE MWCNT were connected to the oscilloscope HDO6104 (LeCroy, USA). The oscillogram of comparison of a single pulse signal is shown in Fig. 41.7. The speed capability of the sample was defined by the amount of delay time of the signal from the SE MWCNT relative to the generator's signal, which came to the high-speed LED, and rise time up to 0.9 of maximum voltage amplitude at the sample.

From the Fig. 41.7, it was clear that the delay time of the signal from the SE MWCNT relative to generator's signal coming on the high-speed LED converges to a minimum (<100 ns). Thus, speed capability can be characterized by a rise time of the voltage. From derived measurements, it was clear characteristic SE MWCNT speed capability, about 30 ms. This time, probably, was due to high resistances and capacity in contacts, as well as inconsistent impedance of oscilloscope input (1 M Ω) with the samples, in the future these parameters of the contacts can be improved by the technological optimization and speed capability will increase.

The valuation of transformation coefficient of energy of infrared radiation into electric for the case of maximum value of the sensitivity of 12.2 mA/W and

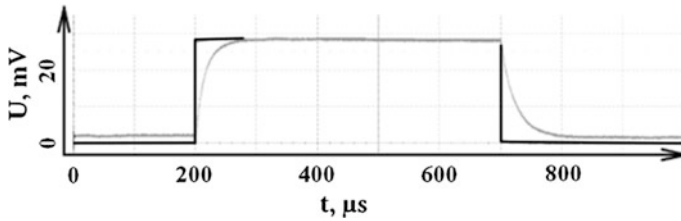


Fig. 41.7 Evaluation of the SE MWCNT speed capability (U signal, t time): *black curve* signal of generator, *grey curve* signal of SE MWCNT

photo-emf of ~ 110 mV (Fig. 41.5) gives $C_F \sim 0.13$ %. This value can be considered satisfactory, since it is an order higher than C_F in the IR radiation detector on MWCNT studied in the paper [17].

It is expected that with decreasing of sizes and increasing of cells quantity, in which exist MWCNT arrays, there will occur growth of C_F and accordingly the effectiveness of IR radiation detector that, we proposed, will increase.

41.4 Conclusions

A new type of sensitive elements for detectors of visible and IR radiation was developed. The sensitive element was represented by a two-electrode square-shaped matrix with linear dimension of 2 mm containing cells (holes) in which arrays of multi-walled carbon nanotubes are synthesized. The cells had 2 μm diameter, 2.3 μm depth, and a distance between them 6 μm . The upper electrode was represented by a layer of a pure aluminum with a thickness of 0.5 μm , and the lower electrode was represented by a silicon plate having electron type of conductivity. All measurements have been conducted at a room temperature.

Maximum photo-emf ~ 100 mV was reached in the visible and short-range IR of 500–1500 nm and minimum photo-emf ~ 0.1 mV in range of 1500–8000 nm. Maximum photosensitivity ~ 12.2 mA/W was realized at 1100 nm emission wavelength and its capacity of 50 μW . Speed capability was equal to ~ 30 μs and efficiency factor of energy transformation of infrared radiation into electric—0.13 %.

It is expected that the optimization of the parameters of the sensitive element and the mode of operating temperature, characteristics of IR radiation detector on the arrays of multi-walled nanotubes will significantly improve. In particular, the operating range of wavelength, photoconductivity, speed capability and efficiency of energy transformation of IR radiation into electric will increase.

Acknowledgments This work was supported by Russian Ministry of Education (Contract No.14.430.11.0006).

References

1. <http://www.pro-lite.co.uk/File/OPTRONIK%20Photometer%20Brochure.pdf>
2. <http://www.mpia.de/IRSPACE/herschel/links.php?print=yes>
3. J.D. Vincent, J. Vampola, G. Pierce et al., *Fundamentals of Infrared and Visible Detector Operation and Testing*. Wiley Series in Pure and Applied Optics, 2nd edn. (2015)
4. I.A. Andreev, O.Y. Serebrennikova, G.S. Sokolovskii et al., *Semiconductors* **47**(8), 1103 (2013)
5. D. Jariwala, V.K. Sangwan, L.J. Lauhon, *Chem. Soc. Rev.* **42**, 2824 (2013)
6. C.A. Merchant, N. Markovic, *Appl. Phys.* **92**, 243510 (2008)
7. J. Zhang, N. Xi, K. Lai, *SPIE Newsroom* 1, (2007)
8. B. Pradhan, K. Setyowati, H. Liu et al., *Nanoletters* **8**(4), 1142 (2008)
9. L. Wei, N. Tezuka, T. Umeyama, H. Imahori, Y. Chen, *Nanoscale* **3**, 1845 (2011)
10. Z. Qingsheng, W. Sheng, L. Leijing, *Opt. Mater. Express* **2**(6), 839 (2012)
11. X. Jimmy, *ACS Nano* **12**(10), 2154 (2008)
12. K. Mizuno, J. Ishii, H. Kishida et al., *Proc. Nat. Acad. Sci. USA* **106**(15), 6044 (2009)
13. V.A. Krivchenko, S.A. Evlashin, K.V. Mironovich et al., *Sci. Rep.* **3**, 3328 (2013)
14. S. Evlashin, S. Svyakhovskiy, N. Suetin et al., *Carbon* **70**, 111 (2014)
15. D.F. Santavicca, J.D. Chudow, D.E. Prober et al., *Appl. Phys. Lett.* **98**, 223503 (2011)
16. A.Y. Glamazda, V.A. Karachevtsev, W.B. Euker, I.A. Levitsky, *Adv. Funct. Mater.* **22**, 2177 (2012)
17. R. Hatakeyama, Y.F. Li, T.Y. Kato, T. Kaneko, *Appl. Phys. Lett.* **97**, 013104 (2010)
18. M.E. Kozlov, *J. Appl. Phys.* **113**, 1643079 (2013)

Chapter 42

Combined Magnetic Field Sensor with Nanosized Elements

L.P. Ichkitidze, S.V. Selishchev and D.V. Telishev

Abstract We investigate a superconducting film ring with a narrowed part (active strip) used as a magnetic field concentrator or magnetic flux transformer in combined magnetic field sensors. Fragmentation (nanostructuring) of the active strip in numerous branches and cuts and simulation of their nanoscale size and positions make it possible to significantly enhance the efficiency of the combined magnetic field sensor with a resolution of ≤ 10 pT, which operates on the base of superconductivity and spintronics phenomena. It was established that the efficiency of concentration of a measured magnetic field on a magnetosensitive element based on the giant magnetoresistive effect can be enhanced using fragmentation of an active strip by cuts with a width of 20–350 nm. The magnetic field concentrator with low-temperature superconductor (e.g., niobium with the London penetration depth $\lambda \sim 60$ nm) films exhibits higher efficiency, than the concentrator with high-temperature superconductor films of the Y-123 or Bi-2223 systems with $\lambda \sim 250$ nm. The magnetic field resolution and maximum field values estimated for a combined magnetic field sensor based on different low- and high-temperature layers and spintronic elements are ≤ 1 fT and ≤ 40 μ T (the Earth's magnetic field), respectively. Characteristics of the investigated sensor are comparable with the parameters of SQUIDs.

42.1 Introduction

Magnetic fields, induced by biological objects, are usually detected by magnetic field sensors (MFSs) with the magnetic field resolution $\delta B \leq 10$ pT. In most of MFSs, the high resolution in the range $\delta B \leq 1$ nT is attained with the use of superconducting magnetic field concentrators (MFCs) or magnetic flux

L.P. Ichkitidze (✉) · S.V. Selishchev · D.V. Telishev
National Research University of Electronic Technology “MIET”, Zelenograd,
Moscow 124498, Russian Federation
e-mail: leo852@inbox.ru

transformers (MFTs),¹ which are applied in many magnetometers for the lossless transfer of the magnetic flux of a measured field to the magnetosensitive element (MSE). The role of MSEs can be played by Josephson junctions, Hall-effect sensors, spintronic sensors, etc. [1].

The main field of application of high-resolution ($\delta B \leq 1$ pT) MFSs is medical diagnostics, including magnetocardiography (MCG) and magnetoencephalography (MEG). The magnetic field sensors that are the most widely used in medicine are superconducting quantum interference devices (SQUIDs) [2, 3]. In low-field (≤ 200 mT) magnetic resonance tomography (MRT) or magnetic resonance imaging (MRI) systems intensively developed in recent years, the SQUIDs are used as the basic MFSs due to their record magnetic-flux sensitivity [4–6]. It is believed that the highly sensitive MFS will allow non-invasive continuous monitoring of the active implanted devices such as artificial hearts [7], and various stimulants (pacemakers) [8], and non-invasive monitoring of indicators of systemic hemodynamics [9]. On the other hand, SQUIDs do not directly measure the absolute value of the magnetic field B and they measure only magnetic flux, they difficult to manufacture and their use is limited by the high cost [10–12].

The parameters comparable with those of the SQUIDs are exhibited by the so-called combined MFSs (CMFSs) consisting of a superconducting film MFC and an MSE based on spintronics phenomena [13, 14]. The widely spread elements based on the giant magnetoresistive effect (GMR) have a low magnetoresistance, which is enhanced with the use of superconducting film MFCs. The advantage of the CMFSs for application in MRT and nuclear magnetic resonance systems is that these sensors can operate at higher magnetic fields than the SQUIDs.

In studies [13–18], various CMFSs were proposed, which contained thin-film MFCs based on low-temperature superconductors (LTS) with the working temperature $T_w \sim 4$ K and on high-temperature superconductors (HTS) operating at $T_w \sim 77$ K. The simplest version is the MFC in the form of a square or circular film ring with a narrowed part (active strip) and an MSE located under it. As was shown in [19–21], the optimal fragmentation (nanostructuring) of the MFC or MFT active strip in parallel micro- or nanosized branches and cuts leads to an additional increase in the efficiency of the MFC or MFT and, consequently, in the efficiency of the CMFS; in particular, the δB value decreases.

The aim of this study was to investigate the CMFS consisting of an MSE based on a spintronic (effect GMR) structure and a superconducting MFC in the form of a closed ring from an LTS or HTS film. The active strip of the ring is fragmented in parallel superconducting branches and cuts with the simulated nanoscale size and position

¹The superconducting ring works as an MFC when the detected element is sensitive to the magnetic field and as an MFT when the detected element is sensitive to the magnetic flux.

42.2 Methods and Materials

The object of study was factor F of multiplication (concentration) of a magnetic field of the film MFC on the MSE with the active strip divided into parallel superconducting branches and cuts. It was assumed that $F = 1$, when there is no fragmentation, i.e., the active strip is continuous. The investigated MFS structure comprises a superconducting film ring with the narrowed active strip and an MSE from the GMR film. The active strip of the MFC overlaps the MSE separated by an insulating film (Fig. 42.1).

The F value was estimated in the following way. In external magnetic field B , the magnetic flux, which screens ring 1 (Fig. 42.1), is determined as $\phi = A \cdot B$, where A is the ring square. The screening current is $I_S = \phi / (L + M)$, where L is the inductance of the ring, and M is the sum of mutual inductances between the superconducting MFC and MSE parts. The L value exceeds the resulting mutual inductance M by an order of magnitude and more. For a ring with the diameter D we write

$$I_S = \frac{\pi D^2 \cdot B}{4L}. \tag{42.1}$$

Inductance L of the MFC ring is much higher than inductance L_s of the active strip. When the latter consists of several branches with inductances L_i ($i = 1, 2, \dots, n$, where $n \geq 2$ is the number of cuts in the active strip), their resulting inductance is insignificantly higher, than L .

We calculated the maximum F value at different widths of branches and cuts, their number, topology, and characteristics of a superconducting MFC material. For optimal nanostructuring of the active strip and, consequently, attaining the maximum F value, we determined the magnetic fields on the MSE induced by

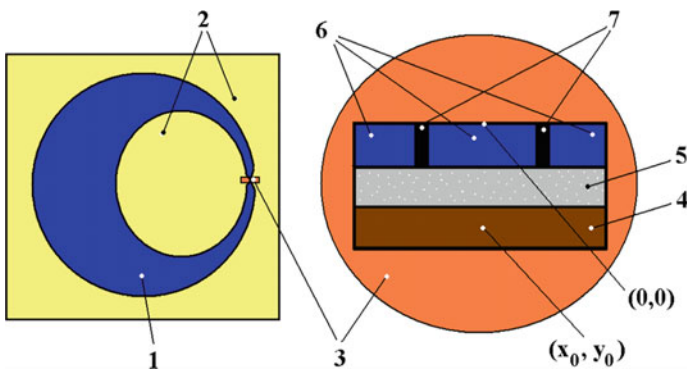


Fig. 42.1 Schematic of the MFS and its elements: (1) superconducting MFC ring, (2) dielectric substrate, (3) MFC active strip enlarged without keeping proportions, (4) MSE, (5) isolating film, and (6) branches and (7) cuts of the active strip

superconducting currents in branches of the active strip. In the calculation, we took into account only the magnetic field component parallel to the substrate surface, since it strongly affects the MSE in the form of the GMR element.

We used the well-known formulae:

$$B = \frac{\mu_0 \cdot I_s}{8\pi \cdot \lambda \cdot h} \cdot \left[\int_{-2h}^0 \int_{-l}^0 \frac{e^{-\frac{y+l}{\lambda}} \cdot (y_0 - y)}{(y_0 - y)^2 + (x_0 - x)^2} dx dy + \int_{-2h}^0 \int_0^{+l} \frac{e^{-\frac{l-x}{\lambda}} \cdot (y_0 - y)}{(y_0 - y)^2 + (x_0 - x)^2} dx dy \right], \quad (42.2)$$

$$F = \frac{\langle B \rangle}{\langle B_0 \rangle} \cdot \frac{1}{K_L}, \quad (42.3)$$

$$K_L = \frac{(\sum_{i=1}^{n+1} L_i^{-1})^{-1}}{L} \sim \frac{w_s}{\sum_{i=1}^{n+1} w_i}. \quad (42.4)$$

Here l and h are the half-width and half-thickness of the active strip film, respectively; μ_0 is the magnetic field constant; $I_s/(4\lambda h) \leq J_c$, I_s is the screening superconducting current in the active strip above the MSE and acting on the latter at the point (x_0, y_0) with the reference point $(0, 0)$ located at the center of the upper film surface; J_c and λ are the critical current density and London penetration depth for the MFC film material, respectively; $\langle B \rangle$ and $\langle B_0 \rangle$ are the averaged magnetic fields induced by the active strip with numerous branches and without them (continuous strip), respectively; K_L is the growth factor of the resulting inductance of the active strip; L and L_i are the inductances of the active strip and its i th branch, respectively; n is the number of cuts in the active strip; $n + 1$ is the number of branches in the active strip; and w_s and w_i are the total width of the active strip and the width of its i th branch, respectively.

The physical base of operation of our CMFS is concentration of a magnetic field on the MSE by the MFC. High magnetic field concentration on the MSE allows enhancing its relative magnetic-field sensitivity S_0 by a factor of multiplication F_0 (no fragmentation) and improving the CMFS resolution. Here, $S_0 = (R_B/R_0 - 1)/B$, where R_B is the MSE resistance in an external magnetic field, i.e., at $B \neq 0$ and R_0 is the resistance of the MSE without magnetic field, i.e., at $B = 0$. Indeed, for configurations with the MSE in the form of the GMR element with width w_{GMR} approximately coinciding with width w_s of the active strip, the external magnetic field variation ΔB is reflected on the MSE under the action of the MFC as the variation ΔB_{GMR} . The ratio $\Delta B_{GMR}/\Delta B = F_0$ is the factor of multiplication (concentration) of the magnetic field under the action of the MFC. We may expect that the value $F_0 \sim D/w_{GMR}$ characterizes an increase in S_0 to $\sim F_0 S_0$; thus, the parameters of the MFS improve,

specifically, the minimum detected magnetic field δB decreases. In the CMFS with the continuous active strip, we have

$$\delta B \sim \frac{\delta U}{IR_0 F_0 S_0}. \tag{42.5}$$

Here, δU is the minimum signal detected by the MFS and I is the MFS measuring current. It can be seen that the high F_0 value leads to improvement of the parameters of the MFS, in particular, to a decrease in δB .

The F value was calculated for different numbers of cuts with width w_p , insulating layer thicknesses h_{ins} , and λ . In the calculation, we took into account only the magnetic field component parallel to the substrate surface, since it strongly affects the MSE.

42.3 Results and Discussion

At $i = 1$ and $n = 0$, we have $F = 1$, which corresponds to the MFC with the continuous active strip. Upon nanostructuring ($i \geq 2$) of the continuous active strip into parallel branches and cuts, the F value significantly changes (Fig. 42.1). In the simple case of two cuts ($n = 2$), the F value changes insignificantly, depending on the positions of cuts in the active strip, which can be seen from the data given in Table 42.1 for $\lambda = 50$ nm. The F value noticeably decreases, when the cuts are located near the strip edges; the maximum F value is attained, when the cuts are far from the active strip edges.

Figure 42.2a, b present the dependencies $F(n)$ obtained at $\lambda = 50$ nm (LTS, e.g., niobium) and $\lambda = 250$ nm (HTS, e.g., a material of the Y-123 system) [22]. In the

Table 42.1 The factor F in the fragmentation of the active strip for the case $\lambda = 50$ nm^a

No.	Fragmentation of the active strip, nm	F
1	3375–100–50–100–3375	2.967
2	3300–100–200–100–3300	3.624
3	3200–100–400–100–3200	3.809
4	3100–100–600–100–3100	3.832
5	3000–100–800–100–3000	3.835
6	2900–100–1000–100–2900	3.834
7	2800–100–1200–100–2800	3.834
8	2700–100–1400–100–2700	3.833
9	2600–100–1600–100–2600	3.833
10	2500–100–1800–100–2500	3.832
11	50–100–6700–100–50	1.989

^aNote The regular font—the width branch, italics—the width of the cuts in nanometers. The total width of the active strip $w_s = 7000$ nm

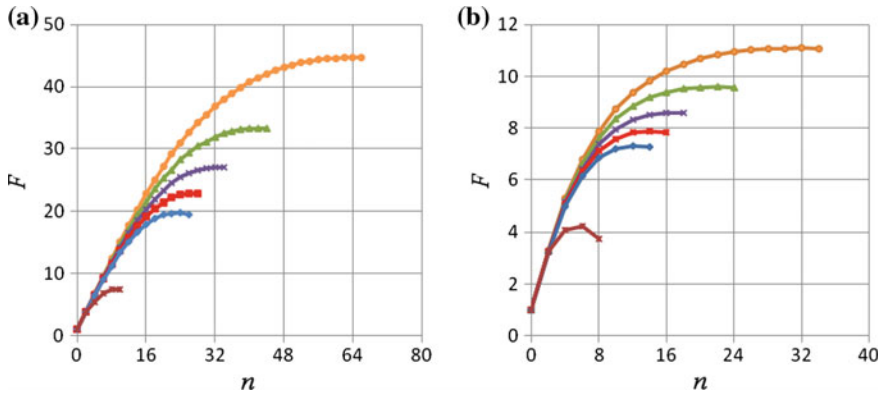


Fig. 42.2 Dependences $F(n)$ obtained at **a** $\lambda = 50$ nm and **b** $\lambda = 250$ nm for different w_p , nm: Orange 20, Green 40, Violet 60, Red 80, Blue 100, Brown 350

calculation, we used the following MFS parameters: $h_{ins} = 20$ nm, $h = 25$ nm, $w_S = 7000$ nm, $h_{mse} = 50$ nm, and $J_C = 10^7$ A/cm².

It was established that with increasing number of nanosized cuts formed on the active strip surface the concentration factor F significantly increases. However, at a certain number of cuts, this effect becomes negative. In particular, at $w_p = 20$ nm, we can reach the largest F values, while with increasing w_p the concentration factor significantly decreases. For example, at $w_p = 350$ nm and $\lambda \sim 50$ nm, we have $F_m = 7.5$ (Fig. 42.2a) and at $w_p = 350$ nm and $\lambda \sim 250$ nm, $F_m = 4.2$ (Fig. 42.2b).

Comparison of the behavior of the concentration factor at $\lambda \sim 50$ nm and $\lambda \sim 250$ nm shows that the F values obtained in the former case are larger than those obtained in the latter case by a factor of 4. The large value $F \sim 44$ at small λ values indicates the higher efficiency of pure LTS materials (e.g., heteroepitaxial niobium layers with $\lambda = 60$ nm [23]) as compared with the efficiency of granular or HTS materials with $F \sim 11$ (e.g., Bi-2223 ceramics with $\lambda \sim 250$ nm [24]) used in the film MFCs.

A significant role in improving the efficiency of the MFSs is played by the insulating layer. Figure 42.3 presents the F values calculated for the active strip with the fragmentation 2200–100–2400–100–2200, where the italics stand for the cut width and the Roman, for the branch width.

It can be seen that at $\lambda \sim 50$ nm the F value grows faster upon variation in the insulating layer thickness than at $\lambda \sim 250$ nm. Varying h_{ins} , one can increase the F value by almost 20 % as compared with the case $h_{ins} \approx 0$.

In all the calculations, we took into account the variation in the total inductance of the active strip upon its fragmentation. In (42.3), we assumed $L_i \sim 1/w_i$, but the exact calculation shows that L_i weakly depends on w_i . Hence, the F values obtained by us are somewhat underestimated. If the dependence of L_i on w_i is ignored, we have $K_L = 1$ and, according to (42.2), the maximum F_m values and the

Fig. 42.3 Dependence F (h_{ins}): Blue $\lambda = 50$ nm; Brown $\lambda = 250$ nm

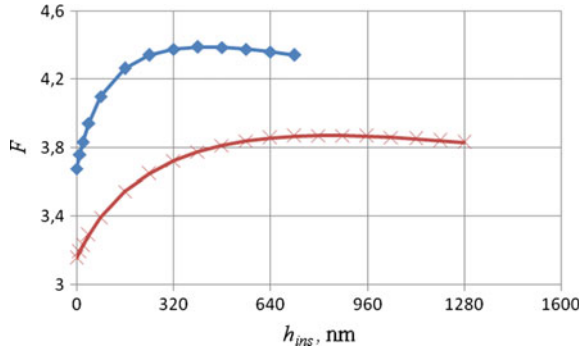


Table 42.2 The F_m and n_m values obtained with and without correction of the total inductance of the active strip

Parameters of active strip		F_m		n_m	
		$K_L = 1$	$K_L \neq 1$	$K_L = 1$	$K_L \neq 1$
$w_p = 20$ nm	$\lambda = 50$ nm	~ 57	~ 45	90	64
	$\lambda = 250$ nm	~ 12	~ 11	44	32
$w_p = 350$ nm	$\lambda = 50$ nm	~ 16	~ 8	12	10
	$\lambda = 250$ nm	~ 6	~ 4	8	8

corresponding numbers of cuts n_m change (see Table 42.2 for the cases $w_p = 20$ nm and $w_p = 350$ nm).

It follows from Table 42.2 that the F_m and n_m values differ from each other by a factor of no more than two at $K_L \neq 1$ and $K_L = 1$. Consequently, the allowance for the variation in the total inductance of the active strip upon its fragmentation does not significantly affect F_m and n_m ; therefore, the efficiency of the MFC remains almost invariable.

The analysis of the results obtained shows that fragmentation of the active strip in nanosized branches and cuts allows us to significantly increase the concentration factor of the film MFC relative to the case of the continuous active strip and, thus, to enhance the CMFS efficiency.

Indeed, in the MFC with the nanostructured active strip, we can reach the F_m value; then, the total magnetic field multiplication is $\sim F_0 \cdot F_m$ and, according to (42.4), we have

$$\delta B \sim \frac{\delta U}{IR_0 F_0 F_m S_0} \tag{42.6}$$

It follows from this formula that we can decrease the δB value by decreasing F_0 and increasing F_m . In addition, decreasing the D ($F_0 \sim D/w_s$) and I values, we can reduce δB and enhance the CMFS efficiency.

Let us estimate the δB value for the MFS consisting of different MSEs. First, we should determine the F_0 value (the presented F_0 values can be somewhat higher,

since they are calculated on the active strip surface rather than at the MSE center) using the formulae

$$F_0 = \frac{B_a}{B}, \quad (42.7)$$

$$F_0 = \frac{\pi D}{4w_s \cdot \left\{ \ln\left(\frac{4D}{w_L}\right) - 2 + \frac{7w_L}{2D} \right\}}, \quad (42.8)$$

with allowance for inductance L , diameter D , and width w_L of the ring, as well as for magnetic field B_a on the active strip surface induced by current I_s :

$$L = \left(\frac{\mu_0 D}{2}\right) \cdot \left(\ln\left(\frac{4D}{w_L}\right) - 2 + \frac{7w_L}{2D}\right), \quad (42.9)$$

$$B_a = \frac{\mu_0 I_s}{2w_s}. \quad (42.10)$$

In study [15], the F_0 values for different ring sizes were obtained. For instance, for the ring with $D = 3$ mm and $w_L = 6$ μm , the magnetic field multiplication is $F_0 \sim 200$. In (42.5), we take $\delta U/(IR_0) \sim 10^{-7}$ and $S_0 \sim 10$ %/(mT) = 100 T^{-1} (the MSE works as a GMR resistor) and obtain $\delta B \sim 10^{-12}$ T. This factor increases with F_0 and S_0 . Indeed, the authors of [16] managed to reduce the δB value by an order of magnitude and more by increasing the ring diameter to about 25 mm and decreasing the ring active strip width to about ~ 3 μm , i.e., by increasing the F_0 value.

In this study, we considered the case when the active strip is fragmented in nanosized superconducting branches and cuts (non-superconducting branches). The fragmentation additionally enhances concentration of an external magnetic field on the MSE, which is reflected in the occurrence of the term $F_m > 1$ in (42.6) and in additional reduction of δB . For $D = 3$ mm, $w_L = 7$ μm , and the rest parameters as previously, we have $F_0 \sim 200$ and $F_m \sim 50$ and, according to (42.6), $\delta B \sim 10^{-14}$ T. As was established in [19–21], the optimal fragmentation yields $F_m \sim 100$. Thus, to reduce the δB value, we should neither increase the MFC ring diameter nor decrease the active strip width. The minimum δB value was attained for the CMFS with a MFC ring diameter smaller than that reported in [16] by almost an order of magnitude.

It is interesting to estimate maximum external magnetic field B_{ex} of the CMFS operation. In accordance with (42.1), relation $I_s/(4hl) \leq J_c$, MFC size, and L value, we obtain $B_{ex} < 40$ μT at $J_c \sim 10^7$ A/cm². Such a high density $J_c \geq 10^6$ A/cm² is implemented in LTS films, e.g., heteroepitaxial niobim layers [23] at $T_w \sim 4$ K or single-crystal HTS film of nanocomposite materials Y-123 system at $T_w \sim 77$ K [24, 25]. Ceramic HTS materials have the low values $J_c \leq 10^4$ A/cm² (e.g., Bi-2223 [22, 26]); therefore, the MFCs based on them can have $B_{ex} < 40$ nT. On the other hand, ceramic HTS materials and layers represent Josephson media, so the MSEs based on them can have the high values $S_0 \geq 10^4 \text{ T}^{-1}$ [27]. The MSE with the

Josephson media are sensitive to the magnetic flux and strongly depend on geometrical sizes. As the latter are decreased, the S_0 value drops. Implementation of the mechanism of δB reduction considered in this study makes certain difficulties in CMFSs with the MSE based on the Josephson media.

42.4 Conclusions

The main field of application of high-resolution (≤ 10 pT) MFSs are medical magnetic systems, including magnetocardiographs, magnetoencephalographs, and low-field magnetic resonance tomographs or low-field magnetic resonance imagines. In these systems, SQUIDs are mainly used as MFSs. Although the SQUIDs require cryogenic cooling, they have been widely used due to their high sensitivity, wide dynamic measurement range $D_r \geq 140$ dB, and other parameters unattainable in other MFSs. The high performances of the SQUIDs are caused, in particular, by using the superconducting film MFTs with large dimensions ($D \sim 7\text{--}10$ mm). The latter complicates application of a large number (hundreds) of SQUIDs for improving the characteristics of magnetic systems.

In a combined magnetic field sensor based on the superconductor (MFC)/non-superconductor (MSE) film structures, such as LTS/GMR (e.g., niobium/permalloy) ones, the value $\delta B \sim 1$ fT was obtained at $T_w \sim 4$ K [13, 14], which is noticeably higher than the resolution of the HTS SQUIDs ($\delta B \geq 5$ fT at $T_w \sim 4$ K) [1–3]. The used ring MFCs with a 3- μm -wide continuous active strip have the diameter $D \sim 25$ mm; the value $F_0 \sim D/w_s \sim 1100$ is attained [13–18]. On the other hand, in the investigated MFC with the nanostructured active strip, the F_m values of a few tens can be implemented, which can be used for additional enhancement of the magnetic field multiplication (concentration) on a magnetosensitive element. Thus, size D can be multiply decreased ($D \leq 1$ mm) at the invariable parameters w_s and δB in the CMFS with the continuous active strip with $D \geq 4$ mm. The proposed CMFS will obviously have much smaller dimensions as compared with SQUIDs ($D \sim 7\text{--}10$ mm) at the same resolution. Thus, the number of MFSs in magnetic systems, such as magnetocardiographs, magnetoencephalographs, low-field magnetic resonance tomographs or low-field magnetic resonance imagines, can be significantly increased, which will make it possible to improve their functionality, in particular, to enhance spatial resolution. For example, the helmet of a widely used magnetoencephalography Elekta Neuromag MEG contains an MSE from 306 SQUIDs [28]. The use of CMFSs as MSEs will allow increasing the number of the latter to 1000 and more, i.e., increasing the spatial resolution of the apparatus several times (≤ 1 mm).

The new combined magnetic field sensors with the fragmented active strip consisting of the simulated nanosized elements (the resolution $\delta B \leq 10$ fT in the external magnetic field $B_{ex} \leq 40$ μT , i.e., in the Earth's magnetic field) can apparently replace the SQUIDs in the widely used medical magnetic systems, including magnetocardiographs, magnetoencephalographs and low-field magnetic

resonance tomographs or low-field magnetic resonance imagines. Thus, such a sensor can be an alternative to SQUIDs in different applications [26].

At present, novel biocompatible materials and advanced treatment and diagnostic techniques are intensively introduced, e.g., vector drug delivery by magnetic nanoparticles, nanomaterials with ferromagnetic or superparamagnetic particles, carbon nanotubes, etc. In addition, active implanted apparatus, such as artificial heart and various stimulators, require permanent control, which can be implemented using the magnetic systems with high-sensitivity magnetic field sensors for non-invasive diagnostics and control. The urgent problems of modern medicine can probably be solved with the use of the combined magnetic field sensors with nanostructured active strips investigated in this work.

Acknowledgments We are grateful to Profs. V.M. Podgaetskii for useful discussions and N.S. Shichkin for help in the calculations. The investigation was performed by a grant from the Russian Science Found (Project No. 14-39-00044).

References

1. D. Robbes, *Sens. Actuators, A* **129**(1), 86 (2006)
2. D. Drung, C. Assmann, J. Beyer et al., *IEEE Trans. Appl. Supercond.* **17**(2), 699 (2007)
3. C.M. Wilson, *Nature* **479**(7373), 376 (2011)
4. V.S. Zotev, A.N. Matlashov, P.L. Volegov et al., *Supercond. Sci. Technol.* **20**, S367 (2007)
5. P.T. Vesanen, J.O. Nieminen, K.C.J. Zevenhoven et al., *Magn. Reson. Med.* **69**, 1795 (2013)
6. V.S. Zotev, A.N. Matlashov, P.L. Volegov et al., *J. Magn. Reson.* **194**, 115–120 (2008)
7. V.A. Mal'gichev, A.M. Nevzorov, S.V. Selishchev et al., *Biomed. Eng.* **44**, 2019 (2011)
8. J.C. Oliveira, M. Martinelli, S.A. D'Orio Nishioka S et al., *Circ Arrhythmia Electrophysiol.* **2**(1), 29 (2009)
9. P.E. Marik, M. Baram, *Critical Care Clins.* **23**, 383 (2007)
10. www.tristantech.com
11. www.starcryo.com
12. www.supracon.com
13. M. Pannetier-Lecoer, C. Fermon, G. Le Goff et al., *Science* **304**(5677), 1648 (2004)
14. M. Pannetier, C. Fermon, G. Le Goff et al., *IEEE Trans. Appl. Supercond.* **15**(2), 892 (2005)
15. M. Pannetier-Lecoer, C. Fermon, A. de Vismas et al., *J. Magn. Mater.* **316**, e246 (2007)
16. M. Pannetier-Lecoer, L. Pakkonen, N. Sergeeva-Chollet et al., *Appl. Phys. Lett.* **98**(15), 153705 (2011)
17. N. Sergeeva-Chollet, H. Dyvorne, H. Polovy et al., *Adv. Biomagn. BIOMAG2010 IFMBE Proc.* **28**, 70 (2010)
18. N. Sergeeva-Chollet, H. Dyvorne, J. Dabek et al., *J. Phys: Conf. Ser.* **303**, 012055 (2011)
19. L. Ichkitidze, A.N. Mironyuk, *Physica C* **472**(1), 57 (2012)
20. L.P. Ichkitidze, A.N. Mironyuk, *J. Phys.: Conf. Ser.* **400**(Part 2), 022032 (2012)
21. L.P. Ichkitidze, *AIP Adv.* **3**(6), 062125 (2013)
22. V.V. Schmidt, *Introduction to the Physics of Superconductors*, 411pp. Moscow. ISBN 5-900916-68-5. (In Russian)
23. L.P. Ichkitidze, V.I. Skobelkin, *Fizika Nizkih Temperature (USSR)*, **11**(8), 839 (1985) (In Russian)
24. M.A. Bodea, J.D. Pedarnig, T.D. Withnell et al., *J. Phys: Conf. Ser.* **234**, 012006 (2010)

25. http://www.htspeerreview.com/2008/pdfs/presentations/tuesday/plenary/europe_update.pdf
26. B.P. Mikhailov, L.P. Ichkitidze, YuE Grigorashvili et al., *Inorg. Mater.* **39**(7), 749 (2003)
27. L.P. Ichkitidze, *Bull. Russian Acad. Sci. Phys.* **71**(8), 1145 (2007)
28. <http://www.mrn.org/collaborate/elekta-neuromag-meg>

Chapter 43

New Methods and Transducer Designs for Ultrasonic Diagnostics and Therapy

A.N. Rybyanets

Abstract Ultrasound has found usage in all aspects of the medical field, including diagnostic, therapeutic, and surgical applications. Recent advances in the field of physical acoustics, imaging technologies, piezoelectric materials, and ultrasonic transducer design have led to emerging of novel methods and apparatus for ultrasonic diagnostics, therapy and body aesthetics, as well as to expansion of traditional applications fields. The chapter presents new multi-frequency and harmonics methods for dynamical focusing of high intensity focused ultrasound (HIFU), methods of supersonic generation and resonant amplification of shear waves, and ultrasonic standing waves (USW) technique for ultrasonic diagnostics, therapy and body aesthetics applications. Technological peculiarities of the ultrasonic transducer design as well as theoretical and numerical models of such transducers and the corresponding HIFU fields are discussed. The results of ex vivo experiments with different tissues that prove the efficacy, safety and selectivity of new methods and developed HIFU transducers are present and analyzed.

43.1 Introduction

The use of ultrasound as a valuable diagnostic and therapeutic tool in several fields of clinical medicine is now so well established that it can be considered essential for good patient care [1]. However, remarkable advances in ultrasound imaging technology over last decade have permitted us now to envision the combined use of ultrasound both for imaging/diagnostics and for therapy. Traditional therapeutic applications of ultrasound include the treatment of soft tissue and bone injuries, wound healing, hyperthermic cancer treatment, focused ultrasound surgery of Parkinson's disease, glaucoma and retinal detachment and for sealing traumatic

A.N. Rybyanets (✉)
Institute of Physics, Southern Federal University, 194, Stachki Ave.,
344090 Rostov-on-Don, Russia
e-mail: arybyanets@gmail.com

capsular tears, benign prostatic hyperplasia, the liver, the kidney, prostate and bladder tumours, vascular occlusion therapy, and tool surgery [1, 2].

Ultrasound beyond the diagnostic ranges can bring about various kinds of reactions when insonated into biological tissue [3]. The resulting effects include thermal, mechanical, chemical and optical reactions. Mechanical effects, more specifically, may consist of acoustic cavitation, radiation force, shear stress, and acoustic streaming/microstreaming. Among them, the thermal effect and acoustic cavitation are the most significant, and their mechanisms of action have been relatively well-understood [1, 4]. It is, however, often extremely difficult to identify positively the mechanisms involved in producing biological change, and indeed to isolate non-thermal effects from thermal ones.

Despite the fact that medical ultrasound is a relatively older field compared to Magnetic resonance imaging (MRI) and Positron Emission Tomography (PET), ongoing advances have allowed one to continuously expand as a field in its numerous applications. In the past decade, with the advent of faster processing, specialized contrast agents, understanding of nonlinear wave propagation, novel and real-time signal and image processing and complex ultrasound transducer manufacturing, ultrasound imaging and ultrasound therapy have enjoyed a multitude of new features and clinical applications [1, 3, 4].

Systems and methods for performing a surgical, therapeutic or aesthetic medical procedure in target tissues of patient's body by using high-intensity focused ultrasound (HIFU) are well known in the art [1, 3]. The HIFU systems are used particularly for body aesthetic therapy by adipose tissue lysis [3, 5, 6]. The main disadvantage of HIFU application for treatment of large volumes of tissue is small treated volume in lateral direction. Other drawback of conventional HIFU treatments of tissue is a restricted number of body areas suitable for treatment because of low fat thickness, complex body shapes, and close proximity of bones or vital organs elsewhere in the body. Therefore the need exists for new safe and effective methods and devices aimed for treatment of large volumes of subcutaneous adipose tissue and skin using ultrasound energy [3].

The chapter presents new methods for ultrasonic diagnostics, therapy and body aesthetics applications. Ultrasonic transducers design as well as theoretical and numerical models of focused ultrasonic transducers and corresponding HIFU fields are discussed. The results of *ex vivo* experiments with different tissues that prove the efficacy, safety and selectivity of new methods and developed HIFU transducers are presented and analyzed.

43.2 Basic Principles of HIFU

HIFU continues to be a very attractive option for minimally invasive procedures. Using well-established principles, this ablative therapy can be used to treat a number of benign and malignant diseases with few side effects. During the last

15 years, there has been an enormous amount of work, both laboratory based and in the form of clinical trials, aimed at developing devices that can deliver treatments with safe and effective outcomes [1, 7–11]. However, the application of this technology still has many drawbacks. It is expected that current obstacles to implementation will be resolved in the near future.

The various methods of focusing ultrasonic waves have been proposed [1, 3]. The simplest and cheapest (often most accurate) method may be a shelf-focusing, for instance, a spherically curved ultrasonic source (transducer). An ultrasonic transducer constructed according to this method, has a beam focus fixed at the position determined from the geometrical specifications of the transducer. Recently, a phased-array ultrasonic transducer technique was adopted for HIFU therapy. By sending temporally different sets of electronic signals to each specific transducer component, this technique enables beam-steering and focusing, which can move a focal spot in virtually any direction within physically allowed ranges. However, the flexibility provided by phased arrays is achieved at the expense of their intricate design; in addition, the field of these arrays contains side lobes (often called grating lobes). The latter fact may cause some undesired effects, such as tissue damage away from the target region, and this is unacceptable in ultrasonic surgery.

Today, the search for new efficient methods of dynamic focusing of ultrasound that allows steering the focus (foci), while retaining a low level of grating lobes in the field of the focusing system is in progress.

Major differences of HIFU therapy from other interventional therapeutic modalities are its complete non-invasiveness and sharp, tailorable treatment margins, which may lead to treatments with very low complication rates. However, several complications have been known to occur after HIFU therapy. These are mostly due to high-energy ultrasonic waves reflected on gas or bony structures, as well as due to poor acoustic coupling between the skin and HIFU transducer (skin-burning) [12, 13]. In addition to these complications, HIFU therapy has displayed several other limitations, which are hampering the effective use of this modality in clinical practice. These include a long procedure time, difficulty in targeting and monitoring moving organs, sonic shadowing by bones or gas in bowels, and the relatively high cost of this technique in relation to its effectiveness and limitations.

A major limitation of current ultrasound thermal and cavitation HIFU therapy is a small size of focal zones and a small thickness of target tissues along with its spatial extension, leading to long procedure time, pain and injury of bones and vital organs. In the field of body aesthetic applications, implantation of new HIFU techniques in combination with other therapeutic and diagnostic modalities, promising a more revolutionary clinical impact, can be anticipated [7–11].

43.3 Dynamical Focusing Method

The method of direct synthesis of dynamically focused acoustic fields is based on the continuous cyclic generation of different focal patterns at optimal repetition frequency by simultaneous applying of “M” different frequency signals to “N” sectors of spherically shaped sectored transducer [3, 5]. For illustration of basic principles of the method HIFU transducers comprising a spherical piezoceramic caps with back electrodes divided circumferentially into 4 regular shaped sectors were designed and tested. The sectors were simultaneously powered by 4 sinuses or burst drive signals with different frequencies from 6 dB bandwidth of the transducer.

Dynamical acoustic fields were calculated and modeled for HIFU transducer comprising a spherical piezoceramic cap (radius of curvature of 50 mm, aperture of 80 mm) with back electrode divided circumferentially into 4 regularly shaped sectors. FEM modeling and calculations were performed using ANSYS and Matlab software packages. Calculations were made for water loading and different pressures on the surface of piezoelement.

A result of summary of ultrasonic beams with different frequencies in the focal area is an equivalent of continuous changes in phase shifts of signal for i th sector according the following formula: $\varphi_i = 360^\circ \Delta f_i (F/C - t)$, where Δf_i is the frequency shift from f_0 , F is the focal distance, C is the sound velocity, t is the time. Frequency excitation protocols: $f_1 = 700$ kHz, $f_2 = 690$ kHz, $f_3 = 700$ kHz, $f_4 = 690$ kHz for 4 regularly shaped sectors. Repetition rate of focal patterns appearance was a common divider of the applied frequencies (10 kHz). The results of FEM calculations of acoustic field structure for regularly sectored dynamically focused transducer are shown in Fig. 43.1.

Acoustic measurements of the dynamically focused sectored transducers were made in an oil bath using calibrated hydrophone and acoustic intensity measurement system (AIMS). The electric power and hydrophone signal were measured using LeCroy WS 24Xs oscilloscope. Transducer sectors were powered using function generator Agilent 33220A and power amplifier AG 1012 LF. For measurements of acoustic field patterns for 4 regularly shaped sectored transducer, the sectors were powered by single frequency bursts at appropriate phase shifts, corresponding to initial and final focal zones.

The results of AIMS 2D Scan in the focal plane of dynamically focused transducer at low power excitation (power = 40 W, burst length = 20 cycles) are listed in Table 43.1. The photos of focal zones patterns of dynamical acoustic fields in a mineral oil are shown in Fig. 43.2.

The HIFU dynamical focusing transducers comprising 4 regular sectors were used for tissue treatment (aperture 80 mm, focal length 50 mm, resonant frequency 700 kHz). The sectors were simultaneously powered by sinus bursts drive signals with different frequencies from 6 dB bandwidth of the transducer using two function generator and power amplifier. The acoustic intensity was kept at 750 W/cm² (ISAL).

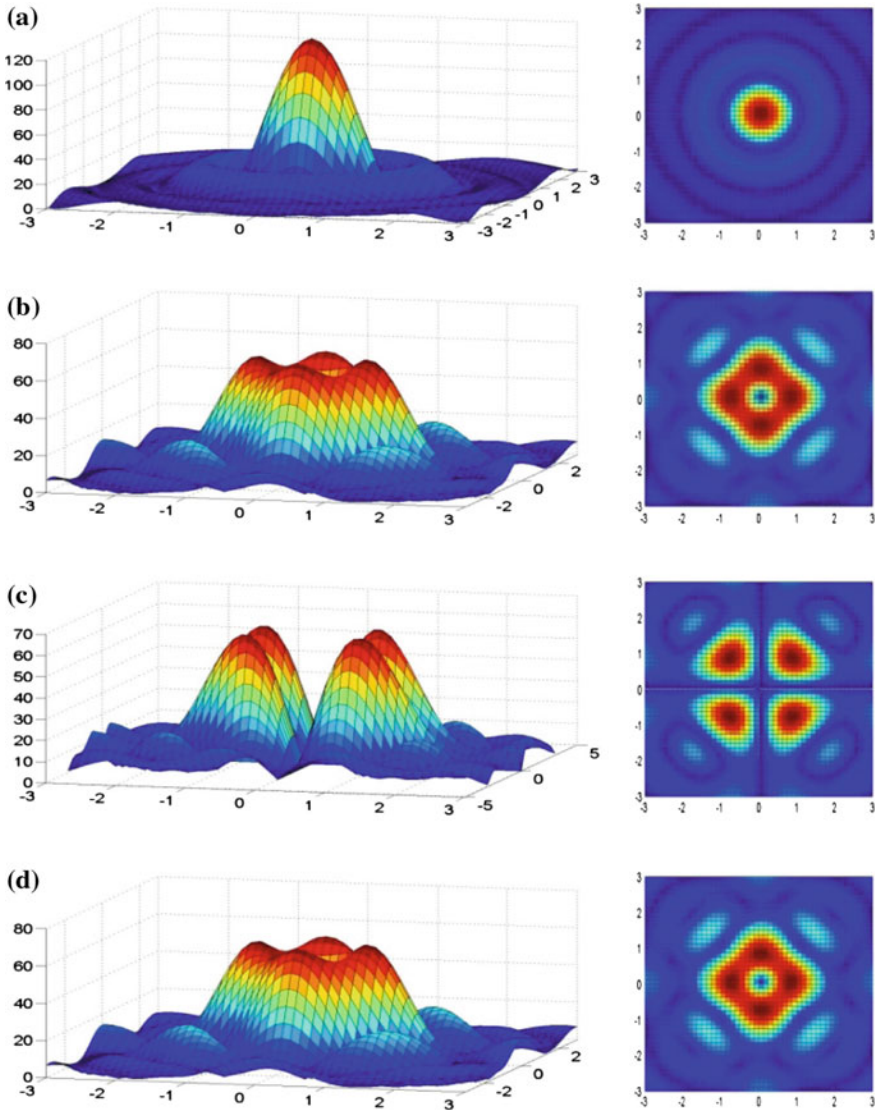


Fig. 43.1 FEM calculated sequential samples of focal zones for regularly sectored dynamically focused transducer. Corresponding phase shifts for neighbor sectors are: **a** $\Theta = 0^\circ$; **b** $\Theta = 90^\circ$; $\Theta = 180^\circ$; $\Theta = 270^\circ$

The fresh porcine adipose samples were placed in an oil bath and positioned right under the transducer such that focal point was placed inside the sample. The samples were irradiated by the dynamical HIFU for 3–10 s. After exposure, the samples were sectioned along the beam axis respectively to compare the

Table 43.1 Results of AIMS 2D Scan

Single Focus			Four Focuses		
$f_1, f_2, f_3, f_4 = 700$ kHz			$f_1, f_2, f_3, f_4 = 700$ kHz		
$\Theta_1, \Theta_2, \Theta_3, \Theta_4 = 0^\circ$			$\Theta_1, \Theta_3 = 0^\circ, \Theta_2, \Theta_4 = 180^\circ$		
Focal diameter @ 3 dB (mm ²)	Peak pressure (kPa)	Power @ 40 dB (W)	Focal diameter @ 3 dB (mm ²) for each of four focuses	Peak pressure (kPa) for each of four focuses	Power @ 40 dB (W) for each of four focuses
1.5×1.6	6110.6	28.5	1.4×1.6	3090.3	7.3

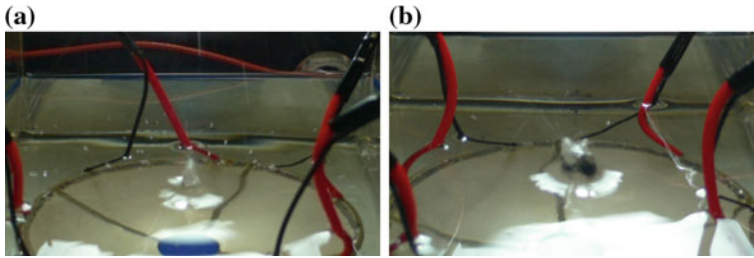


Fig. 43.2 Visualization of dynamical acoustic fields (end points of dynamical cycle) generated of sectored focusing transducer at 700 kHz in a mineral oil: **a** single focus $\Theta_1, \Theta_2, \Theta_3, \Theta_4 = 0^\circ$; **b** four focuses $\Theta_1, \Theta_3 = 0^\circ, \Theta_2, \Theta_4 = 180^\circ$

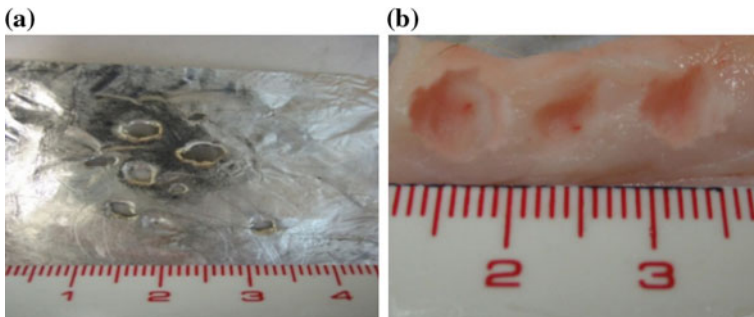


Fig. 43.3 Photographs of cavitation holes in Al-foil **(a)** and cavitation lesions **(b)** in the porcine samples, induced by HIFU transducers at single and dynamical focusing excitation. Frequency excitation protocols: dynamical focusing $f_1, f_3 = 700$ kHz, $f_2, f_4 = 699$ kHz (*big holes* and lesions), single focusing $f_1, f_2, f_3, f_4 = 700$ kHz (*small holes* and lesion). The exposure time = 10 s, duty cycle = 1/10, burst length = 100 cycles, the acoustic intensity ISAL = 750 W/cm²

dimensions of the lesions. Preliminary experiments on thin Al foil in oil bath were also made for cavitation detection.

The photographs of cavitation holes in thin Al foil as well as cavitation lesions in the porcine samples induced by HIFU transducer working in the dynamical focusing and single focusing regimes are shown in Fig. 43.3.

Obviously, the cavitation tissue lesion generated by dynamical focusing method during one sonification is larger than at single frequency excitation under

the same exposure conditions. Enhancement of the cavitation lesions and tissue ablations obvious from Fig. 43.3 was reached due to dynamical focusing method (cyclic generation of different focal patterns) providing cavitation enhancement, inhomogeneous ultrasound beam patterns with higher pressure gradients and shear deformations, as well as nonlinear interactions of harmonics frequencies. Additional increase in lesions activity is provided by optimal repetition frequencies and bursts lengths that correspond to specific resonance/relaxation times of cavitation “clouds” and/or tissues as well as to natural tissues reaction times.

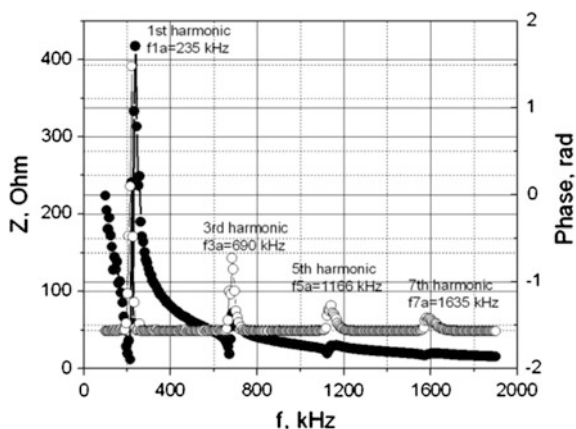
43.4 Multi-frequency Harmonics Method

The multifrequency harmonics method consists in simultaneous or alternative (at optimal repetition frequency) excitation of single element HIFU transducer on a frequencies corresponding to odd natural harmonics of piezoceramic element at ultrasound energy levels sufficient for producing cavitation, thermal or mechanical damage of fat cells at each of aforementioned frequencies [3, 6].

Any piezoelement can be excited on odd harmonics of main resonant frequency [10], but $k_{eff,n}$ will be less than for main mode. Effective electromechanical coupling factor $k_{eff,n}$ for n th harmonics of a piezoelement can be found as $k_{eff,n} = 8k_t^2 / [(2n + 1)\pi]^2$. However at proper electrical matching and excitation power a piezoelement can work on odd harmonics very efficiently. Odd harmonic frequencies can be calculated as $f_{a,n} = (2n + 1)f_{a,1}$, where $f_{a,n}$ is the antiresonance frequency of n th harmonics, $f_{a,1}$ is the antiresonance frequency of main mode, n is a integer. Antiresonance frequencies must be used because of electromechanical contribution to the sound velocity of piezoelectric body. Corresponding resonant frequencies can be calculated from antiresonant ones using standard formulae [10].

Impedance spectra illustrating odd harmonics of thickness vibrations of focusing piezoceramic element are shown in Fig. 43.4. Frequency dependencies of

Fig. 43.4 Impedance spectra (frequency dependencies of impedance and phase) of spherical focusing piezoelement with odd harmonics of thickness vibrations



impedance and phase of piezocomposite elements were determined by impedance spectroscopy method using 4294A Agilent Impedance Analyzer. Measurements were made for focusing piezoceramic element with the aperture 85 mm and radius of curvature 55 mm having resonance frequencies 205 kHz (1st harmonic) and 670 kHz (3rd harmonic), respectively.

FEM modeling was performed using ANSYS software package. Calculations were made for the same focusing piezoceramic element with harmonics frequencies 205 and 670 kHz, respectively. The results were compared with the focusing piezoceramic element with first harmonic resonance frequency 670 kHz (Fig. 43.5).

FEM calculations of acoustic pressure and efficiency at the same input electric power show that the piezoceramic element working on 1-st harmonic resonance frequency (670 kHz) produces 1.8 times higher focal pressure compared to the piezoceramic element excited on the same frequency at 3-rd harmonic. Calculations and modeling of acoustic pressure in the focal plane for 1-st and 3-rd harmonics excitation of focusing piezoceramic element were made by solving standard wave equations at the Fresnel approximation using Matlab software. Calculations were made for water loading and different pressures on the surface of piezoelement.

Acoustic measurements of the focusing piezoceramic elements were performed in oil bath using calibrated hydrophone and acoustic intensity measurement system (AIMS). The electric power and hydrophone signal measurements were made using LeCroy WS 24Xs oscilloscope. Piezoceramic element was powered using function generator Agilent 33220A and power amplifier AG 1012 LF. The total acoustic output was measured by acoustic force balance AFB. The results of AFB measurements at 205 and 690 kHz are listed in Table 43.2.

2D-scans of acoustic pressure distribution in the focal plane of the focusing piezoceramic element measured by hydrophone using acoustic intensity measurement system (AIMS) at low power excitation (4 W, burst length = 20 cycles) are shown in Fig. 43.6. The results of acoustic field measurements for 1-st and 3-rd harmonics are listed in Table 43.3.

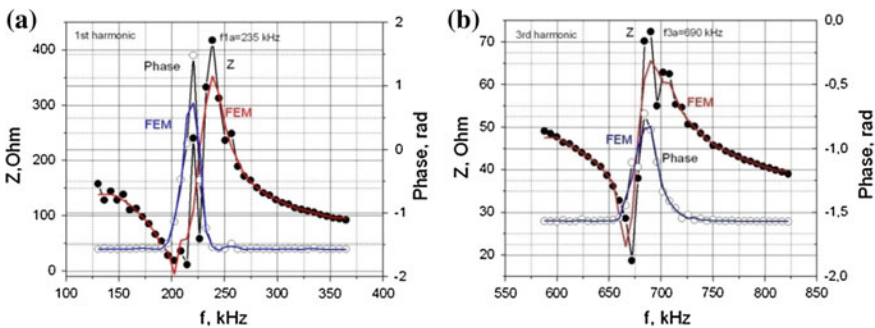


Fig. 43.5 Measured and FEM modeled impedance spectra for first (a) and third (b) harmonics of focusing piezoceramic element

Table 43.2 Results of AFB measurements

Frequency (kHz)	Power (W)	Force (g)	Efficiency (mg/W)
205	20	0.25	125.1
690	20	0.09	45.3

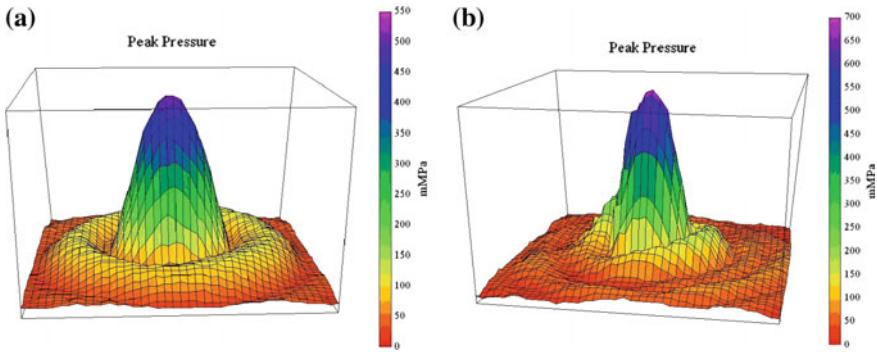


Fig. 43.6 AIMS 2D-scan of acoustic pressure in the focal plane for 1-st and 3-rd harmonics ($f_r = 205$ kHz, $f_3 = 690$ kHz)

Table 43.3 Results of acoustic field measurements

Focal length (mm)	Focal diameter (mm ²)	Peak pressure (kPa)	Power @ 40 dB (mW)
<i>First harmonic $f_r = 205$ kHz</i>			
21.0	5.5 × 5.4	521	619
<i>Third harmonic $f_r = 690$ kHz</i>			
6.3	1.5 × 1.7	695	196

Fresh porcine liver and adipose was obtained from a butcher within 24 h of slaughter. A single element spherical PZT transducer (aperture 85 mm, focal length 55 mm, resonance frequency 205 kHz) was used for experiments. For comparison, spherical PZT transducer with 1-st harmonic resonant frequency 690 kHz was measured also. Piezoceramic element was powered simultaneously on 1-st and 3-rd harmonic frequencies 205 and 690 kHz using two function generators and power amplifiers. The acoustic intensity in the focal plane was kept as 250 and 500 W/cm² (ISAL) for 1-st and 3-rd harmonics, respectively. The acoustic intensity for PZT transducer with the main resonant frequency 690 kHz was 750 W/cm² (ISAL). The samples were placed in an oil bath and positioned right under the transducer such that focal point was placed inside the sample. The samples were irradiated by the harmonics frequency HIFU for 3–20 s at different duty cycles (from 1/2 to 1/100) and burst lengths (from 10 to 200 cycles) of the signals. After exposure the samples were sectioned along the beam axis, respectively, to compare the dimensions of the

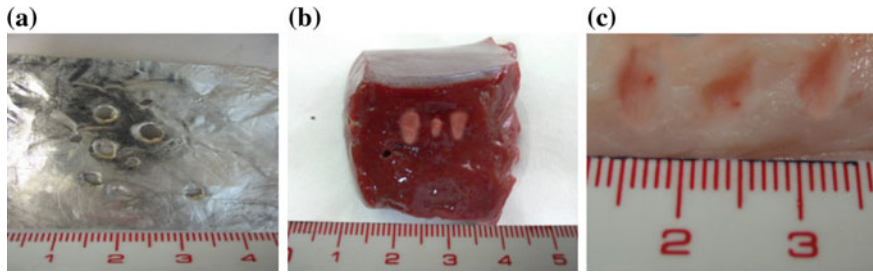


Fig. 43.7 Cavitational holes in Al-foil (a), thermal (b) and cavitational (c) lesions in the liver and porcine samples induced by HIFU transducers at single- (*small holes* and lesions) and dual-frequency harmonics excitation. Treatment parameters: **a** exposure time = 3 s, duty cycle = 1/20, burst length = 10 cycles; **b** exposure time = 9 s, duty cycle = 1/5, burst length = 200 cycles; **c** exposure time = 9 s, duty cycle = 1/20, burst length = 10

lesions. Preliminary experiment on thin Al foil positioned at the focal plane of HIFU transducer in oil bath were also made for cavitation detection.

The photographs of cavitational holes in thin Al foil as well as thermal and cavitational lesions in the liver and porcine samples induced by HIFU transducer at simultaneous excitation on 1-st (205 kHz) and 3-rd (690 kHz) harmonics and by HIFU transducer working on 1-st harmonic (690 kHz) only are shown in Fig. 43.7.

Enhancement of the lesions and tissue ablations obvious from Fig. 43.4 was reached due to simultaneous or sequential influence of harmonic frequencies providing cavitation enhancement of tissue heating, inhomogeneous ultrasound beam patterns with enhanced pressure gradients and shear deformations, as well as nonlinear interactions of harmonics frequencies. Additional increase in lesions activity is provided by optimal repetition frequencies, bursts lengths and sonification times that correspond to specific resonance/relaxation times of cavitation “clouds” and/or tissues as well as to natural tissues reaction times.

43.5 Applications of Shear Waves for Soft Tissues Diagnostics and Therapy

43.5.1 The Acoustic Radiation Force in Soft Tissues

By focusing an ultrasonic beam at a given location, it is possible to create a volumetric radiation force inside a dissipative medium. This force is due to the momentum transfer from the acoustic wave to the medium, caused by dissipation or reflection of the acoustic wave [14–17]. For a dissipative medium, it is common to write: $F = 2\alpha I/v$, where v is the speed of sound in the medium, α is the ultrasound attenuation, and I is the local intensity of the ultrasonic beam that is proportional to the square of the acoustic pressure-field pattern. This force will generate bulk and shear waves propagating in the medium with respective speeds, depending on the

elastic moduli λ and μ of the medium. The shear wave, generated by focused ultrasonic beam, has axial directivity pattern and mainly propagates along the transverse direction. Its velocity, typically a few meters per second in soft tissues, is directly linked to shear elasticity if the medium is assumed to be purely elastic: $\mu = \rho c^2$, where c is the speed of the shear wave and ρ is the density of the medium. This assumption is still valid in a viscoelastic model at the assumption that dispersion induced by viscosity is negligible. As we are dealing with soft tissues, $\lambda \gg \mu$, the Young's modulus of the medium E can be quantitatively estimated by measuring the shear-wave speed: $E \approx 3\mu = 3\rho c^2$.

This estimation is not possible along the acoustic beam axis in which the shear term is negligible. The small displacements along this axis are induced by the coupling term and vanish quickly in the near field of the radiation force source. In the presence of noise, the estimation of elastic parameters is not relevant.

The first experimental confirmation of shear wave excitation by focused ultrasound in a rubber-like medium was presented in [17]. It was shown that high-shear displacements at focal point in the medium (up to 40 μm in phantoms) can be achieved using 100 μs bursts of 1.8 MHz HIFU at acoustic power 45 W. Shear waves with a frequency 10 kHz, observed in these experiments in viscoelastic medium, were strongly attenuating and were intended for diagnostic purposes only.

43.5.2 Resonant Amplifications of Remotely Induced Shear Waves in Soft Tissues

As was mentioned above the peculiarities of shear waves remotely generated by HIFU in tissues are very high attenuation and very low intensity. These low frequency and low intensity shear waves are used now for visualization and tissue assessments [14, 15]. For visualization purposes, it is impossible to use high intensity pumping HIFU. According FDA requirements three parameters with respect to the acoustic output of the ultrasound system should be evaluated: the mechanical index ($MI < 1.9$), the spatial peak pulse average intensity ($I_{SPPA} < 190 \text{ W/cm}^2$), and the spatial peak temporal average intensity ($I_{SPTA} < 720 \text{ mW/cm}^2$) [3]. Thus, the intensity of shear waves generated by this HIFU outside a focal point is very weak. Increase in shear wave amplitude generated in supersonic regime [15] on Mach cone boundary is only 1.5–2 times, as maximum, because of strong attenuation of shear waves. Application of more intensive HIFU, usually used for therapy purposes, for generation of more intensive shear waves is also impossible because of thermal tissue modification in the vicinity of focal point. From other point of view, it is well known that any physical body is less stable mechanically (on orders of magnitudes) to shear deformations than to compression ones.

Thus, meeting these contradictory demands regarding generation of intensive shear waves for diagnostic and therapy applications requires the development of new ultrasonic transducer designs and improved methods of shear waves generation.

A new concept for resonant amplifications and supersonic generation of remotely induced shear waves in soft tissues for therapy and diagnostics purposes were proposed recently [3, 8, 9]. The method consist in a remote formation of the “virtual resonators” of shear waves inside a tissue by exciting a cyclically morphing pattern of focal regions of pumping HIFU. In a morphing pattern, focal regions cyclically appear at different locations. Radiation force generated by the HIFU in each focal region contributes to generating the shear wave. The distance between adjacent locations of focal regions in the pattern, frequency and repetition rate of exciting HIFU bursts and a frequency of the shear wave are determined to provide constructive interference and resonant amplification of the shear wave at each focal region. In resonant amplification of a shear wave, radiation force is repeatedly applied in phase with the shear wave to a region of tissue in which the shear wave propagates to amplify the shear wave amplitude. In other embodiment of the method a focal region in the pattern moves laterally, continuously or “discontinuously” between the locations, or rotates around a center axis in a focal plane of HIFU to generate an amplified shear wave. The linear velocity of focal zone movement or rotation can be equal to (wave resonance regime) or greater than (supersonic regime) the shear wave propagation velocity in a tissue. At supersonic regime of shear wave generation by moving or rotation the shear source at a supersonic speed all resulting shear waves will interfere constructively creating intense Mach cone or Mach spiral structure.

Distinctive peculiarities of proposed methods use dynamical HIFU method for remote formation of the “virtual resonators” of shear waves inside a tissue, and application of wave resonance or supersonic generation regimes for amplification of shear waves propagating in wide tissue region. Different types of HIFU transducers may be used for resonant amplifications and supersonic generation of remotely induced shear waves in soft tissues in accordance with proposed concept. By way of example, an ultrasound transducer may be an annular or sectored HIFU transducer, or any of various phased array configurations, such as for example a linear, two or three dimensional phased array ultrasonic transducers.

Modeling of shear wave propagation in tissue, generated by rotating pattern of focal zones around a center axis in a focal plane of HIFU was performed using Wave 3000™ 3D simulation package (CyberLogic Inc.). Shear waves generated by the rotating pattern of focal zones are characterized by a wave front that propagates in a spiral shape away from the pattern in a focal plane. Virtual sources of shear waves disposed symmetrically around central axis of HIFU transducer were switched on sequentially at appropriate delay times, simulating rotation of 1 of-axis or 2 symmetrically positioned HIFU focal zones. Shear wave propagation traced using Wave 3000 algorithm. The resulting single and double Mach spiral structures of shear waves generated at supersonic regime are shown in Fig. 43.8.

For preliminary feasibility test of the method, the experimental setup comprising sectored HIFU transducer, controller and multi-channel driving circuitry was designed and tested in oil bath and on tissues *in vitro*. Sectored HIFU transducer comprising a spherical piezoceramic cap (radius of curvature 54 mm, aperture 85 mm, frequency 1 MHz) with back electrodes divided circumferentially into 8

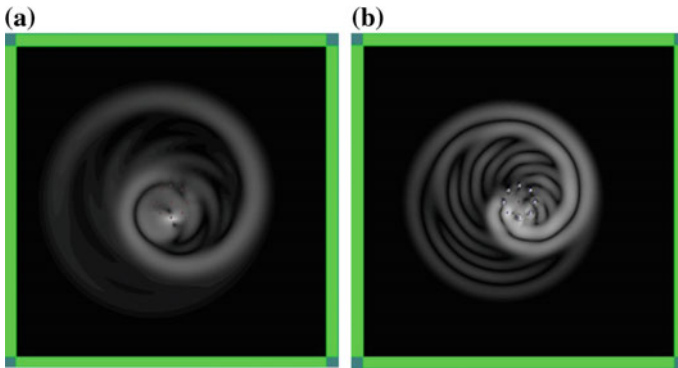


Fig. 43.8 Mach spirals, resulting from constructively interfered shear waves, generated by the rotating pattern of 1 of-axis (a) and 2 symmetrically positioned HIFU focal zones (b)

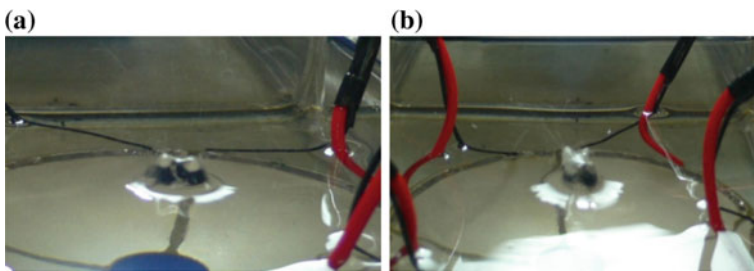


Fig. 43.9 Visualization of rotating focal zones pattern generated by dynamically focusing transducer in a mineral oil: a 2 static symmetrical off-axis focal zones; b rotation of bi-focal zones pattern at angular velocity ω

regular shaped sectors were fabricated. The sectors were combined in 2 symmetrical groups and each group was simultaneously powered by 2 sines or burst drive signals with the same frequency at 180° phase shift.

As a result, 2 symmetrical off-axis focal zones appeared in the acoustic field of the sectored transducer as shown in Fig. 43.9a. For rotation of this bi-focal zones pattern the phase of the drive signal supplied on next sector of each group are sequentially switched. The resulting rotating bi-focal zones pattern visualized in oil bath are shown in Fig. 43.9b.

To provide rotation of the pattern at angular frequency $\omega/2\pi$, switching for the 8-sectored transducer was done at a switching frequency equal to $8\omega/2\pi$. For transducer configuration used in experiments, resonant amplification of shear waves generated by rotating bi-focal zones pattern occurs for an angular velocity $\omega = 2186$ rad/s. For this angular velocity, the focal regions rotate at about 348 rotations per second. At higher angular velocities, supersonic regime of shear wave generation with appropriate Mach spiral formation is realized.

Intensive low frequency shear waves generated in supersonic regime by rotating bi-focal zones pattern in porcine samples in vitro were detected experimentally using specially designed measurement cell equipped by shear deformation piezo-electric sensors. Detected shear waves amplitude at the distance 10 mm far from focal zones pattern was 100 μ (frequency 10 kHz) at pumping HIFU acoustic power 50 W and frequency 1 MHz.

Preliminary feasibility tests showed that intensive shear waves could be generated in wide tissue regions using a new method of resonant amplifications and supersonic generation of remotely induced shear waves at low intensity of pumping HIFU. Dynamical changes in focal zones positions in this case prevent tissue modification by HIFU itself and provide “pure” shear waves diagnostic and imaging tools. Combined effect of high intensity HIFU and resonantly amplified shear waves provides new shear waves therapy modality.

43.6 Ultrasonic Standing Waves Methods for Body Aesthetics Applications

43.6.1 Limitations of HIFU and Prospective Approaches

The main disadvantage of HIFU application for treatment of large volumes of tissue is small treated volume in lateral direction. For example, in the treatment of adipose tissue, which covers all body parts at an average thickness 1–5 cm, the HIFU transducers are applied externally to the patient in the direction perpendicular to the body. To perform the treatment, the transducer needs to be moved step by step over many locations along the body and the procedure is greatly time-consuming. Various attempts to increase the size of treated area in HIFU systems were made [3, 5, 6, 10]. However, all of these techniques still appear to be effective only for treating a limited area of tissue as defined by a small size of a focal zone and are unsatisfactory for practical treatment of big areas of subcutaneous adipose or cellulite tissue regions without damaging skin and other tissues. Other disadvantage of conventional HIFU treatments of tissue is a restricted number of body areas suitable for treatment. Using of HIFU for adipose tissue treatment is restricted practically to include only an abdomen region, because of low fat thickness in other sites, complex body shapes, and close proximity of bones or vital organs elsewhere in the body.

Therefore, the need exists for new methods and devices aimed at treatment of large volumes of tissue, as for example in the case of removing significant amounts of adipose tissue from arbitrary body parts. The need also exists for devices and methods for treating the skin and subcutaneous adipose tissue region using ultrasound energy, wherein the ultrasound energy is applied in a more efficient, safe and effective manner.

Recently, new ultrasonic standing waves (USW) methods and devices were proposed [12, 13] as alternative to HIFU for noninvasive or minimally-invasive

lypolitic, therapeutic or cosmetic treatment of large volumes of tissues including subcutaneous adipose or skin tissue on any desired body areas of patient. The method uses an ultrasonic resonator arranged to generate an ultrasound standing wave field at various resonance frequencies in the target tissue temporarily positioned within that resonator. The ultrasonic resonator is designed for vacuum suction of the target tissue to draw it inside the resonator followed by an automatic supply of acoustic coupling fluid into the contact area. The resonator is made in the shape of a suction cup and comprises an ultrasonic transducer generating cylindrical or plane standing waves in the tissue portion retained inside the resonator. A standing wave is formed in the tissue at each resonance frequency defining a particular nodal pattern associated with that particular frequency. Each different resonance frequency defines a different nodal pattern at different location throughout the tissue consisting of a plurality of pressure nodes and antinodes separated by an acoustic half-wavelength distance. Ultrasonic transducers are enhanced by quarter wavelength acoustic matching layers that also protect the skin contacting the transducers from damage. Introduction of a quarter-wavelength sized layer displaces skin from the pressure maximum point located at the boundary of the tissue. The tissue located in the ultrasonic standing wave field is affected by it with either one or both of thermal or non-thermal mechanisms. Both mechanisms are most effective in the region of ultrasound pressure antinodes, which is the region of the pressure amplitude maxima [13].

43.6.2 Feasibility Test of Tissue Thermal Treatment by Ultrasonic Standing Waves

Modeling of ultrasonic standing wave formation in tissue was performed using Wave 3000™ 3D finite-difference simulation package (CyberLogic, Inc.). The model of transducer configuration and resulting ultrasonic standing waves (USW) in porcine fat are shown in Fig. 43.10.

The experimental setup included two flat rectangular piezoceramic plates facing each other and a high-power generator with a control unit. The transducers were dipped into an oil bath providing effective cooling of the PZT composite piezoceramic plates [18–21] (Fig. 43.11). Samples of freshly excised porcine fat and bovine liver tissues were mechanically clamped between the transducers. The resulting formations of thermal lesion in soft tissues in ultrasound standing wave field are shown in Fig. 43.12.

Ultrasonic standing wave technology providing controllable spatial and temporal concentration of acoustic energy has a great potential and may be employed in numerous applications in biotechnology and in tissue treatment.

Recently, new universal combinational treatment platform based on USW technology for noninvasive surgical, therapeutic, lypolitic or cosmetic treatment of tissues including subcutaneous adipose tissue, cellulite or skin on arbitrary body

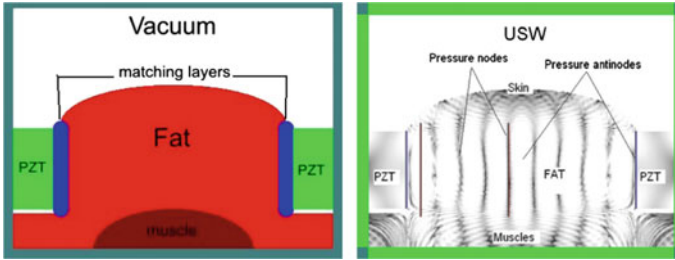


Fig. 43.10 Finite difference model of ultrasonic transducer and resulting standing wave in porcine fat at ultrasound frequency 200 kHz and distance between PZT plates 30 mm

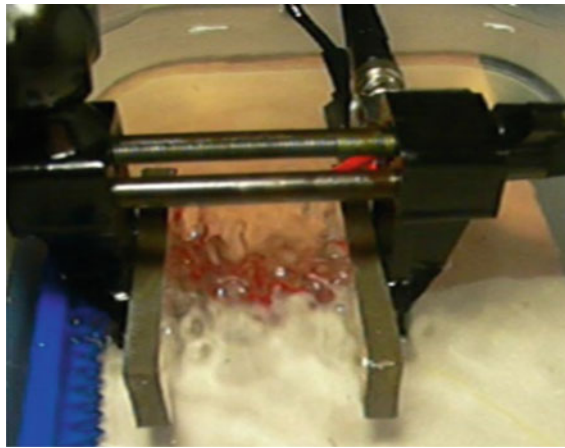


Fig. 43.11 Experimental setup for tissue treatment by USW and corresponding USW formation in mineral oil

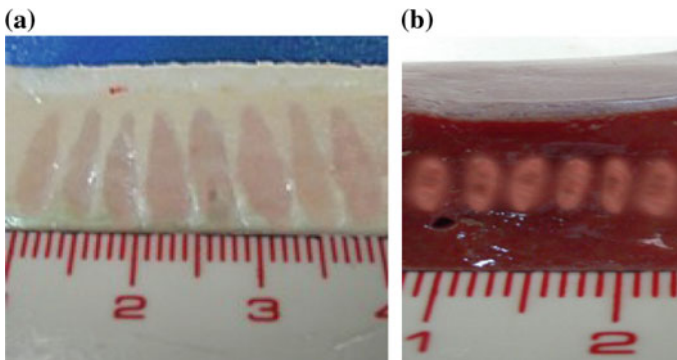


Fig. 43.12 Thermal lesions in porcine fat (a) and bovine liver generated by USW at the excitation protocol: frequency = 350 kHz; burst length = 100–200 periods, driving voltage = 150–250 V, duty cycle 5–10, treatment time 6 s

part of patient were developed [3, 7, 22]. The new method of combinational treatment is based on simultaneous or successive applying of constructively interfering physically and biologically sensed influences: moving ultrasonic standing waves (MUSW), shear waves, radio-frequency (RF) heating, vacuum massage, and ultrasonically assisted drugs delivery.

Unlike all existing HIFU and non-focused systems, ultrasound energy in MUSW directed parallel to the body surface and fully localized in treated body region. Resulting MUSW efficiency is comparable with HIFU at huge increase of treated tissue volume. Continuous cyclic changes of the nodal pattern of MUSW with proper repetition rates corresponding to a specific resonance or relaxation times of living cells or tissue components provide effective dynamical influence of MUSW on tissues. Synergetic combination of MUSW with a vacuum massage that lowers cavitation threshold and intensifies blood flow and clearance of disrupted cell debris, and RF therapeutic heating, along with inherent treatment process control and diagnostic possibilities offers a great future for the technology [23–27].

43.7 Conclusions

New methods for ultrasonic diagnostics, therapy and body aesthetics applications were presented. Technological peculiarities of the ultrasonic transducer design as well as theoretical and numerical models of such transducers and the corresponding HIFU fields were discussed. The results of theoretical modeling and *ex vivo* experiments with different tissues that prove the efficacy, safety and selectivity of new methods and developed ultrasonic transducers for various therapeutic, surgical and cosmetic applications were presented and analyzed.

The main advantages of the developed methods are: bigger treated tissue area, reduced treatment time, arbitrary body part treatment, high selectivity and safety, continuous process and tissue condition control, and variety of applications. The dynamical focusing method based on multi-frequency and natural harmonics techniques brings a new approach to accelerate treatment of big volumes of adipose tissue or tumors ablation with HIFU and also provides a miniaturization of the conventional HIFU transducers. Preliminary feasibility tests showed that intensive shear waves could be generated in wide tissue regions using a new method of resonant amplifications and supersonic generation of remotely induced shear waves at low intensity of pumping HIFU. Combined effect of high intensity HIFU and resonantly amplified shear waves provides new shear waves therapy modality. Synergetic combination of USW with RF therapeutic heating and vacuum massage lowering cavitation threshold and intensifying a blood flow and clearance of disrupted cell debris along with inherent treatment process control and diagnostic possibilities offers a great future for the USW techniques.

Acknowledgments Work supported by the Russian Science Foundation Grant No. 15-12-00023.

References

1. C.R. Hill, J.C. Bamber, G.R. ter Haar (eds.), *Physical Principles of Medical Ultrasonics*, 2nd edn. (Wiley, 2004)
2. G.R. ter Haar, *Prog. Biophys. Mol. Biol.* **93**, 111 (2007)
3. A.N. Rybyanets, in *Piezoelectrics and Related Materials: Investigations and Applications*, Chap. 5, eds. by I.A. Parinov (Nova Science Publishers Inc., New York, 2012), p. 143
4. W. Summer, M.K. Patrick, *Ultrasonic Therapy—A Textbook for Physiotherapists* (Elsevier, London, 1964)
5. A.N. Rybyanets, *AIP Conf. Proc.* **1215**, 287 (2010)
6. A.N. Rybyanets, M.A. Lugovaya, A.A. Rybyanets, *AIP Conf. Proc.* **1215**, 291 (2010)
7. A.N. Rybyanets, US Patents Applications No. 20120123304 (2012)
8. A.N. Rybyanets, US Patents Applications No. 20130051178 (2013)
9. A.N. Rybyanets, US Patent Application No. 20130245444 (2013)
10. A.N. Rybyanets, US Patent No. 8,568,339 (2013)
11. I. Nudelman, A.N. Rybyanets, US Patent No. 7,709,997 (2010)
12. A.P. Sarvazyan, B. Lagutin, US Patent Application No. 20090099485 (2009)
13. A.P. Sarvazyan, L.A. Ostrovsky, A. Rybyanets, *AIP Conf. Proc.* **6**, 020002 (2009)
14. A.P. Sarvazyan, L. Fillingera, L.R. Gavrilov, *Acoust. Phys.* **55**, 630 (2009)
15. M. Fink, G. Montaldo, M. Tanter, *Ann. Rev. Biomed. Eng.* **5**, 465 (2003)
16. A.P. Sarvazyan, *Acoust. Soc. Am.* **123**, 3429 (2008)
17. V.G. Andreev, V.N. Dmitriev, Y.A. Pishchal'nikov, O.V. Rudenko, O.A. Sapozhnikov, A. P. Sarvazyan, *Acoust. Phys.* **43**, 123 (1997)
18. A.N. Rybyanets, *IEEE Trans. UFFC* **58**, 1492 (2011)
19. A.N. Rybyanets, in *Piezoceramic Materials and Devices*, Chap. 3, eds. by I.A. Parinov (Nova Science Publishers Inc., New York, 2010), p. 113
20. A.N. Rybyanets, A.A. Rybyanets, *IEEE Trans. UFFC* **58**, 1757 (2011)
21. A.N. Rybyanets, *Ferroelectrics* **419**, 90 (2011)
22. A.N. Rybyanets, Patent RU No. 2413492 (2011)
23. A. Rybyanets, A.V. Nasedkin, *Ferroelectrics* **360**, 57 (2007)
24. A.N. Rybyanets, A.A. Naumenko, N.A. Shvetsova, in *Nano- and Piezoelectric Technologies, Materials and Devices*, Chap. 1, eds. by I.A. Parinov (Nova Science Publishers Inc., New York, 2013), p. 275
25. A.N. Rybyanets, R. Tasker, *Ferroelectrics* **360**, 90 (2007)
26. A. Nasedkin, A. Rybyanets, L. Kushkuley, Y. Eshel, *IEEE Ultrason. Symp. Proc.* 1648 (2005)
27. A.N. Rybyanets, V.A. Khokhlova, O.A. Sapozhnikov, A.A. Naumenko, M.A. Lugovaya, S.A. Shcherbinin, in *Advanced Nano- and Piezoelectric Materials and Their Applications*, Chap. 23, eds. by I.A. Parinov (New York, Nova Science Publishers Inc., 2014), p. 393

Chapter 44

Theoretical Modeling and Experimental Study of HIFU Transducers and Acoustic Fields

A.N. Rybyanets, A.A. Naumenko, N.A. Shvetsova, V.A. Khokhlova, O.A. Sapozhnikov and A.E. Berkovich

Abstract Recent advances in the fields of physical acoustics, imaging technologies, piezoelectric materials, and ultrasonic transducer design have lead to emerging of novel methods and apparatus for ultrasonic diagnostics, therapy, and anesthetics as well as an expansion of traditional application fields. The chapter presents the results of theoretical modeling and experimental study of different High Intensity Focused Ultrasound (HIFU) transducers. Numerical solutions of parabolic Khokhlov-Zabolotskaya-Kuznetsov (KZK) equation were obtained for nonlinear focused fields. Technological peculiarities of the HIFU transducer design as well as theoretical and numerical models of such transducers and the corresponding HIFU fields are discussed. Several HIFU transducers of different design have been fabricated using different advanced piezoelectric materials. Acoustic field measurements for those transducers have been performed using a calibrated fiber optic hydrophone and an ultrasonic measurement system. The results of theoretical modeling and ex vivo experiments with different tissues (fresh porcine mussels, adipose tissue and bovine liver), as well as in vivo experiments with blood vessels are present that prove the efficacy, safety and selectivity of the developed HIFU transducers and methods.

A.N. Rybyanets (✉) · A.A. Naumenko · N.A. Shvetsova
Institute of Physics, Southern Federal University, 194, Stachki Ave.,
344090 Rostov on Don, Russia
e-mail: arybyanets@gmail.com

V.A. Khokhlova · O.A. Sapozhnikov
Physics Faculty, Moscow State University, Leninskie Gory, 119991 Moscow, Russia

A.E. Berkovich
Sankt-Petersburg Politechnical University, 29, Polytechnicheskaya Str.,
195251 Sankt-Petersburg, Russia

44.1 Introduction

Ultrasound has found usage in all aspects of the medical field, including diagnostic, therapeutic, and surgical applications. The use of ultrasound as a valuable diagnostic and therapeutic tool in several fields of clinical medicine is now so well established that it can be considered essential for good patient care [1]. However, remarkable advances in ultrasound imaging technology over last decade have permitted us now to envision the combined use of ultrasound both for imaging/diagnostics and for therapy. Therapeutic ultrasound has been in use for many years [1–4]. Early applications were those for which tissue heating was the goal, and so it was used to treat soft tissue injuries such as may be incurred during sport activities. More recently, attention has been drawn both to high intensity focused beams that may be used for thermal ablation of selected regions and also to low intensity fields that appear to be able to stimulate physiological processes, such as tissue repair, without biologically significant temperature rises. Ultrasonic tools are used for therapeutic effect in dentistry and are being investigated for use in thrombolysis.

Ultrasound beyond the diagnostic ranges can initiate various kinds of effects when insonated into biological tissue. The ability of ultrasound to interact with tissue to produce biological changes has been known for a long time [3]. Much of the early drive to understand these interactions came from an interest in harnessing ultrasonically induced changes for therapeutic benefit. More recently, the concern has been to understand any possible hazard that may arise from diagnostic ultrasound imaging. It is convenient to divide therapeutic ultrasound into two classes, i.e. applications that utilize ‘low’ ($0.125\text{--}3\text{ W/cm}^2$) and ‘high’ intensities ($\geq 5\text{ W/cm}^2$). The intention of the low intensity treatments is to stimulate normal physiological responses to injury or to accelerate some processes such as the transport of drugs across the skin. The purpose of the high intensity treatments is rather to selectively destroy tissue in a controlled fashion. The resulting effects include thermal, mechanical, chemical, and optical reactions. Mechanical effects, more specifically, may consist of acoustic cavitation, radiation force, shear stress, and acoustic streaming/microstreaming. Among them, the thermal effect and acoustic cavitation are the most significant, and their mechanisms of action have been relatively well-understood [1, 2]. It is however often extremely difficult to identify positively the mechanisms involved in producing biological change, and indeed to isolate non-thermal effects from the thermal ones.

The thermal effect is caused by the absorption of ultrasound in biological tissue. Ultrasonic waves cause vibration or rotation of molecules or part of macromolecules in tissue, and this movement results in frictional heat. Depending on the temperature and the duration of contact, the tissue may become more susceptible to chemotherapy or radiotherapy ($>43\text{ }^\circ\text{C}$, 1 h) or alternatively, protein denaturation may occur (coagulation necrosis) ($56\text{ }^\circ\text{C}$, 1 s) [1, 2, 5]. Beneficial effects that arise from ultrasonically induced heating include an increase in extensibility of collagenous structures such as tendons and scar tissue, a decrease in joint stiffness,

pain relief, changes in blood flow, decrease in muscle spasm, and, at high intensities, selective tissue ablation as achieved in focused ultrasound surgery [4].

Excluding the effects of thermal transfer, the temperature elevation in biological tissue induced by ultrasound (plane wave) absorption is theoretically linearly proportional to acoustic intensity in the following manner ($\partial T/\partial t = 2\alpha I/\rho C_p = 0.014I$, where T is the temperature ($^{\circ}\text{C}$), t is the time (s), α is a absorption coefficient $\approx 0.03 \text{ Np/cm}$ in tissue-like medium at 1 MHz, I = acoustic intensity, ρ is the density $\approx 1 \text{ g/cm}^3$ in tissue-like medium, C_p is the specific heat $\approx 4.2 \text{ J/(g }^{\circ}\text{C)}$ in tissue-like medium) [6, 7]. Because of this linearity and predictability, a thermal effect was traditionally preferred to a mechanical effect in the medical applications of unfocused and focused ultrasound.

Non-thermal mechanisms that can produce beneficial (therapeutic) changes in tissue may be cyclic or non-cyclic in nature. The early literature refers to “micro-massage” [8]. This is presumably thought to be an effect due to the periodic nature of the sound pressure field. The one of non-cyclic effect thought to be involved in ultrasound therapy is acoustic streaming. This may be due to stable, oscillating cavities, or to radiation forces in intra- or extracellular fluids. Streaming may act to modify the local environment of a cell leading, for example, to alter concentration gradients near of an extracellular membrane. The concentration gradient affects the diffusion of ions and molecules across a membrane, and thus streaming may account for the reported changes in the potassium and calcium content of cells following ultrasonic exposure [1].

Acoustic cavitation, defined as the formation and activity of a gas- or vapor-filled cavity (bubble) in a medium exposed to ultrasound, plays a major role in the mechanical effects and minor roles in the chemical and the optical effects of ultrasound medical technology. If biological tissue is insonated by an ultrasound wave, more intense than a specific threshold, negative pressure representing the rarefaction of the wave, may be large enough to draw gas out of the tissue solution to form a bubble. It is easy to understand the underlying mechanism if it is compared to the numerous bubbles formed by vigorous rotation of a motorboat screw. This bubble either repeats radial oscillations being in a resonant size with the ultrasound frequency (stable cavitation; non-inertial cavitation) or oscillates in a similar manner expanding gradually above its resonant size due to net influxes of gas and vapor into the bubble (rectified diffusion), and finally disintegrates by a violent and asymmetrical collapse (unstable cavitation; inertial cavitation) [1, 9]. Acoustic cavitation, particularly inertial cavitation, can cause a significant degree of mechanical and thermal effects as well as chemical and optical effects. The thermal effect caused by acoustic cavitation is larger than that caused by ultrasound absorption alone. Mechanical and thermal effects by acoustic cavitation are generally known to be complex, unpredictable, and, sometimes, detrimental. The threshold of acoustic cavitation depends on the (negative) pressure amplitude, ultrasound frequency, and the tissue where cavitation occurs [1, 8, 10].

Radiation force is a force exerted at an interface between two media or inhomogeneity in a medium due to the passage of ultrasound waves. An acoustic field in fluid may set up acoustic streaming; the transfer of momentum to liquid, by the absorption of energy from an acoustic field, causes acoustic streaming. The fluid velocity caused by acoustic streaming is spatially non-uniform thereby generating a velocity gradient in the field. This gradient causes shear stress. Acoustic streaming caused by an oscillating bubble in a sound field immediately surrounding the bubbles is specifically referred to as acoustic microstreaming. Shear stress formed by microstreaming is an important mechanism underlying many biological reactions [1, 10].

Traditional therapeutic applications of ultrasound include the treatment of soft tissue and bone injuries, wound healing, hyperthermic cancer treatment, focused ultrasound surgery of Parkinson's disease, glaucoma and retinal detachment and for sealing traumatic capsular tears, benign prostatic hyperplasia, the liver, the kidney, prostate and bladder tumours, vascular occlusion therapy, and tool surgery [1–5]. Most physiotherapy units offer spatial average intensities up to 3 W/cm^2 and offer one or more transducers operating at discrete frequencies in the range of 0.75–5 MHz. The choice of transducer depends on the depth of the target to be treated, deeper targets require lower frequencies because of the frequency dependence of ultrasonic attenuation. Devices offer either discrete intensity settings or continuously variable controls. The output may be continuous or pulsed. Pulsed exposures are often chosen when thermal effects are to be kept to a minimum. Commonly available pulsing regimes are 2:2 and 2:8 ms [1].

Therapeutic transducers are usually made of low loss lead zirconate-titanate (PZT) or recently from porous ceramics and piezocomposites [11–13]. In the past decade, with the advent of faster processing, specialized contrast agents, understanding of nonlinear wave propagation, novel real-time signal and image processing as well as new piezoelectric materials, processing technologies and ultrasound transducer designs and manufacturing, ultrasound imaging and therapy have enjoyed a multitude of new features and clinical applications [14, 15].

The chapter presents the results on development and experimental study of different high intensity focused ultrasound (HIFU) transducers. Technological peculiarities of the HIFU transducer design as well as theoretical and numerical models of such transducers and the corresponding HIFU fields are discussed. Several HIFU transducers of different design have been fabricated using different advanced piezoelectric materials. Acoustic field measurements for those transducers have been performed using a calibrated fiber optic hydrophone and an ultrasonic measurement system (UMS). The results of *ex vivo* experiments with different tissues as well as *in vivo* experiments with blood vessels are present that prove the efficacy, safety and selectivity of the developed HIFU transducers and methods.

44.2 Theoretical Calculations and Numerical Modeling of HIFU

The characterization of medical acoustic devices that operate at high output levels has been a research topic and an issue of practical concern for several decades [1, 2]. The importance of nonlinear effects has been considered and addressed even at diagnostic levels of ultrasound [16]. In lithotripsy and HIFU, these effects are critical as acoustic pressures of up to 100 MPa or higher can be reached; such pressures are two or even three orders higher in magnitude than diagnostic ultrasound.

Numerical modeling has been used to predict high amplitude acoustic fields from medical devices. One advantage of modeling is that it can be used to determine the acoustic field in both water and tissue. Numerical algorithms, most commonly based on the nonlinear parabolic Khokhlov-Zabolotskaya-Kuznetsov (KZK) equation, have been developed and applied to the nonlinear fields of lithotripters, unfocused ultrasonic piston sources, diagnostic ultrasonic transducers operating in tissue harmonic imaging mode [17], focused ultrasound sources [18], and HIFU sources [16, 19].

For strongly focused fields non-linear models such as Westervelt equation can be used, which is a generalization of the classical wave equation to the nonlinear case in the approximation of the absence of back propagating waves. Even more complex models based on the solution of the full nonlinear wave equation have been developed [7]. However, these approaches require large computing power and time-consuming calculations (up to several days) on supercomputers, i.e. practically inapplicable to practical problems. This difficulty can be significantly reduced by using the evolution equation for the quasi-plane wave. The corresponding equation in nonlinear acoustics equation is known as the KZK equation [6, 7].

44.2.1 Theoretical Calculation of HIFU Fields

As is known, the system of hydrodynamic equations in the general case cannot be solved analytically, and the basic approach is to use numerical simulation. It is possible to solve numerically the complete system of hydrodynamic equations, but in practice, it is usually unrealizable because of limitations on available computer memory and its computational speed even using the modern computing clusters. However, one can find reasonably accurate solution to the practical problem of interest with some simplifying assumptions.

It is often assumed that the amplitude of acoustic waves is sufficiently low so that the ultrasound field can be described in approximation of linear acoustic. In the linear case we can reduce the problem to considering harmonic (sinusoidal) waves: $p(\mathbf{r}, t) = P(\mathbf{r}) \exp(-i\omega t)/2 + P^*(\mathbf{r}) \exp(i\omega t)/2$, where p is the acoustic pressure, P is its complex amplitude, ω is the angular frequency. The corresponding equation

for harmonic waves in homogeneous medium is the Helmholtz equation: $\Delta P + (\omega^2/c_0^2)P = 0$, where c_0 is the sound speed in the medium. The solution of this equation for one-way propagation from ultrasound transducer can be written as [17]:

$$P(\mathbf{r}) = -i\rho_0 c_0 \frac{k}{2\pi} \int_S \frac{V(\mathbf{r}') e^{ik|\mathbf{r}-\mathbf{r}'|}}{|\mathbf{r}-\mathbf{r}'|} dS' \quad (44.1)$$

This expression is called the Rayleigh integral.

Rayleigh integral can be used for the calculation of acoustic field generated by the source in the shape of a spherical cap under the assumption that the focusing angle is small and the radius of curvature of the radiating surface is much larger than the wavelength [17]. Then locally the surface elements radiate as a flat source, and it can be assumed that the resulting field given by the (44.1) is sufficiently accurate. With a uniform velocity distribution on the cap one can obtain a simple analytical expression for the amplitude of the pressure on the axis of the transducer:

$$P = P_0 \frac{e^{ikz} - e^{ikR_{\max}}}{1 - z/F}, \quad (44.2)$$

where z is the axial coordinate, R_{\max} is the distance from the observation point to the edge of the transducer, P is the complex amplitude of the acoustic pressure on the axis of the transducer (at the point with coordinate z , measured from the center of the bowl), F is the radius of curvature of the bowl, $P_0 = \rho_0 c_0 V$ is the characteristic acoustic pressure on the surface of the transducer, V is the amplitude of the normal velocity component of the radiating surface. The distance $R_{\max} = R_{\max}(z)$ can be written as follows:

$$R_{\max} = F \sqrt{1 + \left(1 - \frac{z}{F}\right)^2 - 2\left(1 - \frac{z}{F}\right) \cos \alpha}, \quad (44.3)$$

where α is the half-opening angle of the cap, i.e. the angle between the rays directed from the geometrical focus ($z = F$) to the center of the bowl and to its edge.

The above result for the sources in the form of a spherical cap can be simply extended to the case of a source in the form of an annular spherical segment. Indeed, since the problem is linear, we can embed in a spherical cap another coaxial one (with the same curvature, but different diameter). Then it is possible to obtain oscillation only of an annular spherical segment if excite the surface of the above mentioned cap in antiphase. Consequently, due to the principle of superposition, the field of the ring can be obtained by subtracting fields of two caps of different diameters.

Therefore, if the center of the transducer has a hole, then the solution will be:

$$p(z, t) = \frac{p_0 e^{-i\omega t}}{1 - z/F} (e^{ikR_{\min}} - e^{ikR_{\max}}), \quad A(z) = \frac{2p_0}{1 - z/F} \left| \sin \left(k \frac{R_{\min} - R_{\max}}{2} \right) \right|, \quad (44.4)$$

where $R_{\min} = F \sqrt{1 + (1 - z/F)^2 - 2(1 - z/F) \cos \beta_1}$, $\sin \beta_1 = a_1/F$.

If the beam propagates in absorbing medium, then attenuation for the pressure amplitude $A(z)$ of the source with a hole can be taken into account as follows:

$$A(z) = \left| \frac{2p_0}{1 - z/F} \sin \left(k \frac{R_{\min} - R_{\max}}{2} \right) \right| \exp(-\alpha z), \quad (44.5)$$

where α is the attenuation at the frequency of the radiation.

For the calculation of the medium heating one can use a standard formula: $Q = 2\alpha I$.

The frequency dependence of the attenuation α , obtained experimentally for a number of liquids and tissues, can be found in [1].

Since the regime of high intensities is required for stopping the bleeding, non-linear propagation of acoustic waves occurs, and theoretical description requires more complex models than for the case of low intensity.

For strongly focused fields, non-linear models such as Westervelt equation can be used, which is a generalization of the classical wave equation to the nonlinear case in the approximation of the absence of back propagating waves [16]. Even more complex models based on the solution of the full nonlinear wave equation have been developed [5, 6]. However, these approaches require large computing power and time-consuming calculations (up to several days) on supercomputers, i.e. practically inapplicable to practical problems. This difficulty can be significantly reduced by using the evolution equation for the quasi-plane wave. The corresponding equation in nonlinear acoustics equation is known as the KZK equation [16].

44.2.2 Numerical Modeling

Numerical modeling of experimental conditions was performed using a KZK-type nonlinear parabolic equation generalized for the frequency-dependent absorption properties of the propagation medium:

$$\frac{\partial}{\partial \tau} \left[\frac{\partial p}{\partial z} - \frac{\beta}{\rho_0 c_0^3} p \frac{\partial p}{\partial \tau} - L_{abs}(p) \right] = \frac{c_0}{2} \Delta_{\perp} p, \quad (44.6)$$

where p is the acoustic pressure, z is the propagation coordinate along the axis of the beam, $\tau = t - z/c_0$ is the retarded time, c_0 is the ambient sound speed, p_0 is the ambient density of the medium, β is a coefficient of nonlinearity, Δ_{\perp} is the Laplacian with respect to the transverse coordinate r , and L_{abs} is the linear operator that accounts for the absorption and dispersion of the medium.

For simulations in water, thermoviscous absorption was included as

$$L_{abs} = \frac{b}{2\rho_0 c_0^3} \frac{\partial^2 p}{\partial \tau^2} \quad (44.7)$$

where b is the dissipative parameter of water. For simulations in gel, the propagation path for ultrasound comprised a two-layer medium consisting of water followed by tissue-mimicking gel phantom. The frequency-dependent absorption of ultrasound in the gel was included in the model according to a nearly linear power law combined with weak thermoviscous absorption, as in the water:

$$\alpha(f) = \frac{2\pi^2 f^2 b}{\rho_0 c_0^3} + \alpha_0 \left(\frac{f}{f_0} \right)^{\eta} \quad (44.8)$$

Here α_0 is the absorption parameter of the gel at the fundamental frequency f_0 , and variation of the sound speed with frequency was calculated for the power law term (η) in (44.8) using the local dispersion relations.

The boundary condition for (44.6) was set by translating the pressure amplitude, p_0 , uniformly distributed over the curved surface of the source to the plane $z = 0$. The translation of the amplitude was performed using a geometrical acoustics approximation following the spherical convergence of the field. The focusing phase shift along the radial coordinate was introduced in the parabolic approximation as

$$p(z = 0, r, \tau) = \frac{p_0}{\sqrt{1 + r_0^2/F^2}} \sin\left(2\pi f_0 \left(\tau + \frac{r^2}{2c_0 F}\right)\right), \quad (44.9)$$

if $r < r_0/\sqrt{(1 + r_0^2/F^2)}$ and $p(z = 0, r, \tau) = 0$, elsewhere. Here, $2r_0$ is the aperture of the source and F is its radius of curvature.

Equation (44.6) was solved numerically in the frequency domain using a previously developed finite difference algorithm. The acoustic pressure waveform was represent as a Fourier series expansion as

$$p(z, r, \tau) = \sum_{n=1}^{\infty} c_n(z, r) e^{in2\pi f_0 \tau}, \quad (44.10)$$

where c_n is the complex amplitude of the n th harmonic. A set of nonlinear-coupled differential equations for the amplitudes of the harmonics was derived and integrated numerically using the method of fractional steps and an operator-splitting

procedure. The simulations were performed assuming radial symmetry of the HIFU source.

To characterize the HIFU output level in the focal zone in water or in gel, two values of the spatial peak intensity were introduced. These values will be referred to in the chapter as focal intensities. The first value, I_N , was calculated from the numerically modeled nonlinear waveform as a combination of the focal intensities of all harmonic components:

$$I_N = f_0 \int_0^{1/f_0} \frac{p^2}{\rho_0 c_0} d\tau = \frac{2}{\rho_0 c_0} \sum_{n=1}^{\infty} |c_n|^2. \quad (44.11)$$

The second value, I_L , was calculated based on the results of the linear acoustic propagation modeling as

$$I_L = \frac{P_F^2}{2\rho_0 c_0}, \quad (44.12)$$

where p_F is the focal (i.e., spatial peak) pressure amplitude in situ. The linear focusing gain of the source was defined as a ratio of the focal and source pressure amplitude obtained from linear modeling in water:

$$G = p_F/p_0. \quad (44.13)$$

The medium heating was calculated as follows:

$$Q = \sum_{n=1}^{\infty} 2\alpha_n I_n, \quad (44.14)$$

where $\alpha_n = \alpha(n\omega_0)$ is the attenuation of n th harmonic and $I_n = |C_n|^2 / (2\rho_0 c_0)$ is the intensity of this harmonic. Thus, total heat source in the non-harmonic (in particular, in non-linear) wave is the sum of the heat sources of the individual harmonics, and each harmonic absorption may be considered in the plane wave approximation.

44.3 Applications of HIFU for Hemostasis, Thrombolysis and Ablation

Acoustic hemostasis may provide an effective method in surgery and prehospital settings for treating trauma and elective surgery patients. Application of HIFU therapy to hemostasis was primarily initiated in an attempt to control battlefield injuries on the spot. High-intensity ultrasound ($ISA = 500\text{--}3000 \text{ W/cm}^2$) is usually

adopted for hemostasis. Many studies on animal models have been successful for both solid organ and vascular injuries [1]. The thermal effect has a major role in hemostasis. The proposed mechanisms of its action are as follows. Structural deformation of the parenchyma of a solid organ due to high temperature induces a collapse of small vessels and sinusoids or sinusoid-like structures. Heat also causes coagulation of the adventitia of vessels, and subsequently, fibrin-plug formation. The mechanical effect of acoustic cavitation also appears to play a minor role in hemostasis. Microstreaming induces very fine structural disruption of the parenchyma to form a tissue homogenate that acts as a seal and induces the release of coagulation factors. No statistically significant hemolysis or changes in the number of white blood cells and platelets have been observed when blood is exposed to HIFU with intensities up to 2000 W/cm^2 . The main drawback of the hemostasis applications is low ultrasound absorption ability of blood and, as a result, low heating and coagulation rate at real blood flow. In this section, HIFU transducer design, nonlinear acoustic field calculations and *in vivo* experiments on blood vessels confirming enhanced hemostasis are described.

Ultrasound can play a significant role in thrombolysis. Ultrasound with/without a thrombolytic agent has been shown to be effective in enhancing thrombolysis. Thrombolysis is achieved with low intensity US ($\text{ISA} = 0.5\text{--}1 \text{ W/cm}^2$) and is known to be associated with non-thermal mechanisms [1–3]. Microstreaming by acoustic cavitation produces a strong mechanical force around the cell membranes that causes the pores or channels to open. This increases the bioavailability of thrombolytic agents on the surface of a thrombus. The radiation force of the ultrasound itself could push the drug to the lesion (“push effect”). The direct mechanical effect with/without microstreaming could cause alterations to the fibrin mesh. These effects, described above, are believed to work synergistically to cause thrombolysis [2]. There are two methods of delivering ultrasound to thrombosed vessels. One is an extracorporeal approach. This is noninvasive, but requires higher ultrasound energy for compensating attenuation through an intervening tissue; in addition, it may have the potential risks of complications and treatment-failure due to the intervening tissues. Clinical trials using the extracorporeal low frequency ultrasound (as in transcranial Doppler ultrasound) for brain ischemia with the assistance of a tissue plasminogen activator have turned out to be successful [3]. The other method is via a miniaturized transducer, at the tip of an arterial catheter, from which a thrombolytic drug releases. This system is minimally invasive and commercially available [3].

Focused ultrasound surgery (FUS) is used for local ablation therapy of various types of tumors using HIFU ($\text{ISA} = 100\text{--}10,000 \text{ W/cm}^2$). The two main mechanisms involved in FUS are thermal effects by ultrasound absorption and mechanical effects involving thermal effects in part, induced by acoustic cavitation. The thermal effect by absorption has been traditionally employed because it is relatively accurately predictable and thus easy to control. This enables the therapy to be safe even though thermal ablation by the conventional method of FUS generally requires a long surgical time for clinical practice. The effects of cavitation have proven to have potential in improving the efficiency of the therapy by enlarging the ablation size

and subsequently reducing the procedure-time for ablation [3]. However, these advantages could be accompanied by a longer cooling time and a relatively high risk of complication.

The shape of a classical thermal lesion resembles a cigar, paralleling the direction of the ultrasound propagation, measuring about 1.5–2 mm in width and about 1.5–2 cm in length when produced by a typical clinical 1.5 MHz HIFU field [3, 8, 9]. This single thermal lesion is extremely small in comparison to the sizes of common clinical tumors. The individual thermal lesions are stacked up closely without leaving intervening viable tissue to form a sufficient ablation zone to cover the tumor itself as well as the safety margin. The tissue-homogeneity influences the shapes of the thermal lesion while the tissue-perfusion may affect its size. The frequency of ultrasound is adjusted to optimize surgical conditions, keeping sonic attenuation low (advantage of low frequency) as well as making energy focused sharply enough (advantage of high frequency) [3].

The histological changes made by FUS have been investigated. Thermal damage after ultrasound absorption has been described as an “island and moat” in which the “island” represents an area of complete coagulation necrosis and complete destruction of the tumor-supplying vessels whereas the “moat” refers to the surrounding rim-like area that is 6–10 cells-thick and composed of glycogen-poor cells (2 h) that usually die within 48 h. Later, granulation tissue, fibroblast infiltrates and finally retraction/scar formation occurs [1, 2]. The changes that occur because of acoustic cavitation are both coagulation necrosis and mechanical tearing. Mechanical tearing, which is attributed to tissue boiling as well as the mechanical effects of acoustic cavitation, manifests as holes or implosion cysts upon microscopic examination [3].

44.4 Limitations and Future Works

Major differences of HIFU therapy from other interventional therapeutic modalities are its complete non-invasiveness and sharp, tailorable treatment margins, which may lead to treatments with very low complication rates. However, several complications have been known to occur after HIFU therapy. These are mostly due to high-energy ultrasonic waves reflected on gas or bony structures [1, 2]. Skin-burn can be caused by poor acoustic coupling between the skin and the therapeutic window (e.g. poor shaving) or a previous operation scar. In cases of liver treatment, reflected ultrasonic waves on ribs can induce overlying soft tissue damage including the skin. Gas-containing bowel loops act in the same manner and can cause thermal injury of the bowel wall. Sciatic nerve injury was also reported after HIFU therapy for uterine leiomyoma. This complication is deemed to be caused either directly by high-energy ultrasonic waves that pass the focal therapeutic zone or indirectly by elevated temperatures of the pelvic bone. If the focal zone locates superficially as in case of breast cancer, direct thermal injury of overlying skin can occur [2]. Likewise, internal organs just anterior or posterior to the focal zone could be

injured. In addition to these complications, HIFU therapy at the time of writing this manuscript, has displayed several other limitations, which are hampering the effective use of this modality in clinical practice. These include a long procedure time, difficulty in targeting and monitoring moving organs, sonic shadowing by bones or gas in bowels, and the relatively high cost of this technique in relation to its effectiveness and limitations.

Main limitation of HIFU for body shaping application (fat reduction, cellulite therapy) is a small size of focal zones and a small thickness of target tissues along with its spatial extension, leading to long procedure time, pain and injury of bones and vital organs.

However, recent technological advances are expected to resolve these problems. One example is the new MR-assisted HIFU device under development, which adopts the technique of an automatic on-line, spatiotemporal temperature control using a multispiral trajectory of the focal point and proportional, integral and derivative principles [2]. This system claims to be able to make a thermal lesion faster and more stably under real-time thermal monitoring even in moving organs than the existing devices [1].

In the field of body aesthetic applications, uses of new HIFU technologies (dynamical focusing and natural harmonics methods) in combination with other therapeutic and diagnostic modalities such as ultrasonic standing waves therapy, shear waves elasticity imaging and therapy, targeted drug/gene-delivery and combinational treatments (ultrasound—RF—vacuum massage), can be anticipated and has a more revolutionary clinical impact [3, 17, 18].

44.5 HIFU Transducers Design

HIFU transducer comprised 1.6 MHz spherical element made from porous piezoceramics [11, 12, 18] with 80 mm aperture and 40 mm centre hole having radius of curvature 54 mm. The piezoelement was sealed in custom-designed cylindrical housing filled with the mineral oil providing acoustic contact and cooling of the element. The housing had an acoustic window made of very thin (0.15 mm) PVC membrane. Centre opening was reserved for ultrasonic imaging transducer (Fig. 44.1).

44.6 Acoustic Field Calculations

Calculations of acoustic fields of HIFU transducers were made using the models and algorithms described above.

Figure 44.2 shows two-dimensional distributions of acoustic intensity in HIFU transducer's acoustic axis plane. Intensity levels are represent in absolute values (kW/cm^2). Calculations were made for two frequencies 1.6 MHz (a) and 2 MHz (b), respectively.

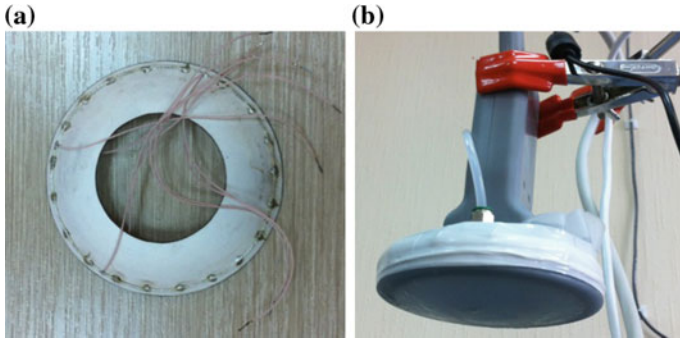


Fig. 44.1 Focusing piezoelement (a) and assembled HIFU ultrasonic transducer (b)

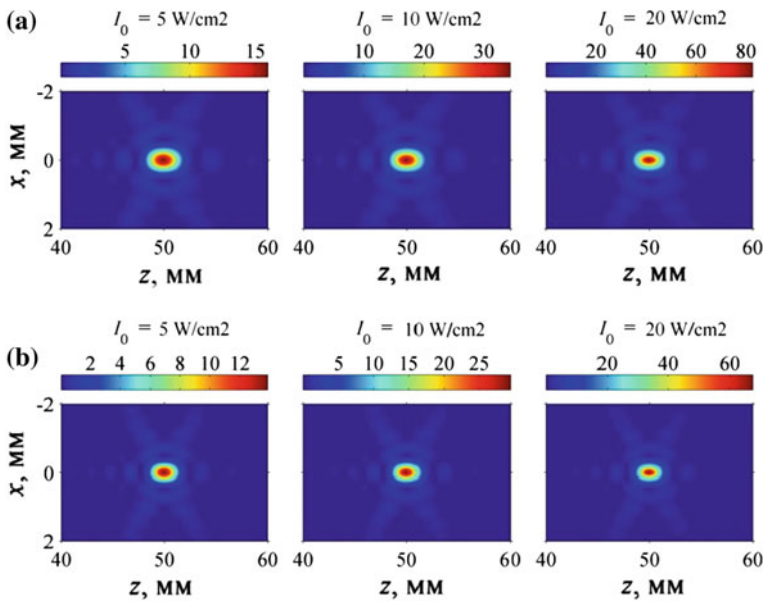


Fig. 44.2 Two-dimensional distributions of acoustic intensity in acoustic axis plane of HIFU transducer for 1.6 MHz (a) and 2 MHz (b) frequencies

Figure 44.3 shows two-dimensional distributions of heat sources power in HIFU transducer’s acoustic axis plane. Power density levels are represent in absolute values (kW/cm^3).

In Fig. 44.4, acoustic pressure signals in the focus, calculated at different initial intensities for 1.6 and 2 MHz, are shown. It is obvious that even at initial intensity level of $5 \text{ W}/\text{cm}^2$, nonlinear effects lead to pressure profile asymmetry that transforms to a shock front in focus at initial intensity $20 \text{ W}/\text{cm}^2$ that give rise to extreme heating.

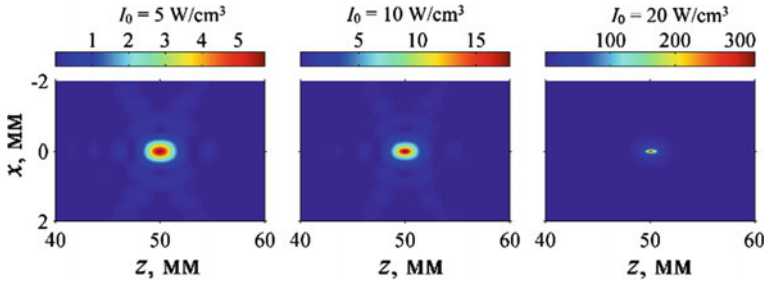


Fig. 44.3 Two-dimensional distributions of heat sources power in acoustic axis plane of HIFU transducer for 1.6 MHz frequency

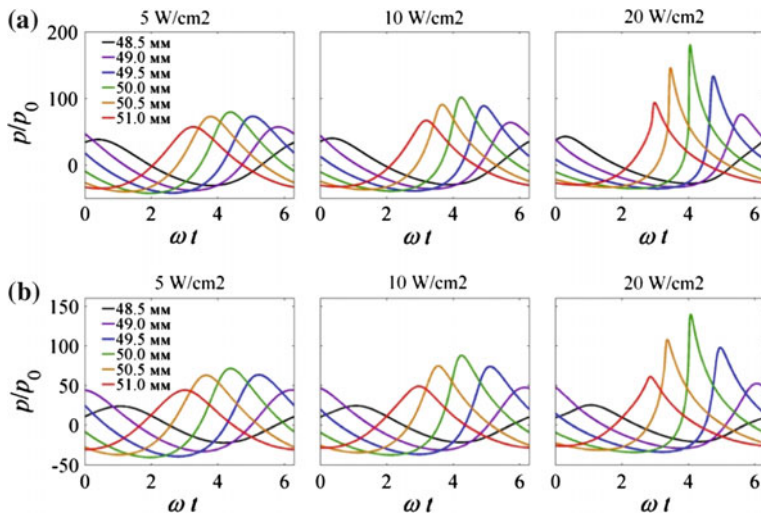


Fig. 44.4 Acoustic pressure signals in the focus calculated at different initial intensities for 1.6 MHz (a) and 2 MHz (b) frequencies

44.7 Ex Vivo Experiments on Tissues

Fresh porcine liver, muscle and adipose tissues were obtained from a butcher within 24 h of slaughter. A single element spherical PZT transducer (1.6 MHz, 80 mm aperture and 40 mm centre hole) has been used for experiments. The acoustic intensity for porous PZT transducer was 750 W/cm^2 (ISAL). The samples were placed in an oil bath and positioned right under the transducer such that focal point was placed inside the sample. The samples were irradiated by the harmonics frequency HIFU for 3–20 s at different duty cycles (from 1/2 to 1/100) and burst lengths (from 10 to 200 cycles) of the signals. After exposure the samples were sectioned along the beam axis respectively to compare the dimensions of the lesions [8, 9].

The photographs of thermal and cavitation lesions in the muscle, liver and porcine samples induced by HIFU are shown in Fig. 44.5.

44.8 In Vivo Experiments on Blood Vessels

The experiments were made on lamb's femoral artery at a standard protocol. During ultrasound exposure, arterial blood flow was temporarily stopped using intravascular balloon. Ultrasonic transducer with 1.6 MHz frequency described in previous sections was used for experiments. All acoustic measurements were performed in 3D Scanning System (UMS3) using a fiber-optic hydrophone (FOPH 2000) from Precision Acoustics Ltd. Waveforms from the hydrophones and the driving voltage were recorded using a digital oscilloscope LeCroy. The transducer was driven by a function generator Agilent 33521B and a linear rf-amplifier E&I model 2400L RF and operates in a CW mode. The acoustic intensity in the focal plane measured in water tank at 5000 W/cm^2 (I_{SAL}) was kept for the object treatment [18–21]. After sonication procedure and angiography study, the samples of femoral artery were extracted to confirm hemostasis and disclose vessel thrombus. The X-ray image of blood vessels obtained using contrast agents and photograph of dissected femoral artery are shown In Fig. 44.6.

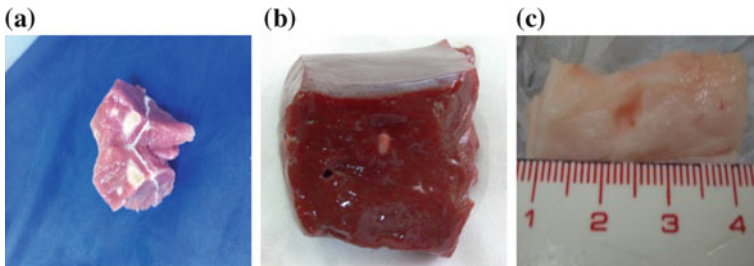


Fig. 44.5 Thermal (a, b) and cavitation (c) lesions in the muscle, liver and porcine samples induced by HIFU transducers. Treatment parameters: **a** CW—exposure time = 3 and 9 s, **b** CW—exposure time = 3 s, **c** burst mode—duty cycle = 1/20, burst length = 10 cycles, exposure time = 9 s

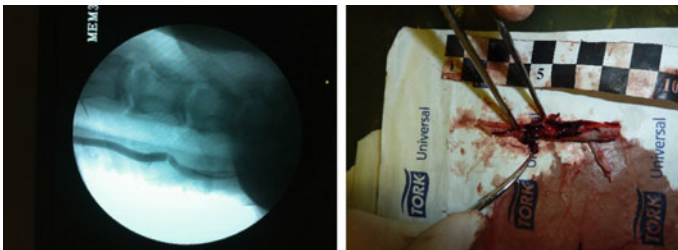


Fig. 44.6 Angiography image of blood vessels showing ultrasound hemostasis and photograph of vessel thrombus in dissected femoral artery

44.9 Conclusions

The results of theoretical modeling and experimental study of different HIFU transducers were presented. Ex vivo experiments in tissues (fresh porcine adipose tissue, bovine liver) and in vivo experiments in lamb's femoral artery were carried out using different protocols. The results of theoretical modeling and tissue experiments prove the efficacy, safety, and selectivity of the developed HIFU transducers and methods enhancing the tissue lysis and hemostasis and can be used for various therapeutic, surgical and cosmetic applications.

We have demonstrated that HIFU can be used to stop active bleeding from vascular injuries including punctures and lacerations. Using HIFU transducers, operated at a frequency of 1 or 2 MHz in continuous mode with intensities of 2000–5000 W/cm², we were able to stop bleeding from major blood vessels that were punctured with an 18- or a 14-gauge needle. Postponed hemostasis was observed at lamb's femoral artery experiments for all HIFU treatments. We have demonstrated that HIFU can be used to stop active bleeding from vascular injuries including punctures and lacerations. Those methods and transducers can be used also for various therapeutic, surgical and cosmetic applications.

Acknowledgments Work supported by the Russian Science Foundation (Grant No. 15-12-00023).

References

1. C.R. Hill, J.C. Bamber G.R. ter Haar (eds.), *Physical Principles of Medical Ultrasonics*, 2nd edn. (Wiley, 2004)
2. G.R. ter Haar, *Prog. Biophys. Mol. Biol.* **93**, 111 (2007)
3. A.N. Rybyanets, in *Piezoelectrics and Related Materials: Investigations and Applications*, Chap. 5, eds. by I.A. Parinov (Nova Science Publishers Inc., New York, 2012), p. 143
4. W. Summer, M.K. Patrick, *Ultrasonic Therapy—a textbook for physiotherapists* (Elsevier, London, 1964)
5. M. Dyson, M. Brookes, in *Ultrasound*, eds. by R.A. Lerski, P. Morley (Pergamon, Oxford, 1983), p. 61
6. V. Khokhlova, A. Ponomarev, M. Averkiou, L. Crum, *Acoust. Phys.* **52**, 481 (2006)
7. V.A. Khokhlova, R. Souchon, J. Tavakkoli, O.A. Sapozhnikov, D. Cathignol, *J. Acoust. Soc. Am.* **110**, 95 (2001)
8. A.N. Rybyanets, *AIP Conf. Proc.* **1215**, 287 (2010)
9. A.N. Rybyanets, M.A. Lugovaya, A.A. Rybyanets, *AIP Conf. Proc.* **1215**, 291 (2010)
10. A.P. Sarvazyan, L. Fillinger, L.R. Gavrilov, *Acoust. Phys.* **55**, 630 (2009)
11. A.N. Rybyanets, *IEEE Trans. UFFC* **58**, 1492 (2011)
12. A.N. Rybyanets, in *Piezoceramic Materials and Devices*, Chap. 3, eds. by I.A. Parinov (Nova Science Publishers Inc, New York, 2010), p. 113
13. A.N. Rybyanets, A.A. Rybyanets, *IEEE Trans. UFFC* **58**, 1757 (2011)
14. M. Fink, G. Montaldo, M. Tanter, *Ann. Rev. Biomed. Eng.* **5**, 465 (2003)
15. A.P. Sarvazyan, *Acoust. Soc. Am.* **123**, 3429 (2008)
16. V.G. Andreev, V.N. Dmitriev, Y.A. Pishchal'nikov, O.V. Rudenko, O.A. Sapozhnikov, A. P. Sarvazyan, *Acoust. Phys.* **43**, 123 (1997)

17. A.N. Rybyanets, V.A. Khokhlova, O.A. Sapozhnikov, A.A. Naumenko, M.A. Lugovaya, S.A. Shcherbinin, in *Advanced Nano- and Piezoelectric Materials and Their Applications*, Chap. 23, eds. by I.A. Parinov (Nova Science Publishers Inc., New York, 393 (2014)
18. A. Sarvazyan, L.A. Ostrovsky, A. Rybyanets, AIP Conf. Proc. **6**, 020002 (2009)
19. A.N. Rybyanets, *Ferroelectrics* **419**, 90 (2011)
20. A. Rybianets, A.V. Nasedkin, *Ferroelectrics* **360**, 57 (2007)
21. A.N. Rybyanets, A.A. Naumenko, N.A. Shvetsova, in *Nano- and Piezoelectric Technologies, Materials and Devices*, Chap. 1, eds. by I.A. Parinov (Nova Science Publishers Inc., New York, 2013), p. 275

Chapter 45

Optimization of the Electric Power Harvesting System Based on the Piezoelectric Stack Transducer

S. Shevtsov, V. Akopyan, E. Rozhkov, V. Chebanenko, C.-C. Yang, C.-Y. Jenny Lee and C.-X. Kuo

Abstract The generation of electrical power from mechanical motion and structural vibrations is an active area of interest both for scientists and for engineers due to its abilities to serve as the power sources for electric and electronic systems with the reduced power consumption. A key aspect of an system is the power electronic circuitry, which interfaces the piezoelectric (PZT) device with the electric load, as a well-designed circuit can increase the amount of energy harvested. Many different circuit topologies have been proposed and studied to achieve this function. Among these types of circuits are passive, which can include combined resistive/capacitive/inductive load with rectifier, semi-active circuits that open or close a switch, when the peak force is achieved across the device, and also an active energy harvesting, that utilizes a bidirectional switch-mode converter to control the voltage on the electrodes of a PZT device. Most investigations of these systems were performed under low power unimorph or bimorph cantilever PZT energy harvesters. However, multilayered piezoelectric stack, whose layers (thin plates with electrically coating surfaces) are parallel connected, may take very high mechanical excitation and can obtain consequently more electric energy. An important feature of the multilayered PZT stack, which differs from the unimorph/bimorph PZT energy harvester, is the very big electric capacitance that affects on the electric energy flow from the PZT energy source to the electric storage device. At the multiplying these layers the electric capacitance of the device multiplies according to the number of layers, but mechanical and electric losses also increase due to mechanical damping in the bonding interlayers and due to leakage in PZT plates. On the base of the finite element (FE) investigation, we formulate the simplified

S. Shevtsov (✉)
South Center of Russian Academy, Rostov on Don, Russia
e-mail: aeroengdstu@list.ru

S. Shevtsov · V. Akopyan · E. Rozhkov · V. Chebanenko
Vorovich Mechanics and Applied Mathematics Research Institute, Southern Federal University, Rostov-on-Don, Russia

C.-C. Yang · C.-Y. Jenny Lee · C.-X. Kuo
National Kaohsiung Marine University, Kaohsiung City, Taiwan, ROC

problem of the energy harvesting, using the lumped model of PZT stack, which experiences the random mechanical excitation in the low-frequency spectrum, and is loaded on a full bridge rectifier, on a filtering circuit with the varied parameters, and charged electric battery. Considering the case of Li-ion battery as an electric energy harvester, we propose the lumped model for the charge-discharge of this battery. Assuming the linearity of the used PZT material and stack's constraints caused by the external dimensions and the mechanical excitation, we are looking for the parameters of the passive electric load, which provide the maximum achievable values of electric power. Our numerical results demonstrated a very weak dependence of harvested electric energy on the passive circuit's parameters and the best efficiency of the power PZT stacks with the largest number of thin piezoelectric layers.

45.1 Introduction

The problem of efficient use of renewable energy sources as solar, geothermal, hydroenergy, ambient vibration energy attracts the growing attention of a wide range engineering specialties. Other type of energy harvesting is the use of piezoelectric materials for direct transformation of ambient vibration into electrical energy. Sources of such mechanical vibrations can be bridges, buildings, railways, surface of highways and even human movement. Most important requirement to the devices, which can convert energy of mechanical vibration directly to the electric energy, is their efficiency. Many difficulties and ways to their overcome are studied and reported in the fundamental monograph [1] and in the overview papers, for example [2–4]. These difficulties are caused, in particularly by complexity of matching impedances of piezoelectric transducer and electric loading circuits at the frequency range of excited vibrations. In the cases when a host vibrating structure is relatively light, energy harvesting is accompanied by increase of structural damping [5–7]. In order to optimize the energy transformation, many different solutions for the load electric circuits are suggested. These solutions include passive circuits, which combine resistive/capacitive/inductive load with rectifier, semi-active circuits that open or close a switch when the peak force is achieved across the device, and also an active energy harvesting that utilizes a bidirectional switch-mode converter to control the voltage on the electrodes of a PZT device [8–13]. Modeling of these harvesters to optimize them implies some conversion of piezoelectric transformer's finite element model to the lumped model, and then couple a solution of these model equations together with equations that describe an electric circuit [8, 10, 11, 13]. Most above cited theoretical works, study performance of light-weight cantilever harvester in a frequency domain that allows one to present an equivalent circuit equations in easiest form.

Reports devoted to the study of high power harvesters based on piezoelectric stacks are very rare. Such works [14–16] derived lumped a single degree of freedom

model of PZT stack from preliminary finite element investigation, then considered this lumped model together with equation of electric circuit in a frequency domain. However, high mechanical stiffness of the stacks leads to very high resonance frequency, which is far from the frequency of mechanical excitations. Wang et al. [17] presented the dynamic analytical model and its solution for piezoelectric composite stack transducers under external harmonic mechanical loads, which based on the linear theory of piezoelectricity. Model correctly describes the behavior of stack in a broad frequency range, but it is cumbersome and uneasy for analysis.

There are three distinct approaches to the problem of PZT harvester's optimization. Whereas the first one bases on a matching impedance of transducer and impedance of electric load [6–8], the second, which assumes the automatic switches, orientes to eliminate discharge of capacitor and the energy return phenomenon [1, 5, 12, 13]. Unlike these two approaches the other one assumes a design space of PZT stack, which is populated with a set of stack's parameters, including piezoelectric layers number, shape, dimensions, thickness, and takes into account some design constraints (total mass, volume, height etc.) [9, 16]. Because the operational conditions, the power PZT stack sufficiently differs from the conditions for low power harvesters (low frequency range, random, high force excitation) and the last approach is more useful to optimize PZT stack's performance. The operating conditions of power PZT stacks introduce an additional constraint that is due to high force excitation. Minimum value of PZT stack's cross-section area is determined by the strength of piezoelectric ceramics. Many works report the significant decrease of cyclic fatigue properties of poled piezoceramics [18], especially experienced the mechanical loading combined with an electric field [19–22]. Such combined electro-mechanical action can twice decrease an admissible cyclic stresses [20].

All cited articles report the investigation of different kinds of harvesters, but even harvesters with a passive load, which consumes the entire electric power. At the random character of mechanical excitation, power PZT stack harvester cannot be a stable source of electric energy, thus generated electric power cannot use effectively. At these operating conditions, the use of electric battery as a sink of generated electric energy is a very promising technical solution. Complexity of using the battery is that its impedance varies during charge and discharge. Consequently, the piezoelectric energy source should work effectively at the varied state of electric load. An additional complexity of the analysis of such a load is caused by the phenomena of charge/discharge accompanied by hysteresis phenomena [23]. Such phenomena are particularly strong for lead-acid, NiMH and NiSD battery, and significantly less in the Li-ion batteries [23–25].

This chapter is organized as follows. We start from the given vibration excitation spectrum, which is characteristic of the highway substrate, and from the maximum possible mechanic loads. In the first part, we investigate the finite element models of PZT stacks with the different number of layers, which area is determined by the maximum admissible mechanic loads and by the fatigue strength values borrowed from [19–22]. For these FE models, we investigate and collect the FRF of output voltage at the different values of resistance load. Then all obtained data are used to

tune the simplified lumped model of PZT stack, which is included to the block-library of Simscape MATLAB toolbox. The complete lumped model of the harvesting system is built and studied using means of this very power tool for model and designs the electronic devices. Assuming constrained dimension of the studied stack, we study an influence of the varied number and thickness of each layer on the efficiency of harvester.

45.2 From the Finite Element to the Lumped Model of PZT Stack

In order to simplify comparison of modeled and experimental data, the piezoelectric stack models were similar to available samples with different number and thickness of PZT layers made from PZT-5H ceramics. FE models were formulated and studied for the cases of 4, 8, 16, 32 PZT layers coated by Ag electrode layers. Thickness of PZT layers was accepted constant of 1 mm, whereas electrodes thickness was 0.1 mm. For any stacks configuration, their FE model for piezoelectric layers assumed the governing equations in the strain-charge form:

$$\begin{aligned} S &= s^E T + d \mathbf{E} \\ \mathbf{D} &= d T + \varepsilon^T \mathbf{E}, \end{aligned} \quad (45.1)$$

where S is the strain tensor, T is the stress tensor, \mathbf{E} , \mathbf{D} are the electric field and electric displacement vectors respectively, s^E is the elastic compliance matrix, d is the piezoelectric constant matrix, and ε^T is the permittivity measured at a constant stress.

All piezoelectric layers were coupled in parallel (see Fig. 45.1) and loaded on the resistance with varied value. Problem was formulated as axially symmetric. At each time step, the electric current through load was calculated by integration of the current density over each piezoelectric layer. Electric voltage generated by PZT stack, we found using Ohm's law:

$$V - R \sum_k \int_{\Omega} J(t) ds = 0. \quad (45.2)$$

At the numerical simulation, PZT stack was slowly pre-stressed by compressive force and excited by the uniformly distributed forces with different frequencies (see Fig. 45.2).

Such simulations were carried out at different number of layers N , load resistance R , and excitation frequency f , which then were used to reconstruct the stack's performance parameters and their dependencies on N , R , and f . These dependencies (see Fig. 45.3) are required to adjust the lumped model of piezoelectric stack, studied subsequently, and compare it with experimental data. At these experiments,

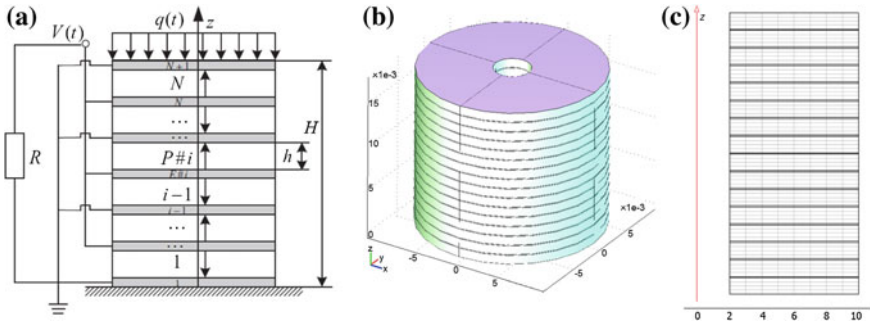


Fig. 45.1 FE model of piezoelectric stack generator under uniformly distributed mechanical load: **a** schematic view [17]; **b** an example of modeled stack geometry; **c** FE meshing of axially symmetric model

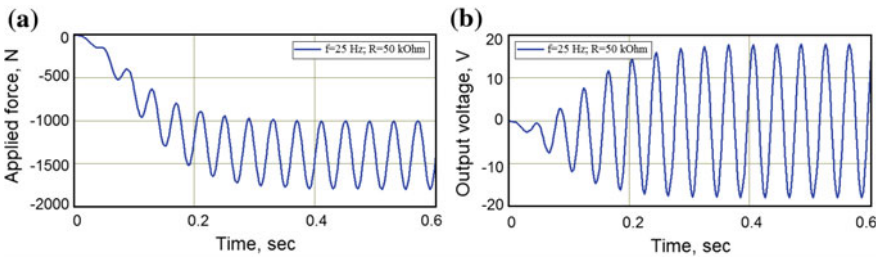


Fig. 45.2 Example of two time histories of the applied excitation force **(a)** and output voltage **(b)** for the piezoelectric stack with 16 layers of 1 mm thickness, surface area 3.016 cm²

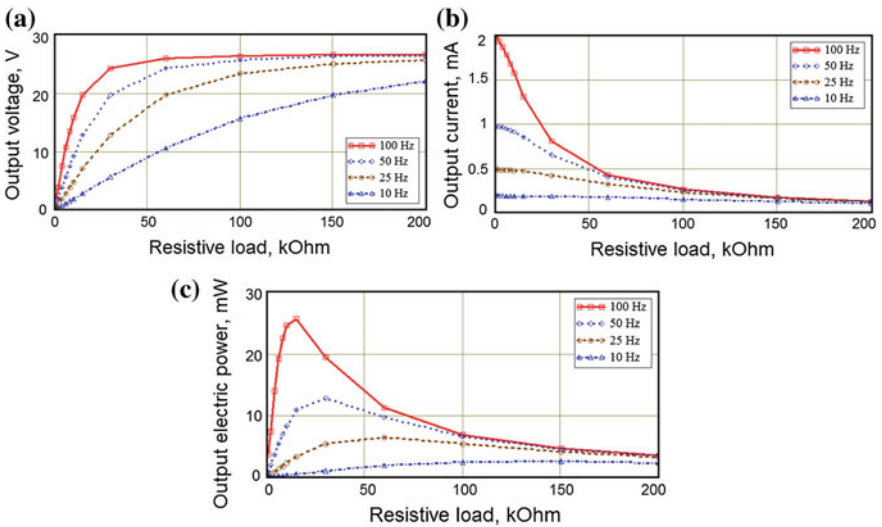


Fig. 45.3 Dependencies of the output voltage **(a)**, current **(b)**, and generated output power **(c)** on the excitation frequency f and load resistance R

the studied PZT stacks were excited using the mechanical exciter driven by numerically controlled machine with wide range of operated frequencies. The found maximum difference between numerical results and experimental data in a studied range of frequencies and load resistance did not exceed 5 %.

Referring to the use of Simscape tools, we accepted as the lumped model of PZT stack the built-in “Piezo Stack” block, whose behavior obeys the one-dimensional (45.1) when only z -axis is active. This block neglects any transverse effects and hysteretic phenomena. Setting of the modeled stack can be implemented by two independent ways. First way assumes a direct setting of piezoelectric ceramics constants together with the dimensions of each piezoelectric layer, and their number. The second one allows one to set the data that obtained in experiments, conducted both in the statics and dynamics. This opportunity can correctly take in account a blocking force, mechanical quality factor, leakage, which difficultly to determine from numerical simulations. In our investigation, we used this opportunity to tune the lumped model of PZT stacks and eliminate substantial deviations from the FE model and experimental data.

45.3 Model of Lithium-Ion Battery Dynamics

Various equivalent circuit models such as the R_{int} -model, the RC -model, the Thevenin model or the PNGV model are now widely used in the studies oriented to ensure an efficient management battery’s state of charge (SOC). This variable is defined as a ratio of an actual battery charge to the maximum battery capacity. The good battery model should represent accurately the voltage dynamics when the current varies and takes into account the open circuit voltage as a function of SOC. There are three main types of battery models, specifically: experimental, electrochemical and electric circuit-based. Most electric circuit-based models are divided into discharge and charge models. We used here the discharge model developed in [23] for the Li-ion batteries:

$$E_{bat} = E_0 - K \frac{Q \cdot it}{it - 0.1Q} + A \exp(-B \cdot it) - R \cdot i, \quad (45.3)$$

where E_0 is battery constant voltage (V), Q is the battery capacity (A h), i is the battery current (A), K is a polarization constant (V/(A h)), A is the exponential zone amplitude (V), B is a inverse constant of the exponential zone time (A h)⁻¹, R is the internal resistance of battery (Ω), and it is the actual battery charge (A h):

$$it = \int idt. \quad (45.4)$$

The charge models proposed in literature are sufficiently complex and our testing of most of them showed their poor stability and lack of precision. We suggest a

simple model, which takes into account the actual state of charge SOC_{in} of the battery and adds charge Q_{add} expressed in terms of SOC:

$$SOC(Q_{add}, SOC_{in}) = 1 - (1 - SOC_{in}) \cdot \exp\left[-\frac{2Q_{add}}{Q \cdot (1 - SOC_{in})}\right]. \quad (45.5)$$

These two models are obtained at the following assumptions. The internal resistance is supposed constant during the charge and discharge cycles and does not vary with the amplitude of the current. The model's parameters are deduced from the discharge characteristics and assumed to be the same for charging. The capacity of the battery does not change with the amplitude of the current. The self-discharge of the battery is not present. The battery has no memory effect.

For the studied battery with nominal capacity 0.25 A h, rated voltage 12 V, and nominal current 12 mA, the dependencies of voltage at discharge according to (45.3), changes of the battery SOC at its charge calculated from (45.5), and corresponding voltage are present in Fig. 45.4. These plots were calculated for the following battery parameters: $K = 0.25$, $A = 1$ V, $B = 30$ (A h)⁻¹. Workflow diagram for harvester's load with the battery, inductance, capacitor and resistor and element supporting Simscape/Simulink interface is present in Fig. 45.5.

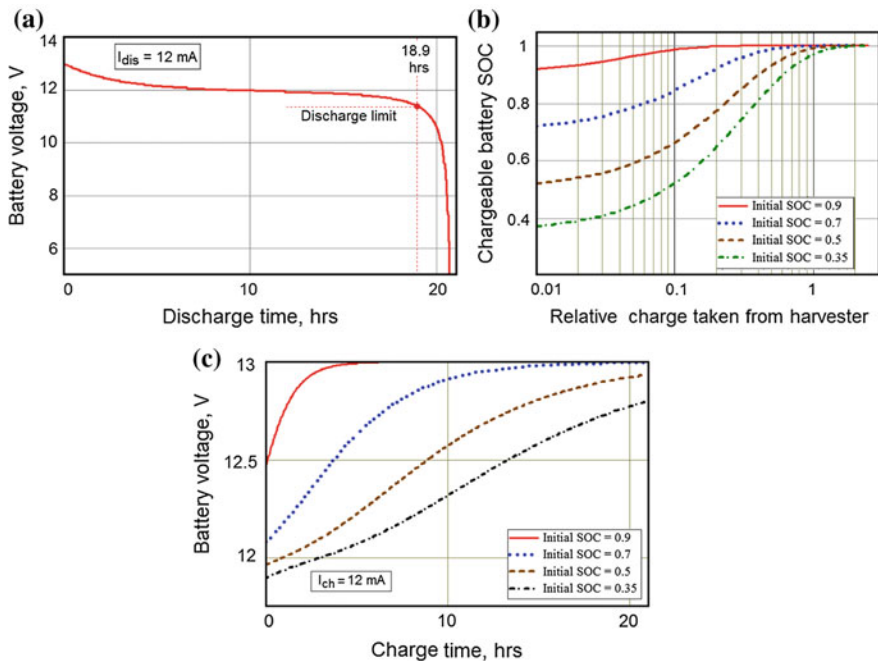


Fig. 45.4 Dependencies of the battery voltage at discharge (a), change of SOC (b) and voltage (c) at the battery charge

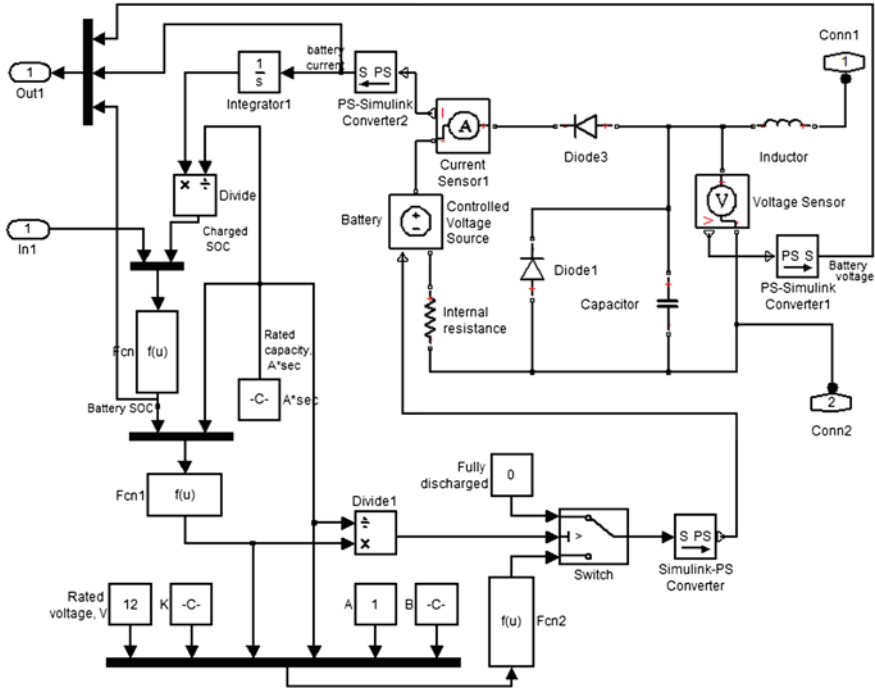


Fig. 45.5 Simscape-Simulink workflow diagram for PZT harvester’s electric load

45.4 Modeling of a Whole Harvesting System

Full equivalent circuit model was built in the Simscape/Simulink environment (see Fig. 45.6). The main modules of a workflow diagram are PZT stack itself, the full bridge rectifier, module generating the random mechanical excitation (see Fig. 45.7), full electric load including battery (see Fig. 45.4) and means for the process monitoring. Initial condition is given by the value of SOC before charging.

Battery charging process was modeled for initial values of SOC 0.3; 0.5; 0.7; 0.85 and 0.95. We studied four different numbers of layers in the stacks with constrained height 96 mm, namely: 80, 96, 120, 160 layers with the thickness 1.2; 1.0; 0.8; and 0.6 mm, respectively. For each studied case, a simulated time was chosen as 60 s. The averaged charging current and rate of SOC (1/min) calculating in a batch mode were chosen as objectives that characterize the harvester’s performance. The optimization algorithm, which calls the harvester’s Simulink model, can change discretely the number of layers, and continuously the value of inductance, capacitance and resistance of load. For the clarity, we present some optimization results for two PZT stack’s structure in Fig. 45.8. These plots demonstrate the ability of all studied PZT stacks for the charging the battery during 10–16 h.

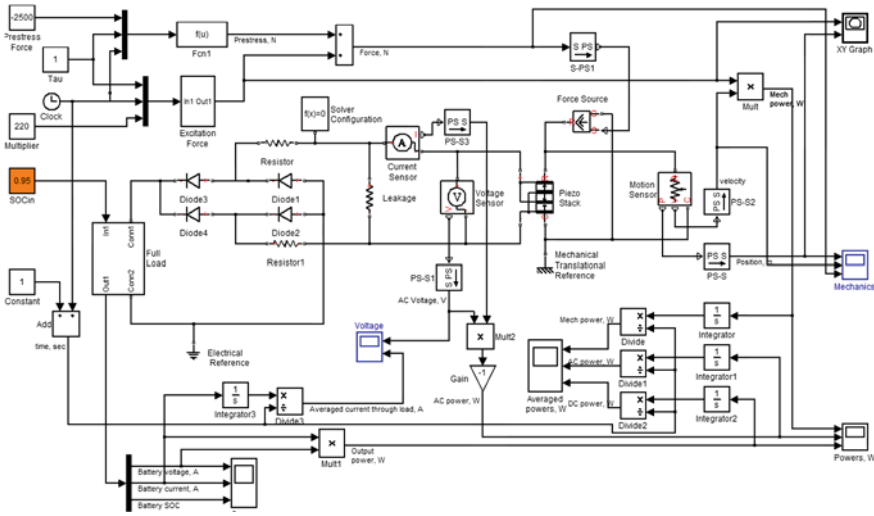


Fig. 45.6 Simscape-Simulink workflow diagram for PZT harvesting system

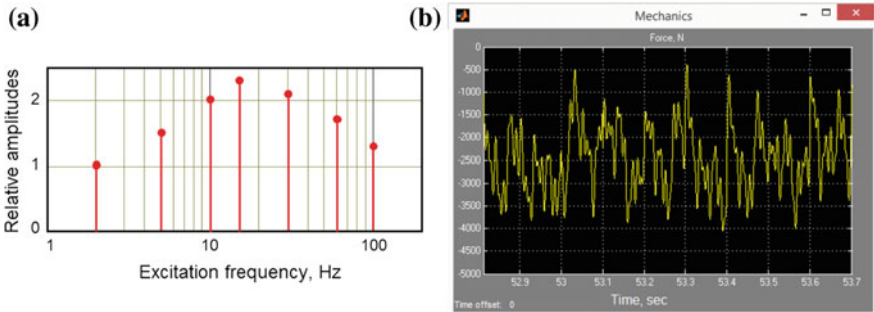


Fig. 45.7 Spectrum of excitation forces (a) and an example of excitation force's time history (b)

Such duration corresponds to the intensive motion of the cars, when this motion can generate mechanical excitation of the highway substrate, and consequently act on the PZT stack harvesters. However, these plots prove the advantage of stacks with greater number of layers at the charging the low-voltage batteries.

Now, we can summarize the area and way of efficient use of obtained results. Such an electric energy harvester can use to provide a battery charge, which is sufficient to supply the LED lamps in the dark. The appropriate places for installing such harvesters are the lighting tunnels and crossroads, remote from the power electric networks. At these cases, the PZT stacks should be mounted under highway cover. These PZT stacks will be excited by the forces from the moving transport, which act on the highway's cover. This mechanical excitation has random amplitude and frequency that depend on the cars weight, speed, and daily traffic intensity.

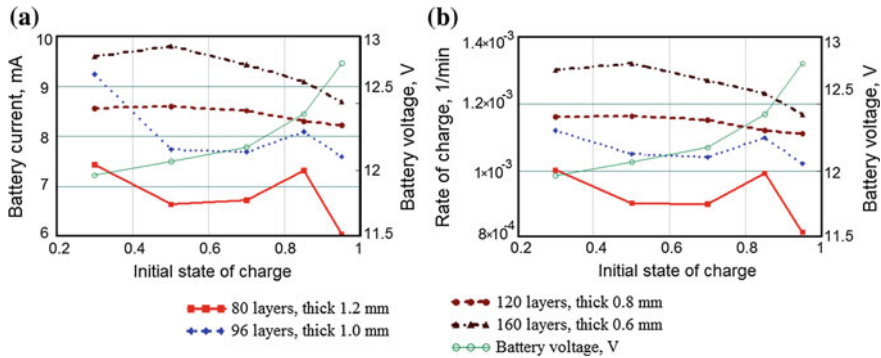


Fig. 45.8 Dependencies of the charging current (a) and the rate of battery charge (b) on the number of PZT layers for the randomly excited piezoelectric stack harvesters with the constrained height 96 mm and section area 3.016 cm²

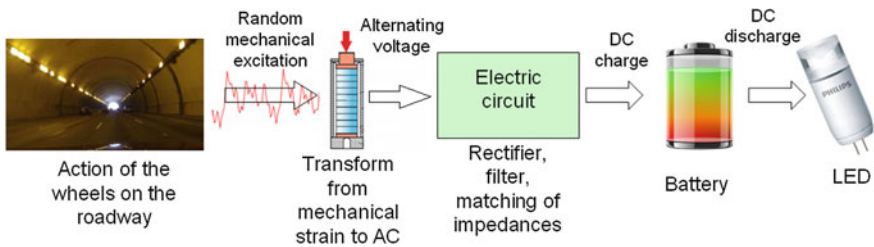


Fig. 45.9 The concept of using the power PZT stack harvester to illuminate dark places in the roads or in the dark

Cross-section of PZT stack should be chosen considering perceived forces and strength of piezoelectric ceramics, whereas number of PZT layers depends on the nominal voltage of lighting devices and battery (see Fig. 45.9). Together with the maximum height dimension, these are main limitations that are constrained on PZT stack harvester. In order to optimize its efficiency and match the impedances we need to find the best number and thickness of layers, and the parameters of passive electric filtering circuit.

45.5 Conclusions

We present the equivalent circuit model for the power PZT stack harvesters and some results of their optimization. Such harvesters can be installed under a surface of highways for the random vibration energy harvesting and charging the batteries, which are intended to supply the lighting (by LED e.g.) at the dark. The input data

for the problem statement are the mechanical vibrations spectrum, their intensity and also required charge capacity and nominal voltage of the batteries. Taking into account the fatigue strength of piezoelectric ceramics, its elastic, electromechanical and electric properties, these input data constraint the dimensions of PZT stack.

Our suggested modeling approach is based on the capabilities of Simscape/Simulink toolboxes, which include full set of electric elements and, particularly, built-in “Piezo Stack” block. This block present a simplified description of the piezoelectric stacks neglecting the effects of hysteresis, non-linearity, leakage, mechanical energy dissipation, but these effects can be easily included using other Simscape and Simulink blocks. In order to correctly describe the dynamic of the battery charge/discharge we proposed the lumped model that allows one to express the evolution of the battery state (state of charge and voltage) at its charging by a current, which is generated by PZT stack and rectified by full bridge with the additional resistance, electric capacitance and inductance.

By using the built lumped model of the harvesting system, which can work in the batch mode, we obtained the optimized values of the electric scheme for the different structures of PZT stack, and we found the expected values of the harvested power that can be stored in the battery during a given time.

Acknowledgments The authors wish to acknowledge the partial financial support from the Russian Foundation for Basic Research (Grants 13-08-00754, 13-08-90912, 14-08-31612, 15-08-00849).

References

1. A. Erturk, D.J. Inman, *Piezoelectric Energy Harvesting* (Wiley, Ltd, 2011)
2. Y. Liu et al., *J. Intell. Mater. Syst. Struct.* **20**, 575 (2009)
3. Y. Liao, H.A. Sodano, *J. Intell. Mater. Syst. Struct.* **20**, 505 (2009)
4. B. Han et al., *J. Vib. Control* **19**(15), 2255 (2013)
5. J.R. Liang, W.H. Liao, *J. Intell. Mater. Syst. Struct.* **20**, 515 (2009)
6. J. Brufau-Penella, M. Puig-Vidal, *J. Intell. Mater. Syst. Struct.* **20**, 597 (2009)
7. S. Shevtsov et al., *Math. Eng. Sci. Aerospace* **2**(2), 145 (2011)
8. C.J. Rup, M.L. Dun, K. Maut, *J. Intell. Mater. Syst. Struct.* **21**, 1383 (2010)
9. J.L. Cauffman, G.A. Lesieutre, *J. Intell. Mater. Syst. Struct.* **20**, 495 (2009)
10. N.G. Elvin, A.A. Elvin, *J. Intell. Mater. Syst. Struct.* **20**, 587 (2009)
11. Y. Yang, L. Tang, *J. Intell. Mater. Syst. Struct.* **20**, 2223 (2009)
12. A.M. Wickenheiser, E. Garcia, *J. Intell. Mater. Syst. Struct.* **21**, 1343 (2010)
13. Y. Wang, D.J. Inman, *J. Intell. Mater. Syst. Struct.* **23**, 2021 (2012)
14. E. Flint, C. Liang, C.A. Rogers, *J. Intell. Mater. Syst. Struct.* **6**, 117 (1995)
15. T. Lee, I. Chopra, *J. Intell. Mater. Syst. Struct.* **11**, 328 (2000)
16. C.J. Rupp, A. Evgrafov, K. Maute, M.L. Dunn, *J. Intell. Mater. Syst. Struct.* **20**, 1923 (2009)
17. K. Wang, Z. Shi, Z. Han, *J. Intell. Mater. Syst. Struct.* **24**, 1626 (2013)
18. H. Weitzing et al., *J. Eur. Ceram. Soc.* **19**(6–7), 1333 (1999)
19. K.L. Le, A.K. So, P.F. H. Scripta Materialia, **49**(9), 849 (2003)
20. Y. Zhan, X. Chen, R. Qian, *Mater. Sci. Eng., A* **351**(1–2), 81 (2003)

21. Y. Zhang et al., *Acta Mater.* **53**(8), 2203 (2005)
22. H. Chen et al., *Ceram. Int.* **33**, 1369 (2007)
23. O. Tremblay, L.-A. Dessaint, *World Electric Vehicle J.* **3**, 1 (2009)
24. H. He, R. Xiong, J. Fan, *Energies* **4**, 582 (2011)
25. S. Wijewardana, *Int. J. Emerg. Technol. Adv. Eng.* **4**(4), 622 (2014)

Chapter 46

Modeling of Non-uniform Polarization for Multi-layered Piezoelectric Transducer for Energy Harvesting Devices

A.N. Soloviev, P.A. Oganessian, T.G. Lupeiko, E.V. Kirillova,
S.-H. Chang and C.-D. Yang

Abstract Mathematical and finite element models of non-uniform polarized piezotransducer are discussed, including implementation in finite-element (FE) package ACELAN. The results of numerical studies of single-layer and multilayered transducers are present. The developed modeling workflow was designed relative to manufacturing process of multi-layered transducers. The results were compared with theoretical model of piezoplate and with numerical experiments performed in ANSYS. Effective scheme of polarization and electrodes placement for three-layered transducer is described with possible preliminary polarization techniques.

A.N. Soloviev (✉) · P.A. Oganessian
Department of Theoretical and Applied Mechanics,
Don State Technical University, Rostov-on-Don, Russia
e-mail: solovievarc@gmail.com

A.N. Soloviev
Vorovich Mathematics, Mechanics and Computer Sciences Institute,
Southern Federal University, Rostov-on-Don, Russia

A.N. Soloviev · P.A. Oganessian
Department of Mechanics of Active Materials, South Scientific Centre
of Russian Academy of Sciences, Rostov-on-Don, Russia

T.G. Lupeiko
Chemical Department, Southern Federal University, Rostov-on-Don, Russia

E.V. Kirillova
RheinMain University of Applied Sciences, Wiesbaden, Germany

S.-H. Chang · C.-D. Yang
Department of Microelectronics Engineering,
National Kaohsiung Marine University, Kaohsiung, Taiwan

46.1 Introduction

The goals of this study are to develop program tools for modeling of non-uniformly polarized materials and to describe an approach to design efficient piezoelectric devices. Finite-element (FE) package ACELAN was used to solve modal and harmonic problems for considered transducer. As was described in [1], applying non-homogeneous polarization field to the single-layer piezotransducer can enlarge the electro-mechanical coupling coefficient and the bandwidth up to 3 times. In this study, we develop the method of multilayered transducers manufacturing with non-uniform polarization independent on each layer. In some cases, we study half-passive transducers with metallic layer.

46.2 Mathematical Model

The mathematical model of each separate elastic or electroelastic body is the same as in [2], namely: the piezoelectric transducer Ω is present by a set of areas $\Omega_j = \Omega_{pk}; k = 1, 2, \dots, N_p; j = k$ with the properties of piezoelectric materials, and a set of areas $\Omega_j = \Omega_{em}; m = 1, 2, \dots, N_e; j = N_p + m$ with the properties of elastic materials. It is appropriate to describe the physical-mechanical processes taking place in the media Ω_{pk} and Ω_{em} within the framework of piezoelectricity (electric elasticity) and elasticity theory.

We assume that the following constitutive equations are satisfied (piezoelectric medium is $\Omega_j = \Omega_{pk}$):

$$\rho_{pk}\ddot{\mathbf{u}} + \alpha_{dj}\rho_j\dot{\mathbf{u}} - \nabla \cdot \boldsymbol{\sigma} = \mathbf{f}_j; \nabla \cdot \mathbf{D} = 0, \quad (46.1)$$

$$\boldsymbol{\sigma} = \mathbf{c}_j^E \cdots (\boldsymbol{\varepsilon} + \beta_{dj}\dot{\boldsymbol{\varepsilon}}) - \mathbf{e}_j^T \cdot \mathbf{E}; \mathbf{D} + \zeta_d \dot{\mathbf{D}} = \mathbf{e}_j \cdots (\boldsymbol{\varepsilon} + \zeta_d \dot{\boldsymbol{\varepsilon}}) + \mathfrak{J}_j^S \cdot \mathbf{E}, \quad (46.2)$$

$$\boldsymbol{\varepsilon} = (\nabla \mathbf{u} + \nabla \mathbf{u}^T)/2; \mathbf{E} = -\nabla \varphi, \quad (46.3)$$

where $\rho(\mathbf{x}, t)$ is the continuous function of coordinates (density); $\mathbf{u}(\mathbf{x})$ is the displacement vector-function; $\boldsymbol{\sigma}$ is the stress tensor, \mathbf{f} are the mass forces; \mathbf{D} is the electric induction vector; \mathbf{c}_j^E are the components of the elastic constant tensor; \mathbf{e}_j is piezoelectric stress coefficients; $\boldsymbol{\varepsilon}$ is the strain tensor; \mathbf{E} is the electric field vector; $\varphi(\mathbf{x})$ is the electric potential function; \mathfrak{J}_j^S are the components of the dielectric permittivity tensor; $\alpha_{dj}, \beta_{dj}, \zeta_d$ are non-negative damping coefficients, and the other symbols are the standard designations for theory of electroelasticity with the exception of index “j”, corresponding to area Ω_j (for elastic media $\Omega_j = \Omega_{ek}$, the piezomoduli \mathbf{e}_j are equal to zero).

For the media $\Omega_j = \Omega_{em}$ with pure elastic properties, only stress fields would be considered. Similar (46.1)–(46.3) and constitutive relationships are used with neglect electric fields and piezoelectric coupling effects. To (46.1)–(46.3) are added

mechanical and electrical boundary conditions, as well as the initial conditions in the case of non-stationary problem. Numerical modeling of devices that can be described with (46.1)–(46.3) are performed using finite element method.

In addition to previous equations, all material properties are defined as functions of coordinates:

$$\rho_k = \rho_{pk}(\mathbf{x}); \mathbf{c}_j^E = \mathbf{c}_j^E(\mathbf{x}); \boldsymbol{\epsilon}_{aj}^S = \boldsymbol{\epsilon}_{aj}^S(\mathbf{x}); \mathbf{e}_j^T = \mathbf{e}_j^T(\mathbf{x}), \tag{46.4}$$

$$g = g^i + |P|(g^a - g^i), \text{ for tensors } \mathbf{c}_j^E \text{ and } \boldsymbol{\epsilon}_{aj}^S \text{ and } g = |P|g^a, \text{ for tensor } \mathbf{e}_j^T, \tag{46.5}$$

There g is corresponding tensor components, i marks isotropic state, a marks anisotropic state. Tensor of piezoconstants \mathbf{e}_j^T will be zero for isotropic bodies.

46.3 Model Implementation and Numerical Results

This model was implemented in FE package ACELAN. The package has been developed to solve specific problems for electro-elastic materials, including non-homogeneous materials. Influence of non-uniform polarization field is taken into account as shown in (46.5). There are different ways to model non-uniform polarization available in ACELAN:

- (i) solving a problem with predefined configuration of electrodes [3],
- (ii) setting individual angle of polarization for each body domain,
- (iii) describing polarization vector field as table or analytical function.

Each approach has its advantages: preliminary polarization analysis is the most accurate way to model manufacturing process, the others two approaches are significantly faster in computation. To keep table data relevant to different lattices, ACELAN provides interpolation utilities based on spline algorithms: (i) thin-plate spline and (ii) Menge algorithm, both implemented in ACELAN. Some of numerical examples presented in this paper were handled using ANSYS package. For verification of numerical results obtained with ACELAN we compared eigen-frequency problems with certain values of polarization angle for each of domains. ANSYS was also used to model electric circuits with layered piezo-transducers.

Let us examine three layered half-passive bimorph. It has two outer layers of PZT-4 and an internal layer made of metal (Fig. 46.1).



Fig. 46.1 Model of three-layered transducer

Top and bottom surfaces of the device covered with electrodes. Study performed for plain model with line of symmetry placed on the left edge. Right end has a fixation for vertical component of displacement. The modeled half of the device is 9 mm long and 0.5 mm thick. Length of metallic layer varied in numerical examples as described below.

Selected non-uniform polarization filed is shown in Fig. 46.2. This polarization was applied to each ceramic layer, vertically revered on the bottom one. Manufacturing process can include preliminary polarization of layers before assembling the whole device.

To implement such polarization we suggest two schemes. Depending of possibilities of polarization equipment, this field can be achieved in one (Fig. 46.3) or two (Fig. 46.4) steps of polrization.

After a polarization is applied, electrodes on the side that will be attached to metal layer, must be removed. Final positioning of electrodes is shown in Fig. 46.5.

After the eigen-frequncy analisys was performed both in ACELAN and ANSYS packages (see Fig. 46.6), electro-mechanical coupling coefficients compared for different polarizations and electrodes confuguartions (see Table 46.1).



Fig. 46.2 Non-uniform polarization of ceramic layer

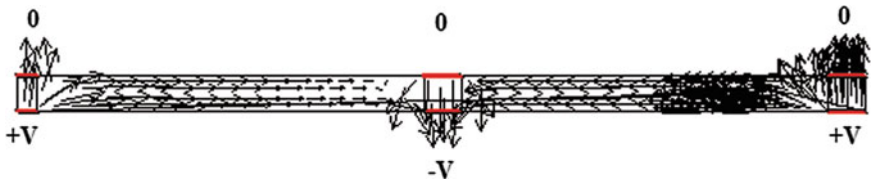


Fig. 46.3 Single-step polarization scheme

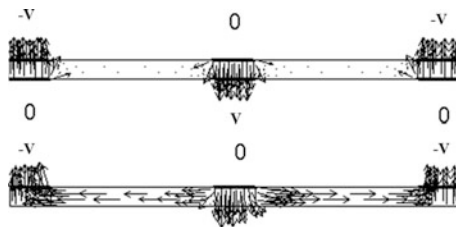


Fig. 46.4 Two-step polarization scheme

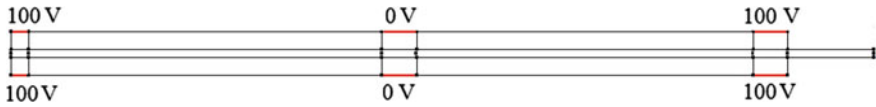


Fig. 46.5 Electrodes for non-uniformly polarized device

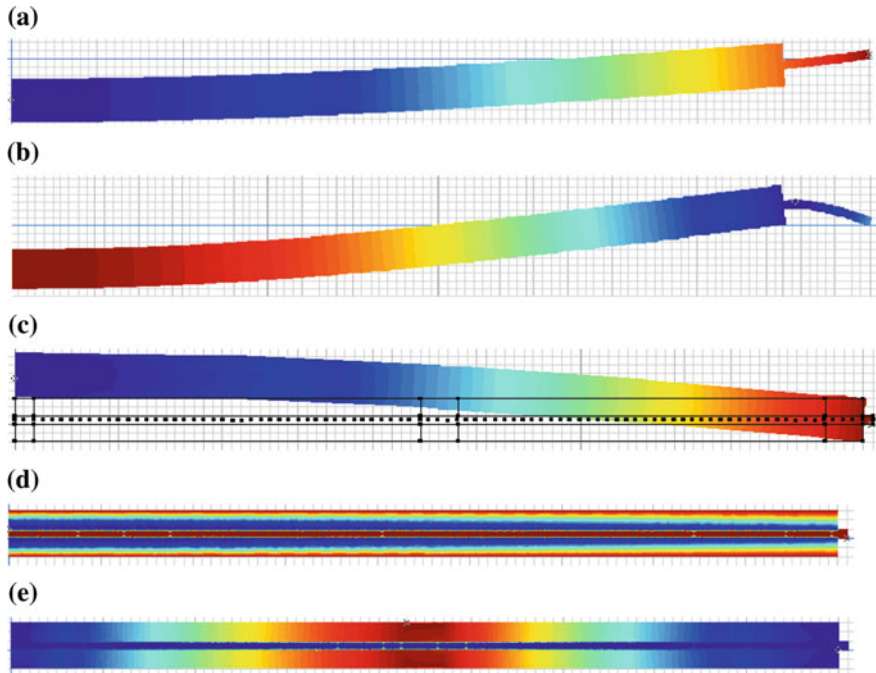


Fig. 46.6 Eigen-values analysis results; displacements for uniform (a) and non-uniform (b) polarizations in models with long metallic layer, non-uniform polarization with short metallic layer (c); electric potential for uniform (d) and non-uniform (e) polarizations

Table 46.1 Comparison of results in eigen-frequency analysis

	Software	Resonance (kHz)	Antiresonance (kHz)	Coupling coefficient (%)
Uniform	ACELAN	2.43	2.67	41.39
	ANSYS	2.43	2.69	42.80
Non-uniform	ACELAN	2.19	2.64	55.83
	ANSYS	2.21	2.72	57.90

As shown in Fig. 46.6, extended metallic layer can affect eigenforms, leading to loss of an efficiency. On this reason, the metallic layer was reduced and was only 0.1 mm longer than the ceramic layer. The results of the analysis showed a growth

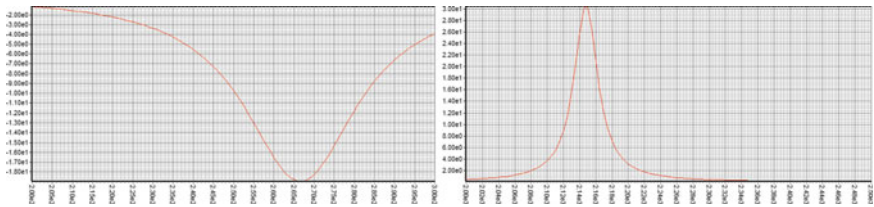


Fig. 46.7 FRA results for vibrations near first eigen-value with mechanical force applied to bottom of the transducer, electric potential on free electrode for uniform (*left*) and non-uniform (*right*) polarization

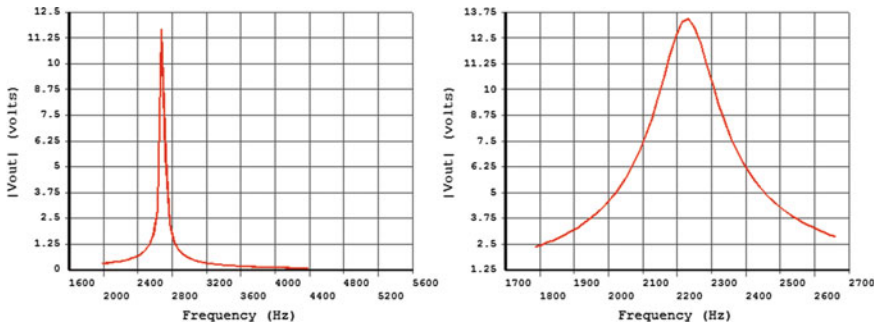


Fig. 46.8 FRA results for electric circuit, uniform (*left*) and non-uniform (*right*) polarization with resistance 10 kΩ

of electro-mechanical coupling coefficient up to 35 %. Higher electric potential was observed in the case of forced oscillations in frequency response analysis (FRA) (see Fig. 46.7); the maximum value on free electrode grew from 180 up to 300 V in the non-uniform case. These models were also used to perform FRA using piezodevice as power source in electric circuit.

Figure 46.8 shows a growth of frequency bandwidth in case of the non-uniform polarization. The maximum voltage is relatively close for selected resistance. With larger resistance, the efficiency of non-uniformly polarized specimen grows (Fig. 46.9).

Another way to perform verification of presented finite element model is to develop applied theory for layered polarized transducers. Various formulations of such a model were described in papers [4, 5]. Using mathematical model of two-dimensional piezoplate, we assume that

$$u = -v'y \tag{46.6}$$

where u is the longitudinal component of displacement, v is the vertical component of displacement, y is the vertical coordinate of point in the body. ACELAN package is capable to export results of computations as XML files with coordinates and

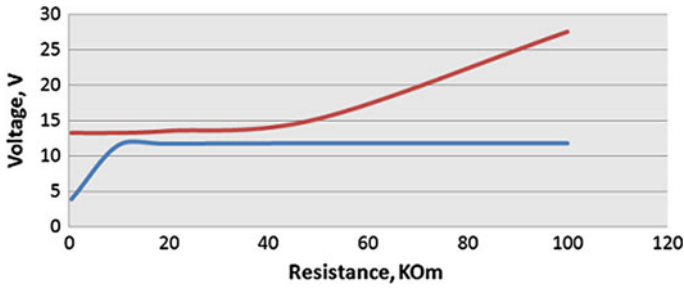


Fig. 46.9 Maximum voltage for different resistance

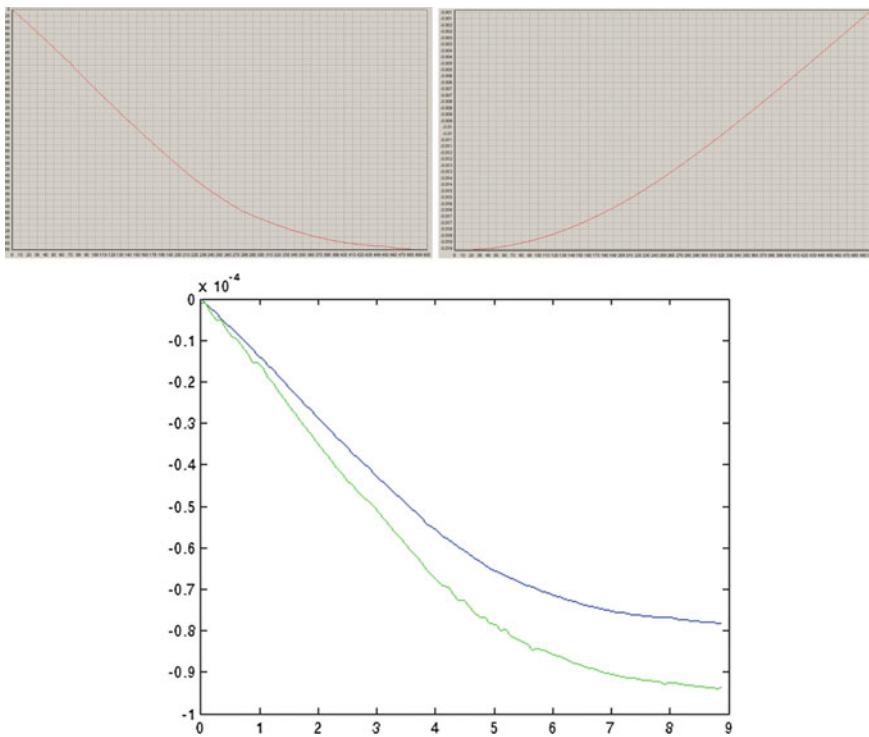


Fig. 46.10 u and v distributions over the top line of device (upper pictures) and comparison between u (blue) and $-v'y$ (green)

values. Such files for model described above were used to perform verification. We observed the line inside the upper layer of ceramics with $y = h$, where h is the thickness of two upper layers of the three-layered device. Values of numerical derivative of table function describing v for non-homogenous model were used in (46.6). Results of the comparison are present in Fig. 46.10.

46.4 Conclusion

The results of the presented study can be used for modeling of piezodevices with higher bandwidth and sensitivity, including energy harvesting devices, sensors and actuators. The suggested research workflow can be performed using ACELAN package for precise polarization analysis and by using ANSYS for electric circuit modeling.

Acknowledgments This work was partially supported by RFBR (grant Nos. 13-01-00943, 13-08-01094).

References

1. A.N. Soloviev, P.A. Oganessian, A.S. Skaliukh in *Advanced Materials—Studies and Applications*, Chap. 12, p. 169, eds. by I.A. Parinov, S.-H. Chang, S. Theerakulpisut (Nova Science Publishers, 2015)
2. A.V. Belokon, V.A. Eremeyev, A.V. Nasedkin, A.N. Soloviev, *Appl. Math. Mech.* **64**(3), 381 (2000)
3. A.V. Belokon, A.S. Skaliukh, *Math. Model. Irreversible Process Polarization* (Fizmatlit, Moscow, 2010). (In Russian)
4. A.O. Vatulian, I.P. Getman, N.B. Lapnitskaya, *Appl. Mech.* **27**(10), 101 (1991)
5. D. Ballhause, M. D'Ottavio, B. Kröplin, E. Carrera, *Comput. Struct.* **83**, 1217 (2005)

Chapter 47

The Multifrequency Sonar Equipment on the Self-action Nonlinear Effect

V.Y. Voloshchenko

Abstract An original operation principles and patented block diagrams for sonar equipment's improvement, such as, sonic direction and range finder, acoustic measurement pulse tube, etc. without complication of reversible interference antenna's design, are present in this chapter. Engineering results can be obtained by means of reception and processing of the "new" sounding echo-signals, i.e. the phase-coupled multiple high-harmonic components $2f, 3f, \dots, nf$ of finite amplitude pump wave with fundamental frequency f generated due to self-action of the radiating pump wave's propagation in nonlinear water medium. The extension of frequency band by additional registration of higher harmonic's echo-signals magnitude allows realizing the original broadband echo-ranging systems with reversible interference antenna's adjustable angular resolution. Phase synchronism and frequency multiplicity of several acoustical signals ($f, 2f, 3f, \dots, nf$) allows designing the equipment for an acoustical reflection/transmission factor's broadband measurements (pulse tube method) for the plane baffle blankets, which operation principle and block diagram are considered.

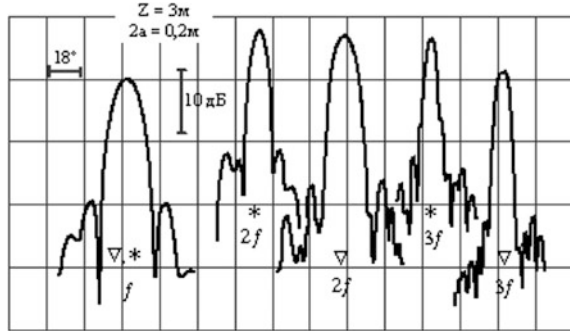
47.1 Introduction

There are known the results of acoustic multiple signal's experimental investigation of self-action regime for active sonar equipment, including the single-beam fish-finding device "Taimen-M", the echo-sounders with navigating mode «Sargan-K, EM, GM», etc. [1, 2].

The directivity patterns of the "Taimen-M" sonar's reversible hydroacoustic interference antenna are represent by diagrams at the Fig. 47.1, where $z = 3$ m and $2a = 0.2$ m are the distance to hydrophone at the acoustic axis and diameter of planar

V.Y. Voloshchenko (✉)
Engineering Technological Academy, Southern Federal University,
347900 Taganrog, Russia
e-mail: voloshchenko.vadim@mail.ru

Fig. 47.1 Beam patterns of “linear” and “nonlinear” regimes for the “Taimen-M” sonar’s reversible interference antenna [1]



antenna appropriately. An angular distributions of multiple signal’s sound pressure amplitude has been registered for two regimes: «linear» regime, antenna’s direct driving at frequencies $f = 50$ kHz, $2f = 100$ kHz, $3f = 150$ kHz (*) by turn and «nonlinear» regime, design mode antenna’s excitation at frequency $f = 50$ kHz, which set to nonlinear generation in water high harmonics $2f, 3f(\nabla)$.

Thus, the “Taimen-M” sonar’s interference antenna possess (∇) the “nonlinear” regime: at frequency $f = 50$ kHz, beam width $\theta_{0,7(f)} = 14.4^\circ$ and sidelobe $P_{sl(f)} = -19$ dB; at frequency $2f = 100$ kHz, $\theta_{0,7(2f)} = 10.8^\circ$, and $P_{sl(2f)} = -23$ dB; at frequency $3f = 150$ kHz, $\theta_{0,7(3f)} = 8.1^\circ$ and $P_{sl(3f)} = -23$ dB; (*) the “linear” regime: antenna’s direct driving at frequency $f = 50$ kHz, beam width $\theta_{0,7(f)} = 14.4^\circ$ and sidelobe $P_{sl(f)} = -19$ dB; at frequency $2f = 100$ kHz, $\theta_{0,7(2f)} = 7.2^\circ$ and $P_{sl(2f)} = -19$ dB; at frequency $3f = 150$ kHz, $\theta_{0,7(3f)} = 4.8^\circ$ and $P_{sl(3f)} = -18$ dB.

As follows from represented measurement data for “linear” radiation regime the sidelobes of angular distributions are without changing, while main beam width decreased in accordance with the prominent physical law. Acoustic fields of high harmonics $2f, 3f, \dots, nf$ possess interesting spatial capabilities: at antenna’s acoustic axis the nonlinear variation of water elastic properties under ultrasonic radiation of high-power pump waves on fundamental frequency f has occurred much greater, in connection with which the width of main lobes for next following harmonic component becomes also narrow. This phenomena at directions of sidelobes occur much lighter, what define the reduction of high harmonic component’s generation efficiency, as a result the sidelobe’s levels for next following harmonic component become also smaller wherewith previous.

47.2 The Multifrequency Navigation System

There is a great need within the area of off-shore marine extraction of oil and gas technology to design the special multifrequency hydroacoustic systems for the navigation and surveillance, which provide the vessel’s safety sailing and maneuvering on the navigable paths, mouth and narrowness of harbors, channels, convergence with drilling platform, etc.

Gage subsystem is composed of the acoustic shipborne devices for sonic location and range of underwater wells equipped by the sonar beacon-pingers, but moreover often observation accuracy and noise immunity occurs insufficient. These difficulties are partially solved by application of the multifrequency sonic direction and range finder, which allows detecting with required accuracy position (bearing and distance) of the powerful source of finite amplitude acoustic waves—sonar beacon-pinger [3, 4].

There is an acoustic subsystem based on angular direction measurements on the bottom beacon at vertical planes transient on axes X and Y of ship's reference system by means of two acoustic arrays, apetalous directional patterns offset one about another on some angle, which forms sonar equisignal zone. This apparatus allows one to take the bearing on the beacon by phase-amplitude method as consistent with it at alignment of the sonar boresight with the bearing on an acoustic pinger. An output error signal from difference block of device is equal to zero, as soon as misalignment of this direction gives rise to appear phase displacements of receiving signals from acoustic arrays. Thus, it is known that sign and variation value of phase displacement depend from magnitude and direction of deflection angle.

Electric error signal in compliance with phase displacement converted to control signal, which supply total mechanical rotation of acoustic arrays until the value of this signal is disappeared. Thus, continuous automatic tracking by means of taking the bearing of acoustic beacon is provided. Unfortunately, the described acoustic subsystem suffers from grave shortcomings. There are modest accuracy of taking the bearing of acoustic bottom beacon, impossibly the range measuring for sound source and necessity of acoustic arrays mechanical turning at the direction finding.

The multi-frequency sonic direction and range of finder functioning occurs in the following way. Electronic units of acoustic beacon-pinger turned on power supply 1 and driving oscillator 2 daisy-chained to chronizator-modulator 3, power amplifier 4 and electroacoustic transducer 5 (see Fig. 47.2). Electroacoustic transducer

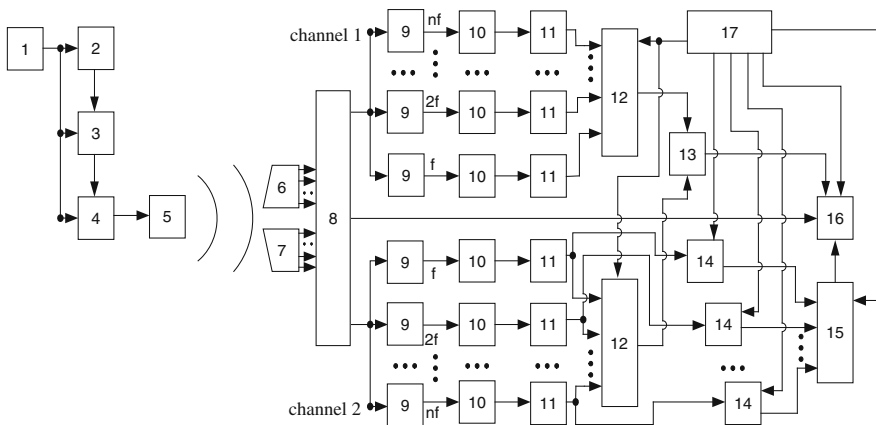


Fig. 47.2 Multi-frequency sonic direction and range finder's block scheme [3]

radiates in nonlinear medium an acoustic sine pulse signal of finite amplitude with sound pressure amplitude P_1 at fundamental frequency f . During its spreading, the saw-tooth distortion of acoustic wave shape will take place, i.e. generating process of higher harmonic components occurs at frequencies $2f, 3f, \dots, nf$ of acoustic pressure, amplitudes of which are equal P_2, P_3, \dots, P_n [5].

An acoustic beacon-pinger can radiate at specified program and may operate until mounting on to the bottom. There are two n -ported reception paths of vessel's aboard receiving apparatus, in which process the electric signals U_1, U_2 from two groups of acoustic transducers 6, 7 process. Both groups of acoustic transducers 6, 7 have the same direction patterns without supplementary lobes, which be away one from other on angle $2\varphi_{cm}$ (Fig. 47.3a), where $\varphi_{cm} = (0.5-0.7)\theta_{0,7f}$, $\theta_{0,7f}$ is the directivity pattern width of each group of acoustic transducers at pump signal. The equisignal-zone method of direction finding can be realized by means of voltage difference determination $\Delta U = U_1 - U_2$ ($-01', 2', -01'', 2''$ in Fig. 47.3a) at the outputs of two identical electric processing channels of both reception paths. Electric signals at frequencies of operation “-” or f , or $2f \dots$, or nf , magnitudes of which are depend of acoustic arrays disposition, what may be specified by tuning callfinding characteristics of equisignal of compensation circuit 8. Retuning of compensation circuit 8 may be carried out as operator manually as well as automatically with subsequent monitoring at the direction on the electroacoustic transducer 5 of acoustic beacon-pinger. If the acoustic beacon-pinger is on the line passing through the intersection point of directivity patterns of two groups of acoustic transducers 6, 7 (it calls the boresight line direction), electric signals of both channels are equal ($U_{1(f)} = U_{2(f)}$ or $U_{1(2f)} = U_{2(2f)} \dots$). Voltage difference ΔU is equal zero, what is indicated by data display unit 16, which shows information

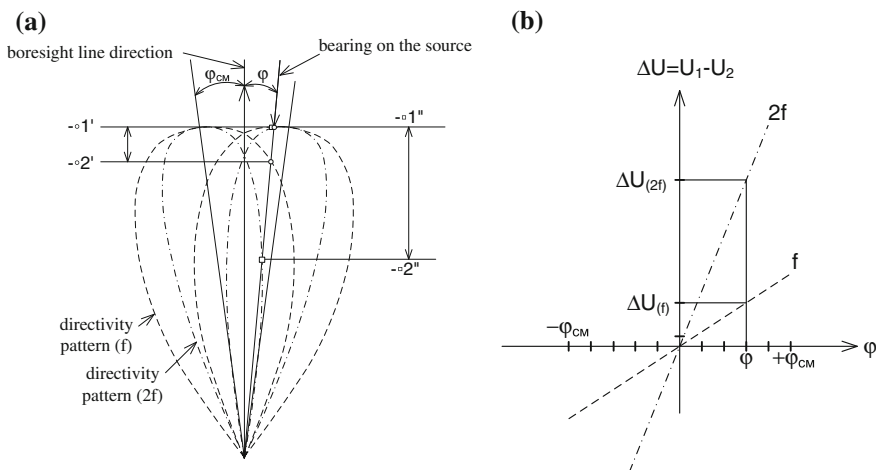


Fig. 47.3 Equisignal-zone method of direction finding (a) and steepness of direction-finding characteristic (b) at operating signals: pump (f) and second harmonic component ($2f$) [3]

about angular coordinate $\Delta\varphi$ taking the bearing on the radiated electroacoustic transducer 5 of acoustic beacon-pinger.

There are several acoustic signals as primary at frequency f as well as generated acoustic fields with frequencies $2f, \dots, nf$. They allow one to regulate the precision of acoustic beacon-pinger direction finding. Direction-finding characteristics of equisignal-zone method on frequencies f (---), $2f$ (-.-.-) for this facility are present in Fig. 47.3b. It is clear from the figure, that steepness of direction-finding characteristic $S = dU(\varphi)/d\varphi$ and therefore direction finding highest possible sensitiveness coincides with the orientation of boresight line direction on the electroacoustic transducer 5 of acoustic beacon-pinger (in this case, $\Delta U = 0$). Therefore, for second harmonic component signal ($2f$), the direction of finding sensitiveness is higher than for fundamental frequency signal. This fact depends of voltage difference magnitude $\Delta U = U_1 - U_2$ ($\ominus 01'$, $2'$, ΔU_f ; $\ominus 01''$, $2''$, ΔU_{2f}) for every angular deflection $\Delta\varphi$ from boresight line direction, what is defined by sharpening of directivity pattern of each group of acoustic transducers in the receipt mode for higher-frequency signals. An angular deflection $\Delta\varphi_{\min(nf)}$ from boresight line direction by which operator or else automatic facility confidently set the presence of voltage difference $U_{1(nf)}, U_{2(nf)}$ expresses by the formula [6]:

$$\Delta\varphi_{\min(nf)} = 0.089\mu(\theta_{0.7(nf)})^2/\varphi_{cm}, \quad (47.1)$$

where $\mu = (0.05 - 0.15)$ or $\mu \geq 0.2$ at operator's direction finding by means of visual or ear indicator, respectively, $\theta_{0.7(nf)}$ are the directivity pattern widths of each group of acoustic transducers at operation signal. Thus, utilization of several operating signals, namely the pump (f) and higher harmonic components (nf) at multi-frequency passive navigation system, which are processed in the n dual-link electric circuits consists of connecting in series band-pass filters 9 tuned up on the frequencies $f, 2f, \dots, nf$, amplifiers 10 and detectors 11. Output signals in pairs of same frequencies f or $2f$ or \dots, nf over two n -ported analog commutators 12 are given for two inputs of subtractor 13, output of which is connected with the second input of data display unit 16. This signal processing allows one to realize the acoustic beacon-pinger's direction finding by means of the equisignal-zone method with required precision, which increase for higher-frequency signals due to the decreasing of directivity pattern widths of each group of receiving array's acoustic transducers at operation signal. The choice of this or another operating signal be carried out by means of giving the signal from the output of control unit 17 to control inputs of two n -ported analog commutators 12, what in this case is determined by necessary precision of ship's sound fixing and range of bottom sonar beacons. Videoimpulse signals $U_{2(f)}, U_{2(2f)}, \dots, U_{2(nf)}$ from outputs of detectors 10 of second reception path enter to the inputs of amplitude measuring devices 14, which register signal's amplitudes on fundamental f and higher harmonic components nf for the moment of precise direction finding. The ratio of signal's levels $U_{2(f)}, U_{2(2f)}, \dots, U_{2(nf)}$ (and so to sound pressure amplitudes $P_1, P_2, P_3, \dots, P_n$) by means of computing unit 15 allows one to determine the range z up to the sonar

beacon-pinger. Output of computing unit 15 connects with the third input of data display unit 16. Control inputs of data display unit 16, computing unit 15 and amplitude measuring devices 14 connect with the corresponding outputs of control unit 17.

There is the derivation of formula for calculation of range z up to taking the bearing of finite amplitude signal of acoustic source by means of three-frequency passive navigation system modification. It is utilized for suitable processing by means of computing unit 15 of the videoimpulse signals $U_{2(f)}, U_{2(2f)}, U_{2(3f)}$. These signals correspond to sound pressure amplitudes P_1, P_2, P_3 acoustic signals of fundamental frequency f and higher harmonics $2f, 3f$ and are received by the one group of acoustic transducers 7. An amplitude ratio of sound pressure amplitudes P_1, P_2, P_3 acoustic signals of fundamental frequency f and higher harmonics $2f, 3f$ are well-known [7]:

$$P_2 \exp(-z\beta_1)/P_1 \exp(-z\beta_2) = [(k+1)2\pi f \ln(z/z_0)P_0 z_0]/(2\sqrt{2}\rho c^3), \quad (47.2)$$

$$P_3 \exp(-z\beta_1)/P_1 \exp(-z\beta_3) = [9(k+1)2\pi f P_0 z_0/(32\rho c^3)]^2 \ln(z/z_0), \quad (47.3)$$

where k is a nonlinear parameter (for water $k = 7$), z is the propagation distance of acoustic signal, $\beta_{1,2,3}$ is the attenuation (neper/meter) of acoustic signal with frequencies $f, 2f, 3f$; ρ is the density of propagation medium (for water 1000 kg/m^3), c is the speed of wave propagation (for water 1500 m/s), P_0 is the sound pressure amplitude of acoustic signal of fundamental frequency f , reduced to the distance $z_0 = 1 \text{ m}$ from the surface of bottom beacon-pinger electroacoustic transducer 5.

Then, one can express $P_0 z_0$ by using expression (2) and put it into (3) $P_3 P_1 / P_2^2 = 3\{\exp[-z(\beta_1 + \beta_3 - 2\beta_2)]\}/2(\ln z - \ln z_0)$. For distance $z_0 = 1 \text{ m}$, we obtain $\ln z = 1.5 \exp[-z(\beta_1 + \beta_3 - 2\beta_2)]P_2^2/(P_3 P_1)$. Thus, exponentiation of expression gives us the following transcendental equation:

$$\exp\{1.5 \exp[-z(\beta_1 + \beta_3 - 2\beta_2)]P_2^2/(P_3 P_1)\} - z = 0. \quad (47.4)$$

It is possible by means of microprocessor hardware to solve the transcendental (47.4) for different values of initial parameters $f, \beta(f), P_1, P_2, P_3$, what allows us to determine unambiguously the range z to taking the bearing for bottom acoustic beacon-pinger.

47.3 An Impulse Method for Broad-Band Acoustical Measurements

High-frequency measurements at (3–100) kHz and (0.5–3) kHz are important, respectively, in marine technology and aero-acoustics in processes of construction of specialized materials in order to apply an acoustic windows, absorbers or

transmission loss systems. The restriction of measuring frequency range by pass band of radiating acoustic transducers and accuracy in determining the modulus and phase of complex acoustic reflection factor for tested material surface are the main difficulties in the gaging of acoustic impedance and material characterization.

Benefits which may be derived from using an improved pulse tube method are undoubted: system proposed uses a convenient technique (radiated and reception paths, temperature controlled water tank, etc.) for acoustic studies, the frequency band extension increases in 2^n times, where n is the even number of applied high harmonic [8]. The schematic diagram of proposed technique is present in Fig. 47.4. Figure 47.5 indicates the voltage waveforms of electrical schematic. The transducer 1 is installed into pulse tube 14 and it radiates in nonlinear medium 2 (water, air, etc.) an acoustic sine pulse signal of finite amplitude U_1 at fundamental frequency f . During it's spreading, because of nonlinear self-action the saw-tooth distortion of acoustic plane wave shape U_2 will take place, i.e., generation of higher harmonic components at frequencies $2f, 3f, \dots, nf$ [5]. All harmonic components of signal U_2 , having phase synchronism with each other, reach the surface of the tested material 3 and reflect from it. Incident and reflected multi-frequency acoustic pulses U_2 and U_5 , respectively, are received by single acoustic probe 4, and then filtered (blocks 5, 6, 7, ...) into harmonic components at frequencies $f, 2f, 3f, \dots, nf$ (electric signals U_6, U_7, U_8, \dots), which correspond to the incident (U_6', U_7', U_9', \dots) and reflected ($U_6'', U_7'', U_9'', \dots$) phased multiple acoustic signals. An acoustic pulse signal U_1 may include (6–10) sine periods of fundamental frequency, varying in measurements at one octave ($f-2f$) range. A single acoustic probe 4 situates on an

Fig. 47.4 Block-scheme of device [8]

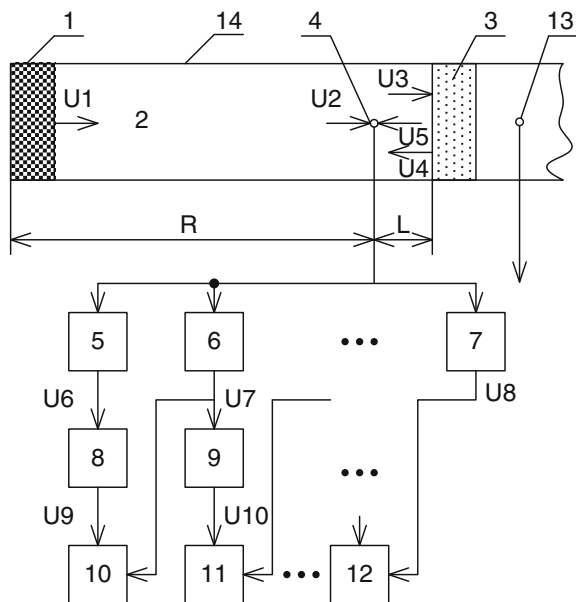
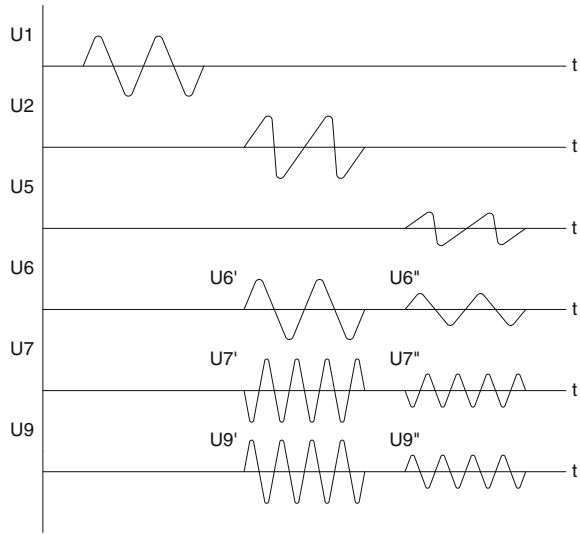


Fig. 47.5 Electric scheme's voltage waveforms [8]



axis of pulse tube near the surface of sample 3, thus, the incident and reflected waves are spatially separated. If $R \gg L$, the attenuation in medium 2 at the distance $2L$ is negligible, and diffraction divergence of acoustical waves does not occur, when the measurements take place in an acoustical tube 14. Thus, signals $U2 \approx U3, U4 \approx U5$ and signal amplitude ratio $U6''/U6' = |\hat{K}(f)|, U7''/U7' = |\hat{K}(2f)|$, will equal to the complex module of acoustical reflection factors for corresponding frequency components $f, 2f, \dots, nf$.

To measure the phase shifts after reflection from the investigated material surface of each harmonic components $f, 2f, 3f, \dots, nf$ for multifrequency signals (incident $U2$ and reflected $U5$) it is necessary to receive several auxiliary support signals with same frequencies. In order to achieve this purpose an electric signals $U6, U7, \dots$, corresponding to acoustic harmonics with frequencies $f, 2f, 4f, 8f, \dots$ are multiplied by the frequency (blocks 8, 9...) by m times, where m equals to the ratio of two neighboring frequency components ($m = 2$). Thus, values of phase shifts between electric signals of the same frequencies (higher-frequency harmonic components $U7, U8, \dots$ and auxiliary support signals $U9, U10, \dots$) determine for incident $U2$ and reflected $U5$ by means of phasometers 10, 11, ...12.

So, for the considered phased multiple acoustic signals of fundamental frequency f and its second harmonics $2f$, we may write

$$\begin{aligned}
 U6' &= U2(f) = U2_{(f)} \cos(\omega t + \alpha_1), \\
 U7' &= U2(2f) = U2_{(2f)} \cos(2\omega t + \alpha_2) \text{---for incident signals;}
 \end{aligned}
 \tag{47.5}$$

$$\begin{aligned}
 U6'' &= U5(f) = U2_{(f)} | \dot{\kappa}(f) | \cos(\omega t + \alpha_1 + 2L\omega/c + \varphi_1), \\
 U7'' &= U5(2f) = U2_{(2f)} | \dot{\kappa}(2f) | \cos(2\omega t + \alpha_2 + 2L\omega/c + \varphi_2) \text{---for reflected waves,} \\
 & \hspace{15em} (47.6)
 \end{aligned}$$

where φ_1, φ_2 are values of the phase shifts for acoustical signals at frequencies f and $2f$ after reflection from tested material 3, $2L\omega/c$ is the current phase increase of acoustical signal because of a double spreading at the distance L , c is the acoustic wave propagation speed in the medium 2. After multiplying signal $U6'$, $U6''$ frequency by 2 times (block 8) we have

$$\begin{aligned}
 U9' &= U2_{(f)} \cos[2(\omega t + \alpha_1)]; \\
 U9'' &= U2_{(f)} | \dot{\kappa}(f) | \cos[2(\omega t + \alpha_1 + \varphi_1 + 2L\omega/c)].
 \end{aligned} \tag{47.7}$$

Phase differences ψ_1 and ψ_2 between signals $U9'$ and $U7'$, and signals $U9''$ and $U7''$, respectively, will be equal $\psi_1 = 2\alpha_1 - \alpha_2, \psi_2 = 2\alpha_1 - \alpha_2 + 2\varphi_1 - \varphi_2 = \psi_1 + 2\varphi_1 - \varphi_2$. Whence $\varphi_2 = \psi_1 - \psi_2 + 2\varphi_1, \psi_1, \psi_2$ are the values, which are successively measured by phasometer 10. Therefore, let the dependence for phase shift φ_1 of the module of complex sound pressure reflection factor $\dot{\kappa}(f)$ is known for the surface of material at one octave ($f-2f$) frequency band. Then simultaneous application in accordance with the described method of the second harmonic $2f$ of acoustic finite amplitude signal makes it possible to obtain additionally the dependence for the phase shift φ_2 . Moreover, we can obtain the modulus of complex sound pressure reflection factor $\dot{\kappa}(2f)$ for the surface of material in the frequency range ($2f-4f$), and when a higher harmonic $4f$ is applied, we can obtain the modulus at the frequency range ($4f-8f$), etc.

Similarly, one can test the acoustical transmission factor through different materials. For this, electrical signals $U6'', U7''$ are received from single acoustical probe 13, located behind the layer of material.

47.4 Conclusion

The chapter presents an original sonar equipment improved development, consisting in an extension of operating frequency band without complication of acoustic antenna's design. This carried out by means of reception and processing of echo-signal amplitude and phase characteristics of generated in nonlinear water medium coupled multiple high harmonic components $2f, 3f, \dots, nf$ of finite amplitude pump waves with fundamental frequency f . For example, upgrading the echo-sounders with navigating mode «Sargan-EM» can extend its operating

capacity: echo-ranging at five operating frequencies (19.7, 39.1, 59.1, 135, 270) kHz allow changing the beam width by 10 times and detecting the singleton/stock of fish at depths of 500 m/1700 m [1].

References

1. V.J. Voloshchenko, *The Fish-Finding Echo-Sounder Based on the Self-action of Nonlinear Effect: Upgraded Prospect* (LAP LAMBERT Academic Publishing GmbH & Co. KG, Germany, 2012) <https://www.ljubljudkni.ru/store/ru/book/isbn/978-3-659-11100-6>, (In Russian)
2. V.J. Voloshchenko, *The Parametric Echo-Sounders for Short-Range Underwater Surveillance* (LAP LAMBERT Academic Publishing GmbH, Omni Scrip. & Co. KG, Germany, 2015) <https://www.ljubljudkni.ru/store/ru/book/isbn/978-3-659-48014-0>, (In Russian)
3. V.Y. Voloshchenko, *Acoustic Direction Finder*. Russian patent No. 2138059 (RU), 20 Sept 1999 (In Russian)
4. V.Y. Voloshchenko et al., *Multi-frequency Navigation System*. Russian Patent No. 86321 (RU), 27 August 2009 (In Russian)
5. T.G. Muir, in *Physics of Sound in Marine Sediments*, p. 241, ed. by L.L. Hampton, Non-linear Acoustics and Its Role in the Sedimentary Geophysics of the Sea (Plenum Press, New York, 1974)
6. A.E.Kolesnirov (ed.), in *Handbook on the Hydroacoustics*, Sudostroenie, 1982 (In Russian)
7. O.H. McDaniel, *J. Acoust. Soc. Am.* **38**(4), 644 (1965)
8. V.Y. Voloshchenko et al., *Apparatus for Measuring the Sound Pressure Reflection Factor of Samples*. USSR Author Certificate on Invention, No. 1196754, 7 Dec 1985 (In Russian)

Chapter 48

Singular Nullor and Mirror Elements for Circuit Design

Quoc-Minh Nguyen, Huu-Duy Tran, Hung-Yu Wang
and Shun-Hsyung Chang

Abstract The singular nullor-mirror pathological elements as universal active elements have been found useful in solving circuit analysis and design problems. They find numerous applications in the synthesis, analysis and design of active networks such as modeling different active elements, nodal analysis, circuit transformations, synthesis of active filters, oscillators and other general networks. A summarization of several applications of singular nullor and mirror pathological elements is given in this chapter.

48.1 Introduction

The singular nullor elements (i.e., nullator and norator) are useful in the synthesis and design of active networks. The main reasons for the popularity of nullor elements are their ability to model a variety of different active elements such as transistors (BJT, FET), Op-Amp, Current Conveyor, Four-Terminal Floating Nullor (FTFN), Voltage follower, Current follower, Operational Transconductance Amplifiers (OTA) etc., independently with the particular realization of the active devices. They provide a unified framework for analysis and design of active networks using different active elements. Nullor elements have been accepted within the network theory community as a basic network element and they have been proven to be a very valuable network analysis, synthesis and design tool. Thus, nullors are fast becoming attractive and prominent active elements for analog signal processing/generation. An attempt to point out all research works related to

Q.-M. Nguyen · H.-D. Tran · H.-Y. Wang (✉)
Department of Electronic Engineering, National Kaohsiung University
of Applied Sciences, 415 Chien Kung Rd., Kaohsiung 807 Taiwan
e-mail: hywang@kuas.edu.tw

S.-H. Chang
Department of Microelectronics Engineering, National Kaohsiung Marine University,
142 Haichuan Rd., Kaohsiung 811 Taiwan

“nullors” and their applications in circuit design, covering the period 1961–2000 has been indicated in [1].

Despite the ability of nullors to represent all active devices elements without the use of resistors, they fail to represent some important analog elements. Therefore, two new pathological elements, called current mirror and voltage mirror are defined [2]. The new defined pathological mirror elements are basically used to represent active devices with current or voltage reversing properties. Their usefulness to circuit synthesis and design has been demonstrated in the literature [3–5]. Recently, the mirror elements with grounded reference node have been extended to include the floating mirror elements [6]. With such extensions, a nullator and a norator can be represented in terms of a floating voltage mirror and a floating current mirror, respectively [7]. Moreover, some pathological sections, which ideally represent most popular analog signal processing properties involving differential or multiple single-ended signals, like conversion between differential and single-ended voltages, differential voltage conveying, and inverting current replication, are concisely constructed from floating mirror elements. Since the better flexibility and simpler configuration of modeling active devices using the combination of singular nullor-mirror elements, the pathological representations of many active devices have been proposed in the literature [7–11].



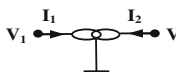
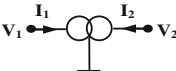
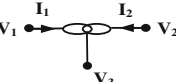
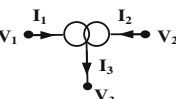
The primary purpose of this chapter is an attempt to summarize several applications of singular nullor-mirror elements for circuit designs proposed in literature. The applications of nullor-mirror elements are classified according to their usage.

48.2 Definitions of Nullor and Mirror Elements

The symbols and definitions of the nullor and mirror elements are shown in Table 48.1. They are singular elements that possess ideal characteristics and are specified on the base of the constraints they impose on their terminal voltage and currents. The nullator and norator own the partial properties of short-circuit and open-circuit. Their symbols and properties are given in Table 48.1a, b, respectively.

The grounded voltage mirror and current mirror shown in Table 48.1c, d are lossless two-port network elements used to represent ideal voltage and current reversing property, respectively. Each of the voltage mirror and current mirror symbols has a reference node, which is set to ground [6]. Although these elements are two-port network elements, they can be used as two terminal elements with the reference node unused [4]. The symbols and definitions of the floating mirror elements are shown in Table 48.1e, f. It can be found that the mirror elements in Table 48.1c–d can be treated as the special cases of the floating mirror elements in Table 48.1e–f, respectively. With the definition of floating mirror elements as Table 48.1, the nullor-mirror models of some active devices with differential voltage input and multiple current output properties can be more concise compared with their pathological representations using mirror elements with grounded reference nodes [11].

Table 48.1 Symbols and definitions of nullor and mirror elements

(a) Nullator		$V_1 = V_2$ $I_1 = I_2 = 0$
(b) Norator		V_1 and V_2 are arbitrary $I_1 = -I_2 = \text{arbitrary}$
(c) Voltage mirror		$V_1 = -V_2$ $I_1 = I_2 = 0$
(d) Current mirror		V_1 and V_2 are arbitrary $I_1 = I_2 = \text{arbitrary}$
(e) Floating voltage mirror		$V_{13} = -V_{23}$ ($V_1 - V_3 = V_3 - V_2$) $I_1 = I_2 = 0$
(f) Floating current mirror		V_{13} and V_{23} are arbitrary $I_1 = I_2 = I_3/2 = \text{arbitrary}$

48.3 Application of Singular Nullor and Mirror Elements in Circuit Design

There are numerous applications of singular nullor-mirror and their combinations in circuit design. In this section, we try to classify them into various categories as follows.

48.3.1 Modeling Active Devices for Nodal Analysis

Symbolic nodal analysis is a formal technique used to calculate the behavior or a characteristic of a circuit with the independent variable (time or frequency), the dependent variables (voltage and current), and the circuit elements represented by symbols. It is mainly used as a means to gain insights into the behavior of the

circuits. The nullor-mirror elements are often used to model all active devices to perform symbolic analysis by applying only nodal analysis. Using the combination of singular nullor mirror elements with grounded reference nodes, the pathological representations of many active devices have been proposed. The various types of operational amplifiers (such as Op-Amp, OTA, OFA, OTRA, COA, etc.) and current conveyors (such as CCIs, CCII, CCIII, MOCCIs, MOCCII, and MOCCIII) have been reported in [12]. Also, the behavioral models of fully-differential active devices such as the fully-differential operational floating amplifier, fully-differential floating operational trans-resistance amplifier, fully-differential operational floating conveyor and fully differential current conveyors (e.g. FD Op-Amp, FD OTA, FD OFA, FD OTRA, FD OCA, FD OFC, DDCCs, DCCII, DXCCII, FDCCII, etc.) have been discussed in [13]. Since the above mentioned models use the combination of nullor-grounded mirror elements and resistors, the circuit complexity is therefore increased. Thus, they increase the complexity of the solution method. In order to improve the speed of finding circuit solution, not only the admittance matrix must be as sparse as possible, but also the size of matrix must be kept as low as possible. Such conditions can be achieved if the behavior of active devices can be modeled with simpler nullor-floating mirror elements instead of nullor-grounded mirror elements resistors. The nullator, norator, differential voltage cell, differential voltage conveying cell, current replication cells, BOCCII, DOICCI, FDCCII and DDCC have been represented by nullor- floating mirror elements in [11].

48.3.2 Applying to Circuit Transformations

Network transformations are the techniques to obtain new functional schemes from available circuits. They are systematic methodologies since each transformation technique can be applied to many circuits to obtain the desired functions or characteristics. By interchange the input voltage or current sources and the output norator of a voltage-mode or current-mode circuit, the new system with inverse transfer function can be obtained [14]. Since the difference between a norator and a current mirror is only their current reversing property, the inverse transformation has been extended to apply to circuits with current mirror output [3]. A convenient network transformation method, exploiting inverse and complementary transformations for deriving linear oscillators from biquadratic band-pass filters was reported in [15]. This method in general can be applied to any band-pass filter without the need of specific requirement of circuits. On the other hand, by interchanging nullators with norators, and voltage mirrors with current mirrors in a circuit, the adjoint transformation can be achieved [16]. The adjoint transformations can be applied for deriving current-mode circuit from voltage-mode circuit and vice versa, generation of equivalent oscillator circuits with the same characteristic equation from an original oscillator and other applications [17–19].

48.3.3 *Applying to Circuit Synthesis Using NAM Expansion*

Recently, a symbolic framework for systematic synthesis of linear active circuit without any detailed prior knowledge of the circuit form was present in [20–24]. This method, named nodal admittance matrix (NAM) expansion, is very useful in generation of specific functional circuits. The matrix expansion process begins by introducing blank rows and columns, representing new internal nodes in the admittance matrix. Then nullor and mirror elements are used to move the resulting admittance matrix elements to their final locations, describing either floating or grounded passive elements properly. Thus, the final nodal admittance matrix (NAM) is obtained including finite elements representing passive circuit elements and unbounded elements, so called infinity-variables [20, 22], representing singular nullor-mirror elements. Two simpler methods for synthesis of voltage-mode and current-mode circuits using NAM expansion was reported in [25, 26]. Based on the above synthesizing method of active network, the generation of several filters, oscillators and gyrators circuits of voltage-mode and current-mode has been proposed [25–32].

48.4 Conclusion

In this chapter, the singular nullor-mirror elements find numerous applications in the synthesis, analysis and design of active networks such as modeling different active elements, symbolic nodal analysis, circuit transformations, synthesis of active filters, oscillators and other general networks. The definition and applications of singular nullor-mirror elements with grounded and floating reference nodes were present. Their practical applications to circuit analysis, synthesis and design in literature have been given.

References

1. P. Kumar, R. Senani, *Analog Integr. Circ. Sig. Process* **33**, 65 (2002)
2. I.A. Awad, A.M. Soliman, *Int. J. Electron.* **86**, 413 (1999)
3. H.Y. Wang, C.T. Lee, C.Y. Huang, *Analog Integr. Circ. Sig. Process* **44**, 95 (2005)
4. H.Y. Wang, S.H. Chang, Y.L. Jeang, C.Y. Huang, *Analog Integr. Circ. Sig. Process* **49**, 87 (2006)
5. H.Y. Wang, C.Y. Liu, S.H. Chang, *Int. J. Electron. Commun. (AEU)* **64**, 828 (2010)
6. R.A. Saad, A.M. Soliman, *Int. J. Circuit Theory Appl.* **38**(9), 935 (2010)
7. R.A. Saad, A.M. Soliman, *Int. J. Circuit Theory Appl.* **38**(2), 148 (2010)
8. R.A. Saad, A.M. Soliman, *Int. J. Circuit Theory Appl.* **38**(9), 935 (2010)
9. A.M. Soliman, *Int. J. Circuit Theory Appl.* **39**(6), 589 (2011)
10. A.M. Soliman, *J. Circuits Syst. Comput.* **21**(3), 1250025 (2012)

11. H.Y. Wang, S.H. Chang, N.H. Chiang, Q.M. Nguyen, *Symbolic Analysis Using Floating Pathological Elements*. Proceedings International Conference on Genetic and Evolutionary Computing, ICGEC, p. 379 (2013)
12. C. Sanchez-Lopez, F.V. Fernandez, E. Tlelo-Cuautle, S.X.D. Tan, *IEEE Trans. Circuits Syst. I* **58**, 1382 (2011)
13. C. Sanchez-Lopez, *IEEE Trans. Circuits Syst. I* **60**(3), 603 (2013)
14. A. Leuciuc, *Electron. Lett.* **33**, 949 (1997)
15. H.Y. Wang, H.D. Tran, Q.M. Nguyen, L.T. Yin, C.Y. Liu, *Appl. Sci.* **4**, 482 (2014)
16. A. Carlosena, G.S. Moschytz, *Int. J. Circuit Theory Appl.* **21**, 421 (1993)
17. T. Dostal, Bielek, K. Vrba, *IEEE Int. Conf. Devices, Circuits Syst T034* (2002)
18. R. Senani, *IEEE Trans. Circuits Syst. I* **41**, 617 (1994)
19. C.A. Papazoglou, C.A. Karybakas, *IEEE Trans. Circuits Syst. II* **45**, 894 (1998)
20. D.G. Haigh, T.J.W. Clarke, P.M. Radmore, *IEEE Trans. Circuits Syst. I* **53**, 2011 (2006)
21. D.G. Haigh, *IEEE Trans. Circuits Syst. I* **53**, 2715 (2006)
22. D.G. Haigh, F.Q. Tan, C. Papavassiliou, *Analog Integr. Circ. Sig. Process* **43**, 297 (2005)
23. D.G. Haigh, P.M. Radmore, *IEEE Trans. Circuits Syst. I* **53**, 2214 (2006)
24. R.A. Saad, A.M. Soliman, *IEEE Trans. Circuits Syst. I* **55**, 2726 (2008)
25. H.D. Tran, H.Y. Wang, Q.M. Nguyen, N.H. Chiang, W.C. Lin, T.F. Lee, *AEU-Int. J. Electron. Commun.* **69**(7), 981 (2015)
26. A.M. Soliman, *Int. J. Circuit Theory Appl.* **39**, 1087 (2011)
27. L. Tan, Y. Bai, J. Teng, K. Liu, W. Meng, *Circuits Syst. Signal Process.* **32**, 1467 (2013)
28. Y.A. Li, *AEU-Int. J. Electron. Commun.* **67**, 754 (2013)
29. Y.A. Li, *AEU-Int. J. Electron. Commun.* **67**, 289 (2013)
30. A.M. Soliman, *J. Electrical Comput. Eng.* doi:[10.1155/2010](https://doi.org/10.1155/2010)
31. A.M. Soliman, *Analog Integr. Circ. Sig. Process* **65**, 43 (2010)
32. A.M. Soliman, *AEU-Int. J. Electron. Commun.* **64**, 971 (2010)

Chapter 49

The Performance Evaluation of IEEE 802.11 DCF Using Markov Chain Model for Wireless LANs

Chien-Erh Weng

Abstract During the past few years, the widespread use of the wireless local area networks (WLANs) communication technique is one of the most popular technologies in data telecommunications and networking. The IEEE 802.11 protocol has achieved worldwide acceptance with WLANs with minimum management and maintenance costs. The theoretical performance and numerical results in terms of saturation throughput and delay of DCF were finished by Ziouva and Antonakopoulous. It takes account the busy medium conditions and how they affect the use of the back-off mechanism. However, the definition of a channel busy probability is not suitable for the operating system architecture. In this chapter, we modified the channel busy conditions and improved Ziouva and Antonakopoulous's (ZA's) model and presented a more accurate analysis of the DCF. The numerical results show that the modified model has a better performance than the ZA's model under an ideal channel scenario.

49.1 Introduction

In recent years, the wireless local area networks (WLANs) market is experiencing an explosive growth. The medium access control (MAC) protocol is the key element that provides the efficiency in accessing the channel, while satisfying the QoS requirements.

The IEEE 802.11 wireless local area network is a shared-medium communication network that transmits information over wireless links for all IEEE 802.11 stations in its transmission range to receive. It is one of the most deployed wireless networks in the world and is likely to play a major role in multimedia home networks and next-generation wireless communications. IEEE 802.11 wireless

C.-E. Weng (✉)

Department of Electronic Communication Engineering,
National Kaohsiung Marine University, Kaohsiung, Taiwan, ROC
e-mail: ceweng@mail.nkmu.edu.tw

networks can be configured into two different modes: ad hoc and infrastructure. In ad hoc mode, all wireless stations within the communication range can communicate directly with each other, whereas in the infrastructure mode, an access point (AP) is needed to connect all stations to a distribution system (DS), and each station can communicate with others through the AP. IEEE 802.11 is composed of both a physical layer (PHY) and MAC specifications for wireless local area networks [1, 2].

In the IEEE 802.11 protocol, the fundamental mechanism to access the medium is called the distributed coordination function (DCF). This is a random access scheme, which is based on the carrier sense multiple access with collision avoidance (CSMA/CA) protocol. The standard also defines an optional point coordination function (PCF), which is based on a polled-response mechanism.

In the DCF, if a station has a frame to transmit, it will monitor the channel. If the channel is busy, the MAC waits until the medium becomes idle, and then defers for an extra time interval, called the DCF inter-frame space (DIFS). After sensing the channel within a DIFS, the station (STA) randomly chooses a back-off interval before transmitting. The back-off counter is decremented in terms of a time slot as long as the channel is sensed as being idle. The counter stops when a transmission with other STAs is detected on the channel and reactivated when the channel is sensed as being idle again for more than a DIFS. The station transmits its frame, when the back-off counter reaches zero. At each transmission, the back-off time is uniformly chosen in the range $[0, W - 1]$, where W is the current back-off window size. W equals the initial back-off window size CW_{\min} . After each unsuccessful transmission, W is doubled until a maximum back-off window size value CW_{\max} is reached. Once it reaches CW_{\max} , W shall remain at the value CW_{\max} until it is reset. W shall be reset to CW_{\min} after every successful transmission or the retransmission counter reaches the retry limit (L). After the destination station successfully receives the frame, it transmits an acknowledgment (ACK) frame following a short inter-frame space (SIFS) time. If the transmitting station does not receive the ACK within a specified ACK timeout or it detects the transmission of a different frame on the channel, it reschedules the frame transmission according to the previous back-off rules. The above mechanism is called the basic access mechanism (ACK CSMA/CA) as shown in Fig. 49.1 [1–3].

There have been many performance analyses of the IEEE 802.11. Bianchi [2] proposed a simple and accurate analytic model to the computer saturation throughput. Ziouva and Antonakopoulous [4] improved Bianchi's model to derive a saturation delay. Wu et al. [5] improved Bianchi's model to consider a retry limit. Hadzi-Velkov and Spasenovski [6] improved Bianchi's model to consider a retry limit in the fading channel. In real-time applications such as voice and video, the STA might take an arbitrarily long time to access the channel.

The rest of this chapter is organized as follows. In Sect. 49.2, a general description of our proposed model is present. Analytical performance deviations of modified model with basic access mechanisms including throughput and delay analysis are present in Sect. 49.3. The numerical results are given with discussion in Sect. 49.4. Finally, conclusions are drawn in Sect. 49.5.

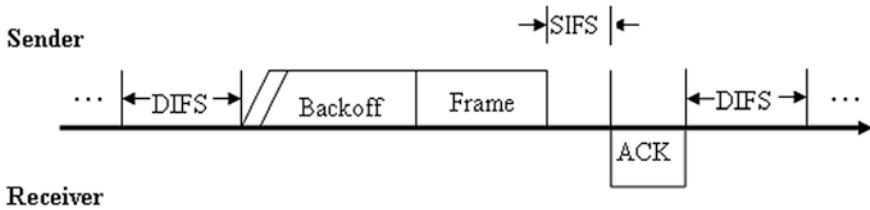


Fig. 49.1 ACK CSMA/CA in DCFDCF

49.2 Overview of the Modified DCF Model

In CSMA/CA protocol, the STA has a frame to transmit. It must sense the channel. If the channel is idle for a period of time equal to a distributed inter-frame space (DIFS), the station transmits. Otherwise, if the channel is sensed busy (either immediately or during the DIFS), the station has to wait for an additional DIFS, and generate a random delay (back-off process) before transmitting its frame. The delay is uniformly chosen in the range $(0, W - 1)$, which is called contention window. When a STA finishes the back-off process and the medium has been idle longer than the DIFS time interval, the frame is transmitted immediately. If there are transmissions from other STAs during this time period, the STA will double up the contention window and enter the next stage, otherwise the STA will enter the $\{-1, 0\}$ state. The STA will freeze its back-off counter until the end of the transmission as there are transmissions from other STAs during this time period. Then, the STA resumes its counter after DIFS. At the first transmission attempt, W is set to be equal to a value CW_{min} , called minimum contention window. After each unsuccessful transmission, W is doubled up to a maximum value $CW_{max} = 2^m CW_{min}$. The back-off time counter is decremented as long as the channel is sensed idle, “frozen” when a transmission is detected on the channel, and reactivated, when the channel is sensed idle again for more than a DIFS. The station transmits, when the back-off time reaches zero.

Since a collision cannot be detected in the CSMA/CA protocol, there are two mechanisms to determine the successful reception of a frame. The first one is called the ACK CSMA/CA mechanism. For each successful reception of a frame, the receiving station immediately acknowledges by sending an acknowledgement (ACK) frame. The ACK frame is transmitted after a short IFS (SIFS), which is shorter than the DIFS. Other stations resume the back-off process after a DIFS time. If an ACK frame is not received after the data transmission, the frame is retransmitted after another back-off process.

We used some similar procedures and index in [4]: $b(t)$ is defined as a stochastic process that presents the value of the back-off counter for a given station at slot time t . We assume that each STA has $m + 1$ stages of back-off delay and that $s(t)$ is the stochastic process representing the back-off stage i at time t . The value of the back-off counter is randomly chosen in the range $(0, W_i - 1)$, where $W_i = 2^i W_{min}$

and depends on the STA's back-off stage i . The state of each STA is depicted by $\{i, k\}$, where i indicates the back-off stage and takes the values $(0, 1, \dots, m)$, and k indicates the back-off time slot and takes the values $(0, 1, \dots, W_i - 1)$ in slot times. The state transition diagram of the Markov chain model is shown in Fig. 49.2. The transition probabilities are listed as follows:

- (1) The back-off counter freezes when the STA senses that the channel has another transmission:

$$P\{i, k|i, k\} = p, 0 \leq k \leq W_i - 1, 0 \leq i \leq m. \tag{49.1}$$

- (2) The back-off counter decrements, when the STA senses the channel does not have any transmission:

$$P\{i, k|i, k + 1\} = 1 - p, 0 \leq k \leq W_i - 2, 0 \leq i \leq m. \tag{49.2}$$

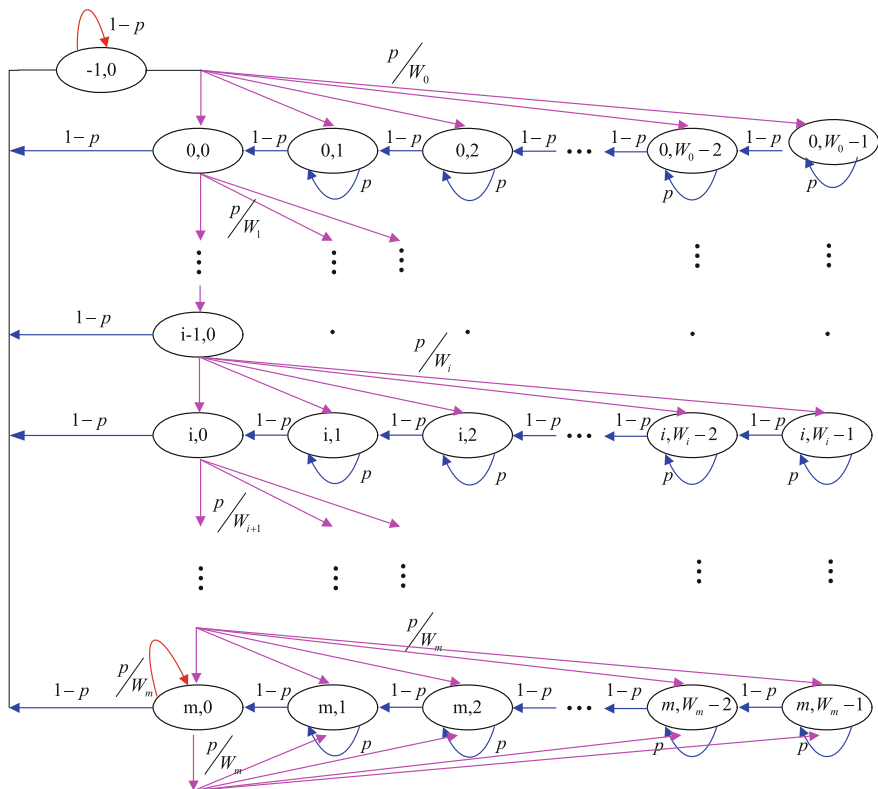


Fig. 49.2 Markov chain model for the back-off window size

- (3) The STA enters the $\{-1, 0\}$ state, if its frame is a successful transmission:

$$P\{-1, 0|i, 0\} = (1 - p), 0 \leq i \leq m. \quad (49.3)$$

- (4) The STA transmits its frame without entering the back-off process, if it detects that its previous transmitted frame was successfully received and the channel is idle:

$$P\{-1, 0|-1, 0\} = (1 - p), 0 \leq i \leq m. \quad (49.4)$$

- (5) If the STA finds that a collision has occurred, the STA defers the transmission of a new frame and enters stage 0 of the back-off process:

$$P\{0, k|-1, 0\} = \frac{p}{W_0}, 0 \leq k \leq W_0 - 1. \quad (49.5)$$

- (6) The STA chooses a back-off delay of the next stage i after an unsuccessful transmission at stage $i - 1$:

$$P\{i, k|i - 1, 0\} = \frac{p}{W_i}, 1 \leq i \leq m, 0 \leq k \leq W_i - 1. \quad (49.6)$$

- (7) The STA has reached the last stage of the back-off process and remains at that state after an unsuccessful transmission:

$$P\{m, k|m, 0\} = \frac{p}{W_m}, 0 \leq k \leq W_m - 1. \quad (49.7)$$

We calculate the probability of a STA at state $\{i, k\}$, where $b_{i,k}$ is the stationary distribution of the Markov chain. The relations are listed as follows:

$$b_{i,0} = p^i b_{0,0}. \quad (49.8)$$

$$b_{m,0} = \frac{p^m}{1 - p} \times b_{0,0}. \quad (49.9)$$

$$b_{-1,0} = p^{-1} \times b_{i,0}. \quad (49.10)$$

$$b_{i,k} = \frac{W_i - k}{W_i} \frac{b_{i,0}}{1 - p}. \quad (49.11)$$

$$b_{0,k} = \frac{W_0 - k}{W_0} \frac{b_{0,0}}{1 - p}. \quad (49.12)$$

$$b_{m,k} = \frac{W_m - k}{W_m} \frac{p^m}{(1 - p)^2} b_{0,0}. \quad (49.13)$$

If τ is the probability of a station transmits frame within a time slot at $\{i, 0\}$ state, we can obtain

$$\tau = b_{-1,0} + \sum_{i=0}^{m-1} b_{i,0} + b_{m,0} = \frac{1}{(1 - p)} b_{-1,0}. \quad (49.14)$$

And if the probability conservation relation states that $\sum_{i=-1}^m \sum_{k=0}^{W_i-1} b_{i,k} = 1$, we have

$$b_{-1,0} = \frac{2p(1 - p)^2(1 - 2p)}{2p(1 - p)^2(1 - 2p) + W(1 - (2p)^m)(1 - p) + (1 + W(2p)^m)(1 - 2p)}. \quad (49.15)$$

To find the value of p , the probability p (channel busy probability) is defined as that of a transmitted frame that encounters a collision, i.e., there are more than one STA transmission during a slot time. This yields

$$p = 1 - (1 - \tau)^{n-1}. \quad (49.16)$$

49.3 Analytical Performance Deviations of Modified Model

49.3.1 Throughput Analysis

Let S is the normalized system throughput, defined as the fraction of time the channel is used to successfully transmit payload bits. The probability that a transmission occurring on the channel is successful is given by the probability that only one STA among all STAs transmits, i.e., there is at least one STA transmission on the channel. The successful transmission probability that at least one STA transmits on the channel is

$$p_S = \frac{n\tau(1 - \tau)^{n-1}}{1 - (1 - \tau)^n}. \quad (49.17)$$

The throughput S is expressed as

$$S = \frac{p_s * E(L)}{(1 - p)\sigma + p_s T_S + [p - p_s]T_C}, \quad (49.18)$$

where $E(L)$ is the average packet payload size, the average amount of payload frame successfully transmitted in a time slot is $p_s * E(L)$, the probability that the channel is idle for a time slot is $(1 - p)$, the channel is either idle nor successful for a time slot is $[1 - (1 - p) - p_s] = (p - p_s)$. T_S is the average time that the frame has a successful transmission, and T_C is the average time the channel is sensed busy by each station during a collision. σ is the duration of a time slot. The value of T_S and T_C depend on the channel access method and are defined as the ACK CSMA/CA mechanism:

$$\begin{aligned} T_S^{ack} &= H + P + \delta + SIFS + ACK + \delta + DIFS, \\ T_C^{ack} &= H + P + \delta + DIFS. \end{aligned} \quad (49.19)$$

49.3.2 Delay Analysis

Delay is defined as the time elapsed between the generation of a frame and its successful reception by the receiving STA. The mean frame delay can be defined by the following relation:

$$E[D] = E[X]\sigma + E[B](p_s T_S + (p - p_s)T_C) + E(N_m)(T_C + T_O) + T_S, \quad (49.20)$$

where $E[N_m]$ represents the average number of collisions before the transmission frame, T_O denotes the time that a station has to wait before sensing the channel again due to its frame collision. From the description we can obtain

$$E(N_m) = \sum_{i=0}^m ip^i(1 - p). \quad (49.21)$$

The average back-off delay depends on the value of a station's back-off counter and the duration, when the counter freezes due to other transmissions. Considering that the counter of the STA is at $\{i, k\}$ state, then a time interval of k time slots is needed for the counter to reach state 0 without taking into account the time the counter is stopped. Let X denote the total number of back-off slots of the STA before accessing the channel without considering the case, when the counter freezes. We then have

$$E(X) = \sum_{i=0}^m p^i(1 - p) \sum_{h=0}^i \frac{W_h - 1}{2}. \quad (49.22)$$

When B denotes the time that the back-off counter of a station freezes and $E[B]$ denotes the average number of time slots that the back-off counter freezes, respectively, we have

$$E(B) = \frac{E(X)}{(1 - p)} p. \tag{49.23}$$

49.4 Numerical Results

To gain a better understanding on how the DCF protocol behaves, the following numerical simulation results have been obtained, assuming the parameters are as follows: Frame payload = 1023 bytes, MAC header = 34 bytes, PHY header = 16 bytes, ACK = 14 bytes, SIFS = 20 μ s, DIFS = 50 μ s, propagation delay = 1 μ s, and slot time = 20 μ s.

Figure 49.3 shows how the normalized back-off probabilities depend on the number of stations, when the back-off counter is equal to 0. When the STA enters either one of both states $\{i, 0\}$ and $\{-1, 0\}$, the normalized back-off probability indicates how frequently each state is used in the medium access process. From Figs. 49.3 and 49.4, we show that the modified model can get a better normalized back-off probability than ZA's model at $\{-1, 0\}$ state. Figure 49.5 is the throughput

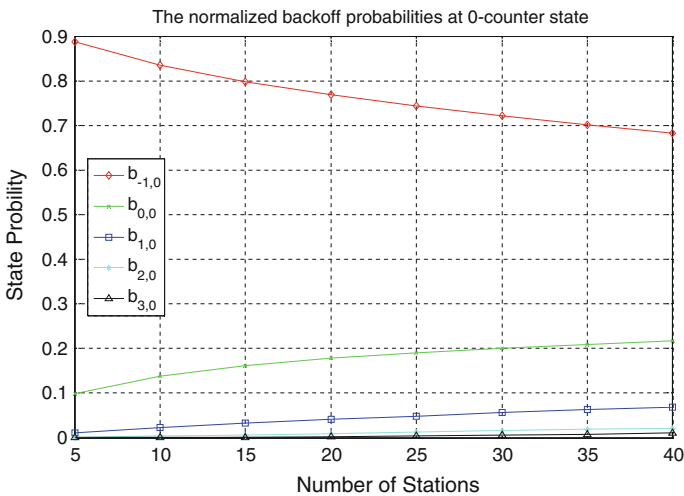


Fig. 49.3 Normalized back-off probability of modified model

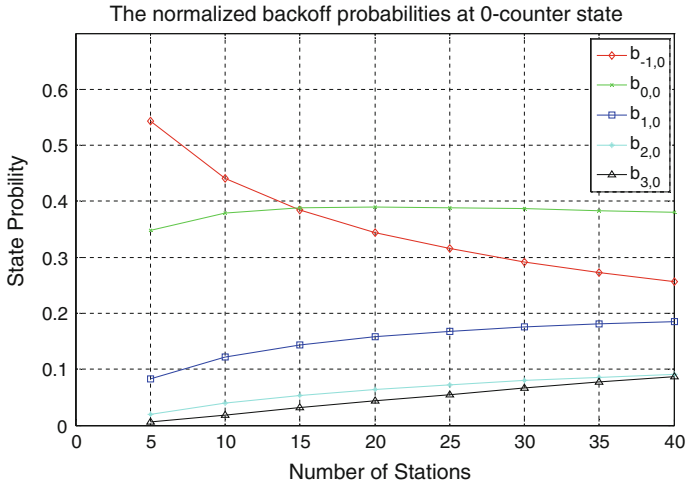


Fig. 49.4 Normalized back-off probability of Ziouva’s model

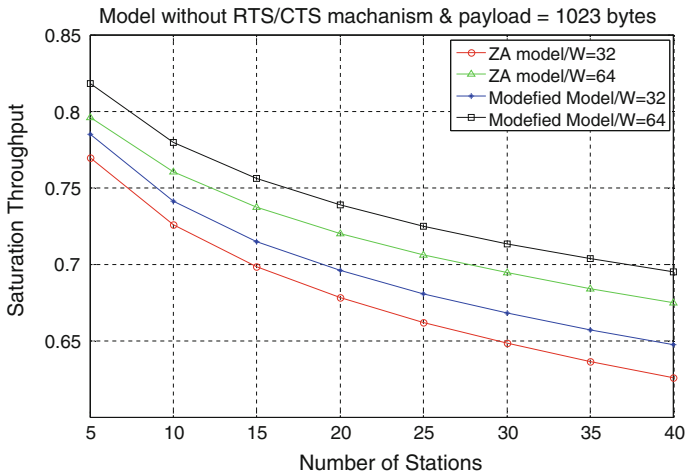


Fig. 49.5 Saturation throughput versus initial window size

without the RTS/CTS mechanism; as the number of the STAs increases, the performance decreases. This is due to the fact that the probability of a collision becomes larger without the RTS/CTS mechanism. As a larger number of STAs without the RTS/CTS mechanism attempt to access the channel, more collisions occur, and the number of retransmissions increase and the stations suffer longer delays as shows in Fig. 49.6.

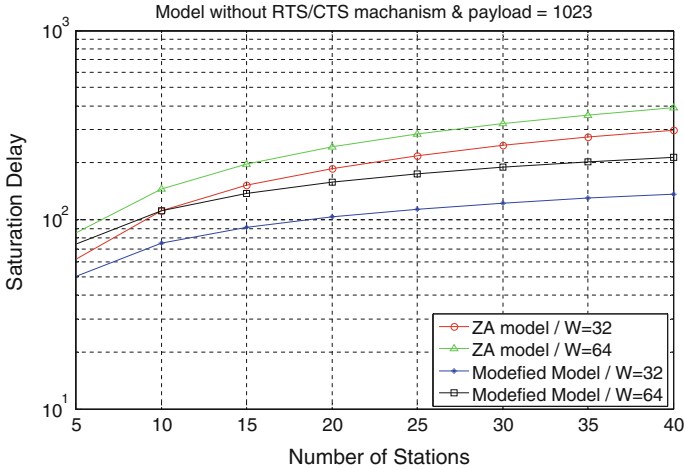


Fig. 49.6 Saturation delay versus initial window size

49.5 Conclusions

The theoretical performance and numerical results in terms of saturation throughput and delay of DCF were finished by Ziouva and Antonakopoulous. Ziouva and Antonakopoulous take account the busy medium conditions and how they affect the use of the back-off process. However, the definition of a channel busy probability is not suitable for the operating system architecture.

In this chapter, we studied the back-off process characteristics of the ZA's model with basic access schemes under an ideal channel scenario. An improved analytical model was proposed to study the behaviors of the back-off process in terms of saturation throughput and saturation delay.

Among the modified model, the numerical results show that the modified model has a better performance than the ZA's model under an ideal channel scenario because the modified model can get a better normalized back-off probability than ZA's model at $\{-1, 0\}$ state.

References

1. IEEE 802.11 WG, *Part 11: Wireless LAN Medium Access Control (MAC) and Physical Layer (PHY) Specification*, 1999
2. G. Bianchi, IEEE J. Sel. Areas Commun. **18**, 535 (2000)
3. Y. Xiao, J. Rosdahl, IEEE Commun. Lett. **6**(8), 355 (2002)
4. E. Ziouva, T. Antonakopoulos, Comput. Commun. **25**, 313 (2002)

5. H. Wu, Y. Peng, K. Long, S. Cheng, J. Ma, in *Proceedings of the IEEE Information Communications (INFOCOM)*, p. 599, 2002
6. Z. Hadzi-Velkov, B. Spasenovski, in *Proceedings of the IEEE International Conference on Communications (ICC 2003)*, vol. 26, p. 121, 2003

Chapter 50

HHT-Based Time-Frequency Features in the Berardius Baird Whistles

Chin-Feng Lin, Jin-De Zhu, Shun-Hsyung Chang, Chan-Chuan Wen,
Ivan A. Parinov and S.N. Shevtsov

Abstract This paper examined five Berardius Bairdii whistle samples and one referred sample, denoted as $ws1(t)$, $ws2(t)$, $ws3(t)$, $ws4(t)$, $ws5(t)$, and $rs1(t)$, respectively. McDonald, [1] recorded these samples in 1994 at $44^{\circ} 16.1' N$, $130^{\circ} 26.8' W$. The current study examined the Hilbert-Huang Transformation (HHT) based time-frequency features of the $ws1(t)$, $ws2(t)$, $ws3(t)$, $ws4(t)$, $ws5(t)$, and $rs1(t)$ samples. The ratios of the energy of the intrinsic mode function 1 (IMF1) to the referred total energy of $ws1(t)$, $ws2(t)$, $ws3(t)$, $ws4(t)$, and $ws5(t)$ were higher than that of the energy of IMF1 to the referred total energy of the $rs1(t)$. The energy ratio of IMF3 to the referred total energy for $ws1(t)$, $ws2(t)$, $ws3(t)$, $ws4(t)$, and $ws5(t)$ were lower than the IMF3 to the referred total energy of $rs1(t)$. The average energy ratio of IMF1 to the referred total energy of the five Berardius Bairdii whistle samples in the 9–10, 10–11, 11–12, 12–13 and 13–14 kHz bands were 10.1141, 15.7863, 17.4510, 14.0474 and 5.2079 %, respectively. The average energy ratio of IMF2 to the referred total energy of the five Berardius Bairdii whistle samples in the 4–5 and 5–6 kHz

C.-F. Lin (✉) · J.-D. Zhu

Department of Electrical Engineering, National Taiwan Ocean University,
Keelung, Taiwan, R.O.C
e-mail: lcf1024@mail.ntou.edu.tw

S.-H. Chang

Department of Microelectronic Engineering, National Kaohsiung Marine University,
Kaohsiung, Taiwan, R.O.C

C.-C. Wen

Department of Shipping Technology, National Kaohsiung Marine University,
Kaohsiung, Taiwan, R.O.C

I.A. Parinov

Vorovich Mathematics, Mechanics and Computer Sciences Institute,
Southern Federal University, Rostov-on-Don, Russia

S.N. Shevtsov

South Scientific Center of Russian Academy of Sciences, Rostov-on-Don, Russia

bands were 4.3647 and 15.9524 %, respectively. The energy ratios of IMF1 to the referred total energy of the $rs1(t)$ sample in the 9–10, 10–11, 11–12, 12–13 and 13–14 kHz bands were 4.4015, 4.2476, 5.8980, 7.6276 and 8.7352 %, respectively. The energy ratios of IMF2 to the referred total energy of the $rs1(t)$ sample in the 4–5 and 5–6 kHz bands were 1.4801 and 1.9135 %, respectively. This study determined the correlations among the whistles in the HHT time-frequency characteristics, and obtained novel information on the vocal features of the *Berardius Bairdii* whistle.

50.1 Introduction

The vocal behavior of whale is an interesting research topic. Winn et al. [2] observed that the frequency distributions of whistles and chirps of Northern bottle whale were 3–16 kHz. In addition, the frequency distributions of clicks of Northern bottle whale were 20–30 kHz. Dawson et al. [3] observed that the frequency distributions of the whistles and clicks of the *Berardius Bairdii* II were 4–8 and 15–25 kHz band, respectively. Frantzisa et al. [4] elaborated that the frequency distributions of clicks of Cuvier's beaked whale were 13–16 kHz in the time durations of 0.7–1.6 ms. Rankin et al. [5] treated that the frequency distributions of click time series of Blainville's beaked whales were 9.4–15.5 kHz in the Hawaii. In [2–5]. Fourier Transform (FT) analysis methods used to understand the physiology of whale and the related behaviors. Huang et al. [6] proposed the Hilbert-Huang transform (HHT) time-frequency method to analyze non-stationary and nonlinear data. The signal resolution of HHT time-frequency (TF) analysis method was better than that of FT and wavelet TF analysis method. Olivier [7] dissertated that the frequency resolution of HHT was better than with Fourier spectrum applying to bio-acoustic signals time-frequency analysis. Frequency evolution for each mode can be analyzed as one-dimensional signal, no need a complex 2D post-treatment using feature extraction. In the paper, the HHT-based TF features of whistles of Bairds Beaked whales studied. McDonald [1] recorded the five *Berardius Bairdii* whistle samples and one referred sample in 1994 at 44° 16.1' N, 130° 26.8' W, and the sampling frequency was 46.88 kHz.

50.2 Methods

The $wcj(t)$ signal was decomposed into N intrinsic mode functions (IMFs) and one residual function (RF) using empirical mode decomposition (EMD) method, and denoted as following:

$$w_{cj}(t) = \sum_{i=1}^N IMF_{w_{cji}}(t) + rf_{w_{cj}}(t), \quad (50.1)$$

where $w_{cj}(t)$ is the j th whistle sample of Berardius Bairdii, $IMF_{w_{cji}}(t)$ is the i th IMFs of the j th whistle sample of Berardius Bairdii, $rf_{w_{cj}}(t)$ is the RF of the j th whistle sample of Berardius Bairdii.

The energy ratios of the i th IMF to its referred total energy for the $w_{cj}(t)$ signal, $IMFERTE_{w_{cji}}$, is given by

$$IMFERTE_{w_{cji}} = \frac{IMF_{w_{cji}}^2(t)}{E_{ref}} \times 100 \%, \quad (50.2)$$

where

$$E_{ref} = \sum_{i=1}^N IMF_{w_{cji}}^2(t) + rf_{w_{cj}}^2(t).$$

The $z_{w_{cji}}(t)$ is defined as

$$z_{w_{cji}}(t) = IMF_{w_{cji}}(t) + jHT\{IMF_{w_{cji}}(t)\} = A_{w_{cji}}(t)e^{i\phi_{w_{cji}}(t)}, \quad (50.3)$$

where

$$A_{w_{cji}}(t) = \sqrt{IMF_{w_{cji}}^2(t) + [HT\{IMF_{w_{cji}}(t)\}]^2}; \quad \phi_{w_{cji}}(t) = \tan^{-1}\left(\frac{HT\{IMF_{w_{cji}}(t)\}}{IMF_{w_{cji}}(t)}\right).$$

The i th instantaneous frequencies (IF) of the j th whistle sample of Berardius Bairdii, $IF_{w_{cji}}(t)$, is defined as

$$IF_{w_{cji}}(t) = \frac{1}{2\pi} \frac{d\phi_{w_{cji}}(t)}{dt}. \quad (50.4)$$

The energy ratios of the i th IMF in the m - n kHz band to its referred total energy for the $w_{cj}(t)$ signal is calculated as

$$IMFERTE_{w_{cjimn}} = \frac{IMF_{w_{cjimn}}^2(t)}{E_{ref}} \times 100 \%, \quad (50.5)$$

where $IMF_{w_{cjimn}}(t)$ is the energy of the i th IMF in the m - n KHz band to its referred total energy for the $w_{cj}(t)$ signal.

50.3 IMFS of the Berardius Bairdii Whistles

The five Berardius Bairdii whistles and one referred samples denoted as $ws1(t)$, $ws2(t)$, $ws3(t)$, $ws4(t)$, $ws5(t)$, and $rs1(t)$, respectively, as shown in Fig. 50.1. McDonald [1] recorded these samples in 1994 at $44^{\circ} 16.1' N$, $130^{\circ} 26.8' W$, and the sampling frequency was 46.88 kHz. The average absolute amplitudes of the $ws1(t)$, $ws2(t)$, $ws3(t)$, $ws4(t)$, $ws5(t)$ and $rs1(t)$ were $0.1146v$, $0.1103v$, $0.1143v$, $0.1119v$, $0.1026v$ and $0.0454v$, respectively. The time interval of observations was 10 ms. The absolute amplitude variances of the $ws1(t)$, $ws2(t)$, $ws3(t)$, $ws4(t)$, $ws5(t)$, and $rs1(t)$ were $0.2387v^2$, $0.2429v^2$, $0.2408v^2$, $0.2345v^2$, $0.2236v^2$ and $0.1140v^2$. The $ws1(t)$ signal was decomposed into 10 IMFs and one RF using EMD method. The IMF1, IMF2, IMF3 and IMF4 of the $ws1(t)$ and $rs1(t)$, respectively. The energy ratios of the IMF1, IMF2, IMF3 and IMF4 to the referred total energy of $ws1(t)$, $ws2(t)$, $ws3(t)$, $ws4(t)$, $ws5(t)$ and $rs1(t)$ signals were drew in Fig. 50.2. The “blue”, “light blue”, “yellow”, and “brown” denoted as the energy ratios of the IMF1, IMF2, IMF3 and IMF4 to the referred total energy, respectively. From Fig. 50.2, we see that the relations of $IMFERTE_{wcji}$ and $IMFERTE_{rs1i}$ were dissertated as the following:

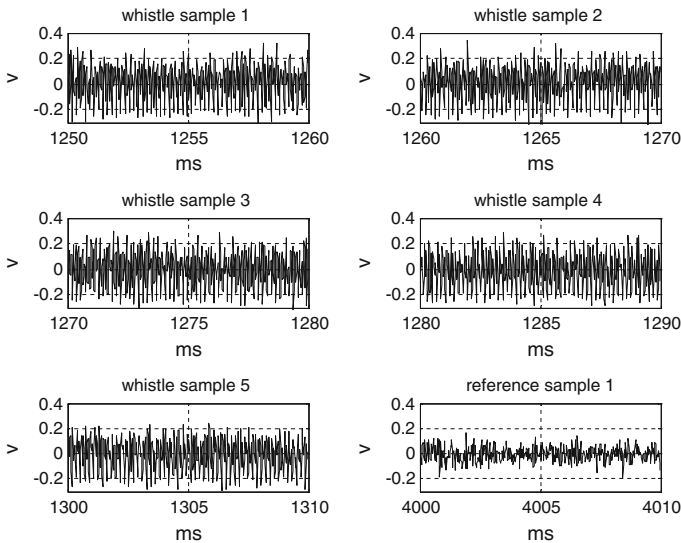
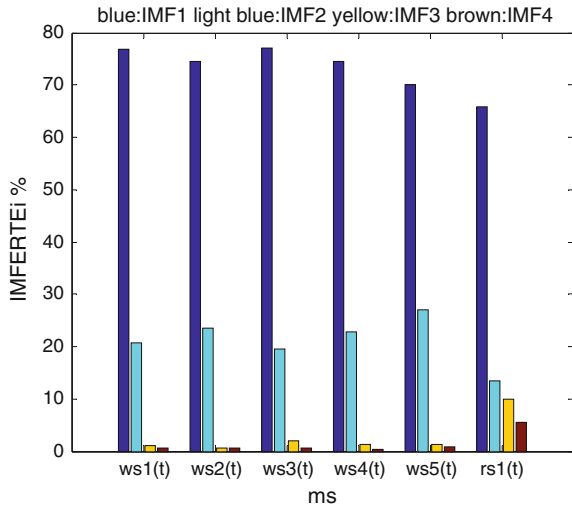


Fig. 50.1 Five Berardius Baird whistle and one referred samples

Fig. 50.2 Energy ratios of the IMF1, IMF2, IMF3, and IMF4 to their referred total energy of the $ws1(t)$, $ws2(t)$, $ws3(t)$, $ws4(t)$, $ws5(t)$ and $rs1(t)$ signals



$$\begin{aligned}
 & IMFERTE_{wc11} > IMFERTE_{wc31} > IMFERTE_{wc21} > IMFERTE_{wc41} \\
 & IMFERTE_{wc41} > IMFERTE_{wc51} > IMFERTE_{rs11} > 65 \% \\
 & IMFERTE_{wc52} > IMFERTE_{wc22} > IMFERTE_{wc42} > IMFERTE_{wc12} \\
 & IMFERTE_{wc12} > IMFERTE_{wc32} > IMFERTE_{rs12} > 10 \% \\
 & IMFERTE_{rs13} > IMFERTE_{wc33} > IMFERTE_{wc43} > IMFERTE_{wc53} \\
 & IMFERTE_{wc53} > IMFERTE_{wc13} > IMFERTE_{rs23}
 \end{aligned}$$

We see that the energy ratios of the IMF1 and IMF2 to its referred total energy of the five whistle signals are higher than that of the IMF1 and IMF2 to its referred total energy of $rs1(t)$, respectively. The energy ratios of the IMF3 and IMF4 to its referred total energy of the five whistle signals are lower than that of the IMF3 and IMF4 to its referred total energy of $rs1(t)$, respectively.

50.4 MFS of the Berardius Baird Whistles

Figures 50.3 and 50.4 show the marginal frequencies (MFs) of IMF1 and IMF2 of $ws1(t)$, $ws2(t)$, $ws3(t)$, $ws4(t)$, $ws5(t)$ and $rs1(t)$. The average ratios of the energy of IMF1 to their referred total energy of the five whistle signals, in the 8–9, 9–10, 10–11, 11–12, 12–13 and 13–14 kHz bands were 5.3857, 10.1141, 15.7863, 17.4510, 14.0474 and 5.2079 %, respectively. The average ratios of the energy of IMF2 to their referred total energy of the five whistle signals, in the 4–5, 5–6, and 6–7 kHz bands were 4.3647, 15.9524 and 2.1056 %, respectively. Figure 50.4 shows the MF1 and MF2 of $rs1(t)$. The average ratios of the energy of IMF1 to the

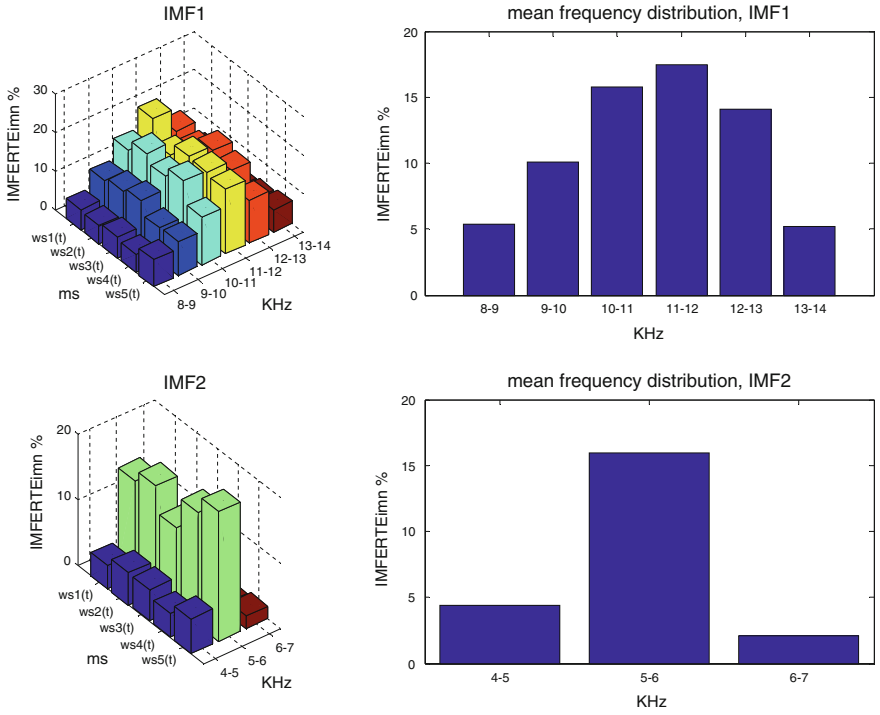


Fig. 50.3 MF1 and MF2 of the five whistle signals

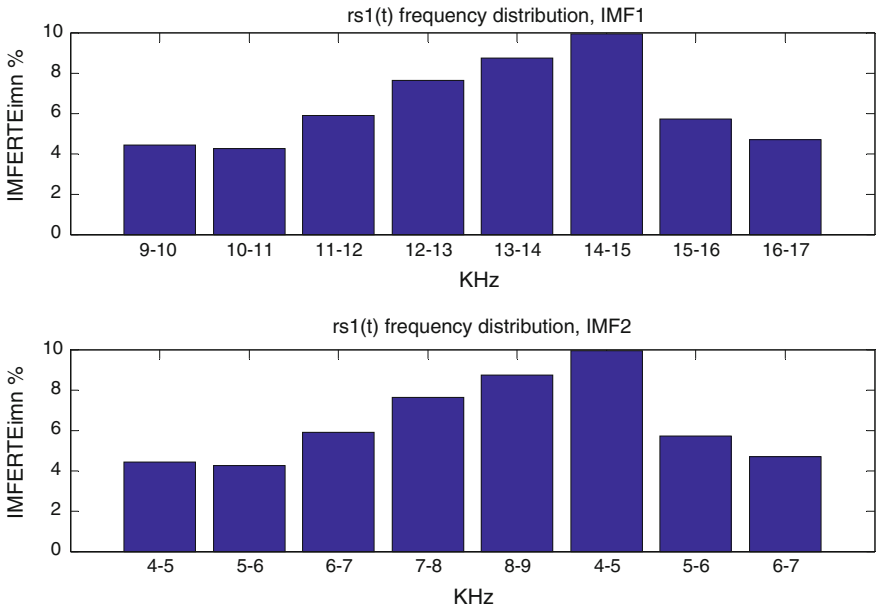


Fig. 50.4 MF1 and MF2 of rs1(t)

referred total energy of $rs1(t)$, in the 9–10, 10–11, 11–12, 12–13, 13–14, 14–15, 15–16 and 16–17 kHz bands were 4.4015, 4.2476, 5.8980, 7.6276, 8.7352, 9.9430, 5.6893 and 4.6933 %, respectively. The average ratios of the energy of IMF2 to the referred total energy of $rs1(t)$, in the 4–5, 5–6, 6–7, 7–8 and 8–9 kHz bands were 1.4801, 1.9135, 2.2181, 3.3650 and 2.0931 %, respectively.

50.5 Conclusions

The energy distributions of the five *Berardius Bairdii* whistle samples concentrate in the IMF1 and IMF2. The average ratios of the energy of IMF1 to the referred total energy of the five whistle samples were higher in the 9–10, 10–11, 11–12 and 12–13 kHz bands than the energy of IMF1 to the referred total energy of $rs1(t)$ in the 9–10, 10–11, 11–12 and 12–13 kHz bands, respectively. The average ratios of the energy of IMF1 to the referred total energy of the five whistle samples, in the 13–14 kHz band was lower than the energy of IMF1 to the referred total energy of $rs1(t)$ in the 13–14 kHz band. The average ratios of the energy of IMF2 to the referred total energy of the five whistle samples in the 4–5 and 5–6 kHz bands were higher than the energy of IMF2 to the referred total energy of $rs1(t)$ in the 4–5 and 5–6 kHz bands, respectively. The average ratio of the energy of IMF2 to the referred total energy of the five whistle samples in the 6–7 kHz band was lower than the energy of IMF2 to the referred total energy of $rs1(t)$ in the 6–7 kHz band.

Acknowledgments The authors acknowledge the support of the NSC 103-2221-E-022-015 and the valuable comments of the reviewers. Ivan A. Parinov acknowledges financial support of the Russian Ministry of Education and Sciences in the framework of “Organization of Scientific Research” Government Assignment (No. 654).

References

1. M. McDonald, *Berardius recordings*, www.whaleacoustics.com
2. H.E. Winn, P.J. Perkins, L. Winn, Sounds and Behavior of the Northern Bottlenose Whale. in *Proceedings of the 7th Annual Conference on Biological Sonar and Diving Mammals*, p. 53 (1970)
3. D. Stephen, J. Barlow, D. Ljungblad, *Mar. Mammal Sci.* **14**(2), 335 (1998)
4. F. Alexandros, C.G. John, K.S. Emmanuel, I.T. Michael, K. Varvara, *J. Acoust. Soc. Am.* **112**(1), 34 (2002)
5. R. Shannon, B. Jay, *J. Acoust. Soc. Am.* **122**(1), 42 (2007)
6. N.E. Huang, S.S.P. Hen, *Hilbert-Huang Transform and its Applications* (World Scientific Publishing Co., Singapore, 2005)
7. A. Olivier, *J. Acoust. Soc. Am.* **120**(5), 2965 (2006)

Curriculum Vitae

Prof. Ivan A. Parinov

Dr. Sc. Ivan A. Parinov received the MSc in Mechanics from the Rostov State University, Mechanics and Mathematics Department in 1978 (Rostov-on-Don, Russia), the Ph.D. in Physics and Mathematics from the Rostov State University in 1990 and the Dr. Sc. in Techniques from the South-Russian State Technical University in 2008. He is Corresponding Member of Russian Engineering Academy (2014) He is working in the Vorovich Mathematics, Mechanics and Computer Sciences Institute of the Southern Federal University (former Rostov State University) from 1978. Today, he is Chief Research Fellow. He has head in 1993–2015 the Research Grants and Programs from Soros Foundation, Collaboration for Basic Science and Education (COBASE, USA), Russian Foundation for Basic Research (10 grants), Russian Ministry for Science and Education (7 grants and scientific proposals). He has published above 260 scientific-technical publications among them 18 monographs (in particular, 3 books published with Springer and 9 books with Nova Science Publishers). He has 10 Russian and Soviet patents and 3 certificates on Russian state registration of programs for computer. Dr. Sc. Ivan A. Parinov is reviewer of *Zentralblatt fur Mathematik* (Germany) and *Mathematical Reviews* (USA) from 1994 (around 450 reviews), review papers of journal *SOP Transactions on Theoretical Physics* (Scientific Online Publishing) from 2013. He was INTAS expert (2004), FP-7 expert (2010), ERA.NET RUS expert (2011, 2015) and he is Russian Federal expert of scientific-technical area (2012–2015). He is winner of competition of the Russian Department of Education and Science (2014–2016) on direction “Organization of Fulfillment of the Scientific Researches” in Southern Federal University. Dr. Sc. Ivan A. Parinov is Active Member of the New York Academy of Sciences (1994), member of the American Mathematical Society from 1996 and the European Mathematical Society from 1998, and has honorary title “Honorary Member of All-Russian Society of Inventors and Rationalizers” (2008). His research interests include R&D of novel materials and composites (in particular, high-temperature superconductors and ferro-piezoelectrics), fracture mechanics and

strength physics, acoustic emission, mathematical modeling, application of advanced materials and composites. More common information locates into INTERNET-page: <http://www.math.rsu.ru/niimp/strl/welcome.en.html>.

Books (2012–2015)

1. *Ferroelectrics and Superconductors: Properties and Applications*, **Ivan A. Parinov** (Ed.). New York: Nova Science Publishers. 2012. 287 p. ISBN: 978-1-61324-518-7.
2. *Piezoelectric Materials and Devices*, **Ivan A. Parinov** (Ed.). New York: Nova Science Publishers. 2012. 328 p. ISBN 978-1-61728-307-9.
3. *Piezoelectrics and Related Materials: Investigations and Applications*, **Ivan A. Parinov** (Ed.). New York: Nova Science Publishers. 2012. 306 p. ISBN: 978-1-61942-387-9.
4. **I. A. Parinov**. *Microstructure and Properties of High-Temperature Superconductors*. Second Edition. Heidelberg, New York, Dordrecht, London: Springer. 2012. 779 p. ISBN 978-3-642-34440-4.
5. *Physics and Mechanics of New Materials and Their Applications*, **Ivan A. Parinov, Shun Hsyung-Chang** (Eds.). New York: Nova Science Publishers. 2013. 444 p. ISBN 978-1-62618-535-7.
6. *Nano- and Piezoelectric Technologies, Materials and Devices*, **Ivan A. Parinov** (Ed.). New York: Nova Science Publishers. 2013. 261 p. ISBN: 978-1-62948-230-9.
7. *Advanced Materials - Physics, Mechanics and Applications. Springer Proceedings in Physics*, V. 152, **Shun-Hsyung Chang, Ivan A. Parinov, Vitaly Yu. Topolov** (Eds.). Heidelberg, New York, Dordrecht, London: Springer Cham. 2014. 380 p. ISBN: 978-3319037486.
8. *Advanced Nano- and Piezoelectric Materials and their Applications*, **Ivan A. Parinov** (Ed.). New York: Nova Science Publishers. 2014. 250 p. ISBN: 978-1-63321-239-8.
9. *Advanced Materials - Studies and Applications*, **I. A. Parinov, S. H. Chang, S. Theerakulpisut** (Eds.). New York: Nova Science Publishers. 2015. 527 p. ISBN: 978-1-63463-749-7.
10. *Piezoelectrics and Nanomaterials: Fundamentals, Developments and Applications*, **Ivan A. Parinov** (Ed.). New York: Nova Science Publishers. 2015 (presented for publication).

Prof. Shun-Hsyung Chang

Dr. Shun-Hsyung Chang received the Ph.D. degree in electrical engineering from National Sun-Yat Sen University, Taiwan, in 1990. Afterwards, he served as an associate professor and has been a professor since 1997 in the Department of Electrical Engineering at National Taiwan Ocean University, Keelung, Taiwan, where he was the chairman 1998–2003. He also had served as the Vice President of National Kaohsiung Marine University, Kaohsiung, Taiwan, during 2003–2006. He is a professor in the Department of Microelectronic Engineering at this university presently. He has published over 280 scientific-technical papers. His research interests include underwater signal processing, electrical engineering, and communication engineering. His outstanding performance in research brought him great honor. In 1984, he was granted “The Creative Youth” prize by the Ministry of Education. He received the Long-Term Paper Award, organized by Acer Incorporated, in 1994, 1996 and 1998. He and his graduate students won the Third Prize of Graduate Team in TI-Taiwan 1994 DSP Design Championship. He also obtained the Distinguished Award in the contest of Special Topic of Communication System in graduate division held by the Ministry of Education in 2000. He contributes greatly in editorship. He was the editor-in-chief of the Journal of Marine Science and Technology 1998–2001, of which he is an editor at present. He is currently the editor-in-chief of the Journal of Ocean and Underwater Technology 2008–2015.

Books, Referred International Journal Papers and Book Chapters (2013–2015)

1. *Advanced Materials - Studies and Applications*, **I. A. Parinov, S. H. Chang, S. Theerakulpisut** (Eds.). New York: Nova Science Publishers. 2015. 527 p. ISBN: 978-1-63463-749-7
2. *Advanced Materials - Physics, Mechanics and Applications. Springer Proceedings in Physics*, V. 152, **Shun-Hsyung Chang, Ivan A. Parinov, Vitaly Yu. Topolov** (Eds.). Heidelberg, New York, Dordrecht, London: Springer Cham. 2014. 380 p. ISBN: 978-3319037486.
3. *Physics and Mechanics of New Materials and Their Applications*, **Ivan A. Parinov, Shun Hsyung-Chang** (Eds.). New York: Nova Science Publishers. 2013. 444 p. ISBN 978-1-62618-535-7.
4. Min Yen Yeh, Yi Cheng Lee, Kun Fu Hsu, Chyi-Da Yang, Cheng-Liang Huang, Po-Hsun Lei, **Shun-Hsyung Chang**. Chapter 2. Hydrothermal Preparation of NaTaO₃ Photocatalyst Materials. P. 29–38. In: *Advanced Materials - Studies and Applications*, **I. A. Parinov, S. H. Chang, S. Theerakulpisut** (Eds.). New York: Nova Science Publishers. 2015. 527 p. ISBN: 978-1-63463-749-7.

5. Chyi-Da Yang, Chia-Hsiang Chou, Yu-Cheng Kung, Cheng-Liang Huang, Min-Yen Yeh, Jiing-Kae Wu, Huoo-Yuan Jenq, Jenq-Der Chen, Chih-Yu Lee, Chiung-Hsing Chen, **Shun-Hsyung Chang**. Chapter 26. Colorful Flashing LED Night Pearls for Marine Application. P. 453–474. In: *Advanced Materials - Studies and Applications*, **I. A. Parinov, S. H. Chang, S. Theerakulpisut** (Eds.). New York: Nova Science Publishers. 2015. 527 p. ISBN: 978-1-63463-749-7.
6. C. F. Lin, T. K. Chan, C. C. Wen, **S. H. Chang, I. A. Parinov**, S. N. Shevtsov. Chapter 28. Hilbert-Huang Transform Based Features for Underwater Voice (II) Transmission. P. 487–498. In: *Advanced Materials - Studies and Applications*, **I. A. Parinov, S. H. Chang**, S. Theerakulpisut (Eds.). New York: Nova Science Publishers. 2015. 527 p. ISBN: 978-1-63463-749-7.
7. A. N. Soloviev, N. D. T. Giang, **S.-H. Chang**. Chapter 12. Determination of Elastic and Dissipative Properties of Material Using Combination of FEM and Complex Artificial Neural Networks. P. 137–148. In: *Advanced Materials - Physics, Mechanics and Applications*. Springer Proceedings in Physics, V. 152, **Shun-Hsyung Chang, Ivan A. Parinov, Vitaly Yu. Topolov** (Eds.). Heidelberg, New York, Dordrecht, London: Springer Cham. 2014. 380 p. ISBN: 978-3319037486 .
8. Andrey Nasedkin, Maria Shevtsova, **Shun-Hsyung Chang**. Chapter 20. Optimal Design of Underwater Acoustic Projector with Active Elements Made from Porous Piezoceramics. P. 251–262. In: *Advanced Materials - Physics, Mechanics and Applications*. Springer Proceedings in Physics, V. 152, **Shun-Hsyung Chang, Ivan A. Parinov, Vitaly Yu. Topolov** (Eds.). Heidelberg, New York, Dordrecht, London: Springer Cham. 2014. 380 p. ISBN: 978-3319037486.
9. C.F. Lin, K. J. Hsiao, C. C. Wen, **S. H. Chang, I. A. Parinov**. Chapter 24. Hilbert-Huang Transform Based Instantaneous Frequency Features for Underwater Voice (I) Transmission. P. 307–312. In: *Advanced Materials - Physics, Mechanics and Applications*. Springer Proceedings in Physics, V. 152, **Shun-Hsyung Chang, Ivan A. Parinov, Vitaly Yu. Topolov** (Eds.). Heidelberg, New York, Dordrecht, London: Springer Cham. 2014. 380 p. ISBN: 978-3319037486.
10. C. F. Lin, **S. H. Chang**, W. C. Wu, W. H. Chen, K. H. Chang, C. Y. Lee Jenny, **I. A. Parinov**. Underwater Acoustic Multimedia Communication Based on MIMO-OFDM // *Wireless Personal Communications*, 2013. Vol. 71, No 2. P. 1231–1245.

Prof. Vitaly Yu. Topolov

Prof., Dr. Sc. Vitaly Yuryevich Topolov received the MSc in Physics from Rostov State University, Physics Faculty in 1984 (Rostov-on-Don, Russia), the Ph.D. in Physics and Mathematics from Rostov State University in 1987 and the Dr. Sc. in

Physics and Mathematics from Rostov State University in 2000. He is working in Physics Department of Southern Federal University (former Rostov State University) from 1984. Today, he is professor of the Chair for Technical Physics at Southern Federal University. He is corresponding member of Russian Academy of Natural Science from 2010. He was Soros's Assistant Professor in 1997, 1998, 2000, 2001. Prof. V.Yu. Topolov 7 times has been included into list of active Russian scientists having more 100 citations on his papers, and the total number of citations of his papers exceeds 1100 since 1987. He published more than 380 works, including four books with Springer. He conducted joint investigations in Switzerland (1992, 1995), Germany (1994–95, 1998, 2002, 2003–04), Great Britain (2006, 2007, 2012, 2013, 2014), Italy (2008). He has led Research within the framework of Grants and Programs from Soros Foundation, German Research Society, Helmholtz Society, Royal Society (London), University of Bath (GB), Russian Foundation for Basic Research, Russian Ministry for Science and Education (1994–2013). W. Leibniz medal and Gold medal “European Quality” (2014). His research interests include physics of ferro-, piezo-active and related materials, electromechanical effects, domain structures and heterophase states in ferroelectrics and related materials.

<http://www.phys.rsu.ru/index.php?l=rus&c=poluprovodniki&id=topolov>

Referred International Journal Papers and Books (2013–2015)

1. *Advanced Materials - Physics, Mechanics and Applications. Springer Proceedings in Physics*, V. 152, **Shun-Hsyung Chang, Ivan A. Parinov, Vitaly Yu. Topolov** (Eds.). Heidelberg, New York, Dordrecht, London: Springer Cham. 2014. 380 p. ISBN: 978-3319037486.
2. **Topolov V.Yu.**, Bisegna P., Bowen C.R. Piezo-active Composites. Orientation Effects and Anisotropy Factors. Berlin, Heidelberg: Springer, 2014. 169 p.; XV. ISBN 978-3-642-38353-3.
3. **Vitaly Topolov**, Paolo Bisegna, Christopher R. Bowen. *Piezo-Active Composites: Orientation Effects and Anisotropy Factors*. London: Springer. 2013. 200 p., ISBN: 978-3642383533
4. Topolov V.Yu. *Heterogeneous Ferroelectric Solid Solutions. Phases and Domain States*. Berlin, Heidelberg: Springer, 2012. 156 p.; XIII. ISBN 978-3-642-22482-9.
5. Bowen C.R., Taylor J., Le Boulbar E., Zabeka D., **Topolov V.Yu.** A modified figure of merit for pyroelectric energy harvesting // *Mater. Letters*. 2015. Vol. 138, N 1. P. 243–246.
6. **Topolov V.Yu.**, Bowen C.R. High-performance 1-3-type lead-free piezo-composites with auxetic polyethylene matrices // *Mater. Letters*. 2015. Vol. 142, N 1. P. 265–268.

7. **Topolov V.Yu.**, Bowen C.R., Bisegna P., Krivoruchko A.V. New orientation effect in piezo-active 1-3-type composites // Mater. Chem. Phys. 2015. Vol. 151, N 1. P. 187–195.
8. **Topolov V.Yu.**, Filippov S.E., Panich A.E., Panich E.A. Highly anisotropic 1-3-0 composites based on ferroelectric ceramics: Microgeometry - volume-fraction relations // Ferroelectrics. 2014. Vol. 460. P. 123–137.
9. Bowen C.R., **Topolov V.Yu.** Polarisation orientation effects and hydrostatic parameters in novel 2-2 composites based on PMN-xPT single crystals // Ferroelectrics. 2014. Vol. 466. P. 21–28.
10. Filippov S.E., Vorontsov A.A., **Topolov V.Yu.**, Brill O.E., Bisegna P., Panich A.E. Features of the piezoelectric effect in a novel PZT-type ceramic / clay composite // Ferroelectrics Lett. Sec. 2014. Vol. 41, NN 4–6. P. 82–88.

Index

0-9

- 0-3 FC, 186, 189, 193
- 0-3 matrix, 179, 181-183, 185-191, 193
- 1-0-3 composite, 179, 180, 182, 183, 185-193
- 1-0-3 relaxor-ferroelectric, 181
- 3d, 512
- 3d poroelastic column, 512

A

- A1-type of symmetry, 264
- Ab initio*, 279, 280, 282, 292, 295
- Accelerometer, 563, 564, 571, 572, 574
- ACELAN, 651, 653, 654, 658
- ACK CSMA/CA, 681
- Acknowledgement (ACK), 676, 677, 682
- Acoustic, 622-635
- Acoustic fields, 606, 608
- Acoustic measurement, 664
 - pulse tube, 659
- Acoustic signals, 664, 666
- Active strip, 591-600
- Analytical electron microscopy, 3, 5, 10, 11
- Anatase, 51-55, 59
- Anisotropy, 157, 169, 517
- ANSYS, 651, 653, 654, 658
- Antiferroelectrics, 251
- Antifriction fillers, 539
- Atomic force microscopy (AFM), 61, 67, 72, 74, 564, 568-571, 573-575, 577-579

B

- Berardius Baird whistle, 690, 691
- Berardius Bairdii, 688, 689
- Berardius Bairdii whistle, 687, 688, 690, 693
- $\text{Bi}_{1-x}\text{La}_x\text{FeO}_3$, 259-266
- $\text{Bi}_{1-x}\text{La}_x\text{FeO}_3$ solid solutions, 261
- BiFeO_3 , 79, 81, 82, 84, 259-261, 263, 265, 266
- BiFeO_3 phase formation, 80

- Binary composite, 541
- Bismuth ferrite (BiFeO_3), 79, 81, 259, 260
- Bleustein-Gulyaev wave (BGW), 413, 424-426
- Boundary-element method (BEM), 505, 506, 509, 517, 518, 524
- Boundary element scheme, 506
- Boundary integral equation (BIE) method, 431, 433, 437
- Braking, 551-554, 556, 557

C

- Carbon, 551
- Carbon composites, 552, 556
- Carbon nanotube (CNT), 299, 300, 302-304, 312, 581, 582, 584-586, 589
- Carrier sense multiple access with collision avoidance (CSMA/CA) protocol, 676, 677
- Cauchy's argument principle, 321
- Ceramic, 79-86, 245-247, 250
- Ceramic matrix composites, 224
- Ceramic matrix piezocomposites, 211, 213
- Ceramic technology, 245, 250, 260
- Circuit, 670, 671, 673
- Circuit elements, 671
- Circuit transformations, 669, 672, 673
- Clay, 198, 200-208
- Clay composite, 198, 199, 201
- Column, 511, 512, 514, 515
- Combined magnetic field sensor, 599, 600
- Complex, 321
- Complex constants, 211, 221
- Complex propagation constant, 318, 322
- Components, 663
- Composite, 197, 198, 201-209, 363-366, 539-544, 547, 548, 550
- Composite laminates, 450
- Composite material, 539, 540, 544, 547, 550

- Composite structures, 449
 Conducting polymer, 62, 64
 Connectivity, 197, 203, 205, 206
 Continuous, 619
 Control object, 341, 342
 Copper oxides, 301
 Constitutive relations, 374, 394, 395, 399, 401, 405, 407, 409–411, 413, 652
 Crack closure, 489, 492, 493, 502, 503
 Cracks, 432
 Crack-tip residual stress, 498, 503
 Crystal growth, 88–90
 Cu, 117, 119, 120, 126
 Cu₂O, 300–306, 308–313
 CuO, 300–313
 Czocharski method, 88
- D**
- Damping, 374, 375, 378, 380, 386, 388, 389
 DCF inter-frame space (DIFS), 676, 677, 682
 Defect detection, 476
 Deformation, 393, 394, 397–400, 402, 403, 405, 408, 410
 Density functional theory (DFT), 279, 280, 282, 284, 285, 289–296
 Density matrix, 157, 159–165, 177
 Design, 117, 126
 Design constraints, 641
 Dielectric permittivity, 229–232, 238, 242
 Diffraction, 81–83, 86, 141, 142, 144, 145, 148
 Diffraction grating, 153
 Diffusion kinetics, 498, 499, 501
 Disorder, 261, 263
 Disordered, 259, 264
 Disordering, 266
 Dispersion, 320, 321, 323–326
 Dispersion characteristics, 318, 322, 325
 Distributed coordination function (DCF), 675–677, 682
 Distributed inter-frame space (DIFS), 677
 Distribution of temperature, 107
 Dopant, 90
 Doped, 87, 89, 91
 Doping, 87, 88
 DRIFTS, 5
 DRIFTS analysis, 19
 Dynamic, 374, 376, 506, 507
 Dynamical treatment, 619
 Dynamic analysis, 641
 Dynamic problem, 374, 378, 380, 389
- E**
- Effect, 591, 592
 Efficient modules, 539, 547
 Efficient moduli, 540
 Eigenvalue, 384, 385
 Elastic guided waves (GWs), 450
 Elasticity, 517
 Elastic wave, 431–433, 444, 445
 Electric field, 280–282, 287, 288, 291–293, 296
 Electric load circuit, 639, 640
 Electro-mechanical coupling coefficients, 654
 Electrocatalyst, 37, 45, 48
 Electrochemical deposition, 299–303, 312
 Electrode potential, 3, 6, 15, 16, 18, 19
 Electrolyte, 329–336, 338
 Electromechanical interaction, 201, 207, 208
 Electromotive force (EMF), 329, 332–336, 338
 Electron distribution, 157, 165, 166, 168
 Electron interaction, 167
 Elements, 670
 Energy gap, 157, 174
 Energy harvesting, 329, 330, 639, 640, 648
 Experiments, 621, 624, 630, 634–636
- F**
- Fast compression wave, 506
 Fatigue limit, 489, 490–493, 496, 502
 FC composite, 205
 Fenton-like reaction, 115, 117, 118, 120–123, 126
 Fenton-like reaction procedure, 118
 Fenton oxidation reaction, 116
 Fenton reaction, 116
 Fermi level, 333, 337, 338
 Ferroelectric, 229, 231, 246–248, 251, 394–397, 405, 410, 411
 Ferroelectric ceramic (FC), 180–193, 197, 198, 201, 203, 205–209, 229, 230, 232–234, 237, 239, 242
 Ferroelectric materials, 393
 Ferromagnets, 259, 260
 Fiber-reinforced laminate composite plates, 456
 Filler, 539–543, 547, 550
 Film, 591–594, 596–599
 Finite amplitude, 661
 Finite amplitude pump waves, 667
 Finite element, 374, 376, 381–383, 534, 542, 651
 Finite-element analysis, 539, 543
 Finite element approaches, 389
 Finite element method, 384, 478, 528
 Finite-element modeling, 530
 Finite element models, 389
 Finite element problems, 389
 Finite element technique, 381

Flotation, 4, 6, 15, 18–20
 Focusing, 431–433, 440, 441, 445, 446
 Formulation, 389
 Frequency response, 384
 Frequency response analysis (FRA), 656
 Friction transfer film (FTF), 536, 537
 Fuel cell, 37, 38, 48
 Full factorial, 126
 Full factorial design (FFD), 116
 Functionally graded, 417, 419, 421–423
 Functionally graded material, 413

G

GaAs, 577–579
 GaAs nanowires (NWs), 563, 565, 577–579, 579
 Giant magnetoresistive effect, 591, 592
 Gel, 51, 52, 55
 Gel method, 304, 305
 Geometrical parameters, 317, 322, 563, 564, 568, 570
 Giant, 591, 592
 Glass-dipole state, 229, 238, 242
 Graphene, 279–284, 286–288, 292, 294–296
 Graphene-based nanoelectronic devices, 281
 Graphene nanoribbons (GNRs), 280, 281
 Graphene semiconductor, 279
 Grating, 143, 144
 Green's matrix, 449–451
 Growing conditions, 98
 Growing of the crystals, 90
 Growth, 94
 Growth conditions, 87, 90
 Growth from melt, 98
 Guided wave (GW), 449, 450, 452–455, 457, 475–477, 480, 481–484
 Gyroscope, 563, 564, 571, 572, 574

H

Hamiltonian, 160–164
 Harmonic, 389, 603, 609–612, 619
 Harmonic analysis, 385
 Harmonic law, 383
 Harmonic oscillations, 413
 Harmonic problem, 385, 378, 383, 385, 389
 HDC method, 102, 103, 105
 Heating due to friction, 532
 HIFU transducer, 608, 609, 612, 614, 621
 High-cycle fatigue (HCF), 489, 490
 High-harmonic components, 659, 667
 High-intensity focused ultrasound (HIFU), 603–608, 611, 613–616, 619, 621, 624, 625, 629–636
 Higher harmonic, 663, 664

Higher harmonic components, 663
 High-power (high-voltage) nanosecond pulses, 3, 4
 Hilbert-huang transformation (HHT), 687, 688
 Horizontal directed crystallization (HDC), 101, 104
 Hydrostatic parameters, 180, 183, 185, 189, 193

I

Image segmentation, 270
 Indentation, 544, 546
 Inhomogeneous coating, 413
 Initial stressed state, 423
 Initial stresses, 413, 424–428
 Initially deformed state (IDS), 414, 423–428
 Integral approach, 431, 435
 Integral equations, 459
 Integral representations, 450
 Interaction energy, 157
 Interference pattern, 343–347
 Intrinsic mode function (IMF), 687–691, 693
 Inversion of Laplace transform, 506
 Inverting Laplace transform, 505
 IR-pyrolysis, 68
 IR radiation, 581, 584, 585, 589

L

Laminate composite materials, 449
 Laminate structures, 450
 Laplace domain, 517, 520, 521, 525
 Laplace transform, 505, 518–521
 Laplace transform inversion, 510
 Laplace transform numerical inversion, 506, 510
 Laser interferometer, 341
 Layered composites, 457
 Layered fiber-reinforced composite structures, 450
 Lead zirconate-titanate, 229
 Leonardite, 129–134
 Librational vibrations, 266
 Librations, 266
 Librations (torsional oscillations) of oxygen octahedrons O₆, 264, 266
 Lignin degradation, 115, 117, 118, 120–126
 Lithium niobate, 88, 90, 91, 94
 Localization, 431–433, 440–442, 444, 446
 Long-range ultrasonic guided waves, 475
 LPAHs, 29

M

Magnetic field concentrator (MFC), 591
 Magnetocardiographs, 599

- Magnetocardiography, 592
 Magnetolectric, 259, 260, 374, 375, 384
 Magnetolectric bodies, 375, 378, 380, 389
 Magnetolectric material, 373, 376, 388
 Magnetolectric media, 376, 389
 Magnetolectric medium, 376
 Magnetolectric solid, 378
 Magnetoencephalography, 592, 599
 Magnetoresistive, 591, 592
 Material, 539
 Material temperature measurement, 357, 358
 Mathematical models, 211, 212, 217, 227
 MCM-41, 116, 117, 119, 120, 126
 Measurement of displacements, 341, 342
 Mechanical stress, 395, 397, 403–408, 411
 Medium access control (MAC), 675, 676, 682
 MEMS, 564
 Mesh electrode, 330–332, 334, 335
 Metal fatigue, 489–491, 494, 499, 502, 503
 Metal–insulator–semiconductor–metal (MISM), 335, 338, 339
 Method, 51, 52, 57, 59, 104
 Method of mode expansion, 385
 Method of mode superposition, 385, 389
 Method of variables separation, 317, 318
 Methods of fabrication, 211, 227
 Microindentation, 544
 Microdomains, 229, 231, 232
 Microstructure, 211, 216–218, 224, 227, 363, 370
 Microwave, 245–248, 250, 252–256
 Mobility, 279–281, 285, 294, 295
 Mode, 384, 385
 Modeling, 621, 625, 627, 629, 636
 Mode superposition method, 385, 386
 Molecular beam epitaxy (MBE), 565, 577, 578
 Monocrystals, 101
 Morphological, 310
 Morphology, 299–302, 304–306, 310, 312, 313
 Multiferroics, 79, 80
 Multifractal, 260, 269, 271
 Multifractal analysis, 265, 266
 Multifrequency navigation system, 660
 Multinomial measurement, 270, 271
- N**
- Nano, 26
 Nanocomposites, 299–308, 308, 310, 312
 Nanoindentation, 544
 Nanomaterials, 564
 Nanoparticles, 37–39, 42, 45, 47, 48, 52, 299–305, 312, 313
 Nanoribbon, 285, 288, 290
 Nanostructure, 565, 567, 574–576
 Nanotechnology, 564
 Nano–zero–valent iron (nZVI), 23, 26–28, 30–33
 Near-threshold crack growth, 496, 501
 NEMS, 374
 Non-contacting method, 357, 358
 Non-uniform, 651, 652, 655, 656
 Non-uniform polarization, 652, 653, 655
 Normal incidence, 460
 Nullor, 669
 Nullor-mirror, 669–671
 Nullor-mirror elements, 670, 672, 673
 Numerical, 621, 624, 625, 627–629
 NZVI–PS, 23
- O**
- One-mode propagation, 460, 462
 Ordering, 259, 264
 Ordering of structure, 264, 266
 Ordering of structure units, 259
 Ordering processes in structure, 260
 Output power optimization, 643
 Oxidation state, 299, 300, 302, 304, 305, 310–312
 Oxygen octahedrons librations, 259, 264
- P**
- PAN thin films, 67, 76
 Parameters, 260
 Partially saturated, 505
 Partially saturated poroelastic column, 513
 Partially saturated poroelasticity, 508
 Pathological, 670
 Pathological elements, 669
 Pathological representations, 670
 Peltier, 335, 336
 Peltier heat, 329, 335
 Periodic composites, 432
 Perovskite, 261, 263, 264, 266
 Persulfate (PS), 23–28, 27, 32, 33
 Phase-coupled multiple, 659
 Phase analysis, 260
 Phase formation, 79, 82
 Phase transition, 229–232, 236, 238, 240, 242
 Phononic crystal, 431–433, 435, 438–442, 445, 446
 Photocatalysis, 51

- Photoconductivity, 583
Photodetectors, 583
Photosensitivity, 581–583, 589
Piezoceramics, 231
Piezoelectric, 373, 374, 376, 378, 388, 389
Piezoelectric coefficient, 182–185, 187–191, 193, 198, 201–204, 205, 206, 208
Piezoelectric stack, 639, 640, 642, 643, 648, 649
Piezoelectric structure, 413, 414, 418, 427, 428
Piezoelectric wafer active sensors (PWAS), 449, 450, 453–455
Piezoelectricity, 383
Piezotransducer, 651
Plackett-Burman, 115–117, 126
Plackett-Burman design, 117
Plackett-Burman full factorial design, 115–118, 120, 126
Plasmon-polariton resonances, 144
Point coordination function (PCF), 676
Polarization, 393–400, 402–410, 651, 653–655
Polyacrylonitrile (PAN), 61–66, 68–76
Polycrystalline ferroelectric material, 393, 395, 398, 410, 411
Polycyclic aromatic hydrocarbons (PAHs), 23, 25, 27–33
Polymer, 180–183, 187–190, 192
Polymer composite, 181, 188, 189, 193
Polymer matrix, 186, 189, 193
Polysilicon, 563, 564, 571–574
Polysilicon surface micromachining, 563
Poroelectric, 505–507, 511
Poroelectrodynamics, 506
Porous ceramics, 216
Porous piezoceramics, 211–221, 225, 227
Problems, 374
Propagation constant, 321
PS/nZVI, 32
PS oxidation, 23
Pt/C, 37–43, 45–48
Pt/C electrocatalyst, 37, 41, 43, 48
Pulsed laser deposition (PLD), 565, 574, 576
Pump, 662, 663
- R**
Radio absorbing covers (RAC), 246
Radio absorbing materials (RAM), 246
Raman, 263
Raman spectra, 259–266
Raman spectrum, 261, 266
Rectangular cracks, 459
Reflection, 459, 460, 462, 471, 473, 474
Reflection coefficient, 473
Relaxor-ferroelectric, 180
Relaxor-ferroelectric single crystal, 179, 180
Representative element of the volume, 541
Representative volume, 539–543, 550
Residual, 394, 399
Residual polarization, 393, 394, 396–398, 400, 403–408, 410
Residual stress, 489–491, 493, 498–503
Resonance frequencies, 144, 154, 384, 609, 610, 617
Resonant, 143, 144, 153
Resonant frequencies, 389
Resonant gratings, 141
Rice straw, 129, 131–134
- S**
Sapphire, 101–103
Sapphire crystal, 101–103, 105–107, 110
Sapphire monocrystal, 106
Saturated poroelasticity, 509
Saturation, 505, 508, 509, 513, 514
Scanning electron microscopy (SEM), 61, 67, 69, 299, 301–307, 309, 310
Self-action of pump waves, 659
Self-organization, 37
Semiconductor, 279–282, 286, 290, 293–296
Semiconductor-semimetal, 296
Semiconductor-semimetal transition, 281, 290, 292, 295
Sensitive element, 581, 582, 584, 585, 589
Set of integral equations, 437
Shear wave, 603, 612–616, 619
Short inter-frame space (SIFS), 676, 677, 682
Single crystals (SCs), 180
Single crystals growth, 87
SiO₂, 299, 311
SiO₂CuO, 305–308, 310–313
SiO₂CuO_x, 310, 311
SLG, 279, 280, 282, 286, 288, 295
Slow compression wave, 506, 511
Slow release fertilization, 135
Slow release fertilizer (SRF), 129–134, 136
Slow wave, 505, 506, 512
SnO, 300, 301, 310–313
Sol-gel technique, 301
Solid solution, 229–231, 234, 242, 259–266
Solid solutions Raman spectra, 261
Solid solutions structure, 266
Sonochemical, 51, 52, 56, 57
Sonochemical method, 51, 55, 58, 59
Sorption, 3–5, 15–19
SQUIDs, 591, 592, 599, 600
Standing waves, 616–619
Station (STA), 676–683
Stepping method, 506

- Stepping schemes, 506
 Stress, 378
 Stress-strain state, 475, 477
 Strip-like crack, 431, 432, 435, 438, 440, 441
 Structural modification, 19
 Structure, 299–302, 304, 305, 308, 310, 312
 Structure “metal–insulator–semiconductor–metal” (MISM), 329
 Structure ordering, 259
 Studies, 260
 Sub-lattice orders, 265
 Sub-lattices structure units order, 265
 Sulfide minerals, 3–6, 15, 16, 19
 Superconducting, 591–594, 598, 599
 Superconducting film, 591–593, 599
 Superconductivity, 157–159, 173, 177
 Superconductor, 599
 Superposition method, 384, 385
 Surface, 378
 Surface acoustic waves (SAW), 426–428
 Surface effects, 373, 374, 378, 380, 388, 389
 Surface micromachining, 564, 574
 Surface plasmon, 143
 Surface plasmon polariton (SPP), 143, 321, 323, 325
 Surface stresses, 374, 376, 388, 389
- T**
 T6 heating, 364, 367
 T6 heat treatment, 363, 367, 370
 T6 heat treatment process, 363, 367
 Techniques, 381
 Technology, 79
 TEM, 61, 67, 69, 70
 Temperature distribution, 105
 Therapeutic treatment, 617
 Thermoelastic instability (TEI), 551, 553, 556, 557
 Thermoelastic two-phase composite material, 540
 Thermoelectric generator, 330, 335
 Thin film, 61, 66, 68, 73, 299, 301, 304–308, 310–313
 Threshold stress intensity, 489, 492, 501, 502
 Time-frequency, 688
 Time-frequency features, 687
 Time-step, 506
 Time-step method, 510, 512
 Time-step procedure, 505
 Titanium dioxide, 51, 52, 55, 56, 59
- Torsional wave, 476
 Totally symmetrical librations of oxygen octahedrons, 264
 Totally symmetrical libration of oxygen octahedrons as whole of A1-type of symmetry, 266
 Transducer, 603–608, 611, 613–619, 621, 624, 625, 632, 635, 636
 Transfer matrix, 434, 440
 Transient problems, 517
 Transition, 296
 Transmission, 460, 474
 Transmission coefficient, 459, 460, 462, 471, 473
 Tribo-contact, 527–529
 Tribosystem, 527, 528
 Triple periodic, 461
 Triple periodic structure, 460
 Two-phase composite, 539, 541, 542
 Two-phase composite material, 540
- U**
 Ultrasonic, 619
 Ultrasonic standing waves (USW), 603, 616–619
 Ultrasound, 603–605, 609, 612, 613, 616–619, 621–626, 628–632, 635
 Ultrasound transducer, 614
- V**
 Vertically aligned carbon nanotubes (VACNTs), 563, 564, 568–571
 Viscoelasticity, 517
- W**
 Waste materials, 129
 Water treatment, 51
 Wave resonance, 440–444
 Weak, 378, 382, 389
 Weak formulations, 389
 Weak solution, 381
 Weak statements, 373
 Whistle, 688, 689, 691–693
 Wireless local area networks (WLANs), 675
- X**
 X-ray, 80–85, 260, 265, 266
 X-ray absorption spectroscopy, 306
 X-ray diffraction (XRD), 67, 69–71, 80, 81, 83
 X-ray phase analysis, 264, 266

X-ray photoelectron spectroscopy (XPES), [5](#),
[12–14](#), [19](#), [61](#), [67](#), [72](#), [299](#), [308](#), [306](#),
[309](#), [311](#), [312](#)
XANES, [299](#), [301–307](#), [309–311](#)
XPD, [61](#), [69](#)
XPES and DRIFTS analysis, [3](#)

Z

Zeolite, [129–136](#)
Zero-valent iron (ZVI), [25–27](#), [32](#), [33](#)
ZnO, [564](#), [565](#), [574–576](#)
ZnO nanorod, [141](#), [148](#), [149](#), [317](#)
ZTS-19 FC, [198–203](#), [207](#)
ZTS-19 FC composite, [204](#)